REVIEW OF THE VKI DOCTORAL RESEARCH

2022 - 2023



von Karman Institute for Fluid Dynamics

Front cover:
GP multi-fidelity inference of the total pressure field at the compressor outlet (right) with 33% experimental measurements sampled and fully sampled experimental reference (left): Overall match of flow features; RMSE lower than the experimental uncertainty. Picture of Gonçalo Granjal Cruz doctoral research work: A Bayesian Data Driven Multi-Fidelity Modelling Approach for Experimental Under-Sampled Flow Reconstruction

©2023 by the von Karman Institute for Fluid Dynamics
Waterloosesteenweg 72, B-1640 Sint-Genesius-Rode
To order: https://www.vki.ac.be

ISBN 978-2-87516-199-4

D/2023/0238/768, D. Laboureur, Editor-in-Chief

The contents of this book are the property of the von Karman Institute for Fluid Dynamics. No part of this book may be reproduced or distributed in any form of by any means, or stored in a database or retrieval system, without the prior written permission from the Publisher.

PREFACE

The 14th symposium on the doctoral research of the von Karman Institute for Fluid Dynamics took place during the period March 7 to 10, 2023. The doctoral students present the progress of their research work carried out in the three departments: Aeronautics and Aerospace, Environmental and Applied Fluid Dynamics, Turbomachinery and Propulsion. The first-year students have presented a poster on their research plans and some preliminary results, while the most advanced students have proposed a presentation followed by a session of questions.

This event was attended by the faculty of the von Karman Institute, as well as by colleagues from universities and industrial partners. The Symposium is open to external attendees free of charge. In addition to the presentations of the PhD candidates, we had the pleasure to welcome three prominent keynote lecturers who open each day the Symposium:

- Prof. Francesca di Mare, Professor and Chair of Thermal Turbomachines & Aeroengines Group and Managing Director of the Institute of Energy Technology at the Ruhr-University of Bochum, "*A holistic approach to modern turbomachinery research: the role of hierarchical simulation approaches,*"
- Prof. Peter Jordan, Professor, CNRS PPRIME Institute, "*Modelling turbulent jets and their sound*,"
- Mrs. Paola Cinnella, Sorbonne Université, UPMC, Institut Jean Le Rond d'Alembert**, "***Synergy of high-fidelity simulations and machine learning for turbulence modelling.*"

This year, the best presentation award has been attributed to Gonçalo Granjal Cruz for his research on "A Bayesian Data Driven Multi-Fidelity Modelling Approach for Experimental Under-Sampled Flow Reconstruction." The best poster presentation has been awarded to Karel Van Den Borre for his research on "Reduced order combustion modelling of propulsion systems for variable cycle engine jet fighter applications." We would like to congratulate them on their achievement.

This proceedings volume contains 61 papers, which are divided into the following topics: Compressor Aerodynamics and Heat Transfer, Turbine Aerodynamics and Heat Transfer, Shape Optimization, Instrumentation and Measurement Techniques, Propellant Management, Liquid and Solid Propulsion, Rarefied and Plasma Flows, Aerodynamics and Aeronautics; Aerothermochemistry, Aerothermodynamics, Aeroacoustics, Liquid Metal and Industrial Flows, Environmental Flows and Safety.

We would like to emphasize that this publication serves as a tool for communication and aims to enhance exchange between the doctoral candidates, the faculty, and external attendees. The annual publication of their results in proceedings is of crucial importance to the VKI research providing a thorough review of the different activities within the three departments.

As such, the doctoral candidate students play a key role in strengthening the expertise in experimental research, computational methods, and physical modelling. In addition to basic research, works carried out at the von Karman Institute often leads to implementation of real-life industrial applications critical to the fluid dynamics community.

Delphine Laboureur
Editor-in-Chief

Christelle Debeer
Organizer

The contribution of all VKI members who helped with this event is deeply acknowledged in particular the faculty and the communication and marketing team.

TABLE OF CONTENTS

Editorial notes i

Table of contents iii

COMPRESSOR AERODYNAMICS AND HEAT TRANSFER

Riccardo TORACCHIO 3
Aeroelasticity analysis of a highly-loaded low-pressure compressor under inlet flow distortions

Gonçalo GRANJAL CRUZ 17
A Bayesian data driven multi-fidelity modelling approach for experimental under-sampled flow reconstruction

TURBINE AERODYNAMICS AND HEAT TRANSFER

Federico BERTELLI 29
On the design and characterization of a modular active turbulence generator for a low-speed turbine cascade rig

Gustavo LOPES 43
Steady Aerodynamics of a Transonic low-pressure turbine cascade with purge flow and unsteady wakes

Antonino Federico Maria TORRE 55
Adaptation of CT3 to test high speed low-pressure turbines

Giacomo PASTORINO (first-year PhD) 67
Experimental assessment and modelling of the effect of free-stream turbulence on turbomachinery boundary layers

Patrick TENE HEDJE (first-year PhD) 69
Wall resolved large-eddy simulations of the SPLEEN low-pressure blade cascade

SHAPE OPTIMIZATION

Thanh-Son TRAN 73
Advance optimization concept for axial compressor

Wassim ABDEL NOUR 83
A stabilized finite element framework for anisotropic adaptive topology optimization of incompressible fluid flows

Tom DE BRUYN 91
Non-linear harmonic method for adjoint-based turbomachinery optimisation

Romain HOTTOIS 99
Gradient-based aeroacoustic optimization of NASA Rotor37

Marco CASTALDI (first-year PhD) 109
Development of a novel rotor-stator reactor for decarbonizing the steam cracking process through high-fidelity data-driven optimization

Duc Huy Marco HOANG (first-year PhD) 111
Shape optimization of impeller blades in centrifugal compressors including fillet radii, leading edge sweep and tangential lean

INSTRUMENTATION AND MEASUREMENT TECHNIQUES

Muhsin Can AKKURT 115
Flow field investigation of a diffuser blade using endoscopic PIV

Adrien VASSEUR 125
Modeling and exploitation of aerothermal probes in helicopter engines

Bora Orcun CAKIR 137
Sensitivity and resolution response of optical flow based background oriented Schlieren to speckle patterns

Marcello NITTI 153
Cyclostationarity indicators in combination with blind filtering technique for fault detection of rotating machine elements

PROPELLANT MANAGEMENT, LIQUID AND SOLID PROPULSION

Domenico FIORINI 163
On the role of dynamic wetting in the management of cryogenic space propellants

Lorenzo VALLISA 175
NURBS-based immersed boundary method for arbitrarily shaped particles modelling

Pedro MARQUES 187
Data assimilation for the thermodynamic modeling of a cryogenic fuel tank

Ward HAEGEMAN (first-year PhD) 199
Multi-fluid model with two kinematic scales for the simulation of liquid-gas interface in solid propulsion

Karel VAN DEN BORRE (first-year PhD) 201
Reduced order combustion modelling of propulsion systems for variable cycle engine jet fighter applications

RAREFIED AND PLASMA FLOWS

Nicolas CORTHOUTS 205
Hybridized Discontinuous Galerkin Method for multidomain problems

Giuseppe Matteo GANGEMI 215
A multicomponent approach for plasma-sheath physics: potentialities and limits

Pedro JORGE 225
Towards measuring ABEP intake efficiency parameters: Experimental characterization of the DRAG-ON facility

Pietro PARODI.....237
Analysis of implicit PIC schemes and their application to electric propulsion

Anatole BERGER (first-year PhD).....247
Moment method for electric propulsion modelling

Simone DEL MONTE (first-year PhD).....249
Characterization and testing methodology of woven materials with application to innovative flexible thermal protection systems for re-entry vehicles

AERODYNAMICS AND AERONAUTICS

Tomas LEVY.....253
Conservative solution transfer between anisotropic meshes for high-order methods

Emilio LOPEZ FIGUEIRAS.....263
Stability of crossflow by means of small, discrete roughness elements: An approach to receptivity

Romain POLETTI.....271
A multi-fidelity environment for the simulation and control of flapping wings

Carlo BRUNELLI (first-year PhD).....283
Variational multiscale method in Julia

AEROTHERMODYNAMICS

Fabio Miguel PEREIRA MORGADO.....287
Development of a multi-fidelity framework for destructive atmospheric entry simulation

Ata Onur BASKAYA.....299
Influence of ablation on atmospheric entry aerothermodynamics

Daniel Gábor KOVÁCS.....309
Aerodynamic investigation of space debris separation: Space debris interaction across a two-dimensional oblique shock wave

Paolo SCUDERI (first-year PhD).....321
Direct simulation of turbulent hypersonic nozzle flows using high-order discontinuous Galerkin methods

AEROTHERMOCHEMISTRY

Enrico ANFUSO.....325
Comparison of the state-of-the-art enthalpy rebuilding procedures for inductively coupled plasma facilities

Michele CAPRIATI.....337
Determination of a stochastic finite-rate nitridation model consistent with molecular beam and plasma wind tunnel data

David HENNEAUX 345
Assessment of curvature filtering strategies for high-order sharp interface simulation of surface tension driven flows

Diana LUÍS 357
Experimental measurements of radio signal attenuation and Faraday rotation in an inductively coupled plasma facility

Greyson KALE 369
OES and PLIF studies of graphite ablation products in ICP facilities

Sander HOLUM (first-year PhD) 379
Supersonic off-stagnation point ground testing of atmospheric entry

Roemer SPREIJ (first-year PhD) 381
Dynamic flight-to-ground duplication of atmospheric entry stagnation point flows

AEROACOUSTICS

Kartik VENKATRAMAN 385
Numerical investigation of noise radiated by helical Darrieus turbines in the operational regime

Erica GALLO 393
Aerodynamic and Acoustic Investigation of a Dual-Rotor Coaxial Drone Propulsion System

Rui GONCALVES 401
Aerodynamic and aeroacoustic installation effects of building-integrated wind turbines

ENVIRONMENTAL FLOWS AND SAFETY

Benoît FOLOPPE 411
Potential increase in annual energy production of the Belgian offshore wind-farm cluster through wake steering: farm-based versus cluster- optimization

Emmanuel GILLYNS 419
Wind turbine wakes impact on the dynamics of high-voltage cables for fatigue assessment and optimization

Trond-Ola HAGBO 427
Parametric sensitivity analysis of precursor generated inflow profiles including atmospheric stability for RANS based ABL microscale wind simulations

Tsvetelina IVANOVA 429
Data assimilation of multiple local observations in WRF for improved weather and power predictions at the Belgian offshore wind farms

Pierrette ATIKPO 437
Buried detonation airblast characterization

Rebeca MARINI 463
Wind field reconstruction with offshore nacelle-mounted LiDAR measurements

Adithya VEMURI 471
A new scale-aware planetary boundary layer scheme in Weather Research and Forecasting model

Alexandros PALATOS-PLEXIDAS (first-year PhD) 479
Improving wind energy forecasting through high-resolution weather models combined with wind farm parameterization and statistical post-processing methods

Lorenzo SCHENA (first-year PhD) 481
Reinforced (Model) based control of wind turbines and wind farms

LIQUID METALS AND INDUSTRIAL FLOWS

Matilde FIORE 485
Thermal turbulence modelling of low Prandtl number flows with data-driven techniques

Jan VAN DEN BERGHE 499
An overview on the development and calibration of a 1D ejector model

Yohanna HENROTEL 509
Phase change in porous media for heat exchanger applications

Tommaso CARLESI 517
Experimental analysis of natural convection in differentially heated cavity

Florentin PRUD-HOMME (first-year PhD) 525
Development of a data-driven bridging turbulence model

Carlo SANAPO (first-year PhD) 527
Experimental and numerical assessment of supersonic jets dispersion

COMPRESSOR AERODYNAMICS AND HEAT TRANSFER

Aeroelasticity Analysis of a Highly-Loaded Low-Pressure Compressor Under Inlet Flow Distortions

Riccardo Toracchio

Turbomachinery and Propulsion Department, von Karman Institute for Fluid Dynamics, Belgium, riccardo.toracchio@vki.ac.be

Supervisor: Fabrizio Fontaneto

Associate Professor, Turbomachinery and Propulsion Department, von Karman Institute for Fluid Dynamics, Belgium, fabrizio.fontaneto@vki.ac.be

University Supervisor: Koen Hillewaert

Associate Professor, Aerospace and Mechanical Engineering Department, University of Liège, Belgium, koen.hillewaert@uliege.be

Abstract

Latest developments in propulsion technology, directed toward the achievement of higher propulsive performance, led turbofan engines to be subjected to inlet flow distortions. In such conditions, especially when the external excitation becomes close to the natural frequency of the blade at its operational speed, not only aerodynamic performance are altered but also the structural integrity of the system. In this context, this paper aims at analysing the flutter and the forced-response of a new-generation low-pressure compressor (LPC), subjected to intake total pressure distortions. An aerodynamic damping analysis is performed to identify the critical flow phenomena impacting the aero-mechanical stability of the blade. This will be done at a vibration mode with natural frequency close to the excitation induced by an engine representative distortion. The forced-response induced by such distortion will be assessed, at different distortion amplitudes, with the intent of characterizing the mechanisms and the flow parameters altering the link between forcing and displacements. It will be found, contrarily to what was initially expected for this compressor, that the tip leakage flow plays a major role in the development of large pressure fluctuations in the flow field. Moreover, the linearity of the blade vibration with the distortion amplitude will be quantified and assessed.

Keywords: LPC, Inlet Distortions, Unsteady, Aerodynamic Damping, Forced-response

1. Introduction

Modern aircraft systems, such as Short-Nacelle Geared High-Bypass (SNGHB) turbofans and Boundary-Layer-Ingestion (BLI) engines, shown strong potential to improve fuel burn and propulsive efficiency [1; 2; 3; 4]. However, these configurations could be characterized by large distortions at the engine inlet with consequent impact on the efficiency and stall margin of the engine [5; 6; 7]. Along with the effect that this could have on the aerodynamic behavior of the engine, also its structural response can be altered [8; 9] by a distortion with spatial frequency close to the natural vibration of the rotor blade at its operational speed. The literature presents numerous studies focused on the structural interaction of front fans and compressors with the distortion. In [10; 11] the authors proposed modern design techniques for distortion-induced vibrations in presence of circumferential and radial inlet total pressure distortions, highlighting their role for the natural excitation of the rotor and flutter. Hub and tip pressure distortions were found to impact the shock location and the separated region near the tip in a NASA Rotor 37 [12]. Similar findings were highlighted in [13; 14], where the shock motion was responsible of a dominant excitation in the flow passage. In the same work, the authors found that larger distortion extents were not necessary linked to a more detrimental impact on the machine, but some spoiled angles had larger influence than

others. Several experimental and numerical activities were conducted on compressors with the intent of predicting distortion-induced fan forced-response. Low-order models and higher fidelity approaches were, indeed, developed [15; 16; 17; 18]. However, no much studies are available on modern compressor stages, neither on engine representative distortions, and still a lot work needs to be done in the field. For this reason, the present paper proposes an aeroelastic study on a 1.5 stage axial compressor representative of the first stage of a modern engine booster. The Non-Linear Harmonic (NLH) method is employed to compute the unsteady fluctuations of the flow field. A flutter stability analysis is first performed considering the mode shape corresponding to the blade natural response induced by the distortion at the nominal speed of the machine. The distortion pattern considered comes from a modification of a realistic distortion present at the outlet of the fan in a Ultras High ByPass Ratio (UHBR) turbofan engine, and able to excite the resonant behavior of the rotor at 100% corrected speed. Moreover, the linearity between forcing and vibration amplitude under distortion is finally assessed. This paper wants to provide an overview of the aero-mechanical phenomena taking place in a modern generation low-pressure compressor, highlighting the flow mechanisms driving the loss of flutter stability and the flow parameters playing a major role in the excitation of the blade vibration.

2. Methodology

The methodology employed for the present study is characterized by three main steps: 1) Modal analysis: to identify the resonant modes and frequencies of the compressor at its nominal speed 2) Aerodynamic damping analysis: to compute the overall critical damping ratio of the structure (used in the forced-response analysis) and to understand the impact that the local flow field has on the damping distribution over the blade surface 3) Forced response analysis: to quantify the vibration induced by the distortion and find the flow features impacting the linearity between forcing and displacement at several distortion amplitudes. Figure 1 reports the aforementioned methodology. The picture specifies that the aerodynamic damping analysis corresponds to a 1-way coupled aeroelastic simulation with imposed blade deformation, and the resulting damping ratio is used for an undeformed blade analysis where the distortion is imposed at the inlet.

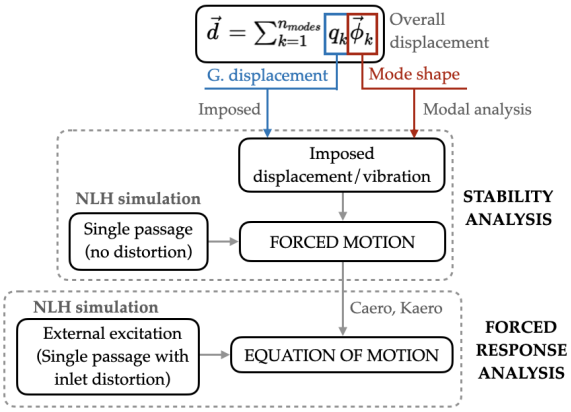

Figure 1: Methodology used for: (A) Modal Analysis (B) Aero-damping analysis (C) Forced-response analysis

2.1. Modal analysis

Ansys Modal was used to perform the modal analysis and to retrieve mode shapes and eigenfrequencies of mode k_{th} (respectively $\vec{\phi_k}$ and Ω_k)

$$[M]\ddot{\vec{d}} + [K]\vec{d} = 0 \iff det([K] - \lambda[M]) = 0 \quad (1)$$

Which leads to:

$$\Omega_k = \sqrt{\lambda_k} \qquad [K]\vec{\phi_k} = \lambda_k[M]\vec{\phi_k}. \quad (2)$$

Suction and pressure side pressure distributions of the rotor blade retrieved from a RANS simulation were used to compute the pre-stress in presence of static loads. The eigenmodes are mass-normalized.

2.2. Aerodynamic damping analysis

The blade displacement is computed as:

$$\vec{d}(x,t) = \sum_k q_k(t)\vec{\phi_k}(x) \quad (3)$$

Which represents a linear combination of all k modes considered. In this equation, $q_k(t)$ is the generalized displacement, while $\vec{\phi_k}$ is the mode shape retrieved with the modal analysis. They represents respectively the time and space information of the blade displacement. Since $q_k(t)$ is imposed, this stability analysis represents a 1-way coupled aeroelastic approach with imposed displacement. Moreover, the NLH method allows to compute $q_k(t)$ as:

$$q_k(t) = \sum_j q'_{jk}(t) \quad (4)$$

$$q'_{jk}(t) = 2[q_{jk,R}cos(j\Omega t) - q_{jk,I}sin(j\Omega t)] \quad (5)$$

where $q_{jk,R}$ and $q_{jk,I}$ represent real and imaginary components of the jth harmonic considered for the kth mode. Blade $n+1$ (adjacent to n) has a discrete phase-shift with respect to n. This shift is called Inter Blade Phase Angle (IBPA) $\sigma = 2\pi ND/N_b$, where N_b represents the blade count. Computing the maximum blade displacement δ_{max} it is possible to retrieve the critical damping ratio:

$$\xi_c = \frac{W_{aero}}{m\omega_n^2 2\pi\delta_{max}^2} \tag{6}$$

$$W_{aero} = -\int_0^T \left(\int_A p(x,t)\vec{V}_w(x,t)\vec{n}(x,t)dA\right)dt \tag{7}$$

Where W_{aero}, m, and ω_n are the work exchanged between fluid and structure over one vibration cycle, the modal mass and the natural frequency. The pressure fluctuation on the blade surface, the wall velocity and the surface normals are $p(x,t)$, $\vec{V}_w(x,t)$ and $\vec{n}(x,t)$, computed by means of an harmonic diplacement imposed at a specific IBPA. In this work, the imaginary components of mode shape and generalized displacement are neglected. Moreover, as mentioned earlier, the mode shape considered is the one with frequency closest to the blade resonant condition at 100% nominal speed ($\Omega = \omega_n$). This aerodynamic damping study aims at understanding the stability of the blade against flutter at all nodal diameters, computed the critical damping ratio to use in the forced-response analysis in presence of the distortion, and find the critical flow features driving the loss of stability in clean conditions. As shown later, the inlet distortion is not considered for the computation of the damping and the clean undisturbed flow was assumed to provide the same damping as in distorted conditions. Although this could not exactly correspond to reality, and the distortion could have an impact on the computed damping, it was proven that, at least for small distortion amplitudes, the operating point of the compressor was not largely impacted from the presence of the distortion, giving validity to the present assumption.

2.3. *Forced-response analysis*

Given the modal force $F^m(t)$, which represents the force integrated over the blade and projected in the direction of the mode shape, the equation of motion for a mass-normalized mode shape is expressed as:

$$I\ddot{q} + diag(2\xi_c\omega_n)\dot{q} + diag(\omega_n^2)q = F^m(t) \tag{8}$$

$$F^m(t) = \int_A p(x,t)\vec{n}(x,t)\vec{\phi^T}(x)dA \tag{9}$$

Since the NLH approach is employed, the time reconstruction of the pressure $p(x,t)$ is performed by:

$$p(x,t) = p_A(x)cos(\Omega t + \psi) \tag{10}$$

$$p_A(x) = 2\sqrt{p_R^2(x) + p_I^2(x)} \tag{11}$$

$$\psi = arctan(p_I(x)/p_R(x)) \tag{12}$$

where p_A and ψ are the amplitude and phase of the fluctuation.

3. Rotor natural vibration

As previously mentioned, the rotor resonant behavior was obtained as result of the modal analysis performed with Ansys Modal. Several Engine Order (EO) excitations were compared with the natural response of the rotor blade to retrieve the Campbell diagram, as reported in Figure 2. In particular, Figure 2a and 2b report respectively the first six natural modes of the rotor and the intersection of its 1st bending mode with the external excitation. The latter highlights that at the compressor nominal speed, an intersection is present between the 6 EO excitation and the 1st natural mode, meaning that a circumferential periodicity of 6 would excite the natural vibration of the rotor. Figure 3 shows, instead, the computed

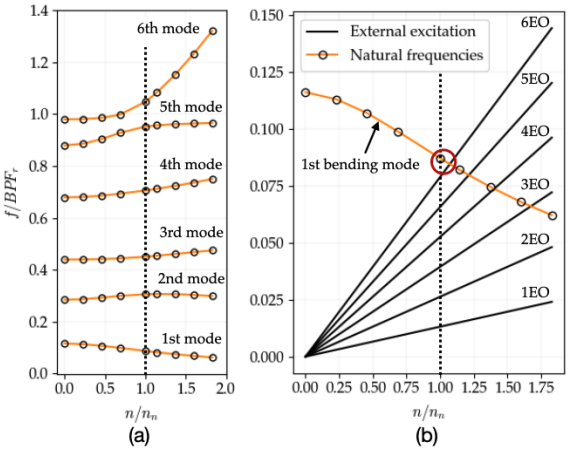

Figure 2: Modal analysis: (a) Rotor natural modes at different speeds (b) Campbell diagram with focus on 1st bending mode and several EO external excitations.

1st bending mode. This means that an inlet distortion with circumferential periodicity equal to 6 would excite the rotor natural vibration at the nominal speed of the machine. It represents therefore a critical condition for the present compressor, and for this reason it is further detailed in the paper.

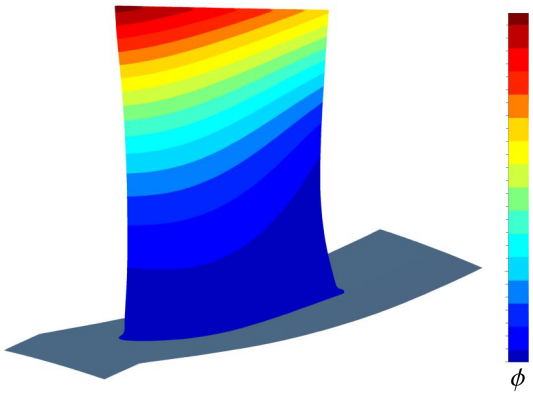

Figure 3: Rotor 1st bending mode at 100% speed of the compressor.

4. External excitation - inlet distortion

To generate a 6 EO excitation, a realist fan-outlet total pressure pattern measured in a UHBR turbofan (Figure 4a) was modified in its circumferential periodicity to excite the rotor natural vibration. The clean inlet total pressure distribution of DREAM was therefore circumferentially reduced by a sinusoidal function (Figure 4b). Several distortions amplitudes, from 1% to 7.5% of the clean inlet total pressure (Figure 4c), were considered to ideally reproduce an increase of the 6th harmonic of the reference distortion up to a point that could aeromechanically destabilize the rotor. Although a 7.5% inlet total pressure reduction is much more than a realistic value in a turbofan, it is important to specify that the objective of this study is to find a limiting value where the onset of critical flow structures is visible. P_{ref} in the pictures is the experimental mass-averaged inlet total pressure measured in plane 0 in clean condition, which is therefore not altered by the presence of the distortion. This value is also the same for all the operating points considered, and it will be used as constant value to non-dimensionalize all the pressures reported in the paper. It is important to notice that for the way the distortion has been generated, the averaged inlet total pressure in plane 1 (considered as the inlet of the numerical domain, where the distortion is applied) is reducing for larger distortion amplitudes. The impact on the modification of the operating point of the compressor induced by the distortion will be later investigated in the paper. Moreover, only total pressure distortions are considered in the paper, and no temperature and swirl distortions will be discussed. As last point, Figure 4d reports the Fourier decomposition of the 6 EO distortion at the rotor inlet. As expected, the 6th harmonic of the distortion is the one with largest amplitude, justifying therefore the choice of analysing only the effects induced on the rotor from this excitation.

5. Numerical method

5.1. Numerical setup

A finite volume formulation on a multi-block structured grid was used in the FineTurbo suite of Cadence to run steady and unsteady simulations. Experimental total quantities and straight flow were imposed at the inlet, along with measured mass-flow at the outlet. Turbulent quantities, such as turbulence intensity and turbulent viscosity ratios, were imposed at the inlet. For the latter there was not an experimental value available, and for this reason it was imposed at an averaged value suggested for turbomachinery applications. A sensitivity study showed that no large influence on the obtained results existed changing this parameter. These turbulent parameters were used for the closure of a 2-equation $k-\epsilon$ Chien turbulence model, which has shown to have superior performance at near-stall conditions for the present machine [19]. Non-reflecting conditions were imposed at the boundaries of the domain and at the rotor-stator interfaces.

Two different setups were employed for the NLH simulations. The first considers only the rotor row, with inlet conditions retrieved from RANS simulation at the experimental location of the inlet section. It was used for a 1-way coupled aeroelastic approach in the aerodynamic damping analysis. A single harmonic perturbation was imposed with deformation equal to the natural mode of interest. Radial basis functions with transfinite interpolation have been considered for the mesh deformation. For the distortion analysis with forced-response, the numerical domain was considered from the experimental plane 1 to 4 (as introduced later in the description of the test-section) and rotor-stator interactions were therefore taken into account. Specifically, 6 harmonics of the distortion were solved, along with the excitation coming from the larger harmonics of the IGV, rotor and stator BPF (up to the 2nd). Also the distortion/rotor-stator interactions was considered. In the present study, since the rotor-stator interactions act at a much larger frequency than the one of the distoriton, only the 6th harmonic of the distortion is taken into account for the analysis of the results. Moreover, only one limitation of the present simulation exists due to the specific software employed: A perturbation (e.g. distortion) can propagate to maximum two rows downstream of the inlet

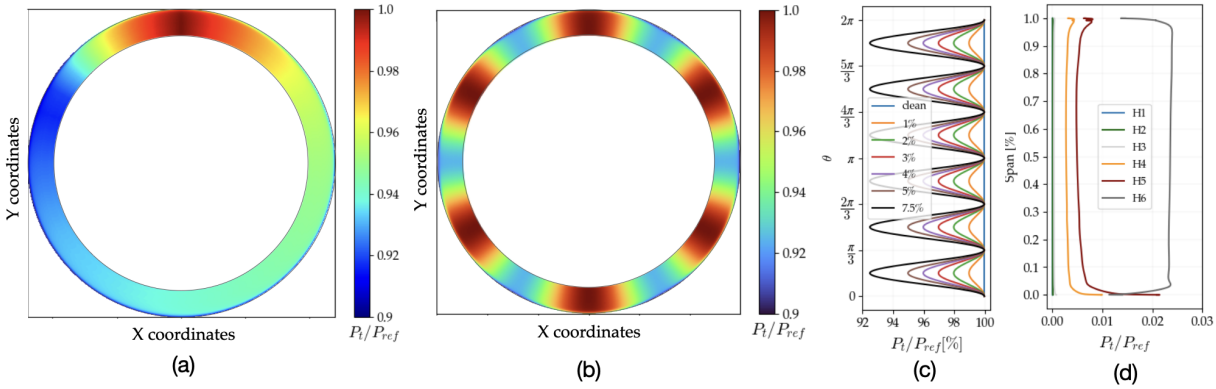

Figure 4: Inlet distortion: (a) Reference distortion measured at the outlet of a fan (b) Distortion used to excite the rotor natural vibration (c) Distortion amplitudes considered for the 6EO distortion (d) Amplitude of the Fourier mode at the rotor inlet for 7.5% inlet total pressure reduction.

section, meaning that the distortion effects on the outlet stator can not be assessed. However, this does not represent a problem in the present case since only the impact on the rotor is assessed.

For the structural simulation, the same domain as in the aerodamping analysis was employed, and the Modal package of Ansys was considered. Only displacements of the rotor were allowed clamping the entire base of the blade and its connection to the disk. A pre-stress analysis was performed at 100% speed solving the first six natural modes of the rotor blade.

As mentioned before, the variation of the averaged inlet total pressure for larger distortion amplitudes could bring to a modification of the compressor operating point. Moreover, the distortion itself is thought to produce a reduction of the performance with consequent modification on the aeromechanical response of the machine. Figure 5 reports, therefore, the compressor map, computed between plane 1 and 4 (on both planes the distortion has an impact). It can be noticed that the reduction of total pressure in plane 4 induced by the growing flow phenomena in the passage generates a reduction of performance, which is higher than the reduction of the total pressure in plane 1 induced by the modification of the inlet boundary condition. However, in a small range of inlet total pressure reductions (here highlighted as "Linear" regime) the operating points all over the operating range of the machine are kept almost constant, while the same does not happen after a specific limiting value of the distortion amplitude. In the so called "Non-linear" regime, a large drop of performance is, indeed, observed. This justifies, at least partially, the choice of not considering the distortion in the computation of the critical damping ratio. It will be therefore assumed that the

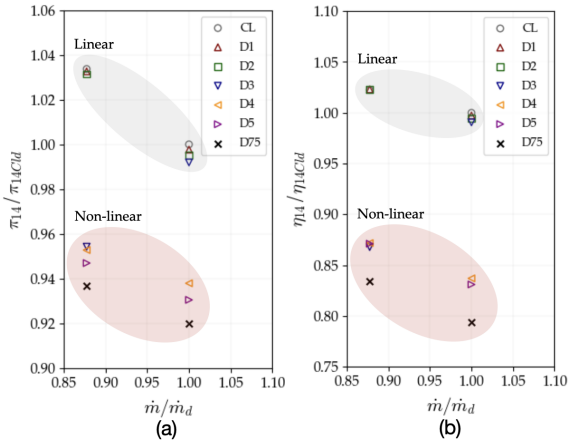

Figure 5: Performance map retrieved from NLH simulations between plane 1 and 4 at different distortion amplitudes: (a) Total to total pressure ratio (b) efficiency.

damping induced by the clean flow is the same as the one induced by the distortion. Despite it is arguable that the same can not be assumed for larger distortion amplitudes, where a drop of performance is visible, it is still true that the onset of critical flow structures, which is the main objective of the present paper, can still be detected.

5.2. Numerical domain and mesh

CFD and structural domain

Technical features, such as fillets and rotor tip gap were considered in the CFD and structural domains. It is, indeed, well known the impact that fillets could have both on the aerodynamic and structural performance of the rotor. Cavities were instead not considered in the final configuration of the numerical do-

main. Figure 6 and 7 show the domain used for CFD and FEM respectively.

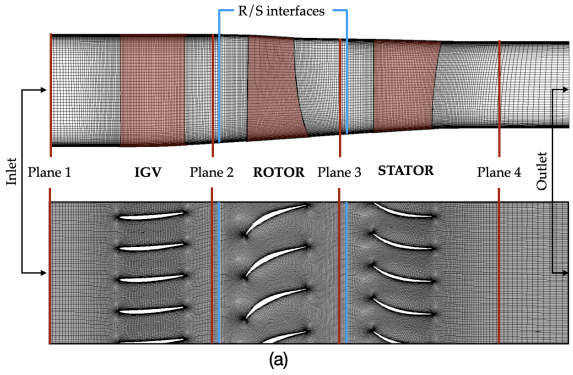

Figure 6: CFD domain: Meridional (top) and B2B (bottom) view at 50% span

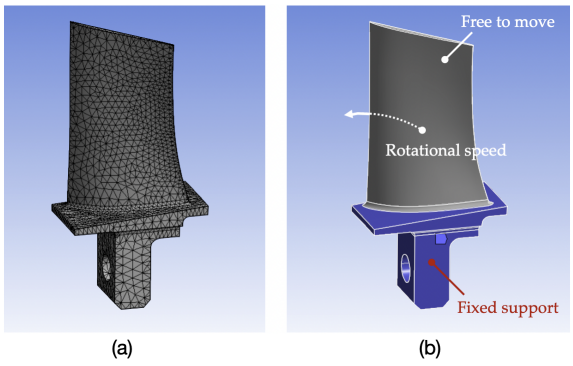

Figure 7: Structural domain: (a) Mesh detail and (b) boundary conditions applied.

Grid quality assessment

A grid refinement study was performed using three mesh levels with 0.87, 7 and 56 million cells, generated through a mesh refinement of 2 in each direction. The selected mesh is characterized by 129, 133 and 125 cells in the spanwise direction for IGV, rotor and stator with 40%, 35% and 40% of mid-flow cells respectively. 32 cells in the tip gap region were employed. The y+ was everywhere lower than 1.2, and the maximum expansion ratio was 1.2 at the interface of the tip gap block and 1.05 over the blade surface. Moreover, since the NLH method is based on a spatial Fourier decomposition, at least 30 and 15 nodes in the circumferential direction are suggested to solve correctly the first and second harmonic respectively of a perturbation. Given the number of IGV/rotor/stator blades (100/76/100) and the harmonics solved, as stated in section 5.1, 40 and 48 cells in the circumferential direction were used for IGV/stator and rotor respectively. O4H and OH symmetric topology were considered for the blade channel and tip gap respectively. Figure 8 shows the numerical performance of the stage comparing the three mesh levels (Figure 8a) and the medium mesh with the experimental pressure ratio (Figure 8b). It is visible that

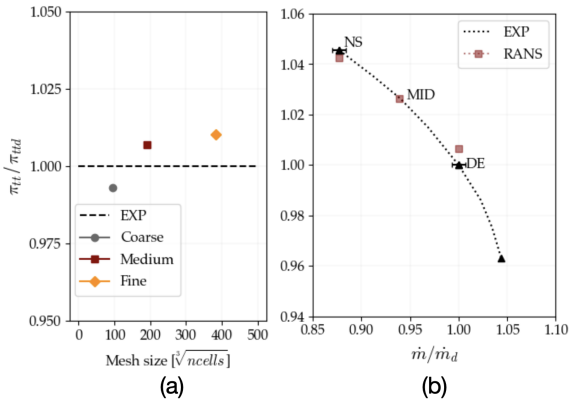

Figure 8: (a) Pressure ratio for coarse, medium and fine grid levels at DE conditions (b) Performance of the medium mesh compared to the experimental results.

the medium mesh provides results close to the finest mesh in terms of performance with much reduced number of grid nodes. The coarsest mesh performs, instead, quite worse with respect to the other mesh levels. 0.16% and 0.62% is the difference between the medium mesh with respect to the finest and the experimental value at design respectively. Figure 9 shows, instead, the skin friction lines on the rotor suction side for the three mesh levels. The low performance predicted by the coarsest mesh is probably induced by the large separation visible from the skin friction lines on the rotor suction side, which is not physical and never predicted from the experiments. The medium mesh is, instead, qualitatively in agreement with the finest mesh, despite a different length of the shock-boundary layer separation is present especially in the tip region. Despite these minor discrepancies, the medium mesh provides results quite in line with both experiments and fine mesh, but with reduced computational cost, and it is therefore chosen to run the steady and unsteady simulations reported in this paper.

18000 cells were used for the structural simulation, which were considered enough to run this type of simulation. No mesh refinement study was therefore performed.

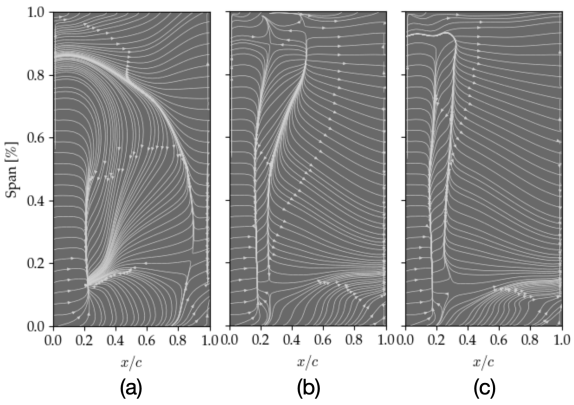

Figure 9: Comparison among mesh levels about the skin friction lines on the rotor suction side for the (a) coarse (b) medium and (c) fine mesh at DE conditions.

The structured mesh used in the CFD simulations was performed by means of Autogrid5 and IGG softwares, while an internal Ansys mesher was used for the unstructured mesh.

6. Test-section and instrumentation

The compressor considered is installed in the R4 high-speed compressor test rig of von Karman Institute for FLuid Dynamics, which is characterized by: 1) tank 2) compressor test-section 3) collector 4) return channel to drive the air back to the reservoir, and 5) the throttling valve for the definition of the compressor operating point (Figure 10). The closed loop configuration and the heat-exchanger located at the compressor inlet allow the independent adjustment of Reynolds and Mach numbers, giving the possibility to test in realistic aircraft conditions.

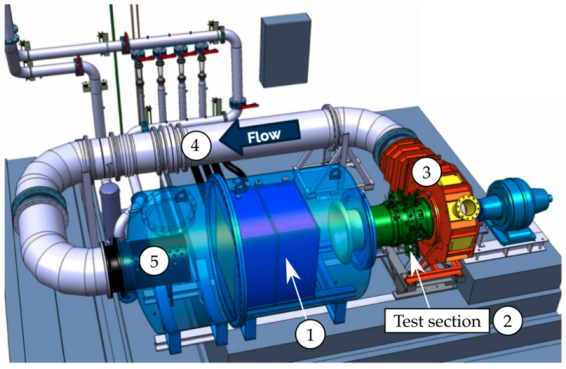

Figure 10: Closed-loop high-speed compressor test rig R4 available at VKI

The compressor considered is a 1.5 stage representative of the first stage of a modern low-pressure compressor. Figure 11 reports its sectional view with the experimental measurement planes visible. This compressor was characterized in clean conditions within the EU FP7 DREAM project (valiDation of Radical Engine Architecture systeMs – GA: 211861), which compressor map is reported in Figure 12. Given the large blade loading and the high degree of reaction, the compressor is prone to develop critical flow structure in the rotor hub region, as confirmed by experiments and CFD. Moreover, the absolute mass-flows corresponding to the design (DE) and near-stall (NS) operating points, which are the ones analysed in the present paper, are used as outlet boundary conditions to run the aforementioned simulations.

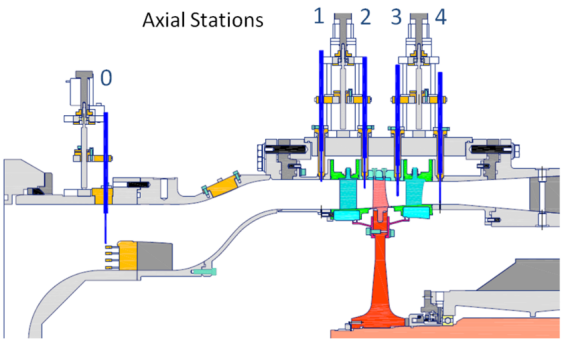

Figure 11: Compressor test-section: DREAM.

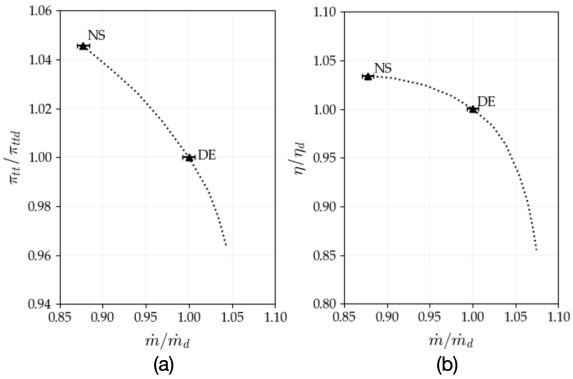

Figure 12: Experimental performance of the DREAM stage: (a) Total to total pressure ratio (b) Efficiency.

The instrumentation here reported is only the one that allows to retrieve the performance of the stage. It is characterized by inlet and outlet rakes located in plane 0 and 4 at 90° from each other, used to measure total pressure and temperature. Moreover, static pres-

sure taps at hub and casing allow a linear reconstruction of the static pressure and therefore of the Mach number. Radial traversing of probes is possible at all measurement planes, and the circumferential traversing of the stator can be performed. For the present paper, the 100% corrected speed of the compressor is considered. The uncertainty associated to the pressure ratio and mass-flow are respectively +/- 0.00053 and +/- 0.04 kg/s calculated with the ASME method [20] in a confidence interval of 95%. The reader should refer to [21] for further details about the experimental setup and instrumentation.

7. Results

Results of the modal analysis are not here reported as they have already been presented in section 3. Following, results retrieved from the aerodynamic damping and forced-response analysis are reported.

7.1. Stability analysis

The critical flow features impacting the flutter stability of the rotor blade are here analysed in clean conditions. As explained earlier, the clean conditions are reported mainly to analyse the aeromechanical behavior of the rotor without any inlet disturbance, but also to isolate the effect of the distortion.

Local aerodynamic damping

Figure 13 reports the critical damping ratio at several nodal diameters for DE and NS operating conditions. In the picture, suction and pressure sides

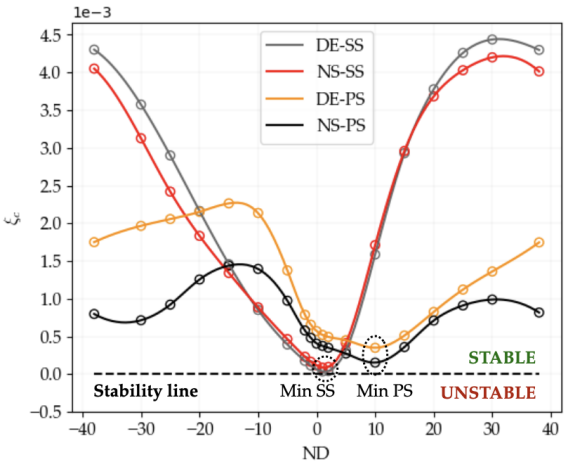

Figure 13: Critical damping ratio at DE and NS operating points.

are shown separately to identify the region that contributes more negatively to the damping, but, however, the overall critical damping ratio should be computed consider both contributions of suction and pressure sides on the work exchanged between fluid and structure. Their sum in the present case is always positive, denoting therefore a stable behavior of the blade against flutter across the two operating points considered. The minimum damping is present at nodal diameter 1 and 10 for suction and pressure sides respectively. Moreover, the suction side shows a smaller damping ratio than the pressure side.

Figure 14 is used to understand which are the flow phenomena in the passage, and their link with the low value of damping visible on the suction side. The latter seems, indeed, the most critical region for the compressor from the aero-mechanical point of view, as it is the region closest to the stability line. The picture reports the local work per cycle on suction (top) and pressure side (bottom) for DE (left) and NS (right) operating points. Nodal diameter 1 and 10 for suction and pressure sides are reported since those are the most critical conditions for the two surfaces considered separately. On top of the work per cycle the averaged skin friction lines are reported. Two points are highlighted through Figure 14: 1) The work exchanged between fluid and structure is larger on the suction side, therefore motivating the smaller damping ratio from the stability map at ND1 2) The work exchanged at DE on the suction side is larger than at NS condition, despite on the aerodynamically it should be the NS condition to be more critical. To explain the reasons behind these two observations, the instanteanous flow in the passage is shown in Figure 15a,b,c for Power, pressure fluctuation and wall velocity respectively. 1) At $t = 0$, large pressure fluctuations are induced by the movement of a sonic pocket developing all over the blade span 2) At $t = T/4$, a change of phase is present on the blade surface, which induces a different sign of pressure fluctuation in the front and rear part of the blade surface. Figure 15d and Figure 15e present pressure fluctuations inside the passage at two spanwise locations (50% and 80% span). At location A and B, larger fluctuations are induced by the presence of a shock motion, located at the end of a sonic bubble developing all over the blade span. It is even more visible, at location C and D, that the shock generates a region of zero pressure fluctuation, therefore altering the phase and the pressure distribution on the blade surface.

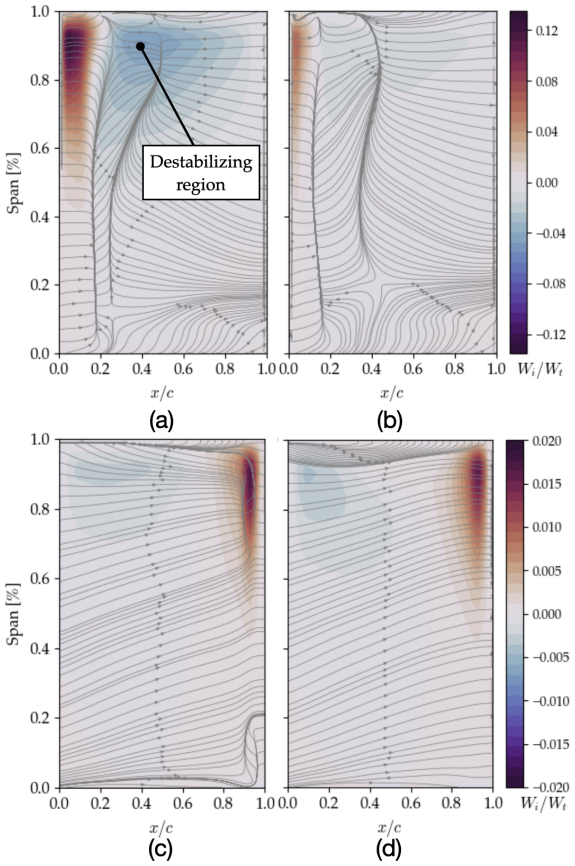

Figure 14: Local work per cycles: (a, b) suction side at DE and NS conditions for ND1 (c, d) pressure side at DE and NS conditions for ND10.

Critical flow features for stability

The origin of the pressure fluctuation previously analysed could be better understood through Figures 16b and 16c, showing the pressure fluctuation in the flow passage at DE and NS operating points for ND1 (shown to be the most critical condition for the suction side, which is responsible for the low damping ratio visible in the stability analysis). Also the incidence variation due to the blade twist is reported (Figure 16a). As expected, the incidence variation reaches its maximum value toward the tip, where the maximum displacement is present. From Figures 16b and 16c, two regions of large pressure fluctuation can be identified: Point A) At the location of the tip leakage flow, Point B) At the location of the sonic bubble in the front part of the blade. A focus of the tip region is instead visible in focus A and B for DE and NS respectively, which allow a better visualization of the unsteadiness. The sequence of phenomena at the base of the large tip fluctuation is thought, therefore, to be: 1) A large incidence variation is observed at the tip rotor inlet 2) This incidence variation promotes the motion of the sonic pocket, and of the shock at its boundary, on the rotor suction side 3) The same incidence variation induces a tip leakage vortex fluctuation 4) The motion of the sonic pocket alter the pressure difference between suction and pressure sides, therefore impacting again on the evolution of the tip leakage vortex (TLV). It seems therefore that the TLV propagation is altered by the incidence variation itself, together with the motion of the sonic bubble on the blade suction side, increasing the fluctuation level in that region. However, at NS condition (Figure 16c), the absolute value of the incidence is larger, and the tip leakge flow is forced to propagate on a more inclined B2B trajector with respect to DE condition, therefore generating a weaker interaction with the rotor suction side. Moreover, the spillage point seems shifted toward the LE, reducing the amplitude of the fluctuation in the rear part of the rotor blade. Such explanation could be at the origin of the larger work exchanged with the rotor suction side at DE conditions: a less inclined tip vortex brings to an increased interaction with the suction side, which is the surface impacting on the damping of the structure.

The present compressor, thought to be hub-critical from the aerodynamic point of view due to the development of an hub corner separation, could rather become tip-critical due to a critical evolution of the tip leakage flow if its 1st bending vibrational mode is considered.

7.2. Forced-response analysis

The effect of the distortion on the generalized force is reported in Figure 17a and 17b respectively at DE and NS conditions. In both pictures only part of the distortion amplitudes is reported for clarity. In the first picture, a clear phase shift and an increase of the force amplitude is present for 4% distortion amplitude, and the same happens at NS for 3% distortion. To understand the reasons behind this behavior, Figure 18 and 19 present the generalized displacement and the amplitude of the pressure fluctuation as a function of the distortion amplitude for DE and NS operating points respectively. Averaged skin friction lines are reported with the amplitude of the pressure fluctuation. From these pictures, it is visible that at both operating points the displacement increase linearly for small increase of the distortion amplitude, while the opposite is visible when the inlet total pressure reduction increases. The flow features in the passage are indeed the same for smaller distortion amplitudes, and a linear increase

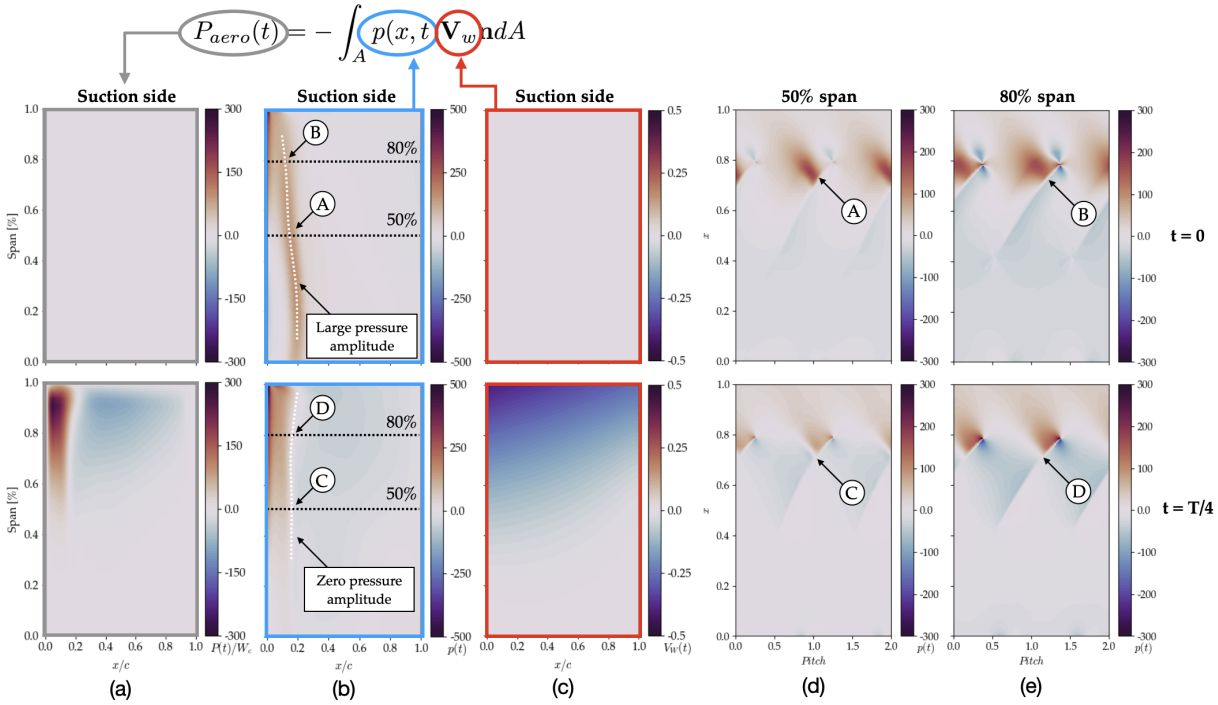

Figure 15: Instantaneous distribution of: (a) Power (b) pressure fluctuation and (c) wall velocity on rotor suction side. Moreover, the pressure fluctuation is shown at (d) 50% span and (e) 80% span. DE operating condition is reported.

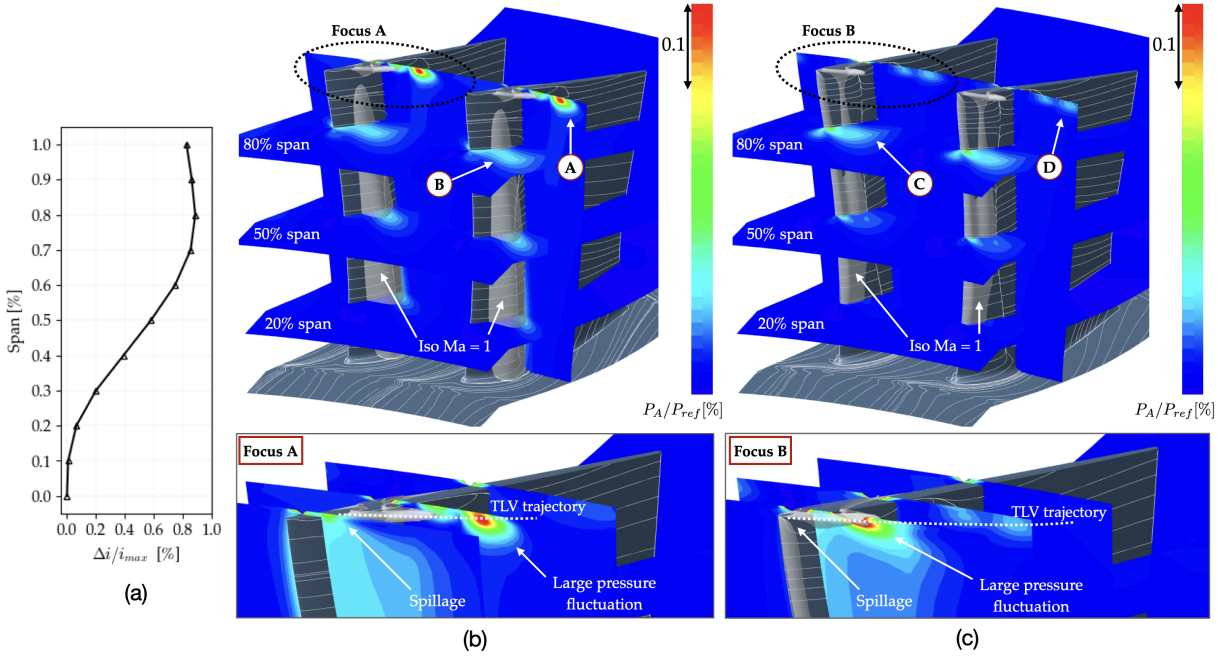

Figure 16: (a) Rotor incidence variation, Pressure amplitude in the passage at (b) DE conditions and (c) NS conditions. Both operating points are shown at ND1.

of the pressure fluctuation is observable. However, at larger amplitudes, a separation appears on the rotor suction side which totally alter the aeromechanical behavior of the blade (Figure 18d and 19d, point C).

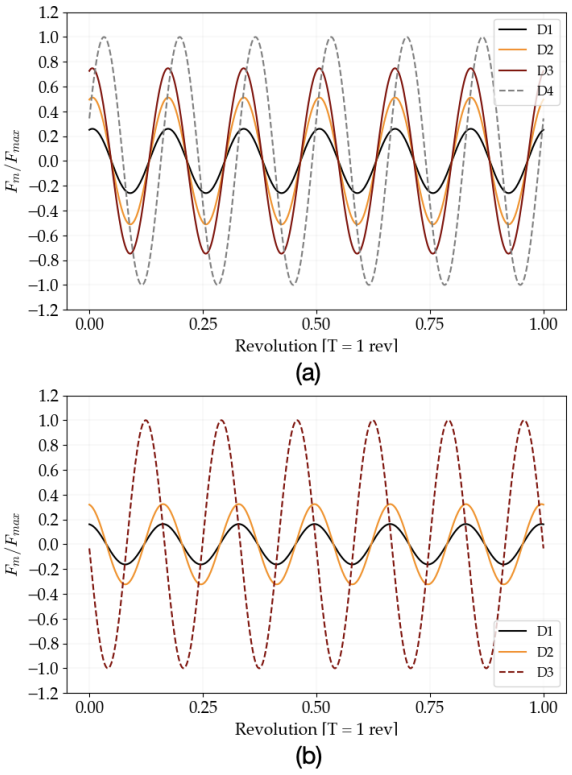

Figure 17: Modal force as result of the forced response analysis with inlet distortion: (a) DE and (b) NS operating points.

The only difference present at DE and NS conditions is that the onset of this separation appears after 3% and 2% inlet total pressure reduction, which therefore represents a limiting value after which the critical behavior of the flow field appears. The incidence variation between clean and distorted region for the 3% distortion case at DE and NS conditions respectively is 2.16° and 2.06°, and in absolute terms, the maximum operating incidence in the distorted region differs at DE and NS by 4.6°.

It should be specified that the periodic behavior of the flow in the linear regime makes the NLH method suitable for the quantitative computation of displacements and forces. However, the same can not be said in the non-linear regime, where the appearance of large scale flow structures make the flow totally non-periodic. However, this still allows the qualitative computation of the flow features appearing on the rotor surface for larger inlet total pressure reductions.

Compressor designers should therefore consider that a linear relation between forcing and displacement exists for small values of the distortion amplitudes, while the same cannot be assumed for lower inlet total pressures. This gives to a designer even the possibility to choose a cheaper computational approach (NLH) when smaller distortion amplitudes are expected, with respect to full-annulus URANS needed when the distortion amplitude increases.

8. Conclusion

This paper proposes a flutter and forced-response analysis on a highly-loaded low-pressure compressor under inlet total pressure distortions. The main focus of the paper was the detection of the critical flow features lowering the stability of the machine against flutter. The main findings of the paper are:

1. The critical damping ratio is positive all over the operating range of the machine, meaning that the compressor is stable against flutter.
2. The incidence variation induced by the blade twist is thought to be at the origin of the main pressure fluctuations in the rotor passage in clean conditions. The core of the tip leakage flow reaches a maximum pressure fluctuation enhanced by the movement of the sonic bubble developing all over the blade span.
3. DE conditions are more critical than NS for flutter stability due to a reduced inclination of the TLV in the passage, which enhances a stronger interaction with the rear part of the rotor blade.
4. 3% and 2% distortion amplitudes were found to be the limiting distortion amplitudes after which a separation appears on the rotor suction side, altering the aero-mechanical performance of the rotor blade. This means that for small distortion amplitudes the relation between forcing and displacements is linear, and it becomes non-linear for larger inlet total pressure reductions.

The results presented are valid specifically for the described compressor, and the same findings cannot be directly extended to different kind of compressors. This work aims anyway at identifying critical flow features of a modern compressor blade with and without the presence of the distortion, which is considered by the authors an added value to the literature and for compressor designers.

Acknowledgments

The authors would like to express their gratitude to Safran Aero Boosters to make the DREAM compressor stage and the inlet distortion pattern available

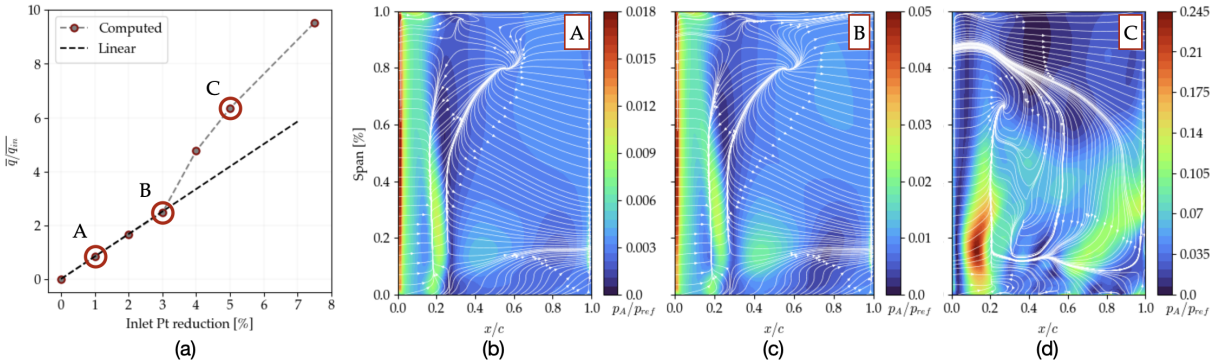

Figure 18: Forced response at DE condition: (a) amplitude of the generalized displacement, pressure fluctuation with (b) 1% (c) 3% and (d) 5% distortion reduction.

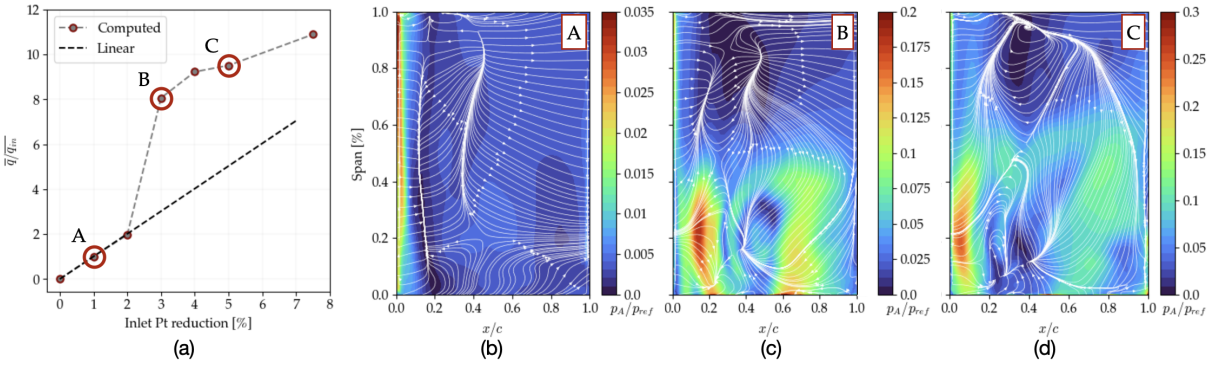

Figure 19: Forced response at NS condition: (a) amplitude of the generalized displacement, pressure fluctuation with (b) 1% (c) 3% and (d) 5% distortion reduction.

for the present study, and Cadence to grant the use of the softwares employed. The F.R.S-FNRS is gratefully acknowledged for funding the FRIA scholarship of Mr. Riccardo Toracchio.

References

[1] C. Hall, E. Schwartz, J. Hileman, Assessment of technologies for the silent aircraft initiative, Journal of Propulsion and Power 25 (6) (2009) 1153–1162.

[2] A. Plas, M. Sargeant, V. Madani, D. Chricton, E. Greitzer, T. Hynes, C. Hall, Performance of a boundary layer ingesting (bli) propulsion system, in: 45th AIAA Aerospace Sciences Meeting and Exhibit, 2007.

[3] A. Uranga, M. Drela, E. Greitzer, D. Hall, N. Titchener, M. Lieu, N. Siu, C. Casses, A. Huang, G. Gatlin, J. Hannon, Boundary layer ingestion benefit of the d8 transport aircraft, AIAA Journal 55 (11) (2017) 3693–3708.

[4] M. Waters, E. Schairer, Analysis of turbofan propulsion system weight and dimensions, Tech. Rep. NASA-TM-X-73199, A-6890, NASA Ames Research Center, CA, US (1977).

[5] E. Gunn, C. Hall, Aerodynamics of boundary layer ingesting fans, in: Proceedings of ASME Turbo Expo, no. GT2014-26142, 2014.

[6] A. Peters, Z. Spakovszky, W. Lord, B. Rose, Ultrashort nacelles for low fan pressure ratio propulsors, Journal of Turbomachinery 137 (2) (2015) 14p.

[7] J. Longley, E. Greitzer, Inlet distortion effects in aircraft propulsion system integration, in: AGARD, no. Steady and Transient Performance Prediction of Gas Turbine Engines, 1992.

[8] J. Ryman, W. O'Brien, D. Rabe, Multi-stage fan and compressor transfer of inlet total pressure distortion with emphasis on high cycle fatigue, in: 39th AIAA/ASME/SAE/ASEE Joint Propulsion Conference and Exhibit, no. p. 4979, 2003.

[9] A. Hamed, K. Numbers, Inlet distortion considerations for high cycle fatigue in gas turbine engine, in: 33rd AIAA Joint Propulsion Conference and Exhibit, no. AIAA 1997-336, 1997.

[10] C. Danforth, Distortion-induced vibration in fan and compressor blading, Journal of Aircraft 12 (4) (1975) 216–225.

[11] S. Fleeter, Aeroelasticity research for turbomachine applications, Journal of Aircraft 16 (5) (1979) 320–326.

[12] Y. Zhang, J. Pan, , Y. Zhu, X. Dong, J. Luo, Investigation of the flutter stability of a transonic fan with inlet distortion, in: Proceedings of Global Power and Propulsion Society, no. GPPS-TC-2022-0024, 2022.

[13] T. Pan, Z. Yan, H. Lu, Q. Li, Numerical investigation on the forced vibration induced by the low engine order under boundary layer ingestion condition, Aerospace Science and Technology 115 (106802) (2021) 10.

[14] T. Pan, Z. Yan, H. Lu, Q. Li, R. Kielb, Forced response induced by low engine order under circumferential inlet distortions with different extents, Journal of Turbomachinery 145 (4) (2022) 12.

[15] Z. Zhang, A. Hou, W. Tuo, A. Xia, S. Zhou, Forced response analysis of compressor blades under unsteady inlet distortion, in: 31st AIAA Applied Aerodynamics Conference, 2013.

[16] C. Bréard, M. Vahdati, A. Sayma, M. Imregun, An integrated time-domain aeroelasticity model for the prediction of fan forced response due to inlet distortion, Journal of Engineering for Gas Turbine and Power 124 (1) (2002) 196–208.

[17] F. Eichner, J. Belz, Application of the modal approach for prediction of forced response amplitudes for fan blades, Journal of Engineering for Gas Turbine and Power 141 (3) (2018) 8.

[18] F. Eichner, J. Belz, P. Winkelmann, R. Schnell, T. Lengyel-Kampmann, Prediction of aerodynamically induced fan blade vibration due to boundary layer ingestion, in: 13th European Conference on Turbomachinery Fluid Dynamics Thermodynamics ETC13, 2019.

[19] R. Toracchio, F. Fontaneto, K. Hillewaert, On the impact of the turbulence model on the secondary flow structure of a highly-loaded compressor stage, in: Proceedings of ASME Turbo Expo, no. GT2022-83163, 2022.

[20] ANSI, ASME, ANSI/ASME PTC 19.1-2005 Measurement Uncertainty, American Society of Mechanical Engineers, 2006.

[21] G. Dell'Era, N. Habotte, J. Desset, J. Brouckaert, S. Hiernaux, Experimental characterization of stall phenomena in a single-stage low-pressure axial compressor, Journal of Power and Energy 229 (5) (2015) 549–559.

A Bayesian Data Driven Multi-Fidelity Modelling Approach for Experimental Under-Sampled Flow Reconstruction

Gonçalo Granjal Cruz

Turbomachinery and Propulsion Department, von Karman Institute for Fluid Dynamics, Belgium, goncalo.cruz@vki.ac.be

Supervisor: Fabrizio Fontaneto

Associate Professor, Turbomachinery and Propulsion Department, von Karman Institute for Fluid Dynamics, Belgium, fabrizio.fontaneto@vki.ac.be

University Supervisor: Xavier Ottavy

Professor, LMFA - Laboratoire de Mécanique des Fluides et d'Acoustique, École Centrale de Lyon, France, xavier.ottavy@ec-lyon.fr

Abstract

This study employs a multi-fidelity approach that combines experimental techniques and numerical models in a Bayesian data-driven framework, which can substantially reduce the need for instrumentation, making it useful for applications that require minimal intrusiveness and minimal testing time. To implement this approach, the study uses a CFD model to generate a belief of the flow, which is then updated based on randomly undersampled experimental observations within a multi-fidelity Gaussian Process framework. The effectiveness of this approach is demonstrated on a small aspect ratio axial compressor with an available experimental database. By randomly undersampling 70% of the complete measurement test, the results show that the approach can successfully reconstruct the mean flow and typical flow features, with the reconstructed flow error comparable to the experimental measurement uncertainty. Furthermore, the study evaluates the approach's robustness and finds that the location of measurements can affect the flow reconstruction, but this effect decreases as more flow measurements are taken. Overall, the multi-fidelity approach showcased in this study provides a useful tool for assessing uncertainties and reducing experimental campaing testing times.

Keywords: Machine Learning, Experimental, Numerical, Instrumentation, Compressor

1. Introduction

Despite advances in alternative fuel sources for aircraft engine applications, such as hydrogen and biofuel [1; 2; 3], future gas turbine engines will continue to operate using the typical Joule-Brayton cycle. To enhance thermal efficiency, these engines will feature compressors that operate at higher overall pressure ratios.

Recent developments in engine design have resulted in a drastic decrease in blade height in the latest stages of the compressor. However, the miniaturization of measurement devices has not kept pace with the increased compactness of the compressor core. As a result, instrumentation-induced blockage and local flow field variation can significantly impact the evaluation of overall performance. Additionally, the thourough experimental testing of engines components requires demanding facilities with a high required electrical power and substantial costs.

Given the sensitivity of flow evaluation to instrumentation intrusiveness and high testing costs, it is necessary to adopt procedures that minimize the potential for instrumentation-induced experimental errors and reduce the number of required measurements, thus reducing the experimental campaign time. While optical techniques [4; 5], offer promising solutions, their applicability in industrial facilities and engine testing is yet to be demonstrated.

A practical way to mitigate the effects of instrumentation blockage is to minimize the instrumentation effort by employing data-driven approaches. Ven-

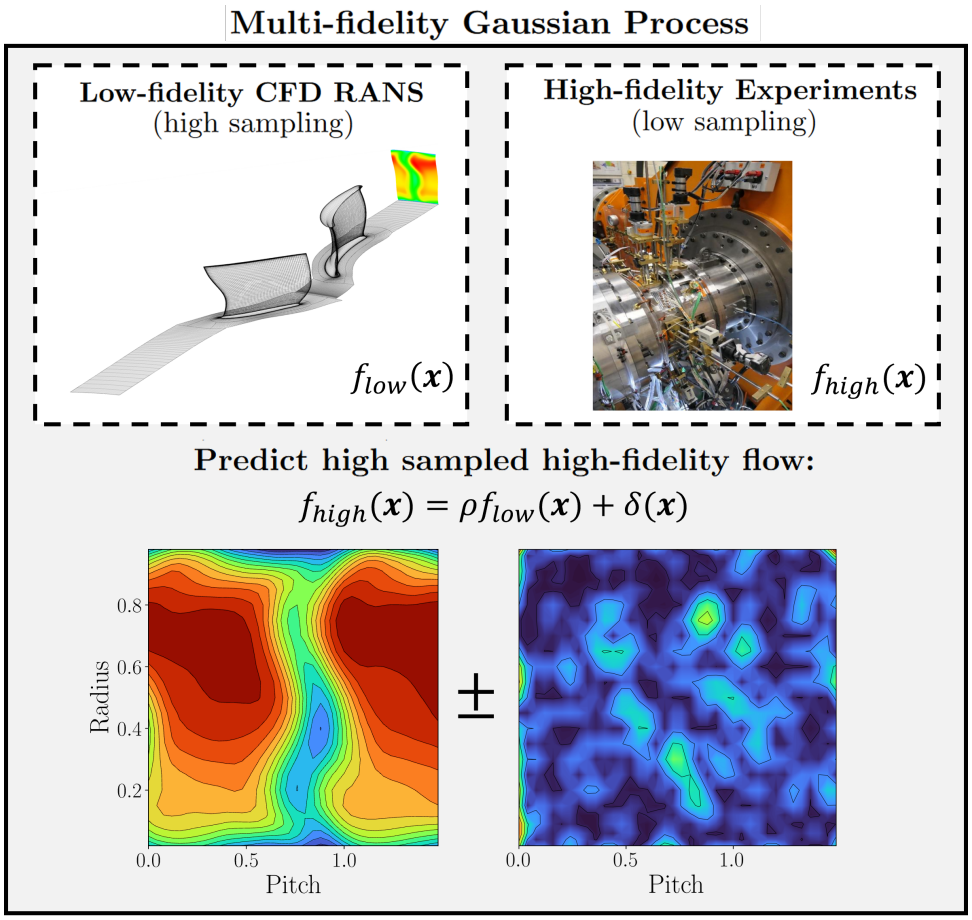

Figure 1: Scheme of the proposed Gaussian process multi-fidelity framework applied to reconstruct the H25 outlet flow.

turi et al. [6] employed proper orthogonal decomposition (POD) to reconstruct the flow past a cylinder using incomplete data sets. Similarly, Lou et al. [7; 8] developed a successful methodology for flow reconstruction across an undersampled compressor through wavelet analysis, utilizing optimally placed experimental probes. Seshadri et al. [9; 10] utilized Bayesian methods to model and average an engine temperature field from sparse experimental data, and decomposed the model uncertainty into measurement error and insufficient sampling.

Recent advancements in the computational paradigm have made numerical simulations, particularly computational fluid dynamics (CFD), a standard practice in industrial flows. Sousa et al. [11] implemented a data assimilation approach to infer the inflow boundary conditions for CFD simulations with a reduced number of experimental sensors. Foures et al. [12] employed data assimilation to match the divergence of the Reynolds stress tensor in a steady RANS formulation to DNS data of a flow across an infinite cylinder, while Symon et al. [13] adapted this approach to improve the resolution of 2D PIV data over an airfoil.

A data assimilation approach can address two separate issues: the limited availability of accurately measured experimental data in terms of space and time, and numerical simulations that may fail to accurately represent the state of the real flow due to numerical discretization or inaccurate boundary conditions [14]. This paper aims to tackle the former problem by coupling low-fidelity CFD RANS simulations with limited high-fidelity experimental data in a real engineering test case, specifically a high-pressure axial compressor stage, using a multi-fidelity Gaussian process (GP) approach proposed by Kennedy and O'Hagan [15],

This paper begins with an overview of the proposed

data-driven multi-fidelity GP approach in Section 2. Section 3 provides a description of the experimental and numerical setups of the test case, the H25 compressor stage, followed by the mean flow results and a sensitivity analysis study in Section 4. Finally, the paper concludes with a summary of the findings and prospects for future improvements to the current implementation.

2. Gaussian Process Regression

The multi-fidelity framework used in this work has its foundation in Gaussian Processes (GPs). Gaussian Processes are a non-parametric method that constructs "Gaussian distributions over functions" [16] rather than in parameters. This makes GPs a powerful tool for regression problems (predict unknown data $\boldsymbol{y}_*$ from noisy observed data $\boldsymbol{y}$). A Gaussian process defines a multivariate Gaussian prior distribution over functions for every point in the input space $\boldsymbol{x}$:

$$p(f \mid \boldsymbol{x}) \sim \mathcal{N}(f \mid \boldsymbol{\mu}, \mathbf{K}) \tag{1}$$

where $f(\boldsymbol{x})$ is a multivariate random variable from which noisy observations $\boldsymbol{y} = f(\boldsymbol{x}) + \boldsymbol{\epsilon}$ are available. The assumption that the noise follows an independent, identically distributed Gaussian distribution with zero mean and fixed variance is taken and thus $\boldsymbol{\epsilon} \sim \mathcal{N}\left(\mathbf{0}, \sigma_y^2 \mathbf{I}\right)$. $\boldsymbol{\mu}$ is the prior mean function and is usually assumed to be 0. $\mathbf{K}(\mathbf{x_i}, \mathbf{x_j})$ is a kernel function that defines the joint covariance of the given inputs $\boldsymbol{x}$.

Given the above assumptions and available noisy observations $\boldsymbol{y}$, the log marginal likelihood function can be derived in Eq. 2:

$$\log p(\boldsymbol{y} \mid \boldsymbol{x}) = -\frac{1}{2}\log\left(\det\left(\mathbf{K} + \sigma_y^2 \boldsymbol{I}\right)\right) - \frac{1}{2}(\boldsymbol{y}-\boldsymbol{\mu})^\top \left(\mathbf{K} + \sigma_y^2 \boldsymbol{I}\right)^{-1}(\boldsymbol{y}-\boldsymbol{\mu}) - \frac{n}{2}\log(2\pi) \tag{2}$$

the first term is a model complexity term, defined by the prior selection of the kernel function. The second term is a likelihood data-fit term showing the Bayesian weighting of prior assumptions with the observed data. Notice the strict dependence of the log marginal likelihood in the kernel function $\mathbf{K}$. Multiple kernel function families exist in the literature for different function modeling behavior (e.g. smoothness, stationary) making this choice a prior input of our knowledge of the problem. In the present work, the kernel function selected is the stationary anisotropic Matérn 5/2 kernel due to its demonstrated performance in engineering applications [17]:

$$\mathbf{K}(\boldsymbol{x}_i, \boldsymbol{x}_j) = \sigma_f^2\left(1 + \frac{\sqrt{5\left(\boldsymbol{x}_i, \boldsymbol{x}_j\right)^T\left(\boldsymbol{x}_i, \boldsymbol{x}_j\right)}}{\ell} + \frac{5\left(\boldsymbol{x}_i, \boldsymbol{x}_j\right)^T\left(\boldsymbol{x}_i, \boldsymbol{x}_j\right)}{3\ell^2}\right)\exp\left(-\frac{\sqrt{5\left(\boldsymbol{x}_i, \boldsymbol{x}_j\right)^T\left(\boldsymbol{x}_i, \boldsymbol{x}_j\right)}}{\ell}\right) \tag{3}$$

where the l is the length scale and controls the smoothness and σ_f acts as a scaling factor. Equation 3 ensures a twice differentiable function without forcing an extreme smooth modelling, typically observed with more default choices. It is of interest to optimize these parameters to fit the available data $\boldsymbol{y}$. This is achieved by finding the hyperparameters that maximize the log marginal likelihood (Eq. 2).

Predictions of the unknown states $\boldsymbol{y}_*$ can be obtained by conditioning their input locations $\boldsymbol{x}_*$ on the previous distributions, giving, a predictive posterior distribution:

$$p\left(\boldsymbol{y}_* \mid \boldsymbol{x}_*, \boldsymbol{x}, \boldsymbol{y}\right) = \mathcal{N}\left(\boldsymbol{y}_* \mid \boldsymbol{\mu}_*, \boldsymbol{\Sigma}_*\right) \tag{4}$$

$$\boldsymbol{\mu}_* = \boldsymbol{\mu} + \mathbf{K}(\boldsymbol{x}, \boldsymbol{x}_*)(\mathbf{K}(\boldsymbol{x}, \boldsymbol{x}) + \sigma_y^2\mathbf{I})^{-1}(\boldsymbol{y} - \boldsymbol{\mu}) \tag{5}$$

$$\boldsymbol{\Sigma}_* = \mathbf{K}(\boldsymbol{x}_*, \boldsymbol{x}_*) - \mathbf{K}(\boldsymbol{x}_*, \boldsymbol{x})(\mathbf{K}(\boldsymbol{x}, \boldsymbol{x}) + \sigma_y^2\mathbf{I})^{-1}\mathbf{K}(\boldsymbol{x}, \boldsymbol{x}_*) \tag{6}$$

where $\boldsymbol{\mu}_*$ is the posterior function mean and $\boldsymbol{\Sigma}_*$ its covariance from which the propagated uncertainty is obtained. The predictions standard deviation is computed directly in the diagonal of the covariance matrix of Eq. 4.

One can extend the GP regression to model functional behaviour from different data sources. Following the approach of O'Hagan [18] we use an autoregressive linear method (AR1) to model the following two level fidelity functional relationship:

$$f_{high}(\boldsymbol{x}) = \rho f_{low}(\boldsymbol{x}) + \delta(\boldsymbol{x}) \tag{7}$$

where ρ is a scaling factor weighting the cross-correlation between fidelity levels, assumed constant in this work. $\delta(\boldsymbol{x})$ is a bias term in the data modeled as $\delta(\boldsymbol{x}) \sim \mathcal{N}(\boldsymbol{\mu}_{bias}, \mathbf{K}_{bias})$. To summarize, Eq. 7 models a high-fidelity function as equal to a fraction of a low-fidelity model plus an error between the two. This allows to predict the complete domain of the high-fidelity function and its uncertainty, as schemed in Fig. 1.

The AR1 method inputs to each fidelity level a GP prior. A joint multivariate GP prior can then be defined in Eq. 8, using Gaussian distribution properties and concatenating the different fidelity data.

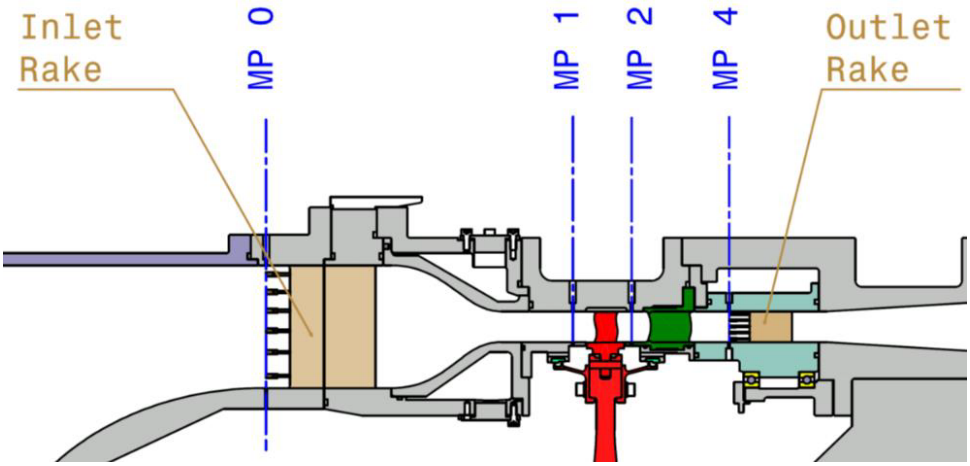

Figure 2: H25 compressor stage test section meridional view

$$\begin{bmatrix} f_{low}(\boldsymbol{x}) \\ f_{high}(\boldsymbol{x}) \end{bmatrix} \sim \mathcal{N}(\begin{bmatrix} \boldsymbol{\mu}_{low} \\ \boldsymbol{\mu}_{high} \end{bmatrix}, \begin{bmatrix} \mathbf{K}(\boldsymbol{x},\boldsymbol{x})_{low} & \rho\mathbf{K}(\boldsymbol{x},\boldsymbol{x})_{low} \\ \rho\mathbf{K}(\boldsymbol{x},\boldsymbol{x})_{low} & \rho^2\mathbf{K}(\boldsymbol{x},\boldsymbol{x})_{low} + \mathbf{K}(\boldsymbol{x},\boldsymbol{x})_{bias} \end{bmatrix}) \quad (8)$$

After hyperparameter training, the low-fidelity component of the joint distribution is marginalized and predictions on the high-fidelity level can be performed. Two main approaches for solving the GPs inference problem are found in literature. The first one is a fully coupled inference of both fidelity simultaneously[18], while the second one performs the inference recursively from low to high fidelity[19]. The latter allows faster computation but requires the data to have a nested structure ($\mathcal{D}_{high} \subseteq \mathcal{D}_{low}$), in this work, since one would have to apply an error-prone interpolation to ensure the nested condition and because we are dealing with only two fidelity levels, the fully coupled approach is used. The interested reader is referred to [20, Chapter 3] for a mathematical derivation.

3. Test case

The H25 compressor stage serves as the primary test case for this study. This research stage represents the final stage of a multi-stage axial compressor for aircraft gas turbine applications and features a low aspect ratio (span-to-chord ratio). In addition, the H25 stage has a blade height of only 25mm, which makes it an ideal test case for investigating a reduction in instrumentation effort and blockage since a standard probe stem diameter is a significant fraction of the pitch size.

3.1. Experimental setup

Fig. 2 displays the meridional view of the H25 test section, with the rotating components and stator row highlighted in red and green, respectively. The measurement instrumentation was distributed axially across four measurement planes denoted as MP in the figure. To obtain the overall performance, combined total pressure-total temperature rakes were deployed at measurement planes 0 (inlet) and 4 (outlet).

The measurement instrumentation at plane 4 allowed for a complete sampling of a 2D (R, θ) map of the flow field across a 1.5 blade passage. Total pressure, angle, and Mach number were measured using an in-house designed miniaturized three-hole probe. The pressure probe was designed to achieve a 2% span end-wall proximity. A detailed flow field was obtained through thorough sampling, with a maximal flow cross-section blockage induced by a probe of 0.6%. The total-to-total pressure ratio uncertainty budget was estimated to be around 1% at nominal speed, while the total temperature uncertainty was 0.6 K.

3.2. CFD RANS simulations

NUMECA FINE Turbo 12.1 which employs a finite volume formulation and a multi-block structured grid to solve fully turbulent compressible steady RANS

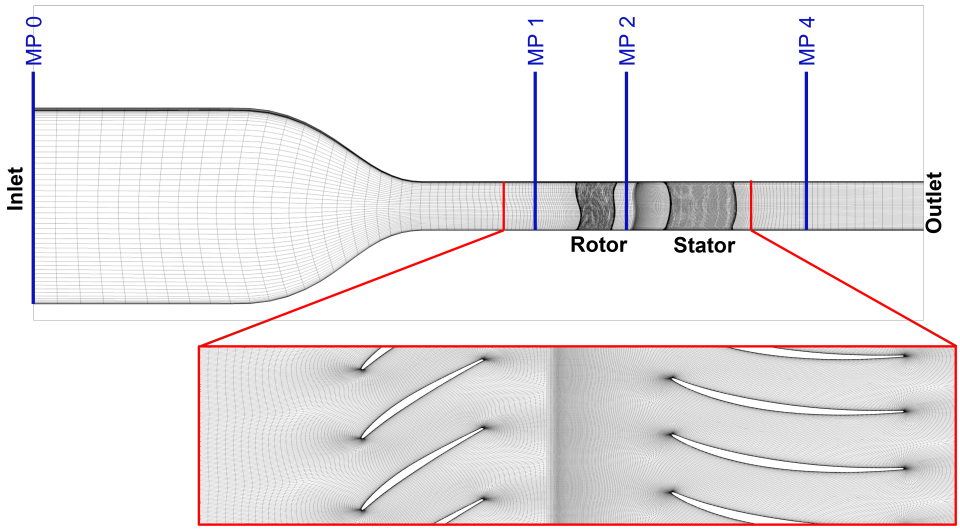

Figure 3: H25 compressor stage numerical domain meridional view and blade-to-blade zoom cut (distorted blade geometry).

equations was used to conduct the numerical simulations of the H25 compressor stage. The k-ω SST turbulence model [21] was chosen as the closure model. Only one blade passage was simulated under a periodicity assumption. A mixing plane interface was utilized to couple the rotor rotating block with the non-rotating stator block.

The computational grid, shown in Figure 3, was generated with Autogrid5 and consisted of a structured mesh. An O-4H mesh topology was used for both blade rows, while an OH topology was employed in the rotor tip gap region. The mesh retained the blade fillets in both the rotor and stator and removed cavities from the numerical domain. All non-dimensional wall distances $y+$ were lower than 2. The mesh convergence was analyzed at 3 levels (with 0.6 million cells, 4.55 million cells, and 19.45 million cells). The RANS data for this work were obtained using the mesh with 4.55 million cells.

The study's operating regime was set to the compressor's design point at nominal speed, with total quantities and flow direction imposed at the inlet and absolute mass flow imposed at the outlet. The computations were adiabatic, assuming adiabatic walls for all domain walls.

In this work, the focus is on studying the outlet flow of the H25 compressor (Plane 4). Figure 4 presents the outlet total pressure P_{T4} flow fields obtained with the fully sampled experimental data (left) and the low-fidelity RANS approach (right). The pressure contours show the main flow structures that match their location. However, a clear discrepancy in values is observed. The average pressure ratio of the flow shows a difference of around 0.084, which is higher than the experimental uncertainty. The experimental flow exhibits an overall higher pressure due to higher loading of the blade at a higher span, as expected from the 3D blade design of the compressor. The experimental flow also shows a narrow and shallow wake compared to the RANS simulation. On the other hand, the RANS simulation is over-predicting the hub losses from $r = 0.02$ until around $r = 0.2$. In-depth flow analysis of the CFD simulation allowed for tracking the origin of these structures and relating them to the modeling assumptions. The mixing plane approach averages the rotor outlet flow, inducing a local incidence change at the stator inlet in the pitch-wise direction at high-span locations (from $r = 0.75$ to $r = 0.98$). In parallel, the CFD simulation predicts a flow breakdown at the mid-chord of the rotor at the hub, which propagates to higher span regions due to the 3D rotor blade design. This flow separation is believed to be overestimated by the turbulence closure model assumption of isotropic turbulence [22]. These two effects propagate together through the stator, leading to higher losses and dislocation of mass flow, which is then visible at the outlet of the stator.

4. Results

This work combines high discretized CFD RANS low fidelity data, $\mathcal{D}_{low} = (\boldsymbol{x}_{low}, \boldsymbol{y}_{low})$, with under-sampled high fidelity experimental data, $\mathcal{D}_{high} =$

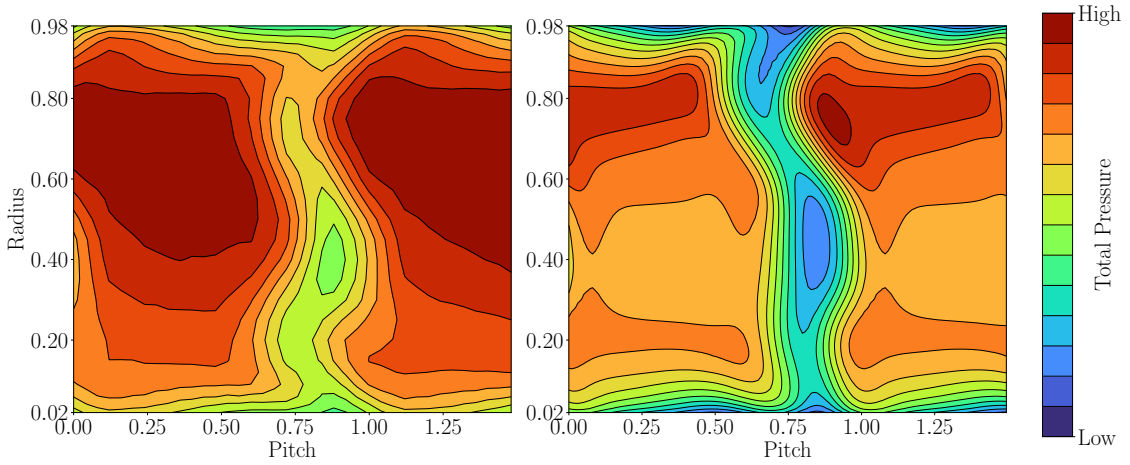

Figure 4: Total pressure (P_{T4}) flow field comparison between experimental data (on the left) and the CFD RANS numerical simulation (on the right) at the compressor outlet (Plane 4). The data is limited to the experimental probe radial sampling limits.

$(\boldsymbol{x}_{high}, \boldsymbol{y}_{high})$ with $\mathcal{D}_{low} >> \mathcal{D}_{high}$. In particular, to tackle the outlet flow assessment, the data set inputs, $\boldsymbol{x} = [\boldsymbol{r}\ \boldsymbol{\theta}]$, are mapped to the outlet total pressure, $\boldsymbol{y} = \boldsymbol{P}_{T4}$.

The high-fidelity experimental data was obtained from a complete 2D (r, θ) flow field that was presented in Fig. 4. This data set has $N_{high} = 950$ sampled points over a grid of 25 points per radius and 38 points over 1.5 stator pitch. The experimental data was divided into two data subsets: the *training* subset, which was used for hyper-parameter learning and flow reconstruction, and the *validation* subset, which was considered as the underlying truth against which the predicted flow reconstruction was to be compared.

In the following analysis, the training subset is one-third of the available experimental measurements randomly selected $N_{high,train} = 313$. This results in a 67% reduction in instrumentation effort. All available CFD low-fidelity data, $\mathcal{D}low$, which consisted of $Nlow = 14900$ data points is used for training the multi-fidelity model. The total number of data points used for training the model were $N_{train} = 15213$, unless otherwise specified. The kernel hyper-parameters of Equation 3 were learned using the L-BFGS optimizer [23].

The remaining two-thirds of the available experimental measurements define the *validation* subset with $N_{high,val} = 637$ with which the model predicted values $\boldsymbol{y}_*$ are evaluated against through the root mean squared error (RMSE) and the maximum absolute error (MaxAE):

$$\text{RMSE} = \sqrt{\frac{1}{N_{val}} \sum_{i=1}^{N_{val}} (y_*^i - y_{val}^i)^2} \tag{9}$$

$$\text{MaxAE} = max_{1 \le i \le N_{val}} \left| y_*^i - y_{val}^i \right| \tag{10}$$

where y_{val}^i and y_*^i denote the true and predicted values at the i-th validation point, respectively.

The RMSE is a commonly used error metric that measures the prediction accuracy of the model. A lower value of RMSE indicates a better performance of the model. The MaxAE, on the other hand, is used to identify the worst prediction made by the model, and can be compared against the experimental measurement uncertainty. If there is a discrepancy between the RMSE and MaxAE, it also suggests that the model's performance might be poor in certain sensitive regions of the flow.

The evaluation of the GP multi-fidelity framework's high-fidelity mean flow reconstruction for the compressor stage outlet's total pressure is presented and compared against the experimental reference total pressure field in Fig. 5, where the white crosses on the experimental reference indicate the $N_{high,train} = 313$ (33%) randomly selected experimental measurements used as high-fidelity samples for multi-fidelity model training.

The reconstructed predicted flow quantities agree with the experiments, with important flow feature regions being well-defined. The wake depth and width are correct, and the spanwise pressure distribution

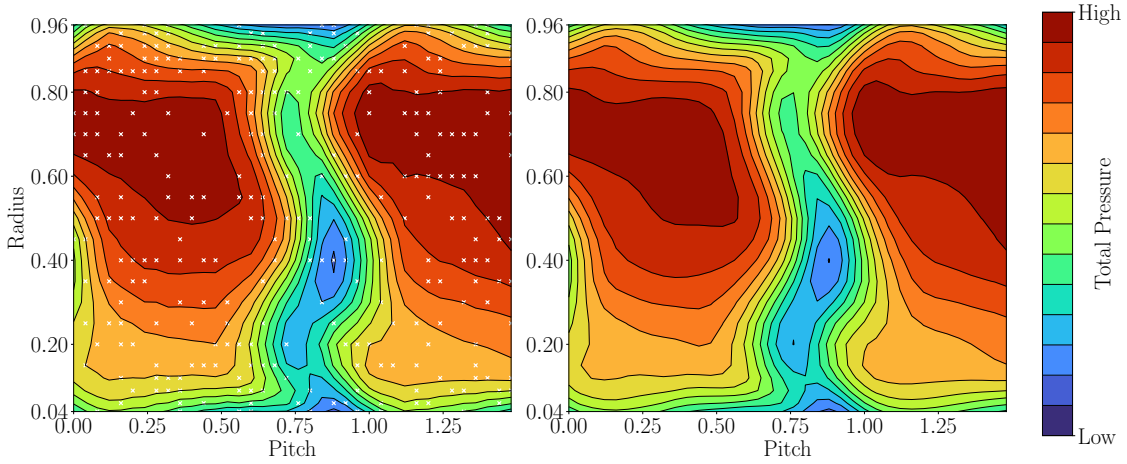

Figure 5: GP multi-fidelity inference of the total pressure field at the compressor outlet (right) with 33% experimental measurements sampled and fully sampled experimental reference (left): Overall match of flow features; RMSE lower than the experimental uncertainty.

agrees with the experimental reference. Other secondary flows, such as the passage vortex near the boundary layer hub region and the losses propagating from the rotor tip vortex, are visible and correctly predicted in size and magnitude. It is worth noting that the Matern 5/2 (Eq. 3) was selected as the kernel covariance function for the model, which, based on the author's experience, outperforms more conventional approaches in predicting high gradients.

The model predicts a small low-pressure region at $\boldsymbol{x} = (r = 0.2, \theta = 0.75)$, which is considered an error due to the lack of experimental measurements in this region during the training data. This region is already outside of end-wall boundary effects and radially far from the deepest wake region, where the only low-pressure values were measured in the reference experiments. The error metrics introduced earlier in this section were used to quantitatively evaluate the performance of the GP multi-fidelity model. The evaluation was conducted in terms of a pressure ratio, and it was found that the model has a RMSE of 0.00057, indicating that it can accurately reconstruct the high-fidelity flow despite the 67% reduction in test instrumentation. This RMSE value is also lower than the propagated measurement uncertainty for the pressure ratio, which is 0.00133. However, the maximum absolute error (MaxAE) in the validation data set is 0.00326, which is one order of magnitude higher than the RMSE and higher than the experimental uncertainty, suggesting the existence of a localized high error area in the flow prediction.

Figure 6 shows the contours of the absolute differ-

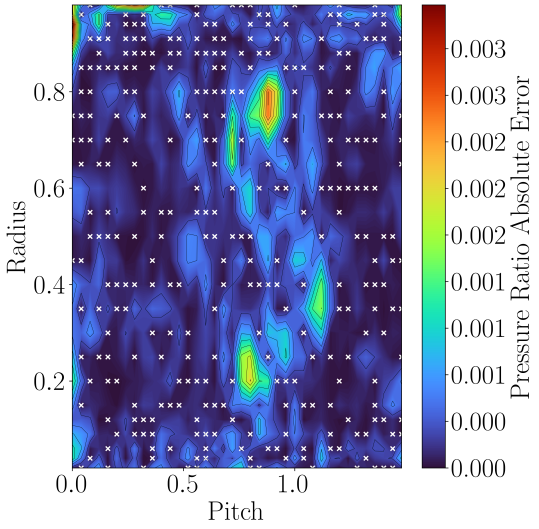

Figure 6: Contour plots of the absolute error between the experimental reference and the multi-fidelity GP model prediction for total pressure ratio. The white dots represent the experimental data used in the model training. Localized areas of error are detected in high gradient flow regions.

ence between the mean flow predictions and the experimental reference for pressure ratio. Generally, the error is lower near the training data indicated by white dots. However, as expected from the error metrics, some flow regions exhibit a higher absolute error than others. The absolute error is higher in the main flow interaction with the blade wake secondary flow, where the stronger pressure field gradients are present, and this error zone is higher than the experimental uncertainty. An optimal selection of high-fidelity measurements a priori could offset the lack of high-fidelity information in this location due to the randomness of the training data selection for the model.

The Bayesian formalism of the model allows a direct measure of the uncertainty in the model predictions. The contour plot of the 95% confidence interval (CI) equivalent of two standard deviations (2σ) of the mean flow prediction for the pressure ratio are shown in Figure 7. The white dots correspond to the high-fidelity experimental measurements used to train the model, and the lowest uncertainty is predicted at those locations. The model uncertainty rapidly increases outside the training data subset, as seen by the higher uncertainty predicted around pitch=0, where no experimental data is present in the training of the model. When comparing the 2σ prediction in Figure 7 to the mean flow absolute error in Figure 6, it is observed that the regions of high uncertainty in the flow match the regions of high absolute error. These regions are characterized by strong flow gradients and a lack of experimental sampling. The model, therefore, predicts higher uncertainty in these regions, while presenting a higher error, making it conservative in its prediction capabilities.

While the presence of high-fidelity experimental measurements tends to result in lower error and uncertainty, the ultimate goal of this study is to obtain accurate flow predictions with a minimal number of measurements. It is therefore important to consider the trade-off between the number and location of high-fidelity measurements and the accuracy of the flow prediction and its standard deviation.

To evaluate the impact of the random selection of experimental data from the full dataset and the effect of the number of measurements used to train the model, a sensitivity analysis is conducted. Figure 8 displays box-plots of the RMSE in the flow reconstruction as a function of the percentage of experimental measurements used for the pressure ratio. Similarly, Fig. 9 shows box-plots of the maximum absolute error.

For each percentage of experimental high-fidelity

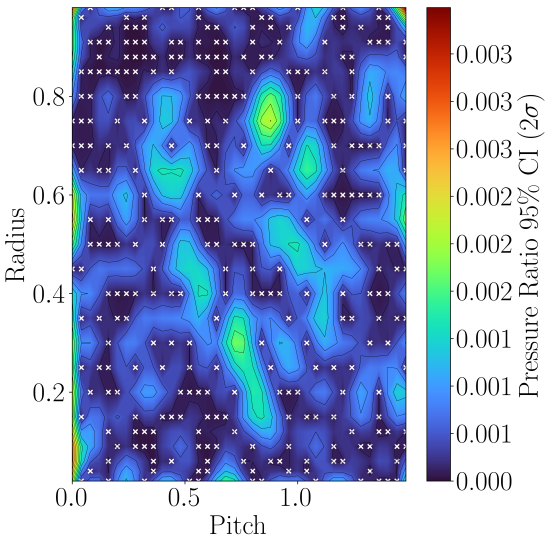

Figure 7: Contour plot of the standard deviation (σ) of the multi-fidelity GP model prediction for the pressure ratio uncertainty.The white dots represent the experimental data used in the model training.

measurements used (represented by each box in the figure), 50 multi-fidelity models (represented by orange dots) are created, where the high-fidelity data used for training is randomly selected from the complete data set. The low-fidelity CFD data used remains the same for all models.

As anticipated earlier, using more high-fidelity experimental data leads to a reduction in both the RMSE and maximum absolute error. This is clearly seen in Fig. 8, where increasing the percentage of high-fidelity data from 10% to 20% results in an average reduction of around 25% in model error. Furthermore, as the amount of high-fidelity data increases, the box-plot spread decreases, particularly for the RMSE, indicating that the model's predictions become more reliable and less sensitive to the random selection of high-fidelity samples. This is expected since more data reduces the probability of inadequate sampling of crucial flow features, such as the strong gradient wake region previously mentioned. Based on this analysis, the choice of presenting the mean flow reconstruction results obtained with 33% of the measurements is justified since it yields a robust flow reconstruction regardless of the random experimental samples used in the model training.

The analysis of the MaxAE metric in Fig. 9 shows that the choice of data has a significant impact for all

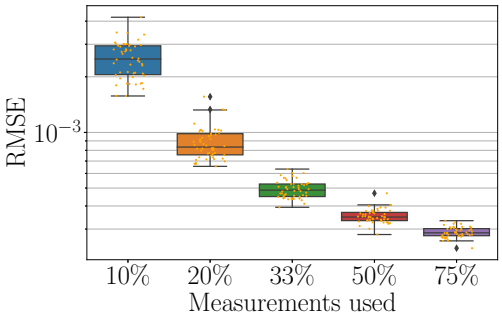

Figure 8: Multi-fidelity GP model total pressure ratio RMSE sensitivity to the random selection of experimental data and the percentage of experimental data used in the model training.

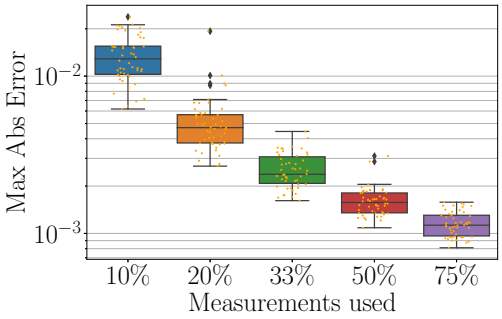

Figure 9: Multi-fidelity GP model total pressure ratio Max. abs. error sensitivity to the random selection of experimental data and the percentage of experimental data used in the model training.

percentages studied. Using the 33% case as an example, some models present a MaxAE from around 0.0017 (close to the experimental uncertainty) to values as high as 0.0043, which is twice as high, but is at the same time the box-plot mean error with 20% measurements. Moreover, the minimum error achievable with 20% measurements is approximately the same as the mean flow solution presented in Fig. 5. These results suggest that if an experimental campaign is designed beforehand to suit the multi-fidelity framework, an even greater reduction in instrumentation effort could be achieved while maintaining the same level of accuracy.

5. Conclusion

The following study presents a multi-fidelity data-driven framework based on Gaussian Processes that uses a combination of RANS CFD simulations and experimental measurements to predict the complete experimental flow. The proposed approach is capable of reducing the instrumentation effort and the experimental testing time required to evaluate the total pressure flow field at the outlet of an axial compressor stage by up to 67% while maintaining a high-fidelity flow reconstruction and no loss of flow feature information.

The study also discusses the use of a Bayesian probabilistic framework to provide a direct uncertainty assessment of the model's predicted flow fields. The uncertainty areas are larger outside of the experimental sampling limits and in strong gradient flow regions. A sensitivity analysis is also presented to show the influence of selected experimental measurements to reconstruct the flow and how it varies with the number of experimental measurements used. The study concludes that a 33% random selection of experimental samples used to train the model presents a good trade-off balance in terms of instrumentation reduction and estimated error. However, if one could evaluate the most relevant experimental locations to sample beforehand, a drastic impact on the instrumentation effort is expected to be achieved at iso-uncertainty levels with respect to traditional fully experimental measurement campaign.

References

[1] A. H. Lefebvre, D. R. Ballal, Gas turbine combustion: alternative fuels and emissions, CRC press, 2010.

[2] P. Chiesa, G. Lozza, L. Mazzocchi, Using hydrogen as gas turbine fuel, J. Eng. Gas Turbines Power 127 (1) (2005) 73–80.

[3] K. K. Gupta, A. Rehman, R. Sarviya, Bio-fuels for the gas turbine: A review, Renewable and Sustainable Energy Reviews 14 (9) (2010) 2946–2955.

[4] G. Zambonini, X. Ottavy, J. Kriegseis, Corner separation dynamics in a linear compressor cascade, Journal of Fluids Engineering 139 (6).

[5] J. Klinner, A. Hergt, S. Grund, C. E. Willert, High-speed piv of shock boundary layer interactions in the transonic buffet flow of a compressor cascade, Experiments in Fluids 62 (3) (2021) 1–19.

[6] D. Venturi, G. E. Karniadakis, Gappy data and reconstruction procedures for flow past a cylinder, Journal of Fluid Mechanics 519 (2004) 315–336.

[7] F. Lou, N. L. Key, Reconstructing compressor non-uniform circumferential flow field from spatially undersampled data – Part 1: Methodology and sensitivity analysis, Proceedings of the ASME Turbo Expo GT2020-14867 (2020) 1–12.

[8] F. Lou, D. R. Matthews, N. J. K. Iii, N. L. Key, Reconstructing compressor non-uniform circumferential flow field from spatially undersampled data – Part 2 : Pratical application for experiments, Proceedings of the ASME Turbo Expo GT2020-15465 (2020) 1–12.

[9] P. Seshadri, A. Duncan, G. Thorne, G. Parks, M. Girolami, Bayesian Assessments of Aeroengine Perfor-

mancearXiv:2011.14698.
URL http://arxiv.org/abs/2011.14698

[10] P. Seshadri, A. Duncan, G. Thorne, Bayesian mass averaging, arXiv preprint arXiv:2011.09240.

[11] J. Sousa, C. Gorlé, Computational urban flow predictions with Bayesian inference: Validation with field data, Building and Environment 154 (November 2018) (2019) 13–22. doi:10.1016/j.buildenv.2019.02.028.
URL https://doi.org/10.1016/j.buildenv.2019.02.028

[12] D. P. Foures, N. Dovetta, D. Sipp, P. J. Schmid, A data-assimilation method for reynolds-averaged navier-stokes-driven mean flow reconstruction, Journal of Fluid Mechanics 759 (2014) 404–431. doi:10.1017/jfm.2014.566.

[13] S. Symon, N. Dovetta, B. J. McKeon, D. Sipp, P. J. Schmid, Data assimilation of mean velocity from 2D PIV measurements of flow over an idealized airfoil, Experiments in Fluids 58 (5). doi:10.1007/s00348-017-2336-8.

[14] T. Hayase, Numerical simulation of real-world flows, Fluid Dynamics Research 47 (5) (2015) 51201. doi:10.1088/0169-5983/47/5/051201.
URL http://dx.doi.org/10.1088/0169-5983/47/5/051201

[15] M. Kennedy, A. O'Hagan, Predicting the output from a complex computer code when fast approximations are available, Biometrika 87 (1) (2000) 1–13. doi:10.1093/biomet/87.1.1.
URL https://academic.oup.com/biomet/article-lookup/doi/10.1093/biomet/87.1.1

[16] C. K. Williams, C. E. Rasmussen, Gaussian processes for machine learning, Vol. 2, MIT press Cambridge, MA, 2006.

[17] M. R. Kianifar, F. Campean, Performance evaluation of metamodelling methods for engineering problems: towards a practitioner guide, Structural and Multidisciplinary Optimization 61 (1) (2020) 159–186. doi:10.1007/s00158-019-02352-1.

[18] M. C. Kennedy, A. O'Hagan, Bayesian calibration of computer models, Journal of the Royal Statistical Society. Series B: Statistical Methodology 63 (3) (2001) 425–464. doi:10.1111/1467-9868.00294.

[19] L. L. Gratiet, J. Garnier, Recursive co-kriging model for design of computer experiments with multiple levels of fidelity, International Journal for Uncertainty Quantification 4 (5) (2014) 365–386. doi:10.1615/int.j.uncertaintyquantification.2014006914.

[20] L. Le Gratiet, Multi-fidelity gaussian process regression for computer experiments, Ph.D. thesis, Université Paris-Diderot-Paris VII (2013).

[21] F. R. Menter, Two-equation eddy-viscosity turbulence models for engineering applications, AIAA Journal-doi:10.2514/3.12149.

[22] F. Gao, W. Ma, G. Zambonini, J. Boudet, X. Ottavy, L. Lu, L. Shao, Large-eddy simulation of 3-d corner separation in a linear compressor cascade, Physics of Fluids 27 (8) (2015) 085105.

[23] J. Nocedal, S. J. Wright, Numerical optimization, Springer, 1999.

TURBINE AERODYNAMICS AND HEAT TRANSFER

On the design and characterization of a modular active turbulence generator for a low-speed turbine cascade rig

Federico Bertelli

Turbomachinery and Propulsion Department, von Karman Institute for Fluid Dynamics, Belgium,
federico.bertelli@vki.ac.be

Supervisor: Sergio Lavagnoli

Associate Professor, Turbomachinery and Propulsion Department, von Karman Institute for Fluid Dynamics, Belgium,
sergio.lavagnoli@vki.ac.be

University Supervisor: Koen Hillewaert

Professor, Aerospace and Mechanical Engineering, University of Liège, Liège,
koen.hillewaert@uliege.be

Abstract

Quantifying free-stream turbulence effects on the fundamental flow physics of fluid dynamic mechanisms is important for improving physical understanding as well as the predictions of the aerodynamic losses for turbomachinery flows and a wide of other internal and external aerodynamic flows. This paper discusses the development and the experimental characterization of a turbulence generator that is capable of generating a wide range of turbulence with the peculiarity to set the turbulence intensity levels and yet tune the turbulence scales independently.

Keywords: Turbulence, Turbulence Scales, Active Turbulence Generator, Jet Grid, Low-Speed Wind Tunnel, Low-Speed Cascade Rig, Blade Passage Flow

1. Introduction

The assessment of the aerodynamic performance degradation for turbine passage flows had and continues to have a key role in performance and efficiency predictability. One prominent effect that plagues this predictive capability is the role of turbulence, as it plays a major role in the dynamics of physical processes that are still not fully understood today. In turbine flows, as well as in many other internal and external aerodynamic flows, the time-dependent and multi-scale interactions between turbulence and flow physics represents the main sources of uncertainty both in experiments and CFD simulations, causing significant discrepancies between measurements and predictions of global flow phenomena and entropy generating mechanisms. While the role of free-stream turbulence intensity has been of primary interest to researchers during the past decades, the individual role of turbulence length/time scales on the aerodynamics of turbine passage flows is still scarcely investigated in open literature. The isolated effects of scales are too often brutally ignored or poorly modeled when not considered as a concurrent/dependent effect of the turbulence intensity, as nowadays the turbulence scales are difficult to generate and measure both in experiments and numerical simulations. However, although there have been only few literature evidences in which there has been a systematic variation of turbulence intensity and scales, the results consistently show the importance of both these two parameters on the flow physics of turbine passages. To advance our physical understanding on the role of turbulence as well as the fidelity of the turbulence-modeled CFD predictions, commonly used as standard practice in today's academic and industrial design and optimization processes, this research field needs a boost. The VKI's turbine research group is contributing to fill this knowledge gap, aiming at producing an unprecedented set of both experimental and

numerical measurements to target the precise identification of scales effects on the fundamental physics of the main flow mechanisms characterizing a turbine aerodynamics and the evaluation of their impact on the performance drop. The rationale behind the scope of this paper is to enable the future experimental campaigns in the VKI C-1 low-speed cascade rig with a novel turbulence generator capable to expose turbine flows to a wide range of free-stream turbulence, characterized by values of turbulence scales that can be systematically varied from the intensity levels, so that the effects of these two key parameters are isolated/decoupled and studied independently each other.

The aim of this paper is threefold. First, this paper describes different concepts for generating free-stream turbulence in low-speed wind tunnels, focusing in particular on the only one that provides the authority for the independent control of turbulence scales. Note that there are now a number of different free-stream turbulence generators that have been presented in the open literature that are able to produce a wide range of turbulence intensities without, however, allowing for an independent control of turbulence scales. Second, this paper focuses on the design process of the turbulence jet grid concept developed to generate different combinations of free-stream turbulence with turbulence intensities between 1% to 15% and an independent control of the integral length scale within the range of 5%-20% of the turbine blade chord. Such desired range of turbulence regimes is representative of turbulence values encountered by a broad class of turbine systems as well as a number of other technologies where turbulence-driven flows play a critical role in the definition of efficiency. Third, this paper presents the complete design of the experiment for the measurement campaign that targets the turbulence jet grid characterization in the auxiliary VKI L-12 low-speed test bench, with the main purpose to validate the turbulence generator concept and the generated turbulent flow fields and inform future design iterations for a scaled-up version to install in the VKI C-1 low-speed cascade rig.

The following sections report a review of relevant past studies, a solid understanding of the concepts used to decouple the turbulence scales effects from the intensity, the analysis and development of the turbulence generator, and finally a description of the entire experiment, describing the experimental facility and measurement techniques used for this study together with strategies, methods and procedures to success the tests.

2. Past Studies

On the Role of Turbulence Scales

Past studies have indicated the importance of both turbulence levels and length scales, however, only few experimental works and only for very specific cases have shown the role of turbulence length scales and the related energy spectra on the aerodynamics and heat transfer mechanisms of turbine flow passages. As pointed out by Ames [1], Carullo et al. [2] and Wang et al. [3], free-stream turbulence scales modulate the leading-edge stagnation heat transfer; larger scales interact with the blade leading edge producing small-scale fluctuations associated with more intense convective heat exchanges. Other investigations have observed the effects of free-stream turbulence scales on turbine vanes aerodynamics [4, 5] concluding that the laminar-to-turbulent transition is highly dependent on a variation of the turbulent structures; larger free-stream turbulence scales grow faster within the boundary layer causing an early laminar-to-turbulent transition on the blade suction side. Mahallati et al. [6] show that the spectrum of smaller integral length scales contains the high-frequency content necessary to trigger boundary layer stream-wise streaks and the generation of turbulent spots. Such results are also in agreement with what reported by analysis of aerodynamics and surface heat transfer in flat plate applications [7, 8].

This high coherence between free-stream turbulence length/time scales and the boundary layer response is indicative of the prominent role that the turbulence scales may play on loss generating mechanisms. As pointed out by Folk et al. [9], smaller scales penetrate deeper into the boundary layer causing a rise in dissipation coefficient and in turn of total losses. Also the recent work of Gakhara [10], solicits further research to address the effects of free-stream turbulence scales on the dissipation coefficient in the laminar boundary layer, and on laminar-turbulent transition. In addition, Gakhara [10] suggests to improve our fundamental understanding about the role of free-stream turbulence scales on: the anisotropy of turbulence withing the boundary layer, the extent of penetration of eddies into the boundary layer (and hence, loss generation), the generation and dissipation of mixing-losses in the wake and on the dynamics of vortical structures.

In line with these conclusions, few numerical works [11–13], using turbulence-resolved CFD simulations, emphasize how the transition location and mechanisms on the blade suction side results to be highly

sensitive to free-stream turbulence scales. The authors reported how the turbulence structures affect the turbulent mixing in the boundary layer such that the transition point and length vary, concluding that the response of the boundary layer to the free-stream turbulence levels depends strongly on the turbulence scales.

The interest to investigate experimentally the turbulence scales effects is particularly strong among the CFD community, since, according to Tucker [13], Dick and Kubacki [14] and Tyacke et al. [15], the lack of experimental data prevents attempts to properly model the role of turbulence in CFD simulations. As numerous experiments do not detail the turbulence scales, such values are too often left to guess or become free parameters to adjust, by the CFD users, the match with available experimental data, limiting thus the specification of the turbulence at the inlet CFD domain. In turbulence modeling simulations (RANS/ URANS) too often the length scale (indirectly captured by the turbulence decay behaviour of the turbulence models) is not seen an input to the simulation, but as a parameter to tune the predictions. However, different prescribed turbulence scales at the CFD domain boundaries would result in different dissipation rates with significantly altered the decay of turbulence that, in turn, strongly affect the flow evolution as reported by Babajee and Arts [16] and Bode et al. [17]. The arbitrary choice of the input turbulence scales is not justified, resulting often in turbulence models that do not correctly represents the flow physics (under/over predicted results) and in a severe mismatch with experimental evidence. For these reasons, it is evident the need to focus on a fundamental understanding of the physics behind the role of turbulence scales in internal flows and to align the accuracy of turbulence-modeled simulations with that of experiments.

What this paper wants to address is, therefore, the development of a new turbulence generator that add the possibility to study the role of turbulence scales, putting thus into evidence their isolated effects. To do that, such device has to be able at generating a wide range of turbulence with the peculiarity to set the turbulence intensity levels and yet tune the turbulence scales independently.

Review of Turbulence Generating Techniques

At the state-of-the-art, several methods for generating turbulence, other than the commonly used passive grids [18], have been presented in the literature with most of these techniques appearing in more recent decades. Turbulence generator methods can be broadly classified into wall jets [19], cross-flow injection [8], combustor simulator [1, 20], active grid [21] and jet grid [22–28]. Among these methods, the passive grids, where the generation of vorticity results from the presence of the flow blockage effects, can offer a well-defined experimental conditions, as they are widely used in a variety of experiments. On the other hand, the passive grids allow to cover the target turbulence intensities without, however, being able to control independently the turbulence length scales in the required range (for a fixed design). Wall jets, cross-flow injections and combustor simulator methods are able to achieve high turbulence levels having, however, inherent problem of a non-uniform mean flow field which makes it complex to apply to a turbine passage flow. Indeed, it is difficult for jets in normal or cross-flows direction to penetrate to the centerline of the test section. Although the homogeneity conditions can be improved, these methods are not take into account due to another limiting factor that is the relatively large size of these devices, as the useful space in test section of the cascade rig is limited. The active grid concept makes use of moving elements (rotating rods with agitator wings) to increase the turbulence levels in the flow field, resulting too complex and not suitable for the present project since it does not allow to control the length scales for a fixed turbulence intensity. Finally, the basic idea behind the jet grid concept is to supply momentum in the mainstream flow by using continuously, adjustable and distributed compressed jet injections. Although the main principle is to inject air by distributed jet injections, this concept also bases on the design of a passive grid. Therefore, a variation of the turbulence levels downstream of the grid is due to their combined effect: namely, interactions and mixing between the turbulent bar wakes and jet injections and the blockage effect of the passive grid. The air injections are blown from an auxiliary pressure system into a hollowed passive grid and injected through small injection holes in the upstream or/and downstream direction. On one side, the upstream jets can be used to control the boundary layer separation on the grid bars by reducing the wake width and consequently reducing the effective solidity and the static pressure drop of the grid. On the other side, downstream jets can smooth the downstream flow field (by filling in the bar wakes) for a better flow homogeneity or, if the jets are strong enough, make the bar wakes unstable (due to the additional shear in the jets themselves) to elevate the turbulence level.

Although at the state-of-the-art no information

were available on how to decouple turbulence intensity from the eddy sizes using a jet grid, the operating principle of this turbulence generator was of significant interest to this paper. Indeed, the jet grid concept looked the most promising in terms of generating a broad range of free-stream turbulence parameters showing the authority to be adapted for the independent control of turbulence scales so as to generate turbulent flow fields where the size of turbulent structure can systematically varied from the intensity. For these reasons we began developing this type of turbulence generator on the base of existing designs.

Jet Grids

As presented in literature, a wide range of different turbulence levels result as a consequence of different jet grid designs [22–28]. All these studies served as basis for the present paper to identify the main parameters driving the design of a new jet grid and the generated turbulent flow fields. However, the works by Young et al. [24], Bangert et al. [25] and Nix et al. [27] were of significant interest, since they highlighted three possible methods being able to independently control the length scales at fixed turbulence levels.

Young et al. [24] used a biplanar grid to inject air through evenly spaced holes either in upstream or downstream direction only. The turbulence decay rate, now also a function of the jet injection, is slower compared to a passive grid where the decay heavily depends only on the grid design and flow conditions. As pointed out by the authors, the turbulence level generated by the jet grid is always higher than a passive grid and its value increases as the injection ratio (or upstream or downstream) increases. In particular, with the same injection ratio and at the same downstream distance from the grid, downstream injection shows higher turbulence intensity than upstream. As the downstream injection increases, additional turbulence and shear of the jets themselves become more important resulting thus in an increase of the turbulence level. At higher injection ratio the jets become unstable and higher turbulence levels are observed, concluding that the jet injections penetrate a distance proportional to the relative jets strength. Unlike the downstream injection, upstream jets seem to increase the grid solidity and/or change its "effective position" and, with relatively small injection ratio, cause flow instability with a subsequent increase of the turbulence level and an effect more pronounced as the injection ratio increase. Finally, as the downstream distance from the grid increases, both upstream and downstream injection produce turbulence levels that converge to the same value (5%) but with different integral length scales (2cm vs. 1.5cm respectively). In light of these conclusions, the *method 1* plans to achieve, with a fixed grid position and at long downstream distance, the same turbulence intensity but with different length scales by separately using the turbulence decay of upstream and downstream injection, as shown in Figure.

The research of Bangert et al. [25] developed a method for generating free-stream turbulence with simultaneous upstream and downstream injections. By adjusting the jet grid design and injection ratio, this turbulence generator produced a turbulence intensity up to 20% and an integral length scale within 2.1 cm and 5.5 cm. Although the preliminary experimental characterization showed promise in generating thigh turbulence levels with upstream injection only, this type of designs caused poor flow homogeneity (grater than downstream injection ± 10%) and the final design was based on simultaneous injection. Also in this case, the turbulence levels for the jet grid were much higher that the passive grid and the turbulence decay is slower. The principle behind the *method 2* is base on the displacement of the jet grid in different position. Indeed, as shown in Figure, by fixing the grid geometry and testing different injection ratio, the obtained turbulence decay curves show the same turbulence level at different downstream distances. Therefore, by adjusting the grid position to obtain the same turbulence intensity imply that the resulted length scales are different.

The *method 3* is obtained from the outcomes of Nix et al. [27], where the authors opted for a jointly use of upstream injection to increase the shear stress for elevating the turbulence level, and downstream injection to fill in the wake behind the bars for a better flow uniformity. As shown in Figure, starting from a passive grid configuration, as the injection is activated and increased, a first decreasing of the turbulence intensity is observed, followed by a steady increase with a continue increase of the injection ratio. The first decreasing, in agreement also with the results reported by Boyle et al. [26] and Gad-el-Hak and Corrsin [22], is a result of a fill up of the wakes behind a grid bar and in literature is only reported for large bar diameter where the effects of the boundary layer development is higher. Therefore, with this method it is possible to obtain at the same downstream distance (close to the grid) the same turbulence intensity but different length scales only by adjusting the injection ratio.

In general, most of the literature results about the

influence of the injection ratio on the turbulence parameters trend are in agreement. For a fixed jet grid geometry, the characteristics curve of the turbulence intensity tends to move to higher values of intensity and at higher downstream distance as the injection ratio increases. It means that, with an increment of the injection ratio is possible to obtain higher turbulence intensity but at higher downstream distance. In the other way around if the injection ratio is decreasing the characteristics curve of the turbulence intensity tends to approach the passive grid configuration. Measurements of the integral length scale show that, with growing distance from the grid the smallest eddies dissipate and the integral length scale growth downstream, even more by increasing the injection ratio.

3. Turbulence Jet Grid Development

The purpose of this section is to highlight the step-by-step procedure that was followed to develop the jet grid concept. From an extensive analysis of the literature evidences [22–28], the main parameters that was identified to drive the design was: the geometry and size of the bars, the array setup of the grid, the size and position of the jet holes along the bars, and the ratio and direction of the jet injection. It is important to note that, unlike a passive grid design, nowadays no empirical correlations exist to follow for designing "a priori" a new jet grid, as most of the effects due to the jet injection are strictly correlated to design itself and test conditions. Therefore, only after the experimental characterization will be possible to validate the choices made and iterate on the final design.

The design process of the jet grid has been put into prospective with the target turbulence values that what we want to reproduce for future experimental campaigns in the VKI C-1 low-speed cascade rig, where the test case will be a turbine flow passage with loading representative of a state-of-the-art low-pressure turbine. The desired free-stream turbulence regimes, representative of turbulence values encountered by a broad class of turbine systems, involve turbulence intensities between 1% to 15% and integral length scale within the range of 5%-20% of the turbine blade chord. Bearing in mind both the constraint imposed by the C-1 test section and the target testing conditions, the early-stage of the design process has been dedicated to obtain the best compromise between varying the blade chord length and:

- maximize the size of the turbulence length scales to be generated and consequently improve the measurement resolution,
- maximize the flow periodicity,
- ensure two-dimensional flow conditions at the mid-section of the blades,
- maximize the measurement resolution,
- maximize the pressure rise so that to maximize the pressure differential to be measured.

Indeed, decreasing the blade chord length decreases the size of the turbulence length scales to generate, which are in turn limited by the design constraints of the jet grid. Moreover, smaller turbulence length scales increase the uncertainty of the measurement. Again, to maintain a pitch-to-chord ratio to value representative of modern low-pressure turbine, low blade chord length decreases the cascade pitch for a better flow periodicity (high number of blades) and increases the aspect ratio for an improved distinction between 2D and 3D flow phenomena. On the other hand, to test at the target Reynolds numbers (within the range 50-250k), the pressure rise requested to the facility increases, resulting in the possibility of exceeding the limits imposed by the performance of the C-1 wind tunnel. Moreover, the spatial resolution of the measurement instrumentation has to be improved to capture and to be sensible of smaller turbulence structures. On the contrary, high blade chord length allows the jet grid to easily reproduce higher integral length scales, which results in improved measurement resolution. Increasing the blade chord length reduces also the pressure rise needed to attain the target Reynolds number and allows a better measurement resolution. However, increasing the chord length leads to a poor flow periodicity (low number of blades) and an aspect ratio that may not ensures two-dimensional flow conditions in the midsection of the blades. Indeed, the end-walls flows generate a huge flow recirculation regions on the blade suction surface which may mix with the midsection flow phenomena. From this analysis, the best compromise is identified in a blade chord length of 75 mm, resulting in a target range of integral length scales within 3.5-15 mm, as shown in Figure 1.

Accordingly to this target turbulence range and the compatibility of the jet grid with the VKI C-1 rig, the design process move through a parametric study of the literature evidences, where the geometry and size of the bars have been varied to optimize all possible jet grid design configurations to meet the project-defined

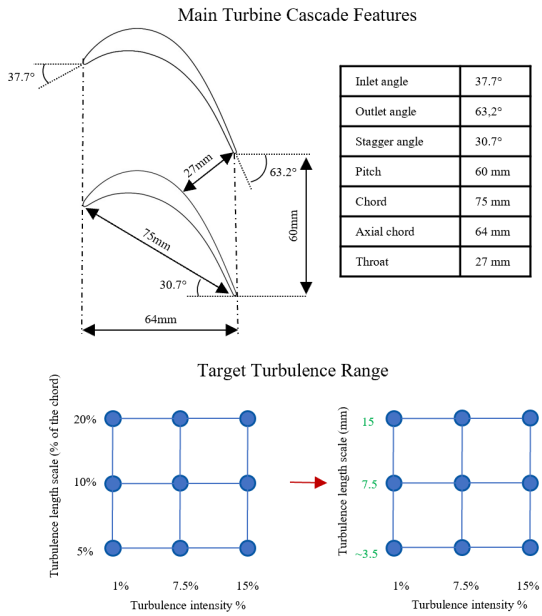

Figure 1: Turbine test case (above) and target turbulence range.

requirements and constraints. The size of the bars has been ranged within from small (5mm) to large (20mm) diameter, whereas the geometry has been varied between a circular and square shape. The choice of the bar shape influences the flow separation and the wake shed downstream of the grid, and consequently his fluid-dynamic solidity and pressure drop. A sharpness of the edges of a square bar shape is less sensitive to variation of the Reynolds numbers and it has a more stationary separation point and wake shape [22], however it produces a more pressure drop with higher turbulence intensity. On the contrary, a circular bar shape generates lower pressure drop and turbulence intensity but, it shows a separation location that depends strongly on the Reynolds number [29], producing more periodic turbulence structure and resulting more inclined to instabilities when the experimental campaigns will vary the Reynolds number. This parametric study can be summarized in the following three steps:

1. the examined bar geometry and shape is found among the literature evidences, seeking to match it with at least one existing jet grid design. The matched design become the baseline on which make the analysis,
2. on the baseline design are applied the methods discussed above that, together with the application of the spatial constraints (some methods involve the displacement of the grid) of the C-1 rig test section, return the turbulence range achievable,
3. following the turbulence parameters trend, resulted by increasing or decreasing the jet injection and/or the bar spacing of the grid, a new scenario is obtained where the baseline design can achieve other turbulence values.

The above steps have been applied for each combination of bar shape and size. When a match with an existing literature designs was not found, an interpolation of data was done to reconstruct the potential turbulence ranges achievable. Note that, while the circular bar shape is commonly used for jet grid design, square bar shape is only used in few experiments. Too few to extract a general trend of the generated turbulence parameters and, therefore, correlations reported by Roach [18] for square passive grids are used to set at least a starting point to predict the turbulence range accessible. The outcomes of this analysis have highlighted that the most promising configurations allowing to cover the target turbulence regimes are three, as reported in Table 1.

	Geometry		*Turbulence Range*	
Conf.	**Shape**	**Size [mm]**	**Intensity**	**Length Scale**
A	Circular	5-7	2-8%	4-10mm
B	Square	5-7	7-15%	4-10mm
C	Circular	9-11	5-11%	8-15mm

Table 1: Promising configurations in terms of bar shape and size.

At this point, the existing jet grid designs has been examined from the point of view of the grid setup. Examination of the experimental evidences shows that a specific design of the grid geometry mainly drives the generated turbulence, as both the pressure losses introduced by the grid and the flow instabilities found downstream scales on the grid array and mesh geometry. Since the turbulence energy generated by a grid is directly related to its design, this study began by fixing the grid array and mesh geometry so as to remove a degree of freedom during the design, focusing thus the study at controlling the turbulence length scales through the only variation of the jet injection and the grid position of the jet grid. By analysing literature evidences, the static pressure drop ΔP of jet grids may be correlated by the equation:

$$\frac{\Delta P}{q} \approx A\left(\frac{\sigma}{1-\sigma}\right)^2 + 2J^2\left(1 + \frac{2}{J} \pm R\right) \qquad (1)$$

where q is the upstream dynamic pressure and σ is the grid solidity. Referring to the Figure 2 the solidity is defined as $\sigma = \frac{A_0 - A}{A_0} = 1 - \beta$, where the porosity β is reported for square-mesh and parallel-mesh array (d is the bar diameter and M the mesh). R is the area ratio, $\frac{A_0}{A_j}$.

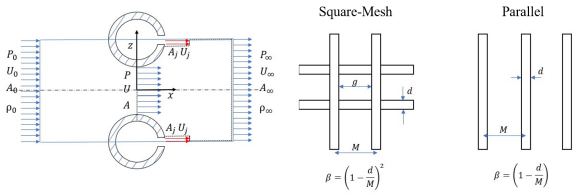

Figure 2: Jet grid representation (left) and grid array setup (right).

When there is not injection ratio, $J = 0$, the equation 1 reduces to $\frac{\Delta P}{q} \approx A\left(\frac{\sigma}{1-\sigma}\right)^2$, as already derived in literature for a passive grid. As reported by Gad-el-Hak and Corrsin [22], an empirical constant, A, multiplied the first term which is function of Reynolds number, Mach number and grid geometry (aerodynamic solidity). Since low pressure drop is given by a parallel-mesh array, the grid is designed based on this setup, choosing in particular an horizontal direction which is coherent with the cascade blade span found in the C-1 low speed rig. In addition, evidences suggest that significant flow instabilities in the wake region of the grid might arise for grid solidity greater than 50%. Since typical values range between $20 - 40\%$, a solidity of around 33% is chosen to allows possible future variations of $\pm 10\%$ without having flow instabilities. Knowing that the solidity is defined as $\sigma = 1 - \beta$, where $\beta = 1 - \frac{d}{M}$ is for parallel-mesh array, this means that the mesh to diameter ratio, $\frac{M}{d}$, is set to 3. Therefore, to match the design constraint of the L-12 test section, the jet grid consists of two configurations of 10 and 6 horizontal-parallel bars for bar diameter of 6 and 10 mm respectively.

Considerable attention has been given to the design of the jet holes, namely, the number, the spacing and the diameter. This because both the flow uniformity of the jet and the jet injection are in function the the jet holes design. As shown in Figure, three different scenario can be arise for the flow uniformity of the jet injections.

In the scenario A, the friction terms due to the inner wall dominate the inertial pressure recovery, which is due to the fact that the flow remaining within the pipe

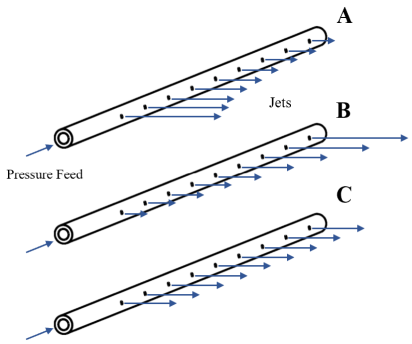

Figure 3: Three possible scenario occurring for the jet injection.

is decelerated along it with a subsequent pressure rise. In this condition, higher flow is biased toward the feed end of the pipe. On the contrary, the scenario B shows as the flow is biased toward the the end of the pipe when the inertial pressure recovery term dominate the friction. To obtain an ideal flow distribution downstream of the grid (scenario C), the inertial pressure recovery and the friction terms have to be balanced. A theoretical models have been used to analysis the perforated pipes.

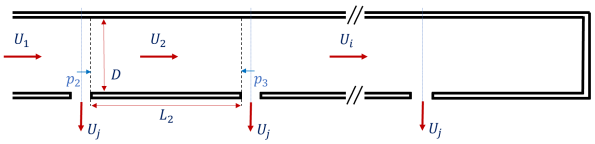

Figure 4: Schematic of the injection pipe.

Referring to the Figure 4, assuming a negligible variation of the density along the injection pipe the pressure rise across a jet hole is:

$$p_{i+1} - p_i = K\rho\left(U_i^2 - U_{i+1}^2\right) \tag{2}$$

where K is the outlet coefficient which considers that the outlet velocity is not totally perpendicular to the pipe, meaning that the pressure variation across the jet holes is only a fraction of an ideal value, $0 < K < 1$. Assuming also an equal distribution of the outlet velocity between n jet holes, $U_i = U_1\left(1 - \frac{i-1}{n}\right)$, the inertial pressure recovery can be written as:

$$p_n - p_1 = K\rho \sum_{i=1}^{n}\left(U_i^2 - U_{i+1}^2\right) = K\rho U_1^2\left(1 - \frac{1}{n^2}\right) \tag{3}$$

Now, by using the Darcy-Weisbach friction factor, f, the pressure loss due to friction between two subsequent jet holes is:

$$p_i - p_{i+1} = \frac{\rho f U_i^2}{2} \frac{L_i}{D} \tag{4}$$

and,

$$p_1 - p_n = \frac{\rho f}{2} \frac{L}{Dn} \sum_{i=1}^{n} U_i^2 = \frac{\rho f}{2} \frac{L U_1^2}{Dn} \sum_{i=1}^{n} \left[\frac{n-(i-1)}{n} \right]^2 \tag{5}$$

Therefore, the balance of the total pressure along the pipe can be written as:

$$\Delta P = \rho U_1^2 \left(\frac{fL}{2D} A - KB \right) \tag{6}$$

where the constant A and B are defined as follow:

$$A = \sum_{i=1}^{n} \frac{1}{n} \left[\frac{n-(i-1)}{n} \right]^2$$
$$B = \left(1 - \frac{1}{n^2} \right)$$

At this point, the goal is to minimize the maldistribution of the jet injections along the pipe. Defining the maldistribution as the percentage variation in jets between the first and last holes, clearly, the pressure variation due to the friction and inertial pressure recovery, ΔP, must be lower than the pressure drop across the holes, ΔP_h, which is defined as $\Delta P_h = \frac{1}{c_d^2} \frac{\rho_h U_h^2}{2}$, where $c_d \approx 0.62$ accounts both for friction and turbulence mechanisms and the approximation of the properties downstream of the orifices. A reasonable value of 5% maldistribution leads to:

$$5\% = 1 - \sqrt{\frac{\Delta P_h - |\Delta P|}{\Delta P_h}} \rightarrow \Delta P_h = 10 \Delta P \tag{7}$$

and substituting all the terms:

$$\frac{\frac{1}{c_d^2} \frac{\rho_h U_h^2}{2}}{\frac{\rho U_1^2}{2} \left| \left[\frac{fL}{D} A - 2KB \right] \right|} = 10 \tag{8}$$

For a number of jet holes greater than 8 the constants A and B are tend to the constant values 0.35 and 1 respectively. The value of K is difficult to assume a priori, however, from literature evidences a value in the order of 0.5 is assumed for discharge manifold. For the expected value of the velocity at the inlet section of the pipe, the Darcy-Weisbach friction factor, f, is assumed ≈ 0.01. The values of $\frac{L}{D}$ are fixed accordingly to the design constraints of the L-12 rig and the bar diameters seen above. Taking into account these approximations, the term $\left| \left[\frac{fL}{D} A - 2KB \right] \right|$ is ≈ 1. Moreover, introducing the definition of the mass flow rate the Equation 8 become:

$$\frac{A_1}{A_h} = \sqrt{10} c_d \sqrt{\frac{\rho_h}{\rho_1}} \tag{9}$$

Referring to the external diameters as reported in Table 1 and assuming a reasonable value for the density ratio across the jet holes, the holes diameter has been computed as 1.1 and 2.1 for bars diameter of 6 mm and 10 mm respectively, resulting in agreement with the existing jet grid designs that report values of the hole-to-diameter ratio ranging between $0.08 - 0.3$. Finally, to match the design constraints of the L-12 test section with the above analysis, the jet holes spacing has been chosen to be 25 mm (the typical values encountered in literature are between $20 - 40$ mm), leading thus to 8 jet holes per bar.

The last analysis is related to the main design parameters: injection ratio and the blowing direction. In reference to the Figure 2, the injection ratio is defined as the ratio of injected mass flow to the mainstream mass flow, $J = \frac{\rho_j A_j U_j}{\rho_0 A_0 U_0}$. The pressurized tubes consist in evenly distributed jet injections, where each tube are connected to a plenum that is pressured by an auxiliary pressure system. In this work, the same type of tube can be integrated in the grid in different ways, namely: for passive grid applications, to inject the flow simultaneous in the upstream and downstream direction [25, 27] or to inject the flow in separated direction at a time [22–24, 26, 28]. This it was thought to characterize the jet grid with respect to possible different uses and to validate the methods described above for the generation of a wide range of turbulence levels. For each of these testing conditions, the plenum to back pressure ratios, P_p/P_{bp}, can be varied to allow both non-choked and choked flow conditions of jets. In the former case, the injection ratio can be set by varying the back pressure of the facility (variation of U_j) or the plenum pressure for the mass flow rate of the injection jets:

$$\dot{m}_j = c_d A_j \sqrt{\gamma \rho_{t1} p_{t1} \left(\frac{2}{\gamma - 1}\right) \left(\frac{p_2}{p_{t1}}\right)^{\frac{\gamma+1}{\gamma}} \left[\left(\frac{p_{t1}}{p_2}\right)^{\frac{\gamma-1}{\gamma}} - 1\right]} \tag{10}$$

where, unless of pressure drops, $P_p \approx p_{t1}$ and $P_{bp} \approx p_2$. In flow condition, the mass flux ratio can be set only by varying the plenum pressure for the mass flow rate of the injection jets:

$$\dot{m}_j = c_d A_j \sqrt{\gamma \rho_{t1} p_{t1} \left(\frac{2}{\gamma + 1}\right)^{\frac{\gamma+1}{\gamma-1}}} \tag{11}$$

Considering the choices made for the jet grid design, the test conditions and, the limitation of the L-12 facility to a 7-bar pressure line, have been computed the plenum pressure needed to meet the target injection ratios. The outcomes are summarized in Table 2, together with all the design parameters.

	Configuration A	*Configuration B*	*Configuration C*
Array Setup	Parallel	Parallel	**Parallel**
Bar Shape	Circular	Square	Circular
Bar outer size	6 mm	6 mm	10 mm
Bar inner size	4 mm	4 mm	8 mm
Bar Spacing M/d	3	3	3
Mesh	18 mm	18 mm	30 mm
Number of bars	10	10	7
Hole diameter	1.1 mm	1.1 mm	2.1 mm
Hole spacing	25 mm	25 mm	25 mm
Number of holes per bar	8	8	8
Intensity range	2 - 8 %	7 - 15 %	5 - 11 %
Length scale range	4 - 10 mm	4 - 10 mm	8 - 15 mm
Pressure supply	1.1 - 5 bar	1.1 - 5 bar	1.1 - 2.5 bar
Injection ratio	1 - 3 %	1 - 3 %	2 - 5 %

Table 2: Summary of the jet grid designs.

4. Design of the Experiment

Experimental facility

The L-12 wind tunnel of the von Karman Institute for Fluid Dynamics is used to characterize the jet grid design and the relative turbulence generation methods. The L-12 rig, reported in Figure 5, is a low speed, open circuit wind tunnel having a contraction ratio of 5.76:1, and a test section designed in plexiglass parts with 0.2m x 0.2m cross section and length of 1 m available. A centrifugal blowing fan is used to push air in the test section with a maximum free-stream velocity of almost 20 m/s with a background turbulence level of about 0.3%. This rig is primarily designed to allow rapid and cost-effective testing of low speed flows, and it is used mainly for laboratory training for boundary layer investigation, three-dimensional velocity measurements, calibration of instrumentation and PIV experiments. The lab is equipped with a 7-bar pressure feed allowing to feed the jet grid. In addition, the L-12 wind tunnel is chosen for its ability to provide easy optical access and modify easily the test sections to accommodate different jet grid designs.

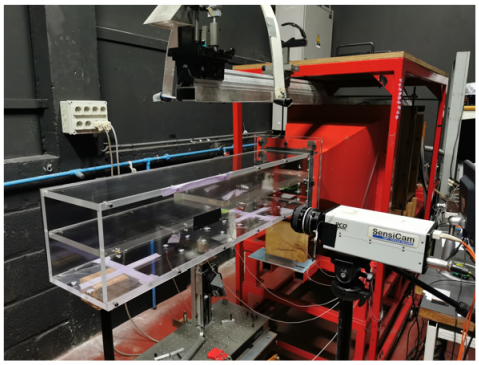

Test Section	20 cm X 20 cm X 100 cm
Maximum Freestream velocity	< 20 m/s
Background Turbulence	0.3 %
Pressure line	7 bar

Figure 5: VKI L-12 low-speed wind tunnel setup.

The idea behind the integration of the jet grid generator concept in the test section is to design an additional section to be added between the end of the contraction and the current test section for two main purposes, namely, to improve the turbulence development and its measurement by increasing the length of the channel and to allow a modular design of the sidewalls to arrange different jet grid configurations. In this sense, the conception of the jet grid was thought as a cassette where the bars, arranged in a horizontal parallel-mesh, are passed in crosswise direction through a slot on the sidewalls of the extension, designed to be compatible with all the jet grid designs. The compatibility is given by coupling the same sidewalls with three couple of supports to assembly different jet grid configurations. Since these slots could be a source of pressure losses/leakage flow, a sealing gasket will be place into a groove designed around the jet grid supports. Similar plexiglass parts of the current test section are used to design those of the extension. Referring to Table 2, except for configuration A and B where, based on literature evidences, the turbulence is supposed to decay in 70 cm, the configuration C needs to be tested in a test section with a channel length of about 110 cm. For this reason, an extension length of about 30

cm is chosen, which is added to the already existing 1 m length. CAD software is employed to digitally support the conception and design of the extension and all the auxiliary parts, as shown in Figure.

The pressure injection into the bars takes place via a pressure line composed by: the 7-bar pressure feed, a plenum and pipelines. The pressure feed will be connected by a pipeline to a plenum chamber that has the main function to equalize the pressure for a more even distribution among the outlets. Indeed, it will be designed relatively large in volume where the air initially resides approximately at rest, and thus has relatively low velocity compared to the outlet pipelines. The contribution to properly design a plenum chamber for an even distribution, and thus to produce a good airflow quality, is often not known. In general, literature reports that the bigger the chamber is the more even the airflow will be. Then, metal sheets are cheap and providing a sufficient plenum chamber is often a simple and cost-effective way to improve air distribution. Gad-el-Hak and Corrsin [22] design a plenum duct with a volume 5 times the volume of the bars, while O'Brien and Van Fossen [23] and Boyle et al. [26] 3 and 2 times respectively. Moreover, open literature reports some guidelines to design a plenum (for air systems): there must be one or more outlet diameter between the inlet and outlet flows, the width of the plenum has to be twice or more the inlet diameter and, the outlet flows have to be on the sides. The plenum will be supplied with compressed air by the pressure feed at gauge pressure: according to the analysis described above, the nominal pressure needed to achieve the target turbulence range between $1.1 - 5$ bar, giving no- and conditions to the jets. To ensure a proper nominal pressure inside the plenum, the pressure feed will be regulated by its own valve and pressure measurements will be performed at the plenum outlets. Each bar is connected by using flexible silicone tubing to the plenum, as is possible throttle and control the flow rate in each bar by squeezing the end of each flexible tube (before entering the hollow bars) with a clamping ring. The bars, made in aluminum, are slightly longer (30 cm) than the test section width (20 cm) so that to allow on one side the air feeding and on the other the measurement through pressure taps.

Jet grid testing are performed to match the conditions found in C-1 cascade rig. At such extent, the main scaling parameter is chosen to be the Reynolds number computed with respect to the grid geometry (bar diameter or mesh). Therefore, the L-12 testing conditions are set ranging the freestream velocity between $5 - 17$ m/s at ambient conditions.

Measurement techniques and planes

The experimental campaign aims to characterize the turbulence downstream of the jet grid as a result of the interactions and mixing between the mainstream flow and jet injections, focusing in particular at controlling the turbulence length scales through the variation of the jet injection and the grid position of the jet grid. The flow features to be characterize are:

Homogeneity and isotropy degree

Homogeneous turbulence is obtained if the property of invariance under spatial translations [30] is satisfied:

$$u_{rms}(\vec{x}_1, t) = u_{rms}(\vec{x}_2, t) \tag{12}$$

In other words, homogeneous turbulence is determined if the turbulent fluctuations are statistically the same at all the points of the flow field. It is often experimentally verified as having relatively constant mean velocity and subsequent constant turbulence intensity profiles, u_{rms}/U , at different traverse planes. In the present experimental campaign, the homogeneity degree should be assessed measuring the streamwise velocity components along different crosswise planes downstream of the jet grid.

Turbulent flows can be considered isotropic if their local statistics of the turbulence fluctuations have the same intensity in all directions [30], i.e. they are invariant under mirroring and axial rotation:

$$u_{rms}(\vec{x}, t) = v_{rms}(\vec{x}, t) = w_{rms}(\vec{x}, t) \tag{13}$$

where v_{rms} and w_{rms} are the root mean square of the velocity fluctuations in crosswise direction with respect to the streamwise direction. Homogeneous and isotropic turbulence (HIT) has same statistical properties in each direction and spatial location. A way to prove the homogeneity of the flow is to show the absence of both turbulent kinetic energy production and transfer among the crosswise fluctuating velocity components, meaning that the flow is shearless (transverse gradients are zero) [31]. Therefore, the ratio w_{rms}/v_{rms} constitutes a measure of the homogeneity degree and a value ideally equal to the unity is expected for homogeneous flows, however value of about 1.2 is found in literature [31]. From the definition, the global isotropy ratio, u_{rms}/v_{rms}, should be the

parameter that defines the change from anisotropic to isotropic flow. Typical values in the range of 1.2-1.4 are found in literature for isotropic flows [32]. Moreover, if the turbulent flow is nearly homogeneous and isotropic then the probability density function should be approximately Gaussian [31], and the PDFs should collapse for different positions in the flows. Therefore, a deviation from a normal probability density function (analysed by means the third and fourth high-order statistics) may be thought as a deviation from the equilibrium itself and thus, the turbulent flow should not be considered neither homogeneous nor isotropic.

Turbulence intensity and length/time scales

Turbulence spectrum is used to characterize turbulence, describing how and how much energy is distributed among eddies of different sizes. On one side is defined the turbulence intensity to quantify how much energy is present in the turbulence and on the other side is defined the length and time scales to quantify the size and frequency of the energy-containing eddies. By measuring at different downstream position from the jet grid both intensity and length/time scales, the turbulence decay can be estimate. To define the level of turbulence in the flow is used:

$$Tu = \frac{\sqrt{\frac{2}{3}k_t}}{U} \tag{14}$$

where the turbulence kinetic energy is defined as: $k_t = \frac{1}{2}(u^2_{rms}+v^2_{rms}+w^2_{rms})$ and U the flow mean velocity. In the case of isotropic flow, turbulence fluctuations have the same intensity in all directions, $k_t = \frac{3}{2}u^2_{rms}$, consequently:

$$Tu = \frac{u_{rms}}{U} \tag{15}$$

To understand the process of energy production and dissipation that occurs in turbulent flow fields must be characterized from the largest (integral) to smallest (Kolmogorov) turbulence scales. The largest eddies are influenced by the geometry and the boundary conditions and they are responsible for the energy transport and mixing. On the contrary, the smallest scales are only influenced by local properties, such as the viscosity and the rate at which the turbulent kinetic energy (TKE) is transported and dissipated in internal energy. Roughly speaking, the integral length scale is used to define the size of the largest eddies in the turbulent flow field. This characteristic length is related to the space correlation coefficient as:

$$L_{ij} = \int_0^\infty R^S_{ij}(\mathbf{r}, t)dr \tag{16}$$

The integral time scale can be computed in the same way by using the time correlation coefficient as:

$$T_{ij} = \int_0^\infty R^T_{ij}(\mathbf{x}, t)dt \tag{17}$$

Considering the most practical methods to compute these quantities:

1. Spatial correlation function can be achieved by using probes array in the flow field. However, the Taylor's hypothesis of frozen turbulence makes possible the relation between the correlation in time and space through a displacement velocity. Then, by measuring with an hot-wire anemometer a velocity component at just one spatial point, the integral length scale is computed multiple the integral time scale by the mean velocity of the flow field: $L_{ij} = U\int_0^\infty R^T_{ij}(\mathbf{x}, t)dt$.
2. The power spectrum obtained from an hot-wire anemometer can be used to extrapolate the value of the power spectrum at zero frequency that results proportional to the integral time scale, $E_{ii}(0) = (u'_i u'_i)/\pi T_{ii}$, and experimentally to the integral length scale, $\Lambda = \left[\frac{E(f)U}{4\overline{u^2}}\right]_{f\to 0}$.

However, one must be careful measuring the integral time and length scales with each of these methods because of their pitfalls. The first method, that makes use of the Taylor's hypothesis and is based on the autocorrelation function, suffers from wide oscillation due to the nature of turbulence. It is clear that, when it is computed a numerical integration of the time correlation, where the autocorrelation function presents negative undershoots around zero, the integration yields to a numerical cancellation and to an erroneous estimation of the time scale and consequently of the integral length scale. Furthermore, while equation to compute the time scales involves the determination of the integral over an infinite domain, the domain of the autocorrelation function from experimental or numerical data is finite, and there is some uncertainty on how best to define the integration domain. However, there are different methodologies presented in literature [33] to compute time scales from the autocorrelation function by using numerical integration: (A) use as the upper limit of the integration the first zero crossing or the first negative minimum of the autocorrelation function, (B) integrate a fit of

the autocorrelation function, (C) integrate the autocorrelation function up to the time when the function reaches the value e^{-1}. The second method is an alternative to compute the turbulence length scale based on the power spectral density function. In theory, methods 1 and 2 are equivalent since the autocorrelation is the transform of the turbulence spectrum. Therefore, the integration and converge problem for the autocorrelation function now is substituted by the form of inaccuracies when dealing with low frequency to compute the spectrum [33]. Typically, the spectrum is extrapolated back to zero frequency by using frequencies above those, corresponding to scales that are physically possible in experiments. Generally, the energy associated to the lower frequency is almost constant and an average of the first frequencies is lead to a reliable estimation of $E(0)$ [34]. Concluding, Lewalle and Ashpis [35] report that the results from methods 1 and 2 are in good agreement, computing around 10% (for the longitudinal integral length scale) to 20% (for the lateral integral length scale) discrepancy. This discrepancy is accounted for by incomplete convergence in the tail of the autocorrelation function and in the low-frequency portion of the turbulence spectrum.

Jet Injection (jet velocity and uniformity)

The air passing through the jet holes can be treated as simple turbulent round free jets since the jet flows into a large space (compared to holes area) being most likely turbulent, carries no additional thermochemical effects (such as density variation, heat release ...) and operates with a simple round nozzle. Measurement of the velocity field at the outlet of the jet holes can be used to provide information useful for the computation of the jet injection and uniformity. Although the hot-wire anemometry technique provides information only at several points, can be used to provide continuous signals of local velocity information as well as information on turbulence properties.

Grid Pressure Loss

The introduction of the jet grid in the main flow field will cause a pressure drop as a function of the design and of the jet injection. Since the pressure drop is defined as the difference in total pressure between two points of a fluid carrying network, the measurement will be done both upstream and downstream of the jet grid, as reported by Nix [27]. On the other hand, Gad-el-Hak and Corrsin [22] characterized the mean drop in static pressure across the grid by experimentally measuring the static pressure at the sidewall both upstream and downstream of the grid. A good pressure distribution (along and among different jet grid bars) is also important to return a good flow uniformity in the channel. Then, by measuring the pressure distribution at different jet holes, in tandem with and jet flow velocity, an estimation of the flow uniformity can be done.

Based on what reported, the test section is instrumented to measure the wind tunnel operating conditions, the jet grid upstream flow, the endwall static pressure distributions, the jet grid downstream flow, the total pressure loss and turbulent flow structures. The instrumentation used for the jet grid characterization are the following:

- Triple hot-wire anemometer. Triple sensor hot-wire from Dantec Dynamics (tungsten wires with diameter of 9 μm and dynamic response of abouth 15 kHz) is traversed in stream- and cross-wise directions at different position both upstream and downstream of the grid. Velocity data from the hot-wire serve to locally characterize: the background turbulence of the wind tunnel, the jet injection and uniformity and, energy spectra and features of turbulence (decay, intensity, length scales, and homogeneity and the isotropy degree),

- Time-resolved particle image velocimeter. Hot-wire measurements are complemented by time-resolved optical PIV measurements in 2D streamwise planes at different downstream distances from the grid to characterize the velocity field and turbulent structures. Two point-correlation PIV and hot-wire measurements is used also to very that Taylor's hypothesis is valid for high turbulence levels.

- Aerodynamic pressure probe. Pitot probe is traversed in crosswise directions to monitor the total and static pressure at both upstream (various axial location from the contraction) and downstream (different planes) section of the jet grid,

- Wall pressure taps. A row of 5 pneumatic taps are positioned upstream and downstream of the grid to monitor the wall static pressure.

As a first step, tests of the wind tunnel performance without the jet grid is performed with the purpose to return a reference value for: background turbulence, mean velocity, total and static pressure. Then, tests are

performed with the jet grid both at the plane of the grid (characterizing the flow uniformity, pressure distribution, jet injection and flow patterns around bars) and downstream (characterizing the turbulent flow fields and the grid pressure drop). The measurement matrix is summarized in Table 3 together with the measurement planes. X indicates the axial location where 0 is the end of the contraction and 130 the end of the test section, S the streamwise plane and C the crosswise planes (y and z directions).

	Plane	***Probe***	Measurement Matrix
W/O Jet grid	Upstream	Triple hot-wire	X= 0 - 10 (Pitch 2cm) S= Centerline
		Pitot probe	X= 5 $C_{y,z}$= 0 - 20 (Pitch 2cm)
		Pressure taps	X=3
W/ Jet grid	Jet grid	PIV	X=10 S= Centerline 2D Planar
		Triple hot-wire	X=10 (in front of jet holes) $C_{y,z}$= 0 - 20 (Pitch 0.5cm)
		Pitot probe	X=10 (in front of jet holes) $C_{y,z}$= 0 - 20 (Pitch 1cm)
		Pressure taps	X= end of the bar
	Downstream	PIV	X=15, 25, 25 S= 2D Planar
		Triple hot-wire	X=20 - 130 S= Pitch x/d=10 $C_{y,z}$= 0 - 20 (Pitch 0.5cm)
		Pitot probe	X=20, 30 $C_{y,z}$= 0 - 20 (Pitch 1cm)
		Pressure taps	X=17

Table 3: Summary of the measurement matrix.

Test matrix

There are three jet grid designs to be characterized and for each of these all the configurations are analysed, namely: passive, active in simultaneous upstream and downstream directions and, active with separated directions at a time. The influence of the injection ratio is tested by varying it between 1.1 – 5 bar.

5. Conclusions

Literature survey highlights the evident need to improve the fundamental understanding of the physics behind the role of turbulence scales on the aerodynamics of bladed-passage flows, so as to better quantify the turbulence effects on the loss generating mechanisms and to align the accuracy of turbulence-modeled simulations with the experiments. A review of the state-of-the-art in turbulence generation has identified several techniques to produce a wide range of turbulence levels, however, only a concept provides the chance for the independent control of turbulence scales: the turbulence jet grid. An extensive analysis of the main jet grid studies return three possible methods allowing to vary the length scales independently from the turbulence intensity as a result of: (1) different injection direction for different turbulence decay, (2) adjusting the injection ratio for different grid positions, (3) continuously variation of the injection ratio with a fixed grid position. In this work, turbulence jet grids capable of ranging from low to high turbulence levels (1-15%) with minimum pressure losses and a low degree of non-uniformity (5%) was successfully designed for a low-speed wind tunnel having a small cross-sectional area. A key feature for the development of this turbulence generator was that the independent control of the integral length scales within the range of 3.5 – 15 mm. The jet grid designs used a horizontal-parallel array of active elements in which non-choked or choked jets are injected in both upstream and downstream directions. Together with the description of the design and scaling parameters, a detailed picture of the future experimental campaign aimed to validate the jet grid designs were documented. The design of the experiment described in detail the experimental facility and the instrumentation used, the measurement techniques, planes and matrix employed and, finally the test matrix planned.

Acknowledgments

This work was sponsored by the von Karman Institute for Fluid Dynamics, monitored by Prof. Sergio Lavagnoli. I would like to thank Prof. Koen Hillewaert at University of Liege for his help and insight into developing the turbulence generator. I would to thank also Prof. Fabrizio Fontaneto, who sponsored the purchase of the instrumentation.

References

[1] Ames, F. E., The Influence of Large-Scale High-Intensity Turbulence on Vane Heat Transfer, ASME Journal of Turbomachinery 119 (1) (1997) 23 – 30.

[2] Carullo, J. S. and Nasir, S. and Cress, R. D. and Ng, W. F. and Thole, K. A. and Zhang, L. J. and Moon, H. K., The Effects of Freestream Turbulence, Turbulence Length Scale, and Exit Reynolds Number on Turbine Blade Heat Transfer in a Transonic Cascade, ASME Journal of Turbomachinery 133 (1) (2011) .

[3] Wang, H. P. and Goldstein, R. J. and Olson, S. J., Effect of High Free-Stream Turbulence With Large Length Scale on Blade Heat/Mass Transfer, ASME Journal of Turbomachinery 121 (2) (1999) 217 – 224.

[4] Butler, R. J. and Byerley, A. R. and Van Treuren, K. and Baughn, J. W., The Effect of Turbulence Intensity and Length Scale on Low-Pressure Turbine Blade Aerodynamics, International Journal of Heat and Fluid Flow 22 (1) (2001) 123 – 133.

[5] Mahallati, A. and Sjolander, S. A., Aerodynamics of a Low-Pressure Turbine Airfoil at Low Reynolds Numbers—Part II: Blade-Wake Interaction, ASME Journal of Turbomachinery 135 (1) (2013) .

[6] Mahallati, A. and McAuliffe, B. R. and Sjolander, S. A. and Praisner, T. J., Aerodynamics of a Low-Pressure Turbine Airfoil at Low Reynolds Numbers—Part I: Steady Flow Measurements, ASME Journal of Turbomachinery 135 (1) (2013) .

[7] Brandt, L. and Schlatter, P. and Henningson, D. S., Transition in Boundary Layer Subject to Free-Stream Turbulence, Journal of Fluid Mechanics 517 (1) (2004) 167 – 198.

[8] Thole, K. A. and Bogard, D. G. and Whan-Tong, J. L., Generating High Freestream Turbulence Levels, Experiments in Fluid 17 (1) (1994) 375 – 380.

[9] Folk, M. and Miller, R. J. and Coull, J. D., The impact of Combustor Turbulence on Turbine Loss Mechanisms, ASME Journal of Turbomachinery 142 (1) (2019) .

[10] Gakhara, K., Effect of Free-Stream Turbulence on Boundary Layer Loss Generation, Ph.D. thesis, Massachusetts Institute of Technology (2020).

[11] R. Pichler, R. D. Sandberg, G. Laskowski, V. Michelassi, High-fidelity simulations of a linear HPT cascade vane subject to varying inlet turbulence, in: ASME Turbo Expo, 2017.

[12] Zhao, Y. and Sandberg, R. D. , By-pass Transition in Boundary Layer Subject to Strong Pressure Gradient and Curvature Effects, Journal of Fluid Mechanics 888 (1) (2020) .

[13] Tucker, P. G., Trends in Turbomachinery Turbulence Treatments, Progress in Aerospace Science 63 (1) (2013) 1 – 32.

[14] Dick, E. and Kubacki, S., Transition Models for Turbomachinery Boundary Layer Flows: A Review, International Journal of Turbomachinery Propulsion and Power 2 (2).

[15] Tyacke, J. and Vadlamani, N. R. and Trojak, W. and Watson, R. and Ma, Y. and Tucker, P. G., Turbomachinery Simulation Challenges and the Future, Progress in Aerospace Science 110 (1) (2010) .

[16] J. Babajee, T. Arts, Investigation of the laminar separation-induced transition with the $\gamma - re_\theta$ transition model on low pressure turbine rotor blades at steady conditions, in: ASME Turbo Expo, 2012.

[17] C. Bode, T. Aufderheide, D. Kozulovic, J. Friedrichs, The effects of turbulence length scale on turbulence and transition prediction in turbomachinery flows, in: ASME Turbo Expo, 2014.

[18] Roach, P. E., The Generation of Nearly Isotropic Turbulence by Means of Grids, International Journal of Heat and Fluid Flow 8 (1) (1986) 82 – 92.

[19] Maciejewki, P. K. and Moffat, R. J., Heat Transfer with Very Hugh Free-stream Turbulence: part II - Analysis of Results, ASME Journal of Heat Transfer 114 (1) (1992) 834 – 839.

[20] J. E. Kingery, F. E. Ames, Stagnation region heat transfer augmentation at very high turbulence levels, in: ASME Turbo Expo, 2015.

[21] Makita, H., Realization of a Large-Scale Turbulence Field in a Small Wind Tunnel, Fluid Dynamics Research 8 (1) (1991) 53 – 64.

[22] Gad-el-Hak, M. and Corrsin, S., Measurements of the Nearly Isotropic Turbulence Behind a Uniform Jet Grid, Journal of Fluid Mechanics 62 (1) (1974) 115 – 143.

[23] J. E. O'Brien, G. J. Van Fossen, The influence of jet-grid turbulence on heat transfer from the stagnation region of a cylinder in crossflow, NASA-TM 87011, NASA (1985).

[24] Young, C. D. and Han, J. C. and Huang, v and Rivir, R. B., Influence of Jet-Grid Turbulence on Flat Plate Turbulent Boundary Layer Flow and Heat Transfer, Journal of Heat Transfer 114 (1) (1974) 65 – 72.

[25] B. A. Bangert, A. Kohli, J. H. Sauer, , K. A. Thole, High freestream turbulence simulation in a scaled-up turbine vane passage, in: ASME Turbo Expo, 1997.

[26] R. J. Boyle, B. L. Lucci, V. G. Verhoff, W. P. Camperchioli, H. La, Aerodynamics of a transitioning turbine stator over a range of reynolds numbers, in: ASME Turbo Expo, 1998.

[27] A. C. Nix, A. C. Smith, T. E. Diller, W. F. Ng, K. A. Thole, High intensity, large length-scale freestream turbulence generation in a transonic turbine cascade, in: ASME Turbo Expo, 2002.

[28] T. Aufderheide, C. Bode, J. Friedrichs, D. Kozulovic, The generation of higher levels of turbulence in a low-speed cascade wind tunnel by pressurized tubes, in: 11th World Congress on COmputational Mechanics, 2014.

[29] J. H. Lienhard, Synopsis of Lift, Drag, and Vortex Frequency Data for Rigid Circular Cylinders, Technical Extension Service 300, Washington State University Pullman (1966).

[30] J. O. Hinze, Turbulence, McGraw-Hill Book Company (1975) 488.

[31] Hearst, R. J., Fractal, Classical, and Active Grid Turbulence: From Production to Decay., Ph.D. thesis, University of Toronto (2015).

[32] Compte-Bellot, G. and Corrsin, S., The Use of a Contraction to Improve the Isotropy of Grid-Generated Turbulence, Journal of Fluid Mechanics 25 (4) (1966) 657 – 682.

[33] Van Fossen, G. J. and Simoneau, R. J. and and Ching, C. Y., Influence of Turbulence Parameters, Reynolds Number, and Body Shape on Stagnation-Region Heat Transfer, Journal of Heat Transfer 117 (3) (1995) 597 – 603.

[34] L. El-Gabry, D. Thurman, , P. E. Poinsatte, Procedure for Determining Turbulence Length Scales Using Hotwire Anemometry, NASA-TM 218403, NASA (2014).

[35] J. Lewalle, D. E. Ashpis, Estimation of Time Scales in Unsteady Flows in a Turbomachinery Rig., NASA-TM 209452, NASA (2004).

Steady Aerodynamics of a Transonic Low-Pressure Turbine Cascade with Purge Flow and Unsteady Wakes

Gustavo Lopes

Turbomachinery and Propulsion Department, von Karman Institute for Fluid Dynamics, Belgium, gustavo.lopes@vki.ac.be

Supervisor: Sergio Lavagnoli

Associate Professor, Turbomachinery and Propulsion Department, von Karman Institute for Fluid Dynamics, Sint-Genesius-Rode, Belgium, lavagnoli@vki.ac.be

University Supervisor: Koen Hillewaert

Myproposition (e.g. Professor), Département d'Aérospatiale et Mécanique, Université de Liège, Liège, Belgium, koen.hillewaert@uliege.be

Abstract

The steady aerodynamics of a transonic low pressure turbine (LPT) cascade is investigated under the impact of unsteady wakes and purge flows. The tests are performed at an outlet Mach (M) and Reynolds numbers (Re) of 0.90 and 70k, respectively. Unsteady wakes are simulated by means of a spoked-wheel type wake generator (WG).

Keywords: High-Speed Low-Pressure Turbine, Linear Cascade, Secondary Flows, Unsteady Wakes, Purge/Leakage Flow

1. Introduction

The Ultra-High By-Pass Ratio Geared Turbofan (GTF) enables a reduction of the specific fuel consumption (SFC), LPT stage count and weight [1] comparatively to modern turbofans. The latter can account for as much as 1/3rd of the overall engine weight [2]. Torre *et al.* [3] performed a thorough investigation of a high-speed LPT in a transonic rotating rig. Their work also highlights the difference in the operating conditions between conventional and high-speed LPTs. Due to the increase in rotational velocity of the low-pressure spool imposed by the gearbox, the LPT operates at transonic exit Mach numbers ($M_{out} > 0.70$) in combination with low-Reynolds numbers encountered during cruising regime [4]. The combination of these flow regimes has been highlighted as one of the main challenges in the development of transonic LPTs for GTFs [5; 6].

The development of secondary flows in axial turbines is a relatively well understood matter due to several models developed under steady flow conditions [7; 8; 9; 10]. However, the flow in axial turbines is dominated by unsteady complex interactions between blade rows [11].

The complexity of the flowfield present in axial turbines is further aggravated by the purge flows emerging from the turbine rim-seal that contribute to the losses due the mixing with the annulus main flow [12] and alter the inlet flow to the upcoming blade row as well as the structure of the endwall flows in the passage. In general terms, investigations performed in turbines report increasing losses and intensification of the endwall flow structures with increasing purge flow rate [13; 14; 15; 16; 17; 18; 19; 20; 21; 22].

This research develops on recent investigations performed in the scope of the EU project SPLEEN, that aims at extensively characterize the interaction of purge flows with endwall flows in high-speed LPTs. Recently, Lopes *et al.*. [23] characterized the steady aerodynamics of an open-access transonic LPT geometry tested at its on- and off-design operating point in a linear cascade environment at engine-relevant Mach and Reynolds numbers. The latter work was extended to include unsteady wakes with similar velocity triangles as the ones found in a real-engine environment [24; 25]. This work aims at extending the previous works and existing literature on the

impact of purge flows on a high-speed LPT under the effects of unsteady wakes. To do so, detailed measurements of the inlet flow field to the cascade are presented before and after the purge flow slot. The impact of an engine-representative cavity geometry on the blade aerodynamics and downstream flowfield is assessed in the absence of purge flow rate, and for two purge flow rates. The blade aerodynamics are characterized by means of static pressure measurements performed in a traversable blade. The downstream flow field flow deviation and losses are characterized by means of a direction pressure probe. The experimental data described in this paper can be obtained at the open access repository https://doi.org/10.5281/zenodo.7264761.

2. Experimental Methods

2.1. SPLEEN Test Case

A thorough description of the test case can be found in [26]. The SPLEEN C1 cascade is representative of a rotor hub geometry of a geared LPT. The linear cascade consists of 23 blades with a span of 165 mm. This investigation is conducted at the nominal operating point ($M_{out} = 0.90; Re_{out} = 70k$). The freestream turbulence intensity is kept fixed at 2.40% by means of a passive turbulence grid. The simulation of unsteady wakes is performed by means of a spoked-wheel type WG mounted with 96 cylindrical bars with 1.00 mm of diameter. The bar tip reaches 73% of the cascade span when parallel to the central blade leading edge (LE). The wake reduced frequency (f^+) at midspan is 0.95, which results in a flow coefficient of 0.80. A slot between the WG and linear cascade is used to inject purge/leakage flow in the test section with purge mass flow ratios in the range of $0 - 1\%$.

2.2. The VKI S-1/C High-Speed Linear Cascade

The measurements are conducted in the high-speed, low-Reynolds linear cascade S-1/C of the von Karman Institute. A schematic view of the wind tunnel is shown in Fig. 1. The wind tunnel is a continuous closed-loop facility driven by a 615 kW 13 stages axial flow compressor. The flow temperature is kept near ambient by means of an air-to-water heat exchanger.

The mass flow is regulated via the adjustment of the compressor rotational speed and a by-pass valve. A vacuum pump regulates the pressure level inside the facility, allowing to reach minimum absolute pressure values in the order of 5000 Pa. The cascade test section is mounted in the first elbow of the loop, following the diffuser. Wire meshes and honeycombs

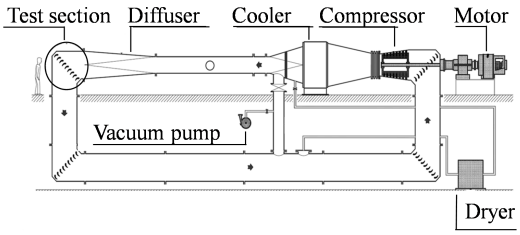

Figure 1: The VKI S-1/C wind tunnel

upstream of the test section ensure homogeneous inlet flow conditions. The outlet Mach and Reynolds numbers can be set independently, hence allowing to test a wide range of engine-relevant conditions. The freestream turbulence intensity (FSTI) is set by means of a movable passive turbulence grid. More details of the facility can be found in [26].

2.3. Purge Flow Circuit

2.3.1. Hardware and instrumentation

A new purge flow system is developed to inject purge flow at the cascade inlet. The latter consists of a circuit that makes use of the pressure drop between a high pressure region within the rig (immediately downstream of the compressor) and the purge location near the test section. The circuit connecting both ends is depicted in Fig. 2.

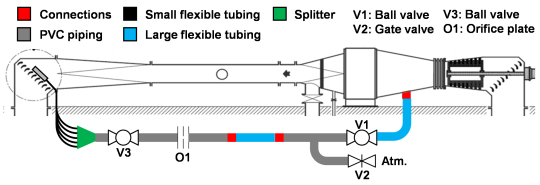

Figure 2: Purge flow circuit constituents in relation to the upper loop of VKI S-1/C

Two ball valves (V1 and V3) are used to fine-tune the amount of bypassed flow to be purged upstream of the cascade. An additional gate valve is used to draw air from atmosphere in case the pressure ratio is not sufficient to accomplish the required mass-flow rate. The measurement of the massflow rate is performed by means of an orifice plate mounted inside a PVC pipe with an inner diameter of 53 mm. The orifice has a diameter of 35 mm. To track the massflow rate inside the circuit, a differential pressure sensor (Validyne DP45 with a range of ±550 Pa) is used to measure the pressure drop across the orifice. Additionally, the static pressure upstream of the

orifice is measured with reference to the cascade reference pressure (shown later). To that effect, an additional Validyne DP45 with a range of ±3500 Pa is used. These measurements are complemented with flow temperature measurements performed by a Type-K thermocouple near the orifice plate. Downstream of the orifice plate, the flow encounters a splitter that splits the flow through 12 small flexible pipes that are fed into the cavity settling chamber (explained later). Upstream of the splitter, the flow total and static pressures, as well as the total temperature are also measured, by means of two Validyne DP45 with a range of ±3500 Pa and referenced to the cascade reference pressure, and an additional Type-K thermocouple, respectively.

2.3.2. Operating principle

The purge flow rate in the rig, $\dot{m}_{rig}$, setup is scaled to respect the purge massflow ratio (PMFR) encountered in the engine. Based on the engine operating conditions and the aerothermodynamic properties encountered in a typical test performed in the VKI S-1/C ($T_{0,rig}$ = 284.1 K; $P_{0,rig}$ = 8880 Pa), the $\dot{m}_{rig}$ that is required to match the engine PMFR can be computed. This value corresponds to the design point (DP) and needs to be adjusted for day-to-day real-time operations. Since the $T_{0,rig}$ varies during the tests, the $P_{0,rig}$ is also adjusted to keep the outlet Mach and Reynolds numbers matched. This causes a mismatch in the mass flow rate required to match the goal PMFR. The required mass flow rate to inject to match the engine point can then be obtained based on the current aerothermodynamic properties during the tests as:

$$\dot{m}_{rig,test} = \dot{m}_{rig,DP} \frac{\sqrt{T_{0,DP}/T_{0,test}}}{P_{0,DP}/P_{0,test}} \tag{1}$$

Where $T_{0,DP}$ and $P_{0,DP}$ and the total temperature and pressure used in the scaling from the engine configuration and $T_{0,test}$ and $P_{0,test}$ are the total temperature and pressure during any test performed in the VKI S-1/C.

The purge flow rate is computed based on the standard ASME MFC-3M-2004 [27], that depends on the orifice plate and connecting pipe geometries, as:

$$\dot{m}_{rig,test} = C_d \epsilon \frac{\pi d^2}{4} \sqrt{\frac{2\rho_{in}\Delta P}{1-\beta^4}} \tag{2}$$

Where C_d is the discharge coefficient, ϵ factor, d is the orifice diameter, ρ_{in} is the density upstream of the orifice, ΔP is the pressure drop across the orifice and β is the ratio of inner to outer diameter. The computation of C_d and ϵ are described in [27]. During the test, the valves in the purge flow circuit are adjusted so that the $\dot{m}_{rig,test}$ computed with Eq. 1. matches the required one computed with Eq. 2.

2.3.3. Cavity geometry

An engine-representative cavity geometry is used. The cavity sits between the WG slot and the cascade. Fig. 3-left highlights the relative position between the WG bar, cavity, and blade in a meridional view of the cascade test section. The splitter feeds the cavity settling chamber through 12 equidistant pipes to reduce flow non-uniformities as the flow develops within the cavity. In addition, a buffer plate (element 1 in Fig. 3-left) is introduced to increase mixing and homogenize the flow within the cavity.

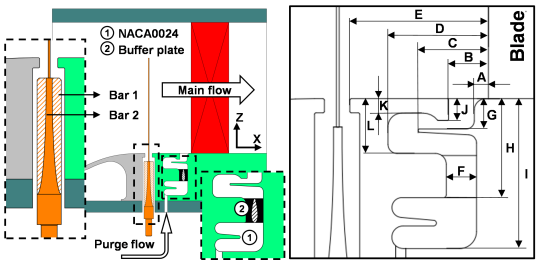

Figure 3: View of test section with detail of WG bar support and cavity structural elements: (1) buffer plate and (2) NACA0024 (left) and cavity geometry key dimensions (right)

In order not to spoil the purge outlet flow, no swirler is mounted near the cavity outlet. The only available location for a possible swirler is where a structural element connecting both sides of the cavity is placed (element 2 in Fig. 3-left). A detailed view of the cavity geometry with key dimensional parameters is displayed in Fig. 3-right. The dimensions are reported in Table 1 for completeness.

Table 1: Key dimensions of cavity geometry

Nom.	Units	Nom.	Units
A	$0.1329C_{ax}$	G	$0.2850C_{ax}$
B	$0.3754C_{ax}$	H	$0.9302C_{ax}$
C	$0.6604C_{ax}$	I	$1.4088C_{ax}$
D	$0.9454C_{ax}$	J	$0.2042C_{ax}$
E	$1.3046C_{ax}$	K	$0.1361C_{ax}$
F	$0.2850C_{ax}$	L	$0.5147C_{ax}$

2.4. Flow conditions

The setups used in this work are combinations of the cavity endwall and the WG bar support. For all the setups the cascade outlet flow conditions and wake reduced frequency correspond to the design point and are the same as investigated in [24].

Tests are performed with a flat endwall and with the cavity endwall. In the presence of the cavity geometry, three cases are investigated: one case without purge flow and two with increasing $\dot{m}_{rig,test}$. The massflow rate was adjusted during the test to achieve PMFR=0.50% and 0.90%.

Preliminary tests are performed with the cavity slot closed (flat endwall) and with a cylindrical WG bar support that occupies as much of the WG slot as possible to reduced ingress/egress from the slot. On the other hand, an elliptical bar support is used in the tests performed with cavity. Table 3 summarizes the investigated cases.

Table 2: Summary of investigated cases

Nom.	Endwall	Bar	PMFR
NC	Endwall	1	0.00%
C	Cavity	2	0.00%
C	Cavity	2	0.50%
C	Cavity	2	0.90%

2.5. Experimental Methodology

2.5.1. Instrumentation

The characteristics of the instrumentation are reported with detail by Simonassi *et al.* [26]. Fig. 4-left shows the meridional view of the test section, the measurement planes, and the cascade reference system. The pitchwise coordinate (y) increases towards passages out of the figure plane.

The cascade total temperature is measured by means of a type-K thermocouple at "Plane Ref". The total pressure at Plane 01 is computed based on a correlation built to estimate the total pressure loss across the TG and WG at different operating points. The static pressure at the outlet is measured by means of static pressure taps on the lower endwall at Plane 06. The taps are connected to a Scanivalve MPS4264 – 1 PSI.

The inlet flow field is mapped by means of a pneumatic Cobra five-hole probe (C5HP) traversed at Plane 02 ($0.50C_{ax}$ upstream of LE). The probe ports are connected to a Scanivalve MPS4264 – 1 PSI and

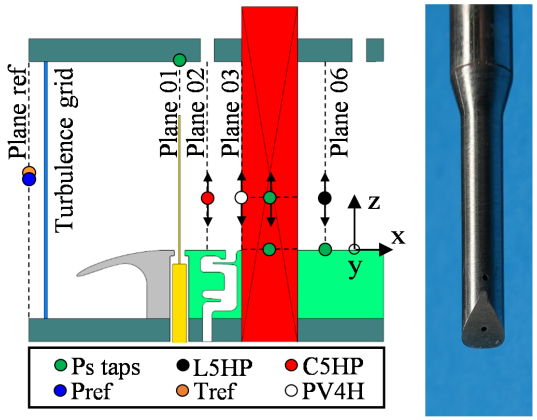

Figure 4: Test section layout and instrumentation at each measurement plane (left) and head of pneumatic virtual four-hole cylindrical probe (right)

aerodynamic calibration coefficients are used to determine the local total and static pressures, as well as yaw and pitch angles in the probe head reference system. The flow angles in the probe reference system are transformed into flow angles in the cascade reference system to compute the incidence (i).

A pneumatic virtual four-hole cylindrical probe (PV4HP) is also used at the inlet. The head geometry, displayed in Fig. 4-right, is inspired by a probe reported in [28; 29]. The probe is used at Plane 03 (between LE) in two slots, one on each side of the central blade, to assess the inlet flow uniformity into to the cascade two central passages in terms of normalized total pressure and flow incidence.

The cascade losses and deviation are obtained through measurements performed with a pneumatic L-shaped five-hole probe (L5HP) at Plane 06 ($0.50C_{ax}$ downstream of TE). The losses are represented by the energy loss coefficient ξ and the flow deviation from the primary flow direction is computed as the difference between the primary flow direction β at each spanwise location and the one at midspan.

In addition to the flow field measurements, phase-averaged blade PS and SS aerodynamics are investigated by means of static pressure taps. Both can be displaced in the spanwise direction from the endwall until midspan. The pressure taps are connected to a Scanivalve MPS4264 – 1 PSI.

3. Results and Discussion

3.1. Inlet Flow Characterization at Plane 02

The profile of the inlet normalized total pressure measured at Plane 02 with the C5HP at $y/g = 0.00$

is displayed in Fig. 5a. The maximum pitch-to-pitch variation of the normalized total pressure can be found in Fig. 5b. The total pressure profiles for the cases with cavity display good agreement. On the other hand, the profiles diverge from the one measured with the flat endwall. Since Plane 02 sits upstream of the cavity slot the variation is attributed to the alteration of the bar support which is likely to have modified the ingress/egress from the WG slot. At $z/H = V0.02$, there is a deficit in the measured total pressure as large as 200 Pa, considering an inlet total pressure of 10,000 Pa. On the other hand, the pitch-to-pitch variation along the span is very similar for all the investigated cases. At $z/H = 0.50$, the pressure variation is within ± 20 Pa. Near the endwall the maximum variation can reach ± 125 Pa for the case tested with a flat endwall.

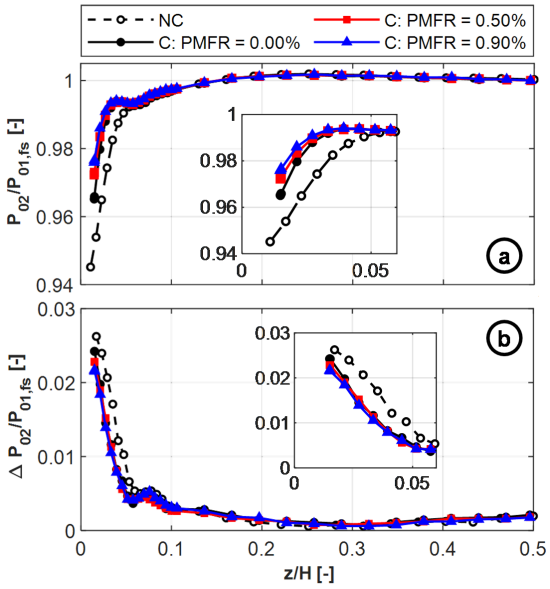

Figure 5: Inlet total pressure profiles measured at Plane 02 with the C5HP for the investigated endwall geometries at $y/g = 0.00$ (a) and maximum pitch-to-pitch variation (b)

The spanwise distribution of incidence at the Plane 02 is displayed in Fig. 6b for $y/g = 0.00$ and in the center of the passages adjacent to the central blade (Fig. 6a and Fig. 6c). The incidence is computed as:

$$i = \beta_{in} - \alpha_{met,in} \tag{3}$$

For all the investigated cases, the spanwise distribution of incidence is negative throughout the span. The incidence decreases towards the endwall up to a local minimum depending on the pitchwise location, after which there is a partial recovery of incidence. A maximum pitch-to-pitch variation of ±0.10 deg exists

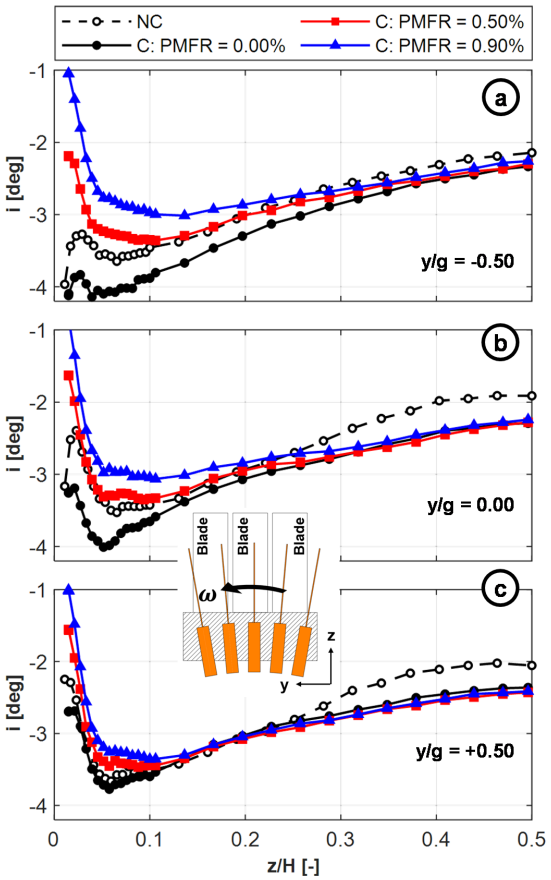

Figure 6: Spanwise distribution of incidence measured at Plane 02 with the C5HP for the investigated endwall geometries at (a) $y/g = -0.50$, (b) $y/g = 0.00$ and (c) $y/g = +0.50$

at midspan for all cases. Near the endwall, the latter reaches ±0.50 deg when purge flow is injected, and as much as ±1.50 deg for the cases with flat endwall and cavity endwall without purge flow injection. For a fixed pitchwise location, the variation in the incidence between the investigated cases is larger at $y/g = -0.50$ (see Fig. 6a), where the variation can reach ±1.50 deg at the location of the closest point measured near the endwall. The difference between the cases is significantly reduced at $y/g = +0.50$ (see Fig. 6c).

3.2. Blade Aerodynamics

Fig. 7 displays the difference in the isentropic Mach number distributions between the case with a flat endwall and the cases with cavity. A subtle difference in the loading is observed for the case where the cavity is present, but no purge flow is injected (see Fig. 7a).

The difference in the isentropic Mach number between the cases with flat endwall and cavity endwall

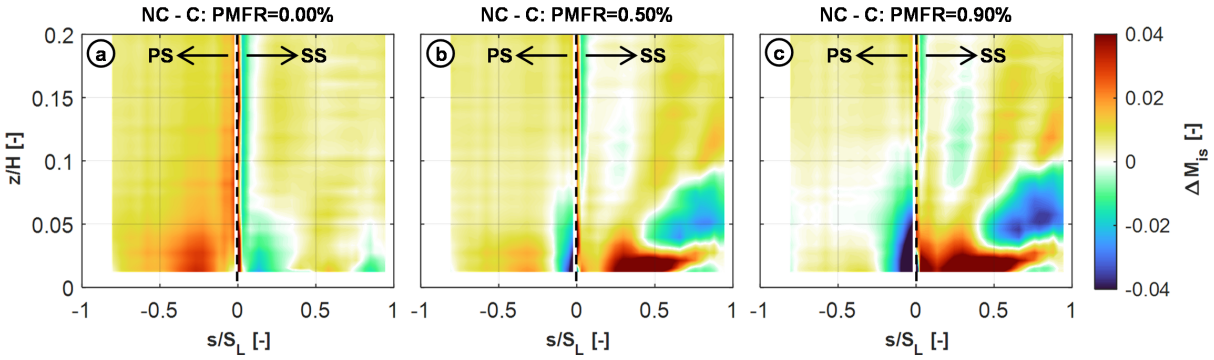

Figure 7: Variation in the isentropic Mach number computed on the blade PS and SS surfaces. The PS is represented in the negative coordinate. The variation is computed between the cases with cavity and purge flow rate of 0.00% (a), 0.50% (b) and 0.90% (c) and the case without cavity

without purge flow (see Fig. 7a) is the largest near the LE on the SS because of the different incidence reported previously. This is further aggravated for the cases with purge flow where a large reduction of the isentropic Mach number on the SS occurs because of the impingement of the purge flows. The regions on the blade SS dominated by the secondary flow structures ($s/S_L > 0.30$), namely the SS corner vortex (CV) and passage vortex (PV), are greatly modified in the presence of purge flow injection. Near the endwall ($z/H = 1.52\%$), the isentropic Mach number is reduced by as much as 0.080 and 0.084 for the cases of PMFR=0.50% and 0.90% at $s/S_L \simeq 0.40$, respectively. These variations occur in the region where the SS corner vortex is expected.

At $z/H \simeq 2.50\%$, the isentropic Mach number is comparable between all cases. After this location, the isentropic Mach number for the cases without purge flow becomes lower than the cases with purge flow injection. The isentropic Mach number at $z/H = 5.15\%$ for the case of PMFR=0.50% and 0.90% is higher than the case with the flat endwall by 0.027 and 0.036, respectively. The region where the isentropic Mach number is higher for the cases with purge flow ends at $z/H = 10.00\%$. As it will be displayed later, the passage vortex is constrained in a region with similar spanwise extent. After $z/H = 20.00\%$ there is little spanwise variation of the isentropic Mach number. The distributions at midspan are in good agreement and suggest that the extent of the impact that the purge flows have on the blade loading is constrained near the endwall.

3.3. Outlet Flow Field

3.3.1. Energy loss coefficient

Contours containing the spanwise and pitchwise distribution of the energy loss coefficient are displayed in Fig. 8-a, b, c, d.

For all cases, a similar topology is observed: a core of higher loss exists at $z/H \simeq 0.10$ (Core 1). This loss core is mainly impacted by the trailing shed vortex (TSV). For the cases with cavity, an additional loss core near the endwall occurs in the region where the SS corner vortex is typically found (Core 2).

The introduction of the cavity impacts the secondary flow development as reported in the works of [30; 31; 32]. Mass and momentum exchange between fluid that recirculates in the slot and the mainstream occurs, mainly in regions of the slot where the static pressure distribution upstream of the LE is lower. Typically, the cavity leakage vortex interacts with the pressure side leg of the horseshoe vortex, giving rise to a stronger passage vortex. Comparing Fig. 8a and b, one can see that the loss magnitude and location of Core 1 did not change significantly. On the other hand, the extent of the region associated with the SS corner vortex enlarged even though the loss magnitude did not increase. The injection of purge flow does not modify the SS corner vortex region nor the magnitude of Core 2. However, the magnitude of Core 1 increases by 11% and 17% compared to the case with cavity and without purge injection for the cases with PMFR=0.50% and 0.90%, respectively. The increase in the purge flow rate also shifts Core 2 away from the endwall because of the translation of the trailing shed vortex (TSV) and PV away from the endwall.

For the cases of PMFR=0.50% and 0.90%, a new loss core is identified (Core 3). The occurrence of this loss peak is due to the larger extent of the PV in the

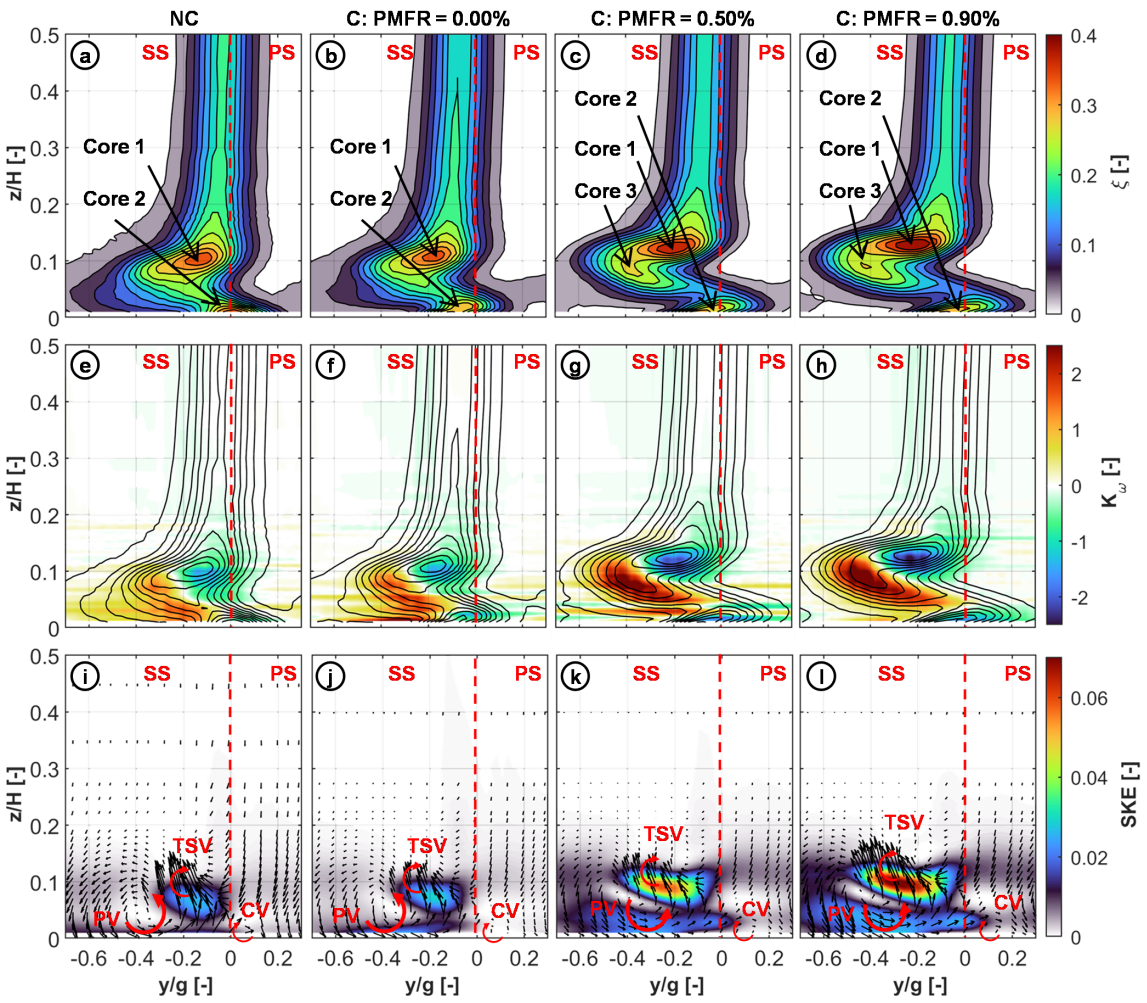

Figure 8: Contours of kinetic energy loss coefficient (a, b, c, d), streamwise vorticity coefficient superimposed with isolines of the energy loss coefficient (e, f, g, h) and secondary kinetic energy superimposed with secondary velocity vectors (i, j, k, l) for the case with flat endwall, with cavity in the absence of purge flow and with cavity with purge flow rate of 0.50% and 0.90%. Observer looks upstream.

passage.

3.3.2. *Streamwise vorticity coefficient*

The contours of streamwise vorticity coefficient, K_ω, superimposed with the kinetic energy loss coefficient isolines are displayed in Fig. 8-e, f, g, h. For all the cases, the PV rotates counter-clockwise (observer looking upstream) in the orange colored region. In addition, the TSV with clockwise rotation can be identified by the blue region at $z/H \simeq 0.10$. Even though limited by the spatial resolution of the L5HP, the SS corner vortex is distinguished by its clockwise rotation located near the endwall.

The streamwise vorticity coefficient in the PV slightly decreases when the cavity endwall is added even in the absence of purge flow. On the other hand, the TSV remains practically unaltered. When purge flow is injected, the size and intensity of the PV region increases. The same occurs to the TSV. Both structures are displaced away from the endwall.

3.3.3. *Secondary kinetic energy*

The contours of secondary kinetic energy (SKE) for the investigated cases are displayed in Fig. 8-i, j, k, l. The secondary velocity vectors are superimposed to the contours to highlight the secondary flow structures present downstream. The SKE provides a good indication of regions of shear between rotating flow structures with surfaces or other structures. In addition, schematic arrows of the structures highlighted in the

previous section are added. The dissipation of SKE is a major contributor to the secondary losses in turbine cascades [33; 34; 35].

The case without cavity endwall displays a region of increased level of SKE resultant from the interaction between the PV and TSV. This is practically unaltered as the cavity endwall is inserted but no purge flow is injected. However, the extent of a region near the endwall increases. MacIsaac *et al.* [32] found similar features and attributed them to the flow overturning in near the endwall region to the cross-passage pressure gradient.

When purge flow is injected, the SKE increases because of the interaction of the PV with the TSV. This region is shifted away from the endwall. Comparatively to the case where the cavity endwall is mounted but no purge flow is injected, an increase in the maximum SKE by 102% and 148% occur for the cases of PMFR=0.50% and 0.90%, respectively. This is supported by the increase in the magnitude of the secondary velocities with PMFR.

3.3.4. Pitchwise averaged

The mass-averaged deviation from the primary flow direction, $\beta - \beta_{MS}$, is used to describe the under/overturning at the cascade outlet (see Fig. 9a). The spanwise distribution of the flow (see Fig. 9a) displays a region of overturning near the endwall that is mainly impacted by the PV. Further away, the underturning resultant from the interaction of the PV and TSV results in a peak in underturning that is dampened as the span increases.

The difference in the streamwise vorticity coefficient in the TSV region between the case with a flat endwall and the one with cavity endwall without purge flow is practically non-existent. This is supported by the similar deviation ranging from midspan to $z/H \simeq 0.10$. Introducing the cavity endwall mainly shifts the distribution away from the endwall because of the shift of the PV. When purge flow is injected the overturning and underturning values are doubled. The overturing peak is shifted away from the endwall because of the larger SS corner vortex. In addition, the SS corner vortex strength promotes a reduction of the overturning caused by the PV near the endwall. Further away from the endwall, the underturning peak is also shifted away from the endwall because of the displaced PV and TSV.

The spanwise distribution of the mass-averaged kinetic energy loss coefficient is displayed in Fig. 9b. Assuming a constant spanwise distribution of the profiles losses [36], the secondary kinetic energy loss

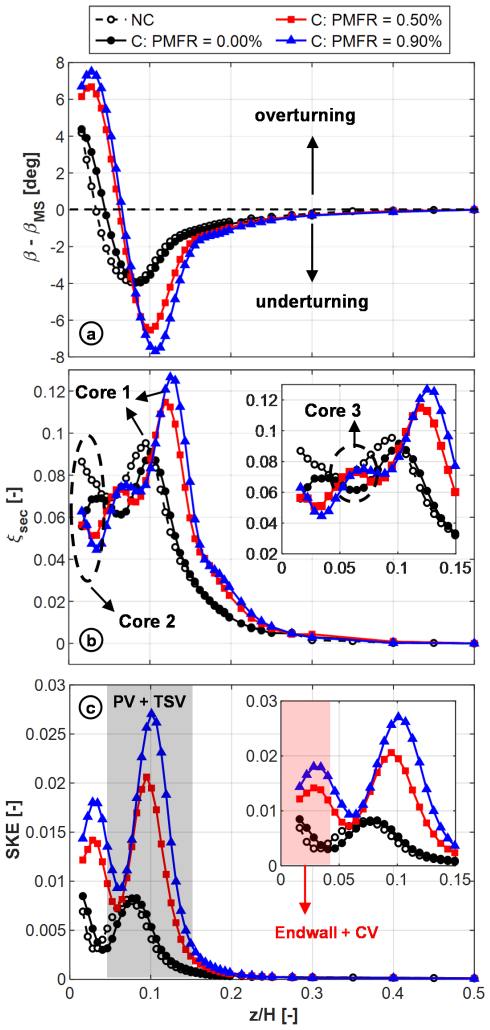

Figure 9: Spanwise distribution of mass-averaged primary flow direction (a), secondary kinetic energy loss coefficient (b) and secondary kinetic energy (c)

coefficient is computed by removing the profile loss from the total energy loss coefficient (see Fig. 9b). The energy loss coefficient is computed using the inlet freestream total pressure and therefore the spanwise distribution includes the contribution of the inlet boundary layer.

Replacing the flat endwall with a cavity slot promotes larger loss content ranging from the endwall to $z/H \simeq 0.10$. Even though the magnitude of the losses in Core 1 does not increase significantly, the pitchwise extent of the losses is higher for the case with flat endwall, resulting in a peak of higher magnitude and closer to the endwall ($z/H \simeq 0.09$ *vs.* 0.10 for case with cavity endwall and no purge) in the span-

wise distribution. In addition, the losses near the endwall region ($z/H \simeq 0.05$) are higher. The later can be justified by the increased size of the SS corner vortex that consists of lower momentum fluid and has a lower contribution to the pitchwise averaging. The peak associated with the SS corner vortex can still be identified at $z/H \simeq 0.03$ for the case with cavity endwall and no purge injection.

The spanwise distribution for the cases with injected purge flow is slightly modified. Near the endwalls, a peak of losses is observed. This is due to the balance between the SS corner vortex induced loss and the region underneath the PV with low losses that does not exist for the cases where purge flow is not present. This low-loss region is cause by the shift of the PV towards the center of the passage. A decay of the losses occurs up to $z/H \simeq 0.03$. The SS corner vortex is contained between the endwall and the valley in the loss profiles. An increase of the losses takes place because of the intensified PV. The peak is displaced away from the endwall with increasing purge flow rate, promoting an increase in the losses of $\sim 3\%$.

Even though the loss peak further away from the endwall is impacted by the PV and TSV, the latter vortical structural is located nearer the loss peak in the contour (see Fig. 8–a, b, c, d). For the case of PMFR=0.50%, the maximum loss peak (mainly impacted by TSV) is shifted from $z/H = 0.10$ to 0.12 and its magnitude increases by 27%. When the PMFR is increased to 0.90%, the location of the peak is further displaced to $z/H = 0.13$.

Respectively to the case with cavity endwall and no purge flow, the maximum loss peak is higher by 40%. The larger extent of the TSV towards the center of the passage is observable up to $z/H \simeq 0.30$, after which the losses for the cases with and without purge are mainly dominated by the profile loss that is the same.

To complement the previous distributions, the mass averaged SKE is displayed in Fig. 9c. For all cases investigated, the SKE produced by the secondary flow structures is constrained between the endwall and $z/H \simeq 0.20$. Starting from the endwall, the combination of the SS corner vortex with the near wall overturning give rise to a first region of increased SKE (red shaded region in zoomed image). Towards midspan, there is a decrease of the SKE due to the weak interaction between the secondary flow structures. A following spike above the latter occurs where the PV and TSV interact (black shaded region).

The SKE distributions for the cases of NC and C: PFMR=0.00% have the same topology along the whole span. Near the endwall, the SKE associated with the endwall flow is higher up to $z/H \simeq 0.05$. On the other hand, the SKE associated with the PV and TSV displays similar magnitude even though it is lifted off towards the center of the passage. The increase of the SKE near the endwall results from the increased level of overturning when purge flow is injected. A distinct peak in this region occurs due to the intensified SS corner vortex that has larger spanwise extent. As the PMFR is increased, the peak associated with the PV and TSV is pushed away from the endwall. Comparatively to the NC case, the magnitude of the SKE associated with this region increases by 154% and 234%, for the increasing PMFR investigated.

3.3.5. Loss breakdown

A loss breakdown is performed to decouple the gross losses computed downstream into inlet BL, profile, and endwall loss. The endwall loss includes the contribution from the endwall BL dissipation and secondary flow mixing. To compute the secondary losses, the profile loss is assumed to be constant along the span:

$$\xi_{end} = \xi_{gross} - \xi_{BL} - \xi_{prof} \tag{4}$$

The gross loss is computed by mass-averaging the kinetic energy loss coefficient from Eq. **??** over the measurement area. Opposite to the contours and pitchwise averaged quantities, the purge flow contribution is considered by substituting the freestream total pressure with the mixed-out inlet total pressure. The method reported by de la Rosa Blanco *et al.* [30], based on the a constant-area mixing calculation of the inlet total pressure is used:

$$P_{0,mix} = \frac{\dot{m}_{main} P_{01,fs} + \dot{m}_{purge} P_{0,cav}}{\dot{m}_{main} + \dot{m}_{purge}} \tag{5}$$

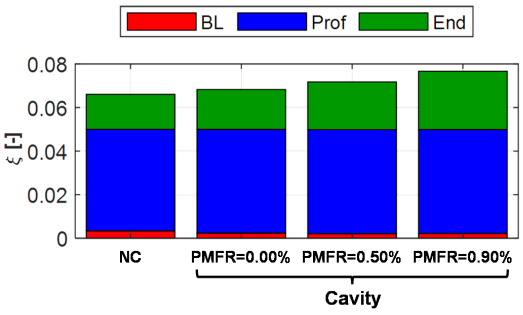

Figure 10: Loss breakdown of investigated cases

The loss breakdown for the investigated cases is displayed in Fig. 10. The gross loss increased when the flat endwall is replaced with the cavity one, and with increasing PMFR in the latter case. The profile loss is similar from case to case as expected since the flow at midspan is not impacted by the purge and secondary flows. The slightly lower loss for the NC is due the slightly higher outlet Mach number when the blade test were performed (L5HP measurements performed in different days). By accounting for the momentum deficit of the inlet BL, it can be concluded that the secondary losses increased with the introduction of the cavity endwall. From the pitchwise distributions, this is justified by the increase in the PV strength. The introduction of the purge flow further increases the endwall loss. This was expected since extent of the secondary flow structures along their strength increased with PMFR.

The contribution of all loss components for the cases investigated is displayed in Table **??**. The introduction of the cavity endwall alone promotes an increase in the endwall loss by 14% compared to the NC case. The purge flow has the impact to further increasing the secondary losses of lowest PMFR case by 37% with respect to the flat endwall. The highest PMFR case promoted an increase of the secondary losses by 67%. Table 4 also contains the planewise mass averaged SKE for completeness. The SKE displays the same behavior as the endwall loss from case to case

Table 3: Summary of loss contributions for all cases

		C w/ PMFR		
ξ	NC	0.00%	0.50%	0.90%
BL	0.0034	0.0024	0.0021	0.0022
Prof	0.0466	0.0476	0.0477	0.0477
End	0.0160	0.0183	0.0219	0.0267
Gross	0.0660	0.0682	0.0718	0.0766
SKE	0.0014	0.0015	0.0034	0.0046

4. Conclusions

The steady aerodynamics of a high-speed linear cascade under the presence of unsteady wakes and cavity purge flow was investigated. The cascade is operated at engine-representative Mach and Reynolds numbers, velocity triangles and purge mass flow ratio. The purpose was to investigate the impact of the cavity geometry and increasing purge flow rate on the aerodynamics of the cascade. The investigation was performed with four different cases: flat endwall, cavity endwall with PMFR=0.00%, cavity endwall with PMFR=0.50% and 0.90%.

Introducing the cavity geometry did not produce meaningful effects on the blade loading near the endwall with exception of the local increase in the isentropic Mach number near the TE. A reduction the isentropic Mach number by as much as 8% between the LE and velocity peak was found when purge flow impinges on the blade. In the PV location, the isentropic Mach number increases by at least 3% near the velocity peak.

Even though the location and extent of the secondary flow structures was not majorly modified by replacing the flat endwall with the cavity endwall, the increasing PMFR displaced the PV and TSV away from the endwall. The mass-averaged analysis allowed to conclude that the loss associated with the TSV can increase as much as 27% and 40% for the cases of PMFR=0.50% and 0.90%, with respect to the flat endwall case. A large region of overturning near the endwall, that is induced by the PV, resulted in a large increase of the SKE near the endwall when purge flow is injected resultant from the intensified PV. The SKE associated with the interaction of the PV and TSV remained constant as the cavity endwall was introduced and it increased by 154% and 234% for the increasing PMFR, relative to the flat endwall case.

The endwall loss was decoupled from the computed gross loss. It was found that the introduction of the cavity geometry alone promoted an increase of the endwall loss by 14% compared with the flat endwall. The endwall loss increased with the PMFR. An increase by 66% was detected for the case of PMFR=0.90%, compared to the flat endwall.

Acknowledgments

The authors gratefully acknowledge funding of the SPLEEN project by the Clean Sky 2 Joint Undertaking under the European Unions Horizon 2020 research and innovation program under the grant agreement 820883. The work of Gene Bryan on the assembling and commissioning of the purge flow circuit is also acknowledged.

References

[1] J. Kurzke, Fundamental differences between conventional and geared turbofans, in: Turbo Expo: Power for Land, Sea, and Air, Vol. 48821, 2009, pp. 145–153.

[2] H. P. Hodson, R. J. Howell, The role of transition in high-lift low-pressure turbines for aeroengines, Progress in Aerospace Sciences 41 (6) (2005) 419–454.
[3] D. Torre, G. García-Valdecasas, A. Puente, D. Hernández, S. Luque, Design and testing of a multi-stage ip turbine for future geared turbofans, in: Turbo Expo: Power for Land, Sea, and Air, Vol. 84911, American Society of Mechanical Engineers, 2021, p. V02BT32A007.
[4] J. Hourmouziadis, Aerodynamic design of low pressure turbines, AGARD, Blading Design for Axial Turbomachines 40 p(SEE N 89-27661 22-07).
[5] M. Giovannini, F. Rubechini, M. Marconcini, A. Arnone, F. Bertini, Analysis of a lpt rotor blade for a geared engine: Part i—aero-mechanical design and validation, in: Turbo Expo: Power for Land, Sea, and Air, Vol. 49705, American Society of Mechanical Engineers, 2016, p. V02BT38A053.
[6] F. Malzacher, J. Gier, F. Lippl, Aerodesign and testing of an aeromechanically highly loaded lp turbine.
[7] H.-P. Wang, S. J. Olson, R. J. Goldstein, E. R. Eckert, Flow visualization in a linear turbine cascade of high performance turbine blades.
[8] C. Sieverding, P. Van Den Bosche, The use of coloured smoke to visualize secondary flows in a turbine-blade cascade, Journal of Fluid Mechanics 134 (1983) 85–89.
[9] L. Langston, Secondary flows in axial turbines—a review, Annals of the New York Academy of Sciences 934 (1) (2001) 11–26.
[10] O. Sharma, T. Butler, Predictions of endwall losses and secondary flows in axial flow turbine cascades.
[11] T. Behr, Control of rotor tip leakage and secondary flow by casing air injection in unshrouded axial turbines, Ph.D. thesis, ETH Zurich (2007).
[12] J. D. Denton, Loss mechanisms in turbomachines, Vol. 78897, American Society of Mechanical Engineers, 1993.
[13] S. D. Hunter, S. R. Manwaring, Endwall cavity flow effects on gaspath aerodynamics in an axial flow turbine: Part i—experimental and numerical investigation, in: Turbo Expo: Power for Land, Sea, and Air, Vol. 78545, American Society of Mechanical Engineers, 2000, p. V001T03A111.
[14] J. Gier, B. Stubert, B. Brouillet, L. De Vito, Interaction of shroud leakage flow and main flow in a three-stage lp turbine.
[15] J. Schlienger, A. Pfau, A. Kalfas, R. Abhari, Effects of labyrinth seal variation on multistage axial turbine flow, Vol. 36894, 2003.
[16] D. Bohn, Investigation of two different axial s̈upersonic compressor stages with special consideration of the interactions between air impeller and guide wheel, Tech. rep. (1977).
[17] C. McLean, C. Camci, B. Glezer, Mainstream aerodynamic effects due to wheelspace coolant injection in a high-pressure turbine stage: Part i—aerodynamic measurements in the stationary frame, J. Turbomach. 123 (4) (2001) 687–696.
[18] S. Schrewe, H. Werschnik, H.-P. Schiffer, Experimental analysis of the interaction between rim seal and main annulus flow in a low pressure two stage axial turbine, Journal of turbomachinery 135 (5) (2013) 051003.
[19] P. Schüpbach, R. S. Abhari, M. Rose, J. Gier, Influence of rim seal purge flow on the performance of an endwall-profiled axial turbine.
[20] P. Schuepbach, R. S. Abhari, M. Rose, T. Germain, I. Raab, J. Gier, Effects of suction and injection purge-flow on the secondary flow structures of a high-work turbine.
[21] B. J. Schreiner, M. Wilson, Y. Li, C. Sangan, Effect of purge on the secondary flow-field of a gas turbine blade-row, Journal of Turbomachinery 142 (10) (2020) 101006.
[22] G. Paniagua, R. De´ nos, S. Almeida, Effect of the hub endwall cavity flow on the flow-field of a transonic high-pressure turbine, J. Turbomach. 126 (4) (2004) 578–586.
[23] G. Lopes, L. Simonassi, A. Torre, M. Patinios, S. Lavagnoli, An experimental test case for transonic low-pressure turbines-part 2: Cascade aerodynamics at on-and off-design reynolds and mach numbers, in: Turbo Expo: Power for Land, Sea, and Air, Vol. 86106, American Society of Mechanical Engineers, 2022, p. V10BT30A027.
[24] G. Lopes, L. Simonassi, S. Lavagnoli, Impact of unsteady wakes on the secondary flows of a high-speed low-pressure turbine cascade, in: 15th European Conference on Turbomachinery Fluid Dynamics Thermodynamics.
[25] L. Simonassi, G. Lopes, S. Lavagnoli, Effects of periodic incoming wakes on the aerodynamics of a high-speed low-pressure turbine cascade, in: 15th European Conference on Turbomachinery Fluid Dynamics Thermodynamics.
[26] L. Simonassi, G. Lopes, S. Gendebien, A. F. M. Torre, M. Patinios, S. Lavagnoli, N. Zeller, L. Pintat, An experimental test case for transonic low-pressure turbines–part i: Rig design, instrumentation and experimental methodology, in: Turbo Expo: Power for Land, Sea, and Air, Vol. 86106, American Society of Mechanical Engineers, 2022, p. V10BT30A012.
[27] ASME, Measurement of fluid flow in pipes using orifice, nozzle, and venturi.
[28] C. Lenherr, A. I. Kalfas, R. S. Abhari, High temperature fast response aerodynamic probe, Journal of engineering for gas turbines and power 133 (1).
[29] I. Bosdas, M. Mansour, A. I. Kalfas, R. S. Abhari, S. Senoo, Unsteady wet steam flow field measurements in the last stage of low pressure steam turbine, Journal of Engineering for Gas Turbines and Power 138 (3).
[30] E. De la Rosa Blanco, H. Hodson, R. Vazquez, Effect of the leakage flows and the upstream platform geometry on the endwall flows of a turbine cascade.
[31] I. Popović, H. Hodson, The effects of a parametric variation of the rim seal geometry on the interaction between hub leakage and mainstream flows in hp turbines, in: Turbo Expo: Power for Land, Sea, and Air, Vol. 44700, American Society of Mechanical Engineers, 2012, pp. 1823–1833.
[32] G. MacIsaac, S. Sjolander, T. Praisner, E. Grover, R. Jurek, Effects of simplified platform overlap and cavity geometry on the endwall flow: Measurements and computations in a low-speed linear turbine cascade, in: Turbo Expo: Power for Land, Sea, and Air, Vol. 55225, American Society of Mechanical Engineers, 2013, p. V06AT36A035.
[33] D. Gregory-Smith, C. Graves, J. Walsh, Growth of secondary losses and vorticity in an axial turbine cascade.
[34] J. D. Coull, Endwall loss in turbine cascades, Journal of Turbomachinery 139 (8).
[35] J. Coull, C. Clark, R. Vazquez, The sensitivity of turbine cascade endwall loss to inlet boundary layer thickness, Journal of the Global Power and Propulsion Society 3 (2019) 540–554.
[36] S. Kacker, U. Okapuu, A mean line prediction method for axial flow turbine efficiency.

Adaptation of CT3 to test High Speed Low-Pressure Turbines

Antonino Federico Maria Torre

Turbomachinery and Propulsion Department, von Karman Institute for Fluid Dynamics, Belgium, antonino.federico.maria.torre@vki.ac.be

Supervisor: Sergio Lavagnoli

Associate Professor, Turbomachinery and Propulsion Department, von Karman Institute for Fluid Dynamics, Belgium, sergio.lavagnoli@vki.ac.be

University Supervisor: Koen Hillewaert

Professor, Department of Aerospace and Mechanics, University of Liège, Belgium, koen.hillewaert@uliege.be

Abstract

This paper presents the commissioning of a newly designed High-Speed Low-Pressure Turbine (LPT) stage, typical of modern geared turbofan (GTF) applications, tested in CT3. The operating conditions stability, as well as on the inlet and cavity injection uniformity are discussed. The commissioning of a traversing system for continuous probe traversing during the short-duration test is also discussed.

Keywords: facility Redesign, High-Speed LPTs

1. Introduction

The geared turbofan engine (GTF) is currently regarded as a key concept to reduce the environmental footprint of modern aircraft propulsion systems. Compared to the direct driven turbofan, the GTF permits an increase of the bypass ratio, with improvement on the propulsive efficiency and sound benefits on the specific fuel consumption [1]. In a GTF, the low-pressure turbine operates at higher rotational speeds and stage expansion ratios compared to the conventional LPT of direct-drive turbofans, offering significant benefits in terms of efficiency and a considerable reduction of the number of stages, hence a decrease of size, weight and cost of the module. However, modern High-Speed LPTs of GTFs face new aerodynamic challenges consisting in a combination of conventional low Reynolds number and transonic Mach numbers, atypical for this module [2]. Open literature is populated by several studies on the aerodynamics of fast LPTs, mainly carried out in cascade environment [3]. For instance, the compressibility effect was studied, among others, by Vera et al. [3]and Vazquez and Torre [4]. Vazquez and Torre [4] compared the results of two rigs designed to have the same loading at two different design exit Mach numbers. The authors showed that the high-speed rig has lower number of airfoil, beneficially reducing the global stage losses. Recently, Lopes et al. [5] examined the on- and off-design results of a transonic LPT linear cascade. They showed that, at nominal Reynolds, profile losses decrease as the Mach number increases, whereas secondary losses remain nearly constant. fExperimental studies of fast LPT stages in engine-representative environments are still a rarity, at least in open literature. Torre et al. [6] conducted an investigation on a fully featured three-stage high-speed intermediate pressure turbine. Their work demonstrated the efficiency gain of the intermediate pressure turbine compared to a reference state-of-the-art conventional low-pressure turbine. Despite the above, many underlying aspect are still unexplored for High-Speed LPTs. For instance, the interaction between cavity purge flows with mainstream have been investigated uniquely on LPTs of the conventional type [7] [8]. Tip-leakage aerodynamics through a light-shroud geometry and its impact on the turbine performance was illustrated by [9] [10] at incompressible regime. Within the scope of the Clean Sky 2 project SPLEEN (Secondary and Leakage Flow Effects in High-speed Low-pressure Turbines), this knowledge gap is filled thorough an experimental in-

vestigation aimed to fully characterize the aerodynamics of a single-stage High Speed LPT. This paper details the design procedure carried out to test the new turbine module in a large-scale blowdown turbine test rig. The reader is rigorously guided though the aerodynamic design of the turbine and though the design solutions found during the refurbishing of the test section, from the mechanical design and instrumentation selection, to the final commissioning of the rig.

2. Definition of the Project objetives

2.1. Investigation of secondary and leakage flow effects in high-speed low-pressure turbines

The EU founded project "Secondary and leakage flow effects in high-speed low-pressure turbines" (SPLEEN) investigates the three-dimensional and unsteady flow field developing in a modern High-Speed Low-Pressure Turbine (HSLPT). The experimental research consists in testing a one-to-one scaled single-stage HSLPT in the compression tube turbine rig CT3, situated at the von Karman Institute [11]. The test campaign pursues the exploration of the interaction between mainstream flow and hub purge flows in an engine-representative environment. Two injection flow rates are investigated to assess the impact of cavity flows on the HSLPT stage efficiency. In addition to the nominal operating condition, an off-design condition is tested at higher stage pressure ratio and rotor speed. In both cases the aerodynamics of the engine-representative interlocking light-shroud featuring the turbine and the impact of tip-leakage on the mainstream are also examined. Finally, the turbine geometry test data, will be collected in an open-access database to provide a unique, consistent set of measurements for code development validation.

2.2. Design Objectives

The test objectives listed in the previous subsection drive the specifications to be satisfied during the design phase. Firstly, the turbine stage has to feature an equal number of blades and vanes, to facilitate the setup of high-fidelity calculations. Secondly, the stage design must recreate the engine representative flow field and losses typical of High-Speed Low-Pressure Turbines, and allowing for installation inside the existing wind tunnel hardware. Thirdly, the test article is required to operate at design and off-design operating conditions and to allow for regulation of the purge flow rate. Lastly, the design shall accommodate high instrumentation density for measurements in the mainstream flow-path and cavities, and allow for ease of access to such instrumentation.

3. Design of the High-Speed Low-Pressure Turbine

3.1. Design Constraints

The isentropic compression tube turbine wind tunnel, CT3 (1), is a blow-down facility that allows to test a turbine stage at engine Mach and Reynolds numbers for a duration up to 500 ms. The wind tunnel consists of three main sections: compression tube, turbine stage (test-section) and downstream dump tank. Prior the test, the test-section and dump tank are evacuated (absolute pressure 40 mbar) and separated from the upstream compression tube by a fast-acting shutter valve. Air from the high-pressure reservoirs is injected at the back of the piston, which slides quasi-isentropically, compressing the fluid upstream of the shutter valve. The test begins when the target pressure and temperature are achieved inside the tube and the shutter valve is opened, releasing the hot gas inside the test section. Downstream of the test section, a variable sonic throat (VST) regulates the mass flow through the turbine, kept constant throughout the testing time. More details on the operation of the rig can be found in [12]. The isentropic compression tube turbine rig can reach relatively high inlet pressures and temperatures, enabling high Reynolds and Mach number, while maintaining gas-to-wall temperature ratios of a real-engine cooled turbine. Thanks to its capabilities, CT3 has been historically used for High-Pressure Turbine (HPT) testing ([13] [14] [15]). In the frame of the SPLEEN project, the rig hosts, for the first time, a low-pressure turbine module, operating at inferior Reynolds numbers of a HPT and at gas-to-wall temperature ratios close to unity. This required a major

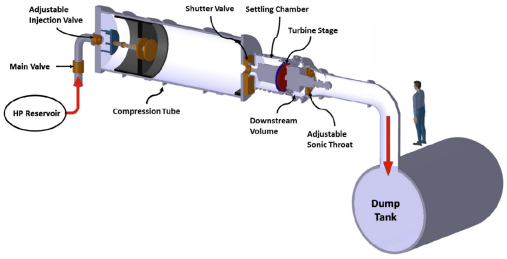

Figure 1: The isentropic compression tube turbine rig of the von Karman Institute for Fluid Dynamics

revamping of the facility, which was constrained by geometrical and operational limits.

The new turbine module is integrated into fixed rig components, constraining the available space to fit the test-section. The minimum inner radius was limited to 260mm by the inner radius of the upstream settling chamber. To fit inside the external casing and to ensure enough space for instrumentation lead-out, the outer radius of the turbine module had to be smaller or equal to 445 mm.

2 shows three corner point solutions for the newly designed turbine. Initially, the geometry of an intermediate 1.5-stage LPT was considered as the baseline engine geometry for designing the test turbine (2-a) because in this section the HSLPT operates under conditions of transonic Mach and low Reynolds number. A 1D model was used to estimate the performances of the facility with the one-to-one scale turbine. Results showed a total test duration below 0.3 seconds, thus too short to ensure sufficient testing time at constant conditions. Because of geometrical and, more importantly, operating limitations, this solution was discarded.

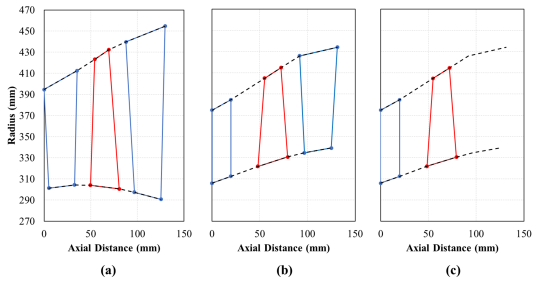

Figure 2: Turbine geometries corner points. (a) 1.5 intermediate stage, (b) 1.5 frontal stage and (c) single frontal stage

An engine 1.5 frontal stage LPT was then tried as baseline geometry and redesigned to operate at intermediate HS LPT conditions (2-b). For this configuration, the 1D model predicted a total test duration of 0.610 seconds, acceptable for blowdown testing in CT3. However, it was found that the insertion of traversable probes for measurements between the blade and the downstream vane was impossible due to the small axial distance between the two airfoils. Any increase of the axial distance between the blade and the downstream vane was not acceptable, since it would have altered the strength of the secondary flow-features exiting the blades and entering the second row of vanes. To prioritize measurements downstream of the rotor, the second vane row was not included in the final design, resulting in the configuration shown in 2-c.

3.2. Aerodynamic design of the SPLEEN Turbine.

The design of the High-Speed Low-Pressure Turbine was carried out by Safran Aircraft Engines (SAE) to match the main aerodynamic parameters for an intermediate stage of a HSLPT. The stage design maintains the rotor blade count and adapts the number of vanes to achieve a 'CFD friendly' design of the test article. In such configuration, the inlet wake reduced frequency on the turbine blade differs from typical engine conditions, nonetheless this modification was estimated to be satisfactory considering the prospect of generating high-fidelity simulation at reasonable cost. Blade and vane airfoils velocity triangles were selected to achieve representative spanwise distribution of deviation, acceleration and outlet relative Mach number encountered in this kind of application. 3 shows the mass-flow averaged radial distributions of Mach number (left) and yaw angles (right) across the stage, obtained from the throughflow computations performed at SAE. Quantities at the inlet of the stage are indicated by solid black lines, rotor inlet absolute quantities by dashed red lines, rotor inlet relative quantities are shown by light-blue long-dashed lines, rotor outlet absolute quantities by dashed-dotted blue lines, and rotor outlet relative quantities by dotted purple lines. The aerodynamic design of the airfoils was done similarly to what is done for industrial application, thus ensuring relevant velocity distributions for each airfoil. Blade sections from hub to tip were selected to have a spanwise distribution of thickness over chord typical of HSLPTs. 4 shows a comparison of the blade hub (red) and tip (black) sections between conventional (4-left) and the high-speed (4-right) LPTs. High-speed profiles are characterized by a strong change in blade section from hub to tip to withstand the high mechanical loads [2]. On the opposite, tip profile is usually thin with a smaller axial chord to minimize weight in regions at high radius. Finally, other main global parameter such as hub-to-tip ratio, aspect ratio and solidity are designed to be consistent with an engine. The airfoil geometrical parameters are collected in Table 1.

The turbine features an interlocking (or scalloped) tip light-shroud (5), typically employed in high-speed applications to limit the stress on the rotating blade [16] [17]. The shroud cartridge located above the rotor is made of a plain material, differently to the honeycomb geometry usually featured on engine applications. Although the honeycomb is significantly

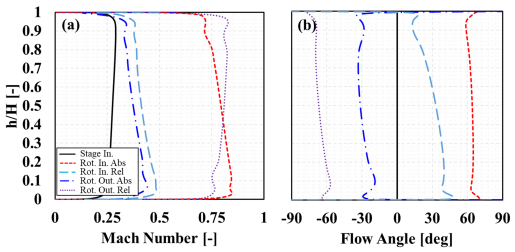

Figure 3: Radial mass flow averaged distributions of (a) Mach numbers and (b) flow angle across the stage

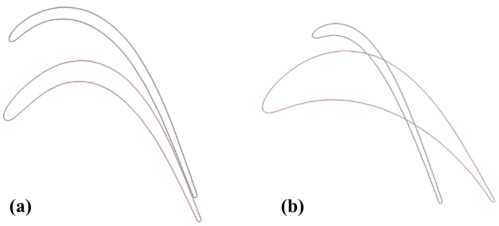

Figure 4: Blade section at hub (red) and tip (black) for a conventional LPT (left) and a high speed LPT (right)

impacting the tangential momentum of the nearby flow by-passing the rotor blade, thus reducing the tip-leakage, a plain part can be better modelled in numerical simulations. Replacing the plain part by a honeycomb one could be one of the interesting development of this rig test sequence beyond the SPLEEN project.

3.3. Operating conditions

The nominal speed-nominal purge test-case represents the reference case at turbine design conditions. Table 2 shows the operating condition of the single-stage LPT at design operating condition. The following data have been obtained from an in-house 1D model employed to scale the turbine from engine operation to laboratory testing.

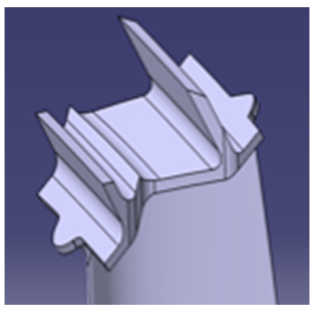

Figure 5: Interlocking Light shroud

4. Rig adaptation to host the newly designed HS LPT

6 shows a cross-section of the newly-designed single-stage high speed Low-Pressure Turbine and its integration on the fixed rig components, here identified by the diagonal hatch. The figure illustrates the static components of the test section colored in gray, except for the vane sectors, here presented in blue. The rotor assembly is colored in red. In light-blue are shown the inserts of plexiglass windows, replaced by metallic inserts when optical measurements are not performed. Finally, in yellow, the Variable Sonic Throat (VST) is presented on the right-hand side of the figure. The figure reports the splitting line (blue dashed double-line) along which the test rig can be opened, thus separating the upstream assembly (grounded) from the downstream components. Thanks to rails, the latter is free to slide axially, ensuring enough space for an easy access to the upstream wheel-space. An o-ring located in the static component constituting the upstream surfaces of the shroud cavity, prevents the flow to exit the test section and bypass the rotor. The figure also reveals a crossing between the splitting line and the black dashed line representing the downstream cavity injection channels. There, purge flow leakage is prevented by o-rings. The test section is constituted by three main assemblies. They are referred to as rotor-upstream, rotor, and rotor-downstream assemblies, depending on their relative position to the LPT rotor.

5. Instrumentation

7 shows a cross-section of the single-stage LPT including the axial and radial locations at which measurements are taken.

Seven regions of interest can be distinguished: three traversing planes placed in the flow-path of the turbine, the vanes region instrumented with pressure taps at 10-50-90% of the span, the two hub cavities and the shroud cavity. The measurement of the rotational speed is performed using a cogwheel and an emitter-receiver photo-diode, both placed on the shaft (not shown in 7). The diode emits a square wave voltage at every cog passage and, knowing the geometrical characteristic of the cogwheel, the rotational speed

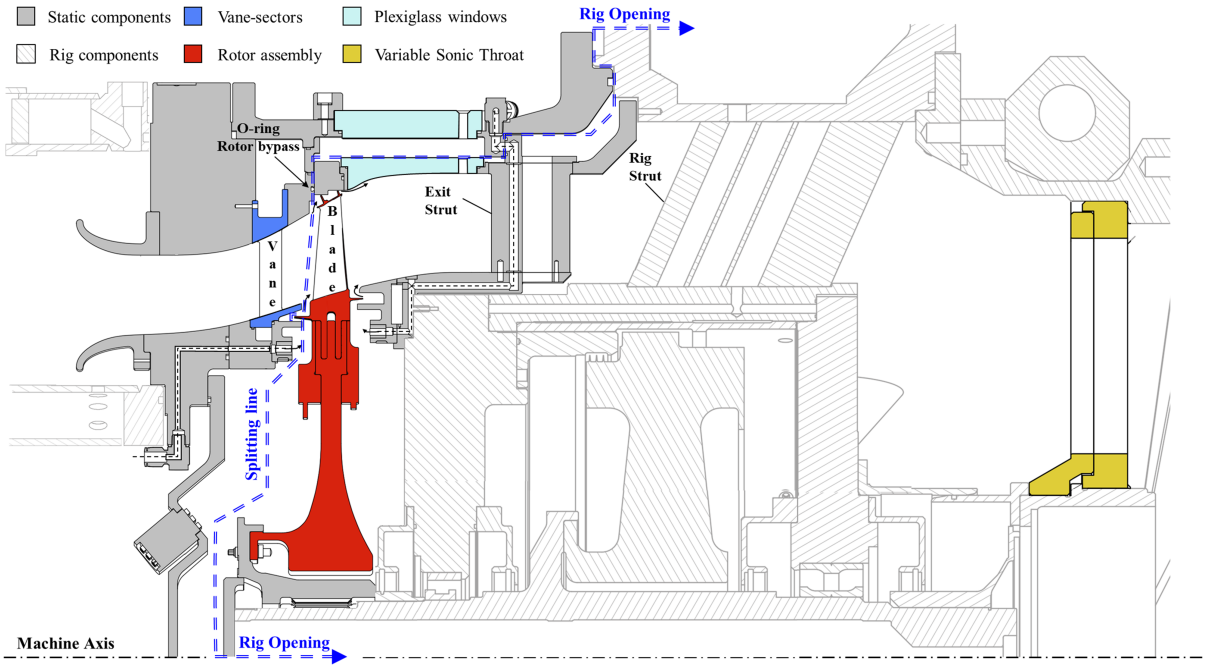

Figure 6: Test article cross section

is computed from the diode signature. Measurement of rotor efficiency are performed, measuring the rotor acceleration during the test and accounting for the rotor inertia, following the procedure described by [18] .

5.1. Measurement planes

At plane 1, the turbine inlet (upstream of the stator vanes) is instrumented to monitor the operating conditions of the turbine and to provide detailed inlet boundary conditions for numerical simulations. Spanwise measurements includes the determination of inlet total pressure by means of a four-head Kiel rake, total temperature using a four-head 25μm type K thermocouple probe, and Free Stream Turbulence Intensity (FSTI) by a copper plated tungsten 5μm hot-wire probe. At hub and tip, wall pressure taps are distributed around the annulus to measure the inlet circumferential uniformity. Every pressure tap in the flow path has a diameter of 0.5 mm, to increase the spatial resolution, than enlarged to diameter of 1.5 mm for a quicker time response. Three additional planes are shown (plane 1a-c) where FSTI decay can be measured.At Plane 2, the rotor inlet is evaluated using aerodynamic probes traversed in both the radial and circumferential directions. Time-averaged and time-resolved flow angles, Mach number and total pressure are measured by one miniaturized pneumatic five-hole probe and one cylindrical fast-response four-hole probe. 13 pressure taps are distributed across 1.5 passages on both the hub and shroud endwalls. The endwalls are instrumented with respectively five and two fast-response pressure transducers across one vane passage to characterize the unsteady endwall pressure distribution. At the hub, two further axial locations for static pressure measurement are placed downstream Plane 2, each comprising 13 pressure taps equally-spaced within 1.5 vane passages. The flow field in Plane 3 is measured to assess the impact of purge and leakage flows on the mainstream. Time-averaged measurements of flow-angles, Mach number and total pressure are measured using two-head five-hole probes, whereas time-resolved measurements are taken using a hemispherical fast response four-hole probe, the latter consisting on a design similar to [15]. The transfer function of the hemispherical four-hole probe is evaluated according to [19], by means of dynamic calibration in a shock tube [20]. Measurements of total temperature are taken using a time-averaged four-head 25μm type K thermocouple probe and an unsteady thin film probe. The latter features nine sensing elements to minimize the number of test runs. In addition to the traversable probes, outlet flow total pressure and temperature are constantly monitored by

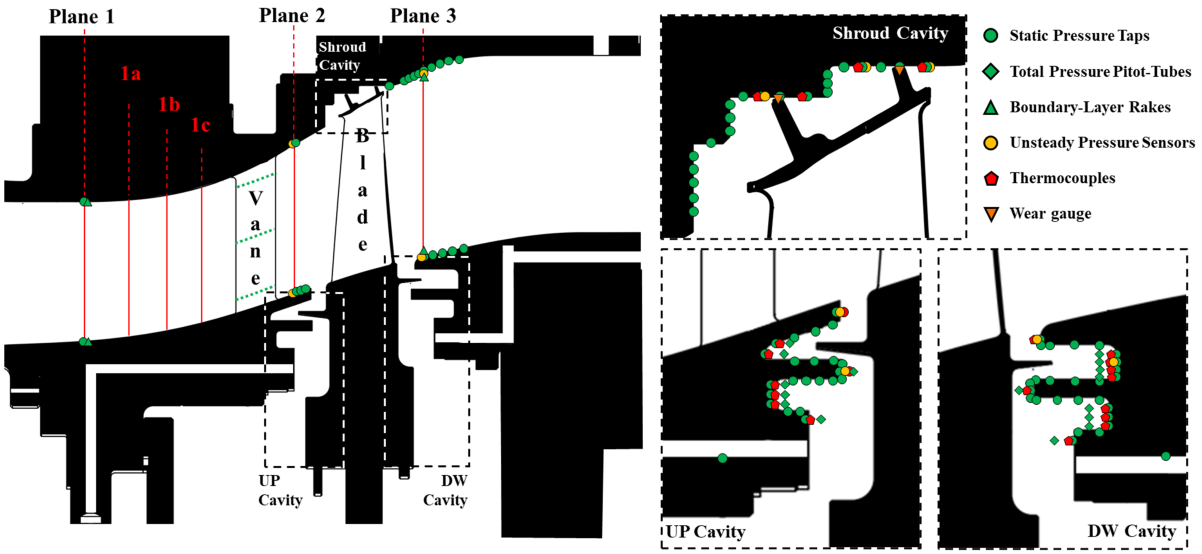

Figure 7: Instrumentation

fixed four-head Kiel and thermocouple rakes. Downstream of the rotor, the time-averaged static pressure on the hub endwall will be measured at five axial locations and on the shroud endwall at 10 axial locations. The unsteady static pressure on the shroud and hub endwalls will be measured at Plane 3 using respectively five and two Kulite pressure transducers, equally spaced across one vane pitch. An additional measurement plane is located 2 mm downstream of the rotating shroud platform edge, where measurements are taken near the shroud cavity for characterizing the tip-leakage flow. Time-averaged measurements of yaw-angle, Mach number and total pressure are taken using a three-hole probe whereas time-resolved measurements of total pressure is taken using a single-hole fast-response probe. Probe placement was carefully selected to avoid any effect on the neighboring probes. Numerical simulations have been performed to assess the impact of the probe at Plane 2 on the surrounding flow field [21]. Simulations have shown that the probe at Plane 2 affects seven vane passages (i.e. 26.25 degrees), and this region is propagated downstream with the wake of the probe itself. It was assumed that the disturbed flow field propagates through the flow path in the same way as a streamline. Given this assumption, the probe location at Plane 3 is chosen having a minimum circumferential spacing to the Plane 2 probes of 45 degrees (or 12 vane pitches) in the direction opposite to the direction of rotation of the disc. Two additional circumferential locations are chosen for probe traversing at Plane 3, which are further spaced of 45 degrees in the opposite direction to the rotor spinning direction.

5.2. Instrumentation in the vane airfoils

Static pressure measurements on the vane airfoils are primarily used for the evaluation of the aerodynamic loading of the vanes. The static pressure will be measured at 10%, 50% and 90% span using pressure tabs, strategically distributed along the two surfaces of the airfoil to capture changes in the static pressure distribution. For the suction side measurements, six taps are used, and for the pressure side measurements, four taps are used.

5.3. Instrumentation in the hub and shroud cavities

Measurements in the upstream and downstream hub cavities are used to characterize the flow structure within the cavities and at the cavity-mainstream interface. Time-averaged and time-resolved static pressure, total pressure, and temperature are acquired at various radial, axial and circumferential locations within the cavities, as shown in 7. In the upstream cavity there are 23 locations at which static pressure

is measured and 11 locations at which temperature is measured. In the downstream cavity there are 27 locations for pressure measurements and 13 locations for temperature measurements. Temperature measurements in the upstream and downstream hub cavities are performed with 80 μm type K thermocouples. Time-resolved static pressure measurements will be taken at the outer and inner stator-side lips in the upstream hub cavity and at the outer stator-side lip and buffer cavity in the downstream cavity, using Kulite transducers placed at eight different circumferential locations. The positions were strategically chosen to create a large variety of small and large angles between any two transducers, necessary to statistically determine the number (and speed) of rotating structures, which are expected to populate wheelspaces (see [22]). Measurements in the shroud cavity are used for characterizing the flow field within this cavity and for determining the performance of the blade tip seals. Measurements of time-averaged static pressure are taken using pressure taps positioned along the cavity stationary walls at 18 different locations. Measurements of time-resolved static pressure will be taken using Kulite sensors positioned in the three cavities formed between the lips of the blade tip-seal. Total pressure measurements will also be taken in this cavity using two pitot-tube rakes to measure the flow tangential velocity. In addition to the pressure measurements, total temperature measurement will also be taken in the shroud cavity using thermocouples measurement upstream and downstream of the two shroud fins.

5.4. Arc-Traverse System

The arc-traverse systems are used for the continuous traversing of the probes in the circumferential direction. They allow for a significant reduction of the number of test runs required for characterizing the flow field [23], compared to the standard point-to-point measurements where probes are kept fixed during each blow-down. The exploded view of the in-house made system is shown in 8.

The traversing system is driven by a FESTO electro-mechanical actuator powered by a stepper motor with integrated encoder. A Nanotec C5-E-2-11 controller allows to operate the stepper motor in closed loop, ensuring a repetition accuracy of ±0.02 mm. A carriage assembly is moved on fixed rails, the latter secured to the external casing of the test section. Sealing is ensured by an o-ring housed in the carriage slot and squeezed against the traverse platform. Four pairs of eccentric bearings engage the two rails. Their

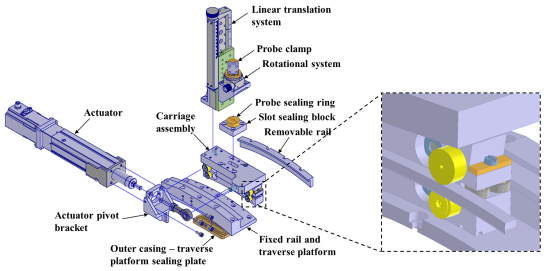

Figure 8: Traversing system

shaft can be rotated to regulate the distance between the carriage and the traverse platform thus regulating the compression of the o-ring. The radial penetration of the probes can be manually adjusted prior to each test-run using a STANDA translation stages whereas probe yaw angle adjustment is done using a STANDA rotation stage. Two magnetic switches (not shown in the picture) serve as either safety limits or homing devices. Three traversing system are employed for the experimental campaign, one located in Plane 2 and two located in Plane 3. 9 shows the position (top) and velocity (bottom) profiles of the three traversing systems tested simultaneously before mounting on the rig. This test is done at higher acceleration and velocity compared to those targeted during the productive tests of the SPLEEN experimental campaign, to assess the capabilities of the newly designed traversing mechanisms. Red circles indicate the profiles of the traversing system located at Plane 2, blue triangles and purple square indicate the traversing mechanisms located at Plane 3. The black line indicate the demanded position and velocity profiles chosen by the operator prior the test. For this test, the linear actuators are demanded to move with a target initial acceleration of 4.5 m/s for 60 ms to reach the nominal speed of 0.246 m/s, followed by 240 ms of motion at constant speed for a length of 1.65 vane passages, resulting on a vane-passing frequency of 6.875 Hz. Lastly a deceleration of 4.5 m/s for 60 ms to slow down the traversing units down to 0 m/s. The velocity profiles show a delay of the traversing units response compared to the target profile. The three traversing mechanisms can reach the demanded traversing constant speed 130 ms after the triggering of the test. In the region of constant traversing speed, the three carriage travels at an higher velocity compared to the aimed value. The traversing system named “Pl. 3b” has the highest average speed reaching a value 2.50% higher of the target velocity and its speed can vary between

± 2.3% of the mean value. The impact on the traverse speed on the measured yaw angle can be evaluated from the velocity triangles of the probe. At plane 2, the impact of the measured angle is below 0.025°, whereas at plane 3 the impact is below 0.09° . The variation of the carriage speed around its mean value is therefore negligible compared to measurement uncertainty.

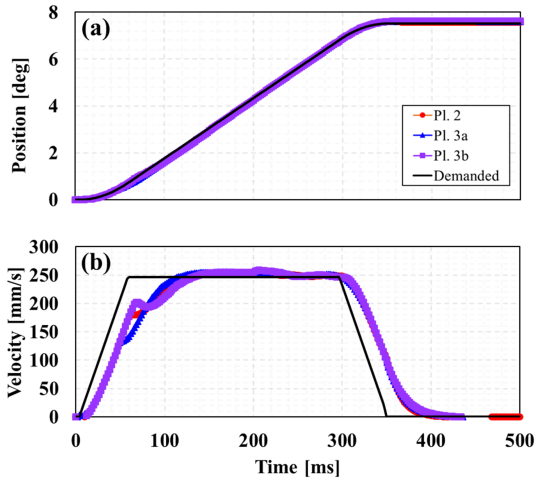

Figure 9: Traversing profiles

5.5. *Commissioning*

In this section, the commissioning of the refurbished test rig is discussed. The design choices at nominal operating conditions (i.e. reference test-case) are verified using experimental data. 10 shows the evolution of meaningful quantities during one blowdown test performed on the High-Speed Low-Pressure Turbine. Shutter valve opening is indicated and occurs at t=0.1874s. 10-a contains the plot of total and static pressures at different measurement planes. The values are normalized by the average inlet total pressure at plane 1c. The solid purple line indicates the pressure inside the compression tube (i.e. upstream of the shutter valve), black triangles indicate the turbine inlet total pressure measured by a fixed Kiel rake located at Plane 1c, blue diamonds show the pitch-wise averaged static pressure on the hub endwall of Plane 1, red circles and green squares indicate the pitch-wise averaged turbine outlet static pressures respectively at the hub and tip endwalls at plane 3. After a transient, the beginning of the useful testing time is t=0.4s. All pressures in the test section are maintained constant within ±1.5 mbar until t=0.6 s, when the change of the slope of the static pressure at Plane 3 indicates the VST un-chocking. This happens because the dump-tank fills up, the static pressure inside it rises thus decreasing the ratio P0,3/Ps,DT below the critical value (i.e. 1.894). Nevertheless, a testing time of 200 ms is considered sufficient to perform time-averaged and time-resolved measurement and to actuate the probe to measure one vane pitch within the testing time (vane passing frequency of 5 Hz).

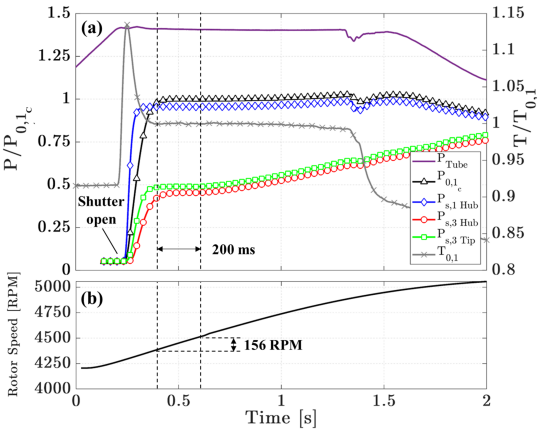

Figure 10: Turbine operation: (a) aerothermal parameters, pressure ad temperature distributions, (b) rotational speed

The gray line with “x” markers shown in 10-a represents the total temperature at Plane 1, normalized by the average during the testing time. This plot reveals an excellent gas temperature stability, within ±0.12510-b shows a rise of the turbine rotational speed during the blowdown. This effect is unavoidable as no brake acts on the shaft. The target rotational speed is achieved at t=0.525 s, roughly in the middle of the 200 ms useful for traversing. Within this timespan, the rotor speed increases by 156 RPM, thus experiencing a variation of the turbine outlet yaw of ±1.6o around the reference value. Although not shown, the position and velocity profiles of the three traversing systems installed on the test rig were acquired during the commissioning test. At the beginning of the testing time, the three traversing mechanisms moved with a velocity 5.6% higher of the demanded value. As previously shown, the effect of the traversing speed on the measured flow angles is negligible at such low traversing velocity. Moreover, during the movement of the traversing unit, an optimal sealing prevented any measurable leakage from the external ambient to the test section.

The turbine inlet uniformity was evaluated looking at the time-averaged static pressure measured at

five locations around the annulus on the hub endwall at Plane 1. The pressure taps showed a value that scatters within ±0.07% of P0,1c around the mean value, thus below the accuracy of a Scanivalve 15 PSI-range ZOC33 pressure transducer used for these measurements, hence showing an extremely good uniformity at the inlet. During the commissioning test, the injected mass flow in the upstream cavity is equal to 0.529% of the mass flow rate in the test section, whereas the injected massflow in the downstream cavity is 0.519%. The uniformity of the upstream injection lines is reported in 11. The figure shows the time-averaged static pressure measured in the 32 injection lines of the upstream cavity. In this plot is reported the pressure difference from the average value, normalized by the average value. The pressure taps show differences from the mean values within ±1% of Pinj, and therefore considered acceptable.

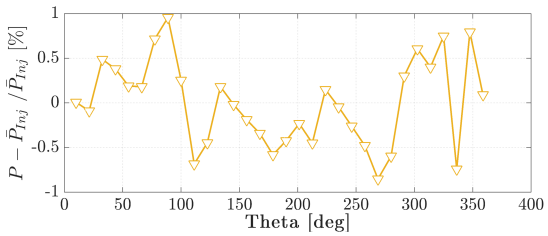

Figure 11: Time-averaged static pressure distribution in the 32 upstream purge supply-lines

12 shows static pressure at Plane 2 hub (black stars), and at the upstream cavity rim seal (cyan line with "+" markers), and at the most inward location in the upstream cavity (magenta triangles), normalized by their average value between t=0.5 s and t=0.6 s, when steady conditions are reached. The values reported in the plot are obtained from pneumatic pressure taps. The plot shows that, differently from the numerical simulations discussed in Chapter 4, the three lines collapse together from t=0.35 s (P/Pend = 0.982) , meaning that the cavity response is quicker than the flow establishment time and does not shorten the available testing time within the cavity.

6. Conclusion

In this paper it was illustrated in detail the procedure followed throughout the design and commissioning of a large-scale blow-down facility, to test High-Speed Low-Pressure Turbines models representative to those employed in modern geared turbofan architectures. At first, the investigation objectives were

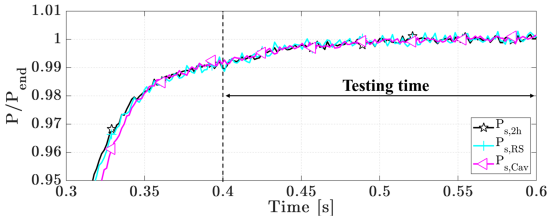

Figure 12: Cavity filling. Static pressure normalized by their value at the end of the transitory

specified, together with the design specifications to be satisfied during the aerodynamic design of the turbine module and the modification of the test rig. Secondly, the design of the high-speed low-pressure research turbine was discussed. Starting from the design constraints, that drove the selection of the test section corner points, was then presented the methodology followed throughout the aerodynamic design of the SPLEEN HSLPT. The final outcome consisted in a one-to-one scale single-stage turbine featuring two hub cavities, the interlocking light shroud geometry and airfoil taper typical of this application. The turbine design was chosen to held an "easy-friendly" geometry constituted by even number of vanes and blades. Third, the instrumentation position selection and design was discussed. The design of the continuous traversing system was illustrated and it was shown to meet the aimed position and velocity profiles. Lastly, the commissioning of the stage was described. The aerothermal parameters revealed a testing time of 200 ms at exceptionally constant conditions. The test started when stable aerothermal conditions were reached, whereas the end of the testing time was set off by the unchocking of the VST, which causes an increase of the static pressure values at Plane 3. During the testing time, a rotor acceleration of 156 RPM is observed, this resulted in a variation of the velocity triangles by ±1.6o around the reference value. The traversing units are operated during the test. They have proven to reach the target velocity during the testing, with deviations having negligible effects on the measured quantities and with an undetectable level of leakage thus to not affect the vacuum level of the test section. The inlet and cavity injection showed to have sufficient uniformity and therefore validated for testing. Finally, the upstream cavity filling time was shown to be shorter than the flow establishment time and not to cause a detrimental effect on the available testing time.

Acknowledgments

Acknowledge here important people for your PhD. Sponsor and financial support acknowledgments are also to be listed in the acknowledgments section.

References

[1] Fundamental Differences Between Conventional and Geared Turbofans, Vol. Volume 1: Aircraft Engine; Ceramics; Coal, Biomass and Alternative Fuels; Controls, Diagnostics and Instrumentation; Education; Electric Power; Awards and Honors of Turbo Expo: Power for Land, Sea, and Air. arXiv:https://asmedigitalcollection.asme.org/GT/proceedings-pdf/GT2009/48821/145/2763386/145_1.pdf, doi:10.1115/GT2009-59745.
URL https://doi.org/10.1115/GT2009-59745

[2] F. J. Malzacher, J. Gier, F. Lippl, Aerodesign and Testing of an Aeromechanically Highly Loaded LP Turbine, Journal of Turbomachinery 128 (4) (2003) 643–649. arXiv:https://asmedigitalcollection.asme.org/turbomachinery/article-pdf/128/4/643/5941668/643_1.pdf, doi:10.1115/1.2172646.
URL https://doi.org/10.1115/1.2172646

[3] A. Perdichizzi, Mach Number Effects on Secondary Flow Development Downstream of a Turbine Cascade, Journal of Turbomachinery 112 (4) (1990) 643–651. arXiv:https://asmedigitalcollection.asme.org/turbomachinery/article-pdf/112/4/643/5570134/643_1.pdf, doi:10.1115/1.2927705.
URL https://doi.org/10.1115/1.2927705

[4] The Effect of Mach Number on the Loss Generation of LP Turbines, Vol. Volume 8: Turbomachinery, Parts A, B, and C of Turbo Expo: Power for Land, Sea, and Air. arXiv:https://asmedigitalcollection.asme.org/GT/proceedings-pdf/GT2012/44748/1131/4233346/1131_1.pdf, doi:10.1115/GT2012-68555.
URL https://doi.org/10.1115/GT2012-68555

[5] An Experimental Test Case for Transonic Low-Pressure Turbines - Part 2: Cascade Aerodynamics at On- and Off-Design Reynolds and Mach Numbers, Vol. Volume 10B: Turbomachinery — Axial Flow Turbine Aerodynamics; Deposition, Erosion, Fouling, and Icing; Radial Turbomachinery Aerodynamics of Turbo Expo: Power for Land, Sea, and Air, v10BT30A027. arXiv:https://asmedigitalcollection.asme.org/GT/proceedings-pdf/GT2022/86106/V10BT30A027/6936975/v10bt30a027-gt2022-82626.pdf, doi:10.1115/GT2022-82626.
URL https://doi.org/10.1115/GT2022-82626

[6] Design and Testing of a Multi-Stage IP Turbine for Future Geared Turbofans, Vol. Volume 2B: Turbomachinery — Axial Flow Turbine Aerodynamics; Deposition, Erosion, Fouling, and Icing of Turbo Expo: Power for Land, Sea, and Air, v02BT32A007. arXiv:https://asmedigitalcollection.asme.org/GT/proceedings-pdf/GT2021/84911/V02BT32A007/6757170/v02bt32a007-gt2021-59219.pdf, doi:10.1115/GT2021-59219.
URL https://doi.org/10.1115/GT2021-59219

[7] S. Schrewe, Experimental investigation of the interaction between purge and main annulus flow upstream of a guide vane in a low pressure turbine, 2015.

[8] P. Jenny, R. S. Abhari, M. G. Rose, M. Brettschneider, K. Engel, J. Gier, Unsteady rotor hub passage vortex behavior in the presence of purge flow in an axial low pressure turbine, Volume 8: Turbomachinery, Parts A, B, and C.

[9] P. S. Rebholz, R. S. Abhari, A. I. Kalfas, C. Zscherp, Tip-shroud cutbacks in a low-pressure gas turbine stage, Journal of Propulsion and Power 32 (2016) 1077–1086.

[10] L. Porreca, T. Behr, J. Schlienger, A. I. Kalfas, R. S. Abhari, J. Ehrhard, E. Janke, Fluid Dynamics and Performance of Partially and Fully Shrouded Axial Turbines, Journal of Turbomachinery 127 (4) (2004) 668–678. arXiv:https://asmedigitalcollection.asme.org/turbomachinery/article-pdf/127/4/668/5569817/668_1.pdf, doi:10.1115/1.2008972.
URL https://doi.org/10.1115/1.2008972

[11] The VKI Compression Tube Annular Cascade Facility CT3, Vol. Volume 5: Manufacturing Materials and Metallurgy; Ceramics; Structures and Dynamics; Controls, Diagnostics and Instrumentation; Education of Turbo Expo: Power for Land, Sea, and Air, v005T16A001. arXiv:https://asmedigitalcollection.asme.org/GT/proceedings-pdf/GT1992/78972/V005T16A001/2402737/v005t16a001-92-gt-336.pdf, doi:10.1115/92-GT-336.
URL https://doi.org/10.1115/92-GT-336

[12] Review of the von Karman Institute Compression Tube Facility for Turbine Research, Vol. Volume 3C: Heat Transfer of Turbo Expo: Power for Land, Sea, and Air, v03CT14A031. arXiv:https://asmedigitalcollection.asme.org/GT/proceedings-pdf/GT2013/55164/V03CT14A031/2420676/v03ct14a031-gt2013-95984.pdf, doi:10.1115/GT2013-95984.
URL https://doi.org/10.1115/GT2013-95984

[13] G. Paniagua, R. Dénos, S. R. de Almeida, Effect of the hub endwall cavity flow on the flow-field of a transonic high-pressure turbine, Journal of Turbomachinery-transactions of The Asme 126 (2004) 578–586.

[14] B. C. Cernat, M. Pátý, S. Lavagnoli, On the unsteady aerodynamics of a high-speed turbine with squealer blade tips, 2018 Joint Propulsion Conference.

[15] Experimental Investigation of a High-Speed Turbine With Rainbow Rotor and Rim Seal Purge Flow, Vol. Volume 6B: Heat Transfer — General Interest/Additive Manufacturing Impacts on Heat Transfer; Internal Air Systems; Internal Cooling of Turbo Expo: Power for Land, Sea, and Air, v06BT14A015. arXiv:https://asmedigitalcollection.asme.org/GT/proceedings-pdf/GT2022/86045/V06BT14A015/6935837/v06bt14a015-gt2022-83129.pdf, doi:10.1115/GT2022-83129.
URL https://doi.org/10.1115/GT2022-83129

[16] R. Corral, J. M. Gallardo, C. Vasco, Aeroelastic Stability of Welded-in-Pair Low Pressure Turbine Rotor Blades: A Comparative Study Using Linear Methods, Journal of Turbomachinery 129 (1) (2004) 72–83. arXiv:https://asmedigitalcollection.asme.org/turbomachinery/article-pdf/129/1/72/5942303/72_1.pdf, doi:10.1115/1.2366512.
URL https://doi.org/10.1115/1.2366512

[17] O. Larrieta, R. Alonso, Ó. P. Escobar, I. Eryilmaz, V. Pachidis, Design space exploration of turbine blade shroud interlock for flutter stability, 2020.

[18] A. Duden, L. Fottner, Influence of taper, reynolds number and mach number on the secondary flow field of a highly loaded turbine cascade, Proceedings of the Institution of Mechanical Engineers, Part A: Journal of Power and Energy 211 (1997) 309 – 320.

[19] E. Boufidi, M. Alati, F. Fontaneto, S. Lavagnoli, Design and Testing of a Miniaturized Five-Hole Fast Response Pressure Probe With Large Frequency Bandwidth and High Angular Sensitivity, Journal of Engineering for Gas Turbines and Power 141 (10), 101010. doi:10.1115/1.4044660.
URL https://doi.org/10.1115/1.4044660

[20] P. Gaetani, A. Guardone, G. Persico, Shock tube flows past

partially opened diaphragms, Journal of Fluid Mechanics 602 (2008) 267 – 286.

[21] A. F. M. Torre, M. Patinios, G. Lopes, L. Simonassi, S. Lavagnoli, Vane–Probe Interactions in Transonic Flows, Journal of Turbomachinery 145 (6), 061010. arXiv:https://asmedigitalcollection.asme.org/turbomachinery/article-pdf/145/6/061010/6974169/turbo_145_6_061010.pdf, doi:10.1115/1.4056578.
URL https://doi.org/10.1115/1.4056578

[22] P. F. Beard, F. Gao, K. S. Chana, J. Chew, Unsteady Flow Phenomena in Turbine Rim Seals, Journal of Engineering for Gas Turbines and Power 139 (3), 032501. arXiv:https://asmedigitalcollection.asme.org/gasturbinespower/article-pdf/139/3/032501/6173139/gtp_139_03_032501.pdf, doi:10.1115/1.4034452.
URL https://doi.org/10.1115/1.4034452

[23] K. J. . N. R. Gomes, R. A., Development and implementation of a technique for fast five-hole probe measurements downstream of a linear cascad, International Journal of Turbomachinery, Propulsion and Power.

Experimental assessment and modelling of the effect of free-stream turbulence on turbomachinery boundary layers

Giacomo Pastorino

Turbomachinery and Propulsion Department, von Karman Institute for Fluid Dynamics, Belgium, giacomo.pastorino@vki.ac.be

Supervisor: Fabrizio Fontaneto

Associate Professor, Turbomachinery and Propulsion Department, von Karman Institute for Fluid Dynamics, Belgium, fontaneto@vki.ac.be

Supervisor: Sergio Lavagnoli

Associate Professor, Turbomachinery and Propulsion Department, von Karman Institute for Fluid Dynamics, Belgium, lavagnoli@vki.ac.be

University Supervisor: Koen Hillewaert

Professor, Faculté des Sciences appliquées, Université de Liège, Belgium, koen.hillewaert@uliege.be

Abstract

The research in the turbomachinery field is headed towards the development of highly-loaded blades. In high-lift machines, the boundary layer state and development are key factors driving the efficiency and the integrity, influencing the operational stability in compressor rows, the heat transfer in high-pressure turbines, and the formation of the separation bubble in low-pressure turbines. Consequently, a proper prediction of the boundary layer state and evolution is of paramount importance to support the development of innovative designs. In particular, the interaction of free-stream turbulence and pressure gradients with the boundary layer is known to be one of the main factors influencing the location and morphology of the laminar-to-turbulent transition. The physics ruling this interaction, known as 'receptivity', is however complex, multi-modal, and still far from being fully understood and modelled. In the scope of the large EU-funded HE-ART project (Hybrid Electric propulsion system for regional AiRcrafT), the ambitious goal of this doctoral research is to provide new insights into the characterization and modelling of the transition mechanisms in turbomachinery boundary layers.

In this work, the physics of the boundary layer transition will be experimentally characterized in the VKI C1 linear cascade facility, under the effect of realistic free-stream turbulence conditions. This investigation will be performed at different conditions of free-stream turbulence intensity and scales, exploiting an active turbulence grid, for two different pressure gradients setups: favorable, in a turbine cascade, and adverse, by means of compressor blades. Specific tests will be performed also to determine the impact of surface finishing on the transition onset. Different instrumentation, such as 5-hole pressure probes, hot-wires and PIV, will be employed to perform extensive and complementary steady and unsteady measurements. These measurements will be employed to develop low-order models of the boundary layer receptivity mechanisms, distinguishing the effects of turbulence intensity and scales, pressure gradients, and surface finishing. This work also aims at providing a unique extensive open-source experimental database, to support the development of innovative designs through the improvement of numerical methods.

Keywords:
Turbomachinery, Boundary layers, Turbulence, Receptivity, Roughness, Transition modelling

Wall Resolved Large-Eddy Simulations of the SPLEEN low-pressure blade cascade

Patrick Tene Hedje

Fluids-Machines Department, Université de Mons, Belgium, patrick.tenehedje@umons.ac.be

Supervisor: Sergio Lavagnoli

Associate Professor, Turbomachinery and Propulsion Department, von Karman Institute for Fluid Dynamics, Belgium, sergio.lavagnoli@vki.ac.be

University Supervisor: Laurent Bricteux

Professor, Fluids-Machines Department, Université de Mons, Belgium, laurent.bricteux@umons.ac.be

Abstract

The field of aircraft propulsion is currently facing major energy and environmental challenges, requiring faster improvements in engine performance and therefore a better understanding of turbine flows. This has led to the development of new ultra-high bypass ratio engine technologies, in which the fan driven by the low pressure turbine through a gearbox is responsible for about 80% of the thrust. As the various experimental investigations carried out are limited by the complex nature of the flows and geometries involved, it becomes important to build numerical methods that can correctly predict such flows. However, accuracy in numerical predictions remains a real challenge.

Low pressure turbine blades in geared turbofan engines operate at transonic exit Mach numbers (between 0.6 and 0.9), and experience fairly low Reynolds number flow regimes, allowing to perform wall resolved large eddy simulation of cascade flows, and avoiding wall modelling issues in presence of adverse pressure gradients. This work focuses on the Wall Resolved Large-Eddy Simulations (WRLES) of flows in High-Speed Low-Pressure Turbine (HS-LPT) transonic cascades. The test case investigated is the "SPLEEN" cascade, a next-generation HS-LPT designed at the von Karman institute for fluid dynamics, in collaboration with Safran aircraft engines within the "Secondary and Leakage Flow Effects in High-Speed Low-Pressure Turbines" EU project. These WRLES are performed with the Explicit Compressible Solver (ECS) of the massively parallel code YALES2, using a high-order Finite Volume Method (FVM). The first simulation campaign presented here concerns the SPLEEN case for the following isentropic exit quantities $M_{2s} = 0.7$ and $Re_{2s} = 70k$; the aim being to access the solver for transonic flows, in terms of prediction of the suction-side separation bubble, the separation-induced laminar-turbulent transition and the wakes. The results obtained, compared with high-fidelity experimental data, show fairly good agreement, further studies are in progress to improve wake prediction.

Keywords: Wall Resolved Large Eddy Simulations, HS-LPT, Explicit Compressible Solver, FVM.

SHAPE OPTIMIZATION

Advance optimization concept for axial compressor

Thanh-Son Tran

Turbomachinery and Propulsion Department, von Karman Institute for Fluid Dynamics, Belgium, TTran@vki.ac.be

Supervisor: Tom Verstraete

Professor, Turbomachinery and Propulsion Department, von Karman Institute for Fluid Dynamics, Belgium, Tom.Verstraete@vki.ac.be

Supervisor: Fabrizio Fontaneto

Associate Professor, Turbomachinery and Propulsion Department, von Karman Institute for Fluid Dynamics, Belgium, Fontaneto@vki.ac.be

University Supervisor: Grégory Coussement

Professor, Service Fluide-Machine, Université de Mons, Belgium, Gregory.Coussement@umons.ac.be

Abstract

High flow turning in conventional single airfoils is hard to achieve without controlling the boundary layer growth in the diffusive flow. An alternative approach consists of distributing the loading over two subsequent airfoils, using a so-called tandem blade, to in some measure restart the boundary layer before flow separation occurs. The so-called tandem blade presents several complexities from a large design space that require advanced design consideration.

Keywords: Shape Optimization, Compressor, Adjoint Method

1. Introduction

The increase in fan bypass ratio has been the largest contributor to the increased fuel savings of around 50% [1] since the introduction of commercial flight. While throughout the year engine size has been expanding, compressors are required to achieve high-pressure ratios, good efficiency, and a wide operating range within as few stages as possible. The circumferential velocity of the rotor is foreseen to increase with the introduction of the novel geared turbofan concept [2], along with higher flow turning in the stator which is hard to obtain with good aerodynamic performance. The latter is achieved in single-blade airfoils by controlling the boundary layer growth in the diffusive flow. An alternative approach consists of distributing the load over two subsequent airfoils, using a so-called tandem blade configuration to restart the boundary layer before flow separation occurs.

This concept was used at the von Karman Institute in the 60ties to handle the strong flow turning of the supersonic compressor R-32 rotor outlet [3]. A three-dimensional annular tandem blade was first designed [4], then the two-dimensional midspan section was tested in the VKI wind tunnel C-2 where the two-airfoil configuration cascade showed promising results in terms of turning due to the gap flow injection [5]. Four main parameters encompass the physical phenomena surrounding the tandem configuration: axial overlap, pitch percentage, gap throat convergence, and blade loading ratio. These variables have been studied, both experimentally [6; 7; 8] and numerically [9; 10; 11]. While tandem blades showed superior performance at design and off-design points in two-dimensional studies, their advantages are hindered by strong secondary flows in a cascade configuration [12]. Multiple studies have investigated tandem blade annular designs [13; 14; 15; 16], which do not perform as well as their direct two-dimensional counterpart [14]. A spanwise variable gap geometry and endwall contouring are suggested to improve the performance of the former [14; 17].

The past decades have seen a large development of optimization algorithms that try to maximize the performance of a design with minimal intervention from the designer while using Computational Fluid Dynamics (CFD) to model the fluid flow [18; 19; 20; 21; 22; 23]. Shape optimization has been gradually introduced into the design process for many industries in the aerospace, turbomachinery, and automotive sector. They can be broadly sorted into gradient-free methods and gradient-based methods. Both aim to solve an optimization problem by maximizing or minimizing one or multiple objectives according to imposed constraints by changing the design parameters. Gradient-free methods such as Evolutionary Algorithms (EA) [24; 25] potentially assisted by surrogate models [20] are widely used for their robustness and ability to find global optima but their usage is computationally expensive for applications with large amount of design variables [26].

On the other hand, gradient-based methods aim to compute the direction towards the optimum from a sensitivity analysis, which offers in general a fast convergence rate. The computational cost of computing the gradient can be reduced using the adjoint technique, where the cost is nearly independent of the number of design parameters [27]. This makes gradient-based adjoint optimization methods more attractive as they can handle very large amounts of design parameters, which are expected for turbomachinery applications [28]. Gradient-based methods are however local methods, which are likely to find local minima.

The evaluation of a tandem configuration presents multiple practical difficulties related to the expanded design space [6]. While conventional assessment methods, such as a parametric study, indicate an improvement for a given design variable, the combined effect from each parameter is difficult to quantify due to the large degrees of freedom. Optimization techniques present to be an efficient approach as they directly reach a design space optimum and circumvent the complex tandem design space intricacy. Several tandem blade design has been lately obtained through the latter [29; 17]. While modern methods can efficiently navigate through the complex design space of the tandem blade configuration, it is unclear whether the benefits of the two-airfoil setup justify the additional flow and manufacturing complexities over the conventional single blade.

The present work aims to fairly compare both tandem and single optimized profiles for high-turning axial compressor stator blade profiles. The best candidate for each concept is obtained using a gradient-based shape optimization technique to improve the pressure loss coefficient at multiple operating points for a given flow turning and geometric constraints. The aerodynamic performance and the operating range of each optimized design are assessed and compared, along with a study of the physical phenomena surrounding the tandem configuration. The effect of secondary flow is not taken into account in the present study as the focus is set on the physical phenomena surrounding the two-airfoil configuration.

2. Optimization Framework

The gradient-based shape optimization framework used in the present work is composed of a geometry and mesh generation, a primal and adjoint CFD solver [30], and a Sequential Quadratic Programming (SQP) optimizer [31]. A CAD-parametrized blade profile is first built from an initial set of design variables. The two-dimensional grid is then automatically generated with an in-house code and improved using an elliptic smoother. The grid refinement near the airfoil wall ensures a $y^+ < 4$ at the main aerodynamic design point.

The steps in the automatic design process are identical to the optimization framework in [32], where the flow solution and the cost functions, are evaluated with a Reynolds Averaged Navier-Stokes (RANS) solver that incorporates the Spalart-Allmaras turbulence model [33], the sensitivities are computed with an adjoint solver using a fully converged flow solution down to a residual of 1e-10, and the gradients are sent to a SQP optimizer which reiterates the optimal search until a stopping criterion is met.

3. Parametrization

Both single and tandem blade profile configurations are represented by a CAD model using a set of geometrical parameters, Fig. 1. The camberline of a single airfoil is obtained by integrating the α-distribution, Eqn.1, described with a set of user-defined control points.

$$y(u) = \int_0^u tan(\alpha(x))dx. \tag{1}$$

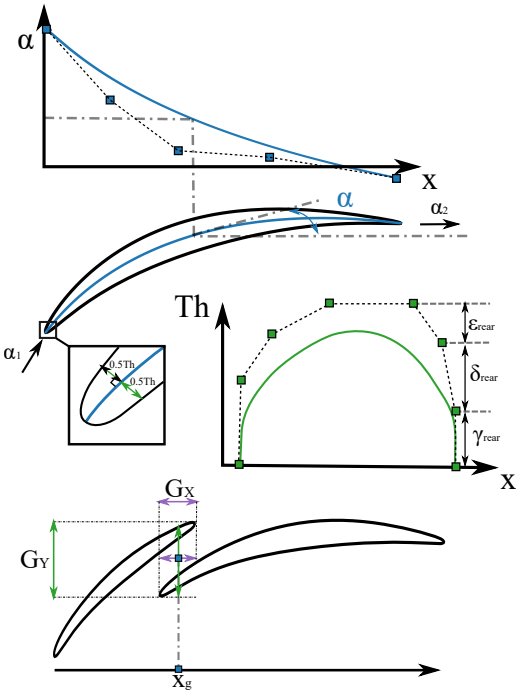

Figure 1: Airfoil Parametrization

The $\alpha(x)$ angle represents the local angle between the camberline and the axial direction. A thickness distribution, Th, defined with a B-Spline curve, is then added to both sides normal to the camberline to generate the pressure and suction side, Eqn. 2. This process is repeated in a tandem configuration for the second airfoil from another set of user-defined α and Th distributions.

$$\begin{aligned} SS(u) &= C(u) + \frac{1}{2} \cdot Th_y(u)N(u) \\ PS(u) &= C(u) - \frac{1}{2} \cdot Th_y(u)N(u) \end{aligned} \tag{2}$$

In the tandem blade configuration, the inter-blade gap is controlled by the axial overlap (AO) distance, G_x, and the pitch percentage (PP) via the pitch distance, G_y. On top of the afore-described parametrization, several control points of the thickness distribution are put into dependent relations, Eqn. 3, where the thickness component, Y_{Th}, are obtained through the sum of external parameters, $(\gamma, \delta, \epsilon)$, to ensure a monotonic increase and decrease of the thickness distribution.

$$\begin{aligned} Y_{Th,0} &= \gamma_{front} \\ Y_{Th,1} &= \gamma_{front} + \delta_{front} \\ Y_{Th,2} &= \gamma_{front} + \delta_{front} + \epsilon_{front} \\ &\cdots \\ Y_{Th,n-2} &= \gamma_{rear} + \delta_{rear} + \epsilon_{rear} \\ Y_{Th,n-1} &= \gamma_{rear} + \delta_{rear} \\ Y_{Th,n} &= \gamma_{rear} \end{aligned} \tag{3}$$

4. Optimization

4.1. Preliminary design

The present work aims to study the performance of a high turning blade, $\alpha_1 - \alpha_2 = 50°$, in a highly subsonic inflow condition, $M_1 = 0.6$. Both single and tandem blades are designed to have an axial outlet flow, $\alpha_2 = 0°$, and the inlet flow angle is consequently set to $\alpha_1 = 50°$. The cascade design characteristic and inlet condition is summarized in Tab. 1.

Inlet flow velocity	M_1	0.6	[-]
Inlet flow angle	β_1	50	[°]
Flow turning	θ	50	[°]
Reynolds Number	Re	800 000	[-]
Total temperature	T_{01}	340	[K]
Axial chord length	c_h	30	[mm]

Table 1: Cascade design parameter summary.

To mitigate the boundary layer separation from the high diffusion occurring in the channel, the preliminary airfoils are aiming for a Leiblein Diffusion Factor (DF) between the recommended empiric range of 0.50 and 0.60 [34]. The resulting solidity of both blade is around $\sigma = \frac{c}{g} \approx 3$, Tab. 2. The latter is defined for the tandem configuration by taking an overall chord starting from the front blade leading edge to the aft blade trailing edge. The diffusion factor, Eqn. 4, of both single and tandem blade baseline design, are respectively 0.52 and 0.54, Tab. 2.

	σ	DF	$\alpha_{m,1}[°]$	$\alpha_{m,2}[°]$
SB Baseline	3.14	0.52	+52.3	-7.2
SB Optimized	2.14	0.60	+53.7	-9.3
TB Baseline	3.09	0.54	+62.0	-7.4

Table 2: Blade parameter summary.

$$DF = 1 - \frac{V_2}{V_1} + \frac{|V_{u,1} - V_{u,2}|}{2\sigma V_1} \tag{4}$$

The baseline single airfoil configuration was obtained from a previous optimization campaign where the objective aims to increase the flow angle without taking into account the pressure losses. The latter started from an initial airfoil drawn with a circular arc camberline and a NACA-65 thickness distribution. The resulting design was able to achieve the desired 50° flow turning with high losses, which allows the main single-blade optimization process to start from a point that satisfies every constraint. This process took place during the framework verification phase where the cautious approach allows a better programming error detection. Subsequent single-blade optimization campaigns have confirmed the ability of the optimizer to reach a good design from a point that does not satisfy all the constraints.

Due to the complexity of the geometry, a myriad of airfoil drawing method exists for the tandem compressor blade. In the present work, the preliminary design is based on the optimized single blade where the camberline angle distribution is split at $u = 0.33$ of the single blade chord to have approximatively the same loading in both segments. A similar thickness distribution is applied to both tandem front and aft airfoils. The second blade is positioned below the front blade, and its inlet blade metal angle, $\alpha_{aft,m,1}$, is increased to handle any eventual poor turning of the front blade. Finally, a high pitch percentage, $PP = \frac{G_y}{g} = 0.86$, is set alongside a zero axial overlap, $AO = \frac{G_x}{c} = 0$, as suggested by the literature [11] to ensure proper performance of the tandem baseline design.

The metal angle, $\alpha_{m,1}(x)$, and the thickness distribution, Th, of the single baseline airfoil are described respectively with 4 and 8 control points, for a total of 24 degrees of freedom where only 16 of the latter are relevant for the optimization process. After including the throat pitch distance to the problem and excluding the axial degree of freedom of the thickness distribution control points for this case, 12 design variables are selected for the single-blade optimization. This amount is triple for the tandem baseline design with 36 design variables from introducing a second airfoil and three parameters acting on the blade split position, the gap pitch distance, and the gap axial distance. The CFD mesh uses around 40 000 cells for both single and tandem blades after a grid convergence analysis Fig. 2.

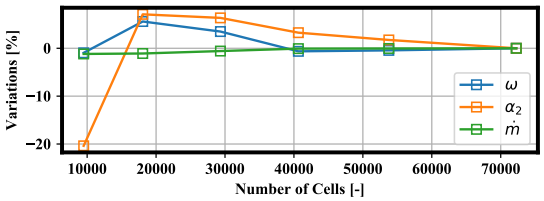

Figure 2: Grid convergence study.

4.2. *Optimization configuration*

Three operating points at different design incidence with the same back pressure, p_2, are used to compute the objective in a weighted sum of pressure loss coefficient, Eqn.5, Table. 3-4, to enforce a wide operating range and a thicker leading edge. The outlet flow angle, α_2, is then constrained below 0° at the design operating point (OP1) to ensure the desired flow turning.

$$\omega = \frac{p_{01} - p_{02}}{p_{01} - p_1} \tag{5}$$

Op. Inci.	$i_{OP1} = 0°; i_{OP2} = +2° ; i_{OP3} = -10°$
Objective	$J = 0.5\,\omega_{OP1} + 0.25\,\omega_{OP2} + 0.25\,\omega_{OP3}$
Flow Angle	$Cstr_1 \equiv \alpha_2 < 0$
Surface	$Cstr_2 \equiv 1 < \frac{S}{S_{ref}}$
Edge Curv.	$Cstr_3 \equiv 1 < \frac{E}{E_{ref}}$

Table 3: Single blade optimization setting.

Op. Inci.	$i_{OP1} = 0°; i_{OP2} = +2° ; i_{OP3} = -10°$
Objective	$J = 0.5\,\omega_{OP1} + 0.25\,\omega_{OP2} + 0.25\,\omega_{OP3}$
Flow Angle	$Cstr_1 \equiv \alpha_2 < 0$
Surface	$Cstr_2 \equiv 1 < \frac{S_{fr}}{S_{fr,ref}}$
	$Cstr_3 \equiv 1 < \frac{S_{af}}{S_{af,ref}}$
Edge Curv.	$Cstr_4 \equiv 1 < \frac{E_{fr}}{E_{fr,ref}}$
	$Cstr_5 \equiv 1 < \frac{E_{af}}{E_{af,ref}}$

Table 4: Tandem blade optimization setting.

In addition, a set of geometrical constraints are defined to ensure a mechanically feasible airfoil. The chord-normalized surface obtained by the integration between the suction and pressure side curves, Eqn. 6, is required to be above a reference value. In other words, the optimizer is not allowed to reduce the blade thickness without reallocating the deducted area elsewhere.

$$A = \int_0^1 P(u) \times \frac{dP}{du} du$$
$$S = \frac{A_{ss} - A_{ps}}{c_h} \quad (6)$$

The TE curvature radius from each airfoil is restricted above a common reference value to produce a realistic TE thickness. Limiting the latter will also allow a better comparison between the single and tandem configurations as lower losses can be achieved with thinner edges. These described constraints aim to complement each other to produce an airfoil geometry with a mechanically feasible blade thickness.

A total of 3 and 5 constraints are respectively used in the single and tandem configuration optimization. After evaluating the cost function, the optimizer finds a design that reduces the objective and satisfies the constraints. The process is repeated until the objective difference between the two iterations is less than 0.1%.

5. Results

5.1. General overview

Convergence is found for the single and tandem blade optimizations respectively after 21 and 25 iterations where both optimized designs satisfy the imposed constraint, Fig. 3. The optimizer manages to reduce the objective value in both cases down to 50% from the initial value. Consequently, the mass-averaged pressure loss, ω, Eqn. 5, is significantly decreased, Tab. 5, for the operating range encompassed by the definition of the objective function.

While every constraint has been respected at convergence, the surface constraint was the most restrictive in both single and tandem blade optimum searches, Fig. 3. The flow angle constraint was also a strong actor during the single blade optimization as the initial design did not conform to the imposed outlet flow angle, α_2.

A first overview shows slightly better performance for the optimized tandem blade at three operating points compared to the optimized single blade, Tab. 5. The lowest pressure loss difference, $\Delta\omega_{OP1} = 0.014$, is observed at design condition, while the highest is at negative incidence.

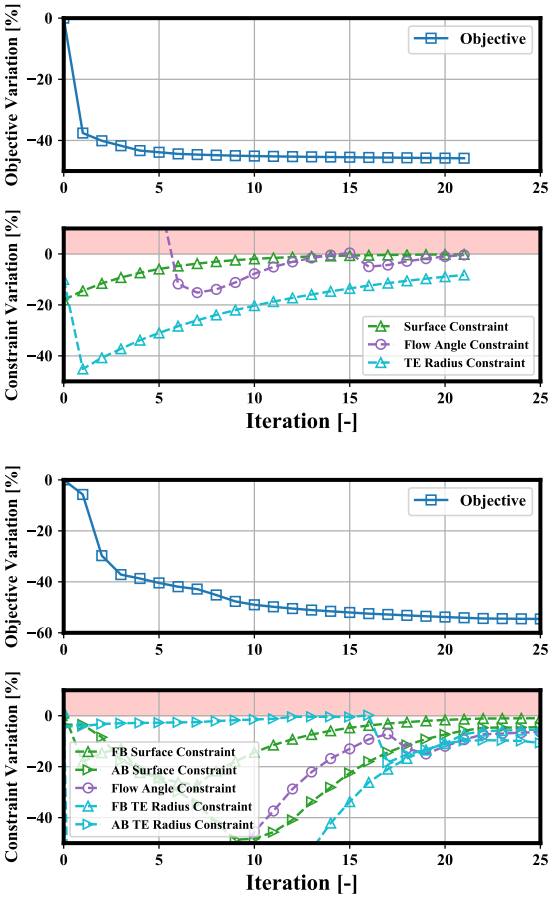

Figure 3: History of the single (Top) and tandem (Bottom) blade optimization.

	ω_{OP1}	ω_{OP2}	ω_{OP3}
SB Baseline	0.083	0.078	0.121
SB Optimized	0.045	0.051	0.049
TB Baseline	0.064	0.070	0.103
TB Optimized	0.031	0.036	0.032

Table 5: Optimization Pressure Loss summary.

Due to non-disclosure reasons, the optimized single blade geometry shown in the present work has been slightly modified, Fig. 4. The performance is however within 1% of the relative difference compared to the optimized airfoils, and the physical phenomena are ensured to remain identical. The optimized tandem blade design is however under an embargo and detailed information surrounding it is restricted at the time of this work. An overall performance analysis will be nonetheless made on both optimized designs.

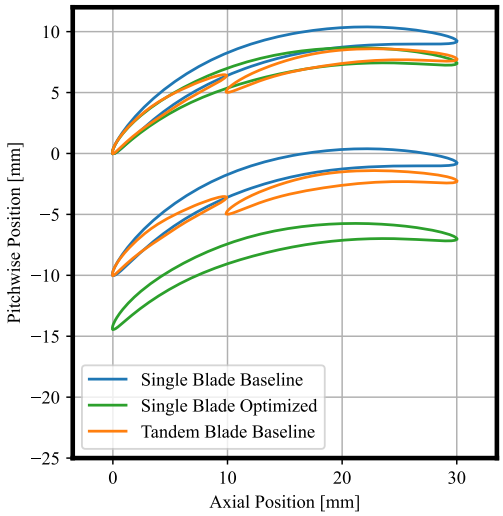

Figure 4: Single blade baseline and optimized geometry.

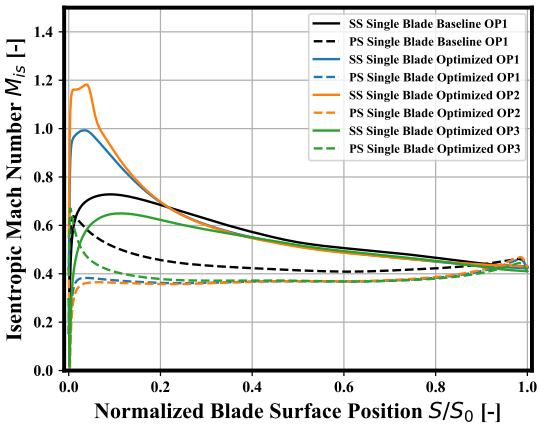

Figure 5: Optimized single blade isentropic Mach comparison.

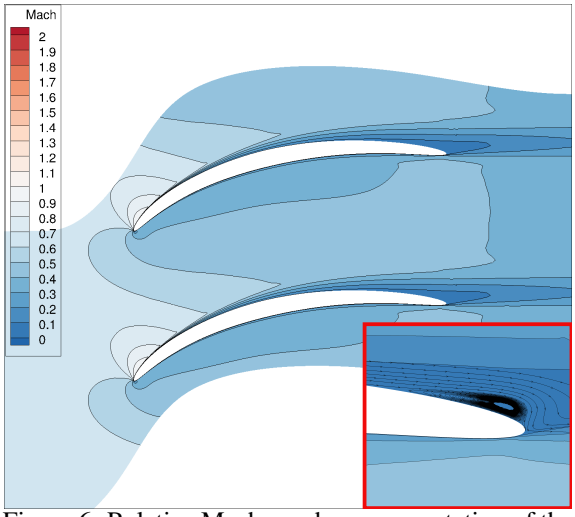

Figure 6: Relative Mach number representation of the single blade at design operating point, OP1.

5.2. *Performance at design point*

At the design operating point, OP1, the isentropic Mach distribution, Fig. 5, underlines an increase in blade loading between the baseline and optimized geometries due to the solidity reduction. The optimized single blade demonstrates multiple characteristics of a control diffusion airfoil [35]. The velocity bump on the baseline suction side near, $s/s_0 = 0.1$, has moved further upstream and increased in amplitude to form a near sonic peak in the optimized design. The flow is then decelerated with a control on the boundary layer growth.

The isentropic Mach number of the optimized blade remains constant throughout the pressure side up to the trailing edge. The deceleration between the peak Mach number and the TE Mach number is about 0.6. A small boundary layer detachment on the single blade rear suction side was permitted by the optimizer at OP1, Fig. 6, from a trade-off between the separation loss and wake loss fraction in the channel. The turning loss is compensated by imposing a more clockwise negative outlet metal angle, $\alpha_{m,2}$, Tab. 2, to have an axial outlet flow angle with the detached flow.

5.3. *Off-design performance*

At positive incidence, OP2, the optimized single blade velocity peak on the suction side is increased beyond sonic speeds while the pressure side velocity distribution remains nearly unchanged, Fig. 5. A larger boundary-layer separation on the suction side near the trailing edge compared to the design operating point is also observed, Fig. 7. The wider wake for a similar amplitude at OP2 confirms a higher loss generation compared to OP1, Fig. 8.

Both suction and pressure side performance of the single blade configuration deteriorate on the front part of the blade at a negative incidence operating point. The velocity peak on the suction side has been replaced by a small bump and the suction side boundary layer separation is reduced as an outcome of the negative incidence flow and the displacement of the stagnation point, Fig. 7. The wake is thinner and taller than the design operating point, Fig. 8.

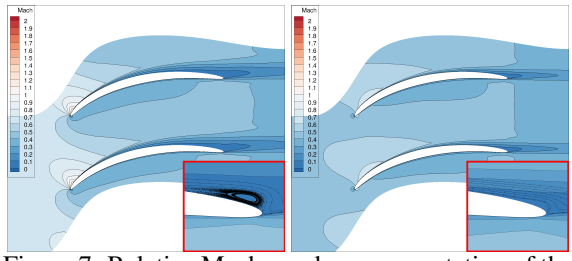

Figure 7: Relative Mach number representation of the single blade at positive (left) and negative (right) incidence operating point, OP2 and OP3.

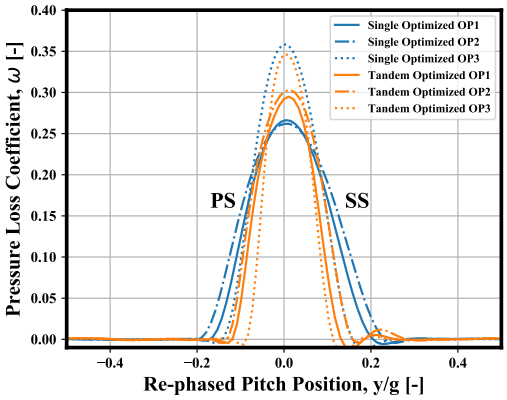

Figure 8: Re-phased pressure loss coefficient at 0.75c

The design and off-design analysis have highlighted three mechanisms made by the optimizer to ensure the desired flow turning with good performance for the optimized single-blade configuration :

- Control of the boundary layer growth by using a controlled diffusion airfoil concept to mitigate the flow separation.
- Reduction of the outlet metal angle towards more negative values to compensate for the loss in flow turning
- Decrease in solidity to lower the wake-loss fraction in the channel.

While a single-blade design with good aerodynamic performance has been found through these mechanisms, the optimizer has interestingly chosen a different set of actions to increase the performance of the tandem blade configuration.

5.4. Loss bucket

Both optimized single and tandem blades have been evaluated at multiple incidences with identical back pressure, Fig. 9a, where the operating point used in the cost function computation are denoted by a

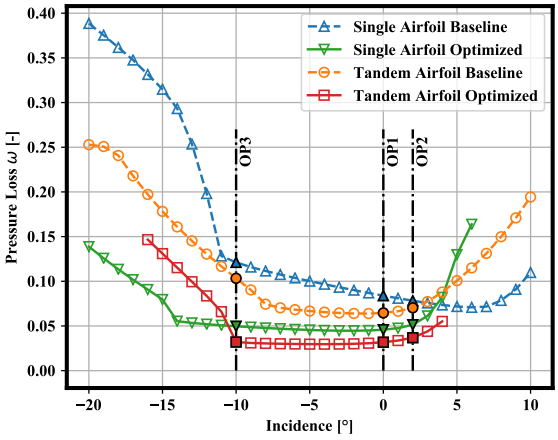

(a) Loss coefficient

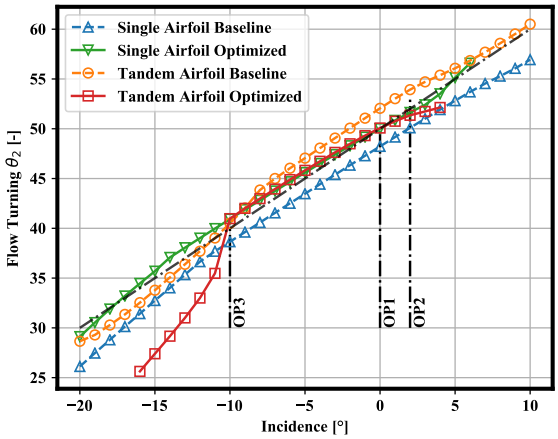

(b) Flow Turning

Figure 9: Performance bucket of the baseline and optimized designs.

filled marker. They both show overall a lower mass-averaged pressure loss than their baseline counterpart with a flatter loss variation in the operating range defined in the objective function definition.

The flow turning within the defined bound is also identical in both blades, Fig. 9b. Finally, the single airfoil demonstrates a larger range in terms of pressure loss and flow turning. A steep increase in pressure loss is denoted right outside of the considered operating bound during the optimization for the optimized tandem design, while the baseline has a smoother evolution.

6. Conclusions

The present work shows two gradient-based multi-point optimizations on a single and tandem blade configuration to find suitable candidates for a fair comparison. The optimizer has demonstrated its capability to find a design that minimizes the losses at three different incidences and satisfies the imposed constraints acting on the flow angle and geometrical parameters to ensure a feasible airfoil shape. Respectively 12 and 36 design variables were used for the optimization of the single and tandem blades. A convergence was found for both configurations after around 20 major iterations.

While the optimized single-blade design converges towards a control diffusion airfoil concept, the optimized tandem configuration has a non-conventional design. The solidity has been lowered in the optimized single-blade configuration to decrease the wake fraction in the flow domain.

The optimized tandem design's overall performance is only slightly better than the conventional single blade in the defined operating range. From the information publicly available in this paper, one can conclude that the two-airfoil configuration would only have a small advantage over the conventional single-airfoil blade in the flow condition described in this paper. The slight performance increase does not justify alone the use of a second airfoil that would increase the manufacturing and maintenance costs. However, the details under embargo might offer a better picture which may put the tandem blade up to a more favorable position.

Both single and tandem blade designs will be optimized in a cascade configuration in future work to take account of the secondary flow. The resulting optimized design will be then investigated experimentally in the VKI CT-2 facility to verify the numerical prediction.

Acknowledgements

The author would like to dedicate this work to Prof. Breugelmans who regrettably passed away during this work. He has been a true inspiration to many colleagues and friends at the von Karman Institute and will be forever in our loving memories.

References

[1] J. J. Lee, S. P. Lukachko, I. A. Waitz, A. Schafer, Historical and future trends in aircraft performance, cost, and emissions, Annual Review of Energy and the Environment 26 (1) (2001) 167–200, publisher: Annual Reviews 4139 El Camino Way, PO Box 10139, Palo Alto, CA 94303-0139, USA.

[2] C. Hughes, D. Van Zante, J. Heidmann, Aircraft engine technology for green aviation to reduce fuel burn, in: 3rd AIAA Atmospheric Space Environments Conference, 2011, p. 3531.

[3] F. A. E. Breugelmans, High Speed Cascade Testing and its Application to Axial Flow Supersonic Compressors, Vol. 79870, American Society of Mechanical Engineers, 1968.

[4] R. Kiock, Stator Design for the High Speed Compressor R-32, von Karman Institute for Fluid Dynamics, 1965.

[5] C. Sieverding, Experimental data for tandem cascade in the high subsonic region, Tech. rep., VON KARMAN INST FOR FLUID DYNAMICS RHODE-SAINT-GENESE (BELGIUM) (1966).

[6] N. L. Sanger, Analytical study of the effects of geometric changes on the flow characteristics of tandem-bladed compressor stators, Tech. rep., National Aeronautics and Space Administration (1971).

[7] J. A. Brent, D. R. Clemmons, Single-stage experimental evaluation of tandem-airfoil rotor and stator blading for compressors, part 8, Tech. rep. (1974).

[8] U. K. Saha, B. Roy, Experimental investigations on tandem compressor cascade performance at low speeds, Experimental thermal and fluid science 14 (3) (1997) 263–276, publisher: Elsevier.

[9] J. Sachmann, L. Fottner, Highly loaded tandem compressor cascade with variable camber and stagger, in: Turbo Expo: Power for Land, Sea, and Air, Vol. 78903, American Society of Mechanical Engineers, 1993, p. V03AT15A086.

[10] G. A. Canon-Falla, Numerical investigation of the flow in tandem compressor cascades, Technische Universität Wien, Diss.

[11] J. McGlumphy, W.-F. Ng, S. R. Wellborn, S. Kempf, Numerical Investigation of Tandem Airfoils for Subsonic Axial-Flow Compressor Blades, Journal of Turbomachinery 131 (2). doi:10.1115/1.2952366.
URL https://doi.org/10.1115/1.2952366

[12] C. Schluer, M. Böhle, M. Cagna, Numerical investigation of the secondary flows and losses in a high-turning tandem compressor cascade.

[13] K. Bammert, H. Beelte, Investigations of an axial flow compressor with tandem cascades.

[14] J. McGlumphy, W.-F. Ng, S. R. Wellborn, S. Kempf, 3D numerical investigation of tandem airfoils for a core compressor rotor.

[15] L. Mueller, D. Kozulovic, D. Wulff, S. Fischer, U. Stark, High Turning Compressor Tandem Cascade for High Subsonic Flows - Part 2: Numerical and Experimental Investigations, in: 47th AIAA/ASME/SAE/ASEE Joint Propulsion Conference & Exhibit, American Institute of Aeronautics and Astronautics, 2011, _eprint: https://arc.aiaa.org/doi/pdf/10.2514/6.2011-5602. doi:10.2514/6.2011-5602.

[16] C. Hertel, C. Bode, D. Kožulović, T. Schneider, Investigations on aerodynamic loading limits of subsonic compressor tandem cascades: end wall flow, in: Turbo Expo: Power for Land, Sea, and Air, Vol. 45608, American Society of Mechanical Engineers, 2014, p. V02AT37A049.

[17] M. Straccia, V. Gümmer, Numerical investigation of non-axisymmetric end wall contouring effects in a low-speed com-

pressor tandem stator, EUROPEAN TURBOMACHINERY SOCIETY, 2021, iSSN: 2410-4833. doi:10.29008/ETC2021-480.

[18] C. S. Ahn, K. Y. Kim, Aerodynamic design optimization of a compressor rotor with Navier—Stokes analysis, Proceedings of the Institution of Mechanical Engineers, Part A: Journal of power and energy 217 (2) (2003) 179–183, publisher: SAGE Publications Sage UK: London, England.

[19] E. Benini, Three-dimensional multi-objective design optimization of a transonic compressor rotor, Journal of propulsion and power 20 (3) (2004) 559–565.

[20] A. Samad, K.-Y. Kim, T. Goel, R. T. Haftka, W. Shyy, Multiple surrogate modeling for axial compressor blade shape optimization, Journal of Propulsion and Power 24 (2) (2008) 301–310.

[21] A. Samad, K.-Y. Kim, Shape optimization of an axial compressor blade by multi-objective genetic algorithm, Proceedings of the Institution of Mechanical Engineers, Part A: Journal of Power and Energy 222 (6) (2008) 599–611, publisher: SAGE Publications Sage UK: London, England.

[22] M. C. Duta, S. Shahpar, M. B. Giles, Turbomachinery design optimization using automatic differentiated adjoint code, in: Turbo Expo: Power for Land, Sea, and Air, Vol. 47950, 2007, pp. 1435–1444.

[23] H. Hu, J. Yu, Y. Song, F. Chen, The application of support vector regression and mesh deformation technique in the optimization of transonic compressor design, Aerospace Science and Technology 112 (2021) 106589, publisher: Elsevier.

[24] D. E. Goldberg, J. H. Holland, Genetic algorithms and machine learningPublisher: Kluwer Academic Publishers-Plenum Publishers; Kluwer Academic Publishers ....

[25] E. Zitzler, Evolutionary algorithms for multiobjective optimization: Methods and applications, Vol. 63, Citeseer, 1999.

[26] S. Chen, J. Montgomery, A. Bolufé-Röhler, Measuring the curse of dimensionality and its effects on particle swarm optimization and differential evolution, Applied Intelligence 42 (3) (2015) 514–526, publisher: Springer.

[27] T. Verstraete, Introduction to optimization and multidisciplinary design, VKI, lecture Series 7 (2010) 93.

[28] M. H. Aissa, R. Maffulli, L. Mueller, T. Verstraete, Optimisation of a turbine inlet guide vane by gradient-based and metamodel-assisted methods, International Journal of Computational Fluid Dynamics 33 (6-7) (2019) 302–316, publisher: Taylor & Francis.

[29] Y. Ju, C. Zhang, Multi-objective optimization design method for tandem compressor cascade at design and off design conditions, in: Turbo Expo: Power for Land, Sea, and Air, Vol. 44021, 2010, pp. 785–796.

[30] L. Müller, Adjoint-Based Optimization of Turbomachinery with Applications to Axial and Radial TurbinesPublisher: Université libre de Bruxelles.

[31] R. Hottois, A. Châtel, G. Coussement, T. Debruyn, T. Verstraete, Comparing gradient-free and gradient-based multi-objective optimization methodologies on the VKI-LS89 turbine vane test case, Journal of Turbomachinery 145 (3) (2023) 031001, publisher: American Society of Mechanical Engineers.

[32] T.-S. Tran, T. De Bruyn, T. Verstraete, CAD Integrated Gradient-Based Aero Optimization of the NASA Rotor 37, in: Turbo Expo: Power for Land, Sea, and Air, Vol. 86120, American Society of Mechanical Engineers, 2022, p. V10DT34A008.

[33] S. R. Allmaras, F. T. Johnson, Modifications and clarifications for the implementation of the Spalart-Allmaras turbulence model, in: Seventh international conference on computational fluid dynamics (ICCFD7), Vol. 1902, Big Island, HI, 2012.

[34] S. Lieblein, F. C. Schwenk, R. L. Broderick, Diffusion factor for estimating losses and limiting blade loadings in axial-flow-compressor blade elements, Tech. rep., NATIONAL ADVISORY COMMITTEE FOR AERONAUTICS CLEVELAND OH LEWIS FLIGHT ... (1953).

[35] D. E. Hobbs, H. D. Weingold, Development of controlled diffusion airfoils for multistage compressor application 106(2) (271-278).

A stabilized finite element framework for anisotropic adaptive topology optimization of incompressible fluid flows

Wassim Abdel Nour

MINES ParisTech, PSL - Research University, CEMEF - Centre for material forming,
CNRS UMR 7635, CS 10207 rue Claude Daunesse, 06904 Sophia-Antipolis Cedex, France, wassim.abdel_nour@mines-paristech.fr

Supervisor: Delphine Laboureur

Associate professor, Enviromental and Applied Fluid Dynamics Department, von Karman Institute for Fluid Dynamics, Belgium,
delphine.laboureur@vki.ac.be

University Supervisor: Elie Hachem

Professor, MINES ParisTech, PSL - Research University, CEMEF - Centre for material forming,
CNRS UMR 7635, CS 10207 rue Claude Daunesse, 06904 Sophia-Antipolis Cedex, France.

Abstract

Shape or topology optimization, aims to find the most convenient material distribution in order to minimize a given criteria, that is the cost function. In this work, we will demonstrate our application of topology optimization based on the Level Set method for reducing head losses. Anisotropic mesh adaptation was applied to capture the interface, and the sensitivity was calculated based on the continuous adjoint method. Three numerical examples were given, where we seek on one hand to validate the algorithm, and on the other hand, to demonstrate the effect of the starting geometry on the final shape.

Keywords: Topology Optimization, Level Set Method, Continous Adjoint, Anisotropic Mesh Adaptation

1. Introduction

Nowadays, with the increase of energy prices, and the increase of the environmental impact of the energy consuming systems, in parallel with the wish of the state to become less energy dependent, the industry is driving research towards reducing the energy consumption of their products by optimizing their energy systems to increase their efficiency.

Bendsøe and Sigmund [1] identified three methods of optimization: parametric, geometric, and topology optimization. Each of these methods is characterized by the architecture of the initial design and the procedure that we follow to reach the final design. Our concern in this work will be about topology optimization.

Topology optimization techniques allow not only to change the size or shape of a structure but also its topology or architecture. In other words, they may result in modifying the connectivity between the inlets and the outlets, and also the connectivity between the fluid ducts that may be in the system by merging already existing ducts or nucleating more of them. This being said, a major advantage of topology optimization techniques is their ability to generate a physical non trivial design without providing them with an initial design or architecture. We can for example begin with a fluid filled design domain, or maybe solid filled domain, or even a combination of both of them.

The density method and the Level Set method are the leading methods for topology optimization[2]. Both methods rely on determining fluid and solid regions. While the density method deals with the entire domain at once, the Level-Set method deals only with surface sensitivities. While the first is faster, more general and less dependant on the initial geometry, the second leads by its ability to generate manufacturable designs with well defined fluid-solid interfaces.

In this paper, we aim to build a numerical framework for topology optimization with hydraulic ap-

plications. Thus, we will first talk about the classic level-set method for interface capturing, then we will explain how we applied automatic anisotropic mesh adaptation to increase the computation precision near the interface and reduce instabilities. Then we will talk about the mixing laws that generate the fluid properties that goes into an Incompressible Navier-Stokes solver. We will also show the weak formulation of the solver with the variational multi-scale approach. After, we will explain the derivation of the convected level-set solver, a powerful tool to precisely transport the interface to the desired position. Then we will talk about the adjoint solver, with the derivation and computation of the control velocity that will be later-on the drive variable of the advection solver. Finally, technical modifications will also be applied: the surface constraint, and the softblocking of the connections with the inlets and outlets. A numerical benchmark will be exhibited in order to validate our framework and prove its effectiveness. Finally we will end up with a conclusion and some perspectives.

2. Numerical Framework

2.1. Eulerian Framework

The level-set method has been used to implicitly track the interface within an Eulerian context. For shape optimization, it consists on separating the fluid regions from the solid ones by a signed distance function α whose zero isovalues correspond to the fluid-solid interface. Let us define Ω the whole computational domain, Ω_{fluid} the fluid domain, and Ω_{solid} the solid domain, and let us denote by $\Gamma_{int} = \Omega_{fluid} \cap \Omega_{solid}$ the interface between them. The level-set function represents the shortest distance to the interface Γ, it is defined at each node x of the domain Ω as follows:

$$\alpha(x) = \begin{cases} \alpha(x,t) = -dist(x, \Gamma_{int}) & \text{if} \quad x \in \Omega_{fluid} \\ \alpha(x,t) = 0 & \text{if} \quad x \in \Gamma_{int} \\ \alpha(x,t) = +dist(x, \Gamma_{int}) & \text{if} \quad x \in \Omega_{solid} \end{cases} \tag{1}$$

2.2. Anisotropic Mesh Adaptation

Anisotropic mesh adaptation allows us to increase the accuracy of capturing the interface. Indeed, since the level set is an implicit definition of the interface, its zero iso-value intersects the elements of the mesh arbitrarily. As a consequence, discontinuities due to the high ratio in the physical properties between the solid and the fluid may lead to numerical oscillations during the resolution of PDEs. Instead, we will consider a regularized interface, meaning that the properties are distributed smoothly over a minimal thickness around the interface. Using anisotropic mesh adaptation with highly stretched elements will help reducing the interface thickness, and will increase the accuracy of the computation due to a higher mesh resolution. To obtain an accurate description of the interface using the level set function, we consider the normal direction as the principal direction of mesh refinement. The anisotropic mesh adaptation procedure is performed using a metric map that prescribes a mesh size according to the principal directions in the domain. These principal directions are given by the eigenvectors of this metric and the mesh size is related to the eigenvalues of this metric. And in order to build the corresponding metric, we start by setting up the error estimator that is according to [3] can then be written as:

$$\|\nabla q_h \cdot x^{ij} - \nabla q(x^i) \cdot x^{ij}\| \leq \max_{y \in |x^i, x^j|} |\nabla^2 q(y) x^{ij} \cdot x^{ij}| \tag{2}$$

Then, as proved in [4], and since for $P1$ finite elements on anisotropic meshes edge residuals dominate a posteriori errors, it is suitable to define an error indicator function e^{ij} associated to the edge x^{ij} as:

$$e^{ij} = |g^{ij} \cdot x^{ij}| \tag{3}$$

However, the gradient is not known at the vertices, thus a recovery procedure has to be considered, The recovered gradient G^i is the solution of the following optimization problem:

$$G^i = arg \min_G \left(\sum_{j \in \Gamma(i)} |(G - \nabla q_h) \cdot x^{ij}|^2 \right) \tag{4}$$

whose solution leads us to as estimation error expressed as:

$$e_{ij} = G^{ij} \cdot x^{ij} \tag{5}$$

In order to relate the error estimation to mesh adaptation, we will introduce a stretching factor s^{ij} defined as the ratio between the length of the edges x^{ij} before and after the adaptation procedure. The stretching factor s^{ij} of the edge ij is chosen so that the total number of nodes in the mesh is kept fixed and is defined as

$$s^{ij} = \left(\frac{e_{ij}}{e(N)} \right) \tag{6}$$

Finally, the metric takes the following expression[5]:

$$M^i = (\tilde{X}^i)^(- 1) \tag{7}$$

where $\tilde{X}^i$ is defines as:

$$\tilde{X}^i = \frac{1}{|\Gamma_i|} \left(\sum_{j \in \Gamma(i)} s^{ij} \times s^{ij} \right) \tag{8}$$

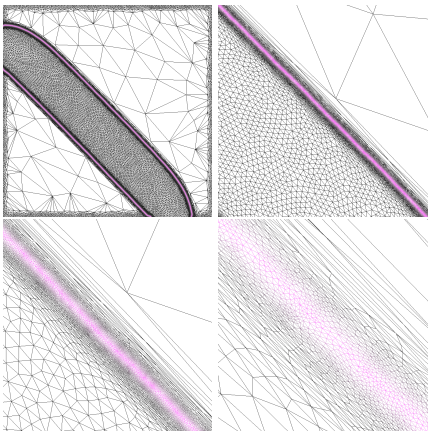

Figure 1: Progressive zoom on the mesh at the interface of the converged solution of the Bend Pipe design

In the following work, the only adaptation criterion will be the interface separating the fluid and solid regions, characterized by the truncated distance function. Figure 1 shows a progressive zoom in on the interface of a converged solution of a test case in section 5. At the left and right sides of the interface, we imposed a constant error in order to eliminate mesh adaptation in these regions and generate an isotropic mesh of constant mesh size. Since no computation is made in the solid region, we set a very small error that thus generates a very coarse mesh. And inversely, we set a relatively larger error in the fluid domain to generate a finer mesh.

2.3. Incompressible Navier-Stokes Solver

So we will consider the following velocity-pressure formulation of the non-linear Navier-Stokes equations:

$$\begin{array}{rcl} \mathbf{u}\cdot\nabla\mathbf{u} - \nabla\cdot\sigma(p,\mathbf{u}) = 0 & \text{in} & \Omega_{fluid} \\ \nabla\cdot\mathbf{u} = 0 & \text{in} & \Omega_{fluid} \end{array} \tag{9}$$

where p and $\mathbf{u}$ are the pressure and the velocity, and σ the stress tensor which reads:

$$\sigma = 2\mu\boldsymbol{\epsilon}(\mathbf{u}) - p\mathbf{I_d} \tag{10}$$

where μ is the dynamic viscosity, $\mathbf{I_d}$ is the identity tensor and $\boldsymbol{\epsilon}$ the strain-rate tensor defined as:

$$\boldsymbol{\epsilon} = \frac{1}{2}\left(\nabla\mathbf{u} + \nabla\mathbf{u}^T\right) \tag{11}$$

The complete description of the variational multiscale (VMS) formulation can be found in [5] and [6].

2.4. Level Set Convection

2.4.1. Standard level set method

Classically, the motion of the interface results from the following advection equation[7]:

$$\frac{d}{dt}\alpha(x,t) = \frac{\partial\alpha}{\partial t} + \mathbf{u}\cdot\nabla\alpha = 0 \tag{12}$$

An interesting feature on using a distance function is that we may ensure the smoothness of the quantity to be convected, which is very important when solving an advection equation with the finite element method. In fact, despite the latest improvements in stabilization techniques, the gradient smoothness remains a key point for having a stable scheme, since $\|\nabla\alpha\| = 1$ is not ensured by just solving 12. Owing to the flow complexity, the gradient of α can become very steep and numerical instabilities may occur. Thus, it is necessary to reinitialize the distance function. Classically, reinitialization is obtained by solving a Hamilton–Jacobi equation that reconstructs the level set with the exact zero isovalue of $\alpha(x,t)$[8]. If we introduce a virtual time τ, we search $\gamma(x,\tau)$ that has the same zero values than $\alpha(x,t)$:

$$\frac{\partial\gamma}{\partial\tau} + s(\alpha)(\|\nabla\gamma\| - 1) = 0 \tag{13}$$

where $s(\alpha)$ is the sign function of α.
Equation 13 can be rewritten as an another advection equation:

$$\frac{\partial\gamma}{\partial t} + \mathbf{U}\cdot\nabla\gamma = s(\alpha) \tag{14}$$

with the velocity $\mathbf{U}$ computed as:

$$\mathbf{U} = s(\alpha)\frac{\nabla\gamma}{\|\nabla\gamma\|} \tag{15}$$

The Hamilton-Jacobi procedure being iterative, the computational cost induced can be prohibitive for large computations. A method to alleviate this burden is the so-called convected level set method.

2.4.2. Convected level set method

The main idea of the convective re-initialization is to avoid the re-initialization step of the standard level-set method[9]. For this purpose, a parameter λ is introduced as:

$$\lambda = \frac{\partial\tau}{\partial t} \tag{16}$$

Thus we have:

$$\frac{\partial\gamma}{\partial t} = \lambda\frac{\partial\gamma}{\partial\tau} \tag{17}$$

And we can rewrite equation 13 to obtain:

$$\frac{\partial \gamma}{\partial t} + \lambda s(\alpha)(\|\nabla \gamma\| - 1) = 0 \tag{18}$$

Since we are in an Eulerian context, the time derivative can be changed in total derivative. Consequently, when using again α as the main variable, and substituting with 12, we finally get the convected re-initialization equation below:

$$\frac{\partial \alpha}{\partial t} + \mathbf{u} \cdot \nabla \alpha + \lambda s(\alpha)(\|\nabla \alpha\| - 1) = 0 \tag{19}$$

Re-written as:

$$\frac{\partial \alpha}{\partial t} + (\mathbf{u} + \lambda \mathbf{U}) \cdot \nabla \alpha = \lambda s(\alpha) \tag{20}$$

2.4.3. Local distance function

The only useful information for our computation is the exact zero isovalue position. Thus, the complete domain level set advection is not necessary, and may be the cause of further numerical instabilities. Another idea is to cut off the level set function at a thickness E using an hyperbolic tangent filter. The truncated level set, denoted $\hat{\alpha}$, is:

$$\hat{\alpha}(\alpha) = E \tanh\left(\frac{\alpha}{E}\right) \tag{21}$$

where E is the cut-off thickness.
The truncated level set now verifies the following property:

$$\|\nabla \hat{\alpha}\| = 1 - \left(\frac{\hat{\alpha}}{E}\right)^2 \tag{22}$$

And by substitution, the final and only equation to solve now reads:

$$\frac{\partial \alpha}{\partial t} + (\mathbf{u} + \lambda \mathbf{U}) \cdot \nabla \alpha = \lambda s(\alpha)\left(1 - \left(\frac{\hat{\alpha}}{E}\right)^2\right) \tag{23}$$

It is shown in [10] that the proposed method reduces the computational cost and ensure a better mass conservation than the classical level set method.

2.5. Control variable and Objective Function

The control variable of the optimization problem is chosen to be the normal velocity of the fluid-solid interface. This velocity is indeed an input to the advection solver (ref section 2.5) that updates the position of the level-set function. Numerically, and with a fixed time-step, this velocity characterises the normal displacement of the interface as shown in figure 2. Here,

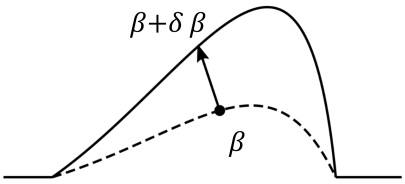

Figure 2: The deformation of the starting geometry (solid line) to the new one (dashed line) causes the total variation in the displacement, which depends on the flow variables

it is important to note that the value of the control velocity does not necessarily indicate the distance that the interface should travel. It is instead a comparative value of the relative displacement between each node and its neighbor. This being said, the convergence criteria is an equal control variable on all the interface rather than particularly a zero control velocity.
In the next section, we will investigate how to find an expression of the control velocity, that moves the interface in a way to minimize a certain objective function. For the rest of the work, we will deal with the following objective function:

$$J = \int_{\Gamma_{in} \cup \Gamma_{out}} \left(p + \frac{1}{2}\|\mathbf{u}\|^2\right) \mathbf{u} \cdot \mathbf{n} d(\Gamma_{in} \cup \Gamma_{out}) \tag{24}$$

which characterizes the minimization of the total power dissipated by a fluid dynamic device.

2.6. Adjoint solver and sensitivity analysis

Based on the continuous adjoint method for sensitivity analysis, the adjoint system that we derived is:

$$\begin{cases} -(\mathbf{u}.\nabla)\hat{\mathbf{u}} + \nabla \mathbf{u}.^T \hat{\mathbf{u}} - \nabla.\sigma(-\tilde{p}, \hat{\mathbf{u}}) = 0 \\ \nabla.\hat{\mathbf{u}} = 0 \end{cases} \tag{25}$$

where $\hat{\mathbf{u}}$ and $\hat{p}$ are respectevely the adjoint velocity and adjoint pressure.
We can easily notice that it is very similar to the Navier-Stokes equations, with two exceptions: the convection term is linear and is followed by the *minus* sign which switches the physical inlets and outlets for the adjoint problem, and we have an additional production term (Second term in equation 25). This is an additional advantage since we've been based on the Navier-Stokes solver to solve the adjoint equations. One main difference is that the adjoint equations are linear, and thus we do not need iterative models to get converged solutions.

The adjoint boundary conditions for equation (25) are:

$$\begin{array}{rcc} \hat{u}_n = -\mathbf{u}_{in} \cdot \mathbf{n} & \text{on} & \Gamma_{in} \\ \hat{u}_t = 0 & \text{on} & \Gamma_{in} \\ \hat{\mathbf{u}} = \mathbf{0} & \text{on} & \Gamma_{wall} \cup \Omega_{solid} \\ \sigma(-\hat{p}, \hat{\mathbf{u}}).\mathbf{n} + (\mathbf{u}.\mathbf{n})\hat{\mathbf{u}} = \mathbf{0} & \text{on} & \Gamma_{out} \end{array} \tag{26}$$

where the subscripts $_n$ and $_t$ refer respectively to the normal and tangential components of the vector that holds them.
The control velocity is therefore, a combination of the state and adjoint variables, and is expressed as follows:

$$\boldsymbol{V_c} = \frac{\partial J}{\partial \beta} = \mu \left[(\mathbf{n} \cdot \nabla) u_t \cdot (\mathbf{n} \cdot \nabla) \hat{u}_t \right] \mathbf{n} \tag{27}$$

For practical reasons, both the primal and the dual systems are solved in the entire design domain Ω. As a result, the control velocity is also computed at every node of the design domain. Whereas, the expression of the derived sensitivity is only valid near the solid-fluid interface. Also, in some cases, it may happen that the maximum of this gradient is not localised on the fluid-solid interface. This may be bluffing, since the maximum gradient is the main criteria that affects the numerical stability of the advection solver. A trivial solution was to implement a Dirac model, whose equation is shown below:

$$D(\alpha) = \begin{cases} \frac{1}{2e}\left[1 + \cos\left(\pi \frac{\alpha}{e}\right)\right] & \text{if} \quad |\alpha| < e \\ 0 & \text{if} \quad else \end{cases} \tag{28}$$

The Dirac model vanishes the value of the control velocity on all the nodes far from the interface. And a numerical treatment, creates a set of binary values that are *True* on a thickness e centered on the fluid-solid interface. This allows us to avoid oscillations, while keeping a maximum of deformation per iteration. And thus, it also allows us to accelerate the convergence of the result without loosing in precision.
Finally, for numerical stability purposes, the calculated gradient is multiplied by a descent factor before it is attributed to the advection solver. But this descent factor is very problematic, because the order of magnitude of the calculated gradient changes with the shape's evolution. With this being said, a fixed step deformation, even if relatively well adapted, causes fluctuations in the rate of shape deformation. To remedy, we implemented an algorithm that re-scales the control velocity, by multiplying it with coefficients that oblige its maximum to oscillate between 0.1 and 1. At the end, this re-scaled velocity is multiplied by a descent factor, set by the user depending on the case, and specially depending on the fictive time step of the advection solver.

3. Technical Modifications

After we built the main framework for topology optimization, some technical modifications are necessary for good functioning of the algorithm: a surface constraint and soft-blocking of the connections.

3.1. Surface Constraint

Previous work shows that, for some objective functions, the optimal shape tends to one of two extreme cases: either fill all the design domain (that is for example the case of pressure drop minimization), or completely disappear (that is the case of drag reduction).Though theoretically correct, the two extremes cases are undesired in the industrial field. For that reason, we put in place a surface constraint that keeps the geometry on a constant surface.
For that, we start by computing the fluid surface. For maximum precision, the surface calculation is done by integrating a Heaviside model on the solid domain. Then we subtract this value from the design domain surface to get the surface of the fluid region. Then, after each deformation, we add an offset value to the distance function ($\alpha = \alpha \pm \delta$), that allows us to recover our desired surface without affecting the geometry's shape. Then, after each deformation, we add an offset value to the distance function, that allows us to recover our desired surface without affecting the geometry. Finally, through the dichotomy method, we deduce the most suitable offset value, which allows us to be more conservative on the translated shape, and be more precise for the same pre-defined admissible error. In order to allow for the geometry to freely deform, we didn't apply the surface constraint at every iteration. Instead, we waited the geometry until it passes by a threshold surface S_{osc}, and we kept on applying the constraint until the surface is included in the interval of the admissible surfaces that is $]S_{ref} - err * S_{ref}; S_{ref} + err * S_{ref}[$. However, like any other constraint, the surface constraint generally end up without reaching the theoretical minimum, and thus, a compromise must be found in order to apply this constraint that is now indispensable.

3.2. SoftBlocking

The minimization of the objective function, might theoretically lead to the modification of the sizes of

the inlets and outlets of the problem. This is, for instance, the case of ducted flows, where the inlets and outlets have big impacts on the evolution of the objective function. At first, rigid blocking was a trivial solution. Although we succeeded in maintaining the positions of the fluid entries and exits, we broke the smoothness on the duct, and created a sudden change in the geometry. That's why we opted for softblocking, where the more it is far from the inlet-outlet, the more the interface is free to move. At each node (x_{node}, y_{node}) where we want to block the connections, we created two circles of diameters d_{V_C} and d_{δ_S}. Inside each circle, we created a scalar function that at each node takes the value of the distance between the node and the blocked node following:

$$d = \sqrt{(x_{node} - x)^2 + (y_{node} - y)^2} \tag{29}$$

For the control velocity, we sought for a filter that is null near the interface, and that reaches 1 steeply and smoothly towards d_{V_C}. The most convenient filter was a hyperbolic tangent one defined as follows:

$$Coef_{V_C} = \frac{1}{2} + \frac{1}{2} * \tanh\left(2.1 * \tan\left(-\frac{\pi}{2} + \pi * \frac{d}{d_{V_C} + \epsilon_1} + \epsilon_2\right)\right) \tag{30}$$

where ϵ_1 and ϵ_2 are two small values that we added to avoid discontinuities in the control velocity blocking zone. Here we set $\epsilon_1 = 0.001$ and $\epsilon_2 = 0.005$. For the surface constraint, the filter is exactly null at the interface, but it increases quicker and smoother to reach d_S with $d_{V_C} > d_{\delta_S}$. The most convenient filter was also hyperbolic tangent but defined as:

$$Coef_{\delta_S} = \tanh\left(1.1 * \tan\left(\pi * \frac{d}{2 * d_{\delta_S} + \epsilon_3}\right)\right) \tag{31}$$

where ϵ_3 is also a small values that we added to avoid discontinuities in surface constraint blocking zone. And here we set $\epsilon_3 = 5e^{-5}$.
For smooth deformation of the interface, our experiments showed that the best is to set d_{V_C} equal 1/40 of the distance orthogonal to the inlet-outlet we are blocking, and that d_{δ_S} fits the most when it is equal to $1.8 * d_{V_C}$. But these diameters remain dependant on the geometry, and it's always better to re-tune them case by case.

4. General Algorithm

Figure 3 shows the general algorithm of the topology optimization we applied. Going from the initial

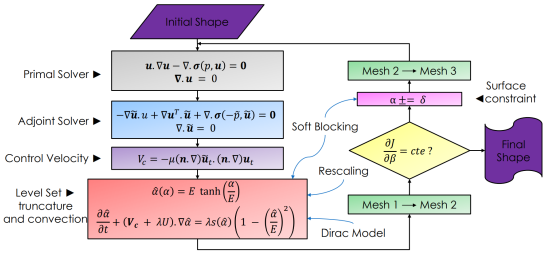

Figure 3: General Algorithm of Topology Optimization

shape, we start by solving the primal and adjoint systems. The state and adjoint equations allows us to compute the control velocity that will be an input for the advection solver that will take in charge moving the interface in the diresction of the steepest gradient of the objective function. Automatic re-meshing here is crucial in order to capture the interface with the highest precision possible. If the displacement of each nodes contributes equally to the minimization of the objective function, then we got our converged solution. If not, we apply the surface constraint and remesh again for precision. Then we re-iterate until convergence.

5. Numerical Benchmark : Design of a Bend Pipe

The design of a Bend Pipe has already been studied by [11][12][2][13]. The design domain is a 1x1 square with an inlet and an outlet of 0.2, centered at 0.8 from the bottom left corner respectively on the left and bottom side of the design domain as shown in figure 4. The inlet velocity has a parabolic profile whose equation, in a system of x and y axes centered on the bottom corner and merged with the edges of the square, is $U_x = 20(y - 0.7)(y - 0.8)$. At the outlet we consider a reference pressure of zero, and constraint the outgoing flow to be in the vertical direction. At the walls, as for the solid domain that will appear later, we consider a no-slip condition for the velocity and free pressure. The kinematic viscosity is 0.044, which leads to a Reynolds number 0.2 based on the averaged inlet velocity.

The starting geometry is composed of regularly distributed circles, in order to assure that there isn't any guess of what could be the final solution. The total surface occupied by the fluid in this configuration corresponds to 25% of the design domain corresponding to a quarter torus connecting the inlet to the outlet. This will indeed serve as a surface reference for the

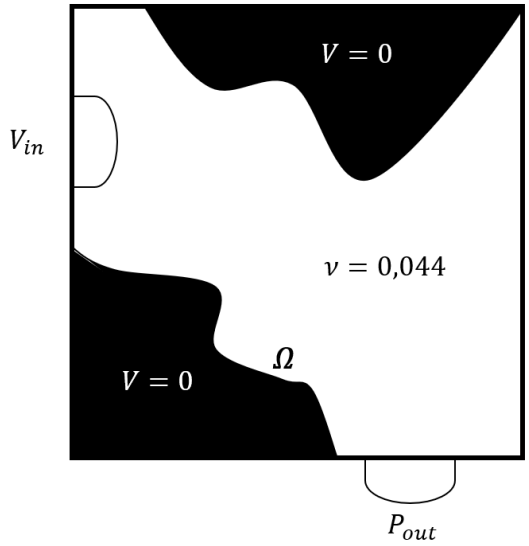

Figure 4: Design a of Bend Pipe Case Setup

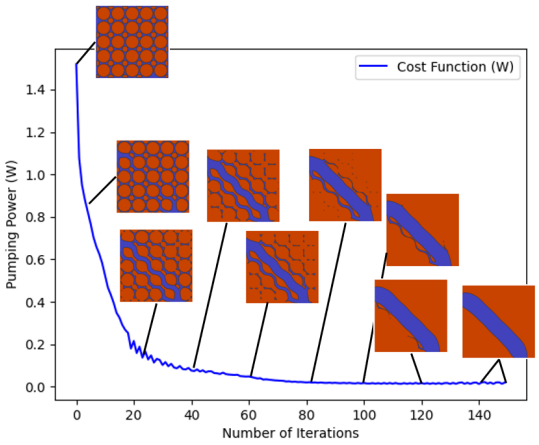

Figure 5: Design a of Bend Pipe Case Setup

rest of the problem with an admissible error on the final surface of 1%. The surface threshold before applying the surface constraint is 0.2525. The descent factor that multiplies the control velocity is 3. And the thickness of the Dirac model applied is equal to twice the minimum mesh size at the interface.

For the meshing, we started with a domain divided into three regions: The fluid and solid regions with interface between them. Since Dirichlet boundary conditions are imposed in the solid domain, no computation is taking place in this region, so we may mesh it coarsely. The mesh in the fluid domain is finer, and should be chosen in a way to ensure convergence of the Navier-Stokes Solution. The fluid-solid interface is the most critical region of the domain. It is important to have precise tracking of the interface when it is advected in order to not lose the desired shape and avoid instabilities. So here is where we make mesh adaptation and where we have the finer mesh with a minimum element size of 0.0001. Finally, the blocking functions of the control velocity and surface displacement are calculated on a distance of 0.025 and 0.045 near the frame, so a relatively fine mesh is applied there. In total, we have a sum of 21500 triangular anisotropic elements in all the design domain.

Beginning with three mesh adaptations, we then launch the CFD simulations. The first CFD simulation (done before any shape deformation), takes about ten iterations to converge. Then, due to velocity and pressure interpolations and to the small displacement per iteration of the interface, steady-state solution is reached after two to three iterations. The convergence criteria being an admissible error of 0.05% on the velocity.

Shape convergence is reached after 140 iterations.The evolution of the objective function with respect of the number of iterations is shown in figure 5. For several values of the objective function, we can also follow the shape evolution.

First of all, it is important to note that, contrarily to an intuitive guess, the optimal shape is not a quarter torus connecting the inlet to outlet, but instead, it is an almost straight channel. According to [6], this can be explained as follows: If a prescribed amount of fluid is to be transported in a pipe, the shears in the fluid are large when the pipe is thin and, conversely, small when the pipe is wide. Since the dissipated power in Stokes flow is due to shears only, an optimal flow pipe is preferably short and wide.

6. Conclusion and Perspectives

In conclusion, we described in this article the procedure we followed to build a numerical framework for topology optimization. Going from the Level-Set method coupled with anisotropic mesh adaptation for capturing the interface, we reached sensitivity computation based on the continuous adjoint method, that led us through moving the interface in the optimal direction.

In order to validate our numerical benchmark, three test cases has been studied: the design of a Bend Pipe, of a Dual Pipe, and of a Four Terminal Device. We launched the optimizations going from regular geometries as a started position, to more complex

starting geometries as a design domain full of circles. These test cases proved the reliability and robustness of our algorithm, even though the second test case showed the dependency of the method on the starting geometry. They also helped us to touch that the minimization of the pumping power for a fluidic device, requires at most to shorten the ducts and to make them as wide as possible. Indeed, the results showed that generally, the most optimal shape is the shortest and widest possible duct connecting each inlet to an outlet.

Even though reliable and robust, our algorithm have several limitations. Until now, we only deal with incompressible laminar flows, and steady state problems. Regarding our future work, we aim to tackle heat exchange problems. We also aim to deal with multi-phase flows, which combines variable densities and unsteadiness of the flow. The additional terms and equations, will be mirrored into complexity in the derivation of the sensitivity. Before the last, we wish to gradually increase the Reynolds number of the flow. And finally, we will switch to three dimension problems.

Acknowledgments

This project has received funding from the Clean Sky2 Joint Undertaking (JU) under grant agreement No 886698. The JU receives support from the European Union's Horizon 2020 research and innovation programme and the Clean Sky 2 JU members other than the Union. This paper reflects only the author's view and that the JU is not responsible for any use that may be made of the information it contains.

References

[1] M. P. Bendsoe, O. Sigmund, Topology Optimization, Springer, 2004. doi:10.1007/978-3-662-05086-6.

[2] T. Borrvall, J. Petersson, Topology optimization of fluids in stokes flow, International Journal for Numerical Methods in Fluids 41 (1) (2003) 77–107. arXiv:https://onlinelibrary.wiley.com/doi/pdf/10.1002/fld.426, doi:https://doi.org/10.1002/fld.426.

[3] T. Coupez, Metric construction by length distribution tensor and edge based error for anisotropic adaptive meshing, Journal of Computational Physics 230 (7) (2011) 2391–2405. doi:10.1016/j.jcp.2010.11.041.

[4] G. Kunert, R. Verfürth, Edge residuals dominate a posteriori error estimates for linear finite element methods on anisotropic triangular and tetrahedral meshes, Numerische Mathematik 86 (2000) 283–303. doi:10.1007/PL00005407.

[5] T. Coupez, E. Hachem, Solution of high-Reynolds incompressible flow with stabilized finite element and adaptive anisotropic meshing, Computer Methods in Applied Mechanics and Engineering 267 (2013) 65–85. doi:10.1016/j.cma.2013.08.004.

[6] E. Hachem, B. Rivaux, T. Kloczko, H. Digonnet, T. Coupez, Stabilized finite element method for incompressible flows with high Reynolds number, Journal of Computational Physics 229 (23) (2010) Pages 8643–8665. doi:10.1016/j.jcp.2010.07.030.

[7] M. Sussman, P. Smereka, S. Osher, A level set approach for computing solutions to incompressible two-phase flow, Journal of Computational Physics 114 (1) (1994) 146–159. doi:https://doi.org/10.1006/jcph.1994.1155.

[8] M. Khalloufi, Y. Mesri, R. Valette, E. Massoni, E. Hachem, High fidelity anisotropic adaptive variational multiscale method for multiphase flows with surface tension, Computer Methods in Applied Mechanics and Engineering 307 (2016) 44–67. doi:https://doi.org/10.1016/j.cma.2016.04.014.

[9] L. Marioni, M. Khalloufi, F. Bay, E. Hachem, Two-fluid flow under the constraint of external magnetic field, International Journal of Numerical Methods for Heat and Fluid Flow 27 (11) (2017) 2565 – 2581. doi:10.1108/HFF-09-2016-0371.

[10] C. Bahbah, M. Khalloufi, A. Larcher, Y. Mesri, T. Coupez, R. Valette, E. Hachem, Conservative and adaptive level-set method for the simulation of two-fluid flows, Computers and Fluids 191 (2019) 104223. doi:https://doi.org/10.1016/j.compfluid.2019.06.022.

[11] X.-B. Duan, Y.-C. Ma, R. Zhang, Shape-topology optimization for navier–stokes problem using variational level set method, Journal of Computational and Applied Mathematics 222 (2) (2008) 487–499. doi:https://doi.org/10.1016/j.cam.2007.11.016.

[12] M. Abdelwahed, M. Hassine, M. Masmoudi, Optimal shape design for fluid flow using topological perturbation technique, Journal of Mathematical Analysis and Applications 356 (2) (2009) 548–563. doi:https://doi.org/10.1016/j.jmaa.2009.02.045.

[13] A. Gersborg, O. Sigmund, R. Haber, Topology optimization of channel flow problems, Structural and Multidisciplinary Optimization 30 (2005) 181–192. doi:10.1007/s00158-004-0508-7.

Non-linear harmonic method for adjoint-based turbomachinery optimisation

Tom De Bruyn

Turbomachinery and Propulsion Department, von Karman Institute for Fluid Dynamics, Belgium, tom.de.bruyn@vki.ac.be

Supervisor: Tom Verstraete[1] and Fabrizio Fontaneto[2]

[1]*Professor, Turbomachinery and Propulsion Department, von Karman Institute for Fluid Dynamics, Belgium, tom.verstraete@vki.ac.be*

[2]*Associate Professor, Turbomachinery and Propulsion Department, von Karman Institute for Fluid Dynamics, Belgium, fabrizio.fontaneto@vki.ac.be*

University Supervisor: Joris Degroote

Professor, Department of Electromechanical, Systems and Metal Engineering, Ghent University, Belgium, joris.degroote@ugent.be

Abstract

As optimisation methods for turbomachinery components become increasingly important to enable further design improvements, there is an interest to extend the capabilities of these methods to cases with significant unsteady effects, such as inlet distortions or strong blade row interactions. In order to do so however, cfd solvers must consider unsteadiness. Harmonic solvers, describing the unsteadiness as set of harmonic perturbations of the mean flow, achieve this at moderate computational cost.

Keywords: CFD, non-linear harmonics, harmonic balance, optimisation

1. Introduction

Several decades after their introduction, Steady Reynolds-averaged Navier-Stokes (RANS) methods remain the dominant approach to turbomachinery CFD, permitting rapid and relatively inexpensive computation. This is especially true in the context of now prevalent optimisation workflows (as considered in the VKI's in-house turbomachinery optimisation framework *CADO*[1], where up to several hundreds of design evaluations may be required. In such cases, higher fidelity methods become prohibitively expensive. RANS methods however insufficiently capture all physical aspects of interest during the optimisation process. Notably vibrational effects (e.g. flutter, vibrations induced by blade row interaction, ...) are by nature unsteady. These effects are of great importance in turbomachinery component development and directly influenced by typical design variables of the optimisation process, hence they must be included directly.

For aircraft engines specifically, recent consideration of novel airplane configurations has led to an increased interest in capturing installation effects such as operation with non-uniform inlet flow. Although steady for the engine as a whole, the solution in each blade passage becomes time-variant in these cases. As full annulus simulation would once again lead to a considerable and in many cases prohibitive computational penalty, these cases also require the solver to consider unsteady operation.

In this paper, a class of methods that incorporates this unsteadiness at reasonable cost is considered. In light of integration in the *CADO* optimisation framework, specific attention is given to the adjoint formulation for these methods. The method and its adjoint are applied to a representative turbomachinery testcase, applying a synthetic inlet distortion to the NASA Rotor 67 test case[2].

2. Harmonic methods

In order to incorporate unsteadiness without suffering the computational penalty of an unsteady RANS (URANS) computation, an harmonic or frequency-domain method is used to capture most of the un-

steadiness at reasonable expense. In order to do so, the solution of the URANS equations for a periodic flow is decomposed into it's temporal Fourier components:

$$U(t, \mathbf{x}) = Re\left[\sum_{k=0}^{\inf} \hat{U}_k(\mathbf{x}) e^{\mathbf{i}k\omega t}\right], \tag{1}$$

where $\omega = 2\pi f$ is the base frequency and U the vector of conservative variables:

$$U = \begin{pmatrix} \rho \\ \rho v_x \\ \rho v_y \\ \rho v_z \\ \rho e \end{pmatrix}. \tag{2}$$

Starting from the unsteady form of the Navier-Stokes equations:

$$\frac{dU}{dT} + R(U) = 0, \tag{3}$$

where $R(U) = F_c(U) - F_v(U) + Q(U)$ is the steady residual comprising of the convective flux, viscous flux and source term respectively, substitution of (1) leads to:

$$k\omega\, Im\left[\sum_{k=0}^{\inf} \hat{U}_k(\mathbf{x}) e^{\mathbf{i}k\omega t}\right] + R(U) = 0. \tag{4}$$

the steady residual R in equation (4) can similarly be decomposed in it's Fourier components:

$$k\omega\, Im\left[\sum_{k=0}^{\inf} \hat{U}_k(\mathbf{x}) e^{\mathbf{i}k\omega t}\right] + Re\left[\sum_{k=0}^{\inf} \hat{R}_k(U) e^{\mathbf{i}k\omega t}\right] = 0, \tag{5}$$

which must hold true for every $t \in [0, T]$, which can be expressed as:

$$\int_0^T f(t)\left(k\omega\, Im\left[\sum_{k=0}^{\inf} \hat{U}_k(\mathbf{x}) e^{\mathbf{i}k\omega t}\right] + Re\left[\sum_{k=0}^{\inf} \hat{R}_k(U) e^{\mathbf{i}k\omega t}\right]\right) = 0 \qquad \forall f(t), \tag{6}$$

where T is the period $2\pi/\omega$. By choosing $f_{k1}(t) = Re\left[e^{\mathbf{i}k\omega t}\right]$ and $f_{k2}(t) = Im\left[e^{\mathbf{i}k\omega t}\right]$ respectively and using the orthogonality of trigonometric functions, the unsteady equations can be formulated in the frequency domain,

$$\begin{aligned} k\omega Im\left[\hat{U}_k(\mathbf{x})\right] + Re\left[\hat{R}_k(U)\right] = 0. \\ k\omega Re\left[\hat{U}_k(\mathbf{x})\right] - Im\left[\hat{R}_k(U)\right] = 0. \end{aligned} \tag{7}$$

which is more simply expressed as:

$$\mathbf{i}k\omega\hat{U}_k(\mathbf{x}) + \hat{R}_k(U) = 0. \tag{8}$$

with $\hat{R}_k$ as above the k-th harmonic of the steady Navier-stokes Residual R, which depend on all harmonics of the solution U. Writing (8) for all k, one obtains a set of balance equations, leading to the name 'harmonic balance' technique[3].

2.1. Finite harmonics

In practice, a finite number of frequencies is used. As the computational effort inevitably increases with an increased number of included harmonics, the number is a trade-off between performance and the improved accuracy representing relevant unsteadiness as more frequencies are included. When the number of harmonics is truncated, (8) is no longer exact. Indeed the non-linearity of the steady RANS residual $R(U)$ means the solution and residual cannot be represented using the same (finite) set of harmonics.

This can be easily understood from the product of two different harmonic components. The multiplication of two variables $f(t)$ and $g(t)$, described using the same number of harmonics can be written out in full:

$$\begin{aligned} f(t)\, g(t) =& \frac{1}{2}\sum_{k=0}^{K}\left[\hat{F}_k e^{\mathbf{i}k\omega t} + \hat{F}_{-k} e^{-\mathbf{i}k\omega t}\right] * \\ & \frac{1}{2}\sum_{l=0}^{L}\left[\hat{G}_l e^{\mathbf{i}l\omega t} + \hat{G}_{-l} e^{-\mathbf{i}l\omega t}\right] \\ =& \frac{1}{4}\sum_{k=0}^{K}\sum_{l=0}^{L}\Big[\hat{F}_k\hat{G}_l e^{\mathbf{i}(k+l)\omega t} \\ & \hat{F}_k\hat{G}_{-l} e^{\mathbf{i}(k-l)\omega t} \\ & \hat{F}_{-k}\hat{G}_l e^{\mathbf{i}(l-k)\omega t} \\ & \hat{F}_{-k}\hat{G}_{-l} e^{-\mathbf{i}(k+l)\omega t}\Big], \end{aligned} \tag{9}$$

where $\hat{F}_{-k}$ and $\hat{G}_{-l}$ are the complex conjugates of $\hat{F}_k$ and $\hat{G}_l$ respectively. It is clear from (9) that if each of the terms has s up to K harmonic, the product contains harmonics up to the $2K$'th harmonic of the base frequency as well as that a particular harmonic of the solution contribute to the residual for several (other) harmonics.

The non-linearity of the RANS residual thus introduces a coupling between the different harmonics, which - depending on the applied methodology - can be neglected, selectively computed or need to be taken into account to prevent aliasing. Regardless of the methodology, a 'harmonic balance' like (8) always neglects harmonics of the residual of higher order than the choice for the decomposition of the solution. However, as the number of harmonics in the solution is increased the approximation error decreases (as generally higher harmonics have a smaller amplitude in the considered cases).

3. Methodology

Writing the residual term in equation (8) first as a Taylor series around the steady solution $\hat{U}_0$ and applying the Fourier transform afterwards leads to the following expressions for the harmonics of the Residual, with K total harmonics considered:

$$\begin{aligned}\hat{R}_0 &= R(\hat{U}_0) + D_0(\hat{U}_0, ...\hat{U}_K)\\ \hat{R}_k &= R(\hat{U}_0) + \left.\frac{\partial R}{\partial U}\right|_{\hat{U}_0} \hat{U}_K + D_k(\hat{U}_0, ...\hat{U}_K) \quad k \neq 0.\end{aligned} \tag{10}$$

The coupling terms D_k are called the deterministic stresses and contain the interaction between the higher harmonics. As the Taylor series expansion introduces polynomials of degree higher than one, these terms are non-linear, maintaining the coupling between the harmonics considered above. Linear harmonic (also called time-linearised) methods neglect all deterministic stress terms in (10), retaining only the first, linear term for the higher harmonics [4].

Non-linear harmonic methods [5; 6] include at least the D_0 term modelling the influence of the unsteadiness on the mean flow field. This term is computed from the higher order harmonics and given by (split in a convective and viscous contribution)[7]:

$$D_0(U) = D_{C0} - D_{V0} = \begin{pmatrix} 0 \\ \overline{(\rho\mathbf{v})'v'_x} \\ \overline{(\rho\mathbf{v})'v'_y} \\ \overline{(\rho\mathbf{v})'v'_z} \\ \overline{(\rho H)'\mathbf{v}'} \end{pmatrix} - \begin{pmatrix} 0 \\ 0 \\ 0 \\ 0 \\ \tau'\mathbf{v}' \end{pmatrix}, \tag{11}$$

where the prime indicates $\rho' = \rho - \hat{\rho}_0$ the unsteady part of the solution. Computation of this term then requires a sum over all harmonics e.g.:

$$\overline{(\rho\mathbf{v})'v'_x} = \frac{1}{4}\sum_{k=1}^{K}\left[\rho\hat{V}_{x_k}\hat{\mathbf{V}}_{-k} + \rho\hat{V}_{x_{-k}}\hat{\mathbf{V}}_k\right]. \tag{12}$$

the evolution of the higher order harmonics is typically modelled by a transport equation using the time-averaged velocity components, neglecting mutual influence of the harmonics on one another, besides through their effect on the mean flow [5; 7]. Including the coupling is however possible as well, though tedious [8].

As such, this method is formulated exclusively in the frequency domain, avoiding the need for Fourier transformations. This does however render the implementation of boundary conditions, classically formulated in the time domain, somewhat more involved. The major drawback is however the neglecting of the coupling terms for the higher harmonics, reducing the overall accuracy of the method in cases where the unsteadiness is more significant.

3.1. time-spectral method

An attractive alternative approach is not to model the deterministic stresses directly, but rather implicitly incorporate these terms by using the discrete Fourier Transform of the non-linear residual. To do so, the solution U is sampled at at least $2K + 1$ sample points (K the index of the highest considered harmonic), for which the Residual is evaluated, resulting in a set of equations:

$$\mathbf{i}k\omega\hat{U}_k(\mathbf{x}) + \mathscr{F}_k(R(\mathscr{F}^{-1}(\hat{U}))) = 0, \tag{13}$$

where $\mathscr{F}_k$ is the k-th component of the discrete Fourier transform and $\hat{U}$ is (1) truncated at K, the approximate reconstruction of the flow field [9; 10]. Particular care is needed for these methods to avoid aliasing in the forward and inverse transforms. As discussed in section 2.1, the residual $R(U)$ contains higher harmonics than U itself, which during the forward Fourier transform may produce spurious contributions to the lower harmonics. In order to reduce the effect, Orszag [11] has suggested to sample at $N \geq 3K + 1$ time instances (50% higher than the lower bound of the Shannon-Nyquist theorem), which is sufficient to eliminate aliasing for quadratic functions. As the residual computation is generally rational, it contains infinitely many harmonics, however these contributions are third order in the perturbation amplitude, and hence drop of quickly. It must be noted that (over)sampling comes at a non-negligible cost,

as at every time instance a residual evaluation is performed.

The time-spectral method holds several important advantages over the 'classic' linear harmonic approach:

- Coupling between harmonics is implicitly included.
- As the RANS residual is evaluated in the time domain, flux evaluation routines developed for steady computations can be applied without modification. This is particularly advantageous for codes with both a steady and harmonic solver, as a single set of routines can be used.
- The joint use of the time and frequency domain, while necessitating the extra cost of the Fourier transforms, means boundary conditions can be formulated in either.

In some cases (13) is cast into the time-domain, corresponding to a pseudo-spectral discretisation of the time-dependent term in the URANS equations[9]. While this removes the need for the forward Fourier transform, the approximation of the time derivative becomes increasingly inaccurate when few (< 16) sampling points are used. Furthermore, it introduces a further coupling between different harmonics, whereas (8) and (as a result) (13) allow one to solve for every wave number independently.

3.2. phase-shift boundary conditions

In order to limit the computational domain, and therefore computational effort, w.r.t. full-annular simulations, periodic boundary conditions are typically applied to a single blade passage. In most turbomachinery computations, the temporal variation of the solution in the blade passage is induced by a spatial (or spatial and temporal) variation of the inlet or outlet conditions along the domain pitch, rather than a solely temporal one. In these cases, the solution in the adjacent blade passages is not instantaneously equal to the solution in the meshed passage, and periodic boundary conditions need to be adjusted to include a 'phase-shift' between trailing and leading side of the periodic boundary [12].

At any given time t, the solution at the leading edge of the meshed blade passage corresponds to the solution at the trailing edge $2\pi/\omega_R N_B$ seconds into the future, when the rotor has rotated over $1/N_B$ part of a full rotation (N_B being the number of blade passages, ω_R the rotational speed of the machine). Hence,

$$\begin{aligned} U_{LE}(t) &= U_{TE}(t + \frac{2\pi}{\omega_R N_B}) \\ U_{TE}(t) &= U_{LE}(t - \frac{2\pi}{\omega_R N_B}), \end{aligned} \tag{14}$$

where the subscripts TE and LE denote trailing and leading edge respectively. Substituting the frequency domain formulation (1) leads for sampling point t_i of the time-spectral method to

$$\begin{aligned} U_{LE}(t_i) &= Re\left[\sum_{k=0}^{K} \hat{U}_{k,TE}(\mathbf{x}) e^{\mathbf{i}k\omega(t_i + \frac{2\pi}{\omega_R N_B})}\right] \\ U_{TE}(t_i) &= Re\left[\sum_{k=0}^{K} \hat{U}_{k,LE}(\mathbf{x}) e^{\mathbf{i}k\omega(t_i - \frac{2\pi}{\omega_R N_B})}\right]. \end{aligned} \tag{15}$$

The term inside the exponential is typically written as a time-dependent part and a phase-shift:

$$k\omega t_i \pm \frac{k2\pi\omega}{\omega_R N_B} = k\omega t_i \pm \sigma_k, \tag{16}$$

where the shift σ_k only depends on the number of blade passages and the ratio between the perturbation (base)frequency and the rotational speed. E.g. in the case of a single rotating blade row following a stationary row of N_V vanes leads to a spatially periodic inlet condition repeating N_V times along the machine's circumference. In this case $\omega = N_V \omega_R$ and (16) depends solely on the blade ratio.

Note that the definition of a phase-shift is a requirement to unique define an unsteady perturbation, as the same perturbation frequency can be the result of either a temporal or spatial variation of boundary conditions, or a mix of both. Lastly note that generally the temporal shift $2\pi/\omega_R N_B$ does not correspond to the interval between sampling points, showing the strength of the time-spectral method for the formulation of boundary conditions.

3.3. treatment of turbulence

For all aforementioned methods, a common assumption is that turbulence models for RANS can be applied for unsteady flow as well, as with a limited number of harmonics, the time scale of the variation of the mean flow (including the harmonic components, but not turbulence), is still orders of magnitude greater than the time scale of the turbulence. Hence existing methods for RANS turbulence modelling such as the (negative) Spalart-Allmaras model[13] can be used. A common simplification is to assume the effect of the

harmonic unsteadiness on the turbulence to be negligible. Under that assumption, the computation of turbulent values (e.g. the Spalart-Allmaras transport quantity) is identical to the treatment for steady flow. The resulting eddy viscosity is used in the computation of all harmonics.

The time-spectral methods offer another approach without the need to express the transport equations in the frequency domain. The same approach used to obtain equation (13) can be applied directly. For the Spalart-Allmaras model used in *CADO* this means expressing the transport quantity as:

$$\rho\tilde{\nu}(t,\mathbf{x}) = Re\left[\sum_{k=0}^{K}\hat{\rho\tilde{\nu}}_k(\mathbf{x})e^{\mathbf{i}k\omega t}\right], \tag{17}$$

leading to an evolution equation:

$$\mathbf{i}k\omega\hat{\rho\tilde{\nu}}_k(\mathbf{x}) + \mathscr{F}_k(R^{TUR}(\mathscr{F}^{-1}(\hat{U},\hat{\rho\tilde{\nu}}))) = 0, \tag{18}$$

where to evaluate the turbulence residual both meanflow and turbulence values are brought to the time domain. Hence the solution strategies used for the mean/harmonic flow can straightforwardly be applied to the turbulence model as well.

4. solution strategy

To solve the system of equations (10) or (13) a pseudo-time marching method is used. Hereto, the pseudo-timestep is added to the left-hand side of (8):

$$\frac{d\hat{U}_k}{dt'} + \mathbf{i}k\omega\hat{U}_k(\mathbf{x}) + \hat{R}_k(U) = \frac{d\hat{U}_k}{dt'} + \hat{R}_k^H(U) = 0. \tag{19}$$

Using m to indicate the pseudo-time step, and using

$$\Delta\hat{U}_k^{(m)} = \hat{U}_k^{(m+1)} - \hat{U}_k^{(m)} \tag{20}$$

a theoretical implicit formulation for the numerical update strategy becomes (linearising the residual around the steady component):

$$\left(\frac{1}{\Delta t'} + \mathbf{i}k\omega + \frac{\partial R_k}{\partial U}\right)\Delta\hat{U}_k^{(m)} = -\hat{R}_k^H(U). \tag{21}$$

In equation (21) different harmonics are generally coupled through the computation of the right-hand side, but also by the Jacobian of the linear system. The latter is somewhat problematic, as by using this formulation all harmonics are solved for simultaneously in a linear system of $2K + 1$ equations. As a result the memory requirements increase with the number of harmonics, and quickly become prohibitive for a larger number of harmonics.

Therefore typically the Jacobian in the left hand site of (21) is approximated for higher harmonics by the one for the steady computation (e.g. [14]:

$$\left(\frac{1}{\Delta t'} + \mathbf{i}k\omega + \left.\frac{\partial R_0}{\partial U}\right|_{\hat{U}_0^{(m)}}\right)\Delta\hat{U}_k^{(m)} = -\hat{R}_k(U), \tag{22}$$

allowing for the updates of the different harmonics to be solved for sequentially (or in fact in parallel, though in that case read access to the stored system matrix may still be serialised, reducing parallelisation effectiveness). As a result, the system matrix must only be computed once for the update of all harmonics.

5. adjoint

The *CADO* optimisation framework the current work is part of makes use of the adjoint method to obtain gradient information. The major advantage of this method is that the cost is roughly proportional to the number of objective functions, rather than to the number of design variables, the former generally being a lot smaller. This way the method allows for large design spaces and a (very) high number of design variables. The method is described in [1], but is generalised here as both the flow solution $U = \left(\hat{U}_0, \hat{U}_1, ..., \hat{U}_N\right)$ and harmonic balance residual $R = \left(\hat{R}_0^H, \hat{R}_1^H, ..., \hat{R}_N^H\right)$ are comprised of complex variables. The objective function J is a functional depending on the solution U and computational grid X:

$$J(U,X) : \mathbb{C}^N x\, \mathbb{R}^M \longrightarrow \mathbb{R}, \tag{23}$$

where N and M are the number of flow variables multiplied by the number of harmonics and number of grid coordinates respectively. Adding the state equations as a constraint through use of Lagrange multipliers Λ the Lagrangian functional is obtained:

$$\begin{gathered} L(U,X) = J(U,X) + \langle R(U,X),\Lambda\rangle : \\ \mathbb{C}^N x\, \mathbb{R}^M x\, \mathbb{C}^N \longrightarrow \mathbb{R}, \end{gathered} \tag{24}$$

where $\langle\cdot\,,\cdot\rangle$ is any inner product on $\mathbb{C}^N$.
Defining the directional (Gateaux) derivative as:

$$d_xF(a;\delta_x) = \lim_{\tau\to 0}\frac{F(a+\tau\delta_x) - F(a)}{\tau}, \tag{25}$$

with δ_x any unit vector of the considered function space. The requirement in the theory of Lagrange multipliers that the minimum must be a stationary point of the Lagrangian (all directional derivatives equal to zero), can be expressed as:

$$\begin{aligned} d_u L(U, X, \Lambda; \delta_u) &= d_u J(U, X; \delta_u) + \langle d_u(R(U, X; \delta_u), \Lambda \rangle \\ &= 0 \qquad \forall \delta_u \in \mathbb{C}^N, \end{aligned} \tag{26}$$

$$\begin{aligned} d_x L(U, X, \Lambda; \delta_x) &= d_x J(U, X; \delta_x) + \langle d_x R(U, X; \delta_x), \Lambda \rangle \\ &= 0 \qquad \forall \delta_x \in \mathbb{R}^M, \end{aligned} \tag{27}$$

and

$$\begin{aligned} d_\lambda L(U, X, \Lambda; \delta_\lambda) = \langle R(U, X), \delta_\lambda \rangle = 0 \\ \forall \delta_\lambda \in \mathbb{C}^N. \end{aligned} \tag{28}$$

Equations (26) through (28) are true for any inner product, though the most convenient and logical choice is the standard complex inner product $\langle A, B \rangle = a_i \bar{b}_i$, where the overbar indicates the complex conjugate. With this choice and unit vectors $\epsilon_{i,R} = \epsilon_i + 0\mathbf{i}$ and $\epsilon_{i,I} = \epsilon_i \mathbf{i}$, equation (28) simply states that all real and imaginary components of the harmonic residual of section 4 must be zero.

This inner product and $\mathbb{C}^N$ define an inner-product space. In this space, a linear operator F defines an adjoint operator F^* according to:

$$\langle F(A), B \rangle = \langle A, F^*(B) \rangle, \tag{29}$$

with F^* the conjugate transpose of F. This, together with the linearisation of (the directional derivative of) the non-linear residual operator:

$$d_u R(U, X; \delta_u) \rightarrow R_u(U, X)\delta_u, \tag{30}$$

allows equation (26) to be written as:

$$\left\langle \delta_u, R_u^*(\Lambda) \right\rangle = -d_u J(U, X; \delta_u) \quad \forall \delta_u \in \mathbb{C}^N, \tag{31}$$

providing a set of equations that can be used to compute the values of Λ in the stationary point. These, together with equation (27) allow the gradient of the functional J with respect to the computational grid to be computed. From here on out, there's no difference with the 'classic' method using only real numbers.

6. results

7. Conclusion

This paper surmises the most commonly used 'harmonic' methods for solving the Reynolds-averaged Navier Stokes (RANS) equations, used when the unsteadiness of the meanflow is periodic and can be accurately represented by small amount of harmonic pertubations. Situated between steady and unsteady RANS solvers, they offer an interesting solution to capture unsteadiness without the - in the context of an optimisation process - prohibitive cost of full annulus URANS. Time-spectral methods are particularly enticing as they can potentially share subroutines with a steady RANS solver, reducing the overal development effort.

Acknowledgments

This PhD research is supported by a fellowship of the Flanders Scientific Research Fund (FWO)

References

[1] L. Mueller, T. Verstraete, Cad integrated multipoint adjoint-based optimization of a turbocharger radial turbine, International Journal of Turbomachinery, Propulsion and Power 2 (3).

[2] A. J. Strazisar, J. R. Wood, M. D. Hathaway, K. L. Suder, Laser anemometer measurements in a transonic axial-flow fan rotor, 1989.

[3] C. Frey, G. Ashcroft, H.-P. Kersken, C. Voigt, A harmonic balance technique for multistage turbomachinery applications, 2014. doi:10.1115/GT2014-25230.

[4] G. Dufour, F. Sicot, G. Puigt, C. Liauzun, A. Dugeai, Contrasting the harmonic balance and linearized methods for oscillating-flap simulations, Aiaa Journal - AIAA J 48 (2010) 788–797. doi:10.2514/1.43401.

[5] S. Vilmin, E. Lorrain, C. Hirsch, M. Swoboda, Unsteady flow modeling across the rotor/stator interface using the nonlinear harmonic method, Vol. 6, 2006. doi:10.1115/GT2006-90210.

[6] L. He, W. Ning, Efficient approach for analysis of unsteady viscous flows in turbomachines, Aiaa Journal - AIAA J 36 (1998) 2005–2012. doi:10.2514/2.328.

[7] S. G. Horcas, F. Debrabandere, B. Tartinville, C. Hirsch, G. Coussement, Extension of the non-linear harmonic method for the study of the dynamic aeroelasticity of horizontal axis wind turbines, Journal of Fluids and Structures 73 (2017) 100–124. doi:https://doi.org/10.1016/j.jfluidstructs.2017.06.008.
URL https://www.sciencedirect.com/science/article/pii/S0889974616306302

[8] P. Vasanthakumar, Three dimensional frequency-domain solution method for unsteady turbomachinery flows, Ph.D. thesis, Durham University (2003).
URL http://etheses.dur.ac.uk/3089/

[9] K. C. Hall, J.P. Thomas and W. Clark, Computation of Unsteady Nonlinear flows in Cascades Using a Harmonic Balance Technique, AIAA Journal 40 (5) (2002) 879–886.

[10] McMullen, Matthew Scott and Jameson, Anthony and Alonso, Juan J., The Application of Non-Linear Frequency Domain Methods to the Euler and Navier-Stokes Equations, Ph.D. thesis, Stanford University, Stanford, CA (3 2003).

[11] S. A. Orszag, On the Elimination of Aliasing in Finite-Difference Schemes by Filtering High-Wavenumber Components., Journal of Atmospheric Sciences 28 (6) (1971) 1074–1074. doi:10.1175/1520-0469(1971)028¡1074:OTEOAI¿2.0.CO;2.

[12] L. He, Method of simulating unsteady turbomachinery flows with multiple perturbations, AIAA Journal 30 (1992) 2730–2735. doi:10.2514/3.11291.

[13] S. R. Allmaras, F. T. Johnson, P. R. Spalart, Modifications and clarifications for the implementation of the spalart-allmaras turbulence model, 2011.

[14] G. Ashcroft, C. Frey, H.-P. Kersken, On the development of a harmonic balance method for aeroelastic analysis, in: E. Onate, X. Oliver, A. Huerta (Eds.), 6th. European Conference on Computational Fluid Dynamics - ECFD VI, 2014, pp. 5885–5896.
URL https://elib.dlr.de/90474/

Gradient-based aeroacoustic optimization of NASA Rotor37

Romain Hottois

Turbomachinery and Propulsion Department, von Karman Institute for Fluid Dynamics, Belgium, romain.hottois@vki.ac.be

Supervisor: Tom Verstraete

Associate Professor, Turbomachinery and Propulsion Department, von Karman Institute for Fluid Dynamics, Belgium, tom.verstraete@vki.ac.be

University Supervisor: Grégory Coussement

Professor, Fluides-Machines department, UMons, Belgium, gregory.coussement@umons.ac.be

Abstract

Within the past decades, numerous optimization methods have been developed to maximize the aerodynamic characteristics of various turbomachinery components. Lately, more attention is being paid to methods able to enhance their aero-acoustic performance due to the increasing demand for quiet propulsion systems for the aircraft industry. In the framework of the present work, a multi-disciplinary, multi-objective, gradient-based shape optimization is performed to minimize the shock-associated tonal noise of NASA Rotor37, while maximizing its isentropic efficiency. The rotor's flow field is obtained through three-dimensional Reynolds averaged Navier Stokes simulations with the Spalart-Allmaras turbulence model, while the corresponding sound power level is obtained using a simple noise prediction model based on the flow perturbations at the rotor inlet. An adjoint approach is used for computing of the gradients of the objective functions with respect to the 41 design variables, which parametrize the geometry of the blade. A Sequential Quadratic Programming optimization algorithm is used to identify several trade-off points of the noise-efficiency Pareto front. Constraints are added to the optimization problem to keep the mass flow within a given range. Results show a substantial improvement in the overall performance of the rotor, with 2.5dB of sound power level reduction and a 1% increase in isentropic efficiency. Compared to a similar study that was conducted with a gradient-free algorithm, these results are obtained at a limited computational effort thanks to the adjoint-based methodology. The flow fields of the baseline and optimized designs are analyzed to understand the mechanisms behind the performance improvements.

Keywords: Aeroacoustics, design optimization, axial compressor

1. Introduction

Many concerns surround noise generation by aerial transportation. European countries are pushing toward the ambitious goal of 65% noise reduction from the levels observed in 2000 [1]. While significant efforts are made towards achieving this objective, the major focus in aviation has been on minimizing fuel consumption for cost-saving reasons and environmental concerns. This has led to the design of high bypass ratio turbofan engines, for which smaller jet velocities and lower turbulence have intrinsically resulted in a drastic reduction of jet noise, positioning the fan and compressor now as the most dominant sources of noise [2].

In the past decades, significant efforts have been made to predict noise through simulations, which ultimately would allow to include noise considerations into the design process. Most of the time, Computational Aeroacoustics (CAA) tools in Turbomachinery are based on Lighthill's acoustic analogy extended to moving solid bodies through the Ffowcs-Williams Hawkings (FW-H) integral method [3]. However, for high speed components, linear calculations of thickness and loading noise are in poor agreement with experimental results, so that alternative methods are

required [4; 5; 6]. In the case of tonal noise generated by shock waves, modal decomposition methods are widely used as a noise prediction method [7; 8]. The first study on acoustic modes was back in the 60's with the work of Tyler and Sofrin [9]. While studying the compressor noise, they focused on the rotating pressure patterns generated by the compressor, which were called spinning modes and were transmitted in the duct enclosing the rotor. During the 70's, a method based on modal decomposition was derived in order to post-process the sound power output of a supersonic 2D ducted rotor due to shock waves [10]. Years later, Wilson [11] proposed the wave splitting method as an extension to the previous work, in order to extract noise information from steady and unsteady CFD calculations, such as the amplitude of the noise sources.

Shape optimization based solely on aerodynamic performance is now a well-established step in the design of turbomachinery components and allows exploring wide design spaces within a reasonable amount of time. However, noise reduction generally requires design features which are conflicting with aerodynamic objectives [12; 13]. A simultaneous aero and acoustic optimization is therefore needed to balance acoustic and aerodynamic requirements of current and future propulsion devices [14; 15; 16]. Efficient optimization algorithms make use of gradients to modify the design in the direction of improved performance. Gradients can be obtained efficiently through the adjoint approach, for which the cost is nearly independent of the number of design variables, enabling the use of very rich design spaces. This paper presents the combination of a noise prediction model with an adjoint-based optimization approach. The test case and acoustic prediction model are first presented. The gradients computation method is then introduced and validated. Finally, optimization results are shown and analyzed.

2. Numerical framework

2.1. NASA Rotor37

NASA Rotor37 [17] is a highly loaded axial transonic compressor stage, which was designed by the NASA John H. Glenn Research Centre in the late seventies. The main characteristics of the compressor are presented in Table 1. It has been a representative stage of advanced air-breathing engines for more than 20 years and for this reason, it has been extensively used for turbomachinery CFD validations as well as to certify experimental test benches [18; 19]. Numerous studies also tackle the aerodynamic design optimization of this compressor. Duta et al. [20] used an adjoint-based optimization method combined with a Sequential Quadratic Programming (SQP) algorithm to obtain an increase of 1% in efficiency. In total, 28 design variables were used to parametrize the blade shape, including the blade sweep, lean, skew, Leading Edge (LE), and Trailing Edge (TE) re-cambering. Similarly, Tran et al. [21] performed an adjoint-based optimization of NASA Rotor37, including the chord length and meridional flow path into the parameterization, which allowed to obtain a 5.52% increase in efficiency while keeping the initial mass flow within a variation range of 0.5%. The first aero-acoustic automatic design optimization of NASA Rotor37 was performed by Wu et al. [22], using modal decomposition to predict noise power levels in the inlet duct. An evolutionary algorithm was used to lead the optimization toward the noise-efficiency Pareto front. The "efficiency-optimal" design was characterized by a 2.9% increase in efficiency, while the "noise-optimal" design allowed reducing the sound power level (SWL) by 3.5 dB. Wu et al. also conducted an aeroacoustic adjoint-based shape optimization of a transonic fan blade, achieving a maximum of 14.1 dB reduction of the SWL when any constraints were not considered [23].

Table 1: NASA Rotor 37 Characteristics

Rotor blade count	[-]	36
Rotor circumferential speed	[rpm]	17188.7
Rotor Tip velocity	[m/s]	454.1
Rotor Tip cleareance	[mm]	0.356
Rotor blade aspect ratio	[-]	1.19

In the present paper, an aeroacoustic optimization is performed using a similar approach for noise prediction. The latter is integrated and differentiated within the existing gradient-based optimization framework, CADO [24], which has been used to improve the Rotor37 performance in a previous work [21].

2.2. Aeroacoustic prediction model

The aeroacoustic prediction model that is used within this work requires the flow quantities at a fixed inlet plane. This is obtained by using a well-validated RANS flow solver coupled with a Spalart-Allmaras

Table 2: Boundary conditions

Inlet flow angle	α_{in}	[°]	0.0
Inlet total pressure	$p_{tot,in}$	[Pa]	101330.0
Inlet total temperature	$T_{tot,in}$	[K]	288.15
Outlet static pressure	p_{out}	[Pa]	114000.0

turbulence model [25]. The reader is referred to [26] for further details on the CFD solver implementation and validation. CFD validation results on the NASA Rotor37 test case using the same CFD solver are given in [21], where also a mesh convergence study was conducted. In the present study, a mesh of 2 million cells is used. The boundary conditions are given in Table 2. During the optimization process, the rotational speed and number of blades are kept constant to their values specified in Table 1.

A schematic view of the noise computation process is given in Fig. 1. First the steady flow solution U is interpolated to a constant axial position in front of the rotor, at a cross-section inside the inlet duct. The area-averaged pressure, and mass-averaged density and axial velocity are subsequently computed. By doing so, pressure and axial velocity perturbations are obtained as the difference between local data (at the center of each grid cell) and the averaged one. A Fourier transform and inverse Fourier transform are then successively applied to filter the perturbed flow data fields at specific harmonics of the blade passing frequency. Starting from Euler's equations and considering the flow as fluctuations on top of a uniform field, one can derive the formula for the axial acoustic intensity [27] presented in Eq. 1:

$$I(x) = (p' + \rho_o u' u_o)(u' + \frac{p'}{\gamma p_o})u_o \ , \qquad (1)$$

where p_o, u_o and ρ_o are the area averaged static pressure, mass averaged axial velocity and mass averaged density, γ is the ratio of specific heat for ideal gas, and $p^{'}$, $u^{'}$ are the fluctuations of static pressure and velocity. Finally, the sound power level (SWL) can be computed as:

$$SWL(x) = 120 + 10 \log [\iint_S |I(x)| \, r \, dr \, d\theta] \ . \qquad (2)$$

The SWL is a metric to quantify the total amount of acoustical energy produced by a source per unit of time and radiated into the surrounding environment as sound. It is expressed in decibels (dB) with reference to a reference power level of 1 picoWatt (pW). The above equations are applied to compute the total acoustic energy at a specific axial position and at a specific frequency. This represents the tonal noise emitted by the rotor. As can be found in [22], a Fourier-Bessel decomposition can also be applied after the inverse Fourier transform to further decompose the acoustic field into spatial duct modes. Then the acoustic energy can be computed individually for each propagating mode. Eventually, the summation of the SWL of each mode corresponds to the total energy computed with Eq. 2. In the present study, the optimization is based solely on the total acoustic energy at the first harmonic of the blade passing frequency, without any spatial decomposition.

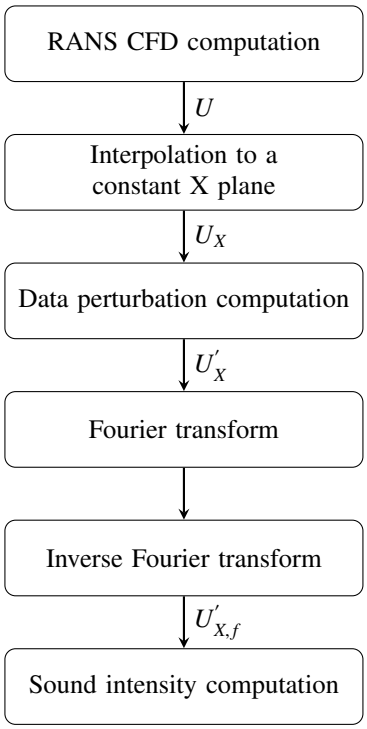

Figure 1: Noise computation process

Results obtained by computing the SWLs at different axial positions in front of the rotor for the first and second harmonics of the blade passing frequency are compared against available results from Wu et al. [22]. One can observe the relatively good agreement between the obtained results and the available numerical data, as shown in Fig. 2. The small differences can be due to a slightly different operating point, or

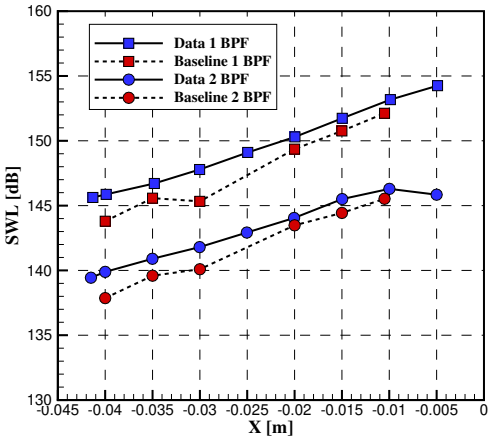

Figure 2: Comparison against numerical data from [22]

to numerical errors, in particular, coming from a different treatment of the non-reflective boundary conditions which have an impact on the propagation of right-propagating waves.

3. Gradients computation

3.1. Adjoint formulation

While gradient-based optimization methods generally offers a better convergence rate compared to their gradient-free counterpart, the former requires to compute the cost function sensitivities. The gradients in the present work are evaluated with an adjoint method [28], where the computational resources scale with the number of cost function, $J(U, \alpha)$, instead of the number of design variables. These techniques can handle large design space and avoid one of the main drawbacks of gradient-free optimizers [29]. The adjoint system of equations, Eq. 3, is first solved based on a fully converged flow U,

$$\left(\frac{\partial R}{\partial U}\right)^T V = \left(\frac{\partial J}{\partial U}\right)^T. \tag{3}$$

The sensitivites with respect to a design variable α are obtained with Eq. 4, where $R(U, \alpha)$ is the residual of the flow solution,

$$\frac{dJ}{d\alpha} = -V^T \frac{\partial R}{\partial \alpha} + \frac{\partial J}{\partial \alpha}. \tag{4}$$

The adjoint optimization framework for NASA Rotor37 is already established and tested by Tran et al. [21] for aerodynamic performance parameters (i.e. efficiency and mass flow). Within the present work, the adjoint solver capability is extended to take into account the acoustic performance of the rotor, that is the sound power level in the inlet duct. Specifically, the right-hand side term of Eq. 3 is re-evaluated for the acoustic objective function, as explained in the following section.

3.2. Acoustic gradient

In the acoustic case, the objective function is the sound power level given by Eq. 2. The variation of the objective function with respect to the flow field can be expressed as shown by Eq. 5, since the acoustic intensity depends only on the static pressure, density and axial velocity fields.

$$\frac{\partial J}{\partial U} = \left(\frac{\partial J}{\partial p}, \frac{\partial J}{\partial u}, \frac{\partial J}{\partial \rho}\right)^T \tag{5}$$

To compute this specific partial derivative, automatic differentiation of each individual module displayed in Fig. 1 is possible, either in forward or in reverse mode. In forward mode, whereby an infinitesimal perturbation is given to each state variable in each cell of the domain, the perturbations to all subsequent quantities are computed using a linearisation of each algorithmic operation. Since the process needs to be repeated for each state variable and each cell, this requires a considerable computational effort. In fact not all cells contribute to the objective function, in particular, only the cells in the neighborhood of the extraction plane are involved, which allows to reduce the computational burden, but requires some additional bookkeeping. In reverse mode, one starts by the last computation and identifies which perturbations to the input variables would match the observed output perturbation. This procedure can be repeated going line by line in reverse through the entire algorithm. In other terms, a perturbation J_b is applied to the output variable and is then back-propagated through the differentiated noise computations modules. Following the chain rule, this mathematically translates into:

$$\begin{aligned} U_b &= \left(\frac{\partial U_X}{\partial U}\right)^T \left(\dots\right) \left(\frac{\partial J}{\partial U'_{X,f}}\right)^T J_b \\ &\Longleftrightarrow U_b = \left(\frac{\partial J}{\partial U}\right)^T J_b \end{aligned} \tag{6}$$

Hence, a unitary perturbation on the output ($J_b = 1$) allows to get all the input perturbations $U_b = (p_b, u_b, \rho_b)$ simultaneously, and therefore the partial derivative $\frac{\partial J}{\partial U}$. This contribution is plugged into Eqn. 3 which is then solved by the adjoint flow solver.

4. Design Optimization

4.1. Optimization problem definition

The aim of the present multi-objective optimization is to minimize the noise generated upstream of the rotor, while maximizing the the total-to-total efficiency. The acoustic intensity is calculated at an axial plane close to the rotor's inflow boundary, at a 60% chord distance from the leading edge, where it can be assumed that the mesh is unaffected by the blade's shape modifications. This has the advantage that the objective function does not explicitly depend on the shape parameters α, so that the last term of Eqn. 4 can be neglected. Since the outlet static pressure is set as boundary condition, a constraint on the mass flow is also imposed to stay within the same operating point. The optimization problem can be expressed as:

$$\begin{aligned} \min_{x} : \quad & \left\{ \omega \left(\frac{SWL}{SWL_{ref}} \right) + (1-\omega) \left(1 - \frac{\eta}{\eta_{ref}} \right) \right\} \\ \text{s.t.} \quad & 0.98 < \frac{\dot{m}}{\dot{m}_{ref}} < 1.02, \end{aligned} \tag{7}$$

where the weight parameter ω allows to balance the two objectives.

The parametrization of the blade is the same as in [21], where a detailed description of the CAD generation process can be found. The camberline surface, which is obtained by stacking every camberline of the rotor along the span, is described with a B-Spline surface by means of 38 design variables acting on the camberline shape and position, Fig. 4. Three parameters are included to control the tangential profile stacking along the span. The thickness distribution is on the other hand kept constant to avoid structural validation. A total of 41 design variables are used to define the design space. The bounds of each design variable act as constraints together with the mass flow. The shape of the duct (meridional flow path) is unchanged, so that the noise computation method remains consistent from one design to another during the optimization process. The optimization loop, presented in Fig. 3, makes use of an in-house developed Sequential Quadratic Programming optimizer [30].

4.2. Gradient quality

Before moving on to the optimization results, the gradients resulting from the adjoint method presented in section 3.2 are validated against a complex step approach [31]. Since the complex step method is much

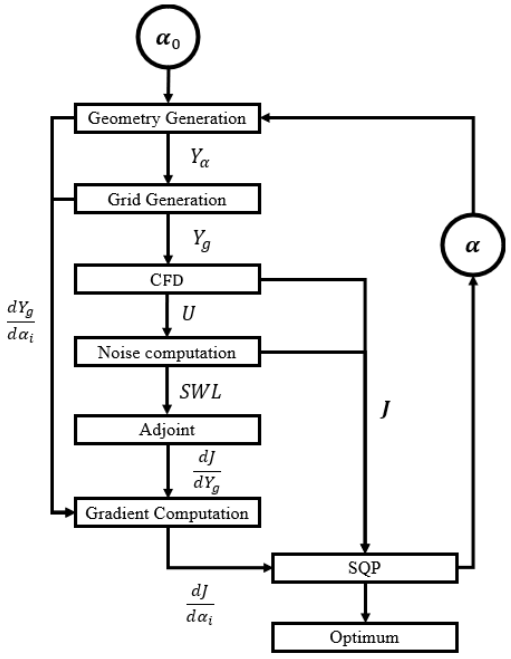

Figure 3: Optimization loop

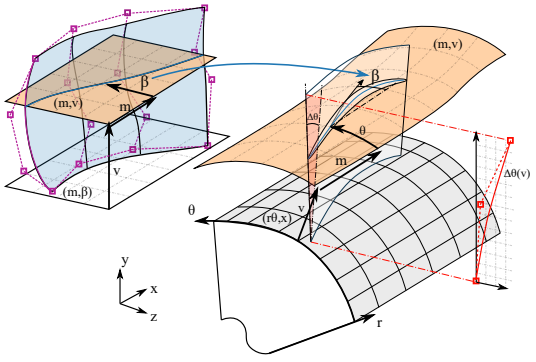

Figure 4: Camberline surface parametrization [21].

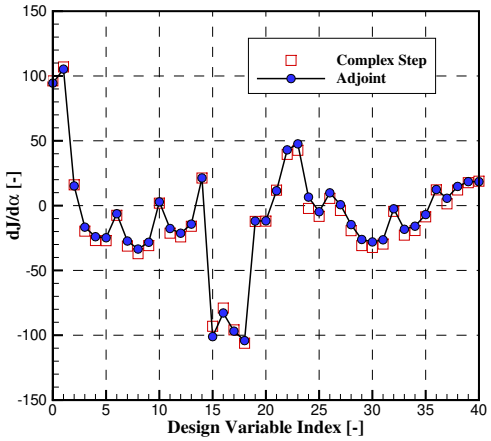

Figure 5: Gradients accuracy validation

less sensitive to the perturbation step size compared to a finite differences method, the gradients can be computed close to machine level accuracy, which makes it a very good benchmark. One should note however that the complex step calculation can only be used for validation but not during an optimization as it requires to run a CFD computation in complex mode for each design variable, which makes its computational cost prohibitively high. The gradients accuracy validation for all 41 design variables is shown in Fig. 5, where one can observe that a good gradients quality is obtained.

4.3. Optimization results

Within this work, two different values of the weight parameter ω in Eq. 7 are tested, which are $\omega = 0.25$ and $\omega = 0.5$. The sound power level and efficiency evolution during the optimization are presented in Fig. 6 and Fig. 7. One can observe that the SWL was reduced by 2.5 dB with $\omega = 0.5$ and that the efficiency was improved by 1.04% in the other case. For $\omega = 0.5$ a slight increase in efficiency of roughly 0.4% is obtained, while for $\omega = 0.25$ the SWL is reduced by 1.3 dB. For each optimization, the constraint on the mass flow is respected, with a maximum variation of -0.4% observed. Each iteration shown in Fig. 6 and Fig. 7 required the evaluation of a design through CFD and noise prediction model, as well as three adjoint computations for each of the performance parameters (which can be run in parallel for time savings). In total, it took two weeks for each optimization to converge, using 11 CPU cores each. It is interesting to put these results into perspective compared to what Wu et al. [22] obtained on the same compressor. As mentioned in the introduction, they were able to obtain a 2.9% increase in efficiency and a 3.5dB SWL reduction, which constitutes better improvements than within this work. It is however important to note that both studies are conducted with different parametrization of the blade, different numerical tools, and more importantly the optimization problem is slightly different. While the mass flow was barely modified in the present work, variations of 1.1% to 4.8% were observed in [22]. Regarding the computational effort, computing the two optimal points with different values of the weight parameter came at a very small cost in comparison to [22], where 8 weeks were necessary to obtain the entire noise-efficiency Pareto front, using a cluster of 864 CPU cores. Finally, it is noteworthy that the SWL is optimized here for the first BPF only, while the objective function in [22] is the time-domain definition of the total SWL, taken before any frequency decomposition.

One could argue that without non-reflective boundary conditions, without modal decomposition or wave splitting technique used to decompose the acoustic field into left and right propagating waves, there is little guarantee that the objective function minimization represents effectively a reduction in acoustic energy leaving the inlet duct. Figure 8 shows the SWL distribution in the inlet duct of the optimized design with $\omega = 0.5$, in comparison to the baseline, for the first and second harmonics of the blade passing frequency. The reduction in SWL obtained at the measurement plane (60% chord from the LE), where the optimization objective was defined, is also achieved at the other axial locations for both frequencies. This suggests that the linear sound propagation is maintained during the optimization and that the possible effect of wave reflections inside the inlet duct is negligible. Modal decomposition and wave splitting techniques could however be added in a future work to further analyze the acoustic content of the spatial modes. This would also allow to include the meridional path into the parametrization, such that the duct shape could be modified, which could lead to a further reduction of the SWL and a better aerodynamic performance.

4.4. Design and flow analysis

In this section, the geometry and flow field of the optimized design from the optimization with $\omega = 0.5$ are compared with the baseline design. Figure 9 shows a comparison of the three-dimensional shapes. The new design is characterized by a backward sweep

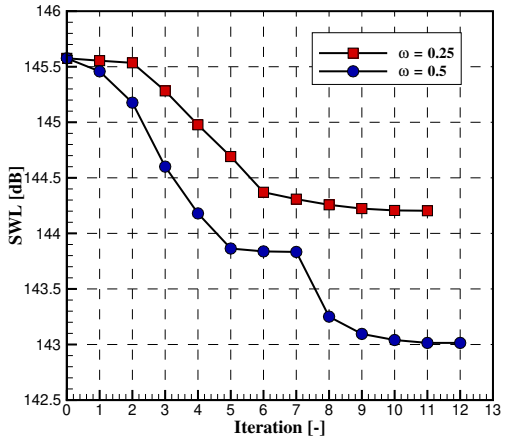

Figure 6: SWL evolution

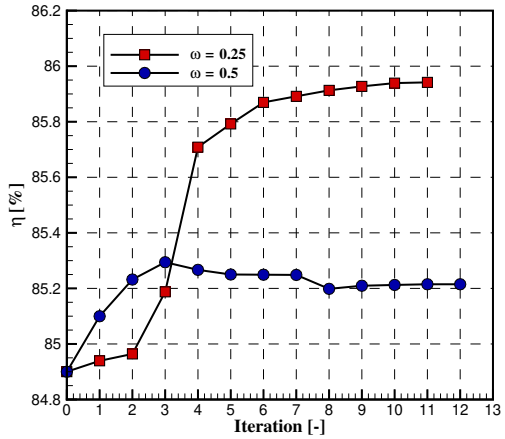

Figure 7: Efficiency evolution

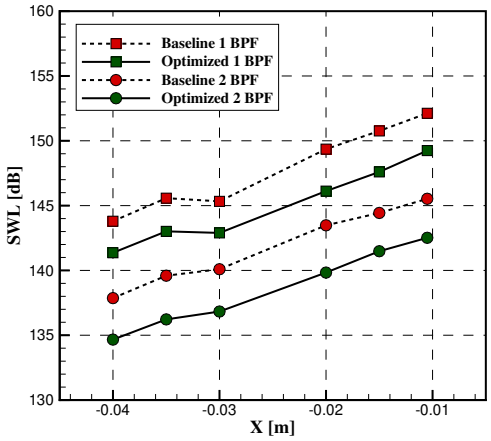

Figure 8: Comparison of SWL distribution in inlet duct for baseline and optimized design with $\omega = 0.5$

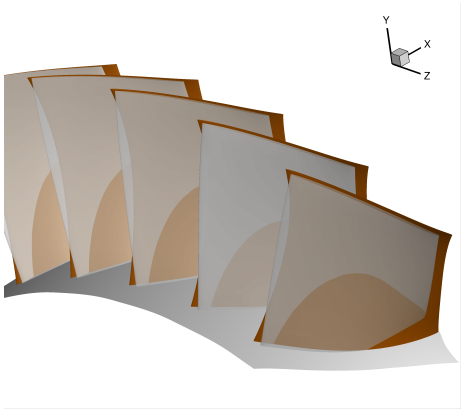

Figure 9: 3D blade comparison of the baseline (grey) and optimized (brown) blade.

compared to the original one, with a chord increase at the hub and at the tip. The blade is also slightly leaned in the rotation direction and the leading edge is curved towards the mid span of the blade. The blade height remains unchanged as imposed by the parametrization of the blade, while the blade width is also increased. Two-dimensional sections at near-hub, mid-span and near-tip locations are presented in Fig. 10. Near the hub, both inlet and outlet metal angle is increased together with the camber line at the aft section. Moreover, a clear increase in chord length is observed both at the hub and tip, while it stays the same in the middle part of the blade. Looking at the mid and tip sections, it is again visible that the blade is swept backwards and is leaned towards the pressure side, i.e. in the rotation direction. It is noteworthy that the shape shown in Fig. 10.b is similar to the noise-oriented design from [22].

In Fig. 11, 12 and 13 the relative Mach number distribution maps are shown for the baseline and optimized geometries at near-hub, mid and near-tip sections respectively. Figure 11 shows a smoother deceleration of the flow at the suction side compared to the baseline with a weaker shock intensity in the passage between the blades. This is due to the chord increase which locally contributes to reduce the blade loading, or to the change in inlet metal angle which modifies the incidence angle. The bow shock in the optimized case demonstrates a change in shape (Fig. 11.b). The flow behaviour at the mid section displayed in Fig. 12 proves to be similar

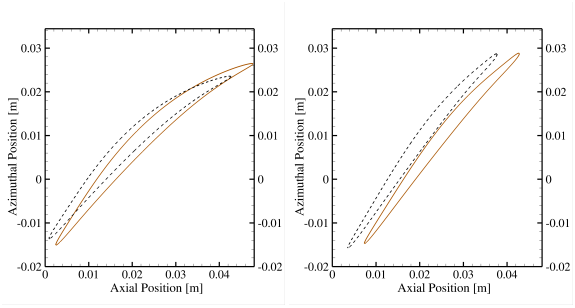

(a) Hub (b) Mid

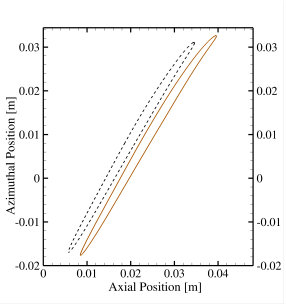

(c) Tip

Figure 10: Blade section comparison in the baseline (black) and optimized (brown) blade.

from the baseline to the optimized design, with a slight acceleration of the flow at the suction side. However, more changes in the flow field can be seen in Fig. 13, near the tip of the blade. The bow shock structure is changed in the optimized design, leading to a more uniform velocity field in front of the rotor. This affects the pressure field which contributes to the reduction in sound power level obtained through the optimization. The passage shock is more oblique compared to the baseline. A supersonic region is then observed which suggest a flow acceleration due to the reduction of the passage, induced by the thickening of the boundary layer. The latter is supported by the wake width increase as shown on Fig. 13.b, which suggests higher diffusion losses. Another supersonic pocket is also observed close to the trailing edge due to its local blade wall curvature and the increased wake width.

A comparison of the static pressure distribution in front of the baseline and optimized rotor geometries is shown in Fig. 14. The diffusion of the inlet shock structure thanks to the optimized shape can be observed. It is more prominent at the hub and tip region of the inlet cross-sectional plane, where the blade shape was altered the most compared with the baseline. This leads to a more uniform pressure field with a decrease of the pressure fluctuations upstream of the rotor, and therefore a reduction of the tonal shock-associated noise.

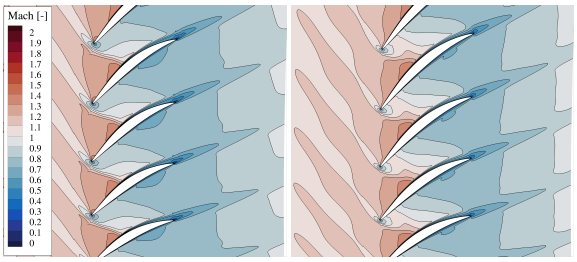

(a) (b)

Figure 11: Comparison of the relative Mach number at the hub for the baseline (a) and optimized (b) blade.

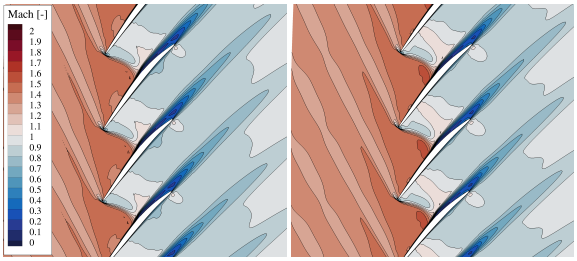

(a) (b)

Figure 12: Comparison of the relative Mach number at mid span for the baseline (a) and optimized (b) blade.

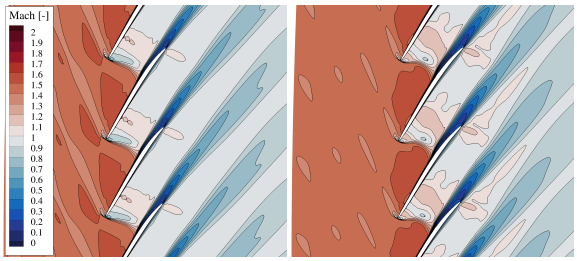

(a) (b)

Figure 13: Comparison of the relative Mach number at the tip for the baseline (a) and optimized (b) blade.

5. Conclusion

In this paper, the aeroacoustic optimization of the transonic axial compressor NASA Rotor37 was conducted, using a gradient-based approach. Two Pareto front trade-off points were computed through the optimization process, with a maximum of 2.5 dB sound

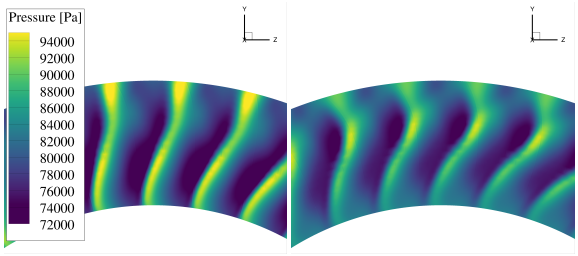

(a) (b)

Figure 14: Comparison of the static pressure distribution in front of the rotor for the baseline (a) and optimized (b) blade.

power level reduction in one case and a 1% efficiency increase in the other. These results were obtained at a very small computational cost, thanks to the adjoint-based method. A more detailed analysis of the optimized design with 50% weight given to each performance parameters in the objective function was also conducted. In particular, it was shown that although the acoustic objective was defined as the SWL at a specific axial position and for the first harmonic of the blade passing frequency, the reduction in SWL can be observed at any other axial position of the inlet duct, and for the second harmonic of the BPF as well. This suggests that the optimization is not affected by wave reflection. It was also shown that the optimized design is characterized by an increase in chord length near the hub and the tip of the blade. Lean in the rotation direction can also be observed. These design modifications allowed to reduce the shock intensity in the inlet duct, thus the shock-associated tonal noise was also decreased. In future works, a wave splitting technique could be added to decompose the acoustic field into left and right propagating waves, such that the shape of the inlet duct could be included into the parametrization.

References

[1] O. Zaporozhets, V. Isaienko, K. Synylo, Pare preliminary analysis of acare flightpath 2050 environmental impact goals, CEAS Aeronautical Journal 12 (2021) 653–667. doi:10.1007/s13272-021-00525-7.

[2] M. Azimi, F. Ommi, Fan noise sources and passive reduction methodlogies in high bypass turbofan engines, Noise and Vibration Worldwide 45 (2014) 18–22. doi:10.1260/0957-4565.45.5.18.

[3] J. Ffowcs Williams, D. Hawkings, Theory relating to the noise of rotating machinery, Journal of Sound and Vibration 10 (1) (1969) 10–21. doi:https://doi.org/10.1016/0022-460X(69)90125-4.

[4] C. L. Morfey, M. J. Fisher, Shock-wave radiation from a supersonic ducted rotor, The Aeronautical Journal 74 (3) (1970) 37–55. doi:10.1017/S0001924000049095.
URL https://doi.org/10.1017/S0001924000049095

[5] E. Envia, A. G. Wilson, D. L. Huff, Fan noise: A challenge to caa (8 2004). doi:10.1080/10618560410001673489.

[6] P. Moinier, M. B. Giles, Eigenmode analysis for turbomachinery applications, Journal of Propulsion and Power 21 (2005) 973–978. doi:10.2514/1.11000.

[7] J. Coupland, A. Wilson, N. Pollard, S. Uellenberg, C. Breard, J. Diamond, Demonstration of a cfd-caa methodology to predict buzz-saw noise propagation to the aircraftdoi:10.2514/6.2007-3517.

[8] M. Daroukh, S. Moreau, N. Gourdain, J. F. Boussuge, C. Sensiau, Tonal noise prediction of a modern turbofan engine with large upstream and downstream distortion, Journal of Turbomachinery 141. doi:10.1115/1.4042163.

[9] J. M. Tyler, T. G. Sofrin, Axial flow compressor noise studies, SAE transactions 70 (1962) 309.

[10] C. L. Morfey, Sound transmission and generation in ducts with flow, Journal of Sound and Vibration 14 (1971) 37–55.

[11] A. Wilson, ROLLS-ROYCE PLC DERBY (Great Britain), A method for deriving tone noise information from cfd calculations on the aeroengine fan stage, Defense Technical Information Center, 2003.

[12] R. Jaron, A. Moreau, S. Guerin, L. Enghardt, T. Lengyel, T. Otten, E. Nicke, Multidisciplinary design optimization of a low-noise and efficient next-generation aero-engine fan, 2020. doi:10.1115/GT2020-14580.

[13] G. Grasso, S. Moreau, J. Christophe, C. Schram, Multidisciplinary optimization of a contra-rotating fan, International Journal of Aeroacoustics 17 (6-8) (2018) 655–686. arXiv:https://doi.org/10.1177/1475472X18789000, doi:10.1177/1475472X18789000.
URL https://doi.org/10.1177/1475472X18789000

[14] J. H. Kim, B. Ovgor, K. H. Cha, J. H. Kim, S. Lee, K. Y. Kim, Optimization of the aerodynamic and aeroacoustic performance of an axial-flow fan, AIAA Journal 52 (2014) 2032–2044. doi:10.2514/1.J052754.

[15] C. Luo, L. Song, J. Li, Z. Feng, A study on multidisciplinary optimization of an axial compressor blade based on evolutionary algorithms, Journal of Turbomachinery 134. doi:10.1115/1.4003817.

[16] A. Wilson, R. Stieger, J. Coupland, N. Smith, N. Humphreys, Multi-disciplinary optimisation of a transonic fan for low tone noise (11 2011). doi:10.2514/6.2011-2950.

[17] L. Reid, R. D. Moore, Design and overall performance of four highly loaded, high speed inlet stages for an advanced high-pressure-ratio core compressor.

[18] R. D. Moore, L. Reid, Performance of single-stage axial-flow transonic compressor with rotor and stator aspect ratios of 1.63 and 1.78, respectively, and with design pressure ratio of 1.82, 1978.

[19] J. Dunham, CFD Validation for Propulsion System Components, AGARD advisory report.

[20] M. Duta, S. Shahpar, M. Giles, Turbomachinery design optimization using automatic differentiated adjoint code, Vol. 6, 2007. doi:10.1115/GT2007-28329.

[21] CAD Integrated Gradient-Based Aero Optimization of the NASA Rotor 37, Vol. Volume 10D: Turbomachinery — Multidisciplinary Design Approaches, Optimization, and Uncertainty Quantification; Turbomachinery General Interest; Unsteady Flows in Turbomachinery of Turbo Expo: Power for Land, Sea, and Air, v10DT34A008. doi:10.1115/GT2022-80906.

URL https://doi.org/10.1115/GT2022-80906
[22] L. Wu, J.-W. Kim, A. G. Wilson, S. Shahpar, Automatic Design Optimization of a Transonic Compressor Rotor for Improving Aeroacoustic and Aerodynamic Performance, Journal of Turbomachinery 144 (8), 081016. doi:10.1115/1.4053916.
URL https://doi.org/10.1115/1.4053916
[23] L. Wu, A. Wilson, J. Kim, D. Radford, S. Shahpar, Low-noise blade design optimization for a transonic fan using adjoint-based approach, AIAA Journal 60. doi:10.2514/1.J060959.
[24] T. Verstraete, CADO: a computer aided design and optimization tool for turbomachinery applications, in: Proceedings of the 2nd international conference on engineering optimization, Lisbon, Portugal, Vol. 69, 2010, p. 69.
[25] S. R. Allmaras, F. T. Johnson, Modifications and clarifications for the implementation of the Spalart-Allmaras turbulence model, in: Seventh international conference on computational fluid dynamics (ICCFD7), Vol. 1902, Big Island, HI, 2012.
[26] L. Müller, Adjoint-based optimization of turbomachinery with application to axial and radial turbines, PhD dissertation, ULB (2019).
[27] C. Morfey, Acoustic energy in non-uniform flows, Journal of Sound and Vibration 14 (2) (1971) 159–170. doi:https://doi.org/10.1016/0022-460X(71)90381-6.
[28] O. Pironneau, On optimum design in fluid mechanics, Journal of Fluid Mechanics 64 (1) (1974) 97–110, publisher: Cambridge University Press.
[29] M. H. Aissa, R. Maffulli, L. Mueller, T. Verstraete, Optimisation of a turbine inlet guide vane by gradient-based and metamodel-assisted methods, International Journal of Computational Fluid Dynamics 33 (6-7) (2019) 302–316, publisher: Taylor & Francis.
[30] R. Hottois, A. Châtel, G. Coussement, T. Debruyn, T. Verstraete, Comparing Gradient-Free and Gradient-Based Multi-Objective Optimization Methodologies on the VKI-LS89 Turbine Vane Test Case, Journal of Turbomachinery 145 (3), 031001. doi:10.1115/1.4055577.
URL https://doi.org/10.1115/1.4055577
[31] J. R. Martins, P. Sturdza, J. J. Alonso, The complex-step derivative approximation, ACM Transactions on Mathematical Software (TOMS) 29 (3) (2003) 245–262, publisher: ACM New York, NY, USA.

Development of a Novel Rotor-Stator Reactor for Decarbonizing the Steam Cracking Process through High-fidelity Data-driven Optimization

Marco Castaldi

Turbomachinery and Propulsion Department, von Karman Institute for Fluid Dynamics, Belgium, marco.castaldi@vki.ac.be

Supervisor: Frank Eulitz

Full Professor, Turbomachinery and Propulsion Department, von Karman Institute for Fluid Dynamics, Belgium, frank.eulitz@vki.ac.be

Co-supervisor: Tom Verstraete

Full Professor, Turbomachinery and Propulsion Department, von Karman Institute for Fluid Dynamics, Belgium, tom.verstraete@vki.ac.be

University Supervisor: Kevin Van Geem

Full Professor, Laboratory for Chemical Technology (LCT), Ghent University, Belgium, kevin.vangeem@ugent.be

Abstract

Steam cracking has been at the core of petrochemical industries for decades. This highly energy-intensive and high-temperature process allows the conversion of naphtha or natural gas liquids into basic blocks (including ethylene and propylene). The latter are afterwards processed to deliver not only daily life products, such as food packaging and medical devices, but also components for renewable energy systems, ranging for instance from polymers in wind turbines to solar panels and batteries of cars. However, steam cracking requires a large amount of energy to heat up tube-shaped reactors, and this is typically obtained through the combustion of fossil fuels.

Rotor stator reactors show great promise in this regard, as they can generate heat for the cracking reactions by direct mechanical energy transfer using sustainable electric motors (Figure 1). Their development has however been lagging behind. The goal of this project is therefore to develop a novel concept of rotor stator reactor, which will mark a significant step forward the decarbonization of the petrochemical industry. At the basis of this innovative technology there is the implementation of both high-fidelity CFD and endothermic models in the optimization loops. As a consequence of its flexible design, in which each axial module is composed of three blade rows and a reaction chamber, the system has the potential to improve the energy transfer and enhance the quality of the overall cracking and heating processes.

The pre-conceptual design of a generic module is depicted in Figure 2. The first section is characterised by a traditional axial compressor stage: the flow is directed through a row of Inlet Guide Vanes (IGV) which pre-swirl and pre-condition the flow. As a second step, the rotating blades (rotors) accelerate the fluid in both the axial and circumferential directions. The rotor airfoils are are installed on a shaft powered by sustainable electricity. Because of their high-loading and high-curvature shape, shock-driven pressure losses are considerable. Differently from axial compressors, this aspect is not crucial, as the purpose of this stage is to maximize the kinetic energy and any pressure increase can negatively affect the endothermic reactions. The increased kinetic energy is then converted into enthalpy rise with dissipative phenomena in the stator vanes. As a last step, an intense turbulent mixing is realised to homogenize the temperature of the reactive flow in the channel after each stage, namely the reaction chamber.

Keywords: Turbomachinery, High-temperature Reacting Systems, Reduced-order CFD Models

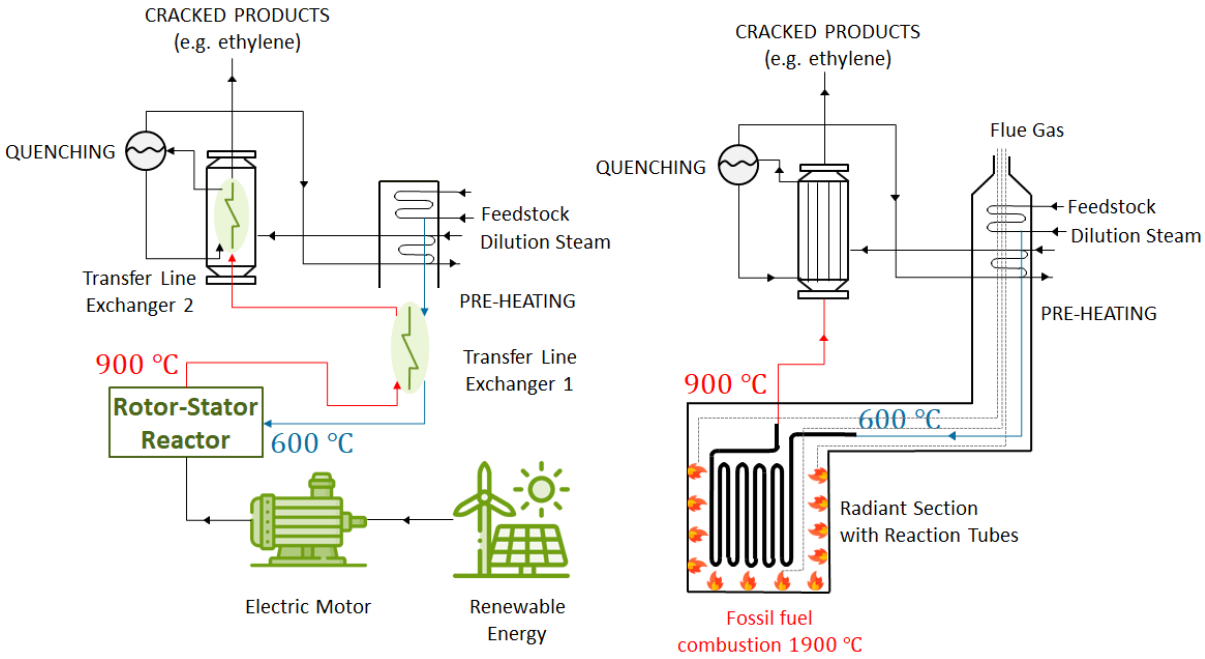

Figure 1: Representation of an olefins production plant. *Left:* turbomachine-based reactor. *Right:* conventional steam cracking furnace.

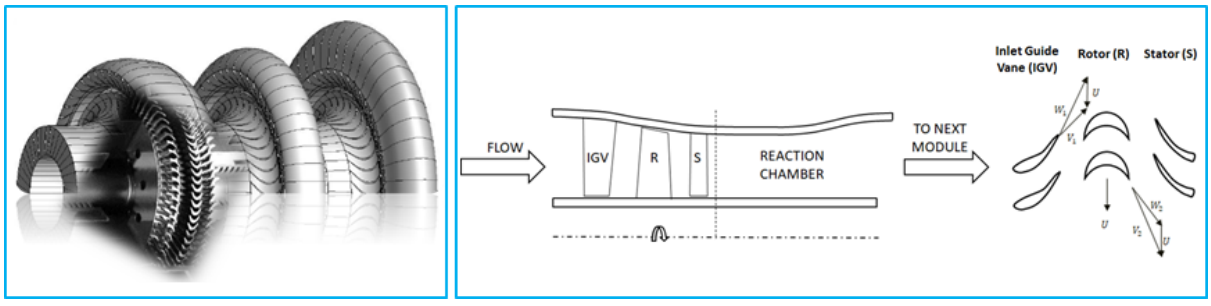

Figure 2: Pre-concept of electrified rotor stator reactor and scheme of a generic module (meridional and blade-to-blade view).

Shape Optimization of Impeller Blades in Centrifugal Compressors including Fillet Radii, Leading Edge Sweep and Tangential Lean

Duc Huy Marco Hoang

Fraunhofer Institute for Environmental, Safety and Energy Technology UMSICHT, Germany , duc.hoang@umsicht.fraunhofer.de

Turbomachinery and Propulsion Department, von Karman Institute for Fluid Dynamics, Belgium, duc.hoang@vki.ac.be

Supervisor: Tom Verstraete

Professor, Turbomachinery and Propulsion Department, von Karman Institute for Fluid Dynamics, Belgium, tom.verstraete@vki.ac.be

University Supervisor: Christian Doetsch

Professor, Cross Energy Systems, Ruhr University Bochum, Germany, christian.doetsch@ruhr-uni-bochum.de

Abstract

In order to improve the aerodynamic performance and the strength behavior of a centrifugal compressor, blade designs with complex three-dimensional features are introduced. Design parameters such as fillet radius, leading edge sweep and tangential lean are varied to achieve these improvements. However, fillets are often assumed to have little influence on the flow field. Due to that assumption and the increased complexity of the geometry, leading to difficulties in the grid generation, fillets are neglected in flow simulation. Therefore, the interactions between those design parameters are unknown.

The goal of the present work is to study the interactions between fillet radius, leading edge sweep and tangential lean on the flow field using CFD simulations. Additionally, a shape optimization under consideration of the aforementioned design parameters is performed. In order to study the interactions properly, a new topology for 3D multi-block structured grid generation of radial impeller blades will be introduced to generate a grid with acceptable quality for geometries with complex three-dimensional features. The adjusted grid generation method will then be integrated into an existing multidisciplinary optimization system to perform a shape optimization of impeller blades in a centrifugal compressor. The aerodynamic performance is evaluated using CFD simulations and the stresses are calculated by a finite element analysis. The objective of the optimization is to maximize the efficiency, while staying below the strength limit of the material.

Keywords: centrifugal compressor, fillet, grid generation, shape optimization

INSTRUMENTATION AND MEASUREMENT TECHNIQUES

Flow field investigation of a diffuser blade using endoscopic PIV

Muhsin Can Akkurt

Environmental and Applied Fluid Dynamics, von Karman Institute for Fluid Dynamics, Belgium, muhsin.can.akkurt@vki.ac.be

Supervisor: Delphine Laboureur

Associate Professor, Environmental and Applied Fluid Dynamics Department, von Karman Institute for Fluid Dynamics, Belgium, delphine.laboureur@vki.ac.be

University Supervisor: Kevin M. Van Geem

Professor, Department of Materials, Textiles and Chemical Engineering, Ghent University, Belgium, Kevin.VanGeem@UGent.be

Abstract

The present work aims a flow field investigation of a diffuser vane in the low-speed cascade C-1 facility located at the von Karman Institute (VKI). An endoscopic PIV technique is successfully implemented in the facility to solve illumination restrictions.

Keywords: steam cracking reactor, diffuser, particle image velocimetry, subsonic flow

1. Introduction

Steam cracking of hydrocarbons has been widely used in the chemical industry to produce light olefins such as ethylene, propylene and butadiene [1]. The conventional steam cracking process is a highly energy-intensive operation in the petrochemical industry, where temperatures up to 1100°C are required due to endothermic chemical processes [2]. This step alone accounts for roughly 8% of this industry's total energy consumption and about 30% of the global industry's carbon dioxide emissions [3].

In traditional steam cracking reactors, the hydrocarbon and high-pressure steam mixture is heated by the combustion of fuel in the furnaces[4]. The primary issue of utilizing furnaces for heat transfer is the fact that the heat transfer walls, instead of the working fluid, are the hottest section of the system. In many cases, the walls can be over 30% hotter than the internal gas.

In contrast, novel concept designs propose a turbomachine to replace the furnaces, where the mechanical energy of the rotor shaft can be transmitted directly to the working fluid, making the fluid the hottest element of the reactor. The design electrified Rotor Stator Reactor (e-RSR), which uses standard turbomachinery components, including a stator (IGV), rotor, and a diffuser, is capable to reduce CO2 emissions by up to 90% compared to conventional steam crackers. Therefore, it has the potential to replace conventional steam-cracking furnaces. The multistage machine is obtained by successively repeating a single stage comprising of these three components.

The use of Computational Fluid Dynamics (CFD) is essential in this type of reactor design process as it provides a cost-effective approach to predict the flow behavior across the machine. However, the accuracy of the flow prediction requires experimental validation particularly [5]. In the present study, the diffuser vane has been selected to be experimentally investigated to provide the validation data. The reason for this is bifold. On the one hand, the diffuser blade row converts the gas kinetic energy -which is increased by the rotor- into an entropy increase resulting in a high level of mixing downstream of this blade row. Secondly, the diffuser reduces the flow velocity which generates stationary shockwaves across which the flow decelerates from supersonic to subsonic speeds over a very small length. Hence, velocity is traded for enthalpy which results in heating times in the order of nanoseconds. Both reasons clearly stress the importance of the diffusers in e-RSR operation and thus the choice to experimentally investigate this blade.

Particle image velocimetry (PIV) has been widely used to investigate instantaneous velocity as it can provide spatially resolved data acquisition with minimal intrusiveness. It is based on fluid velocity measurements via calculation of the displacements of the small tracer particles in two consecutive images recorded with a short time interval [6],[7]. The recent application of PIV offers a valuable opportunity to examine intricate three-dimensional flow structures in turbomachinery applications. Regardless of being rotating or linear stationary cascades, PIV has been successfully implemented into several turbomachinery from the low-speed subsonic [8],[9] to high-speed flows [10],[11],[12].

However, in turbomachinery applications, performing PIV measurements can be quite challenging due to their complex geometries and closed volumes. The optical access, laser reflections, seeding the flow, cleanliness of optics, vibrations, etc. have been the primary challenges in such applications [13]. For the cases when the large optical windows are not suitable on the casings, endoscopes for both camera and the laser can be used. Therefore, the accesses into the closed volumes can be provided through very small holes on the casing that the endoscope can fit. But using endoscopes also brings several drawbacks to be considered. They mainly provide low optical resolution [14] and very low light transmission and contrast [14], [15], [16] compared to conventional objective lenses and thus require high laser powers. But a high-power pulsed laser beam focused down to a smaller diameter to pass through the endoscope possibly destructs the output lenses [14]. Due to the need for very large field-of-view ratios, they cause fish-eye distortions as well as a non-uniform focus throughout the field of view [13].

This study will focus on the subsonic investigation of the flow around the diffuser vane of the e-RSR design. The planar e-PIV measurements are conducted at the low-speed cascade C-1 facility located at the von Karman Institute (VKI). The illumination is made by the laser sheet generated through the endoscope while the traditional objective lens is utilized instead of the camera endoscope due to their constraints. The results are provided along with the evaluation of the post-process quality and the uncertainty analysis.

2. PIV Setup and Facility Preparation

A rig that operates at low subsonic speeds and utilizes a continuous flow system, the C-1 facility is designed and used for the development of axial blade profiles and the investigation of primary and secondary flows in compressor and turbine cascades. A rectangular test section allows atmospheric intake and exhaust through a non-return arrangement on the rig. Air is supplied by a centrifugal blower, which is powered by a DC motor. The flow is guided through a diffuser and three mesh screens before entering a settling chamber. Through a convergent nozzle, the flow is then led to the cascade inlet. The dimensions of the rectangular inlet test section are fixed at 127 mm in height and 250 mm-600 mm (adjustable) in width. This section can host several types and up to 25 blades with the aid of portable end walls. A rotating support is used to mount the cascade, which enables convenient modification of the inlet flow incidence. The rig can simulate realistic engine conditions by varying the Reynolds number based on the airfoil chord of 50mm and exit velocity. Reynolds number can range from 50000 to 250000, while the Mach number achieved is in order of 0.10.

The test rig in the C1 facility can be equipped with a variety of different measurement equipment such as pressure probes, optical endoscopic apparatus and transparent windows for optical access towards the cascade investigated. The diffuser blades were scaled to enable PIV investigation by matching the chord-based Reynolds number at the inlet and preserving the pitch-to-axial chord ratio, $g/C_{ax} = 0.37$, in the original e-RSR design. The pitch of the scaled blade is 37 mm while the chord is 142mm with an axial chord of 100 mm. The blades were manufactured via 3D printing using SLS material. As the leading edge of the diffuser is quite thin, notches were added for the pin connections to provide rigidity. To ensure that they result in minimal influence on the flow, three blades located around the investigation area were placed via the pockets that opened into the transparent window instead of such notches. These blades were also polished to minimize their surface roughness.

24 diffuser blades were mounted to the cassette with a stagger angle, the angle between the chord and the axial direction, of 47.15°. The test section was rotated such that the inlet flow angle would be 71° as shown in Figure 1. The inlet total and static pressures (P_1, P_{01}) were measured by a NACA probe placed upstream of the investigation area, at a distance of four axial chords.

To provide sufficient optical access for the planar PIV measurements a large plexiglass window was needed in the C1 cassette. The prepared access provided a camera observation area of three complete diffuser vane passage, including the inlet and outlet

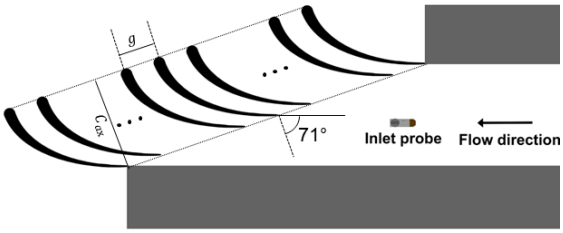

Figure 1: The positioning of 24 diffuser blades in the test section



Figure 2: The transparent window for the optical access together with the new cassette

region (Figure 2). The plexiglass window and a new Aluminium cassette, to which the window is mounted, were manufactured with considerable effort to precisely fit the inner contour of the test section, thereby minimizing disturbances of the near-wall flow. Since the investigation is under non-reactive and subsonic low-speed conditions, the window was installed on the cassette using aluminum screws without extra support. Additionally, plasticine was utilized as a sealant to prevent any possible leakage.

To increase the contrast in the PIV images and avoid possible laser reflections that may result from the highly cambered surface of the diffuser blades, the visible surface of the end wall, the surface across the window, was painted in black.

For the recording of the flow, a CCD PIV camera (Imager SX 4M) with a spatial resolution of 2360 x 1776 pix^2 at a frame rate of 10 Hz was used. The focal length of the chosen camera lens is f = 200 mm. The decision to use such a large focal length was made to reduce the perspective effect (or to minimize the angle of incidence of the rays from the measurement plane to the sensor) by keeping the measurement plane and the sensor further apart (Figure 3). This approach

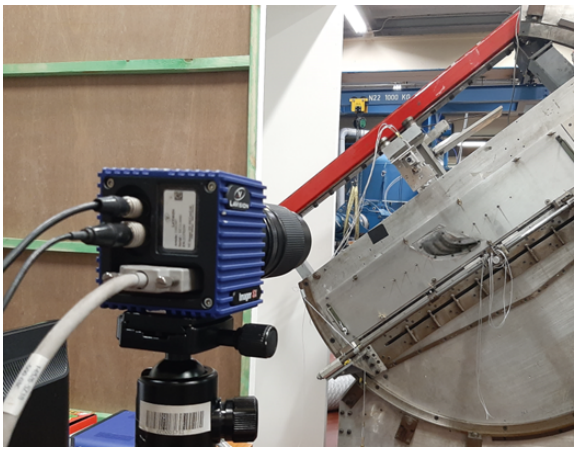

Figure 3: The camera positioning in the PIV setup

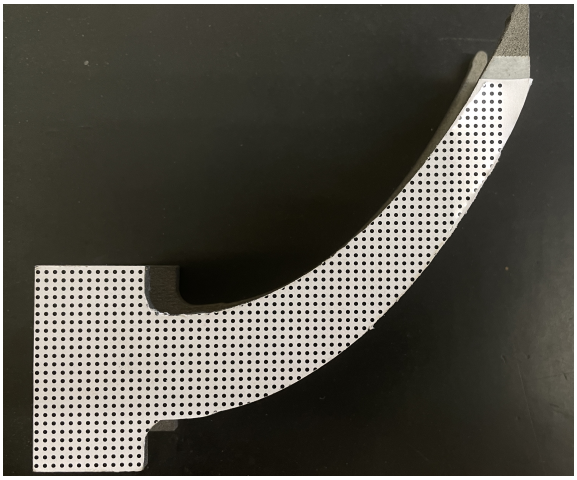

Figure 4: The calibration plate designed to fit the diffuser passage

minimizes the diffuser blade surfaces in the field of view, thereby eliminating any potential laser reflections or image saturation that could arise from those surfaces.

A precise calibration target was used to align the object plane with the PIV camera image plane. The calibration plate has been designed to be precisely placed in the diffuser passage, covering the area between the two blades and the downstream region (Figure 4). It was constructed using SLS material and manufactured through 3D printing. For calibration, a pattern made of black dots on a white background, each with a diameter of 1mm and placed 2mm apart from one another, was attached to the plate.

A Quantel Evergreen ND:YAG laser with a 532 nm wavelength and an applied power of 60mJ was used as

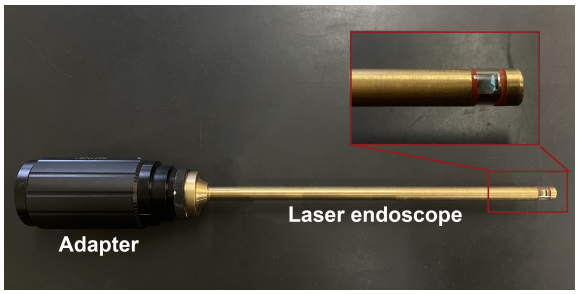

Figure 5: The laser endoscope with an outer diameter of 9mm

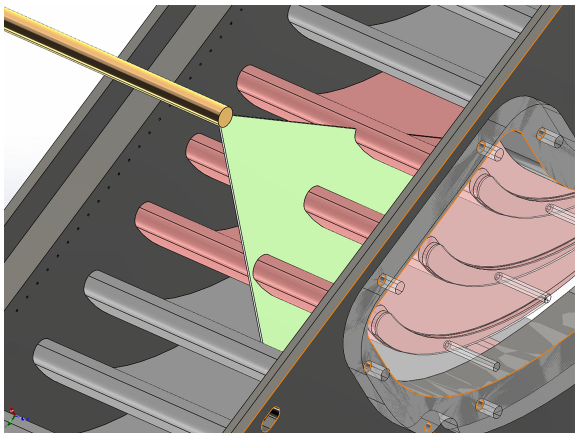

Figure 6: The laser sheet formation via the laser endoscope downstream the diffuser passage

the laser source. A precisely designed laser endoscope (Figure 5) was used to form the laser sheet. A cylindrical lens with convenient AR coating and an ND-YAG prism (for 532nm) were installed manually in the endoscope casing with an outer diameter of 9mm.

The laser sheet is first formed with a divergence angle of about 12° using the cylindrical lens with a focal length of f=-5.79mm, and is then rotated 90° towards the interested plane using the prism (Figure 6). The position and angle of the laser sheet relative to the chord of the diffuser profile can be rotated and adjusted using the endoscope. The endoscope was mounted to the laser head via an adapter (Figure 5) situated between the laser head and the endoscope and inserted through a 9mm hole on the cassette. The probe adapter enables adjustment of the produced light sheet to investigate the flow in the desired blade span positions. To minimize the reflections of the laser beam within the endoscope casing, the spherical lens was placed in the adapter before the beam passes through.

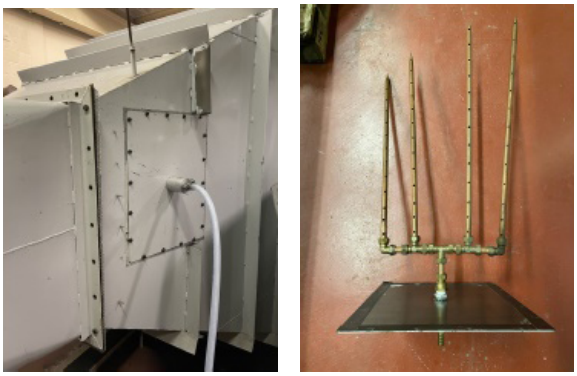

(a) (b)

Figure 7: The seeding positioning on the settling chamber (a) and the seeding rake (b)

A medicinal white oil (Shell Ondina 919) was used as the seeding particles. The oil was vaporized in the seeding generator at around 170°C-180°C to generate the seeding smoke. To introduce the seeding particles to the flow, a seeding rake was inserted upstream of the test section before the settling chamber (Figure 7). To provide uniform seeding distribution, the rake is containing four copper probes with 10 evenly spaced holes along their length.

The smoke blown into the environment from the test rig is collected into a wooden funnel by means of an independent fan and discharged into the atmosphere through a separate pipe system.

3. Experimental configuration

To perform a comprehensive flow investigation, the inlet chord-based Re number Re=183000 was chosen as it matched with that of the original design. Besides the midspan level, the measurement planes at 8%, 15%, 23%, 31%, and 39% blade height (from the window) were investigated at this operating condition (see Figure 8).

Prior to the PIV measurements, the optimum endoscope position was examined as the cambered shape of the diffuser blades blocks the laser sheet to illuminate the entire passage. Because all the mixing process takes place at the downstream of the diffuser of the original design, the first attempt was made by placing the endoscope at the downstream of the blade on the axis perpendicular to the axial direction (Figure 9a). Although the region behind the trailing edge and the downstream side of the passage were sufficiently illuminated according to the scope of the

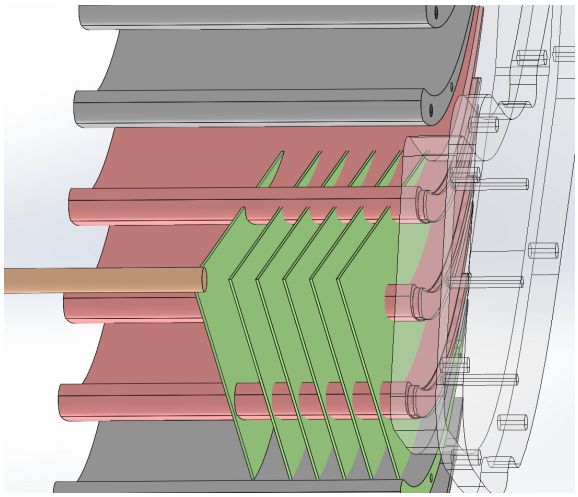

Figure 8: The measurement planes at different blade heights: midspan (50%), 39%, 31%, 23%, 15%, 8%

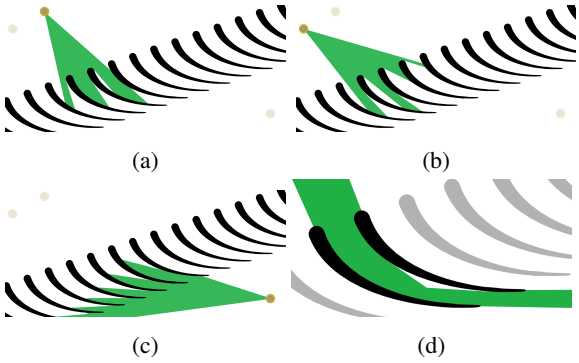

Figure 9: The optical access into the passage with three positions of the laser endoscope: downstream of the investigation passage (a), downstream of the 2nd passage from investigation passage (b) and upstream investigation passage (c); the combination of three accesses for the investigation passage (d)

project, two more endoscope positions were furtherly evaluated. While an area furtherly was retrieved by the second position, the endoscope was placed upstream to retrieve the unilluminated part from the leading edge. The examination of the main case was done by three separate measurement steps with these layouts. The resulting combined observation areas of three endoscope positions are presented in Figure 9d. It should be noted that a small region remained unrecovered due to the profile of the blade. Besides, the resolution of the vector field was enhanced by dividing the observation areas.

To expand the validation case for CFD simulations, the inlet flow regimes of Re=96000, Re=226000 and Re=283000 were also examined for midspan. The combined observation areas approach (mentioned above) was utilized only for the mid-span investigation at Re=183000, due to time constraints. The same calibration, acquisition and post-processing procedure was followed in all cases.

The calibration image was taken after the laser sheet is aligned with the calibration plate. The image plane was scaled out after the image correction was applied by 3rd order polynomial method to eliminate the minimal image distortions caused by misalignments within the setup and minor lens-induced aberrations. In accordance with the guidelines created through the parametric study described in the previous report, the PIV laser was operated at 60% power. Raw PIV images were recorded using Davis 8.4. 1000 image pairs were acquired with the camera's f-number set to 4. To guarantee that the maximum particle displacements would be about 8 pixels, the separation time between two successive PIV images were individually determined for each measurement case.

After the acquisitions, the background images generated separately for each case by a POD-based method, which is proposed by Mendez et al. [17], were removed from the raw PIV images before the image corrections. An example of a raw PIV image, the averaged image and averaged subtracted image are presented in Figure 10.

Instantaneous velocity fields were calculated in Davis 8.4 by the cross-correlation algorithm of the software run with the final interrogation windows of 32x32 pix^2 in three refinement steps. During processing, a 50% effective interrogation window overlap was used. The parameters such as the measurement distance, focal length, camera sensor size, interrogation window size and the overlap resulted in the final spatial resolutions of approximately $1x1m^2$.

4. Cross-correlation quality

Figure 11 exhibits correlation coefficient values that were computed using Davis software, ranging from 0.0 to 1.0. The value 0 indicates the absence of preferred shift direction, whereas 1 signifies identical intensity distributions with minimal noise. Davis recommends a minimum cross-correlation quality of 0.7 to ensure sufficiently accurate PIV results. Barely visible particles in the region where the laser is blocked by the blade resulted in poor correlation values that



(a)

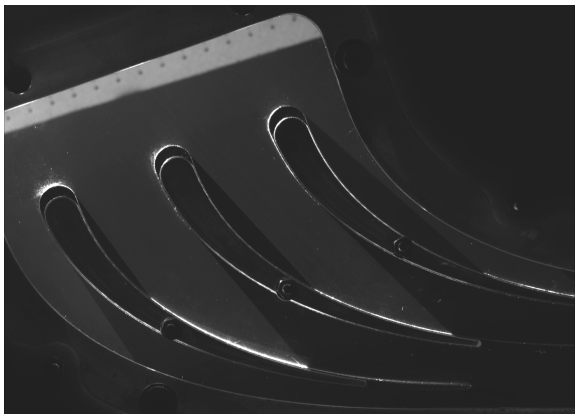

(b)

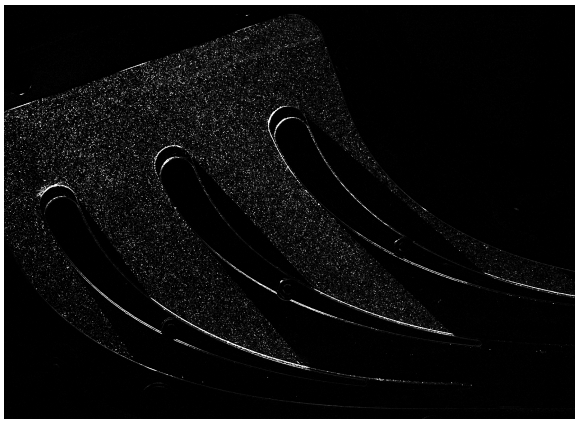

(c)

Figure 10: An example raw PIV image (a), a background image (b) and corresponding background subtracted image (c) in the case of 1st endoscope position at midspan.

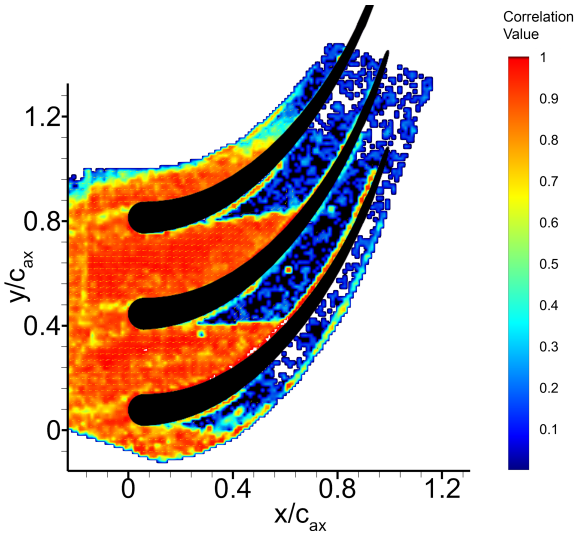

Figure 11: Correlation value distribution in the diffuser passage

are represented in dark blue in the figure. The correlation value ranges from 0.75 to 1 in the other areas properly illuminated, and the average value is calculated as 0.94.

The velocity magnitudes fractions (in pixels) throughout the vector field serve as an indicator of the quality of the cross-correlation algorithm and sub-pixel interpolation, as well as the peak locking effect. Peak locking occurs when the seeding particle diameter is too small (1 pix) for the algorithm to determine the position of the particle in fractional values. In such situations, the correlation peak is biased towards the integer values and precision is lowered. The presence of significant peak locking in a PIV result typically results in the pixel fraction clustering around integers, especially 0 and 1, on the graph. The uniform distribution over the range in Figure 12 suggests that the particle images were captured properly, preventing the peak locking effect.

5. Uncertainty Analysis

Uncertainties are classified as systematic or random uncertainties based on whether they are caused by systematic or random error sources. Random errors are due to irregular factors affecting a measurement, so they can typically yield fluctuant values throughout a series of measurements and their mean value is expected to be zero. However, unlike random errors, systematic errors are constant and can be removed from the total error when their magnitude and sign are

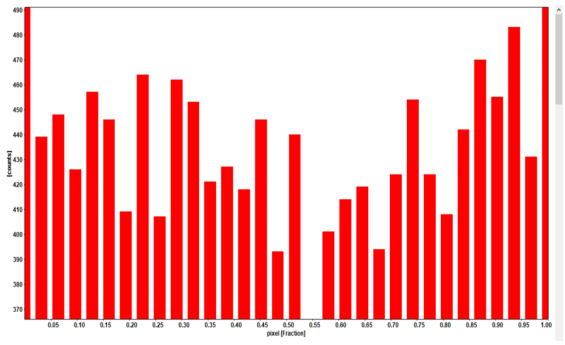

Figure 12: Pixel fractions of corresponding velocity field

known [18]. In this case, the combined standard uncertainty in the quantity of measured velocity vector, V, is expressed as the sum of squares of the systematic, b_V, and random uncertainties, s_v [19]:

$$u_V = \sqrt{b_V^2 + s_V^2}$$

The overall systematic and random uncertainties associated with Nu are then expressed as:

$$b_V = \sqrt{\sum_i (\theta_i b_{V,i})^2}$$

$$s_V = \sqrt{\sum_i (\theta_i s_{V,i})^2}$$

where θ_i is the sensitivity of the velocity vector, V, to the corresponding error source.

In particle image velocimetry, instantaneous fluid velocity, V, is measured by evaluating the particle image displacements, (ΔX), via a magnification factor, M, within a short time interval, (Δt):

$$V[m/s] = \frac{\Delta X[pixel]}{\Delta t[s]} M[m/pixel]$$

where M is calculated in the calibration process as the ratio of position coordinates in the calibration plate (ΔC) to the pixel coordinates in the image (ΔI) representing the same field of view. Therefore, the error sources of these three components were taken into account for the combined standard uncertainty. Magnification-related errors include the standard deviation between the corrected scaled image and ideal position coordinate (RMS fit of the calibration fitting by 3rd order polynomial) and the resolution of the calibration plate. The systematic errors related to the misalignments in the camera and calibration plate were considered by the calibration fitting error. The errors in the cross-correlation and the particle center detection were considered as displacement errors. Although the perspective error is minimized by positioning the camera as far as possible from the measurement plane, it was included in the combined uncertainty. Finally, the error in the separation time was also taken into account according to the estimate in the laser pulse generator. For example, the sensitivity of systematic uncertainty of the RMS fit was computed as:

$$\theta_{RMS,fit} = \frac{\partial V}{\partial \Delta I} = \frac{\Delta X}{\Delta t} \frac{\Delta C}{(\Delta I)^2}$$

All the sensitivities were computed using the partial derivatives method. The uncertainty sources along with the resulting sensitivities of a velocity vector are summarized in Table 1. It should be noted that the sensitivities, therefore the combined standard uncertainty, are not constant as the displacement of the particles is varies across the vector field.

Then, the uncertainty of mean velocity can be expressed as:

$$u_{\bar{V}} = \sqrt{\left(\frac{1}{N}\sum_{j=1}^{N} b_{V,j}\right)^2 + \left(\frac{\sigma_{\bar{V}}}{\sqrt{N}}\right)^2}$$

where $\sigma_{\bar{V}}$ is the standard deviation of the vector samples at a corresponding position and N is the number of samples. Standard deviation, $\sigma_{\bar{V}}$, here was calculated as:

$$\sigma_{\bar{V}} = \sqrt{\left(\frac{1}{N-1}\sum_{j=1}^{N} \left(V_j - \bar{V}\right)^2\right)^2}$$

By the definition of the combined standard uncertainty, the probability of the total error falling within the range of $+/-u_V$ cannot be calculated. Therefore, overall expanded uncertainty was defined at a confidence level of 95% as suggested by ASME PTC 19.1-2005 [17]:

$$U_V = 1.96 u_V$$

Figure 13 presents the expanded uncertainty and the standard deviation distributions across the vector field computed at the midspan measurement in the flow regime of Re=183000 (The same flow field as for the correlation values and pixel fractions). The passage exhibited the highest numerical uncertainty with a maximum of about 0.31 m/s while the wake behind the trailing edge, due to low particle displacements, resulted in lower expanded uncertainties with a minimum value of 0.17 m/s.

Error sources	b_i	θ_i	$(b_i\theta_i)^2$
Image correction error (RMS fit)	0.22 [pixel]	-0.013 [m/spixel]	8E-6
Cross-correlation error	0.05 [pixel]	2.14 [m/spixel]	0.012
Perspective error	0.002 [pixel]	2.14 [m/spixel]	1.8E-5
Laser pulse error	5E-9 [s]	-448200 [m/s^2]	5E-06
Calibration plate accuracy	4E-5 [m]	164 [1/s]	0.007

Table 1: Summary of the uncertainty sources for the midspan measurement

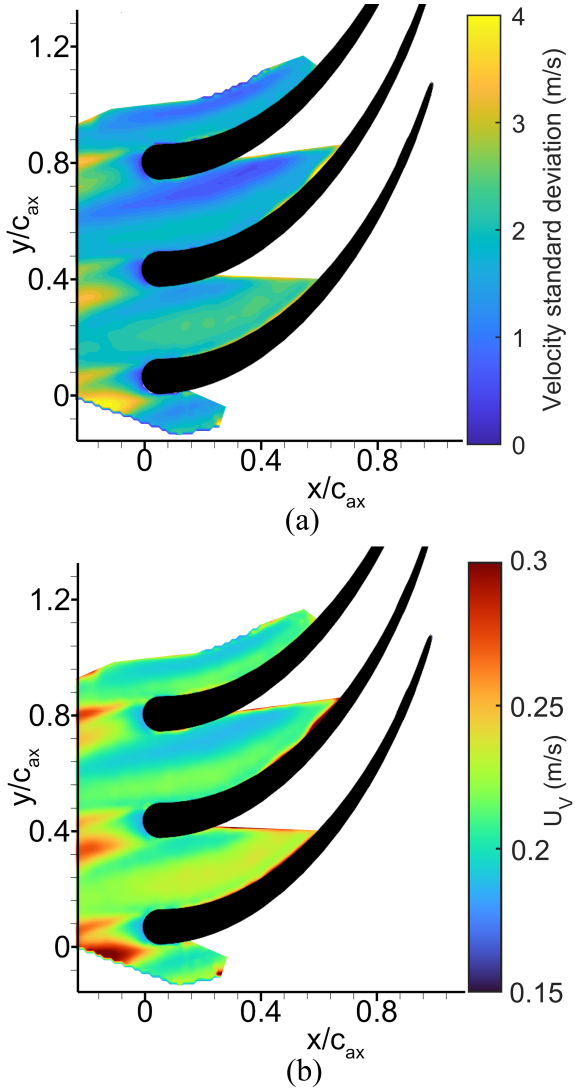

Figure 13: Standard deviation in the velocity field (a) and expanded uncertainty at midspan measurement for the 1st endoscope position (b)

6. Results

Figure 14 illustrates the average absolute velocity fields at midspan height, providing an overview of the various inlet conditions. The data from endoscope position 1 and 2 were merged to obtain the velocity distributions. It is clear that the mean velocity across the entire passage is increasing with the inlet Reynolds number. The streamlines show that the inlet velocity does not have an influence on the flow structure across and downstream the passage within the range of Re=90000-280000. When operating at lower speeds, the high-level mixing which would take place in the original supersonic diffuser design was not observed.

Figure 15 shows the comparison of six measurement planes at several different blade heights where the midspan exhibits the highest velocity. As the cross-section approaches the wall, the maximum velocity in the channel decreases and reaches 8-9 m/s at 8% blade height (z=1 cm). Similarly, the vortices in the wake start to appear and enlarge at trailing edge as the blade height decreases. At the 8% blade height, the wake and the vortices decrease in size despite the lowest velocities.

7. Conclusion

In this study, the planar PIV technique was successfully implemented in the diffuser passage of the e-RSR design. Measurements were performed at different operating conditions of the centrifugal compressor. For flow investigation in the diffuser vane passage, 6 span levels including midspan were chosen to be investigated at the inlet Reynolds number of the original design. To achieve the velocity vector field across the whole passage, three vector fields from three positions of the laser endoscope were combined due to the cambered profile of the blade. The results obtained are of high quality, as the first evaluations have confirmed. An overview of the velocity

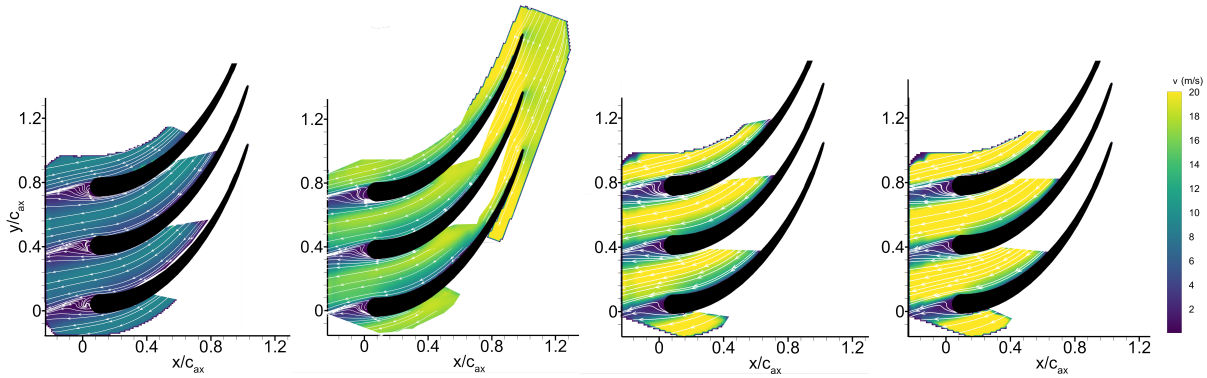

Figure 14: The mean velocity fields at the flow regimes of Re=90000, Re=183000, Re=225000 and Re=265000 respectively

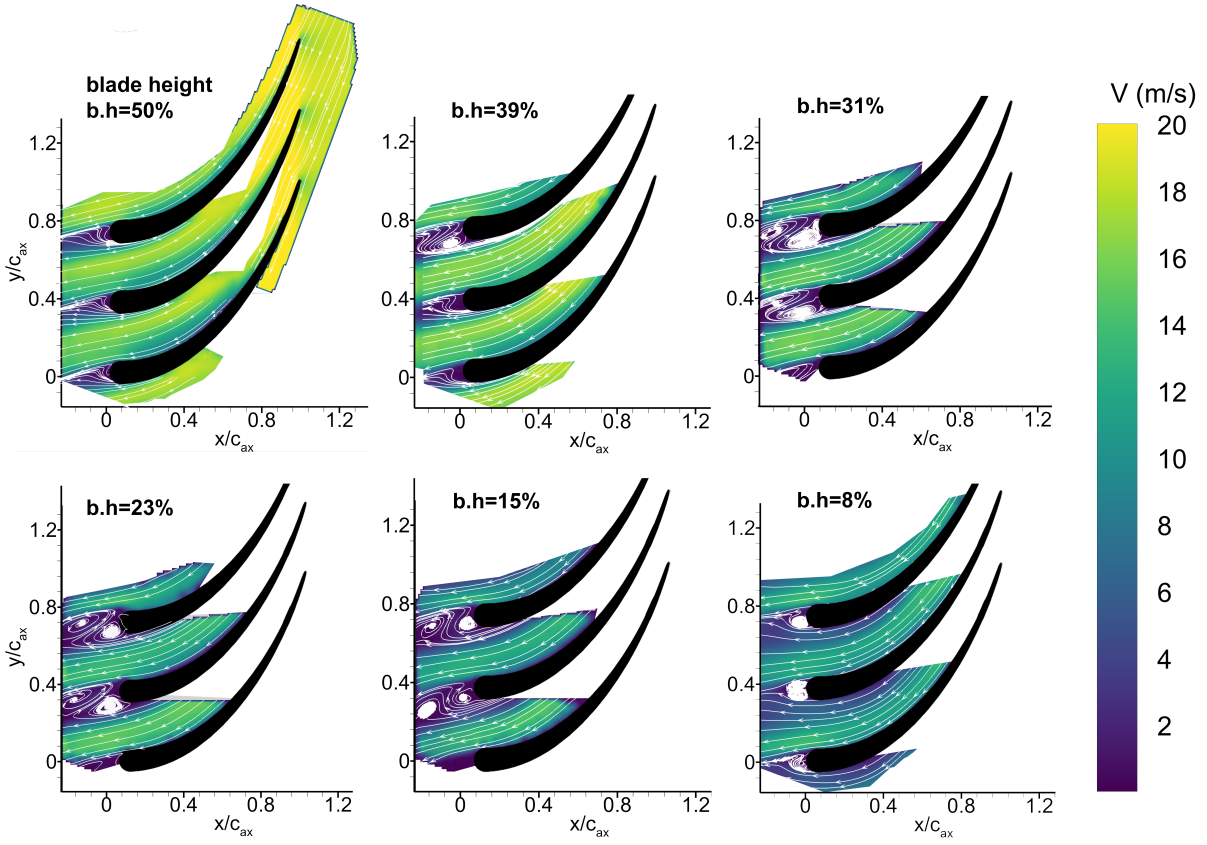

Figure 15: The mean velocity fields for several blade heights (b.h) at the flow regime of Re=183000

distribution in the diffuser vane passage was given, as well as a brief discussion of the influence of the inlet velocities in the flow structures. The PIV methodology followed in this study can be taken as the reference for further supersonic investigations. The established PIV database can be used to validate CFD calculations prior to supersonic evaluation. This PIV campaign shows that stereoscopic PIV measurements with some modifications in the facility can provide a comprehensive understanding of the turbulent flow in and behind the diffuser passage.

References

[1] J. Dedeyne, M. Geerts, P. Reyniers, F. Wéry, K. Van Geem, G. Marin, Computational fluid dynamics based optimization of dimpled steam cracking reactors for reduced co 2 emissions, AIChE Journal 66. doi:10.1002/aic.16255.

[2] D. Rubini, A Novel Turbomachine for Hydrocarbon Cracking, University of Oxford, 2020.

[3] M. Neelis, M. Patel, K. Blok, W. Haije, P. Bach, Approximation of theoretical energy-saving potentials for the petrochemical industry using energy balances for 68 key processes, Energy 32 (2007) 1104–1123. doi:10.1016/j.energy.2006.08.005.

[4] D. Rubini, N. Karefyllidis, L. Xu, B. Rosic, H. Johannesdahl, A new robust regenerative turbo-reactor concept for clean hydrocarbon cracking, Journal of the Global Power and Propulsion Society 6 (2022) 135–150. doi:10.33737/jgpps/150550.

[5] I. Mayo, B. Cernat, M. Virgilio, A. Pappa, T. Arts, Experimental investigation of the flow and heat transfer in a helically corrugated cooling channel, Journal of Heat Transfer 140. doi:10.1115/1.4039419.

[6] C. E. W. S. W. F. S. J. K. M. Raffel, C. J. Kähler, Particle Image Velocimetry: A Practical Guide, Springer Science, 2018.

[7] R. Adrian, J. Westerweel, Particle Image Velocimetry, Cambridge University Press, 2010.

[8] J. Woisetschläger, N. Mayrhofer, B. Hampel, H. Lang, W. Sanz, Laser-optical investigation of turbine wake flow, Experiments in Fluids 34 (2003) 371–378. doi:10.1007/s00348-002-0568-7.

[9] K. Gallier, P. Lawless, S. Fleeter, Development of the unsteady flow on a turbine rotor platform downstream of a rim seal, 2004. doi:10.1115/GT2004-53899.

[10] S. Chemnitz, R. Niehuis, A comparison of turbulence levels from piv and cta downstream of a low-pressure turbine cascade at high-speed flow conditions, Journal of Turbomachinery 142 (2020) 1–14. doi:10.1115/1.4046272.

[11] P. Bryanston-cross, D. Udrea, G. Guenette, A. Epstein, E. d'Hoop, Whole-field visualisaton and velocity measurement of an instantaneous transonic turbine flow, Vol. 1997, 1997, pp. 278 – 286. doi:10.1109/ICIASF.1997.644690.

[12] E. Göttlich, J. Woisetschläger, P. Pieringer, B. Hampel, F. Heitmeir, Investigation of vortex shedding and wake-wake interaction in a transonic turbine stage using laser-doppler-velocimetry and particle-image-velocimetry, Journal of Turbomachinery-transactions of The Asme - J TURBOMACH-T ASME 128. doi:10.1115/1.2103092.

[13] S. Lemay, V. Aeschlimann, R. Fraser, G. Ciocan, C. Deschênes, Velocity field investigation inside a bulb turbine runner using endoscopic piv measurements, Experiments in Fluids 56. doi:10.1007/s00348-015-1991-x.

[14] U. Dierksheide, P. Meyer, T. Hovestadt, W. Hentschel, Endoscopic 2d particle image velocimetry (piv) flow field measurements in ic engines, Experiments in Fluids 33 (2002) 794–800. doi:10.1007/s00348-002-0499-3.

[15] M. Kegalj, H.-P. Schiffer, Endoscopic piv measurements in a low pressure turbine rig, Experiments in Fluids 47 (2009) 689–705. doi:10.1007/s00348-009-0712-8.

[16] A. Nauwerck, J. Gindele, U. Spicher, H. Rosskamp, G. Landwehr, Investigation of the transient in-cylinder flow inside a two stroke engine with particle-image-velocimetry, 2000. doi:10.4271/2000-01-0902.

[17] M. Mendez, M. Raiola, A. Masullo, S. Discetti, A. Ianiro, R. Theunissen, J.-M. Buchlin, Pod-based background removal for particle image velocimetry, Experimental Thermal and Fluid Science (EXP THERM FLUID SCI) 80 (2017) 181–192. doi:10.1016/j.expthermflusci.2016.08.021.

[18] A. Sciacchitano, Uncertainty quantification in particle image velocimetry, Measurement Science and Technology 30. doi:10.1088/1361-6501/ab1db8.

[19] ASME PTC 19.1, Test Uncertainty, American Society of Mechanical Engineers: New York, 2005.

Modeling and exploitation of aerothermal probes in helicopter engines

Adrien Vasseur, Supervisor: Fabrizio Fontaneto

Associate Professor Turbomachinery and Propulsion Department, VKI, Belgium, fabrizio.fontaneto@vki.ac.be

Département Aérodynamique, Énergétique et Propulsion, ISAE-SUPAERO, France, adrienvasseur@isae-supaero.fr

University Supervisor: Nicolas Binder

Professor - Head of Turbomachinery and propulsion research group, DAEP, ISAE-SUPAERO, France, nicolas.binder@isae.fr

Industrial Supervisor: Jean-Louis Champion

BEARCAT Project manager, SAFRAN Tech, France, jean-louis.champion@safrangroup.com

Abstract

The flow after the second HP turbine stage of SAFRAN's BEARCAT test engine is very different from the five-hole probes calibration conditions. The relative size of the probe has a big impact on the flow. Experiments on wall proximity and errors when traversing a wake have revealed errors in flow angle measurements reaching 6°. CFD is expected to complement the understanding of the errors.

Keywords: Five hole probes, pressure probes, measure, corrections, turbulence, shear, errors, metrology

1. Introduction

This PhD was launched in support of the creation of the BEARCAT test bench of SAFRAN Tech. It is a heavily-instrumented helicopter engine [1]. Its aim is to provide numerical models with experimental data, to feed and check them. Original measurements will be performed in the combustion chamber and the high pressure turbine region [1]. One of the probes chosen to that extent is a five-hole aerothermal pressure probe.

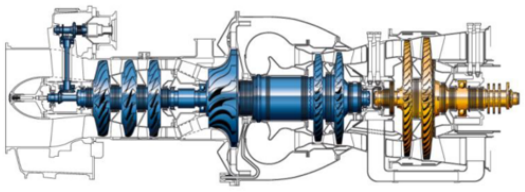

FIGURE 1: CROSS SECTIONAL VIEW OF A MAKILA 2A1 ENGINE

Figure 1: BEARCAT is based on the Makila 2 engine [1]

Five-hole pressure probes are robust probes that give an indirect measure of the flow direction and the Mach number. Adding a temperature reading allows to also get the velocity. As the relationship between flow direction, Mach number and the pressure at each hole is very complex, those probes need to be calibrated. It is usually done in an open jet. The pressures of the five holes are measured at a range of flow conditions and probe orientations. The data is then used, directly or through models, to interpret the set of pressures given by the probe in the unknown flow. The SAFRAN probe studied in this work is depicted in Figure 2.

The use of this probe poses several challenges : its diameter is significant in the engine vein, which changes the studied flow and the flow is very different from the calibration flow which makes the pressure readings harder to interpret correctly.

Figure 3 illustrates several problems encountered: the vein is less than four centimeters high, when the probe has a head diameter of four millimeters. The axial velocity shows strong gradients.

The aim of this PhD is to improve the interpretation of five-hole-probes pressure data sets in engine conditions. The strategy is to identify measurement problems possibly encountered in this kind of set-up, com-

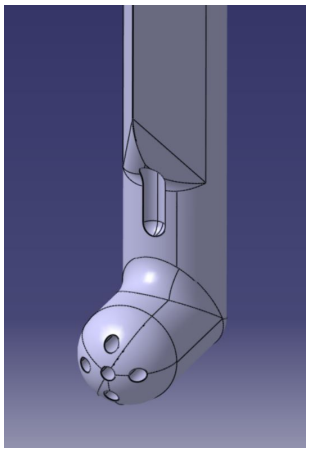

Figure 2: 3D modelling of the probe designed for the BEARCAT project. Above the head is a thermocouple sleeve.

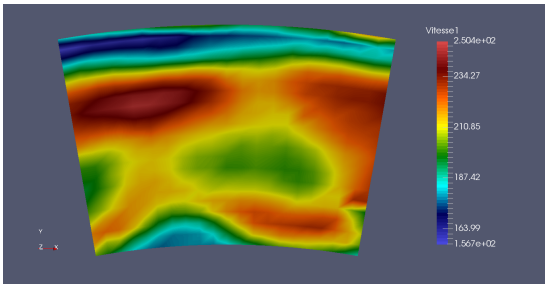

Figure 3: Mean axial velocity field (m/s) at the exit of the second high pressure turbine for 300kW idle engine conditions. BEARCAT data provided by J.-L. CHAMPION

pare and rank them in the BEARCAT context and run experiments and simulations to explore these problems in a unified context with the SAFRAN probe. The possibility of using computational fluid dynamics (CFD) to help with the calibration will be investigated.

This project is a cooperation between SAFRAN and ISAE-SUPAERO in France and the von Karman Institute (VKI) in Belgium. The experimental campaign was carried out in VKI and the rest of the PhD in ISAE-SUPAERO.

2. Bibliographic search

As the specific geometry used by SAFRAN and the flow conditions of interest in this work are hard to find in articles, the bibliographic search as extended to a wide variety of probe shapes, hole numbers and flow conditions. The flow in BEARCAT after the second stage of high pressure turbines can reach Mach 0.6, 1400K and strong turbulence levels. The error sources in the scope of this thesis can be divided in two categories : geometry-related and flow phenomena-related.

2.1. Geometry-related problems

The probe might be of significant size compared to the engine vein it is in. The probe then measures a flow that has been modified by its presence. At the exit of the second high pressure turbine, the probe is as big compared to the vein as a pen is to a post stamp.

The holes of the probe are at a finite distance of each other. When the flow displays strong gradients or the size if the probe is significant compared to the characteristic size of the studied flow, the assumption that the measurement is made on a point becomes wrong. The position of each hole needs to be accounted for [2] [3]. The correction method used in this work is the one described in [4].

When the probe is closer than three diameters to a wall, a blockage effect occurs that bends the streamlines away from the wall [5]. The probe then measures the flow closer to the wall than its actual position. Bailey [5] proposes a correction that accounts for this displacement.

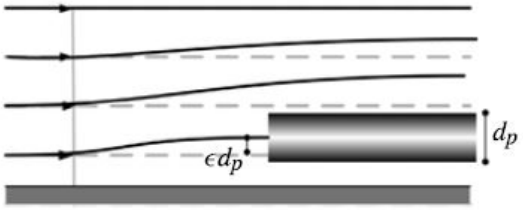

Figure 4: Wall proximity effect. Extracted from [5]

2.2. Flow phenomena-related problems

Crowley [6] in 2013 found a strong hysteresis in the calibration of a five-hole probe. When the probe had a 20° yaw angle, increasing or decreasing velocities triggered hysteresis in one of the calibration factors. However, the hysteresis disappeared when turbulence intensity reached 1%. The hysteresis in one of the calibration coefficients is reported to reach 30%. The reason is an hysteresis in the behaviour of the recirculation bubble on the probe head [6]. This recirculation can also be responsible of a 5° error in angle measurement and 6% in dynamic pressure if the probe was

calibrated in conditions where there was no recirculation bubble according do Dominy [7].

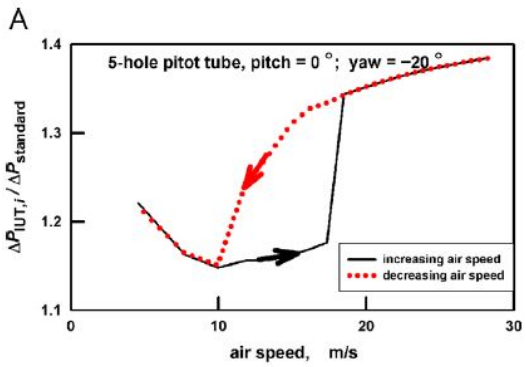

Figure 5: Crowley [6] highlights that the difference between center hole and off-axis holes can display hysteresis

The long tubes in the five-hole probe cause the pressure signal to be the time-averaged value of the pressure at the holes. As the dynamic pressure is a quadratic function of the velocity, turbulence has a increasing effect on the pressure readings. Bailey [5] offers a formula to predict the overestimation of the velocity caused by the turbulence. According to this formula, the error on the velocity is for example 5% for 30% Tu and 0.5% for 10% Tu. Experimental data from the DGEN test bench at ISAE were analysed in this scope. DGEN is a very light turbofan engine produced by Price Induction. The maximum possible overestimation of the velocity due to turbulence in those data was 0.5%. The data is from a little upstream of the fan which makes the turbulence very low.

Turbulence can also affect the measured angle according to Sitaram [3]. A calculation made from his formulas indicates a 0.66% error on pitch angle for 10% Tu. Christiansen [8] reports that turbulence is not a problem for low angles, under 15° in his case. He advises to use the probe in the nulling mode (i.e. the probe is rotated until lateral pressure are the same which makes the angle of the probe the angle reading). Christiansen also reports that the effects of turbulence are worse when the instantaneous velocity direction is out of the linear range of the probe [8].

When in a shear flow, the probes are subject to a displacement effect. The stagnation line is bent the presence of the probe [5]. The probe at location y_0 is actually measuring the flow at the location $y_0 + \Delta y$, where Δy depends on the shear and the probe geometry [5] [9] and the dimension (2D or 3D) [10]. The shear also is responsible of a change in the measured flow angle [9]. The stagnation streamline arrives on the probe with a non-zero angle and the lateral holes are subject to different flows. Several authors like Hall [10] offer formulas to correct the location of the measured velocity, the angle [9], or the velocity at the measurement location [11]. The problem is illustrated in Figure 6.

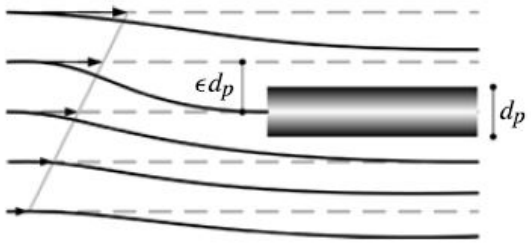

Figure 6: Illustration of the displacement effect. Extracted from [5]

Around unity Mach number the pressure distribution on the probe doesn't change much with the Mach number [12]. It leads to an insensitivity to Mach number changes. This problem can me mitigated by adding a static pressure hole downstream the head for the cobra probe [12]. The uncertainty in Mach number measurement is increased by a factor of five for the five hole probes that Boerned studied [13].

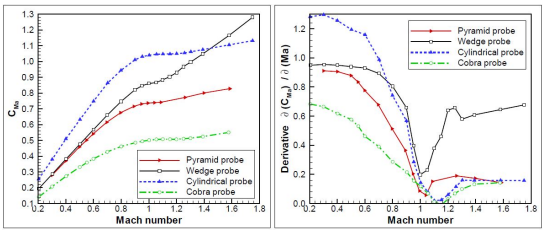

Figure 7: Transsonic insensitivity to the Mach number for different probe geometries. Extracted from [12]

Sitaram [14] reports that the angle measurement is affected by the Mach number. A four hole probe calibrated at a 0.4 Mach number shows a 2.2° standard error in the measurement of the yaw angle between ±20°. Sitaram doesn't specify whether the Reynolds number has been kept constant between throughout the tests so those errors might also be caused by changes in the Reynolds number.

Reynolds number affects the behaviour of the separation, so it has an importance in the recirculation bubble problems mentioned earlier. In a study of various five hole probe geometries, Dominy [7] noted that

for Reynolds numbers higher that 50 000 the yaw coefficient becomes insensitive to yaw between 0 and 4°. Dynamic pressure measurements can display up to a 20% error when the measurement Reynolds number is lower than the calibration Reynolds number [7].

The vortex shedding on the trailing edge of the probe cause pressure fluctuation in the probe holes because of the upstream transmission of pressure information. Liu [15] performed 2D simulations of short oval and trapezoidal probes (see Figure 8) for several Mach number and incidence. He reports that at Mach 0.3 and no incidence, the pressure fluctuation amplitude is between 20 and 25% of the dynamic pressure for both geometries on point *e* and almost zero on *a*. When the probe is at a $-12°$ incidence, it reaches 10% for the oval probe and 5% for the trapezoidal probe. Liu doesn't discuss how the measurements would be affected by this.

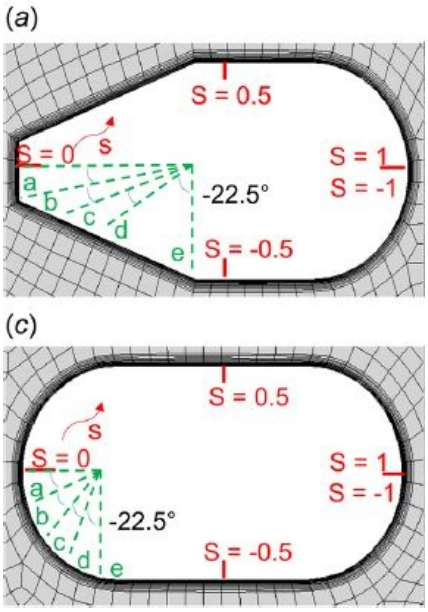

Figure 8: Locations (*a* to *e*) of the pressure signals studied by Liu. Extracted from [15]

Comparable results are to be found in an article by Boufidi [16] that is dealing with a probe with a larger aspect ratio (see Figure 9). She reports that the maximum amplitude of pressure fluctuation in the probe holes is 0.25% of the dynamic pressure. The significant difference between the two articles is probably a consequence of the difference in aspect ratios.

Ranking the errors in the BEARCAT context is complex, because those errors are often geometry-dependant, interdependant and assessed in flow conditions different from the ones sought. The CFD and experimental work will then also be aimed at understanding in what extent the results found in the bibliographic search are applicable to the SAFRAN probe in BEARCAT.

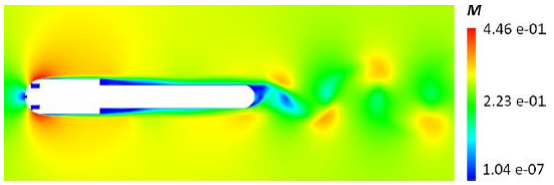

Figure 9: Mach number contour around the probe studied by Boufidi. Extracted from [16]

3. Numerical work

Simulations were first performed on simplified geometries to help with the learning of the CFD tools, and then the 3D SAFRAN probe geometry started to be used.

FineOpen was selected as the CFD software for this thesis, after encountering troubles with elsA and the structured version of Fine. It is a Numeca software that accomodates easily the complex geometry of the probe tanks to hybrid meshes, like the one depicted in Figure 10. The holes are very small and have a sharp inlet, that require a big number of cells.

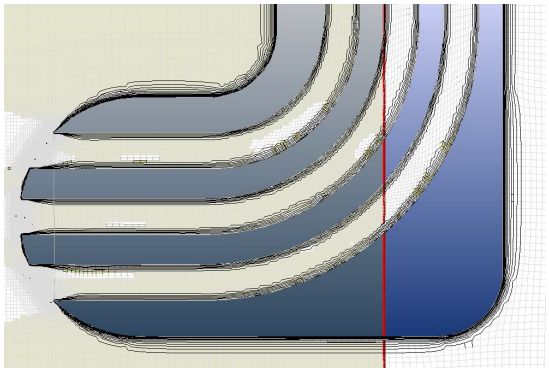

Figure 10: Section of the 3D mesh around the SAFRAN geometry. There are 21 million cells in the whole domain. This mesh was used to compute the calibration coefficients displayed in Figure 12

From 2D simulations ran on different hole geometries and hole boundary conditions, it was observed that they need to have a large aspect ratio and non-slip boundary conditions. In Figure 11, the circulation

reaches the end of the shorter hole in slip conditions whereas viscous walls keep high velocities at the entrance of the hole.

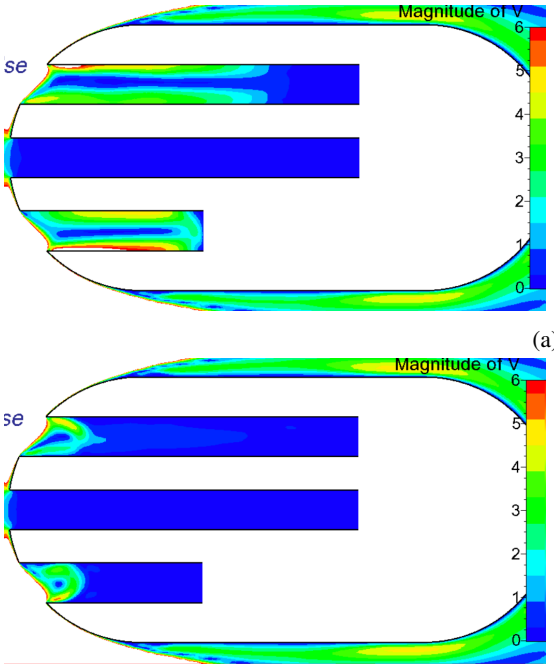

Figure 11: Comparison of $|\vec{V}|$ for slip walls (a) and viscous walls (b)

3D simulations were performed on the geometry depicted in Figure 2 to simulate a calibration of the probe. The domain shown in was extending 30 diameters from the probe in all direction.

RANS and URANS simulations were run and helped build a inexhaustive calibration map at Mach 0.3. At strong incidence, the change of the turbulence model from Spalart-Almaras to $k\omega - SST$ in RANS can change the results by the equivalent of a 0.25° change in the incidence. URANS results at 10° of pitch and yaw are very close to RANS results : the difference in calibration coefficients is equivalent to a negligible 0.04° change in the probe incidence. URANS simulations are thus unnecessary for low incidence simulations. The comparison has yet to be made for high pitch and yaw. The corners of the calibration map stretch as in all the calibration maps found in the literature.

From 3D simulations run with elsA on a simple cylinder in a channel, it was observed that the wake of the cylinder can be asymmetrical when the probe is as far as 13 diameters from a wall. The rule of thumb

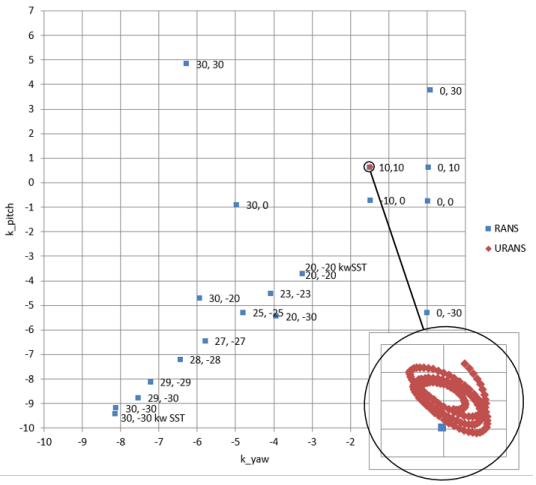

Figure 12: Comparison between RANS calibration coefficients and URANS for 10° of pitch and yaw

found in literature about the effects of wall proximity was that it appeared from 3 diameters distance to the wall. This shows that the shape of the flow isn't sufficient to investigate the wall proximity effect, we should also derive the changes in the calibration coefficients caused by that asymmetry.

A. Bilbault, an engineering student of ISAE-SUPAERO, has conducted a numerical study of the effects of the insertion of the SAFRAN probe in a shear flow. He has compared literature formulas for the displacement effect with the displacement of the stagnation streamline observed for the SAFRAN geometry in various shear conditions. One of his findings was that the mast caused a mast-wise displacement of the stagnation streamline up to 0.27 diameters for no shear and shear, whereas the maximum observed shear-wise displacement was 0.11 diameters. A. Bilbault suggested a revised shear effect correction formula, that includes the mast-wise displacement.

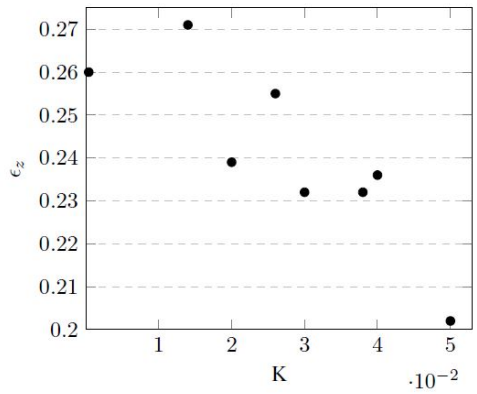

Figure 13: Displacement due to the mast of the probe in [17] as a function of the shear.

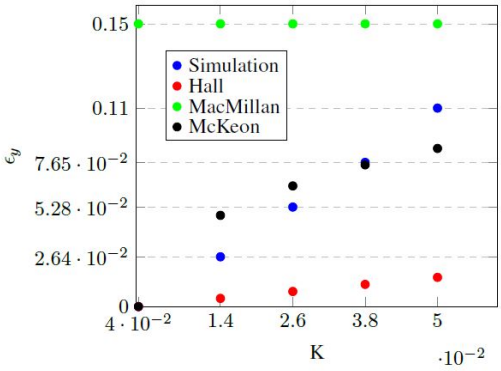

Figure 14: Displacement due to the interaction of the probe and the shear in [17] as a function of the shear.

4. Experimental work

5 experiments were carried out:

- Reynolds and Mach number effects;
- Velocity- and angle-related hysteresis;
- Velocity gradient effects;
- Traverses of an airfoil wake;
- Wall proximity effect.

Three other experiments were planned but were canceled to lack of time and low priority:

- Turbulence effects : a 3D printed grid will produce T_u up to 6.4% ;
- Blockage : the three probe sizes and the small-section sub-vein will help reach a wide range of blockage ;
- Separation on the head.

4.1. Experimental setup

The SAFRAN probe design (L shaped hemispheric head, shown in Figure 2) was simplified for manufacturing purposes. Three heads with diameters of 4 mm, 8 mm and 16 mm were 3D printed, mounted on cylinders and painted black to reduce PIV reflections. All the steps were done in VKI. The different sizes will help change independently the blockage, Reynolds number and Mach number.

The probes heads turned out to not be perfectly aligned with the masts. The heads have a pitch ranging from 1° to 1.7° towards the mast depending on the probe. The reason might be a change in the printed shape during the polymerisation of the resin. This would be very hard to correct thus the angles were measured to incorporate it in the post-processing. The holes of the 4 mm probe had to be drilled to clean the capillaries but this lead to errors in the hole positions, as shown in Figure 15. The result is a 1.2° average rotation of the hole pattern on the face of the probe.

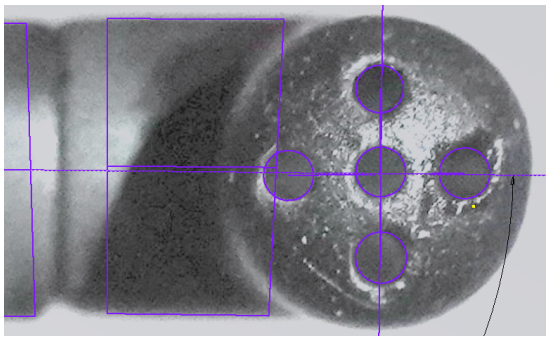

Figure 15: Alignment of the holes on the 4 mm probe

The capability of two different paints to reduce the laser reflections or the brightness of the probes were compared : BLK3.0 and Spectrum black mat spray paint. Their maximum brightness under the laser light were the same, but the bright zone was smaller for the Spectrum paint. In addition, the BLK3.0 suffered from the PIV seeding oil being cleaned from the probe.

The facility chosen for the experimental campaign is the L12 wind tunnel. It is a flexible, easy to operate, low mach, ambient temperature and pressure wind tunnel. It is displayed in Figure 18. It is PIV-ready. A new Plexiglas test section was drawn to perform this project's tests. This wind tunnel can produce flow velocities up to 17 m/s in the standard $0.04m^2$ test sec-



Figure 16: The three probes without paint

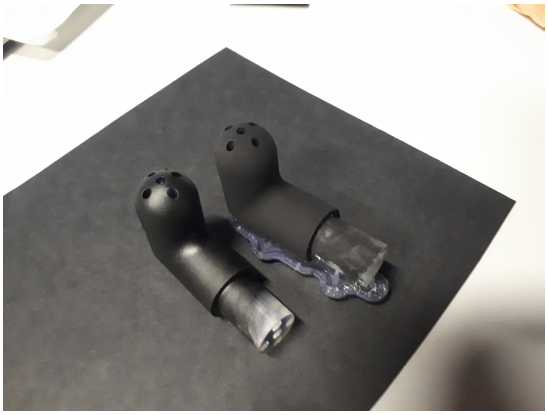

Figure 17: Although the paint from the left appears shinier, it was better suited for the PIV

tion. The test section is 1m long. The settling chamber is equipped with a total pressure probe. Three Validyne relative pressure sensors measured the total pressure in the settling chamber, the pressure from the probe holes and the wall static pressure. The probe sensor was later replaces by five bleed pressure sensors. All pressure sensors are relative sensors with the negative port connected to the ambiant pressure. The range of the sensors was: 0.86 mbar for the static pressure, 2.2 mbar for the other Validyne sensors and 2.5 mbar for the bleed sensors.

A middle plate, obstacle, a turbulent grid and a low section sub-vein can be mounted in the test section. The five hole probe can be inserted just before the exit of the test section to use the developed boundary layers, or just after the converging section to avoid thick

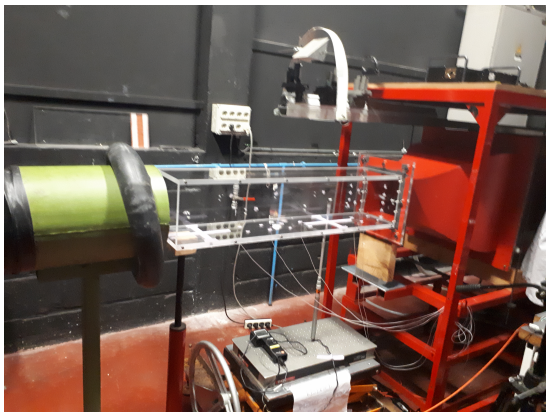

Figure 18: The test section designed for this project mounted on L-12

boundary layers.

4.2. Preliminary tests

Tests of the facility were first ran to get familiar with its possibilities and behaviours, to troubleshoot and verify some assumptions about the campaign.

It was found that when the largest probe head, 1.6 cm in diameter, is in the center of the test section, which is 10 cm away from each wall, rotating it around the mast or around the center of the probe head doesn't change the pressure coefficients. It means the walls are far enough to simplify the tests by not exactly keeping the center of the head in the center of the section. It is consistent with the wall proximity effect threshold of 3 probe diameters mentioned by Bailey [5]. In Figure 19 the yaw pressure coefficient is very similar for each case.

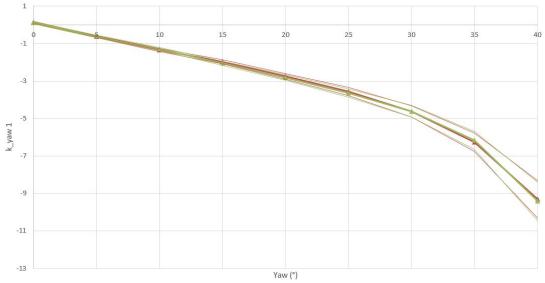

Figure 19: Yaw pressure coefficient for yaw changes made by rotating the probe on its mast axis (blue) or around the center of the head (green).

The evolution of the static pressure on the walls was investigated. A simple model of the displacement

thickness on a flat plate was used to predict the streamwise evolution of the effective section of the tunnel and predict the static pressure depending of the nature of the boundary layer. Figure 20 shows that the boundary layer at low regime is likely to be laminar, whereas at high regimes it is likely to be fully turbulent.

For the 16 m/s case, the velocity is almost 1 m/s higher at the end of the test section. PIV will help know the exact velocity around the probe. In experiments without PIV, the ambient pressure will be used as a reference for static pressure.

Special attention to this boundary layer development will have to be paid when using the sub-test section. For low regimes, the boundary layer will fill all the space of this test section and have large effects on the flow.

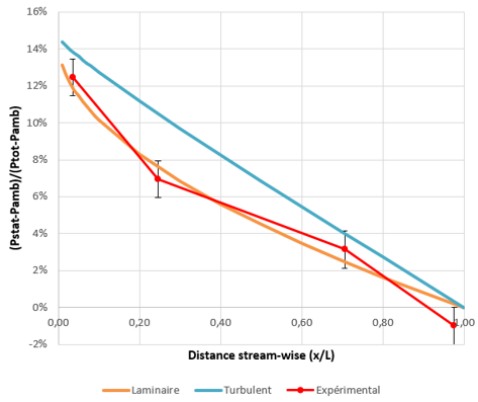

(a)

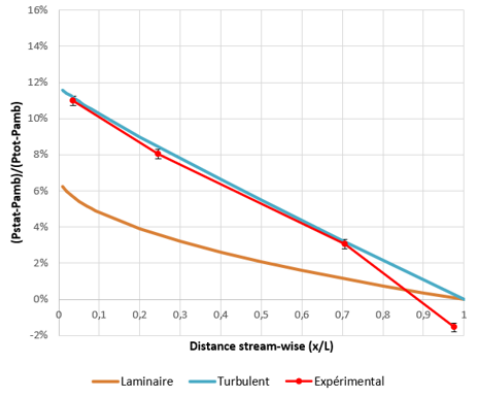

(b)

Figure 20: Evolution of static pressure in the streamwise direction compared to fully laminar or turbulent boundary layer models, at 4 m/s (a) and 16 m/s (b)

4.3. *Hysteresis*

The hysteresis tests were inspired by the article of Crowley [6]. The largest probe was used to match the Reynolds number of 21 000 around mid-velocity of the test section. The velocity was gradually increased to 17 m/s, the full power of the facility, and then decreased to zero. The pressure from the left hole and the right hole were regularly measured to plot the yaw pressure coefficient. This was done at a 20° yaw angle, as in [6] and also 40°. A rotation from −60° to 60° of yaw was also performed at 16 m/s and 8 m/s to check yaw-related hysteresis.

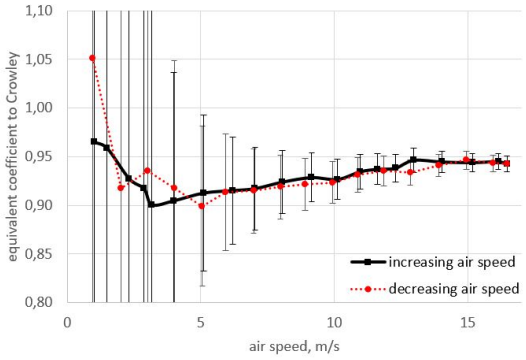

Figure 21: Attempt to reproduce Crowley's findings with the SAFRAN probe.

As can be seen on Figure 21 there is no evidence of any hysteresis. This is good news for BEARCAT but as this facility doesn't cover the whole range of conditions encountered in BEARCAT, this doens't mean this probe geometry will not be subject at all to hysteresis in the engine. This Figure is to be compared to Figure 5.

4.4. *Mach and Reynolds number effects*

The objectives of these measurements were to provide a calibration of the three probes to use in the experimental campaign and to check for changes in the calibration maps caused by changes in Reynolds number and Mach number. The ratio between the maximal and minimal Re used is 16 thanks to the three probe diameters used, 4 mm, 8 m and 16 mm, and the three velocities used : 4m/s, 8m/s and 16m/s. In the following figures, the dots, triangles and squares represent respectively the 16, 8 and 4 mm probes. Some surfaces are displayed for some maps to better visualise the data and have a reference for comparisons.

The coefficients for total pressure and yaw are similar for all probe sizes and flow velocities, as for the

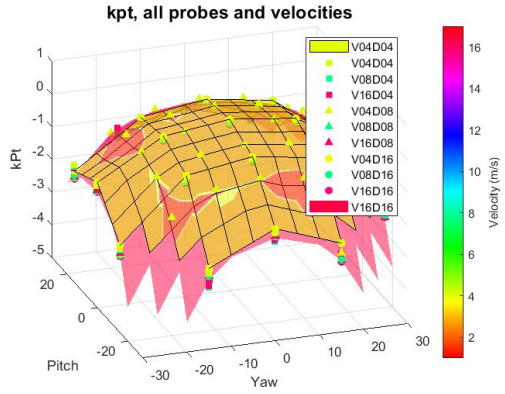

Figure 22: All the maps of total pressure coefficient.

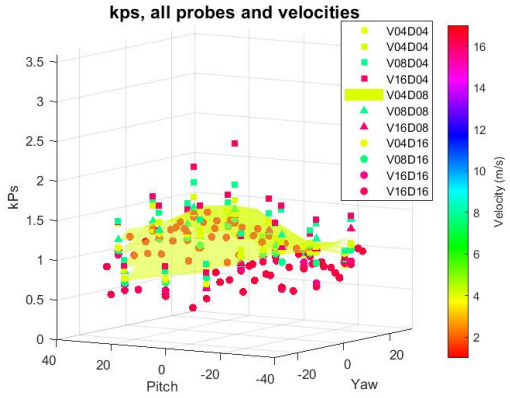

Figure 23: All the maps of static pressure coefficient.

pitch pressure coefficient that is not displayed here. However, the static pressure coefficient changes drastically with low Reynolds number and its behaviour depends on the probe. An increasing Mach number results in an decrease of static pressure coefficient for the two biggest probes, in opposition to what happens for the smallest probe. In addition, there is an inexpected change of slope in the map for low Reynolds numbers at negative pitch angles.

The maps will be measured again in a wind tunnel in ISAE-SUPAERO with finer sensors and in a more controlled environment to try to replicate these observations.

4.5. Wall proximity

The evolution of the pressure coefficients and the pressure in the five holes caused by the proximity of a wall was performed using the 8 mm and 16 mm probes for varying Mach number and boundary layer thickness. This experiment is detailed in the proceedings

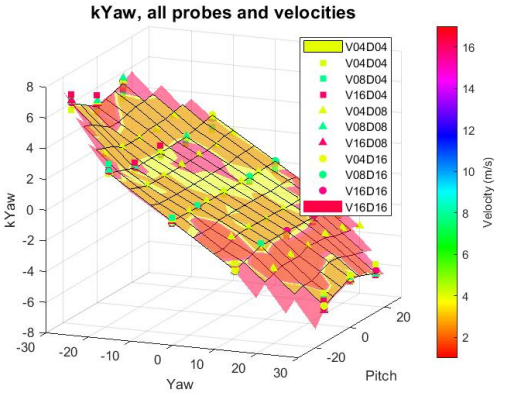

Figure 24: All the maps of yaw pressure coefficient.

of Measurement Techniques in Turbomachinery 2022 [18].

There was no hysteresis shown linked to the direction of the traverse.

The wall proximity effects seem to belong to two categories :

- The immersion in the boundary layer leads to an overestimation of the yaw angle and shifts away from the wall the balance between the hole pressures, as if the flow is directed away from the wall;
- The interaction between the probe and the wall also leads to an overestimation of the yaw angle but shifts towards the wall the balance between the hole pressures, as if the flow is directed towards from the wall.

The two phenomena are competing for the pitch measurement. Their balance seems to be dependant on the boundary layer thickness, the probe diameter and the probe position.

A CFD campain is planned that will help separate further the effects from the boundary layer and the interaction with the wall.

4.6. Wake traverses

The goal of this experiment was to measure the errors in the measurement of the wake, near and far from the trailing edge (TE), for two probes diameters. This situation combines resolution effects, non linear gradients and interactions with an obstacle.

A NACA0012 profile was designed and modified in order to produce a probe diameter to displacement thickness ratio similar to what Fabrizio FONTANETO measured during his PhD [19], for the 8 mm probe.

The profile was placed horizontally at the start of the test section, at equal distance to the top and bottom plate, to get a symmetrical wake.

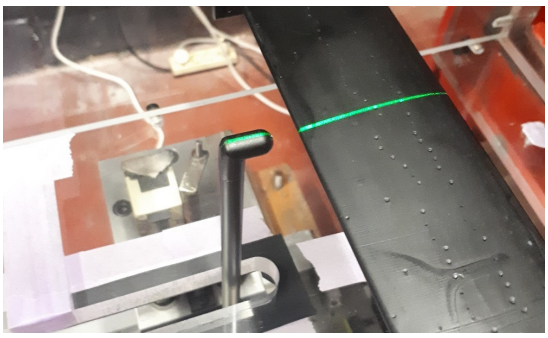

Figure 25: 8 mm probe in front of the profile TE. The position of the laser sheet is visible in green.

Vertical traverses were carried out at 8, 16, 40 and 80 mm downstream of the TE, with the 4 mm and 8 mm probes. At each position, the probe holes, total and dynamic pressures were measured using the same sensors as in the wall proximity study. The flow was recorded using PIV when the probes were at 8, 16 and 40 mm downstream of the TE and in the middle of the wake, 3.5 and 13 mm above and below the wake. The velocity was around 16 m/s for each case. The PIV was also used without the probe in order to have information about the undisturbed flow.

The traverses were interpreted using the calibration described in 4.4. In the figures depicting velocity and pitch angle, the black line is a 5-hole probe traverse reconstructed from the PIV data, the calibration maps and the assumption that the static pressure is equal everywhere to the ambiant pressure. It is supposed to be what a probe transparent to the flow would measure. It is used to assess how much of the differences between the pressure data and PIV data can be attributed to resolution issues. In Figures 26 and 27 the left and right hole pressure were removed for readability. The solid line is the reconstructed pressure and the dashed line is the pressure measurement. Those simulated pressures are then interpreted along the measured pressure to provide the data in Figures 28 to 31. The dashed lines are the pressure measurements corrected for the distance between the probe holes as described in [4]. The right side of the chart is where the probe is below the wake, the left side is where the probe is above the wake, the mast being in the wake.

It appears that there is a lack in pressure in the data predicted from the PIV. It might come from the potential effect of the profile. The overpressure and pressure deficits around ±2 mm are likely to stem from intrusiveness. The PIV data in presence of the probe should help understand it.

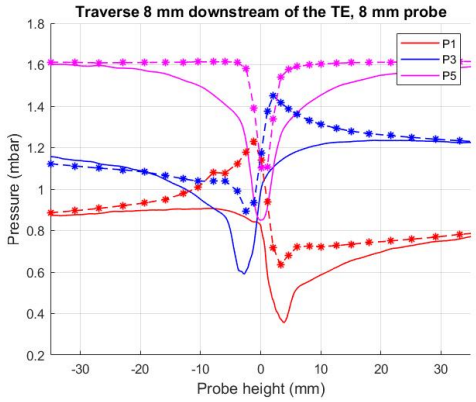

Figure 26: Hole pressure 8 mm away from the TE for the 8 mm probe.

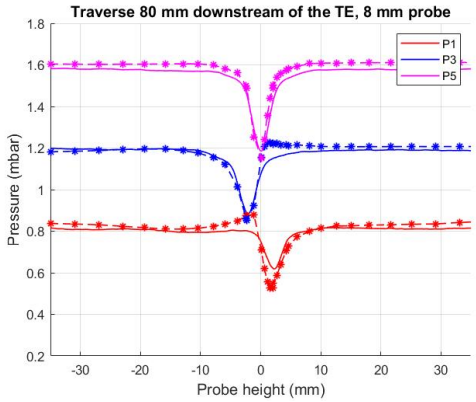

Figure 27: Hole pressure 80 mm away from the TE for the 8 mm probe.

The depth and shape of the velocity agree well between the PIV data and the pressure data corrected for resolution effects 8 mm downstream of the TE. 80 mm downstream the TE, the pressure data from the 4 mm probe do not fit that well. The calibration of the 4 mm probe might be the problem. It is going to be redone in ISAE-SUPAERO in the coming weeks.

The resolution correction divides maximum pitch error by approximately 3 but shifts the location of the measured pitch extrema further from the wake center.

4.7. Shear flow

Shear flow effects on the SAFRAN probe geometry are investigated in this experiment. Two effects are expected according to the bibliographic search :

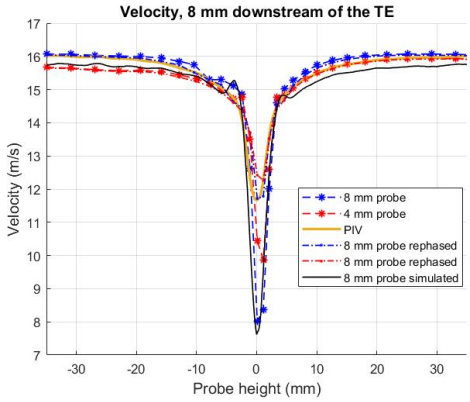

Figure 28: Velocity 8 mm away from the TE.

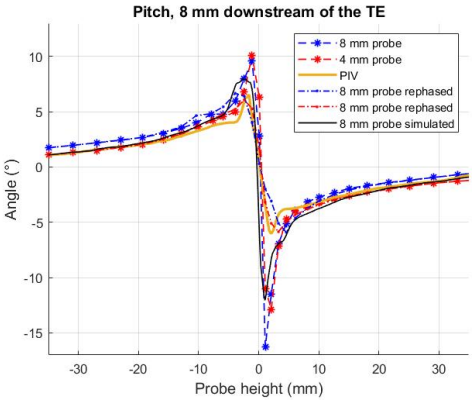

Figure 30: Pitch 8 mm away from the TE.

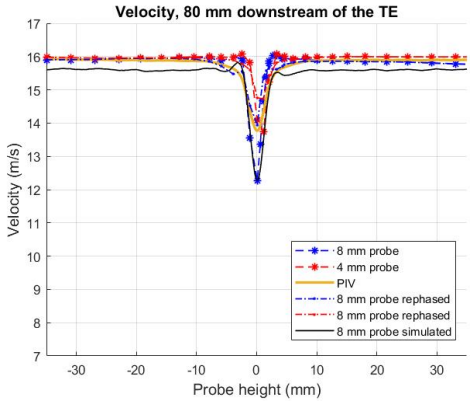

Figure 29: Velocity 80 mm away from the TE.

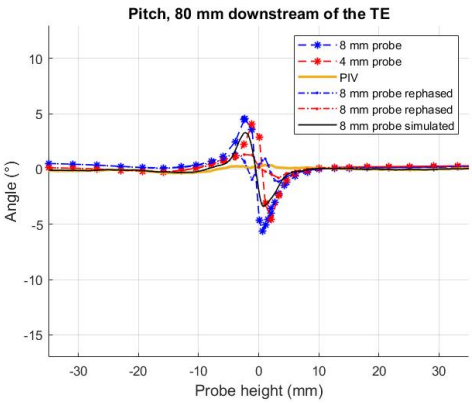

Figure 31: Pitch 80 mm away from the TE.

an artificial angle and a deflexion of the streamlines although the undisturbed flow is parallel.

The shear flow was obtained thanks to the boundary layer developping on the upper wall of the wind tunnel and test section. The probes were inserted in the downstream slit of the test section in order to have the thickest boundary layer possible. The goal was to obtain shear effects out of the wall proximity effects, that start around 2 diameters from the wall.

The expected angle and deflexion are 1° and 0.8 mm two diameters away from the wall, with the 8 mm probe and a flow velocity of 16 m/s. The calculation was made using turbulent boundary layer equations and formulas from McKeon found in [5] and [9]. Differences from the hypothesis of the formulas and the experiment are the shape of the probe and the linearity of the shear.

No hysteresis was observed during the experiment. The measurements set-up was the same as in the wall-proximity effects study. The results haven't been post-processed yet.

5. First conclusions and perspectives

In the range of flow conditions available in the L12 facility, no hysteresis, Reynolds or Mach number effect has been observed. The wall proximity experiment has shown that the SAFRAN probe is subject to distinct effects from the boundary layer and the interaction with the wall : the boundary layer pushes the balance of the holes pressure away from the wall, in opposition to the wall interaction, but both the wall proximity and the boundary layer cause an overestimation of the yaw. The correction of the distance between the probe holes is drastic but not enough to fit the probe measurements to the undisturbed flow. The data on shear flows remains to be post-processed and will shine more light on the observations, as well as futur CFD work.

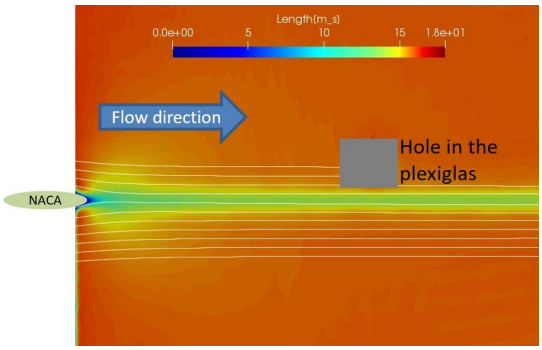

Figure 32: Velocity downstream of the profile without any probe.

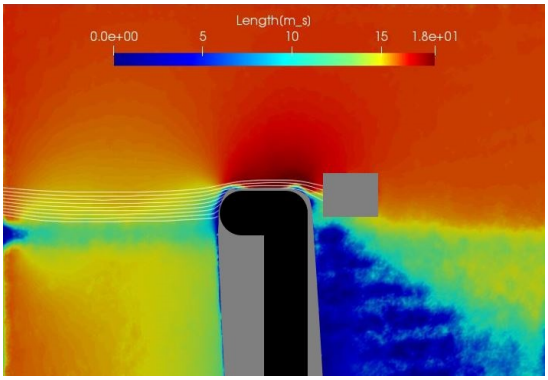

Figure 33: Velocity downstream of the profile with the 8 mm probe 40mm downstream of the TE and 3.5mm above the wake.

Acknowledgments

I would like to express my gratitude to SAFRAN and Association nationale de la recherche et de la technologie for the funding of this project and my heartfelt thanks to Nicolas BINDER, Jean-Louis CHAMPION, Fabrizio FONTANETO and Yannick BOUSQUET for the guidance and help.

References

[1] J.-L. Champion, Bearcat: The safran brand new test engine heavily instrumented for accurate comparison with cfd calculations, no. 2020-14295, 2020.

[2] P. Ligrani, B. Singer, L. Baun, Spatial resolution and downwash velocity corrections for multiple-hole pressure probes in complex flows (1989).
URL https://calhoun.nps.edu/handle/10945/40471

[3] N. Sitaram, B. Lakshminarayana, A. Ravindranath, Conventional probes for the relative flow measurement in a turbomachinery rotor blade passage, Journal of Engineering for Power 103 (2) (1981) 406–414. doi:10.1115/1.3230735.

[4] F. Vinnemeier, L. Simon, W. Koschel, Korrektur des kopfgeometrieeinflusses einer fünfloch- drucksonde auf die meßergebnisse / correction method for the head geometry influence of a five-hole pressure probe on the measurement results, tm - Technisches Messen 57 (JG) (1990) 296–303 [cited 2023-02-17]. doi:doi:10.1524/teme.1990.57.jg.296.
URL https://doi.org/10.1524/teme.1990.57.jg.296

[5] S. C. C. Bailey, M. Hultmark, J. P. Monty, P. H. Alfredsson, M. S. Chong, R. D. Duncan, J. H. M. Fransson, N. Hutchins, I. Marusic, B. J. McKeon, H. M. Nagib, R. Örlü, A. Segalini, A. J. Smits, R. Vinuesa, Obtaining accurate mean velocity measurements in high reynolds number turbulent boundary layers using pitot tubes, Journal of Fluid Mechanics 715 (2013) 642–670. doi:10.1017/jfm.2012.538.

[6] C. Crowley, I. I. Shinder, M. R. Moldover, The effect of turbulence on a multi-hole pitot calibration, Flow Measurement and Instrumentation 33 (2013) 106–109. doi:10.1016/j.flowmeasinst.2013.05.007.

[7] R. G. Dominy, H. P. Hodson, An investigation of factors influencing the calibration of 5-hole probes for 3-d flow measurementsdoi:10.1115/92-GT-216.

[8] T. Christiansen, P. Bradshaw, Effect of turbulence on pressure probes, Journal of Physics E: Scientific Instruments 14 (8) (1981) 992–997. doi:10.1088/0022-3735/14/8/024.

[9] A. Appukuttan, Probe measurement errors caused by shear flows, 2004.

[10] I. M. Hall, The displacement effect of a sphere in a two-dimensional shear flow, Journal of Fluid Mechanics 1 (2) (1956) 142–162. doi:10.1017/S002211205600010X.

[11] K. R. Raju, P. Porey, G. Asawa, Displacement effect in pitot tube measurements in shear flows, Journal of Wind Engineering and Industrial Aerodynamics 66 (2) (1997) 95–105. doi:10.1016/S0167-6105(96)00094-3.

[12] F. Kost, The behaviour of probes in transonic flowfields of turbomachinery, 2009.

[13] M. Boerner, M. Bitter, R. Niehuis, On the challenge of five-hole-probe measurements at high subsonic mach numbers in the wake of transonic turbine cascades, Journal of the Global Power and Propulsion Society 2 (2018) JPRQQM. doi:10.22261/JGPPS.JPRQQM.

[14] N. Sitaram, V. Kumar, V. Pillala, B. Purushothama, B. Prasad, Calibration of multi hole pressure probes for three dimensional flow measurements at high mach numbers, 2015.

[15] Z. Liu, G. Paniagua, Design of directional probes for high-frequency turbine measurements, Journal of Engineering for Gas Turbines and Power 140 (1). doi:10.1115/1.4037640.

[16] E. Boufidi, M. Alati, F. Fontaneto, S. Lavagnoli, Design and testing of a miniaturized five-hole fast response pressure probe with large frequency bandwidth and high angular sensitivity, Journal of Engineering for Gas Turbines and Power 141 (10). doi:10.1115/1.4044660.

[17] A. Bilbault, Obtaining accurate mean velocity measurements on shear flow using five-hole probes, PIR ISAE-SUPAERO.

[18] F. F. A. Vasseur, N. Binder, J.-L. Champion, Evolution of a five-hole probe calibration near a wall, no. MTT2622A39, 202022.
URL https://meastechturbo.com/paper-archives/mtt2622-pisa-2022/item/download/639_125d3f1dc32592f30d7bb95c4645e3a7

[19] F. Fontaneto, Aero-thermal performance of a film-cooled high pressure turbine blade/vane: a test case for numerical codes validation (2014) VKI, Turbomachinery and propulsion department, Università degli studi di Bergamo, Dipartimento di ingegneria.

Sensitivity and resolution response of optical flow based background oriented Schlieren to speckle patterns

Bora O. Cakir

Doctoral Candidate, Turbomachinery and Propulsion Department, von Karman Institute for Fluid Dynamics, Belgium, bora.orcun.cakir@vki.ac.be

Supervisor: Sergio Lavagnoli

Associate Professor, Turbomachinery and Propulsion Department, von Karman Institute for Fluid Dynamics, Belgium, sergio.lavagnoli@vki.ac.be

Co-Supervisor: Bayindir H. Saracoglu

Research Expert, Turbomachinery and Propulsion Department, von Karman Institute for Fluid Dynamics, Belgium, bayindir.saracoglu@vki.ac.be

University Supervisor: Christer Fureby

Professor, Department of Energy Sciences, Lund University, Sweden, christer.fureby@energy.lth.se

Abstract

The degraded resolution and sensitivity characteristics of BOS can be recovered by means of utilizing an optical flow based image processing scheme for the displacement detection stage. However, the background patterns conventionally employed in BOS setups suit the needs of the cross-correlation approach, whereas optical flow is associated with a completely different mathematical background. Thus, in order to characterize the resolution and sensitivity response of optical flow based BOS to the background generation configurations a parametric study comprising synthetic and experimental assessments is performed.

Keywords: Density varying flows, BOS, Optical flow, Speckle patterns

1. Introduction

Background oriented schlieren (BOS) imaging is of great interest to fluid dynamics researchers enabling quantitative characterization of density varying flows by means of an inexpensive and simple setup that can be used for both two and three-dimensional applications. It is performed by acquiring a pair of images with or without the presence of density variations occurring in a flow field. These images contain randomly distributed illumination intensities whose positions on the image plane are modified by the presence of a density varying medium between the recorded scene and the image acquisition system [1]. As the pair of images is processed, the observed variations in the background pattern are traced by means of various digital image processing approaches [2]. However, BOS is associated with a major sensitivity limitation originated by an inherent focusing problem [3]. Considering a generic optical configuration for a BOS setup, increasing the sensitivity demands an amplification of the distance between the object and the background while minimizing the distance between the object and the camera. However this is constrained due to two main reasons of divergence of light rays demanding corrections [4] and the well-documented geometric blur of the flow features of interest [5].

Furthermore, the sensitivity and resolution of a BOS system is also governed by the image processing approach utilized to characterize the deviations of the light rays from their original paths. The most common method employed for this purpose is the cross-correlation based block matching algorithm

[6], which is associated with being prone to over-smoothening due to the averaging effects [7] and a bandwidth limited dynamic range [8]. Nevertheless, the problem of inferior sensitivity and resolution can be addressed through the application of optical flow (OF) image processing technique which defines the motion of objects within the image plane by means of brightness patterns [9]. This is proven to enable OF to go beyond the resolution and accuracy limits of PIV algorithms for reconstructing density field information [10]. Thus, leveraging from its elevated sensitivity and resolution characteristics, various researchers has opted for optical flow to quantify the displacements due to varying refractive index medium using BOS. Accordingly, Nicolas et al. performed 3D reconstruction of a supersonic jet flow employing the Lucas-Kanade optical flow approach which relies on a window based neighborhood dependenc . Moreover, Hayasaka et al. used a variational formulation of optical flow to characterize the laser induced underwater shock waves where the residuals of brightness constancy assumption (non-zero divergence) are utilized to detect the shockwave shape and location [11]. Furthermore, optical flow as the processing tool of choice has been applied to combustion studies for the tomographic reconstruction of flames [12].

The conventional background patterns in BOS are adjusted to suit the needs of the cross-correlation approach, have a high SNR in correlation maps, which yielded random dot patterns based on the optical configuration of the measurement system. Accordingly, concentration, size, intensity profile and interparticle distance of the random speckles are specified to maximize contrast, minimize peak-locking and maximize subpixel interpolation accuracy [13]. Alternatively, in line with the sequential downsampling of images following a coarse-to-fine resolution layout, multi-scale procedural noise patterns can be used as the background image. Thus, the short comings of random noise functions can be avoided which often requires a match between the camera resolution and the background pattern for optimum performance [14]. Hence, the wavelet noise (WN) pattern proposed by [15] is utilized to construct a background image where the scaling factors of the hierarchical OF algorithm is matched to capture both large and small scale structures with high accuracy. Even though synthetic assessments performed in a controlled environment attributed the greatest accuracy to OF application with procedural background patterns, unavoidable experimental uncertainties of illumination and printing artifacts make random dot patterns to be the most robust option as multi-scale patterns are vulnerable against the noise [16]. Nevertheless, due to the scarcity of quantitative assessments on the use of optical flow for PIV and BOS applications, a proper characterization of the influence of background generation parameters yielding a speckle pattern does not exist. This prevents the reaching the full potential of optical flow especially in BOS where a considerably high level of control over the light intensity features is available in comparison to PIV. Therefore, this study aims to perform a quantitative characterization of the sensitivity and resolution limits of optical flow based BOS in response to the computer generated speckle pattern configurations where two synthetic investigations utilizing a 1D shock tube scenario and high resolution DNS datasets as well as an experimental assessment by means of a heated air jet are conducted to demonstrate the theoretical and applicability considerations associated with their employment.

2. Optical flow based BOS

2.1. Optical Flow

Various approaches to OF analysis can be broadly distinguished into two different groups; gradient based and variational algorithms. The common point of these methods is the brightness constancy assumption (Eq.1) where the intensity of pixels moving within the image plane are assumed to be constant [17].

$$\begin{aligned} I(x, y, t) &= I(x + \delta x, y + \delta y, t + \delta t) \\ &= I(x, y, t) + I_t + \delta x I_x + \delta y I_y \end{aligned} \tag{1}$$

Following a gradient based approach, the displacement (δ_x, δ_y) of normalized illumination intensities (I) can be represented as functions of the temporal (I_t) and spatial pixel intensity gradients (I_x, I_y). Nevertheless, underdetermined structure of the resultant governing equation set requires a problem closure to obtain a unique solution which leads to the well known aperture problem galvin1998. Hence, gradient based schemes contain additional energy functions (Eq.**??**) which include quadratic penalization (ρ_D, ρ_S) of the displacement vector residuals, enforcing brightness constancy proposed horn1981. Furthermore, the function to be minimized also contains a penalty contribution from the displacement vector gradients for enhanced robustness while the weighting between the two terms are controlled by a regularization parameter, λ.

$$E(\delta x, \delta y) = \sum \left[\rho_D(I_{t+\delta t} - I_t) + \lambda \rho_S(\nabla \delta x, \nabla \delta y)\right] \quad (2)$$

Moreover, an accurate OF estimation requires adequate handling of the global incoherence and large gradients of displacement vectors. However, as the gradient based formulation relies on small displacements in absence of any discontinuities, additional methods are required to relax the constraints on displacement magnitudes to allow large displacements within the image plane to be reconstructed accurately [18]. Accordingly, hierarchical algorithms are proposed to separate the computation of displacement vectors based on the scales of OF contained within the image plane [19]. The acquired images are assumed to contain a wide spatial-frequency spectrum which is decomposed to its bandwidth limited components by means of a pyramid scheme to prevent any loss of resolution or detail [20].

2.2. BOS background generation

Referring to the aforementioned discussion and the supporting literature on the higher experimental performance of speckle patterns in case of practical BOS setups, the current study concentrates on the generation parameters of computerized speckle backgrounds as well as the influence of major optical configuration features on their image plane representations. A speckle pattern is composed of a binary illumination field when generated on a synthetic environment. Nevertheless, when the pattern is printed and illuminated by means of a light source in experimental setups, the acquired light intensity distribution scattered by a binary dot is in the form a Gaussian function due to the diffraction limited image diameter. Thus, four main features can be identified as the particle size (d_P), particle concentration (N_I), interparticle size (Δ_P) and randomness of particle distribution (RR) as image generation parameters (Fig.1). However, in consideration of the overall uniformity of particle concentrations over the entire image plane, the interparticle distance should be maximized for each d_P and N_I combination to prevent empty spots over the background patterns. Hence, the independently controlled number of parameters reduced to three, eliminating Δ_P.

In addition to the background generation parameters, another two important features influencing the imaged intensity patterns are the magnification factor of the optical setup and the utilized aperture setting for the objective. Due to the fact that BOS is associated

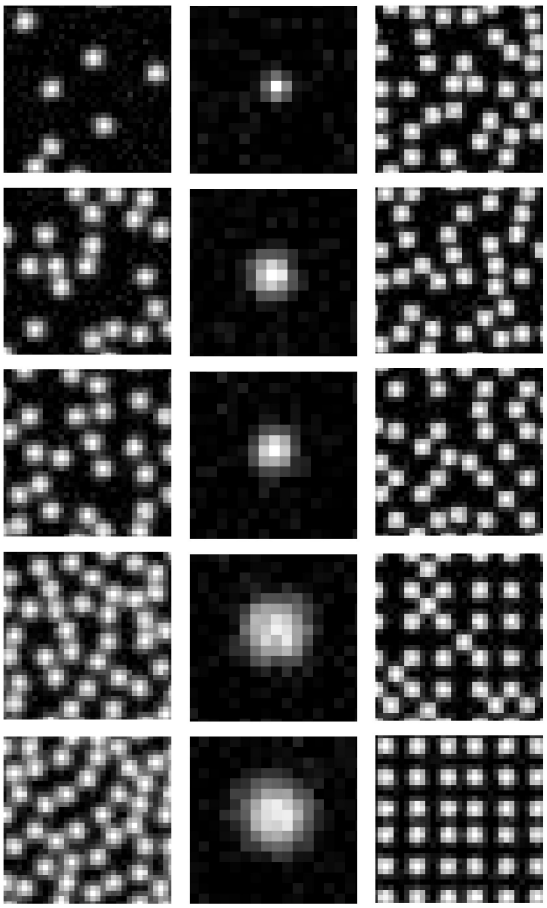

Figure 1: Speckle backgrounds generated with varying features of particle concentrations N_I=0.008 ppp, N_I=0.016 ppp, N_I=0.023 ppp, N_I= 0.031 ppp and N_I= 0.039 ppp (left column top-to-bottom), particle size d_P=1 pix, d_P=2 pix, d_P=3 pix, d_P=4 pix and d_P=5 pix (middle column top-to-bottom) and particle distribution randomness ratio RR=100%, RR=75%, RR=50%, RR=25% and RR=0% (right column top-to-bottom).

with a well known defocusing phenomena originating owing to the distance between the background and the schlieren features of interest (Z_D), a small aperture is preferred in almost most of the situations. There are multiple resources quantifying the theoretical trade-off regarding the influence of aperture ($f_\#$) and magnification (M) on the resolution and sensitivity of the BOS measurement configurations [5]. This trade off exist since the elevation of sensitivity by increasing the distance Z_D also amplifies the geometric blur on the schlieren features. These experimentally verified theoretical predictions hold regardless of the image processing method of choice since they are associated with the physics of optics instead of the mathematics of image processing algorithms. With regard to the

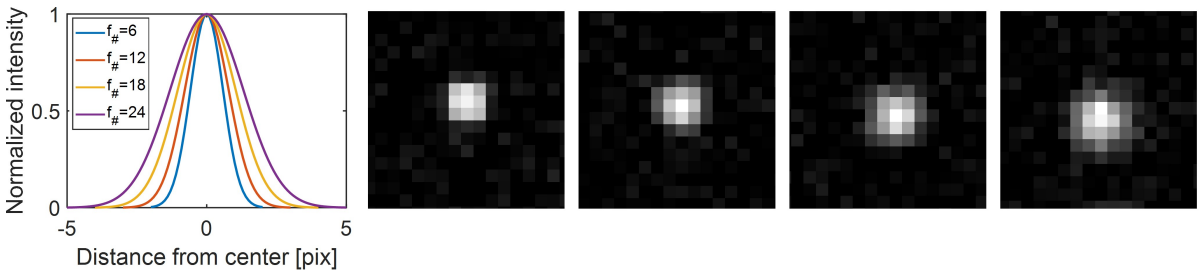

Figure 2: The influence of varying aperture on the normalized illumination intensities of diffraction limited imaging of speckles (left). Corresponding speckle images of particle size d_P=2 pixels with $f_\#$=6, $f_\#$=12, $f_\#$=18 and $f_\#$=24 (2nd to 5th column).

latter, whilst the distance Z_D has no influence in terms of varying the imaged intensity distributions over the backgrounds, the change of $f_\#$ modifies the peak and range of illumination intensities captured surrounding the speckles (Fig.2). Referring to these influences, the geometric blur on the schlieren objects is defined via Eqn. 3.

$$d_i = d_A \left[1 - \frac{1}{f} M'(Z_A - f)) \right] \tag{3}$$

where the M' refers to the magnification of the schlieren object on the image plane ($M' = Z_i'/Z_A$), f and d_A are the focal length and the aperture diameter respectively. This is not an effective factor on the imaging of the background features. Hence, when the images are generated to stimulate a synthetic BOS setup, the defocus on the schlieren object will be neglected to confine the discussion to the influence of aperture on the imaged background patterns which is described through the diffraction limited minimum image diameter d_d using Eqn.4.

$$d_d = 2.44 f_\# (M + 1)\lambda \tag{4}$$

in which λ corresponds to the wavelength of the light source which is in most BOS applications in the range of 450< λ <550 nm. Based on the Eqn.4, it is observed that M also influences the diffraction limited diameter of the imaged speckles. However, practical applications of BOS, especially ones where the flow features of interest require field of views (FOV) significantly larger then the sensor size of the cameras, M has a value in the order of $O(10^{-1})$ hence the contribution of M to d_d is rather insignificant compared to $f_\#$. Thus, in this study the affect of imaging optical configuration is characterized by means of the aperture size only. Then, the nominal imaged particle size d_i is computed by combining the original particle size ($M * d_P$) and the diffracted diameter d_d.

$$d_i = \sqrt{(M d_P)^2 + d_d^2} \tag{5}$$

Hence, the synthetic representation of the diffraction limited speckle image is modelled by means of a Gaussian function where the standard deviation of the Gaussian function (σ) is assigned as the half of computed the diffraction limited image diameter ($\sigma = d_i/2$). The corresponding particle images are provided in Fig.2 with the illumination intensity distributions obtained at various aperture values (Fig. 2, left).

3. Synthetic Assessments

The synthetic assessments of the different background pattern generation and imaging configurations are performed by means of two cases aiming to characterize different capabilities of the optical flow based image processing approaches in presence of various flow scenarios. First, a theoretical solution of the 1D Reimann problem is utilized to simulate a 1D shock tube where supersonic flow features such as expansion fans and shockwaves represented as well as their capturing with BOS using different background pattern features (Sec.3.1). Then, results of a high fidelity DNS simulation is ray traced and displacements originated due to the density field information on the synthetic backgrounds are reconstructed to demonstrate the resolution capability of optical flow over a spatially varying, large range of displacement magnitudes in Sec.3.2. For both cases the set of generated background patterns including the diffraction influence of the aperture size is provided in Tab.1

3.1. Theoretical Assessment

The Sod shock tube problem is an idealized one-dimension model of a rectangular or circular cross-section pipe filled with gas of discontinuously varying properties separated by a diaphragm [21]. Initially

Table 1: Configuration details for the generated synthetic speckle patterns.

Backgrounds	N_I [ppp]	d_P [pix]	RR [%]	$f_\#$ [-]
Min	0.008	1	0	6
Max	0.071	6	100	24

a shock tube is equally divided into a low pressure, low density section (left of the diaphragm) and a high pressure, high density section (right of the diaphragm) separated by a contact discontinuity at the origin. At time t=0, the diaphragm is ruptured and two distinctive compressive flow features are generated. An expansion in the direction of lower pressure from the contact discontinuity travels to the left of the domain while a shockwave in the direction of higher pressure travels to the right of the domain in time. The corresponding flow field information is obtained via solving the 1D Reimann problem in the shock tube exactly which yields the density (Fig.3, top) and density gradient (Fig.3, bottom) profiles.

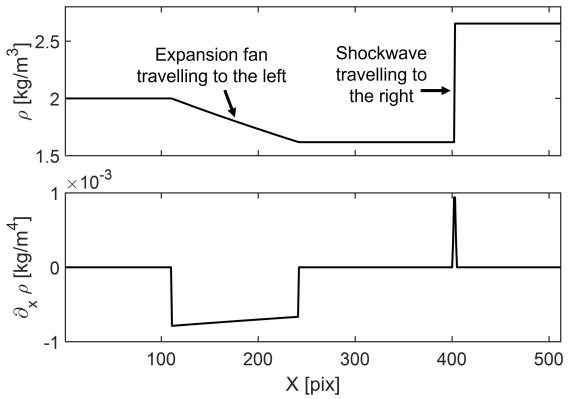

Figure 3: Density (top) and density gradient (bottom) profiles within the shock tube 0.7s after the diaphragm rupture.

The synthetic BOS setup is configured to capture the rectangular shock tube discretized by a sensor of size 512x512 pixels. The two features of the expansion fan and the shockwave are utilized to serve as step and pointwise inputs respectively with 1 pixel displacement vector magnitude to measure the sensitivity and resolution response of optical flow based BOS. In this regard, the sensor size (μ), magnification (M) factor and the distance Z_D are adjusted accordingly when the ray tracing is performed. Fig.4 illustrates the displacement fields computed from the exact solution (Fig.4, top) and reconstructed (Fig.4, middle) by the optical flow approach. As it can be observed from the quantitative extraction of the displacement magnitudes averaged in the y-direction that the optical flow is capable of reconstructing the majority of the displacement vectors with a considerably high level of accuracy that yields an AEPE value of 0.035 pix. Nevertheless, three main regions of deviations from the reference displacement magnitudes are apparent which correspond to the extremities of the expansion fan and the shockwave itself. These regions pose a challenge for the image processing algorithms due to two main reasons, one related to the image processing approach whilst the other being a factor of the experimental measurement technique. Regarding the first one, although Horn-Shunck optical flow is a gradient based scheme, it is equipped with an energy equation that penalizes deviations from the illumination conservation assumption and high level displacement gradients. This is required to resolve the closure problem of optical flow (also referred to as the aperture problem) which also enables an inherent elimination of spurious displacement vectors. While the weighting between the two is controlled via the regularization constant (λ), for every λ >0 there exists a certain degree of neighborhood dependency that prevents the image processing algorithm to exactly capture discontinuous displacements. Furthermore, the second reason that relates to the challenge of resolving the extremities of an expansion fan or a shockwave is the optical distortions associated with regions of large second order gradients of refractive index [22]. As these regions yield light rays to be refracted sharply that would lead the background features to become out of focus locally, capturing the displacement vectors surrounding the locations of high level gradients of light ray displacement is degraded.

Moreover, there is also a physical limitation related to the resolution of the those features. Regarding a typical experimental setup, the shockwave (when generated as a purely planar structure) has a the physical thickness in the order of 200nm [**? ?**] while the BOS system possesses a pixel projection size larger than two orders of magnitude. Hence, the density variation across the shockwave is not resolvable due to the optical limitations of the setup. Although this effect in case of an expansion fan is not as profound as a shockwave due to the fact that expansion fan itself is not discontinuous, the initiation of the density gradients and the corresponding gradients of the displacement vectors are within a physical distance smaller than the optical resolution limit. Hence, the effect associated optical distortions and limitations have on the im-

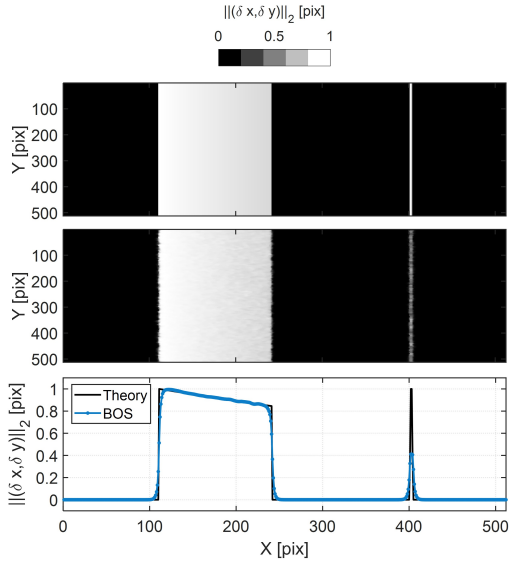

Figure 4: Reference (top) and reconstructed (middle) displacement magnitudes over the entire rectangular cross section of the shock tube and averaged over the y-direction (bottom).

age processing stage of capturing displacement vectors can be observed as an amplication in standard deviation across these features (Fig.4, bottom and Fig.5) and from the fact that only a fraction of the pixel displacement input over the shockwave is reconstructed (Fig.4, bottom and Fig.6).

To start with the influence of particle concentration, where for the comparisons the particle size is kept constant at d_P=2 pix, the resolution increase is obvious with a higher concentration of particles over the background pattern. As optical flow is a gradient based scheme that achieves one vector-per-pixel resolution for the displacement field, the governing set of equations include a brightness constancy based displacement formulation for each pixel. Thus, the rank of the coefficient matrix that represents the linear system decreases with the increasing number of sparse or near zero elements.The coefficient matrix being composed of intensity gradients over the background patterns, the high illumination intensity concentration of the background directly contributes to the non-zero value assignments of the elements of the coefficient matrix which improves not only the accuracy of the computation of the displacement vectors but also the uniqueness of the solution which is captured by means of the decreasing standard deviation of the displacement vectors over the step input. A similar reasoning also exists for the influence of particle size in which backgrounds with different parti-

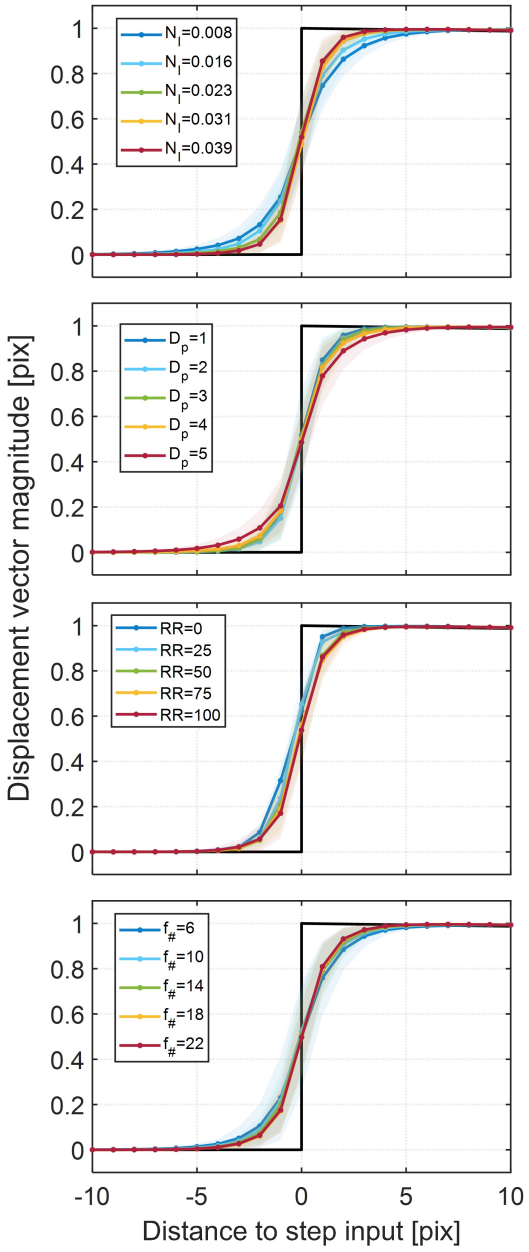

Figure 5: Response of optical flow to a step-like displacement profile for different particle concentrations N_I [ppp] (1st row), particle sizes d_P [pix] (2nd row), distribution randomness ratios RR [%] (3rd row) and aperture settings $f_\#$ [-] (4th row).

cle size are compared where the particle concentration is adjusted to fill the same surface area of the background to isolate the concentration effect. The resolution capability of optical flow is observed to be increasing with lower particle sizes where it converges to a limiting value for d_P >3 pix. The degradation

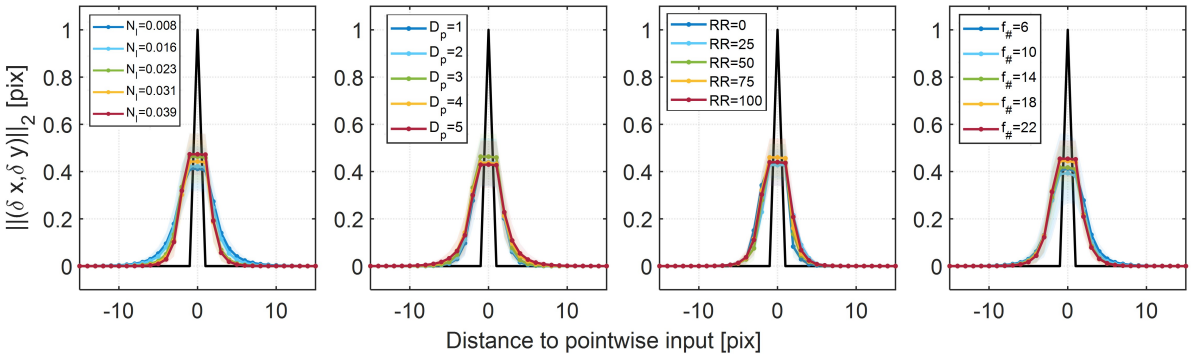

Figure 6: Response of optical flow to a pointwise displacement profile for different particle concentrations N_I [ppp] (1st column), particle sizes d_P [pix] (2nd column), distribution randomness rations RR [%] (3rd column) and aperture settings $f_\#$ [-] (4th column).

of resolution with larger particles is associated with again the rank of the coefficient matrix being lowered due to the reduced amplitude of illumination intensity gradients as the pattern becomes overstuffed. Higher density of smaller particles (d_P ~3 pix) yield a larger variance of intensity gradients over the backgrounds in comparison to a lower number of larger particles (d_P ~5 pix). The gaps between the speckles lack sufficient signal in terms of intensity gradients due to the absence of particles whilst the intensity gradients over the speckles are lower in magnitude owing to the constant high illumination intensity. Nevertheless, it should be noted that increasing resolution and sensitivity demonstrated both over the step (Fig.5, 1st and 2nd rows) and point pixel (Fig.6, 1st and 2nd columns) inputs indicate the higher particle concentration and particle size requirements for optical flow in comparison to its block-matching counterpart of cross-correlation which puts emphasis on the different needs of the respective algorithms.

Furthermore, varying randomness of the speckles is observed not to yield any significant changes between $50 \leq RR \leq 100\%$. However, as the ratio of randomly generated speckles is reduced below 50%, a major shift from the central location of the induced displacement becomes apparent in the reconstructed response to the step input. While the results of RR=50% and RR=25% are rather similar, when a background with completely structured speckles is utilized another modulation in response is present. Although the step response width is not altered significantly between different randomness ratios, the shift in the detection location of the step input yields an inaccurate determination of the response which is associated with the orientation of the structured dot grid with respect to the step response location. Nonetheless, it is worthy to state the decreasing standard deviation with reducing levels of RR that is well expected as the background patterns become more uniform and the determination of the local displacement vector becomes less dependent on the distribution of the speckles. Finally moving on to the influence of aperture on the response of BOS, a clear improvement in sensitivity and reduction in standard deviation with decreasing aperture is observed. Since the influence of aperture on the geometric blur of schlieren features is not implemented, the main driving factor for the aforementioned result is the illumination distributions of the imaged speckles. Hence, the isolated consequence of changing aperture can be treated very similarly as increasing the speckle size but with the addition of the illumination intensity distribution profile being modified. As demonstrated in Fig. 2, decreasing aperture increases the imaged size of a speckle which in turn dissipates the light intensity over the surrounding pixels. This enables a greater portion of the image to be covered which corresponds to a less sparse coefficient matrix that composes the optical flow problem. Even though it is noted that a larger dot would also cause the sensitivity to be reduced due to the low intensity gradients over the region of the dot, when the imaged dot size is increased by increasing $f_\#$, the Guassian profile is preserved (Fig.2, 1st). The importance of the rank of coefficient matrix is again highlighted by the reduction in standard deviation with increasing $f_\#$, referring to the improved uniqueness of the optical flow solution. Nevertheless, it should be noted that particle of size and concentration values larger than a certain threshold would yield a considerably low contrast between the illuminated and non-illuminated areas as the

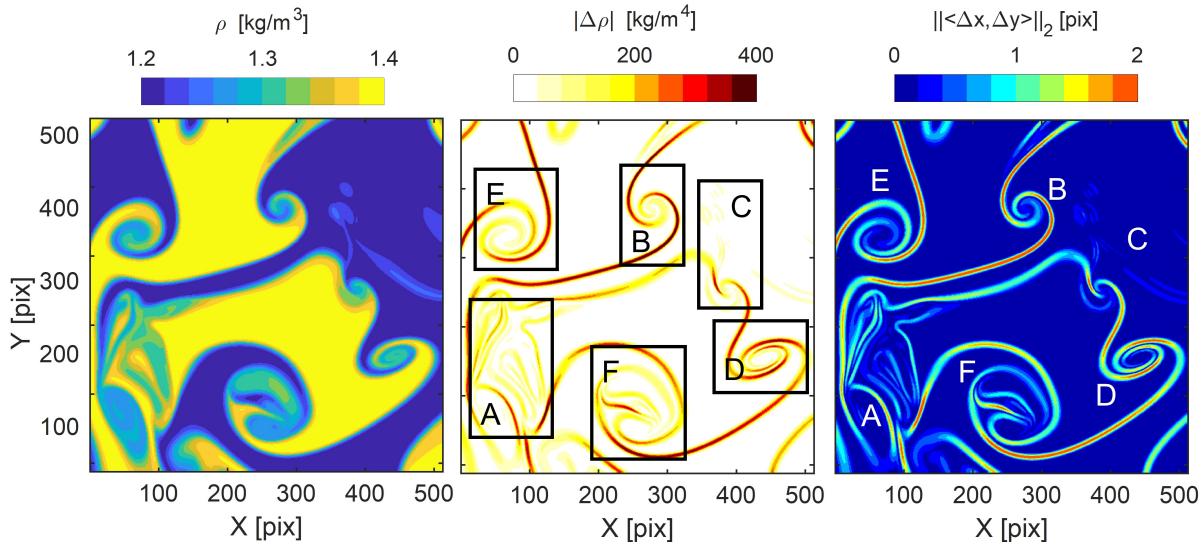

Figure 7: DNS density field (left), DNS density gradients (middle), reference displacement magnitude (right).

speckles on the image plane start to merge.

3.2. *Numerical Assessment*

The synthetic assessment of the influence of background generation and imaging parameters on the accuracy of optical flow based BOS is performed using a direct numerical simulation (DNS) data of homogeneous buoyancy-driven turbulence [23] (Fig.7, left). Density gradients at the central plane of the 3D simulation volume is extruded to create a constant refractive index field along the line-of-sight which is compatible with a planar BOS application (Fig.7, middle). Then, the ray displacements due to the density variations are rendered via a ray-tracing based image generation methodology [24]. The synthetic optical setup is configured such that a maximum displacement value of ~7 pixels is obtained in order to characterize the dynamic range over a relatively large extend of displacement magnitudes (Fig.7, right). In consideration of the spatial dependency of BOS measurements to the distribution of speckles, the characterization of corresponding uncertainty requires sampling of each noise pattern multiple times due to the distribution of density gradients within the flow field modelled by the DNS simulations. Hence, based on the statistical convergence data documented previously, each noise pattern is sampled 50 times [25].

As the ray traced background pairs are processed with optical flow, the regularization parameter (λ) is optimized by means of a bounded non-linear optimization algorithm to obtain the highest reconstruction accuracy of the displacement field with each background pattern. This is performed by computing the the average end-point errors (AEPE) [26] over six dedicated regions (Fig.7, middle) occupied by various levels of displacement vectors which the accumulated value of the AEPE is utilized to compose the cost function for the optimization procedure. Consequently, not only the minimum AEPE value that is achievable with each background but also the corresponding λ value that is necessary to do so is quanti-

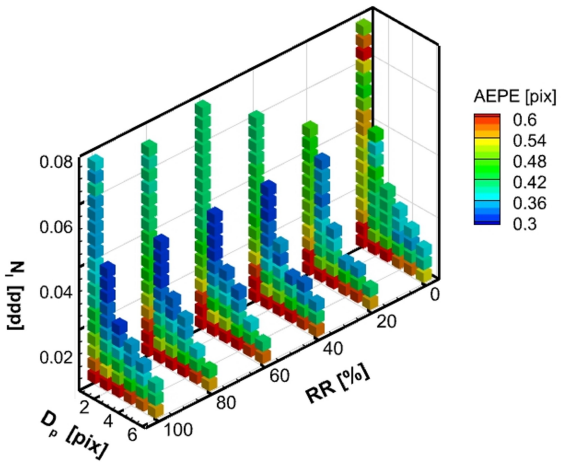

Figure 8: Average end-point error values accumulated over the six regions of interest computed with optimized regularization parameters for varying particle concentration N_I, particle size d_P and particle distribution randomness ratio RR for an aperture setting of $f_\#$=16.

fied.

Accordingly, Fig.9 illustrates the accuracy levels obtained with backgrounds generated using different configurations while the aperture is kept constant. Firstly, an immediate improvement in reconstruction accuracy is observed when speckle size is increased from the conventional value of $d_P = 1$ pix which yields imaged speckles of 2~3 pixels. While the resolution analysis made over the theoretical assessment revealed greater sensitivity with reduction of dot size, the displacement fields under investigation is considerably different in the case of the DNS which is responsible for the observed behaviour of accuracy. In contrast to the step-like input in presence of an expansion fan, the second order gradients of density in the case of DNS although high due to the localized appearance of density gradients, are not discontinuous. This situation relaxes the demand on sensitivity whereas the localization of displacement vectors with a chaotic spatial distribution requires a less sparse coefficient matrix for the optical flow to converge to a higher accuracy reconstruction which is satisfied with of d_P >1 pix. It is also observed that beyond $d_P > 1$ pix a certain threshold of sparsity is exceed which is a limiting factor for d_P=1 pix to achieve low AEPE values since beyond d_P >2 pix, the change in AEPE values is small. Similarly, for constant dot size (d_P), raising concentration of particles allows the reconstruction accuracy to increase. Nonetheless, reduction in AEPE stops when the particle concentration exceeds a certain limit which varies based on the particle size (Fig.9). As this limit is not reached in case of speckles with d_P >2 pix, the trend of reduction of AEPE value with increasing N_I is maintained. This is attributed to the reduction in the rank of the coefficient matrix by the overpopulation of the background which is only possible for the small sizes of speckles as increasing particle size defined in circular shapes yields larger gaps between the speckles allowing larger illumination intensity gradients to be computed in comparison to the overpopulated small speckles. Overall the best combination of these parameters is achieved with d_P=2 pix and N_I=0.039 ppp which yields a pattern that is densely populated to with high-contrast illumination intensity gradients to enable best displacement capturing capabilities.

Regarding the influence of randomness of the dot distributions, no major variation in terms of accuracy for particle concentrations of d_P >1 pix and randomness ratios of 50%≤ RR are observed. When the randomness of the pattern is reduced below 50% significant degradation of reconstruction accuracy is attained

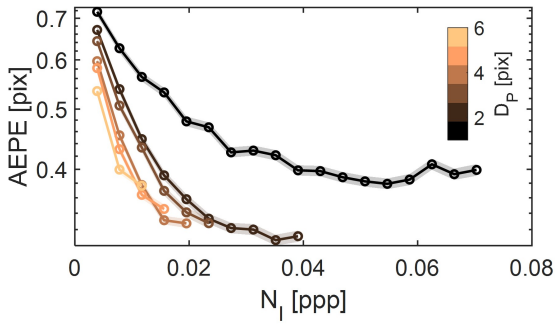

Figure 9: Average end-point error values accumulated over the six regions of interest computed with optimized regularization parameters for varying particle concentration N_I, particle size d_P and aperture setting $f_\#$ for particle distribution randomness ratio of RR=100%.

regardless of the particle size except for particles with d_P >4 pix especially for moderate to high values of particle concentration. This is due to the fact that particles with size and concentration of d_P ≤3 pix and N_I >0.016 ppp respectively are more prone to aliasing errors where the displacement over a region of pixels is misinterpreted by the image processing algorithm due to distributed uniqueness of the solution as RHS of the linear system would lose variance over individual elements. Moreover, the influence of randomness is observed to be most critical for the backgrounds with d_P=1 pix. While randomness levels of 20≤ RR ≤60% did not really vary the performance of the reconstructions, a considerable level of reconstruction accuracy increase is obtained with fully random distribution of speckles with size d_P=1 pix.

Finally, investigating the influence of aperture on the imaged background patterns by means of varying the intensity and radius of intensity gradients, the major impact is observed for d_P=1 pix (Fig.12). The influence is again related to the intensity of the gradients and the total coverage modulation over the imaged patterns. For small particles d_P=1 pix, decreasing aperture increases the diffraction limited particle size allowing a larger portion of the background to be covered with intensity gradients, hence reducing the sparsity of the coefficient matrix. Low concentration of particles always favors high $f_\#$ to increase the nonzero elements in the coefficient matrix. Yet, beyond a certain value of sufficient particle density, diffraction causes the imaged particles to collapse into each other deteriorating the intensity of illumination gradients and reducing the reconstruction accuracy (Fig.11). Thus, while lowest level of errors are obtained with $f_\#$=18, an increase in AEPE values is com-

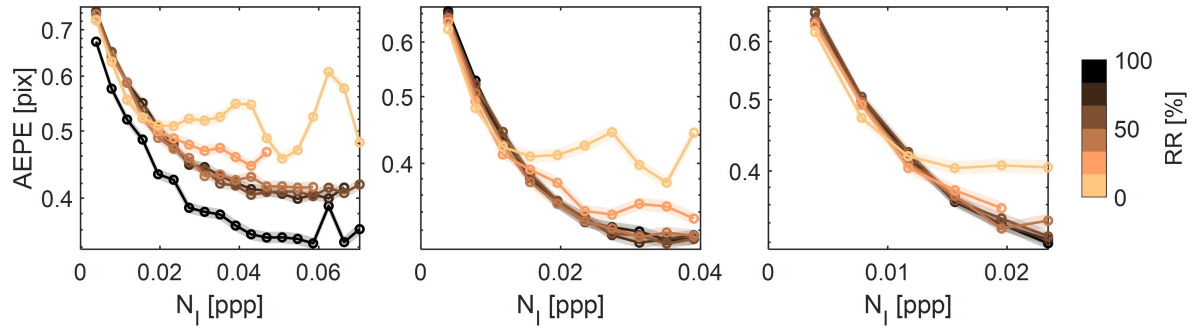

Figure 10: Average end-point error values accumulated over the six regions of interest computed with optimized regularization parameters for varying particle concentration N_I and particle distribution randomness ratio RR for particle sizes of d_P=1 pix (left), d_P=2 pix (middle) and d_P=3 pix (right) for an aperture setting of $f_\#$=16.

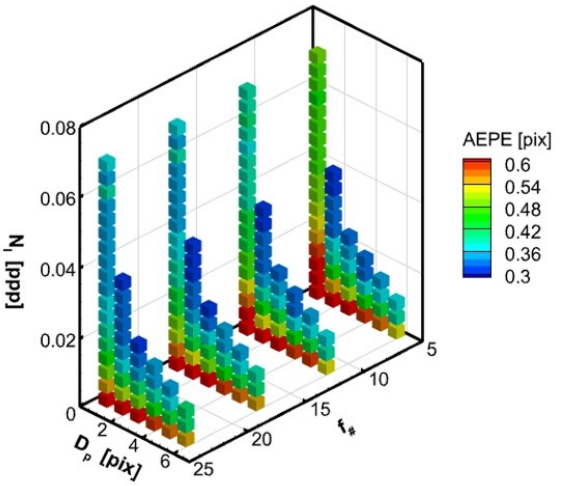

Figure 11: Average end-point error values accumulated over the six regions of interest computed with optimized regularization parameters for particle concentration N_I, varying particle size d_P and aperture setting $f_\#$ for particle distribution randomness ratio of RR=100%.

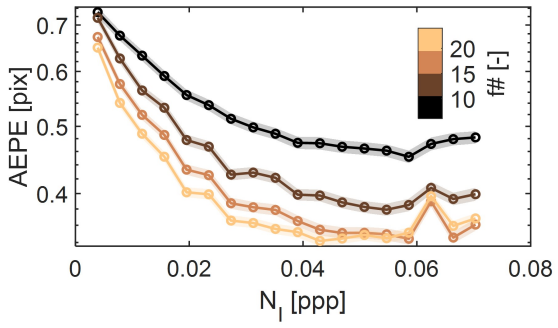

Figure 12: Average end-point error values accumulated over the six regions of interest computed with optimized regularization parameters for varying particle concentration N_I and aperture setting $f_\#$ for particle size of d_P=1 pix and particle distribution randomness ratio of RR=100%.

puted for $f_\#$.

4. Experimental Assessment

The experimental setup employed in this work is implemented around Steinel HL 1610 S heat gun. It has two operation modes ejecting heated air at temperatures of 575 K and 783 K with speeds of 4.7 m/s and 8.2 m/s respectively from an nozzle diameter of 0.033 m. The corresponding nozzle diameter based Reynolds numbers of the operation modes are Re_D = 3200 and Re_D = 3400. For the present experimental assessment, only the first (low speed and low temperature) mode of the heat gun is utilized to enable the spatial and temporal resolution limits of the measurement system to fall within the range of instantaneous flow scales as much as possible.

Configuration of the BOS setup is composed of a Hamamatsu ORCA-Flash4.0 V3 Digital CMOS camera, a f = 100 mm Nikkor lens, four Chazon 100W 10x10 LED arrays as the light source and backgrounds laser printed on 240 g/m^2 paper (Fig.13). The backgrounds are illuminated from the behind to enhance the recorded contrast and remove reflection effects. The distance between the light source and the background is adjusted to optimize the trade-off between light intensity and uniformity. The distances between the camera the background and the heat gun are configured in consideration of three different factors. On top of the trade-off between increased sensitivity and defocusing of the schlieren object, the resolution of the flow features in the spatial domain are aimed to be limited to a spatial resolution level which

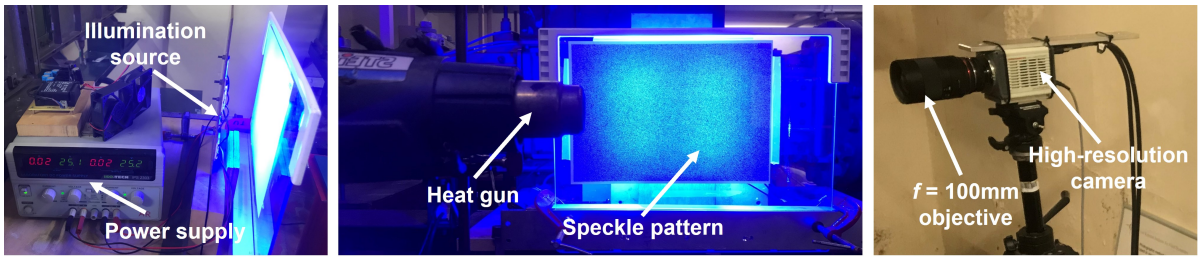

Figure 13: Experimental setup of the background oriented schlieren system with the illumination configuration (left), heat gun and the illuminated speckle pattern (middle) and image acquisition system (right).

can be matched by the maximum shutter speed of the camera while a continuous light source is employed. Accordingly, 100 images for each background pattern at an acquisition frequency of f_{aq}=100Hz are recorded with an exposure time of t=5 seconds to limit the temporal averaging of flow features and to allow sufficient illumination signal to be captured utilizing an aperture of $f_{\#}$=8 (Tab.2). In order to perform a cost efficient investigation of the different background generation configurations discussed previously, latin hypercube sampling based design of experiment approach is followed to sample 15 backgrounds from 230 different combinations (Tab.2).

Table 2: Configuration details for the background patterns and testing conditions.

Backgrounds	N_I [ppp]	d_P [pix]	RR [%]
Min	0.016	1	0
Max	0.062	4	100
Setup measures	Z_A [m]	Z_D [m]	Z_B [m]
	1.8	0.2	1.6
Image acquisition	f_{acq} [Hz]	$f_{\#}$ [-]	M [-]
	100	8	0.054
Testing Conditions	T_{Exit} [K]	U_{Exit} [m/s]	Re_D [-]
	575	4.7	3200

First of all, the instantaneous vertical displacement fields reconstructed at the exit of the heat gun are compared for varying particle concentration (N_I), particle size (d_P) and particle distribution randomness (RR). To start with the particle concentration influence on the capturing capabilities of time resolved features, a major difference in the signal to noise ratio of displacement magnitudes is observed between the backgrounds with particle concentrations N_I=0.015ppp and N_I=0.047 ppp. The low concentration of speckles yielding a less populated pattern results in a low level of signal in terms of displacement magnitudes as the only illumination features optical flow can utilize to trace any displacement induced by the density gradients is the interference pattern of the light source with the irregularities over the paper and the black paint which is of low illumination intensity levels in comparison to the imaged speckles. Thus, in agreement with the synthetic assessments, increasing concentration of particles yields more accurate results. Nevertheless, it was documented in the synthetic assessment with the high fidelity DNS case that there is a limit for the accuracy increase of the reconstructions with the increasing particle concentration after which over population of the pattern results in a reduction of accuracy. Accordingly. it can be deduced that over the results obtained with N_I=0.047 ppp and N_I=0.062 ppp this limit is reached as no differentiable modulation in terms of the captured displacement magnitudes is observed. Comparing these results with the obtained limit of accuracy improvement documented for d_P=1 pix in the synthetic assessment, a very similar behaviour is observed where the accuracy difference between the two particle concentrations for the synthetic assessment is considerably small.

Furthermore, investigating the influence of particle size on the performance optical flow based BOS, a performance jump between the patterns with d_P=1 pix and d_P >1 pix is attained. In very well agreement with the synthetic results, background patterns with speckle sizes of d_P=1 pix yield notably low level of displacement magnitudes in the exact same flow scenarios especially for low to moderate particle concentrations and large aperture settings. It should be reminded that the aperture setting is kept constant for all backgrounds which is selected in accordance with the

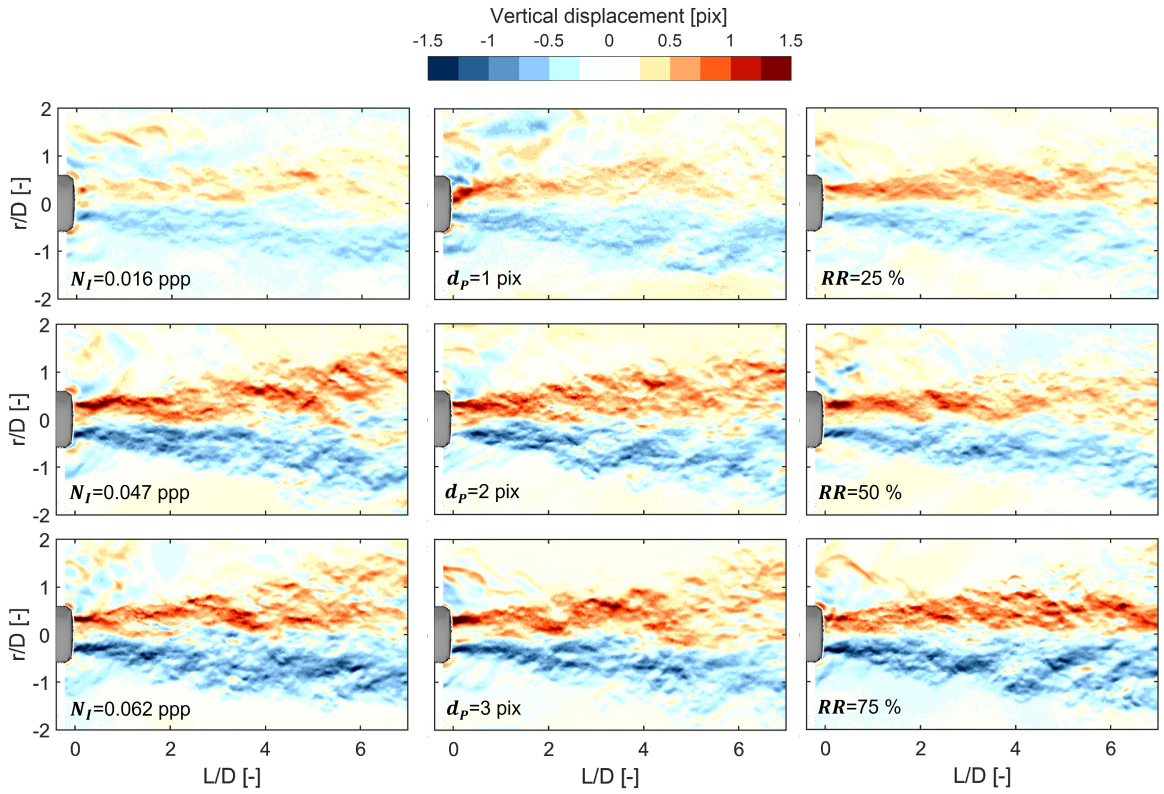

Figure 14: Instantaneous vertical displacement fields obtained with different background configurations of varying particle concentration (1st column), particle size (2nd column) and particle distribution randomness (3rd column).

signal to noise ratio requirements of a low exposure image acquisition configuration. Hence, although the influence of varying aperture is not studied, the high aperture setting of $f_{\#}$=8 limits the diffraction limited particle diameter, confining the speckles of d_P=1 pix to imaged particle sizes of d_i ~3 pix. Whereas speckles with size d_P=2 pix and d_P=3 pix, much larger illumination regions are obtained providing high SNR illumination gradient maps for the displacements induced over the backgrounds and improving the reconstructed vector magnitudes. Again between d_P=2 and d_P=3 no deterministic variations are observed in terms of captured displacement field fidelity and amplitude that is also in agreement with the synthetic assessment in which the differences between the backgrounds with aforementioned size of particles yielded almost identical AEPE values within the range of applicable concentrations to both.

Finally assessing the influence of pattern randomness on the instantaneous resolution of flow features, a constant increase of reconstructed displacement magnitudes is captured with increasing randomness of the pattern. In contrast to the synthetic assessment where no significant variation of reconstruction accuracy is observed for RR≥50%, the experimental assessment revealed improved resolution of time resolved features with increasing RR while the highest resolution capabilities are obtained with RR=100% (Fig.14, 2nd column 2nd row). The variation between the experimental and numerical results is caused by the fact that in the numerical simulations (especially for the time step at which the data is extracted in order to preserve large scale displacement magnitudes), a more organized flow formation is present in comparison to the experimental case which is highly turbulent and the scales of the turbulent fluctuations extend well below the optical resolution limits of the setup. Hence, decreasing scales of the flow features aimed to be reconstructed demands higher level of randomness to prevent any aliasing related issues within the spatial frequency domain.

Moving on to the time averaged vertical displace-

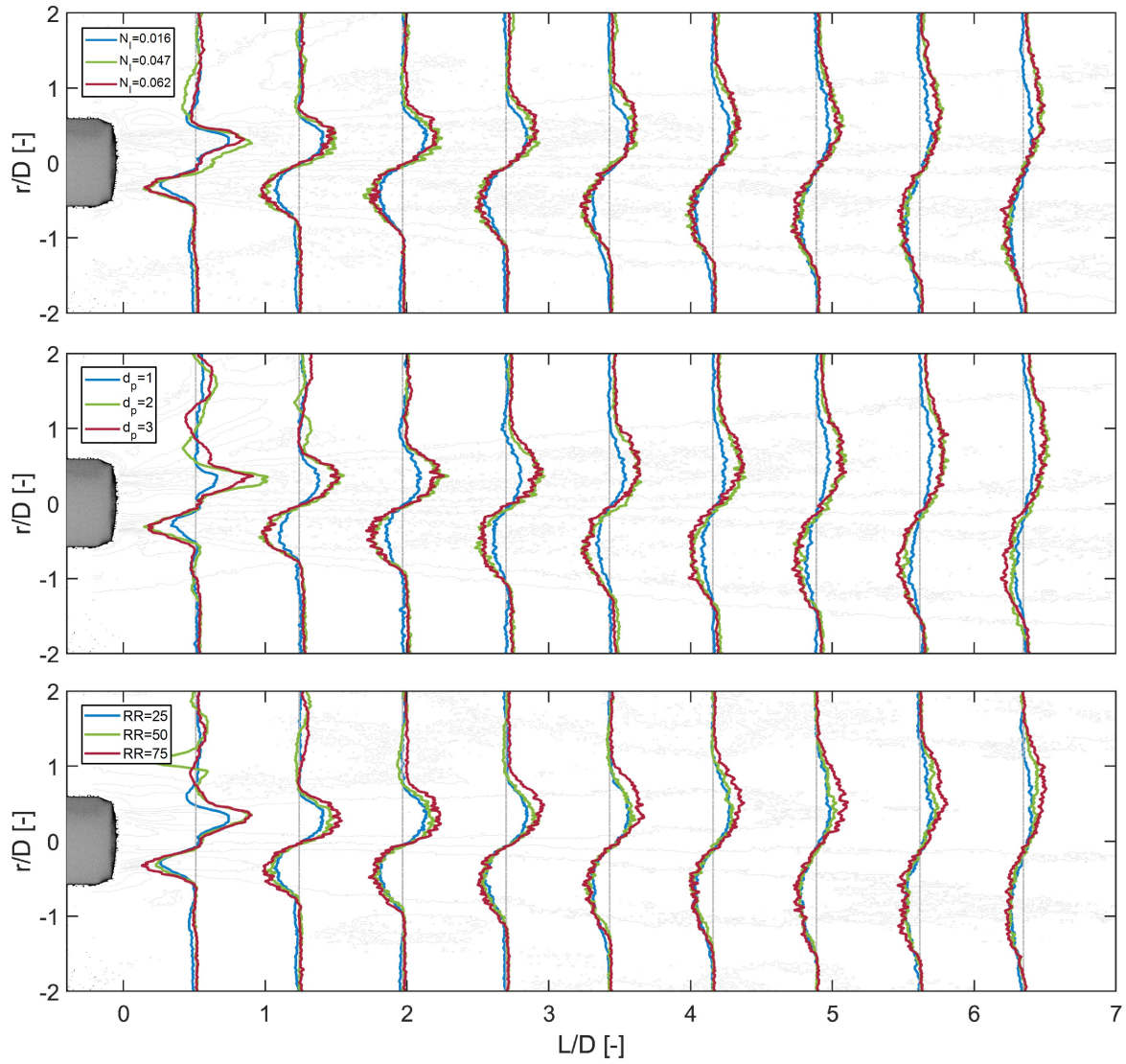

Figure 15: Time averaged vertical displacements extracted over various longitudinal distances from the nozzle exit with varying particle concentration (top), particle size (middle) and particle distribution randomness (bottom).

ment fields reconstructed using the aforementioned background configurations, displacement values over the flow field are extracted over equally distanced locations in the longitudinal direction (Fig15). First of all, comparing the backgrounds with varying particle concentrations yields similar outcomes to the ones observed for the instantaneous fields. The improvement of the reconstructed displacement amplitudes quantitatively shown to be significant between N_I=0.016 and N_I=0.047 ppp. Whilst small modulations are captured between N_I=0.047 ppp and N_I=0.062 ppp, these are confined to the regions close to the jet exit where disturbances due natural convection around the metal exit cone (see Fig.14). Moreover, the differences between the captured magnitudes of reconstructed displacement vectors gets amplified when comparing patterns with different dot sizes. Increasing the particle size in the generated patterns from d_P=1 pix to d_P=2 pix results in a major increase in the reconstructed displacement magnitude. In addition to the variation of performance qualitatively described to be insignificant over the time resolved flow features, the time averaged profiles yield modulations of reconstructed displacement magnitudes especially for loca-

tions further away from the nozzle exit where the imposed displacement magnitudes by the thermal density gradients are dissipated. Thus, it can be stated that while increasing the particle size beyond d_P=2 pixels does not yield major changes for regions of sufficiently high SNR in terms of the density gradients, larger particles might be preferable for regions with lower amplitude of displacement induction where sensitivity to sub-pixel accuracy is more critical. Finally, analyzing the influence of changing background pattern randomness a clear amplification of the reconstructed displacement signals is observed with increasing level of randomness ratios (*RR*) as it is the case for instantaneous flow features. Similar to all the cases, the variation between different levels of *RR* are higher for r/D>0 due to the natural convection driven asymmetry of the heat gun yielding higher amplitude of density gradients above the central axis. Furthermore, specially for regions close to the nozzle exit the length scales of the turbulent structures are smaller which grow as they propagate within the longitudinal direction. Thus, the impact of a higher level of randomness on the resolution of these smaller structures is increased for smaller L/D.

5. Conclusion

Simplicity of application and minimal requirements for its experimental configuration makes background oriented schlieren (BOS) a cost-effective solution for quantitative visualization of density varying flows for which the use of an optical flow (OF) based image processing stage provides a unique opportunity to recover high fidelity density field variations at the deflection detection stage of BOS. However, the background patterns conventionally employed in BOS setups suit the needs of the cross-correlation approach whereas optical flow is associated with a completely different mathematical background in comparison its block matching counterparts. Thus, in order to characterize the resolution and sensitivity response of optical flow based BOS to the background generation configurations, a parametric study comprising a theoretical assessment utilizing 1D shocktube problem, a numerical assessment using a high-fidelity DNS simulation and an experimental assessment with a heat gun is performed. Four main parameters of synthetic speckle background generation and imaging configurations of particle size (d_P), particle concentration (N_I), particle distribution randomness (*RR*) and aperture size ($f_\#$) are investigated.

The theoretical assessment revealed the optimum choice for maximizing local resolution as employing a high density of small speckles which enables the smallest step and point wise response widths representing highest resolution capabilities. Moreover, the increased complexity of the distribution and range of displacement vectors resulted in slight different outcomes in terms of resolving more chaotic structures demanding larger particles to be employed again with a high concentration of particle distributions without overcrowding the background patterns. Finally, the thermally induced density gradients generated by the hot air exiting a heat gun posed an even more challenging case in terms of providing a flow field that is highly turbulent with scales well beyond the spatial and temporal resolution limits of the experimental setup. Accordingly, the conclusions drawn for the influence of particle size and concentration are observed to be in agreement in case of the experimental assessment with the DNS based synthetic assessment. Nevertheless, the effect of randomness ratio observed to be more critical in case of the experimental assessment where highest level of resolution capabilities is achieved with the highest level of pattern randomness which is suggested to be driven by the larger range of turbulent length scales in the case of the experiments.

Acknowledgments

This project has received funding from the European Union's Horizon 2020 research and innovation programme, MORE & LESS (MDO and REgulations for Low-boom and Environmentally Sustainable Supersonic aviation) project under grant agreement No 101006856.

References

[1] G. S. Settles, Basic Concepts, Springer Berlin Heidelberg, Berlin, Heidelberg, 2001, pp. 25–38. doi:10.1007/978-3-642-56640-0_2.

[2] M. J. Hargather, M. J. Lawson, G. S. Settles, L. M. Weinstein, Seedless velocimetry measurements by schlieren image velocimetry, AIAA Journal 49 (3) (2011) 611–620. doi:10.2514/1.J050753.

[3] M. Raffel, Background-oriented schlieren (bos) techniques, Experiments in Fluids 56 (3) (2015) 60. doi:10.1007/s00348-015-1927-5.

[4] G. E. Elsinga, B. W. van Oudheusden, F. Scarano, D. W. Watt, Assessment and application of quantitative schlieren methods: Calibrated color schlieren and background oriented schlieren, Experiments in Fluids 36 (2) (2004) 309–325. doi:10.1007/s00348-003-0724-8.

[5] A. B. Gojani, B. Kamishi, S. Obayashi, Measurement sensitivity and resolution for background oriented schlieren during image recording, Journal of Visualization 16 (3) (2013) 201–207. doi:10.1007/s12650-013-0170-5.

[6] J. Westerweel, Fundamentals of digital particle image velocimetry, Measurement Science and Technology 8 (12) (1997) 1379–1392. doi:10.1088/0957-0233/8/12/002.

[7] M. J. Hargather, G. S. Settles, A comparison of three quantitative schlieren techniques, Optics and Lasers in Engineering 50 (1) (2012) 8–17, advances in Flow Visualization. doi:10.1016/j.optlaseng.2011.05.012.

[8] C. J. Kähler, S. Scharnowski, C. Cierpka, On the resolution limit of digital particle image velocimetry, Experiments in Fluids 52 (6) (2012) 1629–1639. doi:10.1007/s00348-012-1280-x.

[9] E. Davies, Chapter 19 - motion, in: Computer and Machine Vision (Fourth Edition), fourth edition Edition, Academic Press, Boston, 2012, pp. 505–522. doi:10.1016/B978-0-12-386908-1.00019-7.

[10] B. Atcheson, W. Heidrich, I. Ihrke, An evaluation of optical flow algorithms for background oriented schlieren imaging, Experiments in Fluids 46 (3) (2009) 467–476. doi:10.1007/s00348-008-0572-7.

[11] K. Hayasaka, Y. Tagawa, T. Liu, M. Kameda, Optical-flow-based background-oriented schlieren technique for measuring a laser-induced underwater shock wave, Experiments in Fluids 57 (12) (2016) 179. doi:10.1007/s00348-016-2271-0.

[12] S. J. Grauer, A. Unterberger, A. Rittler, K. J. Daun, A. M. Kempf, K. Mohri, Instantaneous 3d flame imaging by background-oriented schlieren tomography, Combustion and Flame 196 (2018) 284–299. doi:10.1016/j.combustflame.2018.06.022.

[13] R. Adrian, J. Westerweel, Particle Image Velocimetry, Cambridge Aerospace Series, Cambridge University Press, 2011.

[14] C. Yang, L. Yao, Z. Xu, X. Chen, J. Liu, R. Kan, Random dots' parameters optimization study of background for background oriented schlieren (bos) environmental research application, in: Light, Energy and the Environment, Optica Publishing Group, 2014, p. EW4A.6. doi:10.1364/E2.2014.EW4A.6.

[15] R. L. Cook, T. DeRose, Wavelet noise, ACM Trans. Graph. 24 (3) (2005) 803–811. doi:10.1145/1073204.1073264.

[16] B. O. Cakir, S. Lavagnoli, B. H. Saracoglu, C. Fureby, Assessment and application of optical flow in background-oriented schlieren for compressible flows, Experiments in Fluids 64 (1) (2022) 11. doi:10.1007/s00348-022-03553-z.
URL https://doi.org/10.1007/s00348-022-03553-z

[17] J. K. Kearney, W. B. Thompson, D. L. Boley, Optical flow estimation: An error analysis of gradient-based methods with local optimization, IEEE Transactions on Pattern Analysis and Machine Intelligence PAMI-9 (2) (1987) 229–244. doi:10.1109/TPAMI.1987.4767897.

[18] E. H. Adelson, J. R. Bergen, Spatiotemporal energy models for the perception of motion., Journal of the Optical Society of America. A, Optics and image science 2 2 (1985) 284–99. doi:10.1364/JOSAA.2.000284.

[19] P. Anandan, A computational framework and an algorithm for the measurement of visual motion, International Journal of Computer Vision 2 (3) (1989) 283–310. doi:10.1007/BF00158167.

[20] P. J. Burt, Fast filter transform for image processing, Computer Graphics and Image Processing 16 (1) (1981) 20–51. doi:10.1016/0146-664X(81)90092-7.

[21] G. A. Sod, A survey of several finite difference methods for systems of nonlinear hyperbolic conservation laws, Journal of Computational Physics 27 (1) (1978) 1–31. doi:https://doi.org/10.1016/0021-9991(78)90023-2.
URL https://www.sciencedirect.com/science/article/pii/0021999178900232

[22] G. E. Elsinga, B. W. van Oudheusden, F. Scarano, Evaluation of aero-optical distortion effects in piv, Experiments in Fluids 39 (2) (2005) 246–256. doi:10.1007/s00348-005-1002-8.
URL https://doi.org/10.1007/s00348-005-1002-8

[23] D. Livescu, J. R. Ristorcelli, Variable-density mixing in buoyancy-driven turbulence, Journal of Fluid Mechanics 605 (2008) 145–180. doi:10.1017/S0022112008001481.

[24] L. K. Rajendran, S. P. M. Bane, P. P. Vlachos, PIV/BOS synthetic image generation in variable density environments for error analysis and experiment design, Measurement Science and Technology 30 (8) (2019) 085302. doi:10.1088/1361-6501/ab1ca8.

[25] B. Cakir, S. Lavagnoli, B. Saracoglu, C. Fureby, Optical flow based background oriented schlieren for compressible flows, in: 20th International Symposium on Application of Laser and Imaging Techniques to Fluid Mechanics, 2022.

[26] S. Baker, S. Roth, D. Scharstein, M. J. Black, J. Lewis, R. Szeliski, A database and evaluation methodology for optical flow, in: 2007 IEEE 11th International Conference on Computer Vision, 2007, pp. 1–8. doi:10.1109/ICCV.2007.4408903.

Cyclostationarity indicators in combination with blind filtering technique for fault detection of rotating machine elements

Marcello Nitti

Environmental and Applied Fluid Dynamics, von Karman Institute for Fluid Dynamics, Belgium, marcello.nitti@vki.ac.be

University Supervisor: Jan Helsen

Professor, Applied Mechanics, Vrije Universiteit Brussel, Belgium, Jan.Helsen@vub.be

University Advisor: Cedric Peeters

Postdoc, Applied Mechanics, Vrije Universiteit Brussel, Belgium, Cedric.Peeters@vub.be

Supervisor: Jeroen van Beeck

Professor, Environmental and Applied Fluid Dynamics, von Karman Institute for Fluid Dynamics, Belgium, jeroen.vanbeeck@vki.ac.be

Supervisor: Sophia Buckingham

Senior Research Engineer, Environmental and Applied Fluid Dynamics, von Karman Institute for Fluid Dynamics, Belgium, sophia.buckingham@vki.ac.be

Abstract

This paper investigates the scalar indicators for higher-order cyclostationarity faults detection in gears and bearings of rotating machines. The performance of these indicators can be hindered by interference from other vibration sources. To overcome this problem their performance is integrated with a blind deconvolution approach. The performance of the proposed methodology is validated on both simulated and experimental vibration data.

Keywords: Vibration signal processing, condition monitoring, higher-order cyclostationarity

1. Introduction

The production of green energy through wind power is experiencing rapid growth. As illustrated in Fig. 1, there has been an increase in the capacity of both onshore and offshore wind turbines in recent years. As can be seen from Fig. 2, wind energy is among the top source for annual capacity in Europe.

The turbines rely on essential rotating components such as gears, bearings, and shafts despite the increasing complexity and size due to advancements in green technology. Any defects in these rotating elements can result in significant financial losses, particularly if they are not addressed promptly, leading to complete component failure. The primary causes of failure in rotating machinery are often attributed to gears and bearings, with the first occupying 76% of the faults in a gearbox and the second 17.1% as

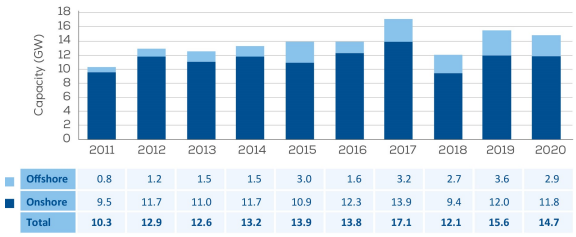

	2011	2012	2013	2014	2015	2016	2017	2018	2019	2020
Offshore	0.8	1.2	1.5	1.5	3.0	1.6	3.2	2.7	3.6	2.9
Onshore	9.5	11.7	11.0	11.7	10.9	12.3	13.9	9.4	12.0	11.8
Total	**10.3**	**12.9**	**12.6**	**13.2**	**13.9**	**13.8**	**17.1**	**12.1**	**15.6**	**14.7**

Figure 1: Onshore and offshore wind energy installation capacity in Europe [1]

also depicted in Fig. 3. The failure of either of these components can impact the machine's performance, affecting power transmission, or in extreme cases, resulting in the complete shut-down of the machine.[3]

To address these challenges, the fields of progno-

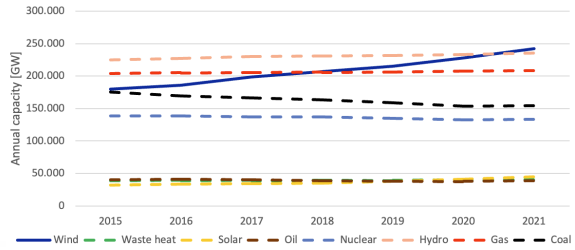

Figure 2: Overview of energy capacity by source in Europe [2]

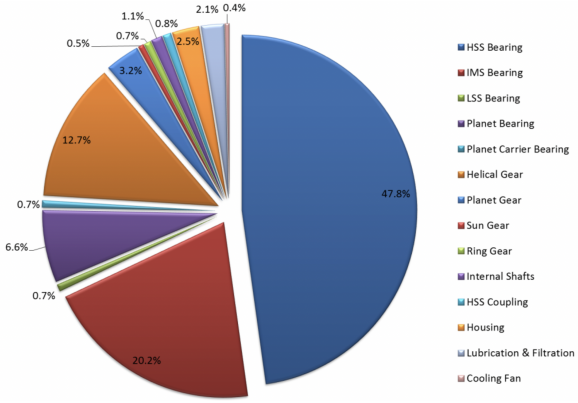

Figure 3: Statistical breaking cause of wind turbine gearbox [4]

sis and health management have become increasingly important in the wind energy industry over the last few decades. Condition Monitoring is the process of collecting and analyse data for health monitoring purposes, and it has become an essential aspect of many industrial projects. There are various methods for implementing condition monitoring, but vibration analysis is widely used and popular in both academia and industry. This is due to its ease of implementation and quick data analysis capabilities, which enable the identification of potential issues with the rotating components of wind turbines. [5]

The typical faults that can occur in gears and bearings include plastic deformation, local defects, distributed surface imperfections, cracks, fractures, corrosion, and wear. These issues can result from a range of factors, such as poor maintenance, excessive loads, or harsh environmental conditions. [6]

The theory of cyclostationarity, which was first proposed in 1958 [7], is an essential concept in advanced vibration analysis for rotating machines. Cyclostationary signals are a family of signals that comprise all waveforms with different periodicities. By decomposing these signals into their periodic and random parts, it is possible to analyze different physical contributions. Although the vibrations of rotating components are usually non-stationary, their signals exhibit some statistical properties that repeat over the shaft rotation cycles. By analyzing changes in these properties, it is possible to detect faults. In the case of gears and bearings, their fault signatures are typically considered as first- or second-order cyclostationary [8] [9]. Although there are differences between these two types of signals, with the former being deterministic and the latter being stochastic, they both exhibit cyclostationary properties that can be analyzed for fault detection purposes.

The cyclostationary approach has been found to be highly effective in detecting weak incipient faults and extracting signals of interest from strong background noise. For example, new indicators of cyclostationarity (ICS) from first to fourth order have been developed, [10], which do not require the computation of *nth*-order polispectra to analyze the data. These indicators were tested on two single-stage gear units with an equal number of teeth mounted back-to-back. The results demonstrated that the first two indicators were suitable for detecting gear faults in the frequency range below 16 kHz, while the last two worked well above 16 kHz. In another experiment involving bearing rolling elements [11], the third and fourth indicators were able to detect faults reliably.

Fig. 4 shows the typical behaviour of a scalar condition indicator of a common machine component degradation. In phase I, there is no fault creation and growth with the value of the indicator being at a low level, indicating a healthy component. On the contrary, phase II exemplifies the fault formation and further growth. Once the indicator value reaches a level above a certain threshold, the component is considered to have critically failed and in need of repair before the machine can continue operation. Hence, the main problem for a condition monitoring methodology is to find a reliable indicator that allows for early fault detection and prediction.

Another potential obstacle to the performance of cyclostationary indicators in detecting faults is interference from other vibration sources. To overcome this, blind deconvolution approaches such as minimum entropy deconvolution (MED), maximum correlated kurtosis deconvolution (MCKD), optimal MED adjusted (OMEDA), multipoint OMEDA (MOMEDA), and cyclostationarity-based blind deconvolution (CYCBD) have been proposed in the literature. [13] The aim of these methods is to increase the signal-to-noise ratio (SNR) of a potential fault signature hidden in the noise level by finding a suitable

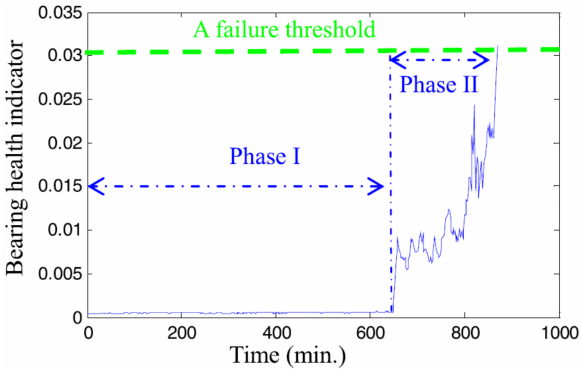

Figure 4: Typical behavior of an indicator health trend of a degrading machine component [12]

filter that maximizes the SNR.

This paper focuses on the potential application of the indicators proposed in [10] in combination with a blind deconvolution approach explained in [14] and [15]. The indicators are tested on simulated signals and real vibration data measured on compelex industrial rotational machinery.

2. Methodology

The indicators are derived from the former definition given by [10] and then evaluated using both simulated and real signals from complex industrial rotational machinery. The simulated signals have different signal-to-noise ratios, while the experimental signals are based on bearings dataset. The goal is to validate the performance of the indicators under different conditions and demonstrate their potential as a fault detection tool. The next section summarizes the general expression of the indicators and their derivation.

The indicators for cyclostationarity rely on cumulants, while the method for blind deconvolution is based on the approach developed in [14]. In this study, the blind filtering technique is utilized to enhance the performance of the indicators.

2.1. Cyclostationarity indicators

A process is said to be cyclostationary if there are hidden periodicities in its statistical structure, or if its *nth* statistical moment or cumulant has periodic components. The cyclostationary indicators rely on the cumulants of a noisy signal $\mathbf{x}$, which are advantageous over moments as they are pure and do not contain lower order cumulants. The indicators applied in this paper are the one defined in [10] as follows:

$$ICS_n = \sum_{\alpha=\varpi,\alpha\neq 0} \frac{|C_n^{\alpha}(0)|^2}{|C_2^0(0)|^n} \tag{1}$$

where α is the frequency of interest of the cycling frequency λ.

2.1.1. Blind filtering tecnique

The ideal input signal $\mathbf{s}$ can be expressed in matrix form as follows:

$$\mathbf{s} = \mathbf{X} * \mathbf{h} \tag{2}$$

$$\begin{bmatrix} s_{N-1} \\ \vdots \\ s_{L-1} \end{bmatrix} = \begin{bmatrix} x_{N-1} & \cdots & x_0 \\ \vdots & \ddots & \vdots \\ x_{L-1} & \cdots & x_{L-N-2} \end{bmatrix} \begin{bmatrix} h_0 \\ \vdots \\ h_{N-1} \end{bmatrix}$$

where $\mathbf{h}$ is the inverse finite impulse responce (FIR) filter of length N, $\mathbf{s}$ has length L and * stands for the convolute product. Vectors are indicated in bold and matrix quantities in capitals and bold in order to distinguish them from scalars. The blind filtering method used in this study is based on the generalized Rayleigh quotient approach, which aims to maximize the eigenvector associated with the highest eigenvalue. In this approach, the ICS values are assigned to the eigenvalue. Therefore, maximizing the first quantity also means maximizing the ICS for the given signal. Additionally, as previously demonstrated in [14], Eq. 1 can also be expressed in the following way:

$$ICS_n = \frac{\sum_{k>0}|c_s^k|^2}{|c_2^0|^n} \tag{3}$$

with

$$c_s^k = \frac{\mathbf{E}^H(|\mathbf{s}|^n)^2}{L-N+1} \tag{4}$$

and

$$c_s^0 = \frac{\mathbf{s}^h\mathbf{s}}{L-N+1} \tag{5}$$

The superscript H indicates the Hermitian transpose, $\mathbf{E}$ is a Fourier matrix and L the signal length structured as follow:

$$\mathbf{E} = \begin{bmatrix} \mathbf{e}_1 & \dots & \mathbf{e}_K \end{bmatrix}$$

with $\mathbf{e}_K$ being:

$$\mathbf{e}_K = \begin{bmatrix} e^{j2\pi\frac{k}{T}(N-1)} \\ \vdots \\ e^{j2\pi\frac{k}{T}(L-1)} \end{bmatrix}$$

Substituting the expression of c_s^k and c_s^0 in ICSN and taking $n = 2$, the ICS2 becomes:

$$ICS_2 = \frac{|\mathbf{s}|^{2H}\mathbf{E}\mathbf{E}^H|\mathbf{s}|^2}{|\mathbf{s}^H\mathbf{s}|^2} \tag{6}$$

Finally, substituting Eq. 2 in Eq. 6, the final expression of the ICS2 becomes the following:

$$ICS_2 = \frac{\mathbf{h}^H\mathbf{X}^H\mathbf{W}\mathbf{X}\mathbf{h}}{\mathbf{h}^H\mathbf{X}^H\mathbf{X}\mathbf{h}} = \frac{\mathbf{h}^H\mathbf{R}_{XWX}\mathbf{h}}{\mathbf{h}^H\mathbf{R}_{XX}\mathbf{h}} \tag{7}$$

where $\mathbf{R}_{\mathrm{XWX}}$ and $\mathbf{R}_{\mathrm{XX}}$ are the weighted correlation matrices and correlation matrix respectively, and with $\mathbf{W}$ being the weighting matrix as follows:

$$\mathbf{W} = diag\left(\frac{\mathbf{E}\mathbf{E}^H|\mathbf{s}|^2}{|\mathbf{s}^H\mathbf{s}|}\right) \tag{8}$$

Eq. 7 is a generalized Rayleigh quotient problem. Maximizing it with respect to $\mathbf{h}$ is the same as maximizing the eigenvector associated with the maximum eigenvalue λ of the following problem:

$$\mathbf{R}_{XWX}\mathbf{h} = \mathbf{R}_{XX}\lambda \tag{9}$$

In this example, maximising λ is equal to maximising ICS2. The procedure is as follows:

1. Provide an initial estimation for $\mathbf{h}$
2. Estimate $\mathbf{R}_{\mathrm{XWX}}$ and $\mathbf{R}_{\mathrm{XX}}$ given the input signal $\mathbf{X}$ and the guessed $\mathbf{h}$
3. Solve Eq. 9 in order to find the corresponding new value of $\mathbf{h}$ associated with λ
4. Once the new value of $\mathbf{h}$ is obtained in step 4, the algorithm returns to step 2 and repeats the process with the updated value of h. This iteration continues until the convergence criteria is met or until the desired level of convergence is reached.

The ICS3 and ICS4 indicator can be obtained by setting $n = 3$ and $n = 4$ in Eq. 3 respectively. The corresponding matrix form is as follows:

$$ICS_3 = \frac{|\mathbf{s}|^{3H}\mathbf{E}\mathbf{E}^H|\mathbf{s}|^3}{|\mathbf{s}^H\mathbf{s}||\mathbf{s}^H\mathbf{s}|^2} = \frac{\mathbf{h}^H\mathbf{X}^H\mathbf{W}\mathbf{X}\mathbf{h}}{\mathbf{h}^H\mathbf{X}^H\mathbf{X}\mathbf{h}} = \frac{\mathbf{h}^H\mathbf{R}_{XWX}\mathbf{h}}{\mathbf{h}^H\mathbf{R}_{XX}\mathbf{h}} \tag{10}$$

$$ICS_4 = \frac{|\mathbf{s}|^{4H}\mathbf{E}\mathbf{E}^H|\mathbf{s}|^4}{|\mathbf{s}^H\mathbf{s}||\mathbf{s}^H\mathbf{s}|^3} = \frac{\mathbf{h}^H\mathbf{X}^H\mathbf{W}\mathbf{X}\mathbf{h}}{\mathbf{h}^H\mathbf{X}^H\mathbf{X}\mathbf{h}} = \frac{\mathbf{h}^H\mathbf{R}_{XWX}\mathbf{h}}{\mathbf{h}^H\mathbf{R}_{XX}\mathbf{h}} \tag{11}$$

and their relative weighting matrix is:

$$\mathbf{W} = diag\left(\frac{diag(\mathbf{s}^H)\cdot\mathbf{E}\cdot\mathbf{E}^H\cdot\mathbf{s}^3}{|\mathbf{s}^h\cdot\mathbf{s}|^2}\right) \tag{12}$$

$$\mathbf{W} = diag\left(\frac{diag(\mathbf{s}^{2H})\cdot\mathbf{E}\cdot\mathbf{E}^H\cdot\mathbf{s}^4}{|\mathbf{s}^h\cdot\mathbf{s}|^3}\right) \tag{13}$$

Solving Eq. 7, Eq. 10 and Eq. 11 allow the maximization of 2nd, 3rd and 4th cyclostationarity indicators.

3. Simulation data

To validate the approach proposed in the study, the authors tested the developed indicators on both a simulated case and an experimental one. The simulated signals used in the study contain impulses of a fault signal with Gaussian distributed amplitudes. Gaussian noise is added to the signal, with a varying signal-to-noise ratio from -40 dB to 40 dB, to test the behavior of the indicators and filtering technique. The total variance of the signal remains constant. The structure of the simulated fault signal is shown in Fig. 5, while the results of ICS2, ICS3 and ICS4 with and without filtering are presented in Fig. 6, Fig. 8 and Fig. 10.

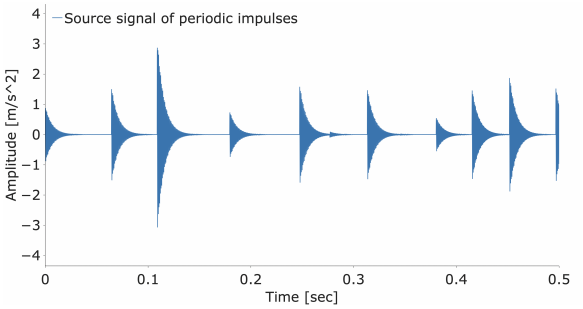

Figure 5: Input signals used for the simulation cases

As shown in Fig. 6, the non filtered ICS2 indicator can detect the fault development in the simulated signals. The application of the filtering technique is applied improves its behaviour. The absolute value increases and the trend of the curve begins to rise at approximately -15 dB, resulting in early fault detection. This is consistent with the expected behavior since the fault exhibits 2nd order cyclostationarity, which causes an increase in the ICS2 indicator.

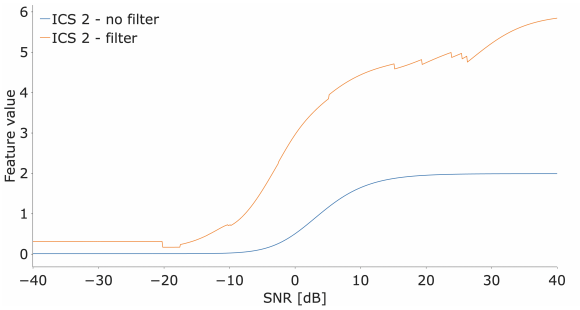

Figure 6: Evolution of the ICS2 indicator with and without filter on simulation data with increasing SNR from −40 dB to 40 dB

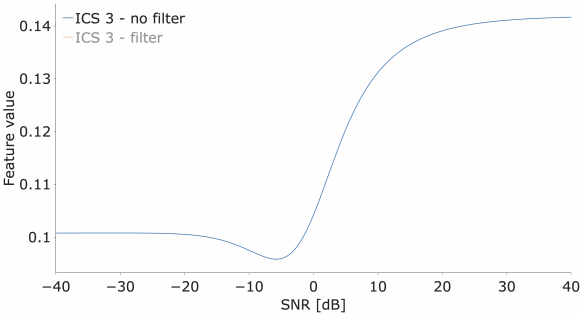

Figure 7: Evolution of the ICS3 indicator without filter on simulation data with increasing SNR from −40 dB to 40 dB

The ICS3 shows a similar behavior as depicted in Fig. 7 and Fig. 8. Its trend is similar to the ICS2 one, but its value is significantly smaller compared to the ICS3 with filter, making it appear as a straight line. In general, the fault could be detected using the indicator even without the filter, but the ICS3 values are too low in such a way that it would be challenging to identify the presence of a fault in a practical scenario. On the other hand, the application of the filter enhances the situation and makes it easier to detect the fault.

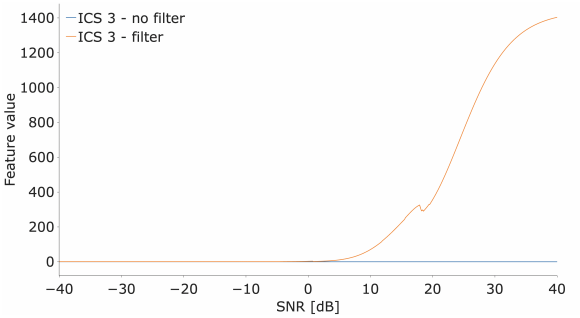

Figure 8: Evolution of the ICS3 indicator with and without filter on simulation data with increasing SNR from −40 dB to 40 dB

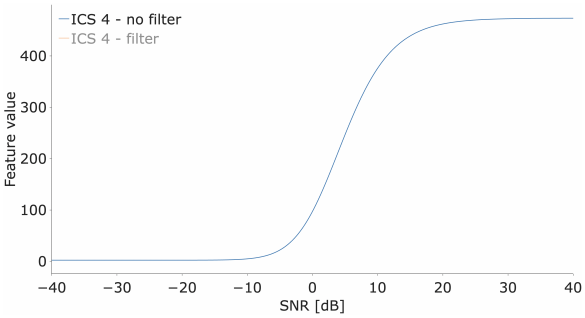

Figure 9: Evolution of the ICS4 indicator without filter on simulation data with increasing SNR from −40 dB to 40 dB

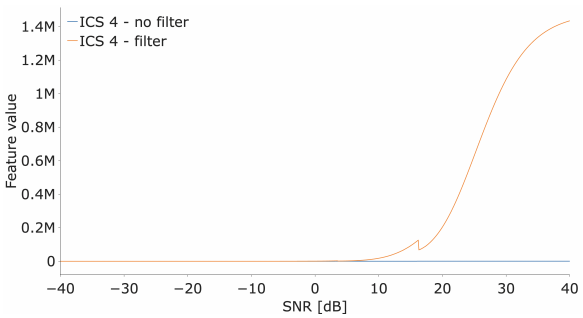

Figure 10: Evolution of the ICS4 indicator with and without filter on simulation data with increasing SNR from −40 dB to 40 dB

The trend of ICS4 is in line with the other two as can be seen in Fig. 9 and Fig. 10. It shows a mild situation compared to the previous two. The indicator without the filter is able to detect the fault (opposite to ICS3), but it start to rise around -5 dB (later compared to the ICS2). The application of the filtering technique improves quite a lot the behaviour or the indicator making sure that the fault is tracked.

4. Experimental data

The experimental dataset originates from a complex industrial test rig. During the experiments, the shaft rotation speed is kept constant and a constant load is applied on the system. The bearings are equipped with accelerometers. Run-to-failure tests were executed until a certain amplitude threshold was reached. At the end of the experiment, defects were found on the bearing raceways. For the blind filtering method, the filter length is set equal to 80 and the maximum number of iterations at 30.

The results of ICS2, ICS3 and ICS4 with and without filtering are depicted in Fig. 11, Fig. 12 and Fig. 13. It has to be pointed out that the results are

showed on a logarithmic scale because the value without the filtering is too low compared to the filter one, making it appearing as a straight line.

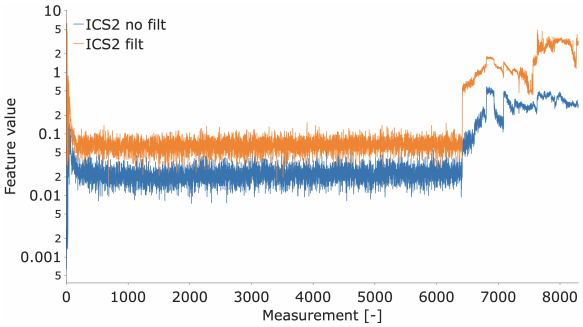

Figure 11: Evolution of the ICS2 indicator with and without filter on experimental dataset

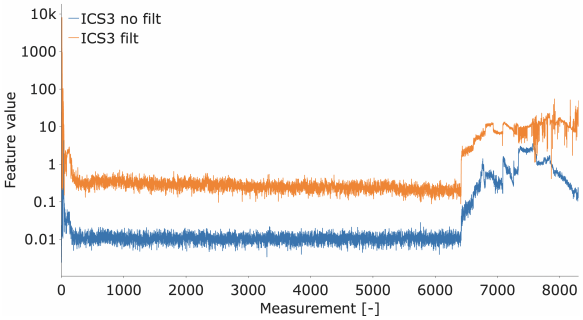

Figure 12: Evolution of the ICS3 indicator with and without filter on experimental dataset

The indicators shows a similar behaviour as the simulated case. All the graphs depict the same trend. There is a first region where the indicators value is at low level, meaning of an healthy bearing. In a later stage the ICS increases. The rise in their values can be attributed to the presence of a bearings' fault. This is in line about what has been mentioned and seen from the technical report given by the company. The presence of the defect enhance the cyclostationarity behavior leading to an higher value of the indicators. All indicators are able to track the faults, with ICS4 displaying the highest absolute value among them. The application of the blind filtering technique further amplifies this behavior making sure that the fault is immediately detected at its formation. This can be clearly seen in the zoom section depicted on Fig. 14.

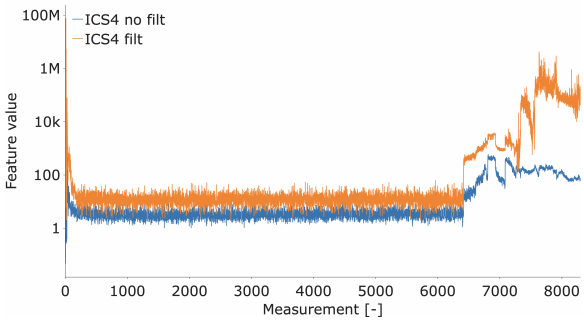

Figure 13: Evolution of the ICS4 indicator with and without filter on experimental dataset

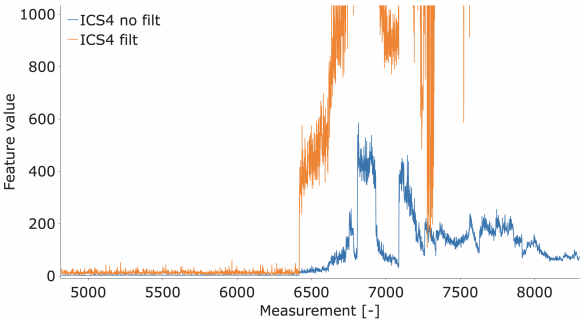

Figure 14: Zoom on the evolution of the ICS4 indicator with and without filter on experimental dataset

5. Critical discussion

The simulation and experimental results demonstrate the effectiveness of using a blind filtering approach for condition monitoring of vibration signals. In general, all the indicators are able to detect the presence of faults. In the simulated case, ICS2 is able to detect the fault earlier and more clearly than ICS3 and ICS4. This is in line with theory, as bearing fault signatures are typically considered as second-order cyclostationary. The application of blind filtering ensures that ICS3 and ICS4 can also be used for such detection.

A different scenario holds for the recorded experimental dataset, as its results do not suggest a clear superiority of any of the three indicators over the others in detecting the fault. However, it demonstrates the blind filtering techniques facilitates the tracking of the faults. This is particularly evident in the sudden increase of the curves at the beginning of the fault. Such a real case highlights the potential of this technique in the presence of noise.

As a remark, the blind filtering technique employed in this paper should not be classified as blind decon-

volution, blind signal separation, or denoising. The method does not aim to deconvolve the signal to recover the source signal, nor does it attempt to separate signals from a mixture or eliminate noise from the signal without causing distortion. Instead, this technique aims to maximize the selected indicator. Thus, the user needs to have this in mind while applying this technique.

The proposed approach combines blind filtering and cyclostationarity indicators to improve vibration signal analysis. However, a major challenge is selecting the appropriate filter length, as it can significantly affect the computation time and results. Longer filter lengths increase computation time and can result in slower convergence or non-convergence. Therefore, it is suggested to use a shorter filter length to minimize computation time and improve convergence.

6. Conclusions

This research investigates the use of scalar indicators for detecting faults in vibration signals by analyzing higher-order cyclostationarity signatures. The indicators are combined with a blind filtering technique based on a generalized Rayleigh quotient problem to improve their performance. The method is easy to implement and computationally efficient. The study evaluates the proposed approach on both simulated and experimental signals and finds that the trend of all indicators is similar for all the analyzed signals.

Among the indicators, ICS2 outperforms ICS3 and ICS4 for simulated signals, resulting in an earlier detection of faults. The blind filtering technique improves ICS3, leading to a clear detection of faults that would not have occurred without filtering. ICS4 without filter is able to track faults, and the application of the filter improves this situation.

All the indicators have a similar behaviour for the experimental case. The blind filtering technique allows to enhance the absolute value of the indicators. There is no early detection compared to the non filter case and the results do not indicate that any of the three indicators have a significant advantage over the others.

In general, the implementation of the blind filtering technique significantly improves the effectiveness of all the indicators, enabling the detection of faults at an earlier stage or providing a clear and unambiguous information of the presence of a fault.

The paper aims to provide inspiration and guidance for future research in vibration monitoring using the blind filtering approach. The study also demonstrates that the Rayleigh quotient iteration is the primary tool for implementing the proposed filters in an efficient manner.

Future work will analyse the impact of the different filter lengths on the results, mainly focussing on computational time and convergence behaviour.

Acknowledgments

Marcello Nitti, Cedric Peeters, and Jan Helsen received funding from the Flemish Government (AI Research Program). They would like to acknowledge FWO (Fonds Wetenschappelijk Onderzoek) for their support through the post-doctoral grant of Cedric Peeters (# 1282221N). The authors are also grateful to the FWO for the support through the SBO Robustify project (S006119N). They would also like to thank the Blue Cluster ICON Rainbow project for their support.

References

[1] W. Europe, Wind energy in europe 2020 statistics and the outlook for 2021-2025, Tech. rep. (2020).

[2] S. G. M. Intelligence, S&p global marketplace: Get the data that gives you an edge.
URL https://www.spglobal.com/marketintelligence/en/campaigns/european-energy-sector

[3] Z. Feng, F. Chu, Cyclostationary analysis for gearbox and bearing fault diagnosis, Shock and Vibration 2015.

[4] W. E. T. Office, Statistics show bearing problems cause the majority of wind turbine gearbox failures.
URL https://www.energy.gov/eere/wind/articles/statistics-show-bearing-problems-cause-majority-wind-turbine-gearbox-

[5] R. B. Randall, Vibration-based condition monitoring: industrial, automotive and aerospace applications, John Wiley & Sons, 2021.

[6] Z. Liu, L. Zhang, A review of failure modes, condition monitoring and fault diagnosis methods for large-scale wind turbine bearings, Measurement 149 (2020) 107002.

[7] W. Bennett, Statistics of regenerative digital transmission, Bell System Technical Journal 37 (6) (1958) 1501–1542.

[8] V. Sharma, A. Parey, Use of cyclostationarity based condition indicators for gear fault diagnosis under fluctuating speed condition, in: Cyclostationarity: Theory and Methods III, Springer, 2017, pp. 241–257.

[9] Z. Ma, Y. Liu, D. Wang, W. Teng, A. Kusiak, Cyclostationary analysis of a faulty bearing in the wind turbine, Journal of Solar Energy Engineering 139 (3).

[10] A. Raad, J. Antoni, M. Sidahmed, Indicators of cyclostationarity: Theory and application to gear fault monitoring, Mechanical Systems and Signal Processing 22 (3) (2008) 574–587.

[11] G. Ishak, A. Raad, J. Antoni, Analysis of vibration signals using cyclostationary indicators, Institute of Technology of Chartres: Chartres, France.

[12] D. Wang, K.-L. Tsui, Q. Miao, Prognostics and health management: A review of vibration based bearing and gear health indicators, Ieee Access 6 (2017) 665–676.

[13] Y. Cheng, B. Chen, G. Mei, Z. Wang, W. Zhang, A novel blind deconvolution method and its application to fault identification, Journal of Sound and Vibration 460 (2019) 114900.
[14] M. Buzzoni, J. Antoni, G. d'Elia, Blind deconvolution based on cyclostationarity maximization and its application to fault identification, Journal of Sound and Vibration 432 (2018) 569–601.
[15] C. Peeters, J. Antoni, J. Helsen, Blind filters based on envelope spectrum sparsity indicators for bearing and gear vibration-based condition monitoring, Mechanical Systems and Signal Processing 138 (2020) 106556.

PROPELLANT MANAGEMENT,

LIQUID AND SOLID PROPULSION

On the role of dynamic wetting in the management of cryogenic space propellants

Domenico Fiorini

von Karman Institute for Fluid Dynamics, Environmental and Applied Fluid Dynamics Department, Belgium, domenico.fiorini@vki.ac.be

Supervisor: Miguel Alfonso Mendez

Assistant Professor, von Karman Institute for Fluid Dynamics, Environmental and Applied Fluid Dynamics Department, Belgium

University Supervisor: David Seveno

Professor, KU Leuven, Dept. of Materials Engineering, Belgium, david.seveno@kuleuven.be

University CoSupervisor: Johan Steelant

Professor, KU Leuven, Dept. of Mechanical Engineering, Belgium,

ESTEC-ESA, Keplerlaan 1, 2200AG Noordwijk, The Netherlands, Johan.Steelant@esa.int

Abstract

The motion of a gas-liquid interface along a solid wall depends on the capillary forces due to the interface shape and its interaction with solid surfaces, where the interface forms a dynamic contact angle. Capillary forces and the dynamic wetting of the surfaces play a major role in the management of space cryogenic propellants. However, traditional dynamic wetting theory has been rarely verified for the case of cryogenic sloshing conditions where inertia cannot be neglected and the fluids hold low viscosity and high volatility. In this work, we investigate a dedicated wetting experiment considering a low-viscosity, highly wetting fluid. We focus on the characterization of the shape of an accelerating liquid interface and the corresponding contact angle comparing normal gravity conditions with a reduced gravity environment. We consider transparent U-tube geometries opportunely modified to perform experiments in microgravity conditions. Our results show that inertial and capillary forces lead the motion of the interface in microgravity, whereas in our previous experiments the interface acceleration resulted as a balance of gravity and inertial forces. The velocity field beneath the interface shows the flow accelerating towards the contact line and the flow field differing significantly from theoretical wedge flow at the scale of our observations.

Keywords: Gas-liquid Interfaces, Dynamic Contact Angle, Inverse method, Cryogenic, Space Propulsion

1. Introduction

Modelling the dynamics of a gas-liquid interface along a solid surface is fundamental in wetting and dewetting (e.g. inkjet printing), coating flows (e.g. slot die coating), and capillary-driven flows (e.g. capillary tubes). These applications have spurred much of the research on the topic and have often been analyzed using semi-empirical or theoretical correlations that link the contact angle at the wall to the contact line dynamics.

One popular approach relates the contact angle to the velocity of the contact line through the Capillary number (e.g. Voinov [1976]; Jiang et al. [1979]; Bracke et al. [1989]; Kistler [1993]), while other authors proposed more complex correlations, in the form of differential equations, to take into account the time history of the contact line dynamics (e.g. Ting and Perlin [1995]; Bian et al. [2003]).

The ability to predict the motion of a liquid interface near walls is essential in developing propellant management devices (PMD) for space applications Jaekle [1997]; Hartwig [2017]; Levine et al. [2015];

White and Troian [2019]. Moreover, capillary forces play a major role in the dynamics of cryogenic propellants in partially filled tanks Kulev and Dreyer [2010]; Kulev et al. [2014]; Schmitt and Dreyer [2015] . The development of engineering models for these applications requires experimental data on the capillary behaviour of cryogenic fluids such as liquid Oxygen, Hydrogen or Methane. These fluids are characterized by low surface tension and the gas-liquid interface meets the solid surfaces with a near zero contact angle.

A critical case study for cryogenic propellant management in microgravity is the axial sloshing of a highly wetting liquid in axisymmetrical containers. This test case was analyzed by Brunet and Baudoin [2022] and Luppes et al. [2009]. Their results demonstrated that the modelling of surface tension strongly impacts the prediction of liquid displacement. Similarly, Li et al. [2018, 2020] conducted a CFD analysis of the oscillations of the gas-liquid interface in a cylindrical tank upon a step reduction in gravity and compared the results with the experimental findings of Li et al. [2020]. Their results showed that the dynamic contact angle models significantly impact the rising velocity of the contact line. Friese et al. [2019] investigated the axial sloshing of cryogenic hydrogen and the corresponding contact line in microgravity conditions and super-heated wall. The authors observed that the axial sloshing was only affected when the apparent wall contact line area recedes and the liquid film at the wall dries out. However, direct observation of the contact line was missing and the authors conclude that the dynamics of the sloshing boundary conditions at a superheated wall needs further understanding.

While these studies highlight the relevance of the capillary forces on the motion of the liquid interface in the absence of gravity and complex geometries, other studies have addressed the fundamentals of dynamic wetting in microgravity using dedicated capillary rise experiments. Stange et al. [2003] performed a capillary rise experiment for a perfect wetting fluid on a large cylindrical tube in a drop tower to reproduce microgravity conditions. Wang et al. [2009] conducted a parametric study of capillary rise in the same configuration to examine the impact of the contact angle and tube size. Both studies observed that that the transient dynamics of the capillary rise results as a competition between viscous and inertial effects, with the former dominating the capillary rise in small-diameter tubes and the latter affecting the initial stage of the rise in large (inertia-dominated) tubes.

The aforementioned studies provide essential data for validating and deriving dynamic contact angle correlations through 1D models of the capillary rise, such as the one developed by Stange et al. [2003]. However, these experiments provide limited information on capillary-dominated conditions as they neglect the role of the flow field beneath the interface, which, in turn, impacts the dynamic contact angle. The velocity field underneath an advancing meniscus has been observed by a few experiments in small capillary tubes, where the motion of the liquid can be assumed to be viscous-dominated. For example, Nasarek et al. [2008] and Waghmare et al. [2012] performed a micro-PIV experiment in a vertical channel and analyzed the advancing motion of a meniscus of ethanol and ethylene glycol, respectively. Both works showed that the common assumption of Poiseuille flow holds until a certain distance from the interface, below which the velocity profile flattens and radial components appear. Similarly, Ratz et al. [2023] analyzed the flow of a quasi-capillary water channel in inertia-dominated conditions and showed that rolling motion under the interface could be produced in advancing and receding conditions.

In this project, we designed a new dedicated wetting experiment for analyzing the impact of the capillary behaviour of cryogenic fluids on the dynamics of a moving gas-liquid interface in a simplified geometry. In Fiorini et al. [2020] we showed the preliminary design of a U-tube facility and its characterization compared to classic experiments. Later work, presented by Fiorini et al. [2021], showed that the dynamic contact angle can be measured for perfect wetting fluids by means of inverse methods and regression of physical-based interface models. The follow-up (Fiorini et al. [2022a]) introduced an inertia-corrected model for the interface shape and used it to perform an analysis of dynamic wetting U-tube experiments performed with demineralized water and HFE7200, a cryogenic substitute fluid. Measurements in accelerating conditions showed that the dynamic contact angle close to the wall retains the classic $\theta \propto \beta Ca^{1/3}$ where the β coefficient needs to be determined for the fluid/surface combination. Fiorini et al. [2022b] showcased the same experiment using a slightly modified U-tube geometry and liquid nitrogen in the cryostat facility of the von Karman Institute. The results showed analogous conclusions of Fiorini et al. [2022a] and demonstrated that nearly identical wetting behaviour could be observed for HFE7200 and Liquid Nitrogen in saturated conditions. Next, Fiorini et al. [2023] compared the motion of the Liquid Ni-

trogen interface with a 1D integral model for the interface shape, analyzing the impact of the main forces involved in the experiment. The results showed that in the U-tube test-case most of the dynamics of the interface is dominated by the balance of inertial and gravity forces with capillary forces playing a relevant role close to the equilibrium conditions of the interface. Fiorini et al. [2023] showed also how classic simplified interface models reveal inadequate to predict the capillary pressure at the interface in large geometries using fluids with small contact angles. Consequently, they propose an equivalent dynamic contact angle representation to correct the capillary pressure prediction. Recently, the project used a parabolic flights setup to study experimentally the the wetting dynamics of highly wetting fluids in microgravity. We modified the baseline test case configuration in a diverging U-tube, sealed to guarantee a saturated gas environment. The different radius of the tube at each side leads to a self-propelled motion of the interface due to capillarity. The experimental conditions achieved through the flights provided a larger duration of the capillary-dominated phase compared to standard capillary rise experiments Stange et al. [2003]; Wang et al. [2009] and allow for characterizing the relationship between the interface shape, its motion and the underlying flow field at different gravity levels. We use particle image velocimetry to measure the velocity field beneath the meniscus and high-speed visualization in backlighting, combined with image processing, to measure the interface evolution.

In this article, we report our latest results on the PIV measurements of a microgravity test case with the capillary rise of HFE7200. Moreover, we present a simple 1D modelling of the interface dynamics on the U tube and compare its prediction with the available experimental data. We validate the model against backlight experiments performed in the same geometry using high viscous Di-propylene glyocol and we analyze the balance of the forces for the two experiment.

In Section 2 we show the facility where the experiment are performed and the test cell for the dynamic experiment. In Section 3 we provide the modeling tools which we use to quantify the impact of surface tension forces on the presented test case. Section 4 and 4.1 characterize the experiment using PIV technique. In the second part of the results, i.e. 4.2, we compare the capillary rise of the interface against the 1D integral model for the interface shape and we discuss the extent of the impact of the capillary force on the dynamics of the liquid column.

The results highlight the role of the capillary forces near the interface and their impact on the capillary rise of highly wetting liquids. The experiment represents an important benchmark for the validation of the models concerning the capillary rise of perfect wetting liquid. Therefore these results are particularly interesting to the management of space propellants, which are also characterized by low (static) contact angles.

2. Experimental Facility

The diverging U-tube (DUT) configuration analyzed in this work is shown in Fig. 1. The experiments were carried out during the 78th ESA parabolic flight campaign.

In the DUT test case, the liquid reservoir used in classic capillary rise experiments is replaced by the larger side of the U-tube. This minimizes the impact of liquid sloshing occurring during a parabolic flight. Moreover, capillary forces have a double effect on the motion of the liquid since both ends of the liquid column create a capillary pressure drop that pulls the interface in opposite directions. This smooths the acceleration profile compared to the step response in experiments with a single driving interface. Moreover, it reduces the inertia-dominated phase and increases the impact of capillary effects on the interface motion. Finally, the lack of a tube entrance reduces viscous losses due to sudden tube constriction, minimizing the effect of viscous forces on the interface motion and reducing the duration of the viscous-dominated phase of capillary rise as identified by Stange et al. [2003].

Figure 1 shows the installation of the DUT quartz tube on its robust structure in aluminium. The structure consists of two plates joined by four cylindrical beams via M8 screws. A resin is poured into two pockets of the structure to clamp the tube. The system is designed to allow optical access while having sufficient rigidity to avoid vibration, which could result in the cracking of the quartz. The complete structure with the U tube and the resin weighs five kg.

The two sides of the tube are connected with a flexible junction. This prevents leakages and creates a closed environment in which saturated conditions are reached before the experiments begin. The flexible is connected to the plate with two fast connectors on the top. The assembly is then installed on a larger breadboard containing the entire experimental equipment, as shown in Fig. 2. A separate electronic rack contains all the electronic devices necessary for the experiment. These include acquisition cards for the ac-

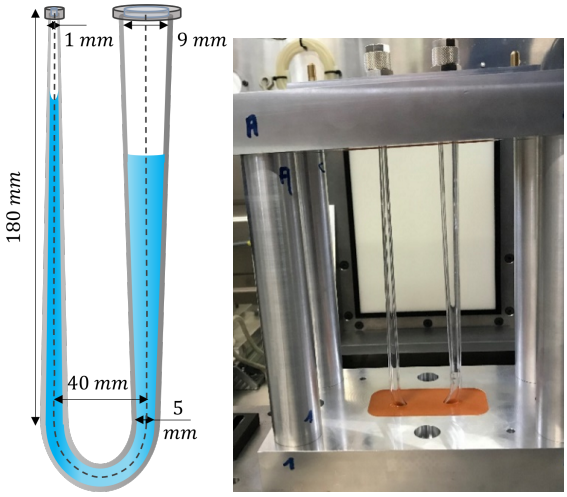

Figure 1: The Figure on the left shows a schematic of the DUT test cell with the characteristic dimensions. The Figure on the right shows a picture of the DUT mounted on a rigid structure to avoid resonance vibrations in the quartz.

celeration and pressure signals connected to a laptop, accelerometer conditioner, laser controller and camera controller connected to a desktop.

Two experiments were performed in parallel, with a camera acquiring images on each side of the two tubes. The motion of each interface is recorded with a high-speed camera (model JAY SP-12000-CXP4), acquiring grey-scale images at 300 fps. The active region of all cameras is restricted to the central region of size $4096 \times n_{px}$ pixels where the lateral size n_{px} is optimized according to the tube geometry to achieve the highest acquisition frequency allowed by the camera. All cameras mount objectives with 105mm focal lenses and are positioned to acquire the full motion of the interface while spanning the largest possible tube length. The final pixel size corresponds to $0.013 \mu m$.

As shown in Fig. 2 on the left, the PIV is carried out using a planar laser sheet produced on one side of the tube. A laser stopper is introduced to avoid optical disturbances on the other side of the tube. The fluid was seeded with FMR-1.3 1-5 μm Red Fluorescent Miscospheres from Cospheric. The particles were illuminated with a continuous laser source (LMX-532 from Oxxius) with a wavelength of 532 nm and a maximum power of 800 mW. The high speed in backlighting conditions is carried out using a LED screen behind the DUTs.

The experiment recordings start with the announcement of the plane being at 40 degrees inclination.

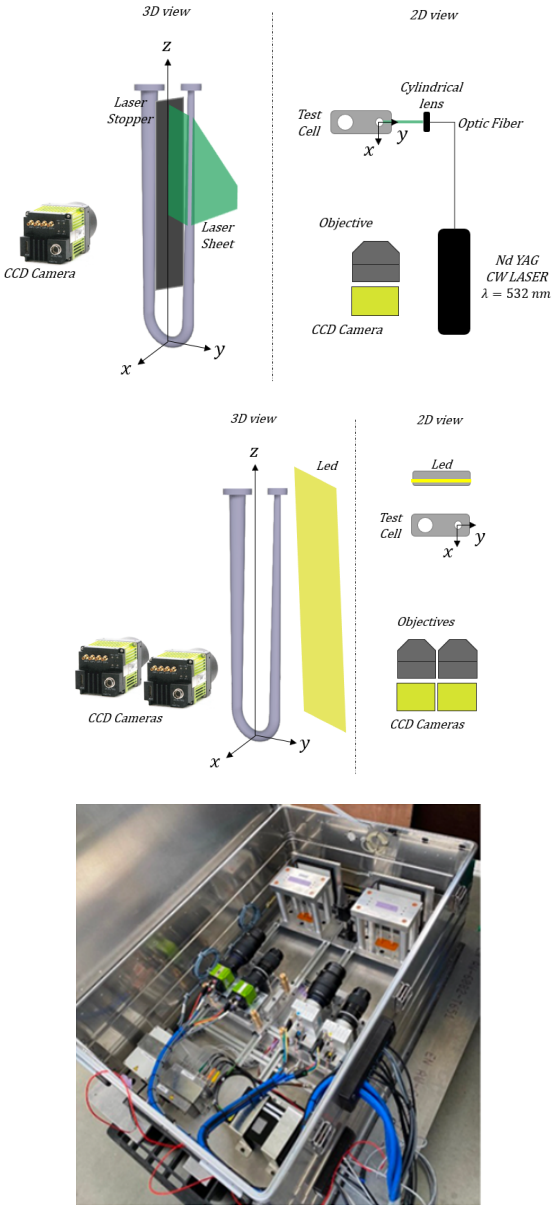

Figure 2: The figures on the top show a schematic of the optical set-up for the PIV measurements. The back-lighting is performed using a LED screen behind the U-tube's aluminium frames as shown by the central Figure. The Figure on the bottom shows the installation on the parabolic flight breadboard: two experiments were carried out in parallel.

Shortly after the announcement, the gravity levels drop from approximately $1.8g$ to approximately $0g$, and the two liquid interfaces begin moving along the axis of the tube due to the unbalanced capillary action of the interfaces. Image processing consists of several stages. First, the images are compensated for the vibrations of the camera objective, which appears as displacement of the image in the vertical (z) and lateral (x) direction (max 4 px.) and without significant image rotation. To compensate for the vibrations, we detect the outer edges of the tube in each image via standard canny edge detection and compute the necessary x and y correction by iteratively minimizing the difference of the global overlap of the image with a reference image acquired at the experiment start. In the second step, the PIV images are preprocessed using the Proper Orthogonal Decomposition (POD)-based background removal introduced by Mendez et al. [2017]. Finally, the PIV interrogation is carried out using OpenPIV processing tool [Liberzon et al., 2020] and windows with a 2:1 aspect ratio, given that velocity component v (along y) is much larger than the velocity component u (along x). We use a Dynamic Region of Interest (DROI) to follow the gas-liquid interface across the available Field of View (FOV). This allows focusing the analysis always in the region below the interface. The DROI is identified by performing standard gradient-based edge detection on the POD-filtered images to detect the element of interest in the image (e.g. the interface). Spurious points and outliers are eliminated through both masking of the tube solid surfaces and unsupervised outlier detection using the Local Outlier Factor (LOF) by Breunig et al. [2000]. A similar procedure is used to identify the interface in the images obtained through backlighting technique. While this approach allows identifying the region of the image where PIV can be applied, the light refraction at the interface of the PIV images prevents extracting the interface contact angle with high accuracy, for which the backlight technique is necessary. The results of the contact angle analysis will be presented in the extended version of this work.

The PIV images are processed using adaptive iterative multigrid interrogation (Scarano and Riethmuller [2000]) to retrieve the velocity fields. The initial window size is set to 128×64 px and reduced over two steps to 32×16 px. Outliers are removed based on the signal-to-noise ratio measured in terms of peak-to-peak in the cross-correlation map.

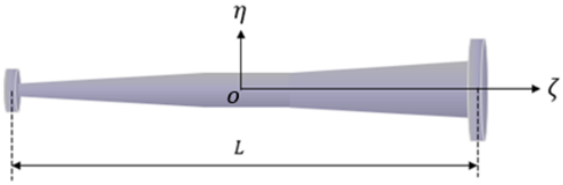

Figure 3: Equivalent cylindrical coordinate system for DUT where gentle curvature of the tube is assumed.

3. Modeling of the capillary rise

We describe the motion of the liquid's center of mass inside the DUT with a 1D integral model balancing the acceleration of the center of mass with the friction, gravity and the interface capillary pressure drop. We derive the model assuming a gentle curvature of the tube and a cylindrical coordinate system (ζ, η) with ζ aligned with the tube axis and η aligned along the tube radius as illustrated in Figure 3. We integrate along the liquid domain the contributions of all forces to obtain the following second-order non-linear ODE:

$$\rho V_l \ddot{Y} = -F_g(Y, a(t)) + F_v(\dot{Y}, Y) + F_c(\dot{Y}, Y, g(t)), \quad (1)$$

where Y, $\dot{Y}$ and $\ddot{Y}$ are respectively the position, the velocity and the acceleration of the liquid column's center of mass along the tube axis $\zeta \in [-L/2, L/2]$. On the right-hand side, F_g denotes the gravitational force acting to the center of mass of the liquid column, F_v denotes the viscous shear applied to the liquid column, and F_c denotes the net result of the capillary pressure due to the two gas-liquid interfaces on the opposite sides of the liquid column. V_l is the volume of liquid within the tube and $a(t) = [a_x(t), a_y(t), g(t)]$ is the local acceleration of the tube.

We denote with $z_A(Y)$ and $z_B(Y)$ the position of the two interfaces along the curvilinear coordinate ζ. The gravity term in 1 results from the contribution of both the height difference $|z_A(Y)| - |z_B(Y)|$ and the local acceleration $a(t)$.

The viscous force term in Eq. 1 results from the integration of the viscous stresses at the walls, thus both across the liquid column length $z_A(Y) - z_B(Y)$ and the radial direction η:

$$F_v(\dot{Y}, Y) = \int_{z_A(Y)}^{z_B(Y)} \int_0^{R(\zeta)} \tau \, 2\pi\eta \, d\eta \, d\zeta + C_U \, . \quad (2)$$

The value of constant $C_U = 2.5 \times 10^{-3} sgn(\dot{Y})$ accounts for the viscous loss in the U-bend and was chosen based on the best fit of the model equation with previous experimental studies on similar materials and geometry (Fiorini et al. [2021, 2022a, 2023]; Delon et al. [2008]). Assuming axisymmetric flow, the viscous stresses τ can be written as

$$\tau = \mu \left[\frac{1}{\eta} \frac{\partial v}{\partial \eta} + \frac{\partial^2 v}{\partial \eta^2} + \frac{\partial^2 v}{\partial \zeta^2} \right] \tag{3}$$

where $v = v(\zeta, \eta, t)$ is the axial velocity of the liquid at the coordinate ζ, η. In normal gravity conditions ($g = 9.8 m/s^2$) and for small diameters, classic capillary rise models assume a Poiseuille velocity profile at each axial position of the channel (see for example Zhong et al. [2019]). Consequently, the velocity profile v can be written as

$$v(\zeta, \eta, t) = 2V(\zeta, t) \left(1 - \frac{\eta^2}{R(\zeta)^2} \right), \tag{4}$$

where V denotes the mean velocity and $R(\zeta)$ the radius of the channel as a function of the channel axial coordinate.

The capillary term is modelled as the net sum of the pressure drop on the two interfaces, which in the analyzed wetting configuration pulls the liquid towards opposite sides. The pressure drop results from the integration of Laplace equation for each interface which reads

$$\begin{aligned} F_c(\dot{Y}, Y) = &\int_0^{R(z_A(Y))} \Delta P_A(\eta) 2\pi\eta d\eta - \\ &\int_0^{R(z_B(Y))} \Delta P_B(\eta) 2\pi\eta d\eta \,, \end{aligned} \tag{5}$$

In the absence of mass transfer and Marangoni effects, the capillary pressure drops $\Delta P(\eta, t)_{A|B}$ become

$$\Delta P(\eta, t) = \sigma \nabla \cdot \mathbf{n} \tag{6}$$

where $\nabla \cdot \mathbf{n}$ is the interface curvature, with ∇ the nabla operator and $\mathbf{n}$ the local normal vectors. If the interface is treated as spherical, the curvature becomes constant and equal to $\nabla \cdot \mathbf{n} = 1/R_s$, with R_s the sphere's radius. With this assumption, introducing the dependency on the apparent and dynamic contact angle θ, one has $R_s(\zeta) \approx R(\zeta)/cos(\theta)$ and thus the capillary pressure drops on each side reads:

$$\Delta P_A = \frac{\sigma}{R(\zeta_A)} cos(\theta_A) \quad \text{and} \quad \Delta P_B = \frac{\sigma}{R(\zeta_B)} cos(\theta_B) \tag{7}$$

4. Results and Discussion

Fig. 4 shows the acceleration profiles for the presented experiments during the $\approx$ 38s constituting a parabola. The Figure on the top shows the envelope of (vertical) gravitational acceleration while the Figure on the bottom report on the lateral accelerations (see Fig. 2).

The micro-gravity phase begins approximately at $t = 10$ s and ends at $t = 30$s. This is preceded and followed by a hypergravity phase. The lateral accelerations are non-negligible during the hypergravity phases and can have an important effect also during the microgravity phase.

Figure 5a shows a sample PIV image acquired during the experiment. All images are pre-processed using the POD background removal; the result for the snapshot in 5a is shown in 5b. The velocity field is computed using the multigrid approach with final-size windows (32, 16). The result is shown in Fig 7 for an extracted axial location near the interface. Figure 6a shows a sample Backlight image acquired during the experiment with di-propylene glycol.

4.1. PIV characterization

In what follows, we focus on the velocity field close to the interface up to 5 mm below the interface. The measured velocity fields in this area are shown in Fig. 7. The red curve in this plot shows the result of the interface detection described in the previous section. These results show that the liquid accelerates towards the contact line as it approaches the interface. This lateral acceleration is due to mass conservation: since the interface shape remains unvaried and hence all its points move at a constant velocity, the flow must adapt from a nearly parabolic profile to a flat one. A similar result was reported by Waghmare et al. [2012] for purely capillary-dominated flow with no evaporation. The classic counter-rotating vortices shown in similar configurations by Davis et al. [1974] and Ratz et al. [2023] are not visible in this case.

At the scale of interest, namely at about the half-width of the channel, the flow appears to be different from the classic wedge flow postulated by Voinov [1976] in the derivation of its classic theoretical model for the dynamic contact angle. This result might thus question the validity of such a model for the investigated test case.

Concerning the stream-wise variation of the velocity profile, at a distance of approximately 3 mm, the velocity profile appears nearly parabolic in all snapshots. At larger acceleration (see snapshot e) the flow

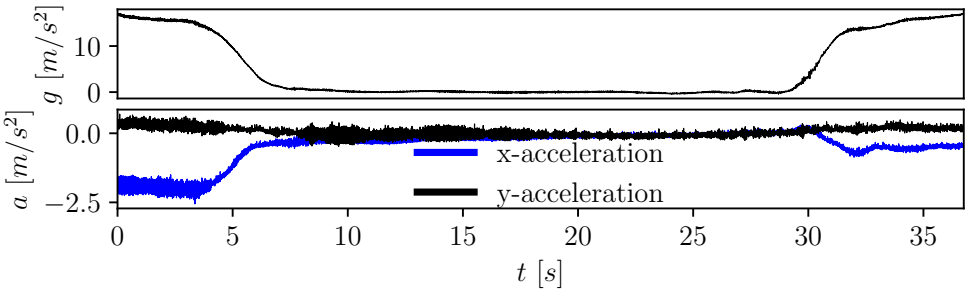

Figure 4: Acceleration profile for the selected experiment

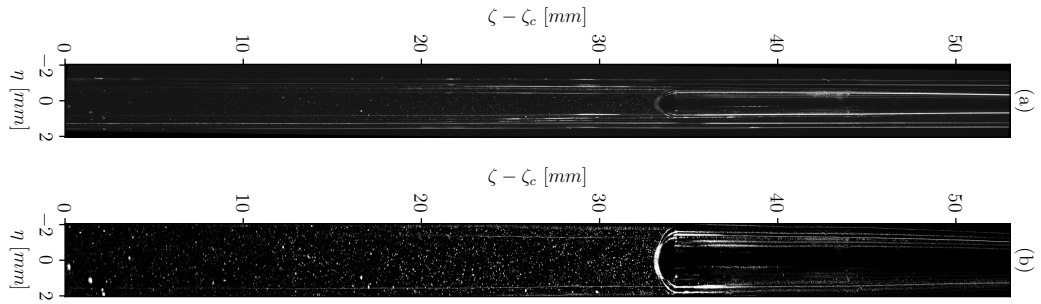

Figure 5: From top to bottom, the Figure shows the raw PIV images and the result from the background removal. All figures are rotated for plotting purposes.

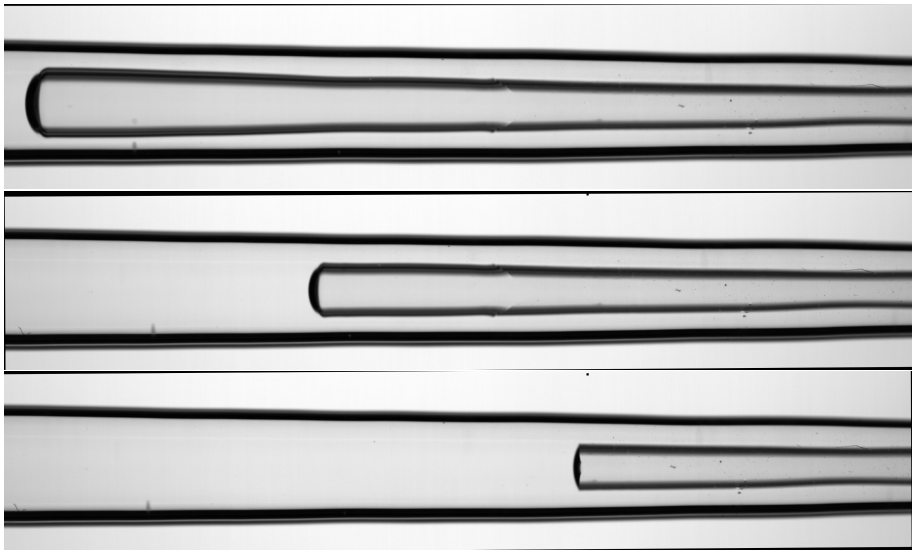

Figure 6: From top to bottom, the Figure shows the raw Backlight images of the di-propylene glycol experiment and at successive instants of the experiment. All figures are rotated for plotting purposes.

inertia appears to push the validity of the parabolic profile closer to the interface (up to nearly 1 mm from it).

Figure 8 compares the velocity profiles at various distances from the interface in this latter snapshot, characterized by larger inertia. The validity of the self-similar assumption is illustrated by comparing the extracted velocity profiles with the classic parabolic profile from the assumption of Poiseuille flow. The progressive flattening of the velocity profile starts appearing at approximately 1 mm from the interface and the parabolic shape of the velocity profile increasingly deteriorates at closer distances from the interface. Fig. 9 use contour plots to provide an indication of a lack of similarity with the Poiseuille flow, measured as

$$P_{\%} = \frac{|v_P - v|}{maxv} \times 100\,, \tag{8}$$

where $v(\eta, \zeta)$ is the measured velocity and $v_P(\eta, R(\zeta), maxv(\eta)$ is the local velocity under the assumption of parabolic profile. This parameter is defined up to the lowest point of the interface, above which the wetting meniscus begins. The figure shows that at the latest stages of the capillary rise, the velocity field is close to that of a Poiseuille flow until a close distance from the interface.

To conclude the analysis of the velocity field, it appears that the assumption of fully developed Poiseuille flow holds until a short distance from the interface, especially when the flow is strongly dominated by inertia as in the last snapshots of Figure 9.

4.2. Analysis of the capillary rise

The results of the previous section validate the assumption of a self-similar profile in the theoretical model presented in 1, particularly in the computation of the viscous term.

In this section we compare the prediction of the model equation 1 with the results of the capillary rise of the interface of di-propylene glycol, obtained using backlight technique, and HFE7200, obtained from the PIV-dedicated visualizations. Figure 10 shows with circular markers the experimental interface position during the capillary rise of Di-Propylene Glycol and compares with the prediction, showed with a dashed line, of the capillary rise of Di-propylene glycol achieved solving numerically Equation 1. The integral model has been solved using python initial value problem solver (scipy.integrate.odeint), which implements an explicit Runge-Kutta method of order 5. We use initial conditions for the interface height corresponding to the initial capillary/gravity balance and zero velocity. The contact angle is initialized with the static value of the fluid and classic Tanner correlation Tanner [1979] is used to model the contact angle dynamics. Figure 10 shows also the acceleration profile in n_g along the axis z, according to the axis convention of Figure 2, as measured by the accelerometer located in the experiment bench. We set conventionally $t = 0$ when $a_z(t) = g(t) = 0.5n_g$.

The comparison appears very satisfactory in the case of Figure 10. The properties of di-propylene glycol compare well with the typical fluids used in dynamic wetting studies as Bracke et al. [1989]; Hoffman [1975]. Moreover, the low inertia of the moving mass of liquid allows tolerating less accurate modeling of not yet known inertial effects that may appear in the force balance of Equation 1. Figure 10 shows a small discrepancy between the model and the prediction at $t \approx 15s$. This difference is due to the different wetting conditions of the quartz surface for which, in this case, the height of the pre-wetted region is located at $h \approx 25mm$. The experimental recordings show that at each rise of the interface a liquid film is left behind until the next experimental run. The film might reduce the local friction of the interface and at each rise, the interface reaches a slightly higher position. The amount of film could not be precisely measured, but a qualitative estimation proposed that the thickness of the film depends on the number of times the fluid traveled within the tube.

Figure 11 compares the model prediction and the experimental data on the interface position retrieved from the PIV visualization of the experiment with HFE7200. The axis on the left reports the interface position while the one on the right reports the instantaneous vertical acceleration.

The Figure illustrates on the right axis the examined gravity profile and on the left the comparison of the model solution with experimental data on the interface position during the experiment. The model correctly shows the oscillation of the interface velocity due to minor oscillation in the gravitational level at about $t \in [6 - 8]$s. Nevertheless, the model significantly under-predicts the interface velocity after $t = 6$s. Since all terms in equation 1 have a comparable order of magnitude during the interface evolution, the accurate modelling of all terms is relevant. Considering that the assumption of self-similarity appears reasonable, the sources of the discrepancy are found either in modelling the pressure losses due to the bend or the treatment of the capillary forces. The first appears less plausible, given that the employed correlation has been well-calibrated in ground exper-

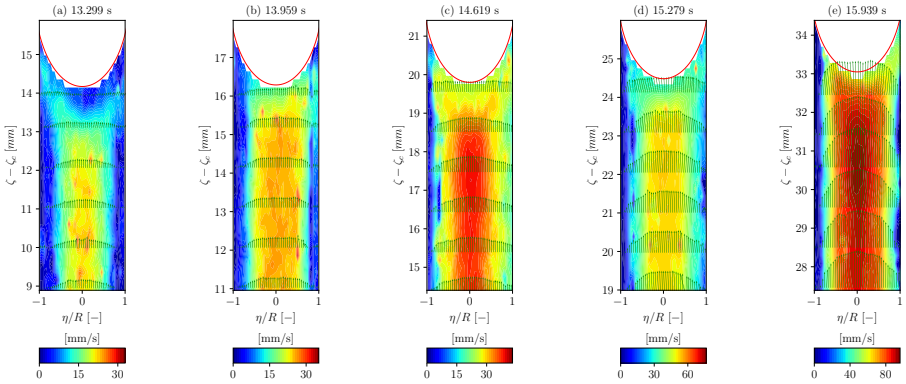

Figure 7: From left to right, the plot shows the axial velocity profile at extracted locations in the axis of the tube and a contour of the velocity magnitude beneath the advancing meniscus.

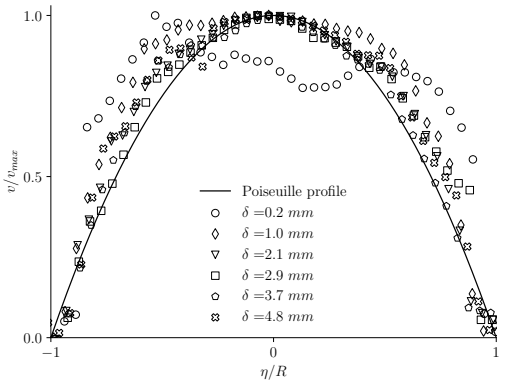

Figure 8: Comparison of experimental radial velocity profiles, sampled at various axial positions along the channel, with theoretical Poiseuille profile.

iments. Therefore, the mismatch is addressed here to the modelling of the capillary term and the impact of the different gravity levels on the interface shape.

For less viscous fluid HFE7200 the same film observed in the experiment of dy-propylene glicol could not be observed through the recordings. However, different levels of saturation of the inner surface of the tube between the different experimental runs are not excluded. Given that the film deposition seems to have an influence on the repeatability of the results, further investigation on the modeling and on introducing the presence of the film in the modeling should be taken into account in the future.

To conclude, Figure 12a and Figure 12b show the force balance on the liquid column computed from the solution of Equation 1 for the experiment shown in Figure 10 and Figure 10. The comparison is restricted to the initial region for $-5 < t < 5s$. The plots show that in both cases the magnitude of the capillary forces has a small step-like increment moving from iper-gravity to microgravity conditions. This is due to the increased curvature achieved by an almost spherical interface shape. The initial acceleration of the fluid column is mostly due to the sudden reduction of gravity force. The main difference between the two experiments concerns the balance of the capillary action (driving force) with the other forces. In the case of di-propylene glycol, the viscous force rises to the level of the capillary force which leads to an almost constant rising velocity. In the case of HFE7200, the magnitude of each force is lower, except for the gravity force, which depends only on the level difference between the two liquid interfaces and the fluid's densities (comparatively similar in this study). This feature implies that small oscillations in the gravity level easily counterbalance the capillary action. Moreover, in the case of HFE7200 the inertia of the flow represents the main balancing force with the capillary force and the fluid is affected by fast downward or upward-directed acceleration which, differently from the case of di-propylene glycol, is not compensated by an equally great viscous action.

5. Conclusion

In this work, we investigated the capillary rise dynamics in a divergent U-tube setup under microgravity conditions using time-resolved Particle Image Velocimetry (PIV). The configuration produces a flow driven by the difference in capillary forces between the two sides of the tube. We followed both the inter-

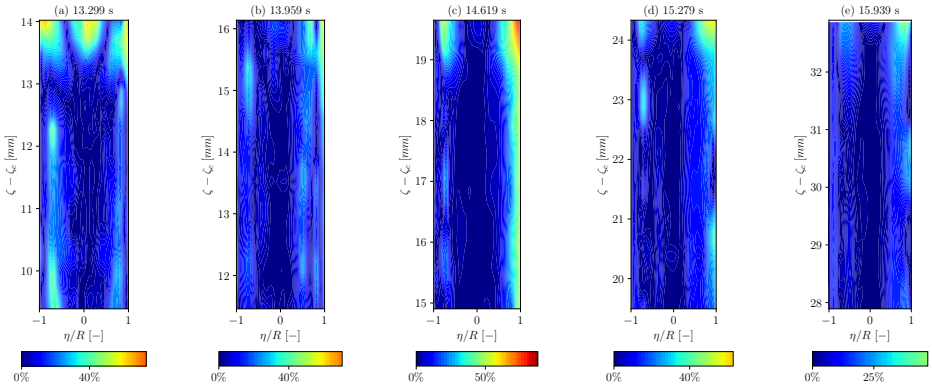

Figure 9: From left to right, the contour plots show the difference of the velocity profile with e corresponding Poiseuille profile at each axial location of the channel. The line plots show the increase of disagreement with the velocity profile moving from the bulk flow toward the meniscus.

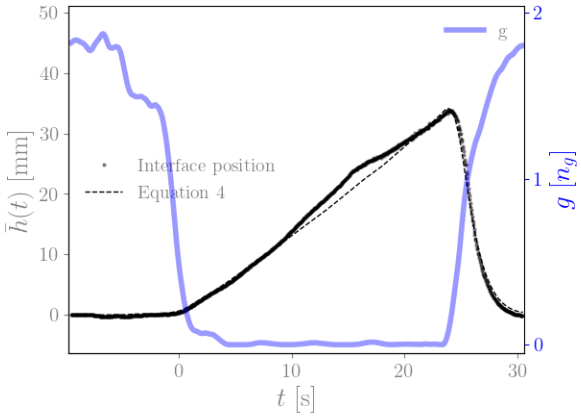

Figure 10: Capillary rise of Di-propylene glycol predicted with capillary rise *DUT* integral model. The small difference found at $t \approx 15s$ is due to the different wetting conditions of the quartz surface due to the previous experimental runs. Nevertheless, an overall good prediction is achieved.

face position and the velocity field during the capillary rise and compared the results with a simple 1D integral model based on self-similarity. The objective was to verify the validity of the self-similar velocity profile assumption and test the accuracy of a simplified 1D formulation of the capillary-driven flow.

The PIV measurements showed the assumption of a parabolic velocity profile until a distance of $\approx$ 1 mm from the interface, thus validating one of the main simplifying assumptions in these flows. The flow profile near the meniscus change from parabolic to nearly flat, with a strong acceleration near the contact line. This suggests that the flow field significantly differs from the wedge flow postulated in the derivation of theoretical models of dynamic wetting, which leads to contact angle correlations of the form $\theta_D = f(Ca)$.

The different prediction accuracies obtained for di-propylene glycol and HFE7200 can be attributed to the different role of inertial effects on the force balance at the interface. The force balance on the liquid column showed that in both cases the magnitude of the capillary forces had a small increment moving from hyper-gravity to microgravity conditions. However, in the case of HFE7200 the PIV visualizations showed the velocity field within the meniscus differing significantly from the theoretical wedge flow, at least at the scale of our observations.

In conclusion, this research has provided insights into the dynamics of the gas-liquid interface in diverging Utubes under microgravity conditions. The results have shown that the specific microgravity profile and the choice of the fluid have a significant impact on the interface motion.

Overall, these findings have important implications for the design and operation of space tanks, as they highlight the need to consider the specific microgravity profile and the fluid properties in order to achieve a stable capillary rise behavior. Additionally, the coupling of the free surface problem with the dynamic behavior of the contact line prompts for further research in wettability studies, such as capillary rise experiments, to deepen the understanding of the dynamics of the interface reorientation and the force balance.

Future study will analyze at a deeper level the capillary rise dynamics in the divergent U-tube using larger

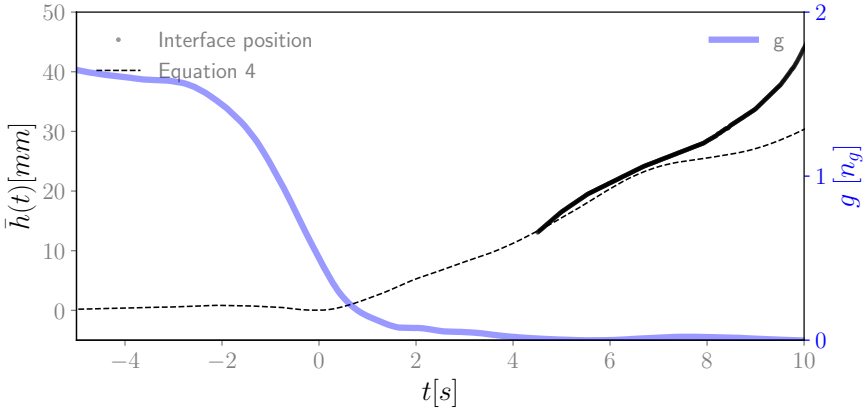

Figure 11: The Figure shows the comparison of the experimental interface position with the prediction achieved by solving eq. 1. The gravity profile corresponding to the time frame examined by the experiment is also shown in the back.

geometries. Parallely, the capillary rise dynamics in this benchmark test case will be also investigated numerically, assessing the impact of the modeling of the contact line and the interface.

Appendix

Acknowledgments

D. Fiorini is supported by Fonds Wetenschappelijk Onderzoek (FWO), Project number 1S96120N. This work was supported by the ESA and BELSPO via the Prodex program and by the ESA-GSTP "Physical and Numerical Modeling of cryogenic sloshing for Space applications" (Contract No. 4000129315/19/NL/MG). We would like to thank also Novaspace for their interest and support to the activities linked to this project, and for the fruitful discussions. The authors acknowledge also Michel Bavier, Louis Carbonnelle and Pedro Marques for the great support in the experiment preparation and execution.

References

Xiaoqiang Bian, William W. Schultz, and Marc Perlin. Liquid slug motion and contact lines in an oscillatory capillary tube. *Journal of Fluid Dynamics (under revision), http://wwwpersonal. umich. edu/schultz/Manuscripts/BianSchultzPerlin. pdf*, 146:151, 2003.

M Bracke, F De Voeght, and P Joos. The kinetics of wetting: the dynamic contact angle. In *Trends in Colloid and Interface Science III*, pages 142–149. Springer, 1989.

Markus M. Breunig, Hans-Peter Kriegel, Raymond T. Ng, and Jorg Sander. Lof: identifying density-based local outliers. In *Proceedings of the 2000 ACM SIGMOD international conference on Management of data*, pages 93–104, 2000.

Philippe Brunet and Michael Baudoin. Unstationary dynamics of drops subjected to mhz-surface acoustic waves modulated at low frequency. *Experiments in Fluids*, 63(1):1–14, 2022.

Stephen H. Davis et al. On the motion of a fluid-fluid interface along a solid surface. *Journal of Fluid Mechanics*, 65(1):71–95, 1974.

Giles Delon, Marc Fermigier, Jacco H Snoeijer, and Bruno Andreotti. Relaxation of a dewetting contact line. part 2. experiments. *Journal of Fluid Mechanics*, 604:55–75, 2008.

D. Fiorini, M. A. Mendez, A. Simonini, J. Steelant, and D. Seveno. Gas-liquid interface dynamics in non-isothermal sloshing: experimental analysis and simplified modeling. In *11th Symposium of VKI PhD Research 2020*, Waterloosesteenweg 72, Sint-Genesius-Rode, Belgium, 2020.

D. Fiorini, M. A. Mendez, A. Simonini, J. Steelant, and D. Seveno. Dynamic contact angle analysis using inverse methods. In *12th Symposium of VKI PhD Research 2021*, Waterloosesteenweg 72, Sint-Genesius-Rode, Belgium, 2021.

D. Fiorini, M. A. Mendez, A. Simonini, J. Steelant, and D. Seveno. Effect of inertia on the dynamic contact angle in oscillating menisci. *Physics of Fluids*, 34(10):102116, 2022a.

D. Fiorini, M. A. Mendez, A. Simonini, J. Steelant, and D. Seveno. Transient dynamics of contact angles. In *13th Symposium of VKI PhD Research 2022*, Waterloosesteenweg 72, Sint-Genesius-Rode, Belgium, 2022b.

D. Fiorini, M. A. Mendez, A. Simonini, J. Steelant, and D. Seveno. Dynamic wetting experiment with cryogenic nitrogen. In *to appear in EPJ Web of Conferences*. EDP Sciences, 2023.

P. S. Friese, E. J. Hopfinger, and M. E. Dreyer. Liquid hydrogen sloshing in superheated vessels under microgravity. *Experimental Thermal and Fluid Science*, 106:100–118, 2019.

J. W. Hartwig. Propellant management devices for low-gravity fluid management: past, present, and future applications. *Journal of Spacecraft and Rockets*, 54(4):808–824, 2017.

Richard L Hoffman. A study of the advancing interface. i. interface shape in liquid—gas systems. *Journal of colloid and interface science*, 50(2):228–241, 1975.

Jr D.E. Jaekle. Propellant management device conceptual design and analysis-galleries. In *33rd Joint Propulsion Conference and Exhibit*, page 2811, 1997.

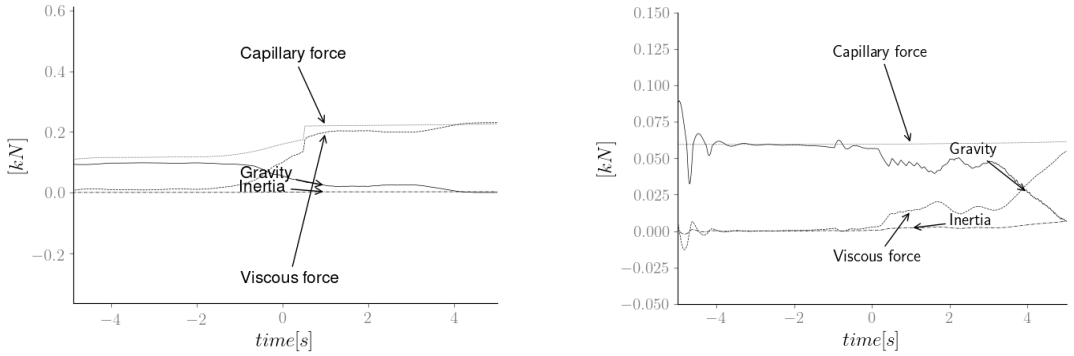

(a) Force balance for DPG capillary rise simulation.

(b) Force balance for HFE7200 capillary rise simulation

Figure 12: Evaluation of the main forces involved in the capillary rise of Di-propylene Glycol (Figure 12a) and HFE7200 (Figure 12b). The figure shows that in the case of viscous liquid the motion of the interface is determined only by capillary and viscous forces. In the case of less viscous HFE7200 all forces play an equally important role in determining the interface motion.

Tsung-Shann Jiang, OH Soo-Gun, and John C Slattery. Correlation for dynamic contact angle. *Journal of Colloid and Interface Science*, 69(1):74–77, 1979.

Stephan F. Kistler. Hydrodynamics of wetting. In John Berg, editor, *Wettability*, chapter 6, pages 311–430. Marcel Dekker, New York, New York, 1993.

N. Kulev and M. Dreyer. Drop tower experiments on non-isothermal reorientation of cryogenic liquids. *Microgravity Science and Technology*, 22(4):463–474, 2010.

N. Kulev, S. Basting, E. Bänsch, and M. Dreyer. Interface reorientation of cryogenic liquids under non-isothermal boundary conditions. *Cryogenics*, 62:48–59, 2014.

D. Levine, B. Wise, R. Schulman, H. Gutierrez, D. Kirk, N. Turlesque, W. Tam, M. Bhatia, and D. Jaekle. Surface tension and contact angle analysis with design of propellant measurement apparatus. *Journal of Propulsion and Power*, 31(1):429–443, 2015.

Ji-Cheng Li, Hai Lin, Jian-Fu Zhao, Kai Li, and Wen-Rui Hu. Dynamic behaviors of liquid in partially filled tank in short-term microgravity. *Microgravity Science and Technology*, 30(6):849–856, 2018.

Ji-Cheng Li, Hai Lin, Kai Li, Jian-Fu Zhao, and Wen-Rui Hu. Dynamic behavior in a storage tank in reduced gravity using dynamic contact angle method. *Microgravity Science and Technology*, 32(6):1039–1048, 2020.

Alex Liberzon, Davide Lasagna, Mathias Aubert, Pete Bachant, Theo Kaufer, Jakirkham, Bauer Andreas, Vodenicharski Boyko, Dallas Cameron, Borg Joe, Tomerast, and Ranleu. Openpiv/openpiv-python: Open-piv-python (v0. 22.2) with a new extended search piv grid option, 2020.

Roel Luppes, Joop A Helder, and Arthur EP Veldman. The numerical simulation of liquid sloshing in microgravity. In *Computational Fluid Dynamics 2006*, pages 607–612. Springer, 2009.

MA Mendez, Marco Raiola, Alessandro Masullo, Stefano Discetti, Andrea Ianiro, Raf Theunissen, and J-M Buchlin. Pod-based background removal for particle image velocimetry. *Experimental Thermal and Fluid Science*, 80:181–192, 2017.

Ralph Nasarek, Steve Wereley, and Peter Stephan. Flow field measurements near a moving meniscus of a capillary flow with micro particle image velocimetry (μpiv). In *International Conference on Nanochannels, Microchannels, and Minichannels*, volume 48345, pages 863–871, 2008.

Manuel Ratz, Domenico Fiorini, Alessia Simonini, Christian Cierpka, and Miguel A Mendez. Analysis of an unsteady quasi-capillary channel flow with time-resolved piv and rbf-based super-resolution. *Journal of Coatings Technology and Research*, 20(1):27–40, 2023.

Fulvio Scarano and Michel L Riethmuller. Advances in iterative multigrid piv image processing. *Experiments in fluids*, 29(1): S051–S060, 2000.

S. Schmitt and M. E Dreyer. Free surface oscillations of liquid hydrogen in microgravity conditions. *Cryogenics*, 72:22–35, 2015.

Michael Stange, Michael E Dreyer, and Hans J Rath. Capillary driven flow in circular cylindrical tubes. *Physics of fluids*, 15(9): 2587–2601, 2003.

LH Tanner. The spreading of silicone oil drops on horizontal surfaces. *Journal of Physics D: Applied Physics*, 12(9):1473, 1979.

Chao-Lung Ting and Marc Perlin. Boundary conditions in the vicinity of the contact line at a vertically oscillating upright plate: an experimental investigation. *Journal of Fluid Mechanics*, 295: 263–300, 1995. doi: 10.1017/S0022112095001960.

O.V. Voinov. Hydrodynamics of wetting. *Fluid dynamics*, 11(5): 714–721, 1976.

Prashant R Waghmare, Debjyoti Sen, David S Nobes, and Sushanta K Mitra. Experimental investigation of the flow front behind a liquid-air interface for capillary flow. In *International Conference on Nanochannels, Microchannels, and Minichannels*, volume 44793, pages 797–806. American Society of Mechanical Engineers, 2012.

Caixia Wang, Shenghua Xu, Zhiwei Sun, and Wenrui Hu. Influence of contact angle and tube size on capillary-driven flow under microgravity. *AIAA journal*, 47(11):2642–2648, 2009.

Nicholas C White and Sandra M Troian. Why capillary flows in slender triangular grooves are so stable against disturbances. *Physical Review Fluids*, 4(5):054003, 2019.

X. Zhong, B. Sun, and S. Liao. Analytic solutions of the rise dynamics of liquid in a vertical cylindrical capillary. *European Journal of Mechanics-B/Fluids*, 78:1–10, 2019.

NURBS-based immersed boundary method for arbitrarily shaped particles modelling

Lorenzo Vallisa

Environmental and Applied Fluid Dynamics, von Karman Institute for Fluid Dynamics, Waterloosesteenweg 72, 1640 Sint-Genesius-Rode, Belgium, lorenzo.vallisa@vki.ac.be

Supervisor: Delphine Laboureur

Professor, Environmental and Applied Fluid Dynamics, von Karman Institute for Fluid Dynamics, Waterloosesteenweg 72, 1640 Sint-Genesius-Rode, Belgium, delphine.laboureur@vki.ac.be

University Supervisor: Michel De Paepe

Professor, Department of Electromechanical,Systems and Metal Engineering, Ghent University, Sint-Pietersnieuwstraat 25, 9000 Ghent, Belgiuml

Abstract

This paper presents a numerical model for the advanced characterization of particle-fluid interaction called *sdfibm++*. An *Immersed Boundary Method* (IBM) is used to accurately identify the boundaries of the particle by means of a *Signed Distance Function*, whereas a *Non Uniform Rational B-Spline* (NURBS) algorithm accurately describes its complex geometry. This formulation allows to model momentum and thermal particle-fluid interaction at local scale. The two-way coupling happens through a discrete forcing approach. The numerical model is validated against numerical and experimental literature test cases for different particles' geometries, in isothermal and non-isothermal conditions.

Keywords: Immersed Boundary Method, NURBS, complex geometries, signed distance function, laminar non-isothermal flows

1. Introduction

Describing accurately the interaction between solid particles and the surrounding fluid is often an intriguing challenge. Indeed, the simplifying assumptions introduced to model the particle-fluid interaction often hide several fundamental aspects. Geometrical features of a particle for example may play an important role in describing collisions, or in the way particles may undergo a spatially non-homogeneous melting or solidification process.

In all industrial applications where these details are fundamental to correctly describe the physics at stake, a thorough description of the particle shape and geometry is not anymore a simplifiable term. In the field of nuclear research for example, after the Fukushima accident, relevant effort has been put in studying the effect of leaked radioactive particles of different shapes and sizes on the thermal stratification at the bottom of reactor's vessel to avoid its collapse [1]. Determining the exact particle's surface is one of the key factors in the design of plasma reactors for the dissociation process of methane into black carbon particles: the quality of the latter ones in fact not only depends on their final shape at the end of chemical reactions chain, but an accurate reproduction of their collisions helps determining the distribution of particles inside the reactor [2]. With the incoming transition to CO_2-free economies, several new technologies to store and transport hydrogen are being investigated: one of these is slush, a biphasic state in which the size of the hydrogen crystals determines the heat transfer coefficient [3] and their shape controls the sedimentation in storage tanks. Experimental studies in these fields are sometimes too expensive or not feasible due to safety reasons. Hence *Computational Fluid Dynamics* (CFD) becomes a fundamental assets for the

detailed analysis of these complex physical processes. *Discrete Element Method* (DEM), introduced by [4], models the collisions among rigid spheres as spring-dashpot interactions. DEM has been extensively used coupled with CFD to predict the behavior of fluid-particle interaction in a dense medium cyclone [5], as well as with *Smoothed Particle Hydrodynamics* (SPH) to simulate slurry flows in grinding operations of mineral processing [6]. However, the DEM does not identify the particles' boundary, thus it deals efficiently solely with spherical particles. Another way to model suspended particles is through adaptive mesh techniques like the *Arbitrary Lagrangian Eulerian* (ALE) method proposed by [7]. Continuous re-meshing and the degenerating quality of the mesh when following strong surface deformation represent however the main limitations of this method. A method that accurately captures the particle interface and is able to reproduce extreme topological deformation of the surface is the *Level Set Method* (LSM) [8]. LSM relies on a *signed distance function* (SDF) to distinguish between two fluids in the mixture. SDF has a positive value in one fluid and a negative value in the other one, and it provides a smooth variation of the physical properties across the interface, which is advected by solving a transport equation. Due to its ability to faithfully represent extreme topological distortion of surfaces, it has been mainly used to simulate droplets and bubbles dynamics [9].

Another numerical method initially introduced to model biological membrane and then extended to particle-fluid interactions is the *Immersed Boundary Method* (IBM) [10]. The idea behind IBM is to determine a force distribution at particle's boundary points, also called Lagrangian points, and to apply it to the flow equations in the fixed reference frame via a regularized Dirac delta function. The initial formulation aimed at determining the damping constant of a system of springs used to represent the force distribution across the particle's interface. Main drawbacks of this formulation were not only the need to resolve the characteristic time scales of the oscillations of the spring-damper systems, but also instabilities generated by the case-dependent tuning of damping constant [11]. To tackle these issues, a direct forcing IBM was first introduced by [12] and further developed by [13]. In this approach the body force term is directly deduced from the momentum equation by setting the velocity at boundary points to the desired velocity using interpolation functions. The main limitations of the first IBM approach were the inaccuracy of imposed boundary condition and some major issues connected with conservation of mass across the boundary [14]. To tackle these aspects, [15] proposed an iterative-procedure to satisfy the no-slip boundary conditions on the solid wall. [16] worked at a method in which a sharp-interface is modeled, whereas [17] developed a method based on a mobile unstructured two-dimensional grid located at the interface between the phases. [18] developed an energy conserving cut-cell method in two dimensions endowed with a control for moving boundaries. [19] recently proposed a numerical model able to finely resolve the particle-fluid and particle-particle interactions by means of an IBM empowered with a SDF function. In the standard direct-forcing procedure of IBM [13], the communication between the two phases at the rigid body's interface happens by means of a projection algorithm. The fluid information is gathered onto the Eulerian grid points, that are discretized points pertaining to the fluid domain, and projected through Dirac delta's function onto the Lagrangian points that identify the boundary of the rigid body. The information is then processed by the solid phase routines and communicated back by the exact same procedure. This projection technique, beside being cumbersome and very sensible to approximation error [20], implies a clear distinction between grid points representing the fluid variable (Eulerian grid points $\boldsymbol{x}$) and grid points located on the rigid body's surface (Lagrangian grid points $\boldsymbol{\xi}$), which need to be initialized and considered separately. Adopting a SDF to track the boundary of the particle using the already existing Eulerian grid points (see FIG.1) enables a simpler numerical model. When it comes then to modelling complex geometries and moving boundaries simulating particle-fluid interaction is still a subject under investigation in the world of CFD.

A way to model arbitrarily shaped particle is provided by the geometrical tool called NURBS (Non Uniform Rational B-Spline). NURBS algorithm, proposed firstly by [21], is widely used in CAD software to reproduce complex shaped geometries. This method allows for an analytical parametrization of non-spherical surfaces, increasing hence the potentiality to model any sort of complex geometry. Several studies have been proposed to study thermal-momentum coupling within an immersed boundary numerical method [22], and some algorithms have also been developed to model arbitrarily shaped particles [23], but to the author's knowledge no investigation has been carried out so far to tackle both problems at the same time. This work describes and validates a numerical solver which combines the advantages of

the SDF applied to the IBM and the accuracy provided by the NURBS algorithm to model thermal and momentum interactions between arbitrarily shaped particles and their surrounding fluid. In the following: section (2) describes the structure of the final solver *sdfibm++*, the numerical methods as well as the numerical routines. Section (3) presents three validation test-cases: a snow crystal falling in a still isothermal fluid and a non-isothermal flow past a sphere and past an ellipsoid. Drag coefficient and Nusselt numbers are compared with literature results.

2. Model description

In this section the set of equations solved for each of the two phases at stake is presented: a solid phase representing the rigid body (subscript p) and a liquid phase representing the surrounding fluid (subscript f). Secondly the numerical methods are introduced together with their interface with NURBS routines of the external library SISL [24], an open source library for the modelling and interrogation of curves and surfaces. An exhaustive outline of the *sdfibm++* solver is given at the end of this section.

2.1. Equations

The governing equations for the fluid phase are the unsteady three-dimensional Navier-Stokes equations for an incompressible flow with temperature dependent thermophysical properties, solved with OpenFOAM routines.

$$\nabla \cdot \boldsymbol{u} = 0 \tag{1}$$

$$\rho_f(T)\frac{D\boldsymbol{u}}{Dt} = -\nabla p + \mu_f(T)\Delta\boldsymbol{u} + \rho_f(T)\boldsymbol{g} + \boldsymbol{f_{IBM}} \tag{2}$$

$$\frac{DT}{Dt} = -\alpha(T,\tilde{\phi})\Delta T \tag{3}$$

where $\boldsymbol{f_{IBM}}$ and $\tilde{\phi}$ are the *coupling parameters* between the two phases. $\boldsymbol{u}$ is the fluid velocity,ρ_i the density of the i-th phase, p is the fluid pressure, Δ is the Laplacian operator, $\boldsymbol{g}$ is the gravitational force term, T is the temperature field, α the thermal diffusivity and μ_f the dynamic viscosity of the fluid. Following the nomenclature proposed by [25], the equations of motion for arbitrarily shaped particles for what concerns translational and angular momentum balance read as:

$$m_p\frac{d\boldsymbol{u_p}}{dt} = \int_{\Gamma_p}(\boldsymbol{\tau}^+[\boldsymbol{n}])dS + V_p(\rho_p - \rho_f)\boldsymbol{g} \tag{4}$$

$$I_p\frac{d\omega_p}{dtt} = \int_{\Gamma_p}\boldsymbol{r}\times(\boldsymbol{\tau}^+[\boldsymbol{n}])dS \tag{5}$$

where m_p is the particle mass, $\boldsymbol{u_p}$ is the particle's translational velocity, V_p is the particle volume, I_p is the moment of inertia, ω_p is the angular velocity of the particle, $\boldsymbol{\tau}^+$ the hydrodynamic stress tensor at the particle surface and Γ_p is the infinitely thin interface between the two phases. In equations (4) and (5) the mathematical notation of operator of higher order acting on an element belonging to a lower order space is adopted. The balance of forces on the particle reads as :

$$\int_{\Gamma_p}(\boldsymbol{\tau}^+[\boldsymbol{n}])dS = \frac{d}{dt}\int_{\Omega}(\rho_f\boldsymbol{u})dV - \int_{\Gamma_p}\boldsymbol{f}_s dS \tag{6}$$

where Ω is the inside of the rigid body domain. Equation (6) relates the drag force exerted on a rigid body p (LHS term) to the rate of change of linear momentum in an arbitrary region moving with the fluid (first term on the RHS)[1] and the force density yielding a stress jump in the fluid across the boundary (second term on the RHS). The last two terms come from the interaction with the fluid and need to be tuned with the *coupling parameters* introduced inside the Navier-Stokes equations.

2.2. Numerical methods

The formulation of the signed field function ϕ is the following one:

$$\phi = \begin{cases} -d_{PF} & \text{if } \boldsymbol{x}\in\Omega_f \\ 0 & \text{if } \boldsymbol{x}\in\Gamma_p \text{ then } \boldsymbol{x}=\boldsymbol{\xi} \\ d_{PF} & \text{if } \boldsymbol{x}\in\Omega_p \end{cases} \tag{7}$$

where Ω_f and Ω_p are respectively the fluid and particle domain. By computing the distance (d_{PF}) of each grid cell point to the particle boundary, the function ϕ detects whether an Eulerian grid point is also a Lagrangian point and hence represents the rigid body's boundary. Through a *Pyramid Decomposition Method* [19] the generated field ϕ is then converted into a field $\tilde{\phi}$ that varies continuously between 0 and 1. $\tilde{\phi}$ represents the volume fraction of the solid within the cell and reads as:

$$\tilde{\phi} = \begin{cases} 0 & \text{if } \boldsymbol{x}\in\Omega_f \\ \varepsilon & \text{if } \boldsymbol{x}\in\Gamma_p \\ 1 & \text{if } \boldsymbol{x}\in\Omega_p \end{cases} \tag{8}$$

[1] Note for a rigid body this contribution corresponds to the added mass term

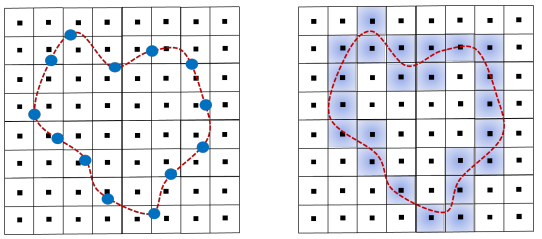

(a) (b)

Figure 1: a) Lagrangian points are a different set of grid points (blue dots) w.r.t. Eulerian grid points (black squares) in the standard IBM formulation. b) In formulation with SDF, Lagrangian points are identified with Eulerian grid points where the boundary of the rigid body is located

where:

$$\varepsilon_i = \frac{V_P}{V_{C,i}} \tag{9}$$

in which V_P is the particle's volume defined as follows:

$$V_p = \sum_i \tilde{\phi}(\boldsymbol{x}_i) V_{C,i} \tag{10}$$

$V_{C,i}$ represent the volume of the i-th cell of the meshgrid. This formulation ensures continuity of thermophysical properties across the interface, thus thermal diffusivity α introduced in equation (3) can be expressed as follows:

$$\alpha(T, \tilde{\phi}) = \alpha_p(T)\tilde{\phi} + \alpha_f(T)(1 - \tilde{\phi}) \tag{11}$$

Function $\tilde{\phi}$ is used moreover to define the particle density ρ_p in (4) through an average procedure over the density values from the cells belonging to the solid particle domain:

$$\rho_p = \frac{1}{V_p} \sum_i \tilde{\phi}(\boldsymbol{x}_i) \rho_i V_{C,i} \tag{12}$$

This technique simplifies typical IBM algorithms in which heat conduction is firstly computed inside the particle, temperature projected onto the Lagrangian points and final thermal energy equation is solved for the surrounding fluid [26]. By using a SDF this step is simplified as the thermal energy equation (convection and conduction in- and outside the particle) is solved only once for both phases (see equation (3)). The same function is used to close the coupling variable $\boldsymbol{f_{IBM}}$. It is in fact possible to link the density force function f_s used in the solid formulation to represent jump stress across the interface, with the volumetric force f_{IBM} for fluid structure coupling, by equating the two following terms:

$$\int_{\Gamma_p} \boldsymbol{f_s} dS = \int_L \boldsymbol{f_{IBM}} dV \tag{13}$$

where L is the layer of cells representing the boundary of the particle, computed as:

$$L = \sum_i V_{C,i} \tilde{\phi}_i \tag{14}$$

Following a direct-forcing approach used by [25], one can derive an expression of $\boldsymbol{f_{IBM}}$ through the following:

$$\boldsymbol{f_{IBM}} = \frac{\partial \boldsymbol{u}}{\partial t} - \boldsymbol{rhs} \tag{15}$$

which comes from a term re-organization of equation (2) in which the term $\boldsymbol{rhs}$ represents all the terms but the temporal derivative and the direct forcing term coming from the solid phase. Integrating over time and enforcing the no-slip boundary condition on the particle boundary, equation (15) becomes:

$$\boldsymbol{f_{IBM}} = \tilde{\phi}\left(\frac{\boldsymbol{u_{p,\Gamma_p}} - \boldsymbol{u}}{\Delta t}\right) \tag{16}$$

where $\boldsymbol{u_{p,\Gamma_p}}$ is the velocity of the particle computed on the boundary by the law of rigid body kinematics, Δt is the discretized timestep and $\boldsymbol{u}$ is the fluid velocity. One can note already that with this formulation there is no need to project the obtained force distribution across the interface, obtaining thus a correct enforcement of the no-slip boundary condition. An operator splitting scheme is used to advance the solution of the Navier–Stokes equations in temporal discretization. This method can accelerate the computational process via the operator splitting to decouple the pressure calculation from that of the velocity field. The spatial derivatives are evaluated by means of second-order operators on a staggered grid. Governing equations for liquid are solved using a Crank-Nicholson method, whereas equation for single particle motion is discretized using a forward Euler scheme, leading thus to an overall formal first-order temporal accuracy. Fluid-momentum, fluid-thermal and particle-motion equations are fully coupled but treated in an explicit way. Given a timestep $\Delta t = t^n - t^{n-1}$, at the n-th iteration the computational algorithm is described from equation (17) to equation (21). Velocity, pressure and temperature update as follows:

$$\tilde{\boldsymbol{u}} = \boldsymbol{u}^{n-1} - \Delta t[\frac{1}{2}((\tilde{\boldsymbol{u}} \cdot \nabla)\tilde{\boldsymbol{u}} + (\boldsymbol{u}^{n-1} \cdot \nabla)(\boldsymbol{u}^{n-1})) + \frac{1}{2}\nu^{n-1}(\Delta\tilde{\boldsymbol{u}} + \Delta\boldsymbol{u}^{n-1}) - \frac{\nabla p^{n-1}}{\rho^{n-1}} + \boldsymbol{g}] \tag{17}$$

$$\Delta p^n = -\nabla \cdot \boldsymbol{f_{IBM}^{n-1}} \tag{18}$$

$$\boldsymbol{u^n} = -\tilde{\boldsymbol{u}} + f(p|^n_{flux}) \tag{19}$$

$$T^n = T^{n-1} - \Delta t[\frac{1}{2}((\boldsymbol{u}^n \cdot \nabla)T^n + (\boldsymbol{u}^{n-1} \cdot \nabla)T^{n-1}) + \frac{1}{2}\alpha^{n-1}(\tilde{\phi}^{n-1})(\Delta T^{n-1} + \Delta T^n)] \tag{20}$$

For what concerns particle motion, translational and angular velocity are computed as:

$$\boldsymbol{u}^n_p = \frac{\boldsymbol{u}^{n-1}_p}{m_p} - \frac{\Delta t}{m_p}[\int_L \rho^n_f \boldsymbol{f^{n-1}_{IBM}} dV + \frac{d}{dt}\int_{\Omega_f} \rho^n_f \boldsymbol{u}^n dV + V_p(\rho^n_p - \rho^n_f)\boldsymbol{g}] \tag{21}$$

$$\boldsymbol{\omega^n_p} = \frac{\boldsymbol{\omega^n_p}}{I_p} - \frac{\Delta t}{I_p}[\int_L \rho^n_f(\boldsymbol{r} \times \boldsymbol{f^{n-1}_{IBM}})dV + \frac{d}{dt}\int_{\Omega_f} \rho^n_f(\boldsymbol{r} \times \boldsymbol{u}^n)dV] \tag{22}$$

$$\boldsymbol{x^n_p} = \boldsymbol{x^{n-1}_p} + \Delta t(\boldsymbol{u}^n_p) \tag{23}$$

According to the new particle position $\boldsymbol{x}^n_p$ the function $\tilde{\phi}$ is recomputed and used to update the $\boldsymbol{f}_{IBM}$ term:

$$\tilde{\phi}^n = \Lambda[\boldsymbol{x}] \tag{24}$$

$$\boldsymbol{f_{IBM}}^n = \tilde{\phi}^n \left(\frac{\boldsymbol{u_{p,\Gamma_p}}^n - \boldsymbol{u}_n}{\Delta t} \right) \tag{25}$$

where the operator Λ is a geometrical operator that identifies whether a grid point is either an Eulerian grid point (belonging to the fluid) or a Lagrangian grid point (belonging to the particle), $f(p|^n_{flux})$ is the function extracting the pressure fluxes out of the pressure scalar field.

2.3. Algorithms for geometry definition

The definition of the geometry uses uniform B-splines[2] basis functions built using parametrized coordinates u and v as independent coordinates, also called *knotvectors*. Basis functions should provide that surfaces have normal and tangent vectors defined everywhere. Their definitions moreover need to be invariant w.r.t. transformations like translations, rotations and scalings (affine invariance). Moreover, each basis function has to be nonzero only on a limited number of sub-intervals. A basis function N that matches all these requirements is defined as follows:

[2]Uniform B-spline function are a generalization of non-uniform rational B-splines functions (NURBS), usually more stable and precise than these latter ones

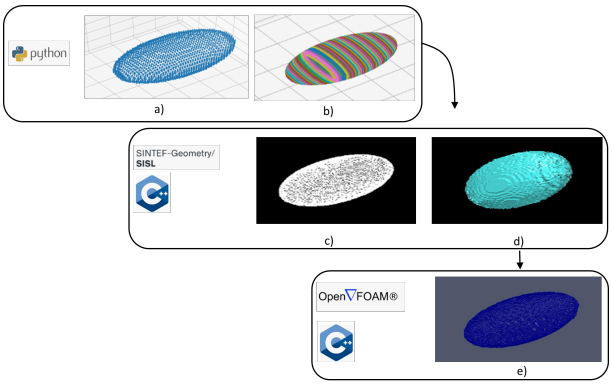

Figure 2: Algorithms for shape assembly: a) Initialization through Voxel file of control point b) Gathering control points into curves c) Definition of shape within SISL library through set of curves d) Creation of the surface object variable inside the SISL library e) Final particle object in sdfibm++

$$N_{i,0}(u) = \begin{cases} 1 & \text{if } u_i \leq u < u_{i+1} \\ 0 & \text{otherwise} \end{cases} \tag{26}$$

$$N_{i,q}(u) = \frac{u - u_i}{u_{i+q} - u_i} N_{i,q-1}(u) + \frac{u_{i+q+1} - u}{u_{i+q+1} - u_{i+1}} N_{i+1,q-1}(u) \tag{27}$$

where q is the order of the basis function. Using such a mathematical tool to describe surfaces provides an analytical[3] expression of the surface itself. The B-spline surface is defined as a function of u and v knotvectors in the following way:

$$S(u,v) = \sum_{i=0}^{n} \sum_{j=0}^{m} N_{i,p}(u) N_{j,q}(v) \boldsymbol{P}_{i,j} \tag{28}$$

where $\boldsymbol{P}_{i,j}$ is a 3rd order tensor of scalars, or equally a 2nd order tensor of 3D coordinates corresponding to the control points given in input. The set of control points $\boldsymbol{P}_{ij}$ is initialized by parsing a voxel file, which can be obtain from the conversion of any STL file format representing the particle's shape. The set of 3D coordinates of particle's control points are then converted into a suitable mathematical structure used as input for the open source NURBS library SISL. First, control points are converted into a set of curves interpolating them with third order polynomial basis (steps a)-b) in FIG. 2). Then, the set of curves is passed as input to the SISL library's routines which create a fully parametrized closed surface (steps c)-d) in FIG. 2). The closed surface is transformed into an object

[3]piecewise C^1

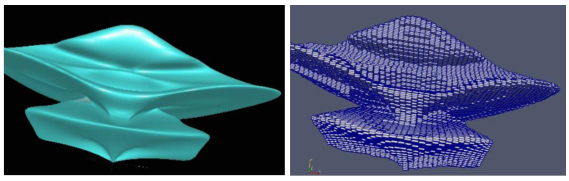

(a) (b)

Figure 3: Concavities detection algorithm: surface with strongly non-linearities reproduced through a) SISL library b) *sdfibm++*

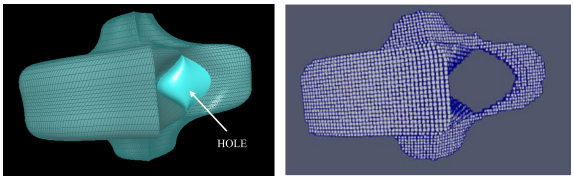

(a) (b)

Figure 4: Hole detection algorithm: rigid body with a hole in it reproduced through a) SISL library b) *sdfibm++*

Algorithm 1: Routines embedded in operator Λ to retrieve final signed function field $\tilde{\phi}$

Given a grid point $\boldsymbol{x}$, operator Λ does:

Step 1. Identify the intersection points between the surface and straight line interpolating point $\boldsymbol{x}$ and the center coordinates of the solid object.

Step 2. Compute the distance between the point $\boldsymbol{x}$ and the detected intersection points on the particle surface

Step 3. Elaborate the number of intersection points to identify whether a point belongs to the fluid, to the particle or to the interface, and in the latter case uses the information of the distance to compute the volume fraction of the cell pertaining to the point $\boldsymbol{x}$.

variable, which is then interfaced with the routines of the multiphase solver for the final initialization of the particle (step e) in FIG. 2). Operator Λ mentioned in equation (24) takes as input a grid point $\boldsymbol{x}$, and operates the routines listed in Algorithm 1 to eventually output the scalar field $\tilde{\phi}$. These three routines mentioned in 1 are then extended by a *concavity detection algorithm* (see FIG. 3) and a *hole detection algorithm* (see FIG. 4). It is important that the algorithm is able to detect strong surface's non-linearities and topological changes that a particle may undergo when, for example, subjected to melting or mechanical deformation. The solver *sdfibm++* can be therefore split into

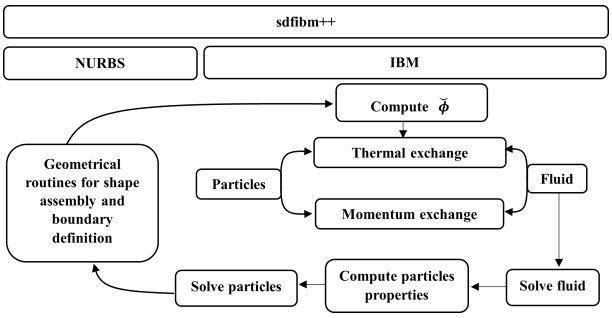

Figure 5: *sdfibm++* solver main structure

two main parts: a part dedicated to the implementation of the geometry and identification of the boundary points, and a second part in which this information is used to create the particle inside the multiphase solver discussed in section 2. A recap of the main structure of the *sdfibm++* solver is proposed in FIG. 5.

3. Validation results

In this section, validation results obtained for three different test-cases are presented. Different shapes are simulated in three-dimensional domains in isothermal and non-isothermal flows and compared to literature in terms of drag coefficient and Nusselt number. To compute the drag coefficient [27] and the Nusselt number [28] the following two formulas are used:

$$F_D = -\int_\Gamma \rho_f u_i \boldsymbol{u} \cdot n_\Gamma dS - \int_\Gamma p n_i dS + \int_\Gamma \mu_f (\nabla \boldsymbol{u} + \nabla \boldsymbol{u}^T)|_i n_i dS \quad (29)$$

$$C_D = \frac{F_D}{\frac{1}{2} S_p v_{x,in}^2 \rho_p} \quad (30)$$

$$Nu = \frac{h_{Avg} L_{Ref}}{k_f} \quad (31)$$

where Γ is an arbitrary closed surface, μ_f is the dynamic viscosity of the fluid, i is the direction taken parallel to the flow in a Cartesian frame of reference, L_{ref} is the reference length for the considered geometry,S_p the particle surface, $v_{x,in}$ the uniform inlet velocity, F_D the drag force term, k_f the fluid thermal conductivity and h_{Avg} is the average convective

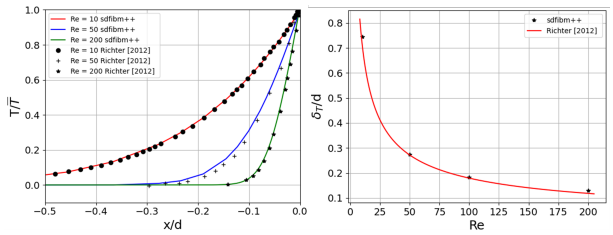

(a) (b)

Figure 6: a) Frontal non-dimensional temperature comparison for sphere case (d is particle diameter). b) Frontal thermal boundary layer thickness comparison for sphere case

heat transfer coefficient computed in the following way:

$$h_{Avg} = \frac{k_f}{T_B - T_\infty}\left[\frac{1}{\Gamma_p}\int_{\Gamma_p}(\nabla T^+ \cdot \boldsymbol{n})dS\right] \tag{32}$$

where T_B is the temperature on the particle's boundary and T_∞ the freestream temperature. The thermal gradients in equation (32) are computed outside of the particle (∇T^+). To evaluate the heat flux at the surface, the particle boundary is identified through the signed field function $\tilde{\phi}$ presented in section 2: according to its definition it is possible to identify the particle's boundary by searching for those grid points $\boldsymbol{x_i}$ such that:

$$0 < \tilde{\phi}(\boldsymbol{x_i}) < 1, \text{ then } x_i \in \boldsymbol{X}$$

where $\boldsymbol{X}$ is the set containing all boundary grid points elements. Then the computation of velocity and thermal gradients from equations (30) and (31) is carried out only on grid points belonging to the set $\boldsymbol{X}$, onto which the average procedure is carried out. A discretized formulation of the averaged convective heat transfer coefficient of equation (32) is the following:

$$h_{Avg} = \frac{k_f}{T_B - T_\infty}\left[\frac{1}{N}\sum_{n}^{N}\frac{(T_n - T_B)}{\delta_n}\right] \tag{33}$$

where $N = |X|$ and

$$T_n \in \overline{T} = [T_i : \boldsymbol{x}_i \in \boldsymbol{X}] \tag{34}$$

$$\delta_n \in \overline{\delta} = [\delta_i = |(\boldsymbol{x}_i - \boldsymbol{x}_B) \cdot \boldsymbol{n}_{\Gamma_p}| : \boldsymbol{x}_i \in \boldsymbol{X}] \tag{35}$$

Note that, thanks to the accurate definition of the parametrized surface through NURBS algorithm, once identified the point on the boundary the value of the normal unit vector on that location ($\boldsymbol{n}_{\Gamma_p}$) can be obtained through the SISL library routines.

3.1. Spherical particle in flow with heat transfer

The first test case presents a flow past a sphere. According to the reference test-case from the study done by [29], the particle is placed in a cross-flow of air at 25°C. The particle has constant and fixed temperature of 125°C in its entire domain, including its surface. The frame of reference is Cartesian and the incoming flow, entirely determined by the inflow, is parallel to the x axis. In the freestream region gradients of velocity and temperature are assumed to be zero, therefore all domain boundaries except inlet and outlet are symmetry boundaries. No buoyancy effect is considered and density, as well as all thermophysical properties, are constant[4] in the whole domain. The flow is initially still. At the inlet of the domain, a uniform velocity is set with only the cross-wise component different from zero. At the outlet of the domain, an atmospheric uniform pressure is set. Thanks to the IBM formulation, there is no need to impose any boundary condition on the particle's boundary, since both thermal and momentum interactions are directly computed as shown in section 2. According to mesh convergence results obtained by [29], the domain size is chosen as 30d x 12d x 30d, where d is the sphere diameter. The number of cells of the uniform tetrahedral mesh is approximately $61e^6$ An high level of refinement is necessary to correctly capture the velocity and temperature gradients respectively in the momentum and in the thermal boundary layer, but also to be able to accurately describe the topological features of the particle's surface. Simulations are run with a steady incompressible solver (SIMPLE) and for the range of Reynolds of interest ($Re < 210$) the flow is laminar, steady-state and axisymmetric. To ensure the correct mesh refinement on the particle boundary, the thickness of the thermal boundary layer as well as the profile of temperature in the forward region of the particle are computed and compared with literature results. In FIG. 6a the non-dimensional profile of temperature along the x-axis centerline is shown for different Reynolds (Re) numbers, where $Re = \frac{ud}{\nu_{Air}}$. For this specific test-case Reynolds number is changed by choosing different values of velocity and reference diameter only. In FIG. 6b the non-dimensional profile of thermal boundary layer thickness along the centerline is presented. Both obtained numerical results show good agreement with those presented by [29], confirming hence that the level of refinement chosen is fine enough to correctly capture the physics at stake.

[4] Properties are considered for air at 25°C and atmospheric pressure

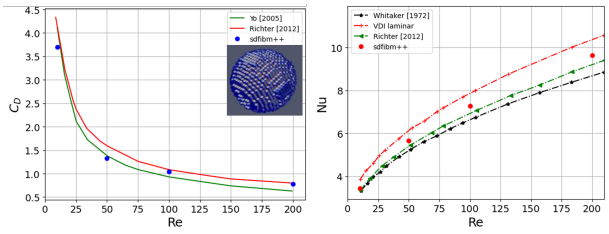

(a) (b)

Figure 7: Validation results for sphere case: a) C_D-Re correlation and b) Nu-Re correlation

The next step is to compute the Nusselt number and the drag coefficient using the discretized formula of equations (31) and (30) following the procedure for boundary tracking shown in equation (33). On the surface Γ_p the first term on the right-hand-side of equation (30) is six order of magnitude smaller than the other two terms, proving the correct enforcement of the no-slip boundary condition. Results are showed in FIG. 7: the overall agreement is within a maximum deviation for the drag coefficient of 8 % with $Re = 10$, and of only 2 % for the Nusselt number with $Re = 200$. A further and final check is proposed in FIG. 8, where the isothermal lines numerically obtained at steady state for cases of $Re = 50$ and $Re = 200$ are plotted against those proposed in the reference paper [29]. Each line i has a temperature value computed according to the following formula:

$$T_i = T_\infty + x_i(T_B - T_\infty)$$

where x_i is the label on the line.

3.2. *Snowflake free-fall in isothermal flow*

The second test case is a snowflake shaped crystal falling in isothermal flow. The validation case is the work done by [30],where the particle shape and the settling velocity are given for $Re < 600$. In all experiments a snowflake is let fall inside a tank until it has reached its terminal velocity. No relevant oscillation nor rotation were observed, which allowed to focus the study on the sole vertical motion of the particle. The drag coefficient is in fact measured when the force balance between the gravitational force and the drag force is reached:

$$C_D = \frac{2gV_P(\rho_p - \rho_f)}{\rho_f v_T^2 S_p} \tag{36}$$

where v_T is the particle terminal velocity and S_p the cross-sectional area of the particle. To reproduce

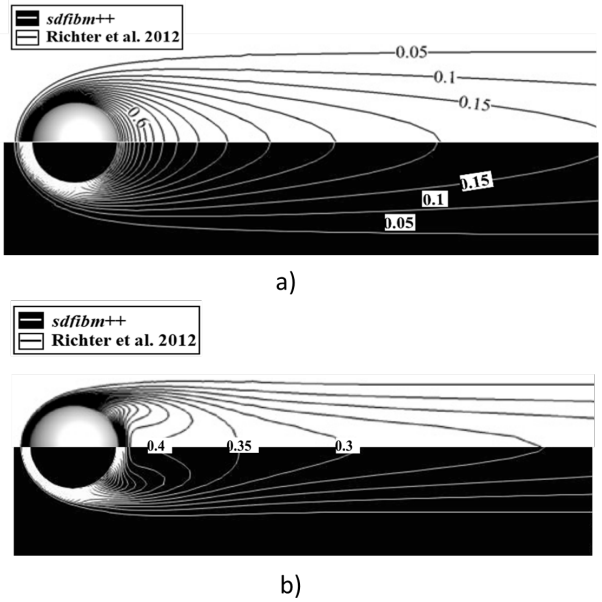

Figure 8: Isothermal lines comparison for sphere case: labels on each line represent the evolution from freestream temperature (0) to the particle's boundary temperature (1). a) Re = 50 b) Re = 200

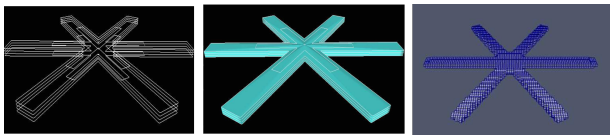

(a) (b) (c)

Figure 9: Snowflake shape assembly: a) Set of curves assembled out of control points b) Surface object in SISL library c) Particle initialized in sdfibm++

the above mentioned experimental test-case a uniform tetrahedral meshgrid of size 4d x 6d x 4d has been chosen, where d is the reference length of the geometry defined as the diameter of the circle circumscribed to the particle. It has been proven that the external's domain boundary patches do not interfere with the dynamics of the falling particle. The number of cells of the discretized domain is $4.5e^6$. This high density of cells is justified by the fact that the trajectory of the snowflake needs to be tracked, hence the refinement region could not be limited to a part of the domain. The cell width h [5] has been therefore chosen such that the level of refinement is high enough to correctly represent the shape and the physic of interest. The frame

[5] By using an uniform tetrahedral mesh h can be computed as $h = (\frac{V_D}{N_C})^{1/3}$ where N_C is the number of cells in the domain

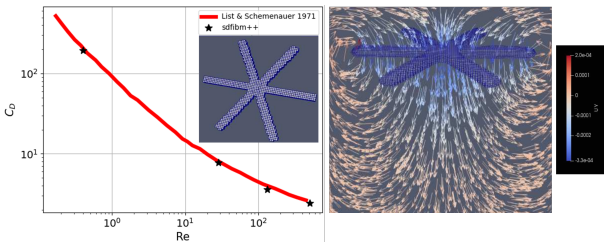

(a) (b)

Figure 10: Snowflake free fall in isothermal fluid: a) Validation of C_D-Re correlation b) Quiver plot on xz plane showing correct enforcement of no-slip boundary condition on particle's boundary (Color-plot shows vertical velocity u_y)

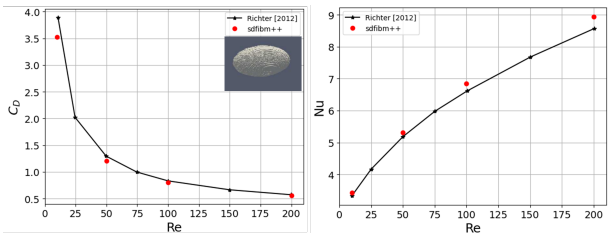

(a) (b)

Figure 11: Validation results for ellipsoid case: a) C_D - Re b) Nu-Re

of reference is Cartesian and gravitational force on the particle entirely determines the flow, which is set parallel to y-axis. The solver chosen is an unsteady incompressible one (PIMPLE) and simulations are run with $CFL = 0.5$: as highlighted by [20] it is in fact important to keep the timestep not too high to let the solid physics correctly follow the much faster fluid dynamic. The particle is initiated into a cuboid where all patches have symmetry boundary conditions: the time needed for the particle to reach stationary velocity is in fact sufficient for the particle to never interact with the boundaries. The fluid is initially still and at the same temperature of the particle, so that thermal interaction is not considered for this specific test-case. No turbulence model is needed for the range of considered Reynolds. The Reynolds number expression is the following:

$$Re = \frac{v_T d}{\nu_f} \tag{37}$$

which means that the value of terminal velocity v_T is uniquely determined by the values of fluid kinematic viscosity ν_f, particle density ρ_p and fluid density ρ_f. The values of these three thermophysical variables used to reproduce the four different Reynolds flow regimes are listed in TABLE 1. The geometry

ν_f [Pa s]	ρ_f [Kg/m3]	ρ_p [Kg/m3]	Reynolds
1.5e-5	896	897	0.4
1e-6	1000	1001	28.4
1e-6	1000	1010	132
1e-6	1000	1100	508

Table 1: Thermophysical properties used for the two phases to reproduce the Reynolds flow regime of interest

is shown in FIG. 9, which corresponds to the *stellar crystal* profile in the work of [30]. To build the geometry, 2000 control points have been used, and converted into a set of curves compatible for with the SISL input. FIG. 10a shows the comparison between the drag coefficient measured in the reference work [30] and the numerical results for different Reynolds number, hence validating the *sdfibm++* implementation. FIG. 10b illustrates a quiver plot on the xz plane showing that the no-slip boundary condition is correctly enforced at the particle's boundary during its vertical motion.

3.3. Ellipsoidal geometry in flow with heat transfer

The third refenrence test case is the flow past a heated elliposide particle described in the work of Richter [29] (identified as *Elliposid 1*). The domain size, discretization and boundaries are the ones used for the flow past a sphere described in Section 3.1. The geometry has been built using over 25000 control points to enable a smooth particle interface. The reference length in the Reynolds number is the diameter of the sphere whose volume is equivalent to the volume of the ellipsoid. FIG 11 shows the comparison between the reference test case and the present study in terms of Nusselt number and drag coefficient. The overall agreement is within 7.5% of deviation for the drag coefficient and 3.5% deviation for the Nusselt number. FIG 12 compares the isothermal lines at Re = 100 and Re = 200. The procedure to derive the isothermal lines is similar to the one explained in section 3.1.

4. Conclusions

In the present work a NURBS-based immersed boundary method was developed to model thermal and momentum interactions between a solid body of complex geometrical shape and its surrounding fluid. The use of a singed distance field function to track the boundary of the solid particle overcame several

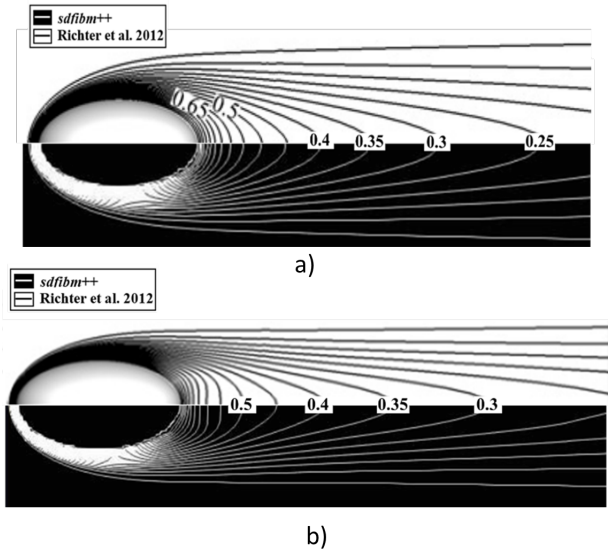

Figure 12: Isothermal lines comparison for ellipsoid case:labels on each line represent the evolution from freestream temperature (0) to the particle's boundary temperature (1). a) Re = 100 b) Re = 200

of the issues that the widely used projection algorithm for IBM was giving, helping moreover to simplify the formulation of the particle-fluid interaction. The presented validation test cases showed that the no-slip boundary condition is respected at the particle boundaries. Moroever, the interaction between the particle and the fluid is modeled with a single equation. The real innovation introduced by this research is the possibility to describe particle's arbitrary shapes by means of routines embedded in the NURBS algorithm formulation. Given in fact a set of 3D coordinates representing the boundary of the particle, the algorithm was able to successfully convert them into an object variable that can be read by the solver as a particle variable. The current numerical method *sdfibm++* is thought as a continuation and an extension of the work started by [19]. The implementation presented in this work focuses first on the geometry definition algorithm developed in Python language and through a C++ NURBS library named SISL. A second part is instead focused on the explicit coupling between the solid and the OpenFOAM fluid routines in a operator-splitting context by means of finite-difference and finite-volume schemes. The solver was eventually validated against three well-known literature test-cases. The NURBS routines were tested first with a spherical geometry and then with ellipsoidal and snow crystal shapes. The obtained particles were then initialized in three-dimensional domains in isothermal (snow crystal) and fully thermally coupled (sphere and ellipsoid) flows. For the isothermal flow test-case drag coefficient was computed and its correlation against Reynolds number shown, whereas for the non-isothermal one also the Nusselt-Reynolds correlation was presented. Both results were compared with very good level of agreement with literature ones. Extending the method to multiple-particle interaction is under way as well as the design of advanced routines for creation of highly deformed particles. Future perspectives of this work also include the implementation of phase change in the *sdfibm++* solver.

5. Acknowledgements

This research is part of the BE-HyFE project, which is a Belgian academic collaboration project, funded by the federal Energy Transition Fund by FPS Economy.

References

[1] L. Vallisa, Radioactive particle dynamics and interactions with liquid metal coolant LBE within MYRRHA nuclear reactor, Tech. rep., Best pitch awarded poster presented at the Nuclear Reactor Thermal Hydraulics 19 (NURETH) conference held in Brussels in collaboration with SCK-CEN (2022).

[2] T. H. B. D. J. Fincke, R. Anderson, Plasma Pyrolysis of Methane to Hydrogen and Carbon Black, American Chemical Society.

[3] M. Scelzo, Experimental and numerical investigation of slurry flows in pipelines: a contribution toward slush propellants for future rocket engines, Ph.D. thesis, von Karman Institute for Fluid Dynamics (2020).

[4] O. S. P.A. Cundall, A discrete numerical model for granular assemblies, Geotechnique 29 (1) (1979) 47–65.

[5] A. Y. K. Chu, J. Chen, Applicability of a coarse-grained CFD–DEM model on dense medium cyclone, Minerals Engineering.

[6] W. Cleary, Prediction of coupled particle and fluid flows using DEM and SPH, Minerals Engineering 73 (2015) 85–99.

[7] N. Z. H. Hu, N. Patankar, Direct numerical simulation of fluid-solid systems using the arbitrary Lagrangian Eulerian technique, Journal of Computational Physics 79 (1988) 12–49.

[8] S. S. S. Osher, Fronts propagating with curvature-dependent speed: algorithm based on Hamilton-JAcobi formulations, Journal of Computational Physics 169 (2001) 427–462.

[9] J. P. W. Zheng, J. Yong, Simulation of bubbles, Graphical Models 71 (2009) 229–239.

[10] C. Peskin, Flow patterns around heart valves: a digital computer method for solving the equations of motion, Ph.D. thesis, Albert Einstein College of Medicine (1972).

[11] J. W. C. Ji, A. Munjiza, A novel iterative direct-forcing immersed boundary method and its finite volume applications, Journal of Computational Physics 231 (2015) 1797–1821.

[12] P. J. M.-Y. E. Fadlun, R. Verzicco, Combined immersed-boundary finite-difference methods for threedimensional complex flow simulations, Journal of Computational Physics 161 (2000) 35–60.

[13] M. Uhlmann, An immersed boundary method with direct forcing for the simulation of particulate flows, Journal of Computational Physics 209 (2005) 448–476.
[14] J. F. T. Kempe, An improved immersed boundary method with direct forcing for the simulation of particle laden flows, Journal of Computational Physics 231 (2012) 3663–3684.
[15] Y. C. C. Shu, N. Liu, A novel immersed boundary velocity correction-lattice Boltzmann method and its application to simulate flow past a circular cylinder, Journal of Computational Physics 226 (2007) 1607–1622.
[16] R. M. H.S. Udaykumar, A shapr interface Cartesian grid method for simulating flows with complex moving boundaries, Journal of Computational Physics 174 (2001) 345–380.
[17] G. T. S.O. Unverdi, A front-tracking method for viscous, incompressible, multi-fluid flows, Journal of Computational Physics 100 (2007) 2999–3011.
[18] O. B. Y. Cheney, The LS-STAG method: a new immersed boundary/level-set method for the computation of incompressible viscous flows in complex moving geometries with good conservation properties, Journal of Computational Physics 229 (2010) 1043–1076.
[19] C. Zhang, sdfibm: a signed distance field immersed boundary field based discrete forcing immersed boundary method in OpenFOAM, Journal of Computational Physics 255.
[20] S. B. K. Zhou, An analysis of the spatio-temporal resolution of the immersed boundary method with direct forcing, Journal of Computational Physics 255.
[21] W. T. L. Piegl, The NURBS book, Springer Verlag, 1997.
[22] T. R.-R. P. J. Pacheco, A. Pacheco-Vega, NUMERICAL SIMULATIONS OF HEAT TRANSFER AND FLUID FLOW PROBLEMS USING AN IMMERSED-BOUNDARY FINITE-VOLUME METHOD ON NON-STAGGERED GRIDS, Numerical heat transfer 48 (2005) 1–24.
[23] S. W.-V. S. H. Kruggel-Emden, S. Rickelt, A study on the validity of the multi-sphere Discrete Element Method, Powder Technology 188 (2008) 153–165.
[24] SINTEF, Sisl - the sintef spline library (2022).
URL https://www.sintef.no/en/software/software-applied-mathematics/sisl/
[25] Kempe, A non-iterative immersed boundary method for spherical particles of arbitrary density ratio, Journal of Computational Physics 17.
[26] W. Y. W. Ren, C. Shu, An efficient immersed boundary method for thermal flow problems with heat flux boundary conditions, International Journal of Heat and Mass Transfer 64.
[27] C. P. M. Lai, An Immersed Boundary Method with Formal Second-Order Accuracy and Reduced Numerical Viscosity, Journal of computational physics 160.
[28] B. F. M. Cheng, HEAT TRANSFER IN FLOW PAST CYLINDERS AT Re ¡ 150 - Calculations for constant fluid properties, Numerical Heat Transfer 12.
[29] P. N. A. Richter, Drag forces and heat transfer coefficients for spherical, cuboidal and ellipsoidal particles in cross flow at sub-critical Reynolds numbers, International Journal of Heat and Mass Transfer 55 (2012) 1343–1354.
[30] R. S. R. List., Free-fall behavior of planar snow crystals, conical graupel and small hail, Atmospheric Science Journal 28.

Data assimilation for the thermodynamic modeling of a cryogenic fuel tank

Pedro Afonso Marques

Environmental and Applied Fluid Dynamics Department, von Karman Institute for Fluid Dynamics, Belgium, pedro.marques@vki.ac.be

Supervisor: Miguel Alfonso Mendez

Associate Professor, Environmental and Applied Fluid Dynamics Department, von Karman Institute for Fluid Dynamics, Belgium, miguel.alfonso.mendez@vki.ac.be

University Supervisor: Benoit Scheid

Professor, Transfers, Interfaces & Processes (TIPs) laboratory, Université libre de Bruxelles, Belgium, benoit.scheid@ulb.be

Abstract

Cryogenic fuels have become promising alternatives to traditional fossil fuels due to their low emissions, high specific energy and efficiency. However, the design and operation of cryogenic fuel tanks presents significant challenges due to their complex thermodynamic behavior. In this article, we present the first steps to the thermodynamic characterization of such systems through a combination of experimental techniques and physical modelling combined with machine learning tools. Our approach provides a comprehensive framework which can be used to optimize the design and operation of efficient cryogenic management systems.

Keywords:

1. Introduction

Cryogenic fuels are managed and stored at extremely low temperatures, typically below -150 degrees Celsius. While historically these fuels have been mainly used in rocket engines [1], they are now actively explored as alternatives to fossil fuels in many applications, such as shipping [2] and aeronautics [3].

This surge of interest is attributed to several reasons. First, cryogenic fuels are very efficient and can generate a lot of thrust for a given fuel mass [4]. This makes them ideal for space exploration and other applications where weight is a critical concern. Second, they are environmentally friendly. In particular, when LH_2 and LOx are burned, they produce only water vapor and do not release harmful pollutants to the atmosphere. While other cryogenic solutions, such as liquefied natural gas (LNG), are not entirely emission-free, they are still candidates to bridge the gap between traditional fossil fuels and a fully renewable energy system [3]. Finally, advances in materials science, cryogenics, and engine design have made it possible to employ these fuels in a wide range of applications. Although this has opened up new possibilities, further research is still required to improve the efficient and reliable management of their storage [5]. This is true for any application requiring long holding times, from marine to aeronautical, ground transportation to deep space exploration.

At cryogenic temperatures (i.e., -253°C for LH_2) no insulating system can entirely prevent heat exchanges with the surroundings, and it is not possible to prevent some of the fuel to evaporate and the tank pressure to rise over time [6]. Additional challenges are present in propellant tanks installed on vehicles, as the external accelerations induce sloshing. Sloshing, defined as the movement of the free liquid surface, can affect the vehicle's stability and manoeuvrability [1] as well as increase heat and mass transfer rates between the liquid and ullage gasses, leading to significant variations of the tank's pressure [7; 8].

This research project aims to contribute to understanding the physics of boil-off and the heat and mass transfer at the gas-liquid interface of a cryogenic tank in a wide range of operating conditions. The work combines experimental techniques, physical modelling and machine learning to derive and val-

idate modelling strategies that can help design new thermal management systems. The following paragraphs summarize the scope of each component of this project.

The experimental characterization of the problem is achieved through a modular approach in which different operating conditions are recreated: pressurization due to heat ingress, pressurization due to vapor injection, system relaxation in storage conditions, and thermodynamic imbalance due to a sloshing event. These test cases will be investigated in reduced-scale laboratorial conditions through three major experimental campaigns: (I) ground-testing with HFE-7000 as a replacement fluid at room temperature, (II) ground-testing with cryogenic nitrogen at ≈ 77.35 K, and (III) microgravity testing through a parabolic flight campaign with HFE-7000 at room tempeature.

The physical modeling of the problem is achieved through simplified representations of the cryogenic fuel tank. These models should be computationally inexpensive yet sufficiently accurate and versatile to predict the state of the system under the different operating conditions (i.e., filling, pressurization, fuel extraction, storage). The governing equations in each control volume are derived from energy and mass balances, whereas the exchanges between fluid regions are dependent on a set of heat transfer coefficients, which must be calibrated to yield accurate predictions over time.

Lastly, the machine learning tools are implemented to improve the predictive ability of the models by computing the closure parameters via a data-driven inverse method. The underlying optimization problem is efficiently solved via gradient-based optimization coupled with the adjoint method.

This first year of research was focused on three main tasks: (1) preparing a preliminary experimental setup on-ground using HFE-7200 as a replacement fluid, (2) implementing and debugging the 0D thermodynamic model of the system, and (3) laying the foundation for the data assimilation and model calibration strategy. These are the main elements of the work presented in this article.

2. Problem set

In typical operating conditions, cryogenic fuel tanks have standard handling sequences, which consist of tank chilling, filling, boil-off, level adjustment, pressurization, and hold [5]. In this project, we focus only on the stages after the level-adjustment has been performed. The scenarios of interest are listed below.

Tank pressurization: achieved by injecting vapor or an inert gas in the ullage of the tank (i.e., active pressurization), or achieved through heat ingress triggering fuel boil-off (i.e., passive pressurization). The pressurization achieved through active methods is typically faster than in passive boil-off [7]. Moreover, since the passive method relies on heat ingress over a longer period, the liquid phase is also warmed up in the process.

Hold: refers to the period during which the tank is maintained in static conditions, with no addition or removal of fuel. Once the pressurization is concluded, the hold phase is characterized by a gradual decrease (i.e., relaxation) of the pressure. This is attributed in part to condensation, and to the heat exchanges with the colder interface and inner tank walls [8]. The magnitude of the pressure-drop during this phase is dependent on the fluid properties, the pressurization method, its duration, and the volume of the tank [7].

Long-term storage: in these conditions, heat ingress from the surroundings inevitably superheats the inner walls in contact with the propellant. As a result, buoyancy-driven fluxes are developed, which create a characteristic thermal stratification in the gas and liquid phases [6]. The main heat transfer mechanisms inside the tank are: (1) wall normal fluxes entering the liquid, transporting warm fluid upwards, and causing a thermal boundary layer to develop at the interface, (2) wall tangent fluxes due to the vertical temperature gradient along the solid walls, (3) exchanges between the warmer gas and the colder liquid, which can trigger condensation or evaporation, while promoting a vertical thermal stratification [9].

Sloshing: due to dynamic perturbations, sloshing is triggered, mixing the temperature field in the system. The warmer liquid in the thermal boundary layer is mixed with subcooled liquid from the bulk, lowering the temperature at the free surface. Since the interface is in saturation, if this surface is cooled, the vapor pressure must decrease, leading to condensation. This is known in the literature as the 'pressure drop effect', which has been investigated by many authors [7; 8]. However, the opposite mechanism can also occur when the fluid travels along the superheated walls, leading to evaporation or even boiling around the contact line [7]. It is this complex interaction between fluid dynamics, heat transfer and phase change which poses such a challenge to current propellant management strategies.

3. Thermodynamic modeling

3.1. 0D model equations

The cryogenic fuel tanks considered in this work are a single-species system composed by a liquid phase l, and its associated vapor v, surrounded by solid walls and a layer of insulation w (cf. Figure 1). The interface i between the gas and liquid is considered as an infinitesimally thin region across which both phases exchange mass and heat. The schematic includes generic inlet and outlet ports for the gas and liquid phases (e.g., pressurization, venting, filling) marked with subscripts "in" and "out", respectively.

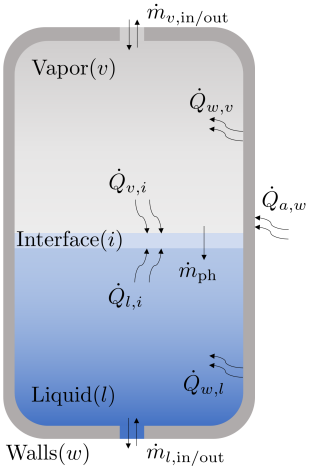

Figure 1: Schematic concept of the experimental setup composed by the donor tank, the pressurization line, and the receiver.

The model's equations are derived from energy, mass and volume balances applied to each of its control volumes, with mass-averaged thermodynamic properties applied to each of them. This results in a coupled system of ordinary differential equations (ODEs) which is integrated in time for a given set of inputs and initial state.

The mass conservation balances in the vapor and liquid phases are given, respectively, by

$$\frac{dm_v}{dt} = \sum \dot{m}_{v,\mathrm{in}} - \sum \dot{m}_{v,\mathrm{out}} - \dot{m}_{\mathrm{ph}} \tag{1}$$

$$\frac{dm_l}{dt} = \sum \dot{m}_{l,\mathrm{in}} - \sum \dot{m}_{l,\mathrm{out}} + \dot{m}_{\mathrm{ph}} \tag{2}$$

where $\dot{m}_{\mathrm{ph}} = \dot{m}_{\mathrm{cond}} - \dot{m}_{\mathrm{evap}}$ is the net mass flux through the interface, accounting for the balance of condensation and evaporation.

The energy conservation balances applied to both fluid regions yield

$$\frac{dU_v}{dt} = \sum \dot{m}_{v,\mathrm{in}} \hbar_{v,\mathrm{in}} - \sum \dot{m}_{v,\mathrm{out}} \hbar_{v,\mathrm{out}} - \dot{m}_{\mathrm{ph}} \hbar_{v,\mathrm{sat}} - \dot{Q}_{v,i} + \dot{Q}_{w,v} + \dot{W}_v \tag{3}$$

$$\frac{dU_l}{dt} = \sum \dot{m}_{l,\mathrm{in}} \hbar_{l,\mathrm{in}} - \sum \dot{m}_{l,\mathrm{out}} \hbar_{l,\mathrm{out}} + \dot{m}_{\mathrm{ph}} \hbar_{v,\mathrm{sat}} - \dot{Q}_{l,i} + \dot{Q}_{w,l} + \dot{W}_l, \tag{4}$$

where U_v and U_l are the internal energies of the vapor and liquid phases, $\dot{Q}$ is the heat flux, $\hbar$ is the enthalpy, and $\dot{W} = -pdV/dt$ represents the expansion/compression work acting on the system.

The heat transfer rates shown in the equations above are estimated using Newton's cooling law:

$$\begin{aligned} \dot{Q}_{v,i} &= A_i h_{v,i}(T_v - T_i) \;\; ; \;\; \dot{Q}_{l,i} = A_i h_{l,i}(T_l - T_i) \\ \dot{Q}_{w,v} &= A_{w,v} h_{w,v}(T_w - T_v) \;\; ; \;\; \dot{Q}_{w,l} = A_{w,l} h_{w,l}(T_w - T_l), \end{aligned} \tag{5}$$

where $h_{v,i}$, $h_{l,i}$, $h_{w,v}$, $h_{w,l}$ are the heat transfer coefficients which must be identified to accurately predict the state of the system, A_i is the area of the interface, $A_{w,v}$ and $A_{w,l}$ are the surface exchange areas between the walls-vapor and walls-liquid phases. These are not constant since the fill level can change due to refueling or due to phase change. Moreover, during a sloshing event the free surface motion along the container walls imposes that A_i is a also a function of time, but trickier to determine than $A_{w,v}(t)$ or $A_{w,l}(t)$. As a result, the calibration of the model should be performed for the lumped $A_i h_{v,i}$ and $A_i h_{l,i}$ terms.

The interface temperature in (5) is assumed to be the saturation temperature evaluated at vapour pressure p_v. Moreover, by applying an energy balance at this surface, the net mass flux due to phase change is expressed as

$$\dot{m}_{\mathrm{ph}} = \frac{\dot{Q}_{l,i} - \dot{Q}_{v,i}}{\mathcal{L}_v} \tag{6}$$

with $\mathcal{L}_v$ the latent heat of vaporization.

If the liquid phase is treated as incompressible, an assumption valid even in extreme cryogenic conditions [9], its density can be written solely as a function of temperature $\rho_l(p,T) \approx \rho(T)$, yielding

$$\frac{dV_l}{dt} \approx \frac{1}{\rho_l}\frac{dm_l}{dt} - \frac{m_l}{C_{p,l}\rho_l^2}\left(\frac{d\rho_l}{dT}\right)_p \frac{du_l}{dt}, \tag{7}$$

where C_p is the specific heat capacity at constant pressure, ρ is the mass-specific density, and $u = U/m$ is the

mass-specific internal energy. From the conservation of volume in the tank, it follows that

$$\frac{dV_v}{dt} = -\frac{dV_l}{dt}. \tag{8}$$

From a zero-dimensional perspective, the insulating walls are considered as a single control volume which can exchange heat with the vapor and liquid phases, as well as with the external environment a at ambient conditions. For a single control volume with mass-averaged properties, the internal energy of the walls is described through

$$\frac{dU_w}{dt} = \dot{Q}_{a,w} - \dot{Q}_{w,v} - \dot{Q}_{w,l} \tag{9}$$

where $\dot{Q}_{a,w}$ is the heat supplied from from the outside environment into the system. This term is computed from existing literature correlations [**?**]. Equation 9 can be directly written as a function of the mass-averaged solid temperature by considering $dU_w = m_w C_w dT_w$.

Thus, the thermodynamic model composed by Equations (1)-(9) can be cast as the following initial value problem:

$$\begin{cases} \dfrac{d\mathbf{x}}{dt} = \mathbf{f}\left(\mathbf{x}, t; \boldsymbol{\theta}\right) \\ \mathbf{x}(0) = \mathbf{x}_0 \end{cases} \tag{10}$$

where $\mathbf{x} \in \mathbb{R}^n$ is the state vector (composed by the masses, volumes and internal energies of each control volume), describing the thermodynamic condition of the system at time-instant t, $\boldsymbol{\theta} \in \mathbb{R}^p$ is the vector of closure terms, in this case expressed by the heat transfer coefficients in (5), and $\mathbf{x}_0 \in \mathbb{R}^n$ represents the (known) initial conditions.

3.2. Non-dimensional equations

In this section, the model equations which comprise the 0D model are turned to non-dimensional form by scaling them with respect to some reference quantities. The main goals of this scaling are to quantify the importance of different phenomena in the system, and to assess whether a reduced-scale model can accurately reproduce the dynamics of the full-scale prototype.

The first step in this analysis requires separating the quantities in the system into two groups: parameters and variables. While variables are scaled with respect to reference quantities, parameters are left in the equations as they are. In this work, the following non-dimensional variables were considered:

$$\hat{t} = \frac{t}{[t]} \;;\; \hat{m} = \frac{m}{[m]} \;;\; \hat{\rho} = \frac{\rho}{[\rho]} \;;\; \hat{p} = \frac{p}{[p]} \;;\; \hat{\Theta} = \frac{T - T_i^0}{[\Delta T]} \tag{11}$$

where the hatted terms $\hat{\cdot}$ denote non-dimensional variables, and square brackets [.] indicate reference quantities. For the purposes of scaling the equations, the energy balances were expressed in terms of temperature by setting $du \approx C_v dT$, no inlets/outlets were considered, and the work term was neglected.

The set of non-dimensional equations obtained from these considerations is given by:

$$\frac{d\hat{m}_v}{d\hat{t}} = -\Pi_1 \frac{d\hat{m}_l}{d\hat{t}} = -\Pi_2^{l,i}\hat{\Theta}_l + \Pi_2^{v,i}\hat{\Theta}_v \tag{12}$$

$$\frac{d\hat{\Theta}_v}{d\hat{t}} = \frac{d\hat{m}_v}{d\hat{t}}\left(\Pi_4^v \frac{\hat{p}_v}{\hat{\rho}_v} - \Pi_3^v\hat{\Theta}_v\right) - \Pi_5^{v,i}\hat{\Theta}_v + \Pi_5^{w,v}\left(\hat{\Theta}_w - \hat{\Theta}_v\right) \tag{13}$$

$$\frac{d\hat{\Theta}_l}{d\hat{t}} = \frac{d\hat{m}_l}{d\hat{t}}\left(-\Pi_3^l\hat{\Theta}_l + \Pi_4^l \frac{\hat{p}_v}{\hat{\rho}_l}\right) - \Pi_5^{l,i}\hat{\Theta}_l + \Pi_5^{w,l}\left(\hat{\Theta}_w - \hat{\Theta}_l\right) \tag{14}$$

$$\frac{d\hat{V}_l}{d\hat{t}} = -\Pi_1\Pi_6 \frac{d\hat{V}_v}{d\hat{t}} = \frac{1}{\hat{\rho}_l}\frac{d\hat{m}_l}{d\hat{t}} - \Pi_7 \frac{\hat{m}_l}{\hat{\rho}_l}\frac{d\hat{\Theta}_l}{d\hat{t}} \tag{15}$$

$$\frac{d\hat{\Theta}_w}{d\hat{t}} = \Pi_8 - \Pi_5^{w,v}\left(\hat{\Theta}_w - \hat{\Theta}_v\right) + \Pi_5^{w,l}\left(\hat{\Theta}_w - \hat{\Theta}_l\right) \tag{16}$$

where the Π_i groups are the non-dimensional numbers which arise from the scaling of equations, presented in Table 1. These groups are then used in the following section to perform the scaling analysis of the problem.

Table 1: Non-dimensional groups obtained by scaling the equations which compose the zero-dimensional model of the fuel tank.

	Definition	Meaning
Π_1	$\frac{[m_l]}{[m_v]}$	Liquid-gas mass ratio
Π_2	$\frac{Ah[\Delta T][t]}{\mathcal{L}_v[m]}$	Convection over latent heat
Π_3	$\frac{C_p}{C_v}$	Specific heat ratio
Π_4	$\frac{[p]}{[\rho]C_v[\Delta T]}$	Potential work per unit mass
Π_5	$\frac{Ah[t]}{[m]C_v}$	Convection over thermal inertia
Π_6	$\frac{\rho_v}{\rho_l}$	Density ratio
Π_7	$\beta_l[\Delta T]$	Thermal expansion
Π_8	$\frac{\dot{Q}[t]}{[m]C_w[\Delta T]}$	Heat ingress over wall inertia

3.3. Scaling analysis

This section compares the responses of the thermodynamic systems subject to sloshing in two distinct tanks, a full-size and a reduced-scale one. The full-size facility is set as Europe's new Ariane 6 launch vehicle. The LH_2 tank is expected to have a cross-sectional diameter of 5.2 m for the core and upper stage's cryogenic propellant tanks [10]. On the other hand, the reduced-scale setup was taken as the VKI quartz cell, used in parabolic flight campaigns and cryogenic experiments, with a diameter of 0.08 m, and a height of 0.120 m, filled with HFE-7000 and with LN_2.

The similarity approach for these test cases is broken down into three categories: geometric, kinematic, and dynamic similarity.

Geometric similarity ensures all body dimensions are linearly related through a scaling factor Λ. On the other hand, kinematic similarity is met if the non-dimensional excitation amplitude A_0/R and frequency $f_e/f_{1,1}$ are matched [7], where A_0 is the forcing amplitude, f_e is the forcing frequency, and $f_{1,1}$ is the natural frequency of the first asymmetrical sloshing mode [1].

Lastly, dynamic similarity is preserved if all non-dimensional numbers are matched. This is generally not possible given that most of the Π groups are defined simultaneously for the gas and liquid phases, while depending on thermophysical properties and on thermodynamic parameters. Given this dilemma, it is necessary to define a scaling strategy to selectively match specific quantities, which will ideally allow for accurately reproducing the physics in the reduced-scale facility.

In this work, we match the sloshing conditions by setting $A_0/R = 0.05$ and $f_e/f_{1,1} = 0.8$ for both setups. Following the empirical correlation derived by Ludwig & Dreyer (2013) [8], we can compute the Nusselt number for sloshing flows in the vicinity of the $f_{1,1}$. This expression allows us to roughly estimate the $h_{l,i}$ and $h_{v,i}$ coefficients in both scenarios. Furthermore, we impose a fill ratio $H_l/H_{\text{tot}} = 0.67$ for both facilities. The reference parameters are set as $[t] = 1/f_e$, $[m_v] = m_v^0$, $[m_l] = m_l^0$, $[\rho_v] = \rho_v^0$, $[\rho_l] = \rho_l^0$, $[p] = p_v^0$, $[\Delta T_v] = T_v^0 - T_i^0$ and $[\Delta T_l] = T_l^0 - T_i^0$. The reference time-scale, heat transfer coefficients, pressure and temperature values are summarized in Table 2.

Figure 2 shows the non-dimensional pressure plotted over non-dimensional time, as well as the differences in the Π_2 and Π_5 groups for the tested scenarios. This figure highlights that matching the sloshing conditions does not guarantee similarity in the heat and mass transfer processes when scaling down the problem. Even when considering H_2 in the reduced-scale tank, the observed pressure drop is higher than in the full-size case. This is partly attributed to the fact that geometrical scaling doesn't preserve the ratio of internal volume to surface area. Thus, the full-scale tank has more inertia as shown from the Π_5 group.

Table 2: Reference conditions for the tested scenarios. The 'FS' and 'RS' abbreviations refer to the full-scale and reduced-scale setups, respectively.

	H_2 (FS)	H_2 (RS)	N_2	HFE-7000
$1/f_e$ [s]	2.81	0.35	0.35	0.35
p_v^0 [bar]	3	3	2	2
T_v^0 [K]	26.8	26.8	90	338
T_l^0 [K]	20.8	20.8	77.4	293
$h_{v,i}$ [W/m^{2}K]	0.71	0.61	0.14	0.24
$h_{l,i}$ [W/m^{2}K]	6.31	5.45	8.84	4.72

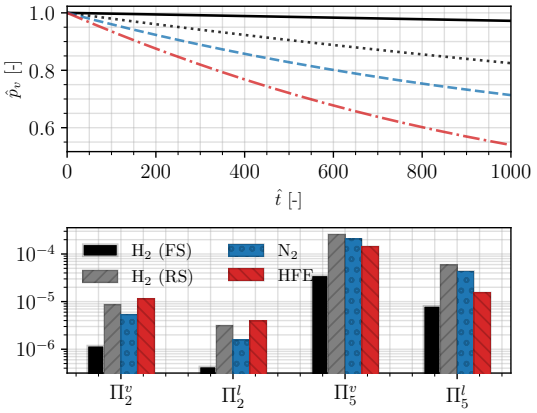

Figure 2: Non-dimensional pressure evolution (top), and non-dimensional groups Π_2 and Π_5 for the vapor and liquid phases (bottom).

Interestingly, the case with N_2 offers better similarity in terms of Π_2, suggesting that the ratio of convective heat transfer over condensation/evaporation enthalpies can be better reproduced in cryogenic conditions. This suggests, that phase change phenomena could be better investigated in these laboratorial conditions. On the other hand, the HFE-7000 setup can better match Π_5, which suggests that the additional thermal inertia of this fluid provides better insight on the temperature transport mechanisms.

4. Model calibration via inverse method

4.1. Data assimilation strategy

Suppose we are provided with a database of reliable observations $\mathbf{w}(t) \in \mathbb{R}^m$ (e.g., from experimental measurements, or high-fidelity numerical simulations) which characterize the thermo-hydraulic state of a cryogenic fuel tank under a wide range of operating conditions. These observations represent physical variables which might not directly correspond to the state vector $\mathbf{x}$ considered in Equation (10). Thus, we introduce the observation operator $\mathbf{h}(\cdot) : \mathbb{R}^n \rightarrow \mathbb{R}^m$ which transforms the state vector into observable quantities

$$\mathbf{w}(t) = \mathbf{h}(\mathbf{x}(t)). \tag{17}$$

This operator is particularly relevant in this work given that the model presented in Section 3.1 is written in terms of internal energies, masses and volumes, yet the observable quantities are often pressure, temperature and fill-level readings.

The aim of the inverse method is to estimate the set of parameters $\boldsymbol{\theta}$ which allows for the model to reproduce the training data, while simultaneously yielding accurate predictions in new (unseen) situations. This methodology relies on minimizing a loss functional $\mathcal{J}$ which evaluates the difference between the observations $\mathbf{w}(t)$ and the predicted outputs of system mapped to the observation space $\mathbf{h}(\mathbf{x}(t))$. The approach implemented in this work is to define $\mathcal{J}$ as

$$\begin{aligned}\mathcal{J}(\mathbf{w}, \mathbf{x}; \boldsymbol{\theta}) &= \int_0^T g(\mathbf{w}, \mathbf{x}, t; \boldsymbol{\theta}) dt \\ &= \int_0^T \frac{1}{2} \left(\mathbf{w}(t) - \mathbf{h}(\mathbf{x}(t))\right)^T \mathbf{R}^{-1} \left(\mathbf{w}(t) - \mathbf{h}(\mathbf{x}(t))\right) dt\end{aligned} \tag{18}$$

where the error between predictions and observations is weighted by the covariance matrix $\mathbf{R}$, accounting for the measurement noise.

The goal is to minimize the objective function defined in Equation (18) by finding the 'optimal' vector of parameters $\boldsymbol{\theta}^*$. The minimizer of $\mathcal{J}$ corresponds to the point at which its gradient, with respect to $\boldsymbol{\theta}$, is zero

$$\nabla_{\boldsymbol{\theta}} \mathcal{J}(\mathbf{w}, \mathbf{x}; \boldsymbol{\theta}) = 0. \tag{19}$$

Differentiating Equation (18) with respect to the vector of parameters yields

$$\nabla_{\boldsymbol{\theta}} \mathcal{J}(\mathbf{x}; \boldsymbol{\theta}) = \int_0^T \frac{\partial g}{\partial \boldsymbol{\theta}} + \frac{\partial g}{\partial \mathbf{x}} \frac{d\mathbf{x}}{d\boldsymbol{\theta}} dt \tag{20}$$

where $\frac{d\mathbf{x}}{d\boldsymbol{\theta}} \in \mathbb{R}^{n \times p}$ represents the sensitivity of the state vector with respect to the closure terms at time t.

The adjoint method simplifies the gradient evaluation in Equation (20) by removing the dependency on the sensitivity $\frac{d\mathbf{x}}{d\boldsymbol{\theta}}$. This term is an $n \times p$ matrix which must be integrated in time, meaning that each gradient evaluation would require solving a system of $n \times p$ ODEs. Although this approach is feasible when the number of closure terms p is small, its computational cost is too much when the number of parameters to tune is large. Thus, the next section is dedicated to describing how the cost functional gradients can be computed via the adjoint method.

4.2. Adjoint method for state estimation

In this article, the adjoint method is derived by minimizing the following constrained optimization problem:

$$\min_{\boldsymbol{\theta}} \mathcal{J}(\mathbf{x}, t; \boldsymbol{\theta}) \quad \text{s.t.} \quad \mathbf{f}(\mathbf{x}, t; \boldsymbol{\theta}) - \frac{d\mathbf{x}}{dt} = 0. \tag{21}$$

The equality constraint can be incorporated in the problem by minimizing the Lagrangian function $\mathcal{L}$

$$\mathcal{L}(\mathbf{w}, \mathbf{x}; \boldsymbol{\theta}) = \mathcal{J}(\mathbf{x}, t; \boldsymbol{\theta}) + \int_0^T \left(\mathbf{f}(\mathbf{x}, t; \boldsymbol{\theta} - \frac{d\mathbf{x}}{dt}\right) \boldsymbol{\lambda}(t)^T dt \tag{22}$$

where $\boldsymbol{\lambda}$ is the adjoint variable. It can be shown that Equation (22) can be minimized without evaluating the sensitivities over time if we satisfy

$$\begin{cases} \dfrac{d\boldsymbol{\lambda}}{dt} = -\dfrac{\partial g}{\partial \mathbf{x}} - \boldsymbol{\lambda}(t) \dfrac{\partial \mathbf{f}}{\partial \mathbf{x}} \\ \boldsymbol{\lambda}(T) = 0 \end{cases} \tag{23}$$

written as a terminal value problem. This is a linear system of quations which must be integrated backwards in time to solve for the adjoint variable $\boldsymbol{\lambda}(t)$. The gradient of the Lagrangian can now be computed as

$$\nabla_{\boldsymbol{\theta}} \mathcal{L} = \int_0^T \frac{\partial g}{\partial \boldsymbol{\theta}} + \boldsymbol{\lambda}(t) \frac{\partial \mathbf{f}}{\partial \boldsymbol{\theta}} dt + \boldsymbol{\lambda}(0) \frac{d\mathbf{x}}{d\boldsymbol{\theta}}(0) \tag{24}$$

where $\frac{d\mathbf{x}}{d\boldsymbol{\theta}}(0) = \frac{d\mathbf{x}_0}{d\boldsymbol{\theta}}$ is known for the prescribed initial conditions.

The main advantage of the adjoint method compared to the forward sensitivities approach, is that its computational effort does not scale with the number of parameters p. It is only required to perform one forward pass of the system to obtain $\mathbf{x}(t)$ and one backward pass to obtain $\boldsymbol{\lambda}(t)$. In addition, it is necessary compute $\partial g / \partial \mathbf{x}$, $\partial g / \partial \boldsymbol{\theta}$, $\partial \mathbf{f} / \partial \mathbf{x}$, $\partial \mathbf{f} / \partial \boldsymbol{\theta}$ over time. In

this work, these terms were first computed through the analytical expressions, and then with automatic differentiation using the JAX package [11]. Although the analytical approach offers evident perfomance gains, its derivation can be cumbersome for a large number of variables, and any modifications to the model's equations force modifications to the analytical derivatives. On the other hand, automatic differentiation allows for these expressions to be obtained through a programmed algorithm, but with the penalty of additional computational effort. Given this trade-off between adaptability and performance, both approaches are tested and compared in the following section.

4.3. Literature verification and performance test

A preliminary test of the data assimilation strategy was implemented using experimental data from Hassan *et. al* (1991) [12]. In this article the authors experimentally characterized the passive pressurization of a 4890 liter spherical LH_2 tank filled up to 84% under varying superheated wall conditions. The authors measured the pressure of the vessel, alongside the temperature of the gas and liquid phases at different vertical coordinates. Thus, the observation vector was composed of $\mathbf{w}(t) = \left[\overline{T}_v(t),\ \overline{T}_l(t),\ p_v(t)\right]$, where the overline indicates spatial averaging. The observation operator $\mathbf{h}(.)$ was implemented using CoolProp [13] to relate the thermodynamic variables of the state vector (i.e., internal energies, masses and volumes) with the measured ones.

Table 3: Performance of the different optimization approaches to minimize the prediction error for the Hassan *et. al* (1991) [12] case. Runtimes evaluated on an Intel Core i7-9750H CPU with 32GB RAM.

Gradient	Iterations	$\mathcal{J}$	Runtime
FD (Custom)	19	298.4	4min51s
FD (SciPy)	19	298.4	3min33s
Adjoint (analytical)	9	284.8	1min40s
Adjoint (auto. diff.)	18	299.5	3min58s

The vector of closure terms was defined as $\boldsymbol{\theta} = [h_{v,i},\ h_{l,i},\ h_{w,v},\ h_{w,l}]$, where each of these coefficients was taken as constant in time. The problem was set up with initial conditions $\overline{T}_v^0 = 21$ K, $\overline{T}_l^0 = 20.1$ K, $p_v^0 = 1.03$ bar, and $\overline{T}_w^0 = 350$ K. The simulations were evaluated throughout the duration of the experiments, which lasted 13.89 hours. Given the low computational cost of the 0D model, each forward pass was executed in 1.9 - 3.5 seconds, whereas the backward pass was performed in 0.2 - 0.3 seconds.

The objective function was minimized using quasi-Newton method L-BFGS-B, where its gradient was computed in four ways: (1) finite-differences (FD) using the built-in SciPy implementation [14], (2) first-order finite-differences implemented manually, (3) adjoint method using analytical derivatives, and (4) adjoint method using automatic differentiation. The outcomes of this test are summarized in Table 3.

From these results, it is clear that the minimization of the objective function through the analytical adjoint method yields evident performance improvements in terms of the number of iterations and overall run-time. However, noting that the adjoint method scales independently from the number of parameters p, and that the finite-difference approach scales linearly with p, it is remarkable, that even for a small problem (i.e., $p = 4$) the auto-diff. approach can nearly match the FD SciPy's runtimes. This results motivates the continued implementation of the adjoint method, especially in future applications where the heat transfer coefficients are parameterized using a much larger number of parameters.

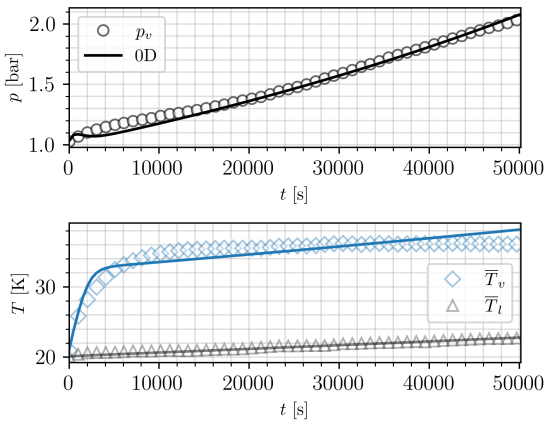

Figure 3: Results of the 0D model calibration based on the Hassan *et. al* (1991) [12] case using the analytical adjoint approach. The obtained coefficients were: $h_{v,i} = 1.8$ W/m^{2}K, $h_{l,i} = 94.3$ W/m^{2}K, $h_{w,v} = 0.05$ W/m^{2}K, and $h_{w,l} = 0.02$ W/m^{2}K.

The experimental and predicted pressure and temperature evolutions are shown in Figure 3. The dots correspond to the experimental data, whereas the solid lines correspond to the numerical predictions. The good agreement found in this test case suggests that the long-term storage heat ingress can be accurately modelled using only constant heat transfer coefficients.

5. Experimental characterization

This section details the advances which have been made during the first year of research on the experimental campaigns planned for this research project. The experimental techniques relevant to this project are associated with measuring thermodynamic variables such as pressure and temperature, as well as the interface dynamics due to sloshing. The common aspects across all campaigns are described here first, whereas their particular challenges, progress and future work are tackled in their respective subsections.

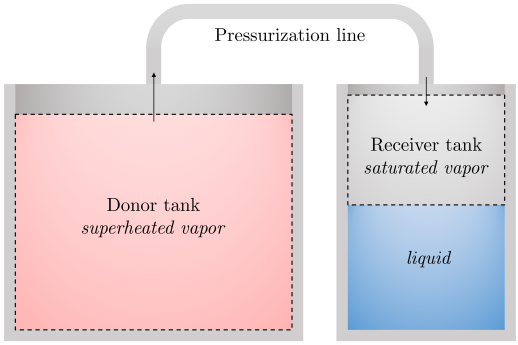

Figure 4: Schematic concept of the experimental setup composed by the donor tank, the pressurization line, and the receiver.

Each experimental setup is composed of two tanks, the 'donor', and the 'receiver', connected to each other through a pressure line. The 'donor' contains superheated vapor at pre-determined operating conditions, whereas the 'receiver' (i.e., the quartz cell) takes the role of the fuel tank which is partly filled with liquid, and in saturation conditions. The connecting line is composed of a series of valves and instrumented with mass flow, pressure and temperature sensors to allow for a complete characterization of the pressurization procedure. The discharge to the 'receiver' is done through a diffuser, which directs the gas radially, minimizing its impact onto the free surface of the liquid.

Given that the aim of these experiments is to fully characterize the thermo-hydraulics of the system, the quartz cell is instrumented with rakes of temperature sensors to measure the thermal distribution in the gas, liquid, inner and outer walls. Moreover, fast-response pressure transducers are also incroporated. Finally, the optical access provided by the quartz cell allows for employing optical techniques such as backlight visualization and Particle Image Velocimetry (PIV) throughout the experiments. These measured quantities are then coupled with the data-assimilation strategy, to determine the closure terms which improve the accuracy of the model's predictions.

Prior to the start of the experiments, each setup must be vacuumed to remove air and any undesired species. Then, both tanks are filled with predetermined amounts of the working fluid (i.e., HFE-7000 or liquid nitrogen). The experiments must be carried out in single-species conditions to allow for a direct relationship between the measured vapor pressure and the temperature of the interface. The last step of the preparation is to ensure that the 'donor' contains superheated vapor, while the 'receiver' remains in saturation conditions.

The experiments themselves are composed of three phases: (1) pressurization, (2) hold, and (3) sloshing. The pressurization stage is primarily achieved by injecting warm vapor into the quartz cell. The key parameters of interest to vary in these tests are the duration of the pressurization, the hold time, and the sloshing intensity.

5.1. Preliminary ground-based measurements

The aims of this campaign were to understand the challenges of implementing an active pressurization system, and to characterize its operation under different working conditions. With this in mind, the measured quantities in the system were: the pressure in the donor and receiver tanks, the temperature inside the donor, in the connecting pipeline, and on the outer walls of the quartz tank. Moreover, the interface dynamics during filling, pressurization and sloshing were captured with a high-speed JAI SP-12000MCXP4 camera with a 60 mm objective, illuminated by diffused LED lights.

A portion of the experimental matrix of this campaign is presented in Table 4. The key parameters varied in these tests were the hold time, and the sloshing excitation. For all tests, the donor tank was pressurized at $\approx$ 0.73 bar and $\approx$ 338 K, while the fluid in the quartz cell was previously cooled in the freezer, starting each experiment at $\approx$ 238 K.

Table 4: Experimental matrix for the preliminary experimental campaign with HFE-7200.

	Press.	Hold	Sloshing	p_0 [kPa]	$p_{\min}$ [kPa]
ID12	60 s	504 s	Swirl	21.5	16.9
ID13	60 s	300 s	Swirl	22.4	17.2
ID15	60 s	485 s	Planar	22.5	19.3

Figure 5 shows the pressure evolution in the quartz cell during test ID13. The steep rise (a) starts at -366

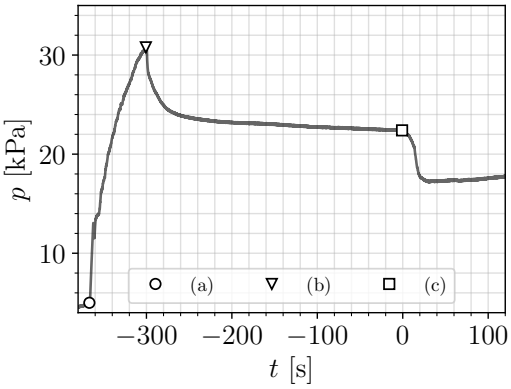

Figure 5: Pressure evolution in the quartz cell during test ID13: a) start of the pressurization, b) start of the hold phase, c) start of the sloshing excitation.

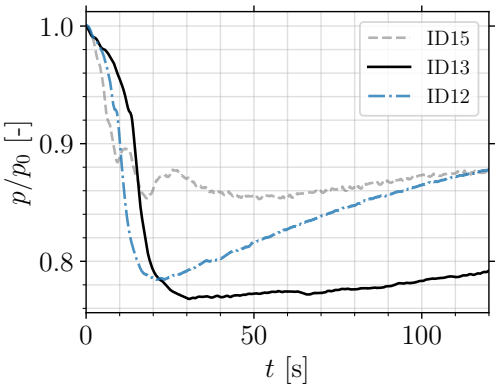

Figure 6: Normalized pressure evolution in the quartz cell at the start of sloshing for tests ID12, ID13 and ID15.

seconds, and is achieved by injecting the system with warm vapor from the donor tank. The pressurization is manually performed until the pressure the in the quartz cell reaches 30 kPa. At this point, the flow-rate is stopped, and the hold stage (b) begins. During this period, the pressure suffers an initial sharp drop, following by a gradual decrease, until the sloshing excitation is initiated at $t = 0$ (c).

Although the implemented procedure allowed pressurizing the cell as expected, the hold stage led to significant condensation, with a relative pressure drop of 27%. The primary mechanism of this drop was attributed to condensation due to the heat exchanges with the colder solid and liquid surfaces. As a result, the fill-level increased by approximately 16% during the pressurization and hold phases.

Figure 6 presents the pressure-drop due to sloshing in the all test cases. Cases ID13 and ID12 were performed under identical swirl sloshing conditions, with different hold durations. The hold period of ID13 was 1.7 times longer than that of ID12. While the minimal pressure reached in both cases is identical, the long-term evolution of the system provides two distinct evolutions. In ID12, the thermal mixing produced by the swirling wave keeps the pressure near the minimum point, whereas in ID13 there is a gradual pressure build-up.

Cases ID15 and ID12 were performed with similar hold times, yet under different sloshing conditions. These measurements confirm that swirl waves produce a more effective mixing of the thermal field, yielding a larger pressure-drop (23%) when compared to the planar case (15%). Interestingly, the pressure evolution in case ID15 is characterized by oscillations which suggest periodic shifts between evaporation and condensation. From the high-speed image sequences shown in Figure 7, the first pressure spike is associated with a thin liquid film rising along the sidewalls of the quartz. This type of free surface motion is not typically observed in planar sloshing [1]. However due to condensation taking place in the cell, droplets are seen falling on the free surface, de-stabilizing its motion, and creating jets which protrude outwards and dramatically altering the expected motion.

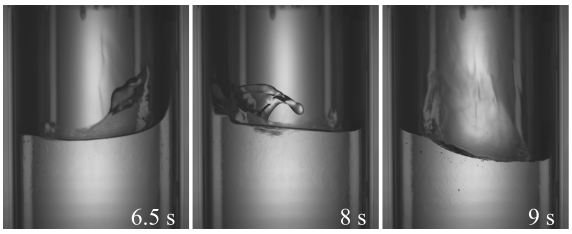

Figure 7: Pressure evolution in the quartz cell during test ID13: a) start of the pressurization, b) start of the hold phase, c) start of the sloshing excitation.

5.2. Ground and μg tests with replacement fluid

The ground-based tests in this campaign are carried out using HFE-7000 as the replacement fluid, using the von Karman Institute's SHAKESPEARE (SHaking Aparatus for Kinetic Experiments of Sloshing Projects with EArthquake Reproduction) facility. The design of this experiment's setup and procedure was a direct result of the lessons learned form the preliminary campaign described in the previous section.

The major technical challenge of designing this campaign, is that its setup must be also used in the microgravity tests aboard the parabolic flight. As a result, it must comply with a stringent set of requirements (e.g., compact design, short pressurization times, reliable and safe procedure, redundancy). The design of the setup has been carried out in a modular approach, focusing on its three primary components: the donor, the pressure line, and the receiver.

From the preliminary campaign, it was found that the manual pressurization procedure was challenging to perform with adequate repeatability. As a result, the new pressure line implements a mass-flow controller provided by Bronkhorst, combined with solenoid valves to better control the discharge of vapor into the quartz cell. Furthermore, the line is wrapped around heating elements connected to a PID controller, and insulated to minimize heat losses through its walls.

A set of heaters are also employed on the upper section of the outer walls of the quartz cell to pre-heat the solid. Similar solutions have been employed by several authors [8] to minimize the condensation and droplet formation observed in the preliminary tests. The instrumentation of the quartz cell consists of a high-frequency response Kulite XTL-190 transducer, three vertical rakes of shielded type K thermocouples (12 sensors in the central rake, with 6 in each of the lateral ones), and four external thermocouples are added to the outer walls to evaluate the thermal stratification imposed on the solid by the heating elements.

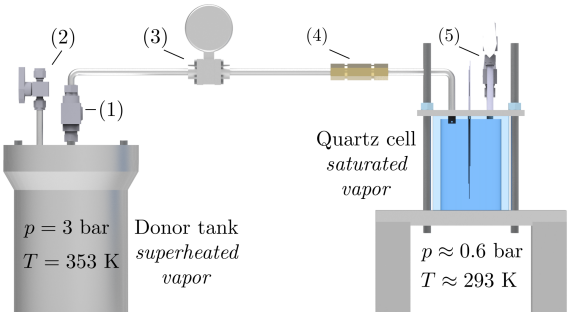

Figure 8: Schematic of the non-cryogenic ground-based and microgravity campaign's experimental setup: (1) solenoid valve, (2) filling and vacuum port, (3) mass-flow controller, (4) check-valve, (5) vacuum port.

The proposed operating conditions, alongside the setup, are shown in Figure 8. These were carefully determined by a compromise of dynamic similarity, ability to perform multiple pressurizations with the same fluid mass, and with safety constraints to respect the structural integrity of the quartz cell during thermal cylcing. To this effect, a parametric study was carried out to determine acceptable ranges for the maximum temperature and pressure, as well as diameter and length of the pressure line.

The design of the donor tank and the pressurization line have been finalized, and they are currently in the commissioning phase, whereas the quartz cell is in its final design iterations. The ground tests with this setup are targeted for the last months of summer 2023. The parabolic flight campaign is planned for the end of November 2023.

5.3. Ground-testing with cryogenic fluid

The cryogenic tests are carried out in the von Karman Institute's cryostat, using LN_2 as the replacement fluid. The main technical challenge of designing the cryogenic experiments is the harsh chill-down to 77.35 K. Given the need to have a pressure-tight setup, all tolerances must be carefully computed, and extensive detail must be placed in the sealing of the setup. To achieve this goal, thermal-stress simulations were performed with Ansys workbench, to estimate the expected thermal deformation and stresses imposed on the assembly.

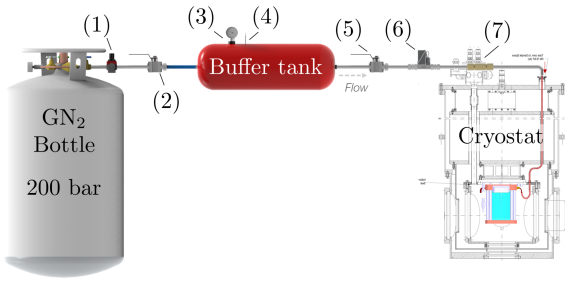

Figure 9: Schematic of the cryogenic campaign's experimental setup: (1) pressure regulator, (2) ball-valve, (3) pressure sensor, (4) thermocouple, (5) ball-valve, (6) mass-flow controller, (7) check-valve.

A schematic of the proposed setup is presented in Figure 9. Given the high-pressures of the LN_2 bottles, a buffer tank must be introduced to lower the pressure differential with respect to the receiver. Moreover, since the quartz cell is subject to cryogenic temperatures, the nitrogen vapor inside the buffer tank can be in ambient conditions.

The instrumentation of the quartz cell follows the same design philosophy as the one described in the previous section, taking advantage of the lessons learned from the preliminary test campaign. As

a result, the setup is instrumented with a high-frequency response Kulite pressure transducer, a rake of Lakeshore DT-670-SD thermo-diodes (7 sensors in the axial center of the tank) distributed along the gas and liquid phases, and two additional sensors attached to the inner walls. Heating elements are also attached to upper outer section of the quartz cell to preheat them and thus reduce the pressure drop during the hold stage. The temperature distribution caused by the heaters is measured through six thermo-diodes.

The design the instrumentation of the quartz cell has been finalized with the exception of the thermal probe, which is still under design. The buffer tank and the pressure line are in the commissioning phase. The ground tests with this setup are targeted, for the early summer of 2023.

6. Conclusions and future outlook

In this study, a physical model of a cryogenic fuel tank was implemented from energy and mass balances applied to its control volumes. A similarity analysis was derived by scaling the model's equations to verify if a reduced-scale setup could reproduce the physics in full-size applications. The results indicate that one cannot simultaneously match all non-dimensional groups. Instead one must break-down the full problem by isolating specific physical phenomena and investigate them separately.

Moreover, the foundations of the data assimilation strategy and inverse method were presented. The presented framework sets up an optimization problem in which the error between available data and model predictions must be minimized. This framework successfully was applied to a literature test case containing experimental data for the pressurization of an LH_2 tank.

Finally, an overview of the experimental campaigns was provided. A preliminary test campaign was carried out during this first year of research using HFE-7200 as the replacement fluid. Simultaneous pressure, temperature and optical measurements were carried to characterize the filling, pressurization and sloshing of the system. The outcomes of these experiments provided crucial insight to the design of microgravity and cryogenic facilities.

Acknowledgments

I would like to express my gratitude to my supervisors, Prof. Miguel Alfonso Mendez and Prof. Benoit Scheid, whose guidance and insights were essential to shaping this work. I would also like to express my appreciation to Dr. Alessia Simonini, for guiding me in the lab, and helping me to advance my skills in this area of research. I must also thank Eng. Mathieu Delsipée and Eng. Louis Carbonnelle for their technical support and design knowledge. Their contributions are critical to ensure the success of these experiments. Finally, I would like to acknowledge the contributions of my students, Francisco Monteiro and Alessandra Zumbo, who have devoted their time, energy, and creativity to this project.

References

[1] H. N. Abramson, F. T. Dodge, H. F. Bauer, G. W. Brooks, W.-H. Chu, J. F. Dalzell, D. D. Kana, W. C. Reynolds, H. M. Satterlee, S. Silverman, The Dynamic Behavior of Liquids in Moving Containers, NASA, 1966.

[2] E. L. Grotle, V. Æsøy, Dynamic modelling of the thermal response enhanced by sloshing in marine LNG fuel tanks, Applied Thermal Engineering 135 (2018) 512–520. doi:10.1016/j.applthermaleng.2018.02.086.

[3] M. Ball, M. Wietschel, The future of hydrogen – opportunities and challenges, International Journal of Hydrogen Energy 34 (2) (2009) 615–627. doi:https://doi.org/10.1016/j.ijhydene.2008.11.014.

[4] P. Fortescue, J. Stark, Spacecraft Systems Engineering, Vol. 3, Wiley, 2003.

[5] J. Joseph, G. Agrawal, D. K. Agarwal, J. C. Pisharady, S. Sunil Kumar, Effect of insulation thickness on pressure evolution and thermal stratification in a cryogenic tank, Applied Thermal Engineering 111 (2016) 1629–1639. doi:10.1016/j.applthermaleng.2016.07.015.

[6] G. Petitpas, Boil-off losses along LH2 pathway-doi:10.2172/1466121.
URL https://www.osti.gov/biblio/1466121

[7] T. Arndt, Sloshing of Cryogenic Liquids in a Cylindrical Tank under normal Gravity Conditions, Ph.D. thesis, Universitat Bremen (2011).

[8] C. Ludwig, M. E. Dreyer, E. J. Hopfinger, Pressure variations in a cryogenic liquid storage tank subjected to periodic excitations, International Journal of Heat and Mass Transfer 66 (2013) 223–234. doi:10.1016/j.ijheatmasstransfer.2013.06.072.

[9] A. van Foreest, Modeling of cryogenic sloshing including heat and mass transfer, in: 46th AIAA/ASME/SAE/ASEE Joint Propulsion Conference and Exhibit, no. July, AIAA, Nashville, TN, 2010, pp. 1–20. doi:10.2514/6.2010-6891.

[10] ESA, Ariane 6, https://www.esa.int/Enabling_Support/Space_Transportation/Launch_vehicles/Ariane_6, accessed: 2022-02-25.

[11] J. Bradbury, R. Frostig, P. Hawkins, M. J. Johnson, C. Leary, D. Maclaurin, G. Necula, A. Paszke, J. VanderPlas, S. Wanderman-Milne, Q. Zhang, JAX: composable transformations of Python+NumPy programs (2018).

[12] M. Hasan, C. Lin, N. Vandresar, Self-pressurization of a flightweight liquid hydrogen storage tank subjected to low heat flux.

[13] I. H. Bell, J. Wronski, S. Quoilin, V. Lemort, Pure and pseudo-pure fluid thermophysical property evaluation and the

open-source thermophysical property library coolprop, Industrial & Engineering Chemistry Research 53 (6) (2014) 2498–2508. arXiv:http://pubs.acs.org/doi/pdf/10.1021/ie4033999, doi:10.1021/ie4033999.

[14] P. Virtanen, R. Gommers, T. E. Oliphant, M. Haberland, T. Reddy, D. Cournapeau, E. Burovski, P. Peterson, W. Weckesser, J. Bright, S. J. van der Walt, M. Brett, J. Wilson, K. J. Millman, N. Mayorov, A. R. J. Nelson, E. Jones, R. Kern, E. Larson, C. J. Carey, İ. Polat, Y. Feng, E. W. Moore, J. VanderPlas, D. Laxalde, J. Perktold, R. Cimrman, I. Henriksen, E. A. Quintero, C. R. Harris, A. M. Archibald, A. H. Ribeiro, F. Pedregosa, P. van Mulbregt, SciPy 1.0 Contributors, SciPy 1.0: Fundamental Algorithms for Scientific Computing in Python, Nature Methods 17 (2020) 261–272. doi:10.1038/s41592-019-0686-2.

Multi-fluid model with two kinematic scales for the simulation of liquid-gas interface in solid propulsion

Ward Haegeman

Aeronautics and Aerospace Department, von Karman Institute for Fluid Dynamics, Belgium, ward.haegeman@vki.ac.be

Supervisor: Thierry Magin

Professor, Aeronautics and Aerospace Department, von Karman Institute for Fluid Dynamics, Belgium, thierry.magin@vki.ac.be

University Supervisor: Marc Massot

Professor, Laboratoire de Mathématiques Appliquées, École polytechnique, France, marc.massot@polytechnique.edu

University Supervisor: Clément Le Touze

Research engineer, Département Multi-Physique pour l'Énergétique, Office National d'Études et de Recherches Aérospatiales, France, clement.le_touze@onera.fr

University Supervisor: Joël Dupays

Head of Research Unit, Département Multi-Physique pour l'Énergétique, Office National d'Études et de Recherches Aérospatiales, France, joel.dupays@onera.fr

Abstract

This thesis aims at developing in the CEDRE code, a CFD platform developed at ONERA for the aerospace and defense industries, the physical models and numerical methods allowing to simulate faithfully the multi-fluid flows which intervene in the interaction of hot supersonic jets with a free surface of water. The complexity of this type of flows results from the presence of many physical phenomena which are challenging from both a modelling and a numerical perspective. Among these features are the large range of Mach numbers, large range of temperatures, phase changes, turbulence... Because of the large disparity in scales (both in time and space) present in the configuration we are interested in, Direct Numerical Simulations are out of reach and thus we focus on reduced order models which belong to the class of diffuse interface models. Our strategy consists in the development of a 5-equation model which allows the two phases to be locally out of thermal equilibrium and will be able to capture the macroscopic features of the flow. This model will be coupled with a sub-scale model in order to get access to the microscopic features of the interface such as the surface area density of the interface, or its mean curvature. The innovation envisaged will be present both in the mathematical models and modelling techniques (continuum mechanics, kinetic theory, variational approaches and thermodynamics of irreversible processes), as well as in the mathematical and numerical analysis allowing the association of new generation numerical methods. The integration of these tools, first in rapid prototyping codes (Josiepy/Samurai) developped at CMAP and then in an industrial code at ONERA in order to carry out simulations that are still unattainable at present. This thesis being carried out at ONERA, the collaboration with VKI will focus on the development of an experimental set-up in order to validate the numerical strategy on the simplified configuration of a cold subsonic jet.

Keywords: Two-phase flows, Diffuse interface models, Finite volume methods, Two-scale modelling, Relaxation schemes.

Acknowledgments

This PhD is sponsored by the Agence Innovation de la Défense (AID) which is duly acknowledged. The author would also like to thank Jean-Baptiste Deuff for his role as technical advisor on behalf of the AID.

Reduced order combustion modelling of propulsion systems for variable cycle engine jet fighter applications

Karel Van den Borre

Turbomachinery and Propulsion Department, von Karman Institute for Fluid Dynamics, Belgium,karel.vandenborre@vki.ac.be

Supervisor: Bayindir H. Saracoglu

Research Expert, Turbomachinery and Propulsion Department, von Karman Institute for Fluid Dynamics, Belgium, saracog@vki.ac.be

Supervisor: Sergio Lavagnoli

Associate Professor, Turbomachinery and Propulsion Department, von Karman Institute for Fluid Dynamics, Belgium, lavagnoli@vki.ac.be

University Supervisor: Julien Blondeau

Myproposition (e.g. Professor), Applied Mechanics, Vrije Universiteit Brussel, Belgium, Julien.Blondeau@vub.be

Abstract

Variable Cycle Engines (VCE) are advanced propulsion systems that possess the ability to dynamically adjust their bypass ratio during flight. This is particularly advantageous in fighter jets, where optimizing engine performance at different flight regimes is essential to improve manoeuvrability, fuel efficiency and top speed. However, the VCE concept complicates engine throttling by introducing more control variables in the form of variable area injectors. Sustainability is an increasingly important consideration in future aircraft design. One approach is to switch to Sustainable Aviation Fuels (SAF), which have lower net carbon emissions when considering the complete fuel life cycle. High-fidelity CFD and experimental research have shown that SAF combustion significantly impacts pollutant formation, flame structure and combustion stability, which are unaccounted for in current preliminary engine design tools. Direct implementation of high-fidelity methods in these preliminary tools is computationally unfeasible.

The goal of this PhD is to improve the current low-cost combustion models by creating a computationally-efficient reduced-order model based on third-party high-fidelity CFD and experimental data. Multiple methodologies will be benchmarked, such as interpolation from pre-calculated tables, equivalent partially stirred reactor networks and artificial neural networks. These models will be used to design and optimise a variable cycle engine for fighter jet applications. The initial step is to use steady mixed 0D/1D tools to calculate the engine performance at multiple critical operating points. At each point, the engine control parameters must be optimised to determine the correct throttle setting. A gradient-free differential evolution algorithm will be used to optimise the engine design in terms of Thrust-Specific Fuel Consumption (TSFC) while meeting the mission requirements at each operating point. A transient digital twin will verify whether the engine design meets the full mission requirements in terms of thrust output, engine operability, stall margins, and transient response time. By coupling the reduced-order combustion model, it is possible to report total fuel consumption, pollutant emissions and combustion stability for multiple sustainable aviation fuels, which is currently not feasible in real-time simulations.

Keywords: Variable cycle engine, reduced order modelling, combustion, sustainable aviation fuels, digital twin

RAREFIED AND PLASMA FLOWS

Hybridized discontinuous Galerkin method for multidomain problems

Nicolas Corthouts

Aeronautics and Aerospace Department, von Karman Institute for Fluid Dynamics, Belgium, nicolas.corthouts@vki.ac.be

Supervisor: Georg May

Associate Professor, Aeronautics and Aerospace Department, von Karman Institute for Fluid Dynamics, Belgium, georg.may@vki.ac.be

University Supervisor: Koen Hillewaert

Associate professor, Design of Turbomachines, Uliège, Belgium, koen.hillewaert@uliege.be

Abstract

This work presents a novel approach in using hybridized discontinuous Galerkin solver for multi-domain problems. A monolithic approach is employed and the formulation and its solution strategy are presented.

Keywords: Hybridized Discontinuous Galerkin, Multi-Domain, Monolithic solver, High-order methods.

1. Introduction

One of the challenges of multi-physics problems are the multi-domain simulations. The mesh of these simulations is composed of several subdomains, possibly governed by very different equations and hosting materials with various properties. They are interconnected with specific interface conditions. For instance in the conjugate heat transfer (CHT) problem, the equations governing the heat transfer in the solid material is a simple heat diffusion equation, while the Navier-Stokes equations are solved for the fluid part. In that case, both the governing equations and the nature of the materials differ. In the case of inductively coupled plasma (ICP), the full system of Navier-Stokes and electric field equation is solved inside the torch, while only the electric field equation rules the domain outside the facility. A last example is the propagation of waves across two media with different refraction indices. The equations are the same but the media and propagation speeds are different. Regarding the vast number of applications of multi-domain problems, the development of solvers for these types of configurations is crucial. In particular, this work is inscribed in the development of Hybridized Discontinuous Galerkin (HDG) ICP solver.

This work is presentd as follows. First, comparisons with the strategies existing in the literature for solving multi-domain problems is performed. Then, the basis of HDG method and its solution strategy is presented. Next, an extension of the HDG method to multi-domain problems is derived. Finally, a comparison of the numerical and analytical solutions of a classic multi-domain case, called the conjugate heat transfer (CHT) problem, is presented.

2. Multi-domain in the literature

There are two main approaches to multi-domain simulations. The first one is the coupled approach, where the domains are handled separately by stand alone solvers exchanging data. The information collected by one domain at its boundary is considered as a known, even though it is the result of the computations from another domain. This approach is conceptually simple and straightforward to implement. However, it does not fully respect the true variation of the boundary values values at the interface, and can lead to slower convergence rate than the conjugate approach, which is discussed below. The method is also know to lead to instabilities and may require to interpolate the solution at the boundary interface, since the mesh is not guaranteed to be continuous between the models. There is a lot of literature on stability analysis of coupled method (see for instance *e.g.* [1; 2]). An example of application for inductively coupled plasma can be found in [3; 4].

The second approach is the fully conjugate one. This time, the system is solved as a whole. This method takes into account the variation of the interface condition with the unknowns on each side. However, it is much more complex to implement, and has a strong impact on the system structure as it links the unknowns from one domain to another. However, the scheme resulting from these considerations are more stable. In this work, a fully-coupled approach is developed for the HDG method. To our best knowledge, this approach has never been tried before in the literature for HDG. The closest examples are found in solution of multi-domain problems with the classic DG method [5].

3. The hybridized discontinuous Galerkin method.

The basic principles of hybridized discontinuous Galerkin (HDG) method is described in this section, following the derivations of [6; 7; 8; 9]. The code is implemented in the Unified Framework, a code developed at the von Karman Institute of Fluid Dynamics and RWTH Aachen by the group of Prof. May [10]. The method belongs to the family of Discontinuous Galerkin method, which have the conservativity properties of finite volumes (FV), the compact stencil and the high-order accuracy of finite elements (FE). Classic DG methods have the disadvantage to present a large number of globally coupled degrees of freedom, leading to expensive computations in several cases. HDG mitigates this drawback by solving first a set of small systems located at each element, then solve for a reduced set of unknowns, called the hybrid unknowns. The local system resolution is an embarrassingly parallel problem. Consequently, the method has a larger number of degrees of freedom, but requires to invert smaller matrices. Note that the HDG method loses all its main advantages when run as a single thread compared to classical DG.

Let us first consider the following general problem on a domain Ω:

$$\partial_t w + \nabla \cdot F(w, \nabla w) = S(w, \nabla w) \tag{1}$$

with $w : \Omega \times \mathbb{R}^+ \to \mathbb{R}^N$ the vector of conserved variables, $F : \mathbb{R}^N \times \mathbb{R}^{N\times D} \to \mathbb{R}^{N\times D}$ is the flux vector and $S : \mathbb{R}^N \times \mathbb{R}^{N\times D} \to \mathbb{R}^{N\times D}$ is the source vector.

Let us define $q = \nabla w$ so that the equation can be rewritten in its mixed form:

$$\begin{aligned} \partial_t w + \nabla \cdot F(w, q) &= S(w, q) \\ q &= \nabla w \end{aligned} \tag{2}$$

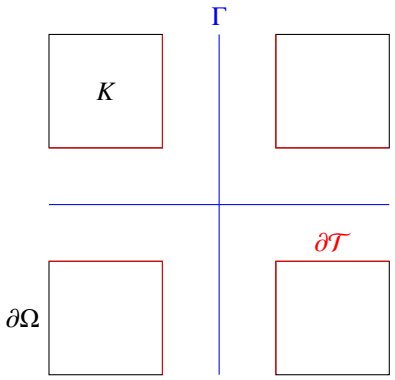

Figure 1: Illustration of the various sets encountered in the HDG method.

The unknowns of the problem are now w and q. This formulation allows to compute the gradient of the variable q with the same precision as the variable w. Indeed, gradients can be very important for certain problems (*e.g.* temperature gradients in heat transfer) and need to be computed with the highest possible accuracy.

3.1. Mesh partition

We will assume that Ω can be meshed by N non-overlapping elements in the set $\mathcal{T} = \{K\}$ such that

$$\Omega = \bigcup_{K\in\mathcal{T}} K \tag{3}$$

The set of element boundaries is defined as

$$\partial\mathcal{T} = \{\partial K \setminus \partial\Omega : K \in \mathcal{T}\} \tag{4}$$

The skeleton of the mesh is the set Γ defined as

$$\Gamma = \{e : e = K \cap K';\ \forall K, K' \in \mathcal{T};\ K \neq K'\} \tag{5}$$

An illustration of each set is given in Fig. 3.1. Note that each element of Γ appears twice in $\partial\mathcal{T}$ and that none of these sets contain the boundary $\partial\Omega$ of the domain.

3.2. Functional spaces

The idea of HDG is to estimate the solution to Eq. 2 by approximating

1. w and q,on the elements $K \in \mathcal{T}$.
2. $\lambda = w|_\Gamma$, called the hybrid unknowns, which will be introduced later, on the trace Γ.

The functional spaces associated with each problem are given as follows:

$$\begin{aligned} \mathbf{V}_h &= \{v \in L^2(\Omega) : v_{|_K} \in \Pi^p(K), K \in \mathcal{T}\}^{N\times D} \\ W_h &= \{w \in L^2(\Omega) : w_{|_K} \in \Pi^p(K), K \in \mathcal{T}\}^{N} \\ M_h &= \{\mu \in L^2(\Gamma) : \mu_{|_e} \in \Pi^p(e), e \in \Gamma\}^{N} \end{aligned} \tag{6}$$

Let us define the set

$$\mathbb{X}_h = \mathbf{V}_h \times W_h \times M_h \tag{7}$$

for convenience. The goal of the method is to find an approximation $(w_h, q_h, \lambda_h) \in \mathbb{X}_h$ using test functions $(\tau, \phi, \mu) \in \mathbb{X}_h$. Remark that $\mathbf{V}_h \in \mathbf{V}$, $W_h \in W$ and $M_h \in M$, with $\mathbf{V}$, W, M the sets of trial functions on the elements for the gradient and scalar unknowns, and on the skeleton elements for the hybrid unknowns respectively.

3.3. Primal formulation

Following the approach adopted by [6], a general primal formulation of the discontinuous Galerkin method is derived. The primal formulation is the weak form of Eq. 2 where the interface fluxes have been replaced by their numerical counterparts. In the case of discontinuous Galerkin method, one has

$$\begin{aligned} &(q_h, \tau)_\Omega - \langle \hat{w}, \tau\rangle_{\partial\mathcal{T}} - \langle w_0, \tau\rangle_{\partial\Omega} + (w_h \nabla\tau)_\Omega = 0 \\ &(\partial_t w_h - S, \phi)_\Omega + \left\langle \hat{f}, \phi \right\rangle_{\partial\mathcal{T}\bigcup\partial\Omega} - (F, \nabla\phi)_\Omega = 0 \end{aligned} \tag{8}$$

where the notations are defined as

$$\begin{aligned} (a,b)_U &= \int_U ab\, dV, \\ \langle a,b\rangle_L &= \int_L ab\cdot n\, dS, \end{aligned} \tag{9}$$

the subscripts h denotes the approximation of a quantity, $\hat{f}$ is the numerical flux vector, $\hat{w}$ is the numerical flux gradient vector and w_0 represents the set of boundary conditions.

The choice of the numerical flux functions $\hat{f}$ and $\hat{w}$ is of capital importance for the method. They must be carefully crafted in order to achieve stability, consistency and convergence. Note that a single physical flux function F is used here with its numerical counterpart $\hat{f}$. Usually, these fluxes are split into two contributions: a convective F_c and diffusive F_v parts:

$$F(w,q) = F_c(w) - F_v(w,q) \tag{10}$$

and their numerical counterparts

$$\hat{f}(w^\pm, q^\pm) = \hat{f}_c(w^\pm) - \hat{f}_v(w^\pm, q^\pm) \tag{11}$$

Where the + and − sign indicated if the value of w and q have been taken on the side where the normal is outward or inward pointing respectively. Let us emphasize that the numerical flux function itself $\hat{f}$ may depend on the facet on which it is applied. For instance, the boundary fluxes can be imposed strongly. Consequently, the relation $\hat{f} = F$ is imposed on the boundary facets, *i.e.* on $\partial\Omega$, while $\hat{f}$ is defined in a different manner on the inside of the domain. Secondly, if one chooses the following approximations

$$\begin{aligned} q_h &= \nabla w_h \\ \hat{w} &= w_h \end{aligned} \tag{12}$$

the first equation of Eq. 8 is trivially satisfied, reducing to the classic DG system

$$(\partial_t w_h - S, \phi)_\Omega + \left\langle \hat{f}, \phi \right\rangle_{\partial\mathcal{T}\bigcup\partial\Omega} - (F, \nabla\phi)_\Omega = 0 \tag{13}$$

Finally, the primal form Eq. 8 only requires the definition of the spaces $\mathbf{V}$ and W.

The HDG method can be defined by extending Eq. 8 and using the full functional space $\mathbb{X}$. The core concept of this discretization is the introduction of the hybrid unknowns $\lambda = w_{|_\Gamma}$ on the trace of the mesh, defined by Γ. The primal formulation of HDG is then obtained by defining

$$\hat{w} = \lambda_h \tag{14}$$

and modifying $\hat{f}$ so that

$$\begin{aligned} &(q_h, \tau)_\Omega - \langle \lambda, \tau\rangle_{\partial\mathcal{T}} - \langle w_0, \tau\rangle_{\partial\Omega} + (w_h, \nabla\tau)_\Omega = 0 \\ &(\partial_t w_h - S, \phi)_\Omega + \left\langle \hat{f}, \phi \right\rangle_{\partial\mathcal{T}\bigcup\partial\Omega} - (F, \nabla\phi)_\Omega = 0 \\ &\left\langle [[\hat{f}]], \mu \right\rangle_\Gamma = 0 \end{aligned} \tag{15}$$

Where $\Gamma^0 = \Gamma \setminus \partial\Omega$, the jump operator $[[\cdot]]$ is defined as

$$[[a]] = \begin{cases} a^+\cdot n^+ + a^-\cdot n^- & x \in \Gamma^0 \\ a\cdot n & x \in \partial\Omega \end{cases}, \tag{16}$$

The last equation of Eq. 15 is the weak form of the continuity of the normal component of the interface numerical fluxes equation. This equation is of capital importance for retaining the conservativity of the scheme.

3.3.1. Discrete system

If a^K is the restriction of quantity a to element K, a_i^K is the ith nodal value of a^K, then for each element

$K \in \mathcal{T}$ and $L \in \Gamma$,

$$\begin{aligned} q_h^K(x) &= \sum_{i=1}^{M} q_i^K \tau_i^K(x) \\ w_h^K(x) &= \sum_{i=1}^{M} w_i^K \phi_i^K(x) \\ \lambda_h^L(x) &= \sum_{i=1}^{M'} \lambda_i^L \mu_i^L(x). \end{aligned} \tag{17}$$

Eq. 15 is solved with respect to $(w_j^K, q_j^K, \lambda_j^L)$ and is thus of the form

$$\mathcal{R}(w_j^K, q_j^K, \lambda_j^L) = \begin{pmatrix} \mathcal{R}_1 & \mathcal{R}_2 & \mathcal{R}_3 \end{pmatrix} = 0, \tag{18}$$

with $\mathcal{R}$ the residual matrix, whose components are defined by

$$\begin{aligned} \mathcal{R}_1 &= \left(q_j^K \phi_j, \tau_i\right)_K + \left(w_j^K \phi_j, \nabla \tau_i\right)_K \\ &\quad - \left\langle \lambda_j^L \mu_j, [[\tau]] \right\rangle_L - \left\langle w_0^L \mu_j, [[\tau]] \right\rangle_L \\ \mathcal{R}_2 &= \left(\partial_t w_j^K \phi_j - S^K, \phi_i\right)_K + \left\langle \hat{f}^L, \phi_i \right\rangle_L \\ &\quad - \left(F^K, \nabla \phi_i\right)_K \\ \mathcal{R}_3 &= \left\langle [[\hat{f}]], \mu_j \right\rangle_\Gamma \end{aligned} \tag{19}$$

where Einstein's summation convention on repeated indices is applied and L represent and element of Γ.

The Newton-Raphson method is used to solve this problem. Note that, since the steady state is of interest in our case, a damping term is added to improve convergence. For computing the $k+1$ step of the Newton iteration, this term is given by

$$\partial_t (w_j^K)_k \simeq \frac{(w_j^K)_{k+1} - (w_j^K)_k}{\Delta (t^K)_k} \tag{20}$$

The final system is of the form

$$\begin{pmatrix} A & B & R \\ C & D & S \\ L & M & N \end{pmatrix} \begin{pmatrix} \delta Q \\ \delta W \\ \delta \Lambda \end{pmatrix} = \begin{pmatrix} -\mathcal{R}_1 \\ -\mathcal{R}_2 \\ -\mathcal{R}_3 \end{pmatrix} = \begin{pmatrix} F \\ G \\ H \end{pmatrix}. \tag{21}$$

The components of the Jacobian are listed in Appendix A.

3.4. Solution strategy

The solution strategy of Eq. 21 is the following. First, one must realize that A, B, C and D are block-diagonal matrices, with each block of size $O(M^2)$, with M the number of degrees of freedom on the element. Consequently, these blocks are small compared to the complete jacobian, and can be easily inverted through direct inversion of the matrices. Following this reasoning, one can split Eq. 21 into two subsystems, namely the local systems

$$\begin{pmatrix} A & B \\ C & D \end{pmatrix} \begin{pmatrix} \delta Q \\ \delta W \end{pmatrix} = \begin{pmatrix} F \\ G \end{pmatrix} - \begin{pmatrix} R \\ S \end{pmatrix} \delta \Lambda, \tag{22}$$

and the global system

$$\begin{pmatrix} L & M \end{pmatrix} \begin{pmatrix} \delta Q \\ \delta W \end{pmatrix} + N \delta \Lambda = H. \tag{23}$$

Eliminating the local variables in Eq. 22 and plugging the expression in Eq. 23, one obtains

$$\begin{aligned} &\left(N - \begin{pmatrix} L & M \end{pmatrix} \begin{pmatrix} A & B \\ C & D \end{pmatrix}^{-1} \begin{pmatrix} R \\ S \end{pmatrix}\right) \delta \Lambda \\ &\qquad = H - \begin{pmatrix} L & M \end{pmatrix} \begin{pmatrix} A & B \\ C & D \end{pmatrix}^{-1} \begin{pmatrix} F \\ G \end{pmatrix} \end{aligned} \tag{24}$$

The solution procedure is represented in Algorithm 1. The main idea is to solve first for the global system Eq. 24, then inject the solution in Eq. 22 to obtain q_h and w_h. Then, the process is repeated until convergence occur. However, it is possible to compute during the assembly of Eq. 24 the local unknowns.

Algorithm 1 Solution procedure for HDG

```
Initialize λ_h, w_h, q_h;
while ||R||_2 > ε do
    for i = 1,..., N do
        Assemble local system (Eq. 22);
        Solve local system;
        Store local solution;
        Assemble global system (Eq. 24);
    end for
    Solve global system;
    Update λ_h, w_h, q_h;
end while
```

4. HDG applied to multi-model problems

The goal of this section is to extend the HDG framework to multi-model problems. Multi-model problems are characterised by various physics on different fixed parts of the domain. For instance, in inductively coupled plasma (ICP) applications, the Maxwell's equation rule inside the ICP torch, while only the electric field is solved outside of the torch. These two physical models must communicate through the torch wall: for Navier stokes, an isothermal wall is present, while the tangential component of the electric field is continuous through the wall (Fig. 2).

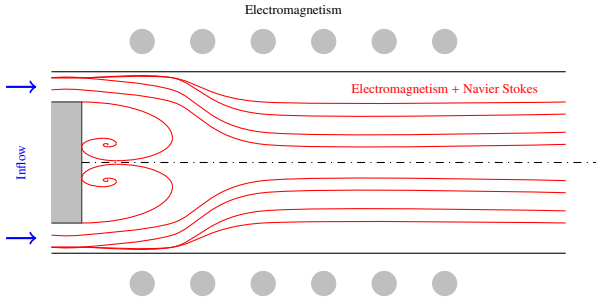

Figure 2: Inductively coupled plasma is an example of multi-physics model. Inside the torch, the electromagnetic and Navier-Stokes equation are solved numerically. On the other hand, only the electromagnetic equations are solved outside the domain. Suitable boundary conditions must be applied at the interface of the domains.

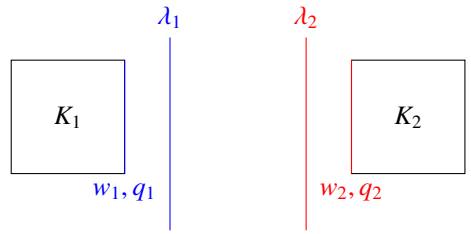

Figure 3: Fundamental concept of multi-domain HDG. The hybrid unknowns at the multi-domain interface are doubled. A relation ship between the hybrid unknowns of these facets and the opposing values must exist for the problem to be well-posed.

4.1. Fundamental concept

The fundamental concept behind this multi-domain formulation is the definition of a double set of hybrid unknowns at the multi-domain interface: one for each model. An illustration is given Fig. 3.

In the classic HDG method, the equation linking all the elements together is the normal flux conservation equation, which is given by

$$\left\langle [[\hat{f}(w_h, q_h, \lambda_h]], \mu \right\rangle_{\Gamma} = 0 \tag{25}$$

At an interface boundary, this equation is replaced by two equations guaranteeing the conservativity of the normal numerical flux through the mesh skeleton,

$$\left\langle \hat{f}(w_h^s, q_h^s, \lambda_h^s) - \hat{f}(\lambda_h^s, q_h^s, \lambda_h^t, q_h^t), \mu \right\rangle_{\Gamma^{s,t}} = 0, \tag{26}$$

Where $\Gamma^{s,t}$ represents the frontier between Ω_s and Ω_t:

$$\Gamma^{s,t} = \partial\Omega_s \bigcap \partial\Omega_t \tag{27}$$

Boundary conditions are imposed weakly on a subset of unknowns. In that case, Eq. 25 is replaced by

$$\left\langle \hat{f}(w_h^s, q_h^s, \lambda_h^s) - \hat{f}(\lambda_h^s, q_h^s, w_h^0, q_h^0), \mu \right\rangle_{\Gamma^{s,t}} = 0 \tag{28}$$

This coupling approach has the non-negligible advantage to keep the same solution strategy as in the single domain case, meaning the successive solution of many small local systems and the resolution of the hybrid unknowns. This is shown in the next section.

4.2. Primal formulation

Let us consider the domain

$$\Omega = \bigcup_s \Omega_s \tag{29}$$

where the equations to be solved might differ on each domain Ω_s. Let us now assume that a domain Ω_s is tessellated using the triangulation $\mathcal{T}_s$. If one assumes that each physical domain is isolated from the other, one can rewrite a primal formulation for each Ω_s as follows:

$$\begin{aligned}
&(q_h^s, \tau)_{\Omega^s} - \langle \lambda_h^s, \tau \rangle_{\partial\mathcal{T}^s} \langle w_0^s, \tau \rangle_{\partial\Omega^s} - (w_h^s, \nabla\tau)_{\Omega^s} = 0 \\
&(\partial_t w_h^s - S^s, \phi)_{\Omega^s} + \left\langle \hat{f}, \phi \right\rangle_{\partial\mathcal{T}^s} - (F^s, \nabla\phi)_{\Omega^s} = 0 \\
&\left\langle [[\hat{f}^s]], \mu \right\rangle_{\Gamma^s} = 0
\end{aligned} \tag{30}$$

all the symbols keep their previous definitions, except that the superscript s denotes the physical domain under consideration. If the interactions between the physical models is now considered, one gets

$$\begin{aligned}
&(q_h^s, \tau)_{\Omega^s} - \langle \lambda_h^s, \tau \rangle_{\partial\mathcal{T}^s} - \langle w_0^s, \tau \rangle_{\partial\Omega^s} - (w_h^s, \nabla\tau)_{\Omega^s} = 0 \\
&(\partial_t w_h^s - S^s, \phi)_{\Omega^s} + \left\langle \hat{f}, \phi \right\rangle_{\partial K} - (F^s, \nabla\phi)_{\Omega^s} = 0 \\
&\left\langle [[\hat{f}^s]], \mu \right\rangle_{\Gamma^{0,s}} = 0 \\
&\left\langle \hat{f}^s - \hat{f}^{s,t}, \mu \right\rangle_{\Gamma^{s,t}} = 0
\end{aligned} \tag{31}$$

where $\hat{f}^{s,t}$ is a numerical flux representing the coupling between the domains, or a boundary condition.

Now, let us focus on an element K^s belonging to the physical model s. The weak formulation for this element is thus given by

$$\begin{aligned}
&(q_h^s, \tau)_{K^s} - \langle \lambda_h^s, \tau \rangle_{\partial K^s} - \langle w_0^s, \tau \rangle_{\partial K^s} - (w_h^s, \nabla\tau)_{K^s} = 0 \\
&(\partial_t w_h^s - S^s, \phi)_{K^s} + \left\langle \hat{f}, \phi \right\rangle_{\partial K^s} - (F^s, \nabla\phi)_{K^s} = 0 \\
&\left\langle [[\hat{f}^s]], \mu \right\rangle_{\partial K^s} = 0 \\
&\sum_t \left\langle \hat{f}^s - \hat{f}^{s,t}, \mu \right\rangle_{\partial K^{s,t}} = 0
\end{aligned} \tag{32}$$

where $\partial K^{s,t}$ is defined by

$$K^{s,t} = K^s \bigcap K^t \tag{33}$$

The matrix representing the linearized global system has a block diagonal and has some coupling denoted by blocks that are off-diagonal. An example

$$\left(\begin{array}{ccc|ccc|ccc} A_1 & B_1 & R_1 & 0 & 0 & 0 & 0 & 0 & 0 \\ C_1 & D_1 & S_1 & 0 & 0 & 0 & 0 & 0 & 0 \\ L_1 & M_1 & N_1 & L_{12} & 0 & N_{12} & L_{13} & 0 & N_{13} \\ \hline 0 & 0 & 0 & A_2 & B_2 & R_2 & 0 & 0 & 0 \\ 0 & 0 & 0 & C_2 & D_2 & S_2 & 0 & 0 & 0 \\ L_{21} & 0 & N_{21} & L_2 & M_2 & N_2 & L_{23} & 0 & N_{23} \\ \hline 0 & 0 & 0 & 0 & 0 & 0 & A_3 & B_3 & R_3 \\ 0 & 0 & 0 & 0 & 0 & 0 & C_3 & D_3 & S_3 \\ L_{31} & 0 & N_{31} & L_{32} & 0 & N_{32} & L_3 & M_3 & N_3 \end{array}\right)\left(\begin{array}{c} \delta Q_1 \\ \delta W_1 \\ \delta\Lambda_1 \\ \hline \delta Q_2 \\ \delta W_2 \\ \delta\Lambda_2 \\ \hline \delta Q_3 \\ \delta W_3 \\ \delta\Lambda_3 \end{array}\right) = \left(\begin{array}{c} -\mathcal{R}_1^1 \\ -\mathcal{R}_2^1 \\ -\mathcal{R}_3^1 \\ \hline -\mathcal{R}_1^2 \\ -\mathcal{R}_2^2 \\ -\mathcal{R}_3^2 \\ \hline -\mathcal{R}_1^3 \\ -\mathcal{R}_2^3 \\ -\mathcal{R}_3^3 \end{array}\right)$$

Figure 4: Example of the structure of the matrix to be solved for a HDG problem with three physical models.

of such a matrix with three physical models is given Fig. 38. The elimination can be performed as in the one model version of HDG. The local equations become

$$\begin{pmatrix} A_s & B_s \\ C_s & D_s \end{pmatrix}\begin{pmatrix} \delta Q_s \\ \delta W_s \end{pmatrix} = \begin{pmatrix} F_s \\ G_s \end{pmatrix} - \begin{pmatrix} R_s \\ S_s \end{pmatrix}\delta\Lambda_s \tag{34}$$

The hybrid equation then becomes

$$\begin{aligned} N_s\delta\Lambda_s \quad &= \delta H_s - \begin{pmatrix} L_s & M_s \end{pmatrix}\begin{pmatrix} \delta Q_s \\ \delta W_s \end{pmatrix} \\ &\quad - \sum_{t\neq s}\left[L_{st}\delta Q_t + N_{st}\delta\Lambda_t\right] \end{aligned} \tag{35}$$

Let us first define

$$\begin{pmatrix} Q_s^0 \\ W_s^0 \end{pmatrix} = \begin{pmatrix} A_s & B_s \\ C_s & D_s \end{pmatrix}^{-1}\begin{pmatrix} F_s \\ G_s \end{pmatrix} \tag{36}$$

and

$$\begin{pmatrix} Q_s' \\ W_s' \end{pmatrix} = \begin{pmatrix} A_s & B_s \\ C_s & D_s \end{pmatrix}^{-1}\begin{pmatrix} R_s \\ S_s \end{pmatrix} \tag{37}$$

the equation can be rewritten

$$\begin{aligned} &\left(N_s - \begin{pmatrix} L_s & M_s \end{pmatrix}\begin{pmatrix} Q_s' \\ W_s' \end{pmatrix}\right)\delta\Lambda_s \\ &\quad + \sum_{t\neq s}\left[N_{st} - L_{st}Q_t'\right]\delta\Lambda_t \\ &\quad = H_s - \begin{pmatrix} L_s & M_s \end{pmatrix}\begin{pmatrix} Q_s^0 \\ W_s^0 \end{pmatrix} - \sum_{t\neq s} L_{st}Q_t^0 \end{aligned} \tag{38}$$

which is formally the same equation as for the single-domain case with additional coupling terms.

5. Validation on conjugate heat transfer

The conjugate heat transfer (CHT) problem is a classic multi-domain problem for which an approximate analytical solution exists [11]. A schematic of the problem is given Fig. 5. There are two distinct sets of equations to be solved.

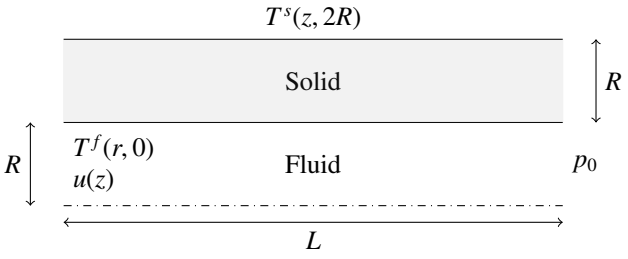

Figure 5: Illustration of the conjugate heat transfer problem. The pipe is made of concrete with finite thickness. Heat is exchanged between the solid and the fluid.

5.1. Navier-Stokes

On the fluid side, the classic Navier-Stokes equations are solved.

$$\begin{aligned} \partial_t\rho + \nabla\cdot(\rho\mathbf{u}) &= 0 \\ \partial_t(\rho\mathbf{u}) + \nabla\cdot(\rho\mathbf{u}\mathbf{u} + p\mathbb{I} - \tau) &= 0 \\ \partial_t(\rho E) + \nabla\cdot(\rho E\cdot\mathbf{u} + p\mathbf{u} - \tau\cdot\mathbf{u}) &= 0 \end{aligned} \tag{39}$$

where ρ is the fluid density, p is the static pressure, $\mathbf{u}$ is the velocity vector, $E = e + \frac{|\mathbf{u}|^2}{2}$ is the total energy, e is the fluid internal energy and τ is the viscous stress tensor.

In the following, it is considered that this set of equations is solved using the primitive variables $(p, \mathbf{u}, T)$, with T the temperature.

5.2. Solid side

On the solid side, only an equation for temperature conduction is solved, namely

$$\rho_s C_s\partial_t T - \nabla\cdot(\lambda_s\nabla T) = 0 \tag{40}$$

with C_s the heat capacity of the solid, ρ_s the solid density and λ_s the solid thermal conductivity.

5.3. Coupling

The coupling between Navier-Stokes and the solid conduction equation occur at the level of the temperature, which must remain constant across the interface,

$$T^f = T^s, \tag{41}$$

with T^f the fluid temperature and T^s the solid one, and through the heat fluxes, which must be equal on both sides, namely that

$$\lambda_s \nabla T^s = \lambda_f \nabla T^f \tag{42}$$

5.4. Analytical solution

The well known anaylytical solution of the CHT problem is given, for a reference mach number

$$M = \frac{u(0,0)}{c(0,0)},$$

with c the speed of sound of the fluid, satisfying $M^2 < 1$, and a maximal temperature variation ΔT over both domains such that $\frac{\Delta T}{T} < 1$,

Fluid.

$$\begin{aligned} \mathbf{u}(z) &= \frac{\beta}{4\mu}(R^2 - r^2)\mathbf{e}_z \\ p(z) &= \beta(l - z) + p_0 \\ T(r,z) &= T_0 - \frac{2\beta}{\rho c_p} z - \frac{Pr}{c_p}\left(\frac{\beta R r}{4\mu}\right)^2 \end{aligned} \tag{43}$$

Solid.

$$\begin{aligned} T^s(r,z) \quad &= T_0 - \frac{\beta^2 R^4}{8\mu\lambda^s_{rr}} \ln\left(\frac{r}{R}\right) - \frac{2\beta}{\rho c_p} z \\ &- \frac{Pr}{c_p}\left(\frac{\beta R^2}{4\mu}\right)^2 \end{aligned} \tag{44}$$

where all symbols previously defined keep their meaning, β is a constant pressure gradient, R and l are the pipe radius and length respectively, μ is the dynamic viscosity, λ^s_{rr} is the solid thermal conductivity coefficient in the radial direction, T_0 is a reference temperature, c_p is the fluid capacity at constant pressure and $Pr = \frac{c_p \mu}{\lambda}$, where λ is the fluid thermal conductivity.

5.5. Boundary conditions

The analytical temperature and velocity profiles are applied at the inlet of the channel. The outlet is at atmospheric pressure. The analytical heat fluxes are applied at the solid left and right boundaries, namely

$$\begin{aligned} \mathbf{q}|_{z=0} &= -\lambda_{rr}\partial_z T|_{z=0}\mathbf{e}_z = \lambda_{rr}\frac{2\beta}{\rho c_p} \\ \mathbf{q}|_{z=l} &= -\lambda_{rr}\partial_z T|_{z=l}\mathbf{e}_z = \lambda_{rr}\frac{2\beta}{\rho c_p} \end{aligned} \tag{45}$$

For the upper boundary, the analytical temperature profile is imposed.

5.6. Numerical values

In order to remain in the hypothesis of validity of the analytical solution, the following numerical values are chosen for the various parameters of the problem:

- $p_0 = 10^5$ Pa.
- $T_0 = 300$ K.
- $M^2 = 0.1$, which leads sets the value of β.
- $\mu = 1.9424 \cdot 10^{-5}$ Pa s.
- $\lambda^s_{rr} = 10^{-2}$ W m^{-1} K^{-1}.
- $\lambda^s_{zz} = 1$ W m^{-1} K^{-1}.
- $\lambda = 2.84695 \cdot 10^{-2}$ W m^{-1} K^{-1}.
- $c_p = 1010.78$ J kg^{-1} K^{-1}.
- $\rho = 1.15663$ kg m$^{-}3$.
- $R = 10^{-4}$ m.
- $l = 3 \cdot 10^{-3}$ m.

5.7. Initial conditions

The initial conditions are a uniform temperature and velocity over the whole domain. The values chosen are the one for the maximal temperatures and velocities respectively.

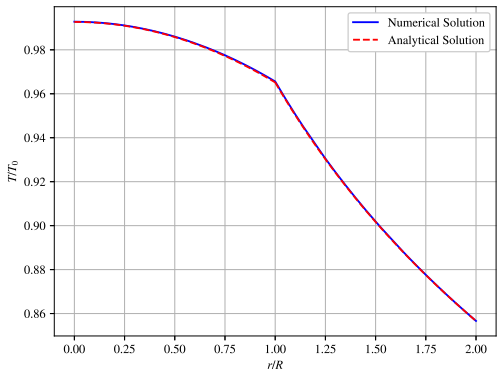

Figure 6: Comparison between the analytical and numerical temperature profiles in the CHT problem.

5.8. Results

In this section, a comparison between the analytical and numerical solution is given Fig. 6. The mesh used for the validation simulation has been generated using Netgen. It is relatively coarse (480 triangular elements, only 4 elements in the radial direction, which is the direction of largest temperature gradients). This is not a problem as the solution is computed using a fourth degree polynomial approximation and is expected to have a polynomial profile of degree 2 at most.

Although there is an obvious match between the solutions, one must keep in mind that the analytical profile has been obtained at the cost of an important hypothesis: the heating of the fluid due to viscous effects has been neglected. Consequently, since our solver is not able to remove these temperature effects, there will always be a discrepancy between the fluid temperature obtained numerically and the analytical solution, making a convergence study impossible. The convergence study is consequently left for future work.

6. Conclusions and future work

This paper presented a new monolithic solver for multi-domain based on the hybridized discontinuous Galerkin method. It opens the path to the numerical simulation of many complex phenomena. Moreover, it is a milestone in the developement of a high order ICP code. An important feature of this new method is the ability to represent discontinuous solutions across the interfaces by the doubling of the hybrid nodes at the mesh skeleton, leading to potential applications in electromagnetics, where the electric field can be discontinuous across the interface, or even light propagation, where the speed of light varies across the boundary of two media having a different refraction index.

However, the scheme has yet to be properly analysed concerning its consistency, stability and convergence. In order to verify the implementation, a convergence study on a true analytical (and not an approximated one, unlike the one that was presented here) solution must be performed.

Appendix A. Jacobian of the classic HDG

The components of the Jacobian matrix of the classic HDG are given in this section. All symbols keep the same definition as previously stated.

$$
\begin{aligned}
A = \frac{\partial \mathcal{R}_1}{\partial q_l^K} &= (\tau_l, \tau_i)_K \\
B = \frac{\partial \mathcal{R}_1}{\partial w_l^K} &= (\phi_l, \nabla\tau_i)_K - \left\langle \frac{\partial w_0}{\partial w_l}, \phi_l \tau_i \right\rangle_{\partial K^\Omega} \\
R = \frac{\partial \mathcal{R}_1}{\partial \lambda_l^L} &= -\langle \mu_l, [[\tau_l]] \rangle_L \\
C = \frac{\partial \mathcal{R}_2}{\partial q_l^K} &= \left\langle \frac{\partial \hat{f}}{\partial q}\tau_l, \phi_i \right\rangle_{\partial K} - \left(\frac{\partial S}{\partial q}\tau_l, \phi_i \right)_K \\
&\quad + \left(\frac{\partial F}{\partial q}\tau_l, \nabla\phi_i \right)_K \\
D = \frac{\partial \mathcal{R}_2}{\partial w_l^K} &= \left(\left[\frac{\mathbb{I}}{\Delta t^K} - \frac{\partial S}{\partial w} \right] \phi_l, \phi_i \right)_K \\
&\quad - \left(\frac{\partial F}{\partial w}\phi_l, \nabla\phi_i \right)_K + \left\langle \frac{\partial \hat{f}}{\partial w}\phi_l, \phi_i \right\rangle_{\partial K} \\
S = \frac{\partial \mathcal{R}_2}{\partial \lambda_l^L} &= \left\langle \frac{\partial [[\hat{f}]]}{\partial \lambda}\mu_l, \phi_i \right\rangle_L \\
L = \frac{\partial \mathcal{R}_3}{\partial q_l^K} &= \left\langle \frac{\partial \hat{f}}{\partial q}\tau_l, \mu_i \right\rangle_{\partial K \cap \Gamma^0} \\
M = \frac{\partial \mathcal{R}_3}{\partial w_l^K} &= \left\langle \frac{\partial \hat{f}}{\partial w}\phi_l, \mu_i \right\rangle_{\partial K \cap \Gamma^0} \\
N = \frac{\partial \mathcal{R}_3}{\partial \lambda_l^L} &= \left\langle \frac{\partial [[\hat{f}]]}{\partial \lambda}\mu_l, \mu_i \right\rangle_L
\end{aligned}
\tag{A.1}
$$

Appendix B. Jacobian of the multi-model HDG

The components of the Jacobian matrix of the multimodel HDG are given in this section. All symbols

keep the same definition as previously stated.

$$
\begin{aligned}
A_s &= \frac{\partial \mathcal{R}_1}{\partial q_l^{K_s}} = (\tau_l, \tau_i)_{K_s} \\
B_s &= \frac{\partial \mathcal{R}_1}{\partial w_l^{K_s}} = (\phi_l, \nabla\tau_i)_{K_s} - \left\langle \frac{\partial w_0}{\partial w_l}, \phi_l \tau_i \right\rangle_{\partial K_s^\Omega} \\
R_s &= \frac{\partial \mathcal{R}_1}{\partial \lambda_l^{L_s}} = -\langle \mu_l, [[\tau_l]] \rangle_{L_s} \\
C_s &= \frac{\partial \mathcal{R}_2}{\partial q_l^{K_s}} = \left\langle \frac{\partial \hat{f}}{\partial q} \tau_l, \phi_i \right\rangle_{\partial K_s} - \left(\frac{\partial S}{\partial q} \tau_l, \phi_i \right)_{K_s} \\
&\quad + \left(\frac{\partial F}{\partial q} \tau_l, \nabla\phi_i \right)_{K_s} \\
D_s &= \frac{\partial \mathcal{R}_2}{\partial w_l^{K_s}} = \left(\left[\frac{\mathbb{I}}{\Delta t^K} - \frac{\partial S}{\partial w} \right] \phi_l, \phi_i \right)_{K_s} \\
&\quad - \left(\frac{\partial F}{\partial w} \phi_l, \nabla\phi_i \right)_{K_s} + \left\langle \frac{\partial \hat{f}}{\partial w} \phi_l, \phi_i \right\rangle_{\partial K_s} \\
S_s &= \frac{\partial \mathcal{R}_2}{\partial \lambda_l^{L_s}} = \left\langle \frac{\partial [[\hat{f}]]}{\partial \lambda} \mu_l, \phi_i \right\rangle_{L_s} \\
L_s &= \frac{\partial \mathcal{R}_3^s}{\partial q_l^s} = \begin{cases} \left\langle \frac{\partial \hat{f}}{\partial q^s} \tau_l, \mu_i \right\rangle_{L_s}, & L_s \in \partial K^s \\ \left\langle \frac{\partial \hat{f}^{st}}{\partial q^s} \tau_l, \mu_i \right\rangle_{L_s}, & L_s \in \partial K^{s,t} \end{cases} \\
M_s &= \frac{\partial \mathcal{R}_3^s}{\partial w_l^s} = \begin{cases} \left\langle \frac{\partial \hat{f}}{\partial w^s} \phi_l, \mu_i \right\rangle_{L_s}, & L_s \in \partial K^s \\ \left\langle \frac{\partial \hat{f}^{st}}{\partial w^s} \phi_l, \mu_i \right\rangle_{L_s}, & L_s \in \partial K^{s,t} \end{cases} \\
N_s &= \frac{\partial \mathcal{R}_3^s}{\partial \lambda_l^s} = \begin{cases} \left\langle \frac{\partial [[\hat{f}]]}{\partial \lambda^s} \mu_l, \mu_i \right\rangle_{L_s}, & L_s \in \partial K^s \\ \left\langle \frac{\partial \hat{f}^{st}}{\partial \lambda^s} \mu_l, \mu_i \right\rangle_{L_s} & L_s \in \partial K^{s,t} \end{cases} \\
L_{st} &= \frac{\partial \mathcal{R}_3^s}{\partial q_l^t} = \left\langle \frac{\partial \hat{f}^{st}}{\partial q^t} \tau_l, \mu_i \right\rangle_{L_s}, \quad L_s \in \partial K^s \\
N_{st} &= \frac{\partial \mathcal{R}_3^s}{\partial \lambda_l^t} = \left\langle \frac{\partial \hat{f}^{st}}{\partial \lambda^t}, \mu_l \mu_i \right\rangle_{L_s}, \quad L_s \in \partial K^{s,t}
\end{aligned}
\tag{B.1}
$$

Acknowledgments

I would like to thank my two promotors, Koen Hillewaert and Georg May, for their continuous support. I would also like to thank the FNRS for supporting my research through a FRIA fellowship.

References

[1] M. B. Giles, Stability analysis of numerical interface conditions in fluid-structure thermal analysis, International Journal for Numerical Methods in Fluids 25 (4) (1997) 421–436.

[2] T. Verstraete, S. Scholl, Stability analysis of partitioned methods for predicting conjugate heat transfer, International Journal of Heat and Mass Transfer 101 (2016) 852–869.

[3] T. Magin, A Model for Inductive Plasma Wind Tunnels, Ph.D. thesis, von Karman Institute for Fluid Dynamics (2004).

[4] A. Lani, N. Villedieu, K. Bensassi, L. Kapa, M. Vymazal, M. S. Yalim, M. Panesi, COOLFluiD: An open computational platform for multi-physics simulation and research, 21st AIAA Computational Fluid Dynamics Conference.

[5] Z. Hao, X. Ren, Y. Song, C. Gu, An investigation of conjugate heat transfer simulations based on discontinuous Galerkin methods on unstructured grids, Proceedings of the ASME Turbo Expo 3 (August 2017). doi:10.1115/GT2013-94498.

[6] D. N. Arnold, F. Brezzi, B. Cockburn, L. D. Marini, Unified Analysis of Discontinuous Galerkin Methods for Elliptic Problems., SIAM Journal of Numerical Analysis 39 (5) (2002) 1749–1779.

[7] N. C. Nguyen, J. Peraire, B. Cockburn, An implicit high-order hybridizable discontinuous Galerkin method for linear convection-diffusion equations, Journal of Computational Physics 228 (9) (2009) 3232–3254.

[8] N. Nguyen, J. Peraire, B. Cockburn, Hybridizable Discontinuous Galerkin Methods, in: J. Hestaven, R. E.M. (Eds.), Spectral and High Order Methods for Partial Differential Equations, lecture no Edition, Springer, 2011, pp. 63–84. doi:10.1007/978-3-642-15337-2.

[9] M. Woopen, G. May, J. Schütz, Adjoint-based error estimation and mesh adaptation for hybridized discontinuous Galerkin methods, International Journal for Numerical Methods in Fluids 76 (September) (2014) 811–834.

[10] M. Woopen, A. Balan, G. May, A unifying computational framework for adaptive high-order finite element methods, in: 22nd AIAA Computational Fluid Dynamics Conference, 2015. doi:10.2514/6.2015-2601.

[11] A. Montenay, L. Paté, D. JM., An investigation of conjugate heat transfer simulations based on discontinuous Galerkin methods on unstructured grids, Proceedings of the ASME Turbo Expo.

A multicomponent approach for plasma-sheath physics: potentialities and limits

Giuseppe Matteo Gangemi

Aeronautics and Aerospace Department, von Karman Institute for Fluid Dynamics, Belgium, giuseppe.gangemi@vki.ac.be

Supervisor: Thierry Magin

Professor, Aeronautics and Aerospace Department, von Karman Institute for Fluid Dynamics, Belgium, magin@vki.ac.be

University Supervisor: Koen Hillewaert

Associate Professor, Aerospace & Mechanical engineering, Université de Liège, Belgium, koen.hillewaert@uliege.be

University Supervisor: Alejandro Alvarez Laguna

Researcher, Laboratoire de Physique des Plasmas, École Polytechnique, Sorbonne Université, France, alejandro.alvarez-laguna@lpp.polytechnique.fr

Abstract

In a wall-confined environment, the plasma behaviour can be identified by dividing the domain in two main regions: the bulk, where the quasi-neutrality prevails (the charge density is close to zero) and the sheath region near the walls, where positive space charge is built. This phenomenon is due to a higher mobility of electrons, creating an electric potential structure that accelerates the ions towards the surface and repels the electrons. In this work we present the effort carried on in order to obtain high order simulations of a mixture of argon plasma: in particular we present a novel physical model (the multicomponent equations in contrast with the most common multifluid approach) and we show the first results of the application of the Discontinuous Galrkin framework, detailing challenges and solutions adopted. Simulations show encouraging results for future developments involving more complex geometries, more variegated mixtures and more accurate time schemes.

Keywords: plasma, sheath, fluid models, discontinuous galerkin

1. Introduction

Understanding the physics behind the formation of the plasma sheath, i.e. a zone of space charge close to the wall that is created due to depletion of electrons, is a problem that fascinated humanity since the beginning of plasma science (the term *plasma* was created in 1928 by Irving Langmuir and the term *sheath* was already present in [1]). Many industrial applications rely on accurate description of this boundary layer for non neutral mixtures, ranging from electric propulsion [2] to laboratory plasmas [3], from arcing in spacecrafts [4] to development of novel thermal protection systems [5].

A great overview of the recent developments on sheath research can be found in [6]: Bohm first proposed a criterion for the ion flux to the walls that now carries his name [7]; since then many efforts have been put in extending the formulation for multicomponent mixtures[8], collisional mixtures [9; 10; 11; 12] and for kinetic simulations [13]. A full asymptotic analysis of the problem of matching the bulk (the quasineutral region away from walls) and the sheath can be found in [14].

Many efforts have been put in experimental investigations [15; 16], but the reduced size of the sheath makes it very challenging; the small width of the space charge region is difficulty in the development of numerical schemes.

Simulating plasma flows can be divided in two great families: kinetic methods, like Particle-In-Cell (PIC)[17; 18], use statistical approach to describe

changes in the species velocity distribution function (VDF) while fluid models (for an extensive review see [19; 20]) implement governing laws for macroscopic quantities: density, momentum and energy. The former are very accurate but computational affordable at low pressures, as their cost increases dramatically with the number of particles simulated; the latter lose accuracy in the rarefied regimes but can produce results with lower computational effort.
Many are the challenges connected with fluid models, that rise mainly from the intrinsic multiscale character of the problem[21]: the small sheath region next to the wall requires high mesh resolution that significantly increases the computational cost; electrons, having much smaller inertia with respect to heavy species, have much faster dynamics that result in stricter numerical constraints; the model developed should remain consistent at low pressures beyond the limit of the continuum regime, preserving the asymptotic of the kinetic equation in absence of collisions; chemical source terms are known to be stiff and require special treatment.

2. Fluid models for plasma

A fluid approach to plasma simulations consists in solving equations for density, momentum and energy: these represent, respectively the 0-*th*, 1-*st* and 2-*nd* moment of the velocity distribution function (VDF) $f_k(\mathbf{x}, \mathbf{c}_k, t)$, where $\mathbf{x}$ is the spatial coordinate, $\mathbf{c}_k$ the *k-th* particle velocity and t the time. Many procedures can be employed in order to obtain governing laws starting from Boltzmann equation [22]: for examples of this procedure, known as kinetic derivation, we refer to [23; 24; 25]. In this chapter we give brief introduction on the equations used for the results in this paper: for a more detailed description see our future publication [26].
In a our simulations we take an isothermal mixture of argon $S = \{e^-, Ar^+, Ar\}$ confined in a one dimensional discharge, where the plasma is in contact with floating walls[27]; heavy species temperature T_h and electron temperature T_e differ but stay constant in time and uniform throughout the domain. The ionization degree, i.e. the ratio of the number of charges with respect to the number of neutrals, is low and decreases with the increase of the neutral pressure; in fact, the neutral act as a background gas, slowing down the dynamics of electrons and ions through elastic collisions.
Table 1 shows the discharge conditions of the testcase used for our numerical experiments.

2.1. Multifluid

Governing laws deriving from the multifluid approach are:

$$\partial_{\bar{t}}\overline{n}_e + \partial_{\bar{x}}(\overline{n}_e\overline{u}_e) = \overline{n}_e\overline{\nu}^{iz}, \tag{1}$$

$$\partial_{\bar{t}}\overline{n}_i + \partial_{\bar{x}}(\overline{n}_i\overline{u}_i) = \overline{n}_e\overline{\nu}^{iz}, \tag{2}$$

$$\begin{aligned}\partial_{\bar{t}}(\overline{n}_e\overline{u}_e) + \partial_{\bar{x}}\left[\overline{n}_e\left(\overline{u}_e^2 + \varepsilon^{-1}\right)\right] &= \varepsilon^{-1}\overline{n}_e\partial_{\bar{x}}\overline{\phi} \\ &\quad - \overline{n}_e\overline{u}_e\overline{\nu}_{en},\end{aligned} \tag{3}$$

$$\begin{aligned}\partial_{\bar{t}}(\overline{n}_i\overline{u}_i) + \partial_{\bar{x}}\left[\overline{n}_i\left(\overline{u}_i^2 + \kappa\right)\right] &= -\overline{n}_i\partial_{\bar{x}}\overline{\phi} \\ &\quad - \overline{n}_i\overline{u}_i\overline{\nu}_{in},\end{aligned} \tag{4}$$

$$\partial^2_{\bar{x}\bar{x}}\overline{\phi} = \chi^{-1}(\overline{n}_e - \overline{n}_i), \tag{5}$$

where we introduced the mass ratio $\varepsilon = m_e/m_i$, the temperature ratio $\kappa = T_h/T_e$ and the non dimensional Debye length squared $\chi = (\lambda_D/L_0)^2$. Equations.1-2 describe the number density n_k conservation for electrons and ions, eqs.3-4 the conservation of momenta $n_k u_k$and eq.5 is the Poisson equation that ensures charge conservation. In this model species are considered separate fluids with their own momentum solved separately as a independent variable. The ionization frequency ν^{iz} is modeled with the iterative procedure from [21], allowing to reach steady state.
All quantities that we are presenting here are scaled following [28]; we recall here the main reference quantities:

$$\begin{aligned}\overline{x} = x/L_0, \quad \overline{u}_k = u_k/u_0, \quad \overline{t} = t/t_0, \\ \overline{n} = n/n_0, \quad \overline{\phi} = \phi/\phi_0, \quad \overline{\nu}^{iz} = \nu^{iz}t_0,\end{aligned} \tag{6}$$

where $L_0 = \lambda_{D0}$ is the initial Debye length, $u_0 = u_B = \sqrt{k_B T_e/m_i}$ is the Bohm velocity and the reference timescale is obtained as $t_o = L_0/u_0$; $n_0 = n_{e0}$ is the initial electron number density and the reference potential is defined as $\phi_0 = k_B T_e/e$ (i.e. the electron temperature in eV. k_B is the Boltzmann constant and e the elementary charge). In this work we are going to investigate how the two different models, multifluid and multicomponent, behave varying the number of elastic collisions in the mixture: Elastic collision frequencies depend on the Knudsen number $\mathrm{Kn}_{kn} = \lambda_{kn}/L_0$ (with $\lambda_{kn} = (n_n Q^{(1,1)}_{kn})^{-1}$ the mean free path for the collision between particle k and a neutral atom. $Q^{(1,1)}_{kn}$ are the collision integrals[29] obtained

Table 1: Argon discharge conditions

Initial electron number density	n_{e0}	$1 \times 10^{16}\,\mathrm{m}^{-3}$	Heavy temperature	T_h	0.05 eV
Electron Temperature	T_e	2 eV	Ion-neutral collision integral	$Q_{in}^{(1,1)}$	$1.41 \times 10^{-18}\,\mathrm{m}^2$
Electron-neutral collision integral	$Q_{en}^{(1,1)}$	$7 \times 10^{-20}\,\mathrm{m}^2$	Electron-to-ion mass ratio	$\varepsilon = m_e/m_i$	1.36×10^{-5}
Ion-to-electron temperature ratio	$\kappa = T_h/T_e$	0.025	Initial Debye length	λ_{D0}	10^{-4} m
Electron plasma period	ω_{pe}^{-1}	1.77×10^{-10} s	Discharge width	L	10^{-2} m

from the thermodynamic library Mutation++[30]):

$$\nu_{en} = \overline{\nu}_{en} t_0^{-1} = \frac{16}{3\sqrt{2\pi}} \frac{1}{\sqrt{\varepsilon}} \underbrace{n_n Q_{en}^{(1,1)} L_0}_{\mathrm{Kn}_{en}^{-1}} \underbrace{\left[\frac{u_0}{L_0}\right]}_{t_0^{-1}}, \tag{7}$$

$$\nu_{in} = \overline{\nu}_{in} t_0^{-1} = \frac{8}{3\sqrt{\pi}} \sqrt{\kappa} \underbrace{n_n Q_{in}^{(1,1)} L_0}_{\mathrm{Kn}_{in}^{-1}} \underbrace{\left[\frac{u_0}{L_0}\right]}_{t_0^{-1}}, \tag{8}$$

2.2. Multicomponent

Multicomponent approach are well known in the scientific community for simulations involving complex mixtures where a large variety of species is involved, in terms of inertia, charges and chemical properties. In this case the plasma is considered a single fluid (so only one momentum equation is solved) and the different species diffuse inside it; in this document we developed a slightly modified version of the equations proposed by Graille et al. [24] that in their work used a non inertial reference frame moving with velocity associated with the heavies v_h. In the discharge testcase previously described, the dynamics of the neutrals is negligible so it is natural to use ions as a reference, with electrons diffusing with respect to them (it is currently under preparation to provide solid mathematical basis for this reasoning). The resulting equations are (scaled with the same procedure detailed for multifluid[1] ones):

$$\partial_t n_e + \partial_x (n_e u_i) + \partial_x (n_e V_e) = n_e \nu^{iz}, \tag{9}$$

$$\partial_t n_i + \partial_x (n_i u_i) = n_e \nu^{iz}, \tag{10}$$

$$\partial_t (n_i u_i) + \partial_x \left[n_i \left(u_i^2 + \kappa \right) + n_e \right] = (n_e - n_i)\, \partial_x \phi - n_i u_i \nu_{in}, \tag{11}$$

$$\partial_{xx}^2 \phi = \chi^{-1} (n_e - n_i), \tag{12}$$

[1] From now on the $\tilde{\cdot}$ notation will be abandoned assumoing all quantities to be scaled

where V_e is the electron diffusion velocity, modeled following the binary diffusion assumption:

$$V_e = \frac{\varepsilon^{-1}}{\nu_{en}} \left(-\frac{\partial_x n_e}{n_e} + \partial_x \phi \right). \tag{13}$$

Equation 11 resembles eq.4, with the addition of the electron pressure $n_e \varepsilon^{-1}$ and the Lorentz force associated to electrons $n_e \partial_x \phi$.

3. Numerical strategies

In this section we detail the numerical approach used for the results in the following chapter. The equations detailed in the first part of this article are discretized using the Discontinuous Galerkin (DG) method [31]; for the seek of clarity we will rewrite them in the following shape:

$$\beta \partial_t \mathbf{U} + \partial_x \mathbf{F}^C (\mathbf{U}) + \partial_x \mathbf{F}^D (\mathbf{U}) = \mathbf{S} (\mathbf{U}) \tag{14}$$

with

$$\mathbf{U}^{\mathrm{MF}} = \begin{bmatrix} n_e \\ n_i \\ n_e u_e \\ n_i u_i \\ \phi \end{bmatrix} \quad \mathbf{U}^{\mathrm{MC}} = \begin{bmatrix} n_e \\ n_i \\ n_i u_i \\ \phi \end{bmatrix} \tag{15}$$

$$\beta = \begin{cases} 1 & \text{Fluid Equations} \\ 0 & \text{Poisson} \end{cases}$$

and

$$\mathbf{F}^{\mathrm{C,\,MF}} = \begin{bmatrix} n_e u_e \\ n_i u_i \\ n_e \left(u_e^2 + \varepsilon^{-1} \right) \\ n_i \left(u_i^2 + \kappa \right) \\ 0 \end{bmatrix} \quad \mathbf{F}^{\mathrm{D,\,MF}} = \begin{bmatrix} 0 \\ 0 \\ 0 \\ 0 \\ \partial_x \phi \end{bmatrix}, \tag{16}$$

$$\mathbf{F}^{\mathrm{C,\,MC}} = \begin{bmatrix} n_e u_i \\ n_i u_i \\ n_i \left(u_i^2 + \kappa \right) + n_e \\ 0 \end{bmatrix} \quad \mathbf{F}^{\mathrm{D,\,MC}} = \begin{bmatrix} n_e V_e \\ 0 \\ 0 \\ \partial_x \phi \end{bmatrix}, \tag{17}$$

(18)

Table 2: Simulation conditions

p_n	$\beta = \frac{n_{e0}}{n_n}$	Kn_{en}		Kn_{in}	
		Sheath	Bulk	Sheath	Bulk
1 Pa	$\sim 10^{-4}$	1143.47	11.43	56.82	0.568
10 Pa	$\sim 10^{-5}$	114.35	1.143	5.68	0.057
100 Pa	$\sim 10^{-6}$	11.43	0.114	0.568	5.68×10^{-3}
1000 Pa	$\sim 10^{-7}$	1.143	1.14×10^{-3}	5.68×10^{-3}	5.68×10^{-4}

and

$$\mathbf{S}^{\mathrm{MF}} = \begin{bmatrix} n_e \nu^{iz} \\ n_e \nu^{iz} \\ n_e \partial_x \phi - n_e u_e \nu_{en} \\ -n_i \partial_x \phi - n_i u_i \nu_{in} \\ \chi^{-1} (n_e - n_i) \end{bmatrix} \qquad (19)$$

$$\mathbf{S}^{\mathrm{MC}} = \begin{bmatrix} n_e \nu^{iz} \\ n_e \nu^{iz} \\ (n_e - n_i) \partial_x \phi - n_i u_i \nu_{in} \\ \chi^{-1} (n_e - n_i) \end{bmatrix},$$

where indices ^{MF} and ^{MC} are used to distinguish the multifluid and multicomponent set of equations. $\mathbf{F}^{\mathrm{C}}$ are the convective fluxes, that introduce directionality in the solution, while $\mathbf{F}^{\mathrm{D}}$ constitutes the diffusive fluxes that tend to uniformise the solution; this last term is usually expressed in a linearized form:

$$\mathbf{F}^{\mathrm{D}} = \mathbf{D} \partial_{\mathbf{x}} \mathbf{U} \qquad (20)$$

with $\mathbf{D}$ the Jacobian matrix.

The derivation of the spatial discretization in the DG framework is classical [31] and won't be repeated here; on the other hand, we focus on the strategies implemented in the time integration in order to fit the problem. As it is clear from eqs.1-5 and eqs.9-12, our problem present time dependent laws (the *fluid* subset) coupled to an instantaneously verified external constraint (the Poisson equation); for this reason classical numerical schemes have to be modified to fit our needs.

With $\mathbf{U} = \left[u_j\right], \quad j \in N_v$ (N_v is the number of variables), the discretised equations in the DG framework:

$$\begin{aligned} \sum_e \int_e \varphi_i \varphi_j \partial_t u_j dV - \sum \int_e \partial_x \varphi_i \left(\mathbf{F}_h\right) dV \\ - \sum_e \int_e \varphi_i \mathbf{S}_h dV \\ + \sum_f \int_f \gamma \left(u^+, u^-; \varphi_i^+, \varphi_i^-; \hat{n}\right) dS \\ - \sum_f \int_f \eta^D \left(u_j, \varphi_j\right) \cdot \hat{n} dS = 0 \end{aligned} \qquad (21)$$

with e the elements and f the interfaces in the mesh, γ is the numerical convective flux (with Roe flux used in this work), η^D the interface diffusive flux (modeled with a symmetric interior penalty method. We will not go into details with the treatment of this term so we refer the interested reader to [31]), $\hat{n}$ the outward normal from the cell interface and the discretized flux and source terms:

$$\mathbf{F}_h = \left(\mathbf{F}^C \left(u_h\right) + \mathbf{F}^D \left(u_h\right)\right), \quad \mathbf{S}_h = \mathbf{S} \left(u_h\right), \qquad (22)$$

the superscripts $^{\pm}$ indicate the two sides of the interface considered. Since a shape function φ_i is supported on a single element, this further simplifies to the semi-discrete form

$$M_{ij} \partial_t u_j = \mathbf{R}_i \qquad (23)$$

with M_{ij} the mass matrix defined as

$$M_{ij} = \int_e \varphi_i \varphi_j dV \qquad (24)$$

with e the common element on which both φ_i and φ_j are defined, and $\mathbf{R}_i$ the (steady) residual associated to

shape function φ_i:

$$\begin{aligned}\mathbf{R}_i = &\sum_e \int_e \partial_x \varphi_i \left(\mathbf{F}_h\right) dV - \sum_e \int_e \varphi_i \mathbf{S}_h dV \\ &- \sum_f \int_f \gamma\left(u^+, u^-; \varphi_i^+, \varphi_i^-; \hat{n}\right) dS \\ &- \sum_f \int_f \eta^D\left(u_j, \varphi_j\right) \cdot \hat{n} dS\end{aligned} \tag{25}$$

This expression can be reformulated as a set of ordinary differential equations for each of the unknowns, by inverting the mass matrix:

$$\partial_t u_i = M_{ij}^{-1} \mathbf{R}_j \tag{26}$$

The mass matrix is defined per element and this allows for exact inversion. In this work we implement a the fourth-order six-stage Explicit first stage Single Diagonally Implicit Runge-Kutta (ESDIRK64) scheme. The multistage algorithm reads then [32]

$$\begin{aligned}u^0 &= u^n \\ u^s &= u^n - \Delta t \sum_{j=1}^{i} a_{ij} \mathbf{M}^{-1} \mathbf{R}(u^j) \\ u^{n+1} &= u_h^s.\end{aligned} \tag{27}$$

A detailed description of the Butcher tableau is in the cited reference. The first stage is explicit as shown in eq.27 with the term $u^0 = u^n$. Conversely, the last stage updates the solution at the next time. Between these two terms, the scheme is composed of s nonlinear problems that is solved using a classical Newton approach.

Boundary Conditions

Setting the correct boundary conditions is fundamental to correctly simulate the interaction of the plasma with the wall. The multifluid equations present an hyperbolic scaling so the quantities to be (or not to be) imposed at the interface have to be chosen accordingly: following Alvarez Laguna et al. [21] we impose the electron flux to both boundaries to be equal to the number of particles crossing the plane with positive velocity component (assuming a maxwellian VDF). In normalized quantities:

$$\Gamma_e^{L,R} = \left(n_e u_e\right)^{L,R} = \mp \frac{n_e}{\sqrt{2\pi\varepsilon}}. \tag{28}$$

Electron density has Neumann boundary on both sides; ion quantities (density and momentum) have the same Neumann condition, as the flux of positive charges arriving at the wall is assumed supersonic. The electric potential is imposed on both sides $\phi\left(x = \pm L/2, t\right) = 0$ but can be easily be biased to different values.
The multicomponent problem has a similar scaling, with the convective part strongly dependent on the ion flow: for this reason the ions density and momentum boundary conditions will remain unchanged (same for the Poisson equation). The flux of electrons must be imposed: the easiest way is to impose the total flux $F^C + F^D$ to be equal to the thermal flux expressed in eq.28.

4. Results

In this section we show the results from the numerical simulations we performed on the argon discharge we described earlier. As mentioned, a key role in our tractation is given by the number of elastic collisions that charges undergo: the level of collisionality is increased in our problem by increasing the pressure of the neutral background gas and the resulting Knudsen numbers are shown in Table 2; the same table details the very low ionization degre α (while the number density of neutrals is changed according the perfect gas law $n_n = p_n / \left(k_B T_h\right)$, the reference number density for electrons n_{e0} is kept constant).
Figure 1 show comparison of number densities for electrons and ions at different pressure level: we see how the two models compare perfectly over the entire domain, predicting a smooth transition between the quasi neutral region to the sheath close to the walls. In fig.2 we can see that both approaches are able to capture the transition between the characteristic ambipolar flow in the bulk (where both ions and electrons move at the same speed) to a region where there is a substancial separation of the two flows due to the presence of the wall; fig.3 shows the species velocity of charges scaled with respect to their thermal speed, highlighting in this way the strong subsonic motion of electrons in comparison to the characteristic supersonic flow of ions. The electric potential profiles are shown in fig.4: once again the agreement of the two solutions is extremely satisfying.

5. Conclusions

We propose a novel physical model: this approach, even though it introduces stiffer numerical terms, it relies on a rigorous kinetic derivation and will reduce

the computational cost and model complexity when we will deal with more complex mixtures (lower number of equations and natural extensions of the terms to multiple species). The comparisons with the reference solution show satisfying results, with the novel proposed approach matching the reference solution on all the quantities checked.
Further developments will include the extension to more complex mixtures and geometries: we plan to add more detailed chemistry and to simulate air plasmas (hence the difficulty of introducing molecules and negative ions); we will remove the isothermal assumption in order to study the temperature variation in the fluid (and the influence of thermal protection systems on the dynamics of the sheath); more complex geometries will be introduced in order to describe real life testcases.
On a pure theoretical level we plan to proposed a rigorous mathematical derivation of the equations that we proposed in this paper only relying on heuristic explanations.

Acknowledgments

The first author is financed by the Fonds National de Recherche Scientifique (FNRS) through the FRIA grant.

References

[1] L. Tonks, I. Langmuir, A general theory of the plasma of an arc, Physical review 34 (6) (1929) 876.
[2] E. Ahedo, F. I. Parra, Partial trapping of secondary-electron emission in a hall thruster plasma, Physics of Plasmas 12 (7) (2005) 073503. doi:10.1063/1.1943327.
[3] I. Hutchinson, Principles of Plasma Diagnostics: Second Edition, Cambridge University Press, 2002.
[4] M. R. Carruth, J. A. Vaughn, R. T. Bechtel, P. A. Gray, Experimental studies on spacecraft arcing, Journal of Spacecraft and Rockets 30 (3) (1993) 323–327.
[5] L. Uribarri, E. H. Allen, Electron transpiration cooling for hot aerospace surfaces, in: 20th AIAA International Space Planes and Hypersonic Systems and Technologies Conference, International Space Planes and Hypersonic Systems and Technologies Conferences, American Institute of Aeronautics and Astronautics, 2015.
[6] S. D. Baalrud, B. Scheiner, B. T. Yee, M. M. Hopkins, E. Barnat, Interaction of biased electrodes and plasmas: sheaths, double layers, and fireballs, Plasma Sources Science and Technology 29 (5) (2020) 053001.
[7] D. Bohm, The characteristics of electrical discharges in magnetic fields, McGraw-Hill, 1949.
[8] K. U. Riemann, The bohm criterion and boundary conditions for a multicomponent system,, IEEE Transactions on Plasma Science 23 (4) (1995) 709–716.
[9] V. A. Godyak, N. Sternberg, Dynamic model of the electrode sheaths in symmetrically driven rf discharges, Physical Review A 42 (4) (1990) 2299.

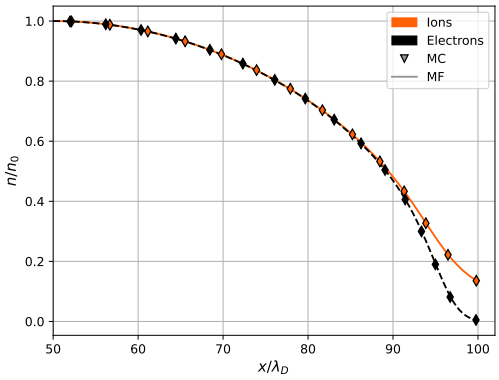

(a) 10 Pa

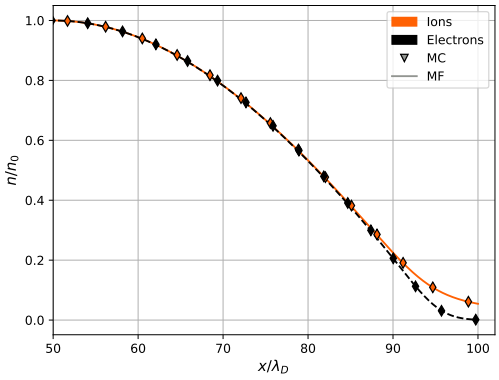

(b) 100 Pa

Figure 1: Comparison of number density under different neutral pressure conditions. Quantities are scaled with respect to the value at the center of the domain.

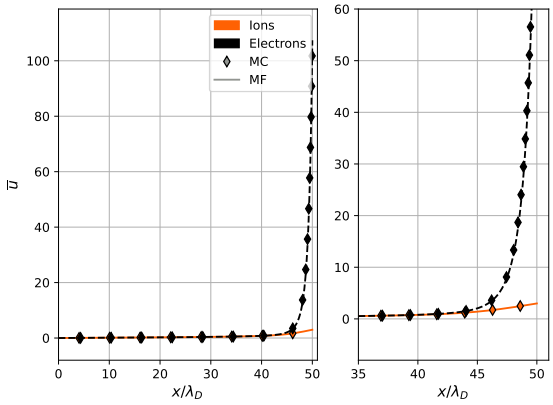

(a) 10 Pa

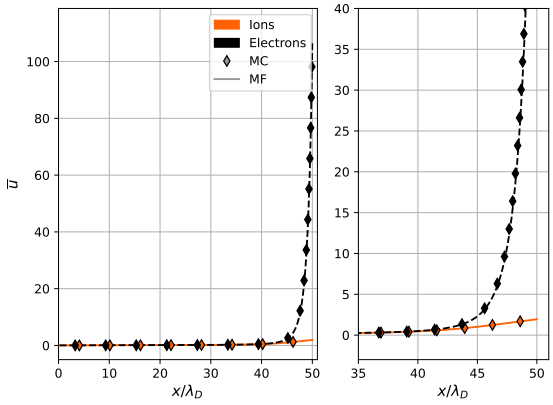

(b) 100 Pa

Figure 2: Comparison of species velocity under different pressure conditions. Value are scaled with respect to the Bohm velocity u_B.

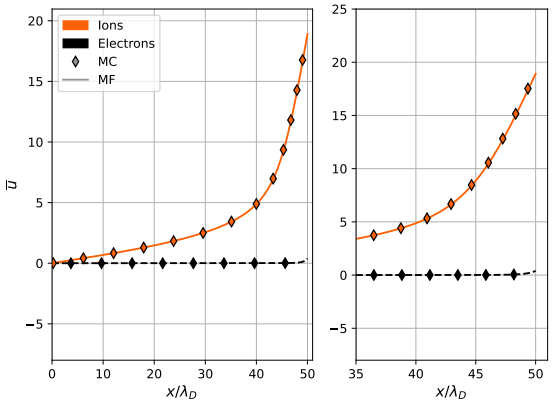

(a) 10 Pa

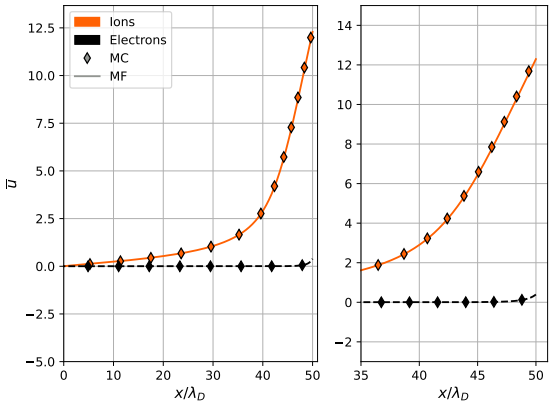

(b) 100 Pa

Figure 3: Comparison of species velocity under different pressure conditions. Value are scaled with respect to the species thermal speed $v_{th,k} = \sqrt{k_B T_k/(\pi m_k)}$.

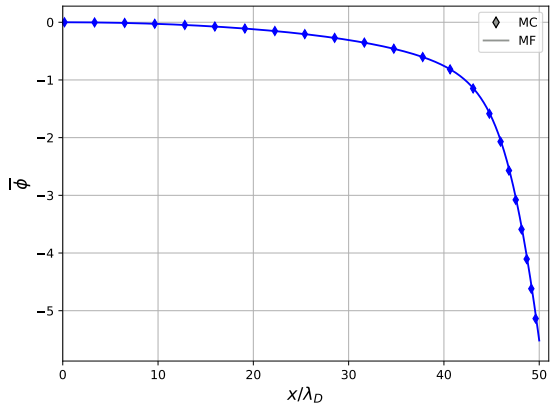

(a) 10 Pa

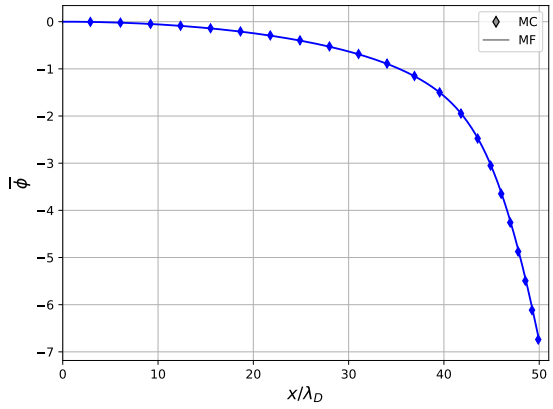

(b) 100 Pa

Figure 4: Comparison of electric potnetial under different pressure conditions. Values scaled with the reference quantity ϕ_0.

[10] H. Valentini, D. Kaiser, Sheath formation in low-pressure discharges, the bohm criterion and the consequences of collisions, Plasma Sources Science and Technology 23 (1) (2013) 015004.

[11] R. Brinkmann, The plasma–sheath transition in low temperature plasmas: on the existence of a collisionally modified bohm criterion, Journal of Physics D: Applied Physics 44 (4) (2011) 042002.

[12] J.-Y. Liu, Z.-X. Wang, X. Wang, Sheath criterion for a collisional sheath, Physics of Plasmas 10 (7) (2003) 3032–3034.

[13] S. Baalrud, C. Hegna, Kinetic theory of the presheath and the bohm criterion, Plasma Sources Science and Technology 20 (2) (2011) 025013.

[14] K. U. Riemann, J. Seebacher, D. D. Tskhakaya Sr, S. Kuhn, The plasma–sheath matching problem, Plasma Physics and Controlled Fusion 47 (11) (2005) 1949–1970. doi:10.1088/0741-3335/47/11/006.

[15] G. D. Severn, X. Wang, E. Ko, N. Hershkowitz, Experimental studies of the bohm criterion in a two-ion-species plasma using laser-induced fluorescence, Physical Review Letters 90 (14) (2003) 145001. doi:10.1103/PhysRevLett.90.145001.

[16] L. Oksuz, N. Hershkowitz, First experimental measurements of the plasma potential throughout the presheath and sheath at a boundary in a weakly collisional plasma, Physical review letters 89 (14) (2002) 145001.

[17] B. Scheiner, S. D. Baalrud, B. T. Yee, M. M. Hopkins, E. V. Barnat, Theory of the electron sheath and presheath, Physics of Plasmas 22 (12) (2015) 123520. doi:10.1063/1.4939024.

[18] L. Beving, M. Hopkins, S. Baalrud, How sheath properties change with gas pressure: modeling and simulation, Plasma Sources Science and Technology 31 (8) (2022) 084009.

[19] L. L. Alves, A. Bogaerts, Special issue on numerical modelling of low-temperature plasmas for various applications – part I: Review and tutorial papers on numerical modelling approaches, Plasma Processes and Polymers 14 (1690011) (2017) 1–2.

[20] A. Bogaerts, L. L. Alves, Special issue on numerical modelling of low-temperature plasmas for various applications – part II: Research papers on numerical modelling for various plasma applications, Plasma Processes and Polymers 14 (1790041) (2017) 4–5.

[21] A. Alvarez Laguna, T. Pichard, T. Magin, P. Chabert, A. Bourdon, M. Massot, An asymptotic preserving well-balanced scheme for the isothermal fluid equations in low-temperature plasmas at low-pressure, Journal of Computational Physics 419 (109634) (2020) 1–29.

[22] J. H. Ferziger, H. G. Kaper, Mathematical Theory of Transport Processes in Gases, American Elsevier Publishing Company, 1972.

[23] M. S. Benilov, A kinetic derivation of multifluid equations for multispecies nonequilibrium mixtures of reacting gases, Physics of Plasmas 3 (4) (1997) 521–528.

[24] B. Graille, T. E. Magin, M. Massot, Kinetic theory of plasmas: Translational energy, Mathematical Models and Methods in Applied Sciences 19 (4) (2009) 527–599.

[25] V. Zhdanov, Transport Processes in Multicomponent Plasma, Vol. 44, Taylor & Francis, 2002.

[26] G. M. Gangemi, A. Alvarez Laguna, K. Hillewaert, T. E. Magin, Drift-diffusion models applied to a low temperature discharge: comparison with multifluid models and novel sheath edge criterion (*In preparation*).

[27] P. Chabert, N. Braithwaite, Physics of Radio-Frequency Plasmas, Cambridge University Press, 2011.

[28] A. Alvarez Laguna, T. E. Magin, M. Massot, A. Bourdon, P. Chabert, Plasma-sheath transition in multi-fluid models

with inertial terms under low pressure conditions: Comparison with the classical and kinetic theory, Plasma Sources Science and Technology 29 (025003).

[29] T. E. Magin, G. Degrez, Transport algorithms for partially ionized and unmagnetized plasmas, Journal of Computational Physics 198 (2) (2004-08-10) 424–449.

[30] J. B. Scoggins, V. Leroy, G. Bellas-Chatzigeorgis, B. Dias, T. E. Magin, Mutation++: MUlticomponent thermodynamic and transport properties for IONized gases in c++, SoftwareX 12 (2020) 100575.

[31] K. Hillewaert, Development of the discontinuous Galerkin method for high-resolution, large scale CFD and acoustics in industrial geometries, Presses univ. de Louvain, 2013.

[32] H. Bijl, M. H. Carpenter, V. N. Vatsa, Time integration schemes for the unsteady navier-stokes equations, Vol. 2612, American Institute of Aeronautics and Astronautics, 2001.

Towards measuring ABEP intake efficiency parameters: Experimental characterization of the DRAG-ON facility

Pedro Jorge

Aeronautics and Aerospace Department, von Karman Institute for Fluid Dynamics, Belgium, pedro.jorge@vki.ac.be

Supervisor: Thierry Magin

Professor, Aeronautics and Aerospace Department, von Karman Institute for Fluid Dynamics, Belgium, magin@vki.ac.be

University Supervisor: Annick Hubin

Professor, Electrochemical and Surface Engineering, Vrije Universiteit Brussel, Belgium, annick.hubin@vub.be

Abstract

The DRAG-ON facility was developed to simulate low Earth orbit conditions and to evaluate Air Breathing Electric Propulsion (ABEP) intake-collectors efficiency parameters. In this study, we describe the experimental assessment of the high vacuum environment and the calibration of ionization gauges on the facility. Additionally, we present a preliminary characterization of the ion outflow from the facility particle flow generator.

Keywords: latex, template, ...

1. Introduction

Satellites operating on Very Low Earth Orbits (VLEO), characterized by altitudes below 450 km and as low as 160 km, offer several advantages, such as improved performance of optical and radiometric payloads, reduced costs of vehicle development and launch, and lower risk of collision with space debris [1]. Nevertheless, VLEO orbits intensify the challenges that exist in higher altitude orbits. These challenges include, firstly, the prevalence of atomic oxygen, a chemically reactive species that results in surface erosion, posing a challenge to mission lifetime. Secondly, the increased atmospheric density in VLEO orbits results in augmented drag that necessitates frequent compensation. Overcoming the challenges associated with VLEO orbits requires the investigation of appropriate erosion-resistant materials and advancements in Air Breathing Electric Propulsion (ABEP) technology. ABEP systems employ an Air Intake-Collector (AIC) that collects and compresses atmospheric gas particles moving towards the satellite at its orbital velocity and directs them to the thruster to be ionized and accelerated, thereby producing thrust and providing drag compensation. Hence, the efficiency of air intake-collectors is critical to the feasibility of ABEP technology [2; 3]. Given VLEO's low density and typical satellite dimensions, gas flow inside intake-collectors is free molecular, implying that collisions between gas particles are infrequent, and flow behavior is controlled by gas-surface interactions. Therefore, the performance of air intake-collectors and overall satellite drag rely heavily on gas surface interaction between atmospheric species and the intake surfaces.

Previous studies on gas surface interactions in Low Earth Orbit (LEO) have primarily relied on flight observations[4; 5; 6] and laboratory testing[7; 8; 9; 6; 10]. These studies have mainly focused on reactive gas surface interactions, particularly the erosion of satellite materials by atomic oxygen. Studies on air intake collectors have primarily focused on full tests of Atmospheric Breathing Electric Propulsion (ABEP) systems, with less emphasis on intake analysis [11; 12], or relied on numerical simulations[13; 14; 15; 16]. Numerical simulations usually rely on the simple Maxwell model to simulate gas surface interaction between flow particles and intake surfaces. Therefore, experimental efforts to characterize non-reactive gas-surface interactions and their effects on

flow behavior and intake performance are crucial to the advancement of Very Low Earth Orbit (VLEO) satellite technology.

Laboratory investigations are currently challenged by the difficulty in replicating orbital flow conditions, as most flow sources compromise between producing the correct gas species, appropriate densities, and particle velocity. Kleiman et al.[17] provided a review of existing facilities for reproducing LEO conditions, which still provides relevant insights into source technologies available today. One modern iteration is the Chamber for Atmospheric and Orbital Space Simulation (CHAOSS) at the University of Colorado Springs, which uses a magnetically filtered oxygen plasma source that produces a plume of streaming atomic oxygen ions with orbital energies(5 eV) and low electron temperature[18]. The facility aims to study momentum exchange through gas surface interactions using a nano-Newton thrust stand and allows the study of GSI without neglecting the effect of solar radiation[19]. However, the use of a plasma source means that the chemical composition for lower orbits is not duplicated, and the facility's single chamber makes qualifying ABEP intake collectors a more challenging task. A more recent facility still under construction is the Rarefied Orbital Aerodynamics Research (ROAR) facility at the University of Manchester, which uses a source based on electron stimulated desorption to generate neutral hyperthermal oxygen atoms[20]. The facility focuses on studying gas-surface interactions through scattering experiments, with planned scaled intake geometry tests[21]. However, the facility's limitations include comprising a single chamber and inherent limitations of its flow source, such as a relatively low flux, high beam divergence, and energy spread[17].

The Dual chamber for RArefied Gas ON-ground testing is designed to duplicate VLEO conditions and with the immediate purpose of characterizing efficiency parameters of ABEP intake-collectors. DRAG-ON consists of two vacuum chambers and comprises an Inductively Coupled Plasma (ICP) source with magnetic beam control. In this paper, we present an overview of DRAG-ON and the detailed experimental investigations carried out to characterize the high vacuum environment. The early tests for the characterization of the ion flow exiting the source are also described, along with a preliminary analysis of the effects of the imperfect duplication of orbital conditions on the measurement of efficiency parameters. Section 2 provides details on the facility, while Section 3 presents the experimental characterization of the vacuum environment. Section 4 shows the ion flow characterization experiments before the main conclusions of this work are drawn.

2. DRAG-ON facility overview

The following section provides a description and rationale for the design of the DRAG-ON facility and outlines the primary intake performance parameters which we aim to measure experimentally.

2.1. DRAG-ON facility overview

The DRAG-ON facility, consists of two interconnected vacuum chambers and a conduit that can house the air intake model under examination. The dimensions of the intake model are constrained by the diameter of the conduit, which measures 0.1317 m in diameter and 0.25 m in length. The technical drawing of the facility and its dimensions are presented in Figure 1. To create conditions that replicate those experienced in low Earth orbit, a Particle Flow Generator (PFG) is employed, which produces particles that traverse the air intake model and are either collected by the secondary chamber or rejected back into the primary chamber.

2.1.1. Pumping system

The facility is comprised of a high vacuum system with enough pumping capacity to allow for free molecular flow conditions with continuous PFG operation. The vacuum pumping system comprises two rotary vane mechanical pump capable of pumping down both vacuum chambers to approximately 10^{-2} mbar, together with one turbomolecular pump on each chamber with enough capacity to reach an ultimate pressure of approximately 10^{-8} mbar with the PFG turned off and approximately 10^{-5} mbar under typical operating conditions. The chamber materials are stainless steel 316 due to its welding, polishing and corrosion resistant properties and are fine glass bead blasted in order to prevent adsorption of gas particles. It is worth to note that the pressure of orbital conditions, approximately 1×10^{-6} mbar, is not duplicated. However, since the flow regime in the facility is free molecular the flow behavior should be duplicated as long as gas surface interactions are not modified by facility pressure conditions, for example through different adsorption dynamics at the two pressures.

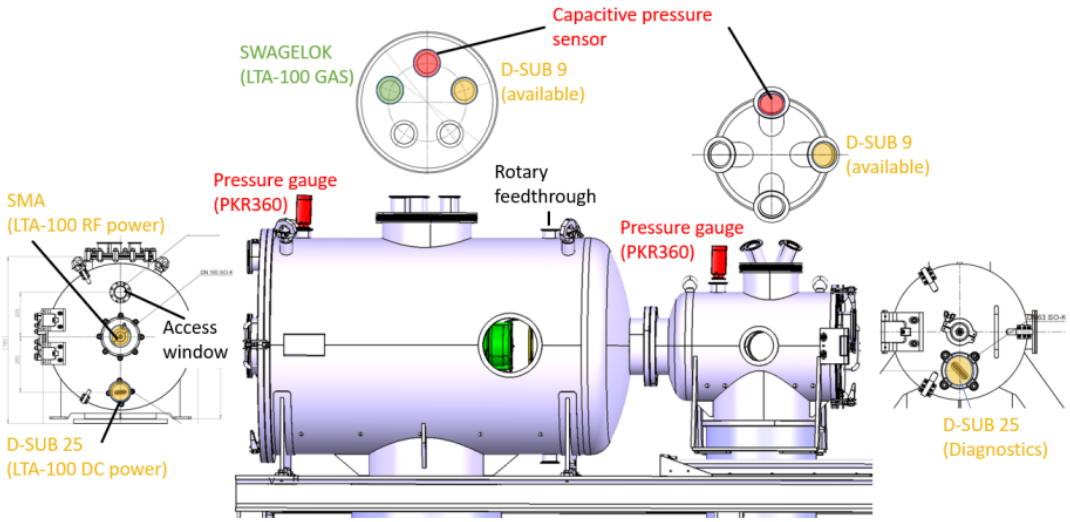

Figure 1: DRAG-ON reference configuration, including typical electrical, mechanical and fluidic interfaces. Conduit now shown.

2.1.2. *Flow generation*

In this study, the Particle Flow Generator (PFG) employed is the LTA-100, which was procured from ThrustMe. The PFG is an Inductively Coupled Plasma (ICP) source that incorporates a magnetic beam control system for variable beam collimation. Figure 2 shows PFG operation with argon in the DRAG-ON facility. The PFG is specifically engineered to replicate orbital flow conditions by producing argon and oxygen ions with a velocity ($u_{ion} \approx 7600\,\mathrm{m \cdot s^{-1}}$) and temperature ($T_{ion} \approx 1000\,\mathrm{K}$) that are commensurate with those experienced in low Earth orbit. We attempt to reproduce orbital conditions on ground by tuning the following LTA-100 source parameters: Changing the acceleration voltage influences mainly the ion mean energy. The focusing current affects primarily the collimation of the beam. Moreover, the power given to the source affects the temperature of electrons and therefore the total beam current. This way, the flow properties can be varied while maintaining a minimum beam ion current of 10 mA. The ion current produced in the DRAG-ON facility generates a lower flux of high-energy particles compared to that experienced in orbit. However, this discrepancy does not pose a significant issue since the primary purpose of the facility is not to perform exposure testing. In fact, a lower flux has certain advantages, as it requires a less intensive pumping system.

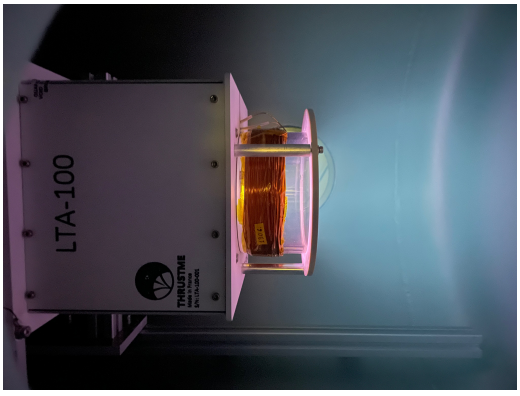

Figure 2: View of the LTA-100 operating with argon.

The source can be operated with a mass flow rate between 3 to 10 sccm while retaining continuous operation. The PFG is mounted on a dedicated aluminium frame that allows PFG translation in the chamber and facilitates the removal of residual heat during operation. This frame is designed to provide support for the PFG and to enable the system to maintain steady operation while utilizing input RF power of up to 80 W.

Two MKS GE50A digital Mass Flow Controllers (MFC) are used to feed the source with argon and/or oxygen. The mass flow controllers rely on a thermal sensor to regulate the mass flow rate and are capable of controlling the throughput with an 1% accuracy for throughputs higher than 20% the 14 SCCM full scale. The MFCs are calibrated for Nitrogen but rely on gas correction models for other gas operation while retaining 1% accuracy.

2.1.3. Diagnostics

To measure operating test conditions and AIC performance parameters several diagnostics are installed in the facility. To this end, Pfeiffer PKR360 Pirani/cold-cathode ionization gauges are installed in each chamber so that the pressure evolution can be monitored in the facility from atmospheric pressure down to high vacuum. These gauges are used mostly for monitoring purposes as their accuracy specifications (30% accuracy) do not allow precision measurements.

For precision pressure measurements, we rely on two MKS 370 Stabil-Ion® Hot-cathode ionization vacuum gauges. The gauges are calibrated for nitrogen and offer a 4% accuracy and 3% repeatability. Other gas measurements are possible through gas correction factors provided by the manufacturer. Thermocouples are installed to track both chamber walls temperature as well as the temperature close to the Hot Cathode Gauge (HCG) ports.

Moreover, plasma beam characterization can be performed with a dedicated 15cm beam target procured from ThrustMe shown in Figure 3. The target is includes an integrated array of Faraday probes to measure the ion current density profile, as well as two grid Retarding Field ion Energy Analyzer (RFEA) to measure the Ion Velocity Distribution Function (IVDF) and Electron Energy Distribution Function (EEDF). Additionally, a single grid Magnetic Retarding Field ion Energy Analyzer (MRFEA) is included in the assembly that allows measurmeents of the IVDF with increased resolution [22]. To measure the integral ion current, all of the elements can be electrically connected to the target body, while an electron repelling potential of -90 V is applied to the target assembly. Additionally, a cylindrical Langmuir probe is positioned in the side of the beam target and swept with bias voltage to measure the electron temperature.

2.2. Performance parameters

Air intake-collectors serve the primary function of channeling the maximum quantity of free stream air particles, which act as the efficient propellant for ABEP systems, towards the electric thruster for ionization and subsequent acceleration to generate thrust. The collection efficiency determines the effectiveness of an intake in allowing the incoming flow to pass through to the ion engine and can be calculated as the ratio of mass flow rates at the inlet and exit of the intake collector, as shown in Equation 1.

$$\eta = \frac{\dot{m}_{out}}{\dot{m}_{\infty}}, \tag{1}$$

where $\dot{m}$ is the mass flow rate and the subscripts *out* and ∞ refer to the outlet and free stream conditions, respectively. However, the ignition of conventional ion thrusters is hindered by the low atmospheric density, necessitating the use of an intake-collector to compress the flow and facilitate ignition. The extent of this compression can be measured by the compression ratio, which is defined as follows:

$$\nu = \frac{n_{out}}{n_{\infty}}, \tag{2}$$

where n is the particle number density. A trade-off between collection efficiency and compression ratio often exists, where higher collection efficiencies may lead to lower compression ratios and vice versa. Analyzing Eqs. (1) and (2) one understands that while the compression ratio can be directly computed by the measurement of pressure and temperature at the appropriate locations, direct measurements of the collection efficiency are not easily realizable without knowledge of particle mass flow rates. Indeed, although measuring flow rates of charged particles at the AIC entrance will be performed through a RFEA probe, at the exit of the intake some of these previously charged particles will have been neutralized through either collisions with walls or background gas particles and would therefore not be measured by the probe, resulting in erroneous measurements. On the other hand, measuring fluxes of neutral particles is not trivial in vacuum conditions [23].

In alternative, conductances are usually measured by measuring the pressure difference between two vacuum chambers connected by the component to characterize [24]. A component's conductance denotes the likelihood of a particle from one chamber to travel through the component and reach the other chamber. Typically, experimental setups involve a chamber that is supplied with a thermalized gas feed and another chamber that is maintained at a lower pressure through the pumping system. Consequently, the net mass exchange is an outcome of the component's geometry and can be assessed by measuring the pressure difference in each chamber. A similar test can be conducted in the DRAG-ON facility. However, unlike the standard conductance experiments, where the flow entering the component from each end is entirely thermalized, the flow in the present study comprises a plume of fast ions, a plume of neutral slow

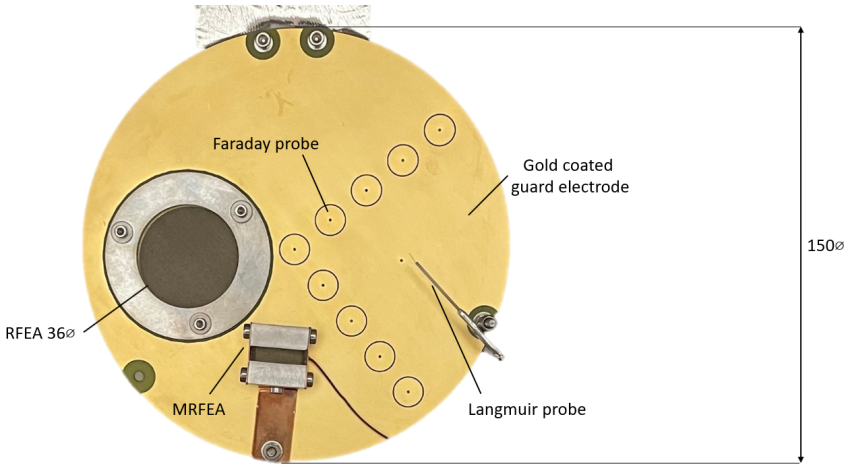

Figure 3: Beam target with the integrated ion diagnostics. All dimensions in mm

particles and a background of residual gas. Thus, estimating the collection efficiency from the pressure measurements of both chambers is achievable, but it necessitates an additional modeling layer of the pertinent flows that traverse the AIC, described in [25], along with a thorough characterization of the facility's operating conditions. In the following section, we describe the experimental campaign carried out to characterize of the facility.

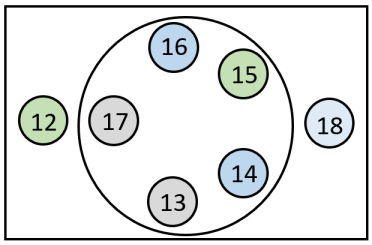

Figure 4: Port schematic used for main chamber tests. Green denotes HCGs, Blue denotes CCGs.

3. High vacuum experimental characterization

In the previous section, an overview of the DRAGON facility was provided and the need for the characterization of the high vacuum environment was stated. In this section, we take advantage of the different feature of the facility to characterize the leaks, pumping speeds and pressure sensors.

3.1. Main chamber tests

The test set-up consists in closing the pneumatic valve upstream of the connecting pipe between the two chambers, effectively isolating the main chamber from the rest of the facility. The LTA-100 is placed inside the main chamber at a distance of 20 cm to the closed pneumatic valve. The two PKRs are installed in ports 14 and 16 and two HCGs in ports 15 and 12. Due to the symmetry of the port distribution, the readings of PKR in port 15 (PKR2) and HCG in port 14 (HCG2) are directly comparable. A capacitance gauge is installed in port 13 and port 17 is used for the feed of the LTA. Figure 4 shows a top view schematic of the ports used in chamber 1. The turbopump is operated at full rotation speed.

A pressure rise test was performed by taking advantage of the current setup and stopping the turbopump. Once the rotation speed is null the angle valve is closed and the chamber is effectively isolated from the environment. Therefore, any increase in pressure can only be due to outgassing and leaks.

Figure 5 shows the pressure time evolution measured by PKR and CMR gauges. We do not take HCG measurements as the pressure is over the gauge operational range. Linear behaviour is observed in both CMR and PKR measurements which should indicate that outgassing is not significant at this stage. However, it is striking that the slope of the curves is significantly different. This discrepancy is also notorious in the absolute values differences between PKR and CMR. At high pressures, when the CMR should be the most accurate the PKR value is roughly 70% higher than the CMR reading. This result puts into question the accuracy of both PKR and CMR readings.

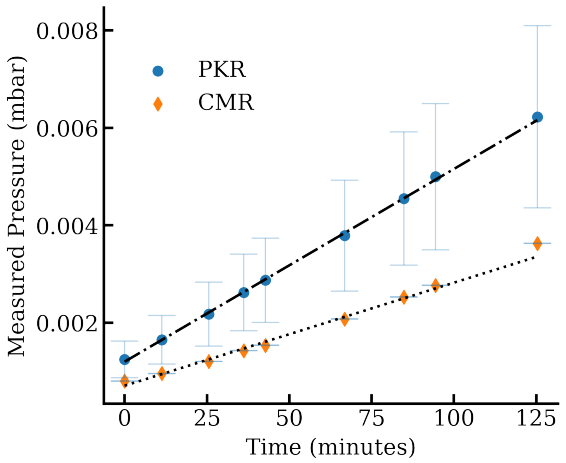

Figure 5: Chamber 1 pressure time evolution after chamber isolation.

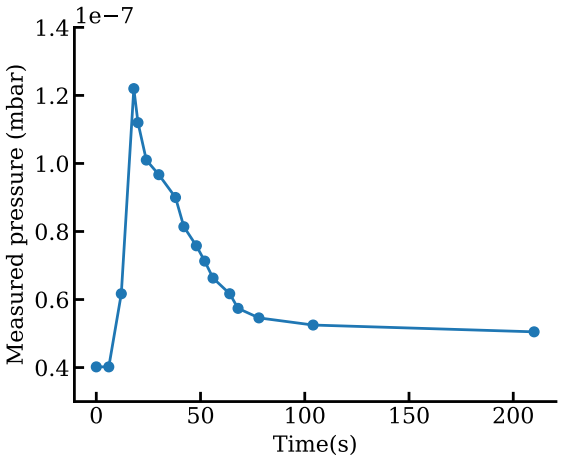

Figure 6: Background pressure (measured by PKR) time evolution during degassing

We estimate the leak flow rate present in chamber 1 using the relation $Q_{leak} = V\Delta P/\Delta t$. Considering a chamber volume of 280L we estimate a leak of $Q_{leak} = 1.05 \times 10^{-4}$ mbar.L/s or $Q_{leak} = 1.86 \times 10^{-4}$ mbar.L/s for CMR and PKR measurements, respectively.

Measurement of the effective pumping speed were performed by taking increments of injected flow rate and waiting until steady state was achieved. An increased complication is introduced due to the higher care needed for HCG measurements. If there was a decrement of injected flow rate that led to a decrease in pressure the HCG would always be degassed to ensure it is not contaminated. Figure 6 shows the pressure increase in the chamber, measured by PKR 2 during the degas process. Particles adsorbed into HCG filament surfaces are desorbed into the chamber increasing its pressure.

To achieve steady state after degassing was a lengthy process which limited the number of data points that were possible to test. Due to this limitation, all injected flow rates were tested with HCG2 but not with HCG1. Figure 7 shows the measurements performed with HCG2 versus the injected flow rate. We cover the expected operational pressure with PFG turned ON.

The effective pumping speed in chamber 1 can be determined with knowledge of the injected flow rateu sing $Q_{inj} + Q_{leak} = S_1 P_1$ and estimating Q_{leak}. In alternative, neglecting Q_{leak} is justified for high values of injected flow rate (Q_{leak} estimated to be $Q_{leak} = 1.86 \times 10^{-4}$ mbar.L/s. Figure 8 shows the effective pumping speed computed for each injected flow rate. The leak flow rate is probably underesti-

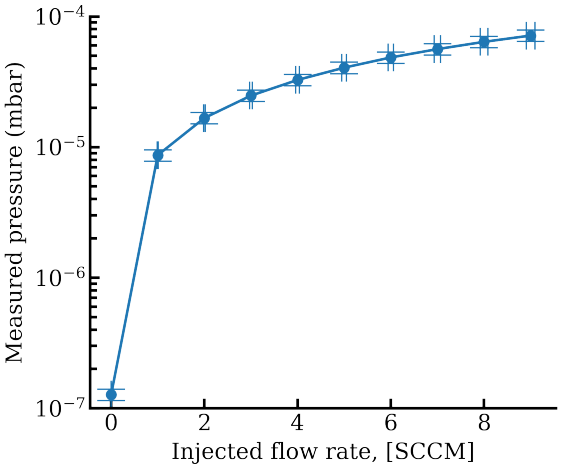

Figure 7: Background pressure measured by HCG2 vs injected flow rate.

mated given the increase in pumping speed with the increase in injected flow rate. We obtain an average pumping speed $S_{1,eff} = 2206$ L/s which compares with a nominal specification of the pump manufacturer of $S_{nominal} = 2900$ L/s. This 24% decrease in pumping speed can be attributed to the presence of a splinter shield which protects the pump from solid particles ingestion, the finite conductance of the connection of the chamber to the pipe entrance, the blockage of the pump entrance with LTA supporting frame, and the fact that we are measuring the pumping speed relative to a position where the pressure is higher than at the entrance of the pump. The uncertainty in the pumping speed calculation are computed through the

propagation of the uncertainty of the mass flow controller and assuming a 10% uncertainty for the pressure measurement arising due to uncertainty in the gas correction factors [24].

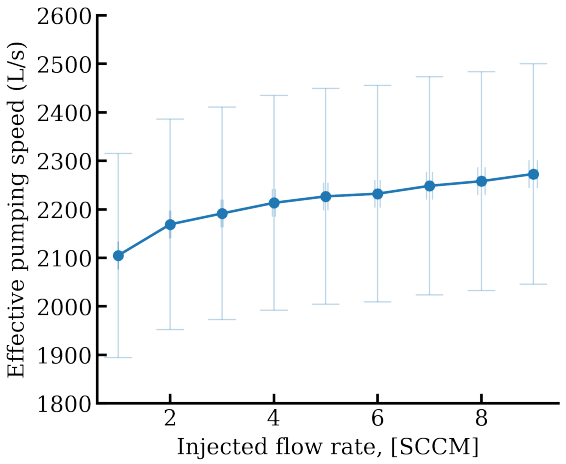

Figure 8: Effective pumping speed vs injected flow rate.

3.2. Secondary chamber tests

The test set-up consists in closing the pneumatic valve upstream of the connecting pipe between the two chambers, effectively isolating the main chamber from the rest of the facility. A pipe is manufactured to feed gas into the middle pipe connecting both chambers. The two PKRs are installed in ports 22 and 24 and two HCGs in ports 26 and 23. The capacitance gauge is installed in port 25. Figure 9 shows a top view schematic of the ports used in chamber 2.

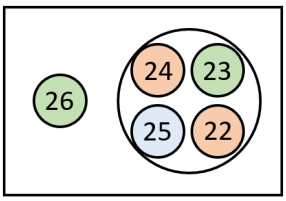

Figure 9: Port schematic used for secondary chamber tests. Green denotes HCGs, Blue denotes CCGs.

A pressure rise test was performed by taking advantage of the current setup in the same fashion as in Section 3.1. Figure 10 shows the pressure time evolution measured by PKR and CMR gauges. Linear behaviour is again observed in both CMR and PKR measurements indicating not significant outgassing. However, the curve slope and absolute values are still significantly different. At high pressures, the PKR value is roughly 50% higher than the CMR reading. This result further questions the accuracy of both PKR and CMR sensors.

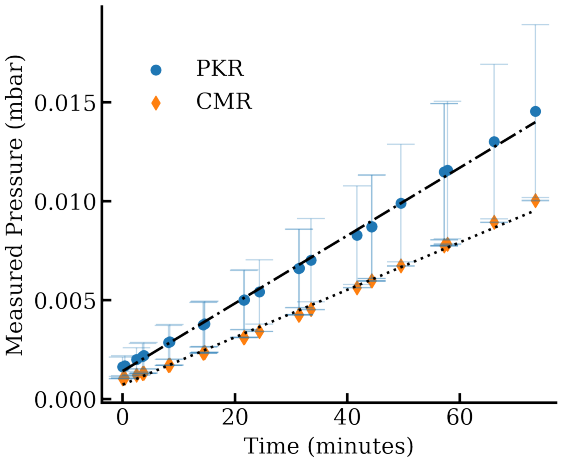

Figure 10: Chamber 2 pressure time evolution after chamber isolation.

Again using $Q_{leak} = V\Delta P \times \Delta t$ and considering a chamber volume of 45L we estimate a leak of $Q_{leak} = 9.13 \times 10^{-5}$ mbar.L/s or $Q_{leak} = 1.3 \times 10^{-4}$ mbar.L/s for CMR and PKR measurements, respectively.

Following the same method as in Section 3.1 the pumping speed is obtained for different background pressures assuming a leak flow rate $Q_{leak} = 1.3 \times 10^{-4}$ mbar.L/s. Figure 11 shows the effective pumping speed variation with background pressure. An average pumping speed $S_{2,eff} = 1575$ L/s which compares with a nominal specification of the pump manufacturer of $S_{nominal} = 1950$ L/s. This 19% decrease is smaller than the one observed in the main chamber even though the splinter shield is less transparent than the one present in the main chamber. This demonstrates the importance of blockage effects in the reduction of effective pumping speeds.

3.3. Hot cathode gauge calibration

As stated in Section 3.1, when using gas correction factors we have to rely on uncertainty estimates that vary significantly within the literature and between gases. To tackle this problem, we use the facility as in a dynamic expander experiment in order to calibrate the hot cathode gauges[26]. Such a set-up, also known as orifice method, is a primary high vacuum standard on the The National Bureau of Standards[27]. In such a standard two chambers are connected by a component of know conductance. Gas is injected in one of

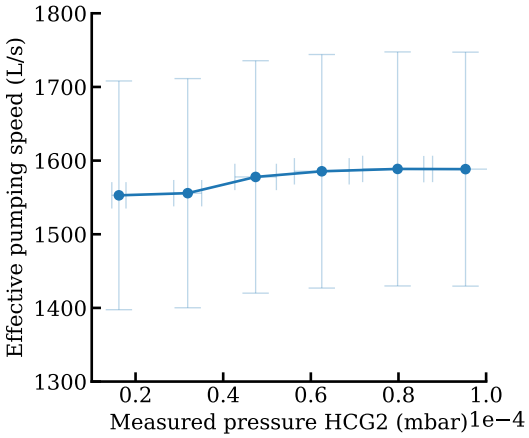

Figure 11: Effective pumping speed vs background pressure.

the chambers and is pumped in the secondary chamber. In order for the conductance to be known, a known distribution of particle velocities at the component entrances needs to be present. Typically, the geometry of the chambers is such that a Maxwell-Boltzmann distribution can be assumed at both entrances.

The DRAG-ON facility does not comply with all the requirements stated in the standard methodology as the secondary chamber should be bigger to ensure a Maxwellian distribution. Nonetheless, we rely on numerical simulations to relate the pressures measured experimentally, to the flow rate entering both ends of the middle section. This flow rate is then related to an effective pressure P_i^* assuming a maxwellian distribution with the relation

$$P_i^* = Z_i \frac{4k_b T_i}{\bar{c}} \tag{3}$$

where k_b is the boltzmann constant, T_i is chamber i wall temperature and $\bar{c}$ is the thermal speed. The experimental set up consists in injecting gas through a middle pipe that directs the flow into the back wall of the main chamber. The main chamber turbopump is turned off and the angle valve is closed to isolate the chamber from the foreline. The chambers are connected by the conduit described in Section 2. The turbopump in the secondary chamber is operated at full rotational speed. One HCG is placed in port 12 of the main chamber and another HCG is placed in port 26, refer to Figures 4 and 9. Performing a mass balance in the main chamber we get

$$Q_{inj} = C(P_1^* - P_2^*), \tag{4}$$

which can be manipulated to yield

$$P_1^* = \frac{Q_{inj}}{C(1 - \frac{P_2^*}{P_1^*})}. \tag{5}$$

Therefore, only the ratio of pressure needs to be accurately known to know the absolute value of P_1^*. If we assume the pressure are not known by a constant multiplication factor, the gas correction factor, then the ratio is not affected by this quantity.

The numerical simulation is performed using CERN's 3-D Test Particle Monte Carlo (TPMC) code Molflow [28]. Figure 12 shows the experiment set-up and simulated pressure field in the y-z plane traversing the facility. From the simulation we relate the measured pressures to the effective pressures P_i^* as $P_1^* = 0.985 P_{HCG1}$ and $P_2^* = 1.025 P_{HCG2}$. We vary the flow

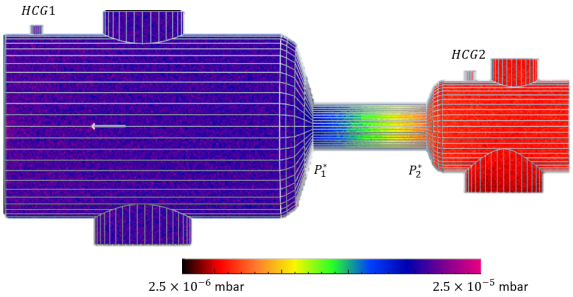

Figure 12: Dynamic expander set-up and pressure field for an injected flow rate of 0.5 SCCM.

rate injected through the pipe to change the pressure in each chamber. Due to the long stabilization times for hot cathode gauge readings only two measurement pairs are performed for each injected flow rate. Figure 13 shows the Gas Correction Factors computed for each injected flow rate. The measured GFCs present a slight increase with background pressure but the values can be reasonably assumed to be approximately constant with a mean of $GCF_{exp} = 0.744$. This value is different from the GCF presented in the manual, $GCF_{man} = 0.775$. The discrepancy may be due to the variations of the GCF with the operating pressure. The manual value is given for all operational pressures while we have tested only on pressure decade.

3.4. Thermalized flow conductance measurements

To evaluate the capability of performing conductance measurements in the facility we design a test to evaluate the conductance of the middle pipe in series with the open pneumatic valve to background flow. To guarantee the gas is thermalized, we inject argon

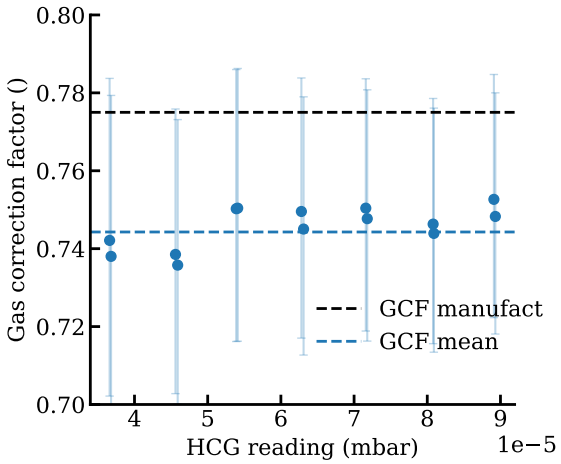

Figure 13: Gas correction factors vs HCG1 pressure reading

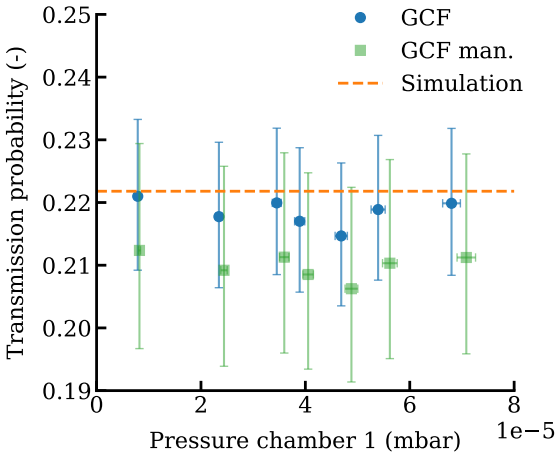

Figure 14: Transmission probability for different main chamber background pressures and assuming GCF provided in the gauge manual (green) and obtained from calibration (blue)

in the main chamber through a pipe directed at the chamber back wall. To replicate the testing environment we keep both turbopumps rotating at full speed and the PFG in the main chamber. The transmission probability of the pipe is computed through

$$\tau_{background} = \frac{S_2 P_2}{C_0(P_1^* - P_2^*)}. \tag{6}$$

where again P_i^* indicates effective pressures relating to the test model entrances and C_0 represents the orifice conductance computed as $C_0 = A\frac{\bar{c}}{4}$, where A is the entrance area. Figure 14 shows the transmission probability of the assembly connecting both chambers as function of the background pressure in the main chamber. The agreement between simulated values of the transmission probability and experiments is remarkable when the GCFs from calibration are used. However, a systematic deviation form the simulation value is introduced when the GCF from the manual are used. Moreover, the uncertainty associated to each GCF are different due the small spread observed in Figure 13. These results highlight the advantages of using calibrated values of the GCFs.

4. Plasma beam diagnostics

To reproduce orbital conditions on ground, the tuning of the following LTA-100 source parameters is necessary: The acceleration potential can be changed between -70V and 0V and changes mainly the ion mean energy. The current fed to the coil for magnetic field generation can be operated from 0 to 2 A and influences the collimation of the beam. Moreover, the power given to the source (varied between 50 and 80W) influences the temperature of electrons and therefore the total beam current. Additionally, the axial distance between the source exit and measurement location affects the electron temperature (due to electron cooling) and beam collimation (due to plume expansion). Finally, changing the flowrate fed to the PFG leads mostly to changes in the total beam current. Flowrates between 3 SCCM and 7 SCCM can be provided without compromising free molecular flow conditions in the chamber. This section describes preliminary experiments performed to characterize the influence of the acceleration potential and the focusing current on the ion velocity distribution function (IVDF) as well as experiments to obtain preliminary estimates of the electron temperature and ion current distributions. In this section, the beam diagnostic target shown in Figure 3 is placed at 5cm from the source and preliminary studies are performed with the MR-FEA and the Langmuir probe.

To study the IVDF, measurements were taken for various values of the acceleration potential relative to the system ground. This entails measuring the current drawn from the RFEA for different values of biasing in the probe collector. The probe collector is biased from 0 to +32 V. The grid and body of the probe are grounded to avoid perturbing the plasma. The IVDF, $f(E)$, can be obtained from the derivative of the measured current as []

$$f(E) \propto -\frac{dI}{dV} \tag{7}$$

The results of these measurements are shown in Figure 15 (a) for a fixed set of operational conditions, including 65W RF power, 3 SCCM flow rate, and focusing current fixed at condition 2-i. The data indicate that the velocity distribution function can be easily manipulated by adjusting the acceleration potential, allowing for the mean ion energy to be reduced to as low as 15 eV for condition 1-p of acceleration potential.

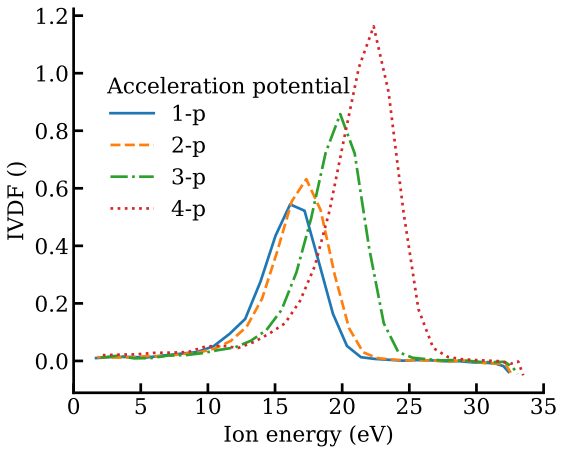

Figure 15: Argon IVDFs as a function of the ion energy measured at 5 cm from the source exit. Operational parameters are 3 SCCM flow rate, 65 W of RF power and focusing current fixed at condition 2-i.

Figure 16 (b) shows the effect of changing the focusing current. The operational parameters are kept fixed as before with 65 W RF power, 3 SCCM flow rate, and acceleration potential fixed at condition 1-p. The focusing current value has an impact on both the shape of the IVDF and the average ion energy. Generally, increasing the focusing current results in a broader IVDF and a decrease in the average energy value. Therefore, both acceleration potential and focusing current can be varied to change the average energy of ions exiting the PFG. A combination of both parameters needs to be found in order to achieve the orbital velocity of 7.6 km/s which translates into an energy $E_i \approx 12$ eV for argon atoms.

Finally, Langmuir probe measurements were performed to obtain information on the plasma electron temperature. We collected the current measured with the Langmuir probe for a bias sweep between -35 V and 0 V. The electron temperature is computed following the procedure detailed by Lobbia and Beal [29] where the electron temperature is given by the the first derivative of the electron current between the floating

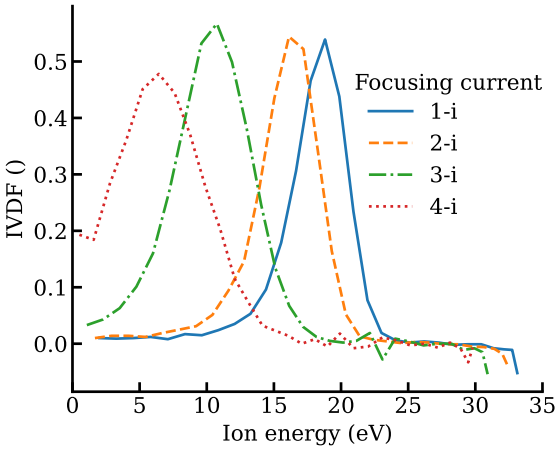

Figure 16: Argon IVDFs as a function of the ion energy measured at 5 cm from the source exit. Operational parameters are 3 SCCM flow rate, 65 W of RF power and acceleration voltage fixed at condition 1-p.

and plasma potential. Figure 17 shows the electron current as function of probe bias voltage. The electron temperature is given by the inverse of this slope $T_e = (d \ln I_e/dV)^{-1}$. For the present case we compute an electron temperature $T_e = 4.4$ eV. To obtain

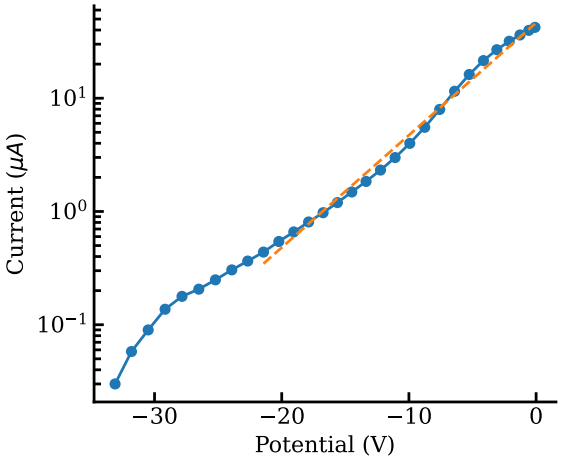

Figure 17: Langmuir electron current versus bias voltage. Operational parameters are 3 SCCM flow, 65 W and acceleration voltage fixed at condition 4-p.

estimates of the electron temperature would require a bigger sweep of potential as the electron saturation current needs to be reached. However, assuming an expected density $n_e \approx 1 \times 10^{-15}\,\mathrm{m}^{-3}$ we compute a Debye length $\lambda_D = 0.4$ mm. Floating sheath sizes are typically 10 times the Debye length [30]. Therefore for an intake with radius 6 cm the sheath size would

be less than 10% of the radius. In future experiments, the electron number density will be measured to have more accurate predictions of the sheath size and the intake will be biased to assess the influence of sheaths in the ions trajectories.

5. Conclusions

In the present study, VKI's DRAG-ON facility is presented. We focus on the characterization of high vacuum that is necessary for the measurement of ABEP intake efficiency parameters. We quantify the throughput of leaks flowing into each chamber through pressure rise tests and measure the effective pumping speeds of the turbomolecular pumps of each chamber.

Moreover, we performed calibrations of the hot cathode gauges that are independent of gas type using the dynamic expander standard. It is found that the calibration factors derived from calibration differ from those provided by the probe manufacturer. Moreover, this procedure allows us to quantify the uncertainty associated with the measured calibration factor. Additionally, we measure the conductance of the middle conduit connecting both chambers for which the measurements of pumping speeds, leaks and calibration factors are required. The measurements agree remarkably with the simulated values when the measures calibration factors are used but present a systematic deviation when the manufacturer values are used instead. This observation together with the quantification of uncertainty highlights the importance of gauge calibration.

Finally, we performed preliminary measurements of the PFG argon plasma outflow. The influence of acceleration potential and focusing current on the IVDF is quantified and we demonstrate the broad range of flow conditions obtainable. More importantly, the ability of the PFG to produce low energy ions that duplicate orbital velocities is demonstrated. Finally, Langmuir probe measurements were performed and an electron temperature of 4.4 eV was measured. A preliminary estimation of the sheath size using this temperature indicates that neglecting the effect of sheaths in the ion trajectory is reasonable as a first approximation.

Acknowledgments

This work was supported by a PhD grant from the Portuguese Foundation for Science and Technology (FCT) with number 2020.05450.BD.

References

[1] N. H. Crisp, P. C. Roberts, S. Livadiotti, V. T. A. Oiko, S. Edmondson, S. Haigh, C. Huyton, L. Sinpetru, K. Smith, S. Worrall, et al., The benefits of very low earth orbit for earth observation missions, Progress in Aerospace Sciences 117 (2020) 100619.

[2] L. A. Singh, M. L. Walker, A review of research in low earth orbit propellant collection, Progress in Aerospace Sciences 75 (2015) 15–25.

[3] P. Zheng, J. Wu, Y. Zhang, B. Wu, A comprehensive review of atmosphere-breathing electric propulsion systems, International Journal of Aerospace Engineering 2020.

[4] B. A. Banks, K. K. de Groh, S. K. Miller, D. L. Waters, Lessons learned from atomic oxygen interaction with spacecraft materials in low earth orbit, in: AIP conference proceedings, Vol. 1087, American Institute of Physics, 2009, pp. 312–325.

[5] K. Moe, G. S. Reiter, Surface-particle-interaction measurements using paddlewheel satellites, Tech. Rep. AD 673 946, DOUGLAS AIRCRAFT CO INC SANTA MONICA CA SPACE SCIENCES DEPT (1968).

[6] I. Harris, A. Chambers, G. Roberts, Preliminary results of an atomic oxygen spaceflight experiment, Materials Letters 31 (3-6) (1997) 321–328.

[7] K. T. Nicholson, T. K. Minton, S. Sibener, Temperature-dependent morphological evolution of hopg graphite upon exposure to hyperthermal o (3p) atoms, Progress in organic coatings 47 (3-4) (2003) 443–447.

[8] T. K. Minton, C. M. Nelson, D. E. Brinza, R. H. Liang, Inelastic and reactive scattering of hyperthermal atomic oxygen from amorphous carbon, JPL Publication 91-34, NASA, Jet Propulsion Laboratory (1991).

[9] J. Zhang, D. J. Garton, T. K. Minton, Reactive and inelastic scattering dynamics of hyperthermal oxygen atoms on a saturated hydrocarbon surface, The Journal of chemical physics 117 (13) (2002) 6239–6251.

[10] C. White, J. Rao, G. Roberts, A. Chambers, K. Lawson, J. Nicholls, The development of carbon-based sensors for the measurement of atomic oxygen, EUROPEAN SPACE AGENCY-PUBLICATIONS-ESA SP 540 (2003) 137–144.

[11] T. Andreussi, G. Cifali, V. Giannetti, A. Piragino, E. Ferrato, A. Rossodivita, M. Andrenucci, J. Longo, L. Walpot, Development and experimental validation of a hall effect thruster ram-ep concept, in: 35th International Electric Propulsion Conference, 2017, pp. 8–12.

[12] M. Tagawa, K. Yokota, K. Nishiyama, H. Kuninaka, Y. Yoshizawa, D. Yamamoto, T. Tsuboi, Experimental study of air breathing ion engine using laser detonation beam source, Journal of Propulsion and Power 29 (3) (2013) 501–506.

[13] F. Romano, T. Binder, G. Herdrich, S. Fasoulas, T. Schönherr, Air-intake design investigation for an air-breathing electric propulsion system, in: 34th International Electric Propulsion Conference, 2015.

[14] S. W. Jackson, R. Marshall, Conceptual design of an air-breathing electric thruster for cubesat applications, Journal of Spacecraft and Rockets 55 (3) (2018) 632–639.

[15] Y. Hisamoto, K. Nishiyama, H. Kuninaka, Design of air intake for air breathing ion engine, in: 63rd International Astronautical Congress, Naples, Italy, 2012.

[16] T. Binder, P. Boldini, F. Romano, G. Herdrich, S. Fasoulas, Transmission probabilities of rarefied flows in the application of atmosphere-breathing electric propulsion, in: AIP Confer-

ence Proceedings, Vol. 1786, AIP Publishing LLC, 2016, p. 190011.
[17] J. Kleiman, Z. Iskanderova, Y. Gudimenko, S. Horodetsky, Atomic oxygen beam sources: A critical overview, in: Materials in a Space Environment, Vol. 540, 2003, pp. 313–324.
[18] C. A. Maldonado, A. Ketsdever, L. P. Rand, K. Xie, C. Farnell, J. D. Williams, Characterization of an atomic oxygen plasma source for ground-based simulation of the leo neutral environment, in: 5th AIAA Atmospheric and Space Environments Conference, 2013, p. 2681.
[19] C. Moldonado, T. Lilly, A. Ketsdever, Development of a space simulation facility to study combined effects, in: 4th AIAA Atmospheric and Space Environments Conference, 2012, p. 2941.
[20] V. T. A. Oiko, P. C. Roberts, A. Macario-Rojas, S. Edmondson, S. Haigh, B. Holmes, S. Livadiotti, N. Crisp, K. Smith, L. Sinpetru, et al., Ground-based experimental facility for orbital aerodynamics research: Design, construction and characterisation, in: Proceedings of the International Astronautical Congress, IAC, Vol. 2020, IAF, 2020.
[21] V. Oiko, P. C. Roberts, S. Edmonson, D. García-Almiñana, S. Rodríguez Donaire, M. Sureda Anfres, Design and development of a hyper-thermal atomic oxygen wind tunnel facility, in: Proceedings of the 14th ISMSE & 12th ICPMSE, Biarritz, France, 1 to 5 October 2018, Centre National d'Études Spatiales (CNES), 2018, pp. 1–6.
[22] D. Rafalskyi, S. Dudin, A. Aanesland, Magnetized retarding field energy analyzer measuring the particle flux and ion energy distribution of both positive and negative ions, Review of Scientific Instruments 86 (5) (2015) 053302.
[23] D. J. Economou, Fast (tens to hundreds of ev) neutral beams for materials processing, Journal of Physics D: Applied Physics 41 (2) (2008) 024001.
[24] K. Jousten, K. Galda, Handbook of Vacuum Technology, John Wiley & Sons, Ltd, 2016. doi:https://doi.org/10.1002/9783527688265.ch9.
[25] P. Jorge, D. le Quang, A. Hubin, T. Magin, Modeling and estimating measurement uncertainty of vki's new low density facility, in: 9 th EUROPEAN CONFERENCE FOR AERONAUTICS AND SPACE SCIENCES (EUCASS), 2022. doi:https://doi.org/10.13009/EUCASS2022-7334.
[26] W. Steckelmacher, The calibration of vacuum gauges, Vacuum 37 (8-9) (1987) 651–657.
[27] K. E. McCulloh, C. R. Tilford, S. D. Wood, D. F. Martin, Summary abstract: The national bureau of standards orifice-flow primary high vacuum standard, Journal of Vacuum Science & Technology A 4 (3) (1986) 362–362. arXiv:https://doi.org/10.1116/1.573928, doi:10.1116/1.573928.
URL https://doi.org/10.1116/1.573928
[28] R. Kersevan, M. Ady, et al., Recent developments of monte-carlo codes molflow+ and synrad+, in: 10th International Particle Accelerator Conference, Vol. 6, 2019.
[29] R. B. Lobbia, B. E. Beal, Recommended practice for use of langmuir probes in electric propulsion testing, Journal of Propulsion and Power 33 (3) (2017) 566–581.
[30] P. Chabert, What is the size of a floating sheath?, Plasma Sources Science and Technology 23 (6) (2014) 065042.

Analysis of implicit PIC schemes and their application to electric propulsion

Pietro Parodi

Department of Mathematics, KU Leuven, Belgium;
Aeronautics and Aerospace Department, von Karman Institute for Fluid Dynamics, Belgium, pietro.parodi@vki.ac.be

Supervisor: Thierry Magin

Professor, Aeronautics and Aerospace Department, von Karman Institute for Fluid Dynamics, Belgium,
Professor, Aero-Thermo-Mechanics Department, Université libre de Bruxelles, Belgium, magin@vki.ac.be

University Supervisor: Giovanni Lapenta

Professor, Department of Mathematics, KU Leuven, Belgium, giovanni.lapenta@kuleuven.be

Abstract

Advanced Particle-in-Cell schemes could facilitate the numerical replication of full electric propulsion devices. In this work, we extend the previously presented semi-implicit PIC formulation to a fully-implicit one that features exact charge conservation. We formulate and implement the Jacobian of the implicit update, as well as two approximate versions. Finally, we evaluate the performance of the different schemes and Jacobians through a numerical experiment.

Keywords: Particle-in-Cell, Particle methods, Air-Breathing Electric Propulsion, Newton-Krylov, Jacobian, preconditioner, anisotropic mesh

1. Introduction

The Knudsen number Kn is the ratio of characteristic dimension of a physical system and the molecular mean free path. It is in the range $\approx$ 0.1-10 for typical plasmas involved in Electric Propulsion and laboratory applications. This means that a high degree of nonequilibrium is present, but gas phase collisions are still relevant. A fluid approach would not represent accurately the plasma in such conditions because of the high degree of translational nonequilibrium. Particle methods, on the other hand, can efficiently represent the six-dimensional *phase space* of 3D particle positions and 3D particle velocities in nonequilibrium. Such methods have been independently developed for collisional gases and for collisionless plasmas, under the names Direct Simulation Monte Carlo (DSMC) [1, 2], and Particle-in-Cell (PIC) [3]. The underlying assumption of both methods is that computational particles can represent a large number F_p of real particles. In DSMC, collision events instantaneously change the velocity of particle pairs undergoing the collision at each time step.

In PIC, the velocity of charged particles is affected by the electromagnetic field computed on a computational grid, which takes into account charged particle currents or densities. The two methods can be merged in a hybrid PIC-DSMC code, where both particle collisions and long-distance charge effects are accounted for. In plasmas of our interest, the electron number density n_e is typically in the range 10^{13}-10^{17} m^{-3}, with temperatures of the order of 1 eV ($\approx$ 11605 K). Ions are relatively cold, typically below 1000 K. This means that the length- and time scales of interest are often much larger than the smallest natural scales of the plasma, which are dictated by the light electrons. The Debye length, $\lambda_{De} = [(\varepsilon_0 k_B T_e)/(n_e q_e^2)]^{1/2}$, where ε_0 is the permittivity of vacuum, k_B is Boltzmann's constant, and q_e is the elementary charge, is typically the smallest length scale. The plasma frequency, $\omega_{pe} = [(n_e q_e^2)/(\varepsilon_0 m_e)]^{1/2}$, where m_e is the electron mass, typically dictates the smallest time scale. Here lies the second obstacle, since traditional explicit PIC schemes need to resolve these small scales, otherwise disrupting numerical instabilities appear. These re-

quirements can make simulation of an entire physical device extremely expensive, and practically unfeasible above a certain plasma density. An illustrative example is provided in Figure 1. Here, a cylindrical conductor is inserted in a plasma. This gives rise to features of very different spatial and temporal scales.

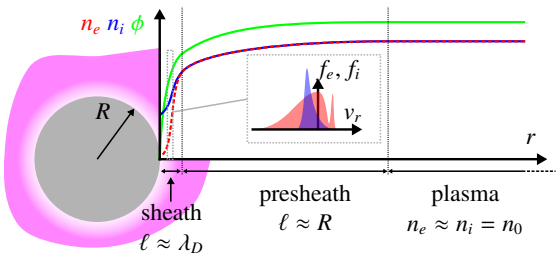

Figure 1: Illustrative example for the nonequilibrium and multiscale nature of plasma. When a conductor is immersed in a plasma, a sheath forms around it, which has a scale of the Debye length λ_{De}. Another region called presheath, where ions are accelerated, can be identified. Its size is comparable to that of the conductor and possibly orders of magnitude larger than λ_{De}. The line plots show the qualitative behavior of electron density n_e, ion density n_i and electric potential ϕ. A sketch of the nonequilibrium velocity distributions of ions and electrons as found in the sheath is also shown.

Recently, different implicit and semi-implicit versions of the energy conserving Particle-in-Cell algorithm have been proposed [4–8]. This type of scheme is designed in such a way that the sum of particle kinetic energy and of field energy is exactly conserved at each time step. An explicit scheme must respect the constraints $\Delta x < \lambda_{De}$ and $\Delta t < \omega_{pe}^{-1}$ [9] to avoid numerical instabilities, most notably the finite-grid instability. Respecting these constraints causes simulations of full plasma devices, such as thrusters for space propulsion or plasma sources, to be extremely expensive, and in many cases unfeasible. It has been shown [10] that energy-conserving schemes present an extended stability region with respect to the common explicit scheme. Electron length and time scales can in fact be well under-resolved, as long as electrons remain in the subsonic regime. An additional complication is that the property of charge conservation is of fundamental importance, especially in many cases of engineering interest where isolated bodies can accumulate electrical charge. This property is enforced in the continuum setting by the charge continuity equation, $\nabla \cdot \mathbf{J} = -\partial\rho/\partial t$, where $\mathbf{J}$ is current density and ρ is the density of charges. When it is not satisfied, an error accumulates in time between the computed electric potential the distribution of charge. Solutions to this problem essentially consist in a correction to either fields or particle properties [11, 12], which is challenging because the energy conservation property must be retained. Alternatively, this requires a nonlinear convergence of the update of fields and particles (i.e. an implicit formulation). The combination of an energy and charge-conserving scheme with a robust time discretization and a flexible, state-of-the-art domain discretization such as anisotropic unstructured meshes could provide a path towards the simulation of full plasma devices at realistic plasma densities. The PIC-DSMC code Pantera is being developed at VKI [13] to tackle these challenges. Building on previous work on the semi-implicit, energy-conserving scheme, we formulate a fully-implicit version which also features charge conservation. In Section 2.1, we introduce the discretization of the particle model and the emerging algorithm to solve the implicit time update. Computation of the Jacobian of the equation's residual with respect to the unknowns is essential for an efficient solution of the Newton iterative procedure. In Sections 2.2-2.4, we formulate the exact Jacobian, based on particle kinetics, as well as two approximate versions. Section 2.5 provides some details of the implementation of these Jacobians. In Section 3, we use a simple but representative test case to compare the performance of the implicit scheme with the previous explicit and semi-implicit schemes. We will also compare the convergence behavior of the three different Jacobians. Finally, in Section 4, we will conclude and discuss the priorities for future work.

2. Model and Methods

2.1. Field equation and particle mover

Differently from most other implementations of the energy-conserving PIC scheme, we employ a finite element discretization, which uses first-order basis functions $\Psi_i(\mathbf{x})$ for the electric potential $\phi(\mathbf{x}, t)$. This can then be represented as:

$$\phi(\mathbf{x}, t) = \sum_i \phi_i(t)\, \Psi_i(\mathbf{x}). \tag{1}$$

Clearly, we obtain a uniform electric field $\mathbf{E}$ in each cell, as given by:

$$\mathbf{E}(\mathbf{x}, t) = -\nabla\phi(\mathbf{x}, t) = -\sum_i \phi_i(t)\, \nabla\Psi_i(\mathbf{x}) \tag{2}$$

This may be considered a crude discretization, since particles experience jumps in electric field along their motion. However, we will show that this allows a significant simplification of some of the computations involved in the algorithm. Additionally, since we require that macroscopic gradients are well resolved by the grid, we expect jumps between adjacent cells to be reasonable. The potential is computed using Poisson's equation, $\nabla^2\phi = -\rho/\varepsilon_0$, where $\rho = \sum_s q_s n_s$ is the total charge density and q_s the charge of species s. It can be cast in the weak form on domain Ω, resulting in the following equation for node i:

$$\sum_j \phi_j \int_\Omega \nabla\Psi_j \cdot \nabla\Psi_i \, dV = \int_{\partial\Omega_N} g \, \Psi_i \, dS + \frac{1}{\varepsilon_0} \int_\Omega \rho \, \Psi_i \, dV, \tag{3}$$

where $g = \frac{\partial\phi}{\partial\hat{\mathbf{n}}}$ is the Neumann boundary condition on boundary $\partial\Omega_N$ with normal $\hat{\mathbf{n}}$. We use the Klimontovich representation for the distribution function f_s of particles of species s:

$$f_s(\mathbf{x}, \mathbf{v}, t) = \sum_{p \in s} F_p \, \delta\Big(\mathbf{x} - \mathbf{x}_p(t)\Big) \, \delta\Big(\mathbf{v} - \mathbf{v}_p(t)\Big), \tag{4}$$

where F_p is the macroparticle weight, and δ is the three-dimensional Dirac delta function. With this particle representation, the charge density accumulated on node i is given by:

$$\rho_i = \int_\Omega \rho \, \Psi_i \, dV = \sum_p F_p q_p \Psi_i(\mathbf{x}_p) \tag{5}$$

Then, Poisson's equation becomes:

$$\sum_j K^{ij} \phi_j = \mathcal{N}_i + \frac{1}{\varepsilon_0} \sum_p F_p q_p \Psi_i(\mathbf{x}_p), \tag{6}$$

where we denoted with $\mathcal{N}_i$ the Neumann boundary term, and with:

$$K^{ij} = \int_\Omega \nabla\Psi_i \cdot \nabla\Psi_j \, dV \tag{7}$$

the integrals of the basis functions. These are in practice stored as per-cell values K_c^{ij} such that $K^{ij} = \sum_c K_c^{ij}$. The definition is:

$$K_c^{ij} = \int_{\Omega_c} \nabla\Psi_i \cdot \nabla\Psi_j \, dV \tag{8}$$

Where $\Omega_c \in \mathbb{R}^d$ is the domain of cell c. This gives rise to the linear system:

$$A_p\{\phi\} = \{b\}. \tag{9}$$

We employ a Crank-Nicholson scheme for particle advection, as is done in many implicit PIC implementations [4, 7, 12]. This allows to have values of particle positions and velocities colocated in time. For each particle, a time step is split into sub-steps of duration Δt_p^ν, such that $\sum_\nu \Delta t_p^\nu = \Delta t$. The mover's equations read:

$$\mathbf{v}_p^{\nu+1} = \mathbf{v}_p^\nu + \frac{q_p}{m_p} \mathbf{E}_p^{\nu+\frac{1}{2}} \Delta t_p^\nu \tag{10}$$

$$\mathbf{x}_p^{\nu+1} = \mathbf{x}_p^\nu + \mathbf{v}_p^{\nu+\frac{1}{2}} \Delta t_p^\nu \tag{11}$$

As suggested in literature [4], we stop the particles at cell boundaries, such that during a sub-step the path of a particle is entirely contained in a grid cell. Since the electric field is uniform in each cell, quantity $\mathbf{E}_p^{\nu+\frac{1}{2}}$ is constant. Substituting Eq. (10) into Eq. (11), we obtain:

$$\mathbf{x}_p^{\nu+1} = \mathbf{x}_p^\nu + \mathbf{v}_p^\nu \Delta t_p^\nu + \frac{1}{2} \frac{q_p}{m_p} \mathbf{E}_p^\nu \left(\Delta t_p^\nu\right)^2. \tag{12}$$

Clearly, particle trajectories within a sub-step are parabolic segments. This greatly simplifies the movement of particles, which in 3D consists of finding the intersection between the parabolic trajectory of the particle and the four faces of the tetrahedral cell. The solution is analytical, and we avoid the burden of an iterative solution. In particular, if a cell's face is described by the plane equation $ax + by + cz + d = \mathbf{n}\cdot\mathbf{x} + d = 0$, the intersection is found as $\mathbf{n}\cdot\mathbf{x}_p^{\nu+1} + d = 0$, which substituting reads:

$$\underbrace{d + \mathbf{n} \cdot \mathbf{x}_p^\nu}_{\gamma} + \underbrace{\mathbf{n} \cdot \mathbf{v}_p^\nu}_{\beta} \Delta t_p^\nu + \underbrace{\frac{1}{2} \frac{q_p}{m_p} \mathbf{n} \cdot \mathbf{E}_p^\nu}_{\alpha} \left(\Delta t_p^\nu\right)^2 = 0. \tag{13}$$

If the determinant $\delta = \beta^2 - 4\alpha\gamma > 0$, the particle's trajectory intersects the cell's face at two possible instants:

$$\Delta t_p^\nu = \frac{-\beta \pm \sqrt{\delta}}{2\alpha}. \tag{14}$$

The solutions for each face of the cell are stored, and then the smallest positive of all solutions is selected. The fact that this solution is analytical avoids an iterative procedure in an already highly nested loop. A time step of the complete implicit algorithm is summarized in Algorithm 1. The implicit update of particle and field quantities with this algorithm requires minimization of the norm of the residual f_k of Poisson's equation at the new time:

$$A_p \tilde{\phi}_k^{n+1} = b_k^{n+1}, \tag{15}$$

Algorithm 1 Time step of the implicit solver

Start with a guess for the updated potential, i.e. $\tilde{\phi}_0^{n+1} = \phi^n$
for $k = 0$ **to** $N_{\text{max iter}}$ **do**
  Compute the expected LHS of Poisson's equation (9): $\tilde{b}_k^{n+1} = A_p \tilde{\phi}_k^{n+1}$
  Compute the electric field $\tilde{\mathbf{E}}_k^{n+\frac{1}{2}} = -\nabla(\tilde{\phi}_k^{n+1} + \phi^n)/2$
  for each particle **do**
    for each sub step **do**
      Look for intersection with cell faces
      Move the particle with $\tilde{\mathbf{E}}_k^{n+\frac{1}{2}}$ (Section 2.1)
      If needed accumulate the Jacobian J from particle motion (Section 2.2)
    end for
  end for
  Deposit particle charge to obtain the new RHS b_k^{n+1} of Poisson's equation (6)
  Compute the residual $f_k = b_k^{n+1} - \tilde{b}_k^{n+1}$ of Poisson's equation at t^{n+1}
  if convergence criteria are met **then**
    $\phi^{n+1} \leftarrow \tilde{\phi}_k^{n+1}$
    Exit the loop
  else
    Correct the potential with a Newton iteration $J(\tilde{\phi}_{k+1}^{n+1} - \tilde{\phi}_k^{n+1}) = f_k$
  end if
end for

where $\tilde{\phi}_k^{n+1}$ is the potential used to move the particles, and b_k^{n+1} is the RHS of Eq. (6), obtained from the updated particle positions. We use a Newton-Krylov solver with line search to solve the nonlinear system. This requires computation of the Jacobian $\partial f/\partial\tilde{\phi}$, or an approximation to it. Often, a Jacobian-free Newton-Krylov (JFNK) approach is used to solve the nonlinear system. In this case, an adequate preconditioner for the Krylov solver, which should approximate the Jacobian matrix, would still be necessary [14]. The following sections will deal with how the Jacobian is derived and computed.

2.2. *Computation of the analytical Jacobian*

We can accumulate the exact Jacobian directly from particle motion. This Jacobian can be written as:

$$\frac{\partial f_i}{\partial \tilde{\phi}_j^{n+1}} = \frac{\partial b_i^{n+1}}{\partial \tilde{\phi}_j^{n+1}} - \frac{\partial \tilde{b}_i^{n+1}}{\partial \tilde{\phi}_j^{n+1}}. \tag{16}$$

One can recognize the second term on the RHS as the (i, j) entry of the matrix of the linear system of Poisson's equation A_p. The first term instead is the effect of particle motion. Since for internal nodes $b_i = \rho_i/\varepsilon_0$, using the chain rule:

$$\frac{\partial b_i^{n+1}}{\partial \tilde{\phi}_j^{n+1}} = \sum_p \left(\frac{1}{\varepsilon_0} \frac{\partial \rho_i^{n+1}}{\partial \mathbf{x}_p^{n+1}} \sum_c \frac{\partial \mathbf{x}_p^{n+1}}{\partial \tilde{\mathbf{E}}_c^{n+\frac{1}{2}}} \frac{\partial \tilde{\mathbf{E}}_c^{n+\frac{1}{2}}}{\partial \tilde{\phi}_j{}^{n+1}} \right), \tag{17}$$

where $\sum_c$ denotes the summation over cells. The first partial derivative can be directly computed from the charge deposition equation:

$$\frac{\partial \tilde{\mathbf{E}}_c^{n+\frac{1}{2}}}{\partial \tilde{\phi}_j{}^{n+1}} = \frac{1}{2} \frac{\partial \tilde{\mathbf{E}}_c^{n+\frac{1}{2}}}{\partial \tilde{\phi}_j{}^{n+\frac{1}{2}}} = \frac{1}{2} \frac{\partial \left(-\nabla \sum_g \tilde{\phi}_g^{n+\frac{1}{2}} \Psi_g(\mathbf{x}_c) \right)}{\partial \tilde{\phi}_j^{n+\frac{1}{2}}} = -\frac{1}{2} \nabla \Psi_j(\mathbf{x}_c), \tag{18}$$

where $\mathbf{x}_c$ is an arbitrary position (since $\mathbf{E}$ is uniform in cells) inside cell c. The last partial derivative can be computed from the electric field equation:

$$\frac{\partial \rho_i^{n+1}}{\partial \mathbf{x}_p^{n+1}} = F_p q_p \nabla \Psi_i(\mathbf{x}_p^{n+1}). \tag{19}$$

The remaining partial derivative in the center is more troublesome to compute. It expresses the effect on the final particle position of the change in electric field in any of the cells it previously visited. It represents an extension of the concept of mass matrix introduced in [5] in the case of particles that traverse more than one cell during a time step. Clearly, this term is zero in case the particle is deleted or deposited at the domain's boundary. Otherwise, it can be computed by examining the equations of the particle mover. Figure 2 can help to visualize the concept

employed to construct this term. It shows how the trajectory, and therefore the final position of the particle, is influenced by a change in the field (in cell 3 in this case). Taking the total differentials of equations (10) and (12), we obtain:

$$d\mathbf{v}_p^{\nu+1} = d\mathbf{v}_p^{\nu} + \frac{q_p}{m_p}\tilde{\mathbf{E}}^{\nu} d(\Delta t_p^{\nu}) + \frac{q_p}{m_p}\Delta t_p^{\nu} d\tilde{\mathbf{E}}^{\nu} \tag{20}$$

for the position, and:

$$\begin{aligned} d\mathbf{x}_p^{\nu+1} = d\mathbf{x}_p^{\nu} + \Delta t_p^{\nu} d\mathbf{v}_p^{\nu} + \frac{1}{2}\frac{q_p}{m_p}(\Delta t_p^{\nu})^2 d\tilde{\mathbf{E}}^{\nu} \\ + \left(\mathbf{v}_p^{\nu} + \frac{q_p}{m_p}\tilde{\mathbf{E}}^{\nu}\Delta t_p^{\nu}\right) d(\Delta t_p^{\nu}) \end{aligned} \tag{21}$$

for the velocity. Both quantities have to be accumulated during particle motion.

The term $d(\Delta t_p^{\nu})$ is a function of $d\tilde{\mathbf{E}}^{\nu}$, and of the way a particle's trajectory terminates in sub-step ν. If this trajectory ends inside a cell, $d(\Delta t_p^{\nu}) = -\sum_{\nu'=0}^{\nu} d(\Delta t_p^{\nu'})$, since the total duration of the time step is fixed at Δt. If, instead, it ends at a cell's boundary, we must compute it from the equation for the intersection of the particle's trajectory with the cell face, Eq. (13), or equivalently by imposing $d\mathbf{x}_p^{\nu+1} \cdot \mathbf{n} = 0$, meaning that the intersection point can only move along the cell face. This gives:

$$d(\Delta t_p^{\nu}) = -\frac{(\Delta t_p^{\nu})^2 d\alpha + \Delta t_p^{\nu} d\beta + d\gamma}{2\alpha\Delta t_p^{\nu} + \beta} \tag{22}$$

where:

$$d\alpha = \frac{1}{2}\frac{q_p}{m_p}\mathbf{n}\cdot d\tilde{\mathbf{E}}^{\nu};\; d\beta = \mathbf{n}\cdot d\mathbf{v}_p^{\nu};\; d\gamma = \mathbf{n}\cdot d\mathbf{x}_p^{\nu}. \tag{23}$$

Equations (20–22) allow us to compute the full, exact Jacobian. The implementation into the code is described in greater detail in Section 2.5.

2.3. A simplified version of the full Jacobian

The computation of the full Jacobian as described in the previous section is cumbersome and its implementation may be prone to mistakes. We suggest the alternative of neglecting the $d(\Delta t_p^{\nu})$ term in equations (20, 21). This significantly simplifies the implementation. Moreover, we noticed that the approximation is good enough that it can be used directly in a Newton method in cases where particles do not traverse more than about 5 cells in a time step. However, the amount of operations to be performed per particle is still very demanding.

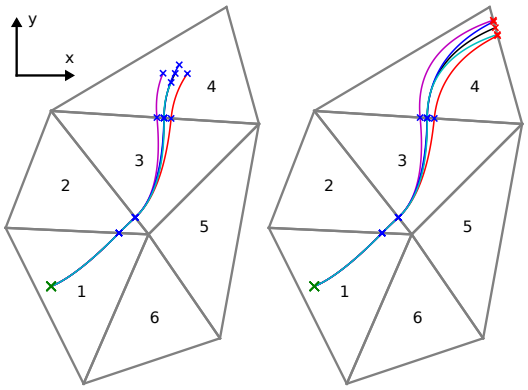

(a) Free trajectory. (b) Bound trajectory.

Figure 2: Example of how particle trajectories are affected by a change in electric field. in these cases, the electric field in cell 3 is varied in the x component (red and magenta curves) and y component (blue and cyan curves). In figure (a), the trajectory terminates inside a cell, while in (b) it terminates at the boundary of the domain. The figures have been generated with a simplified Python code. The same code has also been used to partially verify the procedure for the analytical computation of the Jacobian.

2.4. An even simpler alternative: mass matrix-like implementation

If we suppose that the particle does not leave the cell c where it's located at time n, we only have to take into account the cell where the particle is currently located. The Jacobian becomes:

$$\frac{\partial b_i^{n+1}}{\partial \tilde{\phi}_j^{n+1}} = \sum_p \left(\frac{1}{\varepsilon_0}\frac{\partial \rho_i^{n+1}}{\partial \mathbf{x}_p^{n+1}} \frac{\partial \mathbf{x}_p^{n+1}}{\partial \tilde{\mathbf{E}}_c^{n+\frac{1}{2}}} \frac{\partial \tilde{\mathbf{E}}_c^{n+\frac{1}{2}}}{\partial \tilde{\phi}_j^{n+1}} \right). \tag{24}$$

Since, additionally, all the acceleration of the particle occurs in cell c, Equation (12) is modified into:

$$\mathbf{x}_p^{n+1} = \mathbf{x}_p^n + \mathbf{v}_p^n \Delta t^n + \frac{1}{2}\frac{q_p}{m_p}\mathbf{E}_c^{n+\frac{1}{2}} (\Delta t^n)^2 , \tag{25}$$

so the central term simplifies into:

$$\frac{\partial \mathbf{x}_p^{n+1}}{\partial \tilde{\mathbf{E}}_c^{n+\frac{1}{2}}} = \frac{q_p (\Delta t^n)^2}{2 m_p}. \tag{26}$$

Substituting:

$$\begin{aligned} \frac{\partial b_i^{n+1}}{\partial \tilde{\phi}_j^{n+1}} &= \sum_p \left(-\frac{F_p q_p^2 (\Delta t^n)^2}{4\varepsilon_0 m_p} \nabla\Psi_i(\mathbf{x}_p^n) \cdot \nabla\Psi_j(\mathbf{x}_p^n) \right) \\ &= -\sum_c K_c^{ij} \frac{(\Delta t^n)^2}{4\varepsilon_0 V_c} \sum_{p\in c} \left(\frac{F_p q_p^2}{m_p} \right) = -\sum_c K_c^{ij} M_c. \end{aligned} \tag{27}$$

This expression resembles the mass factor of the semi-implicit method [5, 15]. Then, the Jacobian can simply be written as:

$$\frac{\partial f_i}{\partial \tilde{\phi}_j^{n+1}} = -\sum_c K_c^{ij}(M_c + 1). \tag{28}$$

This represents a computationally much cheaper alternative, since only a particle to grid deposition is required. However, it does not account for the effect of particles visiting multiple cells during a time step. We compare the convergence behavior using these three Jacobians in Section 3.2.

2.5. Details of the implementation

In this section, we illustrate how the Jacobian is accumulated, and how the `PETSc SNES` nonlinear solver suite [16] is integrated with the code. While the terms of Equations (18, 19) are obtained from the finite element basis, the susceptibility of the final position of particles to the electric field must be computed during particle motion. We do this by accumulating quantities $\sum_p q_p \partial \mathbf{x}_p^{n+1} / \partial \tilde{\mathbf{E}}_k^{n+\frac{1}{2}}$ over all particles. Notice that these can be stored as 1, 4, or 9 arrays in 1D, 2D, and 3D respectively. They can then be accumulated into sparse matrices using the `MatSetValues` function of `PETSc`, and finally multiplied by the other partial derivatives to yield the Jacobian matrix.

The implementation has been verified by comparing the computation of the full Jacobian with the finite difference Jacobian computed by `PETSc` in a simple test case. This is done by simply adding the `-snes_test_jacobian_view` flag when running the code, as described in the user manual [16].

3. Results

3.1. Comparison of the explicit, semi-implicit, and fully-implicit schemes

We test the properties of the proposed numerical scheme, by comparing it against the traditional explicit scheme and an electrostatic version of the semi-implicit scheme as initially formulated in [5] and adapted in [15]. The simulation domain is initialized with a uniform and quasineutral hydrogen-electron plasma (ion-to-electron mass ratio $m_i/m_e = 1837.7$) at a density $n_e = n_i = 5 \times 10^{11}$ m^{-3}, electron temperature $T_e = 11600$ K and ion temperature $T_i = 300$ K. Three different domain discretizations are considered, as shown in Figure 3. The first mesh (a) is uniformly fine, with cells of size $\Delta x = 10^{-2}$ m, which respect everywhere the constraint of the explicit scheme, $\Delta x < \lambda_{De}$. The second mesh (b) is uniformly coarse, with cells of dimension $\Delta x = 10^{-1}$ m. Finally, the third mesh (c) is statically adapted such that it resolves the expected macroscopic gradients in fluid and fields quantities at the boundary of the domain, namely the plasma sheath, as illustrated in Figure 1. Notice that we adopted an anisotropic adaptation, which greatly reduces the number of cells required. Regarding the time step, we consider a fine time step $\Delta t = 10^{-8}$ s that satisfies the constraint of the explicit scheme: $\Delta t < \omega_{pe}^{-1}$, and a coarser time step $\Delta t = 10^{-7}$ s that still captures the dynamics of the problem under consideration. Dirichlet boundary conditions for ϕ are applied to the boundary of the domain.

We plot in Figure 4 the number of electrons and ions in the domain as the simulation progresses. The simulations using the explicit scheme and the coarse time step are found to be unstable and the corresponding curves are not shown. Initially, all curves show the same behavior, as no electric field is yet established, and boundary fluxes are dictated by the thermal motion of the particles. As the simulation progresses, the depletion of electrons gives rise to a plasma sheath at the edge of the domain. The characteristic size of this plasma sheath is λ_{De}, as widely demonstrated in literature [17]. The resulting electric field accelerates the ions towards the boundary, and decreases the flux of electrons. As can be seen from the figure, the fluxes of ions and electrons tend to equalize in the reference simulation, performed with the explicit scheme and fine parameters. It is clear from the plot that the simulations performed with the coarse grid are not accurate in every case considered. This is expected, since macroscopic spatial gradients cannot be captured by the grid. However, it can be noted that the fully-implicit algorithm with a coarse time step (FI C C) gives the same (incorrect) result as the explicit algorithm with a coarse grid and fine time step (EX C F). This suggests that: (i) the fully-implicit conserves charge accurately, and (ii) the explicit algorithm is quite robust in these conditions against instabilities caused by low grid resolution. Adapting the grid allows the semi-implicit and explicit scheme to retrieve the reference result (EX F F), but only with a fine time step. Only the fully-implicit scheme in fact allows to capture the reference simulation accurately with a coarse time step (FI A C). In the same conditions the semi-implicit scheme, although stable, is inaccurate, presumably because of the lack of charge conservation. To summarize, these results show that in order to have an accurate solution, macroscopic gradients must be resolved by the grid, and the nu-

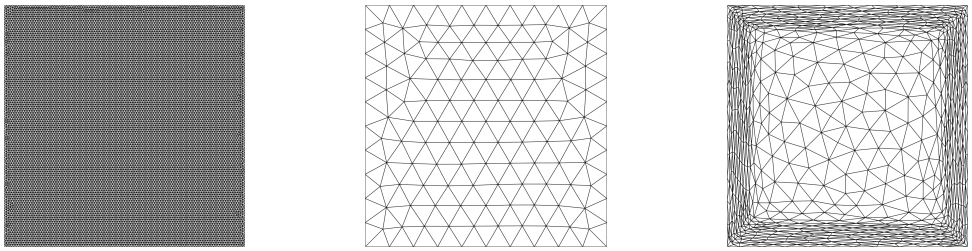

(a) fine grid (b) coarse grid (c) adapted grid

Figure 3: The three grids used for the simulation of the depletion of plasma from a box. Grids (a) and (b) are constituted of uniform triangular elements. Grid (c) is anisotropic. It was generated from a metric field based on the distance from the boundary using the `BAMG` algorithm available in `gmsh`.

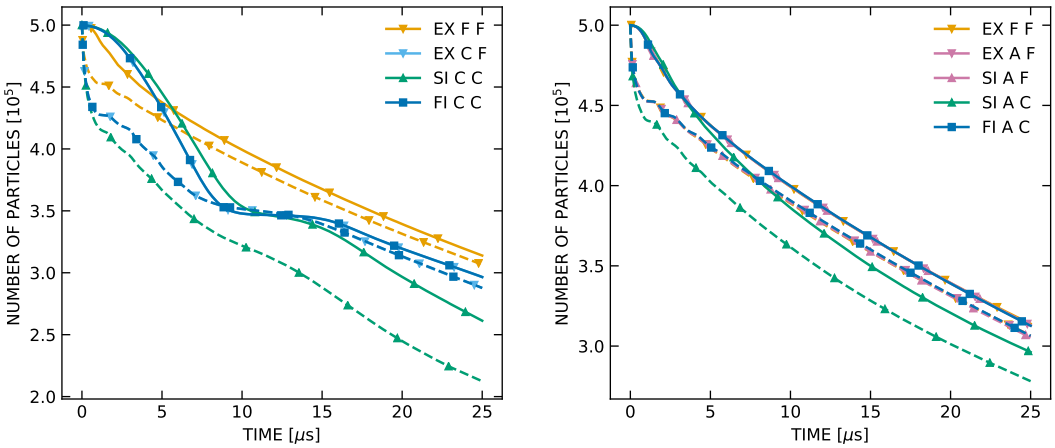

Figure 4: Number of electrons (dashed lines) and ions (solid lines) in the simulation domain as a function of time for the various combinations of algorithms. The label expresses in order the type of scheme (EX = explicit, SI = semi-implicit, FI = fully-implicit), cell size (F = fine, C = coarse, A = adapted), and time step size considered (F = fine, C = coarse). When the coarse grid is used, none of the schemes returns the correct solution (considering EX F F as reference), because the gradients in the sheath are not well captured by the grid. When using the adapted grid and a coarse time step, only the fully-implicit scheme (FI A C) is accurate, because of the charge conservation property.

merical scheme must be stable and conserve charge accurately over each time step.

3.2. Comparison of the three versions of the Jacobian

Finally, we analyze the performance of the three different variations of Jacobian introduced in this paper. The convergence history of the norm of the residual f_k over a few time steps is shown in Figure 5. Notice that with either Jacobian, the residual is reduced enough that the solutions are practically identical. In the figure and the following text we refer to the exact Jacobian as FI1, the version where the $d(\Delta t^\nu)$ terms are neglected as FI2, and the simplified, ECSIM-style Jacobian as FI3. Interestingly, we notice that over the first iteration, all Jacobians perform similarly, with the much simpler FI3 even showing a better reduction than FI2. Over the subsequent iterations, the FI3 Jacobian tends to stagnate, managing a reduction of two orders of magnitude of the residual in 10 iterations. This is probably due to the fact that while being a decent preconditioner, it is not sufficient to point the system towards the exact solution. Notice that this Jacobian remains constant through the iterations since it does not depend on the current solution iterate, which decreases due to the line search procedure. Version FI2 performs much better, managing

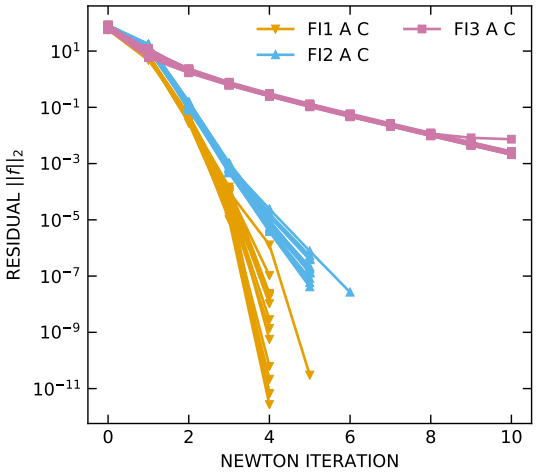

Figure 5: Convergence history for a few time steps of the test case of plasma depleting from a box, for the implicit scheme using the three variations of the Jacobian presented in this paper. Label FI1 refers to the use of the full, exact Jacobian. Label FI2 corresponds to the Jacobian where the $d(\Delta t^{\nu})$ terms are neglected, and label FI3 refers to the simplified, ECSIM-style Jacobian.

a reduction of 8 orders of magnitude in 5 iterations. It too, however, shows an inflection point around the third iteration. This is probably the sign that it becomes less accurate as we get closer to the exact solution. The exact Jacobian shows as expected an excellent performance in this case, with a convergence rate that improves as we get closer to the exact solution. Unfortunately, at the moment the computational cost for this Jacobian is high, and does not justify the fast convergence that can be achieved. This is due to the large number of algebraic operations that must be performed for each individual particle. Clearly, algorithms that consider all particles together (through the moments of their velocities) require first the computation of these moments, which is efficient and easily parallelizable. Then, the remaining operations happen on the far fewer degrees of freedom of the computational grid, as in a fluid-based solver.

4. Conclusion and Future Work

We presented a fully-implicit scheme for the electrostatic, finite element discretization of the Particle-in-Cell method. We have shown through a simple test case of plasma depletion from a box that the simulations using this scheme are stable and that the results are accurate even if the electron time and length scales are locally under-resolved. We also presented three different versions of the Jacobian necessary to achieve nonlinear convergence within a Newton-Krylov method, and compared their performance. We derived the exact Jacobian of the system, starting from the equations of the particle mover, and verified it with finite differences. We showed that this exact Jacobian performs well, especially sufficiently close to the converged solution. Although its computational cost is not competitive at the moment, it is useful to provide a reference against which to compare other simpler and more efficient versions in real application test cases. Jacobians and related physics-based preconditioners have been formulated in literature starting from moment approximations to the field-particle system. We plan to evaluate and benchmark these against our kinetic-based reference. Future work will aim at exploring the best trade-off between the rate of convergence and computational cost of different Jacobians for the implicit formulation presented (or preconditioners in the case of JFNK). We will also consider the extension of the scheme to deal with magnetized electrons in presence of a background magnetic field.

5. Acknowledgements

The research of PP is funded by an FWO Strategic Basic PhD fellowship (reference 1S24022N).

References

[1] G. A. Bird, Approach to Translational Equilibrium in a Rigid Sphere Gas, The Physics of Fluids 6 (10) (1963) 1518–1519.
[2] G. A. Bird, Molecular Gas Dynamics and the Direct Simulation of Gas Flows, Clarendon Press, 1994.
[3] R. W. Hockney, J. W. Eastwood, Computer Simulation Using Particles, CRC Press, 1988.
[4] G. Chen, L. Chacón, D. Barnes, An energy- and charge-conserving, implicit, electrostatic particle-in-cell algorithm, Journal of Computational Physics 230 (18) (2011) 7018–7036. doi:10.1016/j.jcp.2011.05.031.
[5] G. Lapenta, Exactly energy conserving semi-implicit particle in cell formulation, Journal of Computational Physics 334 (2017) 349–366. doi:10.1016/j.jcp.2017.01.002.
[6] G. Chen, et al., A semi-implicit, energy- and charge-conserving particle-in-cell algorithm for the relativistic Vlasov-Maxwell equations, Journal of Computational Physics 407 (2020) 109228. doi:10.1016/j.jcp.2020.109228.
[7] D. Eremin, An energy- and charge-conserving electrostatic implicit particle-in-cell algorithm for simulations of collisional bounded plasmas, Journal of Computational Physics 452 (2022) 110934. doi:10.1016/j.jcp.2021.110934.

[8] G. Chen, L. Chacón, An implicit, conservative and asymptotic-preserving electrostatic particle-in-cell algorithm for arbitrarily magnetized plasmas in uniform magnetic fields, SSRN Electronic Journaldoi:10.48550/arxiv.2205.09187.
[9] R. Hockney, J. Eastwood, Computer Simulation Using Particles, 1st Edition, CRC Press, 1988.
[10] D. Barnes, L. Chacón, Finite spatial-grid effects in energy-conserving particle-in-cell algorithms, Computer Physics Communications 258 (2021) 107560. doi:10.1016/j.cpc.2020.107560.
[11] Y. Chen, G. Tóth, Gauss's Law satisfying Energy-Conserving Semi-Implicit Particle-in-Cell method, Journal of Computational Physics 386 (2019) 632–652. doi:https://doi.org/10.1016/j.jcp.2019.02.032.
[12] M. Campos Pinto, V. Pagès, A semi-implicit electromagnetic FEM-PIC scheme with exact energy and charge conservation, Journal of Computational Physics 453 (2022) 110912. doi:https://doi.org/10.1016/j.jcp.2021.110912.
[13] P. Parodi, Development of a hybrid PIC–DSMC solver for particle flow generators, Tech. rep., von Karman Institute for Fluid Dynamics (2020).
[14] D. Knoll, D. Keyes, Jacobian-free newton–krylov methods: a survey of approaches and applications, Journal of Computational Physics 193 (2) (2004) 357–397. doi:https://doi.org/10.1016/j.jcp.2003.08.010.
[15] P. Parodi, G. Lapenta, T. Magin, Simulation of plasmas for electric propulsion using the energy-conserving semi-implicit PIC scheme, in: 9th European Conference for Aeronautics and Space Sciences (EUCASS), Lille, France, 2022. doi:http://dx.doi.org/10.13009/eucass2022-7331.
[16] S. Balay, et al., PETSc/TAO users manual, Tech. Rep. ANL-21/39 - Revision 3.18, Argonne National Laboratory (2022).
[17] F. Chen, Introduction to Plasma Physics and Controlled Fusion, 3rd Edition, Springer, 2016.

Moment method for electric propulsion modelling

Anatole Berger

Laboratoire de Physique des Plasmas, Ecole Polytechnique, France, anatole.berger@lpp.polytechnique.fr

Supervisor: Thierry Magin

Professor, Aeronautics and Aerospace Department, von Karman Institute for Fluid Dynamics, Belgium, thierry.magin@vki.ac.be

University Supervisor: Alejandro Alvarez Laguna

Chargé de recherche, Laboratoire de Physique des Plasmas, Ecole Polytechnique, France, alejandro.alvarez-laguna@lpp.polytechnique.fr

University Supervisor: Anne Bourdon

Directrice de recherche, Laboratoire de Physique des Plasmas, Ecole Polytechnique, France, anne.bourdon@lpp.polytechnique.fr

Abstract

Hall thrusters are a type of electric propulsion device used on several satellites due to their low propellant consumption. However, some phenomena such as instabilities that develops in certain conditions are still poorly understood.

Current simulations are based on mainly 2 modeling: The most precise is the Particle-In-Cells (or PIC) solver, that solves the Boltzmann kinetic equation in a stochastic manner, however, this method is highly expansive and can therfore not be applied to geometry as complex as a Hall truster. The other method is the multi-fluid simulation which solves the fluid equations for each species, coupled with the Poisson's equation. This model is however less precise and doesn't catch some important kinetic effects. The simplicity of the fluid model comes from the fact that considering only 5 moments of the Boltzmann equation (density, 3-dimensional velocity and temperature) is equivalent to assuming that the Velocity Distribution Functions (VDF) of the particles are Maxwellian, which is usually not the case in low-density plasmas (especially for the electrons). A way to keep the low computational cost of the fluid model (compared to PIC) but still have a more precise description of the physics, namely being able to represent non-Maxwellian distributions, is to consider higher-order moments. However, systems of moments equations are not closed and require a closure to be solved (which are the Navier-Stokes and Fourier laws in classical fluid dynamics). Common methods to do so are the Grad's method that consider VDFs of the form of a Maxwellian perturbed by a sum of Hermit polynomials; and the maximum entropy method that consider a VDF as an exponential of a polynomial in the velocity, and that set the coefficients by maximizing the entropy with some constraints on the moments.

The goal of this PhD is therefore to develop a model of low-density plasma based on a moment method inspired by the two previously cited methods, that would be more precise than classical fluid models while still faster than PIC simulations, and apply this method to the modeling of an electric thrusters.

Characterization and testing methodology of woven materials with application to innovative flexible thermal protection systems for re-entry vehicles

Simone Del Monte

Aeronautics and Aerospace Department, von Karman Institute for Fluid Dynamics, Belgium, simone.del.monte@vki.ac.be

Supervisor: Olivier Chazot

Professor, Aeronautics and Aerospace Department, von Karman Institute for Fluid Dynamics, Belgium, olivier.chazot@vki.ac.be

University Supervisor: Aurelie Bellemans

Assistant Professor, FLOW research group Department of Mechanical Engineering, Vrije Universiteit Brussel (VUB), Belgium, aurelie.bellemans@vub.be

University Co-Supervisor: Lincy Pyl

Associate Professor, Mechanics of Materials and Constructions (MeMC) department, Vrije Universiteit Brussel (VUB), Belgium, lincy.pyl@vub.be

Abstract

The re-entry phase of a space mission is the most critical due to the severe thermal environment of the hypersonic regime to which the spacecraft is subjected and which needs a thermal protection system to ensure its structural integrity. Due to continuous space mission demands and challenging future missions (sample return, human space exploration, etc.), development of innovative solutions made with promising materials is needed. Flexible thermal protection systems with (woven) carbon materials are excellent candidates offering novel opportunities. They can be tailored to specific mission scenarios and designed to fulfill optimized performance to withstand extreme heat conditions in a sustainable and cost-effective way. For example, the reduction of the ballistic coefficient, and thus, of the surface heat fluxes could be achieved. The main objective of this research project is to characterize this kind of materials both from a thermal and mechanical point of view in a reproduced re-entry environment. The ultimate goal is the advancement of their knowledge and the increase of their technology readiness level, with the long-term prospective to implement them in future space missions, such as the ones which regard re-usable spacecrafts, leading to economical return.

Keywords: woven carbon/carbon materials, flexible thermal protection systems, characterization of ablative materials

AERODYNAMICS AND AERONAUTICS

Conservative solution transfer between anisotropic meshes for High-Order Methods

Tomáš Levý

Department of Mechanics, Faculty of Applied Sciences, University of West Bohemia, Czech Republic
Aeronautics and Aerospace Department, von Karman Institute for Fluid Dynamics, Belgium
tomas.levy@vki.ac.be

Supervisor: Georg May

Associate Professor, Aeronautics and Aerospace Department, von Karman Institute for Fluid Dynamics, Belgium
georg.may@vki.ac.be

University Supervisor: Jan Vimmr

Associate Professor, Department of Mechanics, Faculty of Applied Sciences, University of West Bohemia, Czech Republic
jvimmr@kme.zcu.cz

Abstract

We present a solution transfer approach between anisotropically adapted meshes, which preserves conservativity and order of accuracy of a particular high-order method for time-dependent compressible flow problems. Here the discretization scheme of choice is a hybridized discontinuous Galerkin (HDG) method, although the presented approach can be used with any other high-order method where the numerical solution is represented by a linear combination of basis functions on each element of the computational mesh.

Keywords: anisotropic mesh adaptation, time-dependent balance laws, solution transfer, Galerkin projection, hybridized discontinuous Galerkin method

1. Introduction

The use of second-order methods, such as finite volume schemes, has become a standard for the simulation of compressible flows during the last couple of decades. These methods offer a trade-off between the resolution of the numerical solution and the stability of the solution process. The intrinsic artificial diffusivity of these methods greatly contributes to the stability. However, it can also exclude important features of the flow field from the numerical solution.

On the other hand, high-order methods offer superior resolution of the flow field at reduced number of degrees of freedom for a given problem, provided the solution is smooth enough [1]. Since high-speed compressible flow is often accompanied by the presence of shock waves, which in turn disrupts the local regularity of the solution, a finer local resolution is necessary for the high-order method to obtain a reasonably accurate numerical solution. Of course, this need comes with an increased computational cost. Besides the shocks, there could also be other highly anisotropic features of the flow such as boundary layers or wakes in the case of viscous flow simulation.

The ideal high-order method then should be adaptive in the sense that it takes advantage of the smooth flow regions where the resolution may not be as fine as in the regions where rapid changes in the solution are present. One such approach is the anisotropic mesh adaptation where the mesh elements align with the features of the flow based on the numerical solution at hand [2].

The problem at hand is probably even more significant for time-dependent simulations since the shock waves and other anisotropic components of the flow are likely to move over time. In order to fully benefit from the adaptation strategy, the mesh has to be adapted numerous times during the simulation. Such anisotropic mesh refinement generally leads to highly

skewed unstructured grids. Hence, attention must also be paid to the accuracy of the overall numerical method in order to retain the solution precision after each adaptation step.

An essential pitfall in the remeshing procedure for time-dependent problems is the necessity of interpolating the solution from the previous mesh to the adapted mesh that will be used in the subsequent time step. Inappropriate interpolation methods can disrupt conservation of physical quantities of interest, which can ultimately lead to a loss of accuracy. One example is the interpolation method of Grandy [3], which proceeds by mapping from the old mesh to the new one by calculating the volume of intersection of overlapping elements of previous and current meshes. The main drawback of this method is the assumption of constant interpolant across the old-mesh element, which results in a highly diffusive approach. Although some conservative interpolation operators coupled with time-dependent anisotropic mesh refinement can be found in the literature [4; 5; 6], these are usually designed for locally piecewise linear representation of the solution, and the interpolation operator then relies on the Hessian of the solution only [7].

In the present study, we extend the approach presented in [8], where an anisotropic mesh adaptation methodology is built on a Hybridized Discontinuous Galerkin (HDG) solver intended to solve boundary-value problems for steady balance laws. The work has also been extended to initial-boundary-value problems in [9] using static meshes. The resulting numerical solution on a particular mesh is then represented by a polynomial of degree at most p on each element. For this type of representation, the Galerkin projection, which is optimal in the L^2-norm, proved to be particularly well-suited for interpolation of fields between meshes [10]. We further adopt the technique of Farrell [11], who applied the Galerkin projection to fields resulting from simulation of incompressible flow [12]. Following this approach, one constructs a geometry, known as the supermesh, defined as the mesh of the intersection polygons of input meshes. On each element of the supermesh, the basis functions of both old and new meshes are, by construction, continuous polynomials, allowing high-accuracy evaluation of the projection integrals. Coupling of the time advancement with the mesh adaptation is done by successive generation of meshes after a specified number of time steps whereby the adaptation itself is based on the numerical solution resulting from the previous time step.

The paper is organized as follows: In Section 2, we briefly review the type of balance laws under consideration. Next, in Section 3 and 4, we discuss the discretization and mesh adaptation methods used in our solver, while Section 5 is dealing with the solution interpolation between meshes. Finally, in Section 6, we present some preliminary results based on test cases for scalar convection-diffusion equation and the system of Euler equations showing the conservative and accurate nature of the presented methodology.

2. Governing Equations

In this study, we focus on the solution of time-dependent general (possibly nonlinear) convection-diffusion-reaction systems of equations of the form

$$\partial_t \boldsymbol{w} + \nabla \cdot (\boldsymbol{f}_c(\boldsymbol{w}) - \boldsymbol{f}_v(\boldsymbol{w}, \nabla \boldsymbol{w})) = \boldsymbol{s}(\boldsymbol{w}, \nabla \boldsymbol{w}) \quad (1)$$

with appropriate initial and boundary conditions defined on $\partial\Omega$, the boundary of an open bounded domain $\Omega \in \mathbb{R}^d$, $d = 2$. Here, $\boldsymbol{w} \in \mathbb{R}^m$ is the vector of conservative variables, $\boldsymbol{f}_c : \mathbb{R}^m \to \mathbb{R}^{m\times d}$ is the convective flux, $\boldsymbol{f}_v : \mathbb{R}^m \times \mathbb{R}^{m\times d} \to \mathbb{R}^{m\times d}$ is the diffusive flux, and $\boldsymbol{s} : \mathbb{R}^m \times \mathbb{R}^{m\times d} \to \mathbb{R}^m$ is the source term, m being the number of conservative variables.

Besides the scalar convection-diffusion equation, this formulation of the balance law also covers the Euler equations with $m = 4$ and

$$\boldsymbol{w} = \begin{pmatrix} \rho \\ \rho\boldsymbol{u} \\ E \end{pmatrix}, \ \boldsymbol{f}_c = \begin{pmatrix} \rho\boldsymbol{u}^T \\ \rho\boldsymbol{u} \otimes \boldsymbol{u} + P\boldsymbol{I}_d \\ (E+P)\boldsymbol{u}^T \end{pmatrix}, \ \boldsymbol{f}_v = \boldsymbol{0}, \ \boldsymbol{s} = \boldsymbol{0} \quad (2)$$

where ρ is the density, $\boldsymbol{u} = (u, v)^T$ is the fluid velocity vector, E is the total energy, and $\boldsymbol{I}_d$ is $d \times d$ identity matrix. Pressure P is related to the conservative variables by the equation of state of an ideal gas in the form

$$P = (\gamma - 1)\left(E - \frac{1}{2}\rho|\boldsymbol{u}|_2^2\right), \quad (3)$$

where γ is the ratio of specific heats and $\gamma = 1.4$ for air.

In case of the presence of shocks in the flow field, the artificial viscosity approach is followed where the diffusive flux is taken to be $\boldsymbol{f}_v = \varepsilon_{\text{AV}}\nabla\boldsymbol{w}$. Here we assume the artificial viscosity coefficient ε_{AV} obtained by the shock-capturing method of Hartmann [13].

3. Discretization

First, let us begin with some notation that will be used throughout the text. Let the computational

domain Ω be partitioned into a collection $\mathcal{T}_h$ of nonoverlapping elements such that $\Omega = \bigcup_{\kappa\in\mathcal{T}_h} \kappa$ with $\partial\mathcal{T}_h := \{\partial\kappa\backslash\partial\Omega : \kappa \in \mathcal{T}_h\}$ being the set of all edges of the elements, excluding the boundary. We denote the set of all interior edges of $\mathcal{T}_h$ by $\mathcal{E}_h$, and $\mathcal{E}_h^\partial$ contains all boundary edges.

The balance law (1) can be rewritten as a first-order system by introducing an auxiliary variable $\boldsymbol{q}$, which represents the gradient of the solution,

$$\boldsymbol{q} - \nabla\boldsymbol{w} = \boldsymbol{0}, \tag{4}$$

$$\partial_t\boldsymbol{w} + \nabla\cdot(\boldsymbol{f}_c(\boldsymbol{w}) - \boldsymbol{f}_v(\boldsymbol{w},\boldsymbol{q})) = \boldsymbol{s}(\boldsymbol{w},\boldsymbol{q}). \tag{5}$$

In order to obtain a hybridized weak formulation, another additional unknown $\boldsymbol{\lambda}$ is introduced on the element edges. The system of equations is then closed by weakly enforcing continuity of the normal component of convective and diffusive numerical fluxes at the edges. Compared to standard discontinuous Galerkin (DG) methods, this procedure ultimately leads to reduction of the globally coupled degrees of freedom since the method then allows to eliminate the primary variables by a static condensation process and to formulate the global problem in terms of the new variable $\boldsymbol{\lambda}$ only.

Before the weak formulation will be introduced, let us define the discontinuous function spaces in which the solution will be sought. Let $\mathcal{P}^p(D)$ denote a set of polynomials of total degree at most p on some domain D. For a given computational mesh, we consider the following approximation spaces

$$\Sigma_h := \{\boldsymbol{\tau}\in[L^2(\Omega)]^{m\times d} : \boldsymbol{\tau}|_\kappa \in [\mathcal{P}^p(\kappa)]^{m\times d}, \forall\kappa\in\mathcal{T}_h\}, \tag{6}$$

$$V_h := \{\boldsymbol{v}\in[L^2(\Omega)]^{m} \quad : \boldsymbol{v}|_\kappa \in [\mathcal{P}^p(\kappa)]^{m}, \quad \forall\kappa\in\mathcal{T}_h\}, \tag{7}$$

$$\Lambda_h := \{\boldsymbol{\mu}\in[L^2(\mathcal{E}_h)]^{m} \quad : \boldsymbol{\mu}|_e \in [\mathcal{P}^p(e)]^{m}, \quad \forall e\in\mathcal{E}_h\}. \tag{8}$$

Functions $\boldsymbol{\tau} \in \Sigma_h$, $\boldsymbol{v} \in V_h$, and $\boldsymbol{\mu} \in \Lambda_h$ are then piecewise polynomials of degree p, which can be discontinuous across element faces and vertices, respectively.

Now, the task is to find an approximation $\mathbb{x}_h := (\boldsymbol{q}_h, \boldsymbol{w}_h, \boldsymbol{\lambda}_h) \in \mathbb{X}_h := \Sigma_h \times V_h \times \Lambda_h$ such that

$$\begin{aligned}
0 &= \widehat{\mathcal{N}}(\mathbb{x}_h;\mathbb{y}_h)\\
&:= (\boldsymbol{q}_h,\boldsymbol{\tau}_h)_{\mathcal{T}_h} + (\boldsymbol{w}_h,\nabla\cdot\boldsymbol{\tau}_h)_{\mathcal{T}_h} - \langle\boldsymbol{\lambda}_h,\boldsymbol{\tau}_h\cdot\boldsymbol{n}\rangle_{\partial\mathcal{T}_h}\\
&+ \left(\frac{\partial\boldsymbol{w}_h}{\partial t},\boldsymbol{v}_h\right)_{\mathcal{T}_h} - (\boldsymbol{f}_c(\boldsymbol{w}_h) - \boldsymbol{f}_v(\boldsymbol{w}_h,\boldsymbol{q}_h),\nabla\boldsymbol{v}_h)_{\mathcal{T}_h}\\
&- (\boldsymbol{s}(\boldsymbol{w}_h,\boldsymbol{q}_h),\boldsymbol{v}_h)_{\mathcal{T}_h} + \left\langle\left(\widehat{\boldsymbol{f}_c} - \widehat{\boldsymbol{f}_v}\right)\cdot\boldsymbol{n},\boldsymbol{v}_h\right\rangle_{\partial\mathcal{T}_h}\\
&+ \left\langle\left[\!\left[\widehat{\boldsymbol{f}_c} - \widehat{\boldsymbol{f}_v}\right]\!\right],\boldsymbol{\mu}_h\right\rangle_{\mathcal{E}_h} + \mathcal{N}_{h,\partial\Omega}(\boldsymbol{q}_h,\boldsymbol{w}_h;\boldsymbol{\tau}_h,\boldsymbol{v}_h)
\end{aligned} \tag{9}$$

holds for all $\mathbb{y}_h := (\boldsymbol{\tau}_h,\boldsymbol{v}_h,\boldsymbol{\mu}_h) \in \mathbb{X}_h$. Here we have used the abbreviation $(\cdot,\cdot)$ and $\langle\cdot,\cdot\rangle$ to distinguish between element- and edge-oriented inner products, and the jump operator for the vector valued function is defined as $[\![\boldsymbol{v}]\!] := \boldsymbol{v}^+\cdot\boldsymbol{n} + \boldsymbol{v}^-\cdot\boldsymbol{n}^-$, where the signs $\pm$ correspond to elements κ^+ and κ^- separated by edge e. Here, the analytical flux functions are replaced by the numerical fluxes. Our choice of the convective and diffusive numerical fluxes, which we will use, corresponds to Lax-Friedrichs flux and LDG flux, respectively, i.e.,

$$\widehat{\boldsymbol{f}_c}(\boldsymbol{\lambda}_h,\boldsymbol{w}_h) = \boldsymbol{f}_c(\boldsymbol{\lambda}_h)\cdot\boldsymbol{n} - \alpha_c\,(\boldsymbol{\lambda_h} - \boldsymbol{w}_h)\,, \tag{10}$$

$$\widehat{\boldsymbol{f}_v}(\boldsymbol{\lambda}_h,\boldsymbol{w}_h,\boldsymbol{q}_h) = \boldsymbol{f}_v(\boldsymbol{\lambda}_h,\boldsymbol{q}_h)\cdot\boldsymbol{n} + \alpha_v\,(\boldsymbol{\lambda_h} - \boldsymbol{w}_h)\,, \tag{11}$$

where we assume α_c and α_v to be constant scalar values.

The boundary conditions are incorporated into the scheme by evaluating the exact flux functions with a suitably chosen vector of conservative variables at the domain boundary, $\boldsymbol{w}_{h,\partial\Omega} \equiv \boldsymbol{w}_{h,\partial\Omega}(\boldsymbol{w}_h)$, and its gradient $\boldsymbol{q}_{h,\partial\Omega} \equiv \boldsymbol{q}_{h,\partial\Omega}(\boldsymbol{q}_h)$, depending on a particular type of the boundary condition,

$$\begin{aligned}
\mathcal{N}_{h,\partial\Omega} &\equiv \mathcal{N}_{h,\partial\Omega}(\boldsymbol{q}_h,\boldsymbol{w}_h;\boldsymbol{\tau}_h,\boldsymbol{v}_h)\\
&= \langle\boldsymbol{w}_{h,\partial\Omega},\boldsymbol{\tau}_h\cdot\boldsymbol{n}\rangle_{\mathcal{E}_h^\partial}\\
&+ \langle(\boldsymbol{f}_c(\boldsymbol{w}_{h,\partial\Omega}) - \boldsymbol{f}_v(\boldsymbol{w}_{h,\partial\Omega},\boldsymbol{q}_{h,\partial\Omega}))\cdot\boldsymbol{n},\boldsymbol{v}\rangle_{\mathcal{E}_h^\partial}\,.
\end{aligned} \tag{12}$$

The presence of an unsteady term in the semi-discretized scheme (9) gives rise to a system of differential-algebraic equations (DAEs) of index 1. Hence the classical approach using the method of lines with some explicit time integration scheme cannot be used, and one has to choose an appropriate implicit method for solving DAEs. If we split the discretization of the term with the time derivative and the remaining part, we can write the formulation as follows: Find $\mathbb{x}_h \in \mathbb{X}_h$ such that

$$\mathcal{T}(\partial_t\mathbb{x}_h;\mathbb{y}_h) + \mathcal{N}(\mathbb{x}_h;\mathbb{y}_h) = 0 \quad \forall\mathbb{y}_h\in\mathbb{X}_h, \tag{13}$$

where $\mathcal{T}(\partial_t\mathbb{x}_h;\mathbb{y}_h) = (\partial_t\boldsymbol{w}_h,\boldsymbol{v}_h)_{\mathcal{T}_h}$. In this work, we consider the Diagonally Implicit Runge-Kutta (DIRK) methods for the discretization of the time derivative. Applying a general s-stage DIRK method to formulation (13) results in

$$\begin{aligned}
&\frac{1}{a_{ii}\Delta t^n}\mathcal{T}(\mathbb{x}_h^{n,i};\mathbb{y}_h) + \mathcal{N}(\mathbb{x}_h^{n,i};\mathbb{y}_h) =\\
&\qquad = \frac{1}{a_{ii}\Delta t^n}\mathcal{T}(\mathbb{x}_h^{n};\mathbb{y}_h) - \sum_{j=1}^{i-1}\frac{a_{ij}}{a_{ii}}\mathcal{N}(\mathbb{x}_h^{n,j};\mathbb{y}_h),
\end{aligned} \tag{14}$$

which has to be solved to obtain the intermediate solutions $\mathbb{x}_h^{n,i}$ in each stage $i = 1, \ldots, s$. This step can also be seen as an implicit Euler method with modified right-hand side, and coefficients a_{ij}, $i, j = 1, \ldots, s$ are given by a particular DIRK method. The solution at the new time level t^{n+1} is then obtained by

$$\mathcal{T}(\mathbb{x}_h^{n+1}; \mathbb{y}_h) = \mathcal{T}(\mathbb{x}_h^{n}; \mathbb{y}_h) - \Delta t^n \sum_{i=1}^{s} b_i \mathcal{N}(\mathbb{x}_h^{n,i}; \mathbb{y}_h). \tag{15}$$

We consider three types of DIRK methods all being so-called stiffly accurate [14], meaning that the coefficients a_{ij} and b_i in (14) and (15), respectively, satisfy $a_{sj} = b_j$, $j = 1, \ldots, s$, and hence the numerical solution at the time step $n + 1$ is identical to the intermediate solution of the last stage, such that the final step (15) of the scheme is avoided. In particular, we use the two-stage second-order DIRK(2,2) method of Alexander [15], the three-stage third-order DIRK(3,3) of Cash [16], and the five-stage fourth-order DIRK(5,4) method of Hairer and Wanner [14]. The resulting system of nonlinear equations in each stage of a DIRK method (14) is solved by a damped Newton method.

4. Mesh Adaptation

We present a brief overview of metric-based mesh adaptation, of which particular elements are used in our anisotropic mesh adaptation algorithm. The fundamental concept is the mesh-metric duality and the continuous mesh model introduced by Loseille and Alauzet [17; 18]. Given a triangulation $\mathcal{T}_h = \{\kappa\}$ of the computational domain $\Omega \in \mathbb{R}^2$, each nondegenerate simplex element can be characterized by symmetric positive definite matrix

$$\boldsymbol{M} = \begin{pmatrix} a & b \\ b & c \end{pmatrix} \tag{16}$$

such that each of the edges $\boldsymbol{e}_i$, $i = 1, 2, 3$, of a triangular element has a constant length C under the norm induced by the metric

$$\|\boldsymbol{e}_i\|_{\boldsymbol{M}} = \sqrt{\boldsymbol{e}_i^T \boldsymbol{M} \boldsymbol{e}_i} = C, \quad i = 1, 2, 3. \tag{17}$$

Equation (17) now represents a system of linear equations for the elements a, b, and c of the matrix $\boldsymbol{M}$. The mesh element can be inscribed into an ellipse with its origin located at the element centroid, h_1 and h_2 being its principal axes and θ its orientation w.r.t. the Cartesian coordinate system. These quantities can be extracted from the spectral decomposition of the matrix, $\boldsymbol{M} = \boldsymbol{Q}^T \boldsymbol{\Lambda} \boldsymbol{Q}$, where

$$\boldsymbol{Q} = \begin{pmatrix} \cos\theta & -\sin\theta \\ \sin\theta & \cos\theta \end{pmatrix}, \quad \boldsymbol{\Lambda} = \begin{pmatrix} \frac{1}{h_1^2} & 0 \\ 0 & \frac{1}{h_2^2} \end{pmatrix}. \tag{18}$$

One can also define the aspect ratio $\beta := h_2/h_1$ and the local density $d := 1/(h_1 h_2)$, which is inversely related to the area of the element $|\kappa|$. The tuple (d, β, θ) now completely defines the metric $\boldsymbol{M}$ and hence the mesh element $\kappa \in \mathcal{T}_h$. Quantities β and θ can be denoted as the anisotropy of the triangle.

Our adaptation methodology is based on evaluation of the indicated metric for each element of the current mesh and generation of an optimized metric, which is obtained using the solution error estimate, corresponding to the desired mesh element.

The metric described above is discrete in the sense that it is defined for each element. Using a suitable interpolation, one may generate a continuous metric field $\mathcal{M}(\boldsymbol{x})$, $\boldsymbol{x} \in \Omega$, which can then be used in a metric-based mesh generator to produce the desired mesh. In the present work, we use the `BAMG` mesh generator of Hecht [19]. The length of the edge $\boldsymbol{e} = \boldsymbol{x}_2 - \boldsymbol{x}_1$ in the continuous setting is computed using a straight line parametrization,

$$\|\boldsymbol{e}\|_{\mathcal{M}} = \int_0^1 \sqrt{\boldsymbol{e}^T \mathcal{M}(\boldsymbol{x}_1 + s\boldsymbol{e})\boldsymbol{e}}\, \mathrm{d}s. \tag{19}$$

Edges of the resulting triangulation will then satisfy $\|\boldsymbol{e}\|_{\mathcal{M}} \approx C$ where C is the constant in Eq. (17). The generated mesh can be viewed as a discrete approximation of the continuous mesh, which is represented by the continuous metric field $\mathcal{M}(\boldsymbol{x})$.

The aim of the anisotropic mesh adaptation is therefore to optimize both the size and the anisotropy of the mesh elements in such a way that the resulting mesh will have improved approximation properties. In our case, the goal is to obtain triangles that give the smallest interpolation error into the piecewise polynomial approximation space (7) in the L^q-norm.

The optimal metric is obtained by a two-step optimization. First, a locally optimal anisotropy (β^*, θ^*) is obtained from a bound on the interpolation error, which is expressed by the local error model based on the work of Dolejší [20]. With fixed optimal anisotropy, the corresponding error estimate is valid for a family of ellipses where the local density d, hence the size of the triangle, is now a free parameter that can be chosen based on some appropriate optimization strategy. Having a continuous error model,

one may apply analytic optimization techniques to obtain the optimal size distribution given the number of mesh elements as a constraint.

The details of the outlined algorithm can be found in earlier work by Rangarajan et al. [8]. The optimization described above has also been extended to goal-oriented adaptation based on the solution of an adjoint problem, see [21; 22].

5. Mesh-to-Mesh Interpolation

We have seen in Section 3 that in order to solve Eq. (14) for the intermediate solutions in each stage of the DIRK method, a knowledge of the solution from the previous time step is needed. Hence, the use of anisotropic mesh refinement in unsteady simulations relies on the solution transfer between the previous and the current mesh. Furthermore, this interpolation step needs special care since we would like to avoid the disruption of the design order of convergence of the HDG method and/or particular DIRK scheme. Another important property whose absence can have fatal consequences for the evolution of numerical solution in time is the conservativity of the interpolation method.

The solution transfer algorithm used in this study is based on the work of Farrell [11; 12], where Galerkin projection is exploited for the purpose of interpolation between two meshes. The Galerkin projection represents the optimally accurate projection in the L^2-norm, and it is especially beneficial for the piecewise discontinuous fields arising in the DG discretizations, as the interpolation can be done locally on each element. Moreover, from the fact that the resulting field minimizes the interpolation error in the L^2-norm, conservation follows naturally.

Consider field w_{old}, which can also be a component of the vector of conservative variables appearing in the balance law (1), defined on mesh $\mathcal{T}_{h,\text{old}}$, resulting from the n-th time step of a simulation of an unsteady problem. After a mesh adaptation step, a new adapted triangulation $\mathcal{T}_{h,\text{new}}$ based on the solution w_{old} is obtained. Let each element κ of the mesh $\mathcal{T}_{h,\text{old}}$ have N^κ_{old} degrees of freedom corresponding to the basis functions $\varphi^{(i)}_{\text{old}}$, $i = 1, \dots, N^\kappa_{\text{old}}$. Similarly, for the case of the adapted mesh, let N^κ_{new} be the degrees of freedom of each element $\kappa \in \mathcal{T}_{h,\text{new}}$ with basis functions $\varphi^{(i)}_{\text{new}}$, $i = 1, \dots, N^\kappa_{\text{new}}$. Both fields, w_{old} and w_{new}, can then be represented on element κ by the linear expansions

$$w_{\text{old}} = \sum_{i=1}^{N^\kappa_{\text{old}}} W^{(i)}_{\text{old}} \varphi^{(i)}_{\text{old}}, \quad \kappa \in \mathcal{T}_{h,\text{old}}, \tag{20}$$

$$w_{\text{new}} = \sum_{i=1}^{N^\kappa_{\text{new}}} W^{(i)}_{\text{new}} \varphi^{(i)}_{\text{new}}, \quad \kappa \in \mathcal{T}_{h,\text{new}}. \tag{21}$$

The aim is to obtain an interpolant w_{new} on each element of $\mathcal{T}_{h,\text{new}}$, which is optimal in the L^2-norm, i.e.,

$$\|w_{\text{old}} - w_{\text{new}}\|_{L^2(\kappa)} = \min_{w \in V^\kappa_{\text{new}}} \|w_{\text{old}} - w\|_{L^2(\kappa)} \tag{22}$$

where $V^\kappa_{\text{new}} = \text{span}\{\varphi^{(i)}_{\text{new}}, i = 1, \dots, N^\kappa_{\text{new}}\}$. Ideally, we would like to obtain the interpolated solution w_{new} such that $\forall \boldsymbol{x} \in \Omega : w_{\text{old}}(\boldsymbol{x}) = w_{\text{new}}(\boldsymbol{x})$, in which case the left-hand side of (22) is zero. Naturally, this is not possible with $w_{\text{new}} \in V^\kappa_{\text{new}}$. Instead, the equality then can be satisfied in the weak sense by

$$\int_\kappa w_{\text{old}} \varphi^{(i)}_{\text{new}} \, \mathrm{d}\boldsymbol{x} = \int_\kappa w_{\text{new}} \varphi^{(i)}_{\text{new}} \, \mathrm{d}\boldsymbol{x}, \tag{23}$$

$i = 1, \dots, N^\kappa_{\text{new}}$, $\kappa \in \mathcal{T}_{h,\text{new}}$. Since the basis functions $\varphi^{(i)}_{\text{old}}$ in (20) are piecewise polynomials, discontinuous on the edges of each element of $\mathcal{T}_{h,\text{old}}$, integrating the product of different basis functions numerically by evaluating $\varphi^{(i)}_{\text{old}}$ at each quadrature point of $\kappa \in \mathcal{T}_{h,\text{new}}$ would result in inexact integration, and hence the loss of accuracy and conservation, as the quadrature rules are exact for a specified polynomial order.

In order to evaluate the corresponding integral, we utilize the concept of a supermesh [11]. The basis functions $\varphi^{(i)}_{\text{new}}$ are polynomials over $\kappa \in \mathcal{T}_{h,\text{new}}$, and hence the idea is to split the element κ into simplicial intersections with the elements of $\mathcal{T}_{h,\text{old}}$ and evaluate the integral as a sum of integrals over these intersections while avoiding the discontinuities in the basis functions. Therefore, the supermesh is defined as the mesh of intersection polygons of the old and new elements of $\mathcal{T}_{h,\text{old}}$ and $\mathcal{T}_{h,\text{new}}$, respectively, see Fig. 1. The local supermesh construction on element $\kappa \in \mathcal{T}_{h,\text{new}}$ consists of the following steps:

1. Find element $\kappa_1 \in \mathcal{T}_{h,\text{old}}$ intersecting element κ by a brute force method requiring that the centroid of κ lies inside κ_1.
2. The remaining intersecting elements $\kappa_i \in \mathcal{T}_{h,\text{old}}$, $i = 2, \dots, N_I$, are found by the advancing front algorithm [12; 23], which is illustrated in Fig. 2.
3. For each intersecting element $\kappa_i \in \mathcal{T}_{h,\text{old}}$, $i = 1, \dots, N_I$, the nodes forming an intersection polygon are found by searching for an intersection of two lines formed by the faces of elements κ_i and κ that are considered in turn.
4. Once the intersection polygons are identified, they are further split in order to obtain a super-

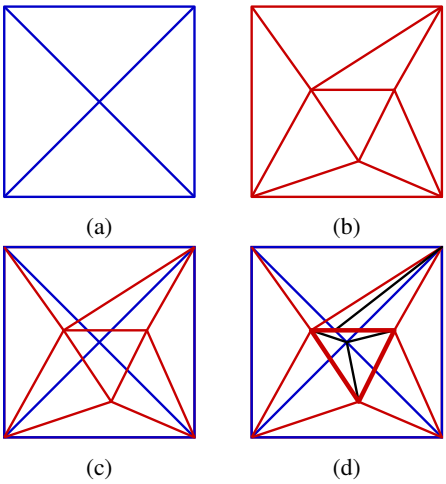

Figure 1: Illustration of a supermesh for a square domain. (a) Initial mesh $\mathcal{T}_{h,\text{old}}$. (b) Adapted mesh $\mathcal{T}_{h,\text{new}}$. (c) Intersection of the meshes $\mathcal{T}_{h,\text{old}} \cup \mathcal{T}_{h,\text{new}}$ including nonsimplicial intersection elements. (d) The global supermesh composed of simplices.

mesh $\mathcal{T}_\kappa = \{\kappa_\ell, \ell = 1, \dots, N_\kappa\}$ composed of triangles only.

Let $\mathcal{T}_\kappa$ be the local supermesh of element $\kappa \in \mathcal{T}_{h,\text{new}}$ having N_κ elements. Now replacing w_{old} and w_{new} in (23) by their finite element representations (20), (21) and taking the supermesh elements into account yields

$$\sum_{\ell=1}^{N_\kappa} \int_{\kappa_\ell \in \mathcal{T}_\kappa} \sum_{j=1}^{N_{\text{old}}^\kappa} W_{\text{old}}^{(j)} \varphi_{\text{old}}^{(j)} \varphi_{\text{new}}^{(i)} \, \mathrm{d}\boldsymbol{x} = \\ = \sum_{\ell=1}^{N_\kappa} \int_{\kappa_\ell \in \mathcal{T}_\kappa} \sum_{k=1}^{N_{\text{new}}^\kappa} W_{\text{new}}^{(k)} \varphi_{\text{new}}^{(k)} \varphi_{\text{new}}^{(i)} \, \mathrm{d}\boldsymbol{x}, \tag{24}$$

$i = 1, \dots, N_{\text{new}}^\kappa$. This representation gives rise to a linear system for the vector of expansion coefficients $\boldsymbol{W}_{\text{new}}$ on each $\kappa \in \mathcal{T}_{h,\text{new}}$ in the form

$$\boldsymbol{M}_{\text{new}} \boldsymbol{W}_{\text{new}} = \boldsymbol{M}_{\text{old,new}} \boldsymbol{W}_{\text{old}}, \tag{25}$$

where $\boldsymbol{M}_{\text{new}}$ is the mass matrix defined with the set of basis functions φ_{new} and $\boldsymbol{M}_{\text{old,new}}$ is the mixed mass matrix of both sets of basis functions φ_{new} and φ_{old} with components

$$(\boldsymbol{M}_{\text{new}})_{ij} = \sum_{\ell=1}^{N_\kappa} \int_{\kappa_\ell \in \mathcal{T}_\kappa} \varphi_{\text{new}}^{(i)} \varphi_{\text{new}}^{(j)} \, \mathrm{d}\boldsymbol{x}, \tag{26}$$

$i, j = 1, \dots, N_{\text{new}}^\kappa$, and

$$(\boldsymbol{M}_{\text{old,new}})_{ij} = \sum_{\ell=1}^{N_\kappa} \int_{\kappa_\ell \in \mathcal{T}_\kappa} \varphi_{\text{new}}^{(i)} \varphi_{\text{old}}^{(j)} \, \mathrm{d}\boldsymbol{x}, \tag{27}$$

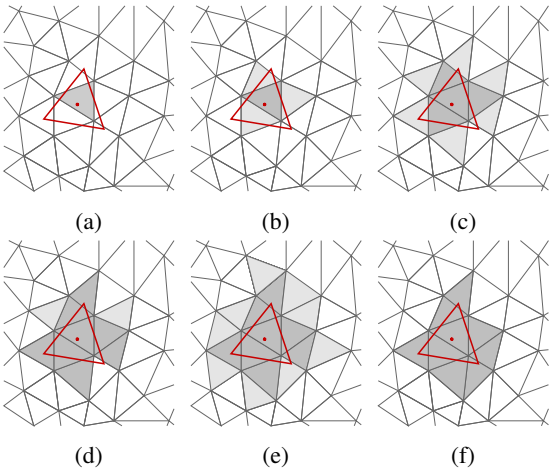

Figure 2: Illustration of element intersection search via the advancing front algorithm. The gray background mesh represents the mesh $\mathcal{T}_{h,\text{old}}$ and the element $\kappa \in \mathcal{T}_{h,\text{new}}$ is shown in red. (a) Element $\kappa_1 \in \mathcal{T}_{h,\text{old}}$ containing the centroid of κ is found. (b) The neighbor elements of κ_1 are identified and tested whether they intersect with κ. (c) - (e) This algorithm is applied for successive neighbors of intersecting elements until no new intersections are found. (f) The resulting set of intersecting elements.

$i = 1, \dots, N_{\text{new}}^\kappa$, $j = 1, \dots, N_{\text{old}}^\kappa$. Note that there is no need to explicitly store the mixed mass matrix as in order to assemble the right-hand side of (25) only the product $\boldsymbol{M}_{\text{old,new}} \boldsymbol{W}_{\text{old}}$ is required.

A bounded Galerkin projection is proposed in [11] in order to preserve minima and maxima of the field defined on the old mesh. However, this boundeness is restricted to linear basis functions only. At this stage, we have not incorporated any bounding procedure into the algorithm.

6. Numerical Results

6.1. Repeated Interpolation

The first test case does not involve any solution of a conservation law (1). Instead, a given function is interpolated several times between structured and unstructured meshes defined on the domain $\Omega = [-1, 1]^2$. The meshes have the same characteristic element size h but different topology, see Fig. 3. The purpose of this test case is to investigate the observed order of convergence of the Galerkin projection for the field represented by polynomials of degrees $p = 1, \dots, 4$ on each element.

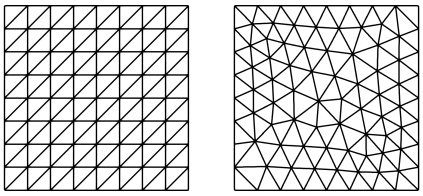

Figure 3: Structured and unstructured meshes with $h = 0.25$ used for the interpolation test case

We consider two functions, namely a sine wave and a smooth approximation to a step function,

$$w_1 = \sin(\pi x)\sin(\pi y), \tag{28}$$

$$w_2 = \frac{10x}{\sqrt{1+(10x)^2}} + \frac{10y}{\sqrt{1+(10y)^2}}. \tag{29}$$

Both of these functions are initialized on the structured mesh and the field is then interpolated onto the unstructured one, followed by interpolation back to the structured mesh. This interpolation procedure is repeated 10 times.

In order to compare the properties of Galerkin projection with some other approach, we assume the solution existing on the old mesh is simply evaluated on the points of the new mesh. This approach is computationally less demanding since no supermesh construction is needed, but, as we will see, this method is generally neither accurate nor conservative.

The convergence results for both functions are shown in Figs. 4(a) and 4(b). As expected, the observed order of convergence is $O(h^{p+1})$ for the case of Galerkin projection. The solution evaluation approach performs slightly worse for the smooth step function w_2. However, if we compare the integral of the final interpolant over the domain Ω, we see that only the Galerkin projection results in a conservative interpolation method. Note that the exact integral is zero for both functions (28) and (29).

6.2. *Rotating Gaussian*

Next, we consider the 2D scalar linear convection-diffusion equation of the form

$$\frac{\partial w}{\partial t} + \nabla \cdot (\boldsymbol{u} w) = \varepsilon \nabla^2 w, \quad \boldsymbol{x} \in \Omega. \tag{30}$$

The idea is to couple the mesh adaptation algorithm with the unsteady solution procedure such that the mesh is adapted in each time step once the current solution is known. Before the mesh is used within the next time step, the solution transfer approach based

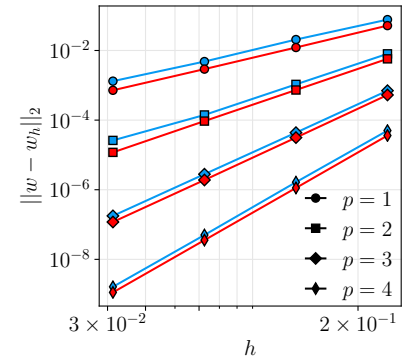

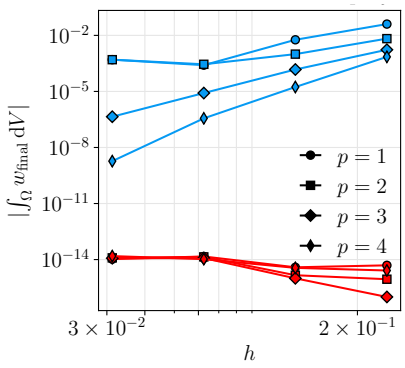

(a) w_1

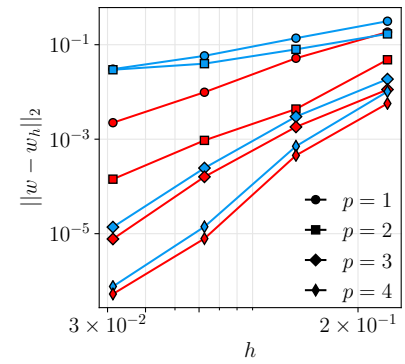

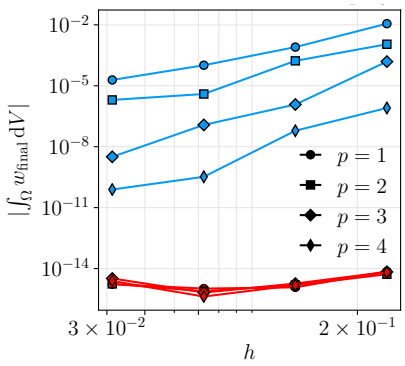

(b) w_2

Figure 4: Convergence results in terms of the L^2-norm error (left) and integral of the function representation over the domain Ω (right), old solution evaluation (—), Galerkin projection (—).

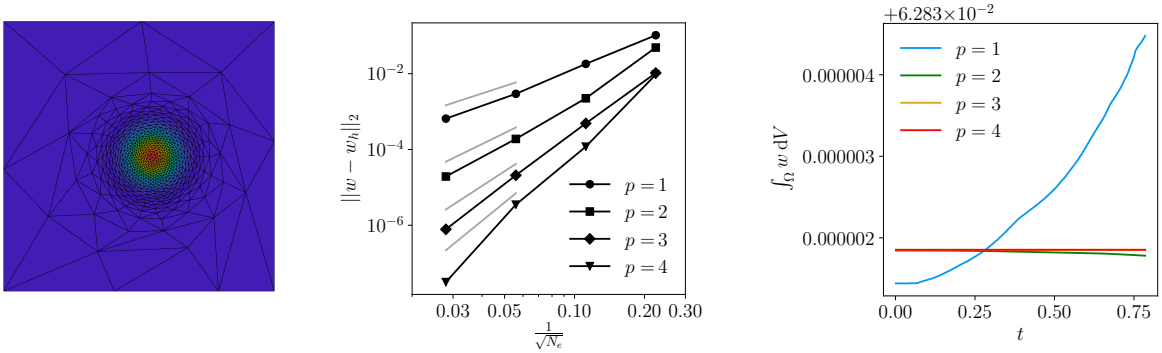

(a) Adapted mesh at the final time $T = \pi/4$ with $N_e = 1280$

(b) Convergence results for the L^2-norm error of the numerical solution at time T

(c) Evolution of the solution integral over the time for $p = 1, \ldots, 4$ and $N_e = 1280$

Figure 5: Rotating Gaussian testcase with anisotropically adapted mesh

on the Galerkin projection is applied as described in Section 5.

The particular test case involving the rotational transport of a Gaussian pulse inside the domain $\Omega = [-1, 1]^2$ has been studied in [24]. With the velocity field set to $\boldsymbol{u}(x, y) = (-4y, 4x)$, the exact solution for this problem is given by

$$w(x, y, t) = \frac{2\sigma^2}{2\sigma^2 + 4\varepsilon t} \exp\left(-\frac{(\widehat{x} - x_c)^2 + (\widehat{y} - y_c)^2}{2\sigma^2 + 4\varepsilon t}\right), \tag{31}$$

where

$$\begin{aligned} \widehat{x} &= x\cos(4t) + y\sin(4t), \\ \widehat{y} &= -x\sin(4t) + y\cos(4t). \end{aligned} \tag{32}$$

The initial center of the pulse is chosen as $(x_c, y_c) = (-0.1, 0)$, the standard deviation of the Gaussian distribution is set to $\sigma = 0.1$, and the diffusivity constant is set to $\varepsilon = 0.001$. Dirichlet boundary conditions taken from the exact solution are assumed at $\partial\Omega$. We are interested in the solution at the final time $T = \pi/4$ that corresponds to one-half rotation of the pulse in counterclockwise direction.

We use the DIRK(5,4) method and perform the unsteady simulation with a fixed number of elements N_e for every mesh adaptation. The test case is run successively with $N_e = 20, 80, 320, 1280$. In order to observe a spatial solution error, the time step size Δt is set to $T/(0.5N_e)$. Based on numerical experiments, this choice is sufficient for the temporal error to be small enough such that the overall error is governed strictly by the spatial discretization error.

The solution together with the adapted mesh at the final time is depicted in Fig. 5(a) for the case $N_e = 1280$. The convergence history is shown in Fig. 5(b). One can see that numerical solutions of polynomial degree $p = 1, \ldots, 4$ converge with order $p + 1$, and hence the Galerkin projection together with the HDG discretization leads to an optimal convergence rate, as in the situation with a fixed mesh. To assess the conservative properties of the interpolation, an integral of the solution over domain Ω is plotted in Fig. 5(c) as a function of time for the case of the mesh with the largest number of elements. It can be seen that even for the piecewise linear solution, the overall integral deviates from the exact one approximately by 2×10^{-6}.

6.3. Shock-Vortex Interaction

To compare the presented method against the classical approach of using a fine static mesh in all time steps, the interaction between a stationary shock and a right-moving vortex is considered [25]. The computational domain is taken to be $\Omega = [0, 2] \times [0, 1]$. A stationary shock wave is initialized at $x = 0.5$ with $\mathrm{Ma} = 1.1$ being the Mach number. The left state upstream of the shock is assumed to be

$$(\rho_L, u_L, v_L, P_L) = (1, \mathrm{Ma}\sqrt{\gamma}, 0, 1). \tag{33}$$

The vortex located at $(x_c, y_c) = (0.25, 0.5)$ is defined by perturbation of the left state mean flow in terms of the velocity vector (u, v), temperature $\Theta = P/\rho$, and entropy $S = \ln(P/\rho^\gamma)$. These perturbations are given by

$$(\delta u, \delta v) = \epsilon \exp\left(\alpha(1 - \eta^2)\right)\left(\frac{y - y_c}{r_c}, -\frac{x - x_c}{r_c}\right), \tag{34}$$

$$\delta\Theta = -\frac{\gamma - 1}{4\alpha\gamma}\epsilon^2 \exp\left(2\alpha(1 - \eta^2)\right), \tag{35}$$

$$\delta S = 0, \tag{36}$$



(a) (b) (c) (d)

Figure 6: Detail of the shock-vortex interaction at time $t = 0.35$. Fixed mesh with 11,000 elements (a) and the corresponding density distribution (b). Contours of density (c) obtained with the adapted mesh (d).

where $\eta = r/r_c$ with $r = \sqrt{(x - x_c)^2 + (y - y_c)^2}$, ϵ is the strength of the vortex, α controls the decay rate of the vortex, and r_c is the critical radius for which the vortex has the maximum strength. Based on [26], we set $\epsilon = 0.3$, $\alpha = 0.204$, and $r_c = 0.05$. Symmetry boundary conditions are assumed on the top and bottom of the domain.

The final time of the simulation is set to $T = 1$, and the time step size is taken to be $\Delta t = 0.005$, using the third-order DIRK(3,3) method and Hartmann's shock-capturing approach. We consider two cases: First, the test case has been run on a fixed mesh with 11,000 triangular elements for the whole computation. For the second case, the mesh is initially adapted based on the initial conditions, and then the anisotropic mesh adaptation algorithm is applied in every other time step. The mesh is limited to 2,000 elements.

The distribution of density for both cases together with the corresponding meshes at time $t = 0.35$ is depicted in Fig. 6. In addition to the improved resolution and suppression of the oscillations near the shock, the computational time for the adapted mesh case including the mesh adaptation procedure itself is approximately one-third of the case with the fixed mesh.

7. Conclusion

The application of anisotropic mesh refinement for time-dependent problems discretized by the HDG method was presented. An algorithm for the conservative interpolation of the numerical solution between two anisotropically adapted meshes has been incorporated into the overall scheme, and the preliminary results show that the spatial and temporal error of the numerical solution is not affected for problems with smooth solution.

So far, the presented approach has been investigated also for the shock-vortex interaction problem for the Euler equations with rather weak shock waves present in the flow field where a significant computational cost reduction is achieved. Ongoing work aims to improve the utilized shock-capturing methods intended to stabilize the solver and to develop a bounding algorithm in order to avoid nonphysical numerical solutions, which may occur during the solution transfer step itself. This improvement would allow solving problems involving strong moving shocks with notably reduced computational cost while maintaining the resolution of the numerical solution near the shock.

Acknowledgments

The work was supported by grant 21–31457S of the Czech Science Foundation and the project SGS–2022–008.

References

[1] Z. J. Wang, K. Fidkowski, R. Abgrall, F. Bassi, D. Caraeni, A. Cary, H. Deconinck, R. Hartmann, K. Hillewaert, H. T. Huynh, N. Kroll, G. May, P. O. Persson, B. van Leer, M. Visbal, High-order CFD methods: Current status and perspective, International Journal for Numerical Methods in Fluids 72 (8) (2013) 811–845.

[2] F. Alauzet, A. Loseille, A decade of progress on anisotropic mesh adaptation for computational fluid dynamics, Computer-Aided Design 72 (2016) 13–39.

[3] J. Grandy, Conservative remapping and region overlays by intersecting arbitrary polyhedra, Journal of Computational Physics 148 (2) (1999) 433–466.

[4] J.-F. Remacle, X. Li, M. S. Shephard, J. E. Flaherty, Anisotropic adaptive simulation of transient flows using discontinuous galerkin methods, International Journal for Numerical Methods in Engineering 62 (7) (2005) 899–923.

[5] F. Alauzet, A. Loseille, G. Olivier, Time-accurate multi-scale anisotropic mesh adaptation for unsteady flows in cfd, Journal of Computational Physics 373 (C) (2018) 28–63.

[6] F. Alauzet, P. Frey, P. George, B. Mohammadi, 3d transient fixed point mesh adaptation for time-dependent problems: Application to cfd simulations, Journal of Computational Physics 222 (2) (2007) 592–623.
[7] F. Alauzet, A parallel matrix-free conservative solution interpolation on unstructured tetrahedral meshes, Computer Methods in Applied Mechanics and Engineering 299 (2016) 116–142.
[8] A. M. Rangarajan, A. Balan, G. May, Mesh adaptation and optimization for discontinuous galerkin methods using a continuous mesh model, in: AIAA Modeling and Simulation Technologies Conference, 2016.
[9] T. Levý, G. May, Comparison of implicit time-discretization schemes for hybridized discontinuous galerkin methods, Applied and Computational Mechanics 16. doi:10.24132/acm.2022.786.
[10] P. George, H. Borouchaki, Delaunay triangulation and meshing: Application to finite elements, Hermès, 1998.
[11] P. Farrell, M. Piggott, C. Pain, G. Gorman, C. Wilson, Conservative interpolation between unstructured meshes via supermesh construction, Computer Methods in Applied Mechanics and Engineering 198 (33) (2009) 2632–2642.
[12] P. E. Farrell, J. R. Maddison, Conservative interpolation between volume meshes by local galerkin projection, Computer Methods in Applied Mechanics and Engineering 200 (2011) 89–100.
[13] R. Hartmann, Adaptive discontinuous galerkin methods with shock-capturing for the compressible navier–stokes equations, International Journal for Numerical Methods in Fluids 51 (9-10) (2006) 1131–1156.
[14] G. Wanner, E. Hairer, Solving ordinary differential equations II. Stiff and differential-algebraic problems, Springer-Verlag, Berlin Heidelberg, 1996.
[15] R. Alexander, Diagonally implicit Runge–Kutta methods for stiff O.D.E.'s, SIAM Journal on Numerical Analysis 14 (6) (1977) 1006–1021.
[16] J. R. Cash, Diagonally implicit Runge-Kutta formulae with error estimates, IMA Journal of Applied Mathematics (Institute of Mathematics and Its Applications) 24 (3) (1979) 293–301.
[17] A. Loseille, F. Alauzet, Continuous mesh framework part i: Well-posed continuous interpolation error, SIAM Journal on Numerical Analysis 49 (1) (2011) 38–60.
[18] A. Loseille, F. Alauzet, Continuous mesh framework part ii: Validations and applications, SIAM Journal on Numerical Analysis 49 (1) (2011) 61–86.
[19] F. Hecht, Bamg: Bidimensional anisotropic mesh generator, User Guide. INRIA, Rocquencourt 17.
[20] V. Dolejší, Anisotropic *hp*-adaptive method based on interpolation error estimates in the l^q-norm, Applied Numerical Mathematics 82 (2014) 80–114.
[21] O. Bartoš, V. Dolejší, G. May, A. Rangarajan, F. Roskovec, A goal-oriented anisotropic hp-mesh adaptation method for linear convection–diffusion–reaction problems, Computers & Mathematics with Applications 78 (9) (2019) 2973–2993.
[22] A. Rangarajan, G. May, V. Dolejší, Adjoint-based anisotropic hp-adaptation for discontinuous galerkin methods using a continuous mesh model, Journal of Computational Physics 409 (2020) 109321.
[23] R. Löhner, Robust, vectorized search algorithms for interpolation on unstructured grids, Journal of Computational Physics 118 (2) (1995) 380–387.
[24] N. C. Nguyen, J. Peraire, B. Cockburn, An implicit high-order hybridizable discontinuous Galerkin method for linear convection-diffusion equations, Journal of Computational Physics 228 (9) (2009) 3232–3254.
[25] J. J. Choi, High-order methods for conservation laws employing embedded structured element method on unstructured hexahedral grid, in: 22nd AIAA Computational Fluid Dynamics Conference, 2015.
[26] F. Zhao, L. Pan, S. Wang, Weighted essentially non-oscillatory scheme on unstructured quadrilateral and triangular meshes for hyperbolic conservation laws, Journal of Computational Physics 374 (2018) 605–624.

Stability of crossflow by means of small, discrete roughness elements: An approach to receptivity

Emilio López Figueiras

Aeronautics and Aerospace Department, von Karman Institute for Fluid Dynamics, Belgium, emilio.lopez.figueiras@vki.ac.be

Supervisor: Christophe Schram

Professor, Aeronautics and Aerospace Department, von Karman Institute for Fluid Dynamics, Belgium, emilio.lopez.figueiras@vki.ac.be

Supervisor: Jure Oder

Research Engineer, Environmental and Applied Fluid Dynamics Department, von Karman Institute for Fluid Dynamics, Belgium, jure.oder@vki.ac.be

University Supervisor: Daniel Rodríguez

Professor, School of Aeronautics, Universidad Politécnica de Madrid, Spain, daniel.rodriguez@upm.es

Abstract

This report will treat the receptivity analysis of the flow over an incompressible flow over a flat plate with an elliptic leading edge under different oncoming free-stream scenarios, such as free-stream turbulence or vorticity modes, updating mainly the partial results obtained from the first unsteady simulations performed and the features to be considered to improve and make more realistic future runs, such as the uniformity for the phases of the incoming disturbances or the reduction of their average amplitude, avoiding the appearance of non-linear interactions.

Keywords: transition, roughness, receptivity, crossflow, DNS, turbulence

1. Introduction

In the search of the aviation industry for more efficient aircraft that reduce fuel consumption, reduce the carbon footprint of commercial flights, and make every airplane more sustainable; the improvement in aerodynamic efficiency is a key goal that can be achieved by reducing as much as possible the aerodynamic drag of the wings. In that sense, the most important contribution to drag is produced by turbulent flow, hence, a lot of effort is put into the delay or control of the processes that lead to the flow transition to turbulence. Among these processes, the mechanism responsible for starting the transition process is called "receptivity" and has its origin in the free-stream perturbations that impinge with the aerodynamic devices or in the interaction of the surface roughness of the aircraft with the flow. This work will treat the stability and receptivity analysis of the flow over a flat plate model with an elliptic leading edge under different oncoming free-stream disturbances, which is a good approximation of the real wings used in nowadays aircraft. The development of more sophisticated models, the numerical study of the processes involving the transition from laminar to turbulent flow and the conclusions obtained about how the leading edge geometry or the flight conditions can affect the stability of the flow over the wing play an important role in the development of strategies for the transition control towards the reduction of the aerodynamic drag and the improvement of the aircraft's aerodynamic efficiency, making future aviation more accessible and sustainable. The receptivity analysis of a 2-D boundary layer flow over a finite-thickness flat plate with an elliptic leading edge will serve as a basis to introduce more complex test cases and geometries in the future, such as the formation of a three-dimensional boundary layer after adding sweep to the model (where the crossflow would appear, generating instabilities), the

addition of discrete or distributed roughness or the change in geometry towards a more applied geometry with airfoil profile.

This work, as the starting point, takes some of the ideas given by state-of-the-art reviews like the one in Saric et al. (2003) [1]. There, the author highlights the importance of considering all the sources of instability, and not a single source isolated. In that sense, to study the way that roughness can start the transition process is essential to consider its interaction with the free-stream turbulence; which, in some cases, may change the nature of the instabilities from the typical stationary wave to traveling waves. Currently, this work treats the modeling of the free-stream turbulence, starting with an approach of sets of vorticity modes and ending with the model of a more "realistic" frees-stream turbulence that could match the energy spectra of real turbulent flows.

Consequently, this work aims to reproduce that free-stream turbulence scenario starting with the simplification given by Schrader et al. (2010) [2], which includes a receptivity analysis of the flow over a flat plate with an elliptic leading edge after considering some vortical perturbations at the inlet of the domain.

Other works, like N. Shahriari (2016) [3], use the geometry of Schrader et al. (2010) [2] to make receptivity analysis to acoustic waves instead of vorticity modes. However, that study has been useful for the setup of the test case of interest for the computation of a symmetric and steady flow field by adapting the boundary condition for the pressure of one of the outlets to a pressure obtained from a precomputed solution.

As a more complex problem, Vincentiis et al. (2022) [4] studies the interactions between free stream turbulence and discrete roughness elements for an incompressible flow over a swept wing, which is quite similar to the long-term goal of this job. Vincentiis et al. (2022) [4] study numerically the effect of the turbulence intensity in the transition process in terms of its interaction with a discrete roughness element. The setup of this test case will be useful in the next stages of this project for the adaptation of the flow field to the addition of free-stream turbulence, avoiding with special treatment the apparition of spurious perturbations near the outlet boundaries.

The immediate next step in this work will be to add the free-stream turbulence at the inlet of the domain, controlling the turbulence intensity to simulate different scenarios. Studies like Hosseinverdi and Fasel (2019) [5], Jacobs and Durbin (2001) [6] or Brandt et al. (2004) [7] apply a turbulence model to their receptivity analysis and serve as a good basis to develop free-stream turbulence at the inlet of the domain, adapting the amplitudes and the phases of the inflow perturbations to match the von Karman energy spectra for turbulent scales, which would generate an isotropic turbulent flow.

2. Methodology

2.1. Numerical method

The numerical approach followed to make the receptivity analysis of vorticity modes is, as it was mentioned before, the same as in Schrader et al. (2010) [2]. Here, an incompressible flow over a semi-infinite flat plate with an elliptic leading edge is solved with direct numerical simulation (DNS) thanks to the Spectral Element Method implemented in Nek5000, from Fischer et al. (2008) [8]. For this case, the polynomial order chosen is $N = 7$ and the spatial discretization has the form $\mathbb{P}_N - \mathbb{P}_{N-2}$, as can be seen in Fig.1 for the velocity field.

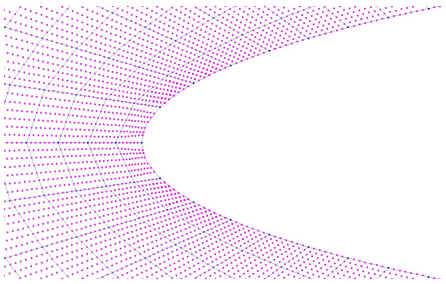

Figure 1: Detailed view of the flat plate leading edge. Gauss-Lobato-Legendre (GLL) points are shown. Every element has $N + 1 = 8$ nodes in each direction of the velocity field.

2.2. Computational domain and mesh

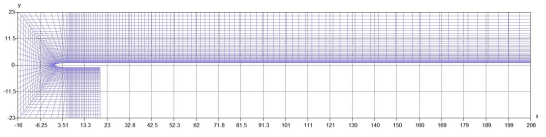

Figure 2: Computational domain and mesh with a number of elements $n_{tg} \times n_{no} \times n_{sp} = 150 \times 34 \times 5$.

The geometry considered is a modification of an ellipse called "super-ellipse", where the junction point between the elliptic curve and the flat plate is

smoother, as even such a small discontinuity could affect the receptivity phenomena. The ellipse equation is given by Eq. 1.

$$\left(\frac{y}{b}\right)^2 = 1 - \left(\frac{a-x}{a}\right)^p; \tag{1}$$

where

$$p = 2 + \left(\frac{x}{a}\right)^2. \tag{2}$$

In our case, the chosen aspect ratio for the super-ellipse was $AR \equiv \frac{a}{b} = 6$ and the semi-minor axis, b, which is the reference length, was chosen to be $b = 1$.

In addition, the computational domain is shortened in its lower half and the far-field boundaries are quite close to the plate, as shown in Fig. 2, to reduce the computational cost, requiring special treatment for those boundary conditions.

2.3. *Base flow*

Before adding the perturbations at the inlet, the computation of a steady flow serves as the base for the vorticity modes and the unsteady simulations.

This base flow solution is obtained from the unsteady, incompressible Navier-Stokes equations implemented in Nek5000. As already mentioned, the reference length is the semi-minor axis of the ellipse, $b = 1$, the free-stream velocity is $U_\infty = 1$ and the kinematic viscosity chosen is such that the reference Reynolds number $Re_b = U_\infty b/\nu = 2400$. With that, the Reynolds number at the end of the flat plate is $Re_L = 500000$.

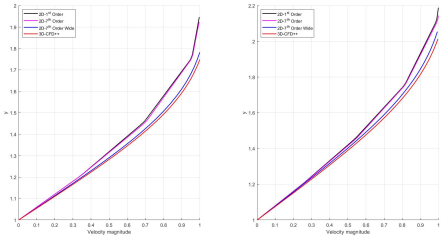

Figure 3: Comparison between the boundary layer profiles obtained from several base-flow computations in two different positions along the flat plate (left: $x = 100$, right: $x = 200$)

The boundary conditions chosen for the far-field boundaries are Dirichlet-type. As the domain size is quite restricted due to the computational cost, flow blockage might appear if those boundaries were uniform. Therefore, it is required to impose a precomputed velocity profile with either a RANS simulation with a wider domain, as in Vincentiis et al. (2022) [4] or as in Schrader et al. (2010) [2], which are obtained from a potential flow solution of the same geometry thickened by the displacement thickness of the boundary layer. The second option was applied in this case, although a RANS simulation with an extended domain size was also run, giving the boundary layer profiles shown in Fig.3, where the solutions for the RANS simulation with extended size and the seventh-order SEM run with wider domain seem to agree accurately. Although the absolute difference between the velocity profiles imposed and the theoretical uniform velocity at the far field seems to be negligible (according to Fig. 4 and Fig. 5), the influence is remarkable in the boundary layer profiles above.

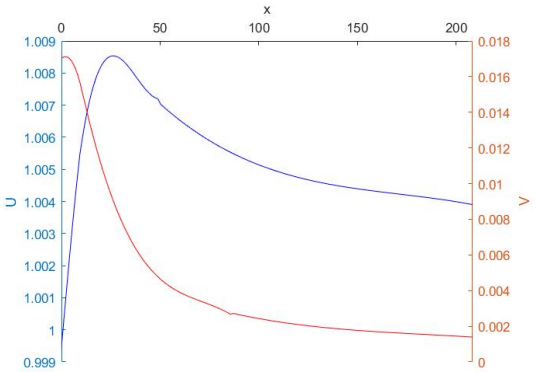

Figure 4: Velocity profiles imposed as Dirichlet boundary conditions at the top wall of the computational domain. Obtained from a precomputed potential flow solution.

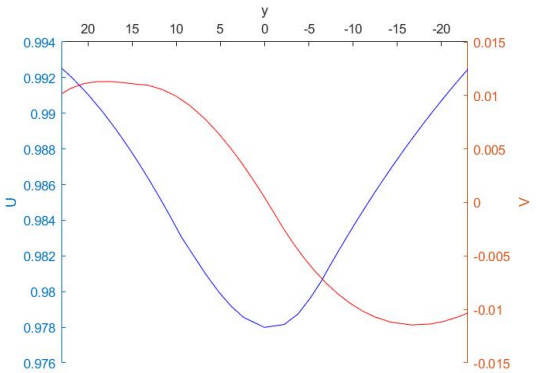

Figure 5: Velocity profiles imposed as Dirichlet boundary conditions at the inlet wall of the computational domain. Obtained from a precomputed potential flow solution.

For the wall, a no-slip condition was applied, while

a periodic boundary condition is set for the spanwise direction.



Figure 6: Pressure slice at half-span with a pressure contour.

Finally, the outlet boundaries have a special treatment, avoiding the dependency of the solution on the length of the lower part and ensuring that the flow field is symmetric over the upper and the lower surface of the flat plate, as shown in Fig. 6. The solution proposed in Shahriari (2016) [3], solves that issue, as it defines natural boundary conditions at both outlet boundaries, imposing a certain ambient pressure profile in the lower half. That pressure profile is obtained from a simulation done for the upper half of the domain, taking the pressure profile at the same x location as the lower boundary.

2.4. Perturbed flow

Once the flow becomes steady and the base flow solution has converged, the three-dimensional, unsteady simulations can be run using Fourier modes of the form $\phi = \hat{\phi} e^{i(\alpha x+\gamma y+\beta z-\omega t)}$., where ϕ can be either the velocity or the vorticity; α, β and γ are the wavenumbers for the axial, vertical and spanwise directions respectively. The amplitude of a function is represented with $\hat{\phi}$, the velocity components for each direction are (u, v, w) and the corresponding vorticity components are (ξ, η, ζ) .

In this work, only axial-dominant vortices, also known as ξ-modes will be considered. Hence, the amplitudes for the velocity and the velocity read

$$(\hat{u}, \hat{v}, \hat{w}) = \frac{i}{\sqrt{\gamma^2+\beta^2}} (0, \beta, -\gamma), \tag{3}$$

$$\left(\hat{\xi}, \hat{\eta}, \hat{\zeta}\right) = \frac{1}{\sqrt{\gamma^2+\beta^2}} \left(\gamma^2+\beta^2, -\alpha\gamma, -\alpha\beta\right). \tag{4}$$

From the expressions in Eq. 3 and Eq. 7 it can be noted that there is no dependency between the disturbance vector $(\hat{u}, \hat{v}, \hat{w})$ and the wavenumber (γ, β), making the energy of each mode independent of its length scale. It is possible to obtain pure axial vorticity if $\alpha = 0$.

When constructing the freestream turbulence with the vorticity modes, it is convenient to ensure that the generated disturbance has a mean amplitude at the inlet $\epsilon_{in} \ll U_\infty$. Otherwise, the magnitude of the disturbances could generate non-linearities within the flow field, non-resolved by the linearized equations. The mean amplitude at the inflow is defined as

$$\epsilon_{in} = \sqrt{\frac{1}{2}\left(\bar{u^2}, \bar{v^2}, \bar{w^2}\right)}. \tag{5}$$

,

where the bar corresponds to the vertical average of the r.m.s. in the z-direction.

The small value for the mean amplitude at the inlet and homogenization of the disturbances, giving a random phase to each of them at the inlet, has not been done for simplicity so far, but they will be implemented to avoid any kind of non-linear interaction between the disturbances. Once that condition is ensured, Taylor's hypothesis is valid in this case, and the chordwise wavenumber α can be substituted with ω, as the phase speed can be considered to be 1 at the inlet. Consequently, a reduced frequency can be defined to get the frequency ω,

$$F \equiv \frac{\nu}{U_\infty^2} 10^6 \omega = \frac{L}{Re_L U_\infty} 10^6. \tag{6}$$

The freestream turbulence generated at the inlet, for the case of this study, will be composed of three different sets of vortical modes. In the case of the pure axial vorticity, with $F = 0$, there are six different vorticity modes with the values $(\gamma, \beta)_j = (0.12, 0.36)\, j$, $j = 1 \cdots 6$.. For the mixed axial vorticity, with frequencies $F = 16$ and $F = 96$, there is a seventh mode $(\gamma, \beta)_0 = (1.344, 0)$. The value of the amplitudes at the inlet for the disturbance modes with finite frequency are shown in Fig. 7, where it is clear that the dominant modes are the ξ-modes, but the other two modes are not zero and dependant of the frequency.

3. Results

3.1. Base flow

The validation of the base flow can be done by taking advantage of the two ways the SEM codes have to refine the meshes for a grid independence study refining in two different ways: h-refinement, which is the classical way of adding more in each direction, and p-refinement, which is exclusive to SEM methods, as it

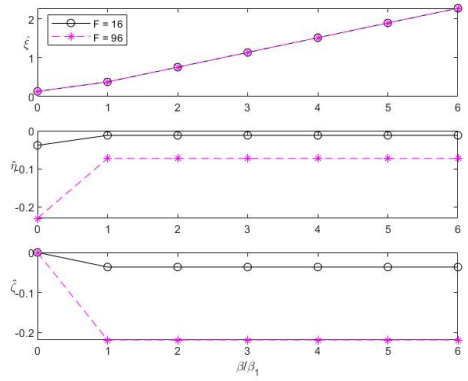

Figure 7: Amplitude of the vorticity components of the inflow disturbances obtained after the addition of the seven stream-wise vorticity modes with reduced frequencies F = 16 and F = 96.

changes the polynomial order of the solver to increase the resolution with the same number of elements. This grid independence study has to be done yet, but it is one of the short-term objectives.

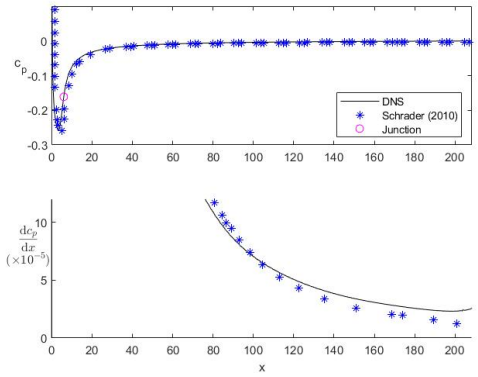

Figure 8: Top: Pressure coefficient distribution over the axial direction. Bottom: Chord-wise derivative of the pressure coefficient.

As a way to validate the steady flowfield used as a base flow for the disturbances, in Fig. 9 there is a comparison between the pressure distribution obtained by Schrader et al (2010) [2] and the one obtained from this work. The graphs show a good agreement. Other comparisons with the references or with analytical solutions, such as the Blasius solution for a boundary layer over a flat plate might be done in future work.

3.2. Perturbed flow

The first feature of the perturbed flow that can be discussed is the fact that the vorticity modes are not uniformly distributed to have random phases and were built without considering the value of the average amplitude ϵ_{in}.

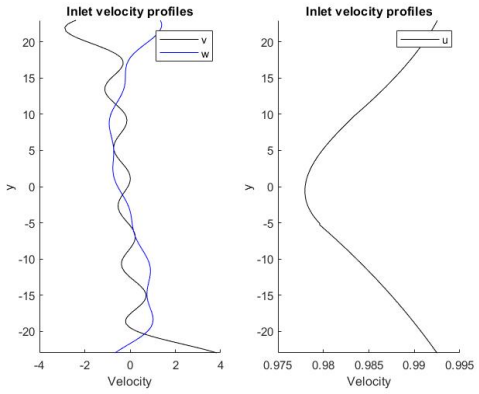

Figure 9: Profiles of the velocity components of the disturbances imposed at the inlet boundary condition.

The calculation of the value of the average amplitude at the inlet ϵ_{in} gave a value of the order of $\epsilon_{in} \sim 1$, while the values of the average amplitude at the inlet deduced from Schrader et al. (2010) [2] are of the order of 5 to 6 orders of magnitude lower. As a consequence, in the simulations of this work, the disturbances could have non-linear interactions that are impossible to resolve with the Linearized Navier-Stokes equations used to solve the unsteady flow.

Despite that possible inaccuracy, the solution states obtained for the cases with $F = 0$ and $F = 96$ can be compared and analyzed comparing their velocity components, shown in Fig. 10 and Fig. 11 respectively.

The patterns observed in both flows give information about the nature of their perturbations. In Fig. 10 the absence of a temporal dependency of the perturbations, as well as the uniformity in the u slice agree with the fact that it is a pure axial vorticity disturbance; opposing to the case with $F = 96$, where the patterns observed for the v and w velocity components are a symptom of η and ζ modes having non-zero values. In addition, Schrader et al. (2010) [2] conclusion about the bigger receptivity of the boundary layer to pure ξ vortices agrees with the fact that the maximum u_{rms} is closer to the wall for the $F = 0$ case than for $F = 96$, where the velocity fluctuations expand closer to the boundary layer edge.

Finally, the surface distributed in the spanwise direction which appears in Fig. 12 and Fig. 13 shows a good result, as the predicted streaky pattern due to the pure axial vorticity disturbance is clearly shown in both figures. However, the effect of the lack of

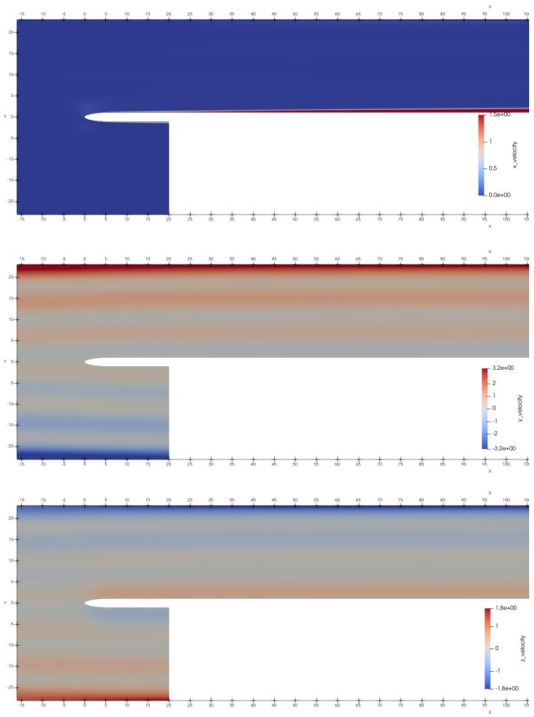

Figure 10: Slices of the velocity components (u,v and w respectively, from top to bottom) of the perturbations with $F = 0$.

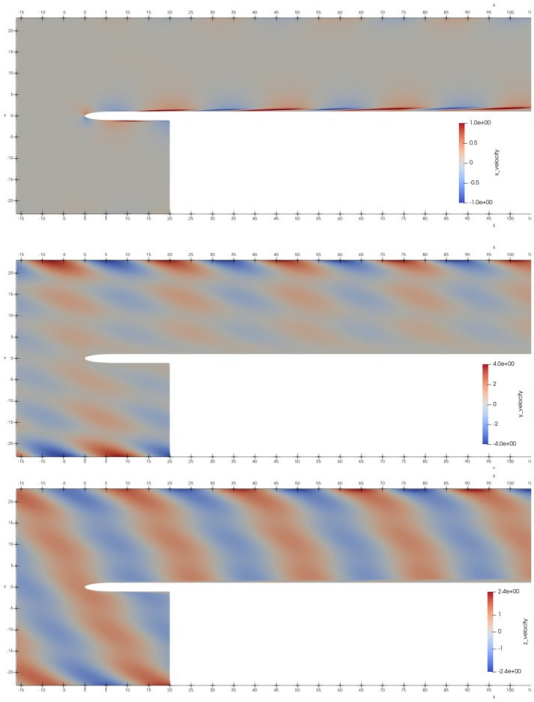

Figure 11: Slices of the velocity components (u,v and w respectively, from top to bottom) of the perturbations with $F = 96$.

uniformity in the phase angles when building the perturbations and the big value of average amplitude, up to six orders of magnitude bigger, generates those regions of high amplitudes near the span ends in Fig. 12. Those regions with high values of disturbance velocity appear due to the interaction of the already big amplitudes of each vorticity mode together with the fact that all the modes coincide in phase.

Fig. 13, obtained from Schrader et al. (2010) [2], shows values for the velocity of the disturbances much lower than the other case and streaks better defined in the middle-span region, as a result of a uniform distribution of the phase angle of the vorticity modes.

4. Conclusion

This work, in origin, was an introduction to the application of the stability and receptivity theory as well as to the software and the analytical tools needed to study the physical phenomena involved in the transition process. In that sense, the model implemented in Nek5000 has been successfully proven to be accurate for both, the base flow and the unsteady simulations, although the unsteady simulations led to discrepancies with the expected results due to the lack of uniformity of the inflow disturbances in the outlet and the huge amplitudes that those disturbances had at the inlet, producing strong interactions between different vorticity modes downstream of the leading edge and in the ends of the flat plate span.

Therefore, the first short-term goal for this work must be the implementation of a uniform, random distribution of the phases of the vorticity modes that are part of the freestream perturbations imposed at the inlet.

Another milestone to be achieved soon should be the execution of a grid independence study, via both, h- and p-refinement. Validation of the base flow obtained by comparing the results with the Blasius solution is also something that could be done in a short period.

As the perturbations introduced from the inlet produce oscillations moving upstream from the outflow boundaries, a sponge region might be needed in the last section of the domain to dissipate the disturbances near the outflow.

In the post-processing of the results, a more complete analysis of the receptivity process can be done also, including the application of Fourier analysis in order to show the disturbances that can get more easily

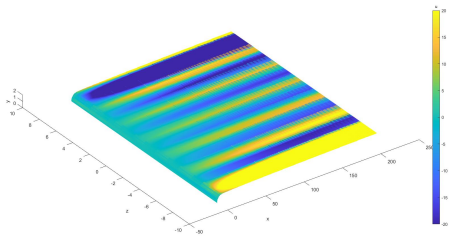

Figure 12: Boundary-layer response to axial free-stream perturbations resulting from the addition of six vorticity modes with $F = 0$ and $\epsilon_{in} = 1.0$. The surface represented contains the points with a wall-normal maximum of u_{rms} and shows the value of the u disturbance

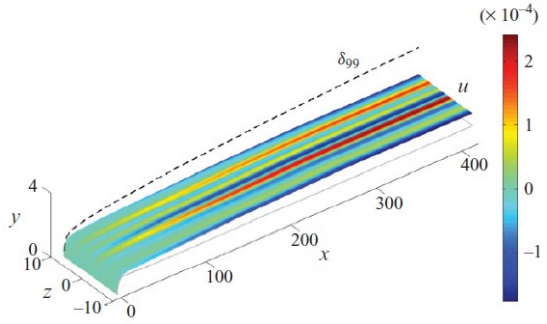

Figure 13: Boundary-layer response to axial free-stream perturbations resulting from the addition of six vorticity modes with $F = 0$ and $\epsilon_{in} = 2 \times 10^{-6}$. The surface represented contains the points with a wall-normal maximum of u_{rms} and shows the value of the u disturbance. δ_{99} is represented also. Source :Schrader et al. (2010) [2]

into the boundary layer. After that, a receptivity coefficient could be computed to compare quantitatively if the boundary layer is more or less receptive to certain vorticity modes.

In the mid-term, adding more complexity to the model would be a good way to continue with the work towards the goal of passively controlling the crossflow instability with discrete roughness elements. In that sense, features like generating isotropic freestream turbulence following the von Karman energy spectrum instead of having just an arbitrary collection of vorticity modes would make the test case much more realistic and close to wind tunnel experiments or real free-flight conditions.

Adding a sweep angle to the flat plate (or a crossflow component to the boundary layer) could give interesting information about the interaction between the vorticity modes or the free-stream vorticity and the crossflow instability. In addition, it would be very valuable to learn about the influence of turbulence in-

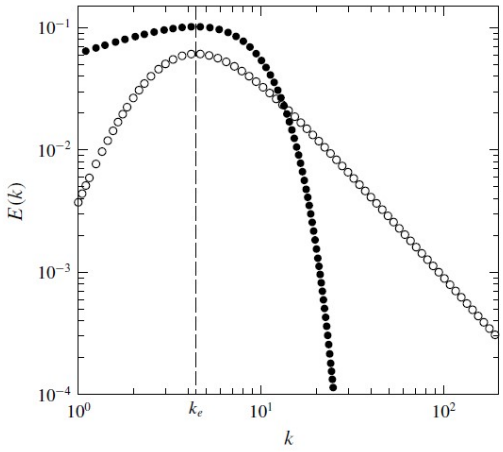

Figure 14: Von Karman energy spectrum (white dot) and alternative spectrum (black dot). Source: Hosseinverdi and Fasel (2019) [5]

tensity on the transition process or in the main instability mechanisms.

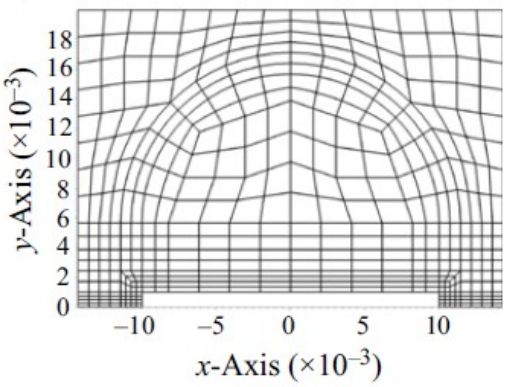

Figure 15: Distribution of the spectral elements around a cylindrical, discrete roughness element. Source: Vincentiis et al. (2022) [4]

Finally, the addition of surface roughness is a key step in the development of this project, mainly in the form of discrete roughness elements, which are meshed and included as part of the geometry, or as distributed roughness modelling the natural roughness of a surface, which is introduced as a non-homogeneous boundary condition in the wall.

Acknowledgments

This project received funding from the European Union's Horizon 2020 research and innovation pro-



gramme under the Marie Skłodowska-Curie grant agreement No 955923.

References

[1] W. S. Saric, H. L. Reed and E. B. White, Stability and transition of three-dimensional boundary layers, Annual Review of Fluid Mechanics 35 (2003) 413–440.

[2] L.-U. Schrader, L. Brandt, C. Mavriplis and D. S. Henningson, Receptivity to free-stream vorticity of flow past a flat plate with elliptic leading edge, Journal of Fluid Mechanics 653 (2010) 245–271.

[3] N. Shahriari, On stability and receptivity of boundary-layer flows, Ph.D. thesis, Royal Institute of Technology (2016).

[4] L. De Vincentiis, D. S. Henningson and A. Hanifi, Transition in an infinite swept-wing boundary layer subject to surface roughness and free-stream turbulence, Journal of Fluid Mechanics 931 (2022) A24.

[5] S. Hosseinverdi,and H. F. Fasel, Numerical investigation of laminar turbulent transition in laminar separation bubbles: the effect of free-stream turbulence, Journal of Fluid Mechanics 858 (2019) 714–759.

[6] R. G. Jacobs and P. A. Durbin, Simulations of bypass transition, Journal of Fluid Mechanics 428 (2001) 185–212.

[7] L. Brandt, P. Schlatter and D. Henningson, Transition in boundary layers subject to free-stream turbulence, Journal of Fluid Mechanics 517 (2004) 167–198.

[8] P. Fischer, J. Kruse, J. Mullen, H. Tufo, J. Lottes and S. Kerkemeier, NEK5000 – Open Source Spectral Element CFD solver, https://nek5000.mcs.anl.gov/index.php/mainpag, Royal Institute of Technology (2008).

A multi-fidelity environment for the simulation and control of flapping wings

Romain Poletti

Environmental and Applied Fluid Dynamics Department, von Karman Institute for Fluid Dynamics, Belgium, romain.poletti@vki.ac.be

Supervisor: Miguel A. Mendez

Professor, Environmental and Applied Fluid Dynamics Department, von Karman Institute for Fluid Dynamics, Belgium, miguel.alfonso.mendez@vki.ac.be

Supervisor: Jeroen van Beeck

Professor, Environmental and Applied Fluid Dynamics Department, von Karman Institute for Fluid Dynamics, Belgium, jeroen.vanbeeck@vki.ac.be

University Supervisor: Joris Degroote

Professor, Department of Electromechanical, Systems and Metal Engineering, Ghent University, Belgium, joris.degroote@UGent.be

Abstract

Flapping drones takes inspiration from natural fliers which outperform quadcopters at small scales. Their exceptional flight builds on complex unsteady aerodynamic phenomena that are challenging to model efficiently. This work presents the development of a multidisciplinary environment to simulate, control and analyze the flapping wings of micro drones in different flight scenarios.

Keywords: Flapping aerodynamics, Reduced Order Model, CFD, FSI, Multibody dynamics, Control

1. Introduction

For the past few years, insects and hummingbirds are inspiring a new generation of drones called Flapping Wing Micro Air Vehicles (FWMAVs). At low Reynolds numbers, flapping wings show excellent aerodynamic performance, adapt to very different wind conditions, and allow unmatched aerobic maneuvers. Those features give flapping drones the potential to outperform standard quadcopters in rescue, surveillance, and civil missions.

The design of micro drones involves a multidisciplinary optimization procedure between electromechanics, control theory, fluid dynamics, etc. The objective of the last two fields is to control the wing shape and motion, such that the drone flies optimally in various scenarios and conditions. This optimization problem is non-trivial since flapping aerodynamics generates complex unsteady phenomena including the absence of stall, rotational circulation, added mass, clap and fling, and wing-wake interaction [1]. Natural flyers also modulate those aerodynamic mechanisms with their flexible wings to increase their flight efficiency [2].

High-fidelity tools such as Computational Fluid Dynamics (CFD) and Fluid-structure interaction (FSI) can explain the details of the flow physics. Nevertheless, its computational cost prevents its use in an optimization or control loop where several wing kinematics are evaluated. For the latter, simplified aerodynamic models are more appropriate but lack accuracy when considering dynamic flapping motions. Separately, the two tools are then ineffective to optimize the motion of flapping wings.

This thesis proposes a comprehensive, multidisciplinary, multi-fidelity environment to teach flapping drones how to learn and continuously optimize their flapping motions (figure 1). First, a given wing shape and kinematics parametrization are chosen. The wing state drives a simplified model which estimates the instantaneous aerodynamic forces and power. The aerodynamic performance feeds a dynamic model

which tracks the drone position and hence computes its trajectory. Depending on the flight objectives and constraints, a controller adapts the wing motion received by the simplified model . In parallel to this control loop, a high-fidelity environment (CFD and FSI) is also developed. Its objective is twofold, to verify and analyze the flow details of a few optimized strategies as well as to improve the simplified models thanks to data regression techniques.

The first year of this PhD was devoted to learn and implement literature tools in each of the building blocks of figure 1. The second year was devoted to extend and exploit the tools as well as to connect them to perform preliminary control of flapping drones.

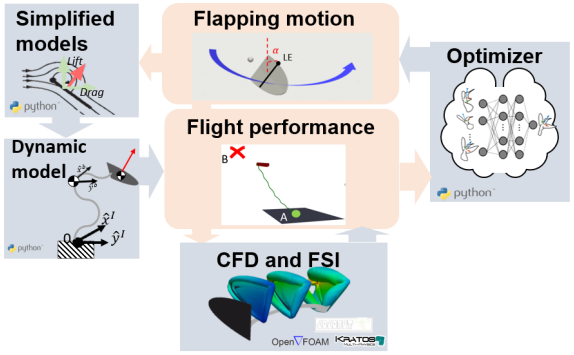

Figure 1: Methodology followed in the PhD to simulate and control flapping wings

2. Research objectives

This article presents the work performed during this second year of PhD. It focuses on four main topics and motivates intermediate goals that are essential to fulfill the control objective of figure 1.

1. *CFD*: development of a CFD environment to simulate 3D flapping wings in hovering conditions (section 3.1). The environment aims to provide high-quality data to a Reduced Order Model (ROM) as well as to allow the study of aerodynamics performance from various flapping kinematics through advanced post-processing techniques (section 4.2).
2. *Simplified models*: development of a CFD data-driven ROM to predict the aerodynamic performance of given flapping motions (section 3.3). The objective is to leverage machine learning techniques to design a fast and accurate model that could improve the literature state-of-the-art (section 4.2).
3. *FSI*: development of an FSI environment to simulate flexible wings (section 3.2). The pursued objective is to validate the implementations on a 2D test case and show their adequacy to perform aeroelasticity analysis (section 4.1).
4. *Dynamic model and control*: development of a dynamic model to simulate the motion of flapping drones according to the wing motion and forces (section 3.4). The objective of this paper is to show the capability of the model thanks to a simple control scenario (section 4.3).

3. Theoretical background

3.1. CFD of rigid wings

According to figure 1, high-fidelity CFD simulations set a mapping between wing motions and aerodynamic forces. The article from the previous PhD symposium described the CFD environment for rigid flapping wings. The environment was validated with 2D foils and 3D elliptical wings stated in section 2.

The open-source software OpenFOAM hosts the CFD simulations based on the finite volume method. The solver is named *overPimpleDyMFoam* which is transient, incompressible, and uses the PIMPLE algorithm. The solver implements the overset method to move the grid according to the flapping wing. Reviews of this dynamic mesh technique are found in [3] and [4]. In short, the overset method splits the computational domain into multiple overlapping grids. For the present case, a small grid, called the component grid, follows the wings and overlaps a large background grid. One equation system solves simultaneously the flow on both grids for which inter-grid interpolation replaces the missing boundary conditions (strong coupling algorithm [4]). The inverse distance interpolation is used but the least square method and cell-volume weights were giving similar results [3].

As seen in figure 2, $430k$ hexahedral cells compose the domain. The component grid has a C-grid topology ($\sim$ 2 chord width) with inflation layers to accurately capture the boundary layer dynamics. The background grid is a cube ($\sim$ 10 span to limit boundary effects [5]). A refinement zone is set where the wing is expected to flap such that the cell size of the background and component grid coincides at their interface. This minimizes interpolation errors [4]. As regards boundary conditions, hovering conditions are simulated so Neumann conditions apply for the velocity field and Dirichlet conditions for the pressure on all the domain external boundaries.

Considering the low Reynolds number $Re = O(10^2 - 10^4)$ of natural flyers [6], a laminar model is often used but a LES model was also tested in [7]: the results were independent of the turbulence model. As regards numerical discretization, second-order schemes discretize the spatial and time terms. Simulation has variable time steps constrained by the Courant number $CFL < 1$.

In order to derive a data-driven ROM (section 3.3), 165 simulations were performed with 2 degrees of freedom flapping kinematics defined by the popular parametrization [8]:

$$\phi(t) = \frac{A_\phi}{\arcsin(K_\phi)} \arcsin[K_\phi \sin(2\pi f t)] \quad (1)$$

$$\alpha(t) = \frac{A_\alpha}{\tanh(K_\alpha)} \tanh[K_\alpha \sin(2\pi f t)]\,. \quad (2)$$

ϕ defines the flapping motion and α the pitching, f the flapping frequency, A_ϕ and A_α the flapping and pitching amplitude while K_ϕ and K_α are the shape factors that can adapt the motion from a smooth harmonic motion (K's low) to a motion with strong accelerations (K's high).

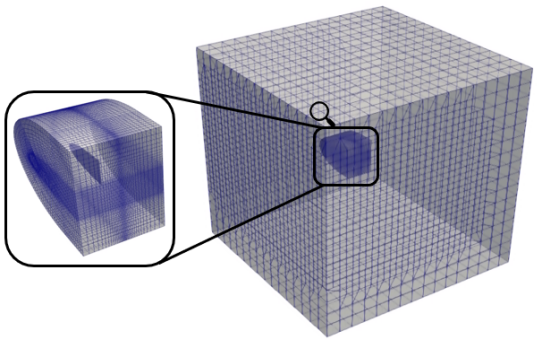

Figure 2: Background grid and its component grid (zoom) for a 3D elliptical wing

Advanced post-processing. Identifying and tracking coherent structures is particularly useful when comes the analysis of unsteady aerodynamics. While the classical $Q - criterion$ and λ_2 criterion are very insightful on the vortex dynamics, those fields are not objective and so can lead to wrong interpretations depending on the frame of analysis [9]. In comparison, finite-time Lyapunov Exponents (FTLE) is an objective scalar field which ridges define Lagrangian coherent structures and unambiguously capture vortex dynamics. The first step in the computation of an FTLE field is to initialize an auxiliary grid of particles, typically more refined than the CFD grid. The second step is to compute the flow map from each particle of the auxiliary grid $\mathbf{x_0}$ toward its final position after a time T_f:

$$\mathbf{\Phi}_{t_i}^{t_i+T}(\mathbf{x_0}, t_i) = \mathbf{x_0} + \int_{t_i}^{t_i+T_f} \mathbf{u}(\mathbf{x}(\tau))d\tau \quad (3)$$

Equation 3 time integrates the trajectories of all the particles from t_i to $t_i + T_f$ (here with a trapezoidal scheme). This operation is extremely computationally intensive since it also involves velocity interpolation from the CFD to the auxiliary grid $\mathbf{u}(\mathbf{x}(\tau))$ at each time step (here with an 8 points linear scheme). The time step $d\tau$ and integration time T_f are then tuned depending on the accuracy needed and computational power available. A small $d\tau$ and large T_f will tend to capture accurately the long structures but might take weeks of computation. The third step computes the Cauchy-Green deformation tensor based on the Jacobian of the flow map:

$$\mathbf{\Delta} = (D^* \mathbf{\Phi}_{t_i}^{t_i+T_f}) D\mathbf{\Phi}_{t_i}^{t_i+T_f} \quad (4)$$

Finite differencing approximates the Jacobian $D\mathbf{\Phi}_{t_i}^{t_i+T_f}$. Finally, the FTLE scalar field is given by:

$$\sigma(\mathbf{\Phi}_{t_i}^{t_i+T_f}, \mathbf{x_0}) = \frac{1}{|T_f|} log\sqrt{\lambda_{max}(\mathbf{\Delta}(\mathbf{x}_0))} \quad (5)$$

It is the scaled, maximum eigenvalue of the deformation tensor at each particle grid. A high FTLE value indicates regions where trajectories stretch the most [10]. Similarly, if equation 3 is integrated backward, the (negative) FTLE shows the attracting lines where particle trajectories gather the most. The present article focuses on negative FTLE since it identifies the boundaries of vortical structures that play a dominant role in force generation. As a final note, for an unsteady flow, equation 5 must be solved for each time step increasing a lot the computation effort.

3.2. FSI of flexible wings

The CFD environment presented in the previous section assumes rigid wings. As described in the introduction, natural species take advantage of their wing flexibility to improve their flight performance. The next section describes the early stages of a fluid-structure interaction environment with the help of a 2D test case. It consists of a rigid teardrop airfoil followed by a flexible plate (in red on figure 3). The airfoil flaps along $\hat{y}$ according to $y(t) = Asin(\omega t)$, which deforms the plate. The main parameters are summarised in table 1. Both experiments and CFD

results are available in the literature [11][12] such that section 4.1 evaluates the trailing edge position of the plate TE and the aerodynamic forces of the developed FSI framework.

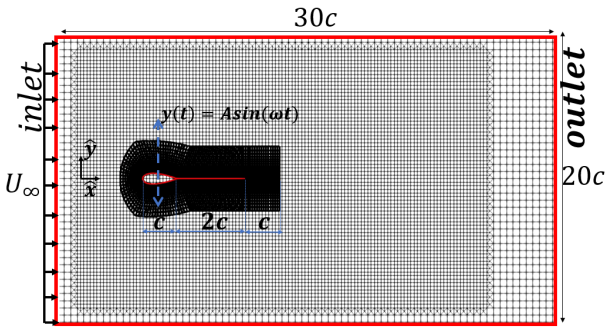

Figure 3: Validation test case of the FSI environment [11]: a flapping foil and a flexible plate in an incoming flow

c	$[m]$	0.03	b/c	$-$	$0.56e-3$
ρ_f	$[kg/m^3]$	1000	E	N/m^2	$2.05e11$
U_∞	$[m/s]$	0.1	ρ_s	$[kg/m^3]$	7850
f	$[1/s]$	0.96	γ	$-$	0.2
Re	$[-]$	9k			
St	$[-]$	0.34			

Table 1: Main parameters of the flapping and flexible foil test case [11]

3.2.1. FSI framework

The airfoil flaps and generates aerodynamic forces due to its surrounding flow. The pressure and shear deform the flexible structure which subsequently alters the aerodynamic forces and so on. The simulation involves then solving flow equations to compute the aerodynamic forces, solving structure equations to compute the wing deformation, and coupling loads and deformations at an FSI interface (i.e. the flexible plate). The FSI environment follows a partitioned approach where flow and structure equations are solved with two independent software (OpenFOAM and Kratos Multiphysics). This strategy allows to reuse available software that use optimal methods to solve flow and structure problems but requires a coupling unit [13]. The open-source Python code CoCoNUT takes care of the coupling thanks to the applications *coconut_overPimpleDyMFoam*, a developed FSI solver with overset capabilities. The latter calls:

A coupling solver: The FSI pursues a staggered algorithm for which multiple flow and structure equations are solved during one time step, until a given convergence is reached at the interface. The interface quasi-Newton with inverse Jacobian method (IQNI) ensures the convergence [13]. The method makes the coupling stable and fast to converge for strongly coupled problems with high added-mass effect. The reader is referred to [14] that describes the IQNI method and other convergence techniques in great details. Parametric studies on the coupling tolerance and other numerical parameters are reported in [15].

Two solver wrappers: they rule the computations inside the CFD and CSM solver as well as the communication between it. It reports when a given computation must be performed and when the results must transmitted/received at the FSI interface.

A solver mapper: it interpolates the loads from the fluid grid to the structural grid of the plate and vice versa. Interpolation is not strictly needed here since the grids of the flow and structure solver coincide. The two next subsections describe the CFD and CSM frameworks.

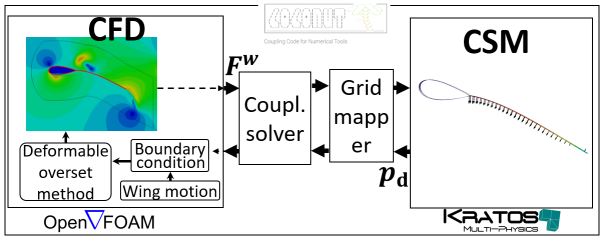

Figure 4: Block diagram of the FSI environment defined with OpenFOAM (CFD), Kratos Multiphysics (CSM) and coupled with CoCoNut

3.2.2. Computational Fluid Dynamics

Based on the deformed wing state, the flow around the wing is solved to compute the pressure and shear stress applied on the plate. Section 3.1 recalled most of the elements involved in the CFD simulations of flapping wings. The CFD from the FSI depends mainly on the same methods and schemes [16]. The grid philosophy is similar (figure 3 and 6) but has two main differences. First, the wing is very thin (table 1) such that a zero-thickness baffle models the plate. Secondly, the dynamic mesh type is different. The overset method is combined with a deforming mesh technique that morphs the component grid cells according to the plate state. This original contribution to OpenFOAM adds another system of equations to emulate the grid deformation.

While various strategies exist [17], the classical Laplace smoothing equation was selected since it is computationally cheap and gave accurate aerodynamic predictions on similar cases [18]. The Laplace equation distributes non-uniformly the mesh deformation in the domain according to:

$$\nabla \cdot (\gamma \nabla(\mathbf{p_d})) = 0 \tag{6}$$

where $\mathbf{p_d}$ is the point displacement of the cells which updates the point coordinates $\mathbf{p_{k+1}} = \mathbf{p_k} + \mathbf{p_d}$ at the next time step $k + 1$. γ is the diffusivity that rules how the mesh motion diffuses from the moving foil to the component grid boundaries. It is function of the inverse distance from the foil in order to strongly deform the cells only near the wing and hence preserve mesh quality [19].

Equation 6 is usually solved with Neumann conditions on the component boundaries. It deforms the mesh and propagates the deformation from the foil towards the boundary which follows the plate motion (region 1 in figure 5). For the region after the plate tip (region 2), the cells remain mainly static (with reference to the moving frame) since no boundary imposes any mesh deformation. Therefore, at the interface between the two regions, mesh quality degrades significantly and rapidly leads to a simulation crash (figure 5). One solution is to enforce the point displacement on the component grid boundaries. Currently, for zone 1, the simplest one-to-one interpolation is implemented, taking advantage of the grid topology. The x and y point displacements at the plate are imposed at the corresponding cells on the upper and lower component boundaries. As regards zone 2, a line is fitted from the last two cell points of the plate. This function is then used to compute the y coordinates of the component patch in zone 2. Finally, the x-point displacement measured at the plate tip is imposed on every boundary point of region 2. As seen in figure 6, the implemented method preserves high-quality cells and extension of the methods for 3D wings is foreseen as the next step (section 5).

3.2.3. *Computational Structural Mechanics*

Kratos Multiphysics is an open-source, multiphysics, FEM software. Its structural solver computes the deformation of the plate nodes p_d according to the applied aerodynamic loads and shear. Corotational, 4 nodes, 3D, 6 dof shell elements model the slender plate model on the same baffle grid defined in the fluid solver. Steel materials compose the plate and table 1 lists the main structural parameters. Finally, the LE

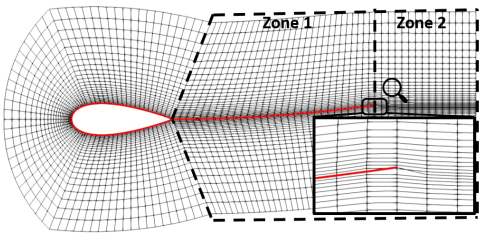

Figure 5: Deformed component grid with zero gradient boundary conditions

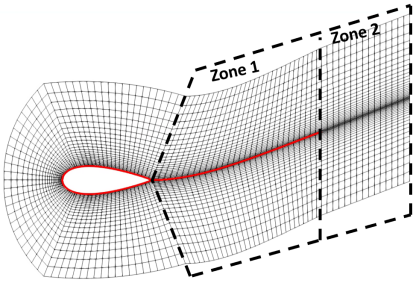

Figure 6: Deformed component grid with interpolation boundary conditions

of the plate moves according to the flapping motion of the airfoil (figure 3). The motion of the TE of the airfoil matches the one of the LE of the plate while the rest of the nodes are solved. More information on the structural set-up in Kratos is given in [15].

3.3. *Simplified aerodynamic models*

Similarly to CFD, simplified aerodynamic models map wing motion to aerodynamic forces but at a much lower computational cost. The article from the previous PhD symposium reviewed the three different time-based aerodynamic models (steady, quasi-steady (QS) and unsteady) [3]. The majority of control applications relies on QS steady models since they benefit from an algebraic expression calibrated with reference data (i.e. fast evaluation with reasonable accuracy). One such literature model was implemented in Python for hovering [20]:

$$C^w(t) = f(Re, AR, Ro) \cdot [C_{tr}(t) + C_r(t) + C_a(t)] \tag{7}$$

where the total dimensionless instantaneous force $C^w(t)$ breaks down into $C_{tr}(t)$ the force due to the translation of the wing, $C_r(t)$ the force due to the pitching of the wing, and $C_a(t)$ the added mass force. The force expression derived from flapping aerodynamics and the reader is referred to the article from

the previous PhD symposium for an introduction [3]. In equation 7, $f(Re, AR, Ro)$ are calibration functions obtained from CFD regressions which modulate the force production as a function of the wing motion and geometry. Overall, the model offers good predictions for smooth motions with simple wing geometries but fails in cases with strongly dynamic flappings in which vortex dynamics becomes strongly unsteady (section 4.2 for more details). Nevertheless, those kinematics are relevant for a number of flight scenarios such as hovering, escape maneuvers, etc [21] [8].

The present research has developed a new data-driven QS model for hovering flight that applies to various different wing kinematics. The results are to be published in [7] and the following briefly summarises the model in order to compare it with model (7) in section 4.2.

The model definition involves a data generation phase and a training phase. First, $n_{CFD} = 165$ CFD simulations were performed with different kinematics (equation 1 and 2) driven by 5 parameters $\mathbf{x} = [R_e, k, A_\alpha, K_\phi, K_\alpha]$. Latin Hypercube sampled the cases from a parameter space typical of natural flyer hovering. The training phase takes then 85 % of the CFD cases, and more specifically their lift and drag, to calibrate a linear Reduced Order Model (ROM) parametrized by some weights $\mathbf{w}$:

$$C(t) = \sum_{j=1}^{n_f} b_j(t) w_j = \mathbf{b}^\top(t)\mathbf{w}\,, \tag{8}$$

$$\begin{aligned}\mathbf{b}(t) = [\,&\cos(\phi), |\ddot{\alpha}|, \dot{\phi}^2, \dot{\alpha}^2, \dot{\phi}\ddot{\phi},\\ &\dot{\alpha}\ddot{\alpha}, \sin(2\alpha)\dot{\alpha}, \sin(2\alpha)\sin(\phi)](t)\,.\end{aligned} \tag{9}$$

$\mathbf{b}(t)$ is a known $n_t \times n_f$ matrix for which n_t is the number of time steps per flapping cycle and n_f the number of features which are computed with (1) and (2). The feature selection in (9) takes inspiration from QS models [22][23] plus some unconventional terms, calibrated through a trial and error procedure. For each n_{CFD} case, the $2n_f$ set of weights $\mathbf{w}$ is optimized with Ridge regression such that lift and drag errors are minimized between CFD computation and (8).

The second stage of the training considers an out-of-cycle regression. It uses the $0.85 \cdot n_{CFD}$ training weights to derive the mapping from each of the $2n_f$ weight $\mathbf{w}$ to the kinematic parameters $\mathbf{x}$. To this end, Gaussian Process Regression is used because of its flexibility, sample efficiency and natural formulation of the model uncertainty. Derivation details are found in [7]. The final stage involves Hyperparameter Optimization (HPO) to find the optimal value of the hyperparameters related to the in and out-of-cycle regression.

3.4. Dynamic models

The aim of the dynamics model is to map the aerodynamic forces of the wings to the drone acceleration through its equation of motion. Most of the literature uses on 6 degrees of freedom drones based on standard aircraft dynamics [24].

The equations of motion formulated in the body frame b are defined by Newton-Euler equations:

$$m_b(\dot{\mathbf{u}}^b + \boldsymbol{\omega}^b \times \mathbf{u}) = \mathbf{F}^b + m_b\mathbf{g} \tag{10}$$

$$\boldsymbol{I_b}\dot{\boldsymbol{\omega}} + \omega^b \times I_b\omega^b = \mathbf{T}^b \tag{11}$$

As elsewhere in the text, the bold notation indicates vectors or matrices such that equations (10) and (11) define a 6 equation system. $\dot{\mathbf{u}}^b = [\dot{u}, \dot{v}, \dot{w}]$ and $\dot{\boldsymbol{\omega}}^b = [\dot{p}, \dot{q}, \dot{r}]$ are the unknown linear and angular body acceleration in the body frame attached to the 6 degrees of freedom of the drone. m_b and I_b defines the body mass and inertia matrix and $\mathbf{F}^b$ and $\mathbf{T}^b$ the aerodynamic forces and torques[1]. In the simplified aerodynamic model and CFD computations, the forces are first computed in the wing frame by the aerodynamic models ($\mathbf{F}^w$, section 3.3) and then transformed into the body frame $x\hat{y}z_b$ thanks to three rotation matrices based on the wing state $s_w = (\phi(t), \alpha(t))$:

$$\mathbf{F}^b = \mathbf{L_y}(\beta)\mathbf{L_z}(\phi)\mathbf{L_y}(\alpha)\mathbf{F}^w \tag{12}$$

$L_z(\phi)$ defines a 3x3 matrix that rotates vector from the $x\hat{y}z_\beta$ to $x\hat{y}z_\phi$ frame along the $\hat{z}_\phi$ axis. β is the stroke plane angle [25]. Until now, $\beta = 0[^\circ]$ but will be varied in section 4.3 to unlock forward flight. $\mathbf{L_y}(\alpha)$ is defined similarly with the help of figure 7.

Equation 10 and 11 can not directly be solved as they also depend on the body orientation with respect to the inertial frame $x\hat{y}z_I$. Indeed, $\mathbf{g}$ is directed along $\hat{z}_I$ and must be projected in the body frame thanks to three consecutive rotations, the Euler angles $\boldsymbol{\Xi} = [\Psi, \Theta, \Phi]$ [24]. Those angles evolve with time and their time derivative can be defined with the linear relation:

$$\dot{\boldsymbol{\Xi}} = \mathbf{A}(\boldsymbol{\Xi})\boldsymbol{\omega}^b \tag{13}$$

[1] $\mathbf{F}^b$ and $\mathbf{T}^b$ are referred to "forces" here after

where $\mathbf{A}(\boldsymbol{\Xi})$ is a matrix function of the Euler angles. Three equations are then added to (10) and (11).

Finally, the Euler angles are also used to convert the body acceleration into the inertial frame $\dot{\mathbf{u}}^I = [\dot{x}^I, \dot{y}^I, \dot{z}^I]$.

$$\dot{\mathbf{u}}^I = f(\mathbf{u}^b, \boldsymbol{\Xi}) \tag{14}$$

where f is a non linear function detailed in [24].

Three additional kinematic equations complete then the dynamical system of 12 ordinary differential equations with 12 unknowns $\dot{s_b} = [\dot{u}, \dot{v}, \dot{w}, \dot{p}, \dot{q}, \dot{r}, \dot{\Psi}, \dot{\Theta}, \dot{\Phi}, \dot{x}^I, \dot{y}^I, \dot{z}^I]$.

Starting from an initial body state $s_{b,0}$ and wing state $(s_{w,0}, \dot{s}_{w,0})$, the wing forces $\mathbf{F}^w$ are computed and transformed in the body frame (equation 12). The body state variables along with the external forces feed equations (10), (11), (13), and (14) that are solved for $\dot{s_b}$ at each time step. $\dot{s_b}$ is then time-integrated with the Runge Kutta integration scheme and hence allows to follow the drone trajectory.

The dynamic system has been implemented in a Python environment. For section 4.3, m_b is 5g as inspired by hummingbirds [26] and the drone is assumed spherical such that only the diagonal terms $I_{b,xx} = I_{b,yy} = I_{b,zz} = 1e-5\ [m^2/s^2]$ are non-zero. The simulation parameters for the wing geometry, wing motion and body are summarised in table 2.

This 6 dof models benefits from its simplicity but relies on strong assumptions. First, the wing mass is neglected. This is often observed in nature for many species where insect body gathers more than 95% of the mass [27]. Secondly, the inertial coupling of the wing and the body is also omitted. The flapping frequency is assumed high enough not to excite body modes. [28] and [27] noted that this assumption rigorously holds only when cycle average dynamics is considered. Otherwise, the trajectories can differ a lot including this effect or not for different representative flapping drones.

In this PhD, the latter hypotheses are adressed thanks to a multi-body drone defined with *PyDy* libraries of Python [29]. The latter generates the equations of motion in a symbolic fashion based on the Kane method and few kinematics and dynamics parameters. The drone's body has 6 dof with respect to the ground (3 translations and 3 rotations) and 4 others between the two wings and the body (i.e. ϕ, α). This complexifies significantly the dynamical system which can be summarised by:

$$\ddot{\mathbf{q}} = fd(model, \mathbf{q}, \dot{\mathbf{q}}, \mathbf{g}, \mathbf{Q}, \mathbf{F^w}) \tag{15}$$

fd is the acronym of forwards dynamics and $\mathbf{Q}$ are the joint forces/torques. The system served as validation for the 6dof in-house environment and will not be further investigated in the frame of this article.

Wing		Body		Flapping	
c	0.015	m	0.005	A_α	45
ΔR	0.0225	I	1e-5	K_ϕ, K_α	0.01
R	0.05			f	20

Table 2: Reference parameters of the drone in SI units

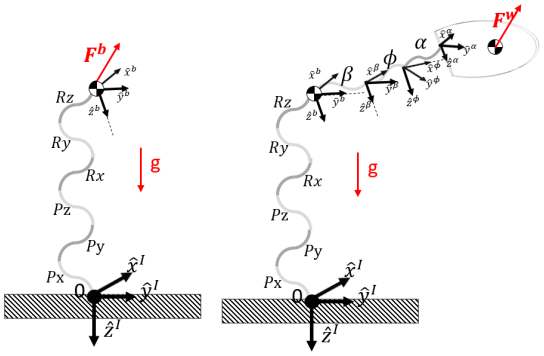

Figure 7: Kinematic illustration of a 6 dof, single body drone (left) and a 18 dof, three body drone (right)

4. Results

4.1. FSI validation

Section 3.2 presented an FSI environment with the help of a 2D flapping and flexible wing (figure 3). The present section validates the implementations thanks to reference data [11] [12] [30].

First, the deformable overset method is validated on a simplified coupled framework (figure 4). A user-defined function replaces the CSM block and enforces the plate deformation at each time step while the airfoil still follows the usual flapping law (figure 3). The deformation function is a parabola between the TE position of the airfoil and the TE position of the plate that was measured experimentally (for $b/c = 0.56e3$) [11]. Figure 8 compares the thrust with the one computed from the CFD of [12]. Both curves match quantitatively well with a mean error below 5%. This confirms the adequacy of the deformable overset method to accurately simulate flapping wings that experience large deformation.

Figure 9 validates the complete FSI environment (figure 4). As a result of the flapping motion from the

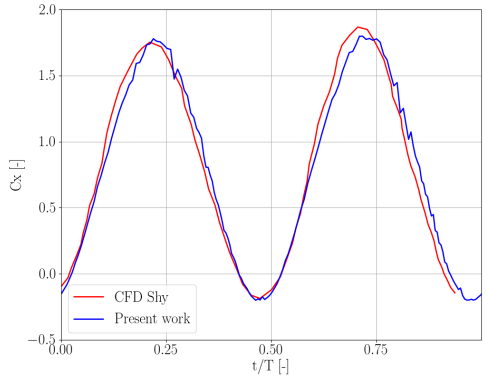

Figure 8: Thrust coefficient computed from OpenFOAM using the deformable overset method and compared with a literature CFD [12]

airfoil, the plate is deforming according to the flow forces. The TE motion of the plate matches well with the experiments [11] (HeathCote) as well as with a literature FSI [30] (Kang). The aerodynamic benefit of flexible structures can already be analyzed in this 2D case by increasing the thickness of the plate (and so increasing the flexibility). [16] highlights that there is an optimal flexible ratio to reach the largest propulsive efficiency (thrust-to-power ratio).

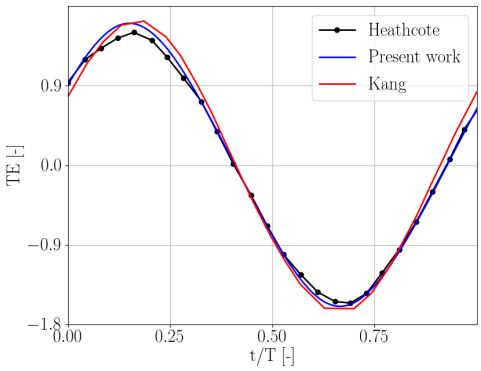

Figure 9: TE displacement predicted by the CoCoNut FSI environment compared with experiments [11] and literature FSI [30]

4.2. *Simplified model comparison*

The present section compares the two aerodynamic models presented in section 3.3: an analytical model with calibrated empirical coefficients [20] and the CFD data-driven ROM developed in the frame of this PhD [7].

Figure 10 compares the root mean square error $\frac{1}{n_t}\| \mathbf{C_{CFD}} - \mathbf{C_{ROM}} \|_2$ of the forces predicted by the simplified models C_{ROM} and the reference CFD C_{CFD} for 25 test cases (not seen during training). The test cases involve very different kinematic parameters $\mathbf{x}$, even sets that natural fliers would not fly or would not be able to fly. Overall, both models reach good accuracy for most of the tested kinematics. This is also noted in the article [7] with Pearson Correlation Coefficient (PCC) between all the CFD data and all the ROM predictions of 0.93 for both drag and lift. The present model reaches better accuracy for lift while worse for drag. This mainly originates from the strongly dynamic cases included in the test pool. For the latter, the features selected (equation 9 which is the same for lift and drag) are sub-optimal [7].

Two force comparisons illustrate the model capability and limits in figure 11 for a moderately dynamic kinematics, and in figure 12 for a strongly dynamic kinematics. In figure 11, the developed *ROM* (red) matches very well the lift curve computed by CFD (black) and the dominant aerodynamic mechanisms are captured. For example, focusing on the lift cuve, the added mass effect is related to the force spikes, the leading edge vortex (LEV) is the main lift contributor and relates to the overall sinusoidal trend while the negative wing-wake interaction can justify part of the difference between ROM and Lee lift during the first half-stroke. Indeed, the Lee model (blue) has no wing-wake interaction contribution while the proposed model, through the features selected (equation 9), has the freedom to model this effect in some cases.

Figure 12 shows much larger discrepancies between the ROM and the CFD. This is due to the very strong dynamic motion, not often encountered in the training data and hence poorly generalized with the Gaussian process regression. Figure 13 gives details on the vortex dynamics thanks to the FTLE ridges and the Q criterion. The figure focuses on three instants corresponding to figure 12. At the beginning of the upstroke (A), the wing is pitching and two small vortices, rotating in the same direction, are formed at the LE and TE. Ridges of the FTLE highlight this behavior. Those vortices do not remain attached to the wing due to the very strong acceleration and high angle of attack. As written above, the wing acceleration (flapping and pitching) generates the added-mass effect but can not be seen through these circulatory fields. On the other hand, the pressure shows a large suction zone on the extrados of the wing. At time (B), FTLE shows that the LEV is still not attached to the wing and that a TEV gets again shed in the wake. When the acceleration reduces, the attached LEV forms and grows until mid-stroke. The attached LEV can be well seen in (C) with both FTLE and Q-criterion.

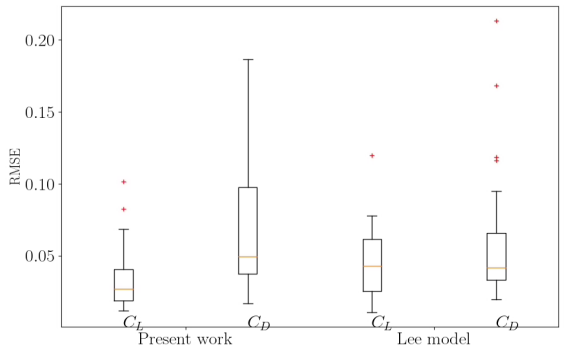

Figure 10: RMSE Box plots on the test data for the lift and drag coefficients for a literature model [20] and the developed model [7]

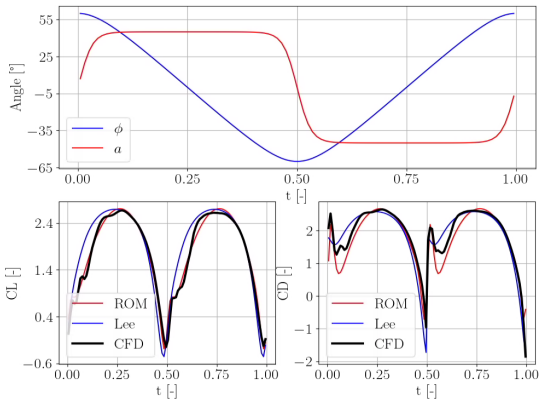

Figure 11: ROM comparison for flapping kinematics with parametrisation according to equation (1) and (2) with $A_\phi = 60°, A_\alpha = 45°, K_\phi = 0.9, K_\alpha = 5, f = 15$

4.3. *Dynamic model simulation*

This section presents one preliminary result of the dynamic environment described in section 3.4 and fully implemented in Python. The main components involved in the simulation are: a wing kinematic parametrization (equation 1 and 2), an aerodynamic model (the literature model, equation 7) and a dynamic system defined with 6 dof equations of motion (equation 10 to 14). The latter are time integrated to compute the drone trajectories as an indirect function of the flapping motion. A controller can also close the loop as shown in diagram 1. Hereafter, a simple PID controller is implemented to make the flapping drone (table 2) move from A = (0,0,0) to B=(0.1,0,0.1) $[m]$. The controller adapts the flapping amplitude A_ϕ and the stroke plane angle β based on the error between the measured position (x, z) and the target position (figure 15 and 16). The simulation lasts 30 flapping cycles (1.5 $[s]$).

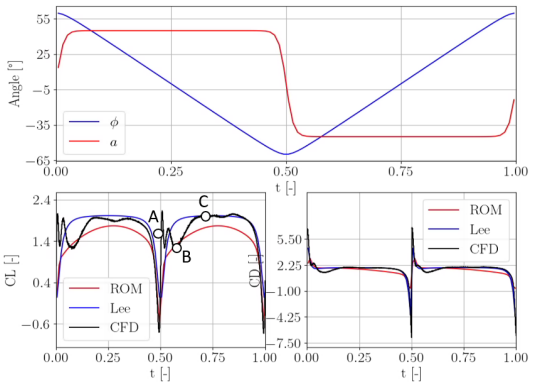

Figure 12: ROM comparison for flapping kinematics with parametrisation according to equation (1) and (2) with $A_\phi = 60°, A_\alpha = 45°, K_\phi = 0.99, K_\alpha = 10, f = 20$

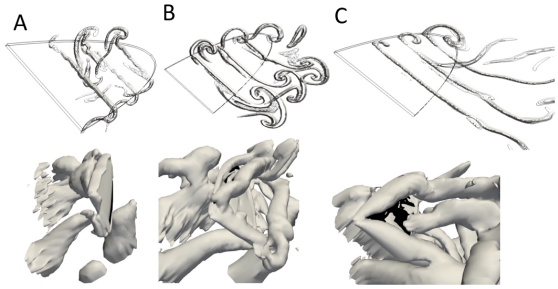

Figure 13: Ridges of the FTLE field on three slices of the wing (upper row) and iso-contour of the Q-criterion (lower row) for the kinematics defined in figure 12

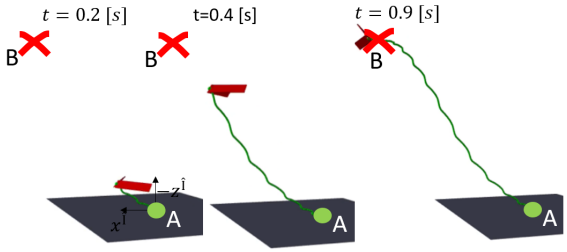

Figure 14: Visualization of the A to B trajectory of a flapping drone controlled by a PID controller

5. Conclusion and future work

This article has reviewed four main tools developed in a multidisciplinary environment that can simulate and control flapping wings in various flight scenarios. A high-fidelity CFD framework, based on the overset method, allows to simulate any rigid wings in flapping motion. Thanks to advanced post-processing techniques, the CFD can evidence the complex vor-

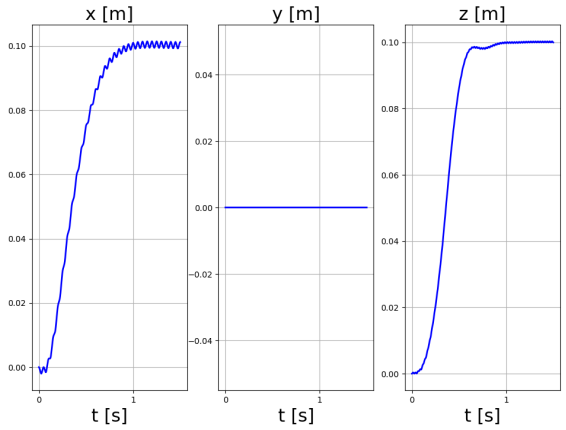

Figure 15: x, y, and z position of a flapping drone during the A to B trajectory controlled by a PID law

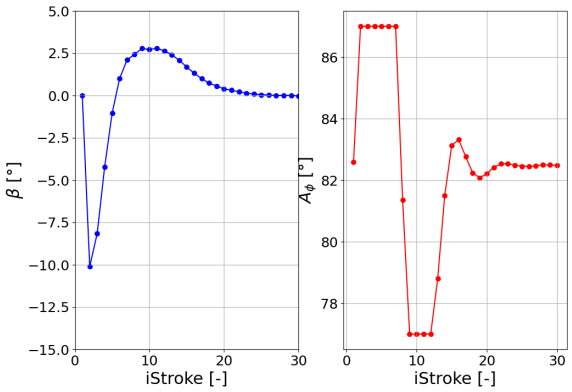

Figure 16: Control of the stroke plane angle β and the flapping amplitude A_ϕ during flight scenario of figure 15

tical phenomena that shape the aerodynamic performance. A simplified model also estimates the aerodynamic performance but in much less computational time. The current research has developed a CFD data-driven ROM based on Ridge regression and Gaussian processes. The model showed accurate results for smooth and reasonably dynamic wing motions, capturing the dominant aerodynamic mechanisms. The model feeds a dynamic model that simulates the drone trajectories. The motion equation of a 6 dof drone as well as a multi-body drone were both implemented in Python. A PID controller applied on a simple flapping motion has demonstrated the work efficiency of the dynamic environment. Finally, an FSI environment was also developed to analyse the influence of wing flexibility on the force generation. The environment was validated on a 2D flapping foil and will be extended in 3D in the future steps. For each of the tools, the upcoming work are:

- *CFD:* 165 simulations have been run to train the ROM. Those simulations abound of precious information on the aerodynamics of flapping wings. An article will be published in a journal paper: "On the aerodynamic analysis of dynamic flapping motions in hovering conditions".

- *FSI:* A 3D environment will extend the current 2D FSI. The results will be published in the conference paper from COUPLED 2023: *Development of an FSI environment for the aerodynamic performance assessment of flapping wings*.

- *Simplified models:* Future work will test other feature set and extend the ROM to more complex flapping conditions (e.g. adding wing flexibility, other wing conditions).

- *Dynamic models:* A throughout comparison of the two dynamic models will be pursued. The influence of different aerodynamic models on the drone trajectory will be also analysed. Then, major part of the work will be devoted to test different control strategies and evaluate which fits best in complex flight scenarios. PID, Bayesian optimisation and reinforcement learning will be the main candidates.

Acknowledgments

This work heavily relies on the contribution of STPs Rebecca Stanciu, Michele Barucca and Emanuele Bombardi as well as RM André Calado.

References

[1] D. D. Chin, D. Lentink, Flapping wing aerodynamics: from insects to vertebrates, Journal of Experimental Biology 219 (7) (2016) 920–932.

[2] W. Shyy, H. Aono, C.-k. Kang, H. Liu, An introduction to flapping wing aerodynamics, Vol. 37, Cambridge University Press, 2013.

[3] R. Poletti, J. van Beeck, D. Joris, On the limits of quasi-steady models for flapping wing aerodynamics.

[4] H. Hadzic, Development and application of finite volume method for the computation of flows around moving bodies on unstructured, overlapping grids, Technische Universität Hamburg, 2006.

[5] C. Badrya, A. Sridharan, J. D. Baeder, C. M. Kroninger, Multi-fidelity coupled trim analysis of a flapping-wing micro air vehicle flight, Journal of Aircraft 54 (5) (2017) 1614–1630.

[6] D. D. Chin, D. Lentink, Flapping wing aerodynamics: from insects to vertebrates, Journal of Experimental Biology 219 (7) (2016) 920–932.
[7] A. Calado, R. Poletti, L. Koloszar, M. A. Mendez, A robust data-driven model for flapping aerodynamics under different hovering kinematics, Physics of Fluid.
[8] G. J. Berman, Z. J. Wang, Energy-minimizing kinematics in hovering insect flight, Journal of fluid mechanics 582 (2007) 153–168.
[9] G. Haller, Lagrangian coherent structures, Annual review of fluid mechanics 47 (2015) 137–162.
[10] S. Krishna, M. A. Green, K. Mulleners, Effect of pitch on the flow behavior around a hovering wing, Experiments in Fluids 60 (2019) 1–17.
[11] S. Heathcote, I. Gursul, Flexible flapping airfoil propulsion at low reynolds numbers, AIAA journal 45 (5) (2007) 1066–1079.
[12] W. Shyy, H. Aono, S. K. Chimakurthi, P. Trizila, C.-K. Kang, C. E. Cesnik, H. Liu, Recent progress in flapping wing aerodynamics and aeroelasticity, Progress in Aerospace Sciences 46 (7) (2010) 284–327.
[13] J. Degroote, K.-J. Bathe, J. Vierendeels, Performance of a new partitioned procedure versus a monolithic procedure in fluid–structure interaction, Computers & Structures 87 (11-12) (2009) 793–801.
[14] N. Delaissé, T. Demeester, D. Fauconnier, J. Degroote, Comparison of different quasi-newton techniques for coupling of black box solvers, in: 14th World Congress on Computational Mechanics/8th European Congress on Computational Methods in Applied Sciences and Engineering, 2021.
[15] M. Barucca, Master thesis report: Fluid structure interaction simulation of a flexible flapping wing, April 2023, VKI, politecnico Milano.
[16] R. Stanciu, Intership report: Cfd study of flapping wings with the deformable overset method, VKI, ESTACA, 2022.
[17] T. Xiao, N. Qin, D. Luo, S. Deng, Deformable overset grid for multibody unsteady flow simulation, AIAA Journal 54 (8) (2016) 2392–2406.
[18] M. Alletto, Comparison of overset mesh with morphing mesh: Flow over a forced oscillating and freely oscillating 2d cylinder, OpenFOAM® Journal 2 (2022) 13–30.
[19] H. Jasak, Z. Tukovic, Automatic mesh motion for the unstructured finite volume method, Transactions of FAMENA 30 (2) (2006) 1–20.
[20] Y. Lee, K.-B. Lua, T. Lim, K. Yeo, A quasi-steady aerodynamic model for flapping flight with improved adaptability, Bioinspiration & biomimetics 11 (3) (2016) 036005.
[21] B. Cheng, B. W. Tobalske, D. R. Powers, T. L. Hedrick, S. M. Wethington, G. T. Chiu, X. Deng, Flight mechanics and control of escape manoeuvres in hummingbirds. i. flight kinematics, Journal of Experimental Biology 219 (22) (2016) 3518–3531.
[22] Y. E. Bayiz, B. Cheng, State-space aerodynamic model reveals high force control authority and predictability in flapping flight, Journal of the Royal Society Interface 18 (181) (2021) 1–10. arXiv:2103.07994, doi:10.1098/rsif.2021.0222.
[23] T. Nakata, H. Liu, R. J. Bomphrey, A CFD-informed quasi-steady model of flapping-wing aerodynamics, Journal of Fluid Mechanics 783 (October) (2015) 323–343. doi:10.1017/jfm.2015.537.
[24] B. Etkin, L. D. Reid, Dynamics of flight: stability and control, John Wiley & Sons, 1995.
[25] F. Leys, D. Reynaerts, D. Vandepitte, Outperforming hummingbirds' load-lifting capability with a lightweight hummingbird-like flapping-wing mechanism, Biology open 5 (8) (2016) 1052–1060.
[26] J. Song, H. Luo, T. L. Hedrick, Three-dimensional flow and lift characteristics of a hovering ruby-throated hummingbird, Journal of The Royal Society Interface 11 (98) (2014) 20140541.
[27] C. T. Orlowski, A. R. Girard, Modeling and simulation of nonlinear dynamics of flapping wing micro air vehicles, AIAA journal 49 (5) (2011) 969–981.
[28] H. E. Taha, M. R. Hajj, A. H. Nayfeh, Flight dynamics and control of flapping-wing mavs: a review, Nonlinear Dynamics 70 (2012) 907–939.
[29] `https://www.pydy.org/`.
[30] C.-K. Kang, H. Aono, C. E. Cesnik, W. Shyy, Effects of flexibility on the aerodynamic performance of flapping wings, Journal of fluid mechanics 689 (2011) 32–74.

Variational multiscale method in Julia

Carlo Brunelli

Aeronautics and Aerospace Department, von Karman Institute for Fluid Dynamics, Belgium, carlo.brunelli@mil.be

Supervisor: Georg May

Associate Professor, Aeronautics and Aerospace Department, von Karman Institute for Fluid Dynamics, Belgium, georg.may@vki.ac.be

Supervisor: Bart Janssens

Associate Professor, Mechanical Engineering Department, Royal Military Academy, Belgium, Bart.Janssens@mil.be

University Supervisor: Mark Runacres

Professor, Engineering Technology Thermodynamics and Fluid Mechanics Group, VUB, Belgium, mark.runacres@vub.be

Abstract

High-Altitude Pseudo-Satellites (HAPS) are Unmanned Aerial Vehicles (UAV), which fly at an altitude ranging from 15 to 20 km, at a low Reynolds ($\lessapprox$ 500000) number regime, offering long-lasting local aerial coverage. Conventional airfoils are not suitable for these vehicles. Different physical phenomena can occur, such as Laminar Separation Bubbles (LSB) [1; 2; 3], flow separation and transition which are extremely sensitive to variations in Reynolds number, and disturbances in the pressure gradient and the environment. The PhD project aims to develop, test and calibrate, suitable numerical methods for this specific use. For achieving this purpose, the main focus is to implement a two–scale Variational MultiScale (VMS) method in the Julia programming language which follows the procedure explained by Bazilevs et al. [4]. It is an evolution of the classic well-known Streamline Upwind Petrov–Galerkin (SUPG) method. In practice, the incompressible and time-dependent Navier-Stokes equations are solved using the Finite Element Method as an implicit Large Eddy Method (LES) for turbulence modelling.

The VMS has been implemented in the Julia programming language using the Gridap library [5; 6]. It has been tested on simple 2D cases with satisfactory results also at higher Reynolds numbers. Specifically, it solves accurately the lid driven cavity problem up to Reynolds 10 000 and captures the laminar boundary layer over a flat plate. The code implementing VMS is capable of capturing correctly also unsteady phenomena as demonstrated by vortex shedding over a cylinder at Reynolds number 1000. Timestepping employs both the θ-method and α-method. It has been shown that for the θ-method θ for the pressure field has to be set to 1 to avoid instabilities. The 2D Taylor-Green vortex case has been used as a further validation but also for evaluating the grid convergence. As expected, the error decreases with the increase of mesh resolution, both for velocity and pressure. The code runs also fully in parallel, using MPI (Message Passing Interface) and PETSc (Portable, Extensible Toolkit for Scientific Computation) as a solver [7]. The parallelization efficiency for the 2D Taylor-Green vortex has been tested with positive results both for the weak and strong scalability.

Keywords: VMS, Variational Multiscale Method, Julia, Finite Element Method, Incompressible Navier Stokes

References

[1] M. S. Selig, J. J. Guglielmo, High-lift low reynolds number airfoil design, Journal of aircraft 34 (1) (1997) 72–79.

[2] A. Mitra, P. Gokul, O. Ramesh, The role of laminar separation bubble on low reynolds number airfoils, in: 51st AIAA Aerospace Sciences Meeting including the New Horizons Forum and Aerospace Exposition, 2013, p. 59.

[3] M. O'meara, T. J. Mueller, Laminar separation bubble characteristics on an airfoil at low reynolds numbers, AIAA journal 25 (8) (1987) 1033–1041.

[4] Y. Bazilevs, V. Calo, J. Cottrell, T. Hughes, A. Reali, Scov-

azzi, Variational multiscale residual-based turbulence modeling for large eddy simulation of incompressible flows, Computer methods in applied mechanics and engineering 197 (1-4) (2007) 173–201.

[5] S. Badia, F. Verdugo, Gridap: An extensible finite element toolbox in julia, Journal of Open Source Software 5 (52) (2020) 2520. doi:10.21105/joss.02520.

[6] F. Verdugo, S. Badia, The software design of gridap: A finite element package based on the julia JIT compiler, Computer Physics Communications 276 (2022) 108341. doi:10.1016/j.cpc.2022.108341.

[7] S. Balay, S. Abhyankar, M. F. Adams, S. Benson, J. Brown, P. Brune, K. Buschelman, E. M. Constantinescu, L. Dalcin, A. Dener, V. Eijkhout, J. Faibussowitsch, W. D. Gropp, V. Hapla, T. Isaac, P. Jolivet, D. Karpeev, D. Kaushik, M. G. Knepley, F. Kong, S. Kruger, D. A. May, L. C. McInnes, R. T. Mills, L. Mitchell, T. Munson, J. E. Roman, K. Rupp, P. Sanan, J. Sarich, B. F. Smith, S. Zampini, H. Zhang, H. Zhang, J. Zhang, PETSc Web page, `https://petsc.org/` (2022). URL `https://petsc.org/`

AEROTHERMODYNAMICS

Development of a multi-fidelity framework for destructive atmospheric entry simulation

Fábio Morgado

Aerospace Centre of Excellence, University of Strathclyde, United Kingdom, fabio.pereira-morgado@strath.ac.uk

Supervisor: Thierry Magin

Professor, Aeronautics and Aerospace Department, von Karman Institute for Fluid Dynamics, Belgium, thierry.magin@vki.ac.be

University Supervisor: Marco Fossati

Professor, Aerospace Centre of Excellence, University of Strathclyde, United Kingdom, marco.fossati@strath.ac.uk

Abstract

The aerothermodynamic environment surrounding bodies undergoing destructive atmospheric entry is characterised by multiple interacting shock waves generated by the presence of several fragments moving close to one another at high speeds. Shock interaction and impingement produce highly localized surface loads influencing the overall dynamics of the fragment, its temperature, and in turn its demise. To increase the confidence level in predicting the re-entry process of fragmenting bodies, a multi-fidelity approach is presented. The proposed multi-fidelity method uses a physics-informed criterion to automatically detect when to transition from low-to-high and then from high-to-low fidelity on the basis of the intersection of shock wave envelopes of different fragments. The complete framework is validated on relevant test cases from the literature.

Keywords: re-entry, multi-fidelity, fragmentation

1. Introduction

Until today, there has been over 11,500 satellites launched, of which 66% are still in orbit, and, with the rise of constellations and CubeSats, more than 100,000 new satellites are expected to be launched to orbit by 2030 [1]. After decommissioned, a spacecraft is either deliberately moved further away from Earth to a graveyard orbit or re-enters the atmosphere through active or passive de-orbit methods, where they undergo a demise process [2].

The entry of space vehicles through a planetary atmosphere occurs at hypersonic speeds, subjecting the vehicle to increasing aerothermodynamic loads. These loads affect the overall dynamics of the vehicle and cause structural deformation. In addition, severe heat fluxes result in a spatially varying thermal response due to the presence of various materials. Furthermore, materials ablate at different rates, promoting further structural deformation. At a critical point during the entry, structural failure may ensue, resulting in the generation of multiple fragments. To ensure minimal risk to life and assets on Earth, the Inter-Agency Space Debris Coordination Committee (IADC) has set standards, requiring that fragments with impact kinetic energy greater than 15 J have a human casualty risk lower than 10^{-4} [3]. Accurately predicting the failure point and state of the fragments resulting from destructive atmospheric entry is computationally demanding and challenging, involving several disciplines such as heat transfer, aerodynamics, and aerothermodynamics for multiple flow regimes, structural dynamics, and flight mechanics [4].

Several state-of-the-art re-entry analysis tools address the multi-physics problem employing engineering and surrogate models based on simplified physical assumptions. Depending on the fidelity level of the geometrical and physical models, the analysis tools can be classified as object-oriented [5; 6; 7], where the spacecraft components are modeled as a set of simple shapes and the break-up event occurs at a given

fixed altitude, usually set to 78 km [8], or spacecraft-oriented [9; 10; 11], where the geometries are discretized through a triangle mesh, allowing the local computation of the different aerothermodynamics parameters [12; 13; 14] and the break-up events are assessed by analyzing the acting mechanical and thermal loads [15]. The spacecraft-oriented tools aim to simulate as real as possible, thus more efforts on physical modeling and computational resources are necessary [16]. In an attempt to combine the advantages of both object- and spacecraft-oriented methodologies, a new component-oriented methodology has started to be explored for re-entry simulations [8]. The new methodology captures the crucial aspects of a spacecraft-oriented model, including the predictive fragmentation and thermal model of the connected components, while achieving a compromise between geometrical complexity and physical fidelity.

However, the methodologies present a severe limitation due to their inability to adequately resolve flow features such as shock-shock interactions and shock impingement, induced by complex geometrical features or the presence of proximal bodies. If these phenomena are not accounted for, the computed distribution of the pressure and heat flux over the vehicle's surface is inaccurate, leading to incorrect trajectory and structural fragmentation predictions [17]. The limitation encountered with the low-fidelity methods can be circumvented through high-fidelity methods, such as Computational Fluid Dynamics (CFD) and the Direct simulation Monte Carlo (DSMC) method. High-fidelity simulations are computationally intensive and require careful set up, especially when dealing with the increasing number of fragments through the demise process. That is why, through the years the concept of multi-fidelity modelling has been introduced as a means to find a trade-off between cost and accuracy.

The present work illustrates the formulation and implementation of the multi-fidelity concept into a framework for atmospheric entry study capable of using either low- or high-fidelity methods to according to the complexity and high-nonlinearity of the flow. In the present work, the switch to high-fidelity methods is considered in relation to the evaluation of the aerothermodynamic loads occurring during fragmentation events. A physics-based trigger based on the Billig formulation for shock envelopes is introduced to determine when to use high-fidelity models, due to the occurrence of shock-shock interactions and shock-impinging characteristics.

The manuscript is organized as follows: Section 2 provides an overview of the proposed multi-fidelity framework along with the aerodynamic, aerothermodynamic, geometry, and ablation modules. Section 3 and Section 4 demonstrate the applicability of the implemented low-fidelity and high-fidelity methods, respectively. Section 5 verifies the use of the switch criteria for a simplified ATV re-entry case, and Section 6 summarises the work and obtained conclusions.

2. A Multi-Fidelity Approach

The framework is conceived to integrate different disciplinary models in a modular and loosely-coupled fashion [18; 19]: a six Degrees of freedom (6DoF) propagator, aerothermodynamics, thermal modeling, structural modeling, material database, and atmospheric models. The destructive phenomena that may occur are set up by specifying different criteria for fragmentation events, including altitude, temperature, and structural stress triggers. A high-level overview of the currently implemented modules is provided in Fig. 1, showcasing the information flow in the framework. The present implementation is currently available open-source as a python-based software called TITAN (TransatmospherIc fligh T simulAtioN)[1].

2.1. Geometry Modelling

The framework has been developed with a hybrid object- and spacecraft-oriented approach in mind. TITAN employs some aspects of both object- and spacecraft oriented methodology. The tool models the full vehicle geometry used for the simulation by connecting different components of the vehicle. The components are divided into fragmentable and non-fragmentable objects, which are referred to as joints and primitives, respectively. The joints connect the different components of type primitive that can undergo structural and thermal failure leading to fragmentation of the vehicle. Depending on the number and complexity of primitives and joints and their geometric arrangement, any level of complexity and detail can be achieved in modeling the spacecraft.

The connection between joint-primitive bodies or primitive-primitive bodies allows to dynamically take into account the separation of different groups of objects during the simulation when a fragmentation event occurs. An illustrative example of the connectivity between primitives and joints is shown in Fig.

[1] https://github.com/strath-ace/TITAN

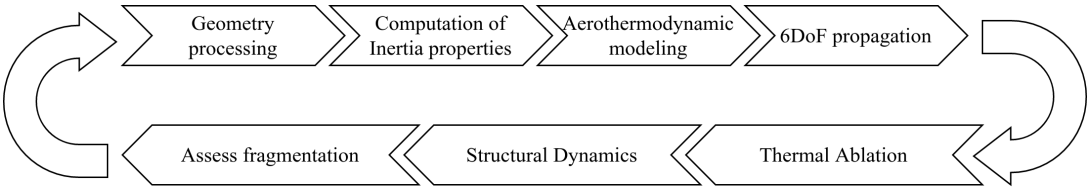

Figure 1: High-level workflow of TITAN.

2, where the circled joints connect the different primitives. In this particular case, the primitives are the solar panels and the main body of the satellite.



Figure 2: Overview of the primitive-joint concept in the geometry modeling of a spacecraft.

Each user-defined component has associated material properties that are retrieved from the European Space maTerIal deMisability dATabasE (ESTIMATE) [20]. The database provides the material characteristics required to compute the inertial properties of the components, as well as the thermophysical properties used to account for the thermal effects. The material database is compatible with the recommendations given in DIVE [21], the guidelines for analyzing and testing the demise of artificial space objects during re-entry.

In the presented methodology, the structural and thermal modeling between components is possible, thus enhancing the physics fidelity with respect to a pure object-oriented tool .Each component can be separated or removed from the simulation due to fragmentation or ablation, but cannot break up into smaller fragments as in spacecraft-oriented codes. However, the level of geometrical fidelity can be enhanced by increasing the number of primitives in the simulation, as showcased in Fig. 3 for a sphere. The user can perform a simulation using as many primitives and joints as required to increase the level of fidelity, ultimately reaching the same level as a spacecraft-oriented code.

2.2. *Multi-fidelity Aerothermodynamics*

The incorporated multi-fidelity aerothermodynamic module enables the computation of aerodynamic and aerothermodynamic loads using fast simplified engineering models or accurate high-fidelity solvers. The low-fidelity models allow for the computation of the aerodynamic and aerothermodynamic quantities at the various flow regimes encountered by the bodies during the re-entry process (e.g. rarefied, transitional, slip-flow and continuum regime) using a fast local panel inclination method.

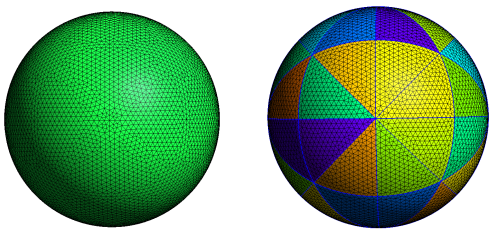

(a) 1 primitive. (b) 48 primitives.

Figure 3: Illustration of a sphere subdivision into several components to increase simulation fidelity.

The high-fidelity simulations in the continuum and slip regimes are computed using the CFD solver SU2-NEMO (NonEquilibrium MOdels solver) [22; 23; 24] for the continuum and slip regime. The use of CFD solvers requires the generation of a grid capable of sharply capturing the flow features inside the computational domain. Therefore, before proceeding to the flow simulation, the tool allows the automatic generation of a computation grid to be used for the flow simulation around the bodies. To achieve a grid-converged solution, anisotropic grid adaptation of the volume mesh and the generation of refined prismatic boundary layers is done to enable the physical surface heating accurate computation using the CFD solver. The generation and manipulation of the computational domain are performed by using third-party tools, referenced during the simulation. The dynamics propagation during a high-fidelity step follows a quasi-steady approach, where a steady flow at each time step is assumed. This approach allows the computation of the integrated loads applied at the body's surface for

each given interval of time that is used for the dynamics calculation. Therefore, at each time step using the high-fidelity solver, the grid has to be regenerated to accommodate the new position of the objects.

The flowchart for both low-fidelity and high-fidelity aerothermodynamic computation methods is showcased in Fig. 4. The free-stream properties are computed using the chemical species density and temperature data at a given altitude from the atmospheric model NRLMSISE-00 [25] or the NASA-GRAM model [26].

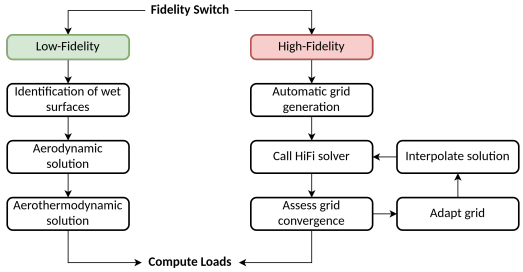

Figure 4: Flowchart of the multi-fidelity aerothermal modeling.

Low-fidelity methods use simplified assumptions and therefore may lead to incorrect predictions for objects with complex shapes and for simulations where the presence of multiple bodies generates several shock waves that can have an impact on the dynamics and structural integrity of neighbor objects. In these situations, the switch of high-fidelity methods is advised to adequately resolve the flow conditions surrounding the objects. The implementation of an automatic method to choose between low- and high-fidelity methods allows for reaching a compromise between computational speed and accuracy while allowing resolving the scenarios that the strict use of low-fidelity models cannot.

2.3. *Physics-informed, Automatic Fidelity Management*

The call of high-fidelity solvers is performed according to the imposed level of compromise between accuracy and computational power, and which can be used in critical scenarios. The presence of multiple fragments in supersonic and hypersonic regimes generates shock waves that can substantially affect the loads and dynamics on the following fragments, and which cannot be fully resolved using low-fidelity methods. In order to detect if the presence of multiple bodies gives rise to intricate flow features, it is necessary to estimate the position of the generated shock, which must be determined at each iteration of time and quickly determining it without advanced tools would greatly lower the cost the simulation.

Despite the fact that accurate shock estimation is difficult, it is possible to quickly compute the shock envelope which, by definition, must encompass the shock generated by the object itself. The generation of the envelope enables the development of a switching criterion based on the objects' relative positions in relation to the shock envelopes of nearby objects. An automatic fidelity switch criteria to choose between low- and high-fidelity models was developed and integrated into the framework of TITAN, using an approach based on Billig's shock estimation for a sphere to generate the shock envelope. This method assumes that the detached shockwave generated by a sphere can be written as a hyperbolic function, asymptotic to the freestream Mach angle, or, in the case of a cone or wedge, to the attached shock angle, θ. The expression formulated by Billig is given as

$$x = R + \Delta - R_c \cot^2\theta \left[\left(1 + \frac{r^2 \tan^2\theta}{R_c^2} \right)^{1/2} - 1 \right] \quad (1)$$

where R is the radius of curvature of the geometry at the stagnation point, R_c is the radius of curvature of the shock at the vertex, Δ the stand-off distance, and θ the asymptotic angle of the hyperbola. The stand-off distance and the vertex radius of curvature are given by the empirical relation proposed in the work of Ambrosio and Wortman in the continuum regime [27] and are respectively formulated as

$$\frac{\Delta}{R} = 0.143 \exp\left(\frac{3.24}{M_\infty^2} \right) \quad (2)$$

$$\frac{R_c}{R} = 1.143 \exp\left(\frac{0.54}{(M_\infty - 1)^{1.2}} \right) \quad (3)$$

where M_∞ is the free-stream Mach number.

Billig's formula is only dependent on the free-stream Mach number and the sphere radius, not taking into consideration the level of flow rarefaction, as stated in the research of Nicolas et al. [28], where it has been verified that with the increase in the Knudsen number, the stand-off distance given by the empirical formula further deviates from the experimental results. Therefore, caution must be taken when applying this methodology in the transitional and rarefied regimes.

To calculate the shock envelope using Billig's approximation, a virtual equivalent sphere must be used

to represent the object. The calculation is performed in the wind frame, where the free-stream velocity vector points towards the positive X-axis. Subsequently, Billig's formula can be applied to compute the shock envelope. An example of this approach is shown in Fig. 5.

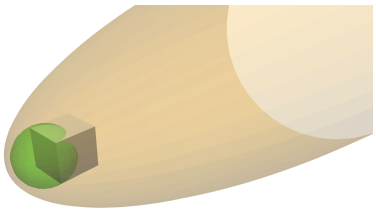

Figure 5: Visualization of the virtual sphere and the equivalent shock envelope for a cube geometry.

Due to the nature of the hyperbolic formula derived by Billig, it is possible to rewrite Eq. 1 for an arbitrarily positioned sphere in the wind frame. For a body i with an equivalent sphere with center at $(x_{s_i},y_{s_i},z_{s_i})$, and assuming the flow direction to be in the positive X-axis direction, the hyperbolic formula for the shock envelope can be rewritten as

$$(x - x_{s_i}) = -R_c - \Delta + R_c \cot^2\theta \times \left[\left(1 + \frac{(r - r_{s_i})^2 \tan^2\theta}{R_c^2}\right)^{1/2} - 1\right] \quad (4)$$

where r is defined as

$$r = \sqrt{y^2 + z^2}. \quad (5)$$

Rearranging equation 6, the inner side of the hyperbola, which defines the shock envelope, can be defined as

$$R_c \cot^2\theta \left[\left(1 + \frac{(r - r_{s_i})^2 \tan^2\theta}{R_c^2}\right)^{1/2} - 1\right] \geq -(R_c + \Delta). \quad (6)$$

For a given body j, with $i \neq j$, the coordinates of the k_{th} vertex of the body are given as $(x_{j_k},y_{j_k},z_{j_k})$. If any of the vertex is inside the hyperbola, a high-fidelity solver is used to compute the aerothermal loads. Otherwise, if they are all outside the hyperbola, low-fidelity methods are used. This means that high-fidelity methods are used if any point complies with the following criteria:

$$(x_{j_k} - x_{s_i}) - R_c \cot^2\theta \left[\left(1 + \frac{(r_{j_k} - r_{s_i})^2 \tan^2\theta}{R_c^2}\right)^{1/2} - 1\right] \geq -(R_c + \Delta), \quad \text{for k = 0, 1, ..., N.} \quad (7)$$

An illustrative example of the proposed methodology for the fidelity switch criteria is presented in Fig. 6, where the vertex inside the envelope are flagged. The considered approach not only allows to account for objects leaving the shock envelope but also for fragments re-entering it, thus eventual interaction with the shock generated by a leading fragment can always be accounted for.

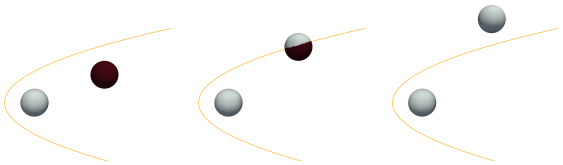

Figure 6: Representation of the sphere positioning in relation to the shock envelope.

2.4. *Low-fidelity Aerodynamic and Aerothermodynamic Modelling*

The use of panel methods for the computation of the aerothermodynamic quantities at hypersonic regimes assume that only the panels facing the flow direction are impacted by the flow particles, resulting in shadow areas that are not affected by the flow. For simple convex objects, it is enough to assess the angle between the flow direction and the surface facet. Thus, if

$$\begin{cases} \arcsin(-\vec{n} \cdot \vec{V}) \leq \pi/2, & \text{The flow is impinging the panel} \\ \arcsin(-\vec{n} \cdot \vec{V}) > \pi/2, & \text{The panel is shadowed} \end{cases} \quad (8)$$

where $\vec{n}$ is the normal vector of the panel, pointing outwards, and $\vec{V}$ is the free-stream velocity vector.

However, this method does not account for occluded sections. For this reason, a back-face culling algorithm based on the projection of the surface mesh into the plane orthogonal to the free-stream velocity vector was developed, as illustrated in Fig. 7. Given the position of the geometrical center of the panels, it is possible to sort them by the relative distance with the orthogonal plane, and individually project them

into the plane, starting with the closest panel. In order to boost the back-face culling methodology speed, the projection is stored in a 2D Cartesian binary matrix. When projecting the geometrical center of the facets, if it falls in on an empty cell, the facet is projected, and if it falls on a filled cell, the facet is shadowed.

To further decrease the computational cost of the mentioned method, TITAN first proceeds to filter the panels that are potentially facing the flow using Eq. 8. An example of the back-face culling method is shown in Fig. 8, where the solar array of the ATV is partially occluding the cargo bay.

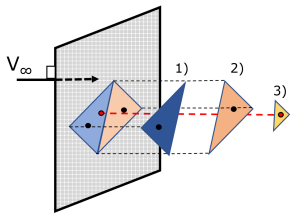

Figure 7: Back-face culling methodology illustration.

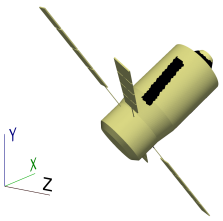

Figure 8: Back-face culling applied for the ATV case.

The aerodynamic and aerothermodynamic contribution in the free molecular regime ($Kn \geq 10^2$) is evaluated using the analytical model by Schaaf and Chambre [13]. For the continuum regime ($Kn \leq 10^{-3}$), the aerodynamic coefficients are estimated with the Modified Newtonian Theory [12], and the the heat transfer is obtained by using Van Driest model [14] if assuming a non-catalytic wall, or by SCARAB [10] formulation for catalytic walls.

2.5. *High-fidelity Modelling in the Continuum Regime*

The SU2-NEMO (NonEquilibrium MOdels solver) [22] CFD solver can be called by the framework to increase the accuracy of the simulations in the continuum and slip regime. The closure of the governing equations for the system of interest is achieved through the linkage between SU2-NEMO and the thermochemistry library Mutation++ [29] (Multicomponent Thermodynamic And Transport properties for IONized gases in C++). The library contains efficient algorithms for the computation of the required mixture properties, such as thermodynamic, transport, and chemical kinetic gas properties for a wide range of temperatures.

The system of governing equations is obtained through the extension of the Navier-Stokes equations to account for chemically reacting, non-equilibrium flows, using the two-temperature model by Park. The translational and rotational energy modes are assumed to be at equilibrium with one another. The same approach is used for the vibrational and electronic energy modes.

2.6. *Thermal Model*

The lumped mass approach ($0D$) is used to simulate the thermal ablation of a re-entering object. It is assumed that the temperature of the object is uniformly distributed where multiple objects can have different values of temperature. The ablation of the object is initiated once the material reaches the melting temperature. The amount of heat remaining after the material reaches the melting temperature (T_{melt}) is given by Eq. 9, where, Q_{in} is the total incoming convective heat flux, Q_{rad} corresponds to the cooling of the surface due to radiation, c_p corresponds to the temperature-dependent specific heat, dt corresponds to the time step of integration, and, m_0 and T_0 correspond to the mass and temperature of the object at previous time step respectively. Finally, the mass lost due to ablation is given by Eq. 10 where Q_{melt} is the latent heat of fusion.

$$Q_f = m_0 c_p \left[\frac{(Q_{in} - Q_{rad}) \times dt}{m_0 c_p} - (T_{melt} - T_0) \right] \quad (9)$$

$$dm = \frac{-Q_f}{Q_{melt}} \quad (10)$$

3. Verification of Low-Fidelity Aerodynamic and Aerothermodynamic Modelling

The verification of the discussed low-fidelity models is performed through the comparison of the computed results with TITAN against numerical data, along with the available results from state-of-the-art spacecraft-oriented tools, retrieved from the work of Annaloro et al. [17].

A 1.6-meter-diameter sphere re-entry case was selected for the accuracy analysis of the low-fidelity models for the transitional and rarefied regime. The computed results are compared with those obtained by the re-entry spacecraft-oriented tool PAMPERO [9], SCARAB [10] and FAST/MUSIC [11], as well as DSMC calculations from Dogra et al. [30]. Free-stream velocity is set to 7.5 km/s. The wall temperature of the sphere is set to be 350 K, uniformly distributed along the surface, which is assumed to

be non-catalytic. The gas-surface interaction was assumed to be diffuse with full thermal accommodation.

A comparative analysis is performed for the altitudes of 90, 130, and 200 km, illustrated in Fig. 9, 10, and 11 respectively. Analyzing the images, it is clear that the discrepancy between the different codes is larger for pressure distribution when shifting towards the free-molecular regime, and for the heat-flux distribution when shifting towards the continuum regime. Overall, the distribution provided by the framework is in good agreement with the reference DSMC solution, with the exception of the heat-flux at 90 km, where the distribution is overestimated, but approximates the reference value at the stagnation point.

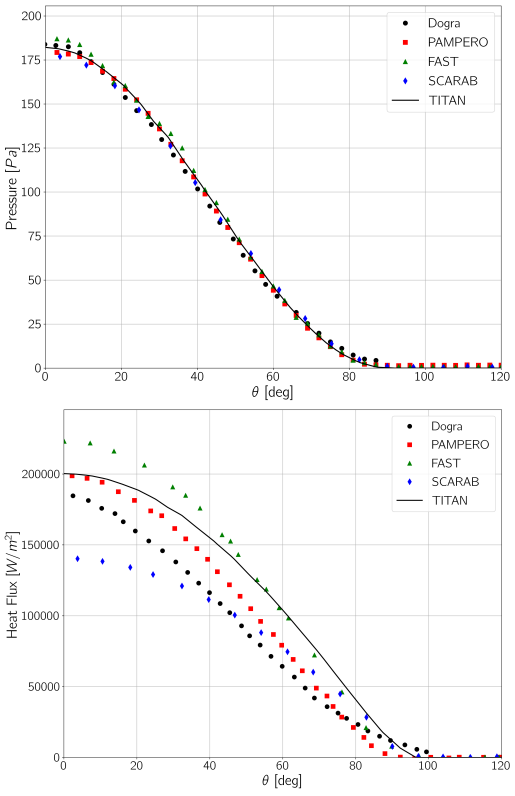

Figure 9: a) Pressure and heat-flux distribution at 90 km

4. Verification of High-fidelity Modeling in Continuum Regime

The use of SU2-NEMO for high-enthalpy flows has been extensively validated in previous works [22; 23; 24]. In order to use the CFD solver, the framework refers to GMSH [31] for the creation of the 3D fully

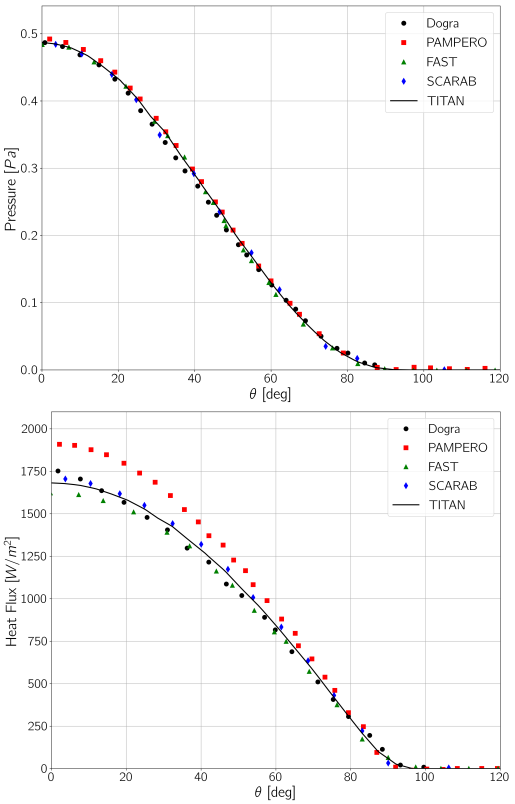

Figure 10: b) Pressure and heat-flux distribution at 130 km

unstructured computational domain using the Delaunay triangulation method. After obtaining an initial CFD converged solution, the grid is anisotropically adapted by the pyAMG library [32; 33; 34]. The pyAMG software is a python wrapper for the Adaptive Mesh Generation library (AMG-lib) that enables the generation of local anisotropic elements to follow the directional flow features (i.e. shock waves, discontinuities) by computing an optimal Riemannian metric tensor field from the solution error estimate. Previous works have analysed the use of highly anisotropic grids for literature re-entry cases using SU2-NEMO [35]. This adaptation procedure is repeated until a grid-converged solution is achieved or the maximum number of grid adaptations is reached.

The adaptation loop was tested for the simulation of a free-flying ring for a hypersonic N_2 flow. The aerodynamic coefficients are compared with experimental results obtained by Grossir et al. [36] using the hypersonic wind tunnel Longshot at Von Karman Institute. Albeit having a simple geometry, the ring is similar to an inter-stage element of a rocket. The presence of

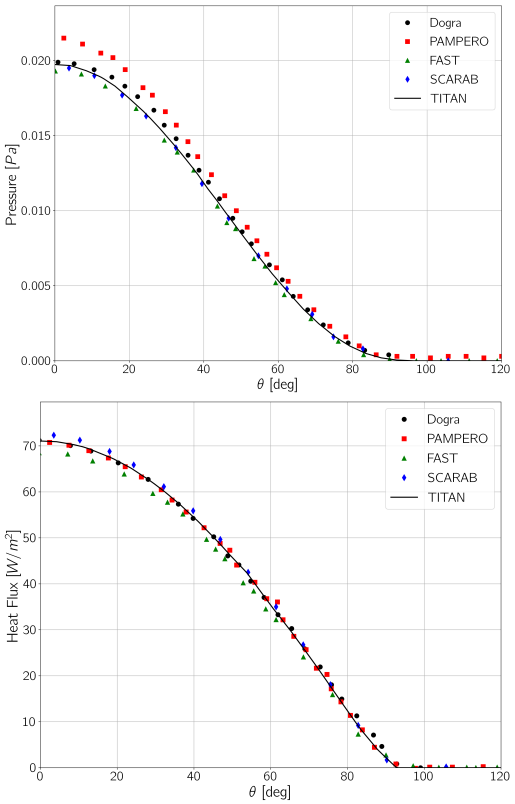

Figure 11: c) Pressure and heat-flux distribution at 200 km

a ring at different angles of attack exhibits complex flow features, such as self-impingement, that need to be carefully addressed in order to compute the correct aerodynamic coefficients. Figure 12 showcases the capabilities of anisotropic grid adaptation into capturing the complex shock interference formed by the ring. A comparison between the numerical and experimental aerodynamic coefficients for different angles of attack (0°, 30°, 45° and 90°) is provided in Fig. 13, where the numerical coefficients are in good agreement with the experimental data, highlighting the benefits of using an adaptation loop for high-fidelity modeling.

5. Verification of the Automatic Fidelity Switch

A conceptual test case of a simplified ATV re-entry scenario was conducted to evaluate the effectiveness of the proposed automatic fidelity switching mechanism and its impact on the dynamics of the fragments. The initial trajectory conditions and fragmentation trigger used in this simulation are summarised

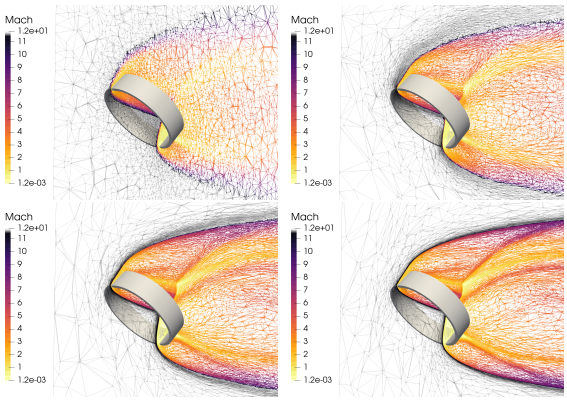

Figure 12: Grid adaptation for a ring with 45° angle of attack.

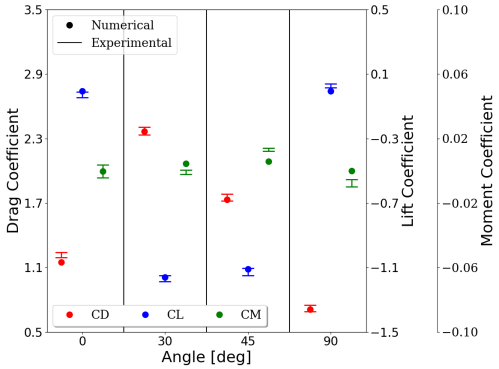

Figure 13: Ring aerodynamic coefficients for different angles of attack.

in Table 1 and the ATV geometry is shown in Fig. 14.

Table 1: Initial trajectory conditions and geometry details.

Parameter	Value
Altitude [km]	120
Velocity [km/s]	7.57
Flight path angle [°]	-1.45
Initial pitch angle velocity [°/s]	10
Fragmentation trigger altitude [km]	78
Number of facets [$\times 10^3$]	40
Time step [s]	0.25

The trajectory is propagated until 78 km of altitude when the joints are set to fragment due to the specified altitude criterion, occurring at t = 172s. Until the moment of fragmentation, there is only one assembly present in the simulation. As a result, low-

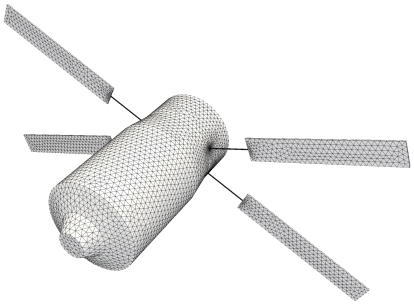

Figure 14: Simplified conceptual geometry configuration of the ATV for methodology verification.

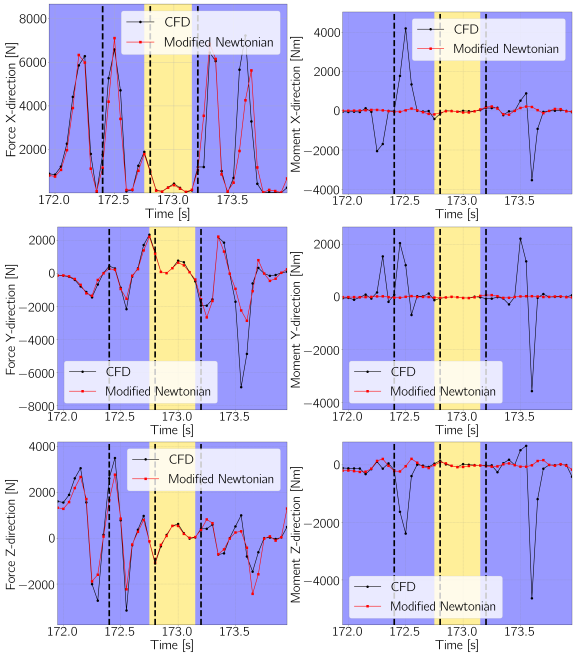

Figure 15: Solar panel forces and moments comparison.

fidelity models are employed to calculate the surface loads until the moment of fragmentation. After the break-up event, the objects are re-entering at Mach 26, leading to the formation of shock waves. Using the described methodology, it is possible to estimate if the fragments are subjected to the influence of the shock generated by leading objects, requiring the use of high-fidelity methods for accurate predictions of surface loads. The forces and moments applied to the fragments were computed for a time interval of $\Delta t = 2.0s$ using a time step of $dt = 0.05s$ for both low- and high-fidelity methods to compare the differences.

The results shown in Fig. 15 illustrate the forces and moments experienced by a single solar panel, circled in red in Fig. 16. The plots show the forces and moments computed for both low and high-fidelity models. The blue background indicates the time interval where the panel is inside a shock envelope generated by the main body or leading panels, thus requiring the use of high-fidelity tools, and the yellow background indicates the time interval where the panel is not interacting with any shock envelope, and low-fidelity models can be used. The difference in the methods is more pronounced when the fragment is inside the shock envelope due to the influence of the leading body. As the fragment leaves the shock envelope, the forces and moments computed using both methods become comparable as there is no further interaction with shock waves. Therefore, after exiting the envelope, low-fidelity methods are sufficient to capture the object's dynamics.

Three different scenarios were sequentially identified and marked with a black dashed line in Fig. 15. After the joints fragmentation, due to the proximity of the solar panels and the main body, high-fidelity methods are required to fully capture the loads applied in the fragments. Afterward, the tracked solar panel leaves the shock influence of the remaining fragments. At this stage, the framework is able to separate the panel whose dynamics can be captured using Modified Newtonian from the fragments that require the use of CFD. This selection process enables the reduction of the number of objects in the high-fidelity simulation, thus minimizing the computational cost. Lastly, a scenario was observed where different clusters of fragments were formed. These clusters do not interact with each other, but the shock influence is still prominent inside each one individually, requiring the use of high-fidelity models. To address them, TITAN is able to run separate high-fidelity simulations, reducing the time and complexity of the flow computation.

In the absence of shock interacting with the fragments, it is expected for the forces and moments computed by both CFD and the Modified Newtonian method to be similar. The use of an analytical function to assess the position of the objects with respect to the generated shock envelopes allows us to quickly assess the level of fidelity required to adequately compute the applied loads at the given instant of time.

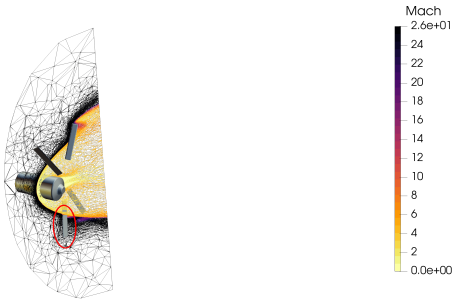

(a) Full CFD simulation at $t = 172.4s$ using one cluster



(b) Solar panel isolation at $t = 172.8s$. Low-fidelity model is used for the circled solar panel

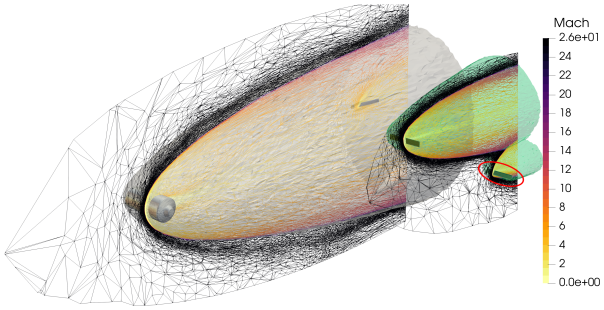

(c) Formation of separate fragment clusters at $t = 173.3s$.

Figure 16: ATV dynamics after fragmentation.

6. Conclusions

An original implementation of the multi-fidelity paradigm in the modeling and simulation of atmospheric entry trajectories is discussed that adaptively and automatically identifies the most appropriate level of fidelity to predict aerothermodynamic loads acting on the surface of the re-entering spacecraft. Differently from other multi-fidelity implementations that aim at improving existing surrogates via model updating, the present implementation selects between high- and low-fidelity models looking for an optimal trade-off between computational cost and accuracy. The introduction of a physics-informed criterion to automatically select the level of fidelity based on the Billig formula has proven effective in identifying conditions where high-fidelity is needed as well as situations where a step back to low-fidelity will not compromise the overall accuracy in the prediction of pressure and heat fluxes.

Validations test cases for the low-fidelity and high-fidelity aerodynamics and aerothermodynamics modules showed satisfactory agreement with the reference data in the literature. The automatic fidelity switch has been tested for a simplified ATV test case. The results presented illustrate the ability of this method to maintain a reasonable degree of accuracy in computing the dynamics of the bodies in the instants after the breakup process.

Despite the present implementation, no model update or correction to the low-fidelity counterpart is considered explicitly, it is one key development currently under development. Future works will focus on the assessment of the present approach in rarefied regimes looking at DSMC methods for high-fidelity aerothermodynamics and more refined modeling of the thermal and thermomechanical processes during re-entry.

Acknowledgments

The authors wish to acknowledge the support of the European Space Agency through the OSIP MIDGARD project, ESA Contract No. 4000130436/20/NL/MH/ac, 2020-2023.

References

[1] C. Pardini, L. Anselmo, The kinetic casualty risk of uncontrolled re-entries before and after the transition to small satellites and mega-constellations, Journal of Space Safety Engineering 9 (3) (2022) 414–426. doi:https://doi.org/10.1016/j.jsse.2022.04.003.

[2] R. Leonard, I. D. Williams, Viability of a circular economy for space debris, Waste Management 155 (2023) 19–28. doi:https://doi.org/10.1016/j.wasman.2022.10.024.

[3] J.-C. Liou, M. Kieffer, A. Drew, A. Sweet, The 2019 u.s. government orbital debris mitigation standard practices, Orbital Debris Quarterly News 24 (1) (2020) 4–8.

[4] W. L. Hankey, Re-entry aerodynamics, American Institute of Aeronautics and Astronautics, Washington, D.C., 1988.

[5] V. Braun, Q. Funke, S. Lemmens, S. Sanvido, Drama 3.0 - upgrade of esa's debris risk assessment and mitigation analysis tool suite, Journal of Space Safety Engineering 7 (3) (2020) 206–212, space Debris: The State of Art. doi:https://doi.org/10.1016/j.jsse.2020.07.020.

[6] J. Annaloro, S. Galera, C. Thiebaut, P. Omaly, DEBRISK V3: new generation of object-oriented tools.

[7] C. Ostrom, B. Greene, A. Smith, M. Matney, J. Opiela, J. Marichalar, J. Bacon, C. Sanchez, R. Toledo, Operational and technical updates to the object reentry survival analysis tool, 2019.

[8] J. Beck, I. Holbrough, J. Merrifield, N. Joiner, Progress in Hybrid Spacecraft/Object Oriented Destructive Re-entry Modelling using the SAM Code.

[9] J. Annaloro, P. Omaly, V. Rivola, M. Spel, Elaboration of a new spacecraft-oriented tool: Pampero, in: Proceedings of the 8th European Symposium on Aerothermodynamics for Space Vehicles, 2015.

[10] G. Koppenwallner, B. Fritsche, T. Lips, H. Klinkrad, Scarab - a multi-disciplinary code for destruction analysis of spacecraft during re-entry, European Space Agency, (Special Publication) ESA SP 563 (2005) 281.

[11] F. Sourgen, Y. Prévereaud, J. l. Verant, E. Laroche, J.-M. Moschetta, Music/fast, a pre-design and pre-mission analysis tool for the earth atmospheric re-entry of spacecraft, capsules and de-orbited satellites, in: Proceedings of 8th European Symposium on Aerothermodynamics for Space Vehicles, 2 March 2015 - 6 March 2015 (Lisbonne, Portugal, 2015.

[12] L. Lees, Hypersonic flow, Journal of Spacecraft and Rockets 40 (5) (2003) 700–735. arXiv:https://doi.org/10.2514/2.6897, doi:10.2514/2.6897.
URL `https://doi.org/10.2514/2.6897`

[13] S. A. Schaaf, P. L. Chambre, Flow of Rarefied Gases, Princeton University Press, 1958.

[14] E. R. van Driest, The problem of aerodynamic heating, Aeronautical Engineering Review 15, 10 (1956) 26–41.

[15] T. Lips, B. Fritsche, A comparison of commonly used re-entry analysis tools, Acta Astronautica 57 (2) (2005) 312–323, infinite Possibilities Global Realities, Selected Proceedings of the 55th International Astronautical Federation Congress, Vancouver, Canada, 4-8 October 2004. doi:https://doi.org/10.1016/j.actaastro.2005.03.010.

[16] J. Annaloro, S. Galera, P. Kärräng, G. Prigent, T. Lips, P. Omaly, Comparison between two spacecraft-oriented tools: Pampero scarab, Journal of Space Safety Engineering 4 (1) (2017) 15–21. doi:https://doi.org/10.1016/j.jsse.2017.02.004.

[17] J. Annaloro, S. Galera, P.Kärräng, Y. Prevereaud, J.-L. Vérant, M. Spel, P. Van Hauwaert, P. Omaly, Space debris atmospheric entry prediction with spacecraft-oriented tools, 2017.

[18] F. Morgado, S. A. Peddakotla, M. Fossati, A multi-fidelity simulation framework for atmospheric re-entering bodies, in: ESA Aerothermodynamics and Design for Demise (ATD3) Workshop, 2021.

[19] F. Morgado, S. A. Peddakotla, C. Garbacz, M. L. Vasile, M. Fossati, Multi-fidelity approach for aerodynamic modelling and simulation of uncontrolled atmospheric destructive entrydoi:10.2514/6.2022-1323.

[20] ESA, Estimate: European space material demisability database (2020).
URL `https://estimate.sdo.esoc.esa.int`

[21] ESA, Dive - demise verification guidelines for analysing and testing the demise of man made space objects during re-entry (2020).

[22] W. T. Maier, J. T. Needels, C. Garbacz, F. Morgado, J. J. Alonso, M. Fossati, SU2-NEMO: An Open-Source Framework for High-Mach Nonequilibrium Multi-Species Flows, Aerospace 8 (7), 10.3390/aerospace8070193.

[23] C. Garbacz, F. Morgado, M. Fossati, W. T. Maier, B. C. Munguía, J. J. Alonso, A. Loseille, Parametric study of nonequilibrium shock interference patterns over a fuselage-and-wing conceptual vehicle, AIAA Journal 59 (12) (2021) 4905–4916. doi:10.2514/1.J060470.

[24] C. Garbacz, M. Fossati, W. T. Maier, J. J. Alanso, J. B. Scoggins, T. D. Economon, T. E. Magin, Numerical Study of Shock Interference Patterns for Gas Flows with Thermal Nonequilibrium and Finite-Rate Chemistry, AIAA Paper 2020-1805, 2020. doi:10.2514/6.2020-1805.

[25] J. M. Picone, A. E. Hedin, D. P. Drob, A. C. Aikin, Nrlmsise-00 empirical model of the atmosphere: Statistical comparisons and scientific issues, Journal of Geophysical Research: Space Physics 107 (A12) (2002) SIA 15–1–SIA 15–16. doi:https://doi.org/10.1029/2002JA009430.

[26] C. Justus, A. Duvall, D. Johnson, Earth global reference atmospheric model (gram-99) and trace constituents, Advances in Space Research 34 (2004) 1731–1735. doi:10.1016/j.asr.2003.04.057.

[27] A. Ambrosio, A. Wortman, Stagnation-point shock-detachment distance for flow around spheres and cylinders in air, Journal of the Aerospace Sciences 29 (7) (1962) 875–875. doi:10.2514/8.9622.

[28] N. Rembaut, R. Joussot, V. Lago, Aerodynamical behavior of spherical debris in the supersonic and rarefied wind tunnel marhy, Journal of Space Safety Engineering 7 (3) (2020) 411–419, space Debris: The State of Art. doi:https://doi.org/10.1016/j.jsse.2020.07.031.

[29] J. Scoggins, T. Magin, Development of mutation++: Multicomponent thermodynamic and transport properties for ionized plasmas written in c++, 2014. doi:10.2514/6.2014-2966.

[30] V. Dogra, J. Moss, R. Wilmoth, J. Price, Hypersonic rarefied flow past spheres including wake structure. arXiv:https://arc.aiaa.org/doi/pdf/10.2514/6.1992-495, doi:10.2514/6.1992-495.

[31] C. Geuzaine, J.-F. Remacle, Gmsh: A 3-d finite element mesh generator with built-in pre- and post-processing facilities, International Journal for Numerical Methods in Engineering 79 (11) (2009) 1309–1331. doi:https://doi.org/10.1002/nme.2579.

[32] A. Loseille, R. Loehner, Boundary layer mesh generation and adaptivity, 2011. doi:10.2514/6.2011-894.

[33] A. Loseille, V. Menier, Serial and parallel mesh modification through a unique cavity-based primitive, in: Proceedings of the 22nd International Meshing Roundtable, Springer International Publishing, Cham, 2014, pp. 541–558. doi:10.1007/978-3-319-02335-9_30.

[34] A. Loseille, V. Menier, F. Alauzet, Parallel generation of large-size adapted meshes, Procedia Engineering 124 (2015) 57 – 69, 24th International Meshing Roundtable. doi:10.1016/j.proeng.2015.10.122.

[35] F. Morgado, C. Garbacz, M. Fossati, Impact of anisotropic mesh adaptation on the aerothermodynamics of atmospheric reentry, AIAA Journal 60 (7) (2022) 3973–3989. doi:10.2514/1.J061071.

[36] G. Grossir, D. Puorto, Z. Ilich, S. Paris, O. Chazot, S. Rumeau, M. Spel, J. Annaloro, Aerodynamic characterization of space debris in the vki longshot hypersonic tunnel using a free-flight measurement technique, Experiments in Fluids 61. doi:10.1007/s00348-020-02995-7.

Influence of ablation on atmospheric entry aerothermodynamics

Ata Onur Başkaya

Aerodynamics Group, Faculty of Aerospace Engineering, TU Delft, The Netherlands, a.o.baskaya@tudelft.nl
Aeronautics and Aerospace Department, von Karman Institute for Fluid Dynamics, Belgium, ata.onur.baskaya@vki.ac.be

Supervisor: Thierry Magin

Professor, Aeronautics and Aerospace Department, von Karman Institute for Fluid Dynamics, Belgium, thierry.magin@vki.ac.be

University Supervisor: Stefan Hickel

Professor, Aerodynamics Group, Faculty of Aerospace Engineering, TU Delft, The Netherlands, s.hickel@tudelft.nl

Abstract

This article considers the development, implementation, and application of a conservative immersed boundary method with gas-surface interactions for simulating atmospheric entry flows. The methodology and the results of relevant case studies involving hypersonic flows under thermochemical nonequilibrium and surfaces undergoing ablation are presented.

Keywords: Atmospheric entry, ablation, gas-surface interactions, immersed boundary methods, CFD

1. Introduction

Atmospheric entry of capsules or space debris involve complex flow environments due to strong shock waves at hypersonic speeds, and high-temperature effects such as thermochemical nonequilibrium (TCNE) and interactions with the surface material. Depending on the characteristics of this material, these gas-surface interactions (GSI) result in catalysis as well as ablation. The latter process alleviates the heat load by means of physicochemical decomposition and mass loss, which alters the shape of the object as its surface recesses. Understanding these fluid-structure interactions is crucial for predicting the surface stresses and heat fluxes as well as the uncontrolled trajectory of space debris. Ground testing is indispensable for validation purposes; however, no facility can simultaneously replicate all aspects of atmospheric entry flows [1]. Hence, computational fluid dynamics (CFD) simulations are essential for the efficient aerothermodynamic analysis and design of future spacecraft.

Investigation of these regimes requires appropriate numerical schemes and computational grids for the accurate representation of strong shock waves and boundary layers. Most solvers used for these applications employ body-conforming structured grids [2; 3; 4]. In these solvers, accurate prediction of the flow field relies on careful alignment of the grid with the shock and the surface. In practice, this requirement demands strenuous effort from the user in generating high-quality body-conforming grids, especially for detailed features and incremental geometry updates [5]. Unstructured grids have also been explored; however, issues affecting the heat flux predictions at the surface were reported [6; 7]. In the presence of strong discontinuities, unstructured body-conforming grids incur larger errors as they usually employ more standard numerical schemes [8]. This stems from the difficulties in the implementation of high-resolution schemes, which provide superior shock capturing properties [9]. A promising alternative is the use of adaptive mesh refinement (AMR) techniques based on piecewise Cartesian grids with immersed boundary (IB) methods, which offer a relatively straight-forward implementation of high-order schemes. There has been a recently growing interest in IB solvers for high-speed viscous compressible flows [10; 11; 12; 13; 14]. Especially for moving and deforming objects with complex shapes, IB methods are more robust and more efficient than body-

conforming mesh-deformation methods.

This paper presents a conservative cut-cell IB method available in the INCA solver (https://www.inca-cfd.com) for the accurate simulation of hypersonic flows including the effects of GSI as encountered in atmospheric entry applications. Cut-cell IB methods are a straightforward extension of the finite-volume flux balance and thus satisfy mass, momentum and energy conservation exactly. Compared to standard cut-cell methods, the present method works on so-called cut elements, which provide sub-cell resolution of the geometry [15]. The verification and validation of the method is presented in a separate publication [16], which demonstrates the accurate modelling of the high-temperature physicochemical interactions and the benefit of having the present conservative IB methodology over nonconservative formulations. In this paper, the underlying numerical methodology is presented and demonstrated for three test cases: hypersonic flow over a compression ramp with perfect gas as well as with thermochemical nonequilibrium models, hypersonic flow in thermochemical nonequilibrium over a cylinder, and a graphite ablator exposed to nitrogen plasma. The governing equations and the thermochemical models are presented in Section 2. The cut-element IB methodology incorporating GSI is detailed in Section 3. Results of the case studies are discussed in Section 4, and concluding remarks are made in Section 5.

2. Governing Equations

The compressible Navier-Stokes equations are solved in their conservative form for a reacting multicomponent fluid under thermochemical nonequilibrium including an additional transport equation for the vibrational energy [17],

$$\frac{\partial \rho_i}{\partial t} + \boldsymbol{\nabla} \cdot (\rho_i \mathbf{u} + \mathbf{J}_i) = \dot{\omega}_i \,, \tag{1}$$

$$\frac{\partial \rho \mathbf{u}}{\partial t} + \boldsymbol{\nabla} \cdot (\rho \mathbf{u} \otimes \mathbf{u}) + \boldsymbol{\nabla} p - \boldsymbol{\nabla} \cdot \boldsymbol{\tau} = 0 \,, \tag{2}$$

$$\frac{\partial \rho E}{\partial t} + \boldsymbol{\nabla} \cdot \left[(\rho E + p)\, \mathbf{u} \right] + \boldsymbol{\nabla} \cdot \mathbf{q} - \boldsymbol{\nabla} \cdot (\boldsymbol{\tau} \cdot \mathbf{u}) = 0 \,, \tag{3}$$

$$\frac{\partial \rho e^{\mathrm{V}}}{\partial t} + \boldsymbol{\nabla} \cdot \rho e^{\mathrm{V}} \mathbf{u} + \boldsymbol{\nabla} \cdot \mathbf{q}^{\mathrm{V}} = \dot{\Omega} \,. \tag{4}$$

Here, ρ_i is the species partial density for the ith species, $\mathbf{u}$ is the mixture average velocity, and $\dot{\omega}_i$ is the source term associated with the production or consumption of species due to chemical reactions. Moreover, ρ is the mixture density, p is the mixture pressure, and $E = e + u^2/2$ is the specific total energy, which is the sum of the thermodynamic internal energy e and the kinetic energy. The species diffusion flux $\mathbf{J}_i$, the viscous stress tensor $\boldsymbol{\tau}$, and the total heat flux $\mathbf{q}$ are detailed below. External forces due to gravitational or magnetic effects, and radiative energy exchanges are not considered for the cases in this study. Park's two-temperature model [17] is employed, which requires solving an energy equation for the vibrational thermal bath, denoted by the superscript V, and $\mathbf{q}^{\mathrm{V}}$ is the heat flux for the vibrational temperature for which the thermal conductivity λ^{V} is obtained by the Euken correction [18]. The energy exchange term $\dot{\Omega} = \dot{\Omega}^{\mathrm{TV}} + \dot{\Omega}^{\mathrm{CV}}$ describes how the system relaxes to equilibrium through energy exchanges between the translational and vibrational modes, $\dot{\Omega}^{\mathrm{TV}}$, and chemical reactions, $\dot{\Omega}^{\mathrm{CV}}$. For the former, the Landau-Teller formulation is used with the relaxation time according to Park's correction to the expression proposed by Millikan and White [17]. A non-preferential dissociation model is used for the energy exchange through chemical reactions [19]. More intricate thermal nonequilibrium models are available [20], yet the current model has proven suitable for our range of applications [21].

The ideal gas assumption leads to the equation of state $p = \rho R T$, where $R = \mathcal{R}/\overline{M}$ is the mixture gas constant with the universal gas constant $\mathcal{R}$ and mixture average molar mass $\overline{M}$. These mixture properties are obtained according to Dalton's law through their constituent species as $p = \sum_i p_i$, $\rho = \sum_i \rho_i$, $R = \sum_i y_i R_i$, with the mass fractions $y_i = \rho_i / \rho$.

Fick's law is used for modeling diffusion with a correction to ensure conservation of mass

$$\mathbf{J}_i = -\rho D_{im} \boldsymbol{\nabla} y_i + y_i \sum_j \rho D_{jm} \boldsymbol{\nabla} y_j \,, \tag{5}$$

where $D_{im} = (1 - x_i) / \sum_{j \neq i} \frac{x_j}{\mathcal{D}_{ij}}$ are the mixture-averaged diffusion coefficients obtained by Wilke's averaging of the binary diffusion coefficients $\mathcal{D}_{ij}$.

The viscous stress tensor is modeled assuming Stokes' hypothesis as

$$\boldsymbol{\tau} = \mu \left[\boldsymbol{\nabla} \mathbf{u} + (\boldsymbol{\nabla} \mathbf{u})^{\dagger} - \frac{2}{3} \boldsymbol{\nabla} \cdot \mathbf{u} \boldsymbol{I} \right] , \tag{6}$$

where μ is the dynamic (shear) viscosity of the mixture.

The heat flux vector includes the contributions from conduction and mass diffusion,

$$\mathbf{q} = -\lambda \boldsymbol{\nabla} T - \lambda^{\mathrm{V}} \boldsymbol{\nabla} T^{\mathrm{V}} + \sum_i \mathbf{J}_i h_i(T, T^V) \,, \qquad (7)$$

where T is the translational temperature and T^{V} is the vibrational temperature. The first two terms stem from Fourier's law and the last term refers to the diffusion of enthalpy with h_i as the species partial enthalpy.

The flow solver INCA has been coupled with the MUlticomponent Thermodynamic And Transport properties for IONized gases in C++ () library of the von Karman Institute, which provides accurate models for thermodynamic data, transport properties, chemical kinetics, and GSI. A detailed description of is presented by Scoggins et al. [19]. Verification and validation of this coupling as well as details on the models being used for the closure of the governing equations are presented by Başkaya et al. [16].

Catalytic and ablative surface boundary conditions are imposed by solving a mass balance [22; 19]

$$(\rho_i v_{blow})_{wall} + (J_i)_{wall} = \dot{\omega}_{i,wall} \,, \qquad (8)$$

with v_{blow} as the surface-normal blowing velocity, which is nonzero only for an ablative boundary. Terms from left to right refer to convective flux due to blowing, diffusive flux, and a species source term due to surface reactions. A probability-based approach is employed for computing this chemical source term for the surface, written as

$$\dot{\omega}_{i,wall} = \gamma m_i \mathcal{F}_{i,impin} \,, \qquad (9)$$

where $\gamma = \mathcal{F}_{i,react}/\mathcal{F}_{i,impin}$ is the ratio of reacting to impinging species fluxes and it describes the efficiency of the process, and m_i is the mass of the ith species [22]. Assuming the species at the wall have a Maxwellian distribution function, the impinging species flux is

$$\mathcal{F}_{i,impin} = n_i \sqrt{\frac{k_B T_w}{2\pi m_i}} \,, \qquad (10)$$

where k_B is the Boltzmann constant, T_w is the wall temperature, and n_i is the number density of the $i^{\mathbf{th}}$ species [23]. The mass blowing rate $\dot{m} = \sum_i \dot{\omega}_{i,wall}$ determines the blowing velocity

$$v_{blow} = \frac{\dot{m}}{\sum_i \rho_i} \,. \qquad (11)$$

Values obtained for species densities and mass blowing speeds are then imposed as boundary conditions for the Navier-Stokes equations.

3. Numerical Methods

The governing equations can be written as

$$\frac{\partial \mathbf{U}}{\partial t} + \boldsymbol{\nabla} \cdot \mathbf{F}(\mathbf{U}) = \mathbf{S} \,, \qquad (12)$$

where $\mathbf{U}$ is the vector of conserved variables, $\mathbf{F} = \mathbf{F}_{inv} + \mathbf{F}_{vis}$ is the sum of inviscid and viscous fluxes, and $\mathbf{S}$ is the vector of source terms. Along the x axis, they take the following forms:

$$\mathbf{U} = \begin{bmatrix} \rho_i \\ \rho u \\ \rho v \\ \rho w \\ \rho E \\ \rho e^{\mathrm{V}} \end{bmatrix}, \quad \mathbf{F}_{inv} = \begin{bmatrix} \rho_i u \\ \rho u^2 + p \\ \rho uv \\ \rho uw \\ u(\rho E + p) \\ u \rho e^{\mathrm{V}} \end{bmatrix},$$

$$\mathbf{F}_{vis} = \begin{bmatrix} J_{\mathrm{x},i} \\ -\tau_{\mathrm{xx}} \\ -\tau_{\mathrm{xy}} \\ -\tau_{\mathrm{xz}} \\ -(\tau_{\mathrm{xx}} u + \tau_{\mathrm{xy}} v + \tau_{\mathrm{xz}} w) + q_{\mathrm{x}} \\ q_{\mathrm{x}}^{\mathrm{V}} \end{bmatrix}, \quad \mathbf{S} = \begin{bmatrix} \dot{\omega}_i \\ 0 \\ 0 \\ 0 \\ 0 \\ \dot{\Omega} \end{bmatrix}.$$

INCA is a high-fidelity finite-volume solver for the compressible chemically reacting Navier-Stokes equations and provides a large number of different discretization schemes on three-dimensional block-Cartesian AMR grids [24; 25]. INCA has been successfully used in many applications such as the simulation of trans- and supercritical jet flow [25], shock-boundary layer interaction [26], reacting shock-bubble interaction [27], and multiphase fuel injection [28].

For the purposes of this study, a third-order weighted essentially non-oscillatory (WENO) scheme [29] with HLLC flux function [30] is selected to discretize the inviscid terms. WENO schemes provide high accuracy in smooth regions, while ensuring stable and sharp capturing of discontinuities. Second-order centered differences are used for the viscous terms and the explicit third-order Runge-Kutta scheme of Gottlieb and Shu [31] is selected for time integration.

Chemical source terms are treated using Strang's second-order time splitting scheme [32]. This leads to a system of ordinary differential equations (ODE) given as

$$\dot{y}_i = \frac{\dot{\omega}_i(\mathbf{y}, p, T, T^{\mathrm{V}})}{\rho} \,, \qquad (13)$$

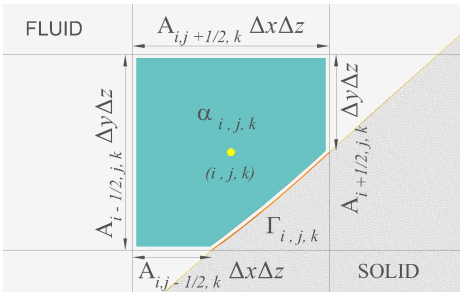

Figure 1: Sketch of a two-dimensional cut-cell in the immersed boundary method of INCA.

where $\dot{y}_i$ is the rate of change of mass fractions. This system is solved by the VODE library [33], which is an external, variable-coefficient ODE-solver using fifth-order backward differences.

3.1. Cut-Element IB Methodology

INCA employs a cut-element based immersed boundary method, which is a consistent and conservative extension of the finite-volume flux balance to accommodate cells being split by boundaries [15; 34]. At the boundary that divides the fluid and the solid regions, fluxes are calculated according to cell-face apertures and interface exchange terms as illustrated in Fig. 1. For a given cell with the geometric indices $[i, j, k]$, the fluid and solid domains are separated by the interface $\Gamma_{i,j,k}$. The aperture $A_{i,j,k}$ denotes the fraction of the cell-face area that belongs to the fluid domain. The fluid volume fraction of a cell is denoted by $\alpha_{i,j,k}$, such that the effective fluid volume of a cut cell is $(V_f)_{i,j,k} = \alpha_{i,j,k}\Delta\mathrm{x}_i\Delta\mathrm{y}_j\Delta\mathrm{z}_k$.

Following the finite-volume methodology, integration of Eq. 12 over the fluid volume V_f for a time step $\Delta t = t^{n+1} - t^n$ yields

$$\int_{t^n}^{t^{n+1}} \left[\int_{V_f} \frac{\partial \mathbf{U}}{\partial t}\, dV + \int_{S_f} \mathbf{F}(\mathbf{U}) \cdot \mathbf{n}\, dS \right] dt = 0\,, \quad (14)$$

where S_f is the wetted surface of a given cell. Defining a volume average for the conserved variables of a cell as

$$\overline{\mathbf{U}}_{i,j,k} = \frac{1}{\alpha_{i,j,k}\Delta\mathrm{x}_i\Delta\mathrm{y}_j\Delta\mathrm{z}_k} \int_V \mathbf{U} dV\,, \quad (15)$$

the three-dimensional discretization of Eq. 14 on a Cartesian grid is

$$\begin{aligned}\alpha^{n+1}_{i,j,k}\overline{\mathbf{U}}^{n+1}_{i,j,k} &= \alpha^{n}_{i,j,k}\overline{\mathbf{U}}^{n}_{i,j,k} \\ &+ \frac{\Delta t}{\Delta\mathrm{x}_i}\left[A_{i-1/2,j,k}\overline{\mathbf{F}}_{i-1/2,j,k} - A_{i+1/2,j,k}\overline{\mathbf{F}}_{i+1/2,j,k}\right] \\ &+ \frac{\Delta t}{\Delta\mathrm{y}_j}\left[A_{i,j-1/2,k}\overline{\mathbf{F}}_{i,j-1/2,k} - A_{i,j+1/2,k}\overline{\mathbf{F}}_{i,j+1/2,k}\right] \\ &+ \frac{\Delta t}{\Delta\mathrm{z}_k}\left[A_{i,j,k-1/2}\overline{\mathbf{F}}_{i,j,k-1/2} - A_{i,j,k+1/2}\overline{\mathbf{F}}_{i,j,k+1/2}\right] \\ &+ \frac{\Delta t}{\Delta\mathrm{x}_i\Delta\mathrm{y}_j\Delta\mathrm{z}_k}\mathbf{X}_{i,j,k}\,. \end{aligned} \quad (16)$$

Note that $\overline{\mathbf{F}}$ refers to the face-averaged fluxes. Here, the discretization in time is presented for a forward Euler scheme, which corresponds to a sub-step of the employed Runge-Kutta scheme. The variable $\mathbf{X}_{i,j,k}$ stands for the interface exchange term, which represents the stresses and the fluxes through the fluid-solid interface. This term is essential for the GSI boundary condition as it will be discussed further on.

Instead of a single planar fluid-solid interface as in Fig. 1, the specific method in INCA accounts for multiple cut elements per cell [15; 34]. These cut-elements directly result from the intersection of the grid with the surface triangulation. The interface of each cut-cell is thus represented by several cut-elements belonging to different surface triangles. The exchange of mass (e.g. with surface reactions), momentum, and energy through these cut-elements is calculated from the prescribed boundary conditions and local fluid values at a point within the fluid domain, which is generally a half cell length away from the interface. The value of a variable at this fluid point is acquired by interpolation from the surrounding cell values and the boundary conditions. In addition, a layer of ghost cells within the solid body is employed to allow for the use of unmodified stencils throughout the domain.

The interface exchange term $\mathbf{X}_{i,j,k}$ is expressed as a sum of the contributions of all cut elements

$$\mathbf{X}_{i,j,k} = \sum_{el} \mathbf{X}_{el}\,, \quad (17)$$

where the index el denotes cut elements for a given cell, and

$$\mathbf{X}_{el} = \mathbf{X}^{p}_{el} + \mathbf{X}^{v}_{el} + \mathbf{X}^{q}_{el} + \mathbf{X}^{m}_{el} + \mathbf{X}^{sp}_{el}\,, \quad (18)$$

where, from left to right, the terms refer to pressure work, viscous stresses, heat transfer, global mass exchange, and species mass exchange. The last two

terms incorporate GSI in addition to the original formulation described by Örley et al. [15] and Pasquariello et al. [34]. We assume that thermal equilibrium is reached at the surface, therefore there is no interface exchange for the vibrational energy.

The pressure term is given by

$$\mathbf{X}^{p}_{el} = \begin{bmatrix} 0 \\ \Delta\Gamma_{el}\, p_{\Gamma,el}\, n^{\Gamma,el}_{\mathrm{x}} \\ \Delta\Gamma_{el}\, p_{\Gamma,el}\, n^{\Gamma,el}_{\mathrm{y}} \\ \Delta\Gamma_{el}\, p_{\Gamma,el}\, n^{\Gamma,el}_{\mathrm{z}} \\ \Delta\Gamma_{el}\, p_{\Gamma,el} \left(\mathbf{v}^{\Gamma,el} \cdot \mathbf{n}^{\Gamma,el}\right) \\ 0 \end{bmatrix}, \tag{19}$$

where $p_{\Gamma,el}$ is the element interface pressure obtained from a one-sided face-normal Riemann solver, $\Delta\Gamma_{el}$ is the interface area per element, $n^{\Gamma,el}$ refers to the normal vector of the element, and $\mathbf{v}^{\Gamma,el}$ is the interface velocity evaluated at the centroid. Similarly, the viscous stresses are

$$\mathbf{X}^{v}_{el} = \begin{bmatrix} 0 \\ \Delta\Gamma_{el} \left(\boldsymbol{\tau} \cdot \mathbf{n}^{\Gamma,el}\right)_{\mathrm{x}} \\ \Delta\Gamma_{el} \left(\boldsymbol{\tau} \cdot \mathbf{n}^{\Gamma,el}\right)_{\mathrm{y}} \\ \Delta\Gamma_{el} \left(\boldsymbol{\tau} \cdot \mathbf{n}^{\Gamma,el}\right)_{\mathrm{z}} \\ \Delta\Gamma_{el} \left(\boldsymbol{\tau} \cdot \mathbf{v}^{\Gamma,el}\right) \cdot \mathbf{n}^{\Gamma,el} \\ 0 \end{bmatrix}, \tag{20}$$

where $\boldsymbol{\tau}$ is the local stress tensor. The velocity gradient in the local stress tensor is approximated by the difference between the interpolation point velocity and the interface velocity. The heat exchange is given by

$$\mathbf{X}^{q}_{el} = \begin{bmatrix} 0 \\ 0 \\ 0 \\ 0 \\ \Delta\Gamma_{el} \left(\mathbf{q}^{\Gamma,el} \cdot \mathbf{n}^{\Gamma,el}\right) \\ 0 \end{bmatrix}. \tag{21}$$

For a reacting surface, exchange of mass with the solid is modeled as

$$\mathbf{X}^{m}_{el} = \begin{bmatrix} \Delta\Gamma_{el}\, \dot{m} \\ \Delta\Gamma_{el}\, \dot{m} \left(\mathbf{v}^{\Gamma,el}_{blow} \cdot \mathbf{n}^{\Gamma,el}\right)_{\mathrm{x}} \\ \Delta\Gamma_{el}\, \dot{m} \left(\mathbf{v}^{\Gamma,el}_{blow} \cdot \mathbf{n}^{\Gamma,el}\right)_{\mathrm{y}} \\ \Delta\Gamma_{el}\, \dot{m} \left(\mathbf{v}^{\Gamma,el}_{blow} \cdot \mathbf{n}^{\Gamma,el}\right)_{\mathrm{z}} \\ \Delta\Gamma_{el}\, \dot{m} \left(h^{\Gamma,el} + \frac{1}{2} \left\| \mathbf{v}^{\Gamma,el}_{blow} \right\|^2\right) \\ 0 \end{bmatrix}, \tag{22}$$

where $\dot{m}$ is the total species production rate, $\mathbf{v}^{\Gamma,el}_{blow}$ is the blowing velocity given by Eq. 11, and $h^{\Gamma,el}$ is the enthalpy of the produced species.

Catalytic GSI are accounted for by the species surface source term $\dot{\omega}_{i,wall}$ introduced in Section 2 as

$$\mathbf{X}^{sp}_{el} = \begin{bmatrix} \Delta\Gamma_{el}\, \dot{\omega}_{i,wall} \\ 0 \\ 0 \\ 0 \\ 0 \\ 0 \end{bmatrix}. \tag{23}$$

Naturally, the sum of the species mass exchange terms yields the global mass exchange and it is only non-zero if the surface is ablative. However, as long as the surface is reacting, catalytic reactions will alter the surface species compositions and therefore lead to non-zero species mass exchange.

4. Results

4.1. Compression Ramp

The first test case is a Mach 11.63 compression ramp flow based on the experimental campaigns of Holden [35]. The numerical setup follows Brahmachary et al. [36] and McQuaid et al. [13] who modeled air as a perfect gas in chemical equilibrium. In addition to this perfect gas assumption, simulations with thermochemical nonequilibrium have also been performed in this work. The geometry consist of a straight section of 0.4394 m and a 15° ramp beyond this point. The total length of the computational domain is 0.7 m. Freestream conditions are given in Table 1. Grid resolutions near the wall are 5×10^{-5} m for the present simulations with INCA, 2×10^{-5} m for Brahmachary et al., and 3×10^{-5} m for McQuaid et al.

The flow field is visualized in Fig. 2, where the separating shock wave is impinging on the ramp. The

Table 1: Freestream conditions for the compression ramp case.

u_∞ [m/s]	T_∞ [K]	T_{wall} [K]	p_∞ [Pa]
1908.9	67.05	294.38	25

results for the pressure coefficient

$$C_p = \frac{p_{wall} - p_\infty}{0.5\rho_\infty u_\infty^2}, \tag{24}$$

and Stanton number

$$St = \frac{q_{wall}}{\rho_\infty U_\infty c_p (T_r - T_{wall})}, \tag{25}$$

distributions along the surface are presented in Fig. 3. Results obtained with the perfect gas and thermochemical nonequilibrium (TCNE) assumptions are compared. The present results are in excellent agreement with the numerical reference data of McQuaid et al. [13] for the perfect gas assumption. Due to the low temperature at the freestream, only a weak vibrational excitation is observed. Nevertheless, results with TCNE move the shock considerably closer to the ramp, while yielding pressure coefficients marginally closer to the experimental results.

For Stanton numbers, corresponding to the different definitions used by the authors of the reference results, two sets of results are shown. Firstly, by taking $T_r = T_{total}$ in accordance with Brahmachary et al. [36], and secondly, by taking T_r based on a recovery factor of 0.89 in line with McQuaid et al. [13]. Both definitions used for the Stanton number agree well with their corresponding reference results with the perfect gas assumption. Stanton numbers match the experimental reference results very well and almost exactly with the TCNE assumption.

4.2. Cylinder

A 5-species air flow at a Mach number of 12.7 over a cylinder of 0.1 m radius is considered to study the method under thermochemical nonequilibrium conditions. Sekhar et al. [37], provide reference results obtained with the well-established DPLR solver. Freestream conditions are presented in Table 2. The 5-species air mixture consists of $[N_2, O_2, NO, N, O]$. A rather coarse grid is used with $7{\times}10^{-4}$ m resolution at the surface, where an adiabatic boundary condition is imposed.

The results for the translational and vibrational temperature contours, and their distributions along the stagnation line are presented in Fig. 4 and in Fig. 5.

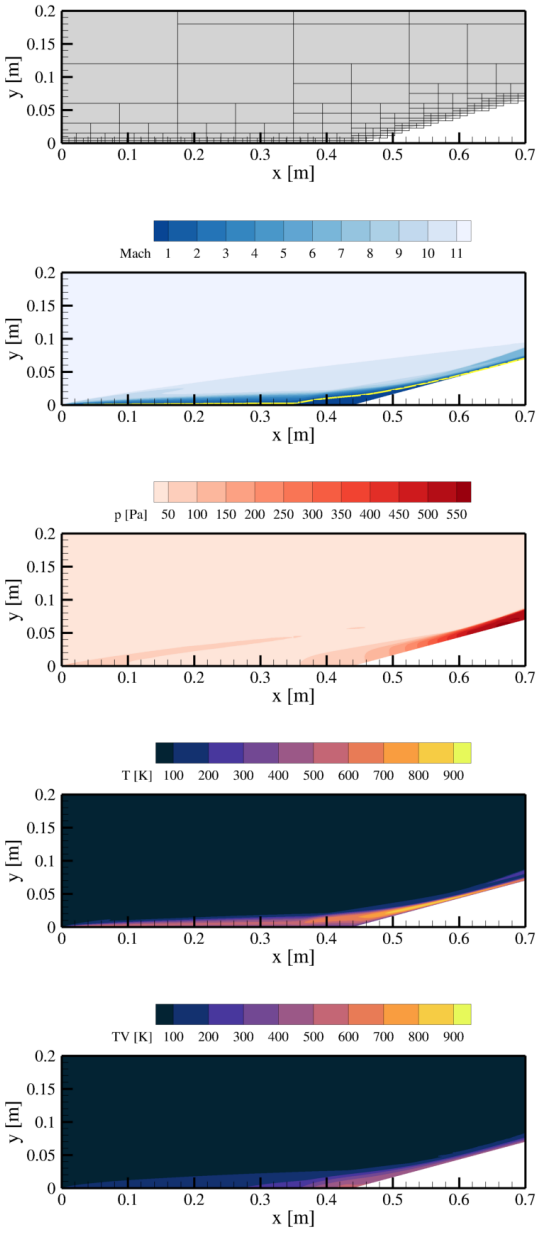

Figure 2: Flow fields showing Mach number (sonic line indicated as the bright line), pressure, translational temperature, and vibrational temperature contours for the compression ramp case with thermochemical nonequilibrium. Block structure of the numerical grid is also shown at the top. Note that this is just a coarse visualisation of the actual fine grid.

Predictions with the present method match almost exactly with the reference results. The thermal nonequilibrium beyond the shock and the relaxation to ther-

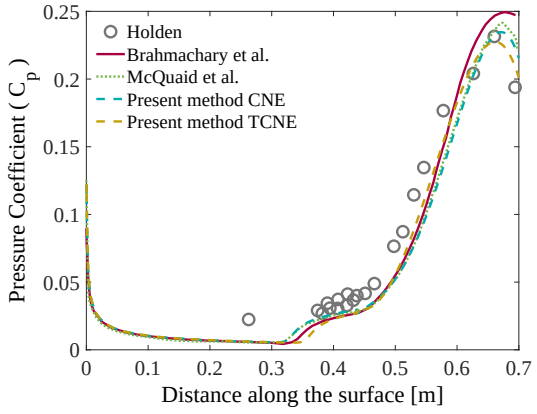

(a)

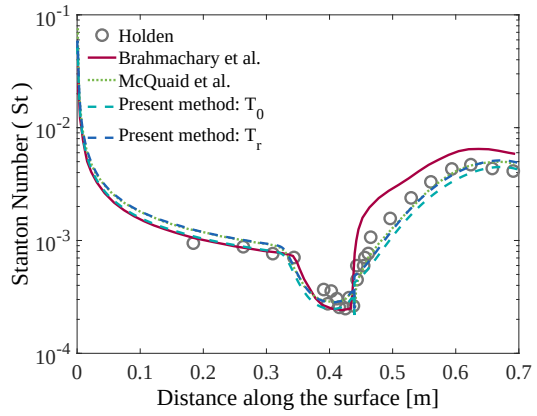

(b)

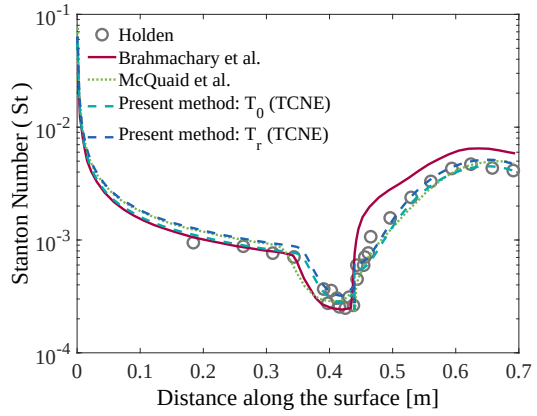

(c)

Figure 3: Comparison of (a) pressure coefficients and (b) Stanton numbers along the surface for the compression ramp case.

mal equilibrium downstream are very well captured. Slight differences are expected to be due to a coarser grid resolution near the shock for the reference simulations.

Table 2: Case specifications for the cylinder case.

u_∞ [m/s]	T_∞ [K]	p_∞ [Pa]	$y(N_2)$	$y(O_2)$
3570	195.96	90	0.7671	0.2329

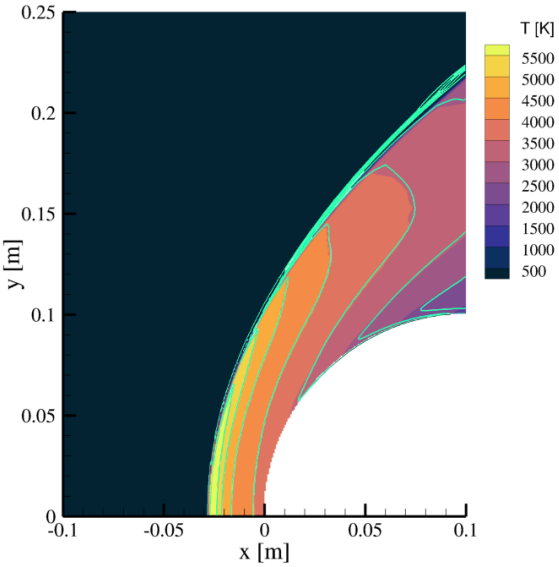

(a)

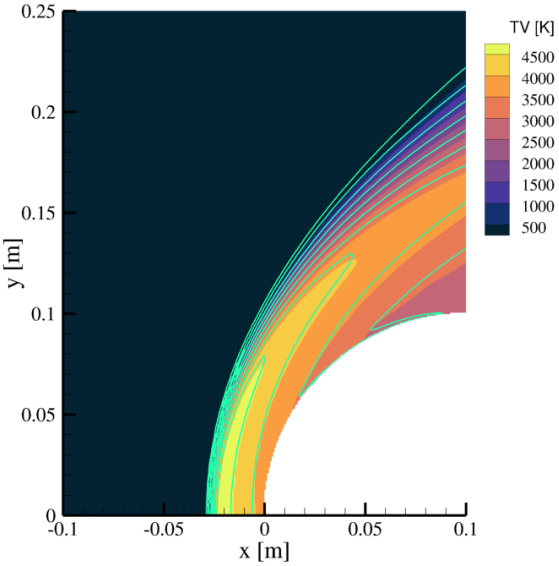

(b)

Figure 4: Comparison of (a) translational and (b) vibrational temperature contours for the cylinder case. Reference data by DPLR [37] is overlaid as bright lines.

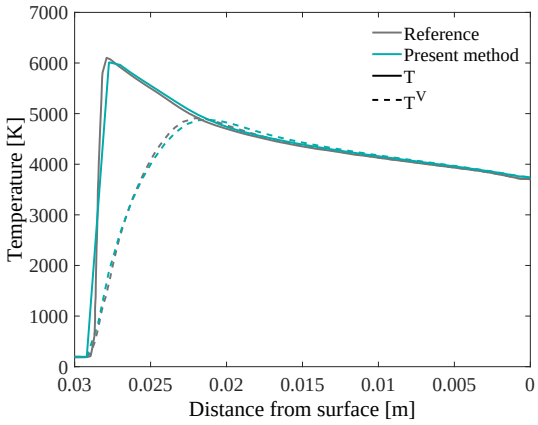

Figure 5: Variation of translational and vibrational temperatures along the stagnation line for the cylinder case. Reference data is provided by DPLR [37].

4.3. Graphite Ablator

A subsonic plasma wind tunnel experiment conducted by Helber et al. [38] at the von Karman Institute is simulated to demonstrate the ablative boundary condition. The experiment exposes a graphite sample with a hemispherical nose of radius 25 mm to nitrogen plasma. The sample undergoes ablation through nitridation reactions

$$\mathrm{C_{(solid)} + N \rightarrow CN}\,, \tag{26}$$

with the reaction probability

$$\gamma = 7.91 \cdot 10^{-2} \exp\left(-\frac{5663}{T_{\mathrm{wall}}}\right). \tag{27}$$

The nitridation efficiency was calibrated based on these particular experiments [38]. The experimental test case was simplified by Başkaya et al. [16] to a 2-D geometry without ionized species to reduce the computational cost. Freestream conditions for this case are given in Table 3. A 6-species mixture of $[N_2, N, CN, C_3, C_2, C]$ is considered. Comparison of the results are made with the US3D solver employing body-conforming meshes. US3D is an extensively validated high-fidelity solver, which uses the same models for thermochemistry and GSI as INCA in this study [16].

The mass fractions along the stagnation line and the mass blowing rates over the wall are shown in Fig. 6. The predictions of the present method agree remarkably well with the results of the reference solver. Coarse results with our method correspond to a grid resolution of 1×10^{-5} m at the wall, in line with the reference. Simulations with a finer grid with 5×10^{-6} m cell size at the wall is also performed to ensure the solution is grid converged.

Table 3: Case specifications for the graphite ablator.

u_∞ [m/s]	T_∞ [K]	T_{wall} [K]	p_∞ [Pa]	$y(N_2)$
1570	10280	2407	1500	9.8e-5

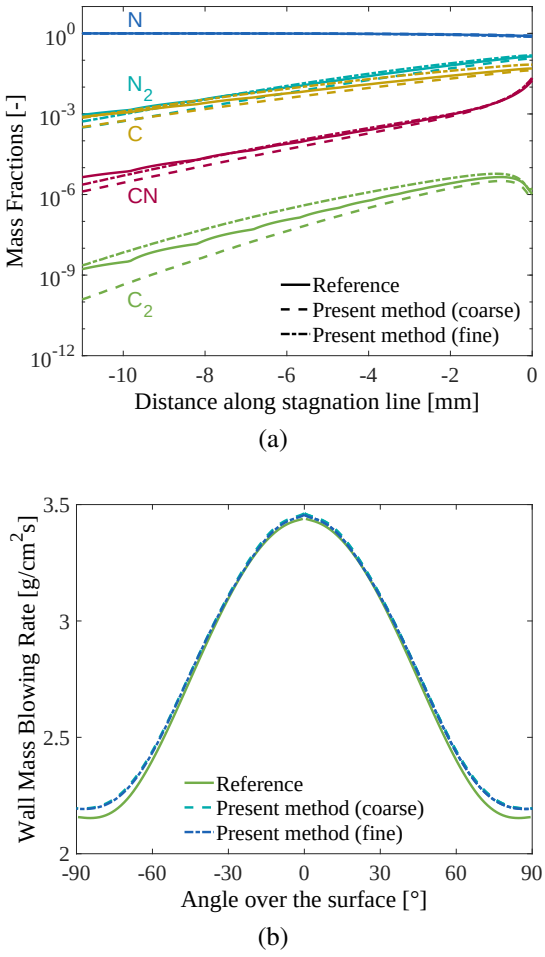

Figure 6: Comparison of (a) mass fractions along the stagnation line and (b) mass blowing rates over the surface for the graphite ablator case. Reference data is provided by the US3D solver [16].

5. Conclusion

A fully conservative cut-element immersed-boundary method for hypersonic flows under the influence of thermochemical nonequilibrium and

gas-surface interactions has been elucidated and demonstrated for hypersonic flow over a compression ramp, hypersonic flow over a cylinder, and a graphite ablator exposed to nitrogen plasma. All of the results have shown good agreement with the references, indicating that the method is highly suitable for simulations relevant in atmospheric entry applications. Future studies will explore more challenging scenarios that exploit the full potential of an adaptive mesh refinement immersed-boundary method for ablative recession and shape change.

References

[1] S. Gu, H. Olivier, Capabilities and limitations of existing hypersonic facilities, Progress in Aerospace Sciences 113 (2020) 100607.

[2] D. Knight, O. Chazot, J. Austin, M. A. Badr, G. Candler, B. Celik, D. de Rosa, R. Donelli, J. Komives, A. Lani, et al., Assessment of predictive capabilities for aerodynamic heating in hypersonic flow, Progress in Aerospace Sciences 90 (2017) 39–53.

[3] D. Knight, J. Longo, D. Drikakis, D. Gaitonde, A. Lani, I. Nompelis, B. Reimann, L. Walpot, Assessment of CFD capability for prediction of hypersonic shock interactions, Progress in Aerospace Sciences 48 (2012) 8–26.

[4] M. J. Wright, T. White, N. Mangini, Data Parallel Line Relaxation (DPLR) Code User Manual: Acadia Version 4.01. 1, National Aeronautics and Space Administration, Ames Research Center, 2009.

[5] G. Candler, D. Mavriplis, L. Trevino, Current status and future prospects for the numerical simulation of hypersonic flows, in: 47th AIAA Aerospace Sciences Meeting Including the New Horizons Forum and Aerospace Exposition, 2009, p. 153.

[6] G. V. Candler, H. B. Johnson, I. Nompelis, V. M. Gidzak, P. K. Subbareddy, M. Barnhardt, Development of the us3d code for advanced compressible and reacting flow simulations, in: 53rd AIAA Aerospace Sciences Meeting, 2015, p. 1893.

[7] L. Scalabrin, I. Boyd, Development of an unstructured navier-stokes solver for hypersonic nonequilibrium aerothermodynamics, in: 38th AIAA Thermophysics Conference, 2005, p. 5203.

[8] R. Boukharfane, F. H. E. Ribeiro, Z. Bouali, A. Mura, A combined ghost-point-forcing/direct-forcing immersed boundary method (ibm) for compressible flow simulations, Computers & Fluids 162 (2018) 91–112.

[9] D. S. Balsara, C.-W. Shu, Monotonicity preserving weighted essentially non-oscillatory schemes with increasingly high order of accuracy, Journal of Computational Physics 160 (2) (2000) 405–452.

[10] R. Arslanbekov, V. Kolobov, A. Frolova, Analysis of compressible viscous flow solvers with adaptive cartesian mesh, in: 20th aiaa computational fluid dynamics conference, 2011, p. 3381.

[11] C. Atkins, R. Deiterding, Towards a strand-cartesian solver for modelling hypersonic flows in thermochemical nonequilibrium, in: 23rd AIAA International Space Planes and Hypersonic Systems and Technologies Conference, 2020.

[12] S. Brahmachary, G. Natarajan, V. Kulkarni, N. Sahoo, V. Ashok, V. Kumar, Role of solution reconstruction in hypersonic viscous computations using a sharp interface immersed boundary method, Physical Review E 103 (4) (2021) 043302.

[13] J. A. McQuaid, A. L. Zibitsker, B. Saikia, A. Martin, C. Brehm, An immersed boundary method for hypersonic viscous flows, in: AIAA Scitech 2021 Forum, 2021, p. 0926.

[14] S. K. Sekhar, S. M. Ruffin, Predictions of convective heat transfer rates using a Cartesian grid solver for hypersonic flows, in: 44th AIAA Thermophysics Conference, 2013, p. 2645.

[15] F. Örley, V. Pasquariello, S. Hickel, N. A. Adams, Cut-element based immersed boundary method for moving geometries in compressible liquid flows with cavitation, Journal of Computational Physics 283 (2015) 1–22.

[16] A. O. Başkaya, M. Capriati, D. Ninni, F. Bonelli, G. Pascazio, A. Turchi, T. Magin, S. Hickel, Verification and validation of immersed boundary solvers for hypersonic flows with gas-surface interactions, in: AIAA Aviation 2022 Forum, 2022.

[17] C. Park, Nonequilibrium hypersonic aerothermodynamics, 1989.

[18] J. O. Hirschfelder, C. F. Curtiss, R. B. Bird, M. G. Mayer, Molecular theory of gases and liquids, Vol. 165, Wiley New York, 1964.

[19] J. B. Scoggins, V. Leroy, G. Bellas-Chatzigeorgis, B. Dias, T. E. Magin, Mutation++: Multicomponent thermodynamic and transport properties for ionized gases in c++, SoftwareX 12 (2020) 100575.

[20] T. E. Magin, M. Panesi, A. Bourdon, R. L. Jaffe, D. W. Schwenke, Coarse-grain model for internal energy excitation and dissociation of molecular nitrogen, Chemical Physics 398 (2012) 90–95.

[21] C. Park, The limits of two-temperature kinetic model in air, in: 48th AIAA Aerospace Sciences Meeting Including the New Horizons Forum and Aerospace Exposition, 2010, p. 911.

[22] G. Bellas Chatzigeorgis, A. Turchi, A. Viladegut, O. Chazot, P. F. Barbante, T. Magin, Development of catalytic and ablative gas-surface interaction models for the simulation of reacting gas mixtures, in: 23rd AIAA Computational Fluid Dynamics Conference, 2017, p. 4499.

[23] P. F. Barbante, et al., Accurate and efficient modelling of high temperature nonequilibrium air flows, Von Karman Institute for Fluid Dynamics, 2001.

[24] S. Hickel, C. P. Egerer, J. Larsson, Subgrid-scale modeling for implicit large eddy simulation of compressible flows and shock-turbulence interaction, Physics of Fluids 26 (10) (2014) 106101.

[25] H. Müller, C. A. Niedermeier, J. Matheis, M. Pfitzner, S. Hickel, Large-eddy simulation of nitrogen injection at trans-and supercritical conditions, Physics of fluids 28 (1) (2016) 015102.

[26] V. Pasquariello, S. Hickel, N. A. Adams, Unsteady effects of strong shock-wave/boundary-layer interaction at high reynolds number, J. Fluid Mech 823 (617) (2017) 014602–19.

[27] F. Diegelmann, S. Hickel, N. A. Adams, Three-dimensional reacting shock–bubble interaction, Combustion and Flame 181 (2017) 300–314.

[28] J. Matheis, S. Hickel, Multi-component vapor-liquid equilibrium model for LES of high-pressure fuel injection and application to ECN spray A, International Journal of Multiphase Flow 99 (2018) 294–311.

[29] G.-S. Jiang, C.-W. Shu, Efficient implementation of weighted eno schemes, Journal of Computational Physics 126 (1) (1996) 202–228.

[30] E. F. Toro, Riemann solvers and numerical methods for fluid dynamics: a practical introduction, Springer Science & Business Media, 2013.

[31] S. Gottlieb, C.-W. Shu, Total variation diminishing runge-kutta schemes, Mathematics of Computation 67 (221) (1998) 73–85.
[32] G. Strang, On the construction and comparison of difference schemes, SIAM Journal on Numerical Analysis 5 (3) (1968) 506–517.
[33] P. N. Brown, G. D. Byrne, A. C. Hindmarsh, Vode: A variable-coefficient ode solver, SIAM Journal on Scientific and Statistical Computing 10 (5) (1989) 1038–1051.
[34] V. Pasquariello, G. Hammerl, F. Örley, S. Hickel, C. Danowski, A. Popp, W. A. Wall, N. A. Adams, A cut-cell finite volume–finite element coupling approach for fluid–structure interaction in compressible flow, Journal of Computational Physics 307 (2016) 670–695.
[35] M. Holden, A study of flow separation in regions of shock wave-boundary layer interaction in hypersonic flow, in: 11th Fluid and PlasmaDynamics Conference, 1978, p. 1169.
[36] S. Brahmachary, G. Natarajan, V. Kulkarni, N. Sahoo, A sharp-interface immersed boundary method for high-speed compressible flows, in: Immersed Boundary Method, Springer, 2020, pp. 251–275.
[37] S. K. Sekhar, M. Zaki, S. Ruffin, V. Kolobov, R. Arslanbekov, Evaluation of viscous flow solvers with adaptive cartesian meshes for hypersonic flows, in: 42nd AIAA Thermophysics Conference, 2011, p. 4035.
[38] B. Helber, A. Turchi, T. E. Magin, Determination of active nitridation reaction efficiency of graphite in inductively coupled plasma flows, Carbon 125 (2017) 582–594.

Aerodynamic investigation of space debris separation: Space debris interaction across a two-dimensional oblique shock wave

Dániel Gábor Kovács

Aeronautics and Aerospace Department, von Karman Institute for Fluid Dynamics, Belgium, / Aerospace and Mechanical Engineering Department, University of Liège, Belgium, daniel.gabor.kovacs@vki.ac.be

Supervisor: Olivier Chazot

Professor and Head of Department, Aeronautics and Aerospace Department, von Karman Institute for Fluid Dynamics, Belgium, olivier.chazot@vki.ac.be

Supervisor: Guillaume Grossir

Senior Research Engineer, Aeronautics and Aerospace Department, von Karman Institute for Fluid Dynamics, Belgium, guillaume.grossir@vki.ac.be@vki.ac.be

University Supervisor: Grigorios Dimitriadis

Professor, Aerospace and Mechanical Engineering Department, University of Liège, Belgium, gdimitriadis@uliege.be

Abstract

Free-flight testing in hypersonic wind tunnels has shown superior capabilities to conventional sting-supported model experiments using aerodynamic balances for analyzing debris objects, providing accurate aerodynamic databases, and testing fragment separation scenarios. The aerodynamics of a free-flying ring that interferes with a two-dimensional oblique shock wave has been tested in the VKI Longshot facility. The ring model was initially suspended at 90 °, 60 °, 0 ° incidence upstream of a transversely mounted cylinder. The interference induces a notable flow-normal velocity even at early stages of the interaction, promoting a shock wave surfing motion.

Keywords: Space debris, re-entry, fragment separation, hypersonic aerodynamics, free-flight testing, VKI Longshot, ATD3 Test Case 2022

1. Introduction

Accumulation of space debris and the production of untraced particles on Earth's orbits increases the possibility of impacts with operational spacecraft, which can cause unpredicted re-entries and eventually prohibit the use of Earth orbits.. To maintain in the long-term a sustainable space environment, space debris mitigation guidelines promote a twofold plan: removal of the actual space junk, and prevention of further accumulation by designing the components to demise during their uncontrolled atmospheric entry. Re-entry prediction software (e.g., DAS, ORSAT, SESAM, DEBRISK, SCARAB, PAMPERO, etc.) are being developed to promote the design of completely demisable spacecraft and hence mitigate the growth of space debris. Such toolkits rely on low fidelity models to compute the re-entry trajectory. They use an aerodynamic databases or simplified theories such as modified Newtonian method [1] which usually fail when predicting complex geometries, concave surfaces, or if shock interactions are present. These engineering correlations are well suited for single bodies, but fail in modeling the break-up process and the dispersion of the fragments (undergoing mutual interactions) due

This preprint has not undergone peer review or any post-submission improvements or corrections. The version of record of this article is published in Experiments in Fluids, August 2023, Vol. 64, Issue 8, Paper 146, and is available online at https://doi.org/10.1007/s00348-023-03686-9

to the complexity of the phenomena and the poor initialization of the fragment trajectories.

The relevance of free-flight testing methodologies to establish accurate aerodynamic databases has been demonstrated earlier [2] and proved ideal for space debris presenting a random entry attitude [3; 4; 5] and testing fragment separation scenarios [6; 7; 8; 9]. Their capabilities are superior to sting-supported model experiments using aerodynamic balances, which modify the wake structure of the model and often require complex acceleration compensations [10] in short duration facilities. Free-flight techniques rely on the analysis of the model's acceleration or trajectory as it is exposed to the flow. These quantities can be determined by placing accelerometers [11], a microcontroller, a data logger [12] or transmitter [13] and a battery inside the model, or by optical techniques relying on contour detection [11; 14; 6; 7; 4], or marker-based stereo tracking [3]. Optical techniques proved to be superior to sensor measurements since they do not pose any spatial constraints regarding the model interior and do not influence the inertia, but require high-speed imaging techniques and image processing algorithms.

Fragmentation studies were established by [15], who described the separation dynamics of meteoroid fragments with an equation expressing the expected lateral terminal velocity. The two-body problem was thoroughly analyzed by [11], [14] focused on shock-wave surfing configurations, and [16] inspected wake interference effects. Studies usually investigate single bodies [3; 4; 17] assuming separate fragment trajectories, or analyze simple proximal body scenarios such as the interaction of spheres [16; 11; 14; 6; 7] or various simple shapes [18, (qualitative analysis)], but the extension of these models to more bodies or clusters is not obvious [8]. Only a few studies have been conducted on larger numbers of objects by [7] and [8]. These works aid the understanding of the behavior of clusters, but a general, representative image of real meteorite and spacecraft break-up events remains to be drawn.

This research aims to advance the free-flight methodology implemented by [4] in the VKI Longshot facility, deepen the understanding of fragment interactions, and supply Design for Demise and CFD tools with experimental data on such proximal body interactions. The present work focuses on the aerodynamics of a ring that interferes with a crossflow cylinder (interstage rocket element and fuselage) at Mach 14 flow conditions. The current experiment and the obtained results serve as a test case and validation data for the Aerothermodynamics and Design for Demise (ATD3) Working Group for 2022.

Section 2 introduces the wind tunnel, the rebuilding of the freestream flow conditions, the flow visualization system, and the measurement setup. Section 3 describes the image and data process techniques. The results of the experimental campaign are presented in Section 4, and Section 5 concludes the work.

2. Experimental tools and measurement setup

2.1. VKI Longshot Facility

The present experimental campaign was carried out in the VKI Longshot (illustrated in Fig. 1) using the Mach 14 contoured nozzle. Since the test gas is continuously expanded through the nozzle while the volume of the reservoir is kept constant, the stagnation conditions are progressively decreasing in time [19]. The targeted initial conditions provide unit Reynolds numbers around $Re_{unit} = 2.3 - 1.9 \cdot 10^6$ 1/m with a core flow diameter of 293 mm for 12 ms and 200 mm for 17 ms [20].

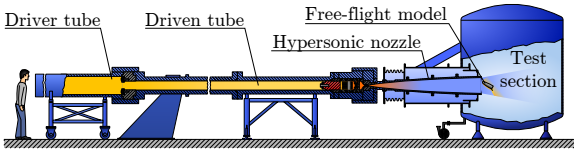

Figure 1: The VKI Longshot facility [4].

2.2. Freestream rebuilding

In order to achieve good accuracy on the flow conditions and derived quantities, a freestream rebuilding technique has been developed for the VKI Longshot facility by [19]. A set of probes (pitot, stagnation point heat flux, and static pressure probe) enables a complete characterization of the flow without the need to involve additional reservoir measurements nor detailed modeling of the nozzle flow, hence contributing to a better accuracy. This set of probes is used for every experiment and set to minimize interactions with the main test articles.

2.3. Flow visualization

The VKI Longshot facility is equipped with a Z-type horizontal schlieren system, which is fixed independently of the facility to avoid vibrations. The schlieren images were captured using a Phantom v2012 monochrome high-speed camera with a

Nikkor 200 mm focal length objective. The images were recorded at 20,000 Hz sampling frequency with 15.98 μs exposure time at a resolution of 1024 × 656 pixels.

2.4. Wind tunnel models

The geometry of the free-flying annular ring model has an external diameter of $D = 60$ mm, its wall thickness is $t = 2$ mm, and its height is $h = 15$ mm. The reference length of the ring is defined as its external diameter $l_{ref} = D$, and its reference surface is defined as $S_{ref} = D \times h$, both for consistency with previous experiments by [4]. The reference point around which moments are determined is the center of gravity, located at the center of the object. The weight of the model was measured by a Kern EW 150-3M precision scale with an accuracy of ±0.01 g.

The crossflow cylinder used to generate an oblique shock wave has a diameter of $D = 60$ mm, which is identical to the diameter of the ring model. This fixed model extends beyond the entire exit of the nozzle ($L = \infty$), hence it creates a two-dimensional bow shock within the coreflow region.

2.5. Design of the model and probe alignment

The test configuration is illustrated in Figure 2. The placement of the Pitot, the static pressure, and the heat-flux probe, and the position of the cylinder model were designed in order to mitigate shock interactions between them. Additionally, the limitations determined during the recent commissioning of the Mach 14 nozzle [20], such as the useful test times, core flow diameters, and typical dynamic pressure behaviour curve, informed the design.

2.6. Test matrix

Three tests were conducted by varying the initial incidence and position of the ring. The world reference frame is fixed to the center of the cylinder. The parameters of the individual tests, such as the free-flight model's weight and mass moment of inertia, the nominal initial incidence, and the relative position with respect to the center of the cylinder are summarized in Table 1.

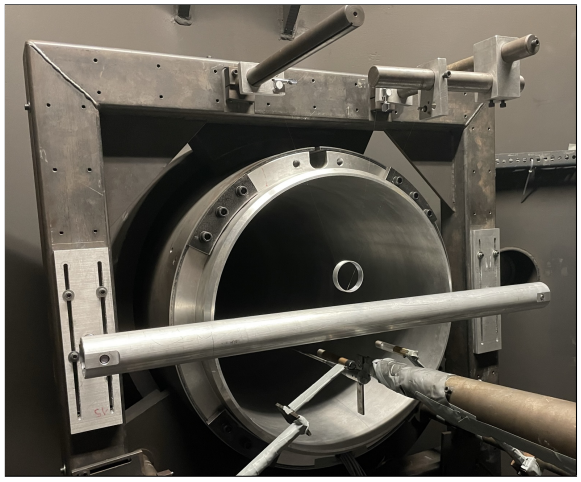

Figure 2: Photo of the test configuration.

Table 1: Test matrix

	Test cases		
Nominal incidence	0 °	60 °	90 °
	Model properties		
Mass, g	13.04	13.01	13.30
Inertia, g · mm^2	5734.3	5721.1	5848.7
	Initial position and attitude		
x_0, mm	−42.33	−9.56	−41.88
z_0, mm	79.35	91.08	76.48

3. Methodology

3.1. Identification of model contours

The localization of the model contours is performed with a sub-pixel level edge detection algorithm accounting for partial area effects [21]. The contour detection procedure involves the application of various masks in order to moderate the search region of the edge detection routine and to differentiate the model features from the flow features and the background. The detection algorithm is illustrated in Figure 3 with the main processing steps applied to a frame of the $\alpha_0 = 90$ ° test.

First, a trajectory mask was created based on the average of the schlieren images. The mask presented in Figure 3a defines the boundaries of the region of interest within which the model is included on all frames. The original images were cropped accordingly at the minimum and maximum of the horizontal and vertical borders of the mask, yielding a reduced 308 × 284 pixel image size. Next, a mask was created for the tunnel wall which is outside of the optical path of the schlieren system, but is part of the camera's field of view. Then, a mask for the bow shock of the crossflow cylinder was constructed. After the definition of the three masks shown in Fig-

ure 3b (which were identical for all images), the edge search was executed for each cropped image. Aiming at a precise model boundary detection limits the ideal threshold level to moderate values, which causes the identification of flow features and random noise as edges. Therefore, to filter out the edges that do not correspond to the model, a fourth, image-dependent, rough enclosing mask was created. The enclosing mask (Figure 3c) was built on the previously defined masks, and was customized for each frame. Examining the influence of the threshold level, the complete processing was repeated for threshold values of 5, 10, 20, and 30. The three lower threshold levels showed a good agreement on the model incidence and trajectory, while the highest level failed to accurately capture the model contours. Consequently, the results obtained with threshold level of 30 were neglected and the mean of the trajectories retrieved with the lower thresholds was used.

3.2. Identification of model position and attitude

The accurate determination of the object position and attitude relies on the following contour matching algorithm. Using an STL CAD geometry, orthogonal projections have been created for the ring model inclined at numerous pitch and roll angle combinations with steps of $\Delta\theta = \Delta\phi = 0.5\,^{\circ}$. The generated contour projections were then assimilated to detected model edges. An optimization algorithm translates the CAD contour until the error between the synthetic points and the model contour points minimizes. This optimization is than repeated for different model attitudes until a search algorithm identifies the incidence yielding the best match. The position retrieved with the offset of the best fit is considered as the location of the model's center of gravity. In order to improve the accuracy of the incidence determination, a 2nd order polynomial surface is fitted on the $\phi - \theta - \mathcal{E}$ points neighbouring the optimum. The minimum of the surface is identified as the model's attitude.

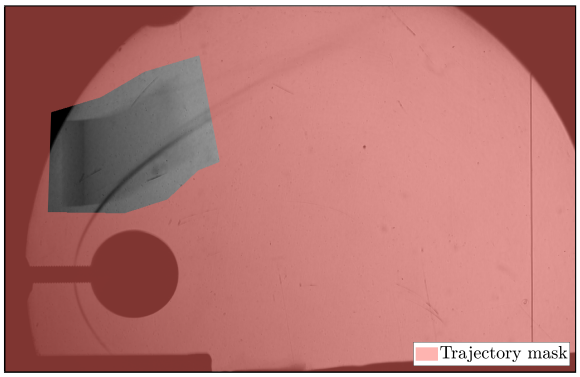

(a) Average of the original schlieren images and the trajectory mask.

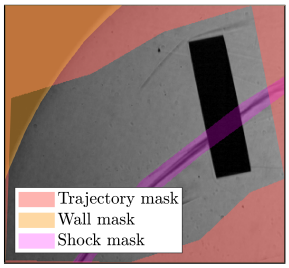

(b) The trajectory, shock, and wall mask.

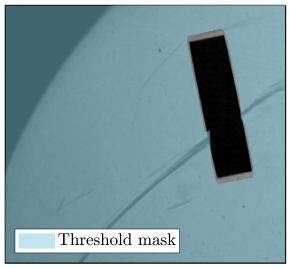

(c) The enclosing mask wrapping around the model.

Figure 3: Edge detection procedure.

3.3. Trajectory processing

Observing the high-speed schlieren video, a processable time frame was selected. It is starting from the arrival of the flow and is bounded by the last frame before the ring model reaches the downstream edge of the uniform core flow. After the position and attitude of the model was detected by the contour matching algorithm on all the images within the useful time frame, the trajectory was obtained in terms of image coordinates.

The inspection of the reference vertical plumb-line yielded a small camera tilt angle. In order to preserve the quality of the images, the correction was not performed directly on the images before the analysis, but on the the detected flight trajectory as a rotation around the center of the field of view. For the following analysis, the relative position of the ring with respect to the crossflow cylinder is of interest. Therefore, the position of the cylinder was determined, and the trajectory was offsetted in order to have the origin of the coordinate system coincide with the cylinder's center.

The determination of the forces acting on the ring model require a double differentiation of the trajectory followed. This makes it quite sensitive to small disturbances along the object path, even though a seemingly smooth trajectory was retrieved from the image analysis technique. To mitigate this, one can fit the trajectories by polynomials [7; 4; 9] or smooth them using various methods, e.g., a moving average or a Savitzky-Golay filter [3; 5]. In the present analysis, a Savitzky-Golay filter was applied.

3.4. Computation of the aerodynamic coefficients

The model's velocities $\left(U_x,\ U_z,\ \omega_y\right)$ and accelerations $\left(a_x,\ a_z,\ \varepsilon_y\right)$ were computed with a second order numerical differentiation scheme. The aerodynamic forces were computed according to:

$$D = \left(a_x - g \cdot \sin\eta\right) \cdot m \ , \tag{1}$$

$$L = \left(a_z - g \cdot \cos\eta\right) \cdot m \ , \tag{2}$$

$$M_y = \varepsilon_y \cdot I_{yy} \ , \tag{3}$$

where a and ε are the directional and angular acceleration respectively, $g = -9.81\ \mathrm{m/s^2}$ is the gravitational acceleration, and η is the nozzle blow angle (due to the recent realignment of the facility this was considered to be zero). Since no variation can be observed in the model's yaw angle and the roll angle was close to zero, no further corrections must be made on the measured forces. The aerodynamic coefficients were computed by normalizing the aerodynamic forces and moment with the time-varying freestream dynamic pressure $\left(q_\infty = 1/2 \cdot \rho_\infty \cdot U_\infty^2\right)$, the reference surface $\left(S_{ref}\right)$, and reference length $\left(l_{ref}\right)$ defined in Section 2.4, according to Equation 4 – 6.

$$C_D = \frac{D}{q_\infty \cdot S_{ref}} \tag{4}$$

$$C_L = \frac{L}{q_\infty \cdot S_{ref}} \tag{5}$$

$$C_{M_y} = \frac{M_y}{q_\infty \cdot S_{ref} \cdot l_{ref}} \tag{6}$$

In order to account for the motion of the model with respect to the freestream flow, two amendments can be performed. First, one can account for the horizontal movement by computing the dynamic pressure based on the relative velocity according to:

$$q_{\infty,corr} = \frac{1}{2} \cdot \rho_\infty \cdot \left(U_\infty - U_x\right)^2 \ . \tag{7}$$

Second, due to the vertical motion and the high pitch rate, an effective angle of attack can be computed by correcting the pitch angle with two additional terms:

$$\alpha = \theta + \arctan\left(\frac{U_y}{U_\infty - U_x}\right) + \frac{\dot{\theta} \cdot l_{ref}}{U_\infty - U_x} \ . \tag{8}$$

This permits the comparison of aerodynamic coefficients retrieved from various studies.

4. Results and discussion

4.1. Annular model at $\alpha_0 = 90°$ (ATD3 Test Case)

4.1.1. Flow properties

The freestream flow conditions were rebuilt with the method discussed in Section 2.2 of the paper, according to [19]. They evolve slightly during a run following the working principle of the Longshot tunnel that operates from a constant volume reservoir. The $t = 0.0$ ms time instant corresponds to the arrival of the flow onto the crossflow cylinder model. The measured freestream Reynolds number decays from $Re = 2.3 \cdot 10^6$ /m to approximately $1.9 \cdot 10^6$ /m, and a fairly constant Mach number of $M = 13.7$ was observed throughout the useful test time of the experiment.

4.1.2. Analysis of the trajectory

Figure 4 illustrates a superimposed schlieren image and a sketch of the free-flight scenario. The superimposed image presents an average of every 2 ms (40th frame) captured between $t = 0{-}14$ ms. The plot on the right hand side indicates the position of the ring model at selected time instants, the location of the crossflow cylinder, its bow shock contour detected at 8.0 ms, and the flow field around the cylinder obtained from a 2D inviscid CFD simulation. The detected flight trajectory is plotted with a dashed black line and the *CG* positions are marked with × symbols.

One can observe in Figure 4 that the trajectory curves upwards and after approximately 8 ms, aligns with the contour of the cylinder's detached shock. Although longer observations would be required to confirm this trend, the ring seems to surf the shock wave. The orientation of the blue arrows indicate the local flow directions around the crossflow cylinder at flow conditions corresponding to $t = 8$ ms. The inclined post-bow shock flow angles and the flow direction behind the shock interaction must be the reason for the ring's lifting trajectory.

Additionally, in Figure 4, one can compare the measured flight path with a simulated, interference-free trajectory (plotted with a dotted red line and + symbols). The trajectory propagation was initiated from the time instant the ring is free of its support wires ($t = 3.8$ ms), using the corresponding flight properties (model incidence, velocity, pitch rate), the dynamic pressure history measured during the experiment, and the freestream ring aerodynamic coefficients determined by [4]. While in an unperturbed configuration the ring would gently sink and slightly pitch in the counterclockwise direction, the present

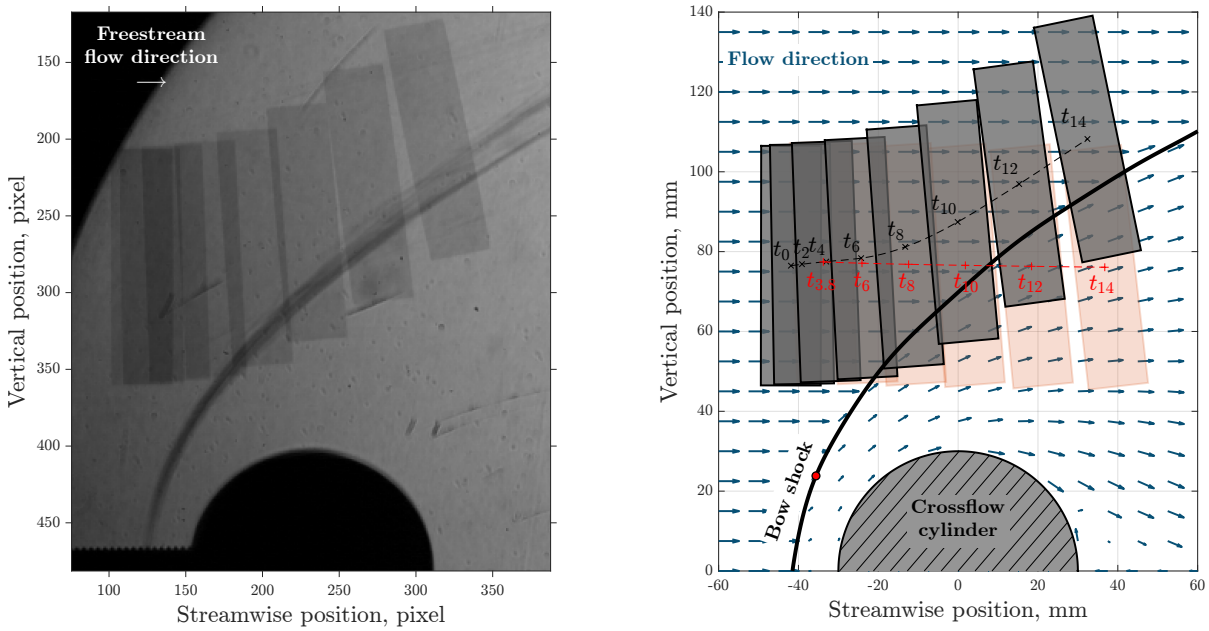

Figure 4: Superimposed schlieren image and trajectory comparison (× measured, + interference-free (simulated)).

experiment shows that the interaction with the cylinder's shock largely influences the trajectory, leading to a significant flow-normal velocity shortly after the interaction begins, and promoting a shock-wave surfing motion.

4.1.3. Aerodynamic coefficients

Figure 5 presents the variation of the drag, lift, and pitching moment coefficients as a function of the effective angle of attack (α). These coefficients (plotted with solid black lines) were normalized by the dynamic pressure accounting for the motion of the ring ($q_{\infty,corr}$). This permits the direct comparison of the deduced aerodynamic coefficients with the interference-free ring aerodynamic characteristics. In Figure 5, 13 time instances corresponding to 13 ms are marked by × symbols. Solid blue lines indicate the aerodynamic properties of this ring geometry computed by modified Newtonian theory using the VKI ANTARES code by [22] (in the absence of shock interactions). The green markers illustrate the experimental results (and their uncertainties corresponding to $1-\sigma$) obtained by [4] for the same annular ring model in interference-free free-flight conditions. One must note, that these results were also obtained in the VKI Longshot wind tunnel, but using a different hypersonic nozzle, at Mach 11 flow conditions. The flow establishment time is illustrated with a dark red zone, the wire ruptures are marked by gray zones, and the end of the useful test time is indicated with a light red zone.

Comparing the aerodynamic coefficients after all cables are detached from the model (3.8 ms), one can observe a fair agreement in the lift between the experiments and the approximate theory, whereas the drag and pitching moment coefficients are different. This implies, that the shock-shock interaction taking place at the bottom of the ring already influences the pressure distribution on the model at this time instance. The enhanced interference at the lower rear edge of the ring after $t = 4.2$ ms strongly lifts the model, while its drag gently decays. The lift-to-drag ratio (L/D) plotted in Figure 6a clearly demonstrates this escalation. As the upper interaction point moves closer to the ring's lower edge (5-6.5 ms), the negative pitching moment (which was close to the interference-free value) decreases and eventually this triple point vanishes. The measured drag coefficient starts to increase as the lower front edge of the ring reaches the cylinder's shock front at 8 ms. The upwards translation of the interaction point exerts increasing pitching moment onto the model whose frontal surface progressively submerses into the cylinder's shock front. As the interaction point reaches the lower internal edge of the ring around 9.35 ms, the lift starts to decay. Around 11 ms, when the shock impingement point approaches the model's surface, the drag and the pitching moment coefficients reach a plateau, and the decay

of the lift coefficient slows down, producing a fairly constant lift-to-drag ratio clearly visible in Figure 6a. On the contrary, observing the corresponding trajectory section in Figure 4, one can notice that its slope is much smaller than unity. The inclination of the flight path is rather approximately 32 °, which must be because the residual streamwise momentum of the

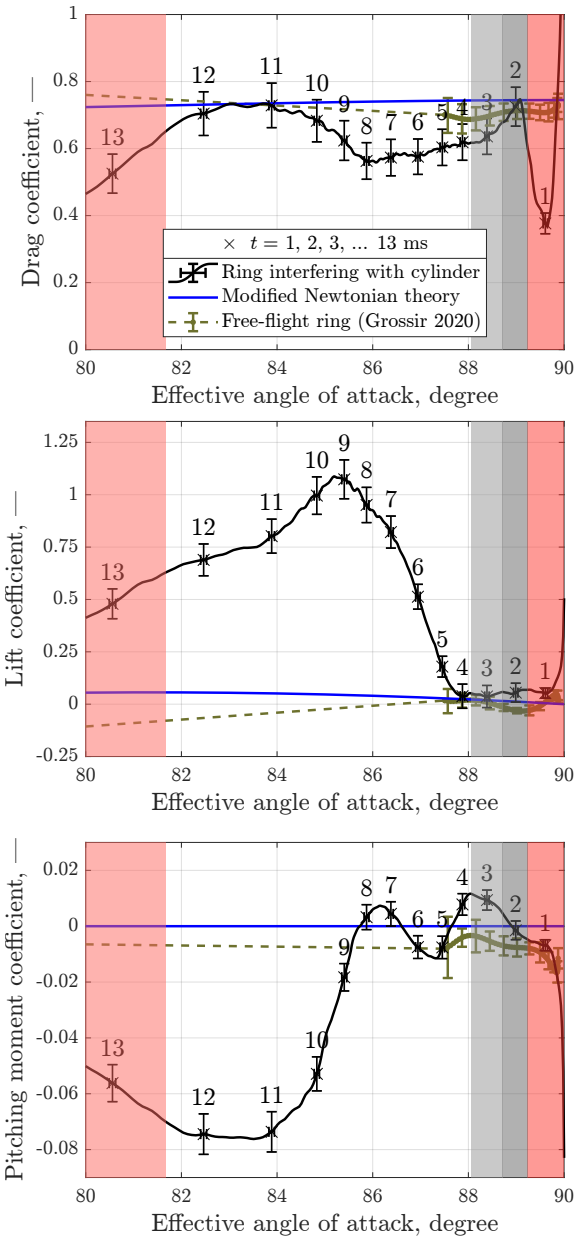

Figure 5: The measured interfering ring aerodynamic coefficients (normalized by $q_{\infty,corr}$) as a function of the effective angle of attack (α).

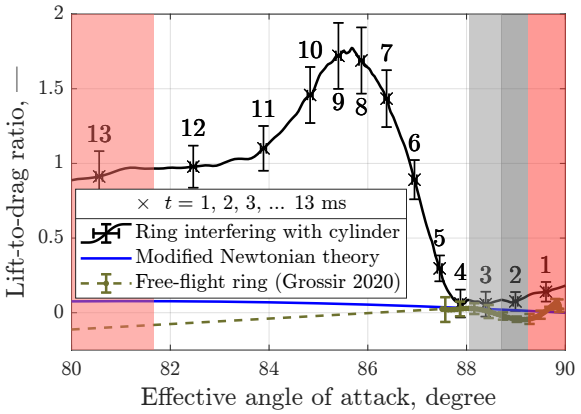

(a) Variation of the lift to drag ratio as a function of the effective angle of attack (α).

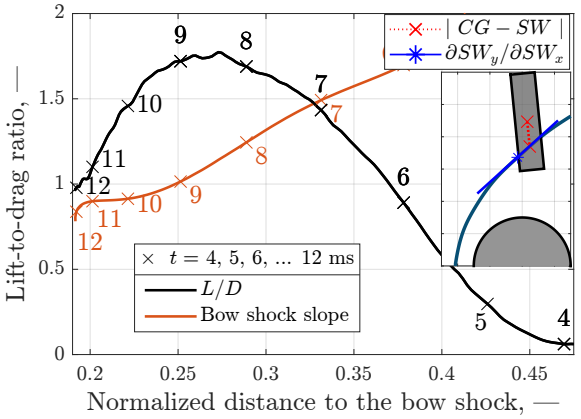

(b) Variation of the lift to drag ratio as a function of the distance between the ring's center of gravity (CG) and the cylinder's bow shock. The distance is normalized by the model diameter.

Figure 6: Lift to drag ratio (L/D) of the interfering ring. The aerodynamic coefficients are normalized by $q_{\infty,corr}$.

model contributes to the motion.

It would be interesting to inspect the formation of the trajectory further downstream, in order to see how long could the surfing motion be maintained, and if the ring would get expelled or entrained. Figure 6b illustrates the variation of the lift-to-drag ratio as a function of the distance between the model's center of gravity and the closest point of the cylinder's detached shock wave. The distance $|CG - SW|$ (illustrated in Figure 6b with × symbols and dotted blue line) is normalized by the model's diameter. An orange line represents the variation of the bow shock's tangent $\left(\partial S\,W_y/\partial S\,W_x\right)$, where the ring's frontal plane would intersects the bow shock (marked with an as-

terisk symbol). The tangent at the virtual intersection line is plotted with a solid orange dash.

The L/D and the bow shock slope curves in Figure 6b seem to converge at the end of the experiment when the lift to drag ratio reaches a plateau, but the normalized distance remains constant through the last 0.5 ms. The final difference between the curves suggests that the ring would get expelled, but the pitching motion of the object makes it difficult to reach a clear conclusion. As a result of the interaction, the ring receives a significant amount of energy leading to a lateral velocity that would contribute to dispersing the objects in case of a fragmentation scenario. The validation of numerical tools with the present experimental results could enable the accurate prediction of the trajectory and interferences further downstream.

4.2. Annular model at $\alpha_0 = 60°$

The initial model placement was slightly too downstream, hence the interaction with the cylinder's bow shock started as soon as the flow was fully established. The rupture of the support wires was delayed, the rear cable remained in contact until 7.65 ms. Figure 7a presents the reconstruction of the measured flight trajectory in comparison with a simulated flight path. The simulated trajectory was started from $t = 7.70$ ms using the parameters (flow conditions and model's position, pitch angle, velocity, and pitch rate) corresponding to this instant as initial conditions, and the ring's freestream aerodynamic coefficients measured by [4]. The simulated flight path in freestream flow is qualitatively similar to the one measured in the post shock region, whereby the model continues to accelerate and its pitch rate also increases. The trajectories cross downstream, but due to the limited test time of the facility, the later parts of the flight are not usable.

4.3. Annular model at $\alpha_0 = 0°$

The model was placed at a $\alpha_0 = 0\,°$ initial incidence upstream of the cylinder. Due to the circular side window, the front of the model is not visible on the first few images, but this did not obstruct the processing algorithm from detecting the attitude. Two support wires ruptured rapidly around $t = 0.65$ ms during the flow establishment, and the last was in contact until $t = 4.40$ ms. Figure 7b presents the measured flight trajectory in comparison with a simulated, interaction free trajectory. Similarly to the $\alpha_0 = 60\,°$ test case, the simulated and experimental flight paths are qualitatively similar, but the simulation predicts less displacement and lower rotational rates than the interfering annular model experiences during the test.

4.4. Comparison

The aerodynamic coefficients measured throughout the useful test time of the three experiments are summarized in Figure 7c. The beginnings and the ends of the useful test times (e.g., $t = 3.8 - 12.45$ ms in case of $\alpha_0 = 90\,°$) are indicated with plus symbols. The current experimental results are plotted with thick black lines, the measurements of [4] are shown with green error bars, and aerodynamic coefficients computed by the Newtonian method are shown with blue solid lines. One can note that in some cases the aerodynamic coefficients measured during the interference with the detached shock wave are almost identical to the ones measured in freestream flow, while in other cases they are significantly different. These diverse results show that no ultimate conclusion can be drawn regarding these interactions, and suggest that there is a high dependency on the way the shock wave is crossed by the secondary object.

5. Conclusion

5.1. Summary

This paper describes an experimental campaign, which investigates the aerodynamics of a free-flying ring that interferes with a two-dimensional detached shock wave. The motion of the ring model was recorded using a high-speed camera coupled with a schlieren system. Due to the late rupture of the support wires, the bow shock of the cylinder was already interfering with the ring model at the time of their detachment, and so that no interference-free frames could be recorded. The model release mechanism should be improved in future tests. On the other hand, the image and data processing framework, i.e., the masking techniques, the contour detection, and model position and incidence identification algorithm based on a CAD contour database interpolation proved satisfactory for the analysis of free-flight experiments.

The comparison with previous experimental data [4] and modified Newtonian computations on an interference-free annular model shows that due to the interaction, the ring receives a significant amount of energy leading to a notable lateral velocity which vastly influencing the flight trajectory. In case of a real fragmentation scenario, such interaction could promote a shock-wave surfing configuration and contribute to object dispersal. Additionally, two other experiments which initiate from different angles of attack have been presented. The comparison

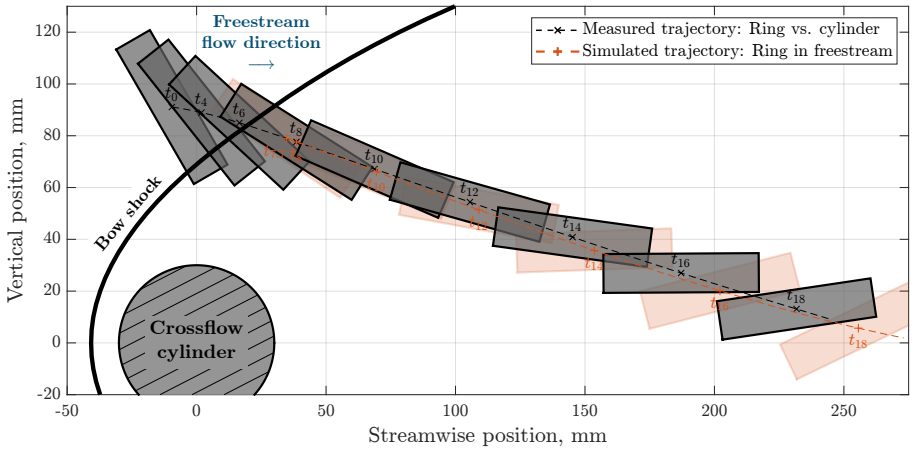

(a) Experiment initiating from $\alpha_0 = 60\,^\circ$. The simulated trajectory is launched from $t = 7.70$ ms.

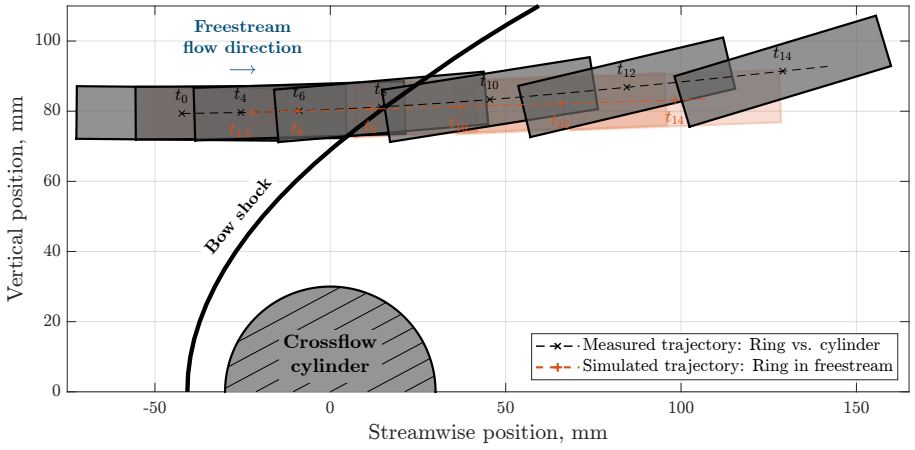

(b) Experiment initiating from $\alpha_0 = 60\,^\circ$. The simulated trajectory is launched from $t = 4.45$ ms.

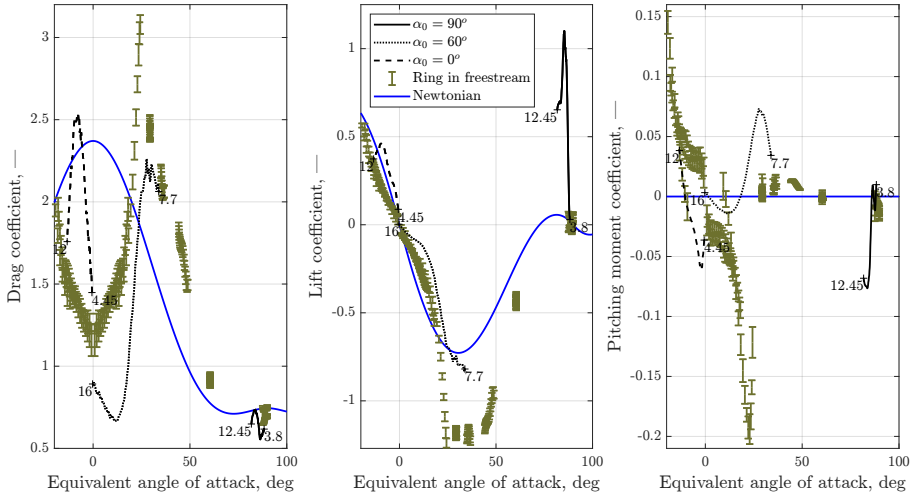

(c) Comparison of the aerodynamic coefficients measured during the interaction in Mach 14 flow with freestream ring aerodynamic coefficients measured in Mach 11 flow, and with modified Newtonian computations.

Figure 7: Comparison of measured interfering and the simulated non-interfering flight trajectories and comparison of interference-free and interfering aerodynamic coefficients.

of the aerodynamic coefficients measured during the various tests does not permit any overarching conclusions regarding the interactions, but suggests a high dependency on the way the shock wave is crossed.

5.2. Future work

In the next part of the present doctoral work, the measurement setup is being extended with a second optical view, hence the model's motion can be traced in six degrees of freedom. This vertical observation will provide a backlit perspective projected image of the model's contour, which requires the upgrade of the processing algorithms. A camera calibration streamline has been already identified, and was inspected with 'dry tests' and with the free-flight testing of two non-interfering spheres. The contour projection method was updated to account for perspective effects and does not require the pre-generation of contour databases. The first results showed that the direct view algorithms have good capabilities in retrieving the flight trajectory in the view-normal directions, but pointed out limited sensitivity along the optical axis. When applying both views together, the model's attitude, streamwise, and vertical position will be identified based on the schlieren images, and the direct view will retrieve only the spanwise motion. This is expected to improve the direct view detection, and eventually the streamwise displacement (well seen by both cameras) could be used for the verification of the measured trajectory. The consecutive step of the research is the testing of multiple interfering objects, hence images of partially overlapping models are expected.

Acknowledgments

This doctoral work is funded by a Ph.D. grant of the von Karman Institute for Fluid Dynamics. Special thanks of gratitude must be expressed to Ing. Mikel Spillemaekers for his help in conducting the experimental campaign.

References

[1] L. Lees, Hypersonic flow, in: 5th International Aeronautical Conference, Vol. 40, AIAA, Los Angeles, USA, 1955, pp. 241–276.

[2] S. J. Laurence, S. Karl, An improved visualization-based force-measurement technique for short-duration hypersonic facilities, Experiments in Fluids 48 (2010) 949–965.

[3] P. M. Seltner, S. Willems, A. Gülhan, Aerodynamic coefficients of free-flying cubes in hypersonic flowfields, Journal of Spacecraft and Rockets 56 (6) (2019) 1725–1734. doi:10.2514/1.A34345.

[4] G. Grossir, D. Puorto, Z. Ilich, S. Paris, O. Chazot, S. Rumeau, M. Spel, J. Annaloro, Aerodynamic Characterization of Space Debris in the VKI Longshot Hypersonic Tunnel Using a Free-flight Measurement Technique, Experiments in Fluids 61 (7) (2020) 163–170. doi:10.1007/s00348-020-02995-7.

[5] P. M. Seltner, S. Willems, A. Gülhan, E. C. Stern, J. M. Brock, M. J. Aftosmis, Aerodynamics of inclined cylindrical bodies free-flying in a hypersonic flowfield, Experiments in Fluids 62 (9) (2021) 1–20.

[6] S. J. Laurence, N. J. Parziale, R. Deiterding, Dynamical separation of spherical bodies in supersonic flow, Journal of Fluid Mechanics 713. doi:10.1017/jfm.2012.453.

[7] S.-H. Park, G. Park, Separation process of multi-spheres in hypersonic flow, Advances in Space Research 65 (1) (2020) 392–406. doi:10.1016/j.asr.2019.10.009.

[8] T. J. Whalen, S. J. Laurence, Experiments on the separation of sphere clusters in hypersonic flow, Experiments in Fluids 62 (4). doi:10.1007/s00348-021-03157-z.

[9] D. Leiser, S. Löhle, F. Zander, D. R. Buttsworth, R. Choudhury, S. Fasoulas, Analysis of Reentry and Break-Up Forces from Impulse Facility Experiments and Numerical Rebuilding, Journal of Spacecraft and Rockets (2022) 1–13doi:10.2514/1.a35204.

[10] D. Joshi, P. Vadassery, F. Lu, Acceleration compensation for force measurements in hypersonic shock tunnel, in: 51st AIAA Aerospace Sciences Meeting including the New Horizons Forum and Aerospace Exposition, 2013, p. 1020.

[11] S. J. Laurence, R. Deitering, H. G. Hornung, Proximal bodies in hypersonic flow, Journal of Fluid Mechanics 590 (2007) 209–237. doi:10.1017/S0022112007007987.

[12] H. Tanno, T. Komuro, K. Itoh, Three-Componet Free-Flight Force Measurement, Proceedings of the 8th European Symposium on Aerothermodynamics for Space Vehicles 8.

[13] C. Kennell, A. Neely, M. Tahtali, D. Buttsworth, R. Choudhury, Free flight testing in hypersonic flows: HEXAFLY-INT EFTV, 54th AIAA Aerospace Sciences Meeting 0 (January) (2016) 1–13. doi:10.2514/6.2016-1152.

[14] S. J. Laurence, R. Deiterding, Shock-wave surfing, Journal of Fluid Mechanics 676 (2011) 396–431. doi:10.1017/jfm.2011.57.

[15] Q. Passey, H. Melosh, Effects of Atmospheric Breakup on Crater Field Formation, Icarus 42 (1980) 211–233.

[16] P. J. Register, M. J. Aftosmis, E. C. Stern, J. M. Brock, P. M. Seltner, S. Willems, A. Guelhan, D. L. Mathias, Interactions between asteroid fragments during atmospheric entry, Icarus 337. doi:10.1016/j.icarus.2019.113468.

[17] T. W. Rees, T. B. Fisher, P. J. K. Bruce, J. A. Merrifield, M. K. Quinn, Experimental characterization of the hypersonic flow around a cuboid, Experiments in Fluids 61 (7) (2020) 1–22. doi:10.1007/s00348-020-02975-x.

[18] A. Gülhan, S. Willems, T. Schleutker, Multibody aerothermodynamics of space debris fragments, in: VKI Lecture Series STO-AVT-262: Space debris reentry and mitigation, 2016.

[19] G. Grossir, B. Dias, Flow characterization of the vki longshot wind tunnel, in: Flow Characterization and Modeling of Hypersonic Wind Tunnels (STO-AVT 325), von Karman Institute for Fluid Dynamics, STO/NATO, Sint-Genesius-Rode, Belgium, 2018, pp. 1–32.

[20] D. G. Kovács, Z. Ilich, G. Grossir, O. Chazot, Experimental Characterization of the VKI Longshot Mach 14 Contoured Nozzle, in: AIAA SciTech 2022 Forum, American Institute of Aeronautics and Astronautics, 2022, pp. 1–22. doi:10.2514/6.2022-1401.

[21] A. Trujillo-Pino, K. Krissian, M. Alemán-Flores, D. Santana-

Cedrés, Accurate subpixel edge location based on partial area effect, Image and Vision Computing 31 (1) (2013) 72–90. doi:10.1016/j.imavis.2012.10.005.

[22] T. Durbin, G. Grossir, O. Chazot, Hypersonic aerodynamic predictions for arbitrary geometries using ANTARES, in: 2nd International Conference on High-SpeedVehicle Science and Technology, CEAS, Bruges, Belgium, 2022, pp. 1–12.

Direct simulation of turbulent hypersonic nozzle flows using high-order discontinuous Galerkin methods

Paolo Scuderi

Aeronautics and Aerospace Department, von Kármán Institute for Fluid Dynamics, Belgium, paolo.scuderi@vki.ac.be

Aéro-Thermo-Mécanique, Univerisité Libre de Bruxelles, Belgium, paolo.scuderi@ulb.be

Supervisor: Georg May[1], Olivier Chazot[2]

[1]*Associate Professor, Aeronautics and Aerospace Department, von Kármán Institute for Fluid Dynamics, Belgium, georg.may@vki.ac.be*

[2]*Professor, Aeronautics and Aerospace Department, von Kármán Institute for Fluid Dynamics, Belgium, olivier.chazot@vki.ac.be*

University Supervisor: Thierry Magin

Professor, Aéro-Thermo-Mécanique, Univerisité Libre de Bruxelles, Belgium, thierry.magin@ulb.be

Professor, Aeronautics and Aerospace Department, von Kármán Institute for Fluid Dynamics, Belgium, thierry.magin@vki.ac.be

Abstract

One of the current unexplored frontiers of fluid dynamics concerns hypersonic turbulence. In the last decade, it was shown that two sound experimental strategies applied to a hypersonic nozzle flow characterization provide different values of the free stream Mach number when applied to the same flow. We hypothesize that some flow phenomena occurring in the nozzle are not correctly modeled in the rebuilding procedure. Having ruled out flow condensation, dense gas effects, and high-temperature effects combined with thermal non-equilibrium phenomena, such as vibrational freezing, we attribute these discrepancies to the presence of Mach shocklets. These are generated by turbulent eddies traveling supersonically within the high-speed turbulent boundary layer and are expected to induce non-isentropic changes in the thermodynamic speed of sound. The aforementioned physical mechanism is not numerically modeled with the over-simplifying Reynolds Averaged Navier-Stokes approach. Consequently, we propose to use high-fidelity direct numerical simulations based on high-order spectral-like Discontinuous Galerkin methods to investigate these complex flow physics and demonstrate our hypothesis. First, the numerical method will be extended to remain robust in the high-speed convection-dominant regime, where Gibbs phenomena occur in the mesh elements situated near the shock location. Subsequently, solutions computed on modern petascale supercomputers will be compared to experimental databases to validate the computational model and better understand the physics of hypervelocity wall-confined flows. Base flow solutions will be coupled with local stability analyses to explore the poorly understood laminar-turbulent transition. In the computational areas where the nozzle walls can be assumed to be flat plates, the results of the laminar regime will be investigated through the self-similar Howarth-Dorodnitsyn transformation. Innovative approaches based on physics-informed artificial intelligence techniques will be employed for the construction of hypersonic turbulent models. State-of-the-art uncertainty quantification methods will allow us to assess the predictive capability of the models developed. Finally, the theoretical advances and numerical tools from this research will be made available to the scientific community in open-access numerical databases for different geometrical and physical configurations.

Keywords: Computational Fluid Dynamics, Hypersonic, Discontinuous Galerkin, Direct Numerical Simulation, High-Order Methods, High-Performance Computing, High-Fidelity Turbulence Modeling.

AEROTHERMOCHEMISTRY

Comparison of the state-of-the-art enthalpy rebuilding procedures for inductively coupled plasma facilities

Enrico Anfuso

Aeronautics and Aerospace Department, von Karman Institute for Fluid Dynamics, Belgium, enrico.anfuso@vki.ac.be

Supervisor: Olivier Chazot

Full Professor and Head of the Aeronautics and Aerospace Department, von Karman Institute for Fluid Dynamics, Belgium, chazot@vki.ac.be

University Supervisor: Aurélie Bellemans

Assistant Professor, MECH Department, Vrije Universiteit Brussel, Belgium, aurelie.bellemans@vub.be

Abstract

Three methods of determining the enthalpy of the flow in an Inductively Coupled Plasma (ICP) wind tunnel that is, the semi-empirical ASTM E-637 formulation, the deterministic procedure employed at the von Karman Institute (VKI) Plasmatron facility and a stochastic inverse method based on a Bayesian framework, are compared. The comparison consists of six test cases at two operating conditions of chamber static pressure p_c and three electrical powers $\mathbb{P}_{el}$. Results show an over-prediction of the VKI standard procedure and an underestimation of the ASTM formulation compared to the Maximum A Posteriori (MAP) prediction of the Bayesian methodology. At $p_c = 100$ mbar and assuming a wall catalytic coefficient (γ) of 0.01, discrepancies range between 12 and 25 % when the VKI and Bayesian formulations are compared. As far as the ASTM is concerned, dissimilarities to the Bayes are roughly constant for all powers (≈ 17 %). At $p_c = 50$ mbar, the VKI rebuilding agrees well (discrepancies < 2.5 %) with the Bayes estimation if $\gamma = 0.1$. However, recent experimental investigations suggest a new value of $\gamma = 2.661 \times 10^{-2}$ leading to differences up to 20 %. Broader discrepancies exist at 50 mbar between the ASTM and the Bayesian formulation of the problem ranging from 20 % to 26 % at the lowest and highest $\mathbb{P}_{el}$, respectively. Finally, if on one hand the Bayesian posterior distribution envelope the VKI standard rebuilding results, ASTM predictions fall outside the 95 % confidence intervals.

Keywords: enthalpy rebuilding procedures, ICP wind tunnel, ASTM method, VKI's Plasmatron procedure, Bayesian methodology

1. Introduction

Among the different solutions presented to tackle the problem of space debris, the end-of-life disposal through aerothermal demise in atmospheric entry is certainly one of the most effective, especially when dealing with small debris (order of millimeters) compared to solutions such as harpoons, nets, and robotic arms. A meticulous design of the demise process plays a crucial role, and plasma wind tunnels are essential in recreating the same aerothermochemical conditions experienced during atmospheric entry. Testing conditions, such as the free-stream enthalpy, must be accurately known to replicate a flight scenario [1; 2] but unfortunately, they cannot be easily measured with dedicated probes and must rely on semi-empirical formula [3] or rebuilding procedures [4; 5]. The latter rebuild the quantities of interest by matching the experimental data with the numerical counterparts.

This work aims to compare three different enthalpy rebuilding procedures in ICP facilities here presented from the simplest to the most reliable according to the assumption made. The first procedure, initially published by Zoby and Sullivan and now stated as standard in the ASTM E-637 [6], is based on a semi-

empirical formulation of the enthalpy as function of the measured heat flux (q_w^{meas}) and total-pressure ($p_{\text{tot}}^{\text{meas}}$) derived from the stagnation-heat transfer theory under the hypothesis of Local Thermo-chemical Equilibrium (LTE) and negligible non-catalytic effects at the surface. The second approach is the standard deterministic procedures currently employed at the von Karman Institute's (VKI) Plasmatron [7] that considers chemical non-equilibrium condition and the recombination of O_2 and N_2 due to the catalytic properties of the copper probe. Recombination reactions are exothermic reactions that may significantly impact the simulated heat flux. Catalysis is described from a macroscopic point of view using the catalytic coefficient γ taken from the literature [8; 4]. The third procedure considered is a stochastic inverse method based on a Bayesian framework recently presented by del Val et al. for catalysis determination [9] and here extended to the inference of the enthalpy. Contrary to deterministic inverse problems, where the optimization problem results in a point-estimate, stochastic inverse problems make use of the probability theory framework including uncertainties stemming from the measurement chain and inadequacies of the selected models. For instance, empirical data on copper catalysis comes from different methods to compute the recombination coefficient and Kovalev et al. [10] already pointed out contradictions among the data. The Bayesian approach here presented allows the inclusion of those uncertainties assuming a-priori unknown catalytic coefficients in the enthalpy inference.

Sec. 2 presents an overview of the VKI Plasmatron describing the constitutive elements, the working principle and summarizing the test conditions considered in this work. Sec. 3 introduces the concept of the Local Heat Transfer Simulation (LHTS) methodology and the role of the enthalpy in the ICP plasma wind tunnels, essential to the ground-to-flight extrapolation. Sec. 4 is dedicated to a general description of the three different enthalpy rebuilding procedures here exploited: the ASTM E-637 method, the VKI rebuilding and the Bayesian procedure. Sec. 5 presents the results of the procedures. In particular, Sec. 5.1 is dedicated to the enthalpy-envelope between the limits of $\gamma = 0$ and 1. Sec. 5.2 and 5.3 present the discrepancies among the methods for the chamber static pressure $p_c = 100$ and 50 mbar, respectively. Sec. 6 draws the conclusion of this work and possible insights for future developments.

2. The VKI Plasmatron

The VKI Plasmatron is the word largest ICP facility powered by a high-frequency, high-voltage, high-power generator (400 kHz, 2 kV, 1.2 MW). The facility is usually operated in subsonic conditions, but sonic and supersonic regimes are achievable through dedicated nozzles (not considered in this work). In subsonic regime, the flow downstream the heater can be assumed quasi-stationary in LTE if the pressure in the chamber p_c is sufficiently high (> 15 mbar) [11]. Contrary to arc-jets plasma wind tunnels, usually preferred for qualification testing of large-scale samples at very high heat flux conditions thanks to their high-power capabilities [12], induction-type facilities use electrodeless technology for the plasma discharge generation ensuring a superior flow purity. They are usually more dedicated to the study of aerothermochemistry and gas-surface phenomena [8]. Fig. 1 depicts a schematic of the facility representing the generator, the torch, surrounded by a coil where the plasma jet is generated by Joule heating effect, the test chamber, where the sample is placed, and the cooling system. The characterization of the flow is performed with a 50 mm hemispherical probe holding a 14 mm calorimeter in the center of the front face, and a 50 mm flat-face (ESA-standard) Pitot probe providing the dynamic pressure $p_{\text{dyn}}^{\text{meas}}$ respect to the chamber static pressure p_c. Probes are located at 385 mm from the torch exit section and injected (not-simultaneously) into the flow through a dedicated actuator system. The stagnation point heat flux, q_w^{meas}, is determined by an energy balance measuring the mass flow with a dedicated flow rotameter and the inlet/outlet temperature difference measured with two type-E thermocouples. The calorimeter is surrounded by a teflon ring to isolate the heat exchange to the surrounding holding probe. The temperature of the hemispherical probe is not measured but assumed equal to the temperature of the surrounding resting gas, $T_w \approx 350$ K. Both the probe and calorimeter have copper surfaces that are highly catalytic to O and N recombination. From a numerical perspective, the catalytic properties are described using a macroscopic approach with the catalytic coefficient $\gamma = \gamma_{N\rightarrow N_2} = \gamma_{O\rightarrow O_2}$ [13]. $\gamma = 1$ indicates a fully catalytic wall that, in the limit, allows a local composition equal to the equilibrium one while $\gamma = 0$ a non-catalytic surface when atoms remain dissociated. Recombination reactions are exothermic and an accurate prediction of γ is fundamental for a truthful estimate of the heat flux. The water-cooled Pitot probe line is connected to a DP45

valydine located outside the test chamber in a vacuum box kept at $p = p_c$. The valydine hosts a M14 membrane ($\Delta P = 220$ Pa) calibrated using a Druck DPI610 digital calibrator (pressure range 2.5 mbar). An absolute pressure transducer (Memberanovac DM 12, Leybold Vacuum) measures the static pressure p_c. As the plasma jet is low subsonic (Ma ≈ 0.1), the static pressure can be assumed constant in the whole test chamber. This assumption is confirmed a posteriori by the numerical simulations of the plasma jet.
The reference testing conditions of the VKI Plasmatron depend on three parameters: the chamber static pressure p_c, the gas mass flow rate ($\dot{m}$) supplied to the torch and monitored through a calibrated mass flow controller, and the electrical power supplied to the coil by the generator $\mathbb{P}_{el}$. The reference conditions considered in this work, as well as the measured heat flux and dynamic pressure are summarized in Tab. 1. Although an uncertainty analysis has yet to be carried out, previous experimental campaigns conducted at VKI [8; 5; 4] assumes unbiased Gaussian distributions with a 2σ confidence level equal to 10 % for q_w^{meas} and $p_{\text{dyn}}^{\text{meas}}$.

Table 1: The VKI Plasmatron reference conditions considered in this work and the corresponding heat flux (q_w^{meas}) and dynamic pressure ($p_{\text{dyn}}^{\text{meas}}$) measurements assuming a 2σ confidence level equal to 10 % of the mean value.

Test ID	$\mathbb{P}_{el}$ [kW]	$\dot{m}$ [g s^{-1}]	p_c [mbar]	q_w^{meas} [kW m^{-2}]	$p_{\text{dyn}}^{\text{meas}}$ [Pa]
$\mathbb{ID}_1$	150	16	100 ± 0.2	825 ± 82.5	14.6 ± 1.4
$\mathbb{ID}_2$	210	16	100 ± 0.2	1660 ± 166	33.2 ± 3.3
$\mathbb{ID}_3$	290	16	100 ± 0.2	2680 ± 268	61.6 ± 6.1
$\mathbb{ID}_4$	150	16	50 ± 0.1	823 ± 82.3	41.4 ± 4.1
$\mathbb{ID}_5$	200	16	50 ± 0.1	1570 ± 157	61.4 ± 6.1
$\mathbb{ID}_6$	300	16	50 ± 0.1	2540 ± 254	113.3 ± 11.3

3. The LHTS methodology

The full potential of Plasma Wind Tunnels (PWTs) is unleashed when test conditions correctly reproduce at least the real flight environment around the stagnation point of the aerospace vehicle [14; 15]. The extrapolation from the ground test conditions to flight is commonly achieved by employing the Local Heat Transfer Simulation (LHTS) technique initially formulated by Kolesnikov for ICP torches at the Institute for Problems in Mechanics (IPM, Moscow, Russia) [2]. The methodology is based on the Fay-Riddell [16] and Goulard [13] formulation of the heat

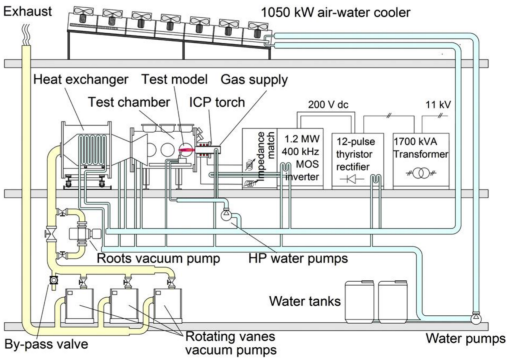

Figure 1: The schematic of the VKI Plasmatron facility.

flux valid for a frozen or equilibrium boundary layer only. It was later adapted by Barbante et al. [1] to the VKI Plasmatron for a chemical non-equilibrium boundary layer. Kolesnikov's works state that, under the assumption of LTE at the outer edge of the boundary layer, the stagnation point heat flux in flight and in ground are identical, if enthalpy h, stagnation pressure p, and the velocity gradient β are locally matched: $h_\delta^t = h_\delta^f$, $p_\delta^t = p_\delta^f$, $\beta_\delta^t = \beta_\delta^f$ where δ denotes the boundary layer thickness (see Fig. 2), the subscript $[.]_\delta$ denotes quantities at the boundary layer edge, and the superscripts t and f the test and flight conditions, respectively.

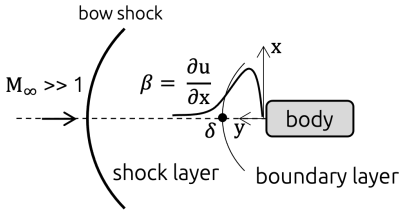

Figure 2: Simplified representation of the bow shock and boundary layer typical of a re-entry body. β represents the gradient of the tangential component (along the $x-$direction) of the velocity.

An accurate estimation of enthalpy is therefore of paramount importance to correlate the flight and ground testing conditions [1].

4. Enthalpy rebuilding procedures

This section presents three procedures exploited in this work to determine the free-stream (at the boundary layer edge) enthalpy of the VKI Plasmatron facility. It starts with the simplest methodology (ASTM E-637 formulation) with an semi-empirical formulation

of h based entirely on q_w^{meas} and $p_{\text{tot}}^{\text{meas}}$, derived from the stagnation-heat transfer theory assuming LTE condition and a fully catalytic surface. It follows with the rebuilding employed at VKI considering a chemical non-equilibrium in the boundary layer region and catalytic coefficient of the copper probe derived from previous experimental campaigns. Lastly, the third procedure introduced is a stochastic method based on a Bayesian formulation of the inference problem that includes uncertainties on the measurements, and assumes the γ-coefficient to be unknown.

4.1. The ASTM E-637 procedure

Due to its simplicity, the ASTM E-637 (or shortly ASTM) procedure is widely used in various plasma wind tunnels in research centers or University laboratories [17; 18]. The local mass-specific enthalpy is only function of the stagnation point heat flux and total pressure [3; 6]:

$$h \approx h - h_w = \frac{1}{K} \frac{q_w^{\text{meas}}}{\sqrt{\frac{p_{\text{tot}}^{\text{meas}}}{R}}} \tag{1}$$

with K the gas-specific constant (for air $0.368\,\text{kWkg}\ \text{m}^{-1.5}\,\text{Pa}^{-0.5}\,\text{MJ}$), R the probe nose radius and h_w the mass-specific enthalpy at the wall. Eq. 1 has been derived from the stagnation-heat transfer theory around a hemispherical probe under several assumptions such as the flow being in LTE, the surface of the probe being fully catalytic, and more (the reader is addressed to [6]) that may significantly contribute to an error in the formulation not addressed in this work. Under these hypothesis and for plasma wind tunnel applications, it is therefore reasonable to approximate $h >> h_w$ simplifying Eq. 1 with h function only of q_w^{meas} and $p_{\text{tot}}^{\text{meas}}$.
For Ma < 2, Eq. 1 requires a modification to take into account that it was derived using the modified Newtonian flow theory. The appropriate expression is [6]:

$$h \approx h - h_w = \frac{K_{\text{M}} q_w^{\text{meas}}}{\sqrt{\frac{p_{\text{tot}}^{\text{meas}}}{R}}} \left[\frac{(\beta D/v_\infty)_{\text{mod.N.}}}{(\beta D/v_\infty)_{y=0}} \right]^{0.5} \tag{2}$$

with K_M the modified gas specific constant (for air $2561\,\text{N}^{1/2}\,\text{m}^{1/2}\,\text{s}\,\text{kg}^{-1}$), D the noise diameter and v_∞ the axial free stream velocity. The velocity gradients can be derived from the Ma number:

$$(\beta D/u_\infty)_{\text{mod.N.}} = \left[\frac{4\left((\gamma-1)\text{Ma}^2+2\right)}{\gamma \text{Ma}^2} \right]^{0.5}, \tag{3}$$

$$(\beta D/u_\infty)_{x=0} = 3 - 0.755\text{Ma}^2 \quad (\text{Ma} < 1). \tag{4}$$

The subsonic Ma number is determined using

$$\text{Ma} = \left[\frac{2}{(\zeta-1)} \left(\left(\frac{p_{\text{tot}}^{\text{meas}}}{p_{\text{c}}} \right)^{\frac{(\zeta-1)}{\zeta}} - 1 \right) \right]^{0.5} \tag{5}$$

with ζ denotes the isentropic exponent and p_{c} the background pressure in the chamber ($\approx$ constant). Eq. 5 holds only for an isentropic flow. However, the variation in the isentropic exponent results in only a small change of the Mach number. Therefore, this equation typically holds for the pressure and temperature regime in plasma wind tunnels. For high enthalpy flows $\zeta = 1.13$ [17].

4.2. The VKI Plasmatron rebuilding procedure

The logic behind the VKI rebuilding code is to infer the enthalpy by matching the experimental values (q_w^{meas}) with the numerical counterparts (q_w) simulated with two steady CFD codes, the Inductively Coupled Plasma (ICP) and the Boundary Layer (BL) solver.

4.2.1. Numerical tools

After being developed as a standalone tool, the VKI ICP code is nowadays integrated into the Computational Object-Oriented Library for Fluid Dynamics (COOLFluiD) [19], developed at the VKI. The VKI ICP code makes use of the MUTATION^{++} library [20] to determine thermodynamic and transport properties of a generic mixture. Here we consider an air mixture of eleven species (O , N , NO, NO^+, O, N, e^-, O^+, N^+, $O_2{}^+$, $N_2{}^+$). The code simulates the steady, subsonic, 2D axisymmetric flow in the torch and test chamber of the Plasmatron facility under LTE assumption. It solves a simplified Maxwell's induction equations coupled with the Navier-Stokes equations through the Lorentz force and Joule heating effect in the momentum and energy equations respectively. The Reynolds number is typically low (Re $\approx$ 100) so the flow is assumed to be laminar. The reference parameters are the chamber static pressure, p_s, the gas flow rate supplied to the torch, $\dot{m}_{gas}$, and the effective power supplied to the plasma by induction $\mathbb{P}_{\text{el}}^{\text{eff}}$. For low subsonic, low Mach number test conditions, p_s and $\dot{m}_{gas}$ are considered constant as verified by the results of numerical simulations and dynamic pressure measurements. As far as $\mathbb{P}_{\text{el}}^{\text{eff}}$ is concerned, it is exact value is still unknown and efforts are underway to overcome the problem. Today, a power efficiency $\eta = \mathbb{P}_{\text{el}}^{\text{eff}}/\mathbb{P}_{\text{el}}$ equal to 50 % is accounted for.
The second solver developed at VKI by Barbante [1]

is NEBOULA (Non-Equilibirum BOUndary LAyer), which provides the solution of the BL equations under thermal equilibrium and chemical non-equilibrium conditions, in the proximity of the stagnation line, of a probe with catalytic surface properties described by the catalytic coefficient γ. The code implements a first order approximation γ, function only of the temperature at the wall T_w, even though Panerai [8] and Viladegut [7] have observed an effect of the static pressure p_s ($\approx p_c$) too. Barbante showed that the equations considering the effects of boundary layer finite thickness and low Reynolds number, reduce to the same set of classical boundary layer equations, valid under the assumption of thin boundary layer and large Reynolds number, when applied to the vicinity of the stagnation line. Thermodynamic and transport data, as well as the parameters to compute the forward and backward reaction rate coefficients of different chemical models (e.g. Dunn-Kang [21], Park [22; 23]), are inquired through the library PEGASE [24] considering the same air mixture of the ICP code. Park's model is considered with 34 chemical mechanisms: 16 third body dissociation reactions of N_2, O_2, NO, 2 exchange reactions for NO, 3 associative ionization, 11 charge exchange, and 2 electron-impact ionization reactions (see Appendix Appendix A). One of the outputs of the boundary layer solver is the numerical heat flux at the wall q_w considering the conduction and diffusion contributions

$$q_{\mathrm{w}} = \lambda_w (\nabla T)_w + \sum_{i=1}^{N_s} V_{i,w} h_{i,w} \rho_{i,w}, \qquad (6)$$

being λ_w the thermal conductivity and $V_{i,w}$, $h_{i,w}$ $\rho_{i,w}$ the species diffusion velocity, enthalpy and density respectively.

4.2.2. Procedure

Reference testing conditions in terms of, p_c, $\dot{m}$, and $\mathbb{P}_{el}$ define the conditions of the ICP solver, assuming an efficiency $\eta = 50\,\%$. The solver provides the boundary layer edge quantities such as temperature T_δ, the pressure p_δ ($\approx p_s = p_c$), the velocity, v_δ, velocity gradient β_δ and the boundary layer thickness δ. v_δ, β_δ and δ are expressed in terms of five non-dimensional parameters

$$\Pi_1 = \frac{\delta}{R}, \qquad \Pi_2 = \beta_\delta \cdot \left(\frac{R}{v_s}\right), \qquad \Pi_3 = \frac{R^2}{v_s} \cdot \frac{\partial \beta_\delta}{\partial y}$$

$$\Pi_4 = \frac{v_\delta}{v_s}, \qquad \Pi_5 = \frac{v_\delta}{v_\infty},$$

with v_s the velocity at the torch exit section and v_∞ the free stream velocity with free stream point assumed to be at half of the distance of the probe from the torch exit section (192.5 mm). Π_5 hides the relationship with the dynamic pressure p_{dyn} being $p_{\mathrm{dyn}} = k_B \frac{1}{2} \rho_\infty v_\infty^2$ with k_B the Barker correction for low Reynolds, high viscous flow (k_B =1.1 in this work).

The measured heat-flux and dynamic pressure, q_w^{meas} $p_{\mathrm{dyn}}^{\mathrm{meas}}$, and the BL edge quantities are then input in a routine called CERBERE (Catalycity and Enthalpy ReBuilding on a REference probe) that calls recursively NEBOULA to compute the numerical heat flux

$$q_{\mathrm{w}} = q_{\mathrm{w}} \left(\gamma, T_{\mathrm{w}}, h_\delta \left(p_\delta,\ T_\delta\right), \Pi_1, \ldots, \Pi_5\right), \qquad (7)$$

The procedure iterates on T_δ until the experimental data match the numerical counterparts providing an estimate of the enthalpy at the boundary layer edge. Fig. 3 summarizes the VKI enthalpy rebuilding procedure.

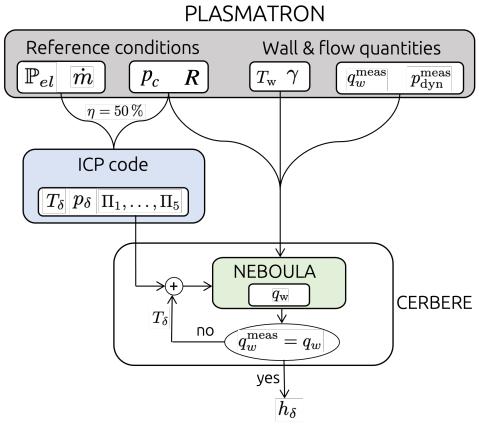

Figure 3: Sketch of the enthalpy rebuilding procedure employed at the VKI Plasmatron facility. The subscript $[.]_\delta$ indicates the boundary layer edge quantities, the superscript *meas* the experimental quantities. Π_i are the non-dimensional parameters and R the radius of the testing probe. p_δ is assumed constant and equal to p_c. T_w is not measured but assumed equal to the surrounding resting gas ≈ 350 K.

4.3. Stochastic method based on a Bayesian framework

Contrary to deterministic inverse problems, where the optimization problem results in a point-estimate, stochastic inverse problems make use of the probability theory framework to enrich the estimation. The main advantage respect to simple forward uncertainty propagation techniques that assume a-priori probability distributions of the model parameters without us-

ing any experimental information, is to exploit experimental data to calibrate such parameters achieving better and more reliable predictions.
The third rebuilding methodology is therefore based on a Bayesian framework that solves the numerical forward problem (NEBOULA) thousands of times providing a complete probability distribution of the quantity of interest including experimental uncertainties and inaccuracies of the γ values proposed by different authors [8; 4].

The Bayes formula can be generically formulated as follows [25]

$$\mathcal{P}(\boldsymbol{q} \mid \boldsymbol{y}_{\text{obs}}) = \frac{\mathcal{P}(\boldsymbol{y}_{\text{obs}} \mid \boldsymbol{q})\mathcal{P}(\boldsymbol{q})}{\int_\Omega \mathcal{P}(\boldsymbol{y}_{\text{obs}} \mid \boldsymbol{q})\mathcal{P}(\boldsymbol{q}) d\boldsymbol{q}} \tag{8}$$

with $\boldsymbol{q}$ the vector of model parameters to be inferred, and $\boldsymbol{y}_{\text{obs}}$ the vector of measurements. The term $\mathcal{P}(\boldsymbol{q})$ is the prior distribution of the parameters, $\mathcal{P}(\boldsymbol{y}_{\text{obs}} \mid \boldsymbol{q})$ the likelihood function of the measurements (or equivalently the probability to obtain $\boldsymbol{y}_{\text{obs}}$ given $\boldsymbol{q}$), and $\mathcal{P}(\boldsymbol{q} \mid \boldsymbol{y}_{\text{obs}})$ the posterior distribution of $\boldsymbol{q}$ (the probability to obtain $\boldsymbol{q}$ given $\boldsymbol{y}_{\text{obs}}$). The symbol Ω refers to the space vector of $\boldsymbol{q}$ and the integral is called the "evidence" or "marginalized-likelihood" which does not depend on the model parameters $\boldsymbol{q}$. Given that the evidence is a constant, we can avoid computing it by working with the proportional relation

$$\mathcal{P}(\boldsymbol{q} \mid \boldsymbol{y}_{\text{obs}}) \propto \mathcal{P}(\boldsymbol{y}_{\text{obs}} \mid \boldsymbol{q})\mathcal{P}(\boldsymbol{q}). \tag{9}$$

In this work, $\boldsymbol{q} = \left(p_{\text{dyn}}, T_{\text{w}}, \gamma, h_\delta\left(p_\delta, T_\delta\right)\right)$ with p_{dyn}, T_{w}, and γ being the nuisance parameters, variables not known but required to compute the quantity of interest h_δ, and $\boldsymbol{y}_{\text{obs}} = \left(p_{\text{dyn}}^{\text{meas}}, p_{\text{s}}^{\text{meas}}, q_{\text{w}}^{\text{meas}}, T_{\text{w}}^{\text{meas}}\right)$ with $p_{\text{s}}^{\text{meas}} = p_c$ and $T_{\text{w}}^{\text{meas}} \approx 350\,\text{K}$ treated as an observation with 10% uncertainty values. Assuming independent unbiased Gaussian measurement errors, with standard deviation σ (for which we assume a 2σ confidence level for the uncertainty values reported in Tab. 1), the likelihood reads

$$\begin{aligned}\mathcal{P}(\boldsymbol{y}_{\text{obs}} \mid \boldsymbol{q}) \propto \exp&\left[-\frac{\left(p_{\text{s}}^{\text{meas}} - p_{\text{s}}\right)^2}{2\sigma_{p_{\text{s}}}^2}\right]\times \\ &\exp\left[-\frac{\left(p_{\text{dyn}}^{\text{meas}} - p_{\text{dyn}}\right)^2}{2\sigma_{p_{\text{dyn}}}^2}\right]\times \\ &\exp\left[-\frac{\left(q_{\text{w}}^{\text{meas}} - q_{\text{w}}(\boldsymbol{q})\right)^2}{2\sigma_{q_{\text{w}}}^2}\right]\times \\ &\exp\left[-\frac{\left(T_{\text{w}}^{\text{meas}} - T_{\text{w}}\right)^2}{2\sigma_{T_{\text{w}}}^2}\right]\end{aligned} \tag{10}$$

The posterior distribution is not known in closed form due the complexity of the mapping between $\boldsymbol{q}$ and the model prediction (q_w) of the forward problem. Therefore, sampling techniques such as Markov Chain Monte Carlo are exploited to estimate the statistics of the posterior (e.g. mean, confidence intervals, etc). The initial point of the MCMC is the Maximum A Posteriori (MAP) defined as $\boldsymbol{q}_{\text{MAP}} = \arg\max_{\boldsymbol{q}} \mathcal{P}(\boldsymbol{q} \mid \boldsymbol{y}_{\text{obs}})$ and computed using the Nelder-Mead algorithm [26].

The prior distributions are summarized in Table 2. For the parameters that have measured counterparts, we are not concerned about the width of their priors as they are expected to converge to their measured values in the posterior distribution. For the catalytic recombination efficiency γ and enthalpy h_δ, the priors are chosen wide enough to encompass known values encountered in the literature, motivated by the work of del Val et al. [27].

As far as the Bayesian methodology is concerned, Park's chemical model with the same 11 species air mixture is considered.

Table 2: Prior distributions of the model parameters from which samples are drawn to evaluate the likelihood function defined in Eq. 10.

Test ID	γ [−]	T_w [K]	p_δ [mbar]	h_δ [MJ/kg]	p_{dyn} [Pa]
$\mathbb{ID}_1$	$\log\mathcal{U}$[−2,0]	$\mathcal{U}$[300,500]	$\mathcal{U}$[70,130]	$\mathcal{U}$[10,70]	$\mathcal{U}$[10,120]
$\mathbb{ID}_2$	$\log\mathcal{U}$[−2,0]	$\mathcal{U}$[300,500]	$\mathcal{U}$[70,130]	$\mathcal{U}$[10,70]	$\mathcal{U}$[10,120]
$\mathbb{ID}_3$	$\log\mathcal{U}$[−2,0]	$\mathcal{U}$[300,500]	$\mathcal{U}$[70,130]	$\mathcal{U}$[10,70]	$\mathcal{U}$[10,120]
$\mathbb{ID}_4$	$\log\mathcal{U}$[−2,0]	$\mathcal{U}$[300,500]	$\mathcal{U}$[20,80]	$\mathcal{U}$[10,70]	$\mathcal{U}$[10,120]
$\mathbb{ID}_5$	$\log\mathcal{U}$[−2,0]	$\mathcal{U}$[300,500]	$\mathcal{U}$[20,80]	$\mathcal{U}$[10,70]	$\mathcal{U}$[10,120]
$\mathbb{ID}_6$	$\log\mathcal{U}$[−2,0]	$\mathcal{U}$[300,500]	$\mathcal{U}$[20,80]	$\mathcal{U}$[10,70]	$\mathcal{U}$[10,120]

5. Results

Results are split into three sections. Sec. 5.1 summarizes the enthalpy-envelopes as function of the measured heat flux for the chamber static pressures considered in this work. The enthalpy-envelope is defined between the limits of $\gamma = 0$ and 1 and computed using the VKI rebuilding procedure. Furthermore, the typical relationship between h_δ and γ is also presented for the $p_c = 100\,\text{mbar}$ case. Sec. 5.2 and 5.3 show the discrepancies between the different methodologies at $p_c = 100\,\text{mbar}$ and 50 mbar respectively with the MAP used as a reference for the Bayesian inference.

The error between a generic procedure P_1 and P_2 is defined as

$$\epsilon_{i,P_1 \to P_2} = \frac{h_{i,P_1} - h_{i,P_2}}{h_{i,P_2}} \tag{11}$$

with the subscript i denoting the testing condition considered. For instance, $\mathbb{ID}_1$, $\mathbb{ID}_2$ and $\mathbb{ID}_3$ are those for $p_c = 100$ mbar, and $\mathbb{ID}_4$, $\mathbb{ID}_5$ and $\mathbb{ID}_6$ for $p_c = 50$ mbar.

5.1. The VKI rebuilding envelope

Fig. 4 depicts the enthalpy-envelope of the Plasmatron facility for the two reference conditions p_c = 50 and 100 mbar obtained through the standard rebuilding procedure currently in use at the VKI. The lower limit corresponds to a fully catalytic copper surface $\gamma = \gamma_{N \to N_2} = \gamma_{O \to O_2} = 1$ while the upper limit is obtained by neglecting any catalytic recombination at the wall, $\gamma = 0$. The rebuilding procedure uses Park's chemical model for an air mixture of 11 species. The enthalpy-envelope using Dunn-Kang's model (not shown) is in good agreement with Park's with a maximum discrepancy below 5 %.
Decreasing the pressure in the test chamber leads increases the temperature, and thus enthalpy, at the boundary layer edge. The effect is more pronounced at low γ-values as shown in the Fig. 4.

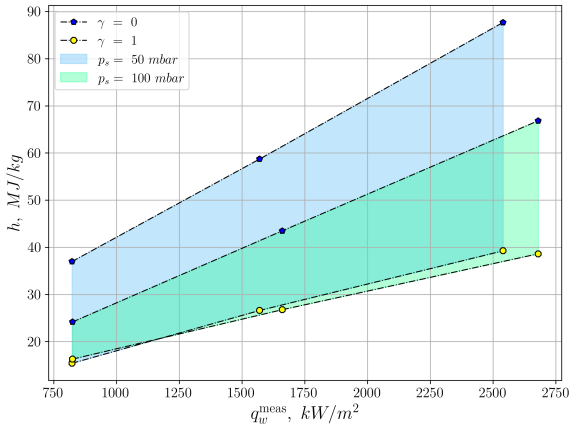

Figure 4: Enthalpy-envelope between the limits of $\gamma = 0$ and 1 using the VKI rebuilding procedure at $p_c = 100$ and 50 mbar. Computation are carried out using Park's chemical model for an air mixture of 11 species and 34 chemical reactions (see Appendix Appendix A).

The change of enthalpy as function of the catalytic coefficient γ, referred in the literature as S-curve, is presented in Fig. 5 for $p_s = 100$ mbar. While the gradient of the curve is almost zero (flat region) for a fully catalytic surface ($\gamma \approx 1$) and when catalysis phenomena are negligible ($\gamma \leq 1 \times 10^{-4}$), the maximum sensitivity of the enthalpy to the catalysis phenomena is reached between $1 \times 10^{-3} \leq \gamma \leq 1 \times 10^{-1}$.

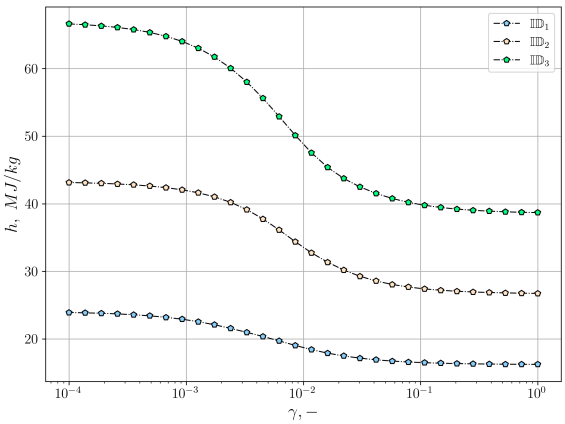

Figure 5: The enthalpy-vs-catalytic coefficient curves, commonly referred to S-curves in literature, at $p_c = 100$ mbar.

5.2. 100 mbar

Fig. 6 shows the comparison between the different methodologies at p_c =100 mbar with discrepancies summarized in Tab. 3. The reference catalytic coefficient, γ, in the VKI rebuilding is set to 0.01 as suggested by Panerai [8] for the chamber static pressure considered. As far as the Bayesian methodology is concerned, the results are presented in terms of mean (orange square) and MAP (yellow diamond) estimators, the latter used as a reference for the two other procedures. Mean and MAP are close to each-other highlighting the symmetry of the probabilistic distribution with the violet region being the 95 % Confidence Interval (CI). On one hand, the VKI standard rebuilding overestimates the enthalpy respect to the Bayes formulation with discrepancies increasing as a function of the power: roughly 12 % at $\mathbb{P}_{el} = 150$ kW and 26 % at the highest power, the latter outside the 95 % CI. On the other hand, the ASTM methodology under-predicts the enthalpy with a difference of $\approx$ 17 % for all electrical powers and predictions falling outside the CI. Discrepancies between the VKI standard methodology and the ASTM formulation are also summarized in Tab. 3 ranging from 35 and 55 % at the lowest and highest $\mathbb{P}_{el}$, respectively. As anticipated in Sec. 4.1, the ASTM formulation lies on several assumptions that may partially explain the discrepancies. For instance, the assumption of LTE is

investigated by running the VKI standard rebuilding boosting the chemical rates coefficients (in particular the pre-multiplication factor of the Arrhenius law) to approach a condition of LTE. Tab. 4 summarized the results showing a significant reduction of h at the edge of the boundary layer. Moreover, if the assumption of negligible wall enthalpy holds in LTE, it becomes questionable in chemical non-equilibrium condition. The assumption of a fully catalytic surface in LTE condition is also verified through VKI standard rebuilding assuming a wall catalytic coefficient $\gamma = 1$ and boosting the reaction rates. Results in terms of enthalpy (see Tab. 4) and mass fractions (not here presented) are in good agreement to those using $\gamma = 0.01$ highlighting the LTE condition.
Fig. 6 also shows the role played by the measurement uncertainties on the enthalpy-envelope. While the VKI rebuilding only considers the point-estimate of the experimental data, the Bayesian approach considers their full distribution as an independent error source. As a result, the lower bound of the CIs fall below the limit of $\gamma = 1$ of 1.1, 1.9, and 2.9 MJ kg^{-1}, for $\mathbb{P}_{el} = 150$, 210, and 290 kW respectively.

Mean or MAP prediction of the Bayesian formulation are a trade-off between all the models' input summarized in Tab. 2 without knowing to which set of inputs the two predictions correspond. It is therefore not clear if the discrepancies existing with the results of the VKI standard rebuilding are mainly due to uncertainties in the catalytic coefficients or the errors in the measurements but higher values of γ in the VKI rebuilding will shift the results downwards decreasing the discrepancies between the two procedures. Future sensitivity analysis may therefore provide insight into the role of each model's input parameter and therefore provide better insight into the role of γ in the enthalpy estimation.

Table 3: The left side summarizes the enthalpy estimations of the different procedures for the three testing conditions. The subscripts $[.]_A$, $[.]_V$, and $[.]_B$ stand for the different methodologies: A for ASTM formulation, V for the VKI procedure using $\gamma = 0.01$ and B for the Bayesian formulation using the MAP as reference. The right side of the table summarized the discrepancies, defined according to Eq. 11, between the different procedures.

Test ID	h_A	h_V	h_B	$\epsilon_{A\to B}$	$\epsilon_{V\to B}$	$\epsilon_{V\to A}$
	[MJ kg^{-1}]			[%]		
$\mathbb{ID}_1$	13.9	18.7	$16.7^{+2.5}_{-1.6}$	−16.7	12.3	35.0
$\mathbb{ID}_2$	22.8	33.5	$28.0^{+5.9}_{-3.2}$	−18.5	19.4	47.2
$\mathbb{ID}_3$	31.6	48.8	$38.8^{+7.4}_{-3.1}$	−18.5	25.8	54.5

Table 4: The table summarizes the values of the enthalpy at the boundary layer edge and at the wall using the VKI standard procedure in: i) chemical non-equilibrium and $\gamma = 0.01$, ii) LTE (by boosting the reaction rates of the chemical reactions) and $\gamma = 0.01$, and ii) LTE and $\gamma = 1.0$.

Test ID	h_V	h_{V_w}	h_V^{LTE}	$h_{V_w}^{LTE}$	$h_{V(\gamma=1)}^{LTE}$	$h_{V(\gamma=1)_w}^{LTE}$
	[MJ kg^{-1}]		[MJ kg^{-1}]		[MJ kg^{-1}]	
$\mathbb{ID}_1$	18.7	2.29	16.1	0.43	16.1	0.43
$\mathbb{ID}_2$	33.5	4.45	26.4	0.44	26.4	0.44
$\mathbb{ID}_3$	48.8	7.55	38.4	0.45	38.4	0.45

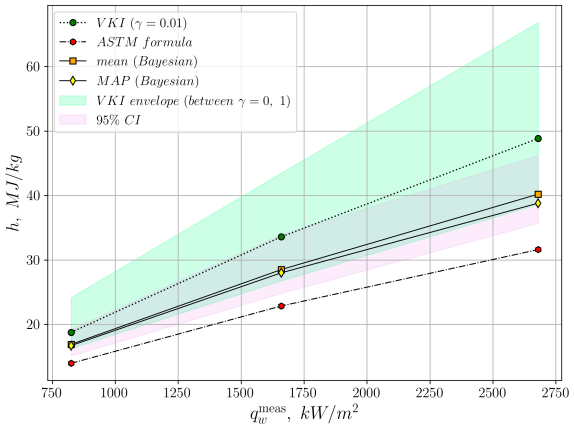

Figure 6: Comparison among the three enthalpy rebuilding procedures at p_c=100 mbar. The VKI rebuilding analysis is carried out with $\gamma = 0.01$ and an 11 species air mixture using Park's chemical model (see Appendix Appendix A).

5.3. 50 mbar

Fig. 7 shows the results at p_c =50 mbar where two catalytic coefficients have been considered for the VKI rebuilding procedure. The former, $\gamma = 0.1$, suggested by Panerai [8] and the latter, $\gamma = 2.661 \times 10^{-2}$, recently presented by Viladegut et al. [4] as the result of the application of the Min-Max methodology that combines heat flux measurements of three different calorimeters (silver, copper and quartz) to retrieve the catalytic coefficient of copper. Discrepancies between the models are summarized in Tab. 5. Results employing γ =0.1 agrees surprisingly well with the Bayes formulation with negligible discrepancies at the lowest and highest heat fluxes (≤ 0.3 %) and a maximum discrepancy of 2.4 % for $\mathbb{ID}_5$. Conversely, the VKI rebuilding employing γ =2.661 $\times 10^{-2}$ over-predict the enthalpy with discrepancies ranging from 10 and 20 % but still enveloped in the confidence interval. As for the $p_c = 100$ mbar, the ASTM under-predict the enthalpy with margins of ≈ 20 % at $\mathbb{P}_{el} = 150$ and

200 kW and 26 % at 300 kW, too large to include the results in the 95 % CIs. Tab. 5 also summarizes the margins between the VKI (γ =2.661 $\times$ 10^{-2}) standard methodology and the ASTM formulation ranging between 37 and 55 % at the lowest and highest electrical power. In general, the discrepancies existing between the empirical formulation proposed in the ASTM and the recent rebuilding procedures are not straightforward to understand. In addition to the assumptions described in Sec. 4.1 and quickly investigated in Sec. 5.2, the K constant presented in Eq.1 was first introduced to include the effect of the thermodynamic and transport properties of the gas at the wall and at the boundary layer edge [3]. The calibration of the constant was performed by means of a linear interpolation between numerical computations and experimental measurements available at that time (60s-70s) that, therefore, can be reasonably questionable. It is, therefore, challenging to find a correlation with the discrepancies found in this work but future development involving sensitivity studies may help quantify the role of the constant in the enthalpy estimation. As for the p_s =100 mbar, the lower bound of the CIs fall below the limit of γ = 1 for the VKI rebuilding method due to the measurement uncertainties. The discrepancies are 0.9, 1.5, and 1.2 MJ kg^{-1}, for $\mathbb{P}_{el}$ = 150, 200, and 300 kW respectively.
Finally, the predictions of the mean and MAP predictions deviate more from previous results suggesting a positive skewness (higher values towards lower enthalpy) of the density distribution.

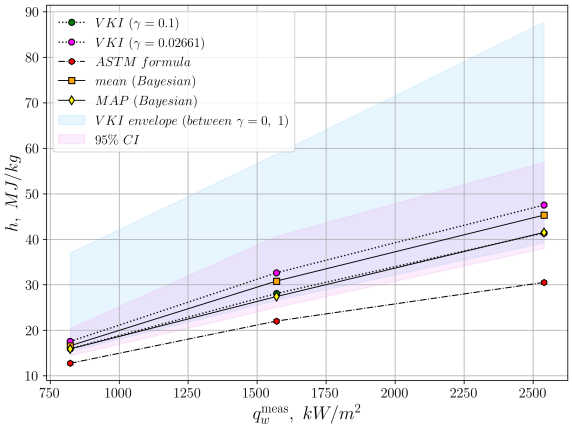

Figure 7: Comparison between the three enthalpy rebuilding procedures with application in the VKI Plasmatron at p_c=50 mbar. The VKI rebuilding analysis is carried out with γ = 0.1 and 2.661 $\times$ 10^{-2} and an 11 species air mixture using the Park's chemical model (see Appendix Appendix A).

Table 5: The left side summarizes the enthalpy estimations of the different procedures for the three testing conditions. The subscripts $[.]_A$, $[.]_{V_{\gamma_1}}$, $[.]_{V_{\gamma_2}}$ and $[.]_B$ stand for the different methodologies: A for ASTM formulation, V_{γ_1} for the VKI procedure using γ = 0.1, V_{γ_2} for the case with γ = 2.661 $\times$ 10^{-2}, and B for the Bayesian formulation using the MAP as reference. The right side of the table summarized the discrepancies, defined according to Eq. 11, between the different procedures.

Test ID	h_A	$h_{V_{\gamma_1}}$	$h_{V_{\gamma_2}}$	h_B [MJ kg^{-1}]	$\epsilon_{A\to B}$	$\epsilon_{V_{\gamma_1}\to B}$	$\epsilon_{V_{\gamma_2}\to B}$	$\epsilon_{V_{\gamma_2}\to A}$ [%]
$\mathbb{ID}_4$	12.7	15.9	17.5	$15.9^{+4.5}_{-1.5}$	−19.8	−0.3	10.3	37.6
$\mathbb{ID}_5$	22.0	28.0	32.6	$27.4^{+13.2}_{-2.4}$	−19.6	2.4	19.0	48.1
$\mathbb{ID}_6$	30.5	41.3	47.5	$41.5^{+15.4}_{-3.5}$	−26.4	−0.28	14.4	55.67

6. Conclusions

Three enthalpy rebuilding methodologies, hereafter presented from the simplest to the most reliable according to the assumption made, have been compared with application at the VKI Plasmatron facility. The ASTM E-637 procedure is based entirely on heat flux, static and dynamic pressure measurements relying on strong assumptions (e.g. LTE equilibrium) in the derivation of the semi-empirical equation of h. The VKI standard deterministic procedure relaxes some hypothesis considering conditions of chemical non-equilibrium and non-fully catalytic surface including the catalytic coefficient, γ. γ is assumed known from literature but, empirical data on copper catalysis suffer many contradictions among the different authors. The last procedure, a stochastic approach based on a Bayesian framework, generalizes the inference assuming a-priori unknown the catalysis coefficient and including measurement uncertainties in the analysis. A total of six experimental campaigns are analyzed at two different chamber static pressures (50 and 100 mbar) and three different electrical powers $\mathbb{P}_{el} \approx$ 150, 210 and 300 kW. In all conditions, the VKI standard rebuilding overestimates the enthalpy respect to Bayes formulation while the ASTM under-predict the thermodynamic variable. At p_c = 100 mbar, the discrepancies between the VKI (γ = 0.01) and the Bayesian formulation range from 12 and 26 % at the lowest and highest $\mathbb{P}_{el}$ while the ASTM shows a roughly constant margin of 17 % for all powers. As far as 50 mbar is concerned, the VKI methodology uses the traditional value of γ =0.1 and γ =2.661 $\times$ 10^{-2} as recently suggested by Viledegut et al. [4]. While the VKI rebuilding using γ =0.1 is almost overlapping the MAP prediction of the stochastic problem (discrepancies below 2.5 %), the case with

γ =2.661$\times 10^{-2}$ shows discrepancies ranging between 10 and 19 %. The ASTM formulation deviates more than the VKI re-building's results with margins in the order of 20 % respect to the Bayes predictions. Furthermore, if on one hand the Bayesian posterior distribution envelope the VKI standard rebuilding results, ASTM predictions fall outside the 95 % confidence intervals. The reasons may lie in the assumptions behind the ASTM formulation. In particular, the LTE and fully catalytic surface hypothesis have been investigated, by boosting the chemical reaction rates in boundary layer computations, for the test cases at p_c = 100 mbar showing how the LTE condition may significantly impact the outcomes of the computations. Future developments can exploit sensitivity analysis studies to quantify the role of other parameters, for instance, the uncertainties of K in the ASTM equation, or in Bayesian formulation to exploit the impact of γ, measurements uncertainties, or other model assumptions (e.g., the power efficiency of 50 %, the role of the NDPs, the uncertainties in Park's chemical model) that may have in the enthalpy estimation. An ongoing effort is to compute the actual uncertainties of the measurement that may benefit the Bayesian methodology instead of assuming uncertainty values from previous works as well as there is an ongoing collaboration with one of the co-authors of the article, A. Fagnani, aims to provide spectroscopic measurements to estimate the temperature, and therefore the enthalpy, to be compared with the results here presented.

Acknowledgments

The research of E. Anfuso is supported by a doctoral fellowship awarded from the Research Foundation Flanders (FWO, dossier #1SF8822N) as well as A.Fagnani's with dossier #1SB3219N. Pascal Collin is acknowledged for his essential help as Plasmatron operator.

References

[1] Barbante, P. F. and Chazot, O., Flight Extrapolation of Plasma Wind Tunnel Stagnation Region Flowfield, Journal of Thermophysics and Heat Transfer 20 (3) (2006) 493–499.

[2] A. Kolesnikov, The concept of local simulation for stagnation point heat transfer in hypersonic flows-applications and validation, in: 21st Aerodynamic Measurement Technology and Ground Testing Conference, 2000.

[3] V. E. Zoby, Empirical stagnation-point heat-transfer relation in several gas mixtures at high enthalpy levels, nASA Technical Note, 1968.

[4] A. Viladegut, O. Chazot, Empirical modeling of copper catalysis for enthalpy determination in plasma facilities, Journal of Thermophysics and Heat Transfer 34 (1) (2020) 26–36.

[5] B. Helber, Material Response Characterization of Low-density Ablators in Atmospheric Entry Plasmas, Ph.D. thesis, Von Karman Institute & Vrije Universiteit Brussel (2016).

[6] A. International, Standard test method for calculation of stagnation enthalpy from heat transfer theory and experimental measurements of stagnation-point heat transfer and pressure, e0637-05. NASA Technical Report, 2005.

[7] A. Viladegut, O. Chazot, Enthalpy characterization and assessment of copper catalysis determination in inductively coupled plasma facility, in: 45th AIAA Thermophysics Conference, 2015.

[8] F. Panerai, Aerothermochemistry characterization of thermal protection systems, Ph.D. thesis, von Karman Institute & Universitá degli studi di Perugia (2012).

[9] A. del Val, P. O. Le Maître, T. Magin, O. Chazot, M. P. Congedo, A surrogate-based optimal likelihood function for the bayesian calibration of catalytic recombination in atmospheric entry protection materials, Applied Mathematical Modelling 101 (2022) 791–810. doi:https://doi.org/10.1016/j.apm.2021.07.019.

[10] V. L. Kovalev, A. F. Kolesnikov, Experimental and theoretical simulation of heterogeneous catalysis in aerother- mochemistry., Fluid Dynamics 20 (2005) 669–693.

[11] A. Cipullo, B. Helber, F. Panerai, L. Zeni, O. Chazot, Investigation of freestream plasma flow produced by inductively coupled plasma wind tunnel, Journal of Thermophysics and Heat Transfer 28 (3) (2014) 381–393.

[12] W. Winovich, W. C. A. Carlson, The 60-mw shuttle interaction heating facility, in: International Instrumentation Symposium, 1979.

[13] R. Goulard, On catalytic recombination rates in hypersonic stagnation heat transfer, Journal of Jet Propulsion 28 (11) (1958) 737–745.

[14] P. F. Barbante, O. Chazot, Flight extrapolation of plasma wind tunnel stagnation region flowfield, Journal of Thermophysics and Heat Transfer 20 (3) (2006) 493–499.

[15] P. F. Barbante, Heat flux duplication between ground facility and hypersonic flight, Journal of Thermophysics and Heat Transfer 23 (4) (2009) 684–692.

[16] J. A. Fay, F. R. Riddell, Theory of stagnation point heat transfer in dissociated air, Journal of the Aerospace Sciences 25 (2) (1958) 73–85.

[17] S. Loehle, F. Zander, M. Eberhart, T. Hermann, A. Meindl, B. Massuti-Ballester, D. Leiser, F. Hufgard, , A. S. Pagan, G. Herdrich, S. Fasoulas, Assessment of high enthalpy flow conditions for re-entry aerothermodynamics in the plasma wind tunnel facilities at irs., CEAS Space 14 (2022) 395–406.

[18] Y. Wang, X. Li, D. Liu, Y. Liu, Estimating the power injection proportion of the plasma jet generator based on the measured enthalpy, Physics of Plasmas 28 (12) (2021) 123508.

[19] A. Lani, An object oriented and high performance platform for aerothermodynamics simulation, Ph.D. thesis, von Karman Institute & Université Libre de Bruxelles (2009).

[20] J. B. Scoggins, V. Leroy, G. Bellas-Chatzigeorgis, B. Dias, E. T. Magin, Mutation++: Multicomponent thermodynamic and transport properties for ionized gases in c++, SoftwareX 12. doi:10.1016/j.softx.2020.100575.

[21] M. G. Dunn, S. Kang, Theoretical and experimental studies of reentry plasmas, Vol. 2232, National Aeronautics and Space Administration Washington, DC, 1973.

[22] C. Park, Review of chemical-kinetic problems of future nasa missions. i-earth entries, Journal of Thermophysics and Heat

transfer 7 (3) (1993) 385–398.
[23] C. Park, R. L. Jaffe, H. Partridge, Chemical-kinetic parameters of hyperbolic earth entry, Journal of Thermophysics and Heat transfer 15 (1) (2001) 76–90.
[24] B. Bottin, D. V. Abeele, M. Carbonaro, G. Degrez, G. S. R. Sarma, Thermodynamic and transport properties for inductive plasma modeling, Journal of thermophysics and heat transfer 13 (3) (1999) 343–350.
[25] T. J. Sullivan, Introduction to uncertainty quantification, Vol. 63, Springer, 2015.
[26] J. A. Nelder, R. Mead, A simplex method for function minimization, The computer journal 7 (4) (1965) 308–313.
[27] A. del Val, Bayesian calibration and assessment of gas-surface interaction models and experiments in atmospheric entry plasmas, Ph.D. thesis, von Karman Institute & École Polytechnique (2021).

Appendix A. Park's mechanisms

Table A.6: $c_{f,j}$, $b_{f,j}$ and $e_{f,j}$ parameters of the Arrhenius law ($k_{f,j} = c_{f,j} T^{b_{f,j}} e^{-e_{f,j}/T}$) for the forward reaction rates coefficients provided by Park et al. [22; 23].

Reaction	M	$c_{f,j}$ [cm^3 s^{-1} mol^{-1}]	$b_{f,j}$ [−]	$e_{f,j}$ [K]
$N_2 + M \rightleftarrows 2\,N + M$	N	3.0×10^{22}	-1.6	113 200
	O	3.0×10^{22}	-1.6	113 200
	N_2	7.0×10^{21}	-1.6	113 200
	O_2	7.0×10^{21}	-1.6	113 200
	NO	7.0×10^{21}	-1.6	113 200
	e^-	1.2×10^{25}	-1.6	113 200
$O_2 + M \rightleftarrows 2\,O + M$	N	1.0×10^{22}	-1.5	59 360
	O	1.0×10^{22}	-1.5	59 360
	N_2	2.0×10^{21}	-1.5	59 360
	O_2	2.0×10^{21}	-1.5	59 360
	NO	2.0×10^{21}	-1.5	59 360
$NO + M \rightleftarrows N + O + M$	N	1.1×10^{17}	0.0	75 500
	O	1.1×10^{17}	0.0	75 500
	N_2	5.0×10^{15}	0.0	75 500
	O_2	5.0×10^{15}	0.0	75 500
	NO	1.1×10^{17}	0.0	75 500
$N_2 + O \rightleftarrows NO + N$	-	5.7×10^{12}	0.42	42 938
$NO + O \rightleftarrows N + O_2$	-	8.4×10^{12}	0.0	19 400
$N + O \rightleftarrows NO^+ + e^-$	-	8.8×10^{8}	1.0	31 900
$O + O \rightleftarrows {O_2}^+ + e^-$	-	7.1×10^{2}	2.7	80 600
$N + N \rightleftarrows {N_2}^+ + e^-$	-	4.4×10^{7}	1.5	67 500
$O + NO^+ \rightleftarrows O_2 + N^+$	-	1.0×10^{12}	0.5	77 200
$N_2 + N^+ \rightleftarrows {N_2}^+ + N$	-	1.0×10^{12}	0.5	12 200
$N + {O_2}^+ \rightleftarrows N^+ + O_2$	-	8.7×10^{13}	0.14	28 600
$NO + O^+ \rightleftarrows N^+ + O_2$	-	1.4×10^{5}	1.90	26 600
$N_2 + {O_2}^+ \rightleftarrows {N_2}^+ + O$	-	9.9×10^{12}	0.0	40 700
$O + {O_2}^+ \rightleftarrows O_2 + O^+$	-	4×10^{12}	-0.09	18 000
$N + NO^+ \rightleftarrows N_2 + O^+$	-	3.4×10^{13}	-1.08	12 800
$O_2 + NO^+ \rightleftarrows NO + {O_2}^+$	-	2.4×10^{13}	0.41	32 600
$O + NO^+ \rightleftarrows N + {O_2}^+$	-	7.2×10^{12}	0.29	48 600
$N_2 + O^+ \rightleftarrows {N_2}^+ + O$	-	9.1×10^{11}	0.36	22 800
$N + NO^+ \rightleftarrows {N_2}^+ + O$	-	7.2×10^{13}	0.0	35 500
$O + e^- \rightleftarrows O^+ + e^- + e^-$	-	3.9×10^{33}	-3.78	158 500
$N + e^- \rightleftarrows N^+ + e^- + e^-$	-	2.5×10^{34}	-3.82	168 600

Determination of a stochastic finite-rate nitridation model consistent with molecular beam and plasma wind tunnel data

Michele Capriati

Aeronautics and Aerospace Department, von Karman Institute for Fluid Dynamics, Belgium, mymail@vki.ac.be

Supervisor: Thierry E. Magin

Professor, Aeronautics and Aerospace Department, von Karman Institute for Fluid Dynamics, Belgium, thierry.magin@vki.ac.be

University Supervisor: Pietro Congedo

Head of the PLATON project-team in CMAP Laboratory (INRIA Saclay Ile-de-France, Ecole Polytechnique), France, pietro.congedo@inria.fr

Abstract

The accurate modelling of gas-surface interaction phenomena is crucial for the prediction of the heat flux and the mass loss experienced by atmospheric entry bodies flying at hypersonic speeds. Gas-surface interactions refer to the set of phenomena occurring between the reactive gas and the material surface, involving heterogeneous chemical reactions together with mass and heat exchange. The surface chemical production rates can be computed using phenomenological or finite-rate chemistry models. In this work, we propose to calibrate nitridation surface chemical rates in a Bayesian framework. The calibration is performed by combining wind tunnel and molecular beam data. The plasma wind tunnel data are explained using a surrogate model that captures the underlying boundary layer in front of the test sample. The molecular beam data are explained through an analytical model. The parameters' posterior distribution is obtained by constructing a Markov Chain Monte Carlo.

Keywords: Ablation, Gas-surface Interaction, Bayesian calibration

1. Introduction

Correctly computing Thermal Protection Material (TPM) thermo-chemical response is important in atmospheric entry applications for a safe spacecraft's landing. The most robust way to characterise TPMs is by means of experimental high-enthalpy facilities, such as the von Karman Institute (VKI) Plasmatron facility. Nevertheless, experiments are generally costly and time-consuming and it is prohibitive to span over too many conditions. Contrarily, numerical experiments are generally cheaper and faster, but one has to model the physics. A suitable way to overcome all these drawbacks is by using experiments to calibrate the models, as sketched in figure 1. When the calibration is done solving a stochastic inverse problem, it is possible to compute a robust estimate of the model's parameters' uncertainty, which can then be propagated when applying the model.

Past the bow shock, particles' internal energy drastically increases and they dissociate and ionize: a chemically reacting boundary layer develops in front of the vehicle. GSIs describe the set of phenomena occurring between the reactive gas and the material surface, involving heterogeneous chemical reactions together with mass and heat exchange. Prediction's accuracy depends, among other things, on the accuracy of the GSI modelling.

In previous works, GSI models were abstracted in the MUTATION^{++} open source software [1; 2] to provide a boundary condition for chemical reacting surfaces. The MUlticomponent Thermodynamic And Transport properties for IONized gases library written in C++ (MUTATION^{++}) has been developed at the von Karman Institute to help centralize physico-chemical models, algorithms, and data into a single software package, which may be shared among several CFD tools. The GSI module of MUTATION^{++}

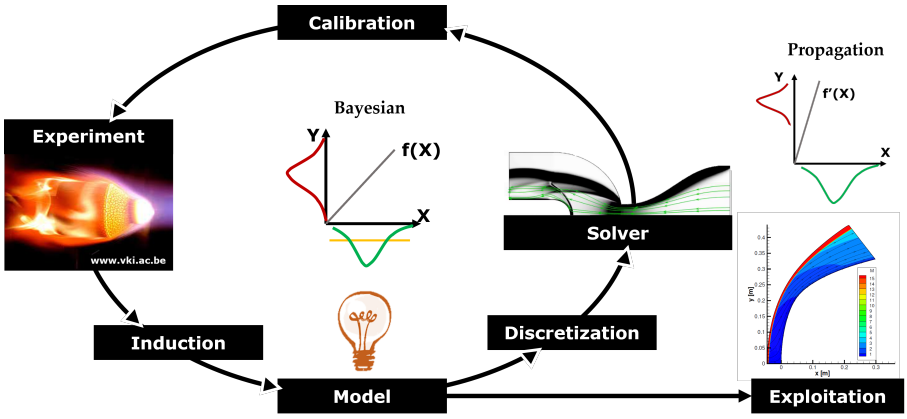

Figure 1: Sketch.

has been used to model catalytic and ablative materials, both assuming thermal equilibrium and non-equilibrium (state-to-state catalysis or two temperature ablation) of the gas near the surface [1; 3].
Among the set of surface reactions, the ones involving nitrogen are of great importance for example for Earth and Titan entry applications. Nitrogen surface recombination has a strong influence on the heat flux experienced by the spacecraft, while the nitridation reaction on the mass loss. In the work [4] it was pointed out that nitridation efficiencies values found in literature span several orders of magnitude. They proposed a temperature dependency to capture the trend.
Recently, a molecular beam experimental campaign [5] was performed to assess the temperature dependency of both the nitridation and the recombination reactions. These data were used to develop a surface finite-rate chemical model [6], which attempts to capture both the temperature and the pressure dependency of the reactions. In [7], this model was used to simulate the experimental campaign in [4]. The model predicted a lower mass blowing rate than what has been experimentally observed. More recently, the work [8] made use of a stochastic environment to robustly assess the values of nitridation efficiency based on the experiment in [4].
In this work, we propose to re-calibrate the model in [6] to make it consistent both with molecular beam and with Plasmatron experiments. To this end, we solve the Bayesian inverse problem. A surrogate model is built on CFD computation to explain Plasmatron data to accelerate the inversion.
The paper is structured as follows: in Section 2 the GSI modelling is presented, as well as the experimental campaigns used for the calibration, in Section 3 the governing equation are presented along with the used CFD solver, in Section 4 the used uncertainty quantification tools are presented, in Section 5 the calibration results are shown, and in Section the conclusions are drawn.

2. Gas-Surface Interaction

The thermo-chemical behaviour of a surface interacting with the gas can be modelled by solving balance equations in the infinitesimal volume containing both the gas and the material.
In this study, we consider the surface temperature known (isothermal condition), and we only solve for the surface mass balance. Assuming the surface recession velocity to be negligible compared to the blowing velocity, the surface mass balance for each species i reads:

$$\dot{\omega}_i^s = (\rho_i \mathbf{u}_g + \mathbf{j}_i) \cdot \mathbf{n}, \quad \forall i \in S, \tag{1}$$

where symbol S stands for the set of species indices and $\mathbf{n}$ is the normal to the surface. The term $\mathbf{u}_g = \sum_{i \in S} \dot{\omega}_i^s / \rho$ is the blowing velocity of the gas at the interface as a result of ablation processes, ρ_i, the mass density of species i, ρ the mass density of the gas mixture, and $\mathbf{j}_i$ the diffusion mass flux of species i. The term $\dot{\omega}_i^s$ is the chemical production rate of species i. It can be computed using phenomenological or finite-rate chemistry models, as described in the following sections.

2.1. Phenomenological approach

Phenomenological models were first introduced to describe the catalytic behaviour of a surface in hypersonic simulations [9], and later to describe ablative

surfaces [4]. They are widely used in the hypersonic community because of their simplicity; they only require the definition of the probability that a macroscopic reaction takes place:

$$\gamma_{\mathrm{i}}^{\mathrm{rea}} = \frac{\mathcal{N}_{\mathrm{i}}^{\mathrm{rea}}}{\mathcal{N}_{\mathrm{i}}}, \tag{2}$$

where $\mathcal{N}_{\mathrm{i}}^{\mathrm{rea}}$ is the number flux of species i subject to the reaction and $\mathcal{N}_{\mathrm{i}} = n_{\mathrm{i}}\sqrt{k_{\mathrm{b}}T_{\mathrm{s}}/(2\pi m_{\mathrm{i}})}$, the number flux of species i impinging the surface. Symbol k_{b} stands for Boltzmann's constant, T_{s} the surface temperature, and m_{i}, the mass of species i. A fully catalytic behavior is obtained when the probability γ approaches unity; whereas a non-catalytic behavior is reached when γ is equal to zero. The chemical production rate reads:

$$\dot{\omega}_{\mathrm{i}}^{\mathrm{s}} = m_{\mathrm{i}}\gamma_{\mathrm{i}}^{\mathrm{rea}}\mathcal{N}_{\mathrm{i}}. \tag{3}$$

2.2. Finite-rate chemistry approach

Alternative formulations to phenomenological approaches are FRC models describing each elementary reaction occurring on the surface (adsorption/desorption, nitridation, recombination, ...). They have the advantage of capturing the pressure dependence of chemical reactions and the surface coverage. In this case, the chemical production rate reads:

$$\dot{\omega}_{\mathrm{i}}^{\mathrm{s}} = \sum_{\mathrm{r}\in R} N_{\mathrm{A}} m_{\mathrm{i}} k_r \prod_{\mathrm{j}\in S} [X_{\mathrm{j}}]^{\nu_{\mathrm{j}}}, \tag{4}$$

where R is the set of surface reactions, $[X_{\mathrm{j}}] = \rho_{\mathrm{j}}/(N_{\mathrm{A}} m_{\mathrm{j}})$, the concentration of species j, ν_{j}, its stoichiometric coefficient, and N_{A}, Avogadro's number. The term k_{r} is the rate coefficient for reaction r, which can assume an Arrhenius-like form, whose parameters need to be computed.

2.3. Experimental campaigns and Modeling

In this Section, we present the Plasmatron and molecular beam experiments, and the relative model derived.

2.3.1. Plasmatron experiments

An experimental campaign was carried out in the VKI Plasmatron facility to assess nitridation efficiency at low-pressure (1500 Pa) [4]. It consists of a nitrogen plasma flow over a 25 mm radius hemisphere carbonaceous sample. The surface temperature was measured by means of a calorimeter, the recession rate using a high-speed camera and the temperature in the BL with a spectrometer. Free stream conditions were numerically rebuilt; further information is provided in [4]. Experimental observables are reported in table 1. The enthalpy in the facility was increased from case G4 to G7, allowing for assessing the effect of the surface temperature on the nitridation efficiency, which read:

$$\gamma_{\mathrm{N}}^{\mathrm{CN}}(T_{\mathrm{s}}) = 7.91 \cdot 10^{-2} \exp\frac{-5653}{T_{\mathrm{s}}}. \tag{5}$$

2.3.2. Molecular Beam experiments

Molecular beams experiments were performed by [5] in order to obtain the efficiency of oxygen and nitrogen reactions with a carbonaceous surface by measuring the flight time of the scattered beams. Differently from Plasmatron experiments, molecular beam experiments are performed at almost-null pressure, such that only gas-surface interaction phenomena appear. The resulting values of the efficiencies relative to the nitrogen reactions [5] are given in the figure 2.

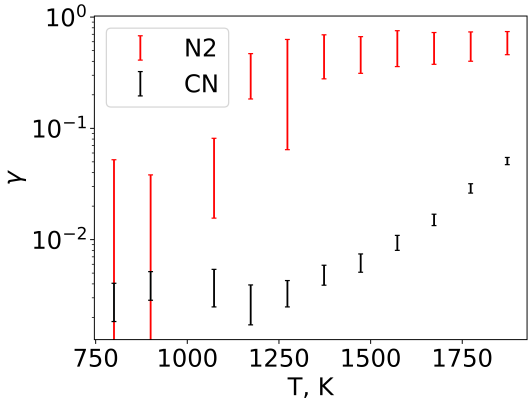

Figure 2: Nitrogen recombination and nitridation efficiency experimentally observed by [5].

2.4. Nitrogen Finite-Rate Chemistry model

An air-carbon ablation model was recently derived by Prata [6]. It was built both from the Plasmatron data and molecular beam experiment data above described. The subset of reactions relevant to this work is listed in table 2. The rate coefficients for each surface reaction are also shown in table 2, where B is the active site density on the surface [mol m^{-2}], s, the surface density of empty sites [mol m^{-2}], $F_{\mathrm{N}} = \sqrt{k_b T/2\pi m_{\mathrm{N}}}$, a quarter of the mean thermal speed of atomic nitrogen, $F_{\mathrm{N,2D}} = \sqrt{\pi k_b T/2m_{\mathrm{N}}}$, the mean thermal speed of the mobile adsorbed nitrogen on the surface, and h, the Planck constant.

Table 1: Overview of Plasmatron test conditions for a nitrogen flow at 1500 Pa over a 25 mm radius hemisphere carbonaceous sample [4]: dynamic pressure P_d, generator power P_{el}, sample mean temperature T_s, mass blowing rate $\dot{m}$, nitridation efficiency γ_N^{CN}, boundary layer edge conditions (density ρ_{edge}, temperature T_{edge}, and velocity u_{edge}).

CASE	P_d [Pa]	P_{el} [kW]	T_{wall} [K]	$\dot{m}$ [g/m^{2}s]	γ_N^{CN} [-]	ρ_{edge} [g/m^3]	T_{edge} [K]	u_{edge} [m/s]
G4	231	280	2225	1.6/3.4	3.2E-3/7.4E-3	0.236	10005	554
G5	268	330	2410	1.9/3.8	4.0E-3/8.6E-3	0.225	10280	562
G6	312	370	2535	3.6/5.2	7.9E-3/1.2E-2	0.184	11040	846
G7	330	390	2575	3.7/5.4	8.1E-3/1.3E-2	0.189	10970	859

Table 2: FRC reactions for nitrogen flows [6].

Reaction	Reaction Rate	Rate Coefficient
$N + s \longrightarrow N_s$	$k_1[N][s]$	$\frac{F_N}{B} \exp \frac{-2500}{T_s}$
$N_s \longrightarrow N + s$	$k_2[N_s]$	$\frac{2\pi m_N k_b^2 T_s^2}{N_A B h^3} \exp \frac{-73971}{T_s}$
$N + N_s + C_b \longrightarrow CN + N + s$	$k_3[N][N_s]$	$\frac{F_N}{B} 1.5 \exp \frac{-7000}{T_s}$
$N + N_s \longrightarrow N_2 + s$	$k_4[N][N_s]$	$\frac{F_N}{B} 0.5 \exp \frac{-2000}{T_s}$
$N_s + N_s \longrightarrow N_2 + 2s$	$k_5[N_s][N_s]$	$\sqrt{\frac{N_A}{B}} F_{N,2D} 0.1 \exp \frac{-21000}{T_s}$
$N_s + C_b \longrightarrow CN + s$	$k_6[N_s]$	$10^8 \exp \frac{-20676}{T_s}$

The set of equations (4) was closed by steady-state assumption ($ds/dt = 0$, meaning that the net production of empty sites in time is zero) and the reaction efficiency is computed by dividing the chemical production rate term by the flux of the species impinging the surface:

$$\gamma_N^{CN} = \frac{\dot{\omega}_{CN}}{m_{CN} \mathcal{N}_N}, \qquad \gamma_N^{N2} = \frac{\dot{\omega}_{N2}}{m_N \mathcal{N}_N}. \tag{6}$$

The efficiency computed in this way leads to the low and high-pressure predictions shown in figure 3. The 0D approach followed by [6] neglected the influence of the boundary layer, which is representative of the molecular beam experiments. Nevertheless, when the model is coupled to a CFD solver to reproduce the Plasmatron experiments report in [4], it predicts lower mass blowing rates then what was experimentally observed [7].

2.4.1. Model Implementation

The FRC model in MUTATION^{++} [1; 2] was extended to use the air-carbon ablation model developed by [6]. A Newton method solves for the system (1), while an internal one solves the chemical production terms (4) under the steady-state assumption. A verification test case for the implementation is shown in figure 4.

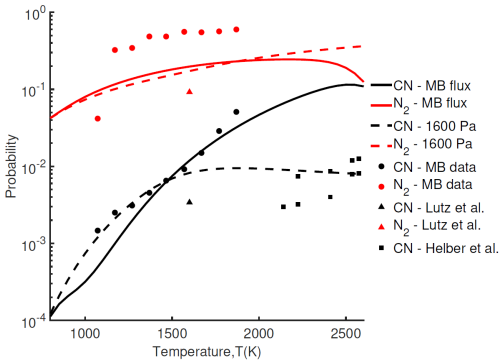

Figure 3: Nitrogen recombination and nitridation efficiency computed in [6].

3. Governing equations and flow solver

Plasmatron experiments are simulated by solving chemically reactive Navier-Stokes equations:

$$\frac{\partial \rho_i}{\partial t} + \nabla \cdot (\rho_i \mathbf{u} + \mathbf{j}_i) = \dot{\omega}_i, \quad \forall i \in S, \tag{7}$$

$$\frac{\partial \rho \mathbf{u}}{\partial t} + \nabla \cdot (\rho \mathbf{u} \cdot \mathbf{u} + p\bar{\bar{\mathrm{I}}} + \bar{\bar{\tau}}) = \mathbf{0}, \tag{8}$$

$$\frac{\partial \rho E}{\partial t} + \nabla \cdot (\rho \mathbf{u} H + \bar{\bar{\tau}} \mathbf{u} + \mathbf{q}) = 0. \tag{9}$$

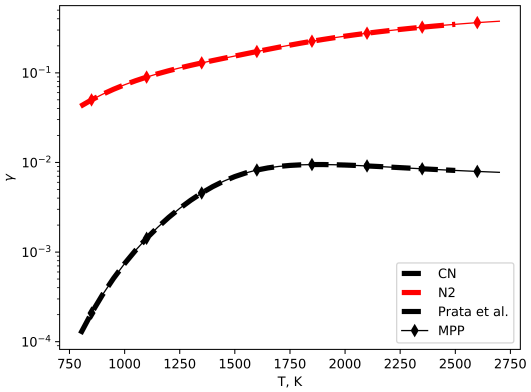

Figure 4: Model verification.

Vector **u** is the mass-averaged mixture velocity, $\dot{\omega}_i$, its chemical production/destruction rate, p, the thermodynamic pressure of the mixture, n_s, the number of species in the mixture, $\bar{\bar{\tau}}$, the viscous stress tensor, E, the total energy, $H = E + p/\rho$, the total enthalpy, and **q**, the total heat flux.
Thermodynamics properties are obtained using the NASA polynomials [10]. Diffusion mass fluxes are computed using the Stephan-Maxwell equations, while viscosity and thermal conductivity are based on Chapman-Enskog solution of the Boltzmann equation [11; 12]. Chemical production rates $\dot{\omega}$ for species i are computed using finite-rate chemistry. The library MUTATION^{++} [2] provides the closure to the models above mentioned to the flow solvers.

3.1. VKI stagnation line solver

When dealing with axisymmetric problems, a Dimensionally Reduced Navier-Stokes Equations (DRNSE) formulation [13] can be used to simulate the flowfield on the stagnation line. The system is written in spherical coordinates (r, θ, ϕ), then, exploiting the axial symmetry, $u_\phi = \partial/\partial\phi = 0$ and letting $\theta \to 0$, the DRNSE formulation is obtained. Munafò [13] developed a software for the DRNSE equations based on a finite volume discretization method, together with an implicit local time-stepping technique to reach the steady state. The code interfaced to MUTATION++ helps us to verify the coupling of US3D to MUTATION++, using the Roe scheme for the numerical fluxes.

4. UQ tools

4.1. Bayesian

We intend to calibrate the pre-exponential factors and the activation energies of the reactions in table 2, as well as the total number of free sites. Input to the Bayesian framework is thus:

$$\mathbf{x} = [X3, X4, X5, X5, E1, E3, E4, E5, E6, B] \quad (10)$$

To their calibration, we used complementary experimental observations:

$$\mathbf{y} = [\gamma^{MB}_{CN,1\ldots11}, \gamma^{MB}_{N2,1\ldots11}, \dot{m}_{G4}, \dot{m}_{G5}, \dot{m}_{G6}, \dot{m}_{G7}] \quad (11)$$

The posterior distribution of the parameters is obtained according to Bayes' theorem:

$$\pi(\mathbf{x}|\mathbf{y}) = \frac{\pi(\mathbf{x})\pi(\mathbf{y}|\mathbf{x})}{\int \pi(\mathbf{x})\pi(\mathbf{y}|\mathbf{x})d\mathbf{x}}, \quad (12)$$

where $\pi(\mathbf{x})$ is the prior distribution of **x** and $\pi(\mathbf{y}|\mathbf{x})$ is the likelihood. To compute the likelihood we need a computational model for expressing the observation as a function of **x**. To explain the molecular beam experiments we used the same 0D approach used in [6], while for the plasmatron experiment a surrogate model was built on CFD simulation. We used a Kriging surrogate model built on an initial 200 latin hyper-cube training points. The set was enlarged to 6200 points to lower the surrogate model to the 3%, as shown in figure 5. The inverse problem, as well as

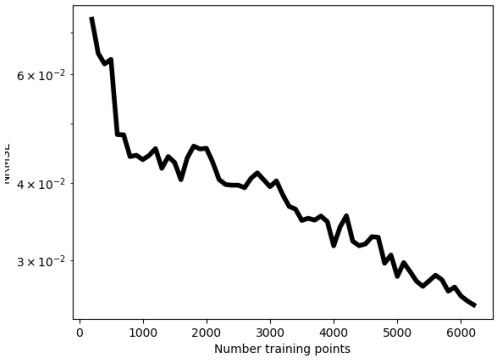

Figure 5: NRMSE.

the construction of the surrogate model, is solved by means of the UQLab library [14].

5. Results

5.1. Calibration only on molecular beam experiments.

We first calibrated the model only on the molecular beam data. The model post predictions at low pressure are shown in figure 7: little model uncertainty is present close to the calibration points. It increases outside this range. Interestingly, the model, which was

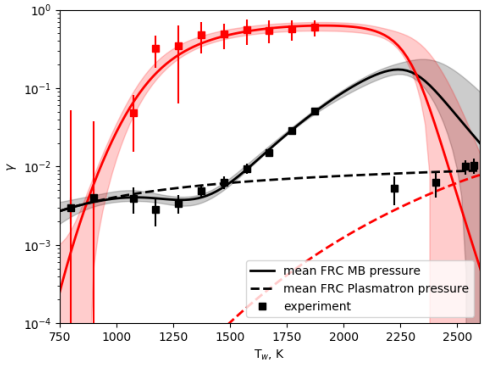

Figure 6: Model post prediction with parameters calibrated only on molecular beam experiments: uncertainty on low-pressure prediction. In red nitrogen recombination probability and in black probability of nitridation reaction.

calibrated only on low-pressure points, is able to well predict higher-pressure nitridation efficiencies. The uncertainty overlaps with the one obtained by [4], as one can see in figure 7. On the other hand, the nitrogen recombination efficiency's uncertainty is very high at this pressure, as a consequence of lack of observations at this pressure. The uncertainty span several order of magnitude.

5.2. Calibration on both molecular beam and Plasmatron experiments.

We then calibrated the model both on the molecular beam and plasmatron data. At high pressure, the uncertainty associated with the recombination reaction drops, as shown in figure 9, in the calibration temperature range. Some tension between the molecular beam and plasmatron data exists on the nitridation efficiency. In fact, the uncertainty associated with its prediction is higher than when the inversion is performed only on molecular beam data. Specifically, one can see in figure 8, that the first two low-pressure nitridation points are characterised by a higher uncertainty. It is contrary to what one expects. It is the

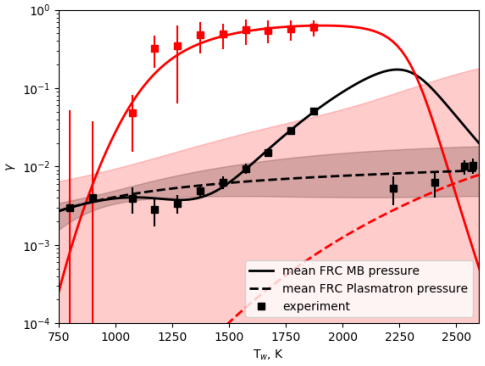

Figure 7: Model post prediction with parameters calibrated only on molecular beam experiments: uncertainty on high-pressure prediction. In red nitrogen recombination probability and in black probability of nitridation reaction.

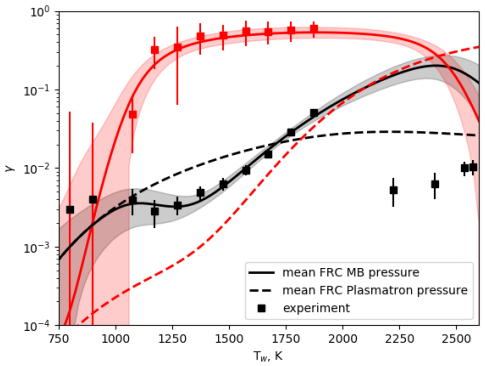

Figure 8: Model post prediction with parameters calibrated on both molecular beam and Plasmatron experiments: uncertainty on low-pressure prediction. In red nitrogen recombination probability and in black probability of nitridation reaction.

author's belief that this tension is caused by a not-enough-accurate surrogate model, which needs a further increase in accuracy to have better predictions.

6. Conclusion

We re-calibrated a nitridation finite-rate chemistry model both based on molecular beam and Plasmatron experiments. The calibration was performed in a Bayesian framework, using as computational model an analytical formulation to explain molecular beam experiments and a surrogate model built on CFD computations for explaining Plasmatron data. The inversion produced good predictions when calibrated only on molecular beam data. On the other hand, when

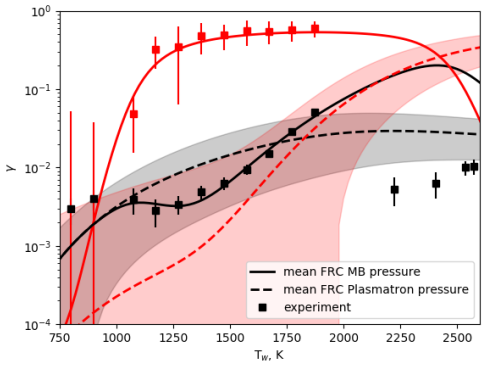

Figure 9: Model post prediction with parameters calibrated only on both molecular beam and Plasmatron experiments: uncertainty on high-pressure prediction. In red nitrogen recombination probability and in black probability of nitridation reaction.

using both molecular beam and Plasmatron data, the tension between the two models drives higher uncertainty on the model's prediction, probably because of the use of a not-enough-accurate surrogate model. It is currently being improved for enhancing the accuracy of the inversion.

7. Acknowledgments

The authors warmly thank Professor Timothy Minton and Thomas Schwartzentruberc for their insights on the molecular beam experiments and the finite rate chemistry models, and Dr Anabel del Val for the insights on the ablative UQ modelling.

References

[1] G. Bellas Chatzigeorgis, A. Turchi, A. Viladegut, O. Chazot, P. F. Barbante, T. Magin, Development of catalytic and ablative gas-surface interaction models for the simulation of reacting gas mixtures, in: 23rd AIAA Computational Fluid Dynamics Conference, American Institute of Aeronautics and Astronautics, 2017. doi:10.2514/6.2017-4499.

[2] J. B. Scoggins, V. Leroy, G. Bellas-Chatzigeorgis, B. Dias, T. E. Magin, Mutation + + : MUlticomponent Thermodynamic And Transport properties for IONized gases in C++, SoftwareX 12 (2020) 100575. doi:10.1016/j.softx.2020.100575.

[3] G. B. Chatzigeorgis, P. Barbante, T. E. Magin, Energy accommodation coefficient calculation methodology using state-to-state catalysis applied to hypersonic flows, AIAA Journal.

[4] B. Helber, A. Turchi, T. E. Magin, Determination of active nitridation reaction efficiency of graphite in inductively coupled plasma flows, Carbon 125 (2017) 582–594. doi:https://doi.org/10.1016/j.carbon.2017.09.081.

[5] V. J. Murray, P. Recio, A. Caracciolo, C. Miossec, N. Balucani, P. Casavecchia, T. K. Minton, Oxidation and nitridation of vitreous carbon at high temperatures 167 (2020) 388–402. doi:10.1016/j.carbon.2020.05.076.

[6] K. S. Prata, T. E. Schwartzentruber, T. K. Minton, Air–Carbon Ablation Model for Hypersonic Flight from Molecular-Beam Data 60 (2) (2022) 627–640. doi:10.2514/1.J060516.

[7] M. Capriati, K. Prata, T. Schwartzentruber, G. Candler, T. Magin, Development of a nitridation gas-surface boundary condition for high-fidelity hypersonic simulations, in: 14th WCCM-ECCOMAS Congress, CIMNE, 2021. doi:10.23967/wccm-eccomas.2020.119.

[8] A. del Val, O. P. Le Maître, T. E. Magin, O. Chazot, P. M. Congedo, A surrogate-based optimal likelihood function for the Bayesian calibration of catalytic recombination in atmospheric entry protection materials, Applied Mathematical Modelling 101 (2022) 791–810. doi:https://doi.org/10.1016/j.apm.2021.07.019.

[9] R. Goulard, On Catalytic Recombination Rates in Hypersonic Stagnation Heat Transfer, Journal of Jet Propulsion 28 (11) (1958) 737–745. doi:10.2514/8.7444.

[10] S. Gordon, J. McBride, Thermodynamic Data to 20,000 K For Monatomic Gases, Tech. Rep. 1999-208523, NASA (1999).

[11] J. H. Ferziger, H. G. Kaper, E. P. Gross, Mathematical Theory of Transport Processes in Gases, American Journal of Physics 41 (4) (1973) 601–603. doi:10.1119/1.1987312.

[12] T. E. Magin, G. Degrez, Transport algorithms for partially ionized and unmagnetized plasmas, Journal of Computational Physics 198 (2) (2004) 424–449. doi:10.1016/j.jcp.2004.01.012.

[13] A. Munafò, T. E. Magin, Modeling of stagnation-line nonequilibrium flows by means of quantum based collisional models, Physics of Fluids 26 (9) (2014) 097102. doi:10.1063/1.4894842.

[14] S. Marelli, B. Sudret, UQLab: A Framework for Uncertainty Quantification in Matlab, in: Vulnerability, Uncertainty, and Risk, American Society of Civil Engineers, 2014, pp. 2554–2563. doi:10.1061/9780784413609.257.

Assessment of curvature filtering strategies for high-order sharp interface simulation of surface tension driven flows

David Henneaux

Aeronautics and Aerospace Department, von Karman Institute for Fluid Dynamics, Belgium, david.henneaux@vki.ac.be

Supervisor: Thierry Magin

Professor, Aeronautics and Aerospace Department, von Karman Institute for Fluid Dynamics, Belgium, thierry.magin@vki.ac.be

University Supervisor: Philippe Chatelain

Professor, Institute of Mechanical, Materials and Civil Engineering, UCLouvain, Belgium, philippe.chatelain@uclouvain.be

Abstract

In this work, we implement several state-of-the-art curvature filtering techniques inside a common high-order discontinuous Galerkin finite element based numerical framework. We conduct an extensive study by considering all the possible combinations in the curvature computation procedure. This allows us to extract the optimal parameters that are expected to minimize instabilities and parasitic current apparition in surface tension driven flows.

Keywords: surface tension, curvature filtering, sharp interface, discontinuous Galerkin

1. Introduction

Because of the imbalance of intermolecular attractive forces that appear at the interface between a liquid and another medium, a resulting localised surface force is present. This force can act both normal and tangential to a fluid interface and is responsible for the phenomenon known as surface tension. Surface tension plays a crucial role in immiscible multiphase flows. It has a determinant effect on interfacial stability, droplet coalescence and break up, surfactant behavior and wetting. Those effects, confined at the interface, can also have a profound impact on the dynamic behavior of the flow in the bulk of each fluid, even when the interface region is small compared to the whole flow. Predicting how surface tension influences the dynamic of a multifluid system is therefore very important for many practical applications in different fields. When it comes to the modeling of surface tension, a momentum balance across the interface is performed from which it can be extracted that the stresses from the bulk acting on the interface are balanced by a pressure force depending on the surface tension coefficient and the interface curvature (neglecting Marangoni effects, this is developed in section 2). The way of accurately incorporating this force into a numerical framework has been the topic of extensive research over the past decades (see e.g. the review of [1]). Three main challenges make this task particularly delicate: (i) the surface tension force is a singular force acting on an interface, (ii) this interface is most of the time moving and can exhibit complex shapes, (iii) the direct computation of the interface curvature often leads to inaccurate estimations affecting the accuracy, stability and robustness of the global method. This work deals with the third challenge which can be addressed in various ways that depend on the type of discretization, the method to treat the singular interface force and the approach selected for interface motion. As we are interested by sharp interface high-order FE-based methods relying on a level-set interface-capturing method, we shall focus the review of the available methods on this category of approaches. Before reviewing them, it is worth explaining the reason why a straightforward computation of the interface curvature is problematic. In high-order FE-based methods employing an implicit interface representation, the interface is approximated by

a high-order polynomial. Contrary to standard low-order method that require a stencil of several neighbhouring elements to be able to reach sufficient accuracy, the curvature in a given cell could in theory be directly computed anywhere in the cell (in particular at the interface) from the level-set interpolant derivatives. However, this will certainly produce an inaccurate and oscillatory curvature field which will in turn generate pressure oscillations inducing spurious currents. The root cause of this issue is that the higher the polynomial order, the higher the frequencies contained in the level-set interpolant (for the most general case in which the interface shape can not be exactly represented by a polynomial). The non-linear combination of the level-set function derivatives to assemble the curvature will magnify the high-order modes contained in the level-set signal and result in a noisy and inaccurate curvature field [2; 3; 4]. [1] Two solutions are then possible. The first one is to avoid having to compute the curvature. This can be achieved invoking a theorem from differential geometry linking the product of the interface curvature and normal with the Laplacian of the identify mapping on the interface. After integration by parts, the original term modeling surface tension forces and involving the curvature is replaced by two terms where the curvature is absent. This Laplace-Beltrami formulation has been followed for FEM in [5; 6; 7] and for discontinous Galerkin (DG) method in [8]. Another interesting approach is to augment the traditional level-set advection equation with an additional equation to explicitly track the interface curvature, thus avoiding the need to compute level-set derivatives [9]. The second solution is to apply some sort of filtering during the computation of the curvature from the level-set equation with the aim of damping the high-order modes when evaluating the derivatives. This can be carried out by different means. A least squares method is proposed in[2] to reconstruct the level-set gradients. For each computational node, the level-set is assumed to behave linearly or quadratically over the adjacent elements. This allows to evaluate the level-set at the center of gravity of those elements and build an overdetermined system for the unknown level-set gradient and Hessian at the considered node. The system is finally solved in a least-squares sense. The curvature approximation is shown to be of second order. In [10], the $P_N P_M$-reconstruction proposed in [11] is followed to reconstruct the level-set polynomial. Starting from a function defined over a given element, the idea is to consider a stencil of neighbouring elements and perform a L_2-projection of an unknown function belonging to a higher order polynomial space on each of the elements in the stencil. This results in an overdetermined system for the unknown reconstructed nodal degrees of freedom. The approach is therefore related to the first one except that instead of a nodal projection, a more accurate L_2-projection is considered. In the same vein, the patch-recovery operator was presented in [3]. It can easily be applied at any level of the process of curvature computation (i.e. on the level-set, on the gradients of the level-set and/or on the final curvature field). It shares some similarities with the $P_N P_M$-reconstruction with the main difference that the L_2-projection is here considered on a composite cell composed by all the adjacent elements on which a smoothly extended polynomial space is defined, rather than on each element separately. There is therefore no need to solve an overdetermined system if the new function space is chosen to be of higher order than the original one. In [4], a similar patch-recovery operator is used and is combined with a partition of unity method. For each element, the best polynomial, in the sense of the L_2 norm, is found matching the original function in the neighbourhood of this element. In a second step, those polynomials which can now be evaluated outside of their original element, are linearly combined with weight functions with compact support in order to obtain a C^∞ smooth function. Thus this procedure involves two steps of smoothing. What those four methods have in common is the way they filter out the small amplitude high frequency modes contained in the level-set by combining neighbouring element information. This is effective because those modes tend to be uncorrelated on adjacent elements and the combination between the elements will favor the accuracy of low-order modes, as explained in [4]. Finally, a last possible approach, employed by [12] and [13], is to solve a diffusion equation for the level-set or curvature, hence introducing some artificial viscosity on the original fields to reduce the spurious peaks in the fields.

The present study is the continuation of the work started by [14]. In order to situate our framework among the numerous available approaches reviewed above, here are the main features of the methods we are using:

- The imposition of the singular surface forces is

[1] It should be remarked here that this problem is expected both for continuous and discontinuous FE approximation. It is therefore not the discontinuous character of the approximation that is the primary cause of the oscillatory curvature, as noted by [2].

done in a sharp manner with the extended discontinuous Galerkin (XDG) method [15; 16]. This method provides a discontinuous high-order enforcement of the balance equations at the interface, thus approximating the effects of surface tension forces with high-fidelity.

- The interface is implicitly represented by a level-set field discretized with a high-order discontinuous Galerkin method combined with high-order reinitialization and velocity extension procedures [17]. The accuracy with which the interface is approximated is therefore consistent with the one of the flow variables.

- The surface tension forces are computed by assembling the curvature from the level-set field. Because of the compressible models considered, the Laplace-Beltrami reformulation of the surface tension forces mentioned earlier does not seem appropriate since the pressure jump induced by the surface tension must be incorporated inside a multiphase Riemann solver.

Based on these features, the purpose of our work is to compare several methodologies designed for accurate curvature estimation and assess their ability to provide robust and stable surface tension computations. Our work is in line with previous analyses comparing different approaches such as [18; 19]. The novelty lies in the fact that we are scrutinizing here state-of-the-art approaches tailored to high-order methods, namely the patch-recovery, partition of unity and artificial viscosity methods. Those filtering strategies are benchmarked based on reference static test cases. To the authors best knowledge, this is the first time that such comparison inside a unique computational framework is conducted, even more so in the context of a high-order two-phase flow solver. From a broader perspective, this paper intends to extract some general guidelines about the estimation of interface curvature for surface tension computation based on sharp interface FE type methods. To this end, we establish a general flow chart composed of decisive steps in the curvature estimation process, in addition to the choice of the filtering strategy: the projection or not of the level-set function on a continuous polynomial space, the use of discrete or lifted derivatives, the interpolation and assembly of the curvature on the interface, and the choice between the Bonnet's formula and the divergence of the normal.

This paper is structured as follows. The physical models, with an emphasis on how the surface tension effects appear in the equations, are first presented in section 2. Section 3 is devoted to the description of the different implemented filtering methods, the associated important steps in the curvature assembly and the global procedure flow chart. The various strategies are then compared on some reference test cases in section 4. Section 5 closes this paper by summarizing its main findings and mentioning some perspectives.

2. Jump conditions and the role of interface curvature

The use of a sharp interface method in this work leads to a so-called local instance formulation requiring the resolution of some jump conditions at the interface, Γ. These conditions specify the exchanges of mass, momentum, and energy through the interface and stand as matching conditions between the two phases. They can be derived by writing the balance laws in a control volume around the interface moving with the interface velocity $\mathbf{v}_\Gamma$. Neglecting interface density, molecular diffusion fluxes contributions to the interface fluxes and interface sources, they can be written under the following generic form [20; 21]:

$$-v_{n,\Gamma}[\![\mathbf{u}]\!]+[\![\underline{\boldsymbol{F}}^c(\mathbf{u})-\underline{\boldsymbol{F}}^d(\mathbf{u},\nabla\mathbf{u})]\!]\cdot\mathbf{n}_\Gamma = \nabla_{s,\Gamma}\cdot\underline{\boldsymbol{F}}_\Gamma\,, \quad \text{on} \quad \Gamma \tag{1}$$

where $v_{n,\Gamma} = \mathbf{v}_\Gamma \cdot \mathbf{n}_\Gamma$ is the normal interface velocity with the unit normal vector $\mathbf{n}_\Gamma$, $\mathbf{u}$ is the set of conservative flow variables, $\underline{\boldsymbol{F}}^c(\mathbf{u})$ are the convective fluxes and $\underline{\boldsymbol{F}}^d(\mathbf{u},\nabla\mathbf{u})$ the diffusive fluxes. The jump operator across the interface Γ at a position $\mathbf{x} \in \Gamma$ for some quantity η defined in the bulk of each phase is given by

$$[\![\eta]\!] = (\eta_{1|_\Gamma} - \eta_{2|_\Gamma})\,, \quad \text{with} \quad \eta_{k|_\Gamma} = \lim_{\epsilon\to 0,\epsilon>0} \eta(\mathbf{x}\pm\epsilon\mathbf{n}_\Gamma)\,, \tag{2}$$

where the adequate sign is related to the phase considered according to the determined orientation of the normal. On the right-hand side of Eq. (1), $\underline{\boldsymbol{F}}_\Gamma$ is the line flux along the interface and the surface divergence operator is defined as:

$$\nabla_{s,\Gamma} = \nabla - \mathbf{n}_\Gamma(\mathbf{n}_\Gamma\cdot\nabla)\,.$$

Focusing on the momentum flux contribution $\underline{\boldsymbol{F}}^{\text{mom}}_\Gamma$, the surface stress tensor can be decomposed into an isotropic and a deviatoric part such that $\underline{\boldsymbol{F}}^{\text{mom}}_\Gamma = \underline{\boldsymbol{F}}^{\text{mom}}_{\Gamma,\text{iso}} + \underline{\boldsymbol{F}}^{\text{mom}}_{\Gamma,\text{dev}}$. In case the system considered does not present a high surface area to volume ratios and that only surface tension effects are taken into account, the dominant interfacial momentum flux is due to the

isotropic part [22, Ch. 1.2]. This part is commonly modeled as $\underline{\boldsymbol{F}}^{\text{mom}}_{\Gamma,\text{iso}} = \sigma(\underline{\boldsymbol{I}} - \mathbf{n}_\Gamma \mathbf{n}_\Gamma^T)$, where σ is the surface tension coefficient [23]. Applying the surface divergence operator to this momentum contribution, the interface curvature κ appears:

$$\nabla_{s,\Gamma} \cdot \underline{\boldsymbol{F}}^{\text{mom}}_{\Gamma} \approx \nabla_{s,\Gamma} \cdot \underline{\boldsymbol{F}}^{\text{mom}}_{\Gamma,\text{iso}} = -\sigma\,\kappa\,\mathbf{n}_\Gamma + \nabla_{s,\Gamma}\sigma\,. \quad (3)$$

The first term gives the normal component force due to the effect of the curved interface whereas the second term represents the tangential force due to surface tension gradient, also known as Marangoni effects, which is not considered in this paper. Thus the imposition of the surface tension forces into the jumps requires the computation of the interface normal and curvature.

3. Numerical strategies for curvature computation

3.1. Global flow chart

As introduced in section 1, the strategies we propose to explore to compute the interface curvature depend on several elements. Those elements determine different paths along the curvature estimation process which is itself composed of several steps. This is illustrated by the flow chart in figure 1, the items of which are described here:

- *Level-set Type*: the discretized level-set field, noted φ, is in general discontinuous across element edges. However, to assemble the XDG variational formulation, a C^0 level-set field is required. To impose the continuity between the elements, an averaging of the nodal values located on the edges is performed. Two level-set fields are then manipulated, the *discontinuous* field φ_{br} which is advected, and the *continuous* one which is provided to the XDG method. At the beginning of the curvature computation process, we can select which level-set field is used, by taking *Cont = None* for the original one, and *Cont = FaceAverage* for the continuous one.

- *Curvature Formula*: the curvature can be obtained by either taking the *divergence of the normal* field,

$$\kappa = -\nabla \cdot \mathbf{n}_\Gamma\,, \quad (4)$$

or by using the so-called *Bonnet*'s formula,

$$\kappa = \frac{\nabla\varphi \cdot \mathrm{H}(\varphi)\nabla\varphi - \|\nabla\varphi\|_2^2\,\mathrm{tr}(\mathrm{H}(\varphi))}{\|\nabla\varphi\|_2^3}\,, \quad (5)$$

where $\mathrm{H}(\varphi)$ is the Hessian matrix of the level-set function and $\mathrm{tr}(\mathrm{H}(\varphi))$ its trace (i.e. the Laplacian). The unit normal vector is computed from the gradient of the level-set,

$$\mathbf{n}_\Gamma = \frac{\nabla\varphi}{\|\nabla\varphi\|_2}\,. \quad (6)$$

Although strictly equivalent for exact continuous function, equations (4) and (5) become different when the level-set field is a function belonging to a discrete functional space. This is the reason why the two formulae are considered here. Note that to apply equation (4), the normal field first need to be assembled with equation (6), which corresponds to the upper branch on the flow chart. For equation (5), both the gradient and the Hessian matrix of the level-set function need to be computed.

- *Derivatives Choice*: in DG methods, a discretized function f is part of a discontinous polynomial space, i.e. that the restriction of the function to each element Ω_m, noted $f|_{\Omega_m}$, belongs to a function space of a given order defined on a reference parametric element. There is no continuity constraint across the element edges. Similarly, the *broken* gradient, noted ∇_{br}, is obtained as the cellwise differentiation of the function:

$$(\nabla_{\text{br}} f)|_{\Omega_m} := \nabla\left(f|_{\Omega_m}\right) \quad \forall\,\Omega_m. \quad (7)$$

This way of computing the derivatives can also be applied to the divergence and Hessian operators. In order to take into account inter-element jumps during derivatives computation, the *lifted* approach can be followed. In this case, the gradient of a function, noted ∇_{DG}, is obtained by:

$$\int_{\Omega_m} (\nabla_{\text{DG}} f)\, w\,\mathrm{d}V = -\int_{\Omega_m} f\,\nabla w\,\mathrm{d}V + \int_{\partial\Omega_m} \{\!\{f\}\!\}\, w\,\mathbf{n}_{\partial\Omega_m}\,\mathrm{d}S \quad \forall\,\Omega_m\,, \quad (8)$$

where $\{\!\{f\}\!\}$ is the average of the traces of f coming from both sides of the edges $\partial\Omega_m$. When applied to the continuous level-set field, equations (7) and (8) produce the same result. But for the gradient of the discontinous level-set field, the divergence of the normal and the Hessian of the level-set, these two ways of evaluating the derivatives will lead to different results.

- *Interpolation on level-set iso-0*: after assembling the curvature field on the nodal degrees of freedom (based on the divergence of the normal or the Bonnet's formula, using broken or lifted derivatives), it must be interpolated to the level-set iso-0. Indeed, to evaluate the interface integrals of the XDG formulation, the curvature is required at every quadrature point located on the interface. The position of the interface is at this stage represented by the zero iso-contour of the continuous level-set field. A specificity of the Bonnet's formula is that we have the choice between assembling the curvature on the nodal degrees of freedom before doing the interpolation on the interface (*Bonnet IP*) and assembling it directly on the interface by interpolating the level-set gradient and Hessian on the iso-0 instead (*Bonnet Iso0*). This second path corresponds to the four arrows in the lower right part of the flow chart. To perform this interpolation, the *classical* approach using the cellwize shape functions is the first possibility. The second one is to involve neighbouring elements information via a *partition of unity* evaluation such that the curvature is continuous across the element edges along the level-set iso-0.

- *Filtering Procedure*: finally, in order to reduce the spurious oscillations in the curvature field, several filtering techniques are available (*Filt* on the figure): *artificial viscosity*, *patch-recovery*, *partition of unity*, *patch-recovery followed by partition of unity*. Those can be applied to the level-set field, the normal field (in case the curvature is obtained via the divergence of the normal), the level-set gradient and Hessian (in case the Bonnet's formula is chosen) or the curvature field itself. The filtering methods are described in section 3.2.

3.2. Filtering methods

Artificial viscosity. The first approach is a PDE-based filter that has been used in [12; 13; 24]. From an input function α, the filter solves the diffusive equation with Neumann boundary equation for the filtered function $\tilde{\alpha}$:

$$\begin{cases} \tilde{\alpha} - \epsilon\Delta\tilde{\alpha} = \alpha & \text{in } \Omega\,, \\ \frac{\partial\tilde{\alpha}}{\partial n} = 0 & \text{on } \partial\Omega\,, \end{cases} \tag{9}$$

where the artificial viscosity coefficient ϵ scales with the square of the local mesh size h through a user-defined parameter ϵ_0: $\epsilon = \epsilon_0 h^2$. Equation (9) can be undestood as a low-pass filter with the artificial viscosity being related to the inverse of the spatial cut-off frequency. It has the property to preserve the signal mean while reducing its energy in the sense that $\int_\Omega \tilde{\alpha}\,\mathrm{d}V = \int_\Omega \alpha\,\mathrm{d}V$ while $\int_\Omega \tilde{\alpha}^2\,\mathrm{d}V \leq \int_\Omega \alpha^2\,\mathrm{d}V$. Equation (9) is discretized by means of the Symmetric Interior Penalty (SIP) DG method (see e.g. the textbook of [25]). The constant matrices resulting from the discretization are assembled once at the beginning of the simulation and are then used to solve the linear system by LU-factorization at every time step.

Patch-recovery. Consider an element Ω_i, and denote by $\boldsymbol{\phi}_i(\mathbf{x})$ the column vector of its shape functions such that the function to filter α writes $\alpha_i(\mathbf{x}) = \mathbf{A}_i\boldsymbol{\phi}_i(\mathbf{x})$ with $\mathbf{A}_i$ the row vector containing its nodal degrees of freedom. Associated with each of the elements Ω_i, we build a patch of vertex-based neighbouring elements $\Omega_i^{\text{patch}} = \{\Omega_{i,1}^{\text{patch}}, \ldots, \Omega_{i,j}^{\text{patch}}, \ldots, \Omega_{i,N_i}^{\text{patch}}\}$ containing N_i elements with the first one being the element Ω_i itself, i.e. $\Omega_{i,1}^{\text{patch}} = \Omega_i$. The patch-recovery technique of [3] consists in computing for each Ω_i the projection of the restriction of α on Ω_i^{patch}, i.e. $\alpha|_{\Omega_i^{\text{patch}}}$, on a polynomial space defined on this patch. This new polynomial space is spanned by the shape functions $\boldsymbol{\phi}_i^{\text{patch}}$. Following the ideas of [4], weighting factors C_{i,Ω_j} giving more importance to the central element are introduced in the projection operator. In practice, we set $C_{i,\Omega_i} = 1.0$ and $C_{i,\Omega_j} = 0.5$ for neighbouring cells $\Omega_j \in \Omega_i^{\text{patch}} \setminus \{\Omega_i\}$. The L_2 projection then reads: for each Ω_i, find α_i^{patch} such that

$$\sum_{\Omega_j \in \Omega_i^{\text{patch}}} C_{i,\Omega_j} \int_{\Omega_j} (\alpha_i^{\text{patch}} - \alpha_j)\boldsymbol{\phi}_i^{\text{patch}}\,\mathrm{d}V = 0\,. \tag{10}$$

The filtered field $\tilde{\alpha}_i$ is then obtained by projecting the restriction of α_i^{patch} to Ω_i on the polynomial space spanned by $\boldsymbol{\phi}_i$. In practice, several sweeps of the patch-recovery procedure are performed. This implies that at the beginning of each new sweep, the functions α_j in equation (10) are replaced by the filtered functions computed from the previous sweep.

It should be noted that in this work, the degree of the polynomial space on which the projection is performed is chosen to be identical to the original polynomial space. As such, the construction of the patch-based shape functions $\boldsymbol{\phi}_i^{\text{patch}}$ is greatly simplified as it is done by extending the shape functions $\boldsymbol{\phi}_i$ to the neighbouring cells $\Omega_j \in \Omega_i^{\text{patch}}$. This extension is encompassed in a matrix-vector multiplication involving the local shape functions $\boldsymbol{\phi}_j$ on $\Omega_{i,j}^{\text{patch}}$ and a coupling

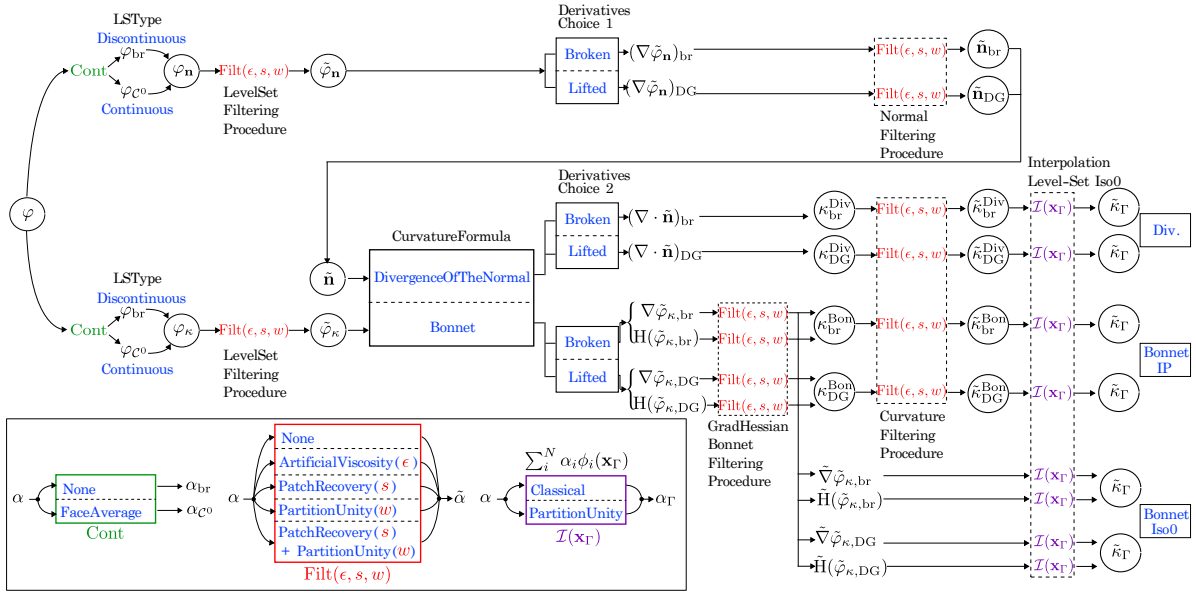

Figure 1: Flowchart showing the organization of the various elements involved in the curvature computation and filtering procedure

matrix $\underline{\boldsymbol{Q}}_{i,j}$ such that

$$\boldsymbol{\phi}_i^{\text{patch}}|_{\Omega_j} = \underline{\boldsymbol{Q}}_{i,j}\boldsymbol{\phi}_j \,. \tag{11}$$

The coupling matrix embodies the projection of the smooth shape function extension onto the considered element in the patch and its definition is taken from the work of [26]:

$$\begin{aligned} \underline{\boldsymbol{Q}}^*_{i,j} &= \int_{\Omega_j} \boldsymbol{\phi}_i^{\text{patch}}|_{\Omega_j}\, \boldsymbol{\phi}_j^T \,\mathrm{d}V \\ \underline{\boldsymbol{Q}}_{i,j} &= \underline{\boldsymbol{Q}}^*_{i,j}\underline{\boldsymbol{M}}_j^{-1} \,, \end{aligned} \tag{12}$$

with $\underline{\boldsymbol{M}}_j$ the local mass matrix of element Ω_j to which shape functions are extended. Notice that $\underline{\boldsymbol{Q}}_{i,i}$ is the identity matrix and therefore we have that

$$\tilde{\alpha}_i = \alpha_i^{\text{patch}}|_{\Omega_i} = \mathbf{A}_i^{\text{patch}}\boldsymbol{\phi}_i \,, \tag{13}$$

with $\mathbf{A}_i^{\text{patch}}$ the degrees of freedom of α_i^{patch} in basis $\boldsymbol{\phi}_i^{\text{patch}}$ which are obtained by solving (10).
It is convenient to manipulate $\underline{\boldsymbol{Q}}_{i,j}$ because they can be assembled in a pre-processing step and re-used during the simulation every time the extension over an adjacent element is required. In the same way, the other expensive steps that are the construction of the patches and the assembly of the inverse of the extended mass matrices and the matrices for the right-hand-side of equation (10) are performed only once at the beginning of the simulation.

Partition of unity. The last filter considered in this work relies on the concept of partition of unity and comes from the work of [4]. Consider the same neighbouring patch elements construction as for the patch-recovery technique. The filtered field $\tilde{\alpha}_i(\mathbf{x})$ at a position $\mathbf{x}$ located in element Ω_i is obtained by a normalized linear combination over the local patch between some weights functions $g_j(\mathbf{x})$ and the functions $\alpha_j^{\text{patch}}(\mathbf{x})$

$$\tilde{\alpha}_i(\mathbf{x}) = \frac{\sum_{\Omega_j\in\Omega_i^{\text{patch}}} g_j(\mathbf{x})\alpha_j^{\text{patch}}(\mathbf{x})}{\sum_{\Omega_j\in\Omega_i^{\text{patch}}} g_j(\mathbf{x})} \,, \tag{14}$$

where $\alpha_j^{\text{patch}}(\mathbf{x})$ are functions evaluated outside of their reference element $\Omega_j \in \Omega_i^{\text{patch}}$ thanks to a smooth extension of the local shape functions into Ω_i through the coupling matrices, equation (12). The weights functions are defined as

$$g_j(\mathbf{x}) = \omega((x - x_j^c)/r_j)\,\omega((y - y_j^c)/r_j) \,,$$

with r_j the radius of the largest ball that can fit inside the patch associated to element Ω_j centered at (x_j^c, y_j^c). The one-dimensional local bump function ω is defined as

$$\omega(\theta) = \begin{cases} \exp\left(C\frac{1}{\theta^2-1}\right) & \text{if } |\theta| < 1 \,, \\ 0 & \text{if } |\theta| \geq 1 \,, \end{cases}$$

where the constant C control the width of the function. Its value is fixed at $C = 32/9$ according to [4].

When the patch-recovery method is used in combination with the partition of unity approach, the nodal expansion weights of the functions evaluated over the patch, α_j^{patch}, are obtained through a patch-recovery procedure before being combined with their associated smoothly extended shape functions. Similarly to the patch-recovery, the neighbours search is done once when starting the simulation, as well as the computation of the inscribed balls.

As a closing remark for this section, we can notice that each of the three filtering approaches studied here depend on user-defined parameters which are not *a priori* obvious to set. The artificial viscosity requires a value for the viscosity coefficient, the patch-recovery depends on the number of sweeps applied, the choice of the neighbouring elements and the weighting factors over the patch, and the partition-of-unity is based on the expression of the bump function and its extent. This makes the design of a completely generic filtering strategy a challenging task.

4. Geometrical test cases for curvature accuracy and oscillations along the interface

Although surface tension computation is only relevant for unsteady test cases, we focus our attention in this work on steady test cases. As pointed out by [27], the accurate computation of surface tension forces is dictated by two main criteria about interface curvature[2]: (i) a fast convergence of the numerical curvature, (ii) minimized oscillations of the curvature along the interface. Because of the huge number of possible combinations the flowchart in figure 1 contains, the objective of this set of test cases is to extract the best features among all the possibilities based on the two identified criteria. We will then be able to proceed with unsteady test cases in future work by using the most promising combinations. To assess the first criterion, the L_2 and L_∞ errors on the elements cut by the interface, Ω_Γ, between the computed and the exact curvatures, κ^h and κ^{ex}, are considered:

$$E_{L_2} = \sqrt{\sum_{\Omega\in\Omega_\Gamma}\int_\Omega (\kappa^h - \kappa^{\text{ex}})^2 \,\mathrm{d}V}\,, \tag{15}$$

$$E_{L_\infty} = \max_{\Omega\in\Omega_\Gamma} |\kappa^h_{\text{QP}} - \kappa^{\text{ex}}_{\text{QP}}|\,, \tag{16}$$

[2]The third criterion mentioned in [27] is related to the variation of the curvature along the interface normal direction, which is only important when a diffusive interface treatment is adopted.

where κ^h_{QP} and $\kappa^{\text{ex}}_{\text{QP}}$ are the values of the curvature evaluated at the quadrature points over the element. The order of convergence on the curvature field is then evaluated based on those two error measures. To evaluate the oscillations of the curvature along the interface, the L_2 measure is obtained by integrating the error along the interface while the L_∞ measure identifies the maximum error on the interface quadrature points:

$$E_{L_2,\Gamma} = \sqrt{\sum_{\Gamma\in\Omega_\Gamma}\int_\Gamma (\kappa^h - \kappa^{\text{ex}})^2 \,\mathrm{d}S}\,, \tag{17}$$

$$E_{L_\infty,\Gamma} = \max_{\Gamma\in\Omega_\Gamma} |\kappa^h_{\text{QP}} - \kappa^{\text{ex}}_{\text{QP}}|\,. \tag{18}$$

The two-dimensional geometries that are selected are a circular and a starfish-shaped droplet defined respectively by

$$\varphi_{\text{drop}} \equiv \sqrt{(x^2+y^2)} = 0.2\,,$$

$$\varphi_{\text{star}} \equiv \sqrt{(x^2+y^2)} - 0.02\sin(5.0\,\text{atan2}(y,x)) = 0.25\,,$$

The analytical expression of the curvature for the starfish-shaped droplet is obtained via symbolic computation using the *Sympy* package. We took inspiration from the exhaustive study conducted in [3] by considering all the possible combinations of the flowchart. More precisely, on a given mesh for a given polynomial order, we run 1200 simulations for the cases where the curvature is obtained from the divergence of the normal (*Div.*), 600 simulations for the Bonnet's formula applied to the interpolation points before interpolation on the iso-0 (*Bonnet IP*) and 120 simulations for the Bonnet's formula directly assembled on the iso-0 from the level-set gradient and Hessian matrix (*Bonnet Iso0*), for a total of 1920 runs. The user-defined parameters of the various approaches are at this stage not varied and are fixed based on some preliminary investigations. The artificial viscosity on the the level-set field is set at $\epsilon_0 = 0.02$ while the one on the level-set derivatives and the curvature is chosen as $\epsilon_0 = 0.05$. The number of patch-recovery sweeps at every stage of the process is taken equal to 2. Let us note also that only two distinct filtering methods on the level-set are applied (contrary to four elsewhere), namely artificial viscosity and patch-recovery. We limit here the study to a single polynomial order $p = 3$ and compute the orders of convergence based on only two meshes, the finest one being the mesh for which the values of the errors are reported. Both geometries are considered in a square domain $[-0.5, 0.5]^2$ discretized by a Cartesian

grid. The grids for the droplet test case are 16×16 and 32×32 while for the starfish test case, grids of 32×32 and 64×64 elements are considered. The results are presented in figures 2, 3 and tables 1, 2. From a general point of view, it appears that:

- compared to the base case scenario, the filtering approaches reduce all the considered errors by one to several orders of magnitude (note the logarithmic scaling in figures 2, 3).
- while the convergence rates for the curvature in terms of the L_2 and L_∞ norms for the base case scenario are in line with the theoretical $p-1$ values, the ones for the filtered situations are significantly increased.
- not surprisingly, the use of filtering techniques increases the CPU time. This must be nuanced by the fact that we only perform the initialization step of the solver here, which involves all the most computational expensive operations related to the filtering methods.

The results also allow to draw up a first list of conclusions regarding the choice of the various methods and parameters in the global flowchart:

- *Curvature formula*: we separate the curvature formula in three approaches for the analysis (see figure 1). For the circle geometry, the divergence of the normal seems to perform globally as good or even slightly better than the Bonnet's formula applied to the interpolation points. For the starfish shape, both approaches based on Bonnet's formula outperform the divergence of the normal. This would require further investigations but it is anticipated that for general complex geometries, the use of Bonnet's formula is more accurate because it involves one less interpolation step.
- *Level-set Type*: the use of the *continuous* or *discontinuous* level-set field to start the process does not have an appreciable effect on the efficiency of the strategies. Since the continuity enforcement is realized though a simple face averaging and that the interface shape is pretty well approximated by the third order polynomial we use here, the deviation between the two level-set fields is only minor.
- *Derivatives choice*: the choice of the lifted derivatives clearly offers the most effective filtering. This looks consistent since taking into account the inter-elements jumps and ensuring a global coupling of the derivatives calculations should favor the stability of the scheme.
- *Fields to filter*: it is manifest that the level-set field itself should not be filtered, or at least not with the parameters and the methods considered here. This indeed perturbs too much the interface shape and leads to inaccurate curvature estimations. For the divergence of the normal, it looks like no filtering on the normal field is required. It turns out that filtering should be applied on the level-set gradients and Hessian matrix (for Bonnet's formula) and/or on the final curvature field (for Bonnet's formula on IP and divergence of the normal). Bonnet's formula on IP, applying two successive filters (possibly different) on the gradient and Hessian and then on the curvature looks promising. Those observations seem to be in contradiction with the ones in [3] in which is it advocated to only filter the level-set field. This could be explained by the different parameters selected and also by the fact that they projected their level-set field on a higher-order polynomial space before starting the process. When they used a continuous level-set belonging to the original space, they found that filtering the gradient and Hessian of the level-set was optimal.
- *Filtering methods*: the most effective filtering technique among the four considered appears to be the succession of the patch-recovery and partition of unity filters. As already suggested by [4], those two techniques provide two complementary filtering effects. It must be highlighted that the artificial viscosity filter, which is barely present here, could potentially be as successful as the others by choosing the optimal viscosity coefficient (which is not *a priori* obvious).
- *Interpolation on level-set iso-0*: interestingly, common to the different curvature formula, is the benefit of applying a last filtering step through the partition of unity technique during the interpolation from the interpolation points to the quadrature points located on the iso-0.

5. Conclusion

The geometrical study presented in this work has demonstrated the ability of the filtering procedures to

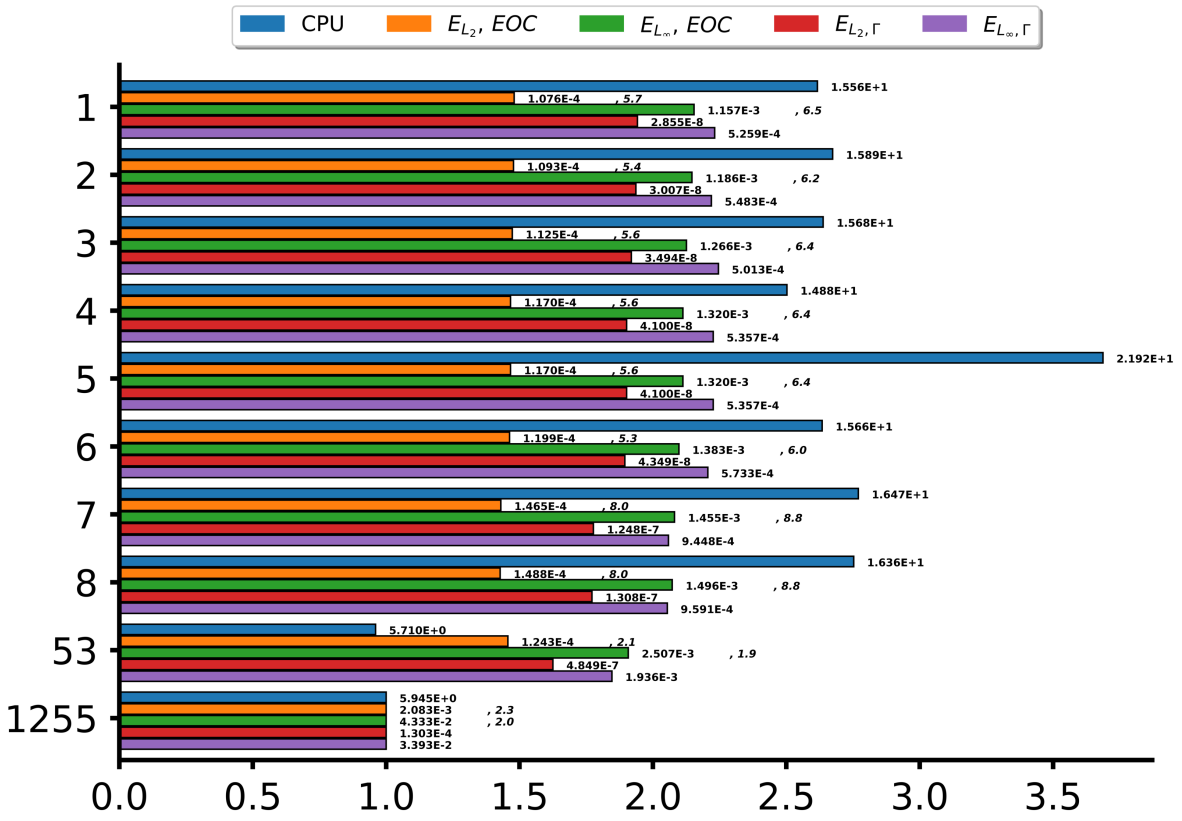

Figure 2: Results for φ_{drop} test case. See caption of figure 3.

	κ formula	LS type	Deriv. choice 1	Deriv. choice 2	Filt. LS	Filt. normal	Filt. grad-Hessian	Filt. curvature	Interp. iso-0
1	Div.	Discont.	Lifted	Lifted	None	None	N/A	PR+PU	PU
2	Bonnet IP	Discont.	N/A	Lifted	None	N/A	None	PR+PU	PU
3	Div.	Discont.	Broken	Lifted	None	None	N/A	PR+PU	PU
4	Div.	Cont.	Lifted	Lifted	None	None	N/A	PR+PU	PU
5	Div.	Cont.	Broken	Lifted	None	None	N/A	PR+PU	PU
6	Bonnet IP	Cont.	N/A	Lifted	None	N/A	None	PR+PU	PU
7	Bonnet IP	Discont.	N/A	Lifted	None	N/A	AV	PR+PU	PU
8	Bonnet IP	Cont.	N/A	Lifted	None	N/A	AV	PR+PU	PU
53	Bonnet Iso0	Cont.	N/A	Lifted	AV	N/A	AV	N/A	CL
1255	Bonnet IP	Cont.	N/A	Broken	None	N/A	None	None	CL

Table 1: The 8 best identified curvature computation combinations for φ_{drop} test case, based on figure 2. The 53th-combination is the best among the ones using the Bonnet formula on iso-0. The 1255th-combination is the reference one, i.e. without any filtering and broken derivatives. The columns name refer to figure 1. AV = Artificial Viscosity, PR = Patch-Recovery, PU = Partition of Unity, CL = classical.

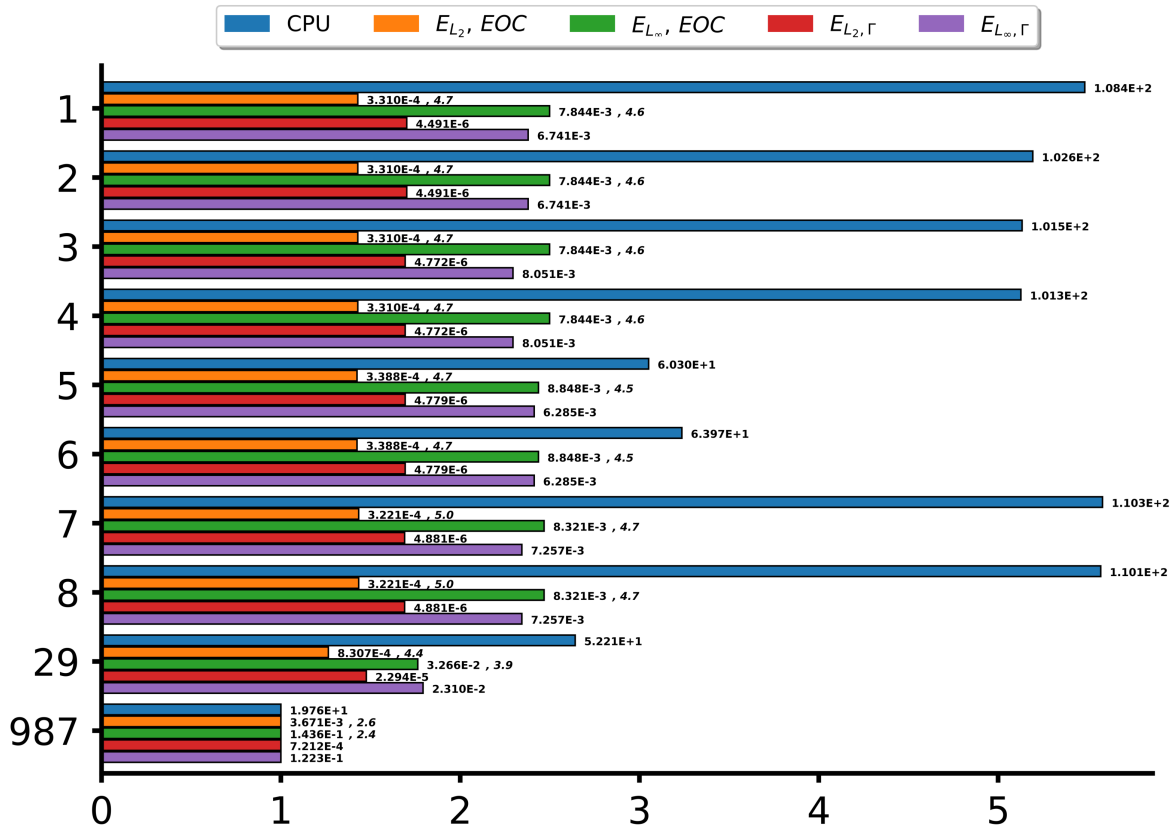

Figure 3: Results for φ_{star} test case. Bar chart presenting the results of the two geometrical curvature accuracy test cases. The five quantities gathered for each situation are the CPU time and the four error measures, eqs. (15, 16, 17, 18). The vertical axis lists the best curvature computation strategies in terms of the $E_{L_2,\Gamma}$ error (eq. (17)), with the labels being the rank of each strategy among the 1920 possible combinations. The last one on the bottom is the reference simulation used to plot the five quantities in a dimensionless form. The CPU time is simply divided by the reference one while the errors are scaled in a logarithmic way, i.e. $\overline{E} = \log_{10}(E)/\log_{10}(E_{\text{ref}})$. The horizontal axis labels are then the ratios between the best combinations quantities and the reference ones. The numbers on the right of each bar are the absolute dimensional values. The estimated order of convergence (EOC) for the two errors E_{L_2} and E_{L_∞} are written on the same line after the comma.

	κ formula	LS type	Deriv. choice 1	Deriv. choice 2	Filt. LS	Filt. normal	Filt. grad-Hessian	Filt. curvature	Interp. iso-0
1	Bonnet Iso0	Discont.	N/A	Lifted	None	N/A	PR+PU	N/A	PU
2	Bonnet Iso0	Cont.	N/A	Lifted	None	N/A	PR+PU	N/A	PU
3	Bonnet IP	Discont.	N/A	Lifted	None	N/A	PR+PU	None	PU
4	Bonnet IP	Cont.	N/A	Lifted	None	N/A	PR+PU	None	PU
5	Bonnet IP	Discont.	N/A	Lifted	None	N/A	PR	PU	PU
6	Bonnet IP	Cont.	N/A	Lifted	None	N/A	PR	PU	PU
7	Bonnet IP	Discont.	N/A	Lifted	None	N/A	PR+PU	PU	CL
8	Bonnet IP	Cont.	N/A	Lifted	None	N/A	PR+PU	PU	CL
29	Div.	Cont.	Lifted	Lifted	None	None	N/A	PR	PU
987	Bonnet IP	Cont.	N/A	Broken	None	N/A	None	None	CL

Table 2: Best identified curvature computation combinations for φ_{star} test case, based on figure 3. The 29th-combination is the best among the ones using the divergence of the normal formula. The 987th-combination is the reference one, i.e. without any filtering and broken derivatives. The columns name refer to figure 1. AV = Artificial Viscosity, PR = Patch-Recovery, PU = Partition of Unity, CL = classical.

substantially improve the curvature accuracy estimation and decrease its oscillations along the interface; two factors that are expected to play a crucial role in the simulation of surface-tension driven flows. It has also highlighted, among a huge set of parameters, the best options in the global procedure for the curvature computation and filtering. The results obtained lay the groundwork for applying the sharp interface solver to unsteady test cases. As perspectives, we can mention the need to vary the user-defined parameters associated to the filtering techniques, to perform a deeper convergence analysis on finer meshes, to evaluate the dependence on the mesh type by considering unstructured simplex meshes, and to conduct the same investigations on a few more complex geometries to build a more representative data set.

Acknowledgments

The first author is supported by the Fonds de la Recherche Scientifique (FNRS) of Belgium, under a FRIA grant. Computational resources have been provided by the supercomputing facilities of the Université catholique de Louvain (CISM UCL) and the Consortium des Equipements de Calcul Intensif en Fédération Wallonie Bruxelles (CECI) funded by the Fond de la Recherche Scientifique de Belgique (F.R.S.-FNRS) under convention 2.5020.11 and by the Walloon Region. The authors would like to acknowledge the contribution of Ward Haegeman who started this work during his VKI RM project (2021-2022) and who has since then continued to actively collaborate with the present authors.

References

[1] S. Popinet, Numerical models of surface tension, Annual Review of Fluid Mechanics 50 (2018) 49–75. doi:https://doi.org/10.1146/annurev-fluid-122316-045034.

[2] E. Marchandise, P. Geuzaine, N. Chevaugeon, J.-F. Remacle, A stabilized finite element method using a discontinuous level set approach for the computation of bubble dynamics, Journal of Computational Physics 225 (1) (2007) 949–974. doi:https://doi.org/10.1016/j.jcp.2007.01.005.

[3] F. Kummer, T. Warburton, Patch-recovery filters for curvature in discontinuous galerkin-based level-set methods, Communications in Computational Physics 19 (2) (2016) 329–353. doi:https://doi.org/10.4208/cicp.191114.140715a.

[4] R. Saye, Implicit mesh discontinuous galerkin methods and interfacial gauge methods for high-order accurate interface dynamics, with applications to surface tension dynamics, rigid body fluid–structure interaction, and free surface flow: Part ii, Journal of Computational Physics 344 (2017) 683–723. doi:https://doi.org/10.1016/j.jcp.2017.05.003.

[5] S. Hysing, A new implicit surface tension implementation for interfacial flows, International Journal for Numerical Methods in Fluids 51 (6) (2006) 659–672. doi:https://doi.org/10.1002/fld.1147.

[6] S. Gross, A. Reusken, Finite element discretization error analysis of a surface tension force in two-phase incompressible flows, SIAM journal on numerical analysis 45 (4) (2007) 1679–1700. doi:https://doi.org/10.1137/060667530.

[7] K.-W. Cheng, T.-P. Fries, Xfem with hanging nodes for two-phase incompressible flow, Computer Methods in Applied Mechanics and Engineering 245 (2012) 290–312. doi:https://doi.org/10.1016/j.cma.2012.07.011.

[8] M. Smuda, F. Kummer, On a marching level-set method for extended discontinuous galerkin methods for incompressible two-phase flows: Application to two-dimensional settings, International Journal for Numerical Methods in Engineering 123 (1) (2022) 197–225. doi:https://doi.org/10.1002/nme.6853.

[9] C. J. Vogl, A curvature-augmented, rea approach to the level set method, SIAM Journal on Scientific Computing 38 (2) (2016) A833–A855. doi:https://doi.org/10.1137/15M1021258.

[10] S. Fechter, C.-D. Munz, A discontinuous galerkin-based sharp-interface method to simulate three-dimensional compressible two-phase flow, International Journal for Numerical Methods in Fluids 78 (7) (2015) 413–435. doi:https://doi.org/10.1002/fld.4022.

[11] M. Dumbser, Arbitrary high order pnpm schemes on unstructured meshes for the compressible navier–stokes equations, Computers & Fluids 39 (1) (2010) 60–76. doi:https://doi.org/10.1016/j.compfluid.2009.07.003.

[12] A.-K. Tornberg, B. Engquist, A finite element based level-set method for multiphase flow applications, Computing and Visualization in Science 3 (1-2) (2000) 93–101. doi:https://doi.org/10.1007/s007910050056.

[13] F. Heimann, An unfitted higher-order discontinuous galerkin method for incompressible two-phase flow with moving contact lines, Ph.D. thesis, Heidelberg University (2013).

[14] W. Haegeman, Implementation of a curvature reconstruction algorithm for a high-order and sharp interface multiphase flow solver, vKI Research Master thesis report (2022).

[15] F. Kummer, Extended discontinuous galerkin methods for two-phase flows: the spatial discretization, International Journal for Numerical Methods in Engineering 109 (2) (2017) 259–289. doi:https://doi.org/10.1002/nme.5288.

[16] D. Henneaux, P. Schrooyen, P. Chatelain, T. Magin, High-order enforcement of jumps conditions between compressible viscous phases: an extended interior penalty discontinuous galerkin sharp interface solver, preprint at ... (2023).

[17] D. Henneaux, P. Schrooyen, L. Arbaoui, P. Chatelain, T. E. Magin, A high-order level-set method coupled with an extended discontinuous galerkin method for simulating moving interface problems, in: AIAA AVIATION 2021 FORUM, 2021, p. 2742. doi:https://doi.org/10.2514/6.2021-2742.

[18] H. Marschall, S. Boden, C. Lehrenfeld, U. Hampel, A. Reusken, M. Wörner, D. Bothe, et al., Validation of interface capturing and tracking techniques with different surface tension treatments against a taylor bubble benchmark problem, Computers & Fluids 102 (2014) 336–352. doi:https://doi.org/10.1016/j.compfluid.2014.06.030.

[19] T. Abadie, J. Aubin, D. Legendre, On the combined effects of surface tension force calculation and interface advection on spurious currents within volume of fluid and level set frameworks, Journal of Computational Physics 297 (2015) 611–636. doi:https://doi.org/10.1016/j.jcp.2015.04.054.

[20] J.-M. Delhaye, Jump conditions and entropy sources in two-phase systems. local instant formulation, International Journal of Multiphase Flow 1 (3) (1974) 395–409. doi:https://doi.org/10.1016/0301-9322(74)90012-3.
[21] W. Dreyer, On jump conditions at phase boundaries for ordered and disordered phases, wIAS preprint (2003).
[22] M. Ishii, T. Hibiki, Thermo-fluid dynamics of two-phase flow, Springer Science & Business Media, 2010.
[23] A. Reusken, X. Xu, L. Zhang, Finite element methods for a class of continuum models for immiscible flows with moving contact lines, International Journal for Numerical Methods in Fluids 84 (5) (2017) 268–291. doi:https://doi.org/10.1002/fld.4349.
[24] M. R. Hashemi, P. B. Ryzhakov, R. Rossi, An enriched finite element/level-set method for simulating two-phase incompressible fluid flows with surface tension, Computer Methods in Applied Mechanics and Engineering 370 (2020) 113277. doi:https://doi.org/10.1016/j.cma.2020.113277.
[25] D. A. Di Pietro, A. Ern, Mathematical aspects of discontinuous Galerkin methods, Vol. 69, Springer Science & Business Media, 2011.
[26] B. Müller, S. Krämer-Eis, F. Kummer, M. Oberlack, A high-order discontinuous galerkin method for compressible flows with immersed boundaries, International Journal for Numerical Methods in Engineering 110 (1) (2017) 3–30. doi:https://doi.org/10.1002/nme.5343.
[27] M. Coquerelle, S. Glockner, A fourth-order accurate curvature computation in a level set framework for two-phase flows subjected to surface tension forces, Journal of Computational Physics 305 (2016) 838–876. doi:https://doi.org/10.1016/j.jcp.2015.11.014.

Experimental measurements of radio signal attenuation and Faraday rotation in an inductively coupled plasma facility

Diana Luís

Aeronautics and Aerospace Department, von Karman Institute for Fluid Dynamics, Belgium, diana.luis@vki.ac.be
Signal Theory and Communication Department, Universitat Politècnica de Catalunya, Spain

Alan Viladegut

Research Engineer, Aeronautics and Aerospace Department, von Karman Institute for Fluid Dynamics, Belgium, alan.viladegut@vki.ac.be

Adriano Camps

Professor, Signal Theory and Communication Department, Universitat Politècnica de Catalunya, Spain, adriano.jose.camps@upc.edu
Researcher, Institut d'Estudis Espacials de Catalunya, Universitat Politecnica de Catalunya, Spain
Professor, College of Engineering, UAE University, United Arab Emirates

Olivier Chazot

Professor, Aeronautics and Aerospace Department, von Karman Institute for Fluid Dynamics, Belgium, chazot@vki.ac.be

Abstract

Spacecraft entering a planetary atmosphere are surrounded by a plasma layer containing high levels of ionization. The high electron number densities cause attenuation and rotation of the emitted signal, leading to communication blackout. This work presents experimental measurements of radio signal attenuation and Faraday rotation due to an ionized plasma flow. These measurements are conducted at the VKI Plasmatron using circularly polarized directive horn lens antennas with a waveguide orthomode transducer. Clear attenuations are observed when the signal is propagating through the plasma, and Faraday rotation measurements show a good agreement with the theoretical estimation.

Keywords: Plasma flow, inductively coupled plasma wind tunnel, communication blackout, radio signal attenuation, Faraday rotation

1. Introduction

Spacecraft enter planetary atmospheres at hypersonic velocities generating shock waves ahead of the vehicle and consequent extreme aerodynamic heating. The high post-shock temperatures dissociate and ionize the atmospheric gases creating a plasma layer that surrounds the spacecraft. High ionization degrees affect the propagation of the electromagnetic waves emitted by the on-board communication antennas, causing attenuation and refraction of the radio waves. Extreme ionization levels lead, ultimately, to communications blackout. Figure 1 shows a schematic representation of this phenomenon. The radio communication blackout in an un-magnetized plasma occurs when the characteristic frequency of the plasma layer around the vehicle exceeds the radio frequency used for communications. The ionization degree of the gas defines the plasma frequency, f_p [Hz], which is related to the electron number density, n_e [m^{-3}], as

$$f_p = \frac{1}{2\pi}\sqrt{\frac{q_e^2 n_e}{m_e \epsilon_0}} \approx 9\sqrt{n_e} \tag{1}$$

where q_e and m_e are, respectively, the electron charge and mass, and ϵ_0 the free space permittivity. Radio blackout typically lasts several minutes, depending on the trajectory and altitude of the vehicle, the properties of the atmosphere [1] and the frequency of the emitting antenna.

From the beginning of space exploration, different methodologies for actively reducing the plasma

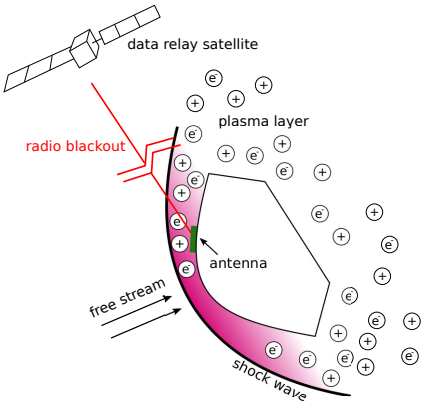

Figure 1: Schematic of the blackout phenomenon during reentry.

layer effects on radio communication attenuation and blackout have been proposed and studied. The most promising areas of research are high-frequency transmission, creation of a magnetic field, aerodynamic shaping effects [2], electrophilic injection [3], and Raman scattering [4]. During the 1960s, NASA's radio attenuation measurement program [5] was conducted to develop diagnostics to characterize the reentry plasma parameters and to begin in-flight testing of some mitigation methods. Those studies confirmed that the most feasible methods mainly contained electrophilic injection, and magnetic windows [6]. Nevertheless, no method has been successfully integrated into a spacecraft for regular flight.

Conversely to flight experiments, several experimental campaigns have been performed in ground facilities. Significant success at mitigating the blackout conditions have been observed using a Remote Antenna Assembly (RAA) in hypersonic wind tunnels for different Mach numbers [7]. A RAA is a small antenna assembly mounted on a pylon sticking out of the bow shock, i.e., outside the thick shock layer. The antennas generate as well a shock wave and are streamlined by plasma. Nevertheless, this study showed that acceptable ionization levels near the antennas can be achieved to allow communications. However, the RAA usually melted without the use of an active cooling system [8]. Savino et al. [9] conducted an experimental campaign in an arc jet plasma wind tunnel to reproduce the plasma frequency on ground and to numerically correlate it with the radio frequency signal loss. For that, they conducted a preliminary characterization of the plasma density and electron temperature using a Langmuir probe. This study demonstrated the capability of duplicating the ionization levels encountered during reentry, and the ability of arc jet facilities, integrated with proper numerical tools, to correctly deal with problems of communication attenuation and blackout. When testing the performance of a heat shield protecting the antenna, Bendoukha et al. [10] explored a new method of communication called end of radio silence using an arc heated facility. A transmitter was located behind the thermal shield and the receiver equipped with a wire antenna was installed in the vacuum chamber and outside the hot gas flow to receive radio signal during the transmissions. Luís et al. [11] studied signal propagation in an inductively coupled plasma wind tunnel using conical horn antennas in the Ka-band. Clear attenuation of the signal have been observed, ranging between 5 and 15 dB depending of the testing conditions. The evolution of the variation of the mean magnitude with power has been found to follow the inverse trend of numerical electron number densities. Preliminary evidence of Faraday rotation has also been stated, but not quantified. Additionally, they have observed clear ripples on the signal due to reflections on the chamber walls.

The Horizon 2020 MEESST (Magnetohydrodynamic Enhanced Entry System for Space Transportation) project aims at designing and testing a proof-of-concept magnetic shielding device to mitigate radio blackout and to reduce heat flux upon the surface of the spacecraft during atmospheric entry. Analytical work [12; 13] showed that the magnetic field required to allow the communication frequencies to penetrate the reentry plasma and the reduction of the heat flux must be very strong, of the order of 1 T [14]. This technique is denominated as magnetohydrodynamic (MHD) flow control. The reduction of the electron density to below the critical one allows to restore communications during reentry [15], by opening a window in the plasma layer through which radio waves can be transmitted [16]. As part of the project, this work presents the effects of an ionized medium on the propagation of the radio signal through an air plasma flow produced with the Inductively Coupled Plasma (ICP) generator in the VKI-Plasmatron facility. The characterization of the radio wave propagation and attenuation through the plasma is conducted resorting to directive horn lens antennas aligned perpendicularly to the flow. The experimental setup also allows to estimate the Faraday rotation caused by the flow.

2. Radio communication theory

2.1. Signal propagation in ionized mediums

The characteristics of electromagnetic wave propagation in the atmosphere depend strongly on the op-

erating frequency. The ionosphere has a major effect on the propagation at medium and high frequencies (0.3-30 MHz), because radio waves in this frequency range are effectively reflected. For frequencies above 30 MHz, the waves propagate through the atmosphere with small attenuation, allowing satellite and deep space communications. At frequencies above 10 GHz, atmospheric conditions play a major role in the signal propagation [17].

The ionosphere is a region of highly charged particles as an ionized gas or plasma. As such, the ionospheric propagation theory can be extended to plasma flow on ground facilities. The "reflections" from the ionosphere are produced by refraction as the wave propagates through this region. The refraction properties of a medium are characterized by the index of refraction n, which can be estimated using the Appleton-Hartree equation [18] derived from the Maxwell's equations and the momentum conservation of electrons as

$$n^2 = 1 - \frac{\left(\frac{f_p}{f}\right)^2}{1 - \frac{i\nu}{2\pi f} - \frac{\left(\frac{f_b}{f}\right)^2 \sin^2\theta}{2\left[1-\left(\frac{f_p}{f}\right)^2 - \frac{i\nu}{2\pi f}\right]} \pm \sqrt{\frac{\left(\frac{f_b}{f}\right)^4 \sin^4\theta}{4\left[1-\left(\frac{f_p}{f}\right)^2 - \frac{i\nu}{2\pi f}\right]^2} + \left(\frac{f_b}{f}\right)^2 \cos^2\theta}} \quad (2)$$

where f is the frequency of the signal, ν is the electron-heavy particle collision frequency, and θ is the angle between the magnetic field vector and the wave vector. The refractive index is dependent on the total electron number density n_e through the plasma natural frequency f_p as expressed in Eq. 1. The gyroscopic frequency of electrons f_b induced by the presence of a magnetic field B is defined as

$$f_b = \frac{1}{2\pi}\frac{q_e B}{m_e}. \quad (3)$$

Figure 2 represents the variation of the refractive index with the f_p/f ratio for a non-collision plasma and different f_b/f ratios. In this case, the refractive index is real, and the cutoff frequency is independent of θ. The presence of a magnetic field increases the cutoff frequency and allows the propagation of lower communication frequencies for the same plasma frequency.

The total electron content (TEC) accumulated along a transmission path penetrating the ionosphere causes the rotation of the wave polarization (Faraday rotation), time delay of the signal, and a change in the apparent direction of the arriving signal due to refraction. As the rotations and time delays are non-linearly

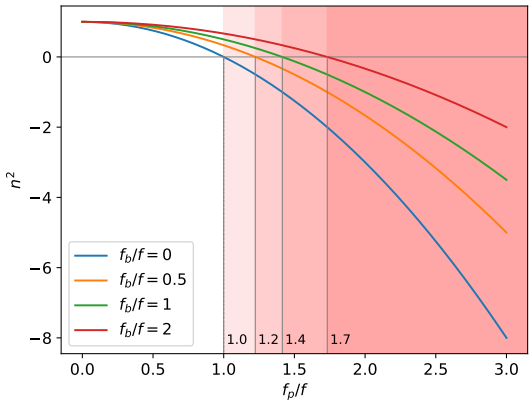

Figure 2: Refractive index for a non-collision magnetized plasma and $\theta = 0°$.

dependent on the frequency, a dispersion or group velocity distortion can also occur. The magnitude of the Faraday rotation, θ_F [rad], depends on the frequency of the radio wave, the magnetic field strength, and the electron density of the plasma as

$$\theta_F = 2.36 \times 10^4 \frac{B N_T}{f^2}, \quad (4)$$

where θ_F is the angle of rotation, B the strength of the magnetic field, f the frequency, and N_T the TEC [m^{-2}] expressed as

$$N_T = \int_S n_e(s) ds, \quad (5)$$

being s is the propagation path and n_e the electron number density.

2.2. *The scattering matrix: S-parameters*

For high frequencies, a network is represented by its scattering matrix. This S-matrix allows to describe the properties of a multi-port network by quantifying how electromagnetic energy propagates through the network. The scattering term refers to the relationship between incident and scattered (reflected and transmitted) voltage or electric field of travelling waves. The S-matrix for a N-port network contains N^2 complex coefficients (S-parameters), each one representing the magnitude and phase of a possible input-output path. The diagonal parameters are referred to as *reflection* coefficient and the off-diagonal as *transmission* coefficients.

The waves going through the N-port are $\mathbf{a} = (a_1, a_2, ..., a_N)$ and the waves travelling away are $\mathbf{b} =$

$(b_1, b_2, ..., b_N)$. The wave a_i going into port i is derived from the voltage wave going into a matched load. For consistency with the conversation of energy, the voltage is normalized to $\sqrt{Z_0}$, being Z_0 the characteristic impedance (often $Z_0 = 50\Omega$). The definitions of the waves a_i and b_i are

$$a_i = \frac{V^+}{\sqrt{Z_0}}, \quad b_i = \frac{V^-}{\sqrt{Z_0}} \tag{6}$$

where V^+ is the voltage of the incident wave and V^- the voltage of the reflected wave. The relation between a_i and b_i $(i \in 1, 2, ..., N)$ can be written as a system of N linear equations [19]

$$b_i = S_{ii}a_i + S_{ij}a_j, \tag{7}$$

where the j subscript stands for the port that is excited (the input port), and the i subscript for the output port. Physically, S_{ii} is the input reflection coefficient with the output of the network terminated by a matched load ($a_j = 0$); S_{ij} is the transmission from port j to port i; and S_{jj} the output reflection coefficient. The S-matrix is symmetric, which means that interchanging the input and output ports does not change the transmission properties, and therefore $S_{ij} = S_{ji}$. Figure 3 represents a generalized four-port network with a characteristic impedance of Z_0.

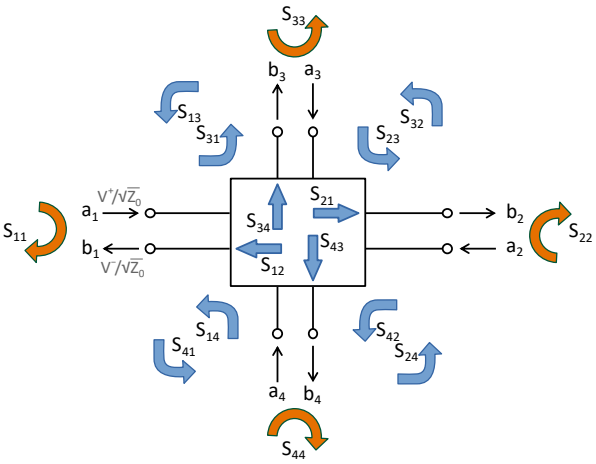

Figure 3: Generalized four-port network.

3. Experimental facility and setup

3.1. VKI Plasmatron facility

The Plasmatron at VKI is an inductively-coupled plasma (ICP) wind tunnel [20], that creates a high enthalpy, highly dissociated subsonic gas flow for reproduction of the aerothermodynamic environment found in hypersonic flight regimes. This facility has been extensively studied by Bottin et al. [20; 21]. Its basic concept consists of a quartz tube surrounded by a coil, which is connected to a 1.2 MW generator that provides high voltage (2 kV) and high frequency (400 kHz) current, that induces an electromagnetic (EM) field inside the tube. The gas injection is done through an annular inlet upstream to the coil. Due to the induced EM field, the gas ionizes and the flow exits the torch to enter into a vacuum chamber of 1.4 m in diameter as a plasma plume of 16 cm in diameter. To operate the facility, Argon is employed as starting gas because of the longer lifetime of the free electrons at low pressure compared to air plasma, facilitating the initial electric discharge. Then, the gas is gradually switched to the desired test gas (air, N_2, CO_2) and the argon is switched off.

An absolute pressure transducer (Memberanovac DM 12, Leybold Vacuum) measures the static pressure (p_s) in the test chamber. As the plasma jet is low subsonic (Ma $\approx$ 0.1), the static pressure is assumed constant inside the chamber. The static pressure uncertainty can be considered to be $\pm 10\%$ due to the stability of the vacuum pumps [22]. The gas mass flow rate ($\dot{m}_{gas}$) supplied to the torch is monitored through a calibrated gas rotameter (Bronkhorst EL-Flow F-203AV), while the Plasmatron control system records the electric power (P_{el}) supplied to the induction coil. Suitable quartz windows installed on the two sides of the vacuum chamber provide the necessary optical access in the direction perpendicular to the plasma flow.

3.2. Instrumentation and calibration

Luís et al. [11] performed a numerical analysis to design a communication system for testing at the Plasmatron, selecting the Ka-band as the most appropriate for signal propagation and blackout testing. Then they performed an experimental campaign with conical horn antennas (23° beamwidth) at the Plasmatron and they stated clear ripples due to interferences caused by the windows and the chamber walls. To minimize the effect of the windows, Luís et al. conducted differential measurements (Eq. 12), which is also done in this work. To minimize the reflections on the chamber walls, a new communication system in the Ka-band is proposed. This new system is required to follow three main constraints: an antenna beamwidth smaller than 5°, a maximum aperture of 18 cm (determined by the window size), and circular polarization. The first two constraints (illustrated in Fig. 4) allow to have the signal propagation concentrated inside of the opposite

window (which has a height of 18 cm) at a distance of 2 m. The final setup consists of two sets each comprising a horn lens antenna of 4.2° beamwidth (MI-wave 258A-6/0.250/381) and a waveguide orthomode transducer (MI-wave 281A-35.75/0.250/381/599), sequentially connected in each port to a waveguide to coax adapter (MI-wave 411A/599/KF), to a flexible microwave cable (Huber-Suhner SUCOFLEX 102) and to a DC block (MI-wave 8141A). Further operating details are summarized in Table 1. The transmission and reception of the signal are measured with a 4-ports vector network analyser (Rohde and Schwarz ZNB40). The antennas are aligned perpendicular to the torch exit and placed outside of the chamber side windows (see Fig. 4).

Table 1: Details about the instruments.

Instrument	Operating frequency [GHz]	Link budget
Antenna	33 - 38.5	32 dBi
Orthomode transducer	33 - 38.5	- 0.5 dB
Adaptor	26.5 - 40	- 0.4 dB
Cables	up to 46	- 2.62 dB/m
DC block	0.01 - 40	- 0.75 dB
VNA	0.01 - 40	10 dBm

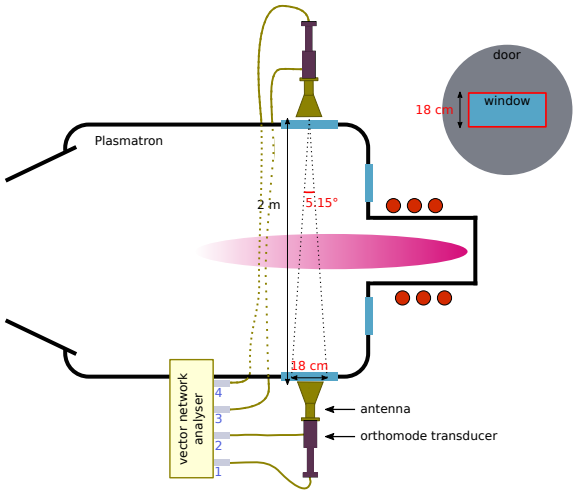

Figure 4: Experimental setup and system constraints.

Alignment and calibration of the test setup are carried out every day of testing. The alignment is done using a 360° self-leveling laser (Makita SK700D), ensuring that the centers of both antennas remain on the horizontal plane passing through the center of the torch, and on the vertical plane at a certain distance from the torch exit. The systematic calibration of the system is performed using a 2.92 mm automatic calibration unit (Rohde and Schwarz ZN-Z54). This type of calibration ensures that the effects of cables and DC blocks, and all systematic errors in general are canceled out before the measurements of the radio signal of the antennas. UOSM (unknown thru-open-short-match) full 2-port calibrations are performed. A combination of three full 2-port calibration ensures that all sixteen S-parameters are fully corrected [23].

3.3. Testing conditions

To study the signal propagation, several conditions covering the operational envelope of the Plasmatron are tested. The test gas is air and the testing conditions are summarized in Table 2. For each of the targeted pressures, twenty measurements without plasma are taken. To proceed with the experiments, the Plasmatron is switched on and the air mass flow is set to 16 g/s with the calibrated rotameter. The vacuum pumps are regulated until the target static pressure is reached inside the chamber. Once the required conditions are reached, fifty consecutive samples are taken. For each condition tested, an average and standard deviation are computed in linear units.

4. Experimental results

4.1. Computation of total attenuation and Faraday rotation

The measured parameters correspond to the S-parameters described in Section 2.2. These parameters are complex numbers,

$$S = |S|e^{i\phi_S}, \tag{8}$$

and both magnitude $|S|$ [dB] and angle ϕ_S [degrees] are acquired experimentally as a function of frequency. In linear units the S parameters are proportional to the electric field $|E|$ and are compute as $10^{|S|/20}$.

The orthomode transducer separates and combines (at the transmitting and receiving antennas, respectively) the two orthogonally linearly polarized signals caused by the circular polarization nature of the antennas. In this case, each component (vertical and horizontal) of the transmitting signal is sent individually and both components of the receiving electric field are actually measured. This means that, besides minimizing the reflections on the walls, this setup allows to uncouple the attenuation and Faraday rotation of the signal that occur simultaneously when propagating through an ionized medium. The computation

Table 2: Summary of testing conditions.

Distance [cm]	Static pressure [mbar]	Electric power [kW]
30	15	100, 125, 150, 175, 200, 250, 300, 320, 350, 400, 450, 500, 550, 600
30	50	100, 125, 150, 175, 200, 250, 300, 320, 350, 400, 450, 500, 550, 600
30	100	125, 150, 175, 200, 250, 300, 320, 350, 400, 450, 500, 550, 600

of the resulting electric field is performed considering both of the components as

$$|E| = \sqrt{|E_V|^2 + |E_H|^2} \tag{9}$$

being V and H the vertical and horizontal components, respectively, and thus neglecting the rotation of the electric field. Considering the notation attributing ports 1 and 2 to the vertical and horizontal components of the transmitting antenna ($1, V$ and $2, H$) and ports 3 and 4 the vertical and horizontal components of the receiving antenna ($3, V$ and $4, H$), the total losses L correspond exactly to the resulting electric field, and in linear units reads as

$$L_i = \sqrt{|E_{3i}|^2 + |E_{4i}|^2}, \quad i \in \{1, 2\}. \tag{10}$$

To study the influence of the plasma, the attenuation between the averaged total losses with and without plasma is considered in this study. This method allows to neglect the influence of the quartz windows and any intrinsic reflections on the metallic walls of the chamber. In linear units, the mean attenuation can be written based on the averaged total losses as

$$\overline{A} = \frac{|\overline{L_{ON}}|}{|\overline{L_{OFF}}|} \tag{11}$$

or, equivalently, in decibels [dB] as

$$\overline{A}_{[dB]} = 20 \log_{10}(\overline{A}). \tag{12}$$

The standard deviation of the mean attenuation due to the plasma is computed according to Taylor's expansion. Ultimately, it can be written as

$$\sigma^2_{\overline{A}} = \left(\frac{1}{|\overline{L_{OFF}}|}\right)^2 \sigma^2_{|\overline{L_{ON}}|} + \left(-\frac{|\overline{L_{ON}}|}{|\overline{L_{OFF}}|^2}\right)^2 \sigma^2_{|\overline{L_{OFF}}|}. \tag{13}$$

being $\sigma_{|\overline{L_{OFF}}|}$ and $\sigma_{|\overline{L_{ON}}|}$ the standard deviations of the mean total losses in vacuum and in a plasma flow, respectively.

To plot the mean attenuation with error bars in decibels [dB], the following method is implemented

$$20 \log_{10}\left(\overline{L} \pm \sigma^2_{\overline{L}}\right), \tag{14}$$

either as function of frequency or as a total averaged values over the frequency range.

Following the same notation, the vertical and horizontal components of the signal received by, respectively, ports 3 and 4 ($3, V$ and $4, H$) can be written as function of the transmitting components as

$$\begin{bmatrix} E_{4,H} \\ E_{3,V} \end{bmatrix} = \begin{bmatrix} \cos\theta_F & -\sin\theta_F \\ \sin\theta_F & \cos\theta_F \end{bmatrix} \begin{bmatrix} E_{2,H} \\ E_{1,V} \end{bmatrix}. \tag{15}$$

If rotation does not occur ($\theta_F = 0$), then the received vertical/horizontal component is equal to the transmitted vertical/horizontal component respectively, and zero at the orthogonal projection.

Uncoupling the attenuation, the Faraday rotation can be estimated with any of the transmitting parameters as

$$\begin{cases} \cos\theta_F = |E_{31}|/L_1 \\ \sin\theta_F = |E_{41}|/L_1 \end{cases}, \quad \begin{cases} \cos\theta_F = |E_{42}|/L_2 \\ \sin\theta_F = -|E_{32}|/L_2 \end{cases}. \tag{16}$$

The theoretical Faraday rotation can be estimated from the expression given in Eq. 4, that depends on the strength of the magnetic field, the wave frequency and the TEC. The magnetic field of the Plasmatron coil can be estimated as the sum of the magnetic field for individual circular loops [24]. Simple analytical expressions for the magnetic field for a circular loop currying a static current are derived by Simpson et al. [25]. For a current loop carrying a current I, with radius a, located in the $x - y$ plane and centered at the origin, the magnetic field components in Cartesian coordinates are given by

$$\begin{aligned} B_x &= \frac{Cxz}{2\alpha^2\beta\rho^2}\left[\left(a^2 + r^2\right)E\left(k^2\right) - \alpha^2 K\left(k^2\right)\right] \\ B_y &= \frac{y}{x}B_x \\ B_z &= \frac{C}{2\alpha^2\beta}\left[\left(a^2 - r^2\right)E\left(k^2\right) + \alpha^2 K\left(k^2\right)\right] \end{aligned} \tag{17}$$

being $\rho^2 = x^2 + y^2$, $r^2 = x^2 + y^2 + z^2$, $\alpha^2 = a^2 + r^2 - 2a\rho$, $\beta^2 = a^2 + r^2 + 2a\rho$, and $C = \mu_0 I/\pi$. μ_0 is the permeability of vacuum, and $E\left(k^2\right)$ and $K\left(k^2\right)$ are the

elliptic integrals in spherical coordinates (r, θ, ϕ) with argument

$$k^2 = \frac{4ar\sin\theta}{a^2 + r^2 + 2ar\sin\theta}. \quad (18)$$

4.2. Estimation of wall reflections

From the gains and losses in the communication system (Table 1), a theoretical transmitted magnitude can be estimated as compared with experimental measurements without plasma. The radio link budget sums the transmitted power along with the gains and losses of every subsystem to determine the signal strength arriving at the receiver input. For this case, the link budget equation for the radio communication system is written as

$$P_R - P_T = G_T - L_T - L_{FS} + G_R - L_R, \quad (19)$$

where $P_R - P_T$ [dB] is the ratio of the received and transmitted powers (converted to dB) as measured by the VNA. G_T and G_R are, respectively, the transmitter and receiver antenna gains [dBi], L_T and L_R are the losses [dB] associated to transmitter and receiver adaptors, mismatching on the line (0.07448 dB for given VSWR of 1.3) and caused by the windows, and L_{FS} the free space loss [dB]. The losses due to the windows are considered to be the same as presented by Luís et al. [11], since the testing frequencies and windows are the same in both works. As the calibration is done between the cable and the adaptor, the losses associated with the cables and DC blocks are considered in the measurements, and therefore do not need to be accounted for in the link budget. The free space loss can be estimated as

$$L_{FS} = 20\log_{10}\left(\frac{4\pi d f}{c}\right) \quad (20)$$

where d is the distance between the antennas, f the operating frequency, and c the speed of light. For this experimental campaign the antennas are positioned 2 m from each other.

Figure 5 presents the magnitude of the S_{31} (blue line) and S_{32} (orange line) coefficients overlapped with the theoretical link budget (grey line) as function of frequency. To remember that ports 1 and 3 correspond to vertical components of the wave, while port 2 (and 4) corresponds to the horizontal component. The theoretical estimation and experimental results for S_{31} are matching very well with a mean difference of 0.8 dB. The same exercise for the data presented by Luís et al. [11] yields a mean difference of 1.8 dB. This shows a clear improvement of the setup, as there is a clear reduction of the reflections on the walls. Regarding the S_{32} coefficient, the values measured correspond to the cross-polar limit which define the minimum measurement threshold. Additionally, the lowest the magnitude of the signal, the higher the associated uncertainty, as thus the higher the ripples measured.

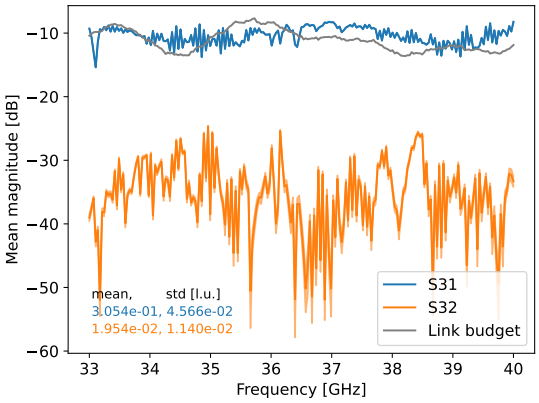

Figure 5: Magnitude of the S_{31} and S_{32} parameters overlapped with the theoretical link budget.

4.3. Signal attenuation due to the plasma

As example, Fig. 6 presents 6 S-parameters out of the 16 measured in function of frequency in vacuum (blue lines) and with plasma (orange lines) for a test case at 15 mbar, 320 kW, 30 cm from the torch exit. Total averaged quantities and standard deviations are also shown. Parameters S_{12}, S_{21}, S_{34} and S_{43} correspond to coefficients between ports on the same antenna, so they do not have a physical meaning. The reflection coefficients in function of the frequency are almost unaltered in the case with and without plasma. The same behaviour is observed for the other two S_{ii} parameters. The reflection coefficients show a clear attenuation of the signal when propagating through the plasma. For the signal propagating through the components with the same orientation ($V-V$ or $H-H$), there is an average signal decay of 30 dB, while for the components aligned perpendicularly ($V-H$ or $H-V$) the average decay is of 16 dB. The decay on the latest proves that there is Faraday rotation (because there is a change of the signal intensity) but also attenuation. The same behaviour is observed for the transmission coefficients not presented, as the S matrix is symmetric and thus $S_{ij} = S_{ji}$.

To estimate the total losses of the signal, neglecting the rotation of the signal, the resulting electric

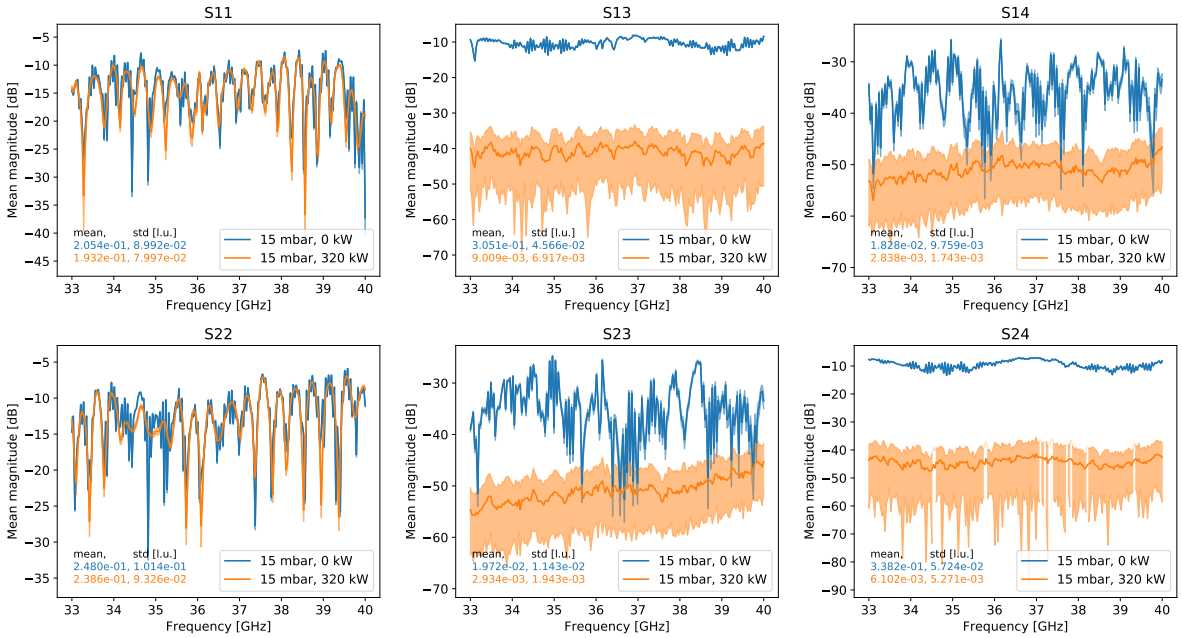

Figure 6: Variation of the mean magnitude of the S parameters for 15 mbar, 320 kW.

field relating each component of the receiving antenna with one of the components of the transmitting antenna (e.g. E_{31} and E_{41}) is computed according to Eq. 10. Figure 7 presents the total losses for the signal sent by the vertical components of antenna 1, for the case without plasma and with plasma. For the case without the plasma, the total attenuation is almost equal to the S_{13} parameter since there is no rotation of the signal, thus the signal is mainly propagating through the co-polar direction, as expected. For the case with plasma there is a slight contribution of the cross-polar component and a mean total loss of 40 dB. Overall, for this case, the total attenuation due to the plasma is around 30 dB. The same behaviour is observable for the L_2, L_3 and L_4 total attenuation coefficients.

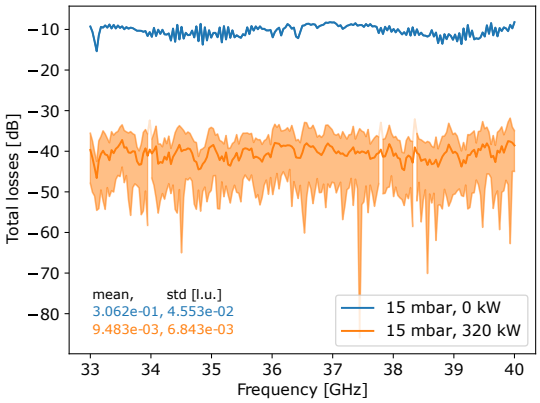

Figure 7: Variation of the total losses L_1 for 15 mbar, 320 kW.

4.4. *Quantification of the Faraday rotation*

Figure 8 presents the effective Faraday rotation obtained experimentally from the S_{31} parameter with respective standard deviation, overlapped with a numerical estimation of the Faraday rotation. The effective Faraday rotation is obtained by subtracting any inherent rotation of the antennas (measurements without plasma) from the rotation calculated with the plasma. The Faraday rotation computed from S_{41} and S_{42} equals exactly, respectively, S_{31} and S_{32}. Small differences between the values of the Faraday rotation for S_{31} and S_{32} are related with the unsteadiness of the plasma (as quantified and explained by Luís et al. [11]) that occurs during the measurement of the different parameters. The numerical estimation is performed by computing the magnetic field for a single loop centered at 127 mm and summing it with the same magnetic field shifted to 177, 227, 277, 327 and 377 mm (position of the coils). The radius is 109 mm, the current carried in the coil is measured by the Plasmatron data acquisition system. The magnetic field of

the Earth in the lab is also considered ($B_x = -22.6\mu$T, $B_y = -45.8\mu$T and $B_z = 11.7\mu$T) and each components in summed to the analytical magnetic field of the coils. The electron number densities are extracted from numerical simulations using an in-house inductively coupled plasma magnetohydrodynamics solver for simulation of the plasma flow field. Overall the experimental and numerical results show a good agreement. This is also observed for the other conditions.

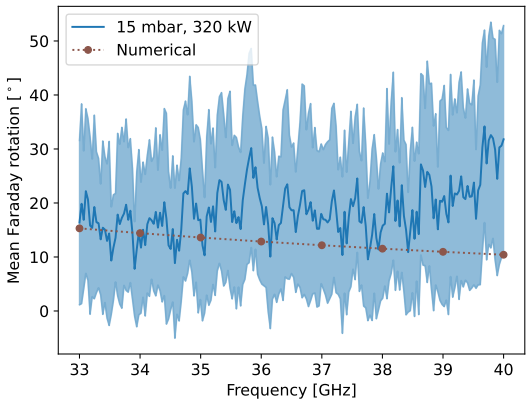

Figure 8: Variation of the Faraday rotation for 15 mbar, 320 kW.

4.5. *Parametric study*

Data analysis considering the dynamic nature of the plasma jet makes drawing conclusions about radio signal propagation challenging. Therefore, it is of interest to neglect the jet fluctuations, assume a steady state flow as normally done for thermal analysis in this type of facility, and consider total averaged quantities throughout the frequency range of each measurement. The same methodology has been been followed by Luís et al. [11]. Thus, the total attenuation (Eq. 11) is plotted as function of power for different chamber pressure and power settings in Fig. 9. Standard deviations are also shown here as error bars around the mean value, following Eq. 14. Clear attenuations are observed when increasing power and, consequently, electron number densities. With this configuration, the mean total attenuation varies between -12 and -37 dB when increasing electric power. Luís et al. [11] have stated total magnitude differences between -5 and -14 dB for the same testing conditions. In their work, the antennas had linear polarization and a much larger beamwidth. The first characteristic of their antennas should actually yield a higher attenuation (more negative) than supposed because the Faraday rotation is neglected. Thus, some of the signal is not actually attenuated but has rotation of its polarization, being just a component of the transmitted signal measured. The latter characteristic is considered to be the main reason for the discrepancies of the results. Since their antennas have higher beamwidth, a higher portion of the signal is transmitted around the jet that consequently reaches the effective measurement area of the receiving antenna undistributed. Additionally, this also increases the reflections on the walls, increasing the signal magnitude read by the receiving antenna. Furthermore, Luís et al. have stated that no significant changes were observed when increasing pressure. In this work, the choice of reduced beamwidth for the antennas has also improved the sensitivity of the results respect to pressure. The attenuation increases with decreasing power, reaching differences of up 10 dB for the same power. This trend contradicts the hypotheses of local thermodynamic equilibrium, where electron number densities increase with pressure. To better understand these results, experimental measurement of electron number densities is proposed as future work.

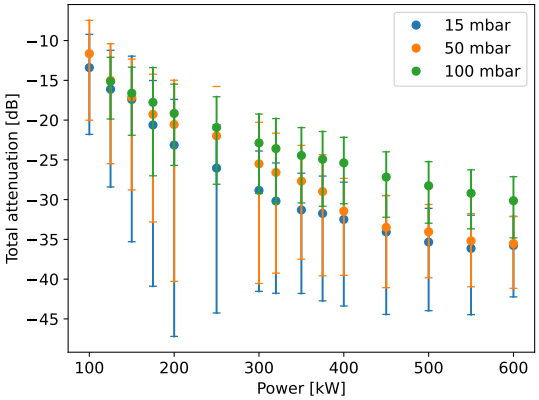

Figure 9: Variation of the mean total attenuation as a function of pressure and power.

Despite the Faraday rotation being related with the transmitting frequency, no significant differences are observed when increasing power (see example in Fig. 8). Thus, as a preliminary way of comparing the results, the evolution of the mean Faraday rotation throughout the frequency range is averaged and presented in Fig. 10 with respectively standard deviations. Once again, clear variations are observed with increasing pressure and power. In fact, the variation observed are consistent with the results from Fig. 9: the higher the electron number densities, the higher the absolute attenuation (Eq. 2) and the higher the po-

larization rotation (Eq. 4).

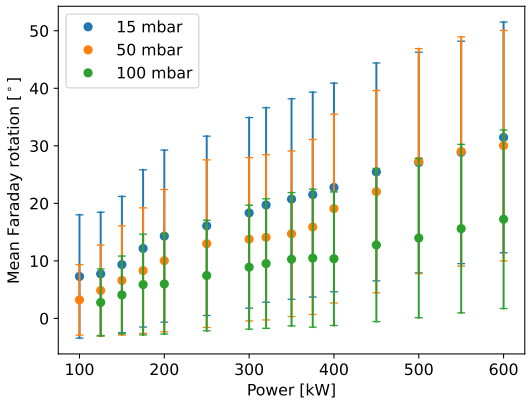

Figure 10: Variation of the mean Faraday rotation as a function of pressure and power.

5. Conclusion

Radio signal propagation in an air plasma flow has been studied for a combination of static pressures and power settings. The tests have been conducted by placing two highly directive antennas across the plasma jet at the VKI-Plasmatron facility, and by measuring their signals with a vector network analyser. The experimental setup proposed has allowed to conduct measurements of attenuation and Faraday rotation (rotation of of the electric field vector) due to the plasma.

The radio signal propagation has been studied initially without plasma to qualify the reflections on the chamber walls. A very good agreement has been observed between the experimental measurements and the theoretical link budget, corroborating the hypothesis that almost no reflection occur.

Nevertheless, to minimize these effects and the free space losses, the effect of the plasma has been studied based on the difference between the signal with and without plasma. To neglect the influence of the plasma unsteadiness, the signal has been averaged over a large number of samples. Analysing the transmission coefficients, clear attenuations have been verified in both co- and cross-polar components. The Faraday rotation has also been computed from experimental results. A good agreement has been observed when comparing the latter with the numerical estimations. As no significant changes have been observed over the frequency range and assuming a steady state flow, the attenuation and Faraday rotation results have been averaged throughout the total frequency range. The evolution of these averages have been analysed in function of pressure and power settings and clear dependencies have been observed. Attenuations of the signal have been verified ranging between -12 and -37 dB depending on the testing conditions, increasing with increase of power (and consequently electron number densities). The mean Faraday rotations have been observed to vary between 4° and 30°, increasing with power and decreasing with pressure. To correlate the variation of the signal attenuation and rotation with electron number densities, tests are planned to measure electron number densities in the Plasmatron facility using emission spectroscopy, by measuring the Stark broadening of the H_β line.

Acknowledgments

Diana Luís research is funded by a doctoral fellowship (2021.04930.BD) granted by Fundação para a Ciência e Tecnologia (FCT Portugal). The MEESST project is funded by the European Union's Horizon 2020 research and innovation programme under grant agreement No 899298.

References

[1] M. Keidar, M. Kim, I. Boyd, Electromagnetic Reduction of Plasma Density During Atmospheric Reentry and Hypersonic Flights, Journal of Spacecraft and Rockets 45 (3) (2008) 455–453, https://doi.org/10.2514/1.32147.

[2] R. P. Starkey, Hypersonic Vehicle Telemetry Blackout Analysis, Journal of Spacecrafts and Rockets 52 (2), https://doi.org/10.2514/1.A32051.

[3] R. P. Starkey, M. J. Lewis, C. H. Jones, Active Flowfield Modification for Plasma Telemetry, in: International Test and Evaluation Association Conference ITEA, 2002.

[4] S. V. Nazarenko, A. C. Newll, V. E. Zakharov, Communication through plasma sheaths via Raman (three-wave) scattering process, Physics of Plasmas 1 (9) (1994) 2827–2834, https://doi.org/10.1063/1.870521.

[5] J. P. Rybak, R. J. Churchill, Progress in Reentry Communications, IEEE Transactions on Aerospace and Electronic Systems AES-7 (5) (1971) 879–894, https://doi.org/10.1109/TAES.1971.310328.

[6] C. Jones, Report from the Workshop on Communications Through Plasma During Hypersonic Flight, AIAA Meeting Paperhttps://doi.org/10.2514/6.2009-1718.

[7] E. Gillman, J. Foster, I. Blankson, Review of Leading Approaches for Mitigating Hypersonic Vehicle Communications Blackout and a Method of Ceramic Particulate Injection Via Cathode Spot Arcs for Blackout Mitigation, Tech. Rep. NASA/TM - 2010-216220, NASA (2010).

[8] I. F. Belov, V. Y. Borovoy, V. A. Gorelov, A. Y. Kireev, A. S. Korolev, E. A. Stepanov, Investigation of Remote Antenna Assembly for Radio Communication with Reentry Vehicle, Journal of Spacecraft and Rockets 38 (2) (2001) 249–256, https://doi.org/10.2514/2.3678.

[9] R. Savino, D. Paterna, M. De Stefano Fumo, M. D'Eli, Plasma-Radiofrequency Interactions Around Atmospheric Re-Entry Vehicles: Modelling and Arc-Jet Simulation, The Open Aerospace Engineering Journal 3 (2010) 76–85, https://doi.org/10.2174/1874146001003010076.

[10] S. A. Bendoukha, K. Okuyama, B. Szasz, S. Takayuki, Experimental Method Using Arc Wind Tunnel to Simulate A New Technique For Communicating With A Reentry Probe Having A Thermal Shield Made Of LATS Materials, International Journal of Research 5 (2017) 1–12, https://doi.org/10.5281/zenodo.345434.

[11] D. Luís, A. Viladegut, A. Camps, O. Chazot, Effect of electron number densities on the radio signal attenuation in an inductively coupled plasma facility, in: 9th European Conference for Aeronuatics and Space Sciences (EUCASS), 2022, https://doi.org/10.13009/EUCASS2022-6128.

[12] R. Starkey, R. Lewis, C. Jones, Plasma Telemetry in Hypersonic Flight, in: International Telemetering Conference, International Foundation for Telemetering, 2002, paper 02-15-2.

[13] R. Starkey, R. Lewis, C. Jones, Electromagnetic Wave / Magnetoactive Plasma Sheath Interaction for Hypersonic Vehicle Telemetry Blackout Analysis, in: 34th AIAA Plasmadynamics and Lasers Conference, no. AIAA Paper 2003-4167, 2003, https://doi.org/10.2514/6.2003-4167.

[14] M. Kim, Electromagnetic manipulation of plasma layer for re-entry blackout mitigation, Ph.D. thesis, Department of Aerospace Engineering, University of Michigan (2009).

[15] M. Kim, I. Boyd, Effectiveness of a Magnetohydrodynamics System for Mars Entry, Journal of Spacecraft and Rockets 49 (2012) 1141–1149, https://doi.org/10.2514/1.A32256.

[16] M. Kim, A. Gülhan, Plasma Manipulation using a MHD-based Device for a Communication Blackout in Hypersonic Flights, in: Proceedings of 5th International Conference on Recent Advances in Space Technologies, Vol. RAST2011, 2011, pp. 412–417, https://doi.org/10.1109/RAST.2011.5966868.

[17] J. G. Proakis, M. Salehi, Fundamentals of Communication Systems, Pearson, 2014, iSBN: 9780133354850.

[18] K. Davies, Ionospheric radio propagation, Vol. 80, US Department of Commerce, National Bureau of Standards, 1965.

[19] F. Caspers, RF engineering basic concepts: S-parameters, CERN Yellow Report CERN-2011-007 (2011) 67–93, https://doi.org/10.48550/arXiv.1201.2346.

[20] B. Bottin, O. Chazot, M. Carbonaro, V. Van Der Haegen, S. Paris, The VKI Plasmatron Characteristics and Performance, Measurement Techniques for High Enthalpy and Plasma Flows.

[21] B. Bottin, Aerothermodynamic Model of an Inductively-Coupled Plasma Wind Tunnel: Numerical and Experimental Determination of the Facility Performance, Ph.D. thesis, von Karman Institue for Fluid Dynamics (1999).

[22] A. Fagnani, D. Le Quang Huy, B. Helber, S. D. ans A. Turchi, O. Chazot, A. Hubin, Investigation of a Free-Stream Air Plasma Flow by Optical Emission Spectroscopy and Comparison to Magnetohydrodynamics Simulations, in: AIAA SciTech Forum, 2020.

[23] M. Hiebel, Vector Network Analyzer (VNA) Calibration: The Basics, Tech. rep., Rohde & Schwarz, https://pchene.files.wordpress.com/2019/08/8e60b68a24a4169eecbd0763d4a9287037e4.pdf, last accessed 25 Oct 2022 (2008).

[24] J. Lane, R. Youngquist, C. Immer, J. Simpson, Magnetic Field, Force, and Inductance Computations for an Axially Symmetric Solenoid, Tech. Rep. 2013-217918, NASA (April 2001).

[25] J. Simpson, J. Lane, C. Immer, R. Youngquist, Simple Analytic Expressions for the Magnetic Field of a Circular Current Loop.

OES and PLIF studies of graphite ablation products in ICP facilities

Greyson Kale

Aeronautics and Aerospace Department, von Karman Institute for Fluid Dynamics, Belgium, greyson.kale@vki.ac.be

Supervisor: Thierry Magin

Professor, Aeronautics and Aerospace Department, von Karman Institute for Fluid Dynamics, Belgium, magin@vki.ac.be

University Supervisor: Noel Clemens

Professor, Department of Aerospace Engineering and Engineering Mechanics, The University of Texas at Austin, Austin, TX, U.S.A, clemens@mail.utexas.edu

Abstract

Optical emission spectroscopy (OES) and laser induced fluorescence (LIF) have been used frequently in ablation studies to measure temperature and quantify freestream and ablation products in the flowfield. This talk first provides background on the ICP facilities used to generate the high enthalpy conditions necessary to initiate ablation, and then gives a brief overview of the application of the OES and LIF diagnostics to this type of work. OES data, mainly emission from the cyano (CN) radical from the Plasmatron Plasmut test campaign is discussed, with attention given to the extent of NEQ in the spectra, and the number density of CN along the sample centerline computed from the OES data. Next, discussion of similar OES measurements in the UT ICP facility is given, including some interesting features of the resulting imaging measurements. Finally, the method of obtaining qualitative planar LIF measurements in the UT torch is covered, and measurements of CN fluorescence in high enthalpy air and nitrogen flows are shown. Notable qualitative results are immediately obvious, including a distinctive stand-off in the CN layer above ablating graphite in air.

Keywords: ablation, graphite, emission spectroscopy, laser induced fluorescence, CN violet.

1. Introduction

With expanded interest in hypersonic flight, the need for robust and high performance thermal protection materials (TPM) is more critical than ever. TPM systems protect the vehicle from the high thermal stress environment experienced during flight, and typically mitigate heating via a physical process known as ablation. Ablating TPMs transport energy from the surface of the vehicle through a combination of mass loss and phase change, the specific physics of which is driven by the current conditions at the surface and the thermo-physical properties and kinetic response of the material itself [1].

As noted above, a key process of interest is the extent of chemical reaction products produced at the surface of an ablation TPM. Understanding the interaction between chemical products generated at the surface and flowfield species can provide information on the heating rate of the TPM and its consumption. Since the internal response of the TPM is difficult to measure in-situ, the flow environment around the ablating TPM must be probed to provide relevant information on the nature of the species produced during ablation. Moreover, duplication of an flight flow environment is key to replicating an accurate ablating condition for a given TPM [2].

If the flow environment can be matched and species can be directly probed within the flowfield, species profiles can be produced for predictive modelers, allowing them to directly tune their simulations to match. These informed predictive capabilities will then allow mission designers to improve mass allocation margins and expand the capabilities of a given payload.

This work discusses the use of two different high enthalpy facilities, the VKI Plasmatron and the UT

PRC torch to make measurements of ablating TPMs. It is planned to expand the collaborative work between the two facilities in the future.

2. ICP Facilities

As previously noted, production of a high enthalpy flow environment is critical to the study of ablation. Ground test facilities typically used to perform this function include both arcjets and inductively coupled plasma (ICP) facilities. While capable of extremely high enthalpy flow conditions, arcjets often suffer from chemical contamination and various degrees of chemical non-equilibrium (NEQ) which can make the resulting analysis of the optical data from the flowfield difficult [2]. In contrast, ICP facilites can produce a clean plasma at near EQ conditions, an ideal situation for making measurements of the thermo-chemical environment of the flowfield.

The von Karman Institute operates one of the worlds largest ICP facilities, the Plasmatron. The Plasmatron facility is capable of achieving a wide range of operating conditions, a broad range of which are given in Table 1 below [1].

Table 1: Plasmatron Operating Parameters

Nozzle Diameter [mm]	160
Working Gas	Air, CO_2, N_2, Ar
Facility Pressure [mbar]	5-300
Heat Flux [kW/m^2]	90-16,000

The University of Texas at Austin operates a similar, smaller scale, 50 kW ICP torch at the J.J. Pickle research campus (PRC) in North Austin. A similar set of operating parameters for the UT PRC torch are likewise given in Table 1 [3]. Note that the main distinction, aside from the accessible plasma powers between the two facilities is the lack of a vacuum chamber for the UT PRC torch, limiting the facility static pressure to atmospheric pressure. This has implications on the applicability of the flow conditions produced in the facility to hypersonic flight.

Table 2: UT Torch Operating Parameters

Nozzle Diameter [mm]	30
Working Gas	Air, CO_2, N_2, Ar
Facility Pressure [mbar]	1013
Heat Flux [kW/m^2]	100-240

3. Optical Diagnostic Techniques

As the name suggests, optical diagnostic techniques rely on the capture of light to provide information on flow conditions and properties. The generation of these photons occur through a variety of processes including conditions where the flow environment provides the excitation energy or where an external source provides the excitation energy. The discussion given in this report focuses on the cynogen radical, CN, an important species in ablation studies of carbon based TPMs, both because it can influence the radiative heat flux to the surface of a hypersonic vehicle, but also because the production of CN impacts the extent of N recombination at the ablating surface [1]. Since the recombination of atomic N is an outsize contributor to the convective heat flux to the surface of the vehicle, and production of CN depletes the available atomic N, understanding the distribution CN across the flowfield is highly relevant. CN radiates strongly in the violet portion of the visible spectrum, and it is this transition that is explored over the duration of this report. Specifically, the CN violet transition results from the release of energy from the second electronically excited state of CN (B) down to the ground electronic state (X), as is noted in Eq. 1 below.

$$B^2\Sigma^+ \leftrightarrow X^2\Sigma^+ \tag{1}$$

3.1. Optical Emission Spectroscopy (OES)

OES is common optical diagnostic technique that has been used widely within the ablation and combustion community. In general, OES probes electronic transitions, specifically transitions from an upper to a lower electronic state. For studies in the aforementioned ICP facilities, the high enthalpy flowfield provides the excitation energy to promote electronic transitions. Two factors can make the interpretation of OES data difficult, the first being that the highly luminous plasma plume can contribute spurious emission that must be accounted for. Since OES setups collect all of the emission over the line-of-sight of the imaging optic, this can pose a major challenge [1], [3]. Second, high temperatures in the plasma plume lowers the overall density and spreads populations over a broader range which can further complication spectral interpretation.

An imaging OES method was used for all OES data presented in this report. Imaging or hyperspectral OES utilizes an imaging spectrograph (Princeton

Instruments HRS-750) and a 2D intensified CCD array (Princeton Instruments PIMax3/PIMax4) to make spectroscopic measurements with both spectral and spatial content. Fig. 1 gives a representative hyperspectral OES image, where both the spatial and spectral coordinates have been highlighted [1]. All credit for the development of the VKI OES setup goes to Andrea Fagnani.

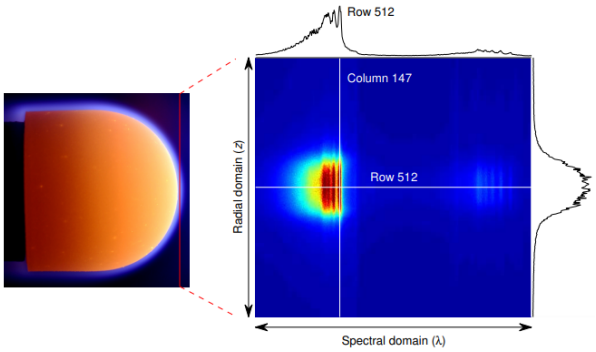

Figure 1: Representative line OES data taken in the VKI Plasmatron for ablating graphite. Note the data is taken along the dashed red line, around 3 mm from the sample surface (Credit: Dr. Bernd Helber).

Note that the slit of the spectrograph acts as spatial filter, permitting line measurements over a length in the object plane determined by the magnification of the optical train in the setup. OES data taken in the UT PRC facility, Fig. 2 is of a slightly different configuration, with the line measurement performed vertically along the stagnation line of the ablating sample.

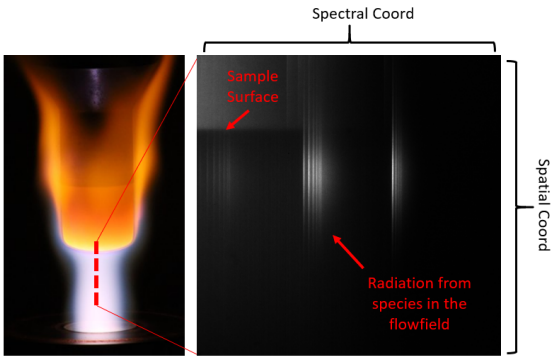

Figure 2: Representative line OES data taken in the UT PRC torch for ablating graphite. Note the data is taken along the dashed red line, starting on top of the surface and moving out into the flowfield.

3.2. *OES Setup*

Optical setups for OES studies are relatively straightforward, where a simple lens or optic is all that is needed to image an area of interest. In the OES setups illustrated in Figs. 3 and 4, the imaging optics are a 250 mm focal length UV-enhanced aluminum concave mirror, and a 50 mm diameter, variable focal length macro lens (Vivitar Series 1 70-210 mm f/3.5) set to a focal length of 200 mm, for the VKI and UT setups respectively. As is noted on Fig. 4, the choice of a variable aperture macro lens in the UT setup was made to allow for measurements with a low (f/3.5) and high (f/22) f/# in an attempt understand the impact the depth of focus has on a given measurement. Since compound camera lenses are designed to be achromatic and aspherical, it is assumed that spherical and chromatic aberrations associated with the UT setup will be negligible.

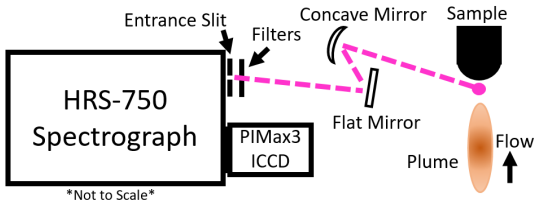

Figure 3: OES setup used in the VKI Plasmatron for the Plasmut test campaign (Credit: Andrea Fagnani).

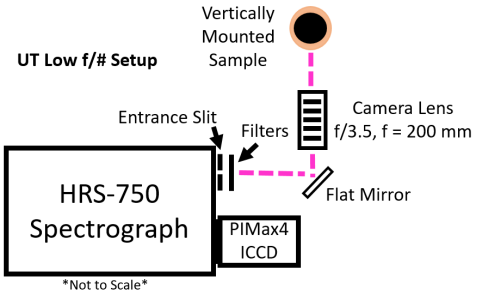

Figure 4: OES setup used in the UT PRC torch for the recent CN campaign.

For both setups, a flat, 25.4 mm UV-enhanced aluminum mirror was used to fold the image back onto the spectrograph slit due to space constraints within each facility. All OES measurements presented here used a 150 g/mm grating, blazed at 500 nm.

3.3. *Laser Induced Fluoresence (LIF)*

Another widely used optical diagnostic technique is LIF, wherein specific electronic transitions are pumped using a laser source. In general, the laser source provides the energy necessary to induce a transition from a lower to upper electronic state. De-

pending on exact photon energy absorbed and the specific transition targeted, fluoresced photons may have a range of energies.

As compared to OES, LIF is a much more specific technique, with the ability to target specific molecular and atomic species. It is also highly sensitive (measurements below 100 ppm are possible), and since the absorption process (the excitation) is resonant, LIF has much higher cross sections than Raman scattering processes, making it an appropriate choice to access minor species in the flowfield. Finally, LIF techniques obviate the line of sight integration issues inherent in OES measurements, improving the overall spatial resolution [4].

However, as may be fairly obvious, the LIF technique is much more involved and complex as compared to OES, requiring a number of additional systems. Furthermore, due to the specificity of LIF, data on only one species may be obtained at a given time, a constraint that should be considered in experimental planning.

3.4. UT planar-LIF Setup

For our specific measurements, the second harmonic at 532 nm of a Continuum Powerlite 9010 Nd:YAG was used to pump a Continuum Vista Dye laser system supplied with LDS750 dye. A Vista FX second harmnonic generator (SHG) was used to frequency double the resulting output from the Vista Dye laser, and was tuned to a wavelengths of 358.5826 and 358.3868 nm to target the (2,1) and (3,2) transitions near of the bandhead of the CN violets $\Delta v = +1$ system. A HighFinesse WS-6 wavelength meter was used to monitor the output from the Vista FX SHG and allows for high fidelity tuning to the required transition [4].

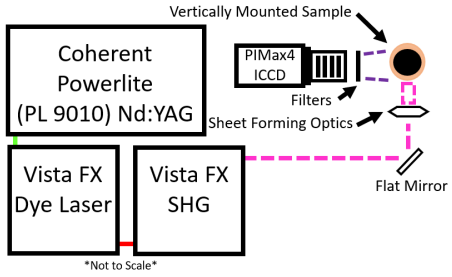

Figure 5: General schematic of the UT PLIF setup. Note the addition of the sheet forming optics.

Fig. 5 details a schematic of the planar LIF setup, note that sheet forming optics (UV fused silica cylindrical lens) are required to form the beam into a sheet. This allows for measurements of a 2D field. It is important to note that the PLIF measurements discussed here are qualitative at best, and serve more of a proof of concept than a quantitative measure of species densities within the flow. Future work is planned to focus on corrections that will allow for quantitative planar LIF measurements.

For qualitative measurements, slightly less is required: the emission spectrum of the target species must be known, an absorption wavelength must be accessible, and the rate of radiative decay of excited state must be known (as the flouresence power is proportional to this rate). In order to perform quantitative planar LIF measurements: two pressing issues must be addressed, (1), the temperature distribution across the measured field and (2), the effect of quenching. To account for quenching three things must be known: (1) the partial pressure of all species other than one of interest, (2) rates of deactivation of species of interest by all others present, and (3) dependence of deactivation rates on temperature [4].

4. OES Processing

As discussed in the previous section, the nature of emission spectroscopy results in a number of challenges to the correct interpretation of the collected spectral data. Moreover, calibrations to the spectrographic setup and corrections due to the choice of optical elements in the OES collection path must likewise be made to ensure reliable quantification and interpretation. The processing steps taken with the OES data from both facilities are detailed below. Please note, all of these steps were performed for both data at the UT and VKI facilities with some minor differences.

1. Background/integration time correction.

   Each data set, regardless of whether it is a measurement, background, calibration image, etc. is immediately corrected for the integration time/gate width it was taken at, resulting in a data set with units of counts/sec.
   Each measurement set is then corrected for the background emission (dark shot noise on the ICCD chip and spurious radiation in the facility) by subtracting the average of a 10 frame measurement at the same camera and spectrograph settings with no plasma or flow in the facility from the measured data.

2. Wavelength correction: based on NIST Hg line positions.

   While a wavelength calibration was performed with the HRS-750 spectrograph prior to the data collection, a systematic shift in line positions was noticed when evaluating the data. Therefore, an additional wavelength correction was performed by imaging a Hg lamp in the focal plane of the OES setup, and constructing a 2nd order correction function based on the line positions given by NIST and their relative position as given by the current HRS-750 wavelength calibration. Fig. 6 illustrates the effect of this correction, changing the spectral positions by an average of ~0.1 nm. This was performed only for a spectral range of 300-510 nm, because the focus was on the evaluation of the CN violet.

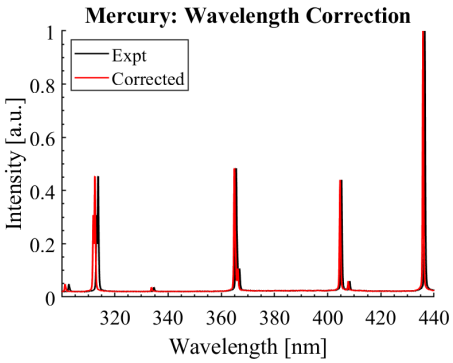

Figure 6: Raw experimental (black) and wavelength corrected (red) data for the spectral region of interest for the CN violet.

3. Intensity correction: raw counts/sec to radiance (W/m^3-sr).

   To perform the intensity correction for each measurement, an instrument function is first constructed based on the measurement of a known source. In the VKI case, a calibrated Osram WI 17/G Tungsten strip lamp is placed in the focal plane of the OES setup, an calibration images were taken at the same camera/spectrograph settings used in the measurement process. To construct the instrument function, the measured calibration image signal at a given spatial location was divided by the known radiance curve from the lamp, producing an instrument response function (IRF) with units of W-sec/m^3-sr-counts at each spatial location. In the VKI case, it was assumed that the IRF would not vary significantly over the spatial coordinate of the chip, so 10 rows on either side of the centerline were averaged to produce the IRF for all measurements at a given set of spectrograph and camera settings. Fig. 7 gives the computed IRF used in the processing.

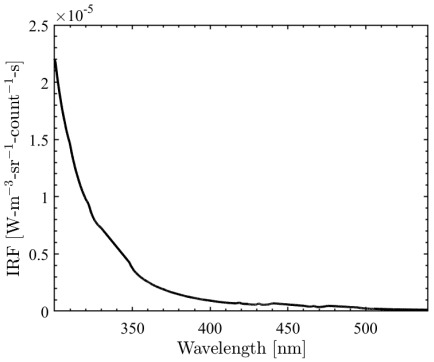

Figure 7: Instrument response function for converting raw measurements in [counts/sec] to radiance [W/m^3-sr].

It should be reiterated that this IRF applies only for measurements with the OES setup taken at a gain setting of 1x and with the 150 g/mm grating for a spectral range of 280-510 nm. Unfortunately, calibration measurements for other gratings/gain settings were not available, so any spectra presented must be considered to be very qualitative. Moreover, to construct the IRF across the whole 280-510 nm range, multiple calibration measurements were required as the grating center wavelength was changed to accommodate the full spectral range. To construct the IRF for the full spectral range, the calibration images were simply averaged at overlapping spectral positions. This produces the small kinks or bumps in the IRF given above, as that is likely due to poor quantum efficiency at locations near the edge of the CCD array.

To convert measurements to radiance, the raw measurement at each spatial location is simply multiplied by the portion of the IRF that corresponds to the spectral range covered by the given measurement. This produces units of radiance as previously discussed, and corrects not only for the transmissivity of the optical elements in the path, but also for the response of the intensifier and the quantum efficiency of the detector CCD array.

In the UT case, a GigaHertz-Optik ISS-8P-VA-100 integrating sphere was used as the known

calibration source. The other portions of the process were identical, with the exception that an IRF curve was constructed for each spatial location and applied, rather than computing an average IRF for use across the whole data field. This is was done because it was noticed that the response of the CCD array on the PIMax4 used at UT had some spatial variation that may impact the processed spectra.

4. Filtering/averaging and Abel Inversion.

   The geometry of the line imaging measurements performed at VKI are of interest, in that they capture the line-of-sight radiation emitted from an axisymmetric source (the plasma plume) in the radial direction. If the gas in the plume is assumed to be optically thin, then the inverse Abel transformation gives the local emission coefficient at a radial position, r, from the centerline of the plume. Prior to the Abel inversion, the two half profiles of the line measurements are averaged and spatially filtered.
   The 3-pt Dasch Abel inversion method, as outlined by Villareal & Varghese, was used to invert the radial measurements made at VKI. The inversion code was validated against two sets of test functions, those outlined by Helber [1] and those given by Villareal and Varghese [5]. The code reproduced the correct radial profiles as can be seen in Fig. 8.

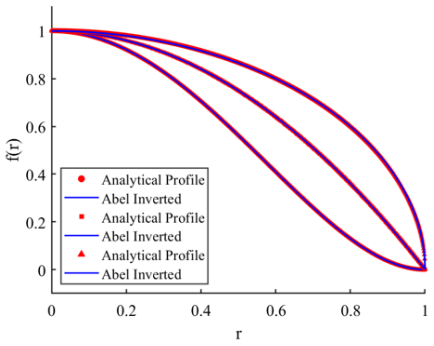

Figure 8: Analytical (red) and Abel inverted (blue) profiles

5. Baseline correction (linear/arPLS).

   The last step prior to more involved interpretation is the baseline correction of the spectra at a given spatial location. In most cases, particularly at higher pressures/densities, some continuum radiation can be seen in the baseline of the spectra, which can impact the subsequent temperature fitting and number density estimates. To improve those estimates, this baseline radiation is removed prior to subsequent analysis.
   All spectra at a given spatial location are baseline corrected with one of two methods: a linear baseline subtraction or an asymmetrically reweighted penalized least squares method (arPLS) [6].

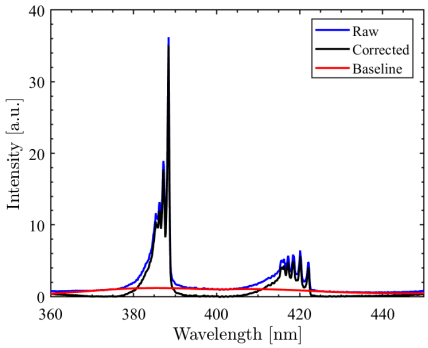

Figure 9: arPLS corrected spectrum, with the raw spectrum (black), the corrected spectrum (blue), and the estimated baseline (red) shown.

   The linear subtraction method requires user input to define the threshold for the baseline and the range over which to apply the subtraction. This process, while simple, is particularly subjective and difficult to apply consistently from spectrum to spectrum. The arPLS method, outlined in Baek et. al., implements a correction method by iteratively changing weights by estimating the baseline in a given signal. This allows for the noise level to be estimated adaptively and the weights to be adjusted accordingly to the level of real signal in the spectrum. As compared to other baseline correction methods, the arPLS does not require individual inspection of corrected spectra, any prior knowledge about the sample composition, peak detection, or mathematical assumption about the background noise distribution. A single user input is required, the smoothing parameter, λ.

6. Temperature fitting (Specair or simplex method w/ NEQAIR).

   Fitting was conducted using two methods: via Specair 3.0 (SpectralFit S.A.S) from 340-430

nm, the spectral region associated with emission from the CN violet system. Specair uses a least squares procedure to solve the radiative transport equation along the simulated line of sight and assumes a Boltzmann distribution for excited state populations. For all fits with Specair, the instrumental broadening profile was assumed to be Gaussian, with a FWHM of 0.365 nm.
Fitting with NEQAIR v15.0 (NASA Ames) relies on a in-house built routine that minimizes a user defined objective function between a theoretical spectrum generated by NEQAIR (via solution of the radiative transport equation) and the experimental spectrum to be fit. The minimization procedure is a modified version of the Nelder-Mead simplex method, known as the globalized constrained Nelder-Mead method (GBNM) as proposed by Luersen et al. [7]. Simple geometric operations are performed on the simplex, allowing it to 'roll' downhill to a local optima. The constrained nature of the GBNM method allows the user to implement physics based constraints on the number of independent parameters to be fit.
Spectra in both cases were fit with 1 temperature LTE (T_{trans} = T_{rot} = T_{vib}= T_{elec}) and 2 temperature models (T_{trans} = T_{rot}, T_{vib}= T_{elec}) to investigate the extent of NEQ behavior in the CN violet spectra.

7. Number density estimates: outlined by Helber and Turchi [8].

The final OES related processing detail is the estimate of CN number densities based on integrated spectral radiance. These estimates are based on the procedure given in Helber and Turchi [8]. Clearly, the assumption is made that the region over which emission is aggregated is assumed to come only from the species of interest. Theoretical spectra are then generated over the range of temperatures relevant to the problem, and the theoretical emission from a given band is integrated for each generated spectrum to obtain the local emission. Since the emission scales linearly with the total number density, an upper bound to the mole fraction can be determined assuming a facility static pressure and an initial mole fraction of 1. After construction of the scaling relationship between the local emission and number density, the experimental number density can be computed by comparison between the integrated experimental emission and that obtain from the theoretical curve.

5. Plasmut Test Campaign

The VKI OES data processed in this analysis originated from the Plasmut test campaign, whose main goal was to study the variation in CN production above graphite as a function of the facility pressure. Two other facility parameters were varied: the grain size of the graphite sample and the facility power. Slight variations in the recession rate had been noted in previous tests of various types of graphite and the appearance of NEQ effects at lower facility powers had motivated interest in further exploration. Table 3 gives the details of facility conditions tested over the course of the campaign.

Table 3: Plasmut Test Campaign

18 tests: (**CN violet**, N_2, N_2+, N).
Facility pressure: 15, 100, 200 mbar.
Graphite grain size: 0.001" (G1), 0.008" (G8).
Facility power: 300 (G8 only), 370, 400 kW.

6. Plasmut OES Results

As a whole, qualitative inspection of the CN violet spectra produced from the Plasmut campaign reveals results that are fairly unremarkable. Only slight NEQ behavior is evident in the higher vibrational bands in the CN violet spectra at higher facility powers and the extent of NEQ behavior becomes more apparent as you move to lower facility powers (in the 300 kW case in particular). Note that some spectra in the G1 cases are missing due to corrupted data. As the facility pressure increases, the emission from the N_2+ 1st negative and Meinel bands grows as well, this is expected with the increase in density. For the G1 grain size, there appears to be some unexpected contamination, in the form of what appear to be atomic lines at around 398 nm, just red shifted from the signal from the N_2+ 1st negative system. A preliminary analysis identified these lines as potentially resulting from Ca atoms, which could have been introduced to the sample during processing or handling. These atomic lines introduce additional uncertainty into the resulting fits.

As previously mentioned, the extent of NEQ in the CN violet spectra is limited, with little to no evidence in the spectra, particularly at the higher pressures and

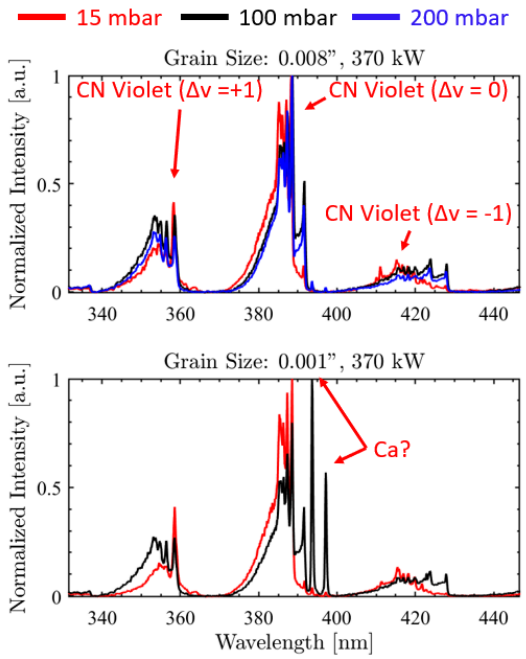

Figure 10: Spectra of the CN violet from the Plasmut campaign for various pressures (colors), and graphite grain sizes (plot rows) at a facility power of 370 kW.

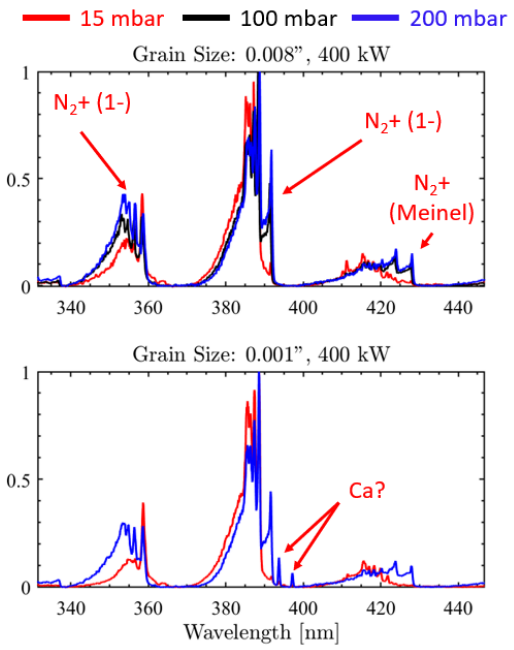

Figure 11: Spectra of the CN violet from the Plasmut campaign for various pressures (colors), and graphite grain sizes (plot rows) at a facility power of 400 kW.

powers in Figs. 10 and 11. However, two lower power tests (300 kW) were conducted with the G8 graphite sample at two pressures, and the appearance of NEQ within the Δv=0 band of the CN violet becomes apparent. This is shown in Fig. 12 where transitions from the upper vibrational levels of the CN B state contribute strongly to the observed emission. To further probe this behavior, additional tests at this power level should be conducted. Following the number density estimation procedure outline above, the CN mole fraction (from the number density and facility pressure) was computed at the centerline of each line imaging measurement. Since reliable spectra were missing for several of the smaller graphite grain (G1) tests, the number densities were computed just for the tests involving the larger graphite grain sizes (G8).

Note, the G5 and G7 labels in the mole fraction estimates below refer to facility test conditions outlined by Helber [1]. The G5 test case was conducted at 330 kW and the G7 test case at 390 kW. Numerical simulations were not conducted at the specific test conditions from the Plasmut campaign due to the lack of accurate boundary conditions. However, referencing the G5 and G7 test conditions provides a good metric for a relative comparison.

The experimental mole fractions are compared to numerically computed mole fractions from a number of Stagline simulations. Stagline is a 1D, finite volume solver developed at VKI that computes flow properties from the surface of a sample out through the boundary layer [9]. The difference between the computational values is the specification of a different chemistry model at the ablating surface. Nonetheless, the experimentally estimated mole fractions show a completely different trend with pressure than the simulations. The reasons for this are currently unclear. Additional uncertainty analysis will be necessary to explore the variation between the results for each power setting. Further, simulations closer to the test conditions may be equally as helpful in revealing additional dependencies.

7. UT OES and PLIF Results

A major goal of this work is to provide an initial framework for comparisons between the two ICP facilities discussed above. To this end, the processing framework for OES data was covered above, and a brief set of analysis on VKI produced data was given. To finish, this section will give a brief set of analysis on UT produced data, including both OES and LIF measurements.

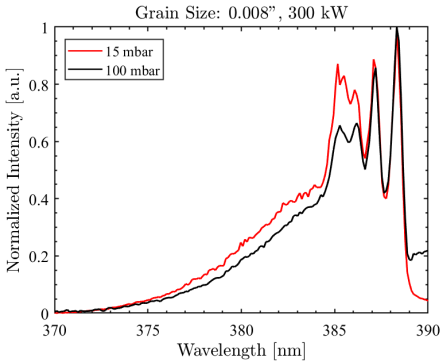

Figure 12: CN violet Δv=0 band at 300 kW for 15 mbar (red) and 100 mbar (black). Note the increased emission around 385 nm in the lower pressure case.

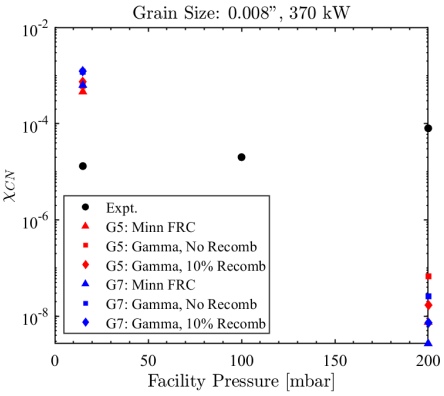

Figure 13: Experimental mole fractions (black) compared to numerically computed mole fractions (red/blue) for Plasmut tests at 370 kW with the G8 graphite grain.

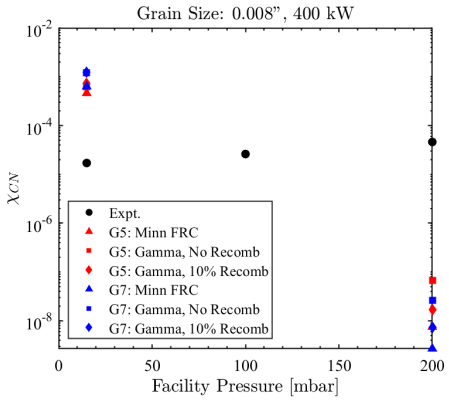

Figure 14: Experimental mole fractions (black) compared to numerically computed mole fractions (red/blue) for Plasmut tests at 400 kW with the G8 graphite grain.

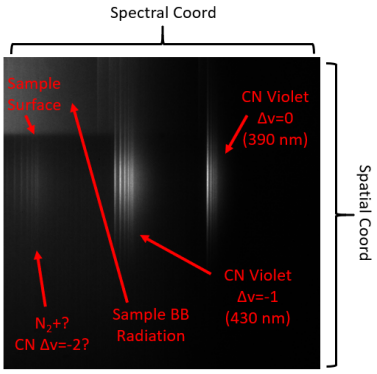

Figure 15: Emission from the CN violet, imaged along a line from the sample surface out through the boundary layer. Test conducted on graphite in an air plasma.

The UT based OES work is ongoing, with line measurements taken vertically from the sample surface out into the boundary layer, see Fig. 15. The hope is that direct comparison between these measurements, and similar ones made at VKI will help inform additional questions on the production of CN, its relationship to pressure, and the performance of different chemistry models in the ablation community.

A number of initial LIF results from the UT facility are given below, starting with a single shot image of CN planar LIF in an air plasma, Fig. 16. All credit for this PLIF work goes to John Murray, another graduate student at The University of Texas at Austin.

Fig. 16 illustrates one of the ultimate goals of the PLIF based analysis, to produce flowfield species profiles along the stagnation line out into the boundary layer. With the ability to bin the intensity over a given ROI as noted, estimates of species profiles can be readily produced. It should also be noted that the planar LIF work can produce highly spatially resolved information about the distribution of flowfield species. Similar measurements in different working gases, air and N_2, (Fig. 17) reveal interesting considerations relative to the chemical production of CN at the ablating graphite surface.

Note the distinct standoff in the CN layer from the graphite surface in the air case. This implies that little to no CN is produced at the surface, and is instead created via gas phase reactivity out in the gas phase, most likely from the CN and CO exchange reaction. In pure nitrogen, peak CN production is at the surface, as is expected via the nitridation reaction. Further, in the pure nitrogen case note an additional peak in the middle of the CN layer, which is well reflected in species profiles produced from simulation. The mechanism for this additional peak is likely due to the balance be-

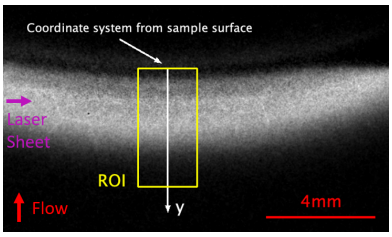

Figure 16: Single shot CN PLIF image of ablating graphite in an air plasma.

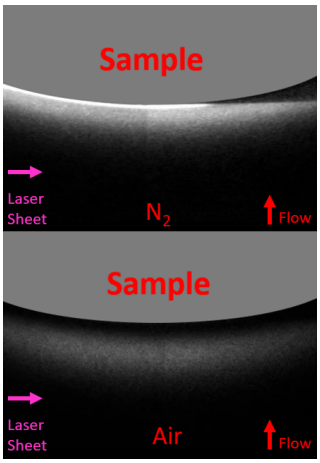

Figure 17: Comparison between the CN layers produced by ablating graphite in N_2 and air plasmas.

tween consumption and production of CN in the gas phase as you move out into the boundary layer.

Note that the LIF studies presented here are all very qualitative, due to the fact that no correction for the temperature field or for quenching effects was done. However, they do serve as an interesting initial set of results that illustrate the potential effectiveness of these techniques. Work is ongoing to correct the LIF measurements in order to generate quantitative measurements. An initial proposal on this front is to work within a saturation regime, where all of the LIF emission is due to photoionization and quenching effects need not be considered. This requires significant laser irradiance, but initial appears to be feasible.

8. Conclusions and Future Work

This report gives an overview of the current progress in optical emission spectroscopy and laser induced fluorescence efforts within the inductively coupled plasma facilities at the VKI and UT Austin. A study of the variation of the cyano radical across the flowfield in both facilities was conducted, and reveals interesting dynamics on its production and evolution.

There are a number of options proposed for future work. One currently underway is the coupled use of both OES and PLIF measurements to produce quantitative estimates of species profiles throughout the boundary layer. Additionally two photon LIF measurements of CO, atomic N, and atomic O are planned, again with the intent to produce quantitative species profiles across the extent of the reaction layer. Additional work on the comparison between OES data taken in the VKI and UT facilities is also planned, with NEQ and number density considerations at the forefront of this work. It is thought, that due to the relatively high pressure (1 atmosphere) in the UT facility, little to no chemical NEQ behavior should be expected. However, preliminary fitting of the CN spectra reveals that this is potentially not the case, showing the same degree of NEQ as seen in the spectra from the VKI facility at lower powers. Therefore, an investigation of the impact of facility power on the extent of chemical NEQ may be worth exploring.

It is also proposed to perform similar LIF based studies at the VKI, starting in the summer of 2023. It is again hoped that similar LIF work performed in two different ICP facilities will expand the overall range of accessible conditions, and allow for a fruitful collaborative exchange.

References

[1] B. Helber, Material Response Characterization of Low-density Ablators in Atmospheric Entry Plasmas, Thesis (2016).
[2] H. O. S. Gu, Capabilities and limitations of existing hypersonic facilities, no. Vol. 13, 2020.
[3] B. Greene, Simulation of Pyrolysis Gas in a Charring Ablative Thermal Protection Material Using Gas Injection through a Porous Graphite Sample, Thesis (2018).
[4] N. C. J. Murray, G. Kale, Comparison of CN in the Boundary Layer of Ablating Graphite in High-Temperature Air and Nitrogen Flows using PLIF, 2022.
[5] F. G. M. A. Luersen, R. Le Riche, A constrained, globalized, and bounded Nelder-Mead method for engineering optimization, 2003.
[6] Y. A. S.J. Baek, A. Park, J. Choo, Baseline correction using asymmetrically reweighted penalized least squares smoothing, no. Vol. 140, 2014.
[7] F. G. M. A. Luersen, R. Le Riche, A constrained, globalized, and bounded Nelder-Mead method for engineering optimization, 2003.
[8] T. M. B. Helber, A. Turchi, Determination of active nitridation reaction efficiency of graphite in inductively coupled plasma flows, no. Vol. 125, 2017.
[9] T. E. M. A. Turchi, J. J. Matesanz Saiz, O. Chazot, Duplication of hypersonic stagnation-region aerothermochemistry and gas-surface interaction in high-enthalpy ground testing, no. Vol. 62, 2021.

Supersonic off-stagnation point ground testing of atmospheric entry

Sander Holum

Aeronautics and Aerospace Department, von Karman Institute for Fluid Dynamics, Belgium, sander.holum@vki.ac.be

Supervisor: Olivier Chazot

Professor, Aeronautics and Aerospace Department, von Karman Institute for Fluid Dynamics, Belgium, olivier.chazot@vki.ac.be

University Supervisor: Parente Alessandro

Professor, Aéro-Thermo-Mécanique Department, Université Libre de Bruxelles, Belgium , Alessandro.Parente@ulb.be

Advisor: Bernd Helber

Senior Research Engineer,Aeronautics and Aerospace Department, von Karman Institute for Fluid Dynamics, Belgium, bernd.helber@vki.ac.be

Abstract

Space debris littering Low Earth Orbit (LEO) greatly threatens the space industry. Without urgent action, small collisions will lead to an exponential growth of space debris and leave LEO completely unusable. The lowest cost method to ensure the removal of current and future space debris is an atmospheric burn-up during reentry. However, due to uncontrolled trajectories and wildly different materials, one can not predict if a full burn-up will occur for all reentries. The old philosophy of reentry design focuses on the highest heat flux possible to design spacecraft for survival, new methodologies need to allow for design for demise (D4D). Supersonic off-stagnation point testing needs to be developed to access these low heat fluxes away from the stagnation point and to closely mimic the reentry situation, including mechanical shear. The experiments will be done on a flat plate attached to a supersonic nozzle in the VKI's inductively coupled plasma (ICP) facility, the Plasmatron. This allows for the recreation of the mechanical and thermal environment during reentry away from the stagnation point. This can also be useful for more conventional reentry vehicles to reduce safety margins or increase trajectory control. Due to the harsh environment recreated, intrusive and complete measurements are difficult. To enhance the extracted data, Computational Fluid Dynamics (CFD) will be done in conjunction to categorize the off-stagnation flow field in the Plasmatron. The final goal of this Ph.D. is to: 1. Develop a systematic methodology to test demise- and TPS-materials in ground testing facilities in supersonic off-stagnation point configuration. 2. Improve/develop ground testing to flight extrapolation 3. Make a material database based on the developed testing methodology.

Keywords: Atmospheric entry, high enthalpy flows, Off-stagnation point, Inductively coupled plasma facility, Space debris

Dynamic flight-to-ground duplication of atmospheric entry stagnation point flows

Roemer Spreij

PhD student, Aeronautics and Aerospace Department, von Karman Institute for Fluid Dynamics, Belgium, roemer.spreij@vki.ac.be

Supervisor: Olivier Chazot

Professor, Aeronautics and Aerospace Department, von Karman Institute for Fluid Dynamics, Belgium, olivier.chazot@vki.ac.be

University Supervisor: Valentijn De Smedt

Associate professor, Department of Electrical Engineering (ESAT), KU Leuven, Belgium, valentijn.desmedt@kuleuven.be

University Supervisor: Jurgen Vanhamel

Assistant professor, Department of Space Engineering, TU Delft, The Netherlands, J.A.M.Vanhamel@tudelft.nl

Abstract

Any object entering an atmosphere experiences changing conditions along its trajectory. Yet ground tests in Plasma Wind Tunnels do not often reflect this reality. This research aims to develop a methodology for dynamic flight-to-ground duplication, based on the Local Heat Transfer Simulation (LHTS) framework [1]. The proposed method will enable the correct representation of the trajectory heating 'history' during a ground test, and thus allow a better assessment of Thermal Protection Systems (TPSs), space debris demisability, and of changing material properties (surface oxidation, emissivity, catalicity, ...) during the flight [2]. Achieving this requires the application of data-driven methods to expedite the current (static) flight-to-ground duplication procedure [3].
The methodology will be applied to the re-entry mission currently under development by the Aether Student CubeSat team at KU Leuven, who are designing a deployable heatshield with a flexible TPS (FTPS) for use on a CubeSat [4]. Initial estimates of the LHTS parameters (stagnation pressure, enthalpy and velocity gradient at the boundary layer edge) along the trajectories of several configurations of the Aether heatshield are given, based on simulations with ROVT (Royal Observatory and VKI Trajectory simulator). Post-shock conditions are computed with Mutation++ [5]. Surface conditions (heat flux, temperature) are estimated using engineering methods to aid mission design.

Keywords: ICP, Ground testing, LHTS, trajectory, CubeSat

References

[1] A. Kolesnikov, The concept of local simulation for stagnation point heat transfer in hypersonic flows - Applications and validation, in: Proceedings of the 21st Aerodynamic Measurement Technology and Ground Testing Conference, Fluid Dynamics and Co-located Conferences, American Institute of Aeronautics and Astronautics, Denver, CO, USA, 2000. doi:10.2514/6.2000-2515.

[2] C. Merhaben, B. Dias, M. Mendez, A. Turchi, Determination of Trajectory-Based Ground Testing Conditions for Space-Debris Materials by Means of a Data-Driven Approach, in: Proceedings of the 2nd International Conference on Flight Vehicles, Aerothermodynamics and Re-entry Missions & Engineering (FAR), ESA, Heilbronn, Germany, 2022.

[3] I. Sakraker, Aerothermodynamics of Pre-Flight and In-Flight Testing Methodologies for Atmospheric Entry Probes, Ph.D. thesis, Université de Liège (Feb. 2016).

[4] J. Vanhamel, N. Eaton, R. Spreij, Using fiber bragg gratings for shape monitoring and adjustment of a thermal protection system aboard a targeted re-entry cubesat, ESA, Heilbronn, Germany, 2022.

[5] J. B. Scoggins, V. Leroy, G. Bellas-Chatzigeorgis, B. Dias, T. E. Magin, Mutation++: MUlticomponent Thermodynamic And Transport properties for IONized gases in C++, SoftwareX 12 (2020) Article 100575. doi:10.1016/j.softx.2020.100575.

AEROACOUSTICS

Numerical investigation of noise radiated by helical Darrieus turbines in the operational regime

Kartik Venkatraman

Environment and Applied Fluid Dynamics department, von Karman Institute for Fluid Dynamics, Belgium
kartik.venkatraman@vki.ac.be

Supervisors: Christophe Schram and Julien Christophe

Professor, Environmental and Applied Fluid Dynamics Department, von Karman Institute for Fluid Dynamics, Belgium,
christophe.schram@vki.ac.be

Research Expert, Environmental and Applied Fluid Dynamics Department, von Karman Institute for Fluid Dynamics, Belgium,
julien.christophe@vki.ac.be

University Supervisor: Stéphane Moreau

Université de Sherbrooke, Canada, stephane.moreau@usherbrooke.ca

Abstract

The aeroacoustic characteristics of three different scaled helix-Darrieus vertical axis wind turbines with end plates and supporting structures are investigated at a fixed rotational speed of 3500rpm. A three-dimensional hybrid Lattice Boltzmann Method-Very Large Eddy Simulation (LBM-VLES) was performed using the PowerFLOW solver and coupled to an in-house aeroacoustic propagation code based on the Ffowcs Williams and Hawkings analogy for noise prediction. The predicted sound pressure levels show excellent agreement with the experimental spectrum and numerical predictions for the helix 45° turbine. Increasing the helix angle at a fixed rotational speed is shown to decrease loading on the blades and reduce both the tonal and broadband noise levels.

Keywords: Darrieus wind turbine, Tip speed ratio, blade-wake interactions, helix angle

1. Introduction

The urgent need to tackle climate change has lead to a growing interest in on-site generation, storage and distribution of electricity as a part of futuristic smart city projects. Vertical axis wind turbines (VAWTs) seem to be a promising prospect for on-site power generation on building rooftops and other areas with high wind potential [1].

However, typical Darrieus VAWT architectures such as the classical (Troposkein) and straight-bladed turbines show poor aerodynamic performance. An alternative concept is the helical VAWT first proposed by Gorlov in 1995. This architecture provides low torque fluctuation per rotational cycle, thereby minimizing the problems due to fatigue and vibrations and power output regulation [2]. The Quiet Revolution wind turbine company also claims that the helical design results in a lower noise signature compared to standard designs [3]. However, no detailed investigations on the impact of helix angle on aeroacoustics characteristics of helix Darrieus turbines are reported yet in the literature.

The majority of the numerical studies on Darrieus VAWTs have focused on H-Darrieus turbines (straight blades) such as by [4; 5; 6; 7; 8; 9]. Very few high-fidelity simulations exist in the literature that focused on Helical VAWTs and are mainly focused on the aerodynamics and wake evolution of the turbine [10; 11; 12; 13; 14]. Accounting for the complex aerodynamics of helical turbines requires high-fidelity 3D simulations capturing the key flow structures close to the blade and the interior of the rotor which is not found present in the literature. This study aims to evaluate the capability of hybrid LBM-VLES methodology to provide an accurate prediction of the

noise of a complete scaled model Helical VAWT with end plates and supporting structures.

The paper is organized as follows: the VAWT geometry used in this work is described in Section 2. The basic notions of terms related to VAWT flow physics are analyzed in Section 3. The numerical methodology is detailed in Section 4. Next, the results are discussed in Section 5 and finally, the conclusions are drafted in Section 6.

2. Baseline VAWT Model

Weber *et al.* [4] studied the noise radiated by 1 : 5 scale helical Darrieus rotors shown in Fig 2. All the models have 3 NACA0018 blades with a chord length of 0.05 m. The height and diameter of the rotor is 0.2 m. Microphone measurements were recorded at the anechoic facility in Institut für Prozessmaschinen und Anlagentechnik (IPAT), Erlagen at 1 m distance from the model at blade mid-span. All measurements were carried out with an inflow velocity of 15 m/s.

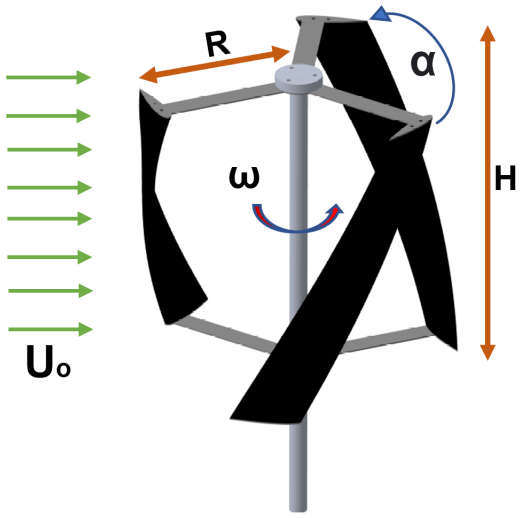

Figure 1: Model helix VAWT rotor studied by Weber *et. al* [15].



Figure 2: Different helix VAWTs studied by Weber *et. al* [15] a) Helix 45°, b) Helix 60° and c) Helix 120°.

3. VAWT Flow Physics

The relative velocity experienced by a VAWT blade is the vector sum of the incoming wind velocity U_o and the velocity of the advancing blade $R.\omega$ as shown in Fig 3. The tip speed ratio (TSR) defined as $R.\omega/U_o$ is the key parameter used to define the different flow regimes for VAWTs. The azimuthal angle θ is defined as an angle with respect to the positive y-axis.

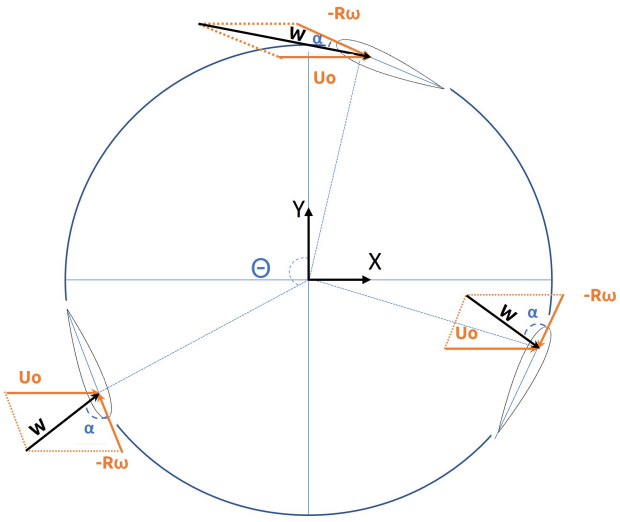

Figure 3: Velocity triangles experienced by Darrieus VAWT blades.

Both the magnitude of relative velocity and the angle of attack experienced by the blades vary over the azimuthal revolution of the blades. As per convention utilized by [16] and shown in Fig 4, the rotation of a Darrieus VAWT can be classified into four different phases. The windward phase between ($315° < \theta < 45°$), upwind phase between ($45° < \theta < 135°$), leeward phase between ($135° < \theta < 225°$), and downwind phase between ($225° < \theta < 315°$).

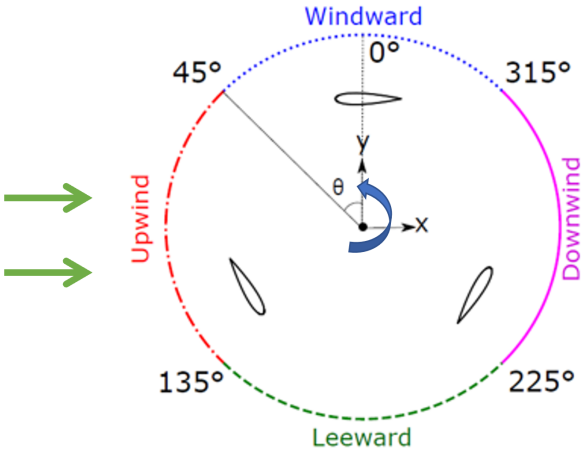

Figure 4: Different azimuthal phases of VAWT for a counter-clockwise rotation.

4. Numerical Model

The present computations are performed via the commercial LBM solver PowerFLOW version 6 from 3DS [17]. Fig 5 and Fig 6 show the simulation domain meant to mimic the anechoic environment at IPAT, Erlangen. Cylindrical zones are used to define different levels of grid refinement. The domain size is set to 50 D on all sides, where D is the diameter of the rotor. The domain comprises an inner rotating zone and outer stationary zone. The inner zone contains the wind turbine blades and the supporting structures and forms the body fixed local reference frame. A sliding mesh interface is imposed between the rotor and stator of the domain. The mesh has 80 million voxels, and the surface mesh comprises of surfels (surface grid elements). The domain is discretized using eleven variable refinement (VR) zones. High mesh refinement is defined close to the VAWT blades and supporting structures as seen in Fig 6 zoomed close to the VAWT blade, medium level refinement in the region close to the rotating zone and microphone probes, and low refinement further away as seen in Fig 6 for the entire domain. To match the experimental tip speed ratio (2.44), the rotational speed (3500 rpm) is imposed, along with the velocity at the inlet. At the outlet, the ambient static pressure is imposed (101,325 Pa).

5. Results

The numerical results are first presented in terms of forces on the blades and power prediction, discussing the effect of helix angle on the loading on the blades at a fixed rotational speed. Next, a visualization of the flow structures is presented using iso-contours of the Q-criterion. For understanding the noise radiation of the turbine, the noise spectra at a given observer position are calculated to first validate the model for the Helix 45° case, and then for all helix turbines.

5.1. Forces on blades

Figure. 7 shows the tangential forces on the blades and for the helix 45°, 60° and 120° turbines respectively. The blade loading decreases as the helix angle increases for a fixed rotational speed. As the helix angle increases, the turbine produces less power at fixed rotational speeds consistent with results similar to the power curves shown for different turbines by [13]. , and the helical twist reduces the next torque on the blade.

5.2. Iso-surfaces of Q-criterion

Figures 8, and 9 depict the iso-surfaces of the Q-criterion with an iso-value of 9500 at three different

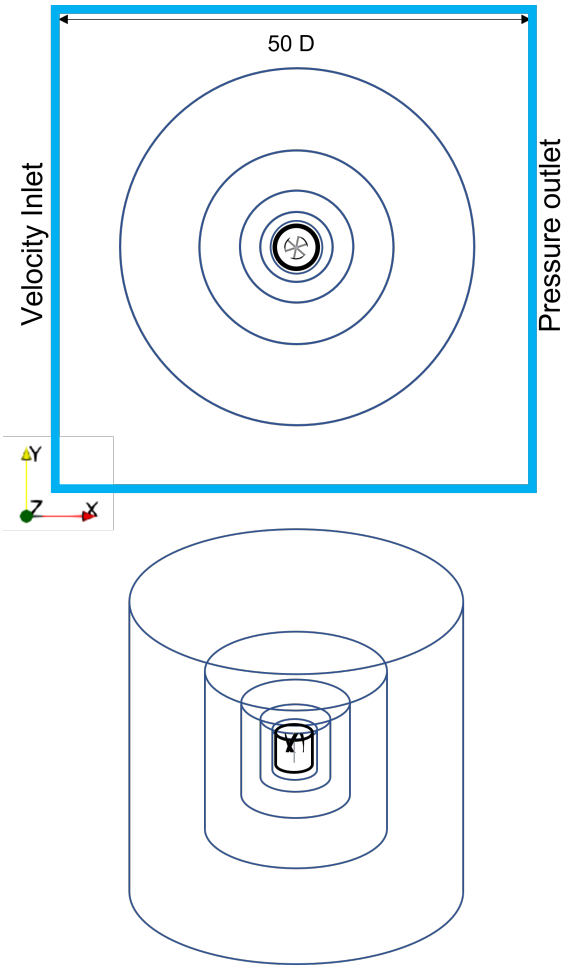

Figure 5: Simulation domain seen from top the top view showing ten cylindrical VR regions.

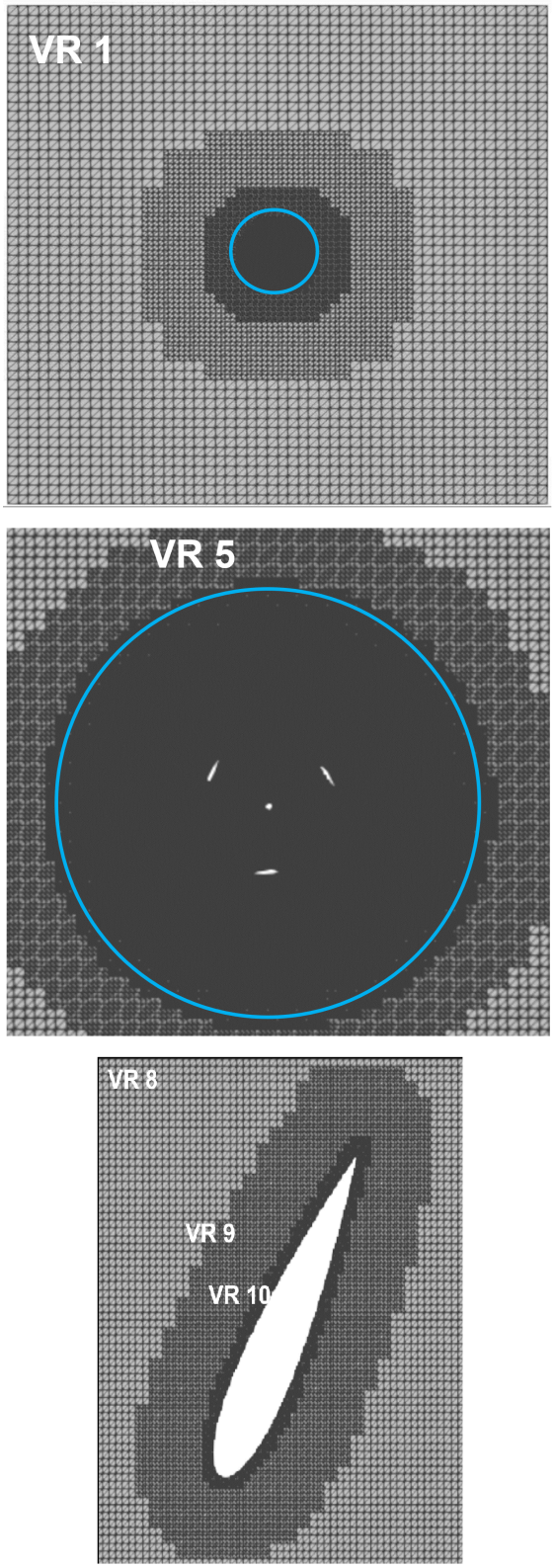

Figure 6: Simulation grid showing different levels of refinement.

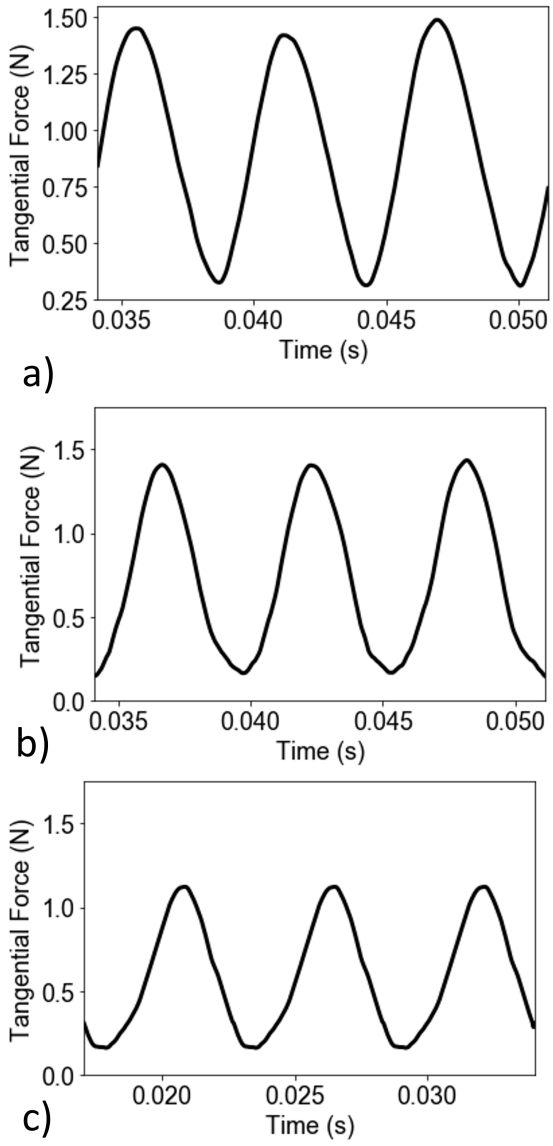

Figure 7: Averaged tangential forces for different helical turbines shown over the azimuthal revolution for a) Helix 45°, b) Helix 60° and c) Helix 120°.

azimuthal positions. A large number of flow structures are noticeable near the blade tip and inside the rotor. These structures are pushed towards the end plate and blade junction. This is consistent with the observations that the helix angle induces a mean vertical velocity in the span-wise direction [14]. Increasing the helix angle increases flow mixing inside the rotor due to a stronger three-dimensional flow. Significant flow structures are shed from the trailing edge of the blades during the leeward phase of rotation, especially for the Helix 120° case near the blade tip. Tip separation noise appears and blade wake interactions are noise generation mechanisms over the azimuthal revolution of the turbine.

5.3. Noise spectra

The experimental spectrum and the present noise prediction using the LBM approach coupled with the Ffowcs Williams and Hawkings (FW-H) analogy show good agreement for both the tonal peaks and broadband components as shown in Figure. 10. The increase in helix angle at a fixed rotational speed alleviates blade loading as seen in Fig. 7 and thereby reduce overall noise levels, as seen in the noise spectra shown in Figure. 11. A more than 10 dB decrease in the tonal level at the first blade passing frequency (BPF) of 175 Hz is seen. An enhanced flow mixing inside the rotor shown earlier in Fig. 9 causes a reduction in tonal peaks.

6. Conclusions

The effect of increasing the helix angle on a helical Darrieus vertical axis wind turbine (VAWT) was investigated at a fixed rotational speed. A 3D hybrid Lattice Boltzmann/Very Large Eddy Simulation (LBM-VLES) model was set up using PowerFLOW to simulate a complete scaled model helical Darrieus VAWT with end plates and supporting structures. The flow solution was then coupled to an in-house aeroacoustic propagation code SherFWH based on the FW-H analogy.

Increasing the helix angle also reduces the loading on the blades and decreases the power coefficient at a given rotational speed. The helix angle induces a spanwise flow and makes the flow inside the rotor three dimensional. The numerical predictions show an excellent agreement between the experimental noise spectrum, both for the tonal peaks at the BPF and the broadband noise levels for the helix 45° turbine. There is a decrease in the tonal peaks at BPFs for the helix 120° turbine due to enhanced flow mixing.

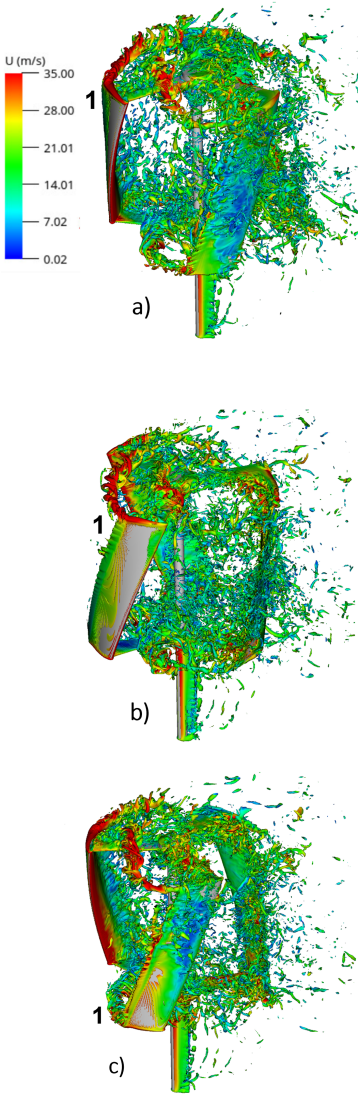

Figure 8: Instantaneous iso surfaces of Q-criterion showing the flow structures at different azimuthal positions for a helix 45° turbine.

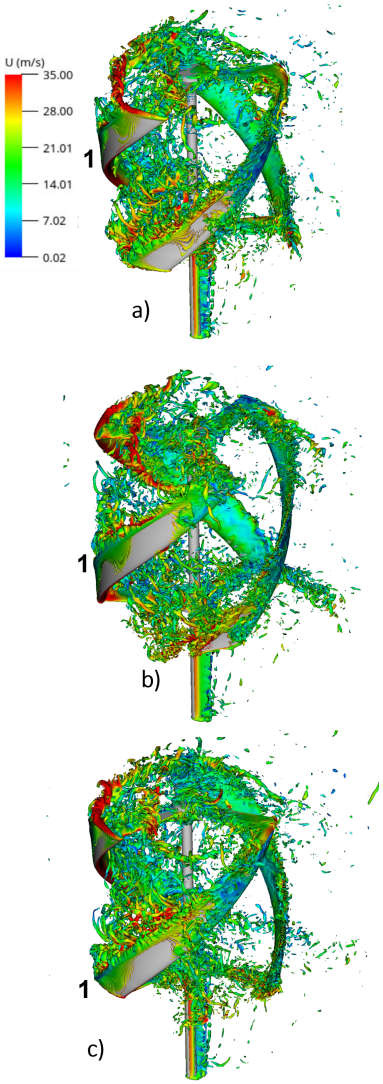

Figure 9: Instantaneous iso surfaces of Q-criterion showing the flow structures at different azimuthal positions for a helix 120° turbine.

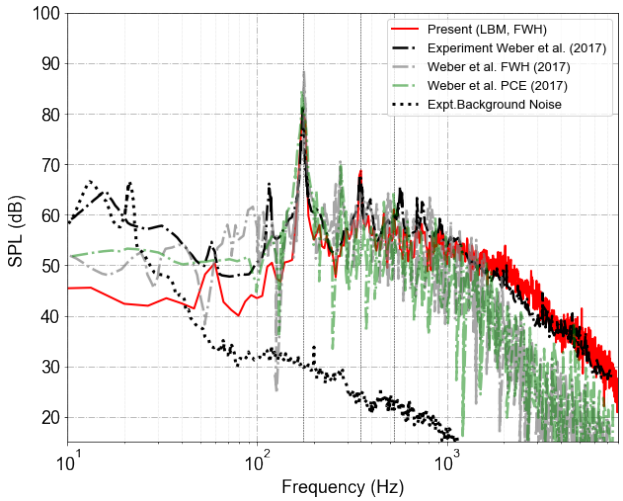

Figure 10: Noise spectrum for a Helical 45° Darrieus turbine for an observer located 1 m away, compared with experimental data and numerical simulations from [15].

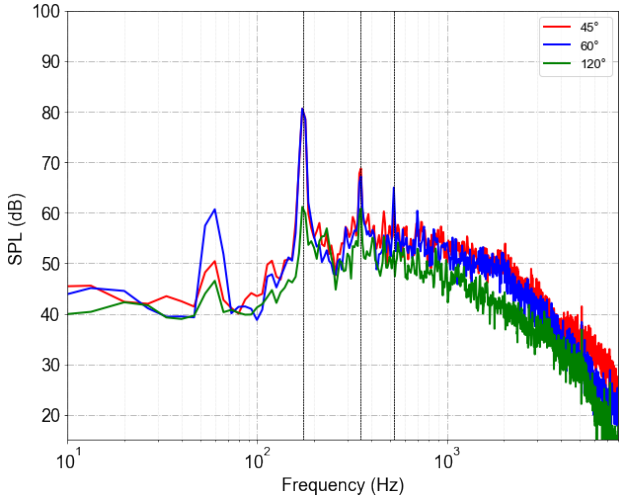

Figure 11: Noise spectrum at an observer located 1 m away with helix angles 45°, 60°, 120°.

Acknowledgments

The authors acknowledge the European Commission for its financial support through the project H2020-MSCA-ITN-2019 zEPHYR (Grant Agreement No. 860101).

References

[1] H. Riegler, HAWT versus VAWT: Small VAWTs find a clear niche, Refocus 4 (2003) 44–46.

[2] W. Tjiu, T. Marnoto, M. Sohif, M. Ruslan, K. Sopian, Darrieus vertical axis wind turbine for power generation I: Assessment of Darrieus VAWT configurations, Renewable Energy 75 (2015) 50–67. doi:10.1016/j. renene.2014.09.038.

[3] V. Power, QR6 helical Darrieus turbine, Available at `https://www.quietrevolution.com/` (2021).

[4] J. Weber, S. Becker, C. Scheit, M. Grabinger, J. Kaltenbacher, Aeroacoustics of Darrieus wind turbine, International Journal of Aeroacoustics 14 (2015) 883–902. doi:10.1260/1475-472X.14.5-6.883.

[5] M. Ghasemian, A. Nejat, Aero-acoustics prediction of a vertical axis wind turbine using large eddy simulation and acoustic analogy, Energy 88 (2015) 711–717. doi:10.1016/j.energy.2015.05.098.

[6] E. Ferrer, M. Viqueira Moreira, Insights into the aeroacoustic noise generation for vertical axis turbines in close proximity, Energies 13 (2020) 4148. doi:10.3390/en13164148.

[7] K. Venkatraman, S. Moreau, J. Christophe, C. Schram, Numerical investigation of the effect of inflow non-uniformity on the noise radiated by a vertical axis wind turbine, in: AIAA AVIATION Forum, 2021, pp. 1–14. doi:10.2514/6.2021-2216.

[8] K. Venkatraman, S. Moreau, J. Christophe, C. Schram, H-Darrieus vertical axis wind turbine power prediction using the Lattice Boltzmann approach, 56th 3AF International Conference on Applied Aerodynamics, Toulouse, France.

[9] L. Brandetti, F. Avallone, D. De Tavernier, B. LeBlanc, C. Simao Ferreira, D. Casalino, Assessment through high-fidelity simulations of a low-fidelity noise prediction tool for a vertical-axis wind turbine, Journal of Sound and Vibration 547 (2022) 117486. doi:10.1016/j. jsv.2022.117486.

[10] A. Alaimo, A. Esposito, A. Messineo, C. Orlando, D. Tumino, 3d CFD analysis of a vertical axis wind turbine, Energies 8 (4) (2015) 3013–3033. doi:10.3390/en8043013.
URL `https://doi.org/10.3390/en8043013`

[11] Q. Cheng, X. Liu, H. S. Ji, K. C. Kim, B. Yang, Aerodynamic analysis of a helical vertical axis wind turbine, Energies 10 (4) (2017) 575. doi:10.3390/en10040575.

[12] Z. Wang, Improvement of the aerodynamic performance of vertical axis wind turbines with leading-edge serrations and helical blades using cfd and taguchi method, Energy Conversion and Management 177 (2018) 107–121. doi:10.1016/j. enconman.2018.09.028.

[13] U. Divakaran, A. Ramesh, A. Mohammad, R. K. Velamati, Effect of Helix Angle on the Performance of Helical Vertical Axis Wind Turbine, Energies 14 (2) (2021) 393. doi:10.3390/en14020393.
URL `https://doi.org/10.3390/en14020393`

[14] M. Gharaati, S. Xiao, N. J. Wei, L. A. Martínez-Tossas, J. O. Dabiri, D. Yang, Large-eddy simulation of helical- and straight-bladed vertical-axis wind turbines in boundary layer turbulence, Journal of Renewable and Sustainable Energy 14 (5) (2022) 053301. doi:10.1063/5.0100169.
URL `https://doi.org/10.1063/5.0100169`

[15] J. Weber, M. Tautz, S. Becker, A. Hüppe, M. Kaltenbacher, Computational aeroacoustic simulations of small vertical axis wind turbine, in: INTER-NOISE and NOISE-CON Congress and Conference Proceedings, InterNoise16, Institute of Noise Control Engineering, Hamburg, Germany, 2016, pp. 4254–4262.

[16] A. Rezaeiha, I. Kalkman, B. Blocken, CFD simulation of a vertical axis wind turbine operating at a moderate tip speed ratio: Guidelines for minimum domain size and azimuthal increment, Renewable Energy 107 (2017) 373–385. doi:10.1016/j. renene.2017.02.006.

[17] Dassault-Systèmes, SIMULIA PowerFLOW User's Guide (2020).

Aerodynamic Performance and Acoustic Assessment of a Dual-Rotor Coaxial Drone Propulsion System

Erica Gallo

Environmental and Applied Fluid Dynamics Department, von Karman Institute for Fluid Dynamics, Belgium, mymail@vki.ac.be

Christophe Schram

Professor, AR/EA Department, von Karman Institute for Fluid Dynamics, Belgium, christophe.schram@vki.ac.be

Emanuele Garone

Professor, Department of Control Engineering and System Analysis, Brussels School of Engineering, Université libre de Bruxelles, Belgium, emanuele.garone@ulb.be

Abstract

A dual-rotor coaxial Urban Air Mobility propulsion system is experimentally investigated to provide noise/propulsive efficiency trade-off. Urban Air Mobility vehicles are likely to be large-scale deployed within a few years. In this scenario, multicopters are conceived as the most advantageous configuration as they offer greener and faster mobility solutions and high maneuverability. Multicopter propulsion systems usually comprise coaxial dual-rotors which can provide redundancy for components failure, as well as more increased flight endurance and payload with respect to single propellers. However, dual-rotor coaxial systems involve complex fluid-dynamics phenomena which make it difficult to predict the noise, let alone propose mitigation strategies. Hence, a significant scientific challenge towards quieter drones is the identification and prediction of the dominant sources of noise. To fill this knowledge gap, this research focuses on measuring and understanding the aerodynamic performance and acoustic features of different configurations of a dual-rotor coaxial model. The experimental setup has been designed, tested, and instrumented with aerodynamic sensors at the ALCOVES anechoic laboratory of von Karman Institute for Fluid Dynamics, Belgium. The experiments consist of a parametric investigation where we analyze the spacing between propellers, the rotational speed and direction, and the number of blades. The objectives will be identifying the optimal configuration in terms of noise vs. Figure of Merit. Furthermore, the characterization of the flow physics in the wake *via* Particle Image Velocimetry technique will be performed to provide new insight into the physical mechanisms. Eventually, the benchmark that will be generated is meant to support the validation of low- and high-fidelity numerical methods.

Keywords: drone noise, low-Re rotor aerodynamic, dual-rotor coaxial system

1. Introduction

While, in the last years, civil Unmanned Aerial Systems (UASs) also known as drones, have been mostly used for remote sensing and surveying, recent breakthroughs in battery technology and propulsion have allowed increasing endurance and payload, and therefore widening the possible range of applications. A new opportunity for the medical sector arises from drones' capacity to avoid urban traffic and swiftly transfer payloads, such as tissues or supplies, increasing transplant success rates [1; 2]. Similarly, package delivery by drones is expected to enable a reduction of traffic congestion in cities and indirectly improve air quality [3]. For the aforementioned applications, multicopters are the most widespread drone configuration for urban travel distances.

However, drone noise pollution can hinder the rapid growth of the technology as public acceptance is not a straightforward matter. Literature studies show that the perceived noise of drones is one of the main upsetting factors for society [4]. In their recent study,

Torija *et al.* carried out subjective analyses to analyze the human response to different drone sound emissions *via* online experiments [5]. Their findings are relevant for the minimization of the drone noise impact on citizens, even though enlarging the test cases to include the effects of the external environment is still needed to provide extended knowledge on the subject.

As new regulations and standardization are fundamental steps toward the inclusion of drones in the community, the new goal in aviation is the design and optimization of low-noise drone technologies [6].

Nowadays, besides the high level of noise emissions, coaxial propulsive systems on small-scale Urban Air Vehicles (UAVs) are interesting as the vehicle volume per thrust output is minimized. Empirical and theoretical research on co-axial configurations were initially reported by Coleman [7]. Nevertheless, these studies mainly concern full-size helicopters that generate different aerodynamic efficiency with respect to small-scale UAVs [8]. In fact, the chord-based Reynolds number Re_c of the small-scale rotors is in the order of 10^5. In this flow regime, a laminar separation bubble responsible for noise radiation can be produced on the blade suction side [9]. The induced drag on the blades becomes even more critical when considering co-axial configurations for the additional flow interactions [10; 11; 12]. The latter are associated with three phenomena:

- the potential field of the propellers interacting with each other,
- the tip vortices detachment from the upstream propeller interacting with the downstream propeller,
- and the wake generated by the upstream propeller interacting with the downstream propeller.

Experimental investigations are carried out to highlight the effects of such mechanisms on aerodynamic performance and acoustics, as well as to generate database benchmarks for optimization purposes. In their work, McKay *et al.* proposed an initial explanation of the mechanisms. They measured the acoustic and aerodynamic performance of different contra-rotating commercial propeller configurations over a wide range of RPM while varying the propeller spacing, the diameter and the blade number [13]. Results of overall sound pressure levels showed that configurations with mismatched blade numbers produced less noise. Similar findings were found when using the upstream propeller with a smaller diameter than the downstream one. A recent study on the optimum separation distance for minimum noise of contra-rotating rotors with zero net torque at hover was carried out by Chaitanya *et al.* [14]. Minimum noise was found in configurations with high aerodynamic efficiency, with separation distances z in the range 0.25 ¡ z/D ¡ 0.5, with D the diameter of the propellers. Analogous conclusions were found by [15]. In their work, they performed experiments and low-order modeling of stacked rotors varying two parameters, the axial distance offset and azimuthal angle offset between rotors, and keeping the blade shape fixed. Eventually, they concluded that the incorporation of variable pitch capabilities at the lower rotor could further improve the overall performance. On the other hand, an investigation of thrust and acoustic performance of a laboratory-scale, coaxial, corotating rotor in hover has been reported in [16]. In their work, the rotor thrust and sound were shown to be more dependent on rotor index angle than stacking distance.

The flow field characteristics of dual-rotor propellers were recently examined by [17] and [18] using Particle Image Velocimetry and high-speed digital schlieren. Overall, the better aerodynamic performance shown by the contra-rotating configuration can be associated with the minimization of the swirl losses.

Nevertheless, in all the above-mentioned studied, a thorough understanding of the interaction mechanisms, and the way they affect the aerodynamic performance and the sound emissions, is still unclear. Hence, this work proposes a parametric investigation of a dual-rotor coaxial system aimed at identifying an optimal configuration in terms of noise vs. thrust. In addition to sound directivity maps, we will provide insight into flow physics by measuring the wake *via* Particle Image Velocimetry technique.

2. Experimental setup

2.1. VKI ALCOVES anechoic laboratory

The experimental campaign is carried out in the ALCOVES anechoic room at the von Karman Institute for Fluid Dynamics, Belgium initially meant to perform simultaneous measurements of the aerodynamic performance and noise emissions of axial fans whose design and specifications are detailed in [10]. The cut-off frequency of the room is 200 Hz. The facility includes two anechoic environments separated by a modular wall partition that can be fitted with rotating components [19; 20]. The initial configuration

of the ALCOVES laboratory is shown in Figure 1. An auxiliary fan drives the flow in the wind tunnel creating a pressure difference across the rooms, and its noise propagation is prevented by acoustic treatments in the pipe which drives the flow.

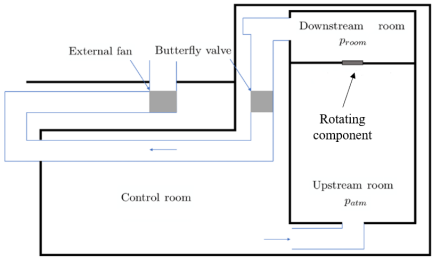

Figure 1: Alcoves facility scheme. Adapted from [21].

The Alcoves facility has been adapted to perform the experimental investigation of the dual-rotor system by removing the partition wall and creating a single environment for the tests.

2.2. *Multi-rotor propulsive system laboratory design*

The multi-rotor propulsion system has been designed, assembled, and partially manufactured at VKI for testing and evaluating the aerodynamic performance and acoustic signature.

The sketch of the setup and the dimensions are illustrated in Figure 2 The test setup is composed of two independent propulsive systems. The two test stands are placed behind each other and aligned on the same axis to minimize aerodynamic interactions and reduce acoustic scattering. The stand placed at the rear is designed with a long shaft supported with several bearings and passes through the first stand. The axial spacing between the front and rear propellers can be varied in a range of 0.5c and 3c (with c the chord of the propeller at its 75% midspan) by moving the front propeller on the long shaft. The front stand is composed of the same elements but the shaft had to be hollow in order to accommodate the long shaft from the rear stand. Furthermore, the long shaft aligns and holds together the rotor and the stator of the front motor. The hollow shaft is also aligned with means of bearings placed between it and the long shaft. Moreover, the presence of the two test stands allows independent change of the RPM and sense of rotation of the two propellers. Hence, both co- and contra-rotating configurations are analyzed. During the experimental campaign, the test stands are shielded by a fairing (see Figure 5).

The experimental tests will be carried out using 2- and 3-blades Mejzlik propellers 13”x4.2 model.

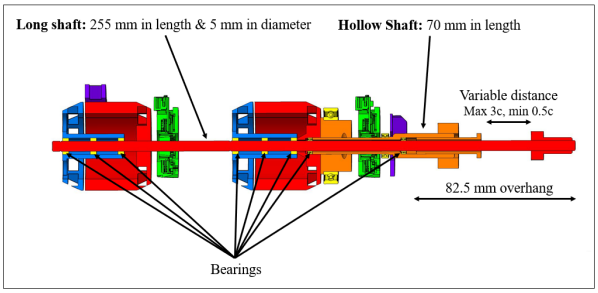

Figure 2: Scheme of multi-rotor setup.

To limit the overheating of the motors, the setup includes an active cooling system, in addition to the passive cooling coming from air movement generated by means of the motors and the cold air flow generated by the propellers. The cooling system is connected to a cold inflow of air, that comes from a pressure line in the ALCOVES facility and envelopes the instrumentation within it (see figure 3). Motors 1 and 2 along with the load-cell implement each a thermo-couple, recording their respective temperature.

The picture of the setup is shown in Figure 4.

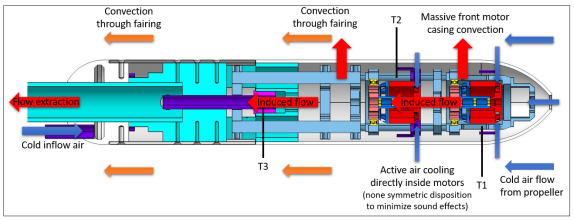

Figure 3: Active and passive cooling system.

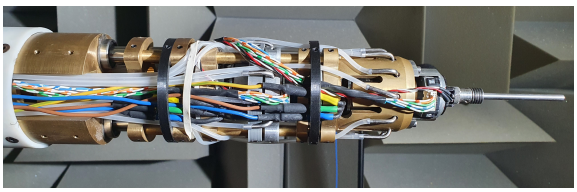

Figure 4: Bullet shape setup.

The test stands are mounted on a supporting structure (see Figure 5) designed to guarantee high stabilization along the vertical and horizontal axis. Hence, vibration-damping elements are mounted on the structure. The structure was mainly designed and manufactured to be installed at the back of the setup in or-

der to minimize noise-scattering effects. The structure is covered by acoustic foam during the experimental tests.

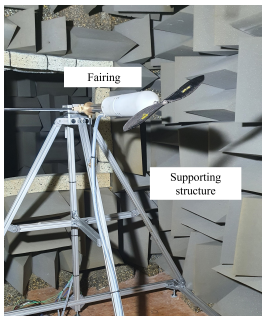

Figure 5: View of the setup adapted in the ALCOVES facility.

2.3. *Instrumentation*

Aerodynamic

Both test stands are equipped with the necessary sensors to measure the aerodynamic performance of the system, shown in Figure 6. More specifically, the rotational speed is measured by means of two tachometers which are two reflective sensors (VISHAY TCRT500). The latter are composed of an infrared emitter and a phototransistor. By placing a reflective surface on the respective shafts, we can measure the frequency at which they are rotating, hence their RPM. The propellers' phase angle is detected by two encoders CUI Devices AMT 22 type. The encoders ensure an accuracy of 0.2° up to 8000 RPM, and they allow control and vary the phase between the front and rear propellers while co-rotating at the same RPM.

The selected motors are T-Motors AT2814 Long Shaft, typical of small UAV applications. Their maximum range of rotation is 10000 RPM, exploiting 70% of the motor power. The motors are controlled using Scorpion Tribunus II 12-80A ESC SBEC controllers.

Furthermore, the overall thrust of the system is measured employing a single Futek LCM100 (FSH03828) loadcell that is placed between the rigid structure of the setup and the free two test stands that are guided with two low friction balls sleeves, shown in Figure 6(b). In order to minimize the impact of induced drag created by the fairing, the fairing is completely decoupled from the load cell.

Finally, the torque is measured by Futek QTA141 (QSH01827) sensors. The latter are hollow reaction torque sensors that are attached between a rigid part of the setup and the stator of each motor and are supported by means of low-friction bearings to minimize extraneous loads.

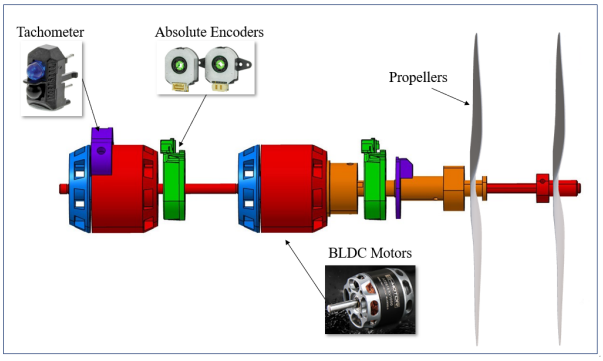

(a)

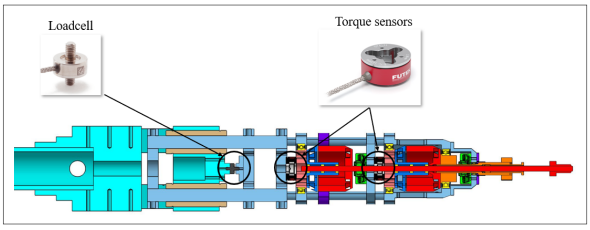

(b)

Figure 6: Schematic of sensor measurements setup.

For the commissioning of the setup, it was important to check that all the aerodynamic sensors were gathering the aerodynamic data of the propellers alone without the influence of the system. Initially, the sensitivity to temperature variation was checked. In detail, this characterization was meant to observe the variation of torque and thrust for different temperatures: each motor was turned long enough to let it heat up. The cooling system was turned on with the pressure line set to about 0.5 bar, which allowed the temperature to rise and then stabilize at a temperature inferior to 36°C (above this temperature the motors can be damaged).

Thereafter, to check the influence of the system on the load-cell measurements, a calibration was realized using a pulley and weights. The pulley was fixed directly to the support using Bosch profiles (see figure 7). A cable was attached to the axis of the Motor 1, allowing the transfer of the stress to the load-cell.

Eventually, the load cell functioning was also compared with the 2-blade Mejzlik propeller 13"x4.2 thrust measurements with data provided by Mejzlik. The tests were carried out at different rotational speeds: 4000 RPM, 5000 RPM, 6000 RPM, and 7000



Figure 7: Load-cell calibration with a pulley

RPM.

The torque-meters of the setup will be calibrated to check the influence of the system as well. However, given that the torque-meters are already installed deep inside the bullet-shaped support, it is not possible to realize a calibration by blocking the axis of the motors and imposing a known couple. A possible solution is to realize unloaded tests for each motor.

Acoustic

A preliminary assessment of the methodology has been performed. The main objective was to observe the ingestion of the propeller wake. In fact, in a closed environment, the wake generated by the rotors propagates, and it is re-ingested by the rotor [15; 22]. This phenomenon has an impact on the acoustic measurements, thus pre-recirculation data are usually isolated and considered for comparison among different configurations.

In this experimental campaign, the auxiliary fan of ALCOVES is expected to ideally ingest the propeller wake at a certain operational point. Consequently, different tests were realized to observe the spectrograms. Initially, the tests were carried out at 7000 RPM in a contra-rotating configuration.

The acoustic measurements were realized using two G.R.A.S. microphones. Microphone 1 was placed at 45° from the motor axis, while microphone 2 was placed at 90° from the motor axis, in the plane of the propellers, at a height of 1.50 m. (see Figure 8). The signal is acquired over 60 s for each test. The sampling frequency f_s used for the acquisition *via* LabView software was set at 51200 Hz.

Future noise experiments will be performed using microphones located in the far field. In detail, 24 microphones will be fitted on an automatic traverse system designed at VKI. Hence, the sound directivity can be investigated by moving the microphone guides vertically in a range of 1.5 m. A schematic view of the measurement setup, along with the dimensions, is shown in Figure 9.

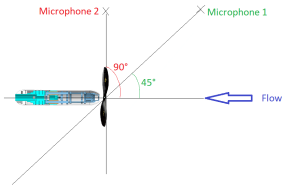

Figure 8: Scheme of the positions of the G.R.A.S. microphones.

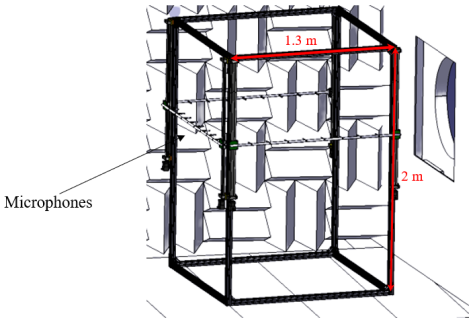

Figure 9: View of the microphones measurement traverse system in the ALCOVES facility.

3. Data analysis

The figure of merit (*FM*) will be used to compare the efficiency of different dual-axis configurations. The *FM* indicates the ratio of the ideal power needed to hover with respect to the actual power. The detailed definition of *FM* for a dual-axis rotors system is reported in [8; 23].

Moreover, the evaluation of the noise radiation is performed by calculating the Sound Pressure Level (SPL) [dB], which is computed as follows:

$$SPL = 10 \log_{10} \frac{PSD\Delta f}{p_{\text{ref}}^2}, \tag{1}$$

where the PSD [dB/Hz] indicates the Power Spectral Density of the signal, Δf [Hz] is the frequency resolution of the signal, and $p_{\text{ref}} = 20 \cdot 10^{-6}$ [Pa] is the reference pressure. The PSD is computed using Welch's method [24].

Finally, the characterization of the wake produced by the dual-axis system will be performed *via* Particle Image Velocimetry. The appropriate technique for the analysis will be selected, and described in the final paper.

4. Preliminary results

4.1. Wake circulation effect

The re-ingestion of the wake produced by rotors in a closed environment is shown to increase the broadband and tonal noise [22]. To observe the phenomenon, initial tests of contra-rotating rotors at 7000RPM were realized (installing and removing the partition wall). The time-frequency analysis for these tests is shown in Figures 10 and 11. However, the results do not show any evidence of ingestion of the propeller wake. There is a chance that the ingestion starts rapidly and that it is covered by the acceleration phase of the motors (from about 10s to 20s).

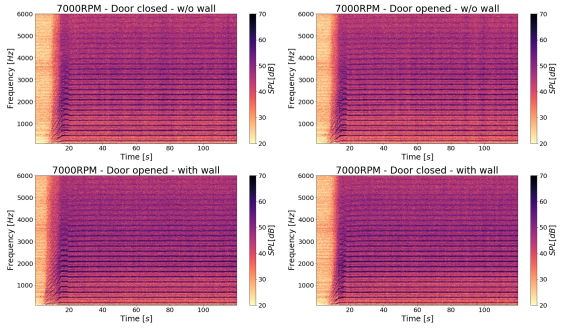

Figure 10: Time-frequency analysis for the acquisition of contra-rotating propellers at 7000 RPM with microphone 1 (45° from the motor axis)

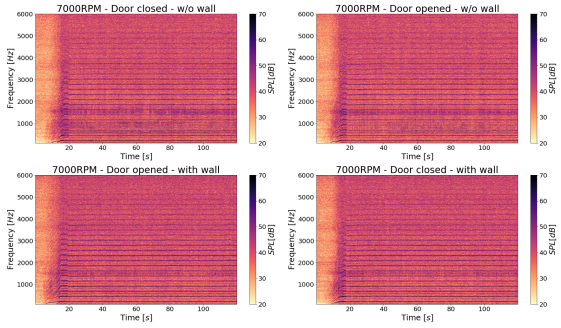

Figure 11: Time-frequency analysis for the acquisition of contra-rotating propellers at 7000 RPM with microphone 2 (90° from the motor axis)

4.2. Acoustic

As part of the preliminary assessment of the experimental measurements, an analysis of the sound emitted by the dual-axis coaxial system at 7000 RPM has been performed, as stated in Section 2.3. Figure 12 shows the SPL measured at microphone 2 (see 8) for the different components of the propulsive system to understand their impacts on the overall system noise. In detail, it is possible to observe the background noise, along with the one produced by the auxiliary fan and the cooling system. The latter emits a broadband spectrum at a very high frequency with a maximum SPL of 35 dB. Additionally, the noise produced when the motors are activated with and without the auxiliary fan running is illustrated. The auxiliary fan has no impact on the noise produced by the motors, as the higher tonal peak is measured when *front* and *back* motors are operating. Finally, the noise measured by the isolated *front* and *back* propellers, and contra-rotating configuration for two different distances (0.5c and 1c, with c the chord at 75% length l of the 13”x4.2 Mejzlik propeller blade in Figure 12(a)) has been measured. Higher tonal noise is measured at the third BPFs and other harmonics when the system is in a contra-rotating configuration at 0.5c distance, as emerged from the literature survey.

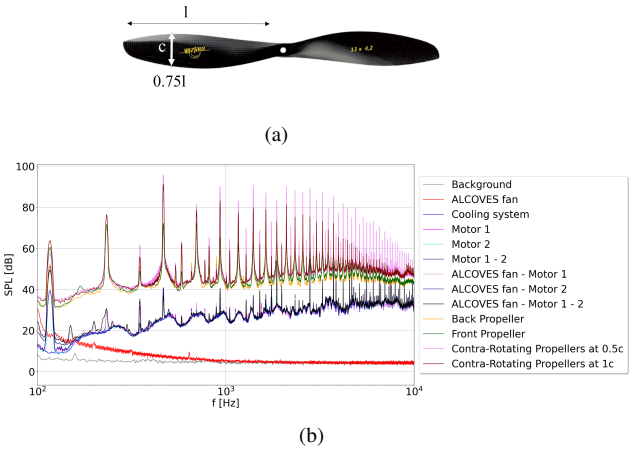

Figure 12: Scheme of a) c, chord at 75% length l of the 13”x4.2 Mejzlik propeller blade used as propeller spacing reference and b) SPL measured of single components of the setup, isolated *front* and **back** propellers, and dual-axis contra-rotating configuration at 7000 RPM at distances 0.5c and 1c.

5. Discussion

Dual-rotor propulsion systems represent a favorable solution for drone technology given the opportunity to improve the efficiency with respect to single rotors. Although those possible benefits, the dual-rotor co-, and contra-rotating systems are responsible for high levels of noise emissions. With this work, we aim at investigating an optimal solution in terms of acoustic signature and aerodynamic performance, whilst interpreting the flow physics involved. A dual-axis rotor propulsive system setup, equipped with aerodynamic measurement sensors, has been designed, manufactured, and assembled at VKI, and preliminary analysis has been carried out to assess the functionality.

The commissioning of the setup involved the calibration of the sensors, the investigation of the wake recirculation phenomenon produced by the rotors in the laboratory, as well as acoustic analysis of different components aimed at evaluating their impact on the final measurements.

In this preliminary investigation, the ingestion by the system of its wake is not observed by the time-frequency analysis, and further analysis is needed to clarify this aspect. Furthermore, it emerges from the acoustic analysis that higher tonal peaks are measured for contra-rotating configuration, specifically if the spacing between rotors is minimized.

Future investigations consits of a parametric investigation of different configurations based on propeller blades, rotational speed, the direction of rotation, and propeller distance will be reported in terms of acoustic and aerodynamic terms. Furthermore, the flow physics of the wake generated by the system will be studied using Particle Image Velocimetry.

The expected outcomes of this research are:

- the identification of the optimal configurations noise vs. performance.
- the analysis of the wake properties
- the generation of a unique benchmark that will be used for numerical simulations.

References

[1] F. Yakushiji, K. Yakushiji, M. Murata, N. Hiroi, K. Takeda, H. Fujita, The quality of blood is not affected by drone transport: An evidential study of the unmanned aerial vehicle conveyance of transfusion material in japan, Drones 4 (1) (2020) 4.

[2] J. R. Scalea, T. Pucciarella, T. Talaie, S. Restaino, C. B. Drachenberg, C. Alexander, T. A. Qaoud, R. N. Barth, N. M. Wereley, M. Scassero, Successful implementation of unmanned aircraft use for delivery of a human organ for transplantation, Annals of surgery 274 (3) (2021) e282–e288.

[3] R. Kellermann, T. Biehle, L. Fischer, Drones for parcel and passenger transportation: A literature review, Transportation Research Interdisciplinary Perspectives 4 (2020) 100088.

[4] A. J. Torija, C. Clark, A psychoacoustic approach to building knowledge about human response to noise of unmanned aerial vehicles, International Journal of Environmental Research and Public Health 18 (2) (2021) 682.

[5] A. J. Torija, R. K. Nicholls, Investigation of metrics for assessing human response to drone noise, International Journal of Environmental Research and Public Health 19 (6) (2022) 3152.

[6] P. Candeloro, D. Ragni, T. Pagliaroli, Small-scale rotor aeroacoustics for drone propulsion: A review of noise sources and control strategies, Fluids 7 (8) (2022) 279.

[7] C. P. Coleman, A survey of theoretical and experimental coaxial rotor aerodynamic research, Tech. rep. (1997).

[8] M. Ramasamy, B. Johnson, J. G. Leishman, Understanding the aerodynamic efficiency of a hovering micro-rotor, Journal of the American Helicopter Society 53 (4) (2008) 412–428.

[9] G. Romani, E. Grande, F. Avallone, D. Ragni, D. Casalino, Performance and noise prediction of low-reynolds number propellers using the lattice-boltzmann method, Aerospace Science and Technology 125 (2022) 107086.

[10] M. Bilka, J. Anthoine, C. Schram, Design and evaluation of an aeroacoustic wind tunnel for measurement of axial flow fans, The Journal of the Acoustical Society of America 130 (6) (2011) 3788–3796.

[11] S. Yoon, H. C. Lee, T. H. Pulliam, Computational study of flow interactions in coaxial rotors, in: AHS Technical Meeting on Aeromechanics Design for Vertical Lift, no. ARC-E-DAA-TN24718, 2016.

[12] R. Jung, M. J. Kingan, P. Dhopade, R. N. Sharma, Investigation of the interaction tones produced by a contra-rotating unmanned aerial vehicle propeller, in: 28th AIAA/CEAS Aeroacoustics 2022 Conference, 2022, p. 2832.

[13] R. S. McKay, M. J. Kingan, R. Go, Experimental investigation of contra-rotating multi-rotor uav propeller noise, in: Proceedings of ACOUSTICS, Vol. 10, 2019.

[14] P. Chaitanya, P. Joseph, S. Prior, A. Parry, On the optimum separation distance for minimum noise of contra-rotating rotors, Journal of Sound and Vibration (2022) 117032.

[15] S. Whiteside, N. Zawodny, X. Fei, N. A. Pettingill, M. D. Patterson, P. Rothhaar, An exploration of the performance and acoustic characteristics of uav-scale stacked rotor configurations, in: AIAA Scitech 2019 Forum, 2019, p. 1071.

[16] C. E. Tinney, J. Valdez, Thrust and acoustic performance of small-scale, coaxial, corotating rotors in hover, AIAA Journal 58 (4) (2020) 1657–1667.

[17] N. Han, Z. Zhang, H. Hu, An experimental investigation on the aerodynamic and aeroacoustic characteristics of dual-rotor propellers for uav applications, in: AIAA AVIATION 2022 Forum, 2022, p. 3892.

[18] J. A. Valdez, C. E. Tinney, The unsteady wake produced by a coaxial co-rotating rotor in hover, in: AIAA SCITECH 2022 Forum, 2022, p. 2166.

[19] J. Dominique, J. Christophe, C. Schram, R. Corralejo, An experimental multi-ports methodology for fan installation effects investigation, in: 24th AIAA/CEAS Aeroacoustics Conference, 2018, p. 3926.

[20] A. Zarri, J. Christophe, C. F. Schram, Low-order aeroacoustic

prediction of low-speed axial fan noise, in: 25th AIAA/CEAS Aeroacoustics Conference, 2019, p. 2760.
[21] A. Zarri, Aerodynamic and acoustic investigation of automotive fan-driven cooling systems, Ph.D. thesis, École Centrale de Lyon, France (June 2021).
URL http://www.theses.fr/2021LYSEC023
[22] D. Weitsman, J. H. Stephenson, N. S. Zawodny, Effects of flow recirculation on acoustic and dynamic measurements of rotary-wing systems operating in closed anechoic chambers, The Journal of the Acoustical Society of America 148 (3) (2020) 1325–1336.
[23] J. G. Leishman, M. Syal, Figure of merit definition for coaxial rotors, Journal of the American Helicopter Society 53 (3) (2008) 290–300.
[24] O. M. Solomon Jr, Psd computations using welch's method, NASA STI/Recon Technical Report N 92 (1991) 23584.

Aerodynamic and aeroacoustic installation effects of building-integrated wind turbines

Rui Gonçalves

Environmental and Applied Fluid Dynamics Department, von Karman Institute for Fluid Dynamics, Belgium, rui.goncalves@vki.ac.be

Supervisor: Christophe Schram

Professor, Environmental and Applied Fluid Dynamics Department, von Karman Institute for Fluid Dynamics, Belgium, christophe.schram@vki.ac.be

University Supervisor: Kees Venner

Full Professor, Engineering Fluid Dynamics, University of Twente, the Netherlands, c.h.venner@utwente.nl

Abstract

With the need to use ducted wind turbine configurations for microgeneration of energy in the urban environment, it is important to be able to accurately predict the noise produced by such a device. A tool to calculate the leading and trailing edge broadband noise of a rotor using Amiet's theory is discussed for this purpose.

Keywords: Wind Turbine, Aerodynamics and Aeroacoustics, Diffuser-Augmented Wind Turbine, Ducted Acoustics

1. Introduction

Facing the trends of concentration of population in large urban centers and the ever-increasing domestic energy consumption, energy management, and sustainable development create discussion about what the energy sources should be, and where they should be located [1]. Furthermore, the demand for carbon neutrality forces us to seek renewable energy sources to reduce dependence on one of the main responsible for carbon emissions, fossil fuels. The transition is already underway, with many European countries consuming more than half of their energy from renewable sources, including wind, hydro, biomass, and solar.

Harvesting wind energy in an urban environment poses challenges, such as maintaining high energy yields, or the inconvenience caused to the population due to noise and visual pollution. However, the integration of turbines within buildings, a concept coined as Building-Integrated Wind Turbine (BIWT), could unlock some doors and be the solution that allows residents inside urban centers to own production of electricity to offset their own needs and consumption.



Figure 1: Example of distinct concepts of BIWT.

The main drawback of installing a wind turbine (WT) in an urban environment is the noise generated during the energy production, which depends on its mechanical and aerodynamic noise. The sound propagation also plays an important role in the perceived sound in adjacent buildings, people living inside the building itself, and on the street/pedestrian level. As cities usually have regulations imposing a maximum noise limit, especially strict at night, noise is a problem that must be dealt with under the penalty of im-

peding the installation of WT.

In order to be able to numerically test aerodynamic noise, it is first necessary to calculate the aerodynamic behavior. To reliably identify noise sources, it is necessary to calculate small pressure fluctuations that propagate in the form of acoustic pressure. Due to the difficulty of calculating such small fluctuations (orders of magnitude lower than the true static pressure), it is often advantageous to use aeroacoustic analogies to simplify sound sources.

The ultimate goal of this study is to consider both aerodynamic and aeroacoustic effects of wind turbines when integrated on buildings in urban environment, in particular for the Diffuser-Augmented Wind Turbine (DAWT) configuration.

2. Diffuser Augmented Wind Turbine

Different configurations can sometimes offer big performance improvements. In Figure 2, a particular example of ducted WT can be seen, in which the casing used is shaped as a diffuser. The diffuser-augmented wind turbine is a ducted configuration that uses a divergent outlet shape, that delays the flow separation downstream of the rotor, lowering the pressure behind the rotor [2].

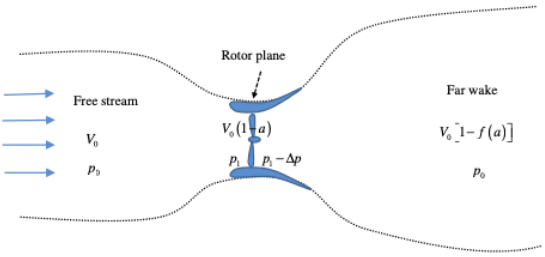

Figure 2: Diffuser-Augmented Wind Turbine Schematic [3].

This effect allows capturing airflow from a greater area with the same rotor size, resulting in higher flow velocities that will improve the Power Coefficient (Cp), as can be observed in Figure 3. Other advantages such as a wider range of operation curve with maximum Cp and possible noise muffling due to the introduction of the casing can be observed. However, it is necessary to evaluate this question and the emergence of trailing edge noise sources in the diffuser.

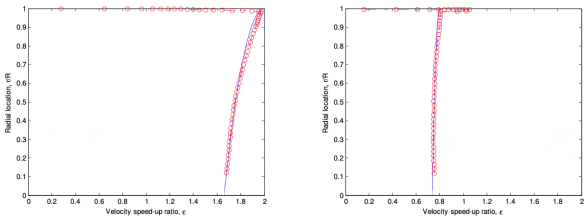

Figure 3: Velocity Speed-up at 0.0 and 1.0 Thrust Coefficient (left and right respectively) [3].

An alternative explanation for the flow acceleration is provided by [4], in which the resultant of aerodynamic forces acting on the diffuser causes circulation, ultimately projected towards the interior resulting in higher induced velocities than the incoming flow.

3. Methods to predict aerodynamic noise

The determination of noise sources from the operation of wind turbines can be done through different methods. Given the difference in complexity, there is associated a different level of fidelity which results in variable computational costs.

Due to the real size of these devices and the various scales at which the problem can be analyzed, it is necessary to reduce the focus into smaller parts, by subjecting the models to adequate assumptions and simplifications.

The scale of the domain depends on the type of problem, and will influence what kind of method should be considered to resolve in a reasonable amount of time. The domain can be as small as a blade or airfoil, or as large as an urban or rural landscape.

The methods to calculate noise sources can be classified into three big categories, by level of fidelity:

- Direct Approach
- Hybrid Approach
- Analytical Approach

The *Direct* approach is regarded as the most accurate, directly calculating the sounds emitted from the source and propagated to a predetermined listener position. As this requires to fully resolve the flow field down to the tiny acoustic pressure perturbations and small-scale turbulent structures, the highly refined mesh exponentially increases the computational requirements. This makes this option unsuitable for most engineering applications. Direct Numerical Simulation (DNS) and Lattice Boltzmann Method

(LBM) are examples of direct aeroacoustic numerical methods.

The *Hybrid* approach consists of using two different solvers to calculate the flow and the acoustic domain separately.

The flow solver is used to calculate the flow field and record the noise sources in the domain. Typical CFD solvers used in this scheme include RANS, URANS, DES and LES, but a wide range of possibilities are available, depending on the accuracy sought, the geometry or even the sound generation mechanism. The acoustics solver focuses on determining the propagation of the previously calculated acoustic sources.

The following methods can be used as acoustic solvers as part of a hybrid approach: BEM, FVM, FEM or integration schemes (FWH).

Given the concept of hybrid approach, the output of the flow solver will be used as input for the acoustic solver. Due to this coupling, the better the accuracy of the flow solver used, the more accurate the determination of the noise sources to be propagated. Once again, this option results leads to a compromise between quality of the results and computational effort/time.

As we move from a *Direct* to *Analytical* approach, we significantly reduce computational costs and fidelity, moving towards methods that often include empiricism and rely on simpler and less accurate descriptions of the geometries, resulting in simpler noise sources. Analytical approaches are often selected for their cost effectiveness and quickness to investigate several geometries in design stages.

These fast running tools and could be used to propose low noise designs for DAWTs. Once the optimal geometry is identified, a 2D RANS simulation is performed to obtain the pressure distribution around the DAWT. The wall pressure fluctuations are then reconstructed and the Amiet's model for trailing edge noise is used.

4. Wind turbine rotor noise

Considering a free stream velocity, U aligned with the airfoil, which is assumed to be a thin flat plate with a chord length $c = 2b$ and span $L=2d$, the aerodynamic noise can be computed using the expressions provided by Amiet [5] [6].

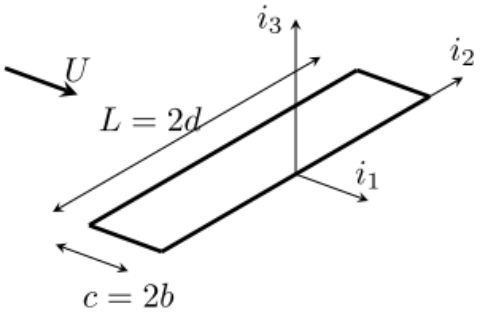

Figure 4: Reference frame [7].

Given an observer position X, the power spectral density produced by the leading edge is calculated with:

$$S_{pp}^{LE}(\mathbf{x},\omega) = \left(\frac{\rho\omega c x_3}{2c_0\sigma_0^2}\right)^2 \pi U d\,|\mathcal{L}(x_1,k_{10},k_{20})|^2 \Phi_{ww}(k_{10},k_{20}), \quad (1)$$

For the case of the trailing edge, the power spectral density can be obtained with:

$$S_{pp}^{TE}(\mathbf{x},\omega) = \left(\frac{\omega x_3 b}{2\pi c_0\sigma_0^2}\right)^2 4d\,|\mathcal{I}(x_1,k_{10},k_{20})|^2 l_y(k_{10},k_{20})\,\Phi_{pp}(k_{10},k_{20}) \quad (2)$$

in which $\mathcal{L}$ and $\mathcal{I}$ are the aeroacoustic transfer functions for leading and trailing edge, respectively [8], $\sigma_0 = \sqrt{x_1^2 + \beta^2(x_2^2 + x_3^2)}$ with x_1, x_2 and x_3 being the observer coordinates (in accordance to **Figure 4** reference) and $\beta = 1 - M^2$. Φ_{ww} and Φ_{pp} are the inflow turbulence spectrum and wall pressure spectrum, respectively. The wall pressure spectrum can be obtained using semi-empirical wall spectrum models, such as Lee [9], Kamruzzaman [10], or others[11], depending on whether it is zero or adverse pressure gradient. For the previously mentioned wall spectrum models, input required is such as turbulent boundary layer characteristics, including BL thickness, BL moment thickness, and BL displacement thickness.

5. Preliminary Results

Accurate and efficient noise prediction tools are essential for the design and optimization of wind turbines.

Amiet's model is a widely accepted method for predicting broadband leading and trailing edge wind turbine noise sources, by considering aerodynamic noise sources and propagation of the sound in the surrounding free far-field. This report aims to validate the use of a computational tool, zEPHYR vertical, that implements Amiet's model for the prediction of wind turbine noise. The validity of the tool will be established through the comparison of the numerical results with experimental field data and other numerical results available in literature or accessible data-sets.

The two test cases selected for the validation study are the NACA0012 airfoil and the SWT 2.3MW wind turbine. The test cases were selected by the availability of geometries/CAD models, numerical and experimental data for sound measurements or turbulent boundary layer parameters (for intermediate validation).

5.1. NACA0012

The NACA0012 airfoil is a widely used reference geometry in aerodynamics [12][13][14][15], while the SWT 2.3MW wind turbine [16] is a commonly used wind turbine model that represents state-of-the-art technology in the wind energy industry, both in terms of power production and noise generation mechanisms.

The comparison of the numerical results with the available literature data should provide insight into the accuracy and reliability of the tool in predicting wind turbine noise.

The simulations were performed using a 2D model, to reduce computational time. The Reynolds-averaged Navier–Stokes (RANS) K-Omega SST turbulence model [17] was selected because of it's robust performance in steady turbulent flows. Since the K-Omega SST turbulence model does not include transition prediction, it was used the Gamma transition model [18] available in the solver STAR-CCM+ for this effect. The aforementioned uses local flow variables to compute flow turbulence intermittency, requiring no additional user input. The use of the transition model allows a more accurate definition of the boundary layer, due to the transition and separation detection, which will lead to more meaningful predictions of the boundary layer thicknesses.

Characteristic	**Values**
Chord Length	0.4 m
Span Length	1 m
Angle of Attack	0 °
Operating Conditions	**Values**
Free Stream Velocity U_∞	56 m/s
Reference Pressure	95429 Pa
Reference Density	1.181 kg/m^3
Speed of Sound	336 m/s

Two slightly different versions of the NACA0012 were tested, to verify whether a blunt trailing edge would significantly affect results. The first model had a perfectly sharp trailing edge, while the second model had a blunted trailing edge. In the case of the NACA0012 blunt model, the trailing edge thickness, h, was of 0.6 mm. The trailing edge thickness may be considered to be weightless, as the TE Thickness to Chord Ratio was 0.15%.

The generated mesh is a hybrid, composed of unstructured and structured parts (around the airfoil). It has a total of 158.9 thousand cells, with a 0.4m target size, which is more refined in the proximity of the airfoil surface.

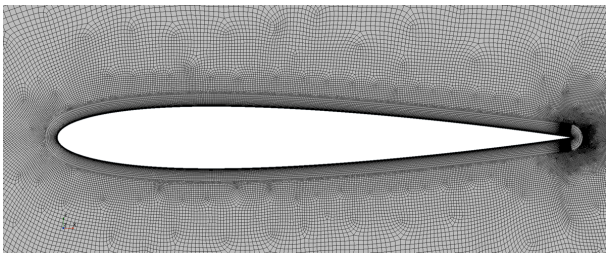

Figure 5: Mesh Scene for Sharp TE NACA0012 model.

As visible in **Figure 5**, 40 Prism Layers are covering the whole chord length, with a thickness decreasing with the proximity to the no-slip wall, for better accuracy of the viscous effects of flow on the boundary layer. The target for the thickness of the first layer, y+, was 0.4. This value is within the recommended range for the turbulence model in use, as it is less than 3 [17]. The mesh underwent several refinement processes, including an airfoil surface control with a cell size target of 1.6 mm, and 0.1 mm to the region of interest, trailing edge.

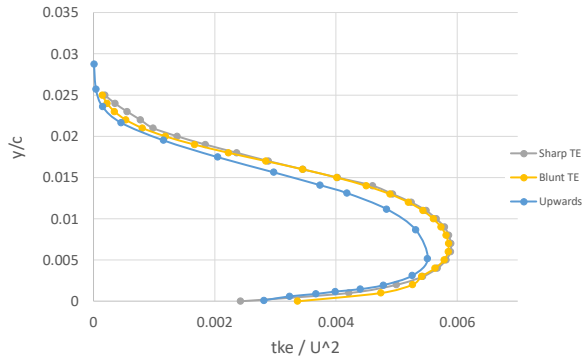

Figure 6: Comparison of Turbulent Kinetic Energy at x/c = 0.95, suction side [19].

Figure 6 shows the Turbulent Kinetic Energy (TKE) profiles in the trailing edge proximity, at x=0.95c. In spite of small local variations, the Blunt and Sharp case's profile is similar to the reference data.

After obtaining the results of the boundary layer parameters, noise predictions were made for the noise produced by the trailing edge in both situations. In **Figure 7** these results are plotted against reference numerical results from [20] and experimental data from [21]. It is observed that there is a large discrepancy between the models that requires further investigation.

After obtaining the results of the boundary layer parameters, noise predictions were made for the noise produced by the trailing edge in both situations. In **Figure 7** these results are plotted against reference numerical results from [20] and experimental data from [21]. It is observed that there is a large discrepancy between the models that requires further investigation.

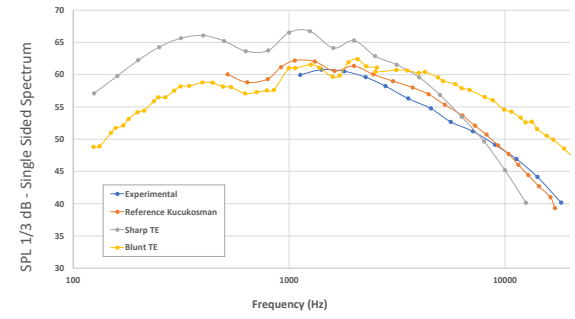

Figure 7: Comparison of the SPL of different airfoil profiles with reference data [20] [21].

The blunt case's SPL provides a close prediction of the values available for comparison. In this case, the results show a good level of correlation in the mid frequencies range, which is no longer true for frequencies > $4000Hz$, where is observed an over-prediction goes beyond 5dB after $10kHz$. The sharp TE model also presents a considerable over-prediction for most of the spectrum, which is not representative of the same situation as the cases of reference, due to the large error, requiring further investigation.

5.2. SWT 2.3

The SWT 2.3-93 is a wind turbine manufactured by Siemens, which has a rotor diameter of approximately 93m. This model has a rated power of 2.3MW, and 13 m/s of rated wind speed.

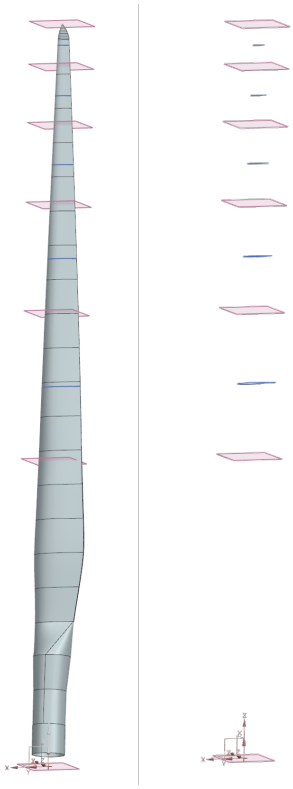

Figure 8: CAD of wind turbine blade (left) and strip sections cut and simulated (right).

To validate the tool's ability to predict the SWL of the rotary wind turbine, the turbine blade was cut into sections, as visible in **Figure 8**, and the workflow from the diagram in **Figure ??** was applied. 3 different operating conditions were also simulated, for which results were available for comparison. WT characteristics and operating conditions for the 3 tests are presented in **Table 1** and **2**, respectively.

Table 1: Dimensions and characteristics for the SWT2.3-93.

Characteristic	**Values**
Blade	SWT 2.3-93
Blade Length	46.5 m
Hub Height	80 m
Angle of Attack	0 °
Operating Conditions	**Values**
Reference Pressure	101325 Pa
Reference Density	1.225 kg/m^3
Speed of Sound	336 m/s

Table 2: Operating Conditions for the 3 cases of SWT2.3-93.

Case #	**Intake U_∞**	**RPM**	**Pitch**	**C_T**
1	6 m/s	13 rev/min	3 °	0.749
2	8 m/s	14 rev/min	-2 °	0.749
3	9.5 m/s	17 rev/min	5 °	0.733

As shown in Table 2, the turbine's behavior was studied in different conditions of wind speed intake, pitch angle alignment, and rotational speed. The different conditions resulted in a different thrust coefficient, which was taken from [14], for this wind turbine model.

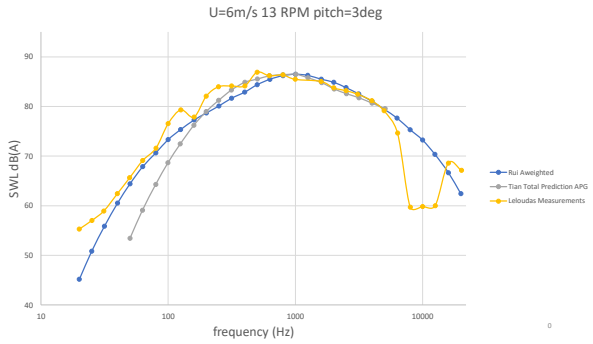

Figure 9: Case 1: SWT2.3 leading and trailing edge broadband noise prediction, SWL dB(A) weighted. Comparison with numerical [22] and experimental data [23] [19].

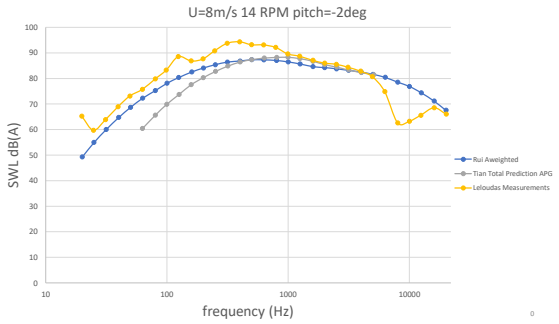

Figure 10: Case 2: SWT2.3 leading and trailing edge broadband noise prediction, SWL dB(A) weighted. Comparison with numerical [22] and experimental data [23] [19].

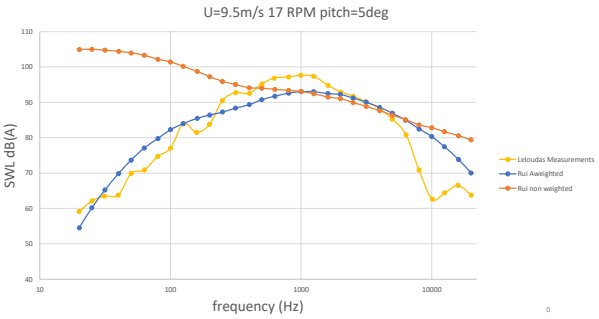

Figure 11: Case 1: SWT2.3 leading and trailing edge broadband noise prediction, SWL dB(A) weighted. Comparison with experimental data [23] and non dB(A) weighted SWL [19].

6. Conclusion

Although the results obtained for NACA0012 showed significant differences in relation to the reference values, this study revealed that the tool used and described in [8] Andrea, is capable of accurately identifying the broadband noise of large wind turbines in different operating conditions.

However, the objective of this work is to extend this analysis to DAWT configurations, which normally have a much smaller size, as well as different operating conditions (rotational speed much higher). It is necessary to evaluate whether the results produced for this type of ducted configuration may prove to be accurate since in this type of configuration there is a tendency to observe a higher angle of attack in each section, which challenges the conditions in which Amiet [5] can be applied.

Since the diffuser is also known to act as a barrier, the problem poses other challenges, such as the scat-

tering effect caused by the diffuser on the noise generated by the surface of the blades. Finally, it should be investigated whether the prediction of broadband noise generated by the trailing edge of the diffuser could be analyzed using a similar strategy as the Amiet for blade trailing edge [5].

Acknowledgments

The authors acknowledge the European Commission for its financial support through the project H2020-MSCA-ITN-2019 zEPHYR (Grant Agreement No. 860101).

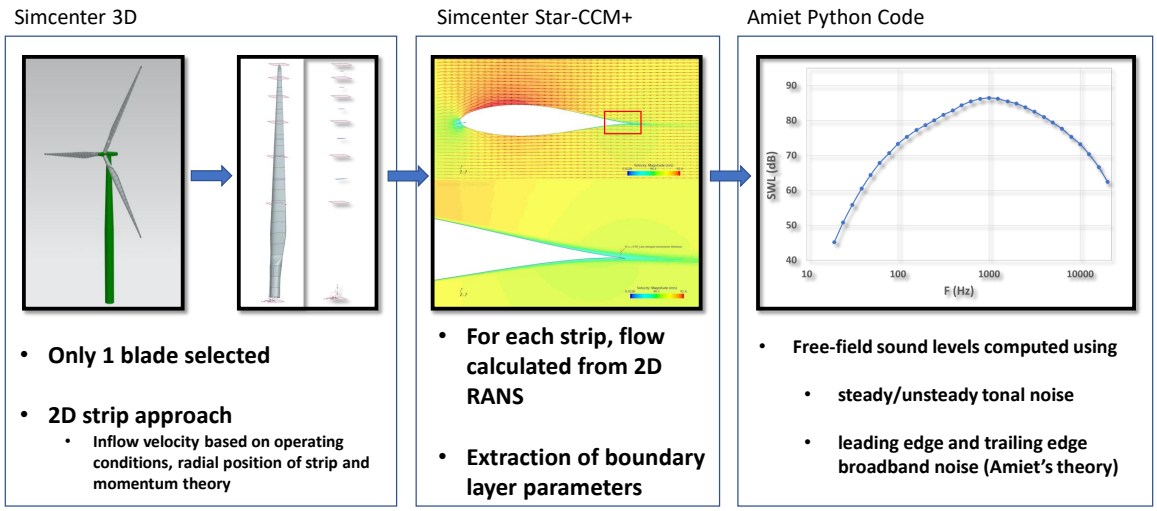

Figure 12: Simulation Workflow for Wind Turbine Rotor TE noise. [8].

References

[1] A review on optimization strategies integrating renewable energy sources focusing uncertainty factor – paving path to eco-friendly smart cities, Sustainable Computing: Informatics and Systems 30 (2021) 100559. doi:https://doi.org/10.1016/j.suscom.2021.100559.

[2] M. O. L. Hansen, N. N. Sørensen, R. G. J. Flay, Effect of Placing a Diffuser around a Wind Turbine, Wind Energy (4) 207–213. doi:10.1002/WE.37.

[3] Y. Liu, S. Yoshida, An extension of the generalized actuator disc theory for aerodynamic analysis of the diffuser-augmented wind turbines, Energy 93 (2015) 1852–1859. doi:10.1016/j.energy.2015.09.114.

[4] O. D. Vries, Fluid dynamic aspects of wind energy conversion.

[5] R. K. Amiet, Acoustic radiation from an airfoil in a turbulent stream, Journal of Sound and Vibration 41 (4) (1975) 407–420. doi:10.1016/S0022-460X(75)80105-2.

[6] R. K. Amiet, Noise due to turbulent flow past a trailing edge, Journal of Sound and Vibration 47 (3) (1976) 387–393. doi:10.1016/0022-460X(76)90948-2.

[7] A. P. C. Bresciani, J. Maillard, L. D. De Santana, Perceptual evaluation of wind turbine noise, Tech. rep. (2022).

[8] A. P. Bresciani, S. Le Bras, L. D. de Santana, Generalization of Amiet's theory for small reduced-frequency and nearly-critical gusts, Journal of Sound and Vibration 116742doi:10.1016/j.jsv.2021.116742.

[9] S. Lee, J. G. Shum, Prediction of airfoil trailing-edge noise using empirical wall-pressure spectrum models, in: AIAA Journal, Vol. 57, American Institute of Aeronautics and Astronautics Inc., 2019, pp. 888–897. doi:10.2514/1.J057787.

[10] M. Kamruzzaman, D. Bekiropoulos, T. Lutz, W. Würz, E. Krämer, A semi-empirical surface pressure spectrum model for airfoil trailing-edge noise prediction, International Journal of Aeroacoustics (5-6) 833–882. doi:10.1260/1475-472X.14.5-6.833.

[11] K. Kücükcoskun, Prediction of free and scattered acoustic fields of low-speed fans.

[12] J. V. Becker, Boundary-Layer Transition on the N.A.C.A. 0012 and 23012 Airfoils in the 8-Foot High-Speed Wind Tunnel, Special Report (1940).

[13] T. F. Brooks, M. A. Marcolini, D. S. Pope, Airfoil trailing-edge flow measurements, AIAA Journal 24.

[14] M. Herr, M. Kamruzzaman, Benchmarking of trailing-edge noise computations-outcome of the BANC-II workshop, 19th AIAA/CEAS Aeroacoustics Conference (2013) 120doi:10.2514/6.2013-2123.
URL https://arc.aiaa.org/doi/10.2514/6.2013-2123

[15] M. Herr, R. Ewert, C. Rautmann, M. Kamruzzaman, D. Bekiropoulos, A. Iob, R. Arina, P. Batten, S. Chakravarthy, F. Bertagnolio, Broadband Trailing-Edge Noise Predictions - Overview of BANC-III Results, 21st AIAA/CEAS Aeroacoustics Conference AIAA 2015–2847doi:10.2514/6.2015-2847.

[16] Siemens SWT-2.3-93 - Manufacturers and turbines - Online access - The Wind Power.

[17] F. R. Menter, Two-equation eddy-viscosity turbulence models for engineering applications, AIAA Journal 32 (8) (1994) 1598–1605. doi:10.2514/3.12149.

[18] F. R. Menter, P. E. Smirnov, T. Liu, R. Avancha, A One-Equation Local Correlation-Based Transition Model, Flow, Turbulence and Combustion 95 (4) (2015) 583–619. doi:10.1007/S10494-015-9622-4.

[19] H. Bériot, J. Christophe, C. Ku-Cukosman, S. Le Bras, Grant Agreement N • 763990 UPWARDS Deliverable D4.1 Assessment of statistical and stochastic approaches for the prediction of WT nearfield noise WP 4 Flow and acoustic simulations Task 4.1 Dedicated statistical / stochastic near-field noise prediction tools Deliverable abstract Deliverable review Reviewer 1: /Coordinator Reviewer 2: Answer Comments Type Answer Comments Type, Tech. rep.

[20] Y. C. Kucukosman, Propositions accompanying the dissertation SEMI-ANALYTICAL APPROACHES FOR THE PREDICTION OF THE NOISE PRODUCED BY DUCTED WIND TURBINES.

[21] M. Herr, C. Bahr, M. Kamruzzaman, Problem Statement for the AIAA/CEAS Second Workshop on Benchmark Problems for Airframe Noise Computations (BANC-II).

[22] Y. Tian, Modeling of wind turbine noise sources and propagation in the atmosphere.
URL https://theses.hal.science/tel-01335869
https://theses.hal.science/tel-01335869/document

[23] G. Leloudas, Optimization of Wind Turbines with respect to Noise, Optimization (November).

ENVIRONMENTAL FLOWS AND SAFETY

Potential increase in annual energy production of the Belgian offshore wind-farm cluster through wake steering: farm-based versus cluster-optimization

Benoit Foloppe

Environmental and Applied Fluid Dynamics Department, von Karman Institute for Fluid Dynamics, Belgium, benoit.foloppe@vki.ac.be

Supervisors: Jeroen van Beeck[1] and Wim Munters [2]

[1]*Professor and* [2]*Research Engineer, Environmental and Applied Fluid Dynamics Department, von Karman Institute for Fluid Dynamics, Belgium,* [1]*vanbeeck@vki.ac.be and* [2]*wim.munters@vki.ac.be*

University Supervisor: Lieven Vandevelde

Professor, Electromechanical and Systems and Metal Engineering Department, Ghent University, Belgium, lieven.vandevelde@ugent.be

Abstract

In recent years, significant research efforts have focused on increasing power extraction using wake steering through yaw misalignment. In the current work, we evaluate the potential increase in annual energy production (AEP) for the Belgian offshore wind-farm (WF) cluster using the FLORIS framework. The 2.2 GW Belgian cluster is an excellent test case for wake mitigation strategies due to its high power density with relatively low turbine spacings. Furthermore, the split of the concession zone into nine individual farms results in a mix of intra- and inter-farm wakes to be considered in one of the largest wind-farm clusters operational to date. First, the Gauss Curl Hybrid and Cumulative Curl velocity deficit models are validated with Large Eddy Simulations data of the Horns Rev wind farm from literature. The new Serial-Refine optimization algorithm is used as more efficient than SciPy's gradient-based SLSQP optimization algorithm. Three different optimization functions are compared. The first one is the complete cluster yaw angles optimization. The other two are farm-based optimizations seeking to maximize either their own AEP or the cluster AEP. Results show that all WFs benefit from every optimization, encouraging operators to implement this strategy. The cluster optimization is found to be the one providing the best AEP increase for all WFs individually and thus for the cluster. The farm-based function optimizing the cluster AEP is in second place, encouraging WF operators to collaborate for their own profits.

Keywords: Belgian offshore wind-farm cluster, AEP, wake steering, optimization

1. Introduction

In modern wind farms, wake interactions between neighbouring turbines are the main drivers of annual energy production (AEP) losses with typical loss values of 10% to 20% compared to lone-standing turbines [1]. . The prospect of mitigating these wake losses through coordinated wind-farm flow control has incited significant research efforts over the last two decades. Furthermore, a recent expert elicitation among stakeholders in academia and industry has shown that 84% of respondents believe that wind-farm control will be broadly adopted in operational wind farms at some point in the future [2]. Over the years, several promising control strategies have emerged to either increase wake mixing through (dynamic) induction control [3][4] or steer wakes away from downstream turbines through intentional yaw misalignments upstream [5]. Comprehensive recent

This preprint has not undergone peer review or any post-submission improvements or corrections. The version of record of this article is published in Journal of Physics: Conference Series, May 2023, Vol. 2505, Paper 012055, and is available online at https://doi.org/10.1088/1742-6596/2505/1/012055

overviews of control techniques and architectures can be found, e.g., in refs. [6] and [7]. In contrast to the complex fluid dynamics of (dynamic) induction control strategies, wake steering flow physics can nowadays be relatively well captured with fast analytical wake models due to significant research efforts in parameterizing phenomena such as wake curling and secondary steering (see, e.g., [8]), avoiding the need for complex flow models in designing control strategies. Combined with an increasing number of wind-tunnel validation studies of simplified setups [9] and field campaigns in small sets of neighbouring turbines [10][11], this has resulted in a significant increase in maturity of wake steering strategies in recent years, with first implementations becoming commercially available [12]. Despite this, studies on the potential AEP increase that wake steering could bring to modern operational wind farms at full scale in actual meteorological conditions have been relatively scarce. Furthermore, with increasing deployments of offshore wind farms, e.g., in the North Sea, multi-gigawatt scale wind-farm clusters, in which farms owned by different stakeholders operate in close proximity, will become more prevalent in the near future. A present-day example hereof is the offshore Belgian-Dutch offshore wind farm cluster located in the North Sea at the border between Belgium and the Netherlands, which consists of a total capacity of 3.7 GW distributed across 7 groups of stakeholders. Although from a fluid dynamics perspective these clusters can often be regarded as a single large wind farm (potentially with different types of turbines), the distributed ownership of individual farms can create distinct borders in operational strategies throughout the cluster. In view of wind-farm control, the absence of full cooperation across different operators would likely result in economic optimality for individual operators yet suboptimal conditions from a systems perspective. To the authors' knowledge, the potential impact of full cooperation on AEP at the farm as well as the cluster level has not been studied to date. In this manuscript, we first describe the methodology used with a focus on three different wake steering optimization functions. Two of them include cooperation of WFs on AEP. Wake models of the FLORIS framework are validated with Large Eddy Simulations data of the Horns Rev wind farm from literature. The result section discusses the potential AEP increase at cluster, farm and turbine levels. Finally, conclusions are given.

2. Methodology

In the current study, the focus is exclusively on the existing Belgian offshore wind farm zone, which was finished in 2020. The zone consists of 9 individual wind farms (Figure 1a), namely Mermaid, Northwester 2, Nobelwind, Belwind, Seamade, Northwind, Rentel, C-Power and Norther, run by 4 distinct operators. For the purpose of this study, we consider each wind farm being operated by a single operator. Furthermore, considering the wind rose (Figure 1b) is dominated by south-westerly winds, for simplicity we omit the Dutch Borssele wind farm zones on the north-eastern border of the considered wind farms.

The wind rose used in this work (Figure 1b) was derived from the ERA5 dataset [13]. An ERA5 subset from hourly data of the wind speed over 10 years (2012-2021) at coordinates 51.5° N, 2.5° E in the northwest of the Belgian North Sea and 100m altitude was processed to generate the wind rose. This altitude lies in the hub heights range of studied turbines and FLORIS extrapolates wind speeds vertically using the wind shear exponential law. As the maximum speed in the set is 27.7 m/s, 28 wind speed bins of 1 m/s width are used. The choice of wind direction bin width can impact the results as it can hide interesting wake-turbine interaction patterns [14], some of which may have high potential for optimisation. After a sensitivity study and mainly for computational cost limitations, the number of bins for the wind is set to 36 (10° resolution of the wind direction). This number is found to be conservative compared to more refined discretisation, meaning that it results in lower AEP increase after optimization of WF yaw angles. The recently developed branch-and-bound algorithm called Serial-Refine (SR) [15] is better suited to this work in opposition to classic gradient-based algorithms which scale as a power law with the number of turbines, each adding a new dimension to the problem, while the SR algorithm scales linearly. Indeed, optimizing the Belgian offshore wind farm cluster has revealed to be a huge process because it involves optimizing the angles of 399 turbines for each combination of wind speed and wind direction which represents around a thousand cases. The optimization of the Belgian cluster is defined by the following function

$$max\left(\sum_{t,s,d=1}^{T=399,S=28,D=36} AEP_{t,s,d}(\alpha_{t,s,d})\right) \quad (1)$$

where α is the wind turbine misalignment with the incoming wind. Indexes t/T, s/S, d/D stand for turbine,

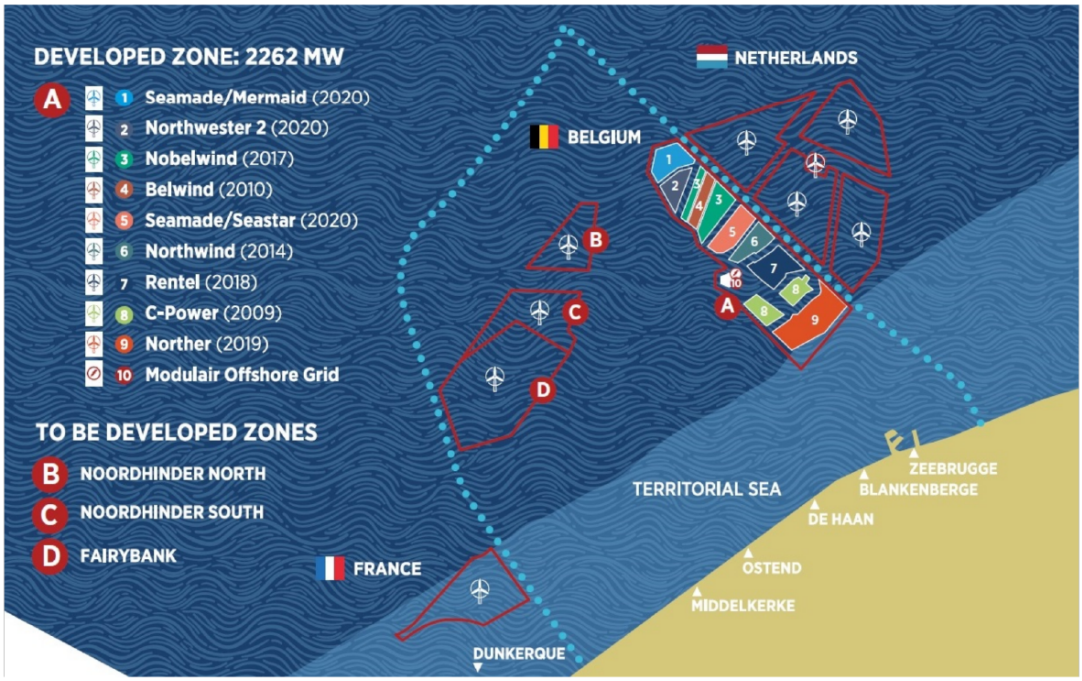

Figure 1: Illustration of the Belgian offshore wind energy zone. Figure courtesy of the Belgian offshore platform

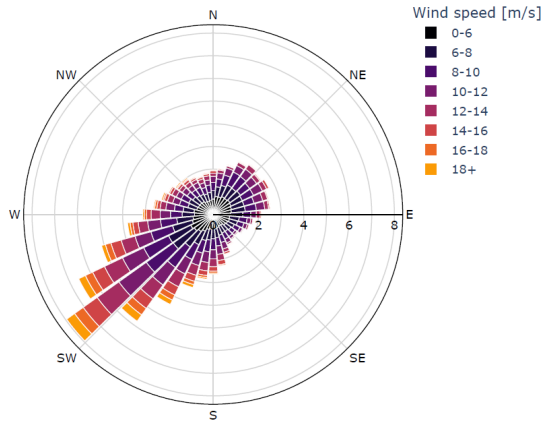

Figure 2: Wind rose of Belgian North Sea conditions at (51.5° N, 2.5° E) derived from the ERA5 dataset[13]

wind speed and wind direction respectively. This optimization function will give the best yaw angle set to maximize AEP of the whole cluster but it will likely not be used in reality as it would require the cooperation of all 9 WF operators. Thus, another approach is studied and compared with the first one. This second optimization function is called "Farm-based" optimization. Only yaw angles from the studied WF are optimized and all other WTs remain aligned with the incoming wind. The optimization function can have two goals: maximizing the AEP of the studied farm (Equation 2) or maximizing the AEP of the cluster (Equation 3)

$$max\left(\sum_{t^*,s,d=1}^{T=T_{wf},S=28,D=36} AEP_{t^*,s,d}(\alpha_{t^*,s,d})\right) \quad (2)$$

$$max\left(\sum_{t,s,d=1}^{T=399,S=28,D=36} AEP_{t,s,d}(\alpha_{t^*,s,d};\alpha_{\bar{t},s,d}=0)\right) (3)$$

where t^*/T_wf are turbines from the studied WF (subset of t) and $\bar{t} = t - t^*$. Finally, optimized yaw angles are used to compute the AEP of the complete cluster. For the farm-based optimizations, the subsets of yaw angles have to be merged before computing the cluster AEP. This merging is mandatory otherwise Equation 2 has only advantages, no negative impacts from neighbouring farms being selfish, and Equation 3 has only drawbacks, making effort for neighbouring farms but not receiving compensations.

3. Validation

The Horns Rev 1 wind farm, consists of 80 Vestas V-80 2 MW turbines, with a rotor diameter of 80

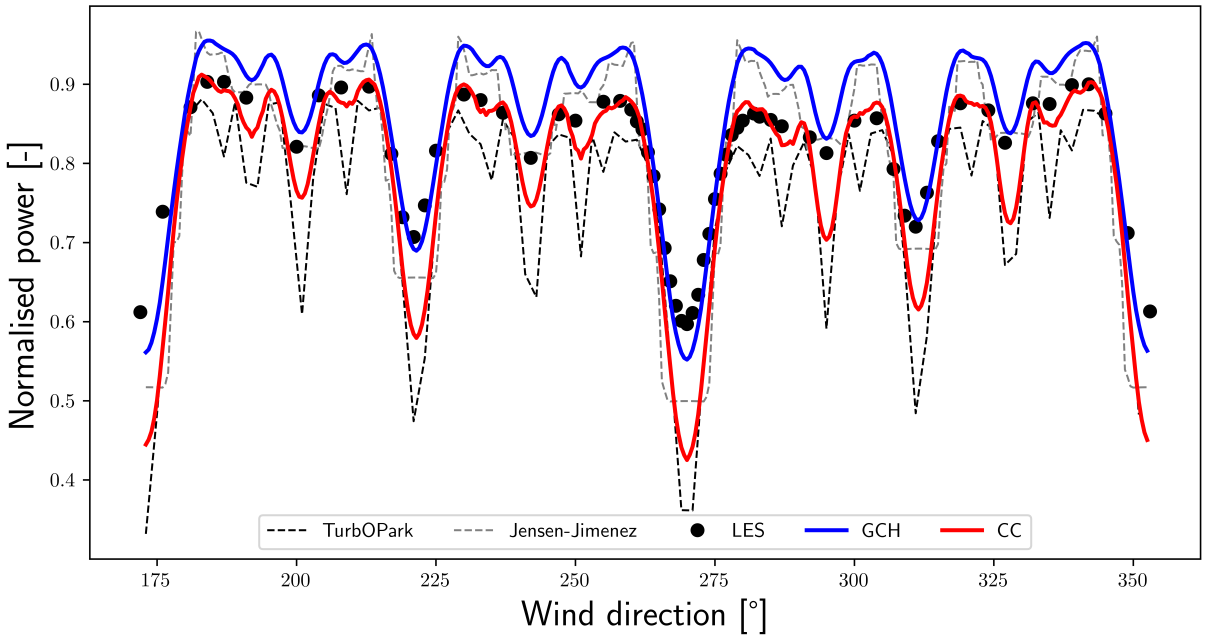

Figure 3: Comparison of FLORIS wake models against reference LES results from [16] for the Horns Rev wind farm.

m and a hub height of 70 m, separated from each other by 7 diameter lengths in both alignment directions. It spans a rhomboidal area of around 20 km^2 with an angle of 7°. Its operation is simulated using Gauss Curl Hybrid (GCH) and Cumulative Curl (CC) wake models (and two other non-gaussian wake models). The results (Figure 2) are compared to reference results from an LES study [16] with a numerical framework validated by wind-tunnel experiments and field data. All calculations were run using a mean velocity of 8 m/s and a turbulence intensity of 7.7% at hub height, which are in good agreement with observations at Horns Rev 1 [16].

It can be seen that CC often exhibits too low dips but is otherwise quite close to LES, with a clear tendency to underestimate the power. On the contrary, GCH tends to overestimate the results although it reaches values very close to LES in the dips. This is consistent with conclusions from the original paper of the CC wake model [17]. Both curves have otherwise highly similar shapes. The CC wake model is selected as designed specifically for large array of turbines. As for the number of wind directions, this wake model is conservative compared to LES results.

4. Results

In the following results, impact of three optimization functions (Cluster optimization, Farm-based optimizations maximizing either the studied farm or the cluster) on wind farm AEPs are compared using the increase in AEP. It is defined as

$$d\left(AEP_{t,s,d}\right) = \frac{AEP_{t,s,d}(\alpha_{t,s,d}) - AEP(\alpha_{t,s,d}=0)}{AEP(\alpha_{t,s,d}=0)} \quad (4)$$

where $AEP_{t,s,d}(\alpha_{t,s,d})$ is the AEP computed after optimizing yaw angles and $AEP(\alpha_{t,s,d} = 0)$ is the AEP without yaw misalignment.

4.1. Farm-based optimizations

In this first part, results assess the effectiveness of the farm-based optimization functions. In Figure 3, results show that all optimizations bring an important increase in AEP with a minimum of 2.14% for Nobelwind. However, wind farms are featuring some discrepancies, with outer WFs (namely Mermaid and Norther) showing less difference, between farm-based optimizations and cluster optimization, than inner WFs. In fact, Mermaid and Norther show a difference of 0.17% and 0.25% respectively where Northwester 2 and Seastar are featuring 1.25% and 1.20% difference respectively. This is due to the fact

that the potential of maximizing the cluster AEP increases with large wake interactions between neighbouring WFs. Outer WFs have only one neighbour on one side (which on top of that is not in the dominant direction) where inner WFs have two.

Northwind, Seastar and Northwester 2 stand out of other WFs with AEP increases of 4.22%, 4.15% and 3.58% for farm-based optimizations maximizing the cluster AEP. One reason for that comes from the power density of WFs as high power density mainly leads to high potential of controlling WTs through wake steering. As seen in Table 1, these three WFs have the highest power density.

With the idea of making the most electricity production out of the Belgian cluster, farm-based optimizations are compared to the complete cluster optimization which represents the highest achievable AEP using wake steering. The first thing to notice is that none of the WF maximizing their own AEP is able to produce more than AEPs resulting from the cluster maximization. This means that all WF operators would have individual interests in collaborating with each other while at the same time maximizing the cluster AEP. As explained before, outer WFs would have lower interest in collaborating than inner WFs. The absolute AEP increases in GWh are showing the important amount of extra electricity produced by each WFs and the cluster. The largely different installed capacities obviously lead to varying benefits.

Figure 4 is focusing on the Seastar WF. The results of the two farm-based optimizations are nicely showing their different objectives. The middle figure depicts the effect of collaboration between WFs. In fact, WTs on the North-East and South-West boundaries are seeing great improvements of AEP compared to the left figure. Finally, the right dot graph does not show a large difference with respect to the middle figure as AEP seems to be increased uniformly over the farm, confirming that the cluster-based optimization is the best solution.

To conclude, the cluster-based optimization is the one improving the most the electricity production of the Belgian cluster with 3.50% of AEP increase. This is highly non-negligible in terms of extra-profits generated by controlling WTs through wake steering. Without collaboration of WF operators, the farm-based optimization seeking to optimize the cluster AEP is out-performing the one optimizing individual AEPs. These are still really important improvement of the AEP that should encourage WF operators to implement individually such control.

4.2. Cluster-based optimization

In an attempt to push the limits of AEP optimization through wake steering using FLORIS, all 399 WTs have been optimised as a single WF. As detailed in the Methodology section, the wind rose is divided in 36 wind directions and 28 wind speeds. It is also dominated by south-westerly winds which is of great importance for the following results. The Serial-Refine yaw angle optimization algorithm is configured with 7 angles being compared during 2 passes (see [15] for description of the configuration).

Looking at Figure 5a, it is clear that the wake steering control is not uniform over the cluster since the absolute yaw misalignment occurrence varies. This metric is defined as

$$\alpha_t^{occ} = \sum_{s,d=1}^{S,D} |\alpha_{t,s,d}| \times f_{s,d} \tag{5}$$

where $f_{s,d}$ is the frequency of wind speed s and wind direction d. A clear trend indicates that south-westly WTs are experiencing more yaw misalignment than downstream WTs along the dominant direction. This is well known in the field of control through wake steering and the goal is to deviate the wake of the front WTs (thus reducing power) to gain even more power at downstream turbines. It is validated with Figure 5b where these south-westerly WTs are the ones featuring a loss of AEP.

As shown previously in Figure 3, Northwind WTs have higher increase of AEP than turbines in the neighbouring farms. This is mainly due to the closely spaced layout of the farm which is well suited for control through wake steering. In fact, wake recovers with downstream distance, reducing the effectiveness of wake steering for largely spaced WF such as Norther. The drawback for Northwind is that its WTs are experiencing high yaw angle occurrences which are increasing loads and fatigue of the WT blades and reducing their lifetime. However, this evaluation is out of the scope of this study. Another closely spaced WF is Belwind, also featuring 3MW WTs but with a smaller diameter. Unlike Northwind, its yaw angle occurences are low. One reason is that its rows of WTs have a significant angle with the dominant wind direction, making the wake naturally out of the downstream WT rotor. This is confirmed in Figure 6 which compares Belwind and Northwind wakes without yaw misalignment for wind speed of 11.5 m/s, 230° wind direction, the wind conditions with highest probability at the cluster location (dominant wind conditions). With small yaw angle occurrence while

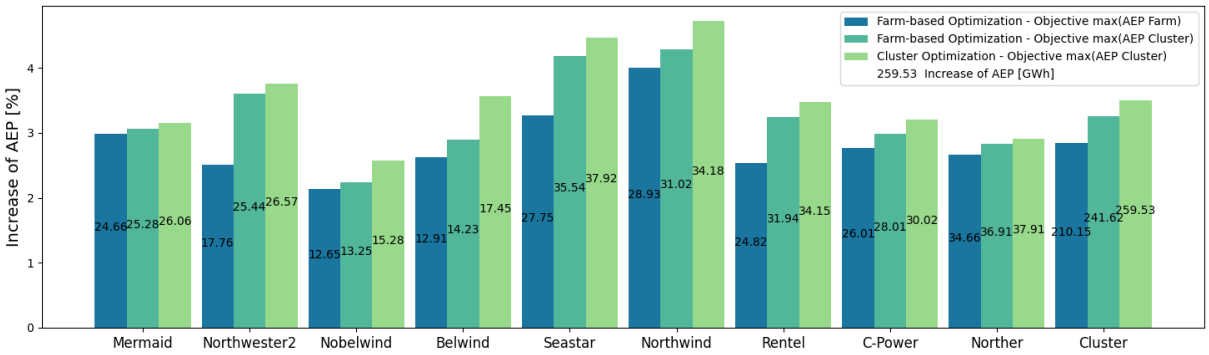

Figure 4: Comparison of the AEP increases for the 9 Belgian wind farms.

Table 1: Power density of Belgian wind farms and the Belgian cluster in MW/km^2

Mermaid	Northwester2	Nobelwind	Belwind	Seastar	Northwind	Rentel	C-Power	Norther	Cluster
14.43	19.01	12.41	14.58	16.18	17.81	13.18	14.89	10.46	14.04

showing a good AEP increase, Belwind might be the WF taking most advantage of this optimization.

Aside from the explanations given, some unknowns could be of important interest. For example, if a wind farm layout is already optimized for the site-specific wind rose, less AEP increase would be expected from the control optimization.

5. Conclusion

This paper studied the potential increase in annual energy production of the Belgian offshore wind-farm cluster through wake steering. The FLORIS framework is used with the Cumulative Curl wake model and the Serial-Refine yaw angle optimization algorithm. Three different optimization functions are compared. The first one is the complete cluster yaw angles optimization. Other two are farm-based optimizations seeking to maximize either their own AEP or the cluster AEP. Results show that all WFs benefits from every optimization function, encouraging operators to implement wake steering. The cluster optimization is found to be the one providing the best AEP increase for all WFs individually and thus for the cluster. The farm-based function optimizing the cluster AEP comes just after, encouraging WF operators to collaborate for their own profits. However, setting up this collaboration may not be an easy task as WF operators are mainly competitors. While increasing the AEP, this collaboration would also create a single consortium of offshore wind energy producers which may prove unsuitable for price competitivity (monopolistic position).

Acknowledgments

The author acknowledge contributions from Loic Dewitte and Wim Munters as co-authors of this article. The author acknowledge support from the PhairywinD project, funded by the Energy Transition Fund of the Belgian Federal Public Service for Economy, SMEs, and Energy (SPF Economy). [13] was downloaded from the Copernicus Climate Change Service (C3S) Climate Data Store. The results contain modified Copernicus Climate Change Service information 2020. Neither the European Commission nor ECMWF is responsible for any use that may be made of the Copernicus information or data it contains.

References

[1] J. C. Y. Lee, M. J. Fields, An overview of wind-energy-production prediction bias, losses, and uncertainties, Wind Energy Science 6 (2) (2021) 311–365. doi:10.5194/wes-6-311-2021.

[2] J. W. van Wingerden, P. A. Fleming, T. Göçmen, I. Eguinoa, B. M. Doekemeijer, K. Dykes, M. Lawson, E. Simley, J. King, D. Astrain, M. Iribas, C. L. Bottasso, J. Meyers, S. Raach, K. Kölle, G. Giebel, Expert elicitation on wind farm control, Journal of Physics: Conference Series 1618 (2) (2020) 022025. doi:10.1088/1742-6596/1618/2/022025.

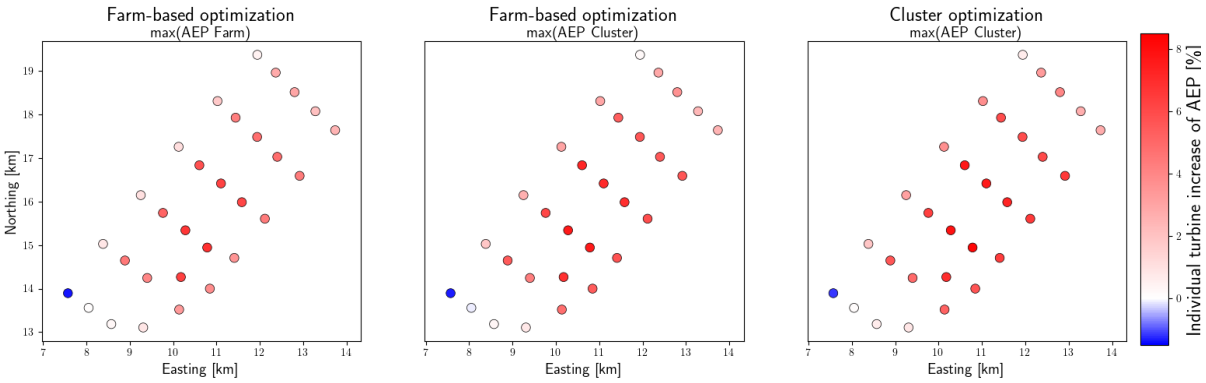

Figure 5: Comparison of Seastar individual turbine AEP increase for every optimization functions.

[3] W. Munters, J. Meyers, Towards practical dynamic induction control of wind farms: analysis of optimally controlled wind-farm boundary layers and sinusoidal induction control of first-row turbines, Wind Energy Science 3 (1) (2018) 409–425. doi:10.5194/wes-3-409-2018.

[4] J. A. Frederik, B. M. Doekemeijer, S. P. Mulders, J.-W. Wingerden, The helix approach: Using dynamic individual pitch control to enhance wake mixing in wind farms, Wind Energy 23 (8) (2020) 1739–1751. doi:10.1002/we.2513.

[5] M. F. Howland, S. K. Lele, J. O. Dabiri, Wind farm power optimization through wake steering, Proceedings of the National Academy of Sciences 116 (29) (2019) 14495–14500. doi:10.1073/pnas.1903680116.

[6] J. Meyers, C. Bottasso, K. Dykes, P. Fleming, P. Gebraad, G. Giebel, T. Göçmen, J.-W. van Wingerden, Wind farm flow control: prospects and challenges, Wind Energy Science 7 (6) (2022) 2271–2306. doi:10.5194/wes-7-2271-2022.

[7] D. R. Houck, Review of wake management techniques for wind turbines, Wind Energy 25 (2) (2021) 195–220. doi:10.1002/we.2668.

[8] P. Fleming, J. King, C. J. Bay, E. Simley, R. Mudafort, N. Hamilton, A. Farrell, L. Martinez-Tossas, Overview of FLORIS updates, Journal of Physics: Conference Series 1618 (2) (2020) 022028. doi:10.1088/1742-6596/1618/2/022028.

[9] F. Campagnolo, V. Petrović, J. Schreiber, E. M. Nanos, A. Croce, C. L. Bottasso, Wind tunnel testing of a closed-loop wake deflection controller for wind farm power maximization, Journal of Physics: Conference Series 753 (2016) 032006. doi:10.1088/1742-6596/753/3/032006.

[10] P. Fleming, J. Annoni, J. J. Shah, L. Wang, S. Ananthan, Z. Zhang, K. Hutchings, P. Wang, W. Chen, L. Chen, Field test of wake steering at an offshore wind farm, Wind Energy Science 2 (1) (2017) 229–239. doi:10.5194/wes-2-229-2017.

[11] M. F. Howland, J. B. Quesada, J. J. P. Martínez, F. P. Larrañaga, N. Yadav, J. S. Chawla, V. Sivaram, J. O. Dabiri, Collective wind farm operation based on a predictive model increases utility-scale energy production, Nature Energy 7 (9) (2022) 818–827. doi:10.1038/s41560-022-01085-8.

[12] P. M. Gebraad, Controlling wind turbines in presence of wake interactions, US Patent Application 15/734,80.

[13] H. Hersbach, B. Bell, P. Berrisford, G. Biavati, A. Horányi, J. M. Sabater, J. Nicolas, C. Peubey, R. Radu, I. Rozum, D. Schepers, A. Simmons, C. Soci, D. Dee, J.-N. Thépaut, Era5 hourly data on single levels from 1959 to present, Copernicus Climate Change Service (C3S) Climate Data Store (CDS).

[14] B. M. Doekemeijer, E. Simley, P. Fleming, Comparison of the gaussian wind farm model with historical data of three offshore wind farms, Energies 15 (6) (2022) 1964. doi:10.3390/en15061964.

[15] P. A. Fleming, A. P. J. Stanley, C. J. Bay, J. King, E. Simley, B. M. Doekemeijer, R. Mudafort, Serial-refine method for fast wake-steering yaw optimization, Journal of Physics: Conference Series 2265 (3) (2022) 032109. doi:10.1088/1742-6596/2265/3/032109.

[16] F. Porté-Agel, Y.-T. Wu, C.-H. Chen, A numerical study of the effects of wind direction on turbine wakes and power losses in a large wind farm, Energies 6 (10) (2013) 5297–5313. doi:10.3390/en6105297.

[17] C. J. Bay, P. Fleming, B. Doekemeijer, J. King, M. Churchfield, R. Mudafort, Addressing deep array effects and impacts to wake steering with the cumulative-curl wake modeldoi:10.5194/wes-2022-17.

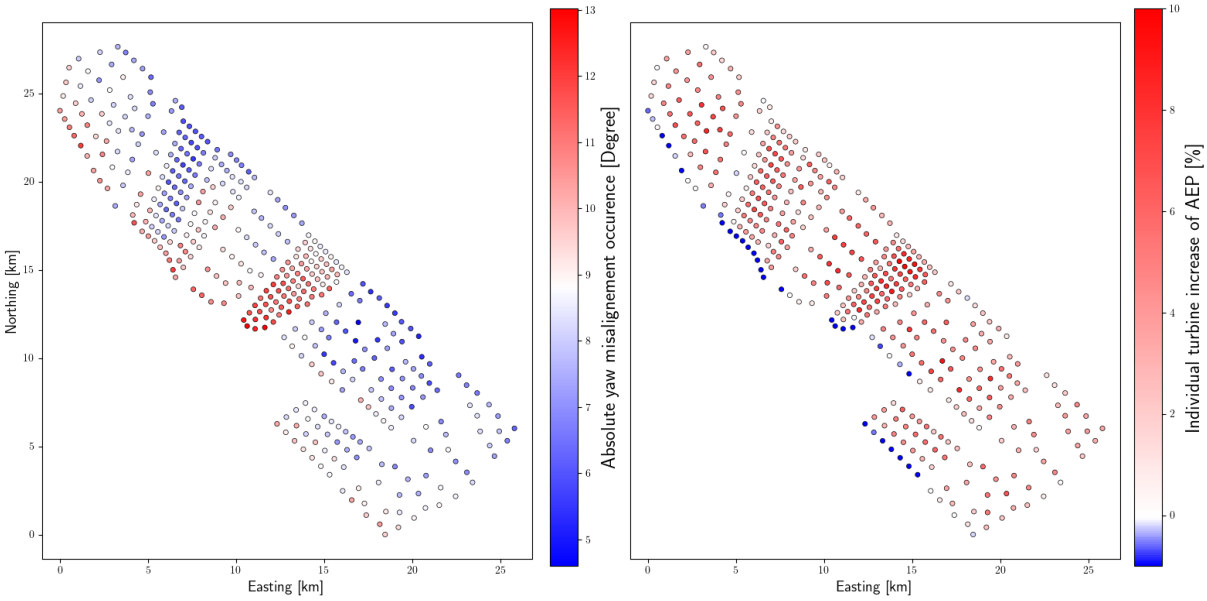

Figure 6: Results of the cluster-based optimization showing (left) absolute yaw misalignment occurence and (right) individual turbine increase of AEP

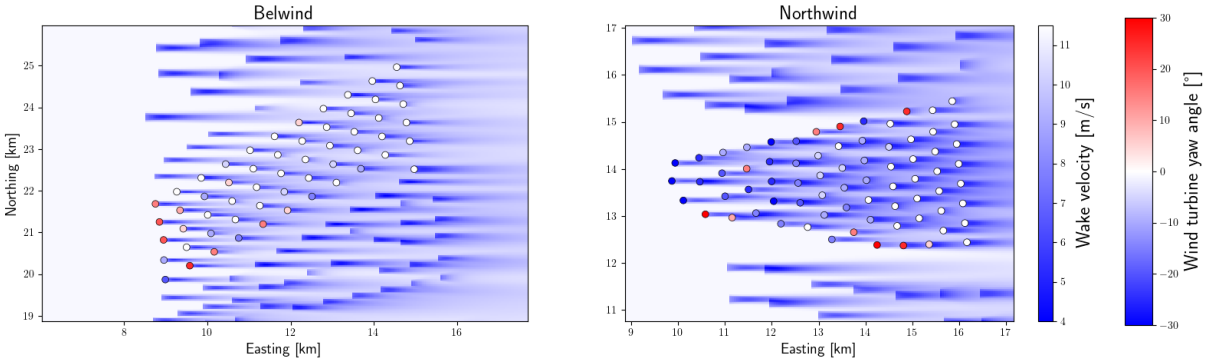

Figure 7: Comparison of Belwind and Northwind wakes without yaw misalignment for wind speed of 11.5 m/s, 230° wind direction and 6% TI. Coloured dots are representing the optimized yaw angle solutions for these wind conditions.

Wind turbine wakes impact on the dynamics of high-voltage cables for fatigue assessment and optimization

Emmanuel Gillyns

Environmental and Applied Fluid Dynamics, von Karman Institute for Fluid Dynamics, Belgium, emmanuel.gillyns@vki.ac.be

Supervisor: Jeroen van Beeck

Professor, Environmental and Applied Fluid Dynamics, von Karman Institute for Fluid Dynamics, Belgium, vanbeeck@vki.ac.be

University Supervisor: Grégoire Winckelmans

Professor, Institute of Mechanics, Materials and Civil Engineering, UCLouvain, Belgium, gregoire.winckelmans@uclouvain.be

Abstract

Wind energy is experiencing a rapid growth and is expected to continue on this trend. With most wind turbines these days larger than 120 m, and a wake 10 times this value, the effect of said wake cannot be neglected. This work aims to provide a better understanding of the phenomena with large eddy simulations, and experimental validation in wind tunnel.

Keywords: wind turbine, wind turbine wake, high voltage cables, galloping, large eddy simulation, actuator line model, atmospheric boundary layer, fluid structure interaction, one-way coupling, fatigue, scale-model wind turbine, Nek5000, LES, spectral element, wind tunnel test.

1. Introduction

With the current trend to the green energy transition, wind power is the leading renewable energy source in Belgium with 12.5 % of the electricity produced in 2022 coming from wind turbines. This number is still increasing, and more wind turbines will be installed, both onshore and offshore..

Wind turbine wakes extend far downstream and correspond to a highly turbulent flow that can have a significant impact on any encountered structure: another other wind turbine, a building, but also electrical cables. Indeed, the large dynamic displacement of cables caused by wake turbulence has be found to lead to significant damages, and even to premature failure.

Numerical simulation can help reveal the driving mechanisms associated to wake turbulence, and also support the development of mitigation strategies. For that, Large Eddy Simulation (LES) can be used as it allows to capture the dynamics of the relevant turbulent scales of the flow, down to the scale of the near tip blade chord. The blades themselves are not resolved by the simulation; instead their effect on the flow is represented using an Actuator Line Model (ALM).

The present paper aims at developing a coherent framework to allow for a detailed comparison between the experimental data collected in a wind tunnel with a scaled wind turbine and the results of LES with ALM run under the same conditions (i.e., same inflow velocity field, blockage, loading distribution over the blades, thrust and power coefficients of the wind turbine).

2. Experimental setup

2.1. Wind tunnel

The results from a numerical simulation should be compared to those of an equivalent experiment in a well controlled environment (such as a wind tunnel).

This preprint has not undergone peer review or any post-submission improvements or corrections. The version of record of this article is published in Journal of Physics: Conference Series, May 2023, Vol. 2505, Paper 012029, and is available online at https://doi.org/10.1088/1742-6596/2505/1/012029

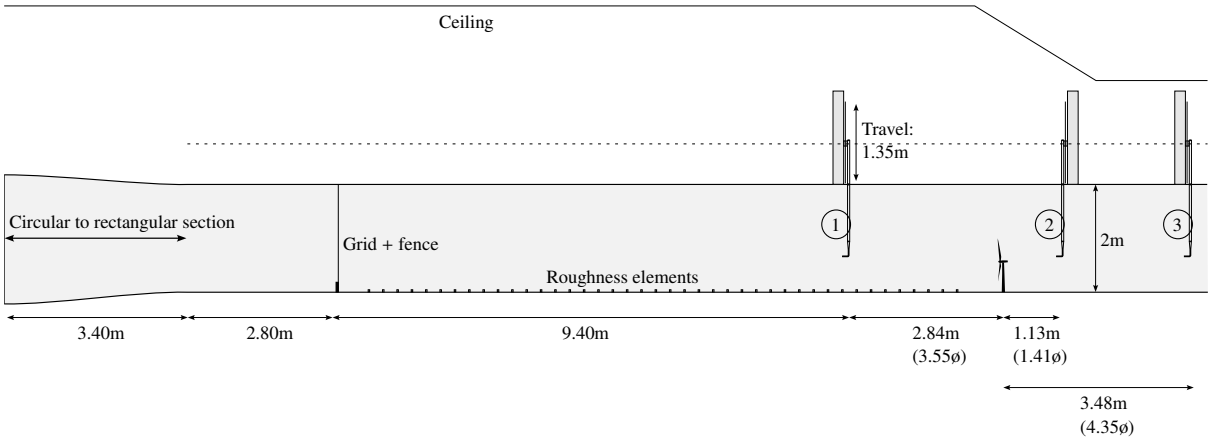

Figure 1: Test section for the L1-B wind tunnel.

This also requires to be able to reproduce the experimental environment numerically, so as to be able to perform a proper validation.

The first thing we consider is the spatial resolution: a fairly large wind turbine model is sought for as it will allow for a better spatial resolution of the measurements. This in turn requires a large wind tunnel as the blockage effects should be kept to a minimum for the results to be representative of a full scale wind turbine.

The wind tunnel used here is the low speed L1-B at the von Karman Institute. It is a closed-loop wind tunnel with test section dimensions of 3 m in width, 2 m in height, and a length of ≃20 m. A schematic of the test section is presented in Figure 1.

The test section is equipped with a roughened floor to allow the growth of a turbulent boundary layer similar to the lower part of an atmospheric boundary layer (ABL) in neutral conditions. The flow can be adjusted from 1 to 50 m/s; the present case will focus on a value of ≃6.5 m/s. This is such that the rotational speed of the wind turbine remains safe to operate.

The wind turbine, detailed in the next section, has a diameter of ø80 cm, and a hub height of 61 cm. It is placed at the beginning of a turntable, where the height of the boundary layer has reached the height of the half-channel (1 m), and where the flow is no longer developing significantly. This location constitutes a trade-off between putting it as far downstream to have a fully developed incoming profile, and as far upstream to allow for the measurement of the wake. As shown in Figure 1, a probe displacement system has been added to measure at three locations (labeled (1), (2) and (3)) using hot wire anemometry. The probe is secured using a pole, displaced in the test section with minimal intrusiveness, as shown in Figure 2. Hot wire anemometry is used to capture the mean flow velocity as well as the fluctuations.



Figure 2: Wind turbine and hot wire setup in the L1-B test section

2.2. *Wind turbine model*

The wind turbine model has been developed for providing a validation case for LES with ALM which reproduces the wake of a wind turbine as close as 1 wind turbine diameter downstream (1D). It is therefore important to have a nacelle as compact as the full scale wind turbines in relative terms.

The first parameter, defining the diameter of the rotor, is the blockage effect in the wind tunnel, which cannot be avoided but should be minimized. The interaction with the ground is desired, therefore this region should be omitted from the blockage calculation. According to [1], the blockage ratio $B = \frac{swept\ area}{wind\ tunnel\ area}$ should be <10 %, and the minimum distance to a wall

should be $> 1D$. With those constrain, the resulting wind turbine is 80 cm in diameter, at a hub height of 61 cm. The blockage, excluding the region below hub height, is 6.0 %, with a clearance to the top wall of 1.0 m.

We also wish to produce a wake whose statistics are independent of the Reynolds number, as described in [2]. According to this reference, this independence start at $Re \approx 9.3 \times 10^4$ (with Re based on the rotor diameter and free steam velocity). The present wind turbine model operates at $Re \geq 35 \times 10^4$, which is well above that recommendation.

The support of the wind turbine allows yaw control. The nacelle has been kept to a minimal size, in an attempt to obtain a realistic ratio to the swept diameter. Components inside the nacelle are kept within a diameter of ø8 cm, thus 10 % of the swept diameter. It contains a swash plate controlled by three electric motors allowing the pitch control, both collective and cyclic. Additionally, to allow the placement of sensors on/in the blade (such as strain gauge at the root and pressure sensor inside the blade), a slip ring is used to transfer the signals from the rotating frame to the stationary one. As those elements occupy space in the nacelle, the generator is placed under the wind tunnel, the aerodynamic power being transmitted through a set of spiral bevel gears. The total length of the nacelle, from the base of the blade support to the furthest part downstream, is 231 mm which is approximately 3 times the nacelle diameter.

With the generator placed under the wind tunnel, a rack and pinion are used to change the height of the wind turbine inside the test section.

The blades have been 3D printed using the plastic PLA+, a variation of PLA with added material making the resulting part more ductile. The ductility of the material allows the blade to flex under load without breaking. It is attached to the wind turbine using a cylindrical hole at the base of the blade, in which a steel rod is inserted, which is then attached to the pitch control mechanism with tight manufacturing tolerance. The airfoil used for the blades is the SD7037-092-88, a low Reynolds airfoil which is suited for such small wind turbine. This airfoil shape is used for the whole blade. Compared to airfoil used in large wind turbine, it is more slender to avoid detachment of the boundary layer at the lower Reynolds numbers. The twist angle and chord distribution of the blades have been designed using a classical BEM approach. A second iteration of the blade design could improve the total power extraction, mostly to improve the region close to the blade root, but the current design can already serve as a validation case, as the same parameters will be used for the ALM model.

Because this wind turbine is being used for experiments regarding the wake, the electrical power generated is dissipated in an electrical resistance. The control strategy for regulating the rotational speed is to vary the load on the generator by connecting more/less electrical resistances on the generator, using a set of relays. Ten resistances are used, each having a resistance double of the previous one. This results in a 10-bit binary code for the load of the wind turbine, which provides 1024 possibles load values; hence an almost continuous set of loadings. The 3 phase alternating current (AC) generator is converted to direct current (DC) using a full bridge rectifier, before being connected to the load. This ensures a balanced load on the three phases at all times, and it eases the control equipment. An encoder is attached to the generator to obtain the rotational speed of the wind turbine, connected to an Arduino, which also controls the relays to act on the load.

In the scope of this study, the wind turbine is operated at constant speed, and with the same inlet velocity profile. One could assume that the load can be set manually once to obtain the desired rotational speed during the tests. However, as the resistances dissipate a significant amount of energy, the temperature changes throughout the experiment. The electrical resistance being proportional to the temperature, there is then a significant drift over time, and the load needs to be adjusted dynamically to maintain the rotational speed constant. For this, a Proportional-Integral (PI) controller is used on the Arduino. It is a Single-Input Single-Output (SISO) controller with the rotational speed as input, and the set of relays loading the generator with resistances as output. The parameters of this controller were adjusted experimentally by linearization around the desired operating point, with effective results.

The rotational speed was defined arbitrarily to 700 RPM (which is a Tip Speed Ratio TSR of 4.6, where the optimum of the current design is $\simeq 5$). This parameter does not have to match the optimum, and can be reproduced in LES easily.

3. Experimental measurements

Measuring the wake is performed using hot wire anemometry. This technique provides high frequency response, hence it is able to measure the turbulent fluctuations. The downside of this methodology is the aging of the wire during its operation, which requires

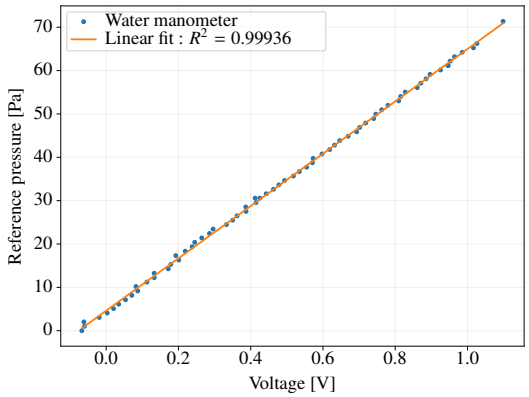

Figure 3: Pressure transducer calibration.

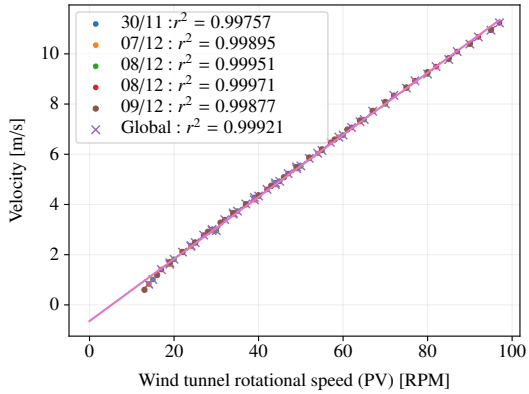

Figure 4: Wind tunnel calibration.

to re-calibrate it periodically. Multiple methodologies were explored for this calibration, but only the selected method is presented here.

3.1. Calibrations

First, a pressure transducer compensated in temperature has been calibrated using both a water manometer and a reference pressure calibrator, see Figure 3, with the combination of them reducing the total uncertainties. This calibration has been repeated over one week, and no drift in time was observed, giving good confidence in the measurements. This pressure transducer is then used to measure the difference in pressure between a pitot tube placed in the center of the test section (at 982 mm from the bottom wall) and a static pressure tap on the wall. Assuming incompressibility, the Bernoulli equation is used to convert the difference of pressure into the local flow velocity. This operation is performed at both locations (1) and (2), where the hot wire will be measuring the profile.

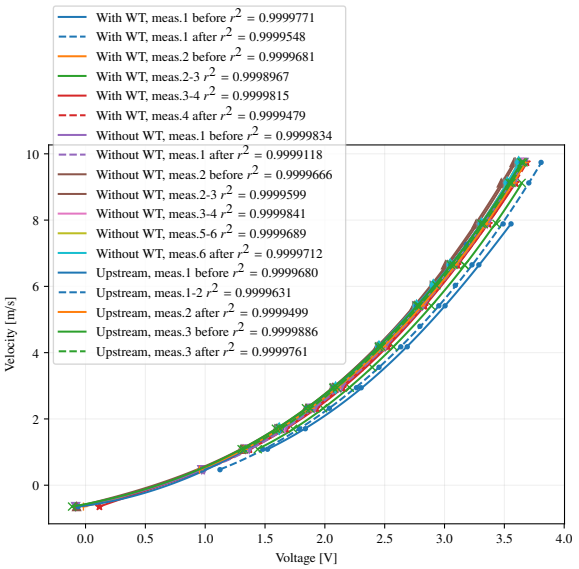

Figure 5: Hot wire calibrations.

Next, the wind tunnel is set at multiple velocities, relating the rotational speed of the motor to the local flow velocity at the center of the channel. This relationship is shown in Figure 4. This step has been repeated over two weeks, with excellent repeatability, giving good confidence in the methodology; then repeated at both locations (1) and (2).

Finally, the pitot tube was replaced with the hot wire mounted on an automated displacement system. Calibration of the hot wire was performed periodically before and after each set of measurements, with a time between calibration ranging from 1 to 1.5 hours. All calibrations curves are shown in Figure 5. It is seen that the curves differ slightly from each other, showing that the calibrations were frequent enough to minimize uncertainties. Overall, one can observe a trend for the curves to move towards the left, as the wire ages over time.

3.2. Measurements

So far, measurements were performed at locations (1) and (2) of Figure 1. They will also be performed at location (3) in the future. We see that the height of the test section (2 m) is bigger than the travel of the hot wire traverse system. Measuring over the entire height of the test section has to be done in two parts, with an overlap region.

Location (1) is ideally positioned to be sufficiently upstream from the wind turbine such that it is unaf-

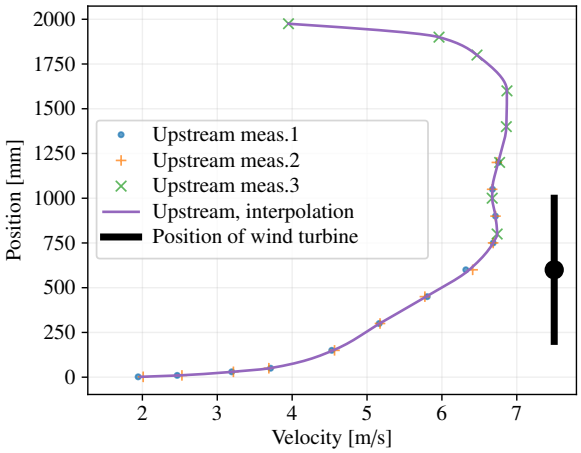

Figure 6: Mean velocity profile.

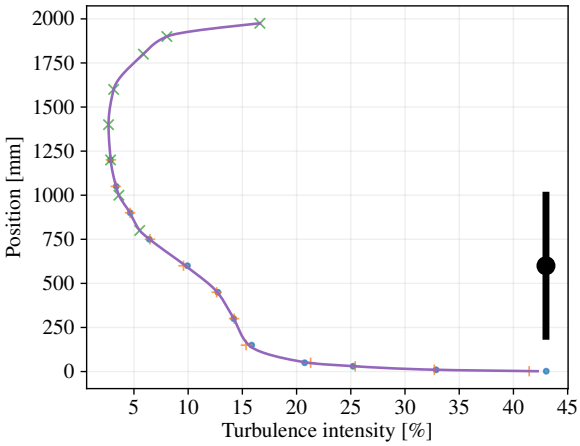

Figure 7: Turbulence intensity profile.

fected by its presence, and sufficiently downstream in the test section to capture the effect of the roughened bottom wall. This profile is also required to impose the inlet in the numerical simulation. The measurement was done in two parts, with significant overlap, and measurements repeated over two days. The overlap is observed between 800 mm and 1200 mm, with a good repeatability. Figure **??** shows the resulting profile, with measurement 1 taken on one day, and measurements 2 and 3 taken on the next day to ensure repeatability. The profile is overall a developing profile, with the bottom boundary layer height being well-developed (reaching close to the half channel height), while the top boundary layer is much thinner due to the smooth wall. The resolution at the top is not as good as that at the bottom, as this region affects very little the wind turbine and only serves to capture the blockage effect of the wind tunnel. The uppermost point is also not as close to the wall as the lowermost point: this is due to the shape of the probe, designed for measuring the boundary layer at the bottom.

The turbulence intensity profile measured is given in Figure 7. This was measured with a hot wire facing the flow horizontally, meaning that it is sensitive to velocity fluctuations in the streamwise and vertical direction (without differentiation), not to the spanwise direction. From the measured signal of the hot wire, the calibration is applied, then its standard deviation is divided by the local mean velocity (shown in Figure 6) to obtain the turbulence intensity.

Measurements at location (2) were made for both cases, with and without the wind turbine, and are presented in Figure **??**. For each case, the profiles were measured on one day, and repeated on the next day to ensure repeatability, and also add resolution in the regions of interest (the measurement 1 was done on the first day, all others were done on the next day). Each reported value uses its own calibration curve, before and after the measurement, with a maximum time of 1.5 h between calibrations.

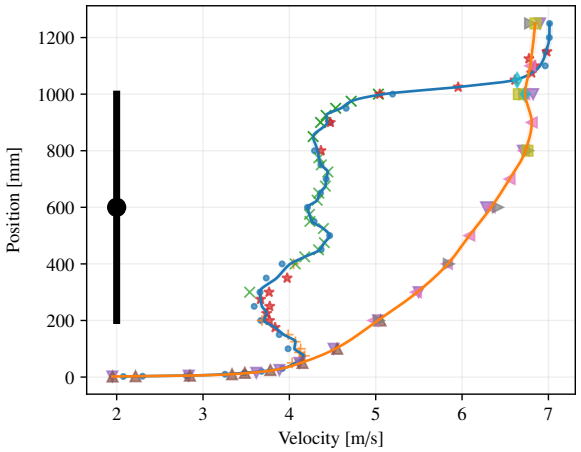

Figure 8: Mean velocity profile.

The profile without the wind turbine (orange curve from Figure **??**) shows a boundary layer height almost reaching the top height of the wind turbine. This depicts that the wind turbine will be subjected to a flow similar to that of an Atmospheric Boundary Layer (ABL) and which indeed encompasses the whole wind turbine. The profile also shows an inflexion point at about 1000 mm, where the bottom boundary layer meets the upper core flow. Measurements at this location were repeated multiple times to ensure that this is not an outlier.

Regarding the flow extraction from the wind tur-

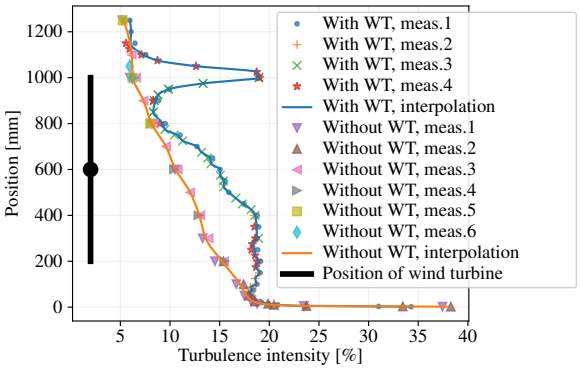

Figure 9: Turbulence intensity profile.

bine, the velocity deficit observed between the two curves shows that the wind turbine indeed extracts energy from the flow. The thrust coefficient is estimated using the two mean velocity profiles (with and without the wind turbine) measured at location (2); which leads to $C_t \simeq 0.46$. For that, the velocity is considered over a disk centered on the wind turbine axis and also slightly enlarged in diameter (to account for the expansion of the wake between the wind turbine location and location (2)). It is assumed homogeneous spanwise. The thrust available in each flow is estimated as $T = \frac{\rho}{2} \sum_i v_i^2 \cdot (w_i \Delta h)$ where ρ is the air density in the test section, v_i is the measured velocity at height i, w_i is the width of the strip associated to the disk at that height and h is the spacing used to discretize the strips. The difference between the two values of T is then used to estimate C_t.

Regarding the power coefficient, the losses between the aerodynamic power at the shaft and the electrical power are not yet quantified; they can only be roughly estimated. Measuring the electrical power of the 3-phase generator is done by measuring the line voltage and current, before the conversion to DC and the load resistances; it is obtained as 18.2 W. If we ignore all losses, the electrical power coefficient is $C_p \simeq 0.25$ (compared to a theoretical designed value of $C_p \simeq 0.37$ at this TSR). The generator efficiency at such low rotational speed typically drops to ≃75 %. An additional efficiency of ≃90 % being applied to account for the bearings and the gears between the two shafts, the estimated aerodynamic power is ≃27.0 W, corresponding to $C_p \simeq 0.36$.

It can be noted that the presence of the wind turbine accelerates the flow in the top region, as seen in Figure **??** (blue curve), which is due to the blockage effect and was expected. Nevertheless, this effect can be considered small, as it only accelerates the flow by ≃ 3 % locally.

Overall the velocity deficit has an interesting shape, that was validated by the repeatability of the experiment. It can be observed that the velocity deficit is greater in the regions of the blade tip and nacelle, and lower in the region of the blade roots. The better extraction near the tip is expected, as this is where the blades were optimally designed. At the blade root, the mechanical link to the shaft forces the design to have a circular cross-section locally: this does not provide any lift contributing to the extraction of energy from the flow, but only drag. Progressing away from the blade root, there is a smooth transition to the airfoil shape which provides lift.

The velocity deficit in the wake of the nacelle is also significant, due to the drag associated with its blockage.

4. LES case methodology

As pointed out from numerous previous works, such as in [3], the wake behavior of a wind turbine is heavily influenced by the inlet velocity profile. The mean profile determines the local flow velocity on the wind turbine blades, affecting how much energy can be extracted for a chosen setup (rotation speed and blade pitch). On the other hand, the turbulence intensity of the inlet affects mostly the length of the wake, higher turbulence resulting in faster wake recovery and hence smaller wake length. It is therefore essential for a proper comparison between an experiment and a numerical simulation to reproduce the inlet with good accuracy. As such, even before introducing the wind turbine model and comparing the wake, it is essential to ensure a solid baseline case without the wind turbine, to ensure that the inlet profile used in the simulation matches well that measured in the experiment.

The case presented here is still work in progress, with results coming up in a near future. Nevertheless, the wind tunnel experiments presented above are also performed to support the development of a LES methodology that is consistent with these experiments. We here solely present the methodology as it is being pursued.

Experimentally, the top wall induces a noticeable blockage, which must also be reproduced numerically. The sides being much further away from the wind turbine, their effect is assumed to be negligible. The experimental profile is considered a developing profile, as the heights of the boundary layer between the top and the bottom do not coincide. To simulate such

flow, a "Recycle and Rescale Method" (R2M) is used, which is suited for generating turbulent inflow conditions for LES. This method is able to produce realistic and self-consistent turbulence structures of a developing flow, as shown in [4]. It consists in sampling a plane downstream (referred as the recycling plane), and copying a scaled version of it at the inlet, repeated at each timestep.

The numerical methodology is split in two cases: the first one focuses on the reproducing the base flow of the test section without the wind turbine, ensuring that the LES profiles are matching fairly well those of the experiment. The second case will be based on the first one, with the added wind turbine modeled using an Actuator Line Model (ALM).

4.1. Simulation of the base flow

The numerical domain is composed of a box with the same height as that of the experiment, and a width large enough for a periodic boundary condition to be applied. Regarding the length, the box starts at the experiment location (1) and ends downstream after location (2) from Figure 1. This is the minimum size that will allow a fair comparison with the experiment at both locations, and includes a buffer zone at the end for the outflow boundary condition. The boundary conditions and the mesh used are shown in Figure **??**. This results in a box of 5 m streamwise, 2 m

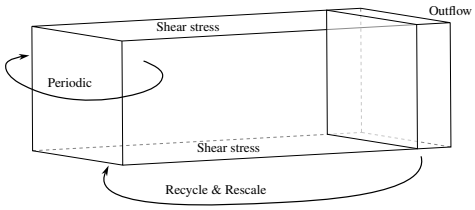

Figure 10: Boundary conditions.

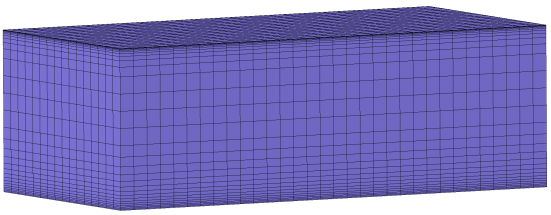

Figure 11: Mesh.

vertically, and 3 m spanwise. The mesh is constructed using a uniform distribution streamwise and spanwise, and is refined near the walls. Based on our previous work [5], we use the newly validated wall-modeled LES (wmLES) within a spectral element method for the wall boundary conditions.

The so-called recycling plane is taken at $x = 4.5$ m, far enough from the outlet such that its effect is negligible. Due to the nature of the spectral element method, Gibbs phenomena are appearing at the element boundaries when performing LES, especially for the resolved turbulent fluctuations, see [5]. The R2M is often used to scale the boundary layer height in a developing flow, by applying the scaling on the position of each point. Doing such in this framework where Gibbs phenomenon are observed at the element interface, would amplify those numerical errors by moving them to the center of an element, hence additional frequency content would appear in the flow. The scaling used here is therefore applied on the magnitude of each node, based on the ratio between the time-averaged recycling plane and the experimental profile.

Once the inlet mean profile is imposed, the remaining degree of freedom consist in adjusting the shear stress of the wall model, such that the mean profile at location (2) matches that of the experiment.

Regarding the turbulence intensity: the wall shear stress will most likely provide the correct turbulence level near the wall. However, the turbulence measured experimentally in the free stream away from the wall is not negligible, even in the region where the mean velocity profile is essentially flat. Since this could also affect the resulting wake, a set of added randomized forces will probably be necessary to perturb the flow locally in the recycling region; with their amplitude being tuned so as to match the turbulence level in the simulation to that of the experiment.

4.2. Simulation of flow with the wind turbine

Once the base flow LES matches sufficiently well that of the experiment without wind turbine, we consider the next case which includes the wind turbine, here modelled using the newly implemented Actuator Line Model (ALM). The domain is similar to the previous one, but it is extended downstream to capture the wake. The parameters of the ALM are based on the effective design of the wind turbine. This includes the polar data for lift and drag of the airfoil used, the chord and twist distributions of the blade, the pitch angle, and the rotational speed.

In order to capture properly the behavior from the wind turbine, the mesh is refined in the region of the wind turbine, to allow the forces from the ALM to be properly captured. An illustration of the resulting mesh is provided in Figure **??**.

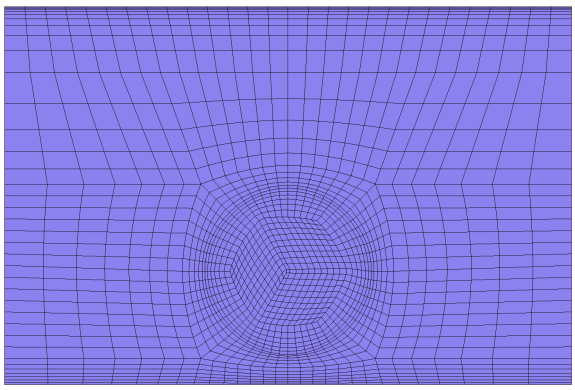

Figure 12: Cross-section of the mesh

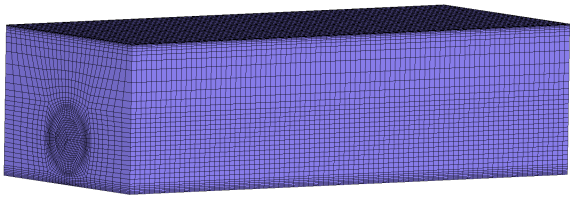

Figure 13: Overview of the mesh

With matching inlet mean velocity and turbulence intensity profiles from the previous case of the base flow (Section 4.1), the difference between the simulated wake and the experimental one shall be investigated, and any mismatch will be clearly identified.

Recall that it remains challenging to properly capture the near tip blade loading and the shedding of tip vortices when using ALM, as this is much influenced by the local resolution. This, in turn, can significantly influence the transition of the near wake to its turbulent state. The ALM in the near tip region will hence be more refined, so that the tip vortices are better captured and can better contribute to a transition to wake turbulence.

5. Conclusions

The presented work aims at reducing the gap between LES and wind tunnel experiments for wind turbine wake, and it is still work in progress. An experimental turbine was designed, built and used for future comparison with LES using an actuator line model. The estimated thrust and power coefficients are within the expected range, giving some confidence that the wake produced is representative of a wind turbine in normal operation.

Measurements have been performed at a location upstream of the wind turbine, to be imposed as inlet to the LES, and at a location downstream of it. The case without the wind turbine was also measured at both locations. The obtained results showed excellent repeatability and will be used to compare with future numerical results. The experimental profile at location (3) will also be measured in the future, bringing added data for the comparison with the LES.

The numerical simulation of this configuration is ongoing work. The pursued methodology was detailed and it is intrinsically linked to the way the experiments were designed and performed. The flow will be simulated in LES over the full height of the test section, and the numerical results will be used for a detailed comparison with those of the experiment. The differences between the two will also allow to fine-tune the parameters of the ALM representing the wind turbine.

References

[1] S. McTavish, D. Feszty, F. Nitzsche, An experimental and computational assessment of blockage effects on wind turbine wake development, Wind Energy 17 (10) (2013) 1515–1529. doi:10.1002/we.1648.

[2] L. Chamorro, R. Arndt, F. Sotiropoulos, Reynolds number dependence of turbulence statistics in the wake of wind turbines, Wind Energy 15 (5) (2011) 733–742. doi:10.1002/we.501.

[3] F. Porté-Agel, M. Bastankhah, S. Shamsoddin, Wind-turbine and wind-farm flows: A review, Boundary-Layer Meteorology 174 (1) (2019) 1–59. doi:10.1007/s10546-019-00473-0.

[4] F. Xiao, M. Dianat, J. J. McGuirk, An LES turbulent inflow generator using a recycling and rescaling method, Flow, Turbulence and Combustion 98 (3) (2016) 663–695. doi:10.1007/s10494-016-9778-6.

[5] E. Gillyns, S. Buckingham, G. Winckelmans, Implementation and validation of an algebraic wall model for LES in nek5000, Flow, Turbulence and Combustion 109 (4) (2022) 1111–1131. doi:10.1007/s10494-022-00378-y.

Parametric sensitivity analysis of precursor generated inflow profiles including atmospheric stability for RANS based ABL microscale wind simulations

Trond-Ola Hågbo[1,2], Kartik Venkatraman[2,3], Sophia Buckingham[2], Knut Erik Teigen Giljarhus[1]

[1]*Department of Mechanical and Structural Engineering and Materials Science, University of Stavanger, Norway, trond-ola.hagbo@uis.no*

[2]*Environmental and Applied Fluid Dynamics Department, von Karman Institute for Fluid Dynamics, Belgium*

[3]*Université de Sherbrooke, Canada*

Supervisor: Jeroen van Beeck

Professor, Environmental and Applied Fluid Dynamics Department, von Karman Institute for Fluid Dynamics, Belgium, jeroen.vanbeeck@vki.ac.be

University Supervisor: Knut Erik Teigen Giljarhus

Associate Professor, Department of Mechanical and Structural Engineering and Materials Science, University of Stavanger, Norway, knut.e.giljarhus@uis.no

Abstract

Atmospheric thermal stability is fundamental in atmospheric science and central to driving global circulation patterns while strongly influencing local weather. The wind behavior within the atmospheric boundary layer (ABL) is commonly modeled using Computational Fluid Dynamics (CFD) tools for numerous applications of microscale wind simulations. However, idealized inlet profiles that do not account for atmospheric stability are usually employed in these simulations, even though these conditions can seriously affect the wind.

No articles found by the authors of this paper utilize a heat flux (heating or cooling of the ground) in their precursor model to tackle the challenge of controlling realistic ABL inflow. Also, the wind profile response to altering the influential parameters is intricate, dependent on multiple conditions, and inadequately understood.

This parametric study addresses the described research gap by investigating the effect of various meteorological, atmospheric, and geographic parameters on ABL wind profiles for precursor-generated inflows. The sensitivity study involved manipulating simulation inputs, including ground heating/cooling, atmospheric pressure difference, roughness length, latitude, and the number of iterations.

Our results show that some parameters have a clear and straightforward effect on wind profiles, while others are more complex and depend on atmospheric stability. This insight has important implications for using realistic inflow profiles for CFD microscale wind simulations. The knowledge can be used to efficiently generate inlet profiles suitable for a range of ABL microscale wind modeling applications.

Keywords: Atmospheric stability, atmospheric boundary layer, microscale, realistic inflow profiles, surface heat flux, parametric study, precursor.

Data assimilation of multiple local observations in WRF for improved weather and power predictions at the Belgian offshore wind farms

Tsvetelina Ivanova

Environmental and Applied Fluid Dynamics Department, von Karman Institute for Fluid Dynamics, Belgium, tsvetelina.ivanova@vki.ac.be

Supervisors: Wim Munters, Sophia Buckingham, Sara Porchetta, Jeroen van Beeck

Environmental and Applied Fluid Dynamics Department, von Karman Institute for Fluid Dynamics, Belgium, wim.munters@vki.ac.be

University Supervisor: Jan Helsen

Department of Mechanical Engineering, Vrije Universiteit Brussel, Belgium, jan.helsen@vub.be

Abstract

The data assimilation techniques (DA) in the Weather Research and Forecasting model (WRF) in combination with a wind farm parameterization (WFP), lead to improved prediction of power, wind speed, and wind direction with respect to SCADA data. In addition, rain has a significant contribution to wind turbine leading edge erosion (LEE) and is therefore also of interest.

Keywords: numerical weather prediction, WRF, data assimilation, wind farm parameterization, ensemble forecasting, offshore wind energy, atmospheric drivers for leading edge erosion, nowcasting

1. Introduction

With ongoing expansion of renewable wind energy, the importance of reliable numerical weather predictions for wind farms is becoming increasingly significant. Wind farms must be operated with well-informed decisions, and accurate weather predictions can aid the decision-making process for more efficient power extraction and wind turbine maintenance. These predictions can also contribute to the further understanding of rain-induced leading edge erosion (LEE) of wind turbine blades.

The atmosphere is a complex nonlinear system and therefore NWP is highly sensitive to initial and boundary conditions. Imposing the initial conditions more accurately is essential for reliable numerical results, and a way to do so is by data assimilation. The main concept of DA is to find the optimal initial state of the atmosphere by combining numerical solutions with observations.

The main tool of this work is the Weather Research and Forecasting model (WRF, v4.4), an open-source NWP modeling system [1]. In this work, a forecasting system is set up by combining in a novel way the specifics of offshore wind energy in the Belgian North Sea with a wind farm parameterization (WFP) from Fitch et al., 2012, and data assimilation (DA) techniques. The WFP represents the effect of the presence of the wind farms by imposing a momentum sink on the flow. The DA techniques aim to reduce the differences between the numerical results and observations, which can be achieved either by introducing tendency terms in the equations (as in "nudging" – four-dimensional DA), or by solving an optimization problem for the atmospheric state (as in variational DA – 3DVar and 4DVar). The observations used in this work are from multiple sources, such as local wind information from LiDAR and SCADA, and rain data from Radar and IMERG (Integrated Multi-satellite Retrievals for Global Precipitation Measurement).

The data assimilation techniques in WRF, in combination with WFP, lead to improved predictions for power production, wind speed, and wind direction

with respect to SCADA data. In addition, rain predictions are also influenced by DA, and rain has a significant contribution among the atmospheric drivers of leading edge erosion of wind turbine blades. The results from this work provide a framework for estimating rain-induced LEE in the Belgian North Sea, and a reliable forecasting system for improved predictions in time scales from minutes-ahead to days-ahead.

This PhD topic is part of the ICON project RAINBOW on optimized prediction and decision support for rain erosion of wind turbine blades. One of the objectives of this PhD is to optimally set up WRF for predicting weather conditions using data assimilation of local observations at the wind farms in the Belgian North Sea. As a consequence, decision support in the offshore wind farms can be improved. Another objective that relies strongly on NWP is to reach a further understanding of the drivers for LEE of the wind turbine blades, and to possibly better predict and mitigate it.

2. Remote sensing for offshore wind energy

IMERG algorithm: Combines info from GPM satellites constellation to estimate precipitation over the Earth's surface (2000 – present). The IMERG dataset has been widely evaluated [2] and can be used for wind turbine leading edge erosion, with rain being the main atmospheric driver for this process [2]. An extensive review on atmospheric drivers on LEE is given in [3].

Rain maps based on observations from meteostations and consequent erosion maps are discussed in [4]

3. Nowcasting

Observation-based nowcasting using the modular and open-source framework for short-term prediction systems, Pysteps [5].

4. Methodology

4.1. Wind farm parameterization (WFP)

In this work, the Fitch scheme is used, in which the effect of the wind farms is represented by imposing a momentum sink on the flow [6].

4.2. Ensemble forecasting

Random perturbations of accumulated physics tendencies of potential temperature, wind and humidity [7].

4.3. Four-dimensional data assimilation (FDDA or Nudging)

Introducing tendency terms in the equations to gradually nudge the solutions towards observations [7].

4.4. Three-dimensional variational data assimilation (3DVar)

Combining forecasts and observations to find the optimal initial state of the atmosphere [7].

4.5. Four-dimensional variational data assimilation (4DVar)

Finding the model trajectory that best fits the observations and the initial estimate of the atmospheric state.

5. Numerical setup

The numerical setup is adapted from the configuration for the New European Wind Atlas (NEWA) [8]. It has 61 vertical levels, 6 of which are below a typical hub height of an offshore wind turbine. The horizontal resolutions of the nested domains are 18 km, 6 km, and 2 km, as indicated also in Figure 2. The sizes in kilometers of the domains are as follows. For D01 – 1980 km by 1980 km, for D02 – 1320 km by 1194 km, and for D03 – 680 km by 596 km.

Fitch wind farm parameterization [6]

Guides from [9]

5.1. Domain

6. Results and Discussion

Forecast evaluation

6.1. Wind farm parameterization (WFP)

- WFP of Belgian-Dutch cluster
- WFP of all fully commissioned wind turbines in the North sea.

6.2. Ensemble forecasting

introducing perturbations and generating ensemble members by using SPPT and SPP

6.3. Four-dimensional data assimilation (FDDA or Nudging)

nudging of u,v components of the wind that are computed from SCADA data;

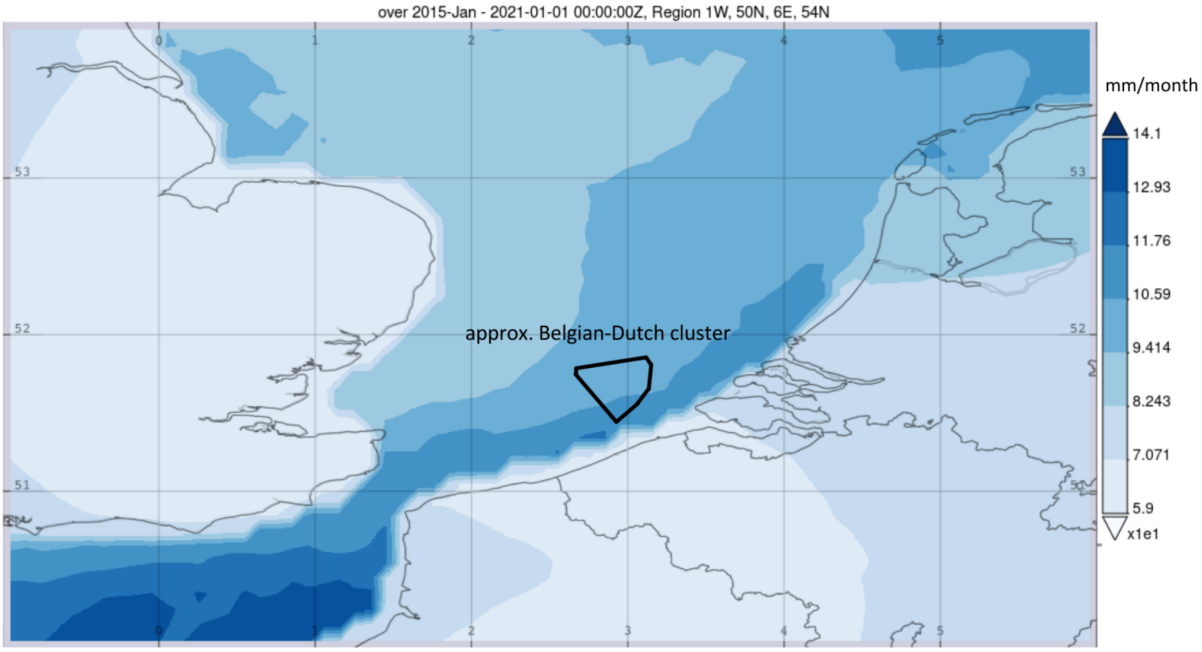

Figure 1: IMERG Rain map at the Belgian North Sea.

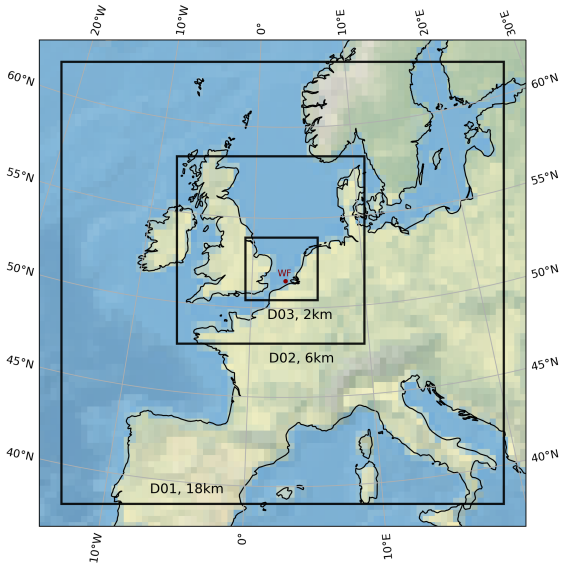

Figure 2: Nested domains with horizontal resolutions of 18 km (D01), 6 km (D02), 2 km (D03).

6.4. Three-dimensional variational data assimilation (3DVar)

- tests with own generated background error matrix: assimilation of LiDAR, assimilation of SCADA
- tests with provided background error matrix that is suitable for any case: response to single observation assimilation

6.5. Four-dimensional variational data assimilation (4DVar)

- tests with provided background error matrix that is suitable for any case: response to single observation assimilation
- next steps: assimilate SCADA over a sufficiently long period and assimilate also accumulated rain observations (GPM IMERG).

7. Conclusion

Possible continuations: Ensemble forecasting with Data assimilation

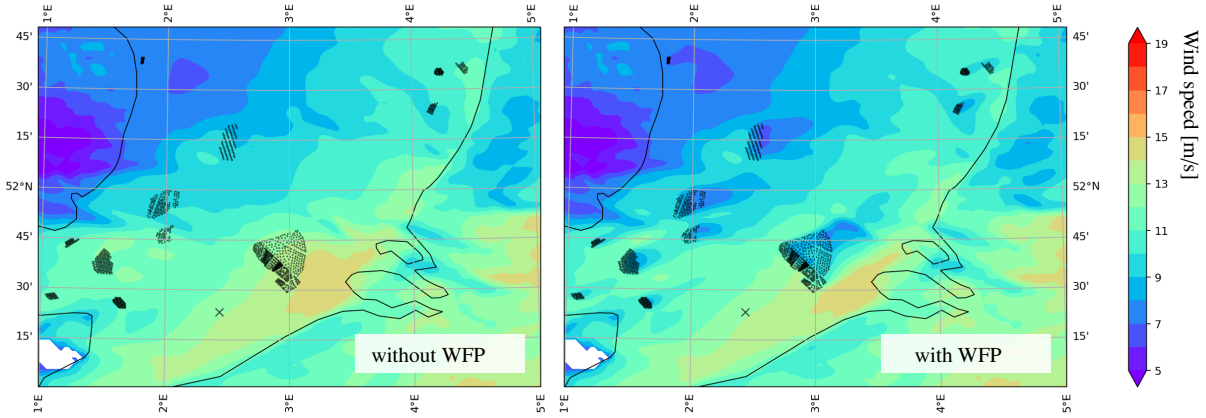

Figure 3: WFP with and without: all fully commissioned wind turbines in the North Sea.

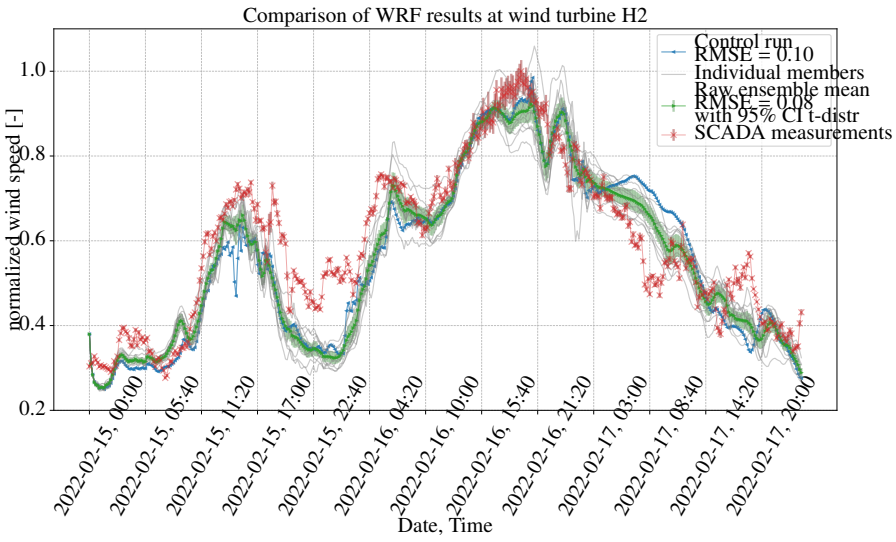

Figure 4: Ensemble forecasting.

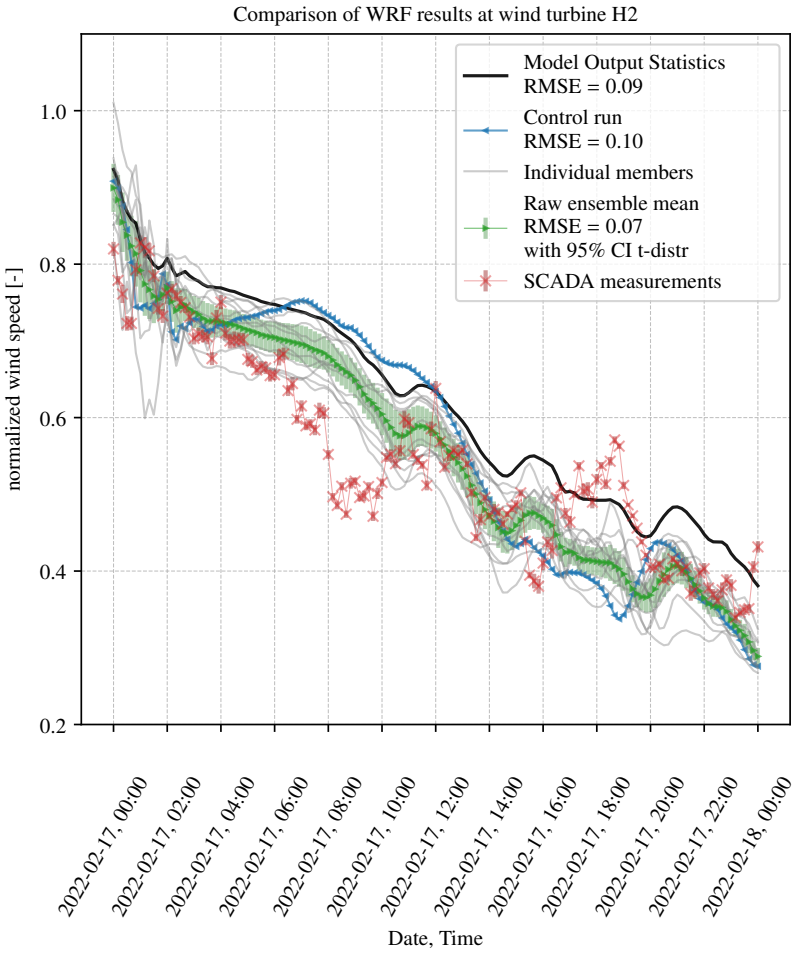

Figure 5: Ensemble forecasting postprocessing MOS.

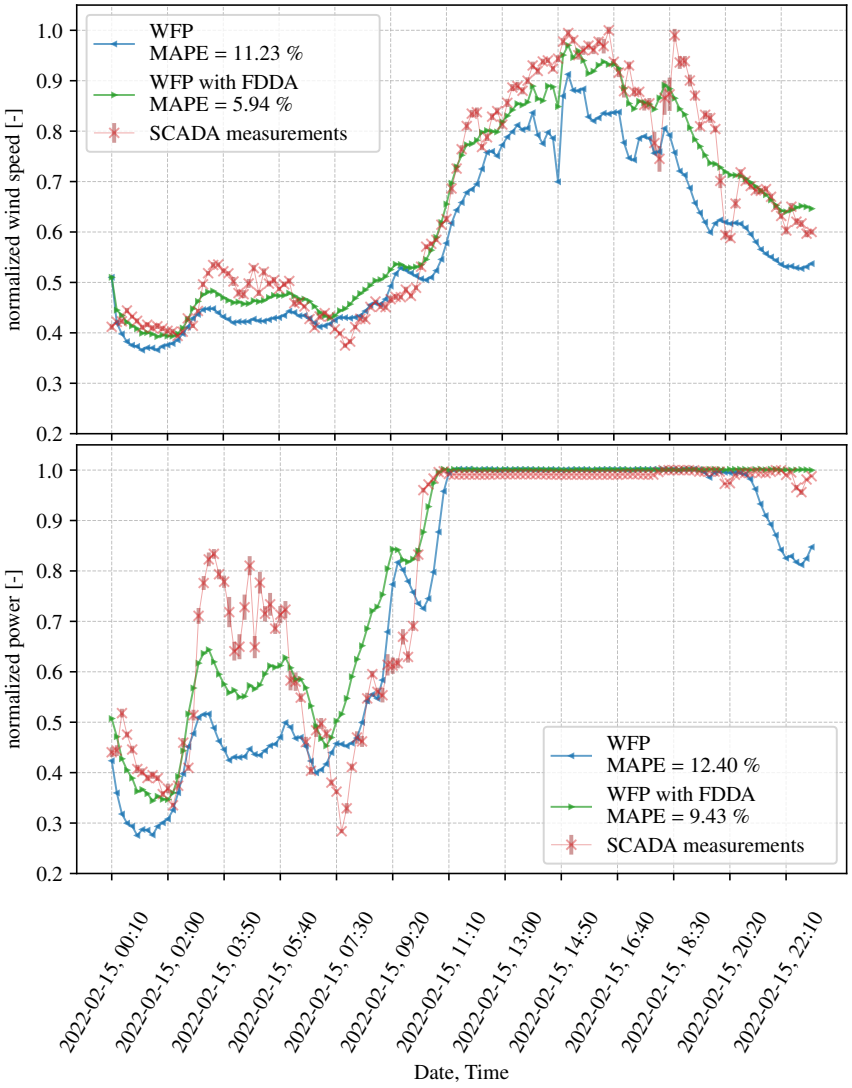

Figure 6: Nudging.

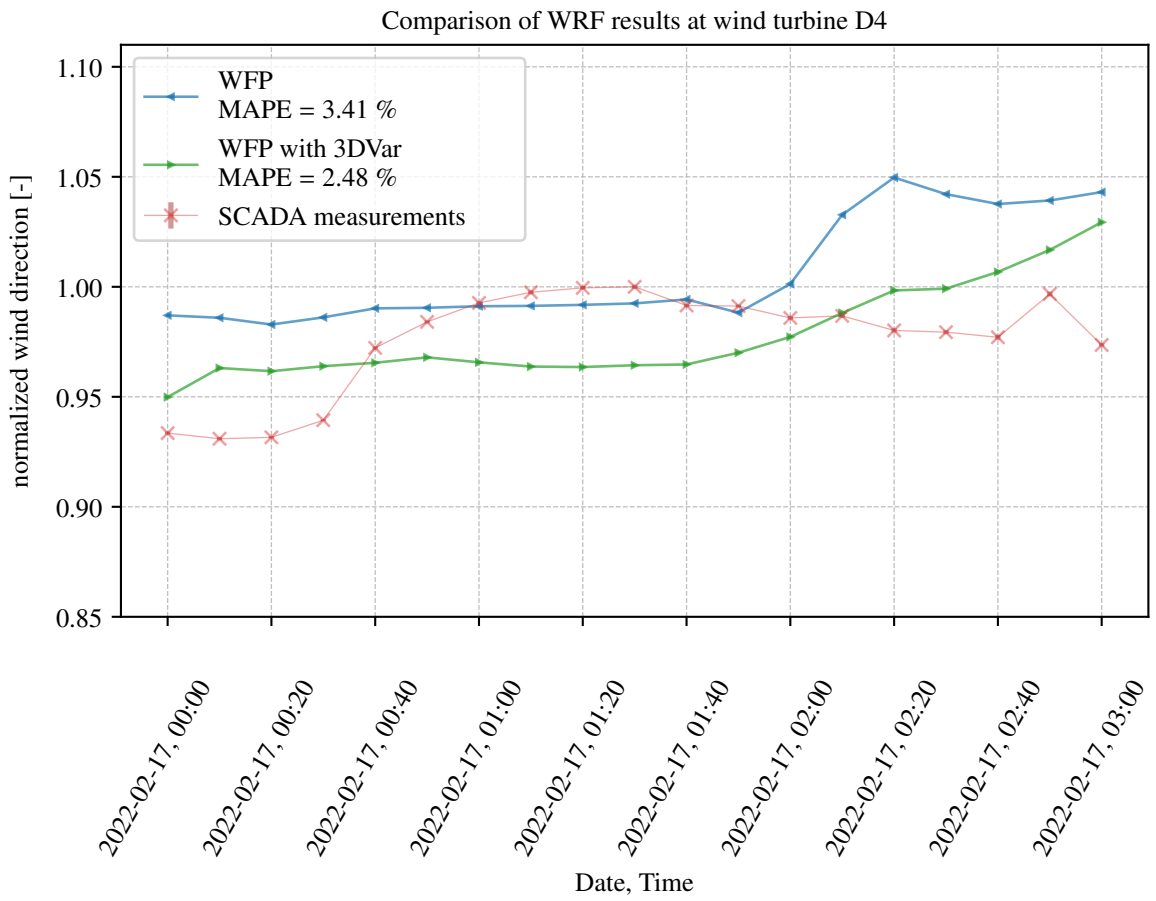

Figure 7: 3DVar.

Acknowledgments

This PhD topic is funded within the framework of the ICON project RAINBOW, which is supported by the Flemish Government via the Agency for Innovation and Entrepreneurship (VLAIO).
This work is performed using free and open-source software: the authors would like to express gratitude to the communities for building powerful tools from which everyone can benefit.

References

[1] W. C. Skamarock, et al., A Description of the Advanced Research WRF Model Version 4, Tech. rep., UCAR/NCAR (2019). doi:10.5065/1DFH-6P97.

[2] M. Badger, H. Zuo, Ásta Hannesdóttir, A. Owda, C. Hasager, Lifetime prediction of turbine blades using global precipitation products from satellitesdoi:10.5194/wes-2022-59.
URL https://doi.org/10.5194/wes-2022-59

[3] S. C. Pryor, R. J. Barthelmie, J. Cadence, E. Dellwik, C. B. Hasager, S. T. Kral, J. Reuder, M. Rodgers, M. Veraart, Atmospheric drivers of wind turbine blade leading edge erosion: Review and recommendations for future research (11 2022). doi:10.3390/en15228553.

[4] K. Pugh, M. M. Stack, Rain erosion maps for wind turbines based on geographical locations: A case study in ireland and britain, Journal of Bio- and Tribo-Corrosion 7. doi:10.1007/s40735-021-00472-0.

[5] S. Pulkkinen, D. Nerini, A. A. P. Hortal, C. Velasco-Forero, A. Seed, U. Germann, L. Foresti, Pysteps: An open-source python library for probabilistic precipitation nowcasting (v1.0), Geoscientific Model Development 12 (2019) 4185–4219. doi:10.5194/gmd-12-4185-2019.

[6] A. C. Fitch, J. B. Olson, J. K. Lundquist, J. Dudhia, A. K. Gupta, J. Michalakes, I. Barstad, Local and mesoscale impacts of wind farms as parameterized in a mesoscale nwp model, Monthly Weather Review 140 (2012) 3017–3038. doi:10.1175/MWR-D-11-00352.1.

[7] W. C. Skamarock, J. B. Klemp, J. Dudhia, D. O. Gill, Z. Liu, J. Berner, W. Wang, J. G. Powers, M. G. Duda, D. M. Barker, X.-Y. Huang, A description of the advanced research wrf model version 4.
URL http://library.ucar.edu/research/publish-technote

[8] A. N. Hahmann, T. Sile, B. Witha, N. N. Davis, M. Dörenkämper, Y. Ezber, E. Garciá-Bustamante, J. F. González-Rouco, J. Navarro, B. T. Olsen, S. Söderberg, The making of the new european wind atlas - part 1: Model sensitivity, Geoscientific Model Development 13 (2020) 5053–5078. doi:10.5194/gmd-13-5053-2020.

[9] J. C. Y. Lee, J. K. Lundquist, Evaluation of the wind farm parameterization in the weather research and forecasting model (version 3.8.1) with meteorological and turbine power data (Jun. 2017). doi:10.5194/gmd-2017-128.
URL https://doi.org/10.5194/gmd-2017-128

Buried detonation airblast characterization

Pierrette Atikpo

Mechanical Engineering Department, Royal Military Academy, Belgium,
pierrette.atikpo@mil.be

Environmental and Applied Fluid Dynamics Department, von Karman Institute for Fluid Dynamics, Belgium,
pierrette.atikpo@vki.ac.be

Promotor: Lieutenant-Colonel Bart Janssens

Associate Professor, Mechanical Engineering Department, Royal Military Academy, Belgium,
bart.janssens@mil.be

Promotor: Lieutenant-Colonel David Lecompte

Associate Professor, Head of Military and Protective Engineering Department, Royal Military Academy, Belgium,
david.lecompte@mil.be

VKI Supervisor: Delphine Laboureur

Associate Professor, Environmental and Applied Fluid Dynamics Department, von Karman Institute for Fluid Dynamics, Belgium,
delphine.laboureur@vki.ac.be

VKI Advisor: Charline Fouchier

Research Engineer, Environmental and Applied Fluid Dynamics Department, von Karman Institute for Fluid Dynamics, Belgium,
charline.fouchier@vki.ac.be

University Supervisor: Mark Runacres

Professor, Mechanical Engineering Department, Vrije Universiteit Brussel, Belgium,
mark.runacres@vub.be

Abstract

Whether buried detonations are used for productive or destructive purposes, the accurate characterization of the blast wave they generate in air is crucial in preventing and mitigating risks associated with them. In this study, 50kg TNT equivalent explosives buried in a pit of 3m deep, 5m diameter and covered with soil up to 2m above ground level was detonated. To measure the blast waves, four blast pencils were placed at 10m, 20m, 30m and 20m90°. Using experimental method and theoretical normal shock approach, an extensive parameters to characterize the blast wave were provided and prediction models were developed for each experimental parameter using second order polynomial interpolation. The blast wave parameters include peak overpressure, arrival time, impulse, duration, shock velocity, Mach number, shock front thickness, wave form parameter, density, pressure, temperature and sound speed. The main observation in this paper is that the blast waves recorded were highly attenuated and their fronts are characterized by two pressure peaks, known as porched shock front waves. To make our models more accurate, more experiments need to be carried out taking into account large range depth of burial, standoff distance, explosive charge mass, chemical composition, geometry, soil type, moisture content and density.

Keywords: shock wave, buried detonation, normal shock theory, explosion

1. Introduction

Since the invention of gun powder in 9th century AD and the invention of dynamite and detonator in 1867 by Albert Nobel, explosives have become important tools in our lives. An explosion is a process resulting from a sudden release of energy [1]. When such energy is released, it activates the adjacent materials. Detonation occurs when adjacent materials are activated due to mechanical forces, that is shock pressure forces. A detonation can happen on the ground (surface detonation) or deep in the ground (buried detonation). When a buried detonation occurs, the shock energy released propagates through the surrounding soil material in all direction and at a very high speed. A big amount of that violent shock energy is used to pulverize and compact the surrounding soil material,leading to the attenuation of the shock wave by the time it reaches the ground surface. Explosives can be used for productive applications such as construction of railways, canals, dams, mining and safe demolition of abandoned buildings. However, they can also be used for destructive purposes such as in terrorism. An important feature of an explosion is the blast wave that it generates in air. Thus, providing an accurate characterization of the blast wave is crucial in preventing and mitigating risks associated with explosions. In the near-field of the explosion, the blast generated is known shock wave. It is characterized by higher Mach number ($M > 1$) [2], thus higher shock front velocity and smaller shock front thickness (in order of few molecular mean free path) [1], [3] . In the far-field, the shock wave disintegrates into acoustic wave which is characterized by smaller Mach number (Mach number around 1), with wave front velocity close to the sonic velocity and with larger wave front thickness.

To fully characterize a blast wave, two categories of parameters are required. The first category is composed of independent parameters [1]. They are the parameters associated with the initial shock intensity (peak overpressure, Mach number and velocity), blast wave duration, specific impulse and arrival time. The second category is made of the derived parameters. They include the density, sound speed, pressure, temperature, shock thickness and the wave form parameter. The blast wave impulse can be divided into positive impulse associated with the positive pressure phase of the blast wave and negative impulse associated with the negative pressure phase. Because the positive impulse is often more significant and more stable to quantify, it is often used as mean to characterize the impulse of the entire blast wave [1]. The specific impulse which is defined as the impulse per unit area is represented graphically as the area under the blast wave pressure - time curve. The impulse is an important characteristic as it is used to evaluate the degree of the damage-causing capacity of the blast. The specific impulse can be found by performing numerical integration of the pressure - time curve. To perform numerical integration of tabulated data, the commonly used algorithms are the Newton-cotes formulae [4] because the polynomials associated with them are less oscillatory [5]. The Newton-Cotes algorithms are the Trapezoidal rule, Simpson's $1/3^{rd}$ rule, Simpson's $3/8^{th}$ rule etc. Theoretically, the shock front is supposed to be an instantaneous discontinuity. However, experimentally, it is observed that the shock front is not an abrupt process but instead comes in gradually because of heat transfer and viscosity. Thus, giving rise to the shock front thickness. The theory of shock front thickness is based on the assumption that in the vicinity of large velocity gradient inside the shock, the viscosity and heat conduction are not negligible. It is observed that the change in velocity inside a shock takes place over a finite, short distance [3]. That distance is known as the shock front thickness. The first theory of the thickness of the shock was developed in 1910 by Rayleigh [6]. He supposed the fluid to be thermally and calorically a perfect gas. He took the viscosity coefficient to be a constant and the heat transfer coefficient to be zero. In 1922, Becker [7] found that a solution exists for a special value of Prandtl number. In 1943, Taylor in Durand's book [8] assumed the heat transfer coefficient to be non-zero and constant by supposing that the velocity jump across the shock is small relative to the local sound speed. In 1948, Puckett and Stewart [3] improved on the theory of the shock thickness by assuming the specific heat at constant pressure, the viscosity and heat transfer coefficient to be function of the absolute temperature for a special case of Prandtl number. This leads to the current shock thickness being defined as the ratio of the velocity difference to the maximum velocity gradient across the wave. The blast wave is characterized by an increased in pressure, followed by a decrease in pressure. The decrease in pressure often goes below the ambient pressure before coming back to the ambient pressure. The rate of decay of the pressure curve is known as the wave form or decay parameter. The positive phase of the wave, is often well modeled using the modified or Friedlander equation [9]. To accurately model the negative phase of the wave, the extended Friedlander [10] is often used.

To study blast wave, three methods can be em-

ployed: numerical method, experimental method and theoretical method. The experimental method consists of using pressure gauges or blast pencils to record the wave pressure-time curve. From this curve, the following parameters can be quantified: the peak overpressure, duration, arrival time, impulse, wave propagation speed, Mach number, shock front thickness and wave form parameter. It is also important to quantify how the medium properties change as a result of the passing of the shock. For this reason, the theoretical method of normal shock wave approach is often employed. The normal shock mathematical approach utilizes the conservation laws (conservation of mass, momentum and energy) and the equations of perfect gas to derive the Rankine - Hugoniot relationships and Rayleigh line equation that connect the parameters before and after the shock [1], [2].

Many empirical relationships, equations, tables and graphs [1] of the blast wave parameters exist in literature based on extensive experimental work of confined, surface and free air bursts of spherical and hemispherical charges around small and full scale explosions [11], [12], [13], [14]. Regarding buried detonations, there is less data, relationships and equations available in literature. The very few full scale buried detonation experiments done are used to characterize the blast crater and not the wave parameters in air [15], [16]. The existing very few studies done to characterize the airblast parameters of buried detonations are mostly based on small scale explosions in controlled environments [17], [18], [19].

In 1993, Reichenbach et al. [17] carried out an extensive laboratory buried detonations of Nitropenta also known as Pentaerythritol tetranitrate (PETN) charges of mass $0.5g$ which is $0.635g$ TNT equivalent and of spherical geometry. They investigated the effect of Depth Of Burst or Depth Of Burial (DOB), Ground Range or standoff distance and soil characteristics (soil type, density and saturation) on blast parameters in air. The scaled DOB (with respect to TNT equivalent) was varied from $-0.23m/kg^{1/3}$ to $0.58m/kg^{1/3}$. The scaled ground range (with respect to TNT equivalent) was varied from $1.05m/kg^{1/3}$ to $9.42m/kg^{1/3}$. A total of seventeen pressure gauges were used, the first gauge was placed on the ground level, thirteen were placed on the same line and three were placed at different angles, that is on different radial. Three types of soil were used: dry aerated YTONG (porous, crushable) with density $0.4g/cm^3$, water-saturated YTONG with density $0.73g/cm^3$ and clay-loam with density $1.8g/cm^3$. Using least square method and third order polynomial fit, they developed prediction functions for blast parameters over ground range between $1.05m/kg^{1/3}$ and $9.42m/kg^{1/3}$ and for DOB between $-0.23m/kg^{1/3}$ and $0.58m/kg^{1/3}$. The prediction functions were developed for the blast overpressure, arrival time, positive phase duration and positive impulse. They found the blast wave parameters vary strongly with DOB and ground range for the three soil types. The peak overpressure and positive impulse decrease with increasing ground range and decrease with increasing DOB. The arrival time in contrary increases with increasing range and increasing DOB. Regarding the positive phase duration, they were unable to measure it precisely but in general it increases with increasing ground range for smaller DOB but for larger DOB it increases then decreases. They observed three types of wave forms (Fig. 8). They found that for smaller DOB ($0 \leq DOB \leq 0.17m/kg^{1/3}$, the wave form is a classical blast wave (Fig. 8a) with a steep shock front and can be modelled by the Friedlander function, they called this the blast wave regime. For $0.17m/kg^{1/3} \leq DOB \leq 0.35m/kg^{1/3}$ a porched wave form (Fig. 8b) was observed characterized by two pressure peaks. They concluded that the first peak was due to the impact of the soil movement (ejecta) on the piston and the ground shock waves. And the second peak is the actual airblast wave. For D0B $\geq 0.35m/kg^{1/3}$ a compression wave (Fig. 8c) was observed. Comparing their results to surface detonation, they concluded the peak overpressure for buried detonation can be compared with surface detonation only for the blast wave regime (($0 \leq DOB \leq 0.17m/kg^{1/3}$).

In 1998, Bergeron et al. [18] conducted a total of 20 experiments divided into two test series of buried detonation. In the experiments, they detonated $100g$ of C4 explosives which is $137g$ TNT equivalent in Silica 20 sand. They investigated the effect of DOB and ground range on blast parameters both in soil and in air. Three scaled DOB (with respect to TNT equivalent) were investigated: $0m/kg^{1/3}$, $0.06m/kg^{1/3}$ and $0.16m/kg^{1/3}$. Using pressure gauges, they measured the pressure-time curve at five locations above the ground level from $0.58m/kg^{1/3}$ to $3.69m/kg^{1/3}$. The wave parameters studied were the peak overpressure, arrival time, positive impulse and propagation speed. They found that the overpressure and propagation speed decrease with increasing DOB and ground range. In general, the positive impulse also decreases with increasing DOB and ground range but near to the explosion center, it increases. They also found that the arrival time increases with increasing DOB and ground range. Contrary to Reichenbach et al., they

did not develop prediction models.

In 2004, Hlady [19] studied buried detonation by conducting over 200 experiments in controlled environment. The explosive used is $25g$ C4 which is $34.25g$ TNT equivalent. The purpose was to study the effect of soil parameters, standoff distance (or ground range) and DOB on the energy transfer in the air. The soil parameters investigated were soil type, moisture content and density. Two soil types were used: coarse grain soil called Concrete Fine Aggregate Sand (CFAS) and fine grain soil mostly made of clay called Suffied Prairie (PS). The moisture was varied from 0.4% to 22%. The density was varied from $1149kg/m^3$ to $2092kg/m^3$. Two scaled standoff distance were used: $0.31m/kg^{1/3}$ and $0.46m/kg^{1/3}$. Seven scaled DOB varying from $0m/kg^{1/3}$ to $0.46m/kg^{1/3}$ were investigated. A Linear Voltage Displacement Transducer (LVDT) and pressure transducers were used to quantify the energy transfer. The study concluded that the energy transfer decreases with increasing DOB. The energy transfer in coarse grain soil (CFAS) decreases with increasing standoff distance but in fine grain soil (PS) the standoff has no impact on the energy transfer. Regarding the effect of moisture, it was observed that in coarse grain soil, moisture has no effect but in fine grain soil, the energy transfer increases with increasing moisture. The energy transfer in wet fine grain soil is 5 time that of dry fine grain soil. Finally, it was concluded that the energy transfer in wet fine grain soil is 6.8 times higher than in coarse grain soil.

Despite the effort made to study buried detonation in the above researches, one can observe the following limitations. All three researches were performed in controlled or laboratory environments, thus did not take into account the uncertainties regarding full scale detonations. The explosive charge mass, geometry and chemical composition were kept constant in each research, making their results unable to take into account how these parameters affect the outputs. The blast parameters investigated did not include the negative phase. Other important parameters such as the shock front thickness and Mach number were not included. A blast wave does not only affect the pressure but also affects the temperature, density, particle velocity and sound speed. But these important parameters were not included. The range of scaled BOD and standoff distance was limited. Finally, not proper consideration was given to large range of soil types, density and moisture content. All these limitations make the prediction models unable to predict accurately full scale explosions [17], [20].

Thus, the purpose of our blast analysis research is to characterize the blast wave in air around full scale buried detonations and develop prediction models for large range of DOB, standoff distance, explosive charge mass, geometry and chemical composition, and soil parameters (soil type, density and moisture content). Our research has four main objectives. The first objective is to provide an extensive parameters characterizing the blast wave in air. The second objective is to develop prediction models for various wave parameters. The third objective is to compare our results to existing buried detonation studies. And finally to analyse the impact of burial on these parameters. To fulfill our objectives, two methods will be employed. Firstly, experimental method will be conducted to collect the pressure-time curve, to extract parameters such as the peak overpressure, arrival time, impulse and duration. Then the normal shock theory will be employed to compute other derived parameters (density, velocity, temperature, Mach number, sound speed, etc).

2. Blast wave characterization - Theory

2.1. Typical blast wave configuration

A typical blast wave is shown in Fig. 1. It is made of the peak overpressure, the arrival time (t_a), positive pressure phase (+), positive duration, negative pressure phase (-), negative duration and total wave duration. The area under the positive and negative pressure phase is known as the positive and negative specific impulse respectively.

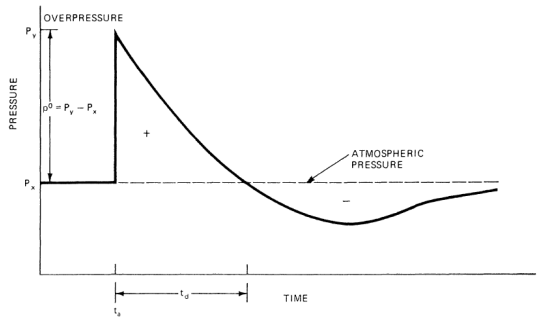

Figure 1: Typical pressure-time curve for an explosive blast wave. [1]

2.2. Experimental results blast wave parameters

Using the pressure-time curve from experiment, the following parameters can be computed.

2.2.1. Peak overpressure

The peak overpressure can be found experimentally as

$$P^o = P_2 - P_1 \tag{1}$$

where P_2 is the peak pressure after the shock and P_1 is the ambient pressure before the shock.

2.2.2. Peak underpressure

The peak underpressure, similarly can be found experimentally as

$$P^u = P_1 - P_{min} \tag{2}$$

where P_{min} is the underpressure.

2.2.3. Duration

The positive duration t_d^+, negative duration t_d^- and the total wave duration t_d can be found experimentally. Here the total wave duration t_d is defined as

$$t_d = t_d^+ + t_d^- \tag{3}$$

2.2.4. Arrival time

The arrival time t_a can be found experimentally as in Fig. 1.

2.2.5. Propagation speed

Using the standoff distance and the arrival time, the propagation speed U_x can be computed as the derivative of the standoff vs arrival time function.

2.2.6. Mach number

The experimental Mach number M_x can be computed as follows

$$M_x = \frac{U_x}{a_1} \tag{4}$$

where a_1 the sound speed of the unperturbed medium is defined as in Eq. 22

2.2.7. Specific impulse

The specific impulse i defined as the impulse per unit area is represented by the area under the blast pressure - time curve. That area can be calculated numerically using any suitable numerical integration algorithm. In this paper, because the time interval is very small $dt = 3.2000e-05$, the Trapezoidal rule can provide an acceptable approximation. Thus,

$$i = \frac{h}{2}\left[f(x_0) + 2\sum_{i=1}^{n-1} f(x_i) + f(x_n)\right] \tag{5}$$

where $h = dt$, $f(x_0) = p(t_0)$, $f(x_i) = p(t_i)$ and $f(x_n) = p(t_n)$.

2.2.8. Shock front thickness

The shock front thickness δ as proposed by Puckett and Stewart [3] is defined as

$$\delta = \frac{U_1 - U_2}{-dU/dx} \tag{6}$$

where U_1 and U_2 are the upstream and downstream velocity respectively as defined in Fig. 2.

For air at ordinary temperatures, the thickness can be approximated as [1]

$$\delta = \frac{11 + 7M_x}{\rho_1(M_x - 1)} \times 10^{-8} \tag{7}$$

The shock thickness is often compared to the molecular mean free path

$$l = \frac{1.88\mu(RT)^{1/2}}{P} \tag{8}$$

where μ is the gas viscosity.
The above equation can be approximated for air at ordinary temperatures as [1]

$$l = \frac{1.2 \times 10^{-7}}{\rho_1} \tag{9}$$

where ρ_1 is the ambient air density.

2.2.9. Wave form parameter

The positive phase of the wave can be modeled using the modified Friedlander equation [10] which can be written as

$$P = P^o\left(1 - \frac{t}{t^+}\right)e^{-\alpha/t^+} \tag{10}$$

where t^+ is the duration of the positive phase decay.

The wave form parameter α can be found analytically as

$$\alpha = \frac{t^+ \ln\left(P^0(1 - t/t^+)\right) - \ln P}{t} \tag{11}$$

2.3. Scaled distance

In literature, the blast wave parameter relationships are often established as function of the scaled distance Z defined as

$$Z = \frac{R}{W^{1/3}} \tag{12}$$

where Z is the scaled distance in $m/kg^{1/3}$, R the standoff distance in m and W the equivalent TNT mass of the charge in kg.

2.4. Normal shock wave approach-preliminaries

2.4.1. Introduction

The normal shock wave approach is employed when the plane of the shock is normal (perpendicular) to the direction of motion and the flow direction does not change before and after the passing of the shock wave. This approach utilizes the ideal gas equations and the laws of conservation to derive the wave parameters equations. Since the parameters are going to be computed from the blast wave in air, the air will be considered as an ideal gas. The normal shock wave theory is based on the following equations and conservation laws [1], [2], [21], [22].

Considering this stationary shock reference frame (Fig. 2), in the upstream medium, P_1 is the ambient pressure, T_1 the ambient temperature, ρ_1 the ambient air density, a_1 the sound speed in the ambient air, $U_1 = U_s$ the speed of the shock front and M_s the shock front Mach number. In the downstream medium, P_2 is the peak pressure, T_2 the peak temperature, ρ_2 the shocked medium density, a_2 the speed of the sound in the shocked medium and U_2 the particle velocity.

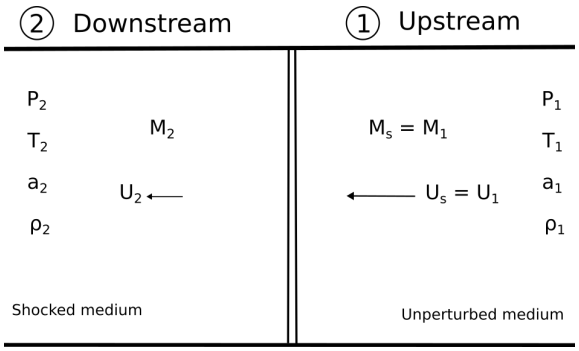

Figure 2: Stationary shock reference frame

2.4.2. Static vs Stagnation quantity

A static or local quantity such as pressure, temperature, density is a quantity measured when the moving fluid is considered as the reference frame. The static quantities are those measured by measurement instruments with no relative velocity. In this paper, the quantities simply called temperature, pressure or density actual mean static temperature, static pressure and static density.

A stagnation quantity is a quantity measured when the fluid is hypothetically decelerated to a zero velocity in an isentropic way. The quantities associated with this state are often greater than those associated with its corresponding static state.

2.5. Conservation laws

Constructing a control volume around the shock front and taking the shock front as the reference frame as in Fig. 2, one can write the governing equations applied to one dimensional compressible flow as follows:

2.5.1. Conservation of mass

For normal shock theory, it is assumed that the area across either side of the shock is the same because the shock thickness is thin, that is in order of molecular mean free path. The conservation of the mass flow rate at the downstream and upstream of the shock can be written as

$$\rho_2 U_2 = \rho_1 U_1 \tag{13}$$

2.5.2. Conservation of momentum

Due to the thinness of the shock, the only force present is the pressure forces, thus the conservation of momentum can be written as

$$(P_1 - P_2)A = \dot{m}(U_2 - U_1) \tag{14}$$

or

$$P_2 - P_1 = \rho_1^2 U_1^2 \left(\frac{1}{\rho_1} - \frac{1}{\rho_2}\right) \tag{15}$$

2.5.3. Conservation of energy

The process across the shock wave happens so rapidly that it can be considered adiabatic, that is there is no heat transfer during the process. This means the stagnation enthalpy across both sides of the shock is conserved because there is no addition or removal of energy during the process. Thus, the equation of conservation of energy can be written as

$$h_1 + \frac{1}{2}U_1^2 = h_2 + \frac{1}{2}U_2^2 \tag{16}$$

or

$$c_p(T_2 - T_1) = \frac{1}{2}\left(U_1^2 - U_2^2\right) \tag{17}$$

2.6. Normal shock wave approach-blast wave parameters

2.6.1. After shock density: Rankine-Hugoniot

Using the conservation of energy equation, the equation of state and the specific heat ratio, one can derive the following equation

$$\frac{k}{k-1}\left(\frac{P_2}{\rho_2} - \frac{P_1}{\rho_1}\right) = \frac{1}{2}(P_2 - P_1)\left(\frac{1}{\rho_1} + \frac{1}{\rho_2}\right) \tag{18}$$

The above equation is known as the shock Hugoniot equation. It connects the pressure and density before and after the shock. The rearrangement of shock Hugoniot equation leads to the following equations known as Rankine-Hugoniot.

$$\begin{aligned}\frac{P_2}{P_1} &= \frac{\frac{k+1}{k-1}\frac{\rho_2}{\rho_1} - 1}{\frac{k+1}{k-1} - \frac{\rho_2}{\rho_1}} \\ &= \frac{2kM_1^2 - k + 1}{k+1}\end{aligned} \tag{19}$$

$$\begin{aligned}\frac{\rho_2}{\rho_1} &= \frac{\frac{k+1}{k-1}\frac{P_2}{P_1} + 1}{\frac{k+1}{k-1} + \frac{P_2}{P_1}} \\ &= \frac{(k+1)M_1^2}{2 + (k-1)M_1^2}\end{aligned} \tag{20}$$

This last equation is used to compute the density after the shock.

2.6.2. Shock front velocity: Rayleigh line

The rearrangement of the momentum equation (Eq. 15) leads to the following equation known as Rayleigh line and is used to find the velocity of the shock front.

$$U_1^2 = \frac{P_1}{\rho_1}\left(\frac{\frac{P_2}{P_1} - 1}{1 - \frac{1}{\rho_2/\rho_1}}\right) \tag{21}$$

2.6.3. Ambient sound speed

The sound speed a_1 in the undisturbed medium before the shock can be written as

$$a_1 = \sqrt{kRT_1} \tag{22}$$

2.6.4. Shock front Mach number

The shock front Mach number $M_s = M_1$ can be written as

$$M_1 = \frac{U_1}{a_1} \tag{23}$$

2.6.5. After shock Mach number

Rearranging the momentum equation (Eq. 15), the continuity equation (Eq. 13) and the sound speed, the Mach number after the shock can be written as:

$$M_2^2 = 1 - \frac{k+1}{2k}\frac{M_1^2 - 1}{M_1^2 - 1 + \frac{k+1}{2k}} \tag{24}$$

2.6.6. Velocity behind the shock

Using the continuity equation (Eq. 13), the velocity U_2 behind the shock can be written as

$$\frac{U_2}{U_1} = \frac{\rho_1}{\rho_2} = \frac{k - 1 + \frac{2}{M_1^2}}{k+1} \tag{25}$$

2.6.7. Blast wind particle velocity

After the passing of the blast wave, the particles inside the shocked air will be moving with the velocity U_p defined as

$$U_p = U_1 - U_2 \tag{26}$$

2.6.8. Sound speed behind the shock

Using the continuity equation (Eq. 13), the sound speed a_2 in the shocked medium can be found using

$$\frac{a_1^2}{a_2^2} = \frac{1 + \frac{k-1}{2}M_2^2}{1 + \frac{k-1}{2}M_1^2} \tag{27}$$

2.6.9. After shock temperature

Using the energy equation (Eq. 17), the temperature T_2 after the shock can be written as

$$\begin{aligned}\frac{T_2}{T_1} &= \frac{P_2}{P_1}\frac{\rho_1}{\rho_2} \\ &= \left(\frac{2k}{k+1}M_1^2 - \frac{k-1}{k+1}\right)\left(\frac{k - 1 + \frac{2}{M_1^2}}{k+1}\right)\end{aligned} \tag{28}$$

2.6.10. Stagnation temperature

Using the energy equation (Eq. 17), the stagnation temperature corresponding to any static state can be written as

$$\frac{T_0}{T} = 1 + \frac{k-1}{2}M^2 \tag{29}$$

where T_0 is the stagnation temperature and T is the corresponding static temperature.

2.6.11. Stagnation pressure

Using the entropy equation, the stagnation pressure corresponding to any static state can be written as

$$\frac{P_0}{P} = \left(\frac{T_0}{T}\right)^{k/(k-1)} = \left(1 + \frac{k-1}{2}M^2\right)^{k/(k-1)} \tag{30}$$

where P_0 is the stagnation pressure and P the associated static pressure.

2.6.12. Stagnation density

Using the equation of stage and the above stagnation temperature and stagnation pressure equations (Eq. 29 and Eq. 30), the stagnation density corresponding to any static state can be written as

$$\frac{\rho_0}{\rho} = \left(1 + \frac{k-1}{2}M^2\right)^{1/(k-1)} \tag{31}$$

where ρ_0 is the stagnation density and ρ the associated static density.

2.6.13. Blast wind stagnation pressure

Using the appropriate equations, the stagnation pressure developed by the blast wind is

$$\frac{P_{stag}}{P_2} = \left[1 + \frac{(k-1)(U_p/a_1)^2}{2(T_2/T_1)}\right]^{k/(k-1)} \tag{32}$$

2.6.14. Blast wind Stagnation temperature

Using the appropriate equations, the stagnation temperature in the stagnation region is

$$\frac{T_{stag}}{T_1} = \frac{T_2}{T_1} + \frac{1}{2}(k-1)\left(\frac{U_p}{a_1}\right)^2 \tag{33}$$

2.6.15. Post shock sound speed

After the passing of the blast wave, the sound speed a_{ps} in the shocked medium is permanently changed and can be computed as

$$\frac{a_{ps}}{a_1} = \left(\frac{a_2}{a_1}\right)\left(\frac{P_2}{P_1}\right)^{(k-1)/2k} \tag{34}$$

2.6.16. Post shock temperature

After the passing of the blast wave, the pressure returns to the ambient pressure but the temperature is permanently changed and is known as post shock temperature T_{ps}. It can be written as

$$\frac{T_{ps}}{T_1} = \left(\frac{a_{ps}}{a_1}\right)^2 \tag{35}$$

3. Experiment

3.1. Experimental procedure

The detonation of the explosives in this experiment followed the DOVO (Belgian Defense Unit in charge of Explosive Ordnance Disposal and Destruction) procedure as described in [23]. The experiment took place in Poelkapelle demolition zone, West Flanders (Fig. 4). Explosives of $50kg$ TNT equivalent were buried in a pit of about $3m$ deep, $5m$ diameter and covered with soil up to around $2m$ above ground level (Fig. 3 and Fig. 4). The blast wave was measured using blast pencil (Fig. 5) which is a PCB Piezotronics Series 137A23 free field blast pressure probe made of a stable quartz piezoelectric element. In this experiment, four blast pencils were placed as in Fig. 6: three were placed on the same line at $10m$, $20m$ and $30m$ from the center of explosion. These three blast pencils were used to investigate the change in blast wave parameters as function of distance. The fourth blast pencil was placed at 90° from the other three and at $20m$ from the center, to investigate the symmetry of the blast wave. Each blast pencil was mounted at $1m$ above ground level. And a weather station placed at about $100m$ from the explosion center was used to measure the ambient temperature.



Figure 3: Explosives being deposited in the pit



Figure 4: Poelkapelle demolition zone



Figure 5: Blast pencil

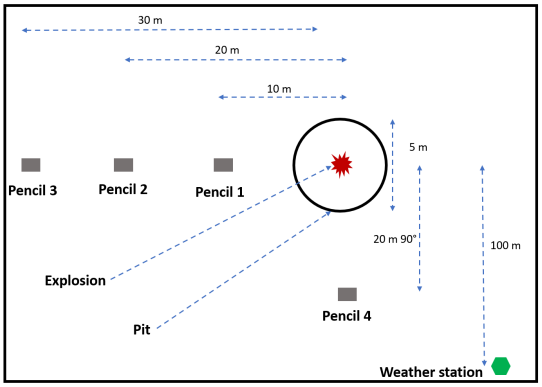

Figure 6: Experimental set-up

3.2. Soil type characterization

To characterize the soil type, soil samples were collected at 4 different depth ($0.8m, 1.2m, 2.3m, 3m$). At each depth, $5kg$ of soil sample was taken and split into three parts: $2kg$ was kept for the dry test, $2kg$ for the wet test and $1kg$ as spare. Several tests were performed using oven, sieve shaker test, plasticity and yield test, blue-methylene test and sand equivalent test. Using the casagrande method [24] and granulometric curve (Fig. 10), it was found that the soil is made of about 90% silt (particles size between $20\mu m$ and $63\mu m$) and about 10% sand (particles size between $63\mu m$ and $2mm$).

Soil moisture content and density were not determined.

4. Results and Discussions

4.1. Recorded blast waves

Each blast pencil recorded a total of 3808485 data points with a time step of $3.2000e-05ms$, thus a total duration of $121.8715ms$ recorded data. The blast data in Fig. 7 shows that the wave arrived at $10m$ first, followed by $20m$ and finally at $30m$. However the wave at $20m90°$ arrived at roughly the same time as that of $10m$.

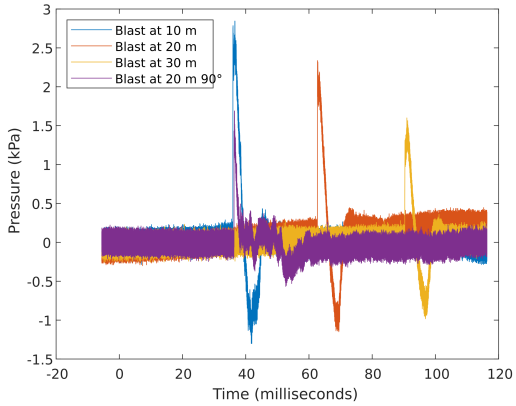

Figure 7: Four blast waves

4.2. Experimental blast wave parameters

Table 1 contains the parameters computed directly from the experimental data. Using second order polynomial interpolation, aprediction model as function of the scaled distance over the range $2.71 \leq Z(m/kg^{1/3}) \leq 8.14$ was developed for each parameter.

4.2.1. Wave form

The form of the blast waves observed is particular. It is not the classical wave form characterised by one peak and that can be modelled with the Friedlander equation. Instead, the wave form is characterized by two peaks (Fig. 11) This type of wave form is termed as "porched shock front" [17]. According to literature [17], the first peak is due to the movement of the ejecta on the pressure sensor and the ground shock wave and the second peak is the actual airblast. In our experiment, the pressure sensors (blast pencils) were placed far from the ejecta, thus, the ejecta did not impact the results. Therefore, the form of the wave can be attributed to the ground shock waves.

4.2.2. Peak overpressure

The peak overpressure decreases with increasing standoff distance (Fig. 15a).

$$P^o(Z) = 3.1229 - 0.0600Z - 0.0156Z^2 \quad (36)$$

4.2.3. Peak underpressure

The peak underpressure decreases with increasing standoff distance (Fig. 15b).

$$P^u(Z) = 1.4358 - 0.0468Z - 0.0011Z^2 \quad (37)$$

4.2.4. Positive decay parameter

Since the observed wave form is not classical, the Friedlander equations were not able to model the entire blast wave. However, the positive decay of the waves were well modeled by the modified Friedlander equation (Fig. 14). The absolute value of the decay parameter α increases with increasing distance as indicated in Table 1 and Fig. 15c.

$$\alpha(Z) = 0.2629 - 0.0563Z + 0.0066Z^2 \quad (38)$$

4.2.5. Arrival time

The arrival time increases with increasing standoff distance (Fig. 15d).

$$t_a(Z) = 10.0856 + 9.3523Z + 0.0614Z^2 \quad (39)$$

4.2.6. Propagation speed

The arrival time as function of the standoff distance which is the second order polynomial interpolation in Fig. 15e is

$$t_a(R) = 10.0856 + 2.5386R + 0.0045R^2 \quad (40)$$

Its derivative is

$$\frac{dt_a}{dR} = 2.5386 + 0.009R \quad (41)$$

The propagation speed U_x is

$$U_x = \frac{dR}{dt_a} \quad (42)$$

The propagation speed decreases with increasing standoff distance (Fig. 15f).

$$U_x(Z) = 393.8319 - 5.0858Z + 0.0548Z^2 \quad (43)$$

4.2.7. Mach number

The Mach number decreases with increasing standoff distance (Fig. 16a).

$$M_x(Z) = 1.1333 - 0.0146Z + (1.5608e - 04)Z^2 \quad (44)$$

4.2.8. Shock front thickness

The shock front thickness increases with increasing standoff distance (Fig. 16b).

$$\delta_x(Z) = 3.2722e{-}06{-}(1.0667e{-}06)Z{+}(1.7620e{-}7)Z^2 \quad (45)$$

4.2.9. Positive duration

The positive duration increases with increasing standoff distance (Fig. 16c).

$$t_d^+(Z) = 3.1208 + 0.1186Z - 0.0061Z^2 \quad (46)$$

4.2.10. Negative duration

The negative duration did not show a specific trend (Fig. 16d).

$$t_d^-(Z) = 7.6153 - 1.0206Z + 0.0806Z^2 \quad (47)$$

4.2.11. Positive impulse

The positive impulse decreases with increasing standoff distance (Fig. 16e).

$$i^+(Z) = 5.8377 - 0.1616Z - 0.0235Z^2 \quad (48)$$

4.2.12. Negative impulse

The negative impulse also decreases with increasing standoff distance (Fig. 16f).

$$i^-(Z) = 5.3081 - 0.7191Z + 0.0432Z^2 \quad (49)$$

4.2.13. Symmetry of the blast wave

It was observed that the blast wave was not symmetrical since the data at $20m$ and that at $20m90°$ have large deviations. The deviations are as follows: overpressure 28%, arrival time 42%, positive duration 46% and positive impulse 69%. The non symmetry of the wave can be due to the pit that is not perfectly symmetrical and the explosive geometry being cylindrical. Future experiments will use more accurate pit dimensions.

4.3. Theoretical blast wave parameters

Air at normal temperatures has heat capacity ratio $k = 1.4$ and specific gas constant $R = 287J/Kg.K$. The ambient absolute temperature $T_1 = 300.5K$ and air mean free path $l = 1.0214e - 07m$.

Table 2. and 3. contain the static and stagnation properties of the medium before and after the shock using normal shock theory. The following observations can be made.

4.3.1. Overall

These tables show that the impact of the shock in the medium is very small or even negligible in some cases. This is due to the low strength of the shock, a little above Mach number = 1. Despite the infinitesimal small effect of the shock, the following observations can be drawn.

4.3.2. Shock front thickness

The shock front thickness increases with distance. According to Puckett and Stewart [3] it is in order of few mean free path. In our study, it is in order of one to two hundreds mean free path, which is relatively a little higher. This can be due to the low strength of the shock. That means the shock is slowly disintegrating into acoustic wave.

4.3.3. Shock velocity

The shock front velocity or upstream velocity decreases with distance. According to the theory, it decreases across the shock wave. This has been proved in our results: at each distance, the upstream velocity is higher than the downstream velocity.

4.3.4. Blast wind velocity

The blast wind velocity also decreases with distance. This makes sense, since the shock front velocity decreases with distance, its blast wind velocity also decreases with distance.

4.3.5. Mach number

According to theory, the upstream of the shock should always be supersonic while the downstream should always be subsonic. This is confirmed by our results. At each distance, the upstream Mach number is always greater than 1 and the downstream Mach number always less than 1.

4.3.6. Pressure

The static pressure decreases with distance and increases across the shock. The downstream stagnation pressure is always less than the upstream stagnation pressure. This is in correlation with the theory which stipulates that there is a loss in stagnation pressure across the shock wave. The blast wind stagnation pressure decreases with distance.

4.3.7. Temperature

The static temperature decreases with distance and increases across the wave. However, there is no loss or gain in stagnation temperature across the shock since the process is adiabatic. The blast wind stagnation temperature and the post shock temperature infinitesimally decrease with distance.

4.3.8. Density

The static upstream density was constant because the ambient temperature was kept constant and was taken from the weather station which was about $100m$. This is a potential source of error in the results. In future work, temperature sensors need to be placed as close as possible. The downstream static density decreases with distance. Both the upstream and downstream stagnation density decrease with distance and infinitesimally decreases across the shock.

4.3.9. Sound speed

Similar to the density, the upstream sound speed was kept constant for the same reason and thus may constitute a potential source of error. It was found that the sound speed increases across the shock, which is predicted by the theory. The downstream and post shock sound speed infinitesimally decreases with distance.

4.4. Experimental vs Theoretical parameters

4.4.1. Propagation speed

Both the experimental and theoretical propagation speed (or shock front speed or upstream velocity) decrease with distance. The experimental speed is 1.78% to 8.19% higher than the theoretical speed. The deviation in the results can be due to the fact that the experimental speed are not collected directly by experimental instruments. It is derived from the distance vs arrival time graph through a second order polynomial interpolation. That means the is some errors associated with it.

4.4.2. Mach number

Similarly, the experimental Mach number is 1.79% to 8.19% higher than the theoretical Mach number since it depends on the speed.

4.4.3. Shock front thickness

The shock front thickness depends on the Mach number and density. The experimental shock front thickness was found to be 72.5% to 86.98% smaller than the theoretical thickness. Potential sources of error include the response time pressure sensors and errors in Mach number and density. Since the shock front thickness is very small, a relatively small error in macroscopic parameters such as Mach number and density can have big impact on it.

Table 1: Computed experimental parameters

Standoff distance R (m)	10	20	30	$20m90°$
Scaled distance Z $(m \cdot kg^{-1/3})$	2.7144	5.4288	8.1433	5.4288
Peak overpressure P^o (kPa)	2.8451	2.3374	1.5998	1.6895
Peak underpressure $P^u(kPa)$	1.3009	1.1500	0.9831	0.5664
Wave form parameter α	0.1590	−0.1528	0.2443	0.7517
Peak pressure ratio P^o/P^u	2.4740	2.0325	1.6272	2.9827
Arrival time t_a (ms)	35.9236	62.6660	90.3128	36.2865
Positive duration t_d^+ (ms)	3.3976	3.5840	3.6800	1.9200
Negative duration t_d^- (ms)	5.4390	4.4509	4.6510	20.5352
Duration ratio t_d^+/t_d^-	0.6247	0.8052	0.7912	0.0935
Total duration t_d (ms)	8.8366	8.0349	8.3310	22.4552
Propagation speed U_x (m/s)	380.4306	367.8364	356.0493	–
Mach number M_x	1.0948	1.0586	1.0247	–
Shock thickness $\delta_x(m)$	$1.6751e-06$	$2.6745e-06$	$6.2704e-06$	–
Shock thickness ratio δ_x/l	16.4004	26.1853	61.3924	–
Positive specific impulse i^+ $(kPa \cdot ms)$	5.2258	4.2674	2.9625	1.3415
Negative specific impulse i^- $(kPa \cdot ms)$	3.6741	2.6760	2.3138	0.9366
Specific impulse ratio i^+/i^-	1.4223	1.5947	1.2804	1.4323

Table 2: Computed normal shock static parameters

Standoff distance R (m)	10	20	30	$20m90°$
Scaled distance Z $(m \cdot kg^{-1/3})$	2.7144	5.4288	8.1433	5.4288
Shock front thickness δ (m)	$1.2867e-05$	$1.5639e-05$	$2.2793e-05$	$2.1582e-05$
Shock thickness ratio δ/l	125.9771	153.1195	223.1603	211.3018
Shock front Mach number M_1	1.0120	1.0098	1.0067	1.0071
Downstream Mach number M_2	0.9882	0.9903	0.9933	0.9929
Mach number ratio M_2/M_1	0.9765	0.9807	0.9867	0.9859
Upstream pressure P_1 (Pa)	$1.01325e+5$	$1.0133e+05$	$1.0133e+05$	$1.0133e+05$
Downstream pressure P_2 (Pa)	$1.0417e+05$	$1.0366e+05$	$1.0292e+05$	$1.0301e+05$
Pressure ratio $P_2/P1$	1.0281	1.0231	1.0158	1.0167
Upstream Temperature T_1 (K)	300.5000	300.5000	300.5000	300.5000
Downstream Temperature T_2 (K)	302.8872	302.4637	301.8471	301.9227
Temperature ratio T_2/T_1	1.0079	1.0065	1.0045	1.0047
Upstream density ρ_1 (kg/m^3)	1.1749	1.1749	1.1749	1.1749
Downstream density ρ_2 (kg/m^3)	1.1983	1.1942	1.1881	1.1888
Density ratio ρ_2/ρ_1	1.0200	1.0164	1.0112	1.0119
Shock front velocity U_1 (m/s)	351.6346	350.8949	349.8197	349.9514
Downstream velocity U_2 (m/s)	344.7478	345.2276	345.9298	345.8435
Velocity ratio U_2/U_1	0.9804	0.9838	0.9889	0.9883
Blast wind velocity U_P	6.8868	5.6673	3.8898	4.1080
Upstream sound speed a_1 (m/s)	347.4779	347.4779	347.4779	347.4779
Downstream sound speed a_2 (m/s)	348.8554	348.6114	348.2559	348.2995
Sound speed ratio a_2/a_1	1.0040	1.0033	1.0022	1.0024
Post shock sound speed a_{ps} (m/s)	347.4780	347.4780	347.4779	347.4779
Post shock temperature T_{ps} (K)	300.5002	300.5001	300.50003	$3.0050004e+02$

Table 3: Computed normal shock stagnation parameters

Standoff distance $R\ (m)$	10	20	30	$20m90^{\circ}$
Scaled distance $Z\ (m \cdot kg^{-1/3})$	2.7144	5.4288	8.1433	5.4288
Upstream stagnation temperature $T_{0,1}\ (K)$	362.0465	361.7878	361.4128	361.4587
Downstream stagnation temperature $T_{0,2}\ (K)$	362.0465	361.7878	361.4128	361.4587
Stagnation temperature ratio	1.0000	1.0000	1.0000	1.0000
Upstream stagnation pressure $P_{0,1}\ (Pa)$	$1.945074e+05$	$1.940234e+05$	$1.933204e+05$	$1.934053e+05$
Downstream stagnation pressure $P_{0,2}\ (Pa)$	$1.945069+05$	$1.940231e+05$	$1.933203e+05$	$1.934052e+05$
Stagnation pressure ratio $P_{0,2}/P_{0,1}$	0.9999978	0.99999879	0.99999961	0.99999954
Upstream stagnation density $\rho_{0,1}\ (kg/m^3)$	1.871931	1.868608	1.8637699	1.8643519
Downstream stagnation density $\rho_{0,2}\ (kg/m^3)$	1.871927	1.868606	1.8637692	1.864351
Stagnation density ratio $\rho_{0,2}/\rho_{0,1}$	0.9999978	0.9999988	0.99999961	0.99999954
Blast wind stagnation pressure $P_{stag}\ (Pa)$	$1.0420e+05$	$1.0368e+05$	$1.0293e+05$	$1.0302e+05$
Blast wind stagnation temperature $T_{stag}\ (K)$	302.9108	302.4797	301.8546	301.9311

5. Comparisons

5.1. Comparison with buried detonation

Here, our experimental results are compared with the results of buried detonations experiments conducted by Reichenbach et al. [17] and Bergeron et al. [18]. Only the trends of the parameters will be discussed. The prediction models in Reichenbach et al. cannot be utilized as they were applicable for $-0.23m/kg^{1/3} \leq DOB \leq 0.58m/kg^{1/3}$ while our experiment DOB = $0.814m/kg^{1/3}$, which is outside their model range.

5.1.1. Wave form

The form of the waves recorded in our experiment (Fig. 11 and 12) is similar to the porched shock front wave forms observed in Reichenbach et al. (Fig. 13). This wave form is characterized by two phases of pressure rise. According to Reichenbach et al., the first rise was due to the impact of the soil movement (ejecta) on the piston and the ground shock waves. Since in our experiment the pressure sensors were far from the ejecta, we can exclude the impact of ejecta as a probable cause and instead assume the ground shock waves as the actual cause. And the second phase of the pressure rise was the actual airblast wave. They observed this wave form when $0.17m/kg^{1/3} \leq DOB \leq 0.35m/kg^{1/3}$. However, in our experiment the DOB is $0.814m/kg^{1/3}$ which is outside their range. This discrepancy in the DOB can be attributed to the mass, chemical composition and geometry of the explosives and the characteristics of the soils used in the two experiments.

5.1.2. Peak overpressure

As observed in Reichenbach et al. and Bergeron et al., the peak overpressure decreases with increasing distance (Fig. 15a).

5.1.3. Positive impulse

In Reichenbach et al. and Bergeron et al., the positive impulse decreases with increasing distance. The similar observation was made in our study (Fig. 16e).

5.1.4. Positive duration

As observed in Reichenbach et al., for large DOB, as the standoff distance increases, the positive duration increases then decreases. Since the maximum distance in our experiment was $8.143m/kg^{1/3}$, we can assume that is the reason why we observed only the increasing phase (Fig. 16c).

5.1.5. Arrival time

In Reichenbach et al. and Bergeron et al., the arrival time increases with increasing distance. The similar observation was made in our study (Fig. 15d).

5.1.6. Propagation speed

Similar to Bergeron et al. it was found that the propagation speed decreases with increasing ground range (Fig. 15f).

5.2. Comparison with surface detonation

Using Kingery-Bulmash [13] equations integrated in the United Nation calculator [25] for estimating surface detonation of hemispherical charge parameters, the following comparison can be made for the same 50 kg TNT equivalent charge between our experimental results (buried detonation) and surface hemispherical detonation. The comparison Table 4 shows the following observations.

It is observed that burying the explosives in the conditions of our experiment considerably impacted the blast wave parameters. The peak overpressure of the buried detonation was attenuated by 92% to 98%. Also the positive impulse for buried detonation was attenuated by 98% to 99%. The arrival time for buried detonation was increased by 48% to 229% compared to the surface detonation. And the shock front velocity was decreased by 5% to 31%.

6. Conclusion

Using experimental and theoretical methods, extensive parameters of the air blast wave were provided. Using second order polynomial interpolation, a prediction model was built for each experimental parameter. The trends in these parameters as function of standoff distance were confirmed by existing literature. A comparison was made between the experimental and theoretical propagation speed, Mach number and shock thickness. Their deviations are reasonably acceptable. A comparison was made between buried and surface detonation and it was observed that the parameters in these two detonations have similar trends but burying the explosives has considerably attenuated the parameters. One stricking observation is regarding the wave form. The waves recorded in our experiment are not the classical Friedlander waves, instead they are known as porched shock front waves. The results and prediction models in the current paper are limited since they are based on only one experiment and

only one independent parameter which is the standoff distance was considered. In future work, the followings need to be taken into consideration. Carry out extensive experiments with a large range of depth of burial, standoff distance, explosive charge mass, chemical composition, geometry, soil type, moisture content and density. Also get more accurate dimensions of the pit and experimental apparatus positioning using geodesy. The wave form parameter of the negative phase of the pressure also needs to be investigated.

Appendix

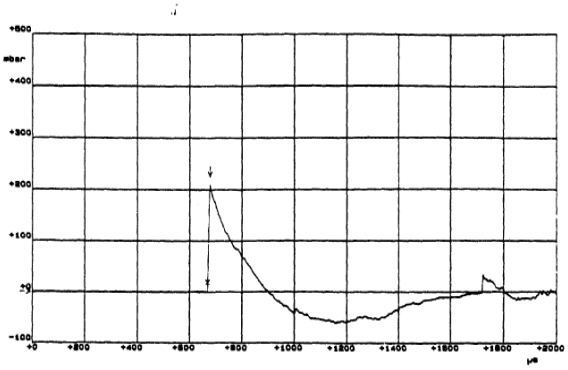

(a) blast wave

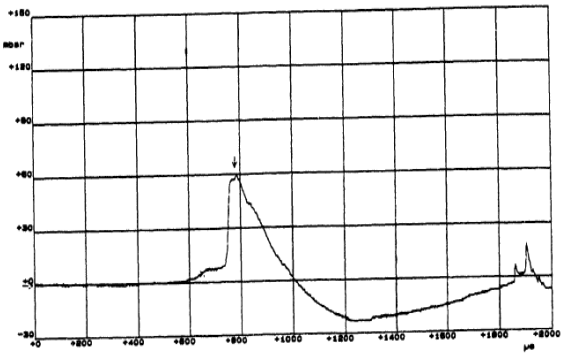

(b) Porched wave

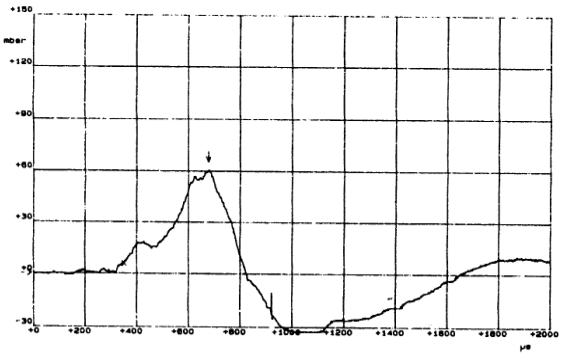

(c) Compression wave

Figure 8: The three wave regimes observed in Reichenbach et al. [17]

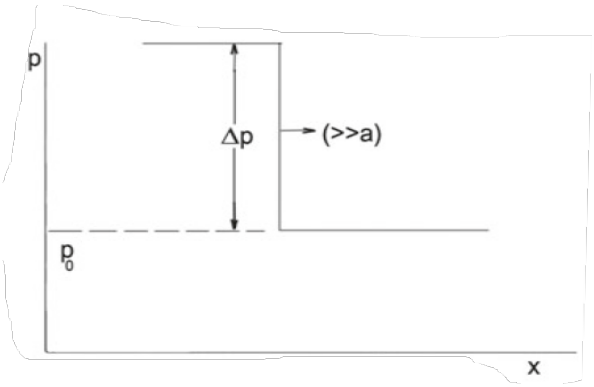

(a) Shock wave (in the near-field) [2]

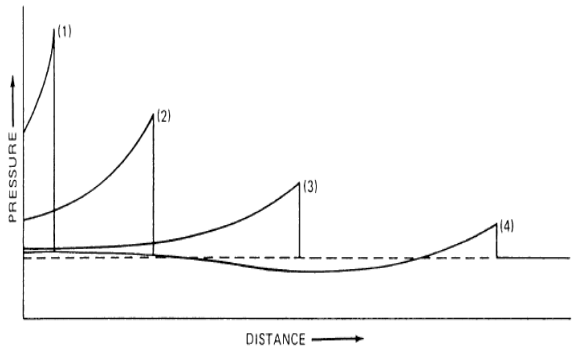

(b) Blast wave in the near field. [1]

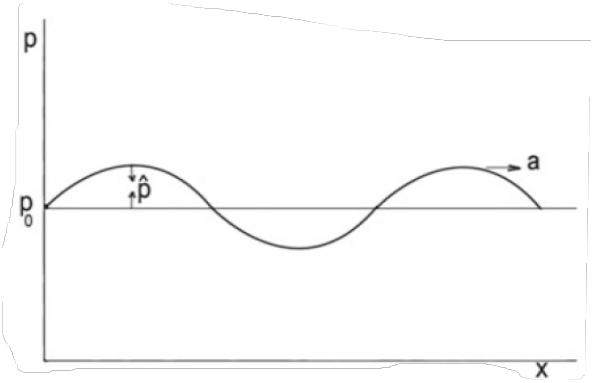

(c) Acoustic wave in the far-field [2]

Figure 9: Evolution of a blast wave

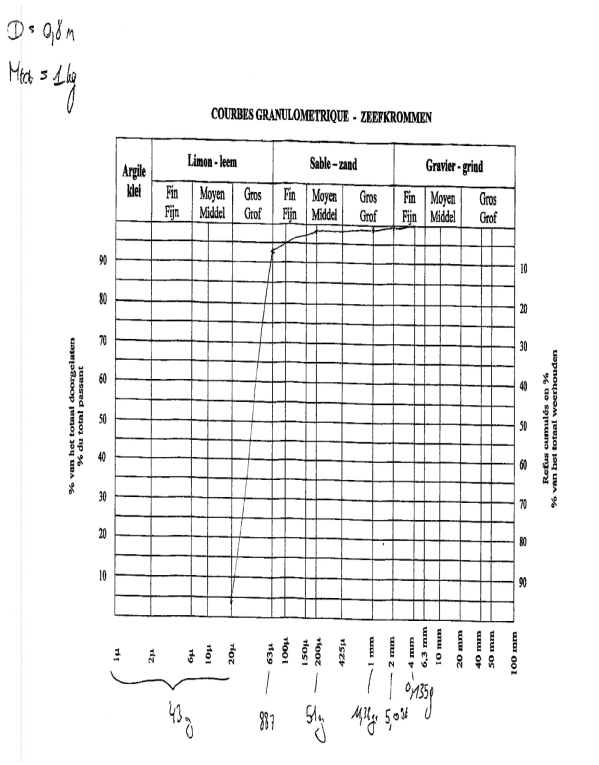

(a) Depth = 0.8m

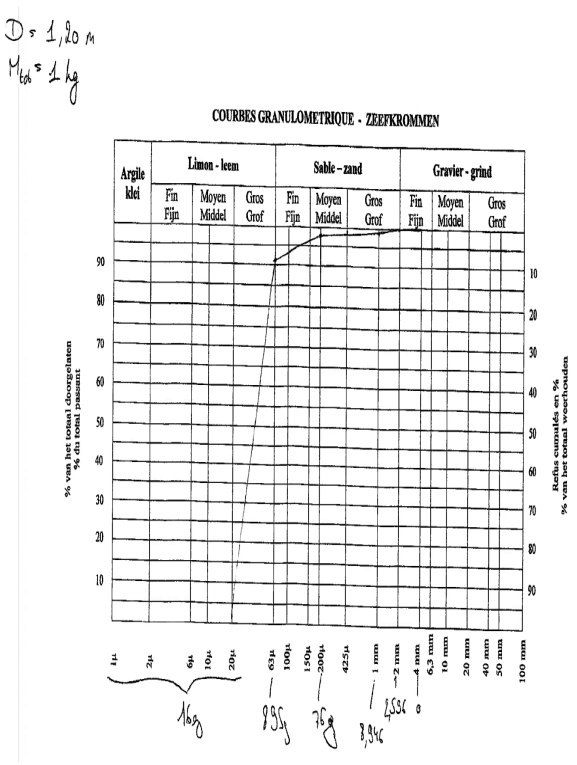

(b) Depth = 1.2m

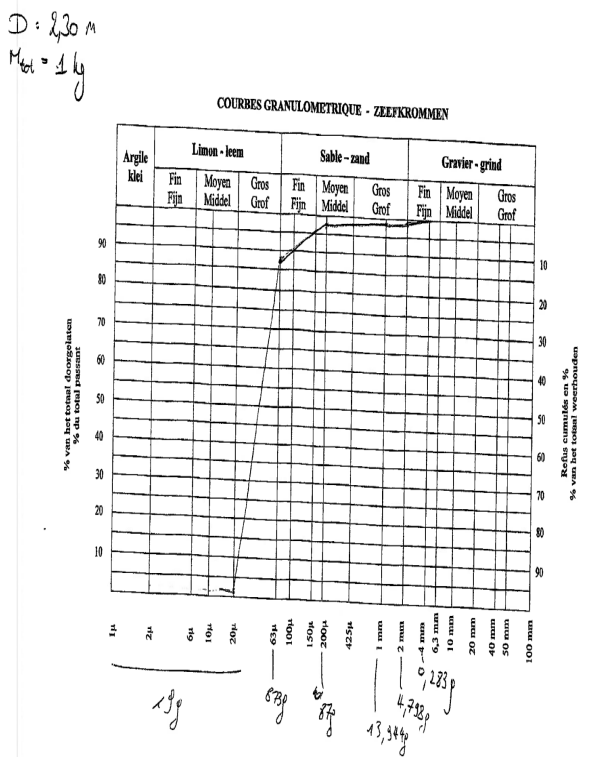

(c) Depth = 2.3m

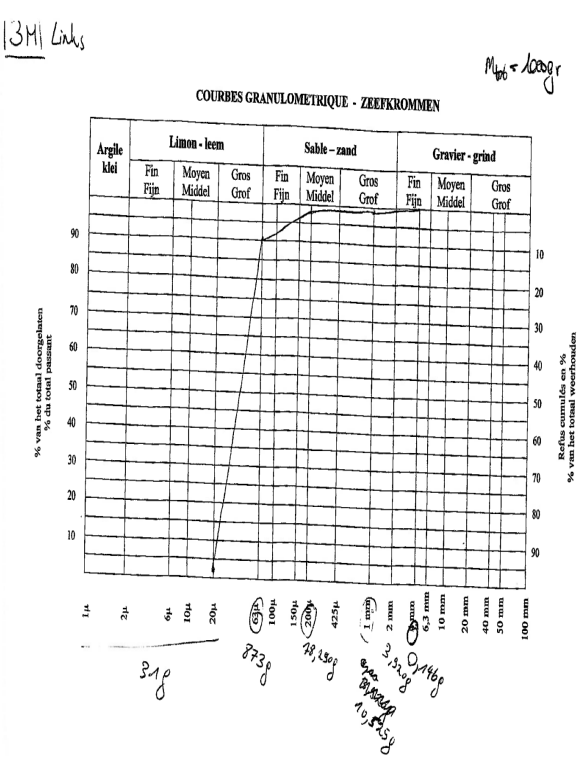

(d) Depth = 3m

Figure 10: Granulometric curves

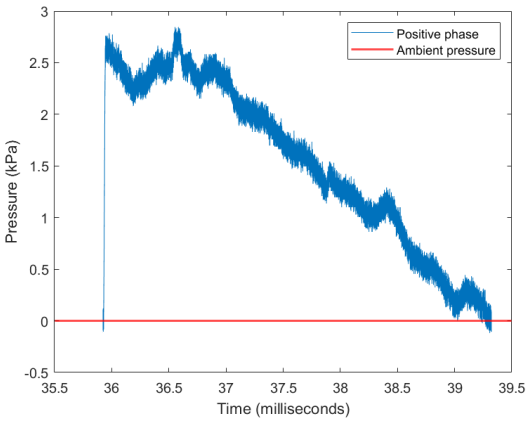

(a) Positive phase at 10m

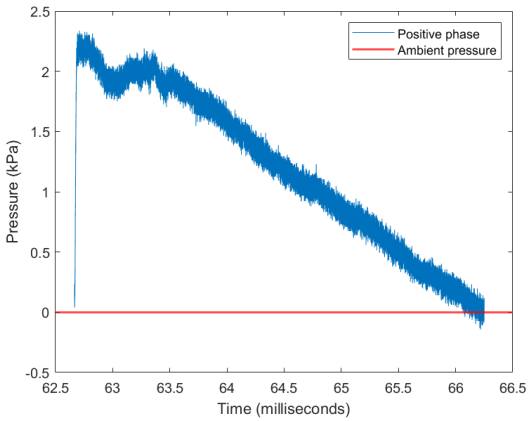

(b) Positive phase at 20m

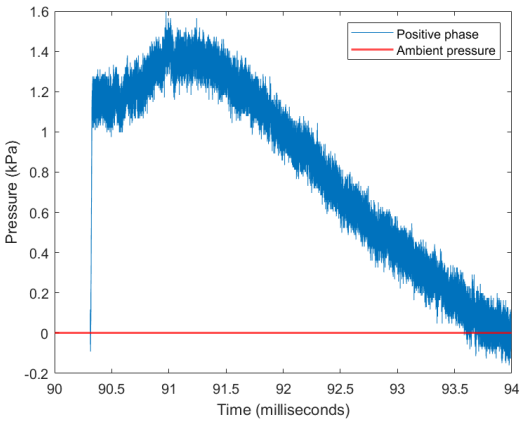

(c) Positive phase at 30m

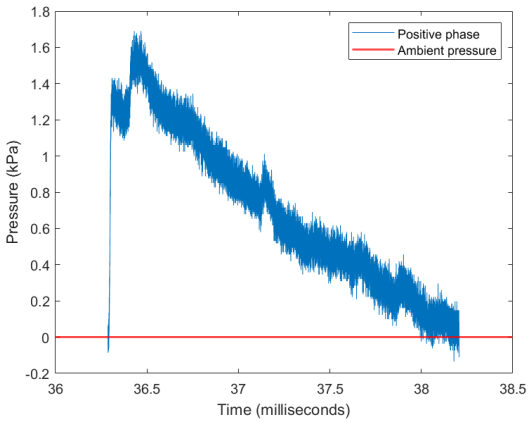

(d) Positive phase at 20m90°

Figure 11: Positive phase of the blast waves

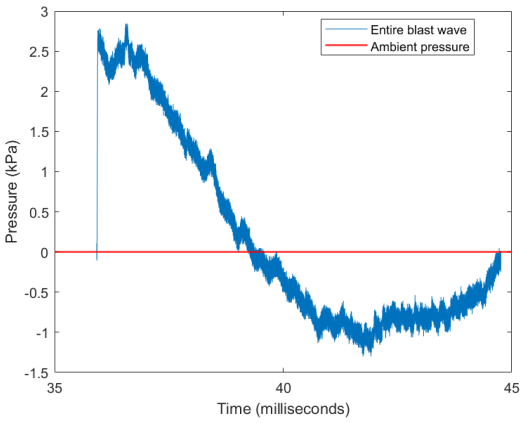

(a) Blast wave at $10m$

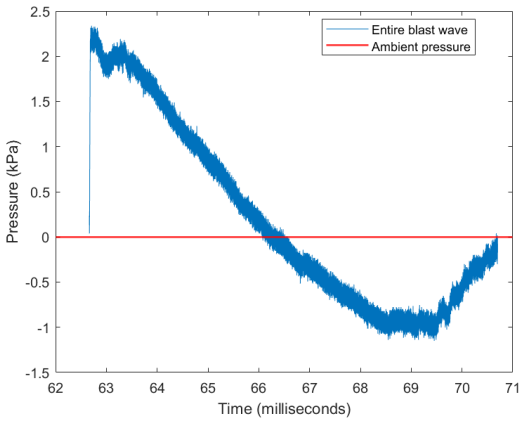

(b) Blast wave at $20m$

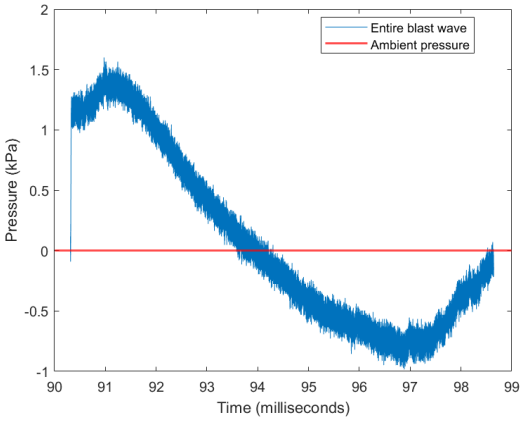

(c) Blast wave at $30m$

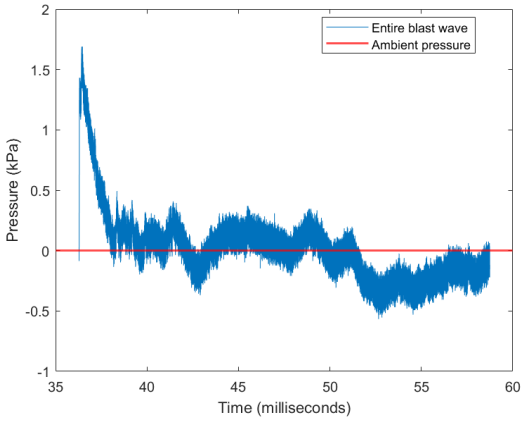

(d) Blast wave at $20m90°$

Figure 12: Entire blast wave

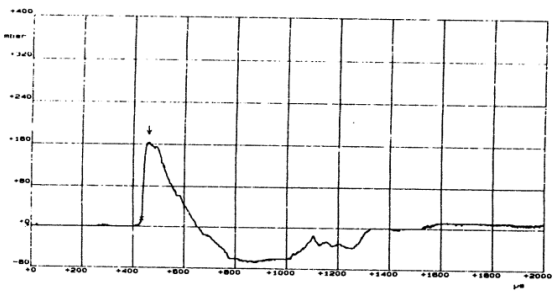

(a) Wave form at DOB = $0.23m/kg^{1/3}$

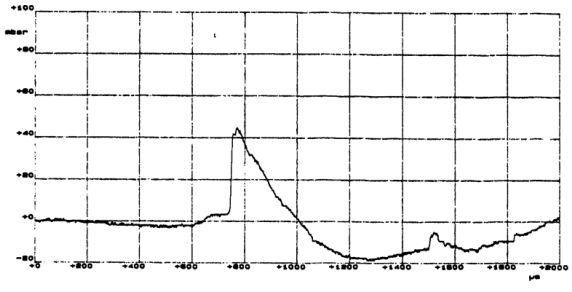

(b) Wave form at DOB = $0.35m/kg^{1/3}$

Figure 13: Porched shock front wave form [17]

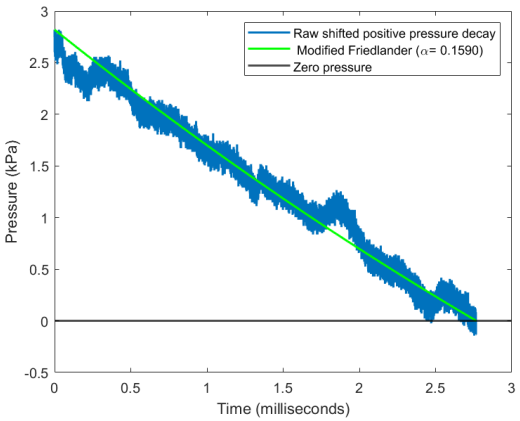

(a) Positive phase decay at 10m

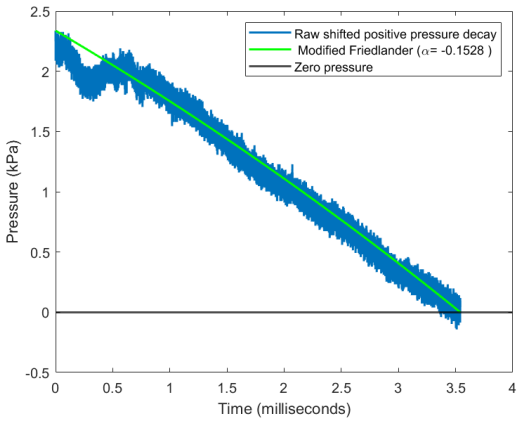

(b) Positive phase decay at 20m

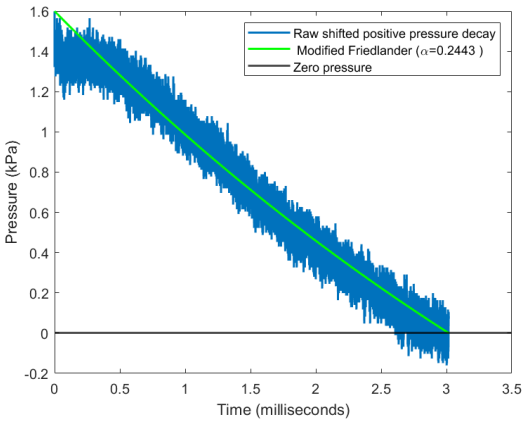

(c) Positive phase decay at 30m

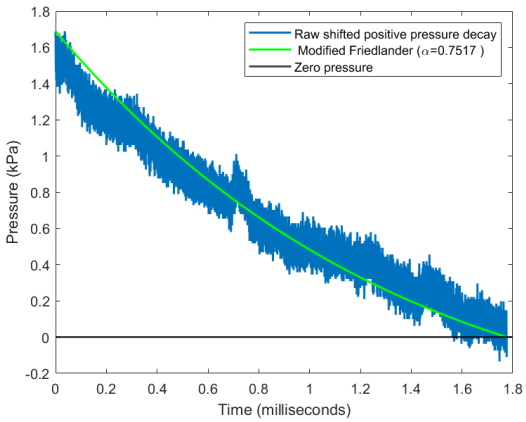

(d) Positive phase decay at 20m90°

Figure 14: Positive phase decay of the blast waves

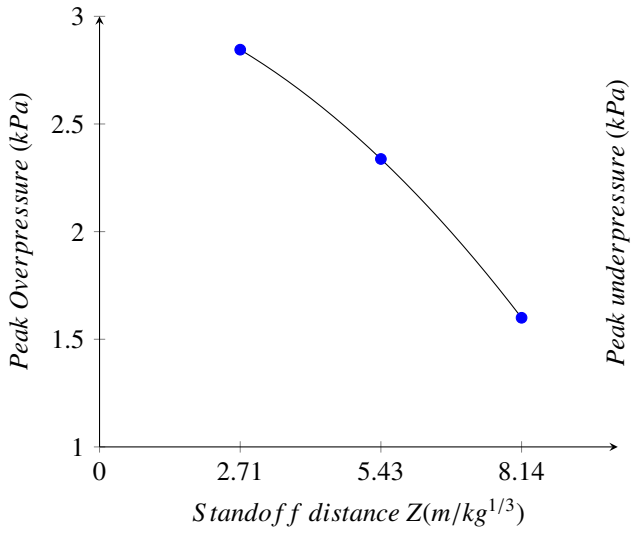

(a) Peak overpressure vs scaled standoff distance

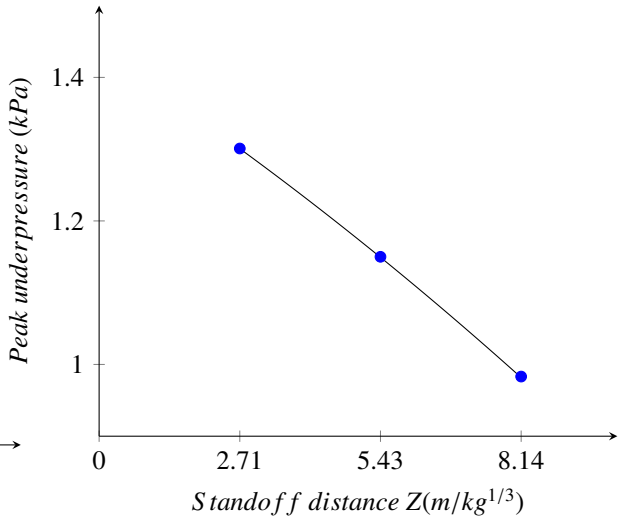

(b) Peak underpressure vs scaled standoff distance

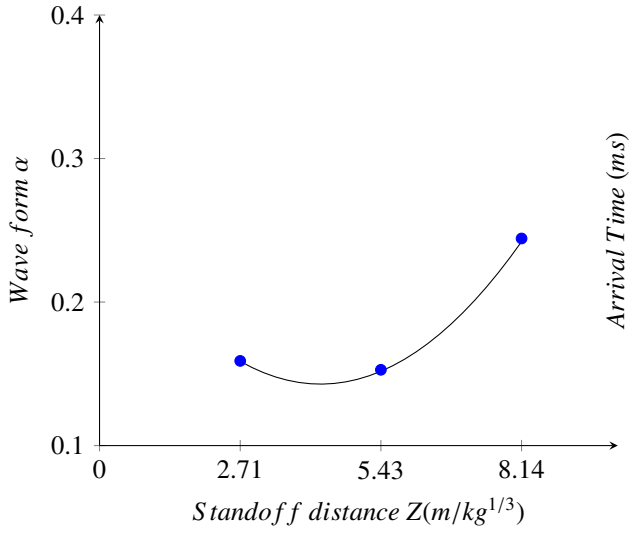

(c) Wave form parameter vs scaled standoff distance

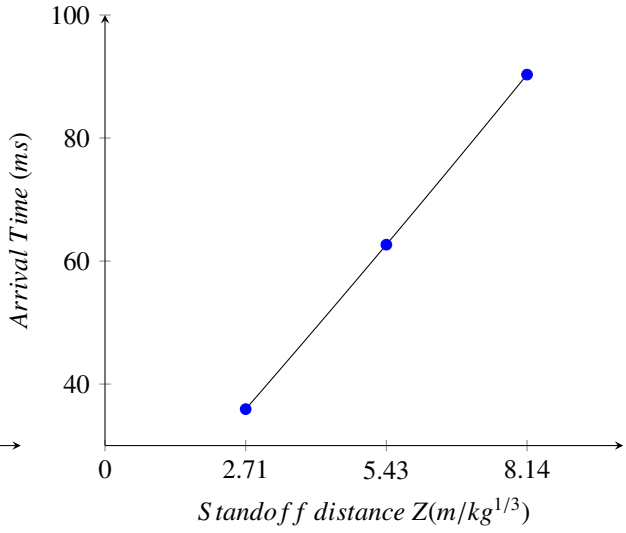

(d) Arrival time vs scaled standoff distance

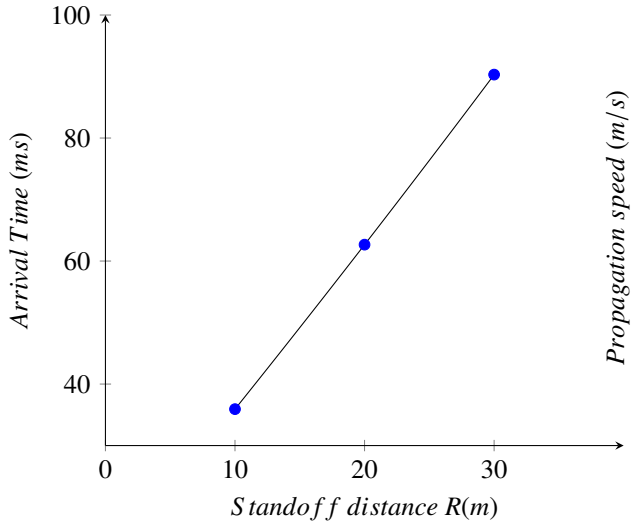

(e) Arrival time vs Standoff distance $R(m)$

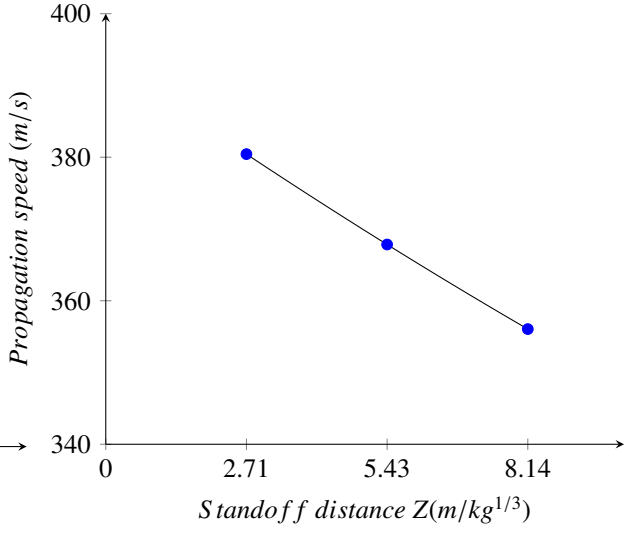

(f) Propagation speed vs scaled standoff distance

Figure 15: 2nd order polynomial interpolation (I)

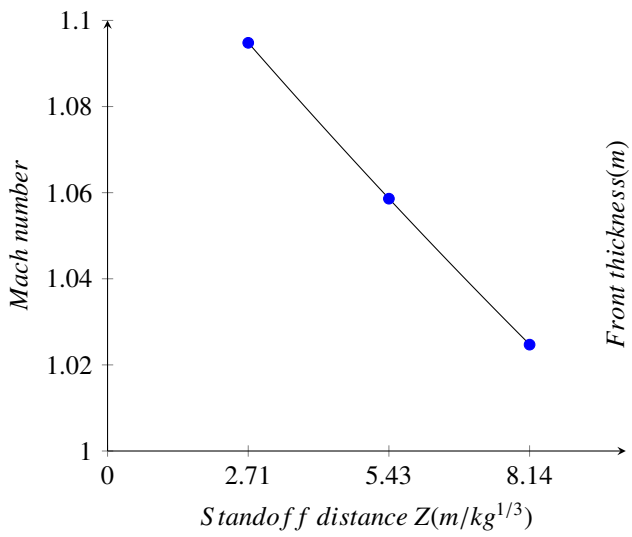

(a) Experimental Mach number vs scaled standoff distance

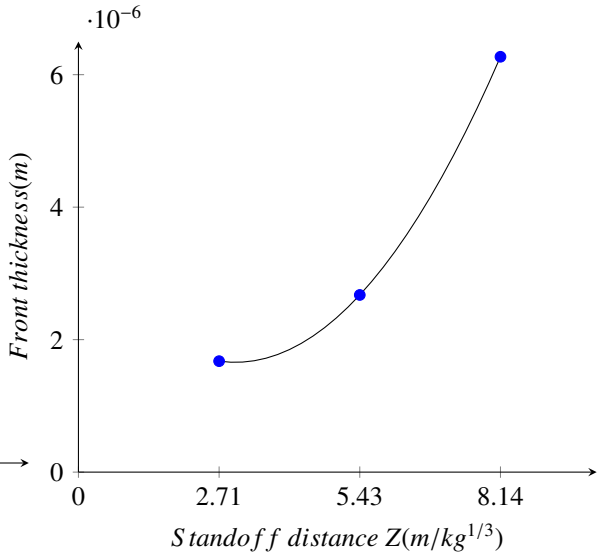

(b) Experimental Shock front vs scaled standoff distance

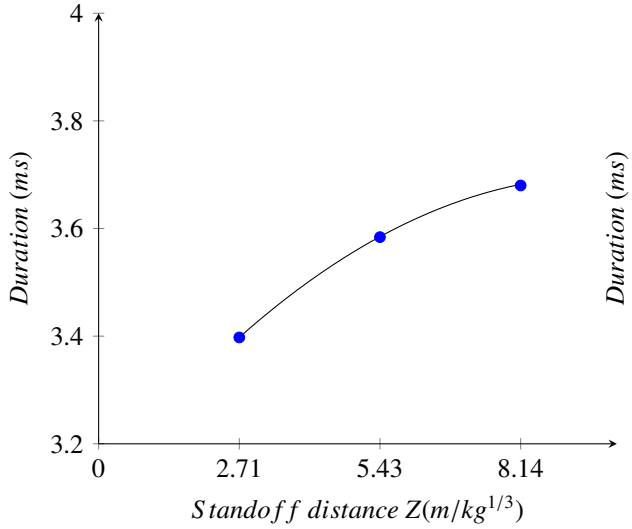

(c) Positive duration vs scaled standoff distance

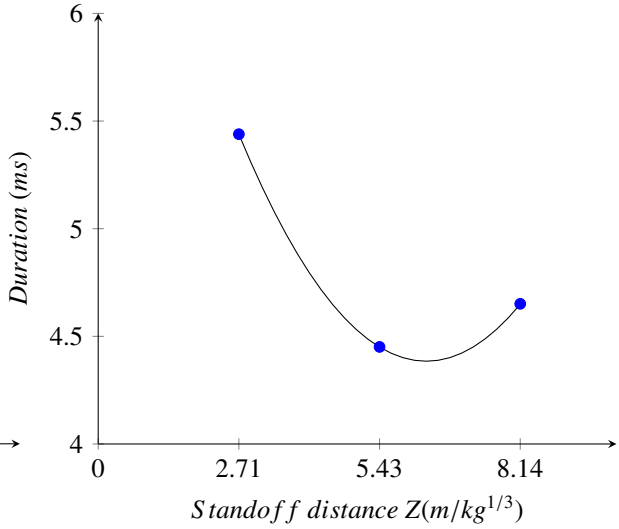

(d) Negative duration vs scaled standoff distance

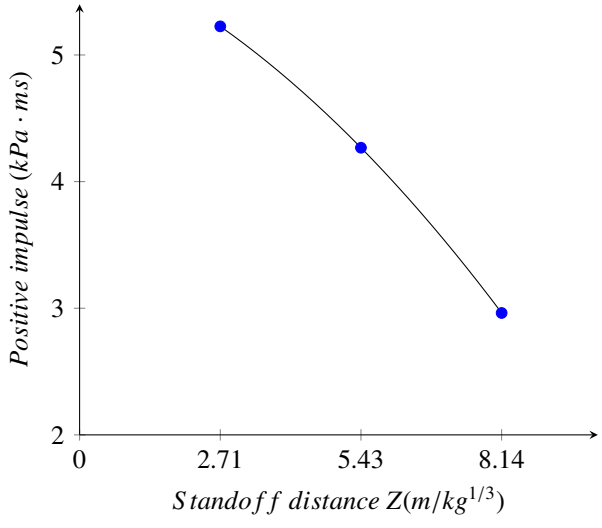

(e) Positive impulse vs scaled standoff distance

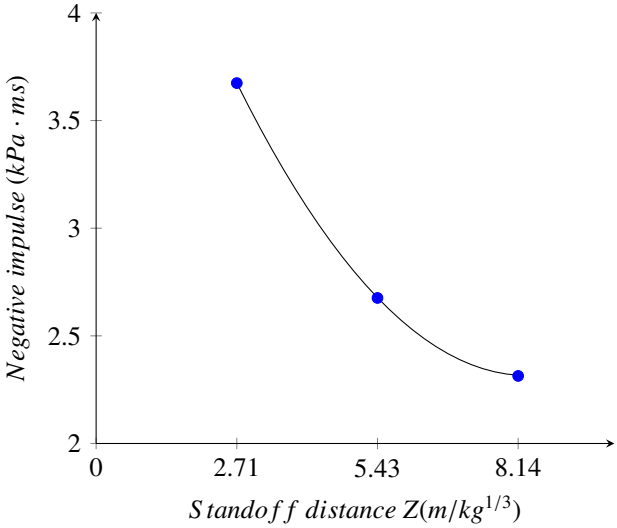

(f) Negative impulse vs scaled standoff distance

Figure 16: 2nd order polynomial interpolation (II)

Table 4: Buried detonation vs surface detonation of hemispherical charge

Standoff distance R (m)	10		20		30	
Scaled distance Z $(m \cdot kg^{-1/3})$	2.7144		5.4288		8.1433	
Detonation type	Buried	Surface	Buried	Surface	Buried	Surface
Peak incident overpressure (kPa)	2.8451	143.24	2.3374	37.49	1.5998	19.82
Incident positive impulse $(kPa \cdot ms)$	5.2258	373.46	4.2674	202.76	2.9625	139.13
Arrival time (ms)	35.9236	10.93	62.6660	34.42	90.3128	61.03
Shock front velocity (m/s)	347.4821	506.50	347.4813	390.45	347.4803	367.43

Acknowledgments

We would like to sincerely thank the following institutions and people for their contribution:

DOVO (Belgian Defense Unit in charge of Explosive Ordnance Disposal and Destruction), for carying out the entire detonation procedure.

Professor Alain Muls from Royal Military Academy, Signal and Image Centre, for Geodesy measurements.

Adjudant Renaat Goorts and his team from Royal Military Academy, Department Génie, for soil samples collection and analysis.

M. Corentin Guinle from École Nationale Supérieure de Techniques Avancées Bretagne, for his assistance with data collection.

References

[1] G. F. Kinney, K. J. Graham, Explosive Shocks in Air, Springer Berlin Heidelberg, 1985.

[2] K. Ramamurthi, Modeling Explosions and Blast Waves, 2nd Edition, Springer, 2021.

[3] A. E. Puckett, H. J. Stewart, The thickness of a shock wave in air, Quarterly of Applied Mathematics 7 (1950) 457–463.

[4] B. Carnahan, H. A. Luther, J. O. Wilkes, Applied Numerical Methods, R.E. Krieger Publishing Company, 1990.

[5] S. K. S. K. Gupta, Numerical methods for engineers, 3rd Edition, New Academic Sciences, 2014.

[6] L. Rayleigh, Aerial plane waves of finite amplitude, Royal Society, 1910, pp. 247–284.

[7] R. Becker, Stoßwelle und detonation, Zeitschrift für Physik 8 (1922) 321–362.

[8] W. F. Durand, Aerodynamic Theory, Vol. 3, Julius Springer, 1943, pp. 209–222.

[9] F. G. Friedlander, The diffraction of sound pulses i. diffraction by a semi-infinite plane, Proceedings of the Royal Society of London. Series A. Mathematical and Physical Sciences 186 (1946) 322–344.

[10] S. E. Rigby, A. Tyas, T. Bennett, S. D. Clarke, S. D. Fay, The negative phase of the blast load, International Journal of Protective Structures 5 (2014) 1–19.

[11] H. J. Goodman, Compiled free-air blast data on bare spherical pentolite (1960).

[12] C. N. Kingery, Air blast parameters versus distance for hemispherical tnt surface bursts (1966).

[13] C. N. Kingery, G. Bulmash, Technical report arbrl-tr-02555: Air blast parameters from tnt spherical air burst and hemispherical surface (1984).

[14] U. F. Criteria, Ufc 3-340-02 structures to resist the effects of accidental explosions (2008).

[15] D. Ambrosini, B. Luccioni, R. Danesi, Influence of the soil properties on craters produced by explosions on the soil surface, Mecánica Computacional XXIII 571–590.

[16] D. Ambrosini, B. Luccioni, Effects of underground explosions on soil and structures, Underground Space 5 (2020) 324–338.

[17] H. Reichenbach, K. Behrens, A. Kuhl, Airblast environments from buried he charges (1 1993).

[18] D. Bergeron, R. Walker, C. Coffey, Detonation of 100-gram anti-personnel mine surrogate charges in sand-a test case for computer (1998).

[19] S. L. Hlady, Effect of soil parameters on land mine blast, 18th Military Aspects of Blast and Shock (MABS), Bad Reichenhall, Germany.

[20] J. Mandal, M. D. Goel, A. K. Agarwal, Surface and buried explosions: An explorative review with recent advances, Archives of Computational Methods in Engineering 28 (2021) 4815–4835.

[21] M. J. Moran, H. N. Shapiro, D. D. Boettner, M. B. M. B. Bailey, Fundamentals of engineering thermodynamics, 8th Edition, Wiley, 2014.

[22] V. Babu, Fundamentals of Gas Dynamics, 2nd Edition, Springer International Publishing, 2021.

[23] P. Atikpo, B. Janssens, D. Lecompte, D. Laboureur, C. Fouchier, Near – field pollutant dispersion due to explosions, von Karman Institute for Fluid Dynamics PhD Symposium 13.

[24] I. Smith, Smith's elements of soil mechanics, 10th Edition, Wiley Blackwell, 2021.

[25] U. SaferGuard, Kingery-bulmash blast parameter calculator — international ammunition technical guidelines.
URL `https://unsaferguard.org/un-saferguard/kingery-bulmash`

Wind field reconstruction with offshore nacelle-mounted LiDAR measurements

Rebeca Marini

Vrije Universiteit Brussel, Pleinlaan 2, 1050 Elsene, Brussels, Belgium, rebeca.marini@vub.be

Supervisor: Jeroen van Beeck

Dean of the Faculty, Environmental and Applied Fluid Dynamics, von Karman Institute for Fluid Dynamics, Belgium, vanbeeck@vki.ac.be

University Supervisor: Jan Helsen

Professor, Industrial Engineering, Vrije Universiteit Brussel, Belgium, jan.helsen@vub.be

Abstract

Using measurements from a LIDAR mounted on an offshore wind turbine in the North Sea, this research estimates wind field characteristics with proposed methodologies. The study includes performance analysis and validation of the LIDAR using wind SCADA measurements from an anemometer. A wind field reconstruction method is then used to estimate wind characteristics, such as wind speed magnitude.

Keywords: Wind field reconstruction, Nacelle-mounted LIDAR, Offshore Wind Turbine

1. Introduction

The European Union (EU) has set guidelines and targets to fulfil the United Nations' Agenda for 2030, to assure a better future for the next generations. One of these is to further decarbonize the current energy system, for example, by further investing in renewable energy research. Wind energy in the last two decades has been rapidly growing, representing more than 35% of the produced renewable energy in the EU during 2020 [FIND CITATION]. The European Wind Energy Association (EWEA) estimates this growth to reach almost 400 GW production by 2030, with 25% being produced in offshore wind farms [1].

The construction costs of an offshore wind farm are higher than an onshore one, due to cabling, mooring and maintenance. However, the increased wind potential and nature preservation lead to a growing number of offshore wind farms every year [2]. Moreover, wind turbines have also been growing in size, reaching more than 100m of blade length. With a higher Levelized Cost Of Energy (LCOE), in comparison with onshore wind farms, it is important to investigate ways of decreasing or at least maintaining, the current LCOE associated with offshore wind farms.

LIght Detection And Ranging (LIDAR) technology has entered the wind energy sector in the last two decades. Much research has been conducted to further improve and develop its applications in wind turbines. The majority of these investigations have a similar objective: the minimization of the LCOE. This can be achieved by either increasing the power production and/or by extending the turbine lifetime [3].

In wind energy, it is important to accurately measure the wind speed and direction at the site of a wind turbine in order to optimize its operation and maximize its energy output. Traditional methods for measuring the wind rely on anemometers mounted on tall masts, which can be expensive and difficult to maintain. Nacelle-mounted LIDAR offers an alternative method that can provide more accurate and detailed measurements of the wind field, but it can be challenging to interpret and process the data.

The use of a better control system is a possible way of going towards either solution. For example, by controlling the pitch of the blades [4] or by decreasing the yaw misalignment [5], it reduces the loads experienced by the wind turbine. The LIDAR can be used to measure the wind turbine's upstream wind, these measurements can be used to reconstruct the incom-

ing wind field, and feed the control system. This has been initially studied in [6] and confirmed its potentiality in simulation investigations [7; 8] and in field experiments [9; 10].

In the current work, an established wind field reconstruction method called the 2-Beam WFR method, is implemented and further validated with real-life LIDAR measurements. This simpler method is widely used by researchers since it is a well-established method with reasonable wind field estimations, but it is too restrictive as it needs flow simplifications to be solved and these can bring larger errors in more dynamic weather conditions. In that sense, researchers have been proposing other more complex methods, in which is possible to estimate wind field characteristics closer to the real wind field. This level of accuracy becomes particularly important when using the incoming wind field for control feeding purposes. Moreover, the combination of this approach with LIDAR technology would further enhance its applicability in the wind energy sector, as well as in other applications. Additionally, since this technology is less expensive than traditional meteorological masts, it is poised to become even more widely adopted. However, as a first step, this simpler method is first investigated and interpreted, in order to proceed to more complex and dynamic methods.

The rest of the paper is outlined as follows. In section 2, related work with wind field reconstruction is discussed. Then, in section 3, the implemented method is explained followed by section 4, where the data obtained from the nacelle-mounted LIDAR is analysed. The results from the method implemented are discussed in section 5. Finally, in section 6 conclusions for the present work are drawn, and future work is suggested to further develop this topic.

2. Wind field reconstruction

Wind field reconstruction methods are techniques that are used to infer the wind field over a certain area of interest, typically using wind measurements from one or more sensors. These methods are necessary since when the LIDAR retrieves the backscattered light, this is detected along a line-of-sight of the direction of the emitted laser beam. Moreover, a single laser beam cannot resolve a three-dimensional wind vector. This limitation causes an ambiguity in the wind field reconstruction, also known as Cyclops dilemma [11]. The Cyclops Dilemma is a challenge encountered in remote sensing measurements of wind speed and direction using single-beam LIDAR. The challenge arises because the LIDAR only measures the component of the wind vector that is along the laser beam. Therefore, in order to determine the full wind vector, multiple measurements from different directions are needed.

To obtain the true wind vector, at least two, line-of-sight measurements are used with a wind field reconstruction method. Wind field reconstruction methods are particularly important for wind turbine control, as accurate knowledge of the wind field can greatly improve the performance and efficiency of wind turbines. In the context of wind turbine control, these methods are used to reconstruct the incoming wind field, using measurements from sensors such as anemometers and LIDARs. As previously mentioned, the measurements are taken from one nacelle-mounted LIDAR in the present work.

These methods can be divided into two main categories: data-driven methods and model-based methods. Data-driven methods rely on historical wind data, typically from a network of weather stations, to derive the wind field. Common techniques in this category include kriging and inverse distance weighting (IDW), as in [12]. These methods can be effective in areas with dense sensor networks, but this is not the case for the majority of wind farms.

On the other hand, model-based methods rely on numerical models to infer the wind field. These models can be either physics-based or data-driven. Data-driven models, such as artificial neural networks and support vector machines as in [13], use historical data to learn patterns in the wind field and make predictions. Physics-based models use equations that describe the physical behaviour of the atmosphere, such as the Navier-Stokes equations, to simulate the wind field. Hybrid methods, which combine the strengths of both data-driven and model-based methods, have also been developed, in [14] a comparison between proposed methods has been made. These methods use observational data and numerical models to infer the wind field.

The choice of method depends on the specific application and the availability of data, computational resources and the quality of data. The accuracy and performance of the method will vary depending on the complexity of the problem and the quality of the input data. In general, the more complex and accurate methods typically require more data and computational resources but may be more effective in areas with sparser data or complex terrain. These methodologies can compute several wind characteristics, such as the shear exponent which is the exponent in the power law

between wind speed and wind shear, or the induction factor.

The reconstructed wind field can then be used for wind turbine control since the measurements used can be from sensors located near or on the wind turbine. The most basic method is the averaging method, which simply takes the average of the wind speed and direction measured by the sensors. However, when using data from a LIDAR, it is necessary to use more advanced methods to reconstruct the wind field. These include Taylor's frozen turbulence assumption for example, which incorporate information about the turbulence intensity and the spatial correlation of the wind field to improve the accuracy of the reconstructed wind field. One step further is the reconstruction by methods that use a combination of observational data and numerical models, and have been shown to be effective in improving the accuracy and robustness of wind field reconstruction for wind turbine control [11].

The focus of this paper will be the physical-based models. Various have been proposed in recent years, such as the five-parameter model by [15], a dynamic reconstruction based on Taylor's Frozen Turbulence Hypothesis by [16], a real-time estimation by [17], estimation based on an induction model in [18] and estimation with a recursive weighted least square method in [19]. In section 3, a detailed description of the method implemented in the current study is given.

3. Methodology

The objective is to derive wind characteristics, such as wind speed, using LIDAR measurements. The current paper focuses on implementing a simpler method, namely the 2-beam wind field reconstruction method. Furthermore, this method will be compared with a so-called naive way of obtaining the wind speed, this being by simply averaging the wind speed measured in the LIDAR's line-of-sight for hub height.

The 2-beam method has to be implemented under certain wind flow assumptions, such as horizontal homogeneity, two- or three-dimensional wind vector, and predefined shear profile [20]. The method is implemented with a Python script with the default mathematical algorithms. Different authors, for example in [21; 22], have implemented a 2-beam reconstruction method with slight differences in methodologies, but with the same principle basis. Figure 1 shows a top-view schematic of the wind turbine with a nacelle-mounted LIDAR (orange dot).

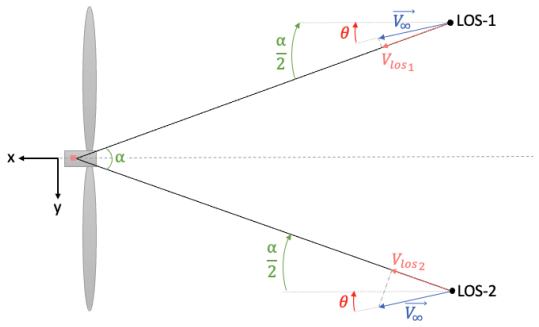

Figure 1: Nacelle LIDAR schematics for 2-beam reconstruction method implementation.

Through this schematic, also represented throughout different literature, it is possible to visualize how the line-of-sight measurements (orange arrows V_{los_1} and V_{los_2}) relate with the incoming wind field (blue arrows $\vec{V_\infty}$). Each line-of-sight vector will make an angle equal to the LIDAR's half-opening angle (green angles $\frac{\alpha}{2}$) with the x-direction. This angle is defined by the LIDAR's manufacturer, being equal to 30 degrees in this case ($\alpha = 30^\circ$). Under the assumption that the incoming flow is homogeneous, as shown in the schematic, it will yield a flow misalignment (red angle θ).

Due to the Cyclops dilemma, a single LIDAR system cannot infer a three-dimensional wind vector by the use of only line-of-sight measurements. So, the implementation of the 2-beam method has to be complemented with certain assumptions of the incoming wind field. For the current work, the following assumptions are made:

- Two-dimensional wind vector: the vertical component (z-axis direction) is equal to zero;
- Horizontal homogeneity: wind speed components are the same horizontally (y-axis direction);
- The LIDAR tilt and roll is 0°;
- The probe volume averaging is neglected.

Following the schematic interpretation and the assumptions made, it is possible to define both wind vector components (V_x and V_y) through both line-of-sight (LOS) measurements [22]:

$$V_x = \frac{V_{los_1} + V_{los_2}}{2 * cos(\alpha/2)} \tag{1}$$

$$V_y = \frac{V_{los_1} - V_{los_2}}{2 * sin(\alpha/2)} \quad (2)$$

Finally, the wind characteristics can be calculated with:

$$V_\infty = \sqrt{V_x^2 + V_y^2} \quad (3)$$

$$\theta = arctan2(V_y, V_x) + \psi \quad (4)$$

being V_∞ the wind speed magnitude and θ the wind direction relative to the rotor centre line (i.e., flow misalignment with respect to the line-of-sight).

The used LIDAR has the capability in measuring the turbine's yaw angle, ψ, via its own sensors, this is added to the relative wind direction, to obtain the true wind direction. However, since in normal functioning, the wind turbine will yaw according to the wind direction, the correction is expected to be minimal.

The 2-beam reconstruction technique is a powerful tool for improving the accuracy of LIDAR wind measurements in complex flow environments, such as those encountered in wind energy applications. However, it does require careful calibration and validation to ensure that the measurements are accurate and reliable. Under this static wind field reconstruction method, it is possible to derive the wind characteristics with a simple implementation, considered sufficient for power performance analysis [21]. However, for control applications, the assumptions made are too simplistic, it is necessary to use methods able to take into account the propagation of the wind field over time. Hence, the so-called dynamic methods or even static methods with fewer assumptions, are necessary to be used in such applications.

4. Experimental Setup

The LIDAR is a remote sensor instrument capable of sampling the wind by means of infrared laser beams. The light of the emitted laser will reflect when encountering aerosol particles in the wind, shifting its frequency due to the Doppler effect. The variation is proportional to the relative movement between light and aerosol, thus it is possible to retrieve the projection of the aerosol velocity in the radial direction [23]. In order to determine the incoming wind field, the measured wind characteristics must be made in multiple spatial locations in the upstream direction and along the rotor area of the wind turbine.

LIDARs can be separated into two categories that depend on the laser source, whether it has a continuous wave (cw) or a collimated laser. In the former configuration, the LIDAR will sample at a single distance from the wind turbine, with sampling frequencies ranging between 50 and 400 Hz. While the latter, allows for a simultaneous multiple-distance backscatter analysis, with a light frequency emission between 10kHz and 20kHz. The present research has employed a 50 Hz continuous-wave nacelle-mounted LIDAR from ZX Lidars. This LIDAR was chosen due to its advantages, such as [24]:

- Up to 10 horizontal measurement ranges, with up to 12 vertical slices for each;
- Circular scan that allows the measurement of the wind field characteristics around the entire rotor;
- Rotor wind equivalent wind speed and wind direction calculations;
- Different data rates of the measured wind field: Raw in 50 Hz, Averaged in 1 Hz and Averaged-10 in 0.002 Hz.

The used LIDAR for the present work will make a circular profile at several distances upstream of the wind turbine. In Fig. 2, the configuration of the measurements along some of the recorded distances can be seen. At each line-of-sight measurement, the azimuthal position is registered with respect to the centre of the probed circle. These measurements are then averaged and a "63-averaged azimuthal positions" LIDAR is created to be used in the implemented methods. Under certain situations, such as when the laser beam hits a blade, the quality of data is compromised. The used LIDAR has the ability to execute quality control on the data, being possible to filter out the measurements of poor quality.

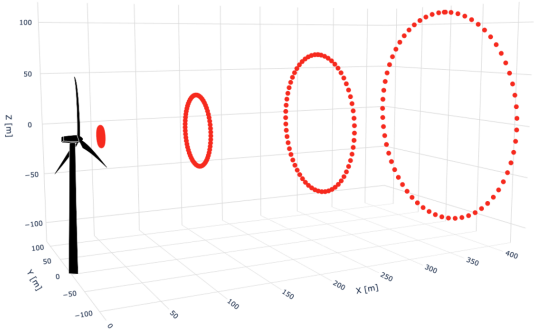

Figure 2: LIDAR's measurement trajectories with 63 azimuth-averaged line-of-sight, at four ranges from the wind turbine.

The deployed LIDAR provides three different data sets for the same time window: a raw file with the 50 Hz frequency measurements, a one-second averaged data and a 10-minute averaged data. The latter data set provides the fit-derived wind parameters, such as the horizontal wind speed at hub height for the different measurement planes. This information was chosen to be used as a comparison with both the SCADA and the studied wind field reconstruction method. After deploying for the measurement campaign, the LIDAR's measurements were then compared with the wind data captured by the sensors installed by the manufacturer of the wind turbine, designated as SCADA from now onward. The comparison of the measured wind speed is shown in Fig. 3. For the studied time window, the measurements show reasonable agreement between them, validating the LIDAR's functioning and positioning.

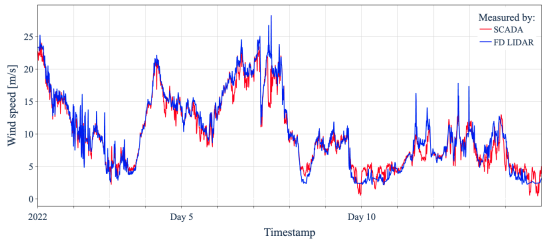

Figure 3: Comparison between LIDAR's fit-derived wind speed measurements and SCADA.

After validating and processing the LIDAR data, the measurements taken in the 15-day time frame shown in Fig. 3 were used in the aforementioned wind field reconstruction method.

5. Results

In this section, the results obtained with the implemented WFR methodologies are presented in comparison with the LIDAR's 10-minutes averaged fit derived wind parameters measurements. The estimated wind field speed magnitude (in green) is compared with the wind field measured parameters (in blue) in Fig. 4. The time series plot also shows a 2-beam average (in orange), further demonstrating the necessity of a proper wind field reconstruction method such as the 2-beam method.

For the studied time frame, around 15 days during the year 2022, the 2-beam wind field reconstruction method reconstructs the wind speed magnitude behaviour quite fairly. Moreover, when comparing with

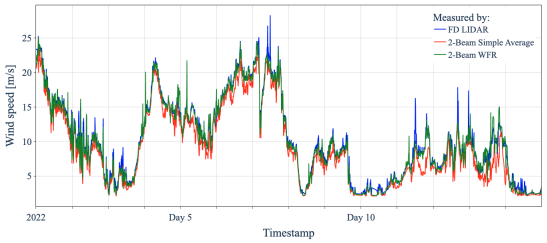

Figure 4: Comparison between LIDAR's anemometer and 2-Beam wind field reconstruction method.

a simple average of the lasers' beam measurements, it has a clear improvement in the wind speed estimation.

The performance of the method becomes more clear in Fig. 5a and Fig. 5b, where a quantile-quantile distribution, respectively, between the "simple averaged" method and 2-beam estimated with the fit derived measured wind speed. This plot further proves that by simply retrieving an average of the measured line-of-sight wind speed, the wind field is not properly estimated. Furthermore, it is visible in both the 2-beam method and the averaged data, a too-high variance of the estimated parameter with respect to the expected value, in order to use it for more input-sensitive applications such as control.

It is also possible to display the locality, spread and skewness of the results with a boxplot, shown in Fig. 6a and Fig. 6b, for both discussed cases. In these figures, the variance of the absolute difference between methods becomes more evident. Being a proven methodology, and as expected, the 2-beam WFR estimates the wind parameter overall better than simply averaging the measurements coming from the LIDAR.

6. Conclusion

Following a measurement campaign on an offshore wind turbine, it is necessary to analyse and interpret the measured data with appropriate methodologies. In that sense, the current research has started and the first results are shown and discussed.

Wind field reconstruction (WFR) methodologies are necessary when a LIDAR is in use in order to obtain wind field characteristics. In this paper, the 2-beam WFR is implemented using Python. The 2-beam WFR method uses two line-of-sight measurements in order to estimate two wind field characteristics (WFC), the wind speed magnitude and wind direction misalignment.

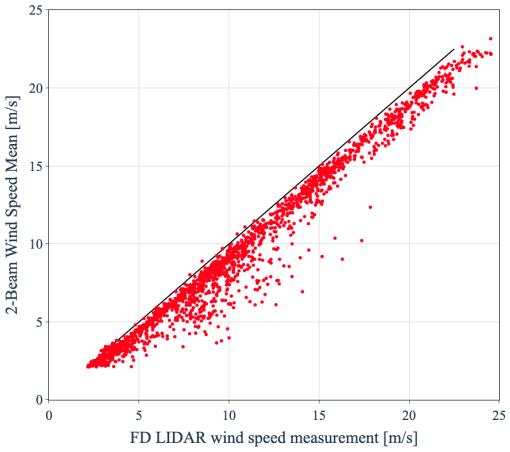

(a) Simple Averaged Wind Speed.

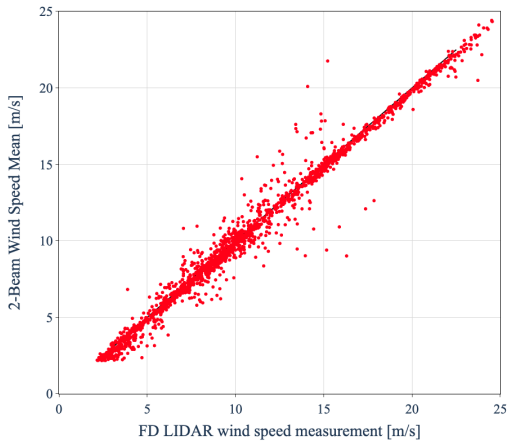

(b) 2-Beam Wind Field Reconstruction method.

Figure 5: Quantile-quantile distribution plots for both methods.

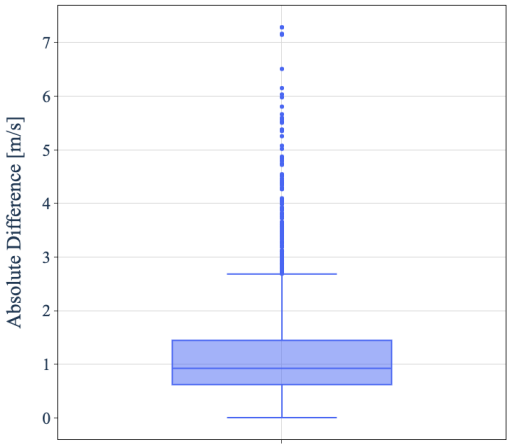

(a) Simple Averaged Wind Speed.

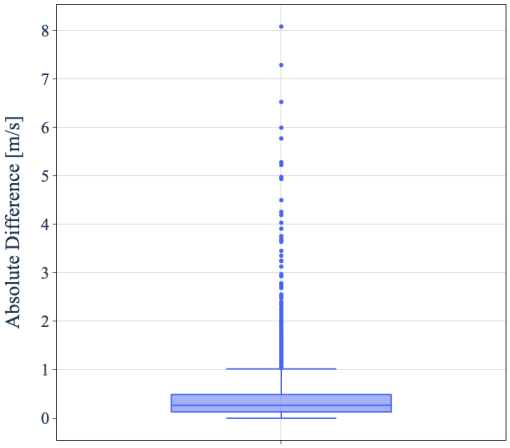

(b) 2-Beam Wind Field Reconstruction method.

Figure 6: Absolute difference between wind field reconstruction methods and measured wind speed.

This was followed by comparing the method estimation and the LIDAR's fit-derived measurements, namely the wind speed magnitude. As initially expected, the 2-beam method performs overall quite reasonably, in particular when compared against a so-called naive method where two-beams measurements are simply averaged with no other considerations. The 2-beam WFR method is widely used by the scientific community, in particular for power curve assessment, but it does has its shortcomings as seen in terms of the variance and overall quality of the estimated wind field. Being a simple method and with wind field assumptions, these differences were not unexpected. However, further investigation could be beneficial to better understand if these occur, for example, due to the induction zone of the wind turbine which is not taken into account in the 2-beam WFR method.

So, in future work, besides a more extensive analysis performed on a larger data set, it will also be on extending the work to more complex wind field reconstructed methods, such as the so-called dynamic methods.

Acknowledgments

For the presentation of this research, I would like to acknowledge the RAINBOW and SEAFD projects.

References

[1] E. B. Intelligence, Tech. rep., EAWE (2015).
[2] P. e. a. Borawski, Development of wind energy market in the european union, Renewable Energy 161 (2020) 691–700.

[3] A. Scholbrock, et al, Lidar-enhanced wind turbine control: past, present, and future, in: American Control Conference (ACC), 2016, pp. 1399–1406.
[4] E. A. Bossanyi, et al, Wind turbine control for load reduction, Wind Energy 6 (3) (2003) 229–244.
[5] D. Song, et al, Wind direction prediction for yaw control of wind turbines, International Journal of Control, Automation and Systems 15 (1).
[6] M. Harris, M. Hand, A. Wright, Lidar for turbine control, Tech. rep., NREL/TP-500-39154 (2007).
[7] D. Schlipf, D. J. Schlipf, M. Kühn, Nonlinear model predictive control of wind turbines using lidar, Wind Energy 16 (8) (2013) 1107–1129.
[8] E. A. Bossanyi, et al, Wind turbine control for load reduction, Journal of Physics: Conference Series 555 (1) (2014) 012011.
[9] D. Schlipf, Field testing of feedforward collective pitch control on the cart2 using a nacelle-based lidar scanner, Journal of Physics: Conference Series 555 (1) (2014) 012090.
[10] A. Kumar, et al, Field testing of lidar assisted feedforward control algorithms for improved speed control and fatigue load reduction on a 600 kw wind turbine, in: EAWE Proc., 2015.
[11] F. e. a. Guillemin, Nacelle lidar online wind field reconstruction applied to feedforward pitch control, Journal of Physics: Conference Series 753 (5) (2016) 052019.
[12] E. Ozelkan, G. Chen, B. Ust unda g, Spatial estimation of wind speed: a new integrative model using inverse distance weighting and power law, International Journal of Digital Earth 9 (8) (2016) 733–747.
[13] C. Tagliaferri, R. Flay, Wind direction forecasting with artificial neural networks and support vector machines, Ocean Engineering 97 (2015) 65–73.
[14] K. Reinhardt, C. Samimi, A comparison of different interpolation methods for wind data in central asia, Climate Dynamics 51.
[15] S. Kapp, A five-parameter wind field estimation method based on spherical upwind lidar measurements, Journal of Physics: Conference Series 555 (1) (2014) 012112.
[16] S. e. a. Raach, Three dimensional dynamic model based wind field reconstruction from lidar data, Journal of Physics: Conference Series 524 (1) (2014) 012005.
[17] P. Towers, B. Jones, Real-time wind field reconstruction from lidar measurements using a dynamic wind model and state estimation, Wind Energy 19 (1) (2016) 133–150.
[18] A. Borraccino, D. Schlipf, F. Haizmann, R. Wagner, Wind field reconstruction from nacelle-mounted lidar short-range measurements, Wind Energy Science 2 (1) (2017) 269–283.
[19] F. e. a. Guillemin, Real-time three dimensional wind field reconstruction from nacelle lidar measurements, Journal of Physics: Conference Series 1037 (3) (2018) 032037.
[20] A. Borraccino, M. Courtney, R. Wagner, Generic methodology for field calibration of nacelle-based wind lidars, Remote Sensing 8 (11) (2016) 907.
[21] D. e. a. Schlipf, Model based wind vector field reconstruction from lidar data, in: Proceedings of the German Wind Energy Conference, 2012.
[22] R. e. a. Wagner, Power curve measurement with a nacelle mounted lidar, Wind Energy 17 (10) (2014) 1441–1453.
[23] D. Trabucchi, Lidar measurements and engineering modelling of wind turbine wakes, Ph.D. thesis, Politecnico di Milano (2020).
[24] ZX Lidars, ZX tm Lidars - product guide, official Product Guide (2019).

A new scale-aware planetary boundary layer scheme in Weather Research and Forecasting model

Adithya Vemuri

Environmental and Applied fluid dynamics department, von Karman Institute for Fluid Dynamics, Belgium, adithya.vemuri@vki.ac.be

Supervisors: Wim Munters, Sophia Buckingham, and Jeroen van Beeck

Research engineer, Research manager, and Professor, Environmental and Applied fluid dynamics department, von Karman Institute for Fluid Dynamics, Belgium, wim.munters@vki.ac.be, sophia.buckingham@vki.ac.be, and jeroen.vanbeeck@vki.ac.be

University Supervisor: Jan Helsen

Professor, Department of Mechanical Engineering, Vrije Universiteit Brussel, Boulevard de la Plaine 2, 1050 Ixelles, Belgium, jan.helsen@vub.be

Abstract

The gray zone problem is the biggest challenge in modern-day numerical weather prediction models. The transition region between mesoscale and large eddy simulation scales could aid in accurately simulating the energy cascade. The following work proposes a new gray zone-capable planetary boundary layer scheme and its implementation in the weather research and forecasting model.

Keywords: Gray zone modeling, mesoscale modeling, planetary boundary schemes

1. Introduction

The 21st century has seen some of the biggest developments and advancements in the field of numerical weather prediction (NWP) [1]. Studies tackling the so-called gray zone challenge have sprung a wide range of modeling techniques for the planetary boundary layer (PBL) [2; 3; 4]. Realistically simulating the PBL plays a major role in key engineering applications and scientific advancements. Fields from aerospace engineering, planetary exploration, and sustainable energy extraction to disaster management heavily rely on its progress.

The gray zone problem is a numerical challenge in modern-day NWP models pertaining to the transition region between mesoscale scales ($\mathcal{O}$(100 km) to $\mathcal{O}$(1 km)) and large-eddy simulation (LES) scales ($\mathcal{O}$(100 m) to $\mathcal{O}$(10 m)). That is, at grid spacings much larger than the largest energy-carrying eddies ($\mathcal{O}$(1 km) to $\mathcal{O}$(100 m)), the LES assumption fails to accurately simulate the PBL [5]. Wyngaard (2004) [2] analyzed and described this transition region as the "terra incognita" (or gray zone). Thus, emphasizing the need for gray zone-capable PBL parameterizations in modern-day NWP models. As a first, Honnert et al. (2011) [3] describe a methodology to extend the existing PBL parameterizations to gray zone scale by blending mesoscale and LES closure assumptions weighed by partitioning functions. Following this, various studies have utilized this approach to propose scale-aware PBL parameterizations for the Weather Research and Forecasting (WRF) model. Schemes such as, Shin and Hong (2013) [6], Ito et al. (2015) [7], SMS-3DTKE PBL scheme [8], amongst others.

The following work proposes a modification and extension to the existing scale-aware SMS-3DTKE scheme to account for partitioning functions as derived by Senel et al. (2020) [9] for all components of the turbulent stress tensor. The new PBL is then tested at gray zone grid spacings using the idealized architecture in WRF for a convective boundary layer (CBL) case.

Section 2 describes the full set of governing equations for the proposed PBL scheme. Following which section 3 details the case study utilizes in this study. Section 4 presents the results and analysis. Finally,

the conclusions are presented in section 5.

2. Governing equations

The WRF model solves the non-hydrostatic Euler's equations with parameterizations for; the evolution of the PBL, the microphysical processes, the cumulus effects, the radiation forcing, and the land surface interaction. This work focuses on the PBL parameterization, specifically for the gray zone. The general form of a PBL parameterization follows the eddy-viscosity assumption relating the turbulent stresses to the gradient of mean flow [10] as described in Eq. 1. Where K is the eddy-viscosity coefficient.

$$\tau_{ij} = K\left(\frac{\partial \bar{u}_i}{\partial x_j} + \frac{\partial \bar{u}_j}{\partial x_i}\right) = KD_{ij} \tag{1}$$

The WRF model primarily defines two methods for determining the eddy-viscosity coefficient: the Smagorinsky closure which relates the eddy-viscosity coefficient to the deformation tensor and a characteristic length scale and the prognostic TKE closure [11; 12] which solves a full TKE equation as in Eq. 2 and relates the eddy-viscosity coefficient to the TKE and length scale.

$$\frac{\partial e}{\partial t} = \bar{u}_j\frac{\partial e}{\partial x_j} - \overline{u_i'u_j'}\frac{\partial \bar{u}_i}{\partial x_j} + \frac{g}{\bar{\theta}_0}\overline{w'\theta'} - \frac{\partial \overline{u_i'(e + p'/\rho_0)}}{\partial x_i} - \varepsilon \tag{2}$$

Focusing on the prognostic TKE closure the determination of the length scale at the mesoscale limit i.e., $\Delta \gg l$ (where Δ is the grid spacing) and the LES limit i.e., $\Delta \ll l$ is very different as the LES assumption fails at mesoscale grid spacing producing unrealistic turbulence diffusion [2]. The gray zone problem is the transitioning region between these limits. At the mesoscale limit, the length scale is usually defined as the master mixing length (L_{Meso}) as derived by Mellor and Yamada (2009) [13] as a harmonic mean of mixing lengths accounting for the surface layer, the turbulent structures, and the thermal stability. At the LES limit the length scale is determined as a function of TKE, Brunt–Väisälä, and the vertical grid spacing. The prognostic TKE closure then defines the eddy-viscosities at the mesoscale limit as $K_{m,Meso} = \kappa\sqrt{e}L_{Meso}$, where the subscript m stands for momentum, κ is the von Karman constant, and e is the TKE and at the LES limit $K_{m,LES} = C_k\sqrt{e}l_{h,v}$, where $l_{h,v}$ stands for length scale defined for horizontal and vertical grid spacing accounting anisotropy in the model [14] and C_k is a constant in the range $(0.15, 0.25)$.

In the WRF model, the eddy-viscosities are further split based on the deformation tensor component as shown in Eq. 3, where $K_h = K_m/Pr$ relating the heat and momentum eddy-viscosity coefficients to the Prandtl number (Pr), η is the terrain (pressure) following vertical coordinate, and the constant C is a function of C_k, length scale, grid spacing, and TKE.

$$\begin{gathered}
\partial(\mu_d e) + \nabla\cdot\mathbf{V}_e = \mu_d(shear\ production + \\
buoyancy + dissipation) \\
Shear\ production = K_hD_{11}^2 + K_hD_{22}^2 + K_vD_{33}^2 \\
+ K_h\overline{D_{12}^2}^{xy} + K_h\overline{D_{13}^2}^{x\eta} + K_h\overline{D_{23}^2}^{y\eta} \\
Buoyancy = -K_vN^2 \\
Dissipation = -\frac{Ce^{3/2}}{l}
\end{gathered} \tag{3}$$

2.1. Non-local effects and gray zone modeling

In order to simulate the realistic evolution of the PBL at mesoscale grid spacings Troen and Mahrt (1986) and Wyngaard (2004) [15; 2] establish the importance of considering non-local diffusion imposed by larger eddies present in the PBL. Eq. 4 describes the general form of of PBL closure including non-local momentum effects in the vertical direction. The counter-gradient term γ_m is defined in Eq. 5 where u_* is the friction velocity, w_* is the convective velocity, w_s is the convective velocity scale, z_i is the height of the PBL, and S_m is an empirical constant 15.9 [16]. The definition of the non-local heat effects follows the methodology introduced by Shin and Hong (2013) [6] relating the vertical heat flux profiles to grid-filtered LES simulations. The non-local effects are only included in the vertical direction following the suggestions of Brown and Grant (1997) [5] and Noh et al. (2003) [16].

$$\overline{u'w'} = -K_{Mv}\left(\frac{\partial \bar{u}}{\partial z} + \frac{\partial \bar{w}}{\partial x}\right) + K_{Mv}\gamma_m \tag{4}$$

$$\gamma_m = -S_m\frac{u_*^2}{w_s z_i}\left(\frac{w_*}{w_s}\right)^3 \tag{5}$$

To bridge the gray zone transitioning gap Honnert et al. (2011) [3] first defined the so-called gray zone partitioning functions to blend mesoscale and LES eddy-viscosities by relating grid-filtered resolved turbulence to the sub-grid scale turbulence. Following this various studies have utilized this approach to parameterizing gray zone capable PBL schemes such as

Boutle et al. (2014) [17] weighing the 1D non-local PBL closure with the 3D Smagorinsky closure, similarly, Ito et al. (2015) [7] extend the Mellor-Yamada PBL scheme by weighing the mesoscale length scale and horizontal diffusion, Shin and Hong (2015) [18] extend the Yonsei State University PBL scheme including non-local effects and gray zone partitioning functions for the vertical momentum and heat components, and Zhang et al. (2018) also called SMS-3DTKE PBL scheme [8] extends Deardorff's 3D TKE closure [11] to the mesoscale limit by considering grid size dependent partitioning functions derived only for TKE and vertical heat fluxes (local and non-local) applied commonly to all components of the stress tensor. Only Shin and Hong (2015) and the SMS-3DTKE scheme derive gray zone partitioning functions using grid averaged top-hat filtered LES simulation of a convective boundary layer. Unlike the SMS-3DTKE scheme, this work utilizes the stability, height, and grid size-dependent partitioning functions derived by Senel et al. (2020) [9] using the Butterworth filter and extends the SMS-3DTKE scheme to include individual partitioning functions for all nine components of turbulent stresses (six momentum fluxes and three heat fluxes) in the PBL closure, i.e., Eq. 3 and Eq. 4.

This work adopts the pragmatic blending approach for the mesoscale and the LES eddy-viscosities using partitioning functions as in the SMS-3DTKE scheme. The respective equations for momentum and heat eddy-viscosities are given in Eq. 6 and Eq. 7. The counter-gradient term in the non-local effects equation (Eq. 4) is blended using partitioning functions at the PBL height.

$$K_m = (1 - \mathcal{P}_{\tau_{ij}}(\hat{\Delta}/z_i, \mathcal{X}_i)) \cdot K_{m,LES} + \mathcal{P}_{\tau_{ij}}(\hat{\Delta}/z_i, \mathcal{X}_i) \cdot K_{m,Meso} \quad (6)$$

$$K_h = (1 - \mathcal{P}_{\theta u_i}(\hat{\Delta}/z_i, \mathcal{X}_i)) \cdot K_m \cdot Pr^{-1} + \mathcal{P}_{\theta u_i}(\hat{\Delta}/z_i, \mathcal{X}_i) \cdot Pr^{-1} \cdot K_m \quad (7)$$

The stability, height, and grid size dependent partitioning functions of an arbitrary stress component $\mathcal{P}_a^{sgs}\left(\hat{\Delta}/z_i, \mathcal{X}_i\right)$ as derived by Senel et al. (2020) [9] for the lower-mixed layer, mixed layer, and the entrainment layer is shown in Eq. 8, where $\hat{\Delta}$ represents the grid spacing and $\mathcal{X}_i = -L_o/z_i$ is the negative inverse convective stability where L_o is the Obhukov length. The constants C_1, C_2, C_3, G_1, G_2, and G_3 for the different layers of the PBL can be found under the said paper.

$$\mathcal{P}_a^{sgs}\left(\hat{\Delta}/z_i, \mathcal{X}_i\right) = \frac{\langle a \rangle_{\Delta}^{sgs}}{\langle a \rangle^{tot}}\left(\hat{\Delta}/z_i, \mathcal{X}_i\right) = \beta + (\alpha - \beta)e^{-e^{(G_1 + G_2 \tanh(G_3 \mathcal{X}_i)) - \left(c_1 + C_2 e^{\mathcal{X}_i^{C_3}}\right)\left(\hat{\Delta}/z_i\right)}} \quad (8)$$

3. Methodology of validation and benchmark LES setup

The WRF model version 4.4.2 is considered in this study the implementation of the new PBL is tested using the idealized architecture present in WRF (WRF-LES). The idealized case study utilized in this work follows that of Shin and Hong (2013) [6]. The details are summarized in Table 1. The simulations are considered to be periodic in the x- and y- directions. A spin-up period of 6 h is considered. The next consecutive hour is then utilized for the analysis presented in this study. The horizontal dimension of the square domain is 12.05 km. The model top is at 2.4 km, with a Rayleigh damping layer at the final 400 m. All simulations are initialized with a geostrophic forcing (u-component) of 10 m/s. The timestep considered is 0.5 s. The Coriolis parameter is set to $f = 10^{-1} s^{-1}$. The surface layer parameterization Monin-Obukhov Similarity scheme is utilized to account for near-surface interactions. The third-order Runge-Kutta time integration scheme is considered. The constants C_s and C_k are set to 0.18 and 0.1 respectively. The acoustic time step is set to the sixth of the aforementioned timestep.

Table 1: Table summarizing the initial conditions and parameters for the idealized simulations considered in this study.

#	Description	Parameter
1	Model top level	2.4 km
2	Domain dimensions	12.05 km, 12.05 km
3	Vertical levels	81
4	Surface heat flux	0.20
5	Damping layer	2 km
6	Geostrophic forcing	10 m/s
7	Time step	0.5
8	Simulation period	7 h
9	Evaluation period	1 h

The new PBL is tested at three horizontal grid spac-

ings 50 m, 300 m, and 600 m. A summary of the simulation matrix is presented in Table 2.

Table 2: Table summarizing the simulation matrix considered in this study.

#	PBL scheme	Grid spacing (Δx)
1	SMS-3DTKE	50 m, 300 m, 600 m
2	SMS-3DTKE + new P-funcs	300 m, 600 m
3	Full TKE eqn	300 m, 600 m
4	Full 3D PBL	50 m, 300 m, 600 m

In order to conserve computational time and storage space the evaluation of the idealized simulations follow probing the domain at different locations as depicted in Fig. 1.

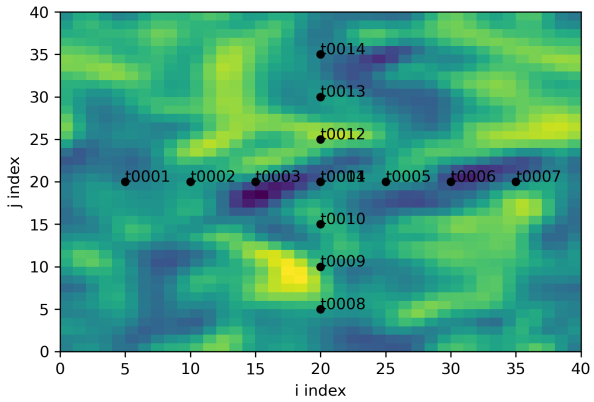

Figure 1: The horizontal plane of streamwise velocity at half the model height. The sampling points are indicated in black.

4. Results and discussion

In order to systematically validate the implementation of the new PBL in WRF. The implementation is split into three stages, first, the partitioning functions of the SMS-3DTKE scheme are replaced with Senel et al. (2020) only for TKE and vertical heat flux, also adding the convective stability and the height dependency nature of the partitioning functions. Second, the full 3D TKE equation is split to consider six partitioning functions for the six momentum fluxes, therein six eddy-viscosities plus the aforementioned vertical heat flux in the non-local equation. Finally, in addition to the full TKE equation, the eddy-viscosities in the horizontal and vertical diffusion equations are extended to account for the new partitioning functions. Therein the horizontal diffusion equation for temperature is also split to consider the influence of $u'\theta'$ and $v'\theta'$ partitioning functions. The following sections 4.2, 4.3, and 4.4 present the results for the aforementioned implementation stage for simulations grid spacings as described in Table 2. The section 4.1 presents the "baseline truth" at below the LES limit at 50 m grid spacing for the new PBL and SMS-3DTKE scheme. The results from this section are then used to compare the subsequent implementation stages. The energy spectra in the following sections are taken at half the vertical domain close to the PBL height. The peaks/kinks in the energy spectra at higher frequencies can be attributed to numerical noise.

4.1. Benchmark results

For simulations at the LES limit, i.e., $\Delta = 50\ m$ there is no impact of the partitioning functions, as for $\Delta < 100\ m$ the turbulence is assumed to be fully resolved. By extension there are no mesoscale effects and non-local effects added to the equations, rendering the simulations to take the form of a standard Deardorff 3D TKE scheme defined in WRF. Therefore by definition, the mean wind spectra of all components and the mean TKE profile must be very similar for the SMS-3DTKE scheme and the new PBL, this is depicted by Fig. 2. Ideally, the mean profiles must overlap, upon considering 4 h time averaging the difference in TKE and spectra profiles is non-existent (not shown). The mean spectra for the v- and the w-components of wind, the temperature spectrum, and the mean profiles also indicate very similar behavior (not shown).

4.2. Modified partitioning functions

The following section presents the results for simulations at 300 m and 600 m grid spacing in comparison to 50 m SMS-3DTKE simulation as the baseline. The physics scheme considered replaces the partitioning functions of the SMS-3DTKE with the new stability, height, and scale-dependent partitioning functions defined in section 2. The results are compared to the standard SMS-3DTKE scheme at the corresponding grid spacing. Figure 3 presents the mean u-component energy spectrum and the resolved vertical TKE profiles.

The cascading drop in the energy spectrum is evident from these plots i.e., the highest energy-carrying simulation is at 50 m and the lowest at 600 m grid

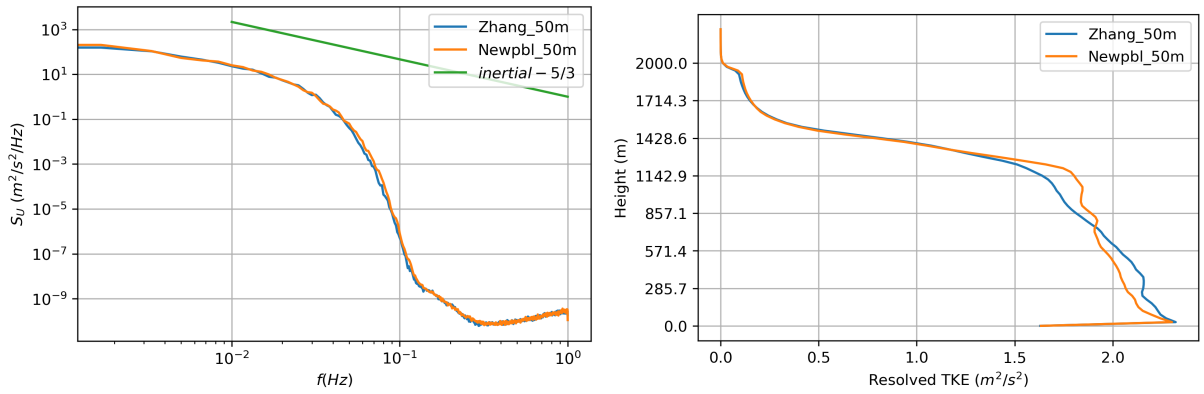

(a) (b)

Figure 2: For simulations at 50 m grid spacing (a) Energy spectrum for the u-component of wind. (b) Resolved turbulent kinetic energy.

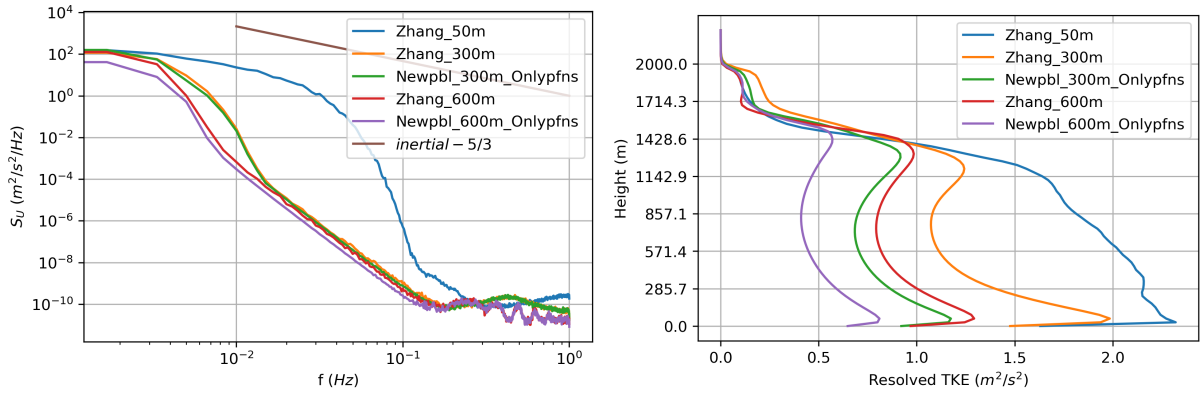

(a) (b)

Figure 3: For simulations at 50 m, 300 m, and 600 m grid spacing considering the change in only the partitioning functions (a) Energy spectrum for the u-component of wind. (b) Resolved turbulent kinetic energy.

spacing. The mean u-component energy spectrum is presented in Fig. 3a indicating the new PBL scheme to have lower energy content in comparison to the SMS-3DTKE scheme at the same grid spacing. This trend is observed for all components of wind spectra. Considering the resolved TKE profiles in Fig. 3b the new PBL simulations produce significantly lower TKE in comparison to the SMS-3DTKE at similar grid spacing. Highlighting the influence of the new stability, height, and scale-dependent partitioning functions.

4.3. Full TKE equation

In a similar manner, the following section presents the results for simulations at 50 m, 300 m, and 600 m grid spacing for the new PBL scheme considering six partitioning for the full TKE equation. Figure 4 presents the mean w spectrum and the resolved TKE profiles.

Unlike the previous section considering the change in only the partitioning functions, the energy spectra at 300 m grid spacings considering the fully partitioned 3D TKE equation is very similar to the SMS-3DTKE scheme for all components of wind spectra, the w-component energy spectrum is presented in Fig. 4a. At 600 m grid spacing the w-component of the wind spectrum observes slightly higher energy content in comparison to the SMS-3DTKE scheme. Considering the resolved TKE profiles as presented in Fig. 4b, the predicted TKE for the new PBL scheme is observed to be higher than SMS-3DTKE at all grid spac-

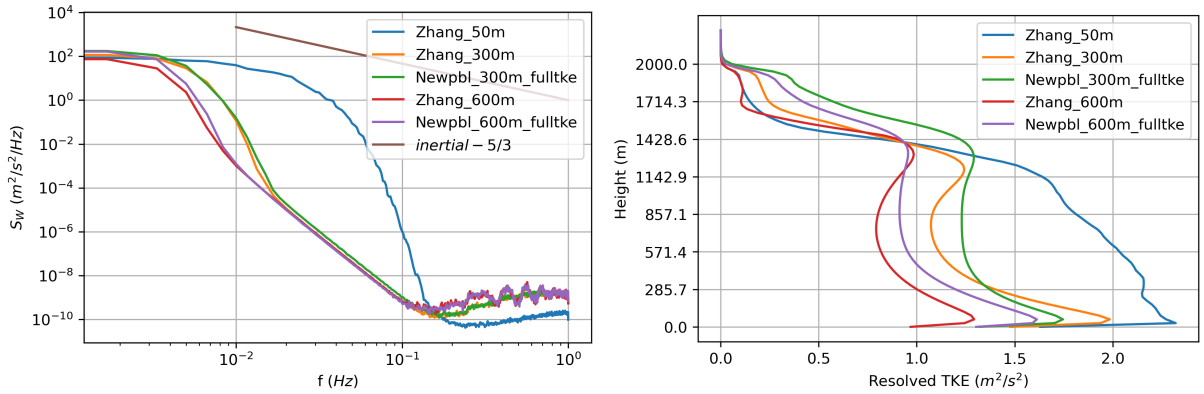

(a) (b)

Figure 4: For simulations at 50 m, 300 m, and 600 m grid spacing considering partitioning functions for the full TKE equation (a) Energy spectrum for the w-component of wind. (b) Resolved turbulent kinetic energy.

ings. Marginally higher PBL height is also predicted in comparison to the SMS-3DTKE simulation. The TKE profiles for the new PBL scheme are observed to be closer to the baseline 50 m grid spacing than the SMS-3DTKE.

4.4. Full 3D PBL scheme

This section presents the results of considering the effects of a fully partitioned TKE equation along with partitioned horizontal, and vertical diffusion equations at 300 m and 600 m grid spacing. The plots comparing the mean u-component spectrum and the resolved vertical TKE profiles are presented in Fig. 5.

The energy spectrum for the u- (Fig. 5a) and v-component observe an increase in energy content at mid frequencies at 300 m and 600 m grid spacing. However, this trend is not observed for the w-component. The resolved vertical TKE profiles are observed to be similar to the section 4.4 (Fig. 4b and Fig. 5b). At 600 m grid spacing, significantly higher TKE is predicted in comparison to the SMS-3DTKE scheme. At 300 m grid spacing, the predicted TKE is found marginally higher than section 4.4. Overall, the predicted TKE for the new PBL is closer in comparison to the SMS-3DTKE scheme.

5. Conclusions

This study elaborates on the implementation of a new planetary boundary layer (PBL) scheme developed at the von Karman Institute for fluid dynamics (VKI) in the weather research and forecasting model. The current implementation of the SMS-3DTKE scheme, based on Deardorff's 3D TKE closure is considered the starting point. The SMS-3DTKE scheme extends the standard Deardorff's 3D TKE closure to mesoscale grid spacings ($\Delta \gg l$) by blending mesoscale and LES eddy-viscosities using scale-dependent gray zone partitioning functions for TKE and vertical heat fluxes. The proposed PBL extends the SMS-3DTKE scheme to include stability, height, and scale-dependent gray zone partitioning functions for all nine components of turbulent stresses (six momentum and three heat). The partitioning functions were previously derived at VKI by Senel et al. (2020) by considering 8 convective boundary layer idealized simulations at different convective stability regimes.

The validation of said PBL scheme is done in three stages, first, by changing only the partitioning functions of the SMS-3DTKE scheme to include stability and height dependency. Second, in addition to the first includes partitioning functions for the full 3D TKE equation. Finally, in addition to the above include partitioning functions for the horizontal and the vertical diffusion equation in WRF. The implementations are validated against the SMS-3DTKE simulation at 50 m grid spacing (LES limit). The simulation matrix includes gray zone grid spacings of 300 m and 600 m. The results indicated all stages of implementation concur with the $-5/3$ inertial range. All stages of implementation indicated slightly higher planetary boundary layer height prediction in comparison to the 50 m baseline simulation. For the final stage of implementation, the energy spectra of the u- and v- com-

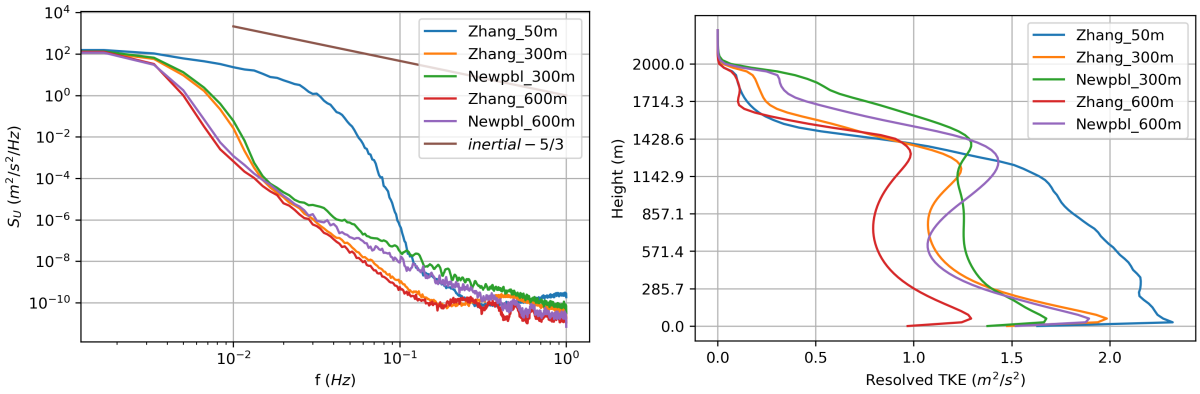

(a) (b)

Figure 5: For simulations at 50 m, 300 m, and 600 m grid spacing considering partitioning functions for both TKE equation and horizontal and vertical diffusion equations (a) Energy spectrum for the u-component of wind. (b) Resolved turbulent kinetic energy.

ponents of wind were found to produce more energy at mid-frequencies. The TKE profiles and mean vertical wind profiles for the last 2 stages of implementation are found to predict closer values to the 50 m grid spacing baseline simulation and higher TKE in comparison to the SMS-3DTKE PBL scheme at 300 m and 600 m grid spacing.

In future work, the effect of horizontal non-local effects may be explored to further understand the final stage of implementation. The new PBL scheme will be tested on real cases of extreme weather events to evaluate its performance against SCADA data. The new PBL scheme may be extended to include the Fitch et al. wind farm parameterization for wind power forecasting applications. Furthermore, the partitioning functions may be extended to include terrain effects using site-tuned LES/DNS simulations.

Acknowledgments

This work has received funding from the Flemish Government through the Agency for Innovation and Entrepreneurship (Vlaams Agentschap Innoveren en Ondernemen, VLAIO) through the cSBO project SeaFD in the context of the MaDurOS program for Material Durability for Off-Shore of the cluster on Strategic Initiative for Materials in Flanders (SIM).

References

[1] P. Bauer, A. Thorpe, G. Brunet, The quiet revolution of numerical weather prediction, Nature 525 (7567) (2015) 47–55.

[2] J. C. Wyngaard, Toward numerical modeling in the "terra incognita", Journal of the atmospheric sciences 61 (14) (2004) 1816–1826.

[3] R. Honnert, V. Masson, F. Couvreux, A diagnostic for evaluating the representation of turbulence in atmospheric models at the kilometric scale, Journal of the Atmospheric Sciences 68 (12) (2011) 3112–3131.

[4] T. W. Juliano, B. Kosović, P. A. Jiménez, M. Eghdami, S. E. Haupt, A. Martilli, "gray zone" simulations using a three-dimensional planetary boundary layer parameterization in the weather research and forecasting model, Monthly Weather Review 150 (7) (2022) 1585–1619.

[5] A. Brown, A. Grant, Non-local mixing of momentum in the convective boundary layer, Boundary-Layer Meteorology 84 (1997) 1–22.

[6] H. H. Shin, S.-Y. Hong, Analysis of resolved and parameterized vertical transports in convective boundary layers at gray-zone resolutions, Journal of the Atmospheric Sciences 70 (10) (2013) 3248–3261.

[7] J. Ito, H. Niino, M. Nakanishi, C.-H. Moeng, An extension of the mellor–yamada model to the terra incognita zone for dry convective mixed layers in the free convection regime, Boundary-layer meteorology 157 (2015) 23–43.

[8] X. Zhang, J.-W. Bao, B. Chen, E. D. Grell, A three-dimensional scale-adaptive turbulent kinetic energy scheme in the wrf-arw model, Monthly Weather Review 146 (7) (2018) 2023–2045.

[9] C. B. Senel, O. Temel, D. Muñoz-Esparza, A. Parente, J. van Beeck, Gray zone partitioning functions and parameterization of turbulence fluxes in the convective atmospheric boundary layer, Journal of Geophysical Research: Atmospheres 125 (22) (2020) e2020JD033581.

[10] D. K. Lilly, On the application of eddy viscosity concept in the inertial sub-range of turbulence, NCAR manuscript 123.

[11] J. W. Deardorff, Stratocumulus-capped mixed layers derived from a three-dimensional model, Boundary-layer meteorology 18 (1980) 495–527.

[12] C.-H. Moeng, A large-eddy-simulation model for the study of planetary boundary-layer turbulence, Journal of the Atmospheric Sciences 41 (13) (1984) 2052–2062.

[13] M. Nakanishi, H. Niino, Development of an improved turbulence closure model for the atmospheric boundary layer, Journal of the Meteorological Society of Japan. Ser. II 87 (5) (2009) 895–912.
[14] W. C. Skamarock, J. B. Klemp, J. Dudhia, D. O. Gill, Z. Liu, J. Berner, W. Wang, J. G. Powers, M. G. Duda, D. M. Barker, et al., A description of the advanced research wrf model version 4, National Center for Atmospheric Research: Boulder, CO, USA 145 (145) (2019) 550.
[15] I. Troen, L. Mahrt, A simple model of the atmospheric boundary layer; sensitivity to surface evaporation, Boundary-Layer Meteorology 37 (1-2) (1986) 129–148.
[16] Y. Noh, W. Cheon, S. Hong, S. Raasch, Improvement of the k-profile model for the planetary boundary layer based on large eddy simulation data, Boundary-layer meteorology 107 (2003) 401–427.
[17] I. Boutle, J. Eyre, A. Lock, Seamless stratocumulus simulation across the turbulent gray zone, Monthly Weather Review 142 (4) (2014) 1655–1668.
[18] H. H. Shin, S.-Y. Hong, Representation of the subgrid-scale turbulent transport in convective boundary layers at gray-zone resolutions, Monthly Weather Review 143 (1) (2015) 250–271.

Improving wind energy forecasting through high-resolution weather models combined with wind farm parametrization and statistical post-processing methods

Alexandros Palatos-Plexidas

Environmental and Applied Fluid Dynamics Department, von Karman Institute for Fluid Dynamics, Belgium, alexandros.palatos-plexidas@vki.ac.be

Supervisors: Dr. Wim Munters, Dr. Sophia Buckingham, Prof. Jeroen van Beeck.

Environmental and Applied Fluid Dynamics Department, von Karman Institute for Fluid Dynamics, Belgium, wim.munters@vki.ac.be

University Supervisor: Lesley De Cruz

Assistant Professor, Department of Electronics and Informatics, Vrije Universiteit Brussel, Belgium, lesley.de.cruz@vub.be

Abstract

Wind energy is an important aspect in moving towards a clean and sustainable energy system and has a significant impact on climate change mitigation. This PhD topic is in the framework of the project BeFORECAST, on wake-effect included offshore wind power forecasting. The purpose is to improve weather models, focusing on the operation of offshore wind farms.

In this study, we focus on advanced Numerical Weather Prediction model (NWP) set-ups and statistical post-processing of power production with operational SCADA data to improve weather forecasting for offshore wind farms. More precisely, we will use the Weather Research and Forecasting model (WRF), an open-source mesoscale model, used both for research and operational forecasting. One major objective is the investigation and improvement of the existing Wind Farm Parametrization (WFP) methods that can be implemented in WRF. Although, WFP methods have been developed in NWP, they are not sufficient for modelling power at the turbine level. The purpose is to implement WFP models able to capture the relations between individual wind turbines within a wind farm and simulate the overall behaviour of the farm. Additionally, even though wind farm measurement data is mostly used for validation purposes we aim to leverage these data on enhancing modelling frameworks (e.g. in data assimilation or statistical post-processing).

Numerical weather forecasts, due to the complex interactions between multiple error sources, often display systematic biases that are hard to avoid. Statistical post-processing methods aim to correct these errors, increasing the reliability of the weather forecasts. Therefore, in this study, we propose to compare different statistical post-processing techniques, focusing both on conventional techniques like Ensemble Model Output Statistics (EMOS) and on machine learning (ML) methods like Neural Networks (NN) for the improvement of the predictions. Furthermore, we aim to investigate advanced tools to incorporate both the measurement data, along with more detailed spatial weather conditions from WRF within the post-processing framework.

Keywords: numerical weather prediction, wind energy, wind farm parametrization, statistical post-processing.

Reinforced (model) based control of wind turbines and wind farms

Lorenzo Schena

Environmental and Applied Department, von Karman Institute for Fluid Dynamics, Belgium, lorenzo.schena@vki.ac.be

Supervisor(s): W. Munters, M. A. Mendez

Research engineer, Associate professor, Environmental and Applied department, von Karman Institute for Fluid Dynamics, Belgium
wim.munters@vki.ac.be, miguel.alfonso.mendez@vki.ac.be

University Supervisor: J. Helsen

Professor, Vrije Universiteit Brussel, Department of Mechanical Engineering, Brussels, Belgium

Abstract

The unsteadiness of the atmospheric boundary layer accounts for more than 65% of flap-wise fatigue loads met by wind turbines [1]. This produces turbulent variation, which varies significantly with weather conditions at time scales of the order of minutes, particularly severe in wind farms due to the superposition of wakes generated by neighbourhood turbines. Moreover, the concern about the mechanical loads grows with the size of the turbine's rotor, as the associated blade slenderness exacerbates aeroelastic responses. To keep wind energy viable, control strategies must handle the variability in the incoming wind, seek optimal power extraction while minimising the loads, meet the machines' life expectation standards, and limit the need for maintenance [2]. This thesis is collocated in this active field of research, seeking to contribute by proposing a combination of model-predictive and model-free strategies for wind energy control [3; 4]. We name such a novel blend *reinforced (model) predictive control* (RPC), which consists of joint training of a controller and a surrogate model of the plant. This RPC is then deployed in three test cases, of growing complexity. This deployment phase consists of both numerical, via a multi-fidelity, multi-physics simulation, and experimental investigations, to be carried out in the L1 wind tunnel at the von Karman Institute (VKI). At first, its performances are compared against state-of-the-art control techniques on a single wind turbine, focusing on the impact of unexpected weather events such as gusts of lulls. The wake-rotor interaction is the core of the second test case, in which the effects of wakes generated by neighbour turbines on energy harvesting and load mitigation are investigated. Finally, the wind-farm flow control is tackled. Therein, the results from the previous assessments are scaled-up, implementing multi-scale control which takes into account the objectives of both the single wind turbine and the full wind farm as a whole. The outcomes of these studies will be a series of controllers fully operative and usable in controlled environments - such as a wind tunnel - serving as a backbone for further research, pointing to the direction of real-world complexity deployment.

Keywords: wind engineering, control systems, reinforcement learning, wind farms

Acknowledgments

This PhD project is supported by Fonds Wetenschappelijk Onderzoek (FWO), Project No. 1S67923N.

References

[1] Fluctuations of angle of attack and lift coefficient and the resultant fatigue loads for a large Horizontal Axis Wind turbine.

[2] Wind farm flow control: prospects and challenges.

[3] J. Freeman, M. Balas, An investigation of variable speed horizontal-axis wind turbines using direct model-reference adaptive control. doi:10.2514/6.1999-28.

[4] M. Soliman, O. P. Malik, D. T. Westwick, Multiple model multiple-input multiple-output predictive control for variable speed variable pitch wind energy conversion systems, Iet Renewable Power Generation 5 (2011) 124–136.

LIQUID METALS AND INDUSTRIAL FLOWS

Data-driven augmentation of a second order heat flux model to extend it to heavy liquid metals

Matilde Fiore

Environmental and Applied Fluid Dynamics Department, von Karman Institute for Fluid Dynamics, Belgium, matilde.fiore@vki.ac.be

Supervisor: Lilla Koloszar

Research Engineer, Environmental and Applied Fluid Dynamics Department, von Karman Institute for Fluid Dynamics, Belgium, lilla.koloszar@vki.ac.be

Supervisor: Miguel Alfonso Mendez

Assistant Professor, Environmental and Applied Fluid Dynamics Department, von Karman Institute for Fluid Dynamics, Belgium, miguel.alfonso.mendez@vki.ac.be

University Supervisor: Yann Bartosiewicz

Professor, Mechanical Engineering Department, Universite catholique de Louvain UCL, Belgium, yann.bartosiewicz@uclouvain.be

Abstract

The thermal-hydraulic design of new generation liquid metal cooled reactors requires advanced numerical models supplemented by accurate Reynolds Averaged Navier-Stokes (RANS) closures. Due to their low Prandtl numbers, heavy liquid metals deserve a specific thermal turbulence modelling that should overcome traditional assumptions of similarity and isotropy. The most detailed approach to model the thermal turbulence dynamics is given by second order closures for the heat flux, including all the mechanisms of generation/destruction, redistribution and transport. The present work seeks to augment a Differential Transport Heat Flux Model (DTHFM) to extend its applicability to low Prandtl number fluids. The choice of the most convenient parametrization of the correction is guided by physical considerations and a sensitivity analysis. The model augmentation is data-driven: a complete Python framework combining inference and regression steps is developed and employed to improve the agreement with the available high-fidelity data. Preliminary results obtained for canonical flow conditions (non-isothermal turbulent channel flow) are promising. The extension of the presented approach to complex flow configurations would increase the generality of the augmentation and allow its application to nuclear engineering flows.

Keywords:

1. Introduction

Liquid metal heat transfer is of primary interest in many engineering applications and flows of academic interest. One of them is their application as coolants in Liquid Metal Fast Reactors (LMFR), whose thermal-hydraulic conditions require a careful analysis for economic and safety reasons. The numerical modelling is a key tool during the design and testing phases, due to the metal opaqueness and chemical aggressiveness and the harsh thermal conditions achieved in the nuclear reactor vessels. However, current thermal turbulence modelling should advance to get reliable predictions for these kind of flows, since the low Prandtl numbers of liquid metals make the similarity between momentum and thermal field less justified. Hence, traditional modelling concepts, as the Reynolds's analogy [1] are not recommended to accurately simulate these flows, as shown in a number of available works on this topic [2; 3; 4]. Several thermal models were recently developed to improve the modelling of the heat flux in the low Prandtl number range [5; 6; 7] and to provide a complete vector representation that over-

comes the alignment with the mean temperature gradient. The models either introduce additional terms to the constitutive relationship of the heat flux [5] or modify the expression of the eddy diffusivity [6; 7] by introducing thermal or mixed time-scales rather than dynamic ones.
In recent years, the modelling and calibration of alternative turbulent closures is aided by Machine Learning techniques that are able to extract knowledge from big data using structured methods. In particular, Artificial Neural Networks (ANNs) earned increasing popularity in the field of turbulence modelling, Thanks to their ability of solving high-dimensional and highly non-linear regression problems, ANNs help to find complex input-output mappings, and in the context of low Prandtl number turbulence they were used to generate a data-driven algebraic closure for the turbulent heat flux [8; 9] that is realizable and rotationally invariant.
On the other hand, despite the power of the regression method used, the algebraic modelling of the turbulent heat flux in the low Prandtl number range is arduous, since the lack of similarity limits the local correlation between the statistics and promotes strong non-linearities. The differential modelling of the heat flux is then needed to overcome the single point approach by introducing historical and non-local effects. The literature provides some examples of second order closure models for the heat flux [10; 11; 12] that have been validated for a limited range of Prandtl numbers and flow configurations. Modelling/calibrating this kind of closures is very challenging as a natural consequence of the differential framework. Indeed, the system of transport equations must be integrated each time a sample model is tested, and conditioning/stability issues pose hard constraints and limit the error tolerance when the fitting is made at the level of the transport terms. According to the peculiar range of the differential equations, these modelling problems are often ill-posed, i.e. multiple solutions are possible. The modeller usually needs to specify additional penalties or constraints to obtain physically consistent solutions.
In this work, we present the development of a data-driven augmentation to extend a Differential Transport Heat Flux Model (DTHFM) to low Prandtl numbers. The parametrization of the augmentation, its field inversion and regression are carried out employing data analysis and machine learning techniques. For the sake of simplicity, the flow conditions are restricted to non-isothermal turbulent channel flow at various Reynolds and Prandtl numbers, for which DNS reference data are available [13; 14].
The paper is organised as follows. Section 2 presents the original DTHFM and its physical/mathematical limitations at low Prandtl numbers. Section 3 introduces the final parametrization of the augmentation based on a global sensitivity analysis. The model correction is inferred in Section 4 and then modelled in Section 5. Finally, conclusions and outlooks are provided in the last section.

2. Original thermal turbulence model

The development of the DTHFM starts from a baseline formulation developed by Dehoux et al. [12] which is based on the elliptic blending concept. The model relies on the definition of a blending function α_θ that accounts for the effects of wall-blockage on the turbulent statistics. In particular, α_θ is the solution of an elliptic blending relaxation equation:

$$\alpha_\theta - L_\theta^2 \nabla^2 \alpha_\theta = 1 \tag{1}$$

in which $\alpha_\theta = 0$ at the wall and L_θ is a turbulent lengthscale given by:

$$L_\theta = C_L \max\left(\frac{k^{3/2}}{\epsilon}, C_\eta \frac{\nu^{3/4}}{\epsilon^{1/4}}\right). \tag{2}$$

where C_η,C_L are model constants and we refer the reader to the nomenclature for the definition of the other symbols. The turbulent heat flux is computed by solving the following transport equation (steady-state conditions):

$$U_j \frac{\partial \overline{u_i \theta}}{\partial x_j} = P_{i\theta} + D_{i\theta} + T_{i\theta} + \Phi_{i\theta} - \epsilon_{i\theta} \tag{3}$$

where $P_{i\theta}$ is the heat flux production term $P_{i\theta} = -\overline{u_i u_j}\frac{\partial T}{\partial x_j} - \overline{u_j \theta}\frac{\partial U_i}{\partial x_j}$ and the molecular diffusion $D_{i\theta}$, turbulent diffusion $T_{i\theta}$, redistribution $\Phi_{i\theta}$ and dissipation $\epsilon_{i\theta}$ are unclosed budget terms that are modelled as indicated in [12]. The elliptic blending parameter α_θ is used to join the correct behaviour of $\Phi_{i\theta}$ and $\epsilon_{i\theta}$ in the near-wall and quasi homogeneous region, to account for the wall-blockage effects [12]:

$$\Phi_{i\theta} = (1 - \alpha_\theta)\Phi_{i\theta}^w + \alpha_\theta \Phi_{i\theta}^h \tag{4}$$

$$\epsilon_{i\theta} = (1 - \alpha_\theta)\epsilon_{i\theta}^w + \alpha_\theta \epsilon_{i\theta}^h \tag{5}$$

The differential model given by eq. (1) and (3) was validated for near unity Prandtl numbers and under condition of forced and natural convection. Its extension to low Prandtl numbers requires to modify

the current formulation. In particular, the following physical/mathematical limitations are identified in the baseline structure of the DTHFM:

- The redistribution and the dissipation terms do not match the DNS ones at low Prandtl numbers. As shown in Figure 1, the redistribution term is largely overestimated by the DTHFM, while the dissipation term is severely underestimated at y^+ higher than 10. In addition, the correct near wall behaviour of the dissipation and molecular diffusion terms is not reproduced.

- The elliptic equation (eq. (1)) to compute the blending parameter α_θ involves the definition of a thermal length scale that is computed based on eq. (2) as a function of momentum statistics only. This is in contrast with what seen from direct numerical simulations, where at low Prandtl numbers the thermal characteristic length scales become significantly larger than the momentum ones.

- The blending parameter α_θ controls the transition between the near-wall and the homogeneous behaviour of thermal turbulence. This transition is expected to be slower at low Prandtl numbers, due to the expansion of the thermal diffusion sublayer. However, if the length scale given by eq.(2) is increased by a constant factor to represent the enlargement of the thermal structures, the agreement in terms of wall-normal heat flux improves, though the error in the streamwise component increases due to the reduction of the corresponding redistribution and dissipation terms. This behaviour is indicated in Figure 2a and suggests that an anisotropic blending, similar to the one introduced by Durbin [15] for the momentum turbulence, is necessary to improve the agreement of both the components at the same time.

3. Parametrization of the correction with global sensitivity analysis

The considerations presented in the previous section lead to a modified mathematical formulation aimed at improving the model predictions at low Prandtl numbers with the aid of four correction scalar parameters named $\beta_{\alpha,x}, \beta_{\alpha,y}, \beta_\phi, \beta_\epsilon$:

$$\mathbf{U}\cdot\frac{\partial\overline{\mathbf{u}\theta}}{\partial x_j} = \mathbf{P}_\theta + \mathbf{D}_\theta + \mathbf{T}_\theta + (\mathbf{1}-\boldsymbol{\alpha}_\theta)\cdot\Big(\beta_\phi\boldsymbol{\Phi}_{w,\theta} - \beta_\epsilon\boldsymbol{\epsilon}_{w,\theta} + \boldsymbol{\alpha}_\theta\cdot\Big(\beta_\phi\boldsymbol{\Phi}_{h,\theta} - \beta_\epsilon\boldsymbol{\epsilon}_{h,\theta}\Big), \tag{6}$$

where matrix $\boldsymbol{\alpha}_\theta$ is a diagonal matrix of anisotropic blending:

$$\boldsymbol{\alpha}_\theta = [\alpha_{x,\theta}, \alpha_{y,\theta}], \tag{7}$$

with

$$\alpha_{i,\theta} - \beta_{\alpha,i} L_\theta^2 \nabla^2 \alpha_{i,\theta} = 1. \tag{8}$$

Inferring and modelling four parameters is an inverse problem of high complexity that is not adequately supported by the small dataset under consideration. The correction parameters are then reduced to two with the aid of a global sensitivity analysis. This approach is aimed at minimising the amount of correction, reducing the inference and modelling efforts and not altering the structure of the original model in the conditions where its predictions are satisfactory.

For such purpose, the unclosed parameters indicated in eq. (8) and (6) ($\beta_{\alpha,x}$, $\beta_{\alpha,y}$, β_ϕ,β_ϵ) are assumed to be uniform random variables in the interval $[0.2, 2.0]$. The sensitivity of the DTHFM to the correction parameters is computed by monitoring the error of the heat flux predictions with respect to the DNS ones:

$$\mathcal{J}_{sens} = \sum_i^N (\hat{\mathbf{q}} - \mathbf{q}(\boldsymbol{\beta}))^2 \tag{9}$$

where $\hat{\mathbf{q}}$ indicates the DNS heat flux, $\mathbf{q}(\boldsymbol{\beta})$ are the heat flux predictions and N is the number of reference points. The flow conditions considered for this analysis are $Re_\tau = 640$ and $Pr = 0.025$. The sensitivity is estimated by computing the Sobol indices, whose definition is reported in detail in ref.[16]. The indices are calculated with a surrogate of the original DTHFM that is based on a Polynomial Chaos Expansion (PCE) series [16]. The details of the PCE construction and training will be provided in an extended version of this article. Figure 2b shows the convergence of the heat flux error mean, variance and of the Sobol sensitivity indices with the number of model evaluations. Figure 3 depicts the first and total Sobol indices as a function of y^+. The parameters β_ϕ and β_ϵ control the most part of the heat flux error variance. In particular, the parameter β_ϵ is the most important in the viscous sublayer, where the dissipation mechanism $\boldsymbol{\epsilon}_\theta$

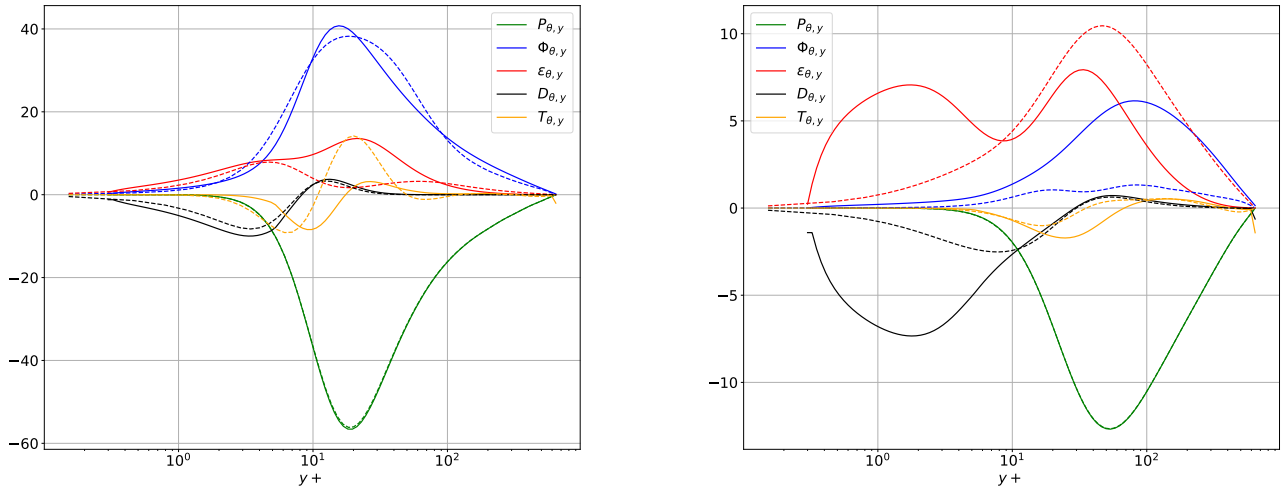

(a) $Pr = 0.71$ (b) $Pr = 0.025$

Figure 1: DNS and modelled budget terms obtained with the DTHFM at equilibrium for $Re_\tau = 640$ and $Pr = 0.71$ (left) and 0.025 (right). DNS data are indicated with dashed lines, the results of the model with solid lines.

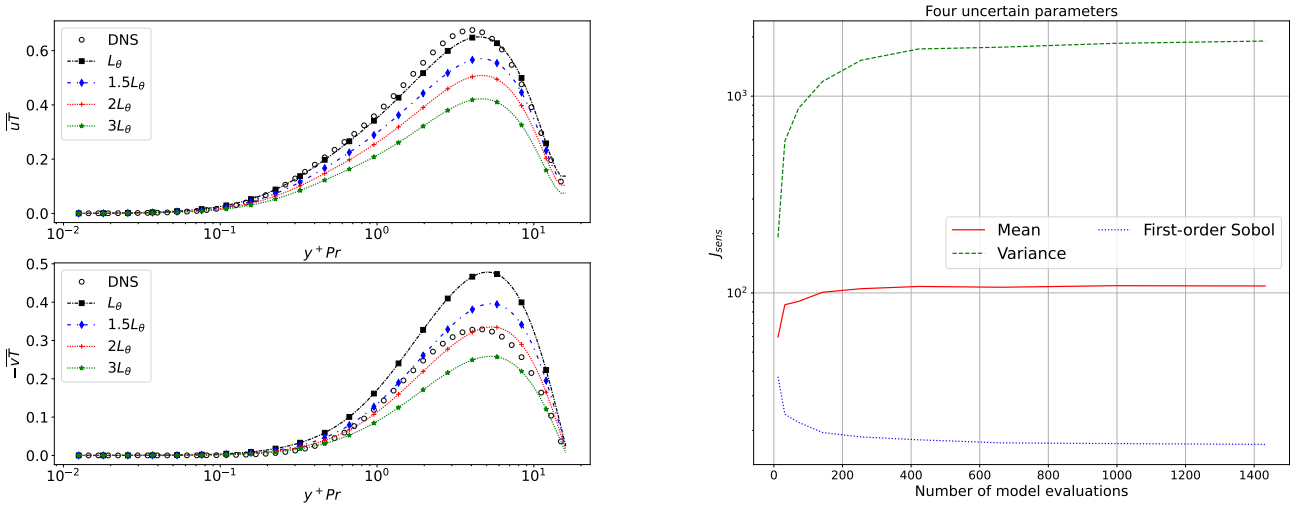

(a) (b)

Figure 2: Left: streamwise and wall-normal heat flux predictions obtained by increasing the thermal length scale (eq.(2)) by a constant factor. Right: convergence of the heat flux error mean, variance and Sobol indices with the number of model evaluations.

balances the molecular diffusion term $\mathbf{D}_\theta$. The parameter β_ϕ controls the variability of the heat flux error in the buffer, logarithmic and homogeneous region of the channel, where the redistribution mechanism $\mathbf{\Phi}_\theta$ is significant (see Figure 1). The output of the DTHFM is not much sensitive to the parameters $\beta_{\alpha,i}$. From a mathematical point of view, this seems a consequence of the closed range of the elliptic equation (8), whose solutions are bounded between 0 and 1. The effect of these parameters is a little more significant in the logarithmic region, though their sensitivity coefficients are significantly lower than the ones of β_ϕ and β_ϵ.
Based on the results of the sensitivity analysis, the most convenient parametrization used hereafter involves the correction factors β_ϕ and β_ϵ only, leading to a simplified version of eq.(6):

$$U_j \frac{\partial \overline{u_i \theta}}{\partial x_j} = P_{i\theta} + D_{i\theta} + T_{i\theta} + \beta_\phi \Phi_{i\theta} - \beta_\epsilon \epsilon_{i\theta}. \quad (10)$$

The following subsections deal with the inference and modelling of these unclosed parameters to improve the model performance in the low Prandtl number range.

4. Resolution of the inverse problem

4.1. Tikhonov regularization

The first approach applied to infer the correction coefficients is based on the Tikhonov regularization. The numerical discretization of eq.(10) in which the DNS heat flux replaces $\overline{\mathbf{u}\theta}$ allows to compute the desired values of β_ϕ and β_ϵ at each mesh point as the solution of the following linear system:

$$\mathbf{A}(\mathbf{q})\hat{\boldsymbol{\beta}} = \mathbf{b}(\mathbf{q}), \quad (11)$$

where $\hat{\boldsymbol{\beta}} = \boldsymbol{\beta} - 1$ and $\boldsymbol{\beta} = [\beta_\phi, \beta_\epsilon]$. However, the analysis of the system (11) reveals that the matrix $\mathbf{A}(\mathbf{q})$ is singular at the mesh points where the values of the redistribution and dissipation terms are negligible. This means that the inverse problem (11) must be solved in a least square sense:

$$\min_{\hat{\boldsymbol{\beta}}} \frac{1}{2}||\mathbf{A}\hat{\boldsymbol{\beta}} - \mathbf{b}||_2^2 + \frac{\lambda}{2}||\hat{\boldsymbol{\beta}}||_2^2 \quad (12)$$

The regularized least squares problem is solved for several values of λ and the results for $Re_\tau = 640$, $Pr = 0.025$ are indicated in Figure 4. For small values of λ, the profiles are non-smooth with large peaks located at the singularity points, where the redistribution and dissipation terms are close to zero. Note that the negative values of β_ϵ achieved for $10 < y^+ < 30$ imply a change of sign of the dissipation term that is not consistent with the physics. The inferred values of $\boldsymbol{\beta}$ can be used to write the linear system for $\mathbf{q}$ that is the counterpart of eq.(11):

$$\mathbf{B}(\boldsymbol{\beta})\mathbf{q} = \mathbf{c}(\boldsymbol{\beta}) \quad (13)$$

When the balance is modified with the values of $\boldsymbol{\beta}$ obtained with low λ, the system (13) is badly conditioned and unstable and the solution $\mathbf{q}$ not convergent. When the values of $\boldsymbol{\beta}$ corresponding to $\lambda = 1$ or higher are applied, convergent solutions of system (13) are found, though the computed $\mathbf{q}$ components do not improve the agreement with the reference data compared to the baseline formulation. Hence, the conditioning of the system (13) is too critical for this approach, and a more sophisticated method is needed to retrieve the values of the correction factors at each point of the mesh. The method should i) enforce the positiveness of the correction factors, ii) account for the conditioning of the system (13) in the neighborhood of the optimal solutions.

4.2. Gradient based adjoint optimization

4.2.1. Gradient-based adjoint optimization

The correction factors β_ϕ and β_ϵ need to be inferred for the available test flows to improve the model predictions in terms of $\mathbf{q}$. This requires to solve a constrained optimization problem:

$$\boldsymbol{\beta}_{opt} = argmin(\mathcal{J}) \quad (14)$$

$$\mathcal{R}(\mathbf{q}(\beta), \beta) = 0 \quad (15)$$

where $\mathcal{J}$ is the cost function employed for the optimization, while eq.(5) enforces the residual of the heat flux transport equation (eq.(13)) to be zero[1]. In the present work, the cost function $\mathcal{J}$ is defined as:

$$\mathcal{J} = \frac{1}{2}(\hat{\mathbf{q}} - \mathbf{q}(\boldsymbol{\beta}))^T \mathbf{C}_m^{-1} (\hat{\mathbf{q}} - \mathbf{q}(\boldsymbol{\beta})) + (\mathbf{D}_2\boldsymbol{\beta})^T \mathbf{C}_\beta^{-1} (\mathbf{D}_2\boldsymbol{\beta}) \quad (16)$$

where $\mathbf{D}_2$ is the second order finite difference matrix computed as indicated in [17]. The first term on the right hand side of eq.(16) represents the mean squared error of the modelled heat flux $\mathbf{q}(\boldsymbol{\beta})$ with respect to the reference one provided by the high-fidelity data ($\hat{\mathbf{q}}$). The second is a regularization term that promotes the

[1] Note that, in order to enforce the positiveness of the inferred β profiles, the inverse problem is solved in practice for $\boldsymbol{\gamma} = \ln \boldsymbol{\beta}$ rather than for $\boldsymbol{\beta}$.

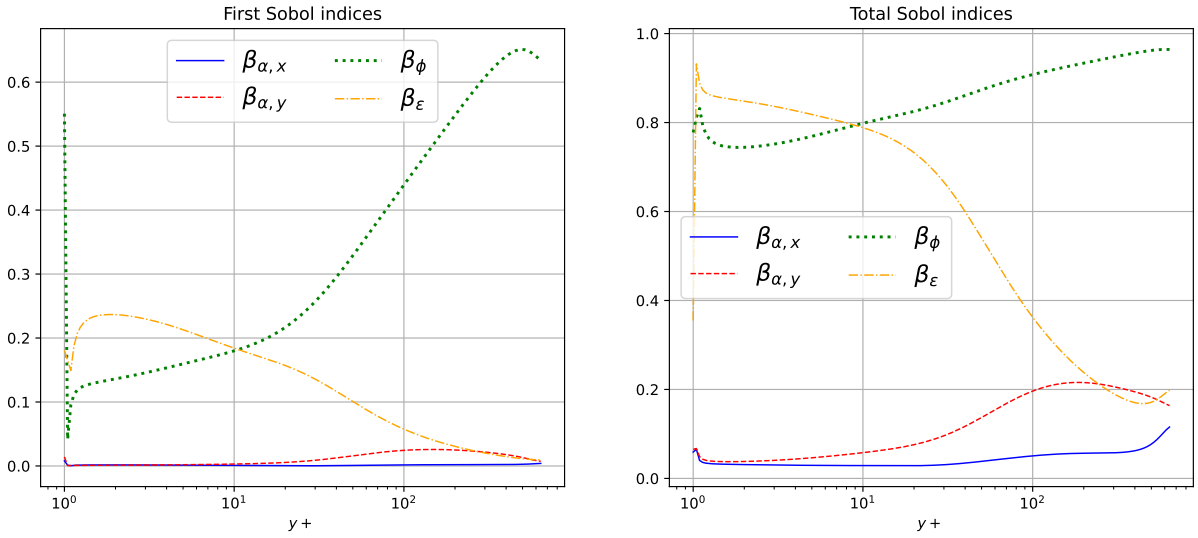

Figure 3: Sensitivity of the heat flux error (eq.(9)) to the correction parameters introduced by eq.(6) and (8) as a function of y^+ ($Re_\tau = 640$, $Pr = 0.025$).

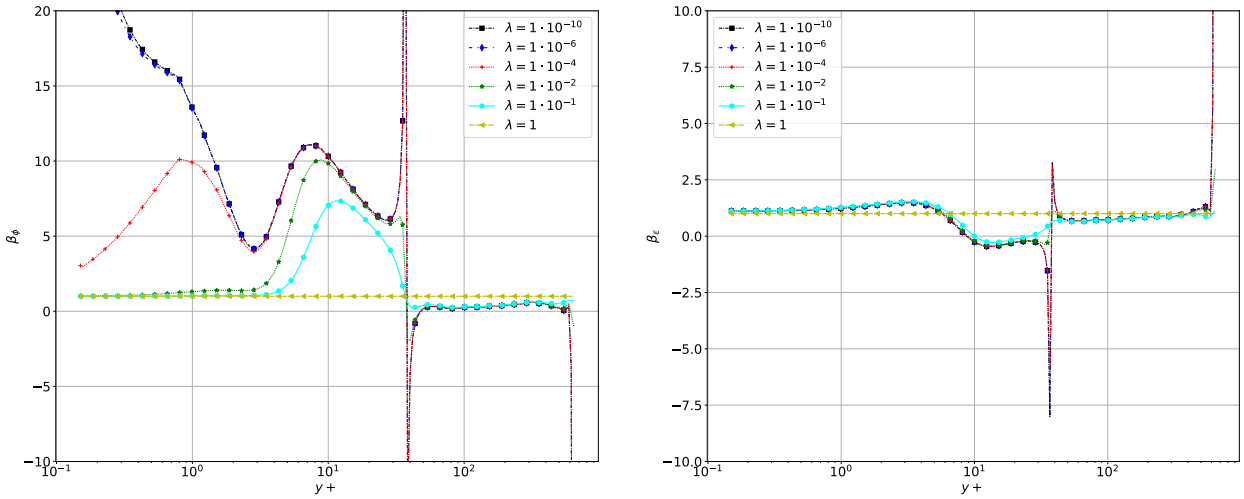

(a) β_ϕ (b) β_ϵ

Figure 4: Distributions of the correction factors over the channel width ($Re_\tau = 640$, $Pr = 0.025$) obtained by solving the least squares problem (eq.(12)) with several values of λ.

smoothness of the inferred correction fields. The covariance matrices $\mathbf{C}_m$ and $\mathbf{C}_\beta$ are defined as $\mathbf{C}_m = \sigma_m^2\mathbf{I}$ and $\mathbf{C}_\beta = \sigma_\beta^2\mathbf{I}$.
The dimensionality of this inverse problem increases with the number of mesh points. Hence, the adjoint method was applied to compute the gradient in order to reduce the computational efforts. Based on this method, the gradient is calculated as:

$$\frac{d\mathcal{J}}{d\boldsymbol{\beta}} = \frac{\partial\mathcal{J}}{\partial\boldsymbol{\beta}} + \psi^T\frac{\partial\mathcal{R}}{\partial\boldsymbol{\beta}} \tag{17}$$

with

$$\left(\frac{\partial\mathcal{R}}{\partial\mathbf{q}}\right)^T\psi = -\left(\frac{\partial\mathcal{J}}{\partial\mathbf{q}}\right)^T. \tag{18}$$

A formal proof of the definitions (17) and (18) is here omitted for brevity. Note that this method avoids the direct evaluation of the sensitivity matrix $\frac{d\mathbf{q}}{d\boldsymbol{\beta}}$ which requires the integration of the system of PDEs for each value of $\boldsymbol{\beta}$. The partial derivatives $\frac{\partial\mathcal{R}}{\partial\mathbf{q}}$ and $\frac{\partial\mathcal{R}}{\partial\boldsymbol{\beta}}$ are computed analytically with a Python library of symbolic calculus (Sympy), after having dicretized all the spatial derivatives of the operating variables ($\boldsymbol{\beta}$ and $\mathbf{q}$) with finite differences. The constrained optimization problem was solved by applying the Conjugate Gradient method (CG).
The uncertainty of the inferred $\boldsymbol{\beta}$ values is estimated by applying the Bayesian rule for conditional probability:

$$p(\boldsymbol{\beta}|\hat{\mathbf{q}}) \propto p(\hat{\mathbf{q}}|\boldsymbol{\beta})\cdot p(\boldsymbol{\beta}) \tag{19}$$

where the likelihood $p(\hat{\mathbf{q}}|\boldsymbol{\beta})$ is assumed to follow a multivariate Gaussian distribution of precision matrix $\mathbf{C}_m$. We assume that the prior distribution $p(\boldsymbol{\beta})$ is also Gaussian, $\boldsymbol{\beta} \sim \mathcal{N}\left(0, \mathbf{C}_\beta\right)$. It can be proved that, for the properties valid for the product of multivariate Gaussian distributions [18], the convariance matrix of the posterior will be given by:

$$\mathbf{C}_{\beta,opt} = \left[\mathbf{C}_\beta^{-1} + \left(\frac{\partial\mathbf{q}}{\partial\beta}\right)^T\mathbf{C}_m^{-1}\frac{\partial\mathbf{q}}{\partial\beta}\right]^{-1}. \tag{20}$$

in which $\frac{\partial\mathbf{q}}{\partial\beta}$ is calculated as:

$$\frac{\partial\mathbf{q}}{\partial\beta} = \left(\frac{\partial\mathcal{R}}{\partial\mathbf{q}}\right)^{-1}\cdot\frac{\partial\mathcal{R}}{\partial\beta} \tag{21}$$

The posterior covariance matrix is then decomposed with Cholesky:

$$\mathbf{R}\mathbf{R}^T = \mathbf{C}_{\beta,opt} \tag{22}$$

and the resulting factorization is used to sample the solution from the approximate posterior distribution to compute the uncertainty ranges:

$$\boldsymbol{\beta} = \boldsymbol{\beta}_{opt} + \mathbf{R}\mathbf{z} \tag{23}$$

where $\mathbf{z}$ is a vector of standard normal variables.

4.2.2. Results of the field inversion

Figure 5 shows the profiles of β_ϕ and β_ϵ obtained over the channel width with two choices of the a priori value of σ_β. Note that the choice of σ_β significantly affects the shape of the profiles. With large values of σ_β, the influence of the regularization term is negligible and β_ϕ and β_ϵ profiles do not exibit a clear trend for the different test flows. When σ_β is smaller, a clear trend is instead visible. This is beneficial for the successive use of the inferred data as reference to train a regression model. The amount of the correction increases with the decrease of the Prandtl and Reynolds numbers. With $\sigma_\beta = 1\cdot10^{-3}$, no corrections are inferred for the near unity Prandtl number cases at $Re_\tau = 395$ and 640.
Figure 6 shows the uncertainty ranges of β_ϕ and β_ϵ obtained with $\sigma_\beta = 1\cdot10^{-2}$ after sampling from the approximate posterior distribution (100 samples). The uncertainty is maximum in the near wall region, where the production term is nil and the values assumed by β_ϕ and β_ϵ have a negligible influence on the computed heat flux profiles. The uncertainty decreases at $y^+Pr > 1.0$ till reaching the centerline of the channel, where the uncertainty grows again due to the vanishing of the redistribution and dissipation terms.

5. Regression model

After the field inversion, a model for the scalar quantities β_ϕ and β_ϵ must be derived based on the inferred fields and their uncertainty ranges. These submodels for β_i should be general functionals of the turbulent and mean flow statistics:

$$\beta_i = \mathcal{F}_i(\mathbf{b}, \mathbf{S}, \boldsymbol{\Omega}, \overline{u\theta}, \nabla T, k, \epsilon, k_\theta, \epsilon_\theta, \kappa, \nu, \alpha_\theta) \tag{24}$$

where

$$b_{ij} = \frac{\overline{u_iu_j}}{k} - \frac{2}{3}\delta_{ij}, S_{ij} = \frac{1}{2}\left(\frac{\partial U_i}{\partial x_j} + \frac{\partial U_j}{\partial x_i}\right), \quad \Omega_{ij} = \frac{1}{2}\left(\frac{\partial U_i}{\partial x_j} - \frac{\partial U_j}{\partial x_i}\right). \tag{25}$$

and the reader is referred to the nomenclature for the definition of the remaining statistics. Eq. (**??**)

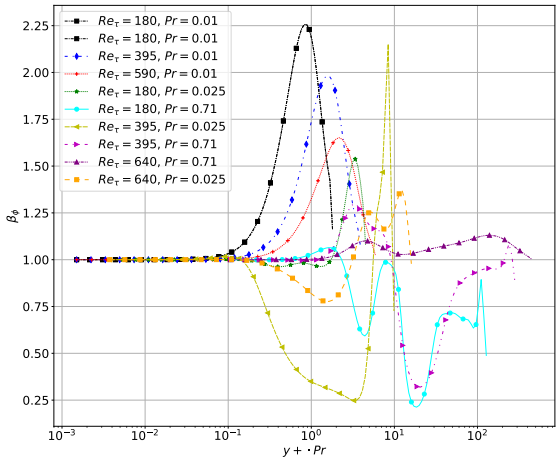

(a) β_ϕ, $\sigma_\beta = 1.0$

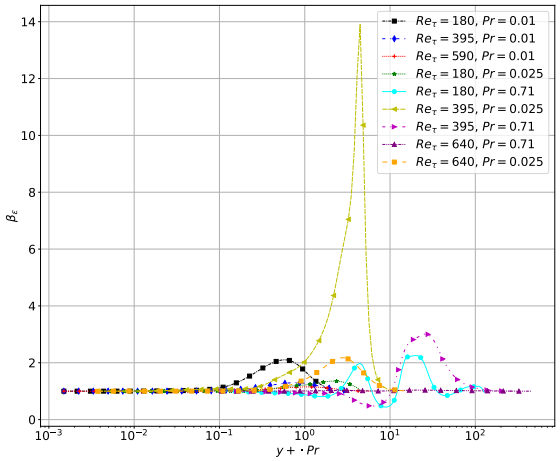

(b) β_ϵ, $\sigma_\beta = 1.0$

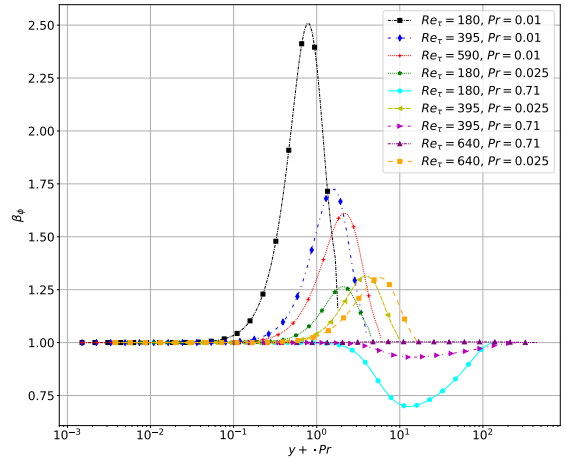

(c) β_ϕ, $\sigma_\beta = 0.01$

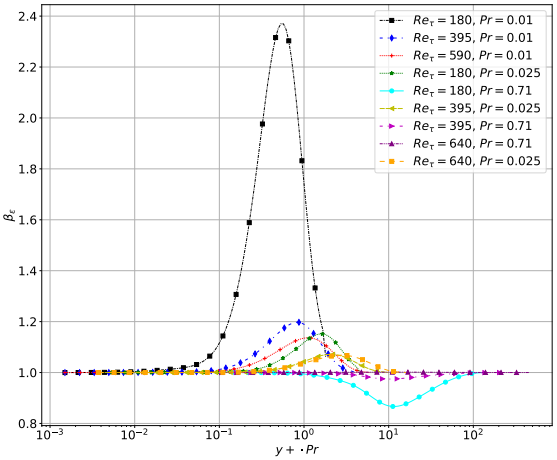

(d) β_ϵ, $\sigma_\beta = 0.01$

Figure 5: Distributions of the correction factors β_ϕ and β_ϵ over the channel width obtained by solving the inverse problem with several choices of σ_β and at different Re_τ and Pr.

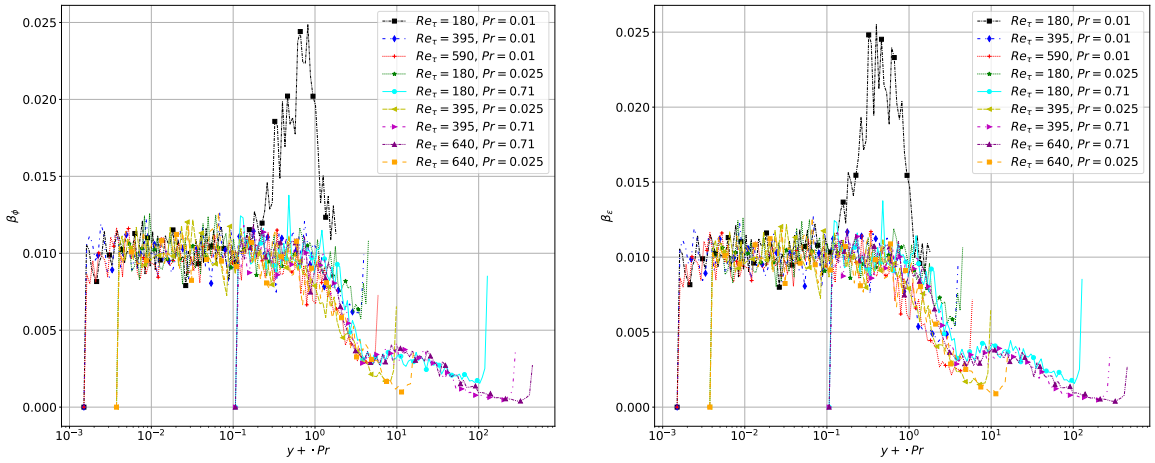

(a) k_θ (b) $\overline{u\theta}$

Figure 6: Distributions of the uncertainties of β_ϕ and β_ϵ over the channel width obtained by solving the inverse problem with $\sigma_\beta = 0.01$ and at different Re_τ and Pr.

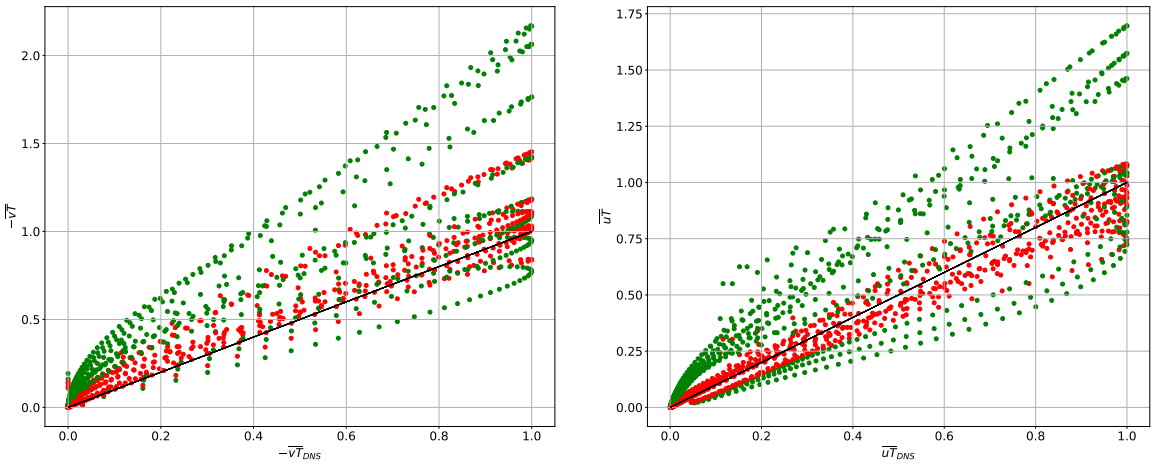

(a) $\overline{v\theta}$ (b) $\overline{u\theta}$

Figure 7: Predictions of the baseline model (green) and the corrected model (red) compared with the corresponding DNS values. Predictions and reference data are normalized w.r.t. the maximum values achieved in each flow condition.

is simplified by eliminating the thermal statistics, according to the linearity principle for scalar turbulence expressed by Pope [19]. Since the β_i are scalar quantities, the Theory of Invariants [20] must be applied to the parameter space to ensure its rotational invariance. The application of the theory and of the Buckingham Theorem leads to the set of dimensionless quantities indicated in Table 1.

This set is formally complete, though not the most suitable choice to develop a model for the correction factors for the flow conditions under consideration. Indeed, the application of the Principal Component Analysis (PCA) to the current dataset states that the set of 9 parameters is redundant. The cumulative sum of the eigenvalues of the correlation matrix, indicated in Figure 8a, shows that only 4 principal components explain more than 90 % of the total variance. On the other hand, β_ϕ and β_ϵ are weakly correlated with most of the momentum invariants, as shown by the correlation matrix represented is Figure 8b. The reason of the lack of correlation is a consequence of the absence of similarity between thermal and momentum fields, as better clarified in Figure 9. While at near unity Prandtl number the growths of β_ϕ and β_ϵ are almost aligned with the change of the momentum parameters, at low Prandtl numbers the two regions are far apart. These considerations suggest to reduce the parameter space to the quantities for which the correlation is significant, i.e. π_5, Re_t, Pr and α_θ:

$$\beta_i = \mathcal{F}_i(\pi_5, Re_t, Pr, \alpha_\theta) \tag{26}$$

An artificial neural network is then built to model the two functionals. The network takes in input the four parameters that are prior normalized to be in the range [0, 1]. The network is characterised by 3 hidden layers of 40 units each with Rectified Linear Unit (ReLU) activation function and a linear output layer. The uncertainty ranges obtained in the inference steps are used in the training to prioritize the fitting of the less uncertain values by minimizing the following cost function:

$$\mathcal{J}_{reg} = \sum_i^N \left(\frac{\beta_i - \beta_{i,FI}}{\sigma_{\beta,i}} \right)^2 + \sum_i^N \left(\sigma_{\beta,i} (\beta_i - 1.0) \right)^2 \tag{27}$$

where $\beta_{i,FI}$ is the inferred reference value at each mesh point and $\sigma_{\beta,i}$ indicates its uncertainty.

The training of the ANN gives a data-driven augmentation that improves the heat flux predictions on both training and test data. In particular, the heat flux predictions obtained for flow conditions excluded from the training set are depicted in Figure 10. The improved accuracy of the augmented model compared to the baseline for several test conditions is shown in Figure 11a. The trend of the data-driven augmentation β_ϕ for Pr ranging from 0.025 to 0.71 is indicated in Figure 11b.

6. Conclusions

A data-driven augmentation of a second order heat flux model based on the elliptic blending concept is proposed to improve the agreement of the predictions at low Prandtl numbers. The approach is based on the parameter selection, their inference via adjoint based optimization and the definition and training of a regression model. The description of these steps highlights the complexity of this second order modelling problem even when applied to a single category of canonical flows (non-isothermal turbulent channel flows). The inverse problem is in fact strongly ill-posed: the selection of convenient correction parameters and the regularized optimization of the fields are essential to retrieve an effective and physically consistent correction. The development of a regression model for the correction parameters is challenged by the poor local correlation between thermal and momentum statistics observed at low Prandtl numbers as a consequence of the lack of similarity.

The first results obtained with this analysis are promising. The data-driven augmentation provides more accurate heat flux predictions in both training and test conditions. Future perspectives of this work cover the extension of the augmentation to flow configurations of interest to the nuclear research community. This progress would require adopting a gradient-free inversion method that by-passes the adjoint gradient calculation, which is invasive for the flow solver and hard to implement into the existing CFD frameworks. The comparison of the "black-box" regression model (ANN) with an interpretable formulation based on genetic programming is also foreseen to better analyse the developed augmentation and promote the understanding of liquid metal thermal turbulence.

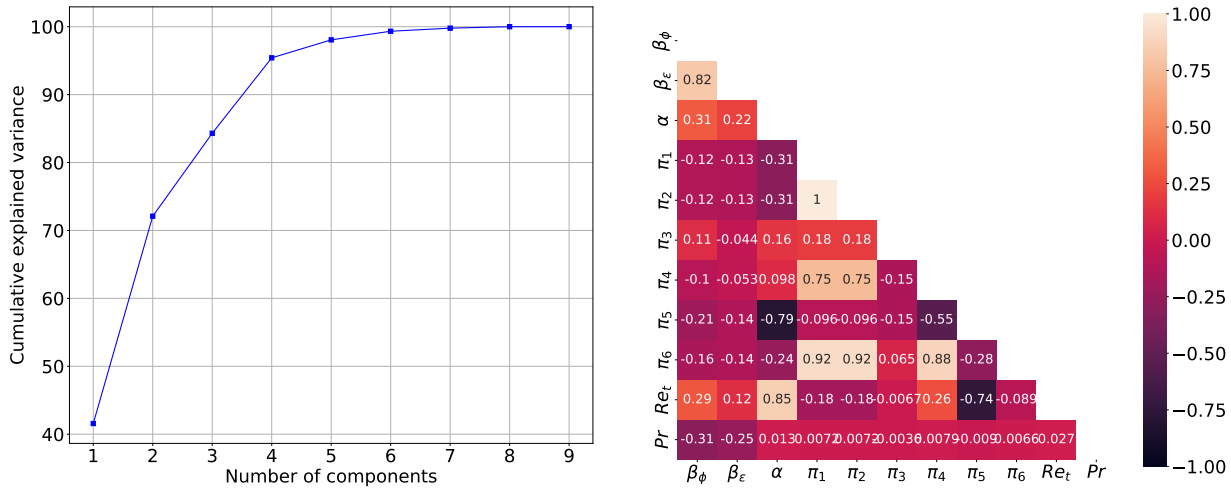

Figure 8: Cumulative sum of the eigenvalues of the correlation matrix constructed with the parameters indicated in Table 1 (left). On the right, the correlation matrix including all the quantities involved in the regression model.

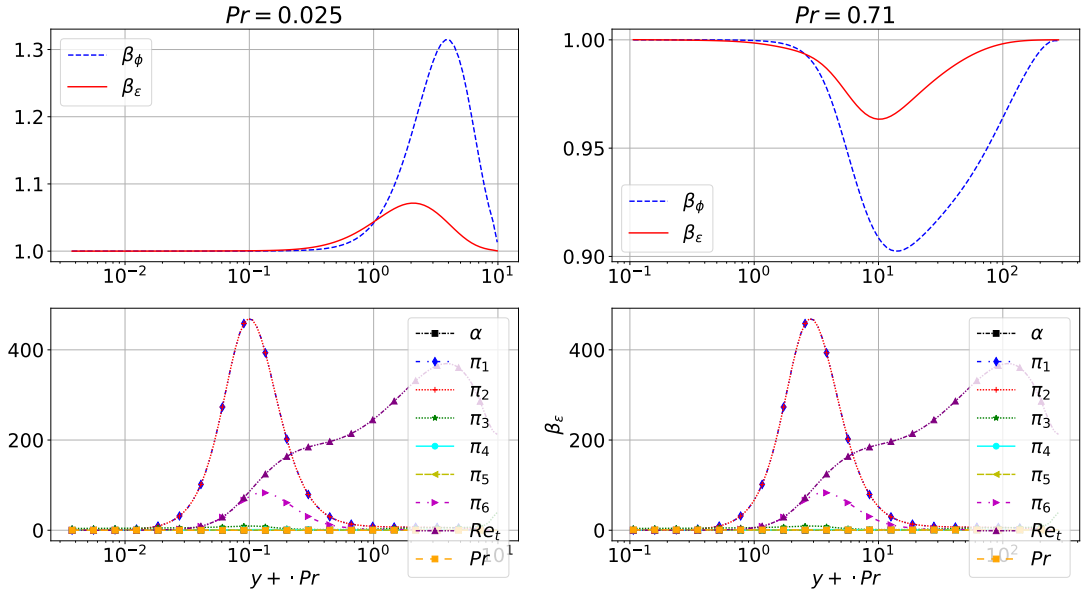

Figure 9: Distributions of the correction factors and the parameters indicated in Table 1 at $Re_\tau = 395$ and $Pr = 0.025$ (left) and 0.71 (right), highlighting the strong misalignment of the corrections with the momentum statistics at low Prandtl number.

Table 1: Minimum set of independent scalar quantities.

Invariants	α_θ	π_1	π_2	π_3	π_4	π_5	π_6	Re_t	Pr
Definition	eq.	$\frac{k^2}{\epsilon^2}\{\mathbf{S}^2\}$	$\frac{k^2}{\epsilon^2}\{\mathbf{\Omega}^2\}$	$\frac{1}{\{\mathbf{b}\}}$	$\frac{k}{\epsilon}\{\mathbf{bS}\}$	$\{\mathbf{b}_2\}$	$\{\mathbf{bS\Omega}\}$	$\frac{k^2}{\epsilon}$	$\frac{\nu}{\alpha}$

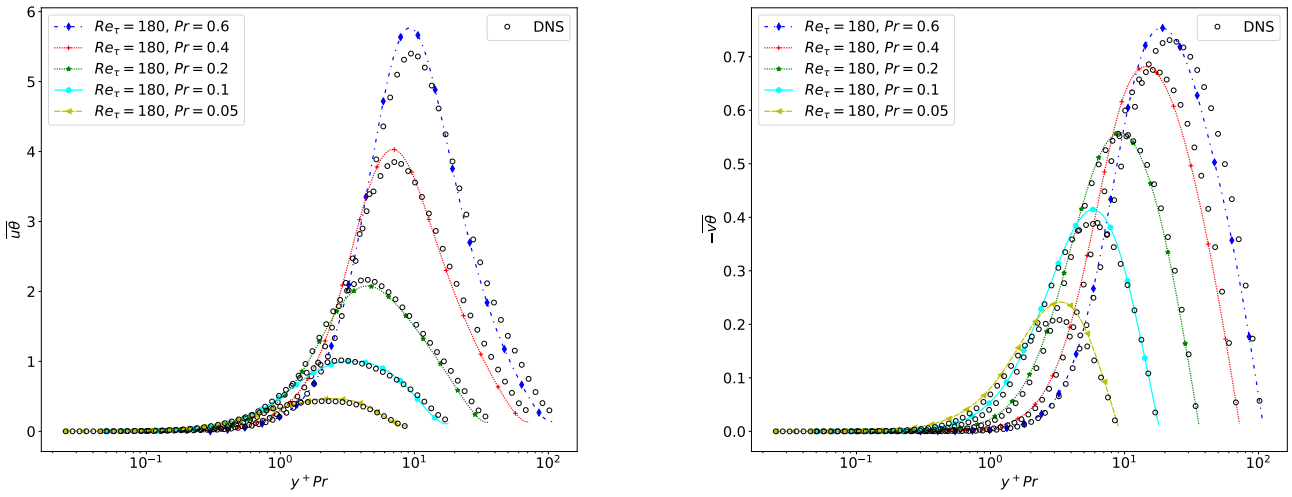

(a) $\overline{v\theta}$ (b) $\overline{u\theta}$

Figure 10: Heat flux predictions of the data-driven augmented model for flow conditions excluded from the training set. Comparison with the corresponding DNS data [13].

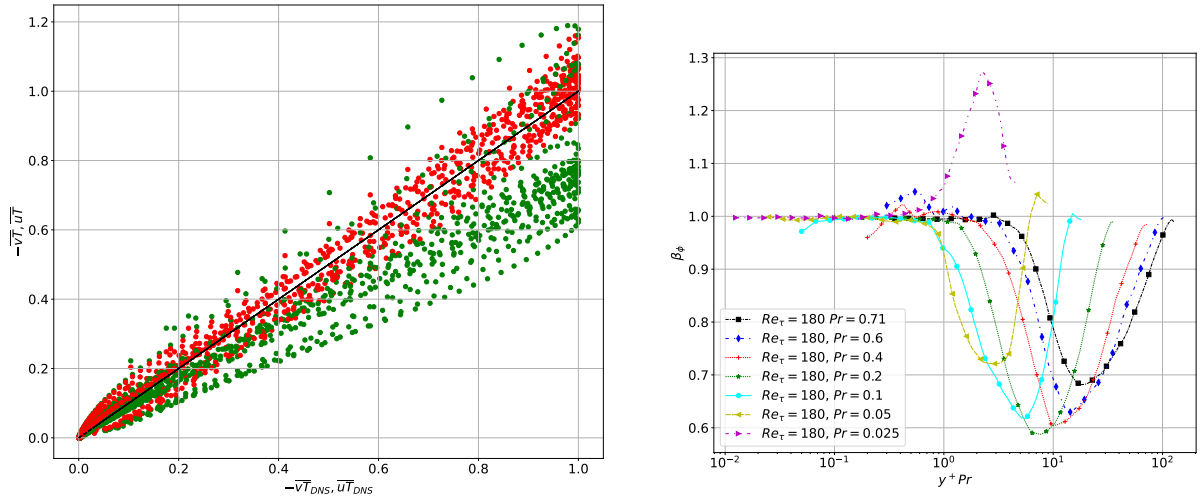

(a) (b)

Figure 11: Left: comparison of the performance of baseline (green) and augmented (red) models for test flow conditions. Right: Predictions of β_ϕ over the channel width for several Prandtl numbers.

NOMENCLATURE

$\mathbf{U}$	[m/s]	Mean velocity
T	[K]	Mean Temperature
$\mathbf{u}$	[m/s]	Velocity fluctuation
θ	[K]	Thermal fluctuation
k	[m^2/s^2]	Turbulent kinetic energy
ϵ	[m^2/s^3]	Turbulent dissipation rate
k_θ	[K^2]	Thermal variance
ϵ_θ	[K^2/s]	Thermal dissipation rate
$\overline{\mathbf{uu}}$	[m^2/s^2]	Reynolds stress
$\overline{\mathbf{u}\theta}$ or $\mathbf{q}$	[mK/s]	Turbulent heat flux
$\mathbf{g}$	[m/s^2]	Gravity vector
ν	[m^2/s]	Molecular viscosity
κ	[m^2/s]	Molecular diffusivity
δ	[m]	Half channel width
α_θ	[-]	Blending parameter
$\mathbf{I}$	[-]	Identity tensor

Appendix

An appendix, if needed, should appear before the acknowledgments. Avoid section numbering.

Acknowledgments

Acknowledge here important people for your PhD. Sponsor and financial support acknowledgments are also to be listed in the acknowledgments section.

References

[1] C. Geankoplis, Transport processes and separation, in: Process Principles, Prentice Hall NJ, 2003.

[2] Z. Ge, J. Liu, P. Zhao, X. Nie, M. Ye, Investigation on the applicability of turbulent-prandtl-number models in bare rod bundles for heavy liquid metals, Nuclear Engineering and Design 314 (2017) 198–206.

[3] A. Shams, A. De Santis, L. Koloszar, A. V. Ortiz, C. Narayanan, Status and perspectives of turbulent heat transfer modelling in low-prandtl number fluids, Nuclear Engineering and Design 353 (2019) 110220.

[4] M. Ziefuß, A. Mehdizadeh, A comprehensive assessment of the reynolds analogy in predicting heat transfer in turbulent wall-bounded shear flows, International Journal of Heat and Fluid Flow 81 (2020) 108527.

[5] A. Shams, F. Roelofs, E. Baglietto, S. Lardeau, S. Kenjeres, Assessment and calibration of an algebraic turbulent heat flux model for low-prandtl fluids, International Journal of Heat and Mass Transfer 79 (2014) 589–601.

[6] S. Manservisi, F. Menghini, A cfd four parameter heat transfer turbulence model for engineering applications in heavy liquid metals, International Journal of Heat and Mass Transfer 69 (2014) 312–326.

[7] W. M. Kays, Turbulent prandtl number. where are we?, ASME Journal of Heat Transfer 116 (2) (1994) 284–295.

[8] M. Fiore, L. Koloszar, C. Fare, M. A. Mendez, M. Duponcheel, Y. Bartosiewicz, Physics-constrained machine learning for thermal turbulence modelling at low prandtl numbers, International Journal of Heat and Mass Transfer 194 (2022) 122998.

[9] M. Fiore, L. Koloszar, M. A. Mendez, M. Duponcheel, Y. Bartosiewicz, Turbulent heat flux modelling in forced convection flows using artificial neural networks, Nuclear Engineering and Design 399 (2022) 112005.

[10] N. Shikazono, N. Kasagi, Second-moment closure for turbu-

lent scalar transport at various prandtl numbers, International journal of heat and mass transfer 39 (14) (1996) 2977–2987.
[11] L. Carteciano, D. Weinberg, U. Müller, Development and analysis of a turbulence model for buoyant flows, in: Proc. of the 4th World Conf. on Experimental Heat Transfer, Fluid Mechanics and Thermodynamics, Bruxelles, Belgium, June, Citeseer, 1997, pp. 2–6.
[12] F. Dehoux, S. Benhamadouche, R. Manceau, An elliptic blending differential flux model for natural, mixed and forced convection, International Journal of Heat and Fluid Flow 63 (2017) 190–204.
[13] H. Kawamura, H. Abe, K. Shingai, Dns of turbulence and heat transport in a channel flow with different reynolds and prandtl numbers and boundary conditions, Turbulence, Heat and Mass Transfer 3 (2000) 15–32.
[14] I. Tiselj, R. Bergant, B. Mavko, I. Bajsic, G. Hetsroni, Dns of turbulent heat transfer in channel flow with heat conduction in the solid wall, J. Heat Transfer 123 (5) (2001) 849–857.
[15] P. Durbin, A reynolds stress model for near-wall turbulence, Journal of Fluid Mechanics 249 (1993) 465–498.
[16] B. Sudret, Global sensitivity analysis using polynomial chaos expansions, Reliability engineering & system safety 93 (7) (2008) 964–979.
[17] J. J. Stickel, Data smoothing and numerical differentiation by a regularization method, Computers & chemical engineering 34 (4) (2010) 467–475.
[18] C. M. Bishop, N. M. Nasrabadi, Pattern recognition and machine learning, Vol. 4, Springer, 2006.
[19] S. Pope, Consistent modeling of scalars in turbulent flows, The Physics of Fluids 26 (2) (1983) 404–408.
[20] A. Spencer, R. Rivlin, The theory of matrix polynomials and its application to the mechanics of isotropic continua, in: Collected Papers of RS Rivlin, Springer, 1997, pp. 1071–1098.

An overview on the development and calibration of a 1D ejector model

Jan Van den Berghe

Environmental and Applied Fluid Dynamics Department, von Karman Institute for Fluid Dynamics, Belgium, jan.vandenberghe@vki.ac.be

Supervisor: Miguel Alfonso Mendez

Assistant Professor, Environmental and Applied Fluid Dynamics Department, von Karman Institute for Fluid Dynamics, Belgium, miguel.alfonso.mendez@vki.ac.be

University Supervisor: Yann Bartosiewicz

Professor, Institute of Mechanics, Materials, and Civil Engineering, Université catholique de Louvain, Belgium, yann.bartosiewicz@uclouvain.be

Abstract

We present a 1D ejector model which combines elements from existing models to reconcile pressure equalization, choking and shear. The compound choking theory is extended with a shear and friction force. Next, the model is calibrated with constant closure coefficients on experimental and numerical data. Finally, we present a physics-constrained machine learning formalism to calibrate systems of ODEs with a neural network term.

Keywords: 1D ejector modelling, compound choking, physics-constrained machine learning, calibration with neural networks, adjoint

1. Introduction

Ejectors are components to drive a flow without moving parts. They expand a primary fluid from a high pressure source through a nozzle which exits in a mixing chamber. A secondary flow is entrained into the resulting low pressure region through shear with the primary jet. The lack of moving parts makes ejectors robust devices, with applications in aeronautics, refrigeration, chemical industry and power generation [1].

Research on ejectors dates back to over a century ago, so an extensive amount of literature is available: experimental works, 2D/3D CFD [2; 3; 4; 5; 6] and 0D/1D modelling [7; 8; 9; 10; 11; 12; 13; 14; 15]. Although the operating characteristics are quite well known and can be predicted accurately, the internal flow field remains a complex combination of flow phenomena. For example, the choking mechanism of the combined primary and secondary jet (the so-called *compound* flow) is still an open question [16]. It can not easily be investigated without the appearance of shock trains at the nozzle exit. Such 2D phenomena complicate the development of 0D/1D models which are inherently limited to an averaged representation. Such compatibility issues partially explain why existing studies usually consider one or two of the modelling options, e.g. a validation of CFD simulations on experiments. Low order models are more commonly compared to both experimental and numerical data in terms of mass flow rates, but are rarely validated against local quantities since most models are based on integral, 0D formulations.

Notable contributions in 1D modelling were made by Clark [10] and Banasiak and Hafner [11], who proposed an ejector model consisting of two interacting 1D domains in the mixing pipe. The shock train at the exit of the primary nozzle is lumped into a 0D junction at the inlet of the mixing pipe. The first considers the two streams as mass tubes which exchange momentum only through shear. Their model is easily interpretable, but has been validated only against global data in the form of mass flow rates and pressure ratios. The second compares well against local pressure measurements, but the high number of closure parameters limits its practical use. Additionally, neither of the models tackle the on-design operating regime,

where the maximal flow rate is achieved and the compound flow is thus choked. This is surprising since it is the most common and desired operating regime. An alternative, quasi-2D approach was proposed by Del Valle et al. [12], which is based on potential flow and Prandtl-Meyer expansion theory to determine the dividing streamline between the primary and the secondary jet from the exit of the primary nozzle. Their model has the advantage of predicting the equalization of the static pressure between the two streams, but requires the assumption of on-design operation and does not include shear.

These models clearly illustrate the complex interaction between three main physical phenomena in the mixing chamber: (1) equalization of the static pressure between the two jets, (2) momentum transfer through shear and (3) choking of the compound flow. Therefore, we propose to develop a 1D ejector model that reconciles existing 0D/1D models with CFD and experiments by including these three main effects and adding data-driven closure relations. The latter are required because the 1D formulation implies the lumping of higher dimensional phenomena into closure coefficients, for example the shear. These coefficients will depend on the local solution through closure relations learned from CFD, to maximally exploit the information from simulations and to minimize the need for ad-hoc calibration. For example, a shear coefficient could depend on the Reynolds number in both streams. The functional relationships will be parametrized and learned with machine learning, e.g. through with artificial neural networks (ANN).

Several ingredients are required to reach this goal: firstly, a robust 1D model which accurately approximates the 2D flow field in multiple operating regimes (on-design, off-design and backflow). Secondly, we need numerical and experimental data for local verification and validation. Finally, we need calibration tools to learn the closure relations from data, which can be stated mathematically as a regression problem constrained by set of ODEs or PDEs. This work presents the progress on these three aspects and closes with perspectives on future work.

2. A 1D ejector model

2.1. Adaptation of existing models

The model proposed in this works combines the structure of [11] with the compound equations proposed in [10]. The structure is illustrated in figure 1: the inlets are modelled as 1D domains, which discharge in a 0D control volume. The static pressures of both streams equalize across this volume and enter two coupled 1D domains for the mixing pipe and the diffuser. The steady Euler equations are solved in each domain. In the mixing pipe, these are complemented by the assumption of equal static pressure and the constraint that the sum of the cross-sections should respect the geometry [17], cf. system (1). These constraints are required since the Euler equations are well-defined if the area is specified, but in this case both cross-sections are unknown. The two constraints cover the two degrees of freedom introduced by the cross-sections. The system is completed with a shear force, which has an equal but opposite effect on the streams, and a wall friction force in the secondary stream. These forces are parametrized with the friction coefficients f_{ps} and f_w. The required boundary conditions are the total pressure and the total temperature at the inlets and the static pressure at the exit.

$$\begin{cases} d_x\left(\rho_i A_i v_i\right) & = 0 \\ d_x\left(\rho_i A_i v_i^2\right) & = -A_i d_x p_i + F_i \qquad i \in [p, s] \\ d_x\left(\rho_i A_i v_i h_{t,i}\right) & = 0 \end{cases}$$
$$\begin{cases} A_p + A_s & = A \\ p_p & = p_s \end{cases} \tag{1}$$

where

$$F_p = -\frac{1}{2} f_{ps}\left(\rho_p v_p^2 - \rho_s v_s^2\right) \tag{2}$$

$$F_s = \frac{1}{2} f_{ps}\left(\rho_p v_p^2 - \rho_s v_s^2\right) - \frac{1}{2} f_w \rho_s v_s^2 \tag{3}$$

The primary nozzle is always assumed to be choked and can therefore be solved individually. The secondary inlet can not be solved directly, since the mass flow rate or Mach number is initially unknown. It can be calculated by first solving the junction. The operating regime is not known either, so the calculation initially assumes on-design operation where the maximal flow rate is reached in the ejector. Practically, we assume the flow is choked at the exit of the 0D junction as in [15], where the mixing pipe consisted of a single domain. The proposed model distinguishes between the two streams in the mixing pipe, so the choking is enforced in the compound sense (cf. section 2.2 and [17; 16]). The procedure iterates on the static pressure at the exit of junction until the flow becomes compound sonic in that section. Assuming an isentropic evolution in the junction, the total pressure and the total temperature are constant from inlet to outlet. With the guessed static pressure at the out-

let, the Mach number in both sections can be calculated from the total and static pressure. The primary cross-sectional area follows from the mass flow rate (known from the choked nozzle) and the secondary area follows from the constraint on the geometry. At this point, the outlet of the junction is fully calculated, allowing to assess the compound state and to iterate on the guessed static pressure. A unique pressure value leads to the sonic condition.

After calculating the junction, the secondary mass flow rate and the inlet of the double flow passage are known, allowing to calculate the secondary inlet and to integrate equations (1) until the exit of the diffuser. It is important to note that a subsonic *and* a supersonic solution exist starting from the sonic boundary condition. In the first iteration we choose the subsonic solution, to obtain the highest pressure at exit of the diffuser (back pressure) for which the ejector is choked. This value is required to assess if the assumption of on-design operation was correct. If the pressure imposed by the boundary condition is lower, the flow will remain choked and the calculation is correct. The calculation can then be repeated to obtain the supersonic solution, which leads to a (much) lower back pressure. Generally, the boundary condition will fall between these values, indicating that a shock should occur somewhere in the mixing pipe. Its position can be determined iteratively by imposing the back pressure to match the boundary condition. If the boundary pressure is higher, the flow must remain subsonic and the ejector operates in off-design conditions. In that case, the procedure should be repeated with a higher static pressure at the exit of the junction until the calculated back pressure matches the boundary condition.

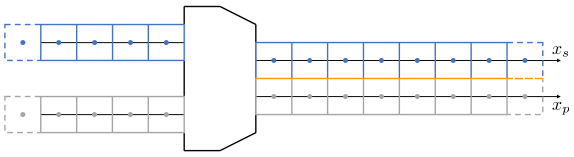

Figure 1: Schematic representation of the adapted 1D model.

The proposed formulation brings several advantages by combining ideas from literature [10; 11; 15].

Firstly, the concept of the compound equations is appealing since there is no mass transfer between the two streams. The evolution of the primary cross-section in x thus takes the physical meaning of a dividing streamline in a 2D slice or a dividing surface in the full 3D case. The model by Banasiak and Hafner contains a mass flux term between the streams, which not only adds to the number of closure coefficients, but also misses the opportunity of providing extra physical information through the dividing surface.

Secondly, the same equations allow a formal description of choking, as discussed below in section 2.2. Choking plays an essential role in ejectors, as the type of operation can be differentiated between on-design, where the maximal flow rate is achieved, and off-design, where the compound flow remains subsonic and depends on the back pressure. It is therefore surprising that it is not covered in [10] and [11].

Finally, additional physical mechanisms can be added if required. In this work, we use focus on ideal gasses and shear since it is the primary driving mechanism of entrainment. Friction is added as a first extension to account for losses. Other phenomena such as heat transfer and real gas effects are not included.

The pain point of the compound equations consists of the assumption of equal static pressure. The primary nozzle is seldom well-expanded and instead shock trains are often observed in the mixing chamber [2]. As a result, the double passage mixing domain can not start directly at the exit of the primary nozzle and the secondary inlet, because the boundary equations would be incompatible with the assumptions in the equations (1). Instead, it can only start in a point downstream where the static pressures have equalized through a shock train. Therefore, this 2D/3D process is lumped in the 0D junction [11].

2.2. *Derivation from first principles*

The model described above is stated as a system of continuous equations, but these are singular in choked conditions. The equations are solved in practice by iterating on the static pressure in the next section $x+\Delta x$. This is unfortunate, since a fully continuous formulation allows efficient integration with state-of-the-art tools, e.g. available in SciPy [18], and for adjoint-based calibration of the closure coefficients, cf. section 4.

The system of equations (1) can be reformulated more compactly in terms of uniform static pressure, two total pressures, two total temperatures and two cross-sections, from which all other quantities follow. In this work, we focus on the equation for the static pressure since it is the source of the singularity in choked conditions. After some operations, the follow-

ing equation can be obtained for the pressure gradient:

$$\frac{d_x p}{p} = \frac{1}{\beta}\left(d_x A + \frac{f_{ps} l_{ps}}{2}\frac{\left(M_p^2 - M_s^2\right)^2}{M_p^2 M_s^2} - \frac{f_w l_w}{2}\left(1 + (\gamma - 1)\, M_s^2\right)\right) \tag{4}$$

where

$$\beta = A_p \frac{1 - M_p^2}{\gamma M_p^2} + A_s \frac{1 - M_s^2}{\gamma M_s^2} \tag{5}$$

The compound choking indicator β plays a similar role as the Mach number in the classic single stream equation. The interested reader can verify that the equation falls back to the quasi-1D Euler equation with a friction term if $M_p = M_s = M$, in which case the numerator becomes $1 - M^2$. The flow is thus *compound sonic* if $\beta = 0$. Note that this condition is reached if both Mach numbers equal 1, but can also be reached if one is subsonic and the other is supersonic. This explains why the secondary flow does not necessarily reach Mach 1 in on-design operation [16; 19]. If $\beta > 0$, the flow is *compound subsonic*, with β going to infinity for stagnant flow. Consequently, $\beta < 0$ corresponds to *compound supersonic* flow.

This equation is an extension of the original compound flow theory proposed by Bernstein [17], who did not include the effect of shear and friction. The second term represents the effect of shear and is always positive. As a result, shear tends to increase the static pressure in subsonic flow ($\beta > 0$). Similarly, the friction term is always negative, leading to a pressure decrease in subsonic flow and a pressure increase in supersonic flow.

A choked section is thus characterized by a singularity in the pressure equation with $\beta = 0$. Nevertheless, the physical pressure gradient remains finite (with the exception of shocks). Therefore, the numerator should also equal zero in a choked section. In absence of shear and friction, this leads to the well-known condition that choking occurs in a throat. The positive shear term tends to push the area gradient to negative values in order to keep the numerator zero. In other words, shear pushes the choked section upstream towards a convergent section, which has been observed numerically [16]. Wall friction has the opposite effect and pushes the choked section into the diffuser. Note that the assumption in section 2.1 of choking at the inlet of the constant area section is thus not strictly coherent with the current analysis!

The choked section can thus be determined, but the equation (4) for the pressure gradient remains singular (0/0). De l'Hôpital's rule brings the solution by deriving the numerator and the denominator with respect to x. This derivation is tedious since it introduces derivatives of the Mach number, which in turn can be formulated in terms of the pressure gradient. The result is a quadratic equation for the pressure gradient. This is logical since the flow can either continue to expand and become supersonic, or remain subsonic. The current analysis thus allows an analytical calculation of the pressure gradient in all admissible physical conditions (e.g. $\beta = 0$ with a non-zero numerator in equation (4) indicates an error in the boundary conditions, such as a mass flow rate higher than the choked conditions). The derivation is too long to be included as an appendix, but will appear in a future technical note.

In summary, the framework in section 2.1 is a practical tool, but it is incoherent with the strict compound equations and needs to be solved iteratively. On the other hand, the set of equations in section 2.2 provide an analytical expression for the pressure gradient, but the assumption of equal static pressure is too restrictive to directly use in an ejector model. Combining these options, either with a 0D junction or with a pressure equalization mechanism, is a challenging task which receives first priority in future work. The next section explores both options through calibration on experimental and numerical data.

3. Data collection and calibration with constant coefficients

3.1. Experimental facility

Figure 2 shows a sketch of the experimental facility. Compressed air is supplied on the top left. The inlet pressures are then regulated independently, allowing to set inlet pressure ratios $\Pi_2 = p_{t,s}/p_{t,p}$ between 0.2 and 1, with a maximal pressure of 5 bar. A 150 kW heater can heat one of the inlets up to a temperature of 200 °C. The flow settles through 2.5 m long straight pipes before passing through two vortex mass flow meters. The maximal achievable flow rate of the facility is 0.7 kg/s. Two flexible tubes allow to connect the heated inlet either to the primary or the secondary inlet of the ejector, which is located on the far right. Both inlets and the outlet are instrumented with four thermocouples and a pressure transducer connected to four pressure taps. With the measured mass flow rates and the known cross-section, these static quantities can be converted to their total counterparts to serve as boundary conditions in the numerical model. Finally, a manual valve at the diffuser exit allows to manipulate the back pressure.

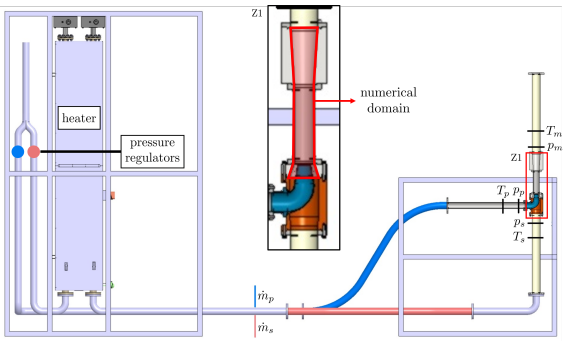

Figure 2: Schematic representation of the ejector facility at VKI.

Two closure coefficients are introduced in the model: the friction coefficient f_p in the primary nozzle and the total pressure loss $\Delta p_{t,s}$ at the secondary inlet. Their calibration allows to respectively match the primary and the secondary mass flow rate. f_p is calibrated independently since we assume that the primary nozzle is always choked. $\Delta p_{t,s}$ lumps all other losses into a total pressure loss at the inlet, changing the boundary condition from the measured value to a lower one. The number of closure coefficients has hence been limited to two, since only two mass flow rates are available to calibrate upon.

The primary friction coefficient has been calibrated on the complete dataset, leading to $f_p = 0.0017$. On the other hand, the secondary pressure loss $\Delta p_{t,s}$ has been calibrated point by point since the secondary and mixed flow field change with the operating conditions. The evolution of $\Delta p_{t,s}$ is shown in function of the pressure ratios at the boundaries on figure 3a. Higher losses are observed at lower back pressures p_b. A plausible explanation could be the higher flow rate in the on-design regime, but more local data is required to determine the source of the losses with more certainty. Note that $\Delta p_{t,s}$ evolves continuously in the plane of pressure ratios, independently of the inlet temperature ratio.

The corresponding mass flow rates are shown on figure 3b with the experimental uncertainty in x and the numerical uncertainty in y, which is obtained by propagating the uncertainties on the boundary conditions of the model. The predictions fall within an error margin of 10 %, indicated by the dashed lines. The numerical uncertainty is higher on the secondary mass flow rate compared to the primary due to the sensitivity to the back pressure in off-design operation.

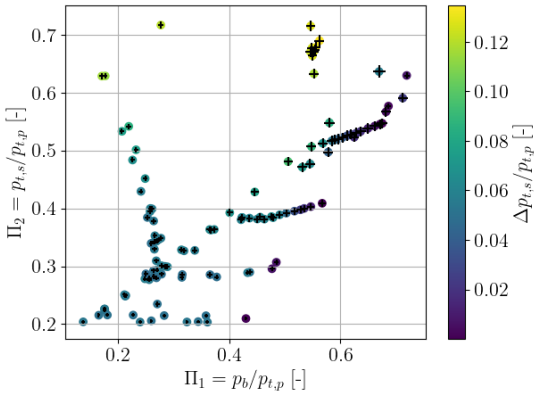

(a) Result of the calibration of $\Delta p_{t,s}$

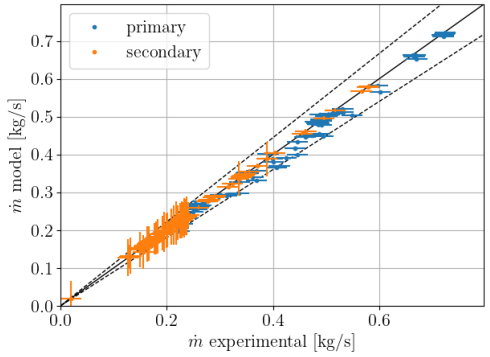

(b) Primary and secondary mass flow rate

Figure 3: Calibration result for the secondary pressure loss $\Delta p_{t,s}$ (left) and comparison of the mass flow rates from the calibrated model and from the experiments (right). The dashed lines indicate a 10 % error margin.

3.2. Numerical simulations

Numerical simulations are available on the same geometry as the experiments in the previous section [20]. The interested reader is referred to the original paper for numerical details. In this work, we post-process these 2D axisymmetric simulations to produce a 1D evolution that serves as reference for the 1D model described in section 2.

The first step consists of extracting the dividing streamline. By definition, no mass can cross this line, so the radius r_{div} of the dividing line at a certain position x can be found by integrating the mass flux until the primary mass flow rate is reached:

$$\dot{m}_p(x) = \int_0^{r_{div}} \rho u \, 2\pi r \, dr \tag{6}$$

where the density ρ and the axial component of the

velocity u depend on x and r. Next, the dividing line is used to average the flow over the two streams. One requirement is that the resulting 1D variables respect conservation, e.g., the mass flow rate computed from the averaged density and velocity should be constant in x and should match the CFD. Several options exist, but in this work we use the following equations:

$$\hat{\rho}_i(x) = \frac{1}{A_i} \int_{A_i} \rho \, dA_i \tag{7}$$

$$\hat{u}_i(x) = \frac{1}{\hat{\rho}_i A_i} \int_{A_i} \rho u \, dA_i \tag{8}$$

$$\hat{e}_{ti}(x) = \frac{1}{\hat{\rho}_i A_i} \int_{A_i} \rho e_t \, dA_i \tag{9}$$

where the hat $\hat{\cdot}$ denotes the averaged 1D variables and the integrals are to be carried out over the two cross-sections depending on the radius r_{div} of the dividing streamline. The choice to average the density is arbitrary, but the other two equations enforce that the 1D variables keep the same mass flow rate and total internal energy as the CFD [16].

Figure 4 shows the resulting dividing streamline for a simulation with a primary total pressure $p_{t,p}$ of 5 bar, a secondary total pressure $p_{t,s}$ of 1 bar and a back pressure p_b of 1 bar. The total temperatures are fixed at 293 K. The primary nozzle is underexpanded, leading to a shock train in the mixing chamber. This illustrates the need for a pressure equalization mechanism in the 1D model, possibly with the 0D junction (cf. section 2). A second shock train appears in the diffuser to recompress the flow to the imposed static pressure at the outlet.

In contrast with the calibration on experimental mass flow rates, local data is now abundantly available, including the evolution of the primary cross-section. The procedure is split in two regions: an upstream region where the static pressures have not equalized and a downstream region. In the first, the cross-sections of the streams are imposed from the CFD to let the pressures equalize, while they are computed with the compound flow equations in the second region (cf. section 2). The on-design procedure assumes so-called Fabri-choking [8], which states that the secondary stream becomes sonic in its minimal cross-section. The actual choking mechanism at play (compound or Fabri) is still an open question [6; 16]. The first step thus consists of finding the minimal cross-section of the secondary stream, where $M_s = 1$ is imposed. Next, the total pressure is defined in the same section such that the mass flow rate matches the CFD (which remains the only free variable with the total temperature from the inlet, the area and the Mach number). In the same section, the primary Mach number and total pressure are tuned to match the CFD as closely as possible. This provides a starting point for integrating the conservation equations with the specified area from the dividing streamline. The equations are integrated backwards from the choked section to the inlets and forwards until the static pressures equalize.

From there on, the continuous compound equations from section 2.2 are integrated to a given coordinate where a shock is introduced. The flow remains supersonic because it was already compound supersonic in the choked section ($M_p > 1$ and $M_s = 1$). The shock is solved with the iterative procedure from section 2.1 with the additional requirement that the flow becomes subsonic. Afterwards, the compound equations are integrated once more until the exit of the domain.

Figure 5 shows the calibrated result on the post-processed CFD simulation from figure 4. The wall friction coefficient is constant throughout and equals 0.002. The shear coefficient varies along x and equals 0.015 in the variable pressure region, 0.002 from the point where the pressure equalize to the shock and 0.010 downstream of the shock. The effect of the operating conditions on these closure coefficients is a target for future work. For now, it suffices to conclude that the 1D formulation is capable of accurately representing the internal flow field of an ejector in this specific operating point. Naturally, it can not represent 2D shock trains. Nevertheless, the approximation with the normal shock allows to match the entire states at the exit of the domain, as was observed earlier on integral quantities in transient conditions [15].

4. Calibration with the adjoint method and artificial neural networks

4.1. Methodology

The ejector model described in section 2 consists of a set of ODEs which contain some closure terms. It has been shown in section 3 that the closure coefficients should vary in x. The goal is to find closure relations not in function of space, but of the local solution, e.g., pressures and velocities. This paradigm can be stated mathematically as follows:

$$\begin{cases} d_t \boldsymbol{u} = f(\boldsymbol{u}, t, \boldsymbol{p}) \\ \boldsymbol{p} = g(\boldsymbol{u}, t; \boldsymbol{w}) \end{cases} \tag{10}$$

where $\boldsymbol{u} \in \mathbb{R}^{n_u}$ denotes the state vector consisting of n_u components, t denotes time (or space in steady 1D

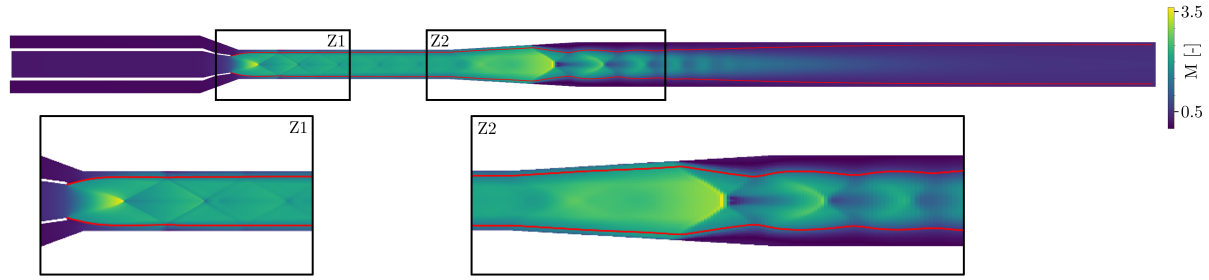

Figure 4: Mirrored Mach number field of a 2D simulation on an axisymmetric ejector with a primary inlet pressure of 5 bar, a secondary inlet pressure of 1 bar and a back pressure of 1 bar. The primary nozzle is underexpanded and the ejector operates in the on-design regime, leading to shock trains in the mixing chamber (zoom 1) and in the diffuser (zoom 2). The red line indicates the dividing streamline obtained in post-processing (cf. equation (6)).

models), $\boldsymbol{p} \in \mathbb{R}^{n_p}$ denotes the vector of n_p closure parameters, which depend on the state, time and a set of weights $\boldsymbol{w} \in \mathbb{R}^{n_w}$ through the function g. The function g is thus the closure relation that we want to infer from data, to be embodied by a regressor such as an artificial neural network (ANN). This approach has been used successfully on a Poisson equation [21] and later in turbulence modelling [22; 23; 24; 25]. The main question is which weights minimize the error compared to available data, measured by a cost function:

$$J(\boldsymbol{w}) = \int_0^T e(\boldsymbol{u}, \tilde{\boldsymbol{u}}) dt \tag{11}$$

where e can be any function that penalizes the mismatch between the numerical solution $\boldsymbol{u}$ and given data $\tilde{\boldsymbol{u}}$. Neural networks are typically trained with gradient-based methods (through back-propagation [26]). Analytically calculating the gradient of equation (11) is challenging because it is linked to the system of ODEs (10). The weights affect the solution at each step of the integration, so the sensitivity $d_{\boldsymbol{w}}\boldsymbol{u}$ of the state with respect to the weights at a given time also depends on the solution at previous time steps. This 'history' effect precludes a direct calculation.

A brute force solution is to use finite differences, which implies solving the system (10) $n_w + 1$ times. This approach is infeasible for neural networks with thousands of weights. The adjoint method provides an alternative by tracing the sensitivities backwards. It requires solving a single additional *adjoint* ODE backwards. Several tutorials are available, see for example [27]. The adjoint system of (10) can be written as follows:

$$\dot{\boldsymbol{\lambda}} = d_{\boldsymbol{u}} e - \boldsymbol{\lambda}(\partial_{\boldsymbol{u}} f + \partial_{\boldsymbol{p}} f \, \partial_{\boldsymbol{u}} \boldsymbol{p}) \tag{12}$$

where $\boldsymbol{\lambda} \in \mathbb{R}^{n_u}$ denotes the adjoint state. This equation can be derived by augmenting the cost function (11) with a Lagrangian multiplier $\boldsymbol{\lambda}$ followed by the system of equations (10). By choosing the adjoint variables such that they respect the adjoint equation, the final expression for the gradient of the cost simplifies to the following equation:

$$d_{\boldsymbol{w}} J = -\int_0^T \boldsymbol{\lambda} \, \partial_{\boldsymbol{p}} f \, \partial_{\boldsymbol{w}} \boldsymbol{p} \, dt \tag{13}$$

In summary, the troublesome Jacobian of the solution with respect to the weights ($d_{\boldsymbol{w}}\boldsymbol{u}$) is avoided and replaced by an adjoint system of linear (!) equations, which require Jacobians that can be calculated from the definition of the original system of equations (10). In case the closure relation g is defined by a neural network, the Jacobians with respect to the input $\boldsymbol{u}$ and the weights $\boldsymbol{w}$ can be computed through backpropagation [26].

4.2. Test case: Burgers' equation

We use a non-linear advection equation as test case:

$$\begin{cases} \partial_t u + a \partial_x u = 0 \\ a = g(u; \boldsymbol{w}) \end{cases} \tag{14}$$

where the advection speed a is prescribed by a neural network with input u and weights $\boldsymbol{w}$. This equation is in fact a PDE, but becomes a set of ODEs after discretizing the space derivative. In this work, a first order upwind scheme is used for simplicity. The integration in time is carried out with a forward Euler scheme for the same reason.

The neural network is arbitrarily defined with two hidden layers of ten nodes with ELU activation functions [28]. The output node has a sigmoid activation function to force the output in the range [0,1], which avoids stability issues with a reference speed of 1 and

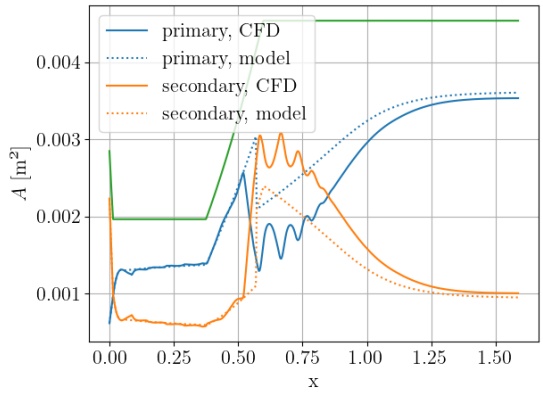

(a) Area

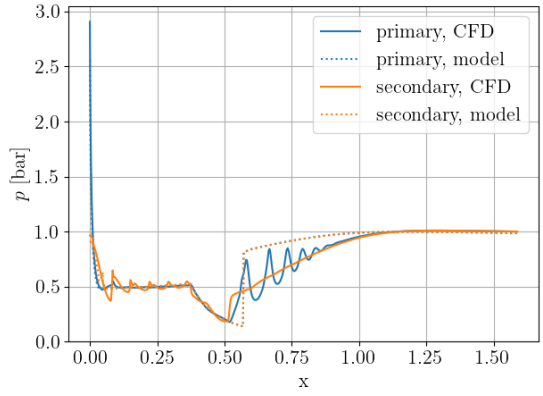

(b) Static pressure

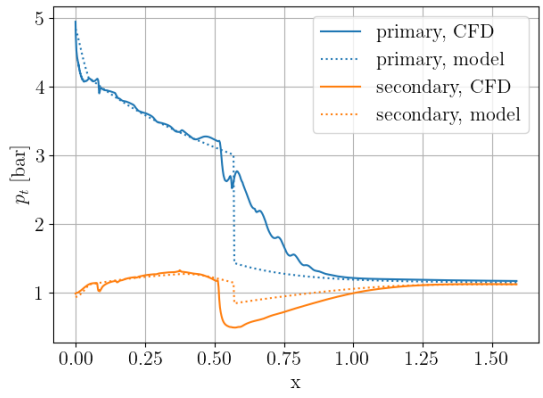

(c) Total pressure

Figure 5: Assimilation of the CFD simulation in figure 4, which was post-processed with equations (7) - (9). The result is obtained through calibration of the shear and the wall friction coefficients.

a CFL number of 0.8. The initial condition and the reference solution are both sinusoidal:

$$u_0(x) = 0.6 + 0.3\sin(2\pi x) \tag{15}$$

$$a_{ref} = 0.5 + 0.4\sin(2\pi u) \tag{16}$$

The cost function is the summed square error at the final time of 0.5 seconds. Figure 6 shows the solution (left) and the closure relation predicted by the neural network (right) as the training progresses. After ten iterations the neural network has learned to lower the advection speeds at high values of u. The main contribution to the cost at the initial time is indeed an overshoot of the peak between $x = 0.1$ and $x = 0.5$. The algorithm converges after 141 iterations. Although the data contains no noise, it remains remarkable that the neural network manages to learn a function indirectly through the integration of a physical equation. Note the large error when extrapolating: values of u below 0.3 never occur during training, so the network can not learn anything in this region.

5. Conclusion

In this work, we presented a 1D model which combines the ideas of three existing models to address the complex interaction between pressure equalization, choking and shear. The compound flow theory is an appealing candidate for the choking mechanism and has been extended to include shear and friction forces. These equations show a discrepancy between the adapted model with the 0D junction and the analytical equations. Reconciling both options is a primary target in future work.

In parallel, experimental and numerical data have been collected to validate the model in development. The data cover all operating regimes of a single ejector. Other geometries can be considered in the future, but are not the main priority. The *global* calibration on experimental data does not allow to localize the losses in the secondary stream, but provides interpretable results in terms of pressure ratios. The calibration on CFD proves that a 1D formulation can also *locally* assimilate the flow field. Understanding the effect of the operating conditions on the calibration is an important future target.

Finally, we proposed a general framework for the adjoint-based calibration of ODE models with an ANN closure term. A non-linear advection equation was used as a proof of concept. A final target is to apply the method on the closure coefficients of the 1D ejector model, which first requires a fully continuous formulation.

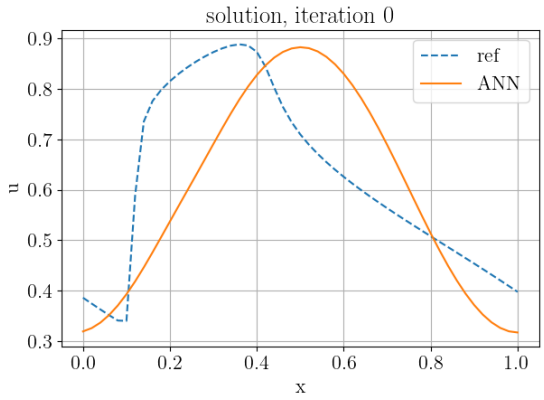

(a) Solution at iteration 0

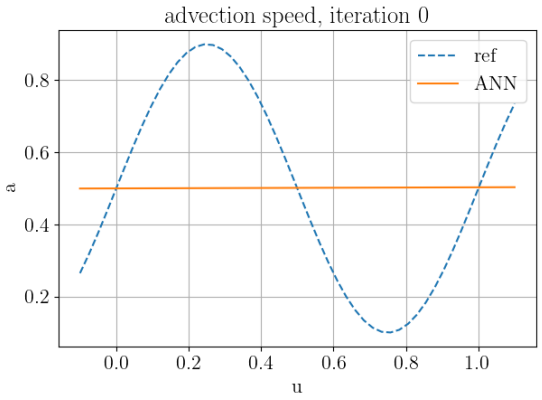

(b) Advection speed at iteration 0

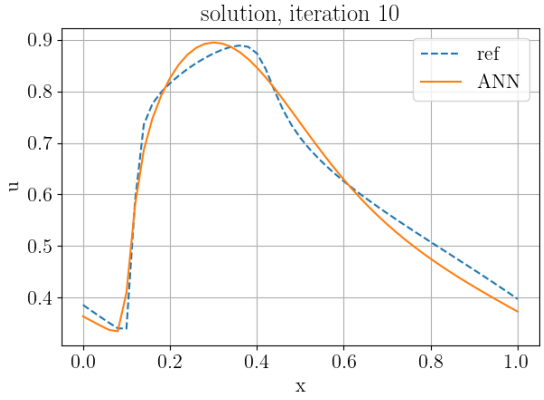

(c) Solution at iteration 10

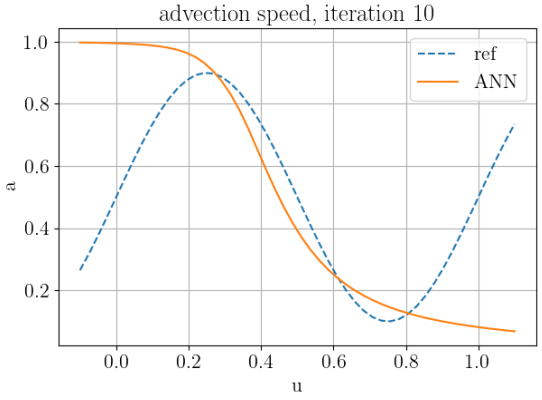

(d) Advection speed at iteration 10

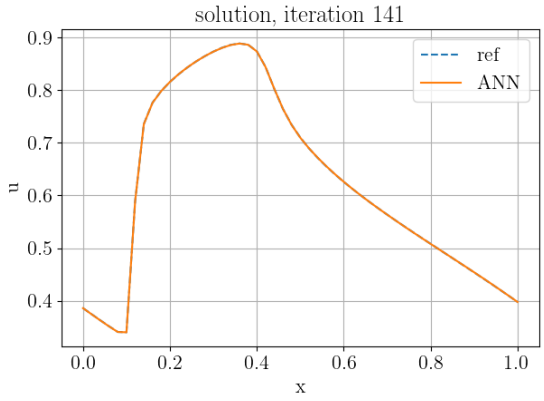

(e) Solution at iteration 141

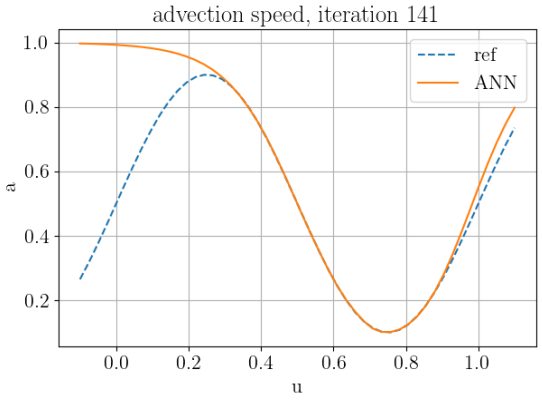

(f) Advection speed at iteration 141

Figure 6: Training history (top-bottom) of a non-linear advection equation where the speed (right) is prescribed by a neural network (cf. equation (14)). The error on the solution at the final time step (left) is penalized through a cost function, which is minimized with an adjoint method for the enhanced physical system (cf. equations (10) to (13)). The network manages to learn a sinusoidal function indirectly through the physical system.

Acknowledgments

J. Van den Berghe is supported by a F.R.S.-FNRS FRIA grant and gratefully acknowledges Dr. Jagadish Babu Vemula for providing the CFD simulations.

This project has received funding from the Clean Sky 2 Joint Undertaking (JU) under grant agreement No 101008100. The JU receives support from the European Union's Horizon 2020 research and innovation programme and the Clean Sky 2 JU members other than the Union.





Disclaimer: The contents presented in this article reflect only the author's point of view: the authors and Clean Sky JU are not responsible for any use that may be made of the information it contains.

References

[1] Z. Aidoun, K. Ameur, M. Falsafioon, M. Badache, Current advances in ejector modeling, experimentation and applications for refrigeration and heat pumps. part 1: Single-phase ejectors, Inventions 4 (1) (2019) 15.

[2] Y. Bartosiewicz, Z. Aidoun, P. Desevaux, Y. Mercadier, Numerical and experimental investigations on supersonic ejectors, International Journal of Heat and Fluid Flow 26 (1) (2005) 56–70. doi:10.1016/j.ijheatfluidflow.2004.07.003.

[3] A. Hemidi, F. Henry, S. Leclaire, J.-M. Seynhaeve, Y. Bartosiewicz, Cfd analysis of a supersonic air ejector. part i: Experimental validation of single-phase and two-phase operation, Applied Thermal Engineering 29 (8) (2009) 1523–1531. doi:10.1016/j.applthermaleng.2008.07.003.

[4] F. Mazzelli, A. B. Little, S. Garimella, Y. Bartosiewicz, Computational and experimental analysis of supersonic air ejector: Turbulence modeling and assessment of 3d effects, International Journal of Heat and Fluid Flow 56 (2015) 305–316. doi:10.1016/j.ijheatfluidflow.2015.08.003.

[5] O. Lamberts, P. Chatelain, Y. Bartosiewicz, New methods for analyzing transport phenomena in supersonic ejectors, International Journal of Heat and Fluid Flow 64 (2017) 23–40. doi:10.1016/j.ijheatfluidflow.2017.01.009.

[6] O. Lamberts, P. Chatelain, Y. Bartosiewicz, Numerical and experimental evidence of the fabri-choking in a supersonic ejector, International Journal of Heat and Fluid Flow 69 (2018) 194–209. doi:10.1016/j.ijheatfluidflow.2018.01.002.

[7] J. H. Keenan, E. P. Neumann, A Simple Air Ejector, Journal of Applied Mechanics 9 (2) (1942) A75–A81. doi:10.1115/1.4009187.

[8] J. Fabri, R. Siestrunck, Supersonic air ejectors, Advances in Applied Mechanics 5 (1958) 1–34.

[9] I. Eames, S. Aphornratana, H. Haider, A theoretical and experimental study of a small-scale steam jet refrigerator, International journal of refrigeration 18 (6) (1995) 378–386.

[10] L. Clark, Application of compound flow analysis to supersonic ejector-mixer performance prediction, in: 33rd Aerospace Sciences Meeting and Exhibit, 1995, p. 645.

[11] K. Banasiak, A. Hafner, 1d computational model of a two-phase r744 ejector for expansion work recovery, International Journal of Thermal Sciences 50 (11) (2011) 2235–2247. doi:10.1016/j.ijthermalsci.2011.06.007.

[12] J. G. del Valle, J. M. S. Jabardo, F. C. Ruiz, J. S. J. Alonso, A one dimensional model for the determination of an ejector entrainment ratio, International Journal of Refrigeration 35 (4) (2012) 772–784.

[13] W. Chen, M. Liu, D. Chong, J. Yan, A. B. Little, Y. Bartosiewicz, A 1d model to predict ejector performance at critical and sub-critical operational regimes, International Journal of Refrigeration 36 (6) (2013) 1750 – 1761. doi:10.1016/j.ijrefrig.2013.04.009.

[14] A. Metsue, R. Debroeyer, S. Poncet, Y. Bartosiewicz, An improved thermodynamic model for supersonic real-gas ejectors using the compound-choking theory, Energy (2021) 121856doi:10.1016/j.energy.2021.121856.

[15] J. Van den Berghe, B. R. Dias, Y. Bartosiewicz, M. A. Mendez, A 1d model for the unsteady gas dynamics of ejectors, Energy 267 (2023) 126551.

[16] O. Lamberts, P. Chatelain, N. Bourgeois, Y. Bartosiewicz, The compound-choking theory as an explanation of the entrainment limitation in supersonic ejectors, Energy 158 (2018) 524–536. doi:10.1016/j.energy.2018.06.036.

[17] A. Bernstein, W. Heiser, C. Hevenor, Compound-compressible nozzle flow.

[18] scipy.optimize.minimize, `https://docs.scipy.org/doc/scipy/reference/generated/scipy.optimize.minimize.html`, accessed: 2023-02-07.

[19] S. Croquer, Y. Fang, A. Metsue, Y. Bartosiewicz, S. Poncet, Compound-choking theory for supersonic ejectors working with real gas, Energy 227 (2021) 120396. doi:10.1016/j.energy.2021.120396.

[20] E. Schillaci, C. Oliet Casasayas, J. B. Vemula, M. Duponcheel, Y. Bartosiewicz, P. Planquart, Air ejector analysis in normal and abnormal modes, oriented to control purposes in aircraft systems, in: 9th European Conference for Aeronautics and Space Sciences (EUCASS), European Conference for AeroSpace Sciences (EUCASS), 2022, pp. 1–12.

[21] R. T. Chen, Y. Rubanova, J. Bettencourt, D. K. Duvenaud, Neural ordinary differential equations, Advances in neural information processing systems 31.

[22] J. R. Holland, J. D. Baeder, K. Duraisamy, Field inversion and machine learning with embedded neural networks: Physics-consistent neural network training, in: AIAA Aviation 2019 Forum, 2019, p. 3200.

[23] J. Sirignano, J. F. MacArt, J. B. Freund, Dpm: A deep learning pde augmentation method with application to large-eddy simulation, Journal of Computational Physics 423 (2020) 109811.

[24] J. Sirignano, J. MacArt, K. Spiliopoulos, Pde-constrained models with neural network terms: optimization and global convergence, arXiv preprint arXiv:2105.08633.

[25] J. F. MacArt, J. Sirignano, J. B. Freund, Embedded training of neural-network subgrid-scale turbulence models, Physical Review Fluids 6 (5) (2021) 050502.

[26] D. E. Rumelhart, J. L. McClelland, Parallel Distributed Processing: Explorations in the Microstructure of Cognition: Foundations, MIT PRess, 1989.

[27] A. M. Bradley, Pde-constrained optimization and the adjoint method. 2019, URL https://cs. stanford. edu/˜ ambrad/adjoint_tutorial. pdf.

[28] A. Géron, Hands-on Machine Learning with Scikit-Learn, Keras, and TensorFlow, 2nd Edition, O'Reilly, 2019.

Phase change in porous media for heat exchanger applications

Yohanna Henrotel

TEMISTh Marignane, France, yohanna.henrotel@temisth.com

Supervisor: Damien Serret

Head of R&D, TEMISTh Marignane, France, damien.serret@temisth.com

Supervisor: Joseph Jabbour

R&D Engineer, TEMISTh Marignane, France, joseph.jabbour@temisth.com

Supervisor: Delphine Laboureur

Associate Professor, von Karman Institute for Fluid Dynamics, Belgium, delphine.laboureur@vki.ac.be

University Supervisor: Olivier Le Metayer

Professor, Mechanical Engineering Energy, Aix-Marseille University - IUSTI / UMR CNRS 7343, France, olivier.le metayer@univ-amu.fr

Abstract

This work presents the definition of the porous model as well as its application. Firstly, we will present a sensitivity analysis of the model on the boundary conditions. The parameters required by the model will be extracted from a series of simulations to replace an experimental device. A volume average per fin element will be used to determine the mass transfer source term and hence the exchange coefficient.

Keywords: CFD, Porous media, Heat exchanger, Heat transfer, Mass transfer, Multiphase flow

1. Nomenclature

α : *Volume fraction*
t : *Time*
ϵ : *Porosity*
Y : *Mass fraction*
ρ : *Density*
e : *Internal energy*
E : *Total energy*
u : *velocity*
μ : *Dynamic viscosity*
P : *Pressure*
m: *Mass*
k_{eff} : *Effective conductivity*
$\dot{m}$: *Mass transfer rate*
μ_p : *Pressure equilibrium coefficient*
λ_v : *Velocity equilibrium coefficient*
H_T : *Thermal equilibrium coefficient*
Cp : *Specific heat*
λ : *Conductivity*
γ : *Heat capacity ratio*
k : *Permeability*
k_1 : *Inertial permeability*
L_{LV} : *Latent heat*
T_{sat} : *Saturation temperature*
P_{sat} : *Saturation pressure*
β : *Inertial resistance coefficient*
S: *Surface*
Nu : *Nusselt number*
Pr: *Prandt number*
Re : *Reynolds number*
j : *Colburn factor*
f : *Fanning friction factor*
Dh : *Hydraulic diameter*
G : *Mass flow rate*
V : *Volume of medium*
V_f : *Volume of fluid in medium*
g : *Chemical potential*
A_I : *Interfacial specific area*

2. Introduction

In a general context of reducing energy consumption and production costs, heat exchangers have become a key element. CFD simulations based on the use of porous media are nowadays the most commonly encountered method for industrial applications to design and dimension heat exchangers with intensification structures such as fins. This enables the best compromise between numerical resource requirements and accuracy of results. In the case of two-phase flows, this is currently not a widespread approach.
This study is based on the use of a two-phase Eulerian mixing model solved by the StarCCM+ software. The pressure drop of the porous medium is modelled by a power law (Darcy-Forchheimer type) per phase. The porous medium is considered to be in thermal imbalance locally, resulting in the addition of a volume source term based on an exchange coefficient. This coefficient integrates heat and mass transfer. It can be spatially variable, reflecting the topology of the two-phase flow (bubble, slug, annular, etc.). We will first present a sensitivity analysis of the model. Different boundary conditions (mass flow, quality, heat flux) will be applied to estimate the influence of each parameter in our two-temperature porous model.
In a second step, we will extract the parameters required by the model from a series of locally resolved simulations (local simulations of a representative finned channel with phase change). A volume averaging method will be used to determine the mass transfer source term and hence the exchange coefficient. The influence of other parameters such as fin geometry or gravity orientation will also be studied. This new model will be applied to the simulation of an evaporator used in a steam cycle, operating with R134a.

3. State of the art

Differents developments were made to simplify the numerical modelization of heat exchangers with porous media. In [1] a procedure for the optimization of heat exchanger geometry is developed. As a part of this program an integral numerical code for modeling of heat exchangers was constructed. The numerical code is derived from Whitaker's [2] presentation of the Volume Averaging Technique (VAT) for a porous media flow. The heat exchanger core can be treated as a porous media to expedite code and make it appropriate for surface optimization computations.

The internal structure of the heat exchanger is composed of isothermal tubes, and it is regarded as a uniform porous medium. [3] provided the local drag and heat transfer coefficient values required to close the transport equations. The conservation features of the finite volume method (FVM) were utilized to discretize the resulting partial differential equations. A preconditioned conjugate gradient approach was then used to solve the resulting system of semilinear equations. Excellent agreement between the predicted drag and heat transfer coefficient values in this paper and published data is observed.

[4] created a multi-scale model for two-phase modeling of multi-stream plate-fin heat exchangers. This model simultaneously takes into account important aspects of a multi-stream HX simulation, including phase change processes, multi-component mixtures, numerous streams, transversal, lateral, and longitudinal conduction, non-uniformity of incoming flow, varying fluid characteristics, and heat leakage. The resulting hypotheses are looked at: steady-state operation, minimal temperature variation along the plate thickness, known mass flow distributions that do not change with flow direction, and a greater emphasis on heat conduction within the solid than on conduction heat transfer across the fluid. In this study, the porous technique was not employed, and the computational elements discretized each domain and sub-domain of the exchanger. The governing equations are calculated independently for each domain, and the common boundary conditions handle thermal interactions.

Another case was simulated by Pozhilov and al. [5], for the heat and mass transfer in a 3D model of a loop heat pipe evaporator. This simulation included the model of Reynolds-averaged Navier–Stokes equations describing the flow in the liquid and vapor regions, Darcy's law for filtration modeling in the wicks (porous structure) and the energy equation with an accurate coupling of connected sub-domains that includes the effects of evaporation on interfaces between the porous and vapor regions.

Pozhilov et al. [5] simulated another scenario involving the mass and heat transmission in a three-dimensional model of a loop heat pipe evaporator. Darcy's law for filtration modeling in the wicks (porous structure), the Reynolds-averaged Navier-Stokes equations model defining the flow in the liquid and vapor regions, and the energy equation with an

accurate coupling of linked sub-domains incorporating the effects of evaporation on interactions between the porous and vapor regions were all included in this simulation.

In [6], a CFD model using a commercial software is developed for simulating the transport phenomena, especially the phase change, in a plate-fin heat exchanger. The flow channels, ducts and passes of the cold box, are considered in the computational geometry. The porous media simplification is introduced in the computational domain due to the excessive increase in the number of computational grids when the fins accounted for in the numerical domain. A flash calculations technique is used with CFD in evaluation of chemical species in the cold box by a user function in this case. This study also looks at the importance of local thermal equilibrium between the porous medium and fluid flow without mass transfer, local thermal equilibrium between the porous medium and fluid flow with mass transfer (LTE), and local thermal non equilibrium between the porous medium and fluid flow with mass transfer (LTNE).

4. Model description

4.1. Macro model: Multi-phase porous model

This approach (multiphase mixture model) models the fluid phases by solving the transport equations for mass, momentum and energy for the mixture of phases. For phase distribution: volume fraction transport equation for each phase.

Phase volume fraction transport equation:

$$\begin{aligned}\frac{d}{dt}\int_V \alpha_i dV + \oint_A \alpha_i v_m \cdot da \\ = \int_V (S_{u_i} - \frac{\alpha_i}{\rho_i}\frac{D\rho_i}{Dt})dV \\ + \oint_A \frac{\mu_t}{\sigma_t \rho_m}\nabla\alpha_i \cdot da \\ - \int_V \frac{1}{\rho_i}\nabla\cdot(\alpha_i\rho_i v_{d,i})dV\end{aligned} \tag{1}$$

Mixture continuity transport equation:

$$\frac{d}{dt}\int_V \rho_m dV + \oint_A \rho_m v_m \cdot da = \int_V S_u dV \tag{2}$$

Mixture momentum transport equation:

$$\begin{aligned}\frac{d}{dt}\int_V \rho_m v_m dV + \oint_A \rho_m v_m \otimes v_m \cdot da \\ = -\oint_A pI \cdot da + \oint_A T_m \cdot da + \int_V S_u dV \\ + \int_V f_b dV - \sum_i \int_A \alpha_i \rho_i v_{d,i} \otimes v_{d,i} \cdot da\end{aligned} \tag{3}$$

Mixture Energy transport equation:

$$\begin{aligned}\frac{d}{dt}\int_V \rho_m E_m dV \\ + \oint_A [\rho_m H_m V_m + p + \sum_i \alpha_i \rho_i H_i v_{d,i}] \cdot da \\ = -\oint_A q \cdot da + \oint_A T_m \cdot v_m \cdot da \\ + \int_V (f_b \cdot V_m + S_u)dV\end{aligned} \tag{4}$$

4.1.1. Porous model

The first characteristic of a porous medium is its porosity: this is the ratio between the volume not containing solids and the total volume of the medium V:

$$\epsilon = \frac{V_f}{V} \tag{5}$$

In the porous domain, the pressure losses are defined by the Darcy-Forchheimer law, for the ΔP in the x-direction it yields:

$$\frac{\Delta P}{\Delta x} = -\frac{\mu}{k}u - \rho k_1 u^2 \tag{6}$$

With k the permeability and k_1 the inertial permeability, the permeability of a porous material is its capacity to let a fluid pass through it. A good permeability therefore implies a good porosity, but the opposite is not necessarily true, it has been shown to be intrinsic to the solid matrix of the porous medium and therefore only a function of its topology and its associated geometric properties.

the porous geometric parameters for this channel are the following:

ϵ	k	k_1
0.87	7.6e-8	78

Table 1: Porous parameters

The heat transfer in the porous media is treated with a local thermal non-equilibrium which yields the following energy formulation on solid and fluid:

$$\begin{aligned}\frac{d}{dt}\int_V \chi\rho_f E_f dV + \oint_A \chi\rho_f H_f v\cdot da \\ = -\oint_A \chi q\cdot da + \oint_A \chi T\cdot v\cdot da \\ + \int_V a_s h_s(T_s - T_f)dV \\ + \int_V (\chi f_b\cdot v)dV + \int_V S_u^e dV\end{aligned} \tag{7}$$

with T, the solid temperature:

$$\begin{aligned}\frac{d}{dt}\int_V ((1-\chi)\rho_s E_s)dVda \\ = -\oint_A (1-\chi)q\cdot da \\ + \int_V a_s h_s(T_s - T_f)dV + \int_V S_u^e dV\end{aligned} \tag{8}$$

Heat transfer between the solid matrix and the fluid:

$$\pm h_s a_s(T_s - T_f) \tag{9}$$

The purpose of this work is to define, in the case of a mini-channel plate-fin exchanger, the source in volume fraction of vapour S_u^i in the associated transport equation (the exchange coefficient h_s representing the convective exchange between the fluid and the porous matrix).

4.2. Micro model: Volume of fluid

This modelling approach consists of an interface capture method that predicts the distribution and movement of the interface of separate phases. It assumes that the resolution of the mesh is sufficient to resolve the position and shape of the interface between the phases. Fluids in the same cell containing the interface are treated as a mixture.

$$\alpha_i = \frac{V_i}{V} \tag{10}$$

$$\sum_{i=1}^{N}\alpha_i = 1 \tag{11}$$

Transport equation volume fraction:

$$\begin{aligned}\frac{d}{dt}\int_V \alpha_i dV + \oint_A \alpha_i v\cdot da = \\ \int_V (S_{\alpha_i} - \frac{\alpha_i}{\rho_i}\frac{D\rho_i}{Dt})dV \\ - \int_V \frac{1}{\rho_i}\nabla\cdot(\alpha_i\rho_i v_{d,i})dV\end{aligned} \tag{12}$$

Transport equation on mass mixture:

$$\frac{d}{dt}(\int_V \rho dV) + \oint_A \rho v\cdot da = \int_V S dV \tag{13}$$

Transport equation on momentum mixture:

$$\begin{aligned}\frac{d}{dt}(\int_V \rho v dV) + \oint_A \rho v\otimes v\cdot da \\ = -\oint_A pI\cdot da + \oint_A T\cdot da \\ + \int_V \rho g dV \int_V f_b dV - \\ \sum_i \int_A \alpha_i\rho_i v_i\otimes v_i\cdot da\end{aligned} \tag{14}$$

Transport equation on energy mixture:

$$\begin{aligned}\frac{d}{dt}\int_V \rho E dV \\ + \oint_A [\rho H v + p + \sum_i \alpha_i\rho_i H_i v_{d,i}]\cdot da \\ = -\oint_A q^{\nu}\cdot da + \oint_A T\cdot v da \\ + \int_V f_b\cdot v dV + \int_V S_E dV\end{aligned} \tag{15}$$

4.2.1. Phase change model

The Rohsenow boiling model (this model is mainly used for low temperature boiling, but a film boiling model can be incorporated for higher temperature boiling) and the transition model (from nucleated boiling to transition) are the main models for modelling boiling flows. The empirical Rohsenow correlation is used to calculate the surface heat flux due to boiling:

$$q_{bw} = \mu_l h_{lat}\sqrt{\frac{g(\rho_{l\rho v})}{\sigma}}\left(\frac{C_{pl}(T_w - T_{sat})}{C_{qw}h_{lat}Pr_l^{n_p}}\right)^{3.03} \tag{16}$$

In this equation, μ_l, h_{lat}, C_{pl}, ρ_l, Pr_l and are the dynamic viscosity, latent heat, specific heat, density and Prandtl number of the liquid phase, n_p is the exponent of the Prandtl number, *sigma* is the surface tension coefficient at the liquid-vapour interface and C_{qw} is an empirical coefficient which varies with the liquid-surface combination.

5. Test case description

In order to capture the flow regime in the channel, the "Volume of fluid" interface tracking model described in 4.2 is used. This modelling approach consists of a method that translates the distribution and movement of the interface of distinct phases (it assumes that the resolution of the mesh is sufficient to resolve the position and shape of the interface between the phases).

The representative elementary channel is a 58 fin offset mini channel with the same geometry as the prototype evaporator that will be experimentally assessed. The dimensions of the channel and the fins are listed in table 2 and illustrated in figure 5.

	channel dimensions	fin dimensions
height	2.42mm	2.02mm
length	260mm	5mm
width	0.55mm	0.25mm

Table 2: Channel and fin dimensions

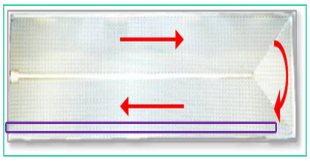

Figure 1: channel element



Figure 2: channels view



Figure 3: channels domain

A trimmed cells mesher was used for the fluid domain, with a boundary layer prism layer cells mesher at the walls. The average cell size is 2.5E-5m with a maximum cell size of 5E-5, the prism layer mesh have a thickness of 0.05mm with a stretching factor of 1.3, the total number of cells is around 3M. The mesh is illustrated in figure 5.

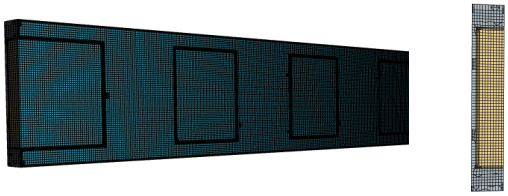

Figure 4: Mesh on micro model

In the determination of the boiling law, the effects of fin conduction are overlooked so a isothermal condition is applied at the solid walls. The boiling fluid used is the R134a. A pressure condition of 3.3 bar is applied at the outlet and a mass flow condition of 6.75E-5 kg/s at 265K and a mass quality of 0 is applied at the inlet. The solid temperature is varied from 279.5 K to 307.5K The complete list of simulations performed is provided in table 3.

Solid T (K)	Δ to saturation (K)
279.5	+2
281.5	+5
287.5	+10
292.5	+15
297.5	+20
302.5	+25
307.5	+30

Table 3: Solid isothermal conditions

6. Mass transfer law

For each of the seven VOF simulations performed, the gas volume fraction and the temperature are extracted with an "average per fin volume method" as in [2].
The mass flow of gas from one fin to the next over the total mass flow is is fitted and then ploted to give the mass transfer law as a function of fluid temperature in the channel. It is also noted that the wall temperature increase, while giving higher gas fraction, follow the same trend as lower wall temperatures.

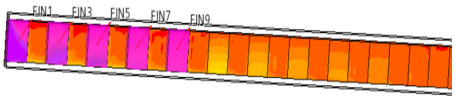

Figure 5: Fin volume discretization

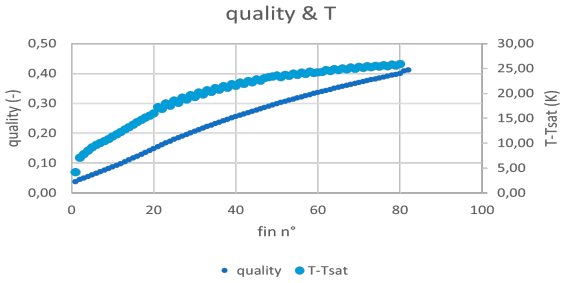

Figure 6: ΔT and quality plot along the channel

with:

$$Quality = \frac{m_{vapor}}{m_{total}} \tag{17}$$

and

$$\frac{m_{vapor}}{m_{total}} = \frac{a_{vapor} * \rho_{vapor}}{\rho_{total}} \tag{18}$$

The results yields the following law (fig:7) as a function of the fluid temperature difference to saturation, the law shows two evaporation regimes and will be divided in two plots.

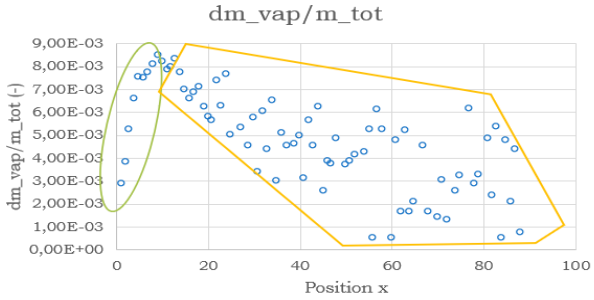

Figure 7: mass transfer law function of temperature

First part of the boiling curve yields the following law:

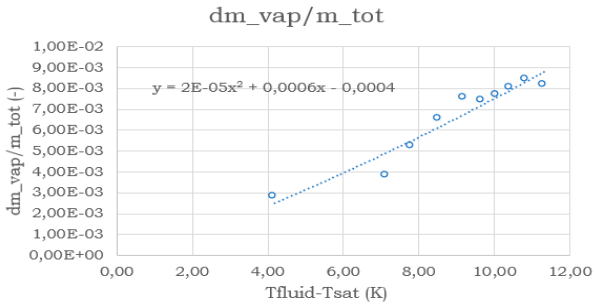

Figure 8: mass transfer law function of temperature: first trend

And the second part:

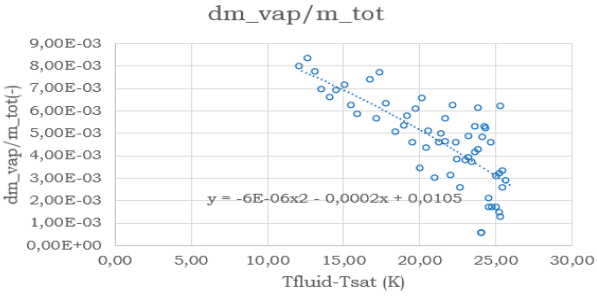

Figure 9: mass transfer law function of temperature: second trend

Second part of the boiling curve give a very low vapor creation compared to the first part, in this work fluid is considered almost entirely evaporated in the first part as the delta of vapor fraction from fin $n-1$ to fin n is close to 0 therefore the second law yields a source terms of 0.

7. Results: VOF-MMP comparison

The boiling law derived from the VOF simulation as described in the previous section has been implemented in the porous equivalent of the channel element. Then the porous two-phase simulations were ran with the mixture multiphase model. The methodology is schematized in figure 10.

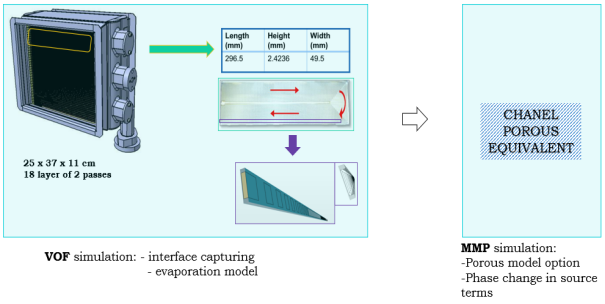

Figure 10: micro to macro model for porous multiphase

The VOF micro model simulation requires a 3 million cells mesh for a run time of 3h to reach a steady state while the MMP simulation in an equivalent porous domain can be ran on a 80k cells mesh for run time of around 20 minutes. The same simulation are performed, this time on the MMP porous model at the highest and lowest wall heating for comparison. The boundary conditions remains the same but the domain is now defined with the porous model described above in 4.1.

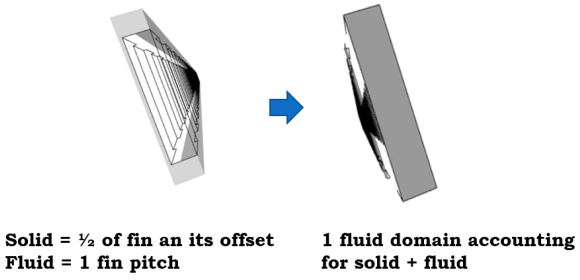

Figure 11: micro VOF computation domain to macro MMP computation domain

The mass transfer law tested on two cases, at low and high wall overheating gives the following results on fluid temperature and quality, at solid temperature of 279.5K in 12 and solid temperature of 307.5K in 13.

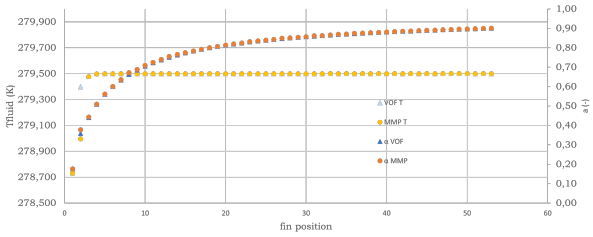

Figure 12: Comparison at Tsolid=279.5K

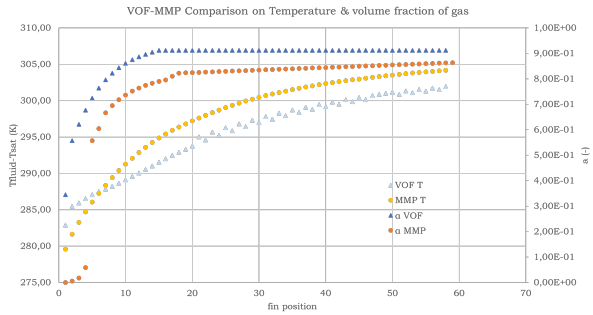

Figure 13: Comparison at Tsolid=307.5K

The law accuracy when modeling boiling at lower temperature, where fluid thermal equilibrium is reached within first fins, is good along the channel, with the highest derivation at the channel inlet where the fluid temperature is at the highest difference to the imposed wall temperature. The quality is still given with a maximum error of 15%.

8. Conclusion

Overall fitting from VOF to MMP gives an error under 20% in temperature and volume fraction. Highest deviation are found in the case of a higher wall overheating since thermal equilibrium is not reached until later, and we will therefore have more instationnarity effects occurring between the two simulations. In a future work this same methodology will be applied to a vertical configuration in order to account for multiple positioning of a heat exchanger. The law would ideally include more variables such as wall temperature, flow topology and solid temperature as well.

Acknowledgments

This project has received funding from the Clean Sky2 Joint Undertaking (JU) under grant agreement No 886698. The JU receives support from the European Union's Horizon 2020 research and innovation programme and the Clean Sky 2 JU members other than the Union. This paper reflects only the author's view and that the JU is not responsible for any use that may be made of the information it contains.

References

[1] A. Horvat, I. Catton, Development of an integral computer code for simulation of heat exchangers.

[2] S. Whitaker, The equations of motion in porous media, Chemical Engineering Science 21 (3) (1966) 291–300.

[3] A. Zukauskas, R. Ulinskas, Heat transfer in tube banks in crossflow.

[4] R. Niroomand, M. Saidi, S. Hannani, A general multi-scale modeling framework for two-phase simulation of multi-stream plate-fin heat exchangers, International Journal of Heat and Mass Transfer 156 (2020) 119730.

[5] A. A. Pozhilov, D. K. Zaitsev, E. M. Smirnov, A. A. Smirnovsky, Numerical simulation of heat and mass transfer in a 3d model of a loop heat pipe evaporator, St. Petersburg Polytechnical University Journal: Physics and Mathematics 3 (3) (2017) 210–217.

[6] A. Zargoushi, F. Talebi, S. Hosseini, Cfd modeling of industrial cold box with plate-fin heat exchanger: Focusing on phase change phenomenon, International Journal of Heat and Mass Transfer 147 (2020) 118936.

Experimental analysis of natural convection in differentially heated cavity

Tommaso Carlesi

Environmental and Applied Fluid Dynamics Department, von Karman Institute for Fluid Dynamics, Belgium
Belgian Nuclear Research Centre (SCK CEN), Institute for Advanced Nuclear Systems, Belgium
Electromagnetism and Telecommunication department, Université de Mons, Belgium
tommaso.carlesi@vki.ac.be

VKI supervisors: Delphine Laboureur and Philippe Planquart

Professor, Environmental and Applied Fluid Dynamics Department, von Karman Institute for Fluid Dynamics, Belgium
delphine.laboureur@vki.ac.be, Chief Project Office, philippe.planquart@vki.ac.be

SCK Supervisors: Julio Pacio and Katrien van Tichelen

Belgian Nuclear Research Centre, Institute for Advanced Nuclear Systems, Belgium
julio.pacio@sckcen.be, katrien.van.tichelen@sckcen.be

University Supervisor: Patrice Mégret

Professor, Electromagnetism and Telecommunication department, Université de Mons, Belgium
patrice.megret@umons.ac.be

Abstract

Turbulent heat fluxes (THFs) in liquid metals are of paramount importance in the determination of primary coolant behaviour n a nuclear reactor. Measurement of these fluxes is challenging as it requires simultaneous measurement of velocity and temperature fluctuations in an hostile environment. In this work the differentially heated cavity designed for liquid metal experiments is described and preliminary results in water are presented and discussed.

Keywords: Liquid metals, Galinstan (GaInSn), natural convection, differentially heated cavity, turbulent heat flux.

1. Introduction

One of the biggest challenges to be faced nowadays is to fulfill the increasing energy demand while meeting the requirements of carbon neutrality imposed by the Paris agreement [1]. Most of the successful scenarios foreseen by the International Energy Agency see an increase in the use of nuclear energy for electricity production [2] and consequently in the amount of nuclear waste to be treated. To tackle the waste problem, transmutation performed in generation-IV nuclear reactor systems seems a valuable solution. This paper is conceived in the framework of the design and construction of such a system: MYRRHA (Multi-purpose hYbrid Research Reactor for High-tech Applications), a pool-type fast-spectrum research reactor under design at SCK CEN (the Belgian nuclear research center). In particular, this work aims at the understanding of the thermal hydraulic behavior of its primary coolant, the liquid metal Lead Bismuth Eutectic (LBE). For the design and safety evaluation of MYRRHA, the temperature of the primary coolant and of the reactor core components must be predicted in nominal operation (forced convection regime) as well as in accidental conditions (mixed and/or natural convection regime). For this assessment, the turbulent heat flux (THF) is a term of paramount importance. It describes the convective heat transfer mechanism related to fast and simultaneous turbulent fluctuations of the local fluid velocity (U) and temperature (T). Their evaluation is usually performed with a combination of numerical simulations and experiments [3], leading to the availability of reliable numerical mod-

els for fluids characterized by higher Pr number like water or air. On the other hand, for lower Pr number fluids (e.g. liquid metals) the available validation data are still scarce and unreliable, especially in the natural convection regime and therefore new experiments are needed for the development of numerical models [4; 5; 6].

Measurement of THF is challenging as it requires simultaneous measurement of velocity and temperature fluctuations. Some attempts have been made in air over a vertical backward facing step with Laser Doppler Velocimetry (LDV) and cold wire anemometry, used to measure the velocity and temperature fluctuations respectively [7]. Other papers address the same issue in water, performing measurements of the turbulent natural convection boundary layer on a vertical plate using hot films and thermocouples [8] or in a closed cavity with an isothermal wall using Particle Image Velocimetry (PIV) and Laser Induced Fluorescence (LIF) [9]. Despite of the difficulties already encountered in these works, these campaigns do not present the additional challenges that must be faced in liquid metals (LMs), especially with respect to high temperatures, opacity and material compatibility. Nowadays techniques for the individual measurement of velocities and temperatures in LMs exist but simultaneous and fast measurements of these two quantities in such environment have not been published yet. In fact, most of the work addressing liquid metal measurements are focused on average quantities [10], finding correlations in a particular setup [11] or large-scale dynamics [12].

To the author's knowledge, there are only two works in recent times that address the issue of a full turbulent heat flux measurement in low Prandtl fluids at low temperature. The first one [13] faces the problem using a transparent Helium-Xenon gas mixture as working fluid. Whereas this fluid allows a strong decrease in the Prandtl number ($Pr = 0.2$) with respect to the common fluids as water and air ($Pr = 1$), the Prandtl number of LBE, $Pr = 0.025$, or of GaInSn, $Pr = 0.021$, is still one order of magnitude lower. This has an impact on the importance of the turbulent heat flux and its modelling approach. In this work, temperature and velocity were measured simultaneously with a frequency of 75 Hz using a double probe combining a hot wire and a thermocouple (TC). Because of the different thermophysical properties between the gas mixture and a liquid metal, the technique cannot be applied straightforward to the present case. Despite of that, the results still remain relevant, especially the comparison with numerical simulations that showed a big influence of the spacing of the probe and of its frequency response. An application more similar to the current project is the turbulence measurement performed in Galinstan (GaInSn) in a non-isothermal vertical confined backward facing step [14]. Both forced and mixed convection regimes have been studied. Velocity measurements have been performed with a newly developed Permanent Magnet Probe (PMP) probe while temperature measurements, useful also for velocity corrections, have been made with standard type K thermocouples. Despite of the high acquisition frequency (5000 Hz with a cutoff frequency of 200 Hz), a full turbulent heat flux measurement has not been performed because the probes were sampled by two different measuring systems. For this reason, synchronization of the two measurements was impossible to achieve and consequently only first order statistics have been calculated.

In this context, the focus of this Ph.D. is twofold:

- Develop a turbulent heat flux sensor (THFS) suitable for THF measurements in liquid metals (EPICURUS, ExPerImental teChnique for tURbUlence in liquid metalS)
- Provide reference data for the development and validation of numerical models for THF in liquid metals

The present paper will give an overview of the selection of the techniques for the measurement of temperature and velocity and will focus on the description of the experimental setup presenting and discussing the first results obtained in water.

2. Methods

In this section, the methodology of the work is analyzed in detail giving insights in the measurement techniques and the experimental setup used. Despite the focus of the work being on the experimental part, also the numerical setup is thoroughly explained.

2.1. Selection of the measurement techniques

The development of a turbulent heat flux sensor (THFS) is driven by the selection of the most suitable instruments currently available.

For the sake of this paper, only a general overview of the sensors chosen and of the motivations that led to these choices are reported. More details about the sensors and their selection can be found in the proceedings of the VKI Symposium 2022. The THFSs

must satisfy specific requirements in terms of spatial resolution, temporal resolution and temperature and velocity measurement range. Because of the final application in liquid metals, the selection was mostly done based on the liquid metal flow characteristics (GaInSn and LBE), assuring at the same time compatibility with water. The characteristic velocity and temperature typically expected in liquid metals are shown in Fig. 1 and are thoroughly explained in the proceedings of the VKI Symposium 2022. As a consequence, the main features of the sensors can be derived.

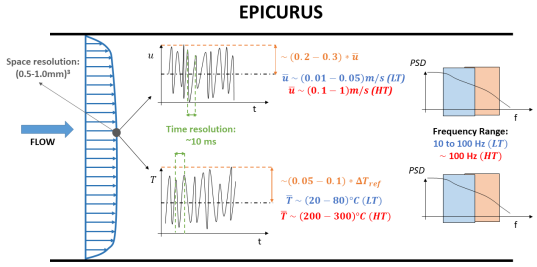

Figure 1: Requirements of the sensors based on the flow characteristics to be measured

2.2. *Experimental setup*

For the first part of the Ph.D., natural convection was chosen as flow regime, not only because the turbulent frequencies are lower and the facility will be easier to operate [15], but mostly because validated turbulence models for natural convection are not available and experimental data for this flow regime are strongly needed. Because most of the studies in literature focus on the Rayleigh-Bénard convection [16; 17; 18; 19], the differentially heated cavity setup was chosen for the purpose of this experiment to fill this knowledge gap. A schematic of the setup is shown in Fig. 2. In differentially heated cavities, a constant temperature difference is maintained between two opposite side walls while all other sides of the cavity are insulated, i.e. ideally adiabatic. This configuration usually gives a flow with similar characteristics to the isothermal vertical plate and for this reason it is also called vertical convection (VC) [11]. Inside the cavity, the imposed temperature difference triggers a natural convection loop rotating in the direction from the warmer side towards the colder side [20]. The main features of the flow change according to the working fluid but in all cases the Prandtl (Pr), Grashof (Gr) and Rayleigh (Ra) numbers control the flow and the

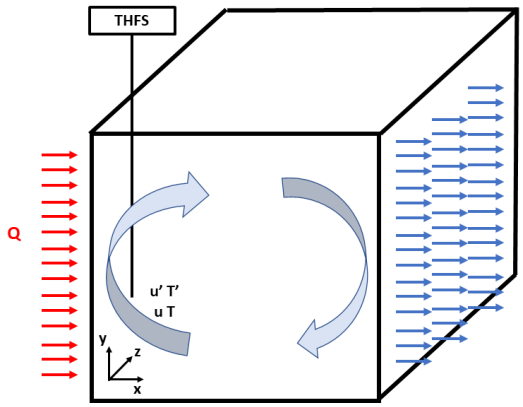

Figure 2: Schematic of the cavity used for the experiments

turbulence phenomena inside the cavity. In particular, increasing the Gr (Ra) number promotes instabilities. Previous studies have shown a critical Grashof number of about 10^8 where the transition to turbulence in buoyant flows in cavities is expected [21; 17].

The tests performed for this paper were conducted in a cubic cavity made of 316L steel with an (inner) edge of 60 mm indicated in Fig. 3 with number 5. The thickness of the walls was 10 mm. Inside natural convection was established through heated/cooled Peltier elements from Laird Thermal Systems capable of reaching a maximum heating power of 800 W and a maximum cooling power of 300 W supplied by an EA-PSI 9000 2U. Full power was not required for the purpose of this experiment. The two elements were positioned oppositely on each side of the cavity in contact with two copper walls inserted in place holders in the cavity.

The copper walls were coated with a 1 µm carbon coating deposited through magnetron sputtering at the University of Namur to ensure material compatibility during future tests with liquid metals. This coating is in fact guaranteed to withstand up to 400 °C avoiding at the same time copper corrosion without worsening the thermal properties of the original material.

Two fans were added in contact with the Peltier elements to avoid overheating. On the hot wall a fan supplied with 12 V in DC was installed while on the cold wall a fan of 24 V was cooling the hotter face of the Peltier element. A picture of the complete setup is shown in Fig. 3. The working fluid (water in the present case) was fed through an opening on the top wall controlled by a ball-valve directly linked to a con-

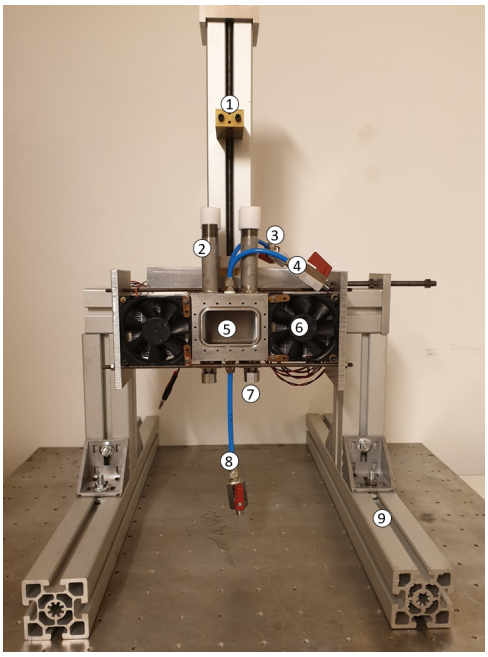

Figure 3: Natural convection setup: 1) Moving chariot moved by an electrical Maxon Motor 110209; 2) TC + FBG access; 3) Valve to feed the fluid; 4) Valve to feed the inert gas; 5) Cavity; 6) Fan; 7) UDV access; 8) Valve to empty the cavity; 9) Support; the whole setup is mounted on a optical table to ensure stability and precision during the measurements.

tainer filled with the fluid. Another ball-valve placed on the bottom of the cell was instead used to empty the cavity. One last ball-valve can be used to feed inert gas used to work in low-oxygen environment during the liquid metal experiments.

As already mentioned in this Section, the four walls that are neither heated nor cooled are ideally adiabatic. To ensure the minimum amount of heat loss from these walls, polyethylene plates of 0.5 cm of thickness were used as thermal insulation. Due to the many valves and openings on the top and bottom wall of the cavity, it was not possible to place effectively the insulation on these two walls. As a result, only two side walls are insulated. The possible consequences of this choice are discussed in Section 3.

Another important point for the design of the experiment was the access for the instrumentation. In fact, in such a small setup it is not trivial to find the best compromise between the available space and the optimal locations of the sensors. Access for the instrumentation was accurately designed according to previous numerical simulations reported in GaInSn [16]. These highlighted the positions where the most important characteristics of the flow can be captured. Fig. 4 shows the four different vertical lines along which measurements of velocity and temperature are possible. The x and z coordinates of the measurements are

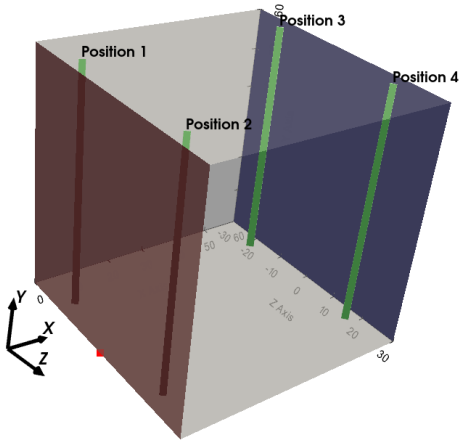

Figure 4: Natural convection setup. The red dot indicates the origin of the reference system whose axes are shown on the bottom left. The hot and cold wall are respectively indicated with red and blue color. The four green lines represent the locations where measurements are possible. The distance from the hot/cold wall of each line is 4 mm while the distance from the side insulated walls is 12 mm.

therefore limited to 4 positions while the y direction is in principle fully accessible by all the sensors.

The access for the temperature sensors (TC and FBG) was guaranteed from the top, while the UDV was flush-mounted on the bottom wall. In this way, the UDV could acquire the profile of the y-component of the velocity while the other sensors could move along the vertical line through the moving chariot (see Fig. 3). At the same time, the UDV is placed such that the axis of the cylindrical sensor (i.e. the center of the ultrasonic beam) is in correspondence with the temperature sensor tip so that the last meaningful point of the velocity profile measured by the UDV coincides with the point where the temperature sensors acquire data. In this way, the theoretical need of measuring temperature and velocity "at the same point" to obtain the THF was satisfied the best way possible. It is to be noticed that all the accesses were proven to be leak-tight in order to sustain vacuum useful to minimize oxidation during the future liquid metal experiments. The sealing should be maintained also during the ver-

tical movement of the instrumentation. More details about the choice of these positions can be found in the proceedings of the VKI Symposium 2022.

2.3. Test matrix

For this paper a total of 24 tests were carried out with one set of boundary conditions. They were performed in all four different available x-z positions (position 1 to 4) while the y positions are reported in Table 1.

Table 1: Test conditions matrix

Position	U	T	y [mm]
1	UDV	TC+FBG	15, 30, 45
2	UDV	TC+FBG	8, 15, 23, 30, 37, 45, 53
3	UDV	TC+FBG	8, 15, 23, 30, 37, 45, 53
4	UDV	TC+FBG	8, 15, 23, 30, 37, 45, 53

An important point to be underlined is the simultaneity of measurements. In fact, all the different techniques use different acquisition systems. For this reason, simultaneous measurements can only be obtained if all the acquisition systems are synchronized, e.g. triggered by an external signal. As this was not yet implemented in the measurement setup, reporting THF results is not yet possible at this stage of the research.

2.4. Numerical simulations

Despite the focus of this paper being on the experimental aspects of the research, Section 3 also presents a comparison with DNS (Direct Numerical Simulation) results. These simulations were performed with the open-source spectral element method code, NEK5000 v19.0, developed by Argonne National Laboratory [22]. The spectral element method is a hybrid finite-element method that uses high degree polynomials as basis functions to resolve the solution within each element. This method presents many advantages as it allows to decrease the numerical dispersion/dissipation errors, reduces the computational cost compared to traditional methods and is highly scalable. Navier-Stokes equations in their dimensional form are used with the Boussinesq approximation. This means flow is assumed incompressible and the temperature variations of density are only present as a force in the source term of the momentum equation. In this work, $30\times30\times30$ elements, with 7 collocation points per spatial direction are used. The elements are increasing in size from the wall towards the center of the domain. The boundary conditions are no slip, adiabatic walls, except for the heated and cooled walls at which constant high and low wall temperatures are imposed, respectively. The results were produced by collecting various statistics of the flow for about 50 flow-around times under statistical steady state condition. More details about the numerical procedure can be found in [16].

3. Results and Discussion

In this section the results obtained following the methodology described in Section 2 are reported and discussed. Experimental results are therefore available in different points along the vertical line of the four positions shown in Fig. 4 but for the sake of clarity only results along the vertical line of position 4 are presented here. The tests were conducted with an average $\Delta T = 58\,^{\circ}\mathrm{C}$. The drift of the temperature difference was $0.16\,^{\circ}\mathrm{C\,min^{-1}}$ leading to a maximum change of $0.25\,^{\circ}\mathrm{C}$ during the time of the acquisition which corresponded to 50 flow-around times like in the numerical simulations. The imposed ΔT can therefore be considered constant during the measurements.

First of all, the average velocity profile along the line is reported in Fig. 5. In order to match the experimental and numerical profiles, it was necessary to average according to their spectral weight the DNS data available. In fact, each point of the UDV profile is an average of the velocity data acquired from

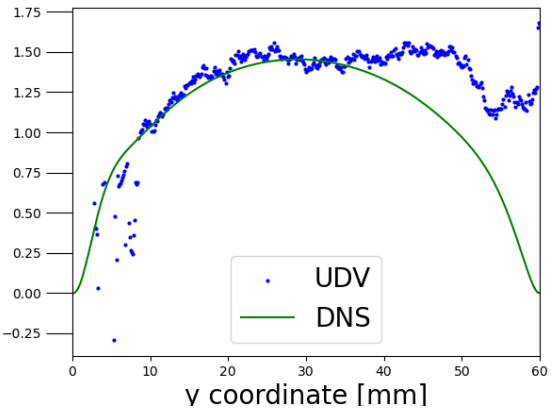

Figure 5: Experimental and numerical results comparison of the vertical (y) component of the velocity

every particle inside a volume (a cone with an aperture of 5°) and this feature must be taken into account when comparing numerical and experimental results. Despite the agreement in the direction and order of magnitude of the velocity, some features of the experimental profile are not present in the DNS results. This might be due to some intrinsic characteristics of the experimental technique. In fact, the first part of the experimental profile is affected by the near field of the UDV. This section is the closest to the emitting sensor and it is common that measurements in this zone are not possible or reliable. In this particular case, to achieve enough signal strength further along the line, a high emitting power was set. As a result, the sensor was fully saturated in this zone and no measurements were possible in the first 10 mm. The velocity along the profile is negative as expected, meaning that at the cold wall the flow is going downwards, i.e. towards the sensor. Moreover, close to the upper-wall, the velocity has a slight increase and change in direction, a phenomenon that is smoothed by the averaged simulations. This might be due to recirculation at the corners due to the impinging jet effect of the horizontal flow along the top surface when it hits the wall. Another meaningful comparison is the one carried out between the rms values of the y-velocity over the measured line. The result is shown in Fig. 6. Also in this

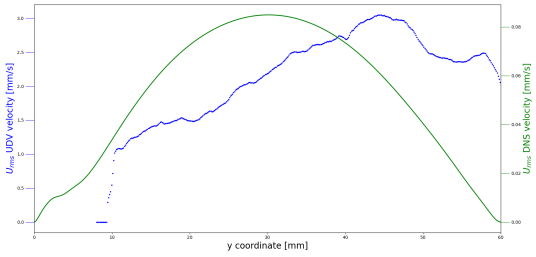

Figure 6: Experimental and numerical results comparison of the rms of the vertical (y) component of the velocity

case a common trend might be seen in both profiles. They tend to be lower at the edges, i.e. close to the walls, and higher at the center. Despite of this similarity, the magnitude of the experimental rms values is almost one order of magnitude higher than the numerical ones. A physical interpretation would lead to the conclusion that in the numerical simulations the fluctuations are lower. This could be explained with the noise and the experimental uncertainty that are not present in the DNS and that in the case of such low velocities have a greater impact on the final results.

Further analyses can be carried out for temperature profiles. The ΔT imposed to the cavity has already been commented at the beginning of this section. The average temperature profile along the position 4 line (see Fig. 4) inside the cavity is shown in Fig. 7. The

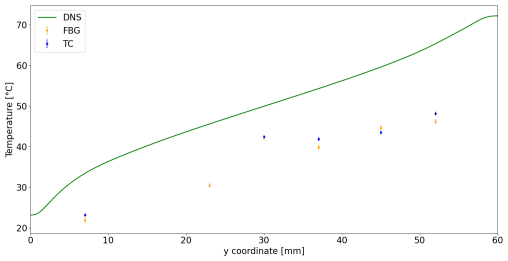

Figure 7: Experimental and numerical results comparison of the rms of the vertical component of the velocity

FBG and the TC measurements seem in good agreement between each other. On the other hand, is clear that the experimental points are far below the numerical profile even when uncertainties are considered. Despite of that, a similar slope can be seen in both trends. This could lead to the conclusion that even if the same wall temperatures have been reached in both cases, heat losses in the experimental setup affect the measurements.

For this reason, the temperature of five out of the six walls of the cavity, i.e. the ones that allow access for thermocouples, were measured during the acquisition. With a constant ambient temperature of 15 °C, the wall temperatures varied from 27 °C to 55 °C. This means that the hypothesis of perfectly adiabatic walls does not apply and heat losses through these walls need to be taken into account. To estimate the heat losses, a convective heat transfer coefficient of $10\,\mathrm{W\,m^{-2}\,K^{-1}}$ was used for air in natural convection. The resulting heat losses were negligible (in the order of Watts) when compared to the power applied by the Peltier (in the order of 80 W), probably because of the small exchange surface $0.02m^2$. Next, the Biot number of the wall was calculated to take into account the thickness of the stainless steel wall of the cavity. The results ($Bi = 0.007$) seem to suggest that the wall can be considered at uniform temperature and therefore conduction losses can also be neglected. For this reason, further investigation is needed to understand the difference between numerical and experimental results.

4. Conclusion

This work addresses the issue of measuring turbulent heat fluxes (THFs) in liquid metals, i.e. the simultaneous and fast velocity and temperature fluctuations of the fluid. Due to the numerous challenges that this task presents, this paper addressed a preliminary stage of the experiment where the experimental setup was designed and water was used as working fluid.

First of all, an overview on the state-of-the-art of the available velocity and temperature measurement techniques was presented. As a consequence of advantages and disadvantages of each technique when used in liquid metals, Ultrasonic Doppler Velocimetry and HWA were chosen for velocity measurements while thermocouple and Fiber Bragg Gratings were chosen for temperature measurements. The second part of this work focused on the design of the differentially heated cavity, the natural convection setup chosen for this study. A detailed description of the setup and motivated design choices were reported. In the end, preliminary results in water were presented and compared with the DNS numerical results available.

With this paper the development of a new experimental setup that allows to get insights on the turbulent heat flux behaviour of different fluids was carried out. Measurements were successfully performed in the newly designed cavity and no major issue with the setup were encountered. In fact, one of the main purposes of preliminary tests in water was to solve unexpected issues so that they could be solved in an easier environment than the one given by GaInSn or LBE.

The measurement results present a large discrepancy between experiments and numerical simulations. Until these are clarified, no major comments can be made from an experimental point of view about the physics of the mass and heat transfer phenomena happening in the cavity. Reasons for this mismatch have been proposed and analyzed in Section 3 and will be taken into account for future improvements. It has to be noticed that the design of the cavity and the measurement techniques selection was made for GaInSn as working fluid, meaning that the same choices can be not optimal for measurements in water. Further investigations are in any case needed to fully understand the source of the discrepancies. First experimental analyses in this sense were already presented in Section 3.

Future works will focus on finding the main causes of the mismatch and solving them. Experiments in water will therefore give meaningful outcomes that will be compared with DNS. Moreover, with the synchronization of the acquisition systems also THF calculations will be possible. After this phase, the expected experiments in GaInSn will be performed and THFs data in liquid metals will be provided to validate numerical models.

Nomenclature

Abbreviations and acronyms

FBG	Fiber Bragg Grating
GaInSn	Galinstan
HW	Hot wire
LBE	Lead Bismuth Eutectic
LMPLM	Low Melting Point Liquid Metal(s)
MYRRHA	Multi-purpose hYbrid Research Reactor for High-tech Applications
Pr	Prandtl number
RANS	Reynolds averaged Navier-Stokes equations
THF	Turbulent heat flux
THFS	Turbulent heat flux sensor
UDV	Ultrasonic Doppler Velocimetry
VKI	Von Karman Institute

Greek letters

μ	Dynamic viscosity ..... $[\mathrm{kg\,m^{-1}\,s^{-1}}]$
ρ	Density ..... $[\mathrm{kg\,m^{-3}}]$

Roman letters

c_p	Specific heat capacity .... $[\mathrm{J\,kg^{-1}\,K^{-1}}]$
k	Thermal conductivity .... $[\mathrm{W\,m^{-1}\,K^{-1}}]$
$\mathbf{r}$	Spatial coordinate (vector) ..... [m]
$\mathbf{u}$	Fluid velocity (vector) ..... $[\mathrm{m\,s^{-1}}]$

Subscripts

$'$	Turbulent fluctuations

Bibliography

[1] Working Group, I. I. I. contribution to the, W. G. I. I. I. Sixth, and Assessment Report. Climate change 2022 mitigation of climate change. Technical report, Intergovernmental Panel on Climate Change, 2022.

[2] IEA International Energy Agency. Global energy and climate model documentation. Technical report, International Energy Agency, 2021.

[3] Katrien Van Tichelen, Graham Kennedy, Fabio Mirelli, Alessandro Marino, Antonio Toti, Davide Rozzia, Edoardo Cascioli, Steven Keijers, and Philippe Planquart. Advanced liquid-metal thermal-hydraulic research for MYRRHA. *Nuclear Technology*, 206(2):150–163, 2020.

[4] A. Shams, F. Roelofs, B. Niceno, W. Guo, D. Angeli, E. Stalio, A. Fregni, M. Duponcheel, Y. Bartosiewicz, I. Tiselj, and J. Oder. Reference numerical database for turbulent flow and heat transfer in liquid metals. *Nuclear Engineering and Design*, 353:110274, nov 2019.

[5] Afaque Shams, Andrea De Santis, and Ferry Roelofs. An overview of the AHFM-NRG formulations for the accurate prediction of turbulent flow and heat transfer in low-Prandtl number flows. *Nuclear Engineering and Design*, 355:110342, dec 2019.

[6] A. Shams, F. Roelofs, I. Tiselj, J. Oder, Y. Bartosiewicz, M. Duponcheel, B. Niceno, W. Guo, E. Stalio, D. Angeli, A. Fregni, S. Buckingham, L. K. Koloszar, A. Villa Ortiz, P. Planquart, C. Narayanan, D. Lakehal, K. van Tichelen, W. Jäger, and T. Schaub. A collaborative effort towards the accurate prediction of turbulent flow and heat transfer in low-prandtl number fluids. *Nuclear Engineering and Design*, 366:110750, sep 2020.

[7] H.I. Abu-Mulaweh, B.F. Armaly, and Chen T.S. Turbulent mixed convection flow over a backward-facing step. *International Journal of Heat and Mass Transfer*, 2001.

[8] G. C. Vliet and C. K. Liu. An experimental study of turbulent natural convection boundary layers. *Journal of Heat Transfer*, 1969.

[9] M. E. Negretti T Caudwell, J.-B Flòr. Convection at an isothermal wall in an enclosure and establishment of stratification. *Journal of Fluid Mechanics*, 2016.

[10] A. Cramer, C. Zhang, and S. Eckert. Local flow structures in liquid metals measured by ultrasonic Doppler velocimetry. *Flow Measurement and Instrumentation*, 15(3):145–153, 2004. Ultrasonic Flowmetering.

[11] Lukas Zwirner, Mohammad S. Emran, Felix Schindler, Sanjay Singh, Sven Eckert, Tobias Vogt, and Olga Shishkina. Dynamics and length scales in vertical and convection of liquid metals. *Journal of Fluid Mechanics*, 2022.

[12] T. Zürner, F. Schindler, T. Vogt, S. Eckert, and J. Schumacher. Combined measurement of velocity and and temperature in liquid metal convection. *J. Fluid Mech. (2019), vol. 876, pp. 1108–1128*, 2019.

[13] Sophia Buckingham. *Prandtl number effects in abruptly separated flows: LES and experiments on an unconfined backward facing step flow*. phdthesis, Université catholique de Louvain, August 2018.

[14] Thomas Schaub, Frederik Arbeiter, Wolfgang Hering, and Robert Stieglitz. Forced and mixed convection experiments in a confined vertical backward facing step at low-prandtl number. *Experiments in Fluids*, 63(1), dec 2021.

[15] NEA. *Handbook on lead-bismuth eutectic alloy and lead properties, materials compatibility, thermal-hydraulics and technologies*. Nuclear Energy Agency, 2 edition, 2015.

[16] Mohammed Alsailani. Numerical simulation of transition in liquid metals. Master's thesis, Von Karman Institute for Fluid Dynamics, 2021.

[17] J. A. Glazier and A. Naert. Evidence against ultrahard thermal turbulence at very high Rayleigh numbers. *Nature*, 398:307–310, 1999.

[18] Janet D. Scheel and Jörg Schumacher. Global and local statistics in turbulent convection at low Prandtl numbers. *Journal of Fluid Mechanics*, 802:147–173, 2016.

[19] S. Paolucci. *The differentially heated cavity*. Sadhana, 1994.

[20] R. J. A. Janssen and R. A. W. M. Henkes. Influence of prandtl and number on and instability mechanisms and transition and in a differentially heated square cavity. *Journal of Fluid Mechanics*, 1994.

[21] S. Cioni, S. Ciliberto, and J. Sommeria. Experimental study of high-Rayleigh-number convection in mercury and water. *Dynamics of Atmospheres and Oceans*, 24(1-4):117–127, January 1996.

[22] Argonne National Laboratory. Nek5000 version 19, 2019.

Development of a data-driven bridging turbulence model

Florentin Prud'homme

Environmental and Applied Fluid Dynamics Department, von Karman Institute for Fluid Dynamics, Belgium, florentin.prudhomme@vki.ac.be

Supervisor: Miguel Alfonso Mendez

Assistant professor, Environmental and Applied Fluid Dynamics Department, von Karman Institute for Fluid Dynamics, Belgium, miguel.alfonso.mendez@vki.ac.be

University Supervisor: Yann Bartosiewicz

Professor, Thermodynamics and fluid mechanics, UCLouvain, Belgium, yann.bartosiewicz@uclouvain.be

Abstract

Bridging turbulence models aiming at filling the gap between the RANS and LES approaches with a unified model offer an attractive option among the RANS/LES hybrid methods to make scale resolving simulations of turbulent flows in industrial configurations at a reasonable computational cost. Various framework (VLES, PITM, PANS, SAS, ...) were already developed to derive such models. However, those models generally tend not to perform satisfactorily for internal flows and more development is needed on the closure modelling. We propose a data-driven approach to develop a bridging turbulence model performing well for internal flows using as background philosophy that the model should be such that all the turbulent scales a given mesh can capture are resolved, hence using the mesh at the maximum of its potential. Furthermore, the model should allow a seamless transition from a RANS to an LES behavior with grid refinement and allow to recover accurate statistics. To this aim, a RANS two equations model will be augmented with a correction involving an artificial neural network. This choice is motivated by the robustness of classical RANS modeling and its ability to represent historical and non local effect. The model will be trained using filtered DNS data from relevant relevant internal flows configurations. Given the scarcity of available full time evolution DNS data, new data will need to be generated. Finally, a CFD integrated training will be preferred despite its high computational cost to take into account the discretizations errors and promote consistency between training and a posteriori conditions. This will require the computation of the solver adjoint to allow the backpropagation of the error.

Keywords: CFD, Turbulence, Machine learning, Hybrid turbulence model, bridging model, neural network

References

Experimental and Numerical Assessment of Supersonic Jets Dispersion

Carlo Sanapo

Environmental and Applied Fluid Dynamics Department, von Karman Institute for Fluid Dynamics, Belgium, carlo.sanapo@vki.ac.be

Supervisor: Delphine Laboureur*, Sara Gonzalez Ruiz◇

*Associate Professor, Environmental and Applied Fluid Dynamics Department, von Karman Institute for Fluid Dynamics, Belgium, delphine.laboureur@vki.ac.be

◇Research Engineer, Environmental and Applied Fluid Dynamics Department, von Karman Institute for Fluid Dynamics, Belgium, sara.gonzalez.ruiz@vki.ac.be

Abstract

Even if a lot of literature can be found on the experimental characterization of supersonic underexpanded jets, a complete experimental dataset characterizing the dispersion phenomena of such a jet when submitted to atmospheric wind conditions is not yet available. As part of a collaboration with the CEA Gramat, the von Karman Institute is continuing research efforts towards the development of optical measurement techniques for the measurement of the velocity and concentration fields of a supersonic jet submitted to crossflow, especially far from the release point, in the self-similar region. The project is called "Supersonic Hot Atmospheric jets DispErsion" (SHADE).

Measurements will take place in the VKI L-1B wind tunnel. The rectangular test section ($3 \times 2 \times 20$ m) has a roughened floor to allow for the growth of a turbulent boundary layer (BL) similar to the lower part of the atmospheric neutral BL. Specific focus is on the proper simulation of turbulence parameters, such as the intensity of fluctuations and power spectra in the 1/250-350 scale range.

Concerning the measurement techniques, LS-PIV (Large Scale Particle Image Velocimetry) has been successfully applied to measure the velocity field. For the concentration, a technique based on the Mie Scattering was adapted and allowed a first experimental assessment of a relative concentration field. However, the differences in the evolution of concentration as the nozzle size changes indicate the need for further improvement of the technique, especially with regard to the correct determination of the reference concentration. A first step will be to determine an absolute concentration value, either using the Light Extinction Spectroscopy technique, or by image processing of a zoomed portion of the jet through particle counting.

A CFD characterization using LES (Large Eddy Simulation) approach will be conducted simultaneously in order to capture the basic characteristics and unsteady effects of such jets, quantifying so the consequences on dispersion.

The other main key challenge will be to adapt the experimental setup and measurement techniques for a high temperature jet. A proper pressurized tank, a capable seeding system and adaptation of the measurements techniques will be needed.

Keywords: supersonic underexpanded jet, dispersion, extinction spectroscopy, LES, LS-PIV